

Proceedings of the
51st IWCS/FOCUS
International Wire & Cable Symposium

November 18-21, 2002
Disney's Coronado Springs Resort
Lake Buena Vista, Florida

IWCS
Focus



*50 Years of
Leadership
& Vision*

DISTRIBUTION STATEMENT A:
Approved for Public Release -
Distribution Unlimited

Sponsored By:
IWCS, Inc., Eatontown, NJ

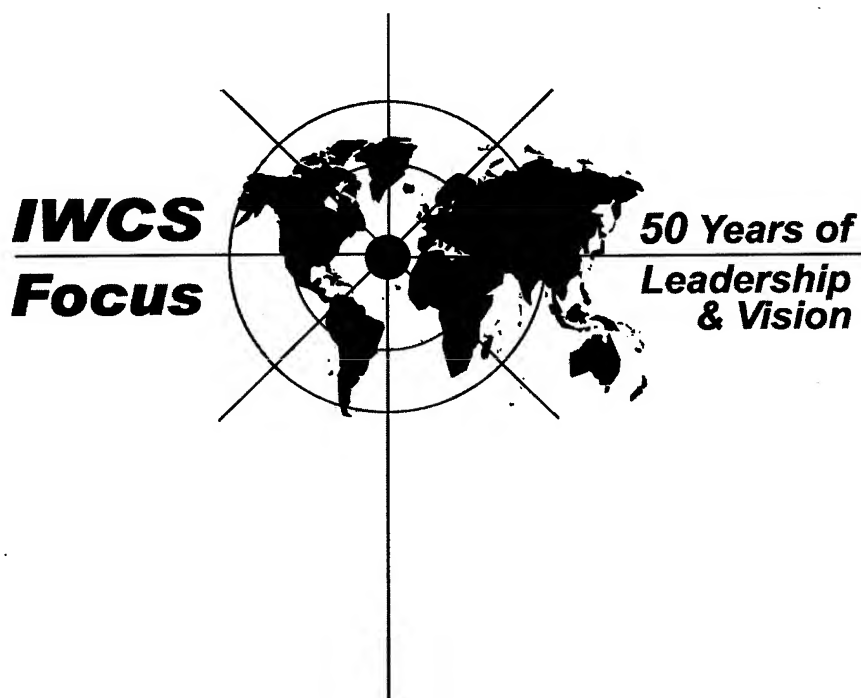
With Participation By:
US Army CECOM, Fort Monmouth, NJ

Supporting Associates:
Europacable, Brussels, Belgium
WCISA - Wire & Cable Industry Suppliers Association
Wire & Cable Technology International
Electronic Components, Assemblies & Materials Association (ECA)

20030923 149

Proceedings of the
51st IWCS/FOCUS
International Wire & Cable Symposium

November 18-21, 2002
Disney's Coronado Springs Resort
Lake Buena Vista, Florida



Sponsored By:
IWCS, Inc., Eatontown, NJ
Website: www.iwcs.org - Email: admin@iwcs.org

With Participation By:
US Army CECOM, Fort Monmouth, NJ

Supporting Associates:
Europacable, Brussels, Belgium
WCISA – Wire & Cable Industry Suppliers Association
Wire & Cable Technology International
Electronic Components, Assemblies & Materials Association (ECA)

APPROVED FOR PUBLIC RELEASE: DISTRIBUTION UNLIMITED

MISSION

The International Wire and Cable Symposium provides a forum for the exchange of technical information amongst suppliers, manufacturers, and users on technological advancements in materials, processes, and products used for voice, data and video signal transmission systems.

TECHNICAL PRESENTATIONS

Monday, November 18, 2002

Special Session

1:00 pm	SESSION	Marketing & Management
---------	---------	------------------------

Tuesday, November 19, 2002

Services and Performance Certification in a Global Environment

Track 1-- Fiber

1:00 pm	SESSION 1	Fiber Optic Cable Design I
---------	-----------	----------------------------

1:00 pm	SESSION 2	Fiber Optic Connectors
---------	-----------	------------------------

Track 2 -- Manufacturing, Processing and Materials

1:00 pm	SESSION 3	Manufacturing/Materials – Fiber I
---------	-----------	-----------------------------------

1:00 pm	SESSION 4	Manufacturing/Materials – Copper I & Fiber
---------	-----------	--

Track 3 -- Copper

1:00 pm	SESSION 5	Copper Networks
---------	-----------	-----------------

New Products

1:00 pm	EXHIBITORS	Presentations (not listed in proceedings)
---------	------------	---

Wednesday, November 20, 2002

Track 1 -- Fiber

1:00 pm	SESSION 6	Fiber Optic Cable Design II
---------	-----------	-----------------------------

1:00 pm	SESSION 7	Fiber Optic Cable Installation
---------	-----------	--------------------------------

Track 2 -- Manufacturing, Processing and Materials

1:00 pm	SESSION 8	Manufacturing/Materials – Fiber II
---------	-----------	------------------------------------

Panel

1:00 pm	SESSION 9	Aerospace/Automotive
---------	-----------	----------------------

Special Invited Session

1:00 pm	SESSION 10	Nano-Structured Photonic Materials & Devices
---------	------------	--

Poster

4:00 pm	SESSION 11	Poster Papers
---------	------------	---------------

Thursday, November 21, 2002

Track 1 -- Fiber

8:30 am	SESSION 12	Optical Fiber Design
---------	------------	----------------------

8:30 am	SESSION 13	Aerial Drop Fiber Optic Cables
---------	------------	--------------------------------

Track 2 -- Manufacturing, Processing and Materials

8:30 am	SESSION 14	Manufacturing/Materials – Copper II
---------	------------	-------------------------------------

8:30 am	SESSION 15	Fire Resistance/Flame Retardant I
---------	------------	-----------------------------------

Track 3 -- Copper

8:30 am	SESSION 16	Cable Performance
---------	------------	-------------------

Track 1 -- Fiber

1:00 pm	SESSION 17	PMD
---------	------------	-----

1:00 pm	SESSION 18	Splicing and Splice Enclosures
---------	------------	--------------------------------

1:00 pm	SESSION 19	Submarine Cables
---------	------------	------------------

Track 2 -- Manufacturing, Processing and Materials

1:00 pm	SESSION 20	Fire Resistance/Flame Retardant II – SESSION CANCELLED
---------	------------	--

PAPERS MOVED TO SESSION 15

1:00 pm	SESSION 21	Fiber Coating
---------	------------	---------------

PAPERS

The papers in this volume were printed directly from unedited reproducible copies prepared by the authors. Responsibility for contents rests upon the authors and not the symposium committee or its members. All rights reserved by the International Wire and Cable Symposium, Inc., 174 Main Street, Eatontown, New Jersey 07724.

PROCEEDINGS/PUBLICATIONS INTERNATIONAL WIRE AND CABLE SYMPOSIUM (IWCS)

Proceedings - Bound - Available from IWCS

39th IWCS Proceedings - 1990 - \$15.00	48th IWCS Proceedings - 1999 - \$15.00
40th IWCS Proceedings - 1991 - \$25.00	49th IWCS Proceedings - 2000 - \$35.00
44th IWCS Proceedings - 1995 - \$40.00	50th IWCS Proceedings - 2001 - \$35.00
46th IWCS Proceedings - 1997 - \$20.00	51st IWCS Proceedings - 2002 - \$50.00
47th IWCS Proceedings - 1998 - \$15.00	

Copies of original proceedings not listed above can be reproduced for \$75.00 per copy plus shipping.

CD's 46th, 47th, 48th & 50th IWCS - \$10; 51st IWCS - \$15.00

Publications - Bound - Available from IWCS

Index of IWCS Papers (1983-1990); PUB #1001RP-1991 - \$15.00

Extra Copies of the 2002 Proceedings can be obtained for: 1 - \$50; 2 - \$100; 3 - \$150; 4 - \$190; 5 - \$230; 6 - \$270; 7 - \$310; 8 - \$350; 9 - \$390; 10 - \$430; 11 and above - \$430 plus \$30 for each additional copy.

Shipping/Handling:

Proceedings

\$10.00 per copy USA only
\$20.00 per copy Canada
\$35.00 per copy Airmail (Europe)
\$40.00 per copy Airmail (Asia)

Publications

\$ 5.00 per copy USA Only
\$10.00 per copy Canada
\$15.00 per copy Airmail
(Europe and Asia)

CDs

\$ 5.00 per copy USA Only
\$ 7.00 per copy Canada
\$13.00 per copy Airmail
(Europe and Asia)

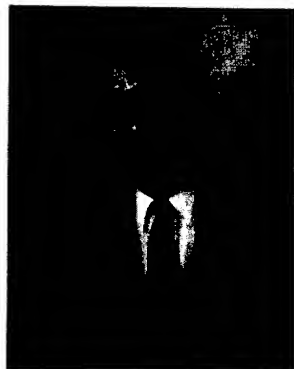
Payment: Make a check or bank draft payable in U.S. Dollars drawn on a U.S. Bank, to the INTERNATIONAL WIRE & CABLE SYMPOSIUM, INC. or use your VISA/MC/AMEX by providing number and expiration date and forward request to: International Wire and Cable Symposium, Inc., 174 Main Street, Eatontown, NJ 07724. Telephone inquiries may be directed to Ms. Charron Wishnick +1-732-389-0990. Prices are subject to change.

Photocopies are available for complete sets of papers for 1964 through 2001. Information on prices and shipping charges should be requested from the: US Department of Commerce, National Technical Information Service (NTIS), Springfield, Virginia 22161, Telephone: +1-703-487-4650

Include Title, Year and "AD" Number

13th Annual Wire Cable Symposium (1964)	- AD 787164
15th Annual Wire Cable Symposium (1966)	- AD A006601
16th International Wire Cable Symposium (1967)	- AD 787165
17th International Wire Cable Symposium (1968)	- AD 787166
18th International Wire Cable Symposium (1969)	- AD 787167
19th International Wire Cable Symposium Proceedings 1970	- AD 714985
20th International Wire Cable Symposium Proceedings 1971	- AD 733399
21st International Wire Cable Symposium Proceedings 1972	- AD 752908
22nd International Wire Cable Symposium Proceedings 1973	- AD 772914
23rd International Wire Cable Symposium Proceedings 1974	- AD A003251
24th International Wire Cable Symposium Proceedings 1975	- AD A017787
25th International Wire Cable Symposium Proceedings 1976	- AD A032801
26th International Wire Cable Symposium Proceedings 1977	- AD A047609
27th International Wire Cable Symposium Proceedings 1978	- AD A062322
28th International Wire Cable Symposium Proceedings 1979	- AD A081428
29th International Wire Cable Symposium Proceedings 1980	- AD A096308
30th International Wire Cable Symposium Proceedings 1981	- AD A110859
31st International Wire Cable Symposium Proceedings 1982	- AD A125662
32nd International Wire Cable Symposium Proceedings 1983	- AD A136749
33rd International Wire Cable Symposium Proceedings 1984	- AD A152119
34th International Wire Cable Symposium Proceedings 1985	- AD A164384
35th International Wire Cable Symposium Proceedings 1986	- AD A180828
36th International Wire Cable Symposium Proceedings 1987	- AD A189610
37th International Wire Cable Symposium Proceedings 1988	- AD A200903
38th International Wire Cable Symposium Proceedings 1989	- AD A216023
39th International Wire Cable Symposium Proceedings 1990	- AD A233634
40th International Wire Cable Symposium Proceedings 1991	- AD A244038
41st International Wire Cable Symposium Proceedings 1992	- AD A259235
42nd International Wire Cable Symposium Proceedings 1993	- AD A279242
43rd International Wire Cable Symposium Proceedings 1994	- AD A293473
44th International Wire Cable Symposium Proceedings 1995	- AD A303506
45th International Wire Cable Symposium Proceedings 1996	- AD A324572
46th International Wire Cable Symposium Proceedings 1997	- AD A338941
47th International Wire Cable Symposium Proceedings 1998	- AD A358377
48th International Wire Cable Symposium Proceedings 1999	- AD A373457
49th International Wire Cable Symposium Proceedings 2000	- AD A393963
50th International Wire Cable Symposium Proceedings 2001	- AD A404389
Kwic Index of Technical Papers, International Wire Cable Symposium (1952-1982)	- AD A027588

MESSAGE FROM THE CEO, DIRECTOR



This will be my last symposium as your CEO/Director. I have been a part of the Symposium for nearly all of its 51 years. Beginning in the mid-fifties, 1954 or 1955 I attended my first IWCS at the Berkley Carteret Hotel in Asbury Park, NJ and I gave my first paper at the Symposium in 1959. Hardly a year passes without someone at the symposium mentioning the years that the symposium was held in Asbury Park or Atlantic City, NJ. The symposium has been such a major part of my life that each year I look forward with joy and excitement in the expectation of another great conference.

My association with the symposium leaves me with many fond memories. The most lasting are the many friends that I have made over the years, especially the many Board/Committee members and their families. During their tenure on the committee, many members became such close friends that at the end of their term, departing became a sad occasion. I will always miss the camaraderie and fellowship of the Board and Committee Members, especially during the international meetings when we visited various companies and symposium supporters.

Last year's 50th Anniversary Symposium in Orlando, Florida was a tremendous success, due largely to the efforts of the past Board Chairman, Dr. Raymond E. Jaeger. The activities planned by Ray and his committee at Disney's Epcot and MGM Studios in support of the symposium were outstanding. The picture displays and the historical artifacts assembled by Ray's committee in the exhibit area helped to revive many memories of past symposiums. I think everyone will agree, that the 50th symposium was both technically rewarding and emotionally exciting.

This year as in the past, an excellent technical program is planned, with over one hundred and thirty papers scheduled to be presented, in addition to one day (Monday) of special educational short courses. The scheduled exhibits and the poster sessions should as always provide the opportunity, especially during the hospitality hours, for everyone to meet and greet old friends.

Last year's winners of best technical/poster papers and best presentation will be recognized and presented with plaques, acknowledging their accomplishments. Retiring Board member Dr. Peter R. Bark of Corning Cable Systems and Committee Member Dr. Howard Wichansky, U.S. Army CECOM will be surely missed. On behalf of the Board of Directors and Symposium Committee, I extend to Peter and Howard our sincere thanks and appreciation for their many years of dedication and service to the symposium.

On behalf of the Board of Directors and Symposium Committee, I extend our gratitude and thanks to the many companies that supported this year's symposium.

I hope this, my last symposium as its CEO/director will be as great as the others that preceded it. As always I am looking forward to seeing and greeting many of you in Florida.

Elmer F. Godwin
CEO, Director

HIGHLIGHTS OF THE 50TH IWCS

International Wire and Cable Symposium

November 12, 13, 14 and 15, 2001

Disney's Coronado Springs Resort, Lake Buena Vista, Florida

*Welcome/Dedication/
Schedule Highlights/IWCS History*

Guest Speaker - Plenary Session



Dr. Raymond E. Jaeger
Chairman, IWCS
Board of Directors
Sturbridge, MA



Dr. Noritaka Kurauchi
President, International Cablemakers Federation (ICF)
Wien, Austria and Chairman of the Board of Directors
Sumitomo Electric Industries, Ltd, Osaka, Japan

Scholarship Recipients

Rutger's Scholarship



**Dr. Ray Jaeger (left) and
Ace Godwin (right)**
Announcing the Elmer F. "Ace" Godwin
Rutger's Scholarship Award

Elmer F. "Ace" Godwin



Aleksandr Pelts
Attending
Drexel University



Jennifer Gaugler
Attending
MIT

Christopher Kenneth Eoll Memorial



Jennifer Shen
Attending
Stanford University

Award Winners



**Jack Spergel Memorial Award for
Outstanding Technical**
John Sach of IWCS (on left)
making presentation to **Manuel Santana**,
Dr. Richard D. Small, **Dr. Peter A. Weimann**,
Dr. Luis M. Bocanegra, **H. Paul Debben, Jr.**,
and **C. Shawn Davis**, Lucent Technologies, Incorporated,
Norcross GA



Outstanding Poster Paper
John Sach of IWCS (on left) making presentation to
Tomotaka Murase, Showa Electric Wire & Cable
Company, Ltd. (who is also accepting for) **Kieko**
Shiraishi and **Haruhito Noro**, Showa Electric Wire
& Cable Company, Ltd., Kanagawa, Japan



**Kitts-Kingsley Award
for Best Presentation**
John Sach of IWCS (on left) making presentation
to **Karthik Krishnamurthy**, Alcoa Fijikura
Limited, Spartanburg, SC

Special Award



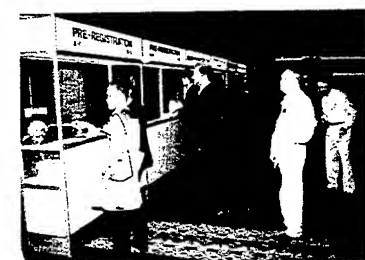
Dr. Ray Jaeger of IWCS (on left) making
presentation to **Irving Kolodny**, also of IWCS

Retiree Award

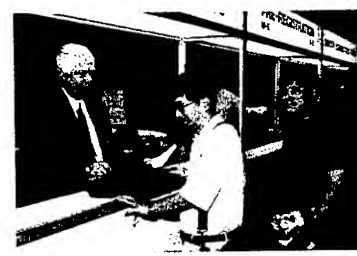


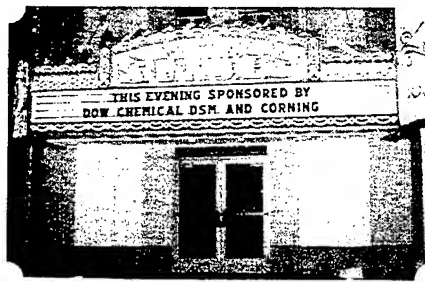
Elmer F. Godwin of IWCS (on left) presenting retirement certificate
to **Nils Artlöve**, Telia International Carrier, Farsta, Sweden





Registration





Hospitality





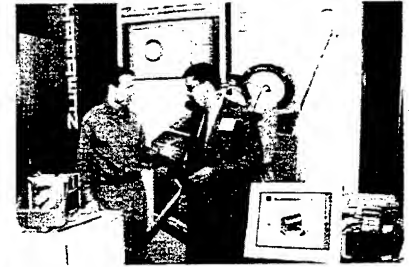
Hospitality



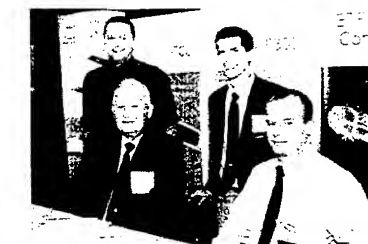
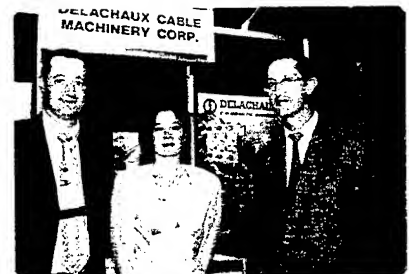


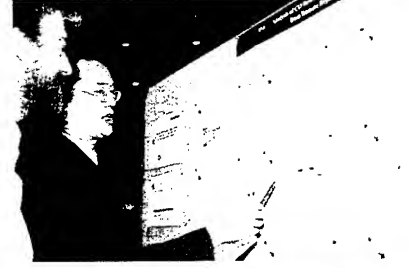
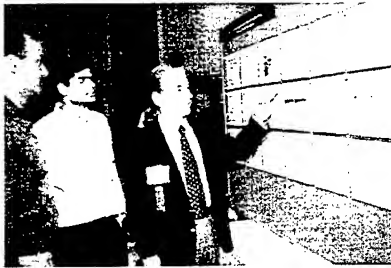
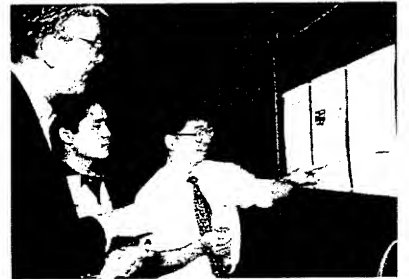
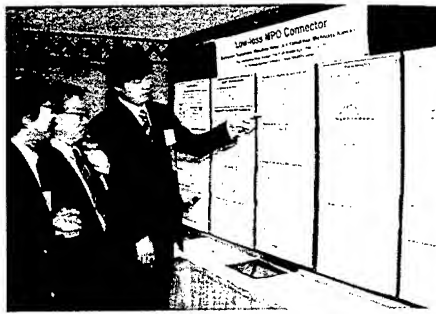
Suppliers Forum





Suppliers Forum





Posters

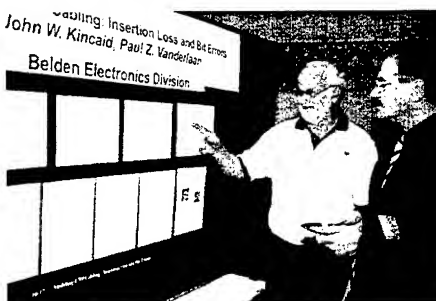
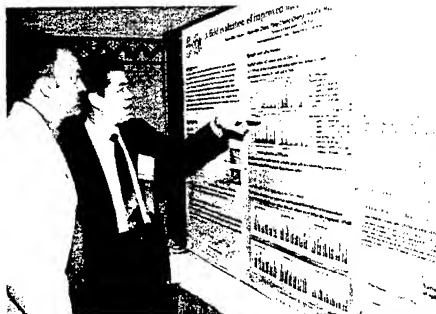
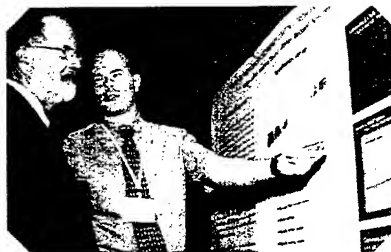
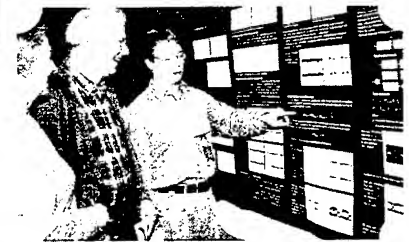
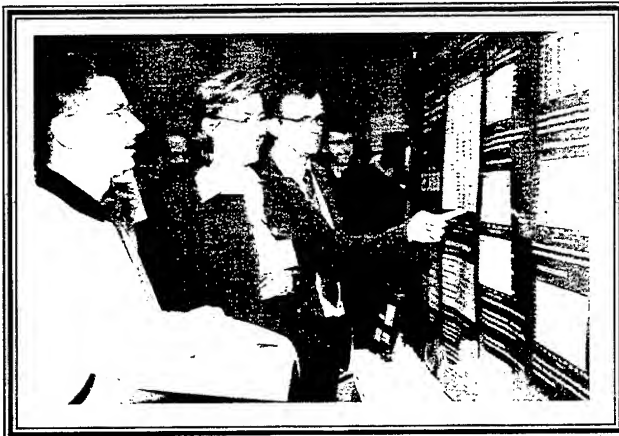


Table of Contents

MISSION	ii
PROCEEDINGS PUBLICATIONS	iii
MESSAGE FROM THE CEO/DIRECTOR	iv
HIGHLIGHTS OF THE 50th IWCS	v-xiii
SCHOLARSHIPS	xxi
AWARDS	xxii-xxiv
51st GOLD SUSTAINING CONTRIBUTORS	xxv
50th ANNIVERSARY SPONSORS	xxvi
51st IWCS/FOCUS SPONSORS	xxvii
51st IWCS/FOCUS ORGANIZATION	
Staff	xxviii
Board of Directors.....	xxviii
Symposium Committee Officers.....	xxix
Symposium Committee Members	xxix
OPENING SPEAKERS	xxx
Dieter S. Nordmann, Chairman, IWCS/Focus Board of Directors, Alcatel Contracting, Hannover, Germany; James Reese, Chairman, IWCS/Focus Symposium Committee, DSM Desotech, Inc., Elgin, IL; David B. Kiddoo, Chairman, IWCS/Focus Plenary Session, AlphaGary Corp., Sparta, NJ	
PLENARY SESSION	xxxi
Loring W. Knoblauch, President & Chief Executive Officer, Underwriters Laboratories Incorporated, Northbrook, IL	
SPECIAL SESSION: Marketing & Management	
Monday Afternoon, Nov. 18, 1:00 – 5:00 PM • Fiesta 5	
Chairperson: M. Edward Fenton, Wire & Cable Clubs/Fenton Group, Inc., Wethersfield, CT	
MM-1 Technology Forecasting Techniques in Communications	1
A. P. Duffy, De Montfort University, Leicester, UK; K. G. Hodge, A. J. Willis, Brand-Rex Ltd., Fife, Scotland	
MM-2 New UL Programs and Standards Proposals; Standards Harmonization Activities and Fire and Electrical Code Issues	9
T. J. Guida, A. D. Wetherell, Underwriters Laboratories Incorporated, Melville, NY	
MM-3 The Future of Copper Cabling Systems; the World versus North America	10
D. O. Nicholson, Intertek Testing Services, ETL SEMKO, Cortland, NY	
MM-4 Fiberoptic Cable: Understanding the Dramatic Shifts in Worldwide Demand	13
P. J. Fay, R. R. Mack, KMI Research, Providence, RI	
MM-5 Global Market Trends in Fiber Optic Cable & Optical Fiber	14
J. P. Barnes, CRU International, London, UK;	
MM-6 Optical Fiber & Cable Industry in China	17
Wei Zhong-cheng, Tang Ren-jie, FiberHome Telecommunication Technologies Co. Ltd., Wuhan, China; He Fang-rong, China Univ. of Geosciences, Wuhan, China	

Track 1 — Fiber	
SESSION 1: FIBER OPTIC CABLE DESIGN I	
Tuesday Afternoon, Nov. 19, 1:00 – 4:30 PM • Fiesta 5	
Chairperson: Manuel R. Santana, OFS Brightwave, Norcross, GA	
1.1	Development of a Ribbon Distribution Cable Utilizing a Stranded Design 22 R. Vaughn, Pirelli Communications Cables & Systems NA, Lexington, SC
1.2	Riser-Rated Dry Core Indoor/Outdoor 12-36 Fiber Count Cables 26 S. Aderogba, K. Chakrabarty, C. Jackson, P. Neveux, W. Newton, M. Shmukler, OFS, Norcross, GA
1.3	Design of Optical Fiber Ribbon Cord 31 H. Shi, Y. Wang, C. Yu, S. Wang, Wuhan Research Institute of Posts & Telecommunications, Wuhan, China
1.4	High Modulus Tight Buffer Design with Improved Microbend Resistance and Low Temperature Performance 37 P. E. Neveux, Jr., W. M. Newton, S. A. Aderogba, M. Nagarajan, C. N. Okafor, OFS, Norcross, GA
1.5	Analysis of Tubing Process for Ribbon Fibers Cable 44 Y.-s. Jung, K.-t. Park, M.-h. Do, J.-h. Kim, Samsung Electronics Co. Ltd., Kyung-Buk, Korea

Track 1 — Fiber	
SESSION 2: FIBER OPTIC CONNECTORS	
Tuesday Afternoon, Nov. 19, 1:00 – 4:30 PM • Fiesta 6	
Chairperson: Bernard J. Cross II, SBC Southwestern Bell, Dallas, TX	
2.1	Development of Chamfer-Type Super Low Loss MPO Connector Using PPS Ferrule 48 W. Sakurai, K. Ohtsuka, Y. Hasegawa, T. Ueda, T. Hosoya, Sumitomo Electric Industries, Ltd., Yokohama, Japan
2.2	Development of 24-fiber Flat Ribbon Cable for Two-Dimensional Array MT Connector 56 K. Hamada, T. Ueda, N. Akasaka, T. Hosoya, Y. Tamekuni, Sumitomo Electric Industries, Ltd., Yokohama, Japan
2.3	Development of Optical Fiber Attenuator using Fusion Splice Technology 61 M. Miura, M. Nakano, Lucent Technologies Yazaki Ltd., Shizuoka-Pref., Japan
2.4	Photodeposition of Bragg Gratings on Nano-Porous Silica Clad Optical Fibers 68 D. Sunil, H. D. Gafney, Queens College, Flushing, NY; B. Skutnik, Fiber Optics Fabrication, Inc., East Longmeadow, MA
2.5	Ring Network Architecture Using Wavelength Division Multiplexing Coupler 72 T. Aihara, M. Kawakami, Y. Enomoto, K. Nakazawa, T. Tashiro, K. Sato, Nippon Telegraph and Telephone Corp., Ibaraki, Japan

Table of Contents

Track 2 — Manufacturing Processing & Materials

SESSION 3: MANUFACTURING/MATERIALS — FIBER I

Tuesday Afternoon, Nov. 19, 1:00 — 4:30 PM • Yucatan 1-3

Chairperson: Russell S. Daniels, Equistar Chemicals, LP, Houston, TX

- 3.1 Improving Geometric Structure of Coloring Device in the Fiber Optics Cabling Process by Numerical Analysis of Flow Characteristics of Coloring Ink.....78
S. m. Yoon, Y. G. Yang, J. S. Kim, I. S. Choi, LG Cable Research & Development Center, Kyungki-do, Korea
- 3.2 Forecasting Optical Network's Components Cost: A Simple Methodology84
E. Cottino, R. Leone, G. Monari, Sirti S.p.A., Milan, Italy
- 3.3 Simulation of Fiber Drawing Using Metallic Wire.....93
H. Ohara, T. Katsuta, T. Shigemoto, Z. Komiya, JSR Corp., Ibaraki, Japan
- 3.4 WITHDRAWN
- 3.5 The Study of UV Foaming Technology for ABF Bundle98
S. Chang, H. J. Kim, J.-H. Oh, D. Lee, E. Kim, Luvantix Co., Ltd., Kyonggi, Korea
- 3.6 WITHDRAWN

Track 2 — Manufacturing Processing & Materials

SESSION 4: MANUFACTURING/MATERIALS — COPPER I & FIBER

Tuesday Afternoon, Nov. 19, 1:00 — 4:30 PM • Monterrey 1-3

Chairperson: Hans A. Mayer, Engineering Consultant, Melbourne, Australia

- 4.1 Extrusion Line for Fine Wires with Highly Expanded Insulation.....103
P.-Y. Bonvin, Maillefer SA, Ecublens, Switzerland
- 4.2 Development of Novel Crosslinkable Polyester Elastomers for Automotive Wire and Cable Applications108
W. Z. Wan, A. E. Listro, Ju'd Wire Inc., Turners Falls, MA; S. Nishikawa, H. Hayami, S. Shukushima, Sumitomo Electric Industries, Ltd., Osaka, Japan
- 4.3 Automotive Applications of Bimetallic Wire117
B. Suwarow, A. Gibson, Copperweld Bimetallic Products, Fayetteville, TN
- 4.4 Alternative Polyolefin Insulation Materials for Communication Cable Applications124
C. D. Lee, T. S. Schloemer, Equistar Chemicals, LP., Cincinnati, OH
- 4.5 Design of New Easy Processing High Modulus Compounds for Fiber Optic Cable Use129
G. D. Brown, K. P. Pang, S. H. Wasserman, The Dow Chemical Company, Somerset, NJ
- 4.6 The Power of Performance Additives136
W. M. Stewart, PolyOne, Solon, OH

Track 3 — COPPER

SESSION 5: CABLE NETWORKS

Tuesday Afternoon, Nov. 19, 1:00 — 4:30 PM • Fiesta 7-10

Chairperson: Helio J. Durigan, Furukawa Industrial S.A. Produtos Eletricos, Curitiba, Brazil

- 5.1 Transmissions Parameter Deviations of a Data Channel Consisting of Cables and Connecting Hardware in Cascade 143
L. Halme, A. Boukalov, R. Kytönen, J. Lisjutin, M. Nupponen, V. Nässi, K. Ranta, E. Törnqvist, Helsinki University of Technology, Espoo, Finland
- 5.2 Generic Cabling for Broadband Access Networks Using Application Independent Universal Cables 150
P. E. Gregor, P. S. Reorda, P. Schnee, P. E. Zamzow, Nexans Deutschland Industries AG & Co KG, Moenchengladbach, Germany
- 5.3 Introduction of Intelligence into Telecom Network Flexibility Points 158
G. Le Traon, F. Fauchoux, D. Morellec, France Telecom R&D, Lannion Cedex, France
- 5.4 Cable for xDSL Technologies with Up to 25 Concentric Pairs in the Same Binder 165
R. T. Tanaka, A. C. Silva, R. F. Cruz, Furukawa Industrial S.A. Produtos Elétricos, Paraná, Brazil
- 5.5 Development of Optical Fibers and Copper Twisted Pairs Composite Cables for Both of FTTH and xDSL Broadband Networks 171
S. Matsumoto, Y. Hamada, F. Shimizu, Nishi Nippon Electric Wire & Cable Co., Ltd., Oita, Japan
- 5.6 Solutions for Business Building Cabling Infrastructures 176
A. C. Réau-Thomas, F. Fauchoux, E. Cressan, France Telecom R&D RTA/LLI, Lannion Cedex, France
- 5.7 Propagation Limits of Twisted Pair Cables 186
J. Poltz, J. Beckett, OptEM Engineering Inc., Calgary, Canada

Track 1 — Fiber

SESSION 6: FIBER OPTIC CABLE DESIGN II

Wednesday Afternoon, Nov. 20, 1:00 — 4:50 PM • Fiesta 5

Chairperson: John R. Sicotte, Corning International K.K., Tokyo, Japan

- 6.1 Performance Aspects of a Novel Two-Rod, Dielectric Sheath Design for Central Tube Cables 192
R. H. Norris, P. A. Weimann, OFS, Norcross, GA; H. M. Kemp, OFS, Chester, NJ
- 6.2 Dry Central Tube Ribbon Cables for the Outside Plant Environment.....202
R. H. Norris, P. A. Weimann, OFS, Norcross, GA
- 6.3 WITHDRAWN
- 6.4 Fiber Optic Cables and Cable Modules with Balanced Mechanical Characteristics Based on Self-Reinforcing Polymers with Controlled Orientation.....211
M. T. Heino, J. T. Ravela, P. E. Korhonen, E. P. Virolainen, NK Cables Ltd., Helsinki, Finland

Table of Contents

- 6.5 **A New Filling Concept for Improved Overall Performance of Fiber Optic Cables**221
B. Lindblom, A. Björk, M. Isacson, Ericsson Network Technologies AB, Hudiksvall, Sweden
- 6.6 **Qualification of Loose Tube Fiber Optic Cables with Reduced Weight and Diameter**227
R. G. Gravely, OFS BrightWave Carrollton, Carrollton, GA

Track 1 — Fiber

SESSION 7: FIBER OPTIC CABLE INSTALLATION

Wednesday Afternoon, Nov. 20, 1:00 – 4:50 PM • Fiesta 6

Chairperson: Nils Artlove, *Telia International Carrier, Farsta, Sweden*

- 7.1 **Optical Fiber Connections Through Existing Sewers and Natural Gas Pipes**231
J. K. Jayapalan, New Milford, CT
- 7.2 **Armored Fiber Optical Cable for Sewer Applications**239
K. E. Bow, T. Kawakita, The Dow Chemical Company, Midland, MI
- 7.3 **A New Fiber Optic Life for Old Ducts**244
W. Griffioen, W. Greven, T. Pothof, Draka Comteq - NKF Telecom, Gouda, The Netherlands
- 7.4 **Development of Lightweight Ribbon Cables for Blown Installation**251
H. P. Debban, Jr., M. S. Rossi, P. A. Weimann, M. Kinard, C. S. Davis, OFS Optical Cable Division, Norcross, GA; J. Pedder, OFS Optical Cable Division, Augsburg, Germany
- 7.5 **Design and High-Speed Processing of New Advanced Blown Fibre Units (EPFU's)**260
T. Jendel, J. Jason, B. Arvidsson, Ericsson Network Technologies AB, Hudiksvall, Sweden; P. Meriläinen, P. Salo, J.-P. Tiesmäki, Nextrom Oy, Vantaa, Finland

Track 2 — Manufacturing Processing & Materials

SESSION 8: MANUFACTURING/MATERIALS — FIBER II

Wednesday Afternoon, Nov. 20, 1:00 – 4:50 PM • Fiesta 7-10

Chairperson: Russell S. Daniels, *Equistar Chemicals, LP, Houston, TX*

- 8.1 **Control of Loose Buffer Tube Properties with Advanced Techniques of Nonlinear Modelling**267
A. Bulsari, Nonlinear Solutions Oy, Turku, Finland; M. Lahti, S. Sneek, Nextrom Oy, Vantaa, Finland
- 8.2 **Raw Materials for Optical Fiber Manufacture**275
A. Shirley, G. Rush, K. Lee, BOC Gases, Murray Hill, NJ
- 8.3 **Novel Manufacturing Method of Graded Index Copolymer Optical Fiber Preform and Its Optical Characteristics**281
J.-S. Choi, H. Cho, M.-G. Kim, B.-J. Ra, J.-Y. Park, J.-T. Hwang, J.-G. Park, Samsung Advanced Inst. of Technology, Suwon, Korea; S.-H. Lee, M.-H. Do, Samsung Electronics Co. LTD., Gyung-buk-Do, Korea; J.-H. Kim, Samsung Advanced Inst. of Technology, Suwon, Korea; E.-G. Lee, S.-H. Park, Yonsei Univ., Seoul, Korea; O.-O. Park, Samsung Advanced Inst. of Technology, Suwon, Korea
- 8.4 **Environmental and Safety Considerations in Premises Cable**288
H. Chen, C. W. Jackson, K. Chakrabarty, W. M. Newton, S. A. Aderogba, P. E. Neveux, Jr., OFS, Norcross, GA

- 8.5 **Helium Recovery in Fiber Optic Production: Benefits and Application**294
R. Busch, L. Schottke, F. Lauricella, Praxair, Inc., Tonawanda, NY/Danbury, CT
- 8.6 **Automation of the Buffer Tube Process Using Active Systems**300
W. Hoerschlaeger, Rosendahl Maschinen GmbH, Pischelsdorf, Austria

Panel

SESSION 9: AEROSPACE/AUTOMOTIVE

Wednesday Afternoon, Nov. 20, 1:00 – 4:50 PM • Monterey 1-3

Chairperson: M. Edward Fenton, *Wire & Cable Clubs/Fenton Group, Inc., Wethersfield, CT*

Moderators: D. Allen, *DuPont, Wilmington, DE &*

Larry Powell, Sr. *Project Engineer, Delphi Packard Electric, Warren, OH*

- 9.1 **Aerospace Cabling-Aircraft Wiring Aging Effects and Recommendations**305
K. V. Hollinger, Mitre Corp., McLean, VA
- 9.2 **Aerospace/Automotive Session**306
R. A. Pappas, Federal Aviation Administration, Atlantic City Int'l Airport, NJ
- 9.3 **Automotive Segment**307
L. Powell, Delphi, Warren, OH
- 9.4 **Automotive Flat Cable Designs**308
V. Perlov, Delphi, Warren, OH
- 9.5 **Future Electrical Systems**309
L. Matola, Delphi, Warren, OH

SESSION 10: NANO-STRUCTURED PHOTONIC MATERIALS & DEVICES

Wednesday Afternoon, Nov. 20, 1:00 – 4:50 PM • Yucatan 1-3

Chairperson: Dr. Howard Wichansky, *US Army Communications-Electronics Command, Ft. Monmouth, NJ*

Organizer: Sam DiVita, *US Army Communications-Electronics Command, Ft. Monmouth, NJ*

- 10.1 **Nanotechnology in Optical Networks and Components**310
G. S. Pomrenke, Air Force Office of Scientific Research, Arlington, VA
- 10.2 **The Organization of Hierarchically Structured Functional Units and Domains in 3-D Composite Fibers and Films**311
G. D. Stucky, University of California, Santa Barbara, CA
- 10.3 **Organic Nanostructured Materials for Photonics**318
T. Goodson III, Wayne State University, Detroit, MI
- 10.4 **Growth and Characterizations of Well-Aligned Carbon Nanotubes**321
Z. F. Ren, Boston College, Chestnut Hill, MA; B. Kimball, Natick Soldier Center, Natick, MA; Z. P. Huang, NanoLab, Inc., Brighton, MA; D. Z. Wang, Y. Tu, W. Z. Li, J. G. Wen, J. Y. Lao, Boston College, Chestnut Hill, MA; D. Steeves, M. Sennett, Natick Soldier Center, Natick, MA; J. Rybczynski, M. Giersig, Hahn-Meitner-Institute, Berlin, Germany; D. L. Camahan, NanoLab, Inc., Brighton, MA; K. Kempa, Boston College, Chestnut Hill, MA

Table of Contents

10.5	Have You Considered Atomic Layer Deposition?326 <i>R. Solanki</i> , Oregon Graduate Institute, Beaverton, OR
10.6	The Role of Nano-Structured Materials Enabling Miniaturization of Photomultipliers330 <i>C. Beetz, R. Boerstler, R. Wright, J. Agresta, D. Winn</i> , NanoSciences Corp., Oxford, CT
10.7	Impact of Preform Fabrication and Fiber Draw on the Optical Properties of Microstructured Fibers339 <i>R. T. Bise, D. J. Trevor, E. Monberg, F. DiMarcello</i> , OFS Laboratories, Murray Hill, NJ
10.8	Giant Optical Transmission Through Nanometer-Scale Apertures344 <i>T. Thio</i> , NEC Research Institute, Princeton, NJ

SESSION 11: POSTER PAPERS

Wednesday Afternoon, Nov. 20, 4:00 – 6:30 PM • Coronado A-G
Chairpersons: **Bernard J. Cross II**, SBC Southwestern Bell, Dallas, TX
& **James R. Leech**, The Dow Chemical Company, Somerset, NJ

11.1	Polypropylene Heterophasic Copolymer for Loose Tube Buffers348 <i>B. Malm</i> , Borealis Polymers Oy, Porvoo, Finland; <i>M. Lahti</i> , Nextrom Oy, Vantaa, Finland; <i>P. Heikkilä</i> , Borealis Polymers Oy, Porvoo, Finland; <i>R. C. Dammert</i> , Borealis AB, Stenungsund, Sweden;
11.2	Shrinkage of PBT, PP and PE in Central Tube Buffering Process352 <i>J. Kotala</i> , Nextrom Oy, Vantaa, Finland
11.3	Investigation of Possibilities for the Proof Testing of Optical Fiber Immediately after Draw357 <i>M. Lipponen</i> , Nextrom Oy, Vantaa, Finland; <i>H. Turunen</i> , Nextrom (USA), Inc., Duluth, Atlanta
11.4	Stress and Index Variation for the Drawing Speed362 <i>J.-H. Lee, S.-K. Oh, M.-H. Do, J.-H. Kim</i> , Samsung Electronics Co. Ltd., Kyung-Buk, Korea
11.5	Feasible Operating Conditions in Optical Fiber Drawing ..365 <i>X. Cheng, Y. Jaluria, C. Polymeropoulos</i> , Rutgers, The State University of New Jersey, Piscataway, NJ
11.6	The Use of a 3-D Computational Fluid Dynamics Simulation in the Design of an Optical Ribbon Coating Applicator371 <i>D. W. Chiasson</i> , Corning Cable Systems, Hickory, NC
11.7	Loss Performance of Standard Single Mode Fibre Cables in the Wavelength Region 1200-1750nm376 <i>S. Hopland</i> , Telenor Networks, Oslo, Norway
11.8	Transmission Capacity and Interference Analysis in ADSL System—Comparison Between a Standard Copper Cable and DSL Cable382 <i>M. A. Andrade, R. C. Federighi</i> , Pirelli Telecomunicações Cabos e Sistemas do Brasil S.A., Sorocaba, Brazil; <i>O. Tozze</i> , Av. Nações Unidas, SP, Brazil; <i>M. A. Garms</i> , Av. Engenheiro Heitor Antônio Eiras Garcia
11.9	Using Flat Steel Wires as Strength Members in Central Core Ribbon Cables387 <i>Y. Guan</i> , Chengdu CCS Optical Fiber Cable Co. Ltd., Sichuan, P.R. China;

11.10	Development of FR-PVC for Compact and High Performance UTP Cable 391 <i>D. H. Park, M. J. Ahn, G. J. Lee</i> , LG Cable Research & Development Center, Kyungki-do, Korea
11.11	Mechanical Stress and Shield Structure Effect on Shield Performance for Screened Twisted-Pair Cables397 <i>S.-H. Chou, J.-C. Lin, J.-C. Lii, Y.-H. Huang, H.-P. Hsu, Y.-c. Lin, J.-Y. Liu</i> , Chunghwa Telecom, Taoyuan, Taiwan
11.12	Recycling of Polyethylene from the Discarded Copper Cable403 <i>F. Nakajima, E. Konda, H. Tajima, M. Hara, Y. Suda</i> , The Furukawa Electric Co., Ltd., Chiba, Japan; <i>H. Hirukawa</i> , Zaikoo Co., Ltd., Chiba, Japan; <i>Y. Kajisa</i> , Okano Electric Wire Co., Ltd., Kanagawa, Japan
11.13	Structure-Property Relationships of Higher Performance Wire & Cable Jacketing Compounds408 <i>D.-C. Lee</i> , The Dow Chemical Company, Somerset, NJ
11.14	Benefits of Chlorinated Flame Retardants for Wire & Cable413 <i>R. L. Markezich</i> , Occidental Chemical Corp., Niagara Falls, NY
11.15	In Situ Cathodic Protection of Existing Lead-Sheathed Cables418 <i>Y. T. Horng</i> , Chunghwa Telecom Co., Ltd., Taoyuan, Taiwan and National Tsing Hua University, Hsinchu, Taiwan; <i>J. H. Wang, H. P. Hsu, Y.-c. Lin, L. J. Liu</i> , Chunghwa Telecom Co., Ltd., Taoyuan, Taiwan; <i>H. C. Shih</i> , National Tsing Hua University, Hsinchu, Taiwan
11.16	Input Impedance of Irregular Cascaded Systems423 <i>M. M. Al-Asadi, A. P. Duffy</i> , De Montfort University, Leicester, UK; <i>K. G. Hodge, A. J. Willis, D. A. Jackson</i> , Brand-Rex Ltd., Scotland, UK
11.17	Development of Novel High Efficient SiC Particle Removing System Based on Thermophoretic Effect428 <i>A. Malinin, T. Mattila</i> , Photonium Oy, Lohja, Finland; <i>M. Rajala</i> , Liekki Oy, Lohja, Finland
11.18	Development of Optical Drop and Indoor Cable of High Fiber Density432 <i>T. Yasutomi, F. Nakajima, M. Hattori, M. Hara</i> , The Furukawa Electric Co., Ltd., Chiba, Japan
11.19	Development of MT Ferrule for Low-Loss 24MPO Connector437 <i>K. Suematsu, M. Shinoda, Y. Ono</i> , The Furukawa Electric Co., Ltd., Chiba, Japan
11.20	Fiber Optic/Carbon Nanotube Skin Friction Sensing Device443 <i>A. K. Sang, M. F. Gunther, P. Stevenson</i> , Luna Innovations Incorporated, Blacksburg, VA; <i>D. L. Camahan</i> , NanoLab, Inc., Watertown, MA;
11.21	Fiber Bragg Grating Sensors for Detection of Acoustic Wave Emission and Seismic Activities448 <i>Y. Zhang</i> , Stevens Institute of Technology, Hoboken, NJ; <i>R. Pastore</i> , Stevens Institute of Technology, Hoboken, NJ and U.S. Army CECOM-RDEC, Fort Monmouth, NJ; <i>J. Ju, H. L. Cui</i> , Stevens Institute of Technology, Hoboken, NJ

Table of Contents

Track 1 — Fiber

SESSION 12: OPTICAL FIBER DESIGN

Thursday Morning, Nov. 21, 8:30 – 12:00 Noon • Fiesta 5

Chairperson: Hiroshi Yokota, Sumitomo Electric Industries, Ltd., Yokohama, Japan

- 12.1 **Understanding Multimode Bandwidth and Differential Mode Delay Measurements and Their Applications**.....453
P. F. Kolesar, OFS, Holmdel, NJ;
D. J. Mazzaresse, OFS, Sturbridge, MA
- 12.2 **Stability of Low Water Peak SMF against Hydrogen Aging**.....461
F. Ohkubo, H. Igarashi, H. Wakiyasu, K. Negishi,
T. Hasegawa, K. Kuwahara, Sumitomo Electric Industries, Ltd., Yokohama, Japan
- 12.3 **Multi- and Single Mode Fiber in One for Higher Bandwidth Applications**.....466
A. Kaczmarek, Pirelli Telecom Cables & Systems Australia P/L, Liverpool, Australia; M. Tanana, CISCO Systems, North Sydney, Australia
- 12.4 **1.25 Gb/s Enhanced Transmission Performance on Standard Single-Mode Fiber Optimized for Operating at 850-nm Using Single-Mode VCSEL**.....471
F. I. Pomarico, M. Artiglia, Pirelli Cables and Systems Telecom SpA, Milano, Italy
- 12.5 **The Study of Optimized Design Fibers for WDM Transmission Systems**.....475
K. Ohsono, Y. Bing, T. Shirogawa, T. Onose, T. Sukegawa, Hitachi Cable, Ltd., Ibaraki-ken, Japan
- 12.6 **Holmium doped Chalcogenide Glasses for U-band (1.62-1.65 μ m) Amplification**.....482
S. H. Park, J. S. Yang, M. H. Do, J. H. Kim, Samsung Electronics Co. Ltd., Gyeong-Buk, Republic of South Korea

Track 1 — Fiber

SESSION 13: AERIAL DROP FIBER OPTIC CABLES

Thursday Morning, Nov. 21, 8:30 – 12:00 Noon • Fiesta 6

Chairperson: Dr. Howard Wichansky, US Army Communications-Electronics Command, Ft. Monmouth, NJ

- 13.1 **A New Method for Validating the Performance of Aerial Drop Cables Under Ice Loads**.....488
J. G. Fitz, M. T. Petryszak, J. Liu, Pirelli Communications Cables and Systems, Lexington, SC
- 13.2 **Optical Ground Wires with Improved Lightning Resistance**.....494
L.-R. S. Casals, J. Martin-Regalado, Pirelli Telecom Cables y Sistemas España S.L., Vilanova i la Geltru, Spain;
A. Ginocchio, Pirelli Cavi e Sistemi Telecom SpA, Milano, Italy
- 13.3 **A Downsized Non-Metallic Drop Cable for FTTH**.....500
K. Kobayashi, M. Kusakari, S. Tanaka, K. Ohashi, Fujikura Ltd., Chiba-ken, Japan;
- 13.4 **Development of Optical Fiber Composite Polyvinylchloride Insulated Drop Wire**.....507
F. Hosoi, F. Nakajima, M. Hara, The Furukawa Electric Co., Ltd., Chiba, Japan; S. Hirukawa, H. Tanaka, Kyushu Electric Power Co., Inc., Fukuoka, Japan

- 13.5 **Results of Qualification of ADSS Cable with Reduced Weight and Diameter**.....512
A. Nunes, OFS, São Paulo, Brazil
- 13.6 **Suggestion of ADSS Cable Standardization Including Installation Procedure**.....516
K.-T. Park, J.-J. Hwang, M.-H. Do, J.-H. Kim, Samsung Electronics Co. Ltd., Kyung-Buk, Korea
- 13.7 **ADSS Cables with Extended Operating Lifetime**.....519
R. Engel, S. Will, Corning Cable Systems, Neustadt, Germany; D. Wartschinski, Technische Universität Ilmenau, Ilmenau, Germany

Track 2 — Manufacturing Processing & Materials

SESSION 14: MANUFACTURING/MATERIALS — COPPER II

Thursday Morning, Nov. 21, 8:30 – 12:00 Noon • Yucatan 1-3

Chairperson: Charles A. Glew, Cable Components Engineering, Framingham, MA

- 14.1 **NEXT Characteristics for the Pitch of Twisted Pair Cable**.....524
Y. Shimoshio, Kumamoto National College of Technology, Kumamoto, Japan; K. Kimura, Tsushin Kogyo Co. Ltd., Saitama, Japan; H. Koga, N. Yamamoto, Kumamoto National College of Technology, Kumamoto, Japan; T. Ideguchi, Kyusyu Tokai University, Kumamoto, Japan
- 14.2 **Thermoplastic Foam Extrusion with Physical Blowing Agents**.....531
T. Reiner, H. Scheid, SIEBE Engineering GmbH, Neustadt/Wied, Germany
- 14.3 **Silane Crosslinked Polyethylene Insulation for Cost Effective Overhead Cables**.....540
R. Carlsson, B.-A. Sultan, Borealis AB, Stenungsund, Sweden; D. Wald, Borealis Polymers NV, Mechelen, Belgium; O. Fagrell, Borealis AB, Stenungsund, Sweden
- 14.4 **Antimicrobial Additives for Use in Wire and Cable Applications**.....548
N. J. Earhart, U. Stadler, Ciba Specialty Chemicals Corp., Tarrytown, NY
- 14.5 **Evaluation of ADSS Jacketing Compounds and Environmental Exposure Effects Using a New Dry Band Arc Test Methodology**.....551
B. G. Risch, S. Neogi, Fiber Optic Cable R&D, Claremont, NC; G. Karady, Y. Lei, B. Shi, Arizona State Univ., Tempe, AZ
- 14.6 **Non-contact Measurement of Copper Diameter and Drawdown Through the Insulation**.....561
C. C. Matthias, Zumbach Electronics Corp., Mt. Kisco, NY
- 14.7 **Composite Cable for Shared Powering System**.....564
S. Park, M. Son, LG Cable, Kumi, Korea; S. Hong, Y. Lee, J. Ha, Korea Telecom, Daejeon, Korea;

Track 2 — Manufacturing Processing & Materials

SESSION 15: FIRE RESISTANCE/FLAME RETARDANT I

Thursday Morning, Nov. 21, 8:30 – 12:00 Noon • Monterey 1-3

Chairperson: David B. Kiddoo, AlphaGary Corp., Sparta, NJ

- 15.1 **Development of Flame-Retardant Optical Fiber Cord**.....569
T. Hayano, O. Kato, T. Shimomichi, K. Ohashi, Fujikura Ltd., Chiba, Japan

Table of Contents

15.2	Development of Flame-Retardant Halogen-Free Fiber Optic Cords with Shrink-Free Jacket574 <i>T. Honjyo, M. Kusakari, K. Kobayashi, K. Ohashi, Fujikura, Ltd., Chiba, Japan</i>
15.3	The Prediction of Flame Retardancy of LSZH Optical Cable Using a Small-Scale Flame Test by Cone-Calorimeter579 <i>H.-s. Lee, E.-s. Um, Samsung Electronics Co., Ltd., Kumi-City, Republic of Korea; J.-h. Kong, Hanwha Chemical R&D Center, Daejeon-City, Republic of Korea</i>
15.4	Nanocomposites as a New Class of Flame Retardants ..584 <i>G. Beyer, Kabelwerk Eupen AG, Eupen, Belgium;</i>
15.5	The Characteristics of a Non-Halogen Flame Retardant Compound Using Advanced Thermoplastic Plastomer589 <i>T. Chen, A. Hendrix, J. M. Huber Corp., Fairmount, GA; T. Glogovski, Basell USA Inc., Lansing, MI; R. Butala, Basell USA Inc., Wilmington, DE;</i>
15.6	Overview of Recent Advances in Flame Retardant Compositions UV Stable Flame Retardant Systems; Fully Formulated Antimony Free Flame Retardant Products for Polyolefins594 <i>N. Kaprinidis, N. Earhart, Ciba Specialty Chemicals Corp., Tarrytown, NY; J. Zingg, Ciba Specialty Chemicals Corp., Basel, Switzerland</i>
15.7	Development of a Tough and Flexible Halogen Free Dual Layer Wire Insulation System for Electronics Applications597 <i>A. H. Trivedi, A. Listro, Judd Wire, Inc., Turners Falls, MA</i>

Track 3 — Copper

SESSION 16: CABLE PERFORMANCE

Thursday Morning, Nov. 21, 8:30 – 12:00 Noon • Coronado E-G

Chairperson: Federic N. Wilkenloh, *CommScope, Inc., Hickory, NC*

16.1	Determining Cable Shield Behaviour602 <i>A. R. Coates, A. Gavrilakis, A. P. Duffy, De Montfort University, Leicester, UK; K. G. Hodge, A. J. Willis, Brand-Rex Ltd., Glenrothes, Scotland</i>
16.2	Coaxial Drop Cable Shielding Fatigue Analysis610 <i>A. Miller, K. Dunn, Corning Cable Systems, Hickory NC</i>
16.3	Impedance Calculation of High Frequency Shielded Cables with the Aid of Conformal Mappings616 <i>A. Gavrilakis, M. Al-Asadi, A. P. Duffy, De Montfort University, Leicester, UK; K. G. Hodge, A. J. Willis, Brand-Rex Ltd., Glenrothes, Fife, Scotland</i>
16.4	Impact of Environmental Effects upon Transmission Performance Data Grade Cables622 <i>J.-H. Walling, Beaconsfield, Quebec, Canada</i>
16.5	Temperature and Flexing Effects on Coaxial Cable Insertion Phase, Insertion Loss, and VSWR633 <i>C. W. Dole, Belden Electronics Division, Richmond, IN</i>
16.6	WITHDRAWN
16.7	Low Cost Assessment of Connector Performance641 <i>A. R. Coates, A. Gavrilakis, M. Al-Asadi, De Montfort University, Leicester, UK; A. P. Duffy, K. G. Hodge, A. J. Willis, Brand-Rex Ltd., Glenrothes, Scotland</i>

Track 1 — Fiber

SESSION 17: PMD

Thursday Afternoon, Nov. 21, 1:00 – 3:05 PM • Fiesta 5

Chairperson: Dr. C. Bertil Arvidsson, *Ericsson Network Technologies, AB, Hudiksvall, Sweden*

17.1	PMD Improving by Fiber Profile Design648 <i>T. Wang, Y. Cao, J. Luo, Yangtze Optical Fiber & Cable Co. Ltd., Wuhan, China;</i>
17.2	Application of Statistical Models to Estimate PMD Coefficient in Telecommunications Optical Links653 <i>C. E. P. Blume, A. A. P. Pohl, CEFET-PR-Departamento de Electronica, Curitiba, Brazil; J. A. de Medeiros Neto, CITS-Centro Internacional de Tecnologia de Software, Curitiba, Brazil; L. F. G. Marques, R. F. Cruz, Furukawa Industrial S.A. Produtos Elétricos, Curitiba, Brazil</i>
17.3	PMD Evaluation in Backbones—A Comparison Between the PMD Value Expected by Calculus and the Field Measurements662 <i>J. A. Brito, Jr., A. Cieslak, Intelig Telecomunicações Ltda., Rio de Janeiro, Brazil</i>
17.4	The Behavior of PMD Parameter in an Optical Cable Link due to Temperature Cycling667 <i>M. M. Simião, J. Dotto, L. F. G. Marques, R. F. Cruz, Furukawa Industrial S.A. Produtos Elétricos, Curitiba, Brazil; J. A. de Medeiros Neto, CITS-Centro Internacional de Tecnologia de Software, Curitiba, Brazil</i>
17.5	Temperature and Humidity Dependence of PMD in Dispersion Compensating Fiber675 <i>J. Zhou, K. Nakajima, NTT Corp., Ibaraki, Japan; M. Ohashi, Osaka Prefecture University, Osaka, Japan</i>

Track 1 — Fiber

SESSION 18: SPLICING & SPLICE ENCLOSURES

Thursday Afternoon, Nov. 21, 1:00 – 3:05 PM • Fiesta 6

Chairperson: John R. Sicotte, *Corning International K.K., Tokyo, Japan*

18.1	Downsized and Enhanced Optical Fiber Cable Transfer Splicing System680 <i>K. Tanaka, M. Zaima, M. Tachikra, M. Nakamura, Nippon Telegraph and Telephone Corp., Ibaraki, Japan;</i>
18.2	Improvements in Splicing Dissimilar Fibers for Dispersion-Managed Ultra Long Haul Network687 <i>M. Nakano, H. C. Chandan, J. Luo, L. R. Pritchett, T. Ellithi, T. Veng, A. D. Yablon, J. F. Ryan, OFS, Norcross, GA</i>
18.3	Development of Buffer Tube Storage Solution for 1728 Fibers696 <i>P. K. Strong, J. C. Lail, Corning Cable Systems, Hickory, NC</i>
18.4	Mid-span Access Tool Designs and Their Impact on Fiber Reliability702 <i>G. Witt, B. Risch, B. Chapman, P. Coat, R. Lovie, B. Overton, Alcatel Fiber Optic Technology, Claremont, NC</i>
18.5	Development of a Mass Fusion Splicing System for up to 24-Fiber Ribbon708 <i>T. Mizushima, S. Morita, H. Sugawara, T. Sato, S. Yaguchi, Fujikura Ltd., Chiba, Japan</i>

Table of Contents

Track 1 — Fiber

SESSION 19: SUBMARINE CABLES

Thursday Afternoon, Nov. 21, 1:00 – 3:05 PM • Yucatan 1-3

Chairperson: Hans A. Mayer, *Engineering Consultant, Melbourne, Australia*

- 19.1 **A New Cost-Effective Approach to Coastal Underwater Cable Installation**716
S. Hopland, Telenor Networks, Oslo, Norway
- 19.2 **High-Voltage Performance and Reliability of Insulated Products in Undersea Cable Systems**721
S. Bernstein, M. L. Jackson, M. E. Kordahi, C.-S. Ma, S. Shapiro, Q. Zhong, Tyco Telecommunications (US), Inc., Eatontown, NJ
- 19.3 **Nonferrous Armor Cable Termination: Ironing Out the Details**727
D. A. Giordano, M. E. Kordahi, R. J. Rue, R. K. Stix, Tyco Telecommunications (US), Inc., Eatontown, NJ

Track 2 — Manufacturing Processing & Materials

SESSION 20: FIRE RESISTANCE/FLAME RETARDANT II

- 20.1 Moved to Session 15, Paper 15.5
- 20.2 WITHDRAWN
- 20.3 Moved to Session 15, Paper 15.6

Track 2 — Manufacturing Processing & Materials

SESSION 21: FIBER COATING

Thursday Afternoon, Nov. 21, 1:00 – 3:05 PM • Coronado E-G

Chairperson: James Reese, *DSM Desotech Inc., Elgin, IL*

- 21.1 **Design of an Efficient Cooling Tube for Optical Fiber Manufacturing at High Draw Speeds**732
D. Tschumperlé, A. Léon, Alcatel, Conflans, France
- 21.2 **Optical Fiber Coating Delamination Using Model Coating Materials**738
C. Aloisio, A. Hale, K. Konstadinidis, R. Moore, M. Tabaddor, J. Turnipseed, OFS, Norcross, GA
- 21.3 **Micro-mechanical On-fiber Analysis of the Interface Between Outer Primary and UV-cured Ink**748
K. Hoekstra, DSM Desotech, Elgin, IL
- 21.4 **Prediction of Ribbon Friction by Matrix Resin Upjacketing of Single Fibers**752
E. Currie, DSM Research, Geleen, The Netherlands; K. Gan, K. A. Hawkinson, B. A. Register, E. P. Zahora, DSM Desotech, Inc., Elgin, IL
- 21.5 **Fiber Optic Coating System Effect Upon Fiber Performance**757
G. L. Workman II, Borden Chemical, Inc., Cincinnati, OH

AUTHOR INDEX763

SCHOLARSHIPS

ELMER F. "ACE" GODWIN SCHOLARSHIPS

2001	Alexander Pelts, Drexel University – A Computer Science/Math Major Jennifer Gaugler, MIT – Mechanical Engineering Major
2000	Stephen Consenza, Cornell University, Freshman — Electrical and Computer Engineering Stephen M. Lopez, The University of North Carolina at Charlotte, Sophomore — Electrical Engineering
1999	Twanaze Mitchell, Auburn University, Freshman — Electrical Engineering Jennifer Gau, University of Pennsylvania, Freshman — Computer Science and Engineering James J. Brown, Georgia Institute of Technology, Sophomore — Computer Engineering
1998	Jothan Bowen, Texas A&M University, Freshman — Digital Communications and Computers John D. Taliaferro, Virginia Tech, Junior — Chemical Engineering
1997	Michael Rich, Georgia Institute of Technology, Freshman — Electrical Engineering Major Billy Oates, Georgia Institute of Technology, Senior — Mechanical Engineering and Math Major Janet Armstrong, Rutgers University, Ph.D. Candidate — Ceramic Engineering Major
1996	Anthony Tindall, Cornell University, Freshman — Mechanical Engineering Major John Belle, North Carolina State University, Sophomore — Electrical Engineering Major
1995	Jason Chang, Princeton University, Freshman — Chemistry Major Fionna Murray, Virginia Tech, Junior — Mechanical Engineering Major
1994	Sara Ransom, Massachusetts Institute of Technology, Freshman — Materials Science Engineering Major Jurron Bradley, Vanderbilt University, Senior — Chemical Engineering Major

CHRISTOPHER KENNETH EOLL MEMORIAL SCHOLARSHIPS

2001	Jennifer Shen, Stanford University – Computer Engineering Major
2000	Peter Galeotti, The University of North Carolina at Charlotte, Senior — Computer Science

AWARDS

	Best Overall Technical Paper	Outstanding Poster Paper	Kitts-Kingsley Award for Best Presentation
2001	Dr. Willem Griffioen, Cees van't Hul, Ignaat Eijpe, Willem Greven and Frans Robbert Bakker – Draka Comteq – NKF Telecom; and Bas Wegbrans – Pirelli Cables – “5.5 km Optical Cables Installed in Small Underwater Tubes Using Waterflow”	Gregory A. Lochkovic, Donald Lockwood, Shail K. Moorjani, John S. Richards, Scott M. Torrey and Karen E. Williams – Corning Cable Systems – “Ribbon Separation Tools & Techniques – End and Mid-Span”	Peter Pleunis – Draka Comteq – “Influences of Profile Variations in PCVD Multimode Fibre on DMD Characteristics for 10 GbE Systems”
2000	H. Paul Debben, Jr., Dr. Luis M. Bocanegra, C. Shawn Davis, Dr. Richard D. Small, Jr., Dr. Peter A. Weimann and Manuel R. Santana – Lucent Technologies – “A New High-Density Central Cable Core Design”	Keiko Shiraishi, Tomotaka Murase and Haruhito Noro – Showa Electric Wire and Cable Company Limited – “Geometric and Mechanical Characteristics of Newly Developed SM-NSP (Single Mode Non-Strippable Primary Coated) Fiber”	Karthik Krishnamurthy – Alcoa Fujikura Limited – “Successful Deployment of ADSS Cables in EHV Environments”
1999	Dr. J. Thomas Chapin and Larry L. Bleich – Lucent Technologies; Dr. Pravin Gandhi and Thomas Ebert – Underwriters Laboratories – “The Development and Performance of a Calibration Cable for the NFPA 262/UL 910 Plenum Cable Fire Test”	Shami S. Sodhi, Allen C. Gregory and Gary E. Grogan – Siecor – “Effect of Temperature, Strain and Installation of PMD in High Fiber Count Ribbon Cables”	Eric R. Logan – Siecor – “The Status and Future of High Fiber Count Cable Designs”
1998	Dr. Bernt-Åke Sultan – Borealis AB; Dr. Thomas Hjertberg and Karin Ericsson – Chalmers University of Technology; and Matti Hirvensalo and Marjo Hänninen – Borealis Polymers Oy – “Novel Halogenfree Flame Retardant Polyolefins Intended for Internal Wiring – Properties and Flame Retardant Mechanism”	Dr. Osman S. Gebizlioglu, Joel D. Mann and C. R. Kurkjian – Bellcore – “The Effect of Preparation Conditions on the Strength of Fusion Splices I: Use of AFM Imaging”	Dr. Priya L. Tabaddor – Lucent Technologies Incorporated – “Mechanics of Delamination Resistance Testing”
1997	Debra A. Simoff, Dr. Mark A. Paczkowski, Dr. Daryl Inniss, Dr. Thomas A. Strasser, J. Renee Pedrazzani, Dr. Rolando P. Espindola, Dr. Robert M. Atkins, Katherine T. Nelson, Valerie J. Kuck, John M. Borick and Jennifer Aspell – Lucent Technologies; and Regina Ragan – California Institute of Technology – “Coatings Having Enhanced UV Transparency for the Fabrication of Optical Fiber Gratings”	Katja Lyytikäinen – Nokia – Maillefer Oy – “Numerical Simulation of Optical Fiber Coating Process”	Dr. Neil R. Haigh – BICC Cables Limited – “Applicability of All – Dielectric Self Supporting Cable Systems to Very High Voltage Overhead Power Lines”
1996	Mitsuru Kamikatan and Matsuhiro Miyamoto – Fujikura Limited; and Osamu Ogawa – Tokyo Electric Power Company – “A Time – Varying Optical Fiber Strain Measurement by Using Brillouin Ring Amplifying System”	Jan Björkman – Telia Network Services; and Dr. Torbjörn Svensson – Telia Research AB – “Aging of Fibres and Ribbon in Water and Filling Compound”	Dr. Priya L. Tabaddor – Lucent Technologies Incorporated, Bell Laboratories – “An Evaluation of Protective Polymer Coatings for Optical Fiber Applications”
1995	Jean Luc Lang and Jean-Francois Libert – Alcatel Submarine Network; David I. Curtis and Peter Worthington – STC Submarine Systems Ltd. – “Optical Performance of Submarine Cables in Optically Amplified High Bit Rate Systems”	Richard S. Wagman, Gregory A. Lochkovic and Kevin T. White – Siecor Corporation – “Component Optimization for Slotted Core Cables Using 8 – Fiber Ribbons”	Dr. Dan L. Philen – AT&T Bell Laboratories – “Optical Fiber for Amplified Undersea Systems”
1994	Toshio Kurashima, Kazuo Hogari, Satoshi Matsuhashi, Dr. Tsuneo Horiguchi, Dr. Yahei Koyamada and Yutaka Wakui – NTT Access Network Systems Laboratories; and Hiroshi Hirano – NTT Technical Assistance & Support Center – “Measurement of Distributed Strain in Frozen Cables and Its Potential for Use in Predicting Cable Failure”	Dr. Sverker Forsberg – Swedish University of Agricultural Sciences; and Jan Björkman – Telia AB – “Release of Lead from Lead – Sheathed Telecom Cables in Soil”	Barry J. Keon – Telstra – “The Effects of Optical Fiber Coating and Ink Materials on the Corrosion of the Glass Surface”

Year	Jack Spergel Memorial Award for Outstanding Technical Paper	Outstanding Poster Paper	Kitts-Kingsley Award for Best Presentation
1993	Dr. Yoshinori Namihira and Toshio Kawazawa – KDD R&D Laboratories; and Naoki Norimatsu – KDD Company, Limited – “PMD Reduction of Optical Fiber Cables for Transoceanic Optical Amplifier Submarine Cable Systems”	Willem Griffioen – PTT Research – “Mechanical Lifetime of Optical Fibers”	Timothy S. Dougherty – AT&T Network Cable Systems – “The Temperature of Aerial Plant and Its Effect Upon Foam – Skin Insulation Life” and Wolfgang Wenski – Kabelmetal Electro GmbH – “First Large Scale FITL Installation: Experience From Opal '93”
1992	Nathan E. Hardwick III and Kris Kathiresan – AT&T Bell Laboratories and J. G. Hartley – Georgia Institute of Technology – “Analysis of Fiber Optic Cable Design Conditions in Vicinity of Steam Lines – Ruptured and Pristine”	Svend Hopland and Albert Klykken – Norwegian Telecom – “Installation of Submarine Fiberoptic Cables in Rugged Coastal Terrain”	Peter Latoszynski – Telecom Australia – “Development of Co – Extruded Polyethylene/Polyamide 12 Insect Resistant Telecommunications Cable”
1991	Shigeru Tomita, Michito Matsumoto, Tetsuro Yabuta and Takuya Uenoya – NTT – “Preliminary Research into Ultra High Density and High Count Optical Fiber Cables”	G. Scott Glaesemann – Corning Inc. – “The Effect of Proof Testing on the Minimum Strength of Optical Fiber”	Sue V. Wolfe – STC Submarine Systems – “Structure and High Voltage DC Behaviour of Submarine Cable Mouldings”
1990	Trevor N. Bowmer, Russell J. Miner, Irene M. Plitz, Joseph N. D'Amico and Lal M. Hore – Bellcore – “Thermal Stability Tests for Polyolefin Insulations”	Steve Lischynsky, Helmut Lukas, Robin McIntyre and Grant Pacey – Bell – Northern Research Ltd. – “New Technology for a Single Mode Mechanical Splice”	Harold W. Friesen – AT&T Bell Laboratories – “An Improved Characteristic Impedance Measurement Technique”
1989	Michel Plasse, Lise Desroches and Paul – Andre Guilbert – Northern Telecom Canada Limited – “High Performance Twisted – Pair Cable for LAN Systems”	Werner Bernard and Susan C. Grant – Siecor Corporation – “Fiber Optic Drop Cables in the Subscriber Loop”	Michel de Vecchis – Les Cables de Lyon – “Results on a Large Scale Installation of a Fibre Optic Distribution Network”
1988	Martin C. Light Jr., James A. Moses, Mark A. Sigmon and Christopher A. Story – Siecor Corp. – “Design and Performance of Telecommunication Cable Optimized for Low Fiber Count”	Dr. R. Raman – Contel Laboratories – “Loss at Dissimilar Fiber Splices”	Janice B. Haber – AT&T Laboratories – “Single – Mode Media and Apparatus for Fiber to the Home”
1987	Stephen B. Pierce – Conel Laboratories – “Digital Transmission on Customer Premises Wiring”	William Wood – Bell Communication Research – “Performance Analysis of Optic Fiber Cleavers”	Richard Rossi – General Cable Company – “Cable Sheathing Design and Performance Criteria”

Year	Outstanding Technical Papers	Best Presentations
1986	Simon D. Dadakarides and Bruce B. Lusignam, Stanford University – “Magnetically Loaded Cables”	Dave Fischer, Superior Cable Corp. – “Progress Towards the Development of Lighting Test for Telecommunication Cables” John C. Chamberlain, Siecor Corp. – “Zero Halogen Fire Retardant Fiber Optic Shipboard Cable”
1985	James A. Krabec and John W. Kincaid, Jr., Belden Technical Research Center – “Advances in the Optimization of Multi – Layer Shield Design”	Stephen Hornung, British Telecom Research Laboratories – “Manufacture and Performance of Fibre Units for Installation by The Viscous Drag of Air”
1984	M. Fujise and Y. Iwamoto, KDD Research & Development Laboratories, Tokyo, Japan – “Self-Core-Alignment Arc-Fusion Splicer Based on a Simple Local Monitoring Method”	William E. Dennis, Dow Corning Corporation, Midland, Michigan – “Hydrogen Evolving Tendencies of Cable Fillers and Optical Fiber Coatings”
1983	V. A. Fentress, Raychem Corp. and D. V. Nelson, Stanford University – “Fracture Mechanics Evaluation of the Static Fatigue Life of Optical Fibers in Bending”	J. R. Bury, Standard Telecommunication Laboratories, Ltd., Hailow, England – “Development of Flame Retardant, Low Aggressivity Cables”
1982	R. H. Whiteley, Raychem Ltd. – “A Comprehensive Small Scale Smoke Test”	A. Yoshizawa, The Furukawa Electric Co., Ltd. – “Structure and Characteristics of Cables for Robots”

Year	Outstanding Technical Papers	Best Presentations
1981	C. J. Arroyo, N. J. Cogelia, Bell Laboratories, and B. J. Darsey, Western Electric – “Thermal Behavior of Experimental Plenum Cable Sheaths Determined in a Radiant Heat Chamber”	G. S. Anderson, Belden Corporation – “Installation of Fiber Optic Cable on 457 Meter Tower”
1980	P. Kish and Y. BeBorgne, Northern Telecom Canada Limited, Montreal, Canada – “General Crosstalk Model for Paired Communication Cables”	J. J. Refi, Bell Laboratories – “Mean Power Sum Far – End Crosstalk of PIC Cables as a Function of Average Twist Helix Angle”
1979	S. Masaki, Y. Yamazaki and T. Ideguchi, Nippon Telegraph and Telephone Public Corporation, Japan – “New Aluminum Sheath Cable Used for Electromagnetic Shielding”	I. Wadehra, IBM Corporation – “Performance of Polyvinyl Chloride Communication Cables in Modified Steiner Tunnel Test”
1978	F. Suzuki, S. Sato, A. Mori and Y. Suzuki; Sumitomo Electric Industries, Ltd., Japan – “Microcoaxial Cables Insulated with Highly Expanded Polyethylene By Chemical Blowing Method”	Richard C. Mondello, Bell Labs. – “Design and Manufacture of an Experimental Lightguide Cable for Undersea Transmission Systems”
1977	T. K. McManus, Northern Telecom Canada Ltd. and R. Beveridge, Saskatchewan Telecommunications, Canada – “A New Generation of Filled Core Cable”	William L. Schmacher, AMP Inc. – “Design Considerations for Single Fiber Connector”
1976	N. J. Cogelia, Bell Telephone Laboratories and G. K. Lavoie and J. F. Glahn, US Department of Interior – “Rodent Biting Pressure and Chemical Action and Their Effects on Wire and Cable Sheath”	Michael DeLucia, Naval Ship Research and Development– “Highly Fire – Retardant Navy Shipboard Cable”
1975	T. S. Choo, Dow Chemical U.S.A. – “Corrosion Studies on Shielding Materials for Underground Telephone Cables”	J. E. Wimsey, United States Air Force – “The Bare Base Electrical Systems”
1974	D. Doty, AMP Inc. – “Mass Wire Insulation Displacing Termination of Flat Cable”	G. H. Webster, Bell Laboratories – “Material Savings by Design in Exchange and Trunk Telephone Cable”
1973	Dr. H. Martin, Kabelmetal – “High Power Radio Frequency Coaxial Cables, Their Design and Rating”	R. J. Oakley, Northern Electric Co., Ltd. – “A Study Into Paired Cable Crosstalk”
1972	J. B. Howard, Bell Laboratories – “Stabilization Problems with Low Density Polyethylene Insulations”	S. Kaufman, Bell Laboratories – “Reclamation of Water – Logged Buried PIC Telephone Cable”
1971	R. Lyenger, R. McClean and T. McManus, Bell Northern Research – “An Advanced Multi – Unit Coaxial Cable for Toll PCM Systems”	S. Nordblad, Telefonaktiebolaget L. M. Ericsson – “Multi – Paired Cable of Nonlayer Design for Low Capacitance Unbalance Telecommunications Network” N. Kojima, Nippon Telegraph and Telephone – “New Type Paired Cable for High Speed PCM Transmission”
1970	D. E. Setzer and A. S. Windeler, Bell Laboratories – “A Low Capacitance Cable for the T2 Digital Transmission Line”	Dr. O. Leuchs, Kable and Metalwerke – “A New Self Extinguishing Hydrogen Chloride Binding PVC Jacketing Compound for Cables”
1969	J. P. McCann, R. Sabia and B. Wargotz, Bell Laboratories – “Characterization of Filler and Insulation in Waterproof Cable”	J. D. Kirk, Alberta Government Telephones– “Progress and Pitfalls of Rural Buried Cable”
1968	H. Lubars and J. A. Olszewski, General Cable Corp. – “Analysis of Structural Return Loss in CATV Coaxial Cable”	N. Dean, B.I.C.C.– “The Development of Fully Filled Cables for Distribution Network”

51st GOLD SUSTAINING CONTRIBUTORS

3M/Dyneon
6744 33rd St No
Oakdale, MN 55128

AlphaGary Corporation
170 Pioneer Drive
Leominster, MA 01453

Cary Compounds, LLC
5 Nicholas Court
Dayton, NJ 08810

Daikin America
20 Olympic Drive
Orangeburg, NY 10962

Fibercore Jena AG
1M Semmicht 1
07751 Jenna
Germany

Fusion UV Systems, Inc.
910 Clopper Road
Gaithersburg, MD 20878

Hitachi Cable, Ltd.
Otemachi Building, 6-1
Otemachi 1-chome
Chiyoda-ku Tokyo 100-8166
Japan

NEPTCO, Inc
30 Hamlet Street
Pawtucket, RI 02861

OFS Brightwave
2000 NE Expressway
Norcross, GA 30071

The Stewart Group
2311-F Distribution Center Drive
Charlotte, NC 28269-4269

T & T Marketing, Inc.
PO Box 120
Allamuchy, NJ 07820

Teijin Twaron USA, Inc.
801-F Blacklawn Road
Conyers, GA 30012

Teknor Apex Company
505 Central Avenue
Pawtucket, RI 02861

UBE Industries, Ltd.
Seavans North Bldg., 1-2-1
Shibaura, Minato-ku
Tokyo, 105-8449
Japan

50th Anniversary Sponsors



Diamond Benefactor

AlphaGary Corp.

Ruby Benefactors

The Dow Chemical Company
DSM Desotech Inc.

Emerald Benefactors

Alcatel Optical Fiber Division
Corning Cable Systems
Corning Inc., Opto-Electronics Group
Equistar Chemicals, LP
Heraeus Tenevo Inc.
Lucent Technologies / Optical Fiber Solutions
Pirelli Communications Cables and Systems NA
Fitel Lucent Technologies
CommScope
Ericsson Cables AB
DuPont Teflon®

Sapphire Benefactors

Borden Chemical, Inc.
Dätwyler Inc.
Degussa AG
Furukawa Industrial S.A.
Nextrom

Benefactors

Nippon Telegraph & Telephone Corp.
Borealis Compounds LLC
Fujikura Limited
The Furukawa Electric Co., Ltd.
Sumitomo Electric Industries, Ltd.
Ciba Specialty Chemicals Corp.
Draka Comteq – Draka Fibre Technology BV
FiberCore Jena GmbH
TyCom (US) Inc.

51st IWCS Sponsors

CommScope Inc.

1100 CommScope Place SE
Hickory, NC 28602

Draka Comteq

PO Box 1442
Eindhoven 5602 BK
The Netherlands

Equistar Chemicals, LP

One Houston Center
1221 McKinney Street, Suite 700
Houston, TX 77252-2583

Nippon Telegraph & Telephone Corporation

1-7-1 Hanabatake
Tsukuba, Ibaraki 305-0805
Japan

51ST IWCS/FOCUS

STAFF

ELMER F. GODWIN
(CEO/Director)

IWCS, Inc.
174 Main Street
Eatontown, NJ 07724
Tel: +1-732-389-0990
Fax: +1-732-389-0991
Email: admin@iwcs.org

RAYMOND P. ZIRKLE
(CEO's Assistant)

Wire & Cable Technology Int'l
107 Mill Plain Rd, Suite 304
Danbury, CT 06811
Tel: +1-203-743-3445
Fax: +1-203-743-4810
Email: rzirkle@bzsales.com

IRVING KOLODNY
(CEO's Assistant)

31 Maple Run Drive
Jericho, NY 11753
Tel & Fax: +1-516-932-0699
Email: ikolodny@msn.com

M. EDWARD FENTON
(CEO's Assistant)

Wire & Cable Clubs/Fenton Group, Inc.
28 Old Common
Wethersfield, CT 06109
Tel: +1-860-721-1292
Fax: +1-860-257-4845
Email: fentongrp@snet.net

MICHAEL A. DELUCIA
(CEO's Assistant)

1776 Crofton Parkway
Crofton, MD 21114
Tel & Fax: +1-410-721-5588
Email: mdelucia@iwcs.org

PATRICIA HUDAK
(Office Administrator)

IWCS, Inc.
174 Main Street
Eatontown, NJ 07724
Tel: +1-732-389-0990
Fax: +1-732-389-0991
Email: admin@iwcs.org

CHARRON WISHNICK
(Administrative Assistant)

IWCS, Inc.
174 Main Street
Eatontown, NJ 07724
Tel: +1-732-389-0990
Fax: +1-732-389-0991
Email: wishnickc@iwcs.org

BOARD OF DIRECTORS

DIETER S. NORDMANN
(Chairman)

Alcatel Contracting
P.O. Box 160; Kabelkamp 20
D30179 Hannover, Germany
Tel: +49-5139-894710
Fax: +49-5139-894111
Email: Norddieter@aol.com

MANUEL R. SANTANA
(Vice-Chairman)

OFS BrightWave
2000 NE Expressway; Rm 1D32
Norcross, GA 30071
Tel: +1-770-798-2754
Fax: +1-770-798-4654
Email: msantana@ofsoptics.com
Email: mrsantana@mindspring.com

HANS A. MAYER
Engineering Consultant

8 Hilton Street
Beaumaris, VIC 3193
Melbourne, Australia
Tel: +61-3-9589-5120
Fax: +61-3-9589-5115
Email: hmayer@compco.com.au

NILS ARTLÖVE

Telia International Carrier
123 86 Farsta
Sweden
Tel: +46-8-713-1212
Fax: +46-70-618-1313
Email: nils.artlove@teliacarrier.com

DAVE FALLOWFIELD

TELUS Communications Inc.
Telus Plaza South, Floor 11
10020 100 Street
Edmonton, Alberta
Canada T5J 0N5
Tel: +1-780-493-4928
Fax: +1-780-424-8312
Email: david.fallowfield@telus.com

JAMES R. LEECH
(Secretary/Treasurer)

The Dow Chemical Co.
1 Riverview Drive
Somerset, NJ 08873
Tel: +1-732-271-7935
Fax: +1-732-271-7949
Email: leechjr@dow.com

DR. PETER R. BARK

Coming Cable Systems
PO Box 489
Hickory, NC 28603
Tel: +1-828-901-6205
Fax: +1-828-901-6264
Email: peter.bark@coming.com

JOHN R. SICOTTE

Coming International K.K.
No. 35, Kowa Bldg., 3F
1-14-14 Akasaka, Minato-ku
Tokyo, 107-0052 Japan
Tel: +81-3-3586-5002
Fax: +81-3-3224-1405
Email: sicottejr@coming.com

SYMPOSIUM COMMITTEE OFFICERS

JAMES REESE

(Chairman)

DSM Desotech Inc.
1122 St. Charles Street
Elgin, IL 60120-8498
Tel: +1-847-468-7720
Fax: +1-847-468-7785
Email: James.Reese@dsm.com

BERNARD J. CROSS II

(Vice-Chairman)

SBC Southwestern Bell
1500 Preston Forrest Sq, 2nd Fl.
Dallas, TX 75230
Tel: +1-972-960-4906
Fax: +1-972-960-8161
Email: bc6024@txmail.sbc.com

XAVIER MANN

(Secretary)

OFS

2000 NE Expressway; Suite C035
Norcross, GA 30071
Tel: +1-770-798-3910
Fax: +1-770-798-3950
Email: xmann@ofsoptics.com

SYMPOSIUM COMMITTEE MEMBERS

DR. C. BERTIL ARVIDSSON

Ericsson Network Technologies AB
SE-824 82 Hudiksvall, Sweden
Tel: +46-650-352-58
Fax: +46-650-360-64
Email: bertil.arvidsson@eca.ericsson.se

RUSSELL S. DANIELS

Equistar Chemicals, LP
One Houston Center
1221 McKinney Street
PO Box 2583
Houston, TX 77252-2583
Tel: +1-713-309-4962
Fax: +1-713-309-2336
Email: Russell.daniels@equistarchem.com

HÉLIO J. DURIGAN

Furukawa Industrial S.A. Produtos
Elétricos
Rua Hasdrubal Bellegard, 820
81450-140
Curitiba - PR - Brazil
Tel: +55-41-341-4085
Fax: +55-41-341-4046
Email: hdurigan@furukawa.com.br

CHARLES A. GLEW

Cable Components Engineering
42 Garvey Road
Framingham, MA 01701
Tel: +1-508-877-4095
Fax: +1-508-877-8845
Email: cglew@cablecomponents.com

JOHN N. KESSLER

KMI Corporation
c/o OCC
22 Farewell Street
Newport, RI 02840
Tel: +1-401-845-0500
Fax: +1-401-848-5705
Email: johnnkessler@cox.net

DAVID B. KIDD00

AlphaGary Corporation
8 Patricia Lane
Sparta, NJ 07871
Tel: +1-973-729-5450
Fax: +1-973-729-5102
Email: dkiddoo@alphagary.com

AGUSTI VALLS PRATS

Pirelli Cavi e Sistemi, SpA
Viale Sarca n. 222
Milan 20126, Italy
Tel: +39-2-6442-7830
Fax: +39-2-6442-5086
Email: agusti.valls@pirelli.com

CAMILLE J. RECHEL

Borden Chemical, Inc
630 Glendale Milford Road
Cincinnati, OH 45215
Tel: +1-513-782-6278
Fax: +1-513-782-6326
Email: rechelcj@bordenchem.com

JOHN R. SACH

Pirelli Communications Cables &
Systems NA
710 Industrial Drive
Lexington, SC 29072
Tel: +1-803-951-4020
Fax: +1-803-951-4044
Email: John.Sach@us.pirelli.com

DR. HOWARD WICHANSKY

Cdr, US Army CECOM
ATTN: AMSEL-RD-ST-WL-AW
Fort Monmouth, NJ 07703-5203
Tel: +1-732-427-4713
Fax: +1-732-427-2150
Email: howard.wichansky@mail1.monmouth.army.mil

FREDERIC N. WILKENLOH

CommScope, Inc.
1100 CommScope Place SE
Hickory, NC 28603-1729
Tel: +1-828-323-4823
Fax: +1-828-323-4854
Email: wlknl@commscope.com

HIROSHI YOKOTA

Sumitomo Electric Industries, Ltd.
Yokohama Research Laboratories
1 Taya-cho, Sakae-ku
Yokohama 244-8588, Japan
Tel: +81-45-853-7172
Fax: +81-45-851-1565
Email: yokota-hiroshi@sei.co.jp

OPENING SPEAKERS



Dieter S. Nordmann
Chairman,
IWCS/Focus Board of
Directors
Alcatel Contracting
Hannover, Germany
Nord Dieter@aol.com

Dieter S. Nordmann holds Diploma Engineering degrees of the Technical Universities of Dresden/Mittweida and Braunschweig in Telecommunications and Electrical Power Engineering.

Dieter has served in various management and board functions of the GHH Group in Germany and for Alcatel in Europe and Overseas. He is a member of various supervisory boards of German based Corporations.

Dieter has been a member of the IWCS/Focus Committee/Board since 1991 and is currently the Chairman of the BOD.

He has been married to his wife Margret for 34 years and they have a son Michael A. age 32. Dieter is engaged in politics and is a very eager golfer and is currently President of one of the leading Golf Clubs in Germany.



James Reese
Chairman,
IWCS/Focus Symposium
Committee
DSM Desotech,
Incorporated
Elgin, IL
James.Reese@dsm.com

Jim Reese is currently Regional Business Manager-Americas for DSM Desotech. He has held various positions within DSM in technology, sales and marketing since 1970. Jim earned his B.S. degree in Biochemistry from the University of Colorado and his MBA from Northern Illinois University. He is currently President of RadTech International, an association for Ultraviolet (UV) Cure Technology and Chair of the IWCS Conference Committee. Jim lives in Arlington Heights, IL with his wife and daughter.



David B. Kiddoo
Chairman,
IWCS/Focus Plenary
Session
AlphaGary Corporation
Sparta, NJ
dkiddoo@alphagary.com

as product development. Before joining AlphaGary, David was the W&C Marketing Manager for Ausimont USA, with responsibility for HALAR fluoropolymer insulations and sheaths. David also has had 11 years of experience with the Du Pont Company in Manufacturing, Technical Service, Market/Product Development, and Sales of W&C materials. His product focus at Du Pont was TEFLON and TEFZEL fluoropolymers as well as KAPTON polyimide films for the communications and aerospace cable market.

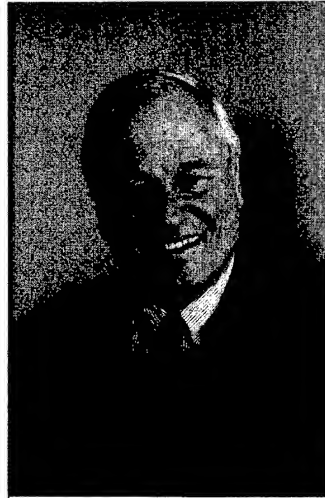
David B. Kiddoo of Sparta, New Jersey, USA, is the Global Business Manager for Wire and Cable insulation and sheathing products at AlphaGary Corp.. AlphaGary Corp. has manufacturing facilities in Massachusetts (USA), North Carolina (USA), Ontario (Canada), and Melton Mowbray (England).

David concentrates on strategic business planning, evolving W&C industry standards, as well

David is a graduate of Bucknell University in Lewisburg, PA with a degree in Chemical Engineering. He is active in various trade organizations, including the Underwriters Laboratories Technical Advisory Panel on Communications Cable (UL TAPCOM), the Vinyl Institute of the American Plastics Council (VI / APC), the National Electrical Manufacturing Association (NEMA), the American Society for Testing and Materials (ASTM), the Society of Automotive Engineers (SAE), the National Fire Protection Association (NFPA), the Fire Protection Research Foundation (FPRF) and Building Industry Consulting Services International (BICSI). He is a member of the Premise Wiring Committee of the Telecommunications Industry Assoc. (TIA/EIA).

PLENARY SESSION

"Services and Performance Certification in a Global Environment"



Loring W. Knoblauch
President & Chief Executive Officer
Underwriters Laboratories Incorporated
Northbrook, IL

Loring W. Knoblauch is Underwriters Laboratories' (UL) ninth President and CEO with two "firsts" to his credit, the first president from outside the company, and its first non-engineering president. He comes to UL with a world-class track record, having run nine different companies in the high technology and manufacturing sectors. His most recent position was President and CEO of Detroit-based Talon Automated Equipment Company, an international industrial processing equipment company.

Prior to that, Mr. Knoblauch served as President, International for Hubbell, a \$2 billion a year, New York Stock Exchange (NYSE)-listed electrical products manufacturer. Most notable, however, was Knoblauch's 20-year career with Honeywell International, where he ran seven different businesses, including a six-year stint in Hong Kong as President of Honeywell's \$2 billion a year Asia Pacific Region. Mr. Knoblauch has established and/or run nine international joint ventures in China, India, Japan, Korea, Malaysia and Brazil.

He has been a member of the Bemis Company's Board of Directors for nine years. (Bemis, which is NYSE-listed, is the world's leader in flexible packaging.)

Most recently, Mr. Knoblauch has been honored to serve on the Board of Directors for the Electrical Safety Foundation International (formerly the National Electrical Safety Foundation). ESFI is the only organization exclusively devoted to promoting electrical safety in the home, school and workplace through education and public awareness.

Knoblauch holds a Bachelor of Arts degree from Yale University, a law degree from Harvard University, and was a Sloan Fellow at Stanford's Sloan School of International Business.

On a more personal note, Mr. Knoblauch has been married for 37 years to his wife, Carol Elnicky Knoblauch. They have one son, Loring, Jr., age 32, and one grandson, age 2.

Mr. Knoblauch is a proactive supporter of the arts, and is currently a Life Trustee of Opera Colorado.

Technology Forecasting Techniques in Communications

Alistair P. Duffy

School of Engineering and Technology
De Montfort University
The Gateway, Leicester, UK.
+44 116 257 7056 apd@dmu.ac.uk

Kenneth G. Hodge

Brand-Rex Ltd.
Viewfield Industrial Estate
Glenrothes, Fife, Scotland

Arthur J. Willis

Abstract

The desire to know "what the future holds" is an holy Grail for both corporate and technology strategy development. While jumps in technology are frequently, apparently, random and only monitoring weak signals in the environmental analysis can provide an insight into what may happen and when, prediction of developments in current technologies is a prime interest of technology forecasting. There are several techniques available to undertake this analysis and, while many of them are used to some extent, others are generally not. Some key techniques include Trend-line analysis, Fisher-Pry analysis and Gompertz analysis. One significant issue is the accuracy of these models, particularly in relation to projection from early data, and, hence, their usability for strategic information. Examples for this include applying poor parameter selection for Fisher-Pry and Gompertz analyses, leading to unrealistic assumptions about saturation values. This paper reviews these, and other, techniques and discusses a number of issues related to the relationship between forecasting and knowledge management and the suitability and the applicability of some of these techniques to the communications industry.

Keywords

Forecasting; S-curve; knowledge management; Fisher-Pry; Gompertz

1. Introduction

Could the impact of the events of 11th September 2001 and/or the global telecoms downturn have been better predicted? Could more companies have been better placed to cope with the effects of these factors? Despite a number of indications that something 'big' would happen in the USA, the nature and effects of the atrocities could probably only have been considered as wild speculation. Perhaps transport related companies could have based a scenario on "What if something happens that reduces peoples desire to travel?" and they could have prepared better but would it have been feasible to consider the effects of something that would have a dire impact on general business confidence which then impacts on the communications business?

Scenario analysis emerged in the 1960s and has been used to great effect by many companies. One of the most popular examples of companies using these is Shell [1,2], who, in the 1960s looked at the unpredictability of oil prices and as a result were well placed to survive the oil crisis in the 1970s. Further, in the 1980s, they looked at what would happen if a virtual unknown (Mr Gorbachev) came to power. It has been suggested [3] that most

companies only look at one scenario, the official future, but development of a variety of scenarios can help to develop managers' mental maps about the future. Clearly, scenarios need a significant basis in qualitative information but backed by quantitative information where possible.

Some aspects feeding into scenario development are inherently more predictable. 'More predictable' in this case meaning 'less uncertain'. For example, perhaps the global communications slowdown was more predictable. If we accept that all growth has limits and products and markets go through periods of slow introduction, rapid adoption and slow decline, limits both in volume and times can be placed on current technologies and markets. The S-curve is the basis of many forecasts using quantitative data. This paper addresses some aspects of forecast generation using S-curve extrapolation.

One significant aspect of forecasting is that the act of undertaking the forecast, or creation of the scenarios, unlocks knowledge held within the organization and available to the organization, and creates new knowledge. Benefits of this can be felt in a number of areas. For example:

- Corporate and technology strategy. A current trend in strategy is the development of a sustainable competitive advantage based on the capabilities leveraged from organizational resources [4]. Knowledge is a key intangible resource.
- Organisational change. The culture of an organization, the way it does things, is a complex interplay of many factors such as management structure and stories and myths [5]. Knowledge and communication are embedded in the culture, so by managing the process of knowledge creation and sharing differently, the culture of the organization can start to change and with cultural change comes scope for organizational change [6].

While forecasts based on 'market data' can feed into the development of scenarios, extrapolation techniques do have a major role to play in the planning for individual products or sections within a company. This paper looks specifically at extrapolation techniques, and notably Fisher-Pry and Gompertz analyses: it being frequently commented on that these are not as widely used as they could be. The paper first looks at the relationship between knowledge management and forecasting, it then puts the extrapolation techniques into context by overviewing a number of related and complementary forecasting techniques. Finally, a number of examples are drawn from the literature, which illustrate their use, issues related to errors are also discussed.

2. Knowledge Management and Forecasting

2.1 Forecasting and knowledge

Knowledge management is an emerging management topic and more companies are now treating knowledge as a key organizational resource. Forecasting requires both the accessing of knowledge that exists and the creation of new knowledge. As the process of forecasting requires the collection and generation of data, and implies that decisions need to be made based on the knowledge, it is helpful to consider the relation between data and knowledge. One useful visualization was presented by Amidon and Skyrme [7] which transposes neatly to the forecasting process:

- Data are the observations made. Clearly these are the facts and figures collected.
- Information can be thought of as data with context. The data is organized.
- Knowledge is the information with meaning. The forecast is made
- Wisdom is knowledge with insight. Decisions are made based on the forecast.

The introduction discussed the benefit of forecasting in accessing organizational knowledge and the effects on organizational culture. There are two factors here that have a bearing on this. The first is the relationship of tacit and explicit knowledge of individuals and groups and the second is whether the organization can, itself, possess knowledge.

Cook and Brown [8] suggested that individuals and groups possess both tacit knowledge and explicit knowledge. The combination of these four types of knowledge come together to fuel the work that is done. Cook and Brown refer to this as Knowing in Action and the interplay of the knowledge types as a generative dance and that while knowledge cannot be converted from one form to another, one type can be created from another. Figure 1 illustrates these epistemologies.

	Individual	Group
Explicit	Concepts: <i>e.g. rules, equations, observations</i>	Stories <i>e.g. success stories, shared phrases which have useful meaning</i>
Tacit	Skills <i>e.g. making use of the concepts</i>	Genres <i>e.g. shared understanding about how things are done</i>

Figure 1 Relational epistemologies

From the standpoint of creating a forecast, individuals may know how to create a questionnaire or they may know equations for some of the trend analyses techniques ("Concepts"), but some will be better able than others to implement these ("Skills"). The group working on the forecast development may share knowledge about previous forecasts ("Stories") and share a certain way of carrying out various meetings and interviews ("Genres").

Together, these dictate the process by which the forecast is created.

Knowledge of individuals and groups, whether tacit or explicit, leads onto the question of where knowledge in an organization is held. The concept of organizational memory is generally vague and confused [9]. However, one of the most widely acknowledged views [10] suggest that there are a number of aspects which contain the acquisition and retention of knowledge, these are:

- The individual memory and personal files
- The organizational culture, such as stories or shared frameworks
- The logic embedded in the transformations from inputs to outputs.
- The roles within an organization as a repository for information storage
- The ecology of the workplace.

While the approach used here does not clearly embody the information systems related repositories, it does reinforce the relationship between individuals and groups and the fact that knowledge creation and sharing is an interplay of many directly and indirectly related factors.

Success of many organizational strategies depends on the identification of weak signals – the hints that suggest what may happen. Identification of these signals may provide an organization with valuable intelligence providing opportunity for competitive advantage over the competition. Weak signals, as their name suggests, could possibly be missed in the background noise (unlike strong signals which encourages companies to take the same sorts of actions: "shoaling"). In order to identify these weak signals early enough to be able to act on them, the factors of both Figure 1 and the organizational memory need to be managed to encourage pooling of, for example, environmental, political, technical and social factors (STEP analysis and its variants). Such approaches may involve encouraging communities of practice, learning networks or simply introducing forms of rewards for sharing this information [11].

This section has attempted to provide some organizational knowledge context for forecasting and the process of undertaking them. The next sections look at the more practical aspects of forecasts.

2.2 Elements of a forecast

Twiss [12] suggests that the forecasting process can be regarded as a means of transforming inputs (in the form of assumptions, data, insight and judgment) to outputs (in the form of qualitative and quantitative data, given a time reference and with the levels of uncertainty acknowledged). The inputs have a clear relevance to the elements of figure 1, particularly in understanding (knowing) the potential deficiencies in input data or the weighting to place on certain qualitative factors.

The next section looks at a number of forecasting typologies and develops further the analysis of the Fisher-Pry and Gompertz approaches.

3. Forecasting Typologies

This section reviews a number of forecasting techniques. There are a number of texts that discuss these in more detail; for example [12, 13, 14, 15]. While various authors and forecasters may categorise the techniques differently, the techniques discussed in this paper are split into Exploratory and Normative techniques, in the manner of [12]. Exploratory techniques project past data into the future, such as technological progress or market penetration. Normative techniques use expert opinion to determine the feasibility of particular options. Whilst perhaps an oversimplification, exploratory techniques can be thought of as being ostensibly quantitative and normative techniques as being ostensibly qualitative.

3.1 Exploratory techniques

The concept of lifecycles, whether industry or product, is embedded in corporate psyche. With time and investment, some parameter being monitored will grow, initially, at an exponential rate and the rate of growth will decline at a decaying exponential rate until a technical, physical or economic limit is reached. In marketing terms this is a concept that may encourage investment or marketing mix modification decisions. Technically, the limit may be determined by the physics of a particular device; nevertheless, the S-curve concept then encourages informed decisions about alternative investment opportunities.

Identifying new technologies and their growth can be assisted by precursor trend analysis. Typically scientific paper or patent monitoring can provide valuable insight into competitor technology

The basic exponential curve is the Pearl curve, given by the formula

$$y = \frac{L}{1 + ae^{-bt}} \quad (1)$$

where y is the value of the parameter being monitored, such as market penetration or bit-rate, L is the maximum value of the parameter y , a and b are parameters which determine the shape of the curve. It does not account for step changes in technology nor investment (Twiss [12] makes the point that investment, rather than time, is the key to technological development). This curve can readily be converted to a straight line (in log-lin format) and linear regression used to project the data, for example, using Excel spreadsheets. Sources of error in the Pearl curve involve the uncertainty associated with both the time and value measurements for the initial observations (most observations should be treated as probability clouds than exact points). While L , a and b can be determined with reasonable accuracy from at least three independent measurements, they are limited by the accuracy of the initial observations.

The maturity of one technology often leads to the substitution by another technology. In the case where this newer technology offers a technical superiority over the older technology it will be

bought/implemented for this reason. One particularly successful approach to quantifying this was proposed by Fisher and Pry [16] who looked at the rate of substitution. The equation they proposed is:

$$\frac{f}{1-f} = ae^{bt} \quad (2)$$

The relationship between equation 2 and the Pearl curve of equation 1 are clear (they are functionally the same). In this case, f represents the proportion of substitution at the observation time.

Projections based on small amounts of data ($f = 0.01$ [14] and $f = 0.05$ [12]) are claimed to produce accurate forecasts.

Where the main driver is not better technical performance but obsolescence then the model proposed by Gompertz [17] is more appropriate. While this model is based in the biological sciences, it has achieved some success in technology forecasting, particularly in consumer applications [15] where an increasing decline in substitution is seen with time. The general form of the equation is:

$$y = Le^{-e^{-b(t-a)}} \quad (3)$$

When successive substitution curves are plotted on the same axis, for the same technical parameter, it has been observed that the envelope of the resulting graph is also an S-curve. It is also possible to combine several related technologies to provide a view of the current state of the technology. The selection of the appropriate parameters to use may rely on the use of normative techniques rather than exploratory techniques.

A further, similar, curve is the learning curve. This is widely understood and relates the cost of a product or the time taken to produce a design to the number (experience) already produced.

Cyclic behaviour is also widely used in forecasting [13]. The basic time series (Kondratieff) cycle relies on the extraction of several deterministic coefficients, with varying time constants [17] such that:

$$Y = TSCI \quad (4)$$

Where Y is the observed variable, T is the trend (obtained by long term smoothing of Y), S is the seasonal variation (obtained from the de-trended observations Y/T), C is the cyclic variation (obtained from the de-trended, de-seasonalised, data by smoothing), and I is the irregular component – the noise residue.

Various statistical packages, such as SAS (Statistical Analysis System) contain a variety of similar and related techniques such as the powerful Box-Jenkins technique.

Precursor trend analysis was briefly discussed above. As well as using product and related data for this, common monitoring data comes from patent or scientific literature monitoring or organizational monitoring. One (large) organisation known to the authors has a generally close working relationship with

another (large) organisation, to the extent that there are many discussions between staff in the respective research departments. However, one indicator of a 'big push' is the fact that the labs of the second organisation become increasingly difficult to get into and staff become less communicative. This is currently the case, with staff of the first company currently speculating what this is: patent applications and scientific literature monitoring have given them a good idea about what is being prepared for launch.

3.2 Normative Techniques

Normative techniques usually concentrate on obtaining and making sense of expert opinion. Some common approaches to this are discussed in this section. Normative techniques are possibly more prone to effects of the investigator's research paradigm than exploratory techniques and acknowledgement of such is generally beneficial. The two key research paradigms are:

- **Positivistic.** Here the researcher is testing an hypothesis and assumes that the act of undertaking the research will have little impact on the results – the information exists and the researcher is uncovering this. It is closely related to the general approach used in engineering research and development. A typical positivistic approach may be to ask the question "I want to confirm or refute that increasing clock speeds of pcs drives the upper frequency of twisted pair cable"
- **Phenomenological.** This acknowledges that the researcher may influence the results of the investigation; it was developed as a reaction to the positivistic, natural science, approach where the researcher is distant and distinct from the research being undertaken. A typical phenomenological approach may be to ask the question "what factors are likely to impact on the upper frequency of twisted pair cable?"

Some of the techniques, which can be used in normative studies, are:

- **Interviews.** While interviews based on closed questions may be easier to undertake, unstructured or semi-structured interviews may be of more benefit in investigating how the interviewee has developed the view that is being discussed and, as such, enable a better understanding of the phenomena which are regarded as being significant.
- **Questionnaires.** The design of these will largely depend on the designer's research paradigm, with a positivist usually asking more closed questions. A good questionnaire will usually start with questions about the general environment and move to the specific. As with the interviews, there may be issues about sample size that need addressing in order to impart any statistical certainty on the results.
- **Nominal Group Conferencing.** This brings together a small group of experts who initially consider a problem on their own and presenting their results to the rest of the group who discuss the panel member's views after all solutions/answers have been posted, and then weight

the solutions posted by the other panel members. This technique can be particularly useful to elicit novel ideas and, when several conferences are held, with different groups, to identify strong themes.

- **Delphi surveys.** Panel approaches to identifying information can suffer from 'weak' individuals with good ideas keeping quiet or 'strong' individuals with poor ideas dominating discussions. The Delphi technique was developed to overcome some of these difficulties. A panel of experts are recruited and briefed on the problem being addressed: they will not know who the other panel members are. Their views are sought and their reply should include timescales and probabilities in order to ensure that all the experts are responding to the same question (thus avoiding perception errors). One variant of the technique requires the respondents whose values are at the extremes of the survey to provide a reason for their responses. The results and the reasons are circulated anonymously to the whole group for them to revise their initial responses if necessary. The final responses are then analysed and circulated. Consensus may suggest a course of action, but so to does a lack of consensus, indicating that further research or analysis may be required before a decision is taken.
- **Relevance trees.** These start with a desired objective and work back to the projects which can be undertaken, or the factors which need to be present, in order for this objective to be realized.
- **Morphological analysis.** This is a technique, which encourages the identification of alternative technical objectives to a current or planned system. It does this by creating a grid in which the key features of the system are listed in a column and rows are created which list possibly ways of achieving each single objective. The matrix is then scanned for new permutations of solutions to the main features and each of these is then analysed for feasibility.
- **Impact analysis.** Panel based impact analysis can be used to identify the effects of a technical development on the business as a whole or society in general. The process is iterative and starts with a central proposition and the immediate impact of this is noted, then the next level of impacts is identified (as a result of the first level impacts). The process may be repeated until a range of impacts has been identified. This can be particularly helpful in analyzing scenarios. Cross-impact analysis takes a more introspective view of potential developments and looks to see what effect, if any, each of the possible changes will cause to each of the others

Scenarios were mentioned in the introduction as a powerful tool to build a view of alternative futures. The knowledge-based view of the firm, combined with some of exploratory and normative techniques can be used to provide the raw material from which to create the. The use of relevance trees and impact analysis can then assist the strategic management to decide which of the

possible options are most appealing to the organization as a whole.

One important point about forecasting is that the further into the future the forecast aims to look, the more important it is to attempt to triangulate the predictions or opinions.

4. Examples

A number of examples are presented here to look at the way in which some of the exploratory techniques can be applied. In some cases, the examples have been taken from the WWW to allow easy further investigation of the approaches used.

4.1 Pearl versus exponential

Reference [14] presents the reduction in the average cell size for cellular radio systems (1st generation) using data from four years to predict the general reduction. The argument for using such an approach is that, generally, technological developments follow an exponential pattern of development. In this reference, Vanston uses the Pearl curve (equation 1) and provides the coefficients. The original data is given in table 1.

Table 1 average 'mobile' cell size approximate values from [14]

Year	Average cell size (miles)
1984	10
1985	6
1986	4.5
1987	3.5

The proposed curve fitted parameters give rise to the predictive equation:

$$y = \frac{1}{1 - 0.9e^{-0.097696t}} \quad (5)$$

This predicts an average minimum cell size of 1 mile. If, however, a simple exponential development had been assumed, the picture would be quite different and an average minimum cell size of nearly three miles would be expected. An exponential of the form of equation 6 was used with the parameters $a = 15.8$, $b = -0.81$ and $c = 2.96$

$$y = ae^{bt} + c \quad (6)$$

The implications for deployment or development strategies are clear. Figure 2 illustrates this difference projecting forward a further six years from the end of the data. The original data is included in the graph. It will be noted that the initial differences

are almost indistinguishable, whereas the differences after half a decade are significant, and potentially costly.

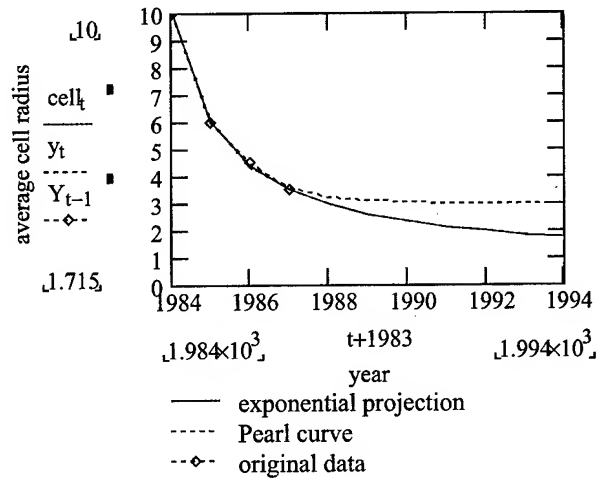


Figure 2 Comparison of Pearl curve and exponential fit to original data

While both the exponential and Pearl curves fit the early data very well, there is an expectation that the values used are precise. There will be, however, some tolerance on both the size measurements and the time value – this has not been taken into account with Figure 2. Figure 3 shows the effect of assuming a 20% tolerance on the measurement values (using the Pearl curve). The effect of this uncertainty can clearly be seen, with an average cell size limit projection of 0.81 to 1.18. More specifically, if a strategic aim depended on a cell size of, for example, 2.5 miles, the 20% tolerance on measurements would result in a time difference of approximately 3 years.

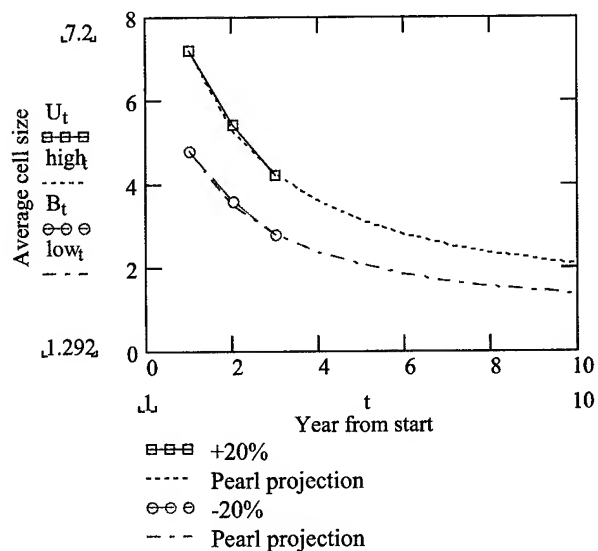


Figure 3 Illustration of the effects of tolerances in measurements.

To give some idea of the value of adopting the Pearl rather than exponential curve, a typical cell size in the mid 1990s was of the order of 1.2 miles, close to the values predicted by the Pearl curve but less than half the value predicted by exponential decay. (There is a health warning with this figure however, as it depends on geography and power, and it does not take into account any step-change developments in technology.)

4.2 Mobile phone adoptions

A study [18] looked at the rate of adoption of mobile phones in Portugal. The study noted the S-shaped adoption profile and projected that 2/3 of the population would eventually have a mobile phone. In their review of the data, they applied both Gompertz and the logistic (Pearl / Fisher-Pry) approaches. It was observed that the Gompertz approach suggested that the saturation level would be 12.5 Million mobile phones. However, the population is only 10 Million! A previous study [19] reported in [18] also used Gompertz and projected a saturation level of 13 Million subscribers. The authors of [18] suggested that the curve fitting used was assuming the data provided represented the exponential phase, whereas, in reality, the data had gone past the point of high growth. Reference [19] used a normative approach to predict that approximately 70% of the population would own a mobile phone and reference [18] used the logistic curve to reach a similar conclusion.

While the authors of [18] suggest a mathematical reason for the poor data correlation, it could be argued that the Gompertz model is philosophically ill suited to such a study (but the logistic curve is). The reason for this is that Gompertz models mortality effects better, that is, initially high growth but with a long tail-off to saturation – from a consumer perspective, people will only buy something new when their current device fails. Until recently, mobile phones were generally bought to replace others because of their improved features/size/battery/aesthetics. Such purchases are best modeled by a Fisher-Pry approach. The recent decline in the sales of new mobile phones may indicate that a Gompertz model may now be more appropriate; however, there is always the promise of the 'killer bundles' associated with third generation systems that will encourage people to update their handsets. Should this happen, the lesson from Portugal may be not to use Gompertz where purchasers are actually discarding the old for the new rather than replacing the old with the new. (One interesting forecasting exercise would be to predict the future of 3G, but this is beyond the scope of this paper).

It is interesting to note that by the end of 2001, on average, 100 people in Portugal owned 77.3 mobile phones [20]. The headline prediction of the model had clearly underestimated the ownership, however, it is not clear whether the authors of [19] had done a sensitivity analysis to provide some bounds for their projection.

4.3 Copper cable

The maximum frequency of copper communication cables was reported in [21] as following the trend shown in Figure 4. It is interesting to note the slight dog-leg in the early 1990s. However, a simple curve fit projects that 10GHz will be achieved by 2005.

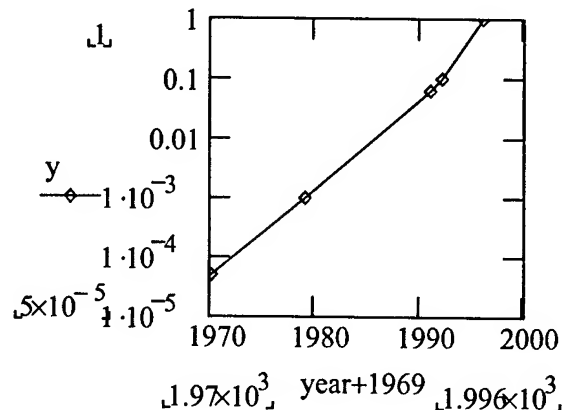


Figure 4 Copper cable maximum frequency in GHz

Adding into this data that 7GHz was possible by 2001 results in Figure 5, which includes the trend line. The implication of this is that 100GHz will be possible by 2010.

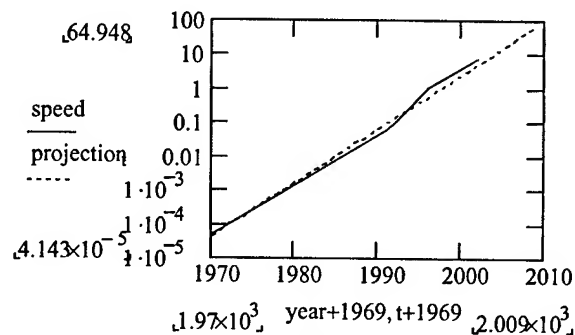


Figure 5 Trend-line extrapolation for copper cable

Figure 4 was based on the date of announcement of frequencies. Difficulties in gaining confidence in this data are primarily due to publication delays. Without original data to discuss, could the dog-leg in the early 1990s simply be due to publication difficulties?

The data used in Figure 5 was also used as the early data for both the logistic and Gompertz equations, using CurveExpert 1.3 [22]. The Gompertz approach gave the data illustrated in Figure 6, the x-axis shows the date as years from 1969. The result of this is that copper communication channels would be expected to reach approximately 850 GHz – in about 100 years time. Closer to the present day, it suggests that 40GHz will be achievable by 2010.

However, the projections being made are clearly using early data, this is evidenced from a sensitivity analysis of the last point being used (which was a clear estimate). A 20% decrease in speed leads to a 10% decrease in 2010 but a 20% increase leads to a 100% increase in 2010.

By comparison, the logistic approach suggested that the maximum copper speed will be an order of magnitude below the Gompertz projection: a clear lesson in careful application of extrapolation techniques.

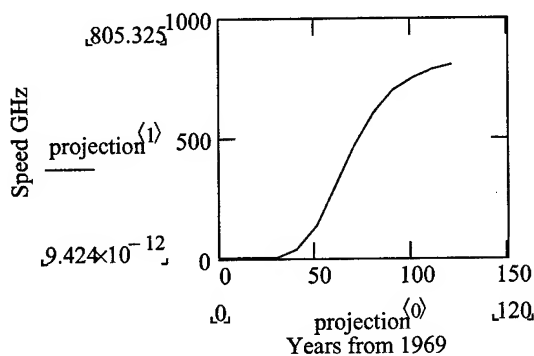


Figure 6 Gompertz projection of copper based channel speeds

Figure 7 shows the history of backbone bandwidth in Gbit/s. Superimposed on the original data are both the Gompertz and logistic curve projections.

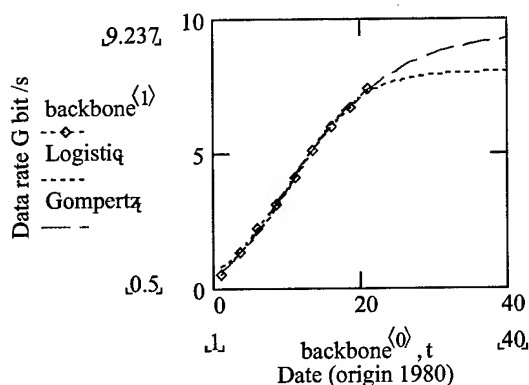


Figure 7 Projections of backbone data rate.

The Gompertz model of a saturation level of about 9.5 Gbit/s is close to the general opinion that 10Gbit/s is the backbone limit for Ethernet. The solution to higher throughput requirements will probably be to change technologies. Perhaps a key to the general accuracy of this model is that the data supplied goes beyond the 50% saturation level, so the projection is not being made from the early data

Figure 8 looks at the data for the operational frequency of twisted pair cable as a function of year of issue of the appropriate standard, the first point is category 2 and the last is category 8 with an estimated issue date of 2004. The x axis uses 1980 as the origin. This data has been used as it combines technical, economic and political factors, rather than just dealing with the technical. It is conjectured that this study may provide some indication of the future path of twisted pair. The interesting feature is the coincidence of categories 6 and 7. One way of looking at this data is that Category 6 is the end of the UTP technology and category 7 was therefore delayed in its introduction due to the debates regarding standards.

As a result of this, applying a logistic curve to categories 2 – 6 suggests that the maximum frequency of UTP cable is approximately 450MHz. This is shown in Figure 8.

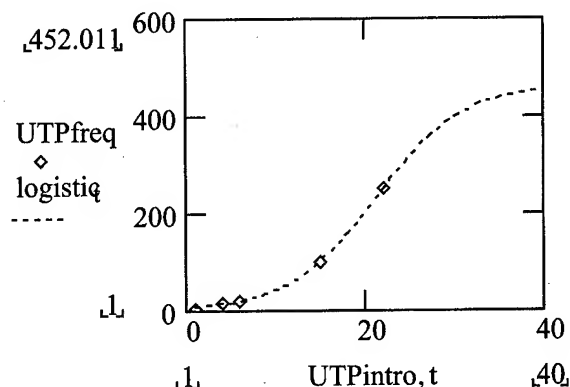


Figure 8 UTP capacity prediction based on issued standards, data rate in MHz versus years from 1980.

The data presented in Figure 7 shows the sigmoid of UTP, on top of which is the start of the sigmoid for STP. The question now is what is the projected upper frequency of STP? It was suggested earlier that the combination of sigmoids is, itself, a sigmoid. The assumption is now made that the data point for category 6 can be ignored from the envelope and that category 7 should have been introduced a couple of years earlier. With these assumptions in place, the Fisher-Pry approach suggests that the maximum shielded twisted pair frequency will be 1.5GHz and Gompertz suggests that it will be 2.6GHz. What is not clear for the purpose of this paper is the reasons for choosing which of the two models to select. Either way, a figure of the order of 2GHz would seem a reasonable estimate without a step change in the technology base.

5. Conclusions

This paper has presented a quick tour of some key forecasting techniques and has attempted to link them to a knowledge management perspective.

Examples have been presented to illustrate the operation of the techniques. While the data is generally widely available, extrapolation techniques have been used to provide additional knowledge. In some cases, the future of systems has been anticipated prior to the analysis presented in this paper, in this case, the extrapolations provide useful triangulation for the normative approaches which have identified some limits. Other cases have used more recent data to verify the performance of previous studies.

In general, the extrapolation techniques used (Fisher-Pry (logistic, Pearl) and Gompertz) have demonstrated their potential for predictions. It was suggested at the beginning of the paper that scenarios are a powerful strategic tool, and the forecasting techniques discussed in this paper can provide substantial input to these. Combining the issues on knowledge management and

forecasting itself, the following points should also be investigated where possible, or their absence acknowledged.

- Triangulation. Comparing the predictions of two or more independent forecasts provides information rather than data.
- Challenge assumptions. Identifying and acknowledging assumptions is the key to overcoming them.
- Sensitivity analysis. There will almost always be a level of approximation in the recording of both the dependent and independent variables. A sensitivity analysis can add bounds to the predicted data, which can be useful in the generation of specific forecasts, in triangulating forecasts or in creating scenarios.

6. References

- [1] G. Ringland, *Scenario Planning: Managing for the Future*, 1998, Chichester, John Wiley.
- [2] P. Schwartz, *The Art of the Long View*, 1991, New York, Doubleday.
- [3] P.J.H. Schoemaker, "Multiple scenario development: its conceptual and behavioral foundation", *Strategic Management Journal*, 1993, Vol 14, pp. 193 – 213.
- [4] R.M. Grant, *Contemporary Strategy Analysis*, 3/e, 1998, Malden, Massachusetts, Blackwell
- [5] G Johnson, "Rethinking incrementalism", *Strategic Management Journal*, 1988, Vol 9, pp 75 –91.
- [6] Y. Carlisle, "Strategic thinking and knowledge management" in *Managing Knowledge – an essential reader*, S Little, P Quintas and T Ray (eds), 2002, London, Sage.
- [7] D Skyrme and D. Amidon, *Creating the knowledge based business*, 1997, Business Intelligence, London
- [8] SDN Cook and JS Brown, "Bridging Epistemologies: the generative dance between organizational knowledge and organizational learning", in *Managing Knowledge – an essential reader*, S Little, P Quintas and T Ray (eds), 2002, London, Sage.
- [9] LJ Bannon and K Kuutti "Shifting Perspectives on Organizational Memory: from Storage to Active Remembering" in *Managing Knowledge – an essential reader*, S Little, P Quintas and T Ray (eds), 2002, London, Sage.
- [10] JP Walsh and GR Ungson, "Organizational memory", *Academy of Management Review*, 1991, Vol 16, pp 57 - 91
- [11] JB Quinn, P Anderson and S Finkelstein, "Managing Professional Intellect: Making the Most of the Best" in *Managing Knowledge – an essential reader*, S Little, P Quintas and T Ray (eds), 2002, London, Sage.
- [12] B.C. Twiss, *Forecasting for technologists and engineers: A practical guide for better decisions*, 1992, London, Peter Peregrinus.
- [13] SM Millet and EJ Honton, *A Manager's Guide to Technology Forecasting and Strategy Analysis Methods*, 1991, Columbus, Ohio, Bettelle Press
- [14] JH Vanston, *Technology Forecasting – An aid to effective technology management*, 1996, Technology Futures Inc, <http://www.tfi.com>
- [15] LK Vanston and JH Vanston, *Introduction to Technology Market Forecasting*, 1998, Technology Futures Inc, <http://www.tfi.com>
- [16] JC Fisher and RH Pry, "A Simple Substitution Model of Technological Change", *Technology Forecasting and Social Change*, 1971, Vol 3, pp. 75 – 88.
- [17] J Hussey and R Hussey, *Business Research – A practical guide for undergraduate and postgraduate students*, 1997, Basingstoke, Palgrave.
- [18] A Botelho and LC Pinto, *Has Portugal gone wireless? Looking back, Looking ahead*, 2000, Working paper series No 5/2000, Nucleo de Investigacao em Microeconomia Aplicada, Universidade do Minho. Available from http://www.ucm.es/info/icae/VjornadasTeleco/Papers/TLM_Anabela.pdf
- [19] PP Barros and N Cadima, *The impact of mobile phone diffusion on the fixed-link network*, CEPR Discussion paper no 2598, 2000, reported in [18]
- [20] Business World Internet Edition, March 25th, 2002. http://itmmatters.com.ph/news_03252002i.htm
- [21] PJ Palmer and DJ Williams, "An analysis of Technology Trends within the Electronics Industry" available from <http://www-staff.lboro.ac.uk/~enpjp/downloads/imappstrends.pdf>
- [22] Curve fitting software available from www.ebicom.net/~dhyans/cvxp.htm

Authors Biographies

Alistair P. Duffy was educated at Conyers School, Yarm; University College, Cardiff, and Nottingham University. He is currently a Principal Lecturer in Communication Engineering at De Montfort University, Leicester and Deputy Head of the Engineering Division. Particular research interests include experimental, numerical and analytical applications for electromagnetics. Particular emphasis for this in recent years has been in communication cable design and analysis.

Other aspects of this interest include microwave and rf heating and novel antennas. A substantial interest is in the formal comparison of complex data sets.

Kenneth G. Hodge holds a BEng from Liverpool University and an MSc from Warwick University. He is currently a representative to BSI and CENELEC committees working on LAN cabling. Ken has been working in the cable industry since 1982, he was initially involved with the development of optical and copper data communication and telecommunication cables, then transferred to the R&D facility as Design Manager Optical Cables. He is now Technical Manager at Brand-Rex (Part of Novar plc).

Arthur J. Willis has been involved in the design and development of cables since joining BICC in 1957, and as Chief Engineer was responsible for the early development of communication cables for information technology. He is currently Technical Consultant to Brand-Rex Limited.

Special Session: Marketing & Management

Chairperson: M. Edward Fenton

Wire & Cable Clubs/Fenton Group, Incorporated, Wethersfield, CT

New UL Programs and Standards Proposals; Standards Harmonization Activities and Fire and Electrical Code Issues



Thomas J. Guida and Austin D. Wetherell

Underwriters Laboratories Incorporated
Melville, NY

+1-631-6200, x22228 · thomas.j.guida@us.ul.com & +1- 631-271-6200, x22818 · austin.d.wetherelljr@us.ul.com

Abstract

This paper addresses the following wire and cable related topics:

- 1 - New proposals and adopted changes to UL's wires and cable standards that have taken place since the 2001 IWCS/Focus.
- 2 - Where the Tri-National (Canada, Mexico, and USA) Standards Harmonization work stands on the four (Thermoplastic-Insulated Wire, Thermoset-Insulated Wire, Flexible Cords, and Test Methods) Standards currently being created.
- 3 - National Fire Code Issues.
- 4 - NEC Issues.
- 5 - Other issues of interest such as Limited Combustible Cables.

Keywords

UL Safety Standards, Tri-National Standards Harmonization (ANCE, CSA, UL), NEC

Biographies

Thomas J. Guida is a Senior Staff Engineer with Underwriters Laboratories Inc. and has been a member of the Conformity Assessment Services section devoted to wire and cable products for over 29 years.

His present responsibilities include standards development, work with technical committees, and he is the technical editor of the UL wire and cable industry newsletter WIRETALK.

Previous to his service at UL, he was a process engineer for both the Okonite and Hatfield Wire and Cable companies.

He was a member of National Electrical Code Making Panel 7 for 18 years and is also a member of ASTM committees B-1 (Electrical Conductors) and D-9 (Electrical Insulating Materials).

Tom is a graduate of Manhattan College with a Bachelor of Chemical Engineering degree and is a Licensed Professional Engineer in New York State.

Austin Wetherell is a Senior Staff Engineer in UL's Conformity Assessment Services Department. He has a B.S.E.E. from Tennessee Technological University and an MS from Long Island University.

Austin has been with UL for 34 years, most of which dealing with wire and cable products. He is currently a principal member of NEC Code Making Panel 6.

Austin served on the International Wire & Cable Symposium Committee from 1981 to 1984. He has served on various committees and working groups of ASTM, SPE, and IEEE/ICC.

Austin is a member of CSA Subcommittee on C22.2 No. 49 - Flexible Cords and an associate Member of Several CSA Subcommittees, including C22.2 No. 0.3 - Test Methods, and the Technical Committee on Wiring Products. He is a member of the CANENA Technical Harmonization Subcommittee for Tri-National Harmonization (Canada, Mexico and USA) of Flexible Cords Standards.

The Future of Copper Cabling Systems; the World versus North America

Donald O. Nicholson

Intertek Testing Services, ETL SEMKO

Cortland, N.Y. 13045

607-753-6711 · dnicholson@etlsemko.com

Abstract

What happens when existing cabling systems can't keep pace and meet expectations?

As it is today, unshielded twisted pair (UTP) cabling is the most common choice of end-users in North American markets. However, some questions have already emerged regarding the ability of an unshielded cabling system to offset electromagnetic interference (EMI) as bandwidth performance is pushed to its limits. For this reason, shielded twisted pair (STP) cabling might be considered a better alternative to ensure long-term system integrity and performance. Shielded cabling has been popular for some time in Europe and in other parts of the world because of its effectiveness in environments with excessive electromagnetic noise, such as airports, electrical power plants and hospitals, as well as where data security is vital, such as brokerage houses.

This presentation will review the differences between UTP and STP cabling and the issues relevant to a possible shift toward STP in North America.

Keywords

Cabling; performance; standards; shielded twisted pair; unshielded twisted pair; STP; UTP; fiber; electromagnetic interference; performance; and bandwidth.

1. Introduction

As it is today, unshielded twisted pair (UTP) cabling is the most common choice of end-users in North American markets. However, some questions have already emerged regarding the ability of an unshielded cabling system to offset electromagnetic interference (EMI) as bandwidth performance is pushed to its limits. For this reason, shielded twisted pair (STP) cabling, the preference of many foreign countries, might be considered a better alternative to ensure long-term system integrity and performance because of its proven effectiveness of EMI protection [1].

Nonetheless, the decision is not a simple one. There are several issues to consider when planning for what type of cabling system end-users will want in the future for optimal performance. Advantages and disadvantages of each have been uncovered under certain conditions and history itself may prevent a shift in end-user habits and preferences.

2. Main Body of Submission

2.1 Historical and geographical perspective

STP cable has long faced an uphill battle against UTP in North America simply because a large majority of homes and businesses were originally outfitted many years ago with UTP for telephone communications, and, as with most anything, people generally stick with what they know and what they have [2]. Moving forward, when demand for Ethernet communication capabilities

was first forecasted in North America, cabling manufacturers chose to work with the familiar UTP to achieve the desired performance results and quickly demonstrated that it could handle the load. EMI was not originally as much of a concern to North American manufacturers or end-users as was bandwidth and speed [3].

The same is true of Australia, Italy, Spain and a majority of the Asia Pacific region [2].

North America's first cabling performance standard, *The Commercial Building Telecommunications Cabling Standard*, EIA/TIA-568, contributed to UTP being the historical choice upon its publication in 1991. It inadvertently set the precedent of cabling choice on the continent for years to come, as the standard identified and approved UTP for cabling networks [2]. It was at this time that the industry truly realized how the standards development process influences the choices of end-users. Unshielded cabling was purchased almost as quickly as it could be produced once the standard was in place. By the time a revision was published in 1995, it was too late for a shielded alternative to gain ground on its unshielded counterpart. Many end-users during these times did not even realize they had the option of shielded or unshielded systems.

Conversely, the mitigation of EMI has long been a concern of many European countries, much more so than in North America. Accordingly, shielded cabling was the initial choice in foreign countries and still remains the desired option for environmentally conscious countries, like Germany.

Fortifying this along the years has been the implementation of many government-enforced electrical emissions limitations on post, telephone and telegraph (PPT) inside buildings [4]. In fact, Germany-based employers can currently be held accountable for employees' medical costs if they develop an ailment that can be traced to stray emissions from unshielded cabling. Other countries that have historically installed STP, and continue to do so, include France, Switzerland and Austria [3]. North American manufacturers of STP cabling should consider taking advantage of these markets' potential.

2.2 EMI protection

UTP and STP are essentially the same. Both contain multiple pairs of twisted copper wire and each twisted pair is encased in an insulated, color-coded jacket. The goal of each is to provide reliable connectivity of electrical equipment, but the way each provides protection from EMI is very different. To pass requirements of low EMI rates, STP cabling primarily relies on its shield and UTP cabling relies on proper balance and filtering techniques [3].

However, UTP's ability to offset EMI as bandwidth is pushed to its limits is still somewhat unclear and something of a design "catch 22."

UTP has long provided EMI protection by varying the length of the twists in nearby cable pairs. However, when increased performance levels were desired, the wire pairs had to be twisted tighter and tighter to achieve the optimal results. It's now known that twisting of the pairs is only effective against EMI up to 30 MHz. At higher frequencies, EMI signals that come in contact with the cable increase the bit error rate (BER) and consequently slow down the network [2].

To help improve EMI protection of UTP at higher frequencies, many installers currently implement some degree of physical separation between cabling runs, power lines and other electrical equipment, but again, beyond 30 MHz, EMI protection is not secure [2]. Manufacturers can help by providing physical separation guidelines to end-users and installers with equipment purchases. Using a shielded system is the preferred alternative for better EMI protection, but several factors can also sway its effectiveness and market popularity.

STP has been prevalent for some time in various parts of the world because of its effectiveness in environments with excessive electromagnetic noise, such as airports, electrical power plants and hospitals, as well as where data security is vital, such as brokerage houses. There are currently three different forms of cabling which provide EMI protection through shielding [5]. These are: the IBM cabling system at 150-ohms with two individually shielded pairs; shielded screened twisted pair at 100-ohms with individually shielded pairs and an overall shield that covers all the pairs; and screened twisted pair or foil twisted pair at 100-ohms with four individually unshielded pairs and an overall shield that covers all of the pairs. The term STP is used very liberally in North America, but often refers to the IBM type of shielded cabling. Elsewhere in the world, the term foil twisted pair is most popular [5].

Similarly to UTP, twisting wire pairs provides protection from EMI in STP up to 30 MHz. Beyond that frequency, a shield is effective against EMI because its reflective barrier performs dual functions: preventing radio frequency interference from coupling with the differential mode signals on twisted pairs and providing a reflective barrier that is intended to prevent energy from broadcasting out of the cable. The shield reflects and absorbs received noise when every component within the system is seamlessly shielded and properly grounded [3].

Many industry experts agree that the most significant problem associated with shielded cable and the reason it is not used more often is the difficulty of maintaining a proper ground. Improper grounding counteracts the benefits of a shielded cabling system, wherein the shield acts essentially as an antenna, converting received noise into current flowing in the shield [4]. Complementing this issue is the fact that many cable installers aren't familiar with shielded systems or how to ground them properly because the majority of their career experience has been working with unshielded systems. Finding an experienced STP installer is key to the effectiveness of the shield [2].

Contributing to STP's lack of popularity and use in North America and elsewhere are its potential size, installation manageability and cost. Shielded cables are often bulkier and thicker than unshielded cables, making these more difficult to work with in small areas, like plenum spaces, and possibly contributes to accidental damage of the cabling or its shield if not handled correctly. Additionally, shielded cabling is typically a bit

more expensive, primarily to cover the cost of the "ninth wire," or shield. There are more materials involved, so the cost is a reflection of that, but manufacturers do not necessarily make more profit from STP than UTP [3].

2.3 Standards drive the future

UTP is currently dominating the cabling market, with well over 15 billion feet installed worldwide, versus 500,000+ feet of various shielded designs. However, the rise in use of wireless devices is certainly contributing to an increase in electromagnetic noise everywhere, leading many to believe that shielded or fiber-based systems will be a necessary alternative if high performance levels are to be maintained [3].

Contributing to this possible shift is current activity on technical committees of the Telecommunications Industry Association (TIA) and the International Electrotechnical Commission (IEC). For example, the IEC has been considering a category 7/class f system specification that will specify bandwidth to 600 MHz, three times that of category 6 [3]. To satisfy this requirement, most agree that a shielded solution will be necessary. And, although the TIA is not currently working on a category 7 standard, it has implied that performance beyond category 6 will not be satisfied with unshielded solutions. Both the TIA and IEC have also generated committees to develop new industrial cabling standards for use in areas of high EMI [2].

The European Union is currently considering the addition of a regulation for electromagnetic performance to its EMC Directive for passive cabling components. There is also a good chance that the Federal Communications Commission may adjust its own radiated emissions regulations as electromagnetic noise increases due to increased usage of wireless devices [2].

3. Conclusion

Given the standards development work and the previously mentioned disadvantages of STP, fiber will be the long-term choice of end-users worldwide, as it is not affected by EMI, under any conditions. However, STP is less expensive than fiber, so there is a chance for it to gain market share, especially with strong marketing initiatives and industry education.

4. References

- [1] Cabling Installation & Maintenance, "Study: worldwide residential cabling market growing 55% annually," May 2002, http://cim.pennnet.com/Articles/Article_Display.cfm?Section=Archives&Subsection=Display&ARTICLE_ID=142581&KEYWORD=BSRIA.
- [2] Dave Hess and Michiel Pelt, "Cable to Cable Coupling," a *BICSI conference presentation* (October, 1997).
- [3] Dave Hess and Michiel Pelt, "The Relationship between EMC Performance and Applications," a *BICSI conference presentation* (March, 1998)
- [4] Cabling Installation & Maintenance, "Fiber to the desk: is it finally coming." (October 2001), http://cim.pennnet.com/Articles/Article_Display.cfm?Section=Archives&Subsection=Display&ARTICLE_ID=121392&KEYWORD=FTM%20consulting.

- [5] Cabling Installation & Maintenance, "Shielded twisted-pair cable fights an uphill battle for market acceptance," (October 1997),
http://cim.pennnet.com/Articles/Article_Display.cfm?Section=Archives&Subsection=Display&ARTICLE_ID=63348&KEYWORD=shielded%20screened%20twisted%20pair.

5. Author

5.1 Name and address

Donald O. Nicholson
3933 US Route 11
Industrial Park
Cortland, NY 13045

5.2 Biographical sketch

Donald O. Nicholson is the general manager of telecommunications and IT products testing at the ETL SEMKO division of Intertek Testing Services, the world's largest product and commodities testing organization. Donald (Don) is based in Cortland, N.Y. He is a graduate of the State University of New York (SUNY) at Alfred, N.Y. where he majored in Electrical Engineering Technology.

He has been employed with ETL SEMKO for over ten years. During which time he has served in such positions as sales manager, industry manager and general manager. Don has participated on numerous cabling industry committees, such as those of TIA/EIA, ISO/IEC, NFPA, NEMA, ASTM and ICEA. Prior to working for ETL SEMKO, he worked as a business telephone installer for AT&T and as general manager for DMC Services. During this period, he oversaw the installation of network infrastructure systems for small and large businesses. Currently, Don is active with the BICSI Membership and Public Relations Committees where he serves as the Region 1 Representative.



Special Session: Marketing & Management

Fiberoptic Cable: Understanding the Dramatic Shifts in Worldwide Demand



Patrick J. Fay and Richard R. Mack

KMI Research
Providence, RI

+1-401-243-8121 · pfay@kmicorp.com & +1-401-243-8113 · rmack@kmicorp.com

Abstract

By the end of 2002, the worldwide market for fiberoptic cable will have dropped about 30% from its peak year in 2000. The rapid growth before this drop, and the two-year drop itself are both the result of a complex group of business, technical, and regulatory factors. This talk will summarize several of these factors and scenarios for when the market will resume a positive growth trend.

The viewgraphs will include market data to show where the fiber was installed—in what regions and in what applications. Historical data will be shown to discuss whether the recent market swing can be analyzed in terms of cyclical trends seen in other industries. This data will show that the long-distance sector has been the most volatile, and that several one-time phenomena drove demand in the late-1990s that probably will not be duplicated again – at least not in Western Europe and North America.

Shorter-distance applications, however, did not track closely with the aggressive investments in long-distance applications. The most recent trend, however, is that Internet applications are contributing to increasing pockets of demand for fiber-in-the-loop (FITL) for business and residential communities. The talk will cover the potential impact of these FITL applications on the future fiberoptic cable market.

Such shifts in the mix of applications and other market developments will have an impact on the type of fiber and cable being produced. The talk will look at the mix of fiber types in the cable market and highlight the demand for higher-performance fiber versus conventional single-mode fiber (G.652). Finally, these factors are all having an impact on prices, and the data will include charts to show the recent trends in average prices. The

market has entered a period of strong pressure to lower prices, and this is contributing to the drop in market value.

Keywords

Fiberoptic Cable, FITL, Single-Mode Fiber, Multi-mode Fiber

Biographies

Patrick J. Fay directs market research on worldwide optical fiber and fiberoptic cable markets. Mr. Fay maintains KMI's FiberGlobe™ database, which includes KMI's forecast for cabled-fiber installations in more than 50 countries. He is the author of KMI's "Worldwide Optical Fiber and Fiberoptic Cable Markets," and "Networks of Fiber-based Pan-European Carriers."

Mr. Fay appeared on CNBC in November 2000 to provide industry analysis of the worldwide fiber shortage, and he was invited to speak at IWCS in 2001, Lucent Technologies, Norcross, GA in 2000, and Optocom 2002 in Taipei, an event organized by the Photonics Industry Technology & Development Association. His articles have been published in *Lightwave* magazine, and he has been quoted in *Business Week Online Communications Technology, Communications, Engineering & Design, and Lightreading*.

Richard R. Mack, Vice President and General Manager of KMI Research, has been involved in the fiber optics industry for more than 20 years. Prior to joining KMI in 1988, he was the managing editor of *Laser Focus World* magazine. At KMI, Mr. Mack has conducted market research in various areas of fiber optics including active and passive devices, optical waveguides, cable, connectors, data-communications systems, metropolitan area networks, rights-of-way, and telecom systems.

Global Market Trends in Fiber Optic Cable & Optical Fiber

Jon P Barnes

Managing Consultant, Wire & Cable

CRU International

31 Mount Pleasant, London, United Kingdom
+44-20-7903 2116 · jon.barnes@crugroup.com

Abstract

This paper will determine the magnitude and timing of the downturn in the global fiber optic business during 2001 and 2002. It will assess both the scale and timing of the downturn on the world's major regional markets – North America, Western Europe, Rest of the World and Asia. The impact of these developments of the financial performance of the sector will also be briefly addressed. This paper will also quantify recent developments in Japan, currently one of the world's largest national market for fiber optic cables. The likely outturn for the global market in 2002 will then be assessed along with factors likely to influence recovery prospects.

Keywords

Fiber Optic Cable; Optical Fiber; FTTH;

Introduction

Thank you very much for the invitation to present at this year's IWCS/Focus Symposium. My name is Jon Barnes, and I am the Managing Consultant of the Wire & Cable Research team at CRU International. The title of my talk today is Global Market Trends in Fiber Optic Cable and Optical Fiber and covers four main areas: -

- 1) Global & Regional Trends & Indicators
- 2) Asian Growth – Focus on the Japanese Market
- 3) Impact of Global Downturn on Sector Financials, and
- 4) Conclusions & Points to Watch

Main Body

Global & Regional Trends & Indicators

Telecom Investment & GDP

Let us begin by looking at the global relationship between GDP and total Telecom Investment. If we compare annual growth rates in nominal US\$ terms over the past decade we see that, at the very least, there has been a strong coincident relationship. Telecom investment growth has been higher, and has tended to outperform strongly towards the peak of the economic cycle. However, the relationship appears to have seriously broken during 2001 and 2002 when we have a major discontinuity, with a big collapse in the global rate of telecom investment relative to GDP. We expect a sizeable recovery, albeit from a much-reduced base in 2003.

World Fiber Optic Cable Demand Trends

World fiber optic cable demand enjoyed uninterrupted year-on-year growth in quarterly consumption volume until Q2 2001. Q3 posted a modest decline, but thereafter the rate of decline accelerated culminating in 50% year-on-year decline in Q2 2002. This was as much to do with an unfavorable comparison to the heights of the previous year. Since then, at least, the rate of decline has not deteriorated further, and may indeed be edging towards parity with depressed prior year levels in Q4 2002.

Regional Fiber Optic Cable Demand Trends

A regional comparison of these quarterly volumes indicates that North America was the first to enter recession, followed by Europe not long afterwards. The magnitude of the decline was in both cases particularly severe. Asia and the Rest of the World only entered recession at the beginning of 2002 and will have to endure several more quarters before they emerge. Even so, we do not expect demand to fall as far from the peak as in North America and Europe thereby cementing Asia's growing relative importance.

Indicators – World Trade Flows

One indicator that I find useful to track is the monthly trend in the dollar value of trade in optical fiber and fiber optic cable. I think this quite nicely illustrates three central points. Firstly, the huge influence of China in the second half of 2001 in supporting the world market after the slowdown in North America and Europe; Secondly, the sharp deceleration in the world market from Q4 2001, And finally, as the rate of decline is no longer accelerating, and may be decelerating, that the prospects of recovery are not too far ahead.

Indicators – Spot Optical Fiber Prices

However, whatever the prospects for the future in the here are now spot prices for optical fiber are languishing at severely depressed levels. Prices would have undoubtedly fallen further but for voluntary capacity idling, and the maintenance of high perform prices by Shin-Etsu, although this in its own way has not been without its implications.

Asian Developments – Japanese Market Focus

Japan National Profile

Let me begin with a brief profile of Japan, drawing out some factors that are relevant to fiber optic cable market situation. Despite having only 4% of the land area, Japan is around half the size of the

USA in measures of population and GDP, and has a GDP per capita only 10% lower. However, the country has however had persistent economic problems since the boom of 1990/91. Japan is very mountainous and as a result the majority of the population live in densely packed conurbations on the coastal plains. The two main centers of Tokyo and Osaka are only 600km apart.

Japanese society is very homogenous and still emphasizes collective goals over individual achievement. But this is changing in business, and even faster in society as a whole. The economy has generally been perceived to be slower to adopt the IT revolution than its neighbors and main competitors. This has now been countered by the embracing of the e-Japan initiative to transform society. Telecom industry privatization has been under way for some years. The number of Type I carriers who are authorized to build networks has climbed from 5 to 330 in the last 15 years.

Japan Cable Market Characteristics

So what are the main characteristics of the Japanese optical cable market? Well, during the last calendar year, volume growth was very rapid, though has subsided during 2002. Although clearly a boom, its intensity did not match the magnitude of those seen in North America or Western Europe. Financing has been more stable and deployment has been more in line with predicted traffic growth. Thus despite the slowdown, volumes have held up reasonably well this year. Growth was initially led by long haul deployment, but since October 2001 a sizeable proportion of demand has been devoted to FTTH with the aim of total national coverage by 2005.

NTT's role and importance in the market has until very recently been a downward trend. The NTT Group still accounts for 50% of the market by volume, but its influence is wider. Amazingly competing carriers are very reluctant to install cables that do not meet NTT specifications, even if they give that carrier a competitive advantage! This is one of the reasons, along with shorter distances, why NZDS fiber has not been at all widely adopted. It would be hard to understate the importance of customer service in Japan. Indeed this was one of the contributing factors to the Corning-Hitachi Cable joint venture in Japan. As we shall see cabled fiber prices have generally been on a downward trend. Slotted core ribbon designs dominate, but this is an over-simplification. It is common practice for the customer rather than the manufacturer to exactly specify the cable design. For this reason the slot depths or the fiber coloring is subtly different from one customer to the next. Consequently all cables are made to order and manufacturers' inventories are minimal.

Quarterly Trend in Fiber Shipments

If we examine the quarterly trend in Japanese optical fiber shipments we can readily see that output growth was initially driven by a rise in export sales, which was supplemented by growing sales to domestic cablemakers. When export sales slowed as the boom subsided the slack was temporarily taken up by stronger sales to cablemakers as large-scale FTTH began. Overall volumes began to

suffer from Q1 2002 as domestic cable shipment growth decelerated.

Cable Shipment Trends by Customer

The Japanese Cable Makers' Association classifies cable demand into 4 main categories: Public Telecom Utilities (NTT); Power Utilities; Other Domestic Demand (mainly NCCs) and Exports. In recent years demand from NTT has been falling with its share being taken up by the Power Utilities and NCCs, with these latter two groups mainly investing in long-haul networks. From mid-FY2001 the share of these two, and particularly the NCCs began to decline as FTTC&H began to develop. NTT has been the main customer for cables of these types, explaining its growing market share.

Cabled Fiber Price Movements

Japanese cabled fiber prices have generally been following a long-term downward trend. The exception was a brief period in mid-2000 at the height of the world boom when cablemakers were able to pass on modest increases to major customers. Average cabled fiber prices have fallen below ¥10,000 (\$70) per fkm. In the past there used to be considerable variation in the prices paid by different Japanese customers. There is now much greater homogeneity, and customers are now more willing to 'beat up' their suppliers on price.

Impact on Cablemakers' Financials

As we are all well aware, the fiber optics segment is not the only segment of the global cable business that has been in recession. Metallic cable markets have also been suffering. In this next slide I have attempted to quantify the impact of the recession on the operating margins by business segment of the largest cablemakers.

As we can see, the operating margins of communications cable businesses have slumped, while energy cable margins, although dipping a little, have not fared anywhere nearly as badly. A closer examination of the operating margins on the communications cable side of the business reveals the differentially adverse impact on the fiber optics segment, compared to copper telecom and datacom.

Conclusions

In the light of regional market developments so far this year, what can we expect as the outturn for 2002? At CRU we expect that world cable market volumes will be in the 60-65mfkm range, a 30-35% decline from the record 95mfkm achieved in 2001. The decline in value has been even more marked due to lower fiber pricing, deteriorating product mix and diluted margins. Global fiber optic cable sales are likely to halve to \$4-5bn from \$9bn in 2001.

It appears that the North American and European markets are stabilizing at a very low level of activity. China is now beginning to recover and it is hoped that Japan will soon follow suit. World fiber volumes in Q4 2002 will not be far different from Q4 2001, but it currently seems that they will still fall a little short.

The pace of recovery in Asia, and particularly in China and Japan, will be an important point to watch, as we can realistically expect no

rapid recovery in North America and Europe. Contractual commitments for perform deliveries from Shin-Etsu remain a concern for many, despite tough ongoing negotiations. In Europe and North America the complex issue of whether fiber installed in bankrupt carriers networks is lost forever or will come back into service is a key factor – this subject is currently being investigated by CRU. Meanwhile the substantial capacity overhang in fiber and cable looks likely to place a ceiling on any price recovery.

Thank you for your attention.

Biography

Jon Barnes (BA Economics) is the Managing Consultant of CRU International's Wire & Cable Research team. In his 11 years with CRU International he has analyzed world-wide metallic and fiber optic insulated wire and cable markets.

Jon is the editor of the regular Optical Fiber & Fiber Optic Cable Monitor and the recently published Cables Industry Analyst. He is also the principal author of CRU's Telecom Cables Service analyzing Fiber Optic and Copper Telecom Cable markets.

Optical Fiber & Cable Industry in China

Wei Zhong-cheng*, Tang Ren-jie

FiberHome Telecommunication Technologies Co.Ltd(wuhan China)

He Fang-rong

China University Of Geosciences(wuhan China)

Abstract

China's optical fiber & cable industry started in middle of 1970's, and now China become one of most potential market over the world. This paper describes the history, domestic situations and development trend of optical fiber & cable industry in China. A detail analysis on production capabilities and market demands for optical fiber & cable also give in this paper.

Key Word

optical fiber, optical cable, industry, market

1. Introduction

In early of 1970's, the researchers in China has pay much interesting in optical fiber telecommunications since Corning developed the first silica fiber with the loss less than 20dB/km^[1-2]. In 1973, as national key research institute, Wuhan Research Institute of Posts & Telecommunications(WRI) first presented a strategy researching plan in China about optical telecommunication which including optical device, optical transmission equipment and optical fiber cable. Therefore, WRI started making optical fiber by MCVD process in 1974. In late 1978, multimode fiber(MMF) with grade index profile(GI) in compliance with CCITT standards were developed. The first trial transmission system with GI-MMF in China was also exhibited in the national science and technology conference in 1978. A year later, the first in-site optical fiber transmission system with transmission speed 8.44Mbit/s and 5.7km aerial optical cable was set up by WRI in China, and then transmission distance was extended to 7.7km. In 1981, optical fiber started to be manufactured using

Now Wuhan Research Institute of Posts & Telecommunications

MCVD process on large scale. The first optical fiber transmission system was applied to public service networks in China in 1982. This indicated that the prelude for optical fiber telecommunication construction was underway in China.

2. Optical Fiber and Cable Industry

2.1 Optical Fiber

As optical fiber telecommunication construction was outspreaded in great force in whole China, the demands for optical fiber and cable were enhanced increasingly. In order to meet such demands, the China government started investing to set up optical fiber factories, such as Shanxi Houma wire cable factory, Peking 605 factory, Shanghai silica glass factory, et al. All of those factories imported MCVD equipments and technologies to manufacture the optical fiber. After a few years, they are all failed, except WRI.

In later of 1980's. Two(2) joint venture companies between China and foreign were set up, known as YOFC(Yangtze optical fiber & cable Co. Ltd) and Shianfu optical fiber & cable Co. Ltd. The former introduced PCVD technology from Phillips of the Netherlands in 1988, and the later introduced the VAD technology from Furukawa Electric Co., Ltd. of Japan. In 1990's, a few new joint venture company which specialty in manufacturing optical fiber(Only drawing fiber, perform were supplied by foreign company) had been set up. Such as Shanghai Lucent (Last year, Corning company got the Lucent's share in Shanghai Lucent and Peking Lucent), Nanjing Walsin-Fujikura optical fiber Co. Ltd., Chengdu SEI(CDSEI) and Zhejiang Futong Showa, etc.

During 1996-2001, especially the fiber shortage period (1999-2001), a few new domestic optical fiber

companies were established, such as Hainan Ruifeng , Nanjing Twentsche (known as TFO) , Fasten Photonics, Hongkong Transtech ,TeFa –Alcatel and Tianjing Tiancai , Shanghai Huayuan ,et al. There are still some projects to set up fiber plant include preform manufacturing are undertaking. Table 1 show the basic state of optical fiber companies in China(excluding the companies in Taiwan prov.)and table 2 estimate the whole production capacity in China. It was obviously that optical fiber manufacturing industry have been made greatly progress during past 20 years, not only in production capacity, but also in manufacturing technologies.

Table 1. optical fiber companies in China

No.	Company	Integrity	Preform Technology
1	YOFC	Preform , fiber	PCVD
2	Shanghai Lucent	fiber	No
3	Walsin Fujikura	fiber	No
4	FiberHome	Preform , fiber	Inside Deposition
5	CDSEI	fiber	No
6	Shianfu	Preform , fiber	MCVD/ VAD
7	Futong Showa	fiber	FSVD
8	Nan Jing (TFO)	Preform , fiber	MCVD
9	Fasten Photonics	Preform , fiber	MCVD
10	Tefa Alcatel	fiber	No
11	Hongkong	Preform , fiber	MCVD
12	Hainan Ruifeng	Preform , fiber	MCVD
13	Shanghai Huanyuan	fiber	No
14	Tianjing Tiancai	fiber	No

2.2 Optical Fiber Cable

R & D on the optical fiber cable was started in early 1980's, the first cable was designed as a slotted-core structure, utilized the wire cable manufacturing equipment through cooperation in whole China. In the

Table 2. The production capacity of optical fiber in China at year 2002 and 2005.(million km)

No.	Company	2002	2005
1	YOFC	5.0	10.0
2	Shanghai Lucent	2.5	3.0
3	Walsin Fujikura	2.0	3.0
4	FiberHome	1.0	3.0
5	Futong Showa	1.0	3.0
6	Tefa Alcatel	1.0	2.0
7	CDSEI	0.5	2.0
8	Nan Jing (TFO)	0.5	2.0
9	Fasten Photonics	0.5	2.0
10	Tianjing Tian Cai	0.3	2.0
11	Hongkong	0.3	2.0
12	Shianfu	0.2	1.5
13	Shanghai Huayuan	0	1.0
14	Hainan Ruifeng	0	1.0
	others	0	2.0
Total		14.8	39.5

middle of 1980's, optical fiber cable was applied mainly among the switch terminations .At end of 1980's , optical fiber cable with a large amount was serviced in backbone networks.

As the policy of open and reform was transacted in depth, China government started investment on foundation facilities. To meet demands of optical fiber cable for telecommunication constructing, a lot of wire cable factories of the state-owner begun to produce optical fiber cable. Using lower cost labor, some foreign companies such as Germany Siemens(now Corning), Lucent technologies(now Corning) begun to set up the JV companies to manufacture optical fiber cable. At present, there are more than 200 optical fiber cable manufacturers in China. Also, the domestic cable factories can design

and manufacture all kinds of optical fiber cable such as center loose tube cable, stranded cable, slotted-core cable, ribbon cable, ADSS , OPGW and premise cable ,et al.

Though there are a lot of optical fiber cable factories in China, more than 80% market in China was shared by the top ten of optical fiber cable manufacturers. Table 3 shows the production capacity of the top ten optical fiber manufacturers. It indicates that the production of optical fiber cable is more and

Table 3. The production capacity of the top ten optical fiber cable manufacturers(10 thousand kmf)

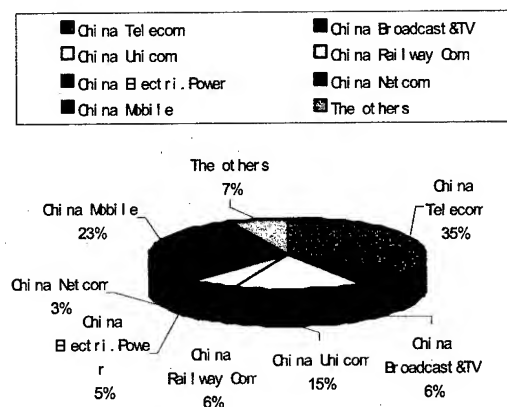
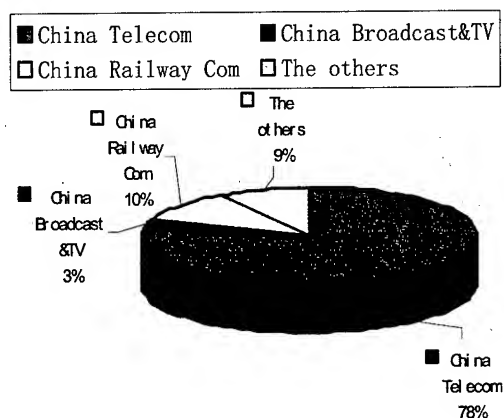
No	Company	Capacity
1	YOFC	300
2	FiberHome	200
3	Peking Lucent	150
4	CDCCS	150
5	Hengtong	150
6	Yongding	120
7	Zhongtian	100
8	Tefa	90
9	Shanghai Walsin	80
10	Huiyuan	80
Total		1420

more concentrating in the several big companies, the supply amounts of total optical fiber cable is over than actual demand .As the top company's brands are more and more famous in this industry, merging among optical cable companies become not reversing trends recently.

3. The Domestic Market of the Optical Fiber and Cable

Going with national telecommunication construction , the demand for optical fiber and cable increased annually with high rate. As a dominant customer in China in past year, China telecommunication has finished the construction of optical cable networks about more than 1.25 millions km in routine length in whole China. After merging and aparting (M/A) of

China telecommunication network operators, the demand share for optical fiber cable in China has changed greatly .Figure 1 and figure 2 present the changing pattern of main network operators in the year of 1995 and 2001,respectively.



According to the national tenth 5 year plan for telecommunication, the lay-out length of the public network for optical fiber cable will reach to 2.5millions km. It means that 1.25 millions km (including 200 thousands km cable using for trunk distance backbone network)optical fiber cable will be laid newly in the following 4 years. Considering other demands for special groups such as LAN for education access network, enterprise access network and residence access network , we reckon total demands for optical fiber in the year of 2001-2005

as following(see table 4). Adding approximately 10%

loss during cabling process, Total demand during the year of 2001-2005 will be about 7360 kmf. So the market of optical fiber cable in China will increase by average 8%-15% annually.

Table 4. The demands for optical fiber cable (2001-2005) (10 thousands km)

Purpose	Routine Length	Average fiber number	Demand Quantity
Trunk Backbone Network	10(Western)	48	480
	10(Eastern)	96	960
Access Network and METRO Network	105	48	5040
Others	35	6	210
Total	160		6690

4. The future of the Optical Fiber and Cable Industry

The following 5 years is very important to the optical fiber and cable industry. Because production capacity of optical fiber and cable is overplus as mentioned above, competition in this industry will become more and more hard while small companies will lose their advantage in future. This industry will encounter drastic M/A and top companies will finally gain the most market share. In order to reduce the cost, the top companies will cover the full production of the preform, fiber and optical fiber cable. The company which covers the full production will win the future market and will gain dominance over the future market.

Of course, the companies of optical fiber and cable will face the potential opportunities of the international marketing as China become a member of WTO. At present, some top company like YOFC and FiberHome has exported the products of optical fiber and cable to foreign countries. The JV companies abroad will be set up in 2-5 years by China company.

5. Summary

For developed nearly 30years, optical fiber and cable industry in China became to more and more well-rounded, they mastered the whole key technologies of manufacturing optical fiber and cable , and can supply all kinds of optical fiber and cable products to customers. Also there are a lot of optical fiber and cable factories in China, however, more than 80% market in China was shared by the top ten of optical fiber cable manufacturers .

Although the international market became depressed since the second half year of 2001 as the bubble of the internet economy was dashed the ground overturn in globe, domestic market of optical fiber and cable was also considered one of most potential markets. It is estimated that the market of optical fiber and cable will increase by 8-15% annually for 2001-2005 and the total demand quantity for optical fiber and cable will reach 6690 kmf .

But compared to the demand of optical fiber and cable, the production capacity is surplus seriously. Competition in this industry will become more and more harder and will encounter drastic M/A .Top companies will finally gain the most market share.

6. Reference

- [1]F.P.Kapron et al., Radiation losses in glass optical waveguides, Appl .phys.lett.Nov.15,1970,pp423-425
- [2]Tosoc Federico, Optical fiber communications in the 0.8-0.9 μ m wavelength region -applications and perspectives, ECOC'1982,pp9-15

Authors

Wei Zhong-cheng

Wuhan Research Institute of Posts and Telecommunications
YOUKEYUAN Road 88, Hongshan District, Wuhan, China

E-mail: zhchwei@wri.com.cn

He received his M.Sc. degree in Material Science in 1989, and then he joined WRI ,where he was involved in the R&D of optical fiber manufacturing technologies ,materials and process of optical cable manufacturing . In 2000 , he was deputy general manager of

optical fiber and cable department of FiberHome Telecommunication Technologies Co. Ltd. After a year, he was general manager of optical fiber department of FiberHome..Now he is head of industry development department of WRI..

Tang Renjie

FiberHome Telecommunication Technologies Co.,Ltd.
No.88 Youkeyuan Road, Hongshan District, Wuhan, China

Tel. +86 27 87691497

E-mail: rjtang@wri.com.cn



Prof. Tang Renjie was born in Shandong prov.,China in 1947. As a national expert, he has been engaged in the R&D of optical fiber in Wuhan

Research Institute of Posts and Telecommunications for more than 20 years. He joined FiberHome Telecommunication Technologies Co.,Ltd in 1999. Now he is the vice general engineer of Optical Fiber Dept.of FiberHome.

He Fang-rong

China University Of Geosciences(wuhan China)
LUMU Road 388, Hongshan District, Wuhan, China

Tel. +86 27 87692894



She graduated from the university in 1986,and then was a lecturer for more than ten years.Now she is a graduate student of the information science faculty of China University

Of Geosciences(wuhan China).

Development of a Ribbon Distribution Cable Utilizing a Stranded Design

Roger Vaughn

Pirelli Communications Cables & Systems NA
Lexington, SC

Abstract

Pirelli Communications Cables and Systems NA recently developed a high fiber count ribbon distribution cable called COLink™ for premises applications. The cable utilizes 12 fiber ribbon stacks inside gel-free buffer tubes stranded around a central strength member, and is either OFNR or OFNP rated. The plenum (OFNP) version may be used for riser applications as well, as it exceeds GR-409-CORE and ICEA 596 riser mechanical and environmental specifications. Fiber counts of up to 576 fibers are available in either riser or plenum versions of the cable.

Stranded design for ribbon distribution cables offers several advantages over a central tube design. The advantage of individually protected sub-units translates into improved handling and minimizes accidental damage to ribbons. Multiple ribbon sub-units in the cable also reduce cost of installation and complexity by limiting the need for furcation tubes within a rack. Buffer tubes can simply be routed from the entry point of the rack to individual panels before exposing the ribbons for individual termination. The stranded nature of the design allows for greater flexibility and kink-resistance, as well as the capability of handling greater tension; and the multiple sub-unit design results in greater compression and impact resistance than traditional central tube designs. This increased overall cable robustness is advantageous when protecting vital revenue generating data streams.

The biggest design challenge in the development of the cables that utilizes gel-free buffer tubes for premises applications is GR-409-CORE compliance to impact and compression resistance, as well as environmental performance. The gel-free nature of the buffer tubes presented various processing challenges as well, particularly with respect to manufacturing repeatability. Careful consideration to minute design and processing details need to be made in order to fully maximize quality without compromising manufacturability and cost.

Keywords

Buffer Tube, Plenum, Riser, Stranded, Central Tube, Parallel Optics, MT ferrule, PVC, PVDF, Mass Termination

Introduction

Ribbon Distribution cables are utilized in various network locations. One of the most common applications is in transitions from OSP environment to the premises where NEC regulations required flame ratings and clean, quick terminations are desired. In this function many of the cables are preconnectorized to panels in stub assemblies where the other end of the cable is simply fusion spliced to the OSP cable. Other applications include use as back-plane jumpers, network backbone, and parallel optics transmission. These cables must have some of the mechanical and environmental performance of both the OSP and premises cables. This means that in addition to exceeding Telcordia GR-409-CORE and ICEA-569, cables are tested to tensile strengths of 600lbs per Telcordia GR-20-CORE.

The high fiber count density attained using ribbon, the limited duct space available in many institutions, CO's, POP's, etc., and the increasing acceptance of OSP ribbon cable all contribute to an increasing use of ribbon cables in the premises. Space is at a premium in many CO's and the more you occupy the more it costs. One way to limit that cost is to increase the port density in the racks. Traditional tight buffered cables are predominate in legacy systems, but are much too large to support this capacity increase. Ribbon distribution cables, especially stranded design, are specially suited for the application. Utilizing the individual buffer tubes to route inside the racks and panels the ribbon is continuously protected until final termination within the panel. By grouping the ribbons in 12 to 144 fibers per tube, up to four panels can be fed from one cable or one panel can be fed from opposite sides to elevate fiber congestion within the panel.

As ribbon distribution cable gained popularity the fiber counts increase to meet the demand for new applications. Ribbon distribution cables originally designed as central tube product has increased in fiber count to such a degree that a stranded design must be used for maximum benefit. Central tube design cable is cost effective and extremely functional for fiber counts of 12-216 fibers and when running from point to point. Once the fiber counts exceed 216 fibers or more complex point to multi-point connections is required stranded design ribbon distribution cables become advantageous. One reason for this is the port density of patch panels currently limited to 216 fibers and many times 72, 96 or 144 count. One can immediately see the benefit in using a stranded ribbon distribution design with limited duct or back-plane access. For example; four 144 port patch panels can be preterminated with one 576 fiber ribbon distribution cable using the individual buffer tubes to route to each panel where as four separate 144 fiber central tube cables would have to be used.

Design

When first tasked with developing stranded ribbon distribution cables several technical specifications including Telcordia GR-409-CORE, Telcordia GR-20-CORE, ICEA-596, as well as customer specifications were taken into consideration. Much more emphasis was placed on customer requirements, but standard specifications were maintained for wide acceptance of product offering. Tensile strength was of major concern for the customer as they expected the same crews that install the OSP to handle the ribbon distribution as well. Another concern was equality between riser and plenum specifications, so the decision was made for both cable ratings to meet the more stringent riser mechanical and environmental specifications.

Several cable designs were considered, but from the beginning the customers' end use of the product was kept in mind. Divisions of 72, 96, 144, & 216 fibers were of utmost importance in the design process, as they would mate with current panel port densities of the most popular panel manufacturers. Using these fiber counts and realizing the space constraints associated with most applications a four-position cable design was decided upon. Both a 288 version with 72 fiber sub-units and a 576 fiber with 144 fiber sub-units were chosen. These fiber counts and tube configurations covered any combination of panel port densities.

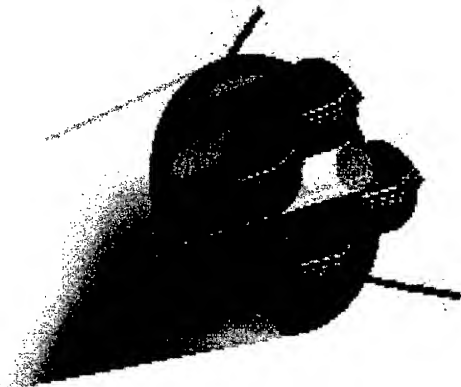


Figure 1. Pirelli COLink™, Stranded Ribbon Distribution Cable

Capitalizing on Pirelli's extensive knowledge of high fiber count OSP ribbon cable development; process technology and equipment was utilized to develop the stranded ribbon distribution cables. Some of the more unique characteristics in contrast to OSP products are the gel-free tubes and flame ratings requiring flame-retardant buffer tube materials.

Development

Buffer tube material selection was the first development consideration and the most important. The tube material is critical in determining the performance of the cable. All material attributes were reviewed and considered. The main characteristics used though were cost, burn characteristics, coefficient of thermal expansion (CTE), and processability. The two basic materials looked at were PVC and PVDF; both have good CTE and process characteristics, but differ substantially in cost and burn characteristics. As one can see from Table 1, PVC is low cost, but

is limited in flame performance for plenum applications. PVDF is costly but excels in burn characteristics.

Table 1. Comparison of PVC and PVDF

	PVC	PVDF
Limited Oxygen Index (LOI)*	30-50%	99%
Cost	\$0.75 - \$1.75/lb	\$6.00-\$8.00/lb
CTE	Low	Very Low
Processability	Excellent	Good

*LOI is the percent oxygen atmosphere required for a material to sustain a flame.

Ultimately the PVDF compound was chosen for the plenum rated cable design and PVC for the riser cable design based on the NEC rating required.

Special consideration was made to process conditions during manufacture of the buffer tubes. As with most fiber optic cable designs the buffering process is the most critical as it is the first operation in making the cable. Any adjustments to buffering can and do transfer to later processing steps with significant outcomes. Some of the variables monitored included the ribbon payoff tension, ribbon pitch, tube ovality, and excess fiber length (EFL). Payoff tension is used to provide an adequate amount of back tension such that the ribbon stack maintains a correct orientation and twist.

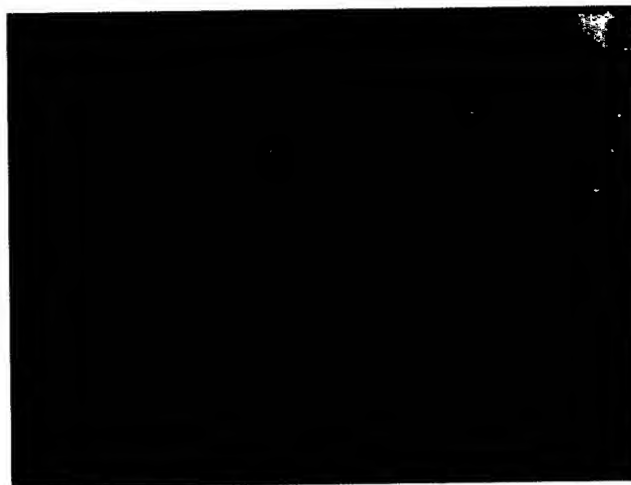


Figure 2. Twisted Ribbon Stack prior to Entry into Buffer Tube.

The unique feature of these cables is the gel-free tube, which caused some changes to the normal process of producing buffer tubes. In a gel filled tube the gel helps to hold the ribbons in position once placed in the tube. Without gel the tube was collapsed at the beginning and end of the buffering run in order to hold the twist induced in the ribbon stack during manufacturing. These sections are later discarded after jacketing.

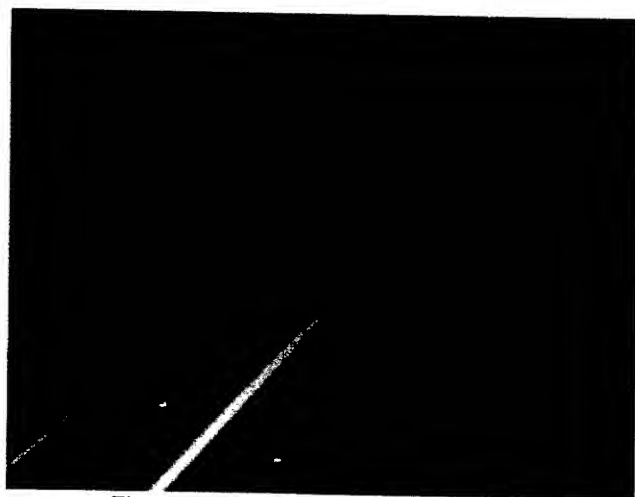


Figure 3. Buffering Tube Production

Ribbon pitch, tube ovality, and EFL all contribute to the cable performance during environmental testing and were monitored closely to insure consistent product. EFL is the most important and is controlled mainly during the stranding process. Ribbon pitch is the distance between twists placed in the ribbon during buffering. The pitch allows for the cable to be bent in any direction without adversely affecting the ribbon.

Stranding and jacketing operations are well understood and are fairly straightforward. It is important to note though that the reverse oscillated lay (ROL) stranding places the ribbon in a configuration such that the amount of excess fiber length is not too much as to adversely affect environmental performance, but is great enough to eliminate stress during tensile loading. As one can see from Figure 4. Below the ROL stranding process wraps the tubes back and forth around a Central Strength Member (CSM). The ROL also, as with OSP cable, allows for mid-span access, which is not capable with taught sheath central tube cable installations.

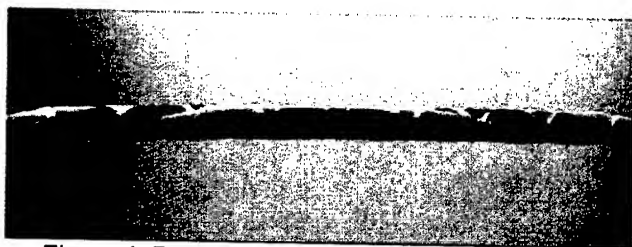


Figure 4. Reversal point in reverse oscillated lay (ROL) stranding.

A cable jacket primarily serves as mechanical protection for the cable components, but in NEC rated cables it must also be highly flame retardant to meet the stringent requirements of burn testing. Again, as with the buffer tube material selection, two materials, PVC and PVDF, were evaluated. PVC is flame retardant but not as much as PVDF, however PVDF is very expensive, typically in the range of eight times greater than PVC. Costs of this magnitude are prohibitive for use in large quantities such as jacketing without a significant benefit. After reviewing the attributes of both, the PVC compound was chosen for the riser design to reduce cost and the PVDF compound was chosen for the plenum version to consistently meet NFPA 262 (a.k.a. UL 910) test requirements.

Testing

Once design and development work was completed the cables were prototyped and readied for testing. Prototypes were constructed of both the 288F design and 576F design in riser and plenum. Results from testing are summarized below in Table 2.

Table 2. Test Results

Test & Method per GR-409-CORE	288 fiber Cable Design	576 fiber Cable Design
Temperature Cycling & Aging Test Method: EIA-455-3A Criteria: Temperature Cycling from, -20C to +50C, <0.2 dB/km increase, Aging <0.4 dB/km	Maximum attenuation delta change recorded 0.09dB/km with average dB change of 0.01dB/km	Maximum attenuation delta change recorded 0.05dB/km with average dB change of 0.01dB/km
Tensile Strength Test Method: EIA-455-33A Load: 2640N (600lbs), Residual: 880N (200lbs) Criteria: <0.2 dB/km attenuation increase	All fibers had <0.20 dB change in attenuation	All fibers had <0.20 dB change in attenuation
Fiber Tensile Strain Test Method: FOTP-38 Load: 2640N (600lbs), Residual: 880N (200lbs) Criteria: <0.6 of fiber proof strain at load, <0.2 of fiber proof strain at residual load.	Maximum recorded Strain at load, 0.21 and 0.065 at residual load	Maximum recorded Strain at load, 0.21 and 0.057 at residual load
Compressive Strength Test Method: EIA-455-41 Load: 100 N/cm (57 lbf/in) Criteria: 0.2 dB/km attenuation increase	All cables tested exceed 100N/cm with <0.2dB	All cables tested exceed 200N/cm with <0.2dB
Impact Resistance Test Method: EIA-455-25A Impact Energy: 5.88 N*m (4.34 lbf*ft) Criteria: 0.2 dB/km attenuation increase	All fibers had <0.20 dB change in attenuation	All fibers had <0.20 dB change in attenuation
In all cables the top, middle and bottom ribbons in each tube were measured. Single mode fiber was used for all testing. Three or more of each cable design were tested.		

From the data shown, one can see that previous experience with ribbon and OSP ribbon cables was quite beneficial in the immediate success of the design.

Field Installation

Acceptance of the design in the market place was quickly confirmed when several orders were placed for 216 & 288 fiber cables by major RBOC and CATV customers only one month after its product release. Installation of the cables ranged from backbone runs from central office to co-location equipment and stub assemblies from the OSP vault rooms to patch panel racks several floors above.

One such installation involved cable runs in 1.25" duct from manhole to the equipment rooms with excellent results. Lengths of cable installed were 600', 1100', and 1450', which validated the requirement for 600lb pull strength as an initial design requirement. Since the cable design borrowed heavily from traditional OSP products, Installers were able to use existing tools and techniques to pull, access, and terminate the cable.

Conclusion

Continuing trends of higher patch panel port densities, developments in parallel optics, and increased space constraints are driving use of ribbon and ribbon distribution cables further into the network. Regulations and concerns over flame propagation in highly congested vault rooms, CO's, POP's, etc. will make the need for NEC rated cables a necessity. Efficiencies gained in OSP construction from mass fusion are also realized in premises environments. Mass termination connectors, such as MTP, MPO, SMC, etc. are being utilized in the network making ribbon a necessity. All of these elements combined contribute to the increasing demand for high fiber count ribbon distribution cable in the premises.

Attention to detail, thoughtful design consideration, and use of tried and true processes made for a smooth product development. The ribbon distribution cable utilizing a stranded design was found and proven to incorporate the functionality our customers needed in a package that was easily manufactured. Through application of proven design, processes, and attention to customer specifications a successful development project was completed exceeding all requirements.

Biography



Roger Vaughn is Product Manager for Ribbon Cable products at Pirelli Communications Cables & Systems NA in Lexington, SC. Key responsibilities include product development, market strategy, sales analysis, and customer account management. After serving an enlistment with the US Air Force, Roger received his Bachelors of Science degree in Material Science and Engineering from North Carolina State University in 1995. During his academic studies he served an internship with CommScope, and following graduation started his career with Berk-Tek as a process engineer. He joined Pirelli in 1997, initially working on high fiber count ribbon cable development, progressing to Product Management in 1998. He has been awarded 3 patents and has 2 previous publications.

Riser-Rated Dry Core Indoor/Outdoor 12-36 Fiber Count Cables

Samuel Aderogba, Kaushik Chakrabarty, Charles Jackson, Paul Neveux,

Wayne Newton, Mark Shmukler

OFS

Optical Connectivity Division

Norcross, Georgia

+1-770-798-2781 · cwjackson@ofsoptics.com

Abstract

Design and development of a series of compact, flexible, tight-buffered, dry core Indoor/Outdoor cables in fiber counts of 12 through 36. Cable features include weather resistant jacket, units and buffer, unique water-blocking approach. Tested to UL 1666 for Riser rating and ICEA-696 environmental/mechanical performance.

Keywords

Premises cable; Indoor/Outdoor.

1. Introduction

There are applications where telecom providers prefer to connect optical fiber cables directly between an outdoor branching location and a frame located within a building some distance from the exterior wall. Such placements typically require that the cable used meet both outdoor environmental and indoor fire requirements. By eliminating the junction near the building wall, connection expense and labor is reduced.

OFS, formerly Lucent Technologies' Optical Fiber Solutions Division, developed several cables for this indoor/outdoor application. This paper presents features and performance of the new designs.

2. Features

Indoor cable installers are accustomed to a dry core, and OFS used dry water-blocking techniques to avoid the mess associated with typical outdoor cable gels or filling compounds in these cables. U. S. customers also prefer a PVC-based tight buffer that can be easily stripped from the fiber. Figure 1 illustrates the 12-fiber cable cross-section, while Figures 2 and 3 illustrate the 24- and 36-fiber constructions, which contain multiple 6-fiber units ROL about a central organizer.



Figure 1. Twelve Fiber Cable

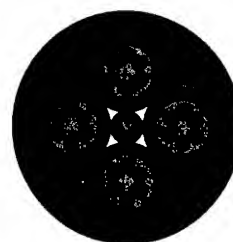


Figure 2. 24 Fiber Cable

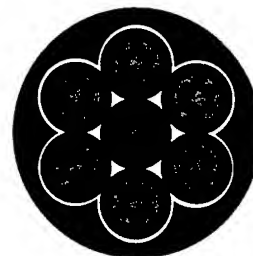


Figure 3. 36 Fiber Cable

The new designs work with singlemode and all types of multimode fibers. The new higher bandwidth multimode fibers were more challenging to cable.

3. Performance

These three cables were designed to meet the mechanical and environmental requirements of ICEA-696. The following sections highlight the fire, mechanical and environmental performance of the designs.

3.1 Fire

These cables have been tested to the UL 1666 standard and listed as Riser (OFNR). The 36-fiber cable was made using both leaded and lead-free PVC buffers. Table 1 shows the results.

Table 1. Fire Performance

Measure	Criterion	12-fiber	24-fiber	36-fiber (leaded, non-leaded)
Flame	< 12 ft	5 ft	6 ft	5.5, 4.5 ft
Temp	< 850°F	389°F	399°F	407, 384°F

3.2 Mechanical

These cables were tested to various mechanical specifications found in ICEA-696. This standard allows added losses of up to 0.6 dB for multimode fibers and 0.4 dB for singlemode fibers under a variety of mechanical loadings. Table 2 lists the tests, and cross-references to Figures 4 through 11 showing added losses on 50 micron multimode, 62.5 micron multimode, and 9 micron singlemode fibers in cables of 12/24/36 counts with lead-containing buffer, and cable of 36 count with non-lead PVC buffer.

Table 2. Mechanical Tests

Key	Test
A	Cold Bend, FOTP-37, 4 wraps at 20X diam, -10°C
B	Hot Bend, FOTP-37, 4 wraps at 20X diam, 60°C
C	External Freeze, FOTP-98A
D	Cyclic Flex, FOTP-104, 25 cycles 180° over 20X diam
E	Impact, FOTP-25, 4.4 N-m twice at 3 locations 150 mm apart
F	Tensile Load and Bend, FOTP-33, -38. 2670 N rating, 30% residual load
G	5 minutes after all load released on above test.
H	Compressive Load, FOTP-41, 220 N/cm, then hold 110 N/cm for 10 minutes, measure

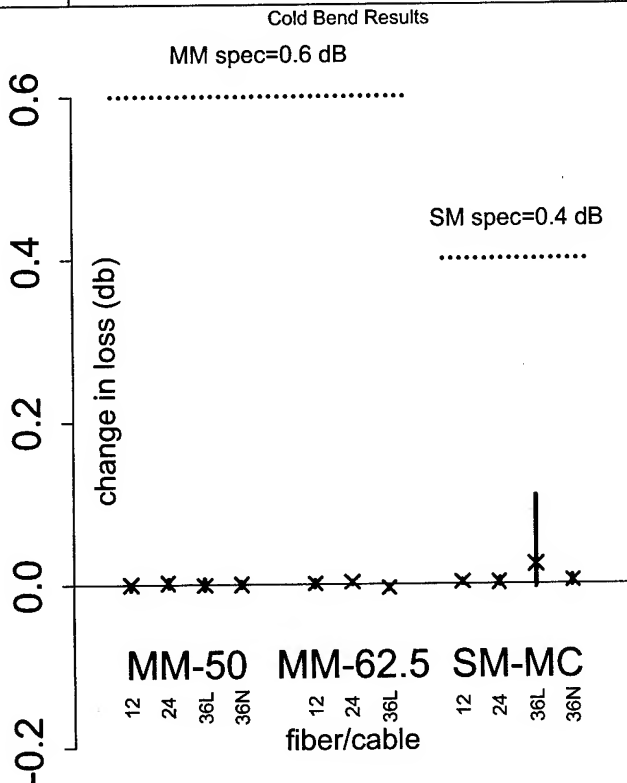


Figure 4. Cold Bend Results

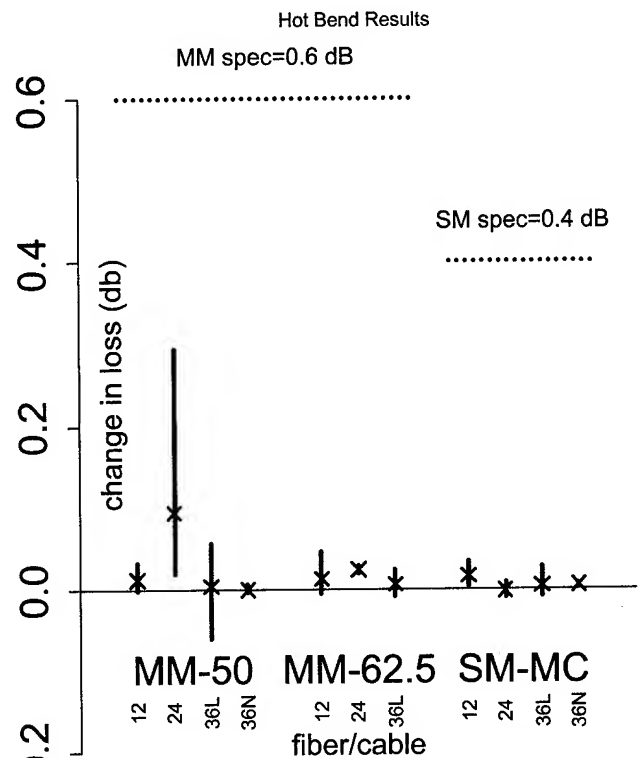


Figure 5. Hot Bend Results

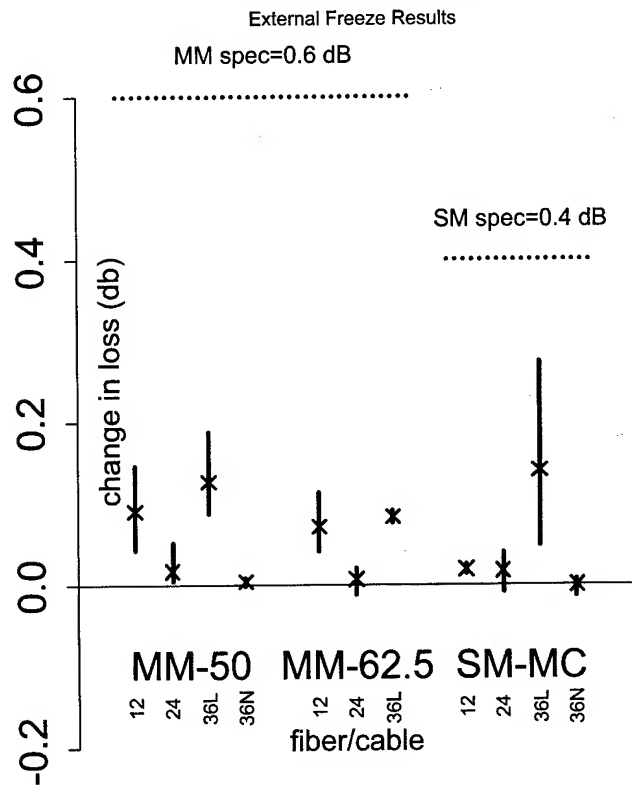


Figure 6. External Freeze Results

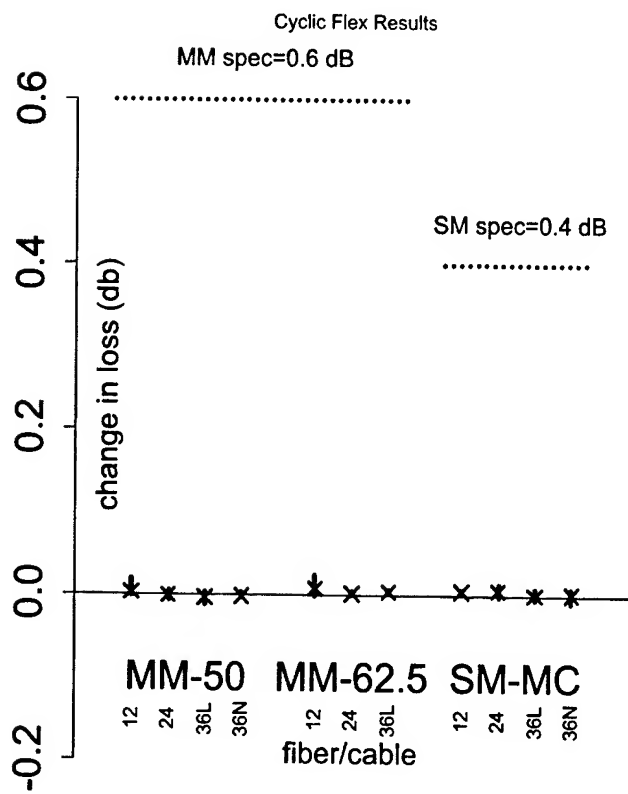


Figure 7. Cyclic Flex Results

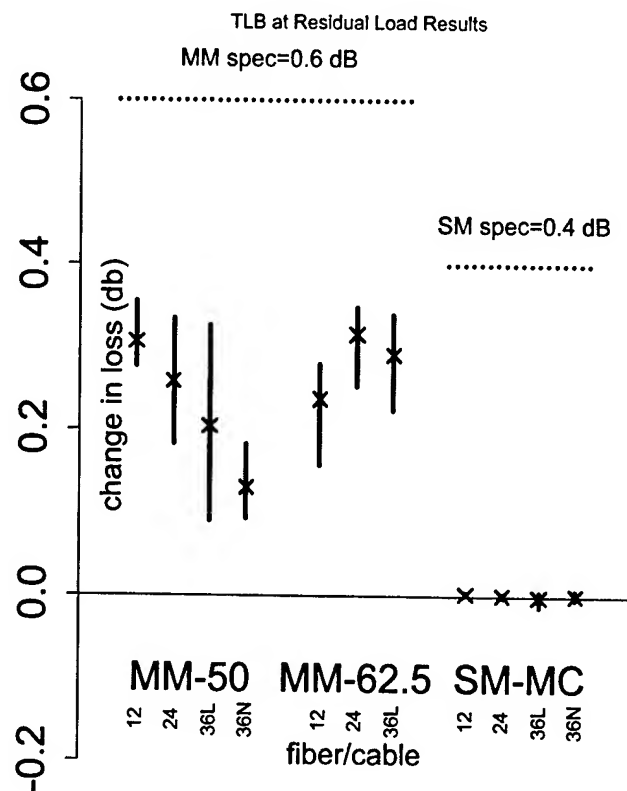


Figure 9. TLB at Residual Load Results

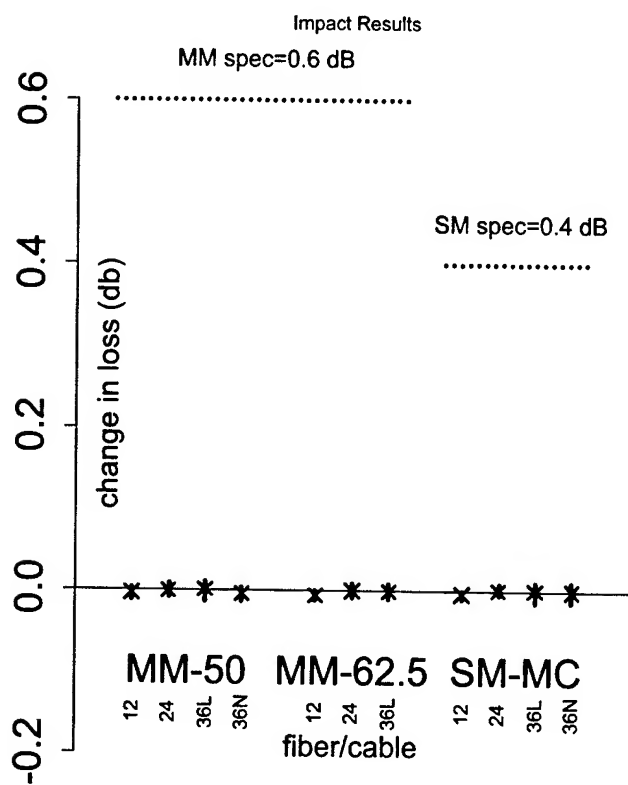


Figure 8. Impact Results

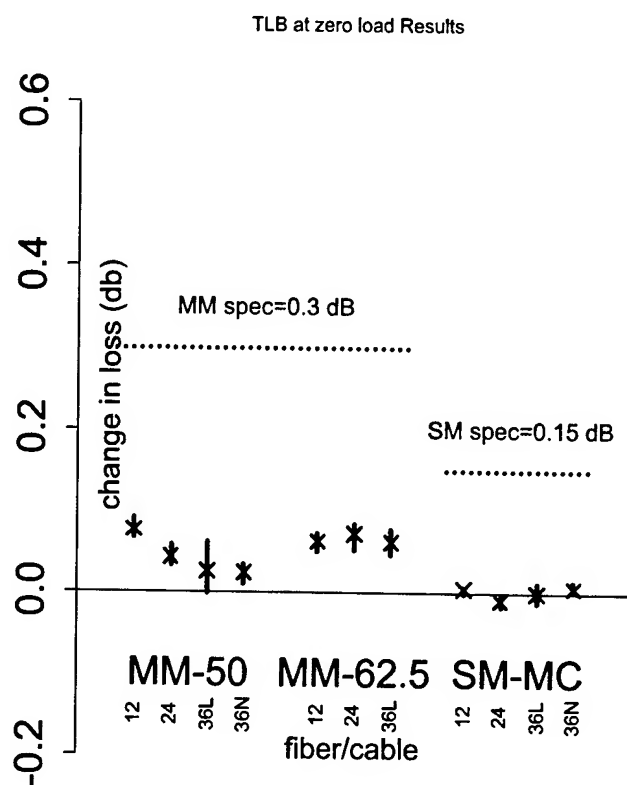


Figure 10. TLB after Load Results

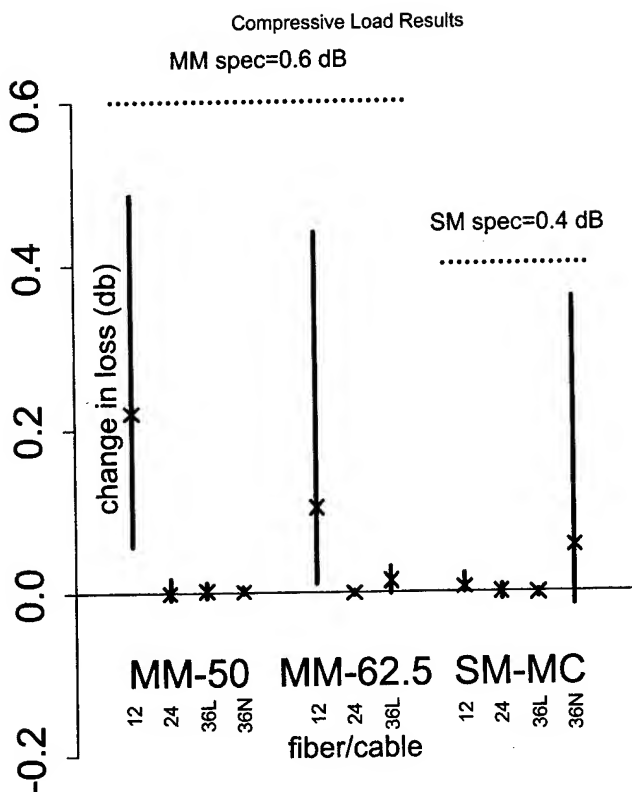


Figure 11. Compressive Load Results

Referring to these figures, it can be seen that the mechanical tests most difficult to pass were the compression and hot bend tests. The added losses in tensile load and bend were similar at all fiber positions. In contrast, the inner three fibers of the 12-fiber cable showed greater losses in the compression and hot bend test than the outer nine.

In addition to the loss change requirements under these loads, ICEA-696 specifies a maximum strain under rated load and under residual load. Table 3 indicates the results of these strain measurements.

Table 3. Strain Limits During Tensile Load and Bend Test

Metric	Limit	12-fiber	24-fiber	36-fiber Leaded	36-fiber NonLead
Strain at rated load	0.6%	0.351%	0.335%	0.227%	0.180%
Strain at resid. load	0.2%	0.099%	0.169%	0.111%	0.067%

3.3 Environmental

Unlike most other premises cables, Indoor/Outdoor cables must operate down to temperatures of -40°C . The ICEA-696 specification limit is a change in loss of no more than 0.6 dB/km at 1300 nm for multimode fiber types and no more than 0.4 dB/km at 1550 nm for singlemode fiber types. Table 4 details the results.

Table 4. Temperature Cycling

Fiber Type / Max limit for Loss change	Maximum Loss Change, dB/km on two cycles from -40°C to 70°C			
	12-fiber	24-fiber	36-fiber Leaded	36-fiber NonLead
50 μm / 0.6 dB/km	0.165	0.226	0.311	0.218
62.5 μm / 0.6 dB/km	0.022	0.056	0.050	N/A
SM-MC / 0.4 dB/km	0.028	0.053	0.035	0.232

4. Conclusions

Three US Riser rated PVC-buffered indoor/outdoor cables with dry core constructions are described. Cables with 12, 24, and 36 fiber counts have been developed. Additional development showed that non-leaded PVC constructions behave similarly in mechanical/environmental/and fire testing.

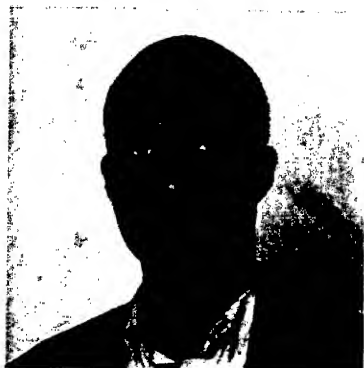
5. Acknowledgments

Thanks to Kelly Johnson, Hal McGinnis, and Tony Simons for manufacturing support, Bill Allen for mechanical and environmental qualification testing, and Hong Chen for fire testing.

6. References

- [1] ANSI/ICEA S-104-596-2000, "Standard for Indoor/Outdoor Optical Fiber Cable"

7. Authors



Mr. Samuel Aderogba

Member of Technical Staff. Responsible for cable design, process development, instrumentation, and optical measurement. He holds a B.Sc. and M.E. degrees in Mechanical Engineering from the University of Ibadan, and the Tennessee State University, respectively. He is a member of the American Society of Mechanical Engineers.



Dr. Kaushik Chakrabarty

Member of Technical Staff. Responsible for product development, materials selection and materials evaluation, for fiber optic apparatus and fiber optic cables. He has a Ph.D. in Polymer Science from The University of Connecticut.



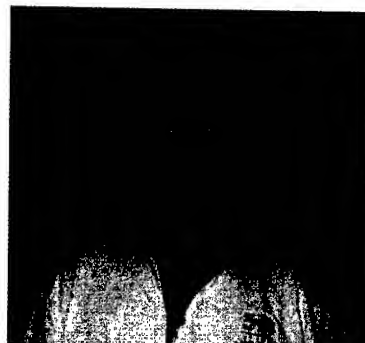
Dr. Charlie Jackson

Member of Technical Staff. Responsible for cable design and testing. He has a Ph.D. in Mechanical Engineering from Stanford University. Previous experience includes optical fiber processing and data analysis.



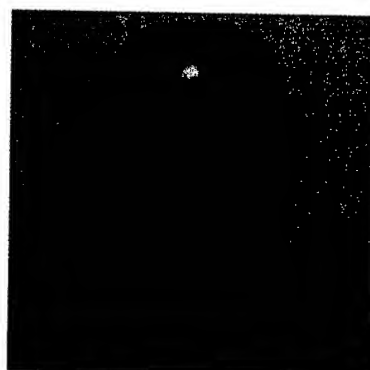
Dr. Paul Neveux

Technical Manager for Premises Cable Design and Development. He has a Ph.D. in Chemistry from University of North Carolina, Chapel Hill. Previous experience includes work at Sumitomo Electric for cable design and manufacturing.



Mr. Wayne Newton

Distinguished Member of Technical Staff. Recently retired after 36 years with Western Electric, AT&T, Lucent Technologies and OFS. For the last 8 years he has been responsible for Process Development Engineering. He obtained a B.S. Degree in Electrical Engineering from Clemson University and an M.S. Degree in Industrial Engineering from Texas Tech University. He has 8 U.S. and 3 Foreign Patents in the Copper and Fiber Optic Cable field.



Mr. Mark Shmukler

Formerly Member Technical Staff. Responsible for process and machine development. He obtained a M.S. in Electro-Mechanical Engineering from Lvov Polytechnic Institute. He is a registered professional engineer and holds 3 patents in the Fiber Optic Cable field.

Design of Optical Fiber Ribbon Cord

Huiping Shi, Yingming Wang, Cilong Yu, Shiyong Wang

Wuhan Research Institute of Posts & Telecommunications
Hongshan Dist. Wuhan Hubei Prov 430074 P.R.China
+86-27-87801093 hpshi@fiberhome.com.cn

Abstract

The growing of optical communications system in recent years has increased a count of indoor optical fiber cable. When the count is demanded to reach over 72 cores, optical fiber ribbon cable is usually chose. The main reason is that optical fiber ribbon cable including many optical fibers may be provided with smaller outer-diameter.

Generally, the structure of indoor optical fiber ribbon cable is that a layer of halogen-free flame retardant sheath covers fibers and aramid yarn. The sheath can expand or contract as environment temperature changes. If cable contains more fibers, the fibers might be stressed and the attenuation loss value might rise. This paper introduces a new structure of optical fiber ribbon cable for indoor use, which has two layer of sheathes. Inner layer is made of polyester material and outer layer is halogen-free flame retardant sheath. The aramid yarn is mounted between two layer sheathes. This cable structure not only protects fibers from producing strain but also meets specifications.

A variety of tests concerning optical transmission loss characteristics, mechanical characteristics, and fire-resistance characteristics have been performed on the cable structure mentioned above. It has confirmed that this cable structure possesses excellent characteristics.

Key Words: optical fiber ribbon cord; Design; Indoor cables

1. Introduction

Indoor cables have been used in building widely by way of indoor leadin of connecting network and trunk subsystem or level subsystem of premises distribution system for building telecommunications because of its more light and soft and more convenient assembly compared to the outdoor cable.

Several years ago, simplex and duplex cables mainly used for jumper and trailer are dominant on market in China. The growing of optical communications system in recent years has increased optical fibers. Cables that contain more than 12 optic fibers appear various constructions based on purpose and situation. Especially in FHHT system, fiber cores of premises distribution will be demanded to increase several times. It is very important to increase cabling port densities in less space [1][2].

When the count is demanded to reach over 72 cores, optical fiber ribbon cable is usually chose. The main reason is that optical fiber ribbon cable including many optical fibers may be provided with smaller outer-diameter to satisfy the requirements.

Generally, the structure of indoor optical fiber ribbon cable is that a layer of halogen-free flame retardant sheath covers fibers and aramid yarn. The sheath can expand or contract as environment temperature changes. If cable contains more fibers, the fibers might be stressed and the attenuation loss value might rise. This paper introduces a new structure of optical fiber ribbon cable for indoor use, which has two layer of sheathes. Inner layer is made of polyester material and outer layer is halogen-free flame retardant sheath. The aramid yarn is mounted between two layer sheathes. This cable structure not only protects fibers from producing strain but also meets specifications. A variety of tests concerning optical transmission loss characteristics, mechanical characteristics, and fire-resistance characteristics have been on performed the cable.

2. Cable Structure

The cable has been designed for 12×12 cores single-mode ribbon fiber. The ribbon dimensions meet

specifications (Table 1).

Two layers of sheath between which aramid yarns are twisted (Figure 1 and Table 2) cover the ribbons. Inner sheath is made of polyester materials having higher modulus of elasticity and lower thermal coefficient. The contraction property of the polyester materials is better than

halogen-free flame retardant materials, so the covered fibers can be protected as better as possible. And the extra length of fibers could be assured. Outer sheath is made using halogen-free flame retardant (HFFR) materials to protect cable from fire.

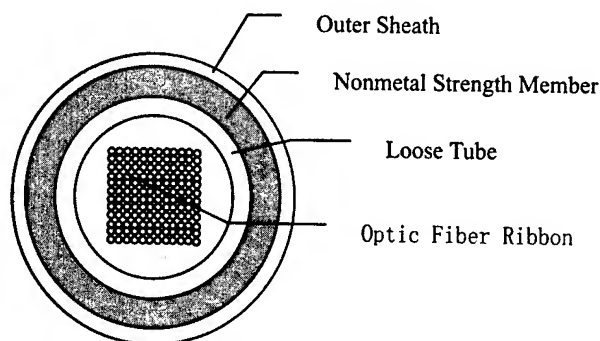


Figure1. Structure of optical fiber ribbon cord

Table1. Optical fiber ribbon dimension

Ribbon Samples	Ribbon Width(μm)	Ribbon Height(μm)	Vertical Separation(μm)
1#	3197.9	312.7	16.2
3#	3195.9	316.1	18.6
4#	3183.3	311.1	21.6
5#	3171.8	317.9	19.9
6#	3178.6	312.3	21.6
11#	3187.5	308.5	22.0

Table2. Structure Specifications of Cable

No.	Name	Material
1	Sheath	HFFR
2	Nonmetal Strength Member	Aramid
3	Loose Tube	Polyester
4	Optic Fiber Ribbon	-----
5	Diameter	17mm

1550nm for single-mode fibers. The maximum optic losses are 0.338dB/km at 1310nm and 0.20dB/km at 1550nm(Table 3).

Table 3. Results of Transmission Characteristics Test

Wavelength	1310nm	1550nm
Maximum attenuation loss	0.338 dB/km	0.20 dB/km

3. Cable Performance

We had performed the optical transmission loss characteristic test, mechanical characteristic test, and fire-resistance characteristic test on the cable according as methods prescribed by IEC 60794-1-2[4].

3.1 Transmission Characteristics

The attenuation loss is tested by OTDR. The measurements were made at transmission wavelengths of 1310nm and

3.2 Mechanical Characteristics

The mechanical characteristic tests had been performed in according with the test procedures specified in the IEC 60794-1-2[1]. Test items, requirements and results are showed in table 4. The added attenuation loss was measured at transmission wavelengths of 1550nm.

The results indicate that there were no fiber breaks and a

permanent or temporary increase in optical attenuation value is lesser than 0.03dB in sample at 1550nm for all the tests.

It is remarkable that the load was larger than the value specified in the standard in the process of crush test but the

added attenuation loss was extremely low (only 0.01dB). Therefor this cable structure can provide better capability of tension and crush resistance to protect fibers from deformation and damage.

Table 4. Results of Mechanical Characteristics Test

Items		Units	Requirements	Results
Tensile	Strain-stress	%	200N applied for 5min	0.02
	Added optical Loss		200N applied for 5min	0.02
Crush			1000N applied for 1min	0.01
Impact			Dots:5; Impact energy:1.0Nm; Number of impacts: 3.	0.025
Repeated Bending			Bending radius:20D; Mass of weights:20N; Number of cycles:1000 times; Requirements: no change in attenuation after test.	0.01
Torsion		dB	Torsion angle: $\pm 180^\circ$; Mass of weights:20N, Number of cycles:10 times, Requirements: no change in attenuation after test.	0.02
Cable Flexing			Pulley diameter:20D; Mass of weights:20N, Number of cycles:10 times, Requirements: no change in attenuation after test.	0.01
Vibration			f:50Hz; Amplitude: ± 3 mm, last 10min; Requirements: no change in attenuation after test.	0.01

3.3 Temperature Characteristics

The cable was tested for attenuation at room temperature and attenuation during temperature cycling. The measurements were made at transmission wavelength of 1550nm.

IEC 60794-1-2-F1 temperature cycling requires that the cable must undergo two cycles consisting of an appropriate low and high temperature for appropriate intervals of time. The low and high temperature limits are to be selected based on purchaser requirements. Therefor, the temperature cycling test according to Figure 2 was performed on cable.

The low and high temperature limits were -30°C and 70°C respectively. The measurements were made after holding 24 hours at each temperature point at transmission wavelength of 1550nm.

The result of statistical data for temperature attenuation of all fibers is expressed as Figure 3. The maximum value is 0.024dB/km with 80% of the measured values no greater than 0.007Db/km. Thus it is can be seen that the inner sheath of cable takes the better effect on improving the temperature attenuation characteristic.

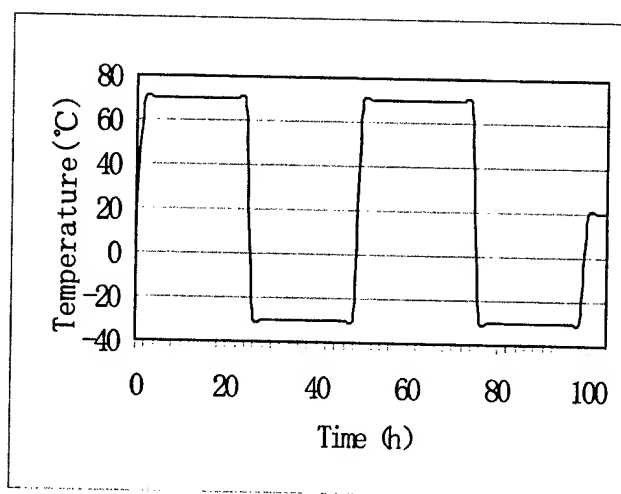


Figure 2. Temperature Cycling

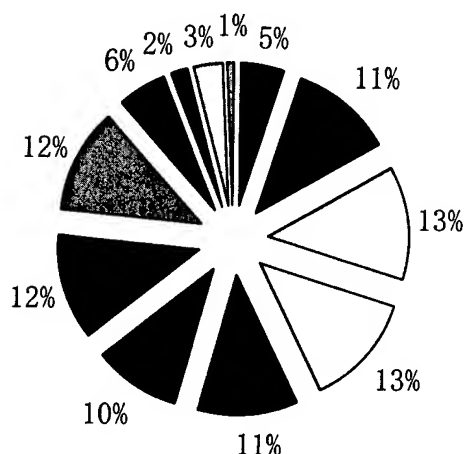


Figure 3. Diagram of Temperature Attenuation statistical Result

3.4 Flame Retardant Characteristic

The flame-retardant test was performed on the sample made using the cable in according with IEC 60332. Figure 4 shows the test arrangements meeting IEC 60332 standard requirement. Figure 4(a) shows the vertical combustion test arrangement and Figure 4(b) shows the horizontal combustion test arrangement. The result of the horizontal combustion test is that flame on the cable samples

extinguished immediately by itself when the flame was taken away. The specification of IEC 60332-1 for the vertical combustion test is that a cable shall pass the test if the distance between the lower edge of the top support and the onset of char shall be greater than 50mm.[5] The tested samples passed the tests (see Figure 5).

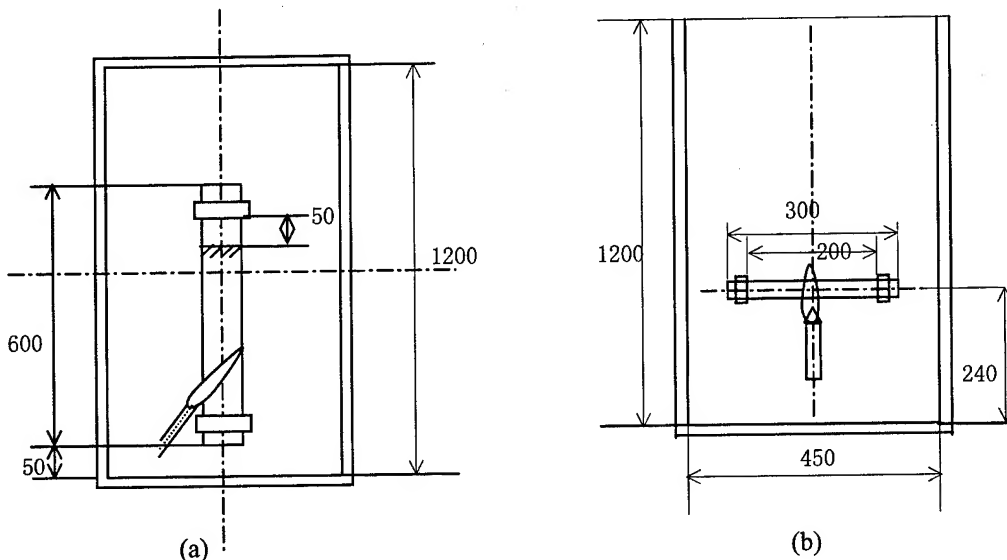


Figure 4. Flame-retardant Arrangement

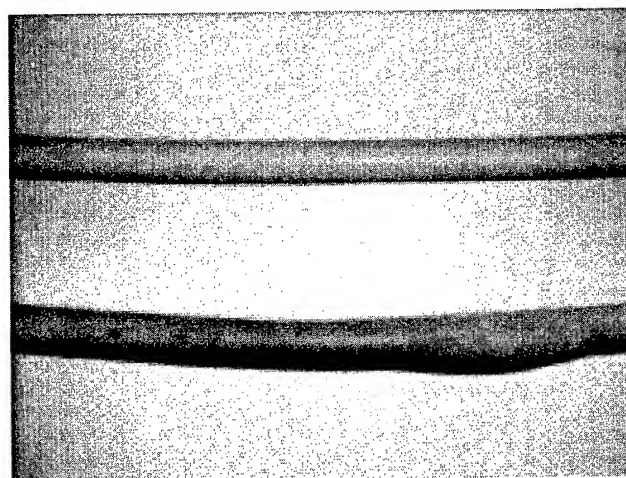


Figure 5. Photos of Combustion Test

4. Conclusions

Optical fiber ribbon cord has predominance in building FTTH system because it can meet the requirement mounting more terminals in limited space. The optical fiber ribbon cord introduced by this paper not only meets above requirement but also has points as follows:

1. The structure having two layers of sheath between which aramid yarns are twisted provides the cord with good tensile performance and crush performance.
2. The cord possesses excellent temperature characteristic because of the lower contraction coefficient of inner sheath.

The maximum value is only 0024dB/km.

3. The outer sheath consisting of HFFR materials provides the cord excellent flame-retardant characteristic to meet the requirement of flame-retardant for indoor using.

The cord cable has been on the Chinese market successfully.

5. References

- [1] Fuminori Nakamjima, Nobuhisa Ishii, Ichiro Kobayashi, Masami Hara, Kuniaki Yamaguchi, and Hitoshi Ishimaru, Development of Halogen-free, Flame-retardant Miniature Optical Fiber cord, 50th IWCS 2001, P201-205

[2]Jianwei Wang, Kaushik Chakrabarty, J.Thomas Chapin and Carla G.Wilson,Development of Low Smoke Non-Halogen MiniCord® Cables, 50th IWCS 2001,P212-218

[3]IEC 60794-2-30 Ed.1-Indoor optical fibre cables-Part 2-30:Family specification for optical fibre ribbon cords,2002

[4]IEC 60794-1-2,Optical fibre cables-Part 1-2:Generic specification-Basic optical cable test procedures,1999

[5]IEC 60332-1, Test method on electric wires or cables under fire conditions Part 1:Test on a single vertical insulated wire or cable.

High Modulus Tight Buffer Design with Improved Microbend Resistance and Low Temperature Performance

**Paul E. Neveux, Jr.; Wayne M. Newton¹; Samuel A. Aderogba;
Mala Nagarajan; Christopher N. Okafor**

OFS Laboratories, OFS, 2000 Northeast Expressway
Norcross, Georgia

+1-770-798-5314 · pneveux@ofsoptics.com

Abstract

A dual layer buffering system employing a new compliant layer is described and its performance is compared with the former dual layer and conventional single layer buffering systems. Buffer materials, whose flexural modulus is higher than typical buffer materials, such as PVC, are needed for high performance and high reliability pull-proof connectors. In addition, systems are now moving towards higher bandwidth capable fibers, like the 50 μm multi-mode LaserWave™ fibers with reduced differential modal dispersion (DMD). Unfortunately, 50 μm multi-mode fibers are approximately three (3) times more microbend sensitive than 62.5 μm multi-mode fibers. While the current dual layer system is adequate for 62.5 multi-mode and single mode optical fibers, a dual layer system with a new compliant layer was developed to handle the more microbend sensitive 50 μm fiber. The new system is shown to have much lower microbend sensitivity minimizing the difference seen between 62.5 and 50 μm buffered fibers. The new dual layer tight buffer system also has much lower attenuation during loose coil temperature cycling tests.

Keywords

Optical, fiber, buffer, multi-mode, modal dispersion, connectors

1. Introduction

1.1 High Reliability Pull-Proof Connectors

The need for high modulus buffer materials starts with the connectors, specifically pull-proof connectors, which maintain optical performance when axial and side loads are applied to the optical fiber cable.¹ These connectors are designed to meet Telcordia's GR-326² which includes active tension tests that require pull-proof cable – retention mechanisms. In addition, when these pull-proof connectors are used, the ferrule assembly inside the connector travels towards the cable when mating with another connector. This results in excess buffered fiber length in the connector/cable assembly. In a properly designed connector-cable system, the buffer has adequate stiffness to push back into the cable and the cable jacket is loose enough to allow the movement of the

buffered fiber, but not so loose as to allow the buffered fiber to pull out of the jacket during stripping of the buffered fiber.

The need for a high modulus buffer is especially important given the current activity in IEC SC86A WG 3. The working group is developing a test method³ as part of a new specification, 60794-2-50, for patch cords. The purpose of the method is to examine the change in attenuation when a buffered fiber in a cable moves during the mating of connectors. The test will assess how cable and buffered fiber designs, used in patch cords and interconnect cables, maintain optical performance with pull-proof connectors.

1.2 High Bandwidth 50 μm Multi-Mode Fiber

The second compelling reason for a dual-layer high modulus tight buffer system is the introduction of new high bandwidth 50 μm fibers with reduced differential modal dispersion (DMD) like LaserWave™ fiber. With the demand for increased bandwidth and longer deployment lengths, 50 μm multi-mode fibers have been redesigned and optimized for 10-gigabit data transmission with lengths of up to 600 meters with LaserWave™ XL fiber, by reducing DMD which causes pulse broadening. As a consequence, low-DMD 50 μm multi-mode fibers, like LaserWave™, are seeing increased penetration in enterprise, central office and OEM applications.

The microbend sensitivity of 50 μm multi-mode fibers is approximately 3 times higher than standard 62.5 μm multi-mode fiber.⁴ Despite this fact, the standards, shown on page 2 in Table 1, still restrict the attenuation change for 50 μm multi-mode fibers to the same levels as standard 62.5 μm multi-mode fibers. For these high performance 50 μm low-DMD multi-mode fibers, a dual-layer high modulus buffer system is ideally suited to provide excellent microbend resistance and low temperature performance that is necessary to meet the most demanding attenuation requirements, as will be shown below.

¹ Retired

Copyright © 2002, Fitel USA Corp. All rights reserved

1.3 Buffer and Cable Requirements

Table 1 summarizes some of the key requirements for the tight buffered fiber and the cables in which they are employed. While there are a number of other requirements, *e.g.* impact resistance, which are not included in the Table, the attributes listed are ones on which this paper will focus. In the case of jumpers or interconnect cable where anti-buckling elements are not typically used, the environmental attenuation performance requirement of cable is essentially the performance requirement of the tight buffered optical fiber. Examining Table 1, the rationale for first item, buffer stiffness, was mentioned above in the requirements for a reliable pull-proof connector.

For many customers, the second requirement, the ability to remove the buffer coating without removing the optical fiber coating, is very important. In single-layer high modulus or stiff buffer design, the buffer material adheres so strongly to the secondary coating of the optical fiber that it is impossible to remove the buffer without destroying the optical fiber coating. Previous designs used a "release" layer between the high modulus material and the secondary coating.^{5, 6} In the dual-layer buffered structure, the compliant layer also acts as a release layer, so that the buffer material can be removed without damaging the optical fiber coating beneath it.

Table 1. Buffer & Cable Requirements

Performance Attribute	Requirement
Buffer Stiffness	Meet connector anti-buckling requirements while keeping "memory" to a minimum
Buffer Strippability	Buffer must be removable such that the primary and secondary coatings of the fiber remain intact for connectorization.
Buffer Microbend Resistance	Resist the rigors of installation and cable manufacturing without increase in attenuation.
Cable Low Temperature Optical Performance:	<p>ICEA 596 (Premises) & 696 (I/O)</p> <p>Single Mode: $\Delta\alpha \leq 0.4$ dB/km @ 1550 nm</p> <p>Multi-mode: $\Delta\alpha \leq 0.6$ dB/km @ 1300 nm</p> <p>Telcordia GR-409</p> <p>Before Aging:</p> <p>Single Mode: $\Delta\alpha \leq 0.3$ dB/km @ 1550 nm</p> <p>Multi-mode: $\Delta\alpha \leq 0.6$ dB/km @ 1300 nm</p> <p>After Aging:</p> <p>Single Mode: $\Delta\alpha \leq 0.6$ dB/km @ 1550 nm</p> <p>Multi-mode: $\Delta\alpha \leq 1.2$ dB/km @ 1300 nm</p>
Plenum: 0 °C Riser: -20 °C Indoor/Outdoor: -40 °C	

As mentioned above, the need for a microbend resistant buffering system is especially important for 50 μ m multi-mode fibers. Another important performance attribute is low temperature optical performance. Unfortunately, by choosing a high modulus buffer material, the amount of force imposed by the contraction of the buffer material on the optical fiber at low temperatures may cause attenuation increase if not properly designed. Meeting the environmental attenuation requirements becomes increasingly

difficult as one designs cables from single mode fiber to 62.5 μ m multi-mode fiber to 50 μ m multi-mode fiber.

1.4 Single vs. Dual-Layered Buffered Fibers

In order to meet all the requirements described above, a dual-layered high modulus buffered structure is used. Figure 1, below, shows the typical structure of a single layer buffered fiber with a standard 250 μ m fiber in the center, surrounded by a buffer material to an outer diameter of 900 μ m. Again, while it is possible to make a high modulus single layered buffered optical fiber, the buffer material will adhere to the optical fiber coating, such that the buffer cannot be removed without also removing optical fiber coating.

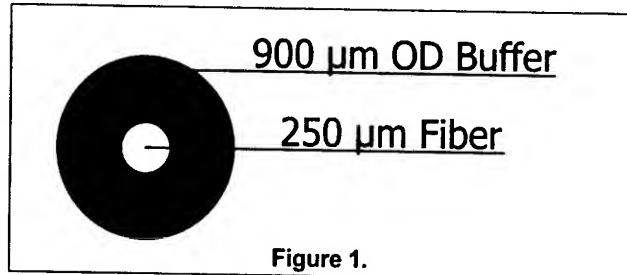


Figure 1.

Figure 2 shows the dual layered buffered fiber structure. The compliant layer, shown in the figure, not only allows the fiber to be stripped off the buffer material without removing the coating, but also greatly enhances its microbend and low temperature performance, as will be shown below.

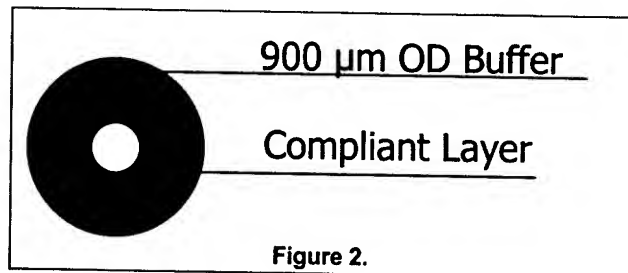


Figure 2.

2. Experimental

2.1 Test Matrix

Shown in Table 2 are the tests that were performed in this evaluation.

Table 2. Testing Matrix

Test	Procedure
Strip Force	FOTP 178
Microbend Resistance	Short Length Method
Environmental Cycling	Modified GR-20
Compliant Layer Modulus	Dynamic Mechanical Analysis

2.2 Strip Force

The test was performed according to FOTP-178 using Instron Series IX or Model 4501 tensiometer with a 10 N (1.02 kg) load cell, a cross-head speed of 0.5 in/min and 15 mm strip length. A

Microstripperⁱⁱ brand stripper was used. The maximum load detected during the test was considered the strip force. A 0.016" (406 μ m, orange) stripper was used to remove only the buffer material and leave the optical fiber coating intact. Samples were tested before and after temperature cycling, which included 5 days of 85°C aging.

2.3 Microbend Resistance

Microbend resistance was performed using a "short length" method where the buffered fibers were pressed against 900 μ m wires between two flat plates where the fiber and wires were perpendicular to each other. The number of wire-to-fiber crossovers was typically 25 (5 - 900 μ m wires X 5 buffered fiber passes). The fiber was connected to the multi-mode power meter output, wrapped around a 1" mandrel mode stripper, run through the microbend apparatus and terminated to the input of the power meter. The reference attenuation of the set-up was measured without the top plate, then weights were added in a step-wise fashion and the attenuation change was recorded. Results are expressed in attenuation versus weight per crossover (lbs/XO). The maximum weight per crossover used was below the elastic limit of the buffer material.

2.4 Temperature Cycling

Temperature cycling was performed in a Tenny Engineering Model WI-40150 walk-in thermal chamber. The attenuation change was measured using an OTDR. Samples were first taken off the reel and made into loose coils. These loose coils were then placed horizontally in trays and put into the walk-in chamber. The temperature cycle used is shown in Figure 3. Each temperature was held for 24 hours and the attenuation was measured at the end of each 24 hour period.

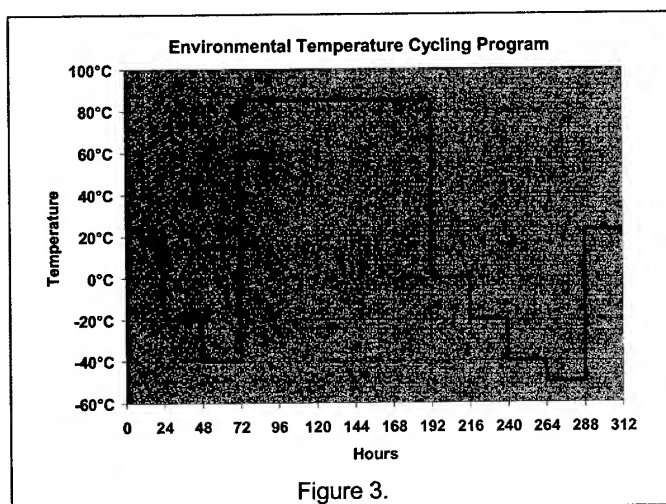


Figure 3.

2.5 Dynamic Mechanical Analysis (DMA)

Samples were tested on a TA Instruments Model 2980 DMA (Version 1.7B Firmware) using a film specimen holder in tension

ⁱⁱ Microstripper is a brand name of Micro Electronics, Inc.

configuration. Samples were tested from -100 °C to 150 °C at the rate of 2 °C/minute.

3. Results and Discussion

3.1 Buffer Removal - Strip Force

Many customers expect to be able to strip the high modulus buffer off the optical fiber without removing the optical fiber coating. They also expect to be able to do this after the cable has aged. The strip force results before and after 5 days of aging at 85 °C, using 16 mil (406 μ m) strippers are shown in Table 3, below. While the strip force values are on the high side of the typical specification (0.5 lbs - 3 lbs.), in all cases, the optical fiber coating was left intact and undamaged. Aging only slightly reduces the strip force. Further, the thickness of the compliant layer does not affect the strip force to any measurable extent.

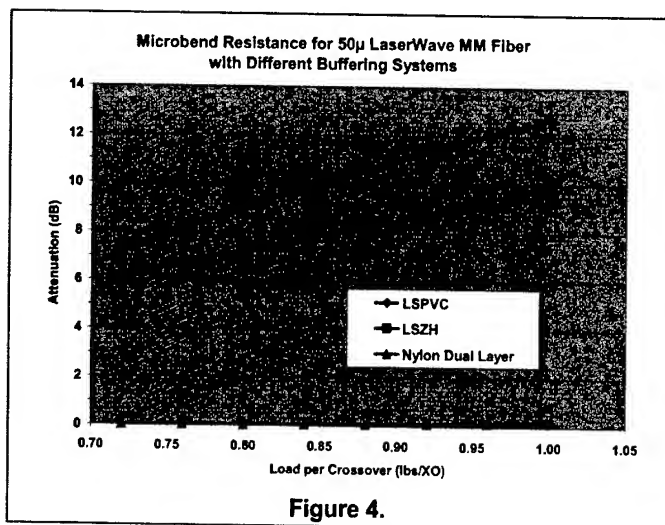
Table 3. Strip Force using 0.016" Strippers

New Compliant Layer Thickness	Unaged Strip Force (lbs)	5 Day/85°C Aged Strip Force	Optical Coating Intact & Undamaged?
58% Ref	2.9 \pm 0.1	2.7 \pm 0.2	Yes
80% Ref	2.9 \pm 0.1	2.4 \pm 0.3	Yes
Reference	2.9 \pm 0.1	2.1 \pm 0.2	Yes

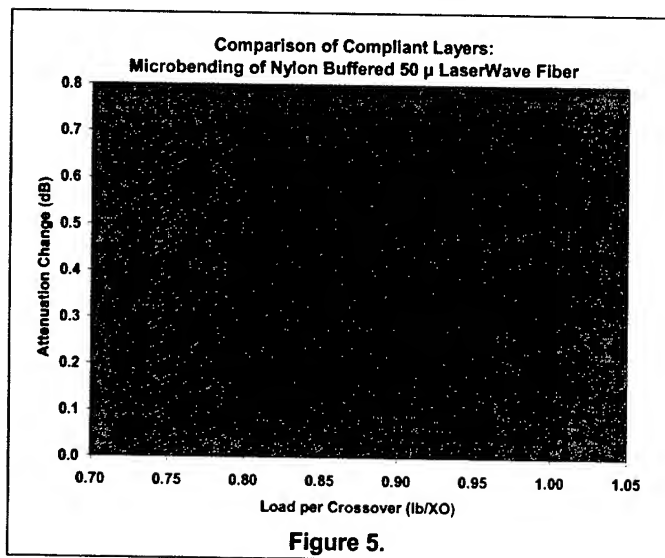
3.2 Microbend Resistance

In order to get a perspective of how different the microbend sensitivity is between a single layer buffered fiber with a relatively soft buffer, like low-smoke zero-halogen (LSZH) or low-smoke PVC (LSPVC), and a dual-layered buffered fiber with a higher modulus buffer, like nylon, and compliant inner layer, the short length microbend test was performed on these two buffer structures using 50 μ m LaserwaveTM multi-mode fiber. Figure 4, on page 4, shows the results of that test where the error bars are 3 standard deviations. Clearly, the dual-layered structure using nylon and compliant inner layer performs much better than either the LSPVC or the LSZH buffered fiber. In critical applications, for example, jumpers or interconnect cables used in the central office, having a dual-layered structure is advantageous.

The microbend performance of the dual-layered structure is dependent on the mechanical properties of both the buffer material and the compliant layer between the buffer and the optical fiber. The microbend resistance between the former and new compliant layers, which have different elastic moduli, are shown in Figure 5, on page 4. Note that the error bars in Figure 5 are only one (1) standard deviation. Following the models used to optimize optical fiber performance, the new compliant layer was designed to have a lower modulus compared with the former. The chart in Figure 5 shows that the lower modulus material performs better than the former higher modulus compliant layer material.

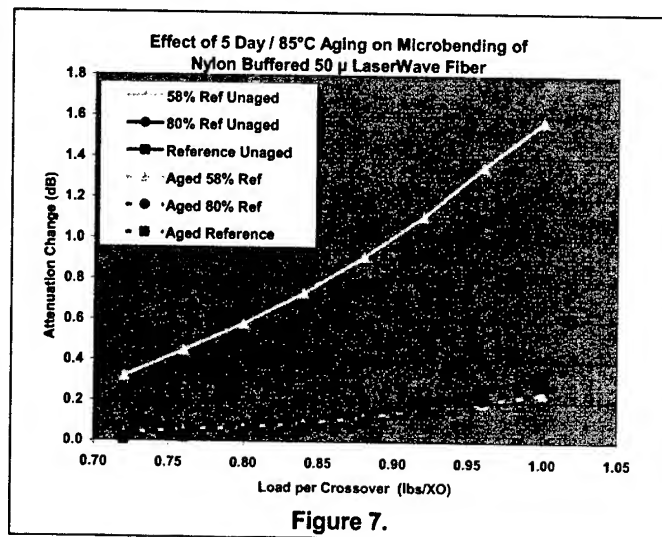
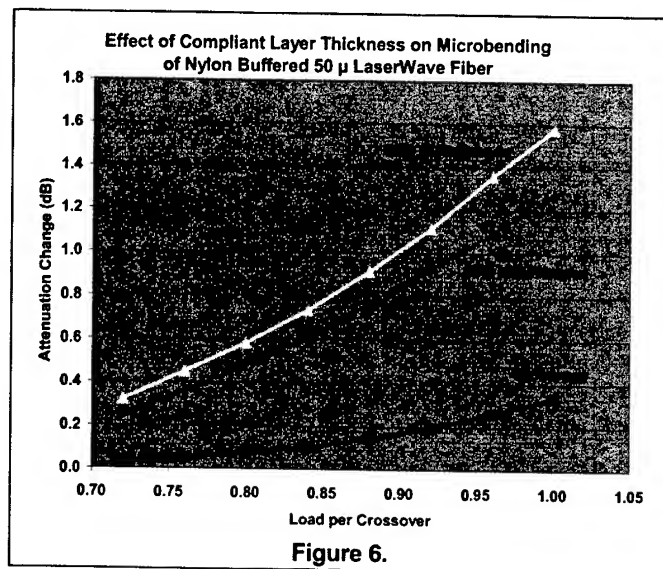


As might be expected as well, microbend resistance of the dual-layered structure also depends on the thickness of the compliant layer. Figure 6, below, shows the effect of varying the thickness of the compliant layer to 80% and 58% of the reference thickness. Note that the same 50 µm LaserWave™ fiber was used for all three thicknesses to insure that the differences were due the thicknesses and not from any difference in the optical properties of the fiber.



In order to ascertain the long term reliability of the new compliant layer, the same samples shown below in Figure 6, were taken from the temperature cycling test, discussed below, and evaluated for microbend resistance. Figure 7, below, shows the results of aging the dual-layer nylon buffered 50 µm LaserWave™ fibers. For the "58%" and "80%" thicknesses, the microbend sensitivity decreased, whereas, for the "Reference" thickness, there was no measurable change in microbend sensitivity. These results demonstrate that the compliant layer maintains its elasticity even after aging. The reason for the decrease in microbend sensitivity of the dual-layer nylon

buffered fiber can be explained by the increase in the modulus of the nylon buffer. As mentioned above, the microbend resistance depends not only on the modulus of the compliant layer, but also on the modulus of the buffer material. The aging temperature is above the glass transition temperature, T_g , of the nylon and allows the crystallinity of the nylon, and hence the modulus, to increase. This conclusion was confirmed using dynamic mechanical analysis.⁷



3.3 Environmental Cycling

While having a high modulus buffer provides substantial improvement in performance for pull-proof connectors and for microbend resistance, a high modulus buffer, like nylon or PBT, while perfectly suited for indoor cable applications, becomes a design challenge when it comes to environmental or temperature cycling at low temperatures for outside plant environments, e.g. indoor/outdoor cables. The reason is a simple mechanical one: as

the temperature decreases, the buffer shrinks in proportion to its thermal expansion coefficient and imposes a force on the optical fiber that is proportional to the cross-sectional area times the modulus of the buffer material. There are a number of methods to counteract or mitigate the compression force imposed by the buffer material at low temperature.

The most commonly used approach is to build in anti-compression or anti-buckling elements, like glass reinforced plastic (GRP), into the cable design. In this approach, the buffered fiber is coupled mechanically to the anti-buckling strength element. Note that aramid yarn does not have any anti-buckling properties. When the buffered fiber is coupled to an anti-buckling strength element, compression, along with concomitant increases in microbending and attenuation, is prevented when the cable is exposed to low temperatures. However, anti-buckling elements not only add significant cost to a cable, but also add stiffness and weight, making the cable less flexible and more difficult to handle than those cables with fewer or no anti-buckling elements.

Another approach is provided by the dual-layer design. In the dual-layer design, the compliant layer reduces the ability of the compression force of the shrinking buffer material to couple fully to the optical fiber. The decoupling action of the compliant layer reduces microbending and, hence, reduces attenuation loss. This decoupling action in the dual layer tight buffer simplifies the design of cables, for example, indoor/outdoor cables, where a reduction in stiff anti-buckling elements produces cables that are lighter, more flexible and easier to handle. As might be expected, both the temperature dependent modulus and the thickness of the compliant layer affect the layer's ability to isolate the optical fiber from the compressive force of the buffer material as the environmental temperature is lowered.

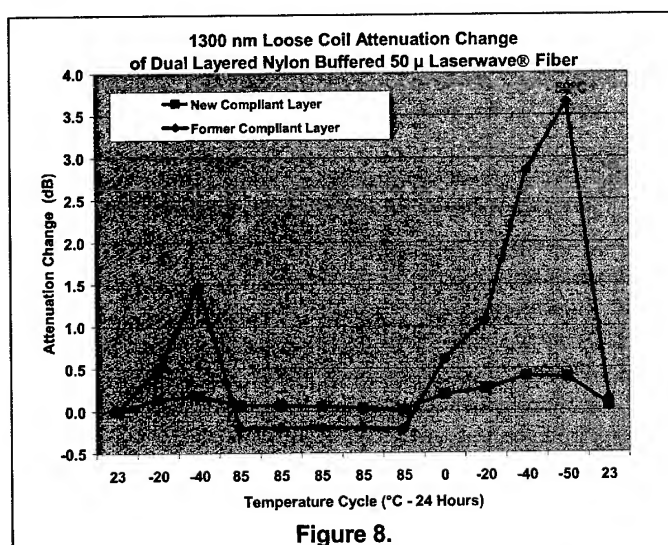


Figure 8.

Shown in Figure 8, above, is the 850 nm attenuation change versus environmental temperature cycling of loose coils of dual-layer nylon buffered fiber with the former and new compliant layers. The

graph clearly shows that, even for the former compliant layer, some anti-buckling elements would be needed to prevent attenuation increase for 50 μ m multi-mode fiber in an outside plant environment. However, for the new compliant layer, the attenuation change is less than 0.5 dB even down to -50°C , easily meeting both ICEA and Telcordia requirements. Note that ICEA does not require an 85°C aging step.

What makes the low temperature performance possible is the low glass transition temperature (T_g) of the new compliant layer compared to the former layer. In Figure 9, below, the dynamic mechanical analysis of the former and new compliant layers clearly shows the difference in the T_g of the two layers. The elastic modulus of the new compliant layer is essentially flat from 150°C down to -20°C .

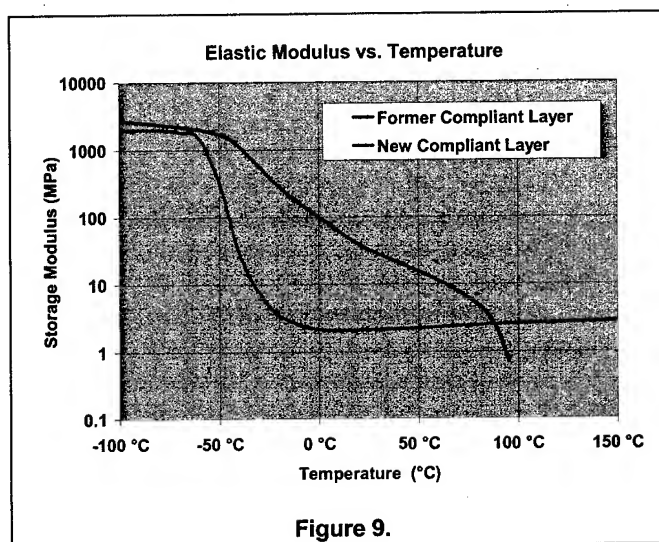


Figure 9.

4. Conclusions

A new compliant layer has been shown which greatly enhances the low temperature and microbend resistance of dual-layered tight buffered fiber, which is especially important for low DMD 50 μ m multi-mode fiber. The new compliant layer provides for new design options, including the use of special thermoplastic buffer materials, for example, which give enhanced fire protection while maintaining good temperature and microbend resistance. The improved performance allows OEM's, system integrators and cable manufacturers to benefit from both the increase bandwidth performance of low DMD fibers, such as LaserWave XL TM, and the exceptional environmental and handling characteristics of dual layered stiff tight buffer optical fiber. Coupling these improvements with the proven performance of pull-proof connector, like the LC connector, provide exceptional performance and long-term reliability for every customer.

5. Acknowledgments

The authors would like to thank the following individuals for their contributions in making this paper possible: Lopa Thakkar, Frank Calabrese, Mark Shmukler, David Au, and Charlie Freeze.

6. References

- [1] Holman, J.R., Jenkins, A.C., Subh, N.T., Travieso, R., "Reliability of Optical Fiber Cables for New Connector Systems," Proceedings of the 43rd International Wire and Cable Symposium, 1994, pp 795 - 801
- [2] GR-326, "Generic Requirements for Single Mode Optical Connectors and Jumper Assemblies," Issue 3, Telecordia, September 1, 1999.
- [3] IEC 60794 Part 2: Indoor optical fiber cables, Section 50: Specification for simplex and duplex cables for use in patch cords,

Method E21, "Fiber Movement Under Compression," Draft dated July 2002

[4] Refi, James J., "Fiber Optic Cable - A LightGuide," abc Teletraining, Inc. 1991

[5] Marx, M. F., Moss, P.A., Presnell, M. J., Shea, J. W., United States Patent #5,011,260; April 30, 1991

[6] Chapin, J. Thomas; Graham, Lionel; Holman, James R.; Viriyayuthakorn, M.; "Buffered Optical Fiber Having A Strippable Buffer Layer," United States Patent #5,684,910; November 4, 1997

[7] Neveux, Jr., Paul E., unpublished results.

7. Authors



Dr. Paul E. Neveux, Jr.,

Technical Manager for Premises Cable Design and Development. He has a Ph.D. in Inorganic Chemistry from University of North Carolina, Chapel Hill. After working 11 years at Sumitomo Electric Lightwave Corp., he joined Lucent Technologies, now OFS, working on optical fiber and copper premises materials, design and process development. He has served on TIA Standard committees 6.6.7 and 6.6.8, authored two FOTP's. He has 4 patents, 6 patents pending and numerous publications.



Mr. Samuel Aderogba

Member of Technical Staff. Responsible for cable design, process development, instrumentation, and optical measurement. He holds a B.Sc. and M.E. degrees in Mechanical Engineering from the University of Ibadan, and the Tennessee State University, respectively. He is a member of the American Society of Mechanical Engineers.



Mr. Wayne Newton,

Distinguished Member of Technical Staff. Recently retired after 36 years with Western Electric, AT&T, Lucent Technologies and OFS. He had been responsible for Process Development Engineering. He holds a B.S. Degree in Electrical Engineering from Clemson University and an M.S. Degree in Industrial Engineering from Texas Tech University. He has 8 U.S. and 3 Foreign Patents in the Copper and Fiber Optic Cable field.



Ms. Mala Nagarajan,

Member of Technical Staff in the Premises Cable R&D group at OFS, Norcross, GA. She has a B.E. Degree in Mechanical Engineering from Bangalore University, India and a M.S. Degree in Mechanical Engineering from University of Maryland. She has been leading the efforts for designing new premises cable products. Her current involvements include process and product development pertaining to premises fiber optic cables.

several capital expansion projects and is currently involved in premises fiber optic cable process development.



Mr. Christopher Okafor,

Member of Technical Staff at OFS Fitel, joined AT&T Bell Laboratories in 1986 after graduating from Alabama Agricultural & Mechanical University in 1983 with BSEE and in 1986 with MS in Applied Physics (concentration Optics). Chris has worked on a broad range of projects including the development of a model that more accurately determines the cutoff wavelength of single mode fiber that is now used industry wide. He has managed

Analysis of Tubing Process for Ribbon Fibers Cable

Young-soo Jung*, Kyung-tae Park, Mun-hyun Do and Jin-han Kim

R&D Group 1, Fiberoptics division, Telecommunication Network Business

Samsung Electronics Co. Ltd

#94.1, Imsoo-Dong Gumi-City, Kyung-Buk, Korea

+82-54-479-7164 ysjung94@samsung.com

pkt1013@samsung.com

Abstract

These days, optical fiber cable has been developed with high density, compact, low cost and high performance. To satisfy these demands, ribbon cable has been developed. Using ribbon technology, the time and cost of termination could be saved. Ribbon technology brings significant advancement in fiber packing density and handling. Recently, to increase efficiency of duct space high fiber count ribbon cable is preferred, however cost of poor quality due to unstable process is heavier to the manufacturer as fiber count increasing. We can categorize the ribbon technology in two models, which are slot core and central core ribbon cable. In this paper, we describe the tubing process, which is the essential in the manufacturing a central core ribbon cable

Keywords

Central core ribbon cable; filling compound; stranding pitch; optic attenuation; ERL; cable.

1. Introduction

For fiber optic ribbon cables, the ideal design is inserting a high number of optical fibers within a small size. Of course, optical loss should be minimized. Proper selection of raw material, idealized OFC (Optical Fiber Cable) design, stabilized manufacturing process and other factors shall be considered

Our work is focused on investigating ERL (excess ribbon length) change and optical attenuation change when applying several filling compounds with different ribbon stranding pitches. Used raw material of ribbon tube was modified-PP (Polypropylene) for better mechanical and environmental properties. With fitting the tube material, the changes of the ERL(Excess Ribbon Length) and the optical attenuation were investigated when applying several filling compounds and stranding pitches. Description of other process parameter conditions for the test is shown in table 1.

Two types of gels are used in the ribbon tube. One is pre-gel, which is applied in the interstices of ribbon stack and the other is main-gel, which is applied between ribbon-stack and core tube. When investigated the properties of the ribbon tube, the viscosities of pre-gel and main-gel differently applied.

Table 1. Process parameter condition for the test

Pay-off tension	Gel's hose temperature	Water cooling temperature	Tension of capstan	Take-up tension
(g)	(°C)	(°C)	(N)	(kg)
70	70	15	20	2.5

* Heating temperature of pre-gel and main-gel hose are same through whole tests

As like described above, ERL and optical attenuation were measured regarding several conditions of gel and stranding pitch. Through the measurements, we could choose the optimal condition and observed several properties when the tube is cabled.

Finally, temperature cycling test was done to the OFC manufactured with the optimal conditions.

2. Experiment

2.1 Material selection and test condition

Function of filling compound in central core ribbon cable is so important that several types of filling compounds were investigated. Because, there are lots of filling compounds in the market for central core ribbon cable application, widely used gels were selected. Gel plays important role in protecting the ribbon fibers. And the ribbon-stack in the core tube has 18 ribbons and each ribbon includes 12 optical fibers.

2.1.1 Filling compound Gel for filling compound has many properties such as density, cone penetration, viscosity, oil separation, volatility and so on. Among them, viscosity should be considered most importantly, because the ERL of ribbon cable and the free movement are influenced by it. So, the gels having different viscosities were used for our test.

2.1.2 Ribbon stranding pitch Applying the stranding pitch to the stacked ribbons makes the structure in the tube symmetric. When the ribbon cable is under bending, the symmetric structure plays a role in maintaining the optical fiber performance through happening the stable relaxation in the direction of minimizing the strain energy. Since the shorter the ribbon stranding pitch is, the smaller the bending radius is possible, so it is desirable to shorten the stranding pitch in OFC design. But if the stranding pitch is too short, the fiber strain may be increased.

2.2 Ribbon tubing

Tubing process is inserting ribbons-stacked into a core tube in manufacturing the OFC.

The gels used in our test have the same properties except viscosity. And, stranding pitches of 2 types were selected. Table 2 shows the test conditions of the gel viscosity and ribbon stranding pitch.

Table 2 Test Condition

(Viscosities of pre-gel & main-gel, stranding pitch)

Test	Viscosity of main-gel (mpa)	Viscosity of pre-gel (mpa)	Stranding pitch
T-1	High	High	60
T-2	High	High	80
T-3	High	Low	60
T-4	High	Low	80
T-5	Low	High	60
T-6	Low	High	80
T-7	Low	Low	60
T-8	Low	Low	80

* Test Method (viscosity of gel): Shear rate $D=50S^{-1}$ (at 25 °C)
Stranding pitch: the multiple number of tube outer diameter

2.2.1 ERL on ribbon tube In manufacturing ribbon cable, controlling ERL is the important factor that determines the cable properties. And not only average value of ERL but also ERL difference (length difference of each ribbon in stacked ribbon) could influence to the properties of ribbon cable. So, ERL and ERL difference should be controlled to improve the properties of ribbon cable. The measurements of ERL were done to the 5m of ribbon tube after 1 hour passed from manufacturing the tube. Figure 1 illustrates the average value of ERL regarding each test condition.

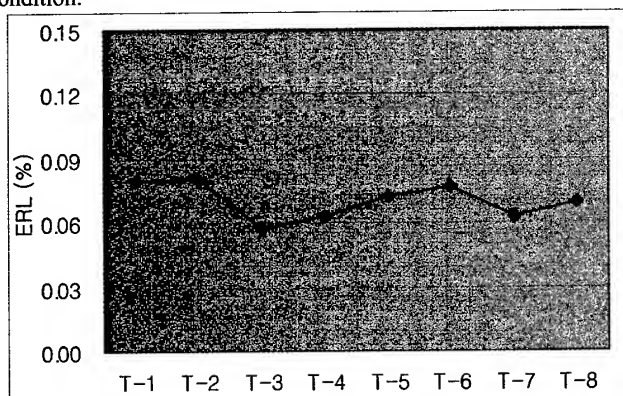


Figure 1. ERL (average) vs. Test condition

Based on average ERL values from Figure 1, we found that there are somewhat differences of them in the ribbon tube with different filling compounds and different stranding pitches. Even though they have their values different from other test results, they are so small to neglect. It means that it is not suitable for finding relationships between viscosity of main-gel, viscosity of pre-gel and stranding pitch. So, we approached with another method to find functions of them. However, another manufacturing process parameters are not varied.

Although, average ERL value did not play an important role in find functions of them, basic concept of designing central core ribbon tube is in ERL value. So, we approached with ERL values of each ribbon-stacks.

From Figure 2, when viscosity of pre-gel is high, edged ribbons showed high ERL values than that of inside ones. This phenomenon comes from the fact that the stranding radius of the edged ribbon is larger than that of the centered ribbon by applying the stranding pitch to the ribbon-stack. But, the ERL values of edged ribbons are longer than other edged ribbons in the case of the high viscosity of pre-gel. This excessive ERL on specific ribbons can influence to the quality of the cable

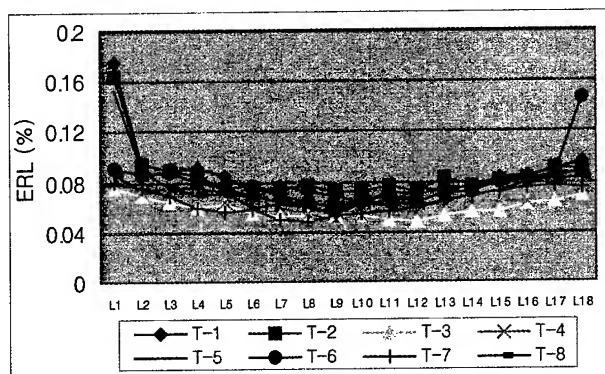


Figure 2. ERL difference vs. test condition

2.2.2 optic attenuation on ribbon tube Figure 3 shows optical attenuation losses of samples. From Figure 3, they show two trends. One is high maximum value and relatively high average optical attenuation value. The other is relatively low maximum value and low average value at 1550nm wavelength. But, there is no difference at 1310nm wavelength. These results give us some useful information that unsuitable selection of pre-gel can cause optical attenuation increase.

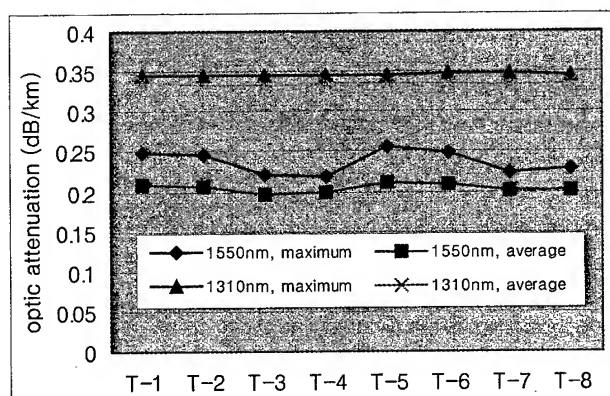


Figure 3. Optic attenuation vs. test condition

From Figure 3, the function of pre-gel in central core ribbon tube can be explained. Sample T-3, T-4, T-7 and T-8 applied low viscosity pre-gel in interstices of ribbon-stacks and they showed low optical loss. It means that friction force between ribbon stacks plays an important role in optical characteristics of ribbon tube. High friction between ribbon-stacks can cause microbending, compression and other unexpected results. In addition, low

friction between ribbon-stacks can minimize optical changes. However, viscosity of pre-gel can control the ERL of ribbon tube. From test results based on ERL, OFC design was done and further tests were conducted.

2.3 Cable Test

2.3.1 Design Among ribbon tube designs in Table 2, OFC for verification was manufactured with the same process parameters. They have stranding pitch of tube outer diameter's 60 times and different pre-gel and main-gel. Figure 4 shows OFC structure.

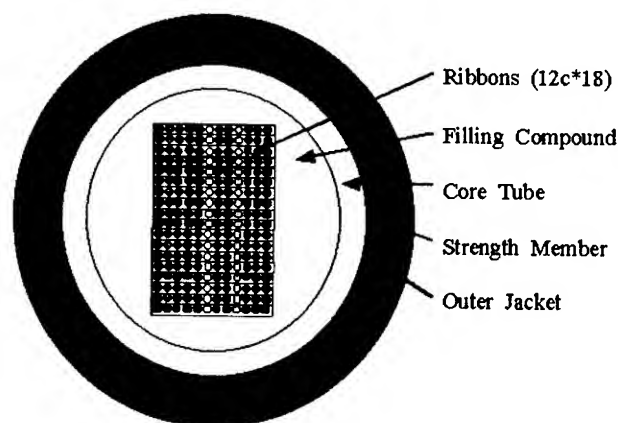


Figure 4. Structure of Cable
(216-Fibers Central Core Ribbon Cable)

2.3.2 Test Cable There is the optical attenuation after cabling in the figure 5. Figure 5 shows the stable optical attenuation in the all types of cable. This comes from the effects of decreasing the strain in the ribbon fiber after cabling.

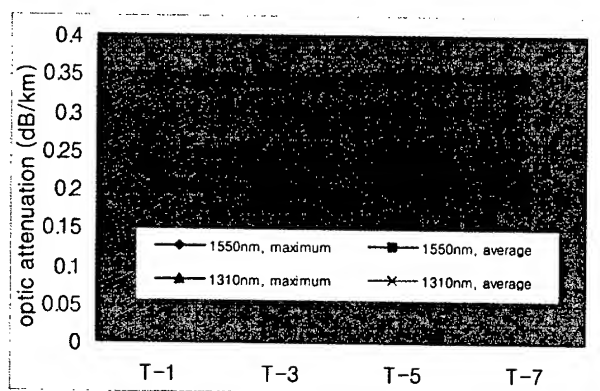


Figure 5. Optic attenuation vs. test condition

The standard defined in GR-20-CORE for temperature cycle test is as follows; 1) Temperature range: $-40^{\circ}\text{C} \sim +70^{\circ}\text{C}$, 2) No. of cycle: 2, 3) duration of each step: 24 hours. And the test results plotted in Figure 6. From the plot we can know that optical attenuation at the low temperature seemed to be very low and stable throughout the cycle and the optical attenuation differences from the reference temperature at both wavelength (1310nm and 1550nm) are much smaller than the value specified in the GR-20-CORE

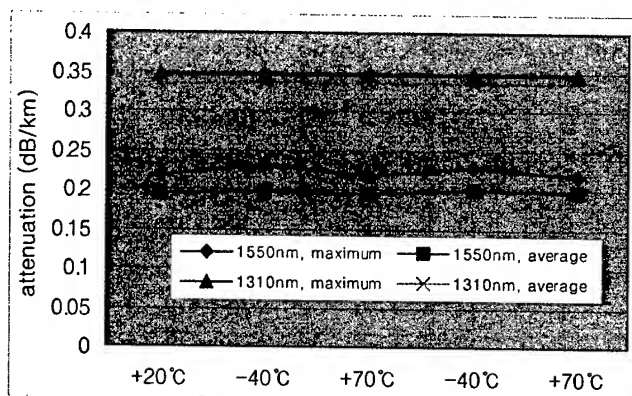


Figure 6. Optic attenuation vs. Temperature during temperature cycling

3. Discussion

In this paper, the effects of the viscosity of gel and the stranding pitch to ERL and optical attenuation were investigated. In conclusion, it was discovered that viscosities of pre-gel and main-gel are important factors to the optical attenuation. The viscosity of gel has property that is inversely proportional to the temperature. From the fact that optical attenuation is influenced by viscosity of gel, we can have the same effect of using low viscosity gel by heating high viscosity gel.

Applied stranding pitches of 60 and 80 times of the tube outer diameter don't degrade the ERL and optical attenuation. But, decreasing less or increasing more may bring other phenomenon. Through addition study about the stranding pitches, the optimal length can be found.

4. Conclusion

The goal of this paper is selecting gel and determining stranding pitch to establish the stable process in manufacturing of central core ribbon tube.

In selecting gel, viscosity is the important factor and by applying the different viscosities of pre-gel and main-gel we could obtain better results. In addition it was discovered that the stranding pitches between 60 and 80 times of the tube diameter don't bring side effects.

Finally, we manufactured 216-fiber central core ribbon cable with the tubes having the optimal tubing conditions and the cable showed good stability in a wide temperature range ($-40^{\circ}\text{C} \sim +70^{\circ}\text{C}$)

5. References

- [1] GR-20-CORE, "Generic Requirements for Optical Fiber and Optical Fiber Cable"
- [2] M.I.Lahti, "High-Speed Buffering of Compact Loose Tubes for Stranded Cables", 50th International Wire and Cable Symposium, USA, (2001)
- [3] L.M.Bocanegra, "Numerical Analysis to Predict Temperatures in Central Core Fiber Optic Cables during Manufacture", 50th International Wire and Cable Symposium, USA, (2001)

- [4] M.Tabaddor, "CONTACT MECHANICS OF FIBER OPTIC RIBBON", 46th International Wire and Cable Symposium, USA, (1997)
- [5] H.P.Debban, "A New High-Density Central Cable Core Design", 49th International Wire and Cable Symposium, USA, (2000)
- [6] N.V.Nechitailo, "Influence of Ribbon Stack Twist Laylength and Bending on the Strain Distribution and Attenuation in Optical Fiber Ribbon Cable", 50th International Wire and Cable Symposium, USA, (2001)

Authors



Young-soo Jung
SAMSUNG Electronics Co., Ltd.
#94-1, Imsoo-Dong Gumi-City,
Kyung-Buk, Korea.
ysjung94@samsung.com



Kyung-tae Park
SAMSUNG Electronics Co., Ltd.
#94-1, Imsoo-Dong Gumi-City,
Kyung-Buk, Korea.
pkt1013@samsung.com



Mun-hyun Do
SAMSUNG Electronics Co., Ltd.
#94-1, Imsoo-Dong Gumi-City,
Kyung-Buk, Korea.
mhdo@samsung.com



Jin-han Kim
SAMSUNG Electronics Co., Ltd.
#94-1, Imsoo-Dong Gumi-City,
Kyung-Buk, Korea.
jinhan@samsung.com

Development of Chamfer-Type Super Low Loss MPO Connector Using PPS Ferrule

Wataru Sakurai, Kenichiro Ohtsuka, Yuuko Hasegawa, Tomohiko Ueda, Toshifumi Hosoya

Sumitomo Electric Industries, Ltd.

1, Taya-cho, Sakae-ku, Yokohama, 244-8588, Japan

Phone: +81-45-853-7163, Fax: +81-45-851-5300, E-mail: sakurai@yklab.sei.co.

Abstract

In order to meet the requirements for multi-fiber and high density optical connection in DWDM (Dense Wavelength Division Multiplexing) systems, we have developed a super low loss MPO connector using injection molded PPS ferrule. Furthermore, we also propose to chamfer around the guide-pin holes near the connection end face to improve durability against repeated mating. We have confirmed that this is highly effective in preventing cracks and damage around the guide-pin holes near the end face and contribute to the stability of insertion loss levels. The trial chamfer-type single-mode MPO connectors have exhibited satisfying characteristics including maximum insertion loss of less than 0.35dB; maximum loss change of less than 0.2dB when repeatedly mated up to 500 times; and maximum loss increase of less than 0.2dB during reliability tests based on GR1435.

Keywords

MPO connector; PPS (Polyphenylene Sulfide); Injection molding; Chamfer;

1. Introduction

In recent years, the advancement of high-speed and large-capacity fiber optic communication systems, based on technologies such as DWDM (Dense Wavelength Division Multiplexing), has been driven by the rapid growth of the Internet. Optical connectors are an essential part of DWDM technology. Although single-fiber SC connectors have been widely used, requirements for multi-fiber and high density connection interfaces of DWDM components, such as the MPO connector and the MPX connector, have been increasing in recent years. The most popular 8-fiber MPO connector has 5 times as high fiber density as the SC connector, enabling users to construct higher capacity systems.

However, it has been very difficult to realize multi-fiber low loss connection equivalent to that of the single-fiber SC connector, because the multi-fiber connector needs highly precise ferrule which positions plural fibers precisely. It has also been very difficult to improve the productivity of conventional ferrule manufacturing processes using thermosetting epoxy resin, since the thermosetting resin requires a certain amount of time to harden. Furthermore, in conventional MPO connectors including MT ferrules, problems have included cracks and damage around guide-pin holes near the end face when repeatedly mated, which can potentially affect stability of connection loss levels.

To meet the demands for multi-fiber and high density connectors with a higher level of productivity, we have been studying these problems, and have developed a chamfer-type super low loss multi-fiber MPO connector using injection-molded ferrule. In this paper, we describe the design concepts of low loss connections, the manufacturing of the highly precise ferrules with injection molding method, optical characteristics and reliability tests of a trial product of 8-fiber MPO connectors. Finally, we mention the trial results of 12-fiber MPO connectors and 16-fiber narrower-pitch MPO connectors as a primary step for a higher density connection.

2. MPO Connector Features

Figure 1 shows the structure of the MPO connector^{[1],[2],[3]}. It was standardized in IEC (IEC61754-7), and is 45mm in length, 12.6mm in width and 7.7mm in height. The MPO connector consists of a pair of MT ferrules, two guide-pins, two housings and an adaptor.

The MT ferrule is a key part which determines the connection characteristics of the connector. The ferrule has two guide holes and plural fiber holes (12 maximum). The guide pin and fiber hole pitch are 4.6mm and 0.25mm, respectively. In order to achieve low insertion loss of single-mode fiber, the offset of fiber hole from the designed position must be less than, or equal to, 1 μ m. Thus, conventional MT ferrules have been manufactured using transfer molding which is easier to obtain accuracy, but have lower productivity.

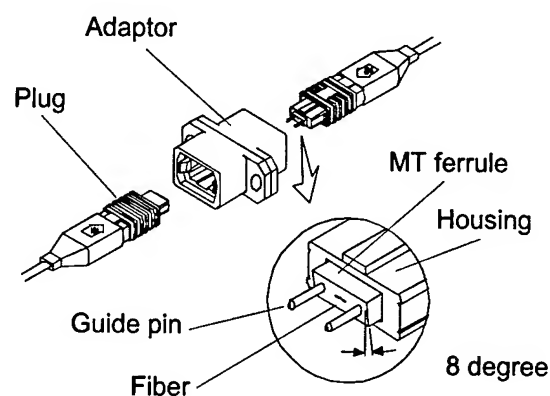


Figure 1. MPO connector

Fibers are inserted into the fiber holes and fixed to the MT ferrule by adhesive. The ferrules at each face are accurately polished and accommodated in each housing, where they are accurately aligned by inserting guide pins into the guide holes of each ferrule. The

MPO connector is easy to connect and disconnect through a MPO adaptor and housings.

To achieve high return loss without refractive index matching material, the end face of the fiber and the ferrule are polished at an angle of 8 degree, and the end faces of fibers must be accurately polished to make contact with opposing end faces of fibers.

3. Design of Low Loss Connector

The dominant factor of insertion loss in optical connectors is the offset of fiber core from the designed position. Fiber-core offset in the MPO connector is expressed by the sum of the influence of offsets in the ferrule, guide pins and fibers^[4]. Namely, fiber-core offset in the MPO connector is expressed by the following: 1) fiber-hole offset from designed position in the ferrule; 2) clearance between the fiber and fiber hole; 3) fiber-core offset from the center of the fiber; 4) clearance between the guide pin and guide-pin hole, as shown in Figure 2.

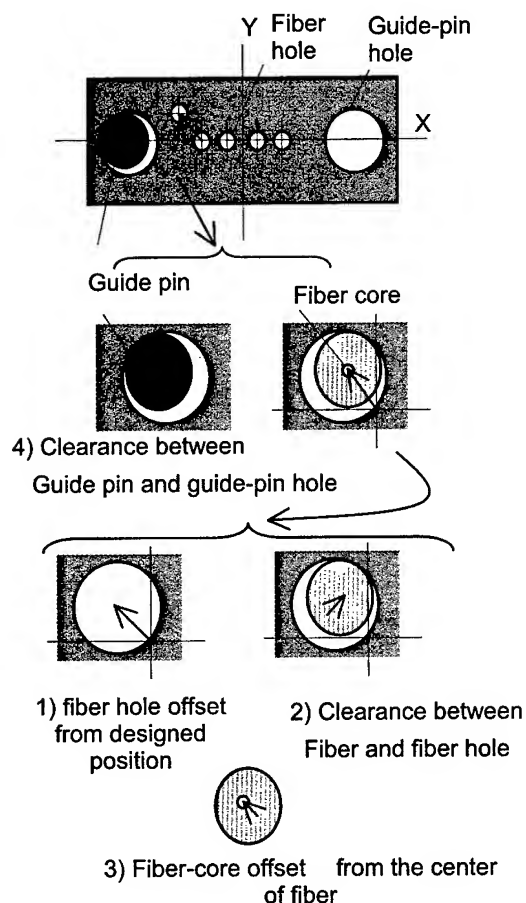


Figure 2. Causes of fiber core offset

On the other hand, if we assume that the distribution of fiber-core offset has an average of zero, we can calculate the theoretical distribution of the random connection loss with the standard deviation of fiber-core offset. By varying the standard deviation of the fiber-core offset as a parameter, we calculated the theoretical

distribution of random connection. As a result of these theoretical studies, we determined that the valid design value of standard deviation for fiber-core offset to achieve random connection loss is 0.35dB maximum, taking into account the present accuracy of each part.

In order to design the MPO connector with a low insertion loss of 0.35dB maximum, we investigated the possibility of reducing the fiber-core offset and the deviation of fiber-core offset. As a consequence of this investigation, we determined that it was necessary not only to reduce the fiber hole offset by adjusting the mold, but also to reduce the clearance between the guide pins and guide-pin holes, and optical fiber and fiber holes.

We designed the size tolerance of the MT ferrule, fiber and guide pin so that the sum of the deviations on each part become equal to the deviation of the fiber-core offset we determined above. Namely, the ideal position for the fiber-hole offset was designed to be less than $0.7\mu\text{m}$, and the clearance tolerance for guide-pin holes and fiber hole was designed to be less than $0.3\mu\text{m}$ respectively. Furthermore, we determined that the tolerance for the fiber-hole tilt to be less than 0.2 degree maximum to reduce insertion loss by influence of angular offset of fiber axis in MPO connector.

4. Manufacturing

MT ferrule, which determines the characteristics of insertion loss in MPO connectors, is the most important part. We manufactured MT ferrules with an injection-molding method of PPS resin. In this section, we describe the precise molding resin, precise mold and molding condition as key technologies to realize the precise MT ferrules. Furthermore, we propose to chamfer around guide-pin holes to avoid cracks or damage by inserting opposing guide pins into the guide-pin holes.

4.1 Manufacturing of MT Ferrules

4.1.1 Development of Molding Resin A resin suitable for molding MT ferrules must have good moldability, dimensional precision, dimensional stability against varying environments, and mechanical strength. However, commodity plastic resins that are available were insufficient in terms of dimensional precision.

Therefore, we started to develop a special-blend resin for molding MT ferrules. In terms of low thermal expansion co-efficiency, low water absorption, and high mechanical strength, we selected PPS resin as a base resin and tried to improve the characteristics of the resin by selecting suitable kinds of filler and compounding them into the resin. As a result of dozens of trial resins, we successfully obtained a plastic resin suitable for molding MT ferrules.

4.1.2 Development of Mold We have developed a precise mold to achieve design value for the above ferrule. Figure 3 shows the schematic structure of mold we have used.

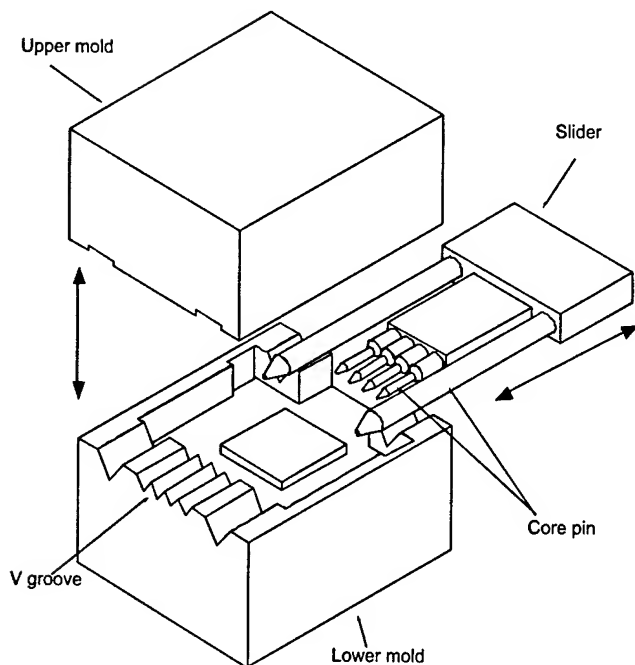


Figure 3. Structure of mold

To align fiber holes precisely, guide-pin-hole-forming and fiber-hole-forming core pins, which are held and aligned with a slider, are inserted into a cavity with precise v-grooves, and are precisely positioned with the v-grooves.

Although this structure was conventionally used for the transfer molding of epoxy resin, in order to reduce fiber hole offset of the ferrules and clearance of guide-pin hole and fiber hole, the precision of the v-grooves were improved and core pins were carefully selected with a diameter tolerance of less than $0.1\mu\text{m}$.

Furthermore, we have improved the runner and the gate of the mold to obtain good moldability against high viscosity molding resin due to the large amount of filler used.

4.1.3 Molding Condition To obtain ferrules with dimensional precision and stability during repeated molding, it is essential to keep excellent transcriptional ability and reduce residual stress in the molding articles.

In particular, molding conditions have more significant meanings for molding of MT ferrules, because the molding process uses fiber-hole-forming pins with very small diameters and high-viscosity molding resin. Through molding experiments, we determined optimum molding conditions, namely, mold temperature, resin temperature, injection rate, injection pressure, and cooling condition. We discovered that a condition of relatively lower injection rate and lower injection pressure exhibits good results.

As a consequence of the above studies on molding resin, molds and molding conditions, we have successfully developed injection-molded MT ferrules that have dimensional precision, dimensional stability, enough mechanical strength for practical use and higher productivity than that of transfer-molded ones.

Not only by shortening the hardening time of the molding process, but also by reducing the mold flash by cleaning it after every process, the molding cycle was reduced to one-third of that for the transfer-molded ones. This enabled us to raise the productivity of manufacturing ferrules.

Furthermore, the injection-molded ferrule exhibits good polishing characteristics. We have confirmed that the ferrule can be polished precisely for a low insertion loss.

4.2 Chamfer around Guide-pin Holes

In conventional MPO connectors including MT ferrules, problems have included cracks or damage around the guide-pin holes near the end face by opposing guide pin when repeatedly mated, which can potentially affect stability of insertion loss levels, as show in Figure 4.

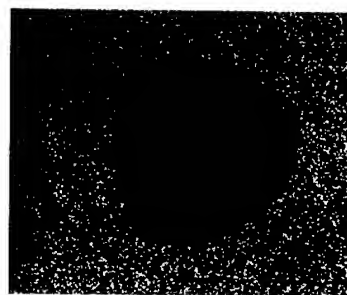


Figure 4. Damage around guide-pin hole near the end face of a conventional MPO connector

Our solution to these problems was to chamfer around the guide-pin holes near the end face. This enables an easier and smoother insertion of guide pins into guide-pin holes. Moreover, this contributes to the stability of the connection loss level when repeatedly mated.

We investigated the optimum chamfer taper angle to obtain better stability of insertion loss and to avoid damage around the guide-pin holes. The connectors with same chamfer diameter but different chamfer taper angle (60, 90, and 120 degree) were subjected to evaluation tests. As a result, we confirmed that connectors with a chamfer taper angle of 120 degree were easier and smoother to insert guide pins into guide-pin holes than others and not damaged at all. Thus, they exhibited the best performance in terms of stability of insertion loss levels among the three. Figure 5 shows the picture of the chamfer-type MPO connector.



Figure 5. Chamfer-type MPO connector

5. Characteristics of trial products

5.1 Ferrule Characteristics

5.1.1 Positional Precision of Fiber Hole Figure 6 shows the positional precision of fiber holes of injection-molded PPS 8-fiber MT ferrules. Positional precision was $0.29\text{ }\mu\text{m}$ on average and $0.51\text{ }\mu\text{m}$ maximum with a standard deviation of $0.10\text{ }\mu\text{m}$, indicating highly precise dimensional characteristics and satisfying the design value of less than $0.7\text{ }\mu\text{m}$. Furthermore, positional precision was stable during repeated molding, which means this manufacturing method is suitable for mass production.

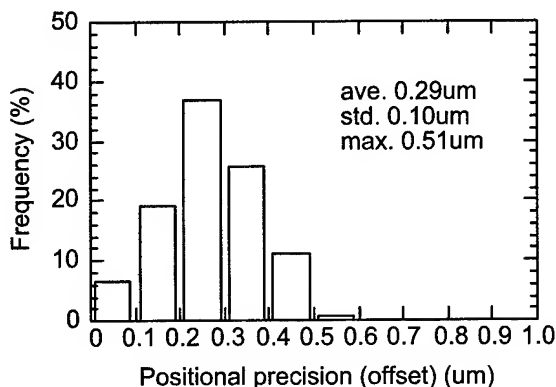


Figure 6. Positional precision of injection-molded 8-fiber MT Ferrules

5.1.2 Fiber hole tilt Figure 7 shows the fiber hole tilt with respect to the axis of guide-pin holes. All of the fiber hole tilts were within 0.2 degree and they were also stable during repeated molding.

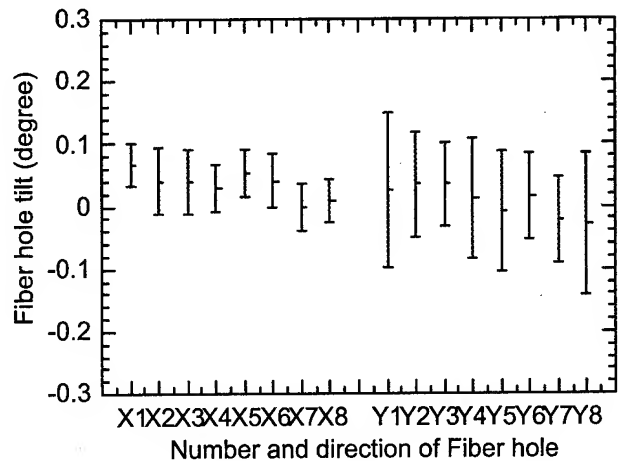


Figure 7. Fiber hole tilt of injection-molded 8-fiber MT ferrules

5.1.3 Precision of the Fiber-hole and Guide-pin-hole Diameter

We measured the diameter of the fiber hole and guide-pin hole with pin gauges. Both of them were extremely stable because of the selected forming pins. Each hole had a clearance of $0.3\text{ }\mu\text{m}$ maximum toward select fibers and select guide-pins, respectively, satisfying design values.

5.2 Optical Characteristics

5.2.1 Random Insertion Loss We manufactured 8-fiber chamfer-type MPO connectors using the PPS ferrules and selected fibers, and measured the insertion loss for random combinations at a wavelength of $1.31\text{ }\mu\text{m}$ with selected guide pins. We have achieved the target of 0.35 dB maximum as shown in Figure 8. The connection loss was less than 0.1 dB on average, with the standard deviation being less than 0.05 dB , indicating good characteristics.

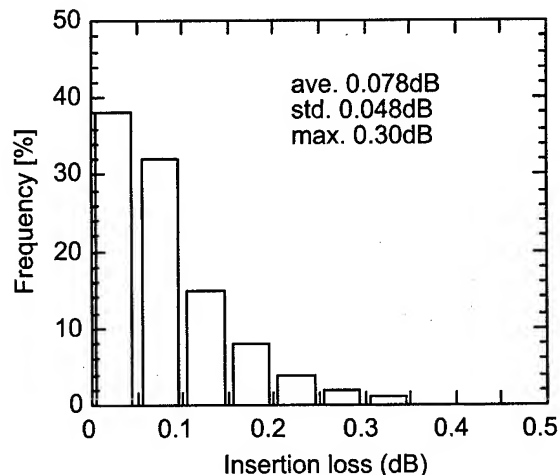


Figure 8. Random insertion loss of 8-fiber MPO connectors

This means that the dimensional tolerance we determined for each part was appropriate, and that we have achieved the target for the standard deviation of fiber-core offset as designed.

5.2.2 Return Loss Figure 9 shows the distribution of return loss at the wavelength of $1.31\mu\text{m}$ for random connections, exhibiting a satisfying characteristic of 56dB minimum.

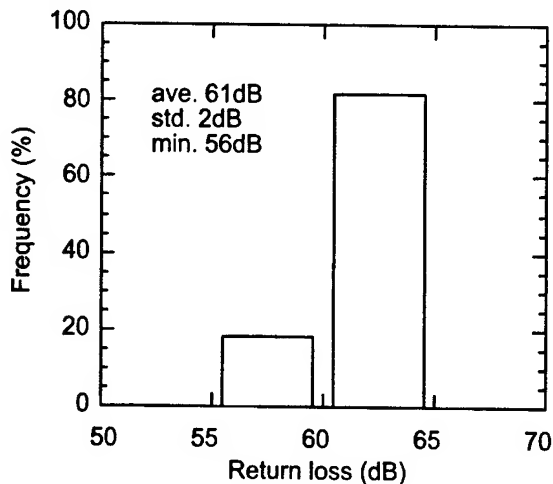


Figure 9. Distribution of return loss

5.3 Reliability Test

We examined the trial products of 8-fiber chamfer-type MPO connector to evaluate their practicality. We prepared 50 plugs for the test.

5.3.1 Durability Test We evaluated the repeatability of insertion loss in repeated mating, which is one of the most important characteristics of connectors. During the up to 500-time mating, at every 25-time mating stage the end face of the connectors was cleaned and measurements were conducted. As shown in Figure 10, the maximum loss increase was less than 0.2dB during the test.

Furthermore, no damage around the guide-pin holes near the end face was observed as shown in Figure 11.

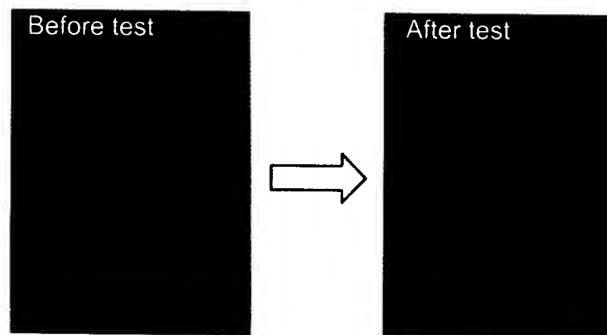


Figure 11. Guide-pin hole of Chamfer-type connector before and after durability test

This means chamfer around the guide-pin holes is highly effective in preventing cracks and damage around guide-pin holes near the end face by inserting guide-pins, and contributes to the stability of insertion loss levels.

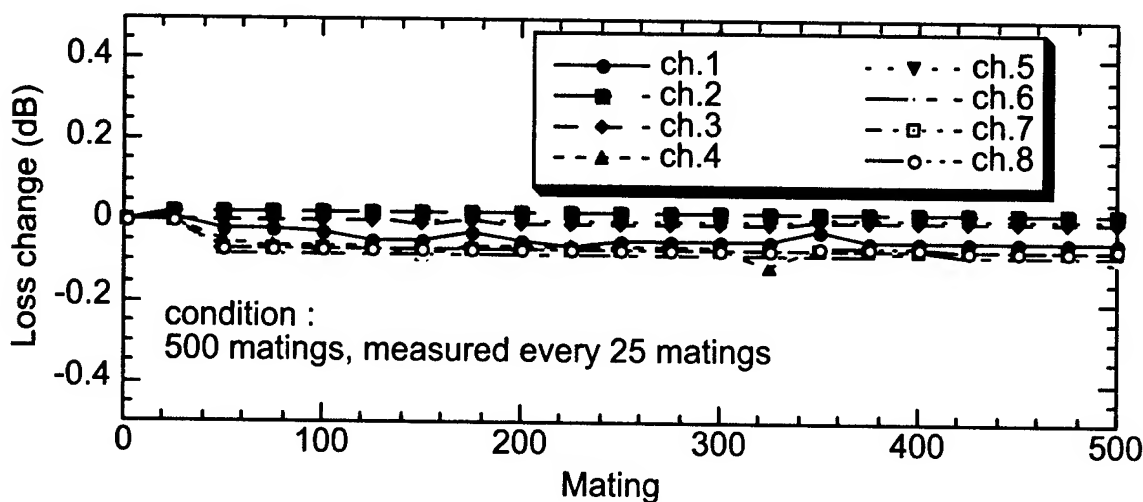


Figure 10. Insertion loss change during durability test

5.3.2 Environmental Test It is also necessary for connectors to have good insertion loss stability when exposed to various environments, such as high temperature, high humidity and varying temperature. To evaluate the environmental performance, we conducted environmental tests based on Telcordia GR-1435-CORE standard. Figure 12 shows the detailed test conditions and a typical measurement data of the tests, indicating excellent stability of maximum loss increase of less than 0.2dB during the tests.

5.3.3 High-Power Laser Incident Test The MPO connectors we have developed will be used in high power transmission system, such as DWDM, and the connector is possibly affected by high-power-signal light. Therefore, we evaluated the durability of the connectors against a high-power laser.

It is known, that in single-fiber connectors, if a high-power laser is used on the mated connectors with dust on the end face of the fiber core it will most certainly cause burning at the end face of the fiber. Thus, the end faces of the connectors were carefully cleaned before the tests.

In this test, three types of connector pairs were prepared; 1) the one of which fiber core has no cracks; 2) the one of which end face of the fiber had some cracks near the core; 3) the one which had an air gap between the end face of the opposing two fibers, namely the one which didn't achieve PC contact.

Incidence tests of a 2-watt laser at a wavelength of 1.48 μ m to mated connectors were conducted for 8 hours. After the test, we measured the connection loss of the three types of connectors and observed the end face each one. As shown in Table 1, the connection-loss changes were less than 0.02dB, compared with the initial loss before the test, is the same as the level of mating error. Furthermore, no damage was observed on the end faces as shown in Figure 13, and there was no heat generation or smell detected. We confirmed that the connectors were durable enough to be used in a high power transmission system, such as DWDM systems.

Table 1. Results of laser incidence test

	Maximum Loss change (dB)	End face of fiber after test
1)	-0.02	No damage
2)	0.01	No damage (shown in Figure 13)
3)	-0.01	No damage

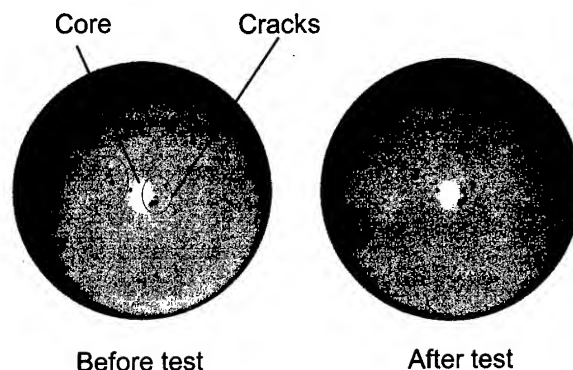


Figure 13. End face of fiber before and after high-power laser incident test (type 2)

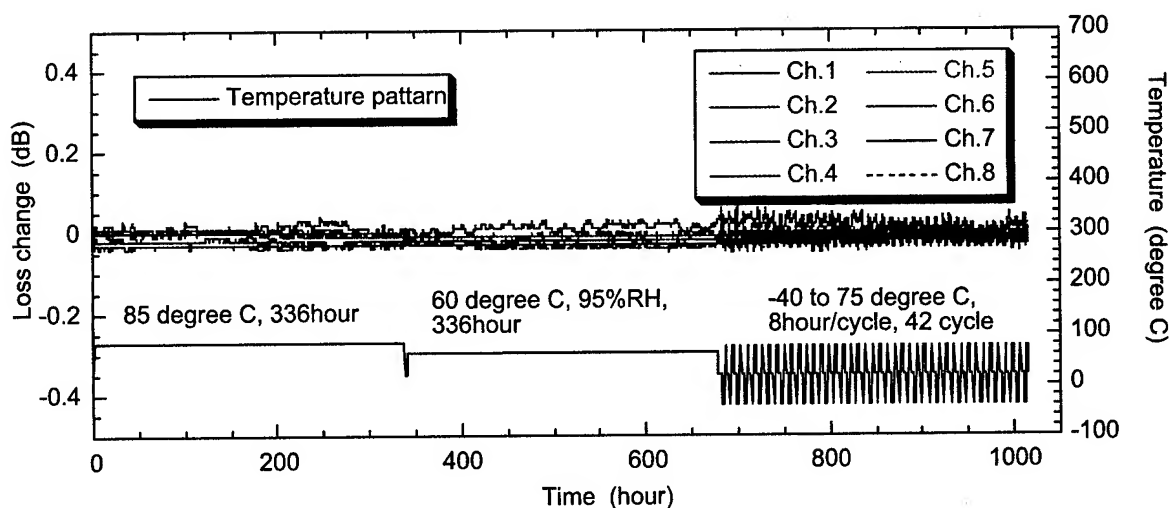


Figure 12. Insertion loss change during durability test based on GR-1435-Core

5.4 A trial of Higher-density Connection

5.4.1 12-fiber MPO Connector We have been developing 12-fiber MPO connector. It has the same size and same fiber pitches as 8-fiber MPO connector, but has 12 fibers, and has 7.5 times the high fiber density as SC connector. Although we were concerned about deterioration in dimensional precision of the ferrule due to inferior moldability, by increasing the fiber hole-forming pins in the cavity, we confirmed that the 12-fiber ferrules have as good dimensional precision as the 8-fiber ferrule. Figure 14 shows the insertion loss for random combinations at a wavelength of $1.31\mu\text{m}$, exhibiting satisfying results of less than 0.1dB on average and 0.35dB maximum with the standard deviation of 0.064dB.

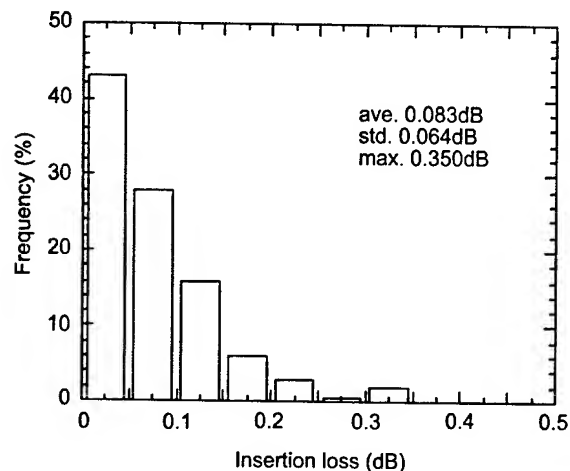


Figure 14. Random insertion loss of 12-fiber MPO connectors

5.4.2 Fine Pitch 16-fiber MPO Connector We have also been studying much higher-density connection. As long as fibers are arranged in a row, it is hardly possible to realize an arrangement of more than 12 fibers in 0.25mm pitch on the end face of an MT ferrule that is a standardized size. We manufactured the MT ferrule, including 16-fiber holes in 0.18mm pitch, which is the same size as the conventional one. Figure 15 shows the end face of a fine pitch 16-fiber MPO connector in comparison with 0.25mm pitch one.

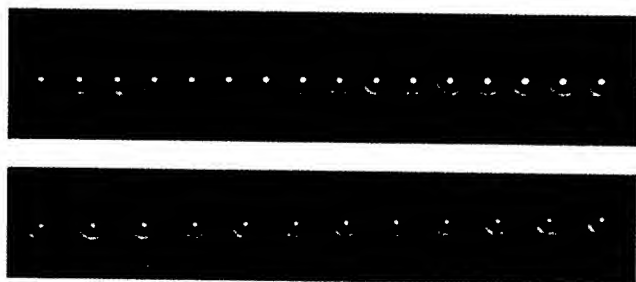


Figure 15. fiber arrangement in 0.18mm pitch and 0.25mm pitch

This fine pitch 16-fiber MPO connector has 10 times the high-fiber density as a SC connector.

We manufactured trial products of the 16-fiber MPO connectors with the above ferrules. Figure 16 shows the distribution of random insertion loss of the fine pitch 16-fiber MPO connectors, indicating 0.131dB on average and 0.54dB maximum.

The results were somewhat inferior to those of 8-fiber MPO connectors and the 12-fiber MPO connectors. We have attributed these results to the inferior moldability due to the increase of fiber-hole-forming pins in the cavity. However, we believe that we can improve the precision of the ferrule by changing the molding condition or structure of the mold.

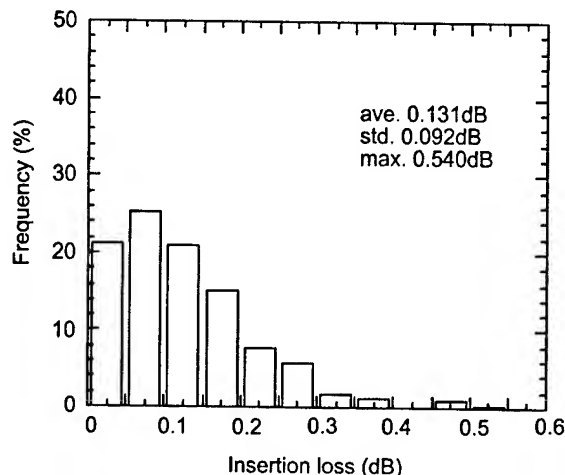


Figure 16. Random insertion loss of fine pitch 16-fiber MPO connectors

6. Conclusions

To meet the requirements for multi-fiber and high density optical connection in DWDM systems, we have developed a super low loss MPO connector using injection-molded PPS ferrule.

Furthermore, we also proposed to chamfer around the guide-pin holes near the connection end face to improve durability against repeated mating. We have confirmed that this is highly effective in preventing cracks and damage around the guide-pin holes near the end face, and contribute to the stability of connection loss levels through evaluation tests.

The trial chamfer-type single-mode 8MPO connectors have exhibited satisfying characteristics including maximum insertion loss of less than 0.35dB; maximum insertion loss change of less than 0.2dB when repeatedly mated up to 500 times; maximum insertion loss increase of less than 0.2dB during reliability tests based on GR1435. Furthermore, incidence tests of a 2-watt laser to a mated connector with cracks on the fiber end face, resulted in no damage on the end face of the connector.

Finally, we introduced the 12-fiber MPO connector and fine pitch 16-fiber MPO connector as a trial of higher-density connection. Fine pitch 16-fiber MPO connector has 10 times the high fiber density as a SC connector, indicating insertion loss of less than 0.6dB.

We believe that these MPO connectors are highly suitable for multi-fiber and high density connection interfaces of high power transmission system, such as DWDM systems and effectively contribute to the construction of the systems.

7. References

- [1] T.Sakata, T.Arikawa, P.W.Blubaugh, C.Parsons and T.Uchida, "MT Multifiber Connectors and New Applications," 44th ETCT, 994-999 (1994).
- [2] S.Nagasawa, Y.Yokoyama, F.Asiya and T.Satake "A High-performance Single-mode Multifiber Connector Using Oblique and Direct Endface Contact Between Multiple Fibers Arranged in Plastic Ferrule," J.Lightwave Technol., vol.13, no.6, 987-994, (1995).
- [3] T.Satake, T.Tatsuno, Y.Oucgu, D.Knasel, K.Knight, J.Lundberg, and D.Keller "Single-Mode Multifiber Connector Design and Performance," 1996 Electric Component and Technology Letters, 494-499, (1996).
- [4] K.Shibata, et al, IEEE Photonics Technology Letters, vol. 13, no.2, 136-138, (February 2001)

Authors



Wataru Sakurai

sakurai@yklab.sei.co.jp

Wataru Sakurai received a M.E. degree from Keio University in 1997. He joined Sumitomo Electric Industries, Ltd. in 1997, and has been engaged in research and development of optical connectors. He is an engineer of the Optical Network R&D Department in Yokohama Research Laboratories.



Kenichirou Ohtsuka

ohtsuka@yklab.sei.co.jp

Kenichirou Ohtsuka received a M.E. degree from Tohoku University in 1994. He joined Sumitomo Electric Industries, Ltd. in 1994, and has been engaged in research and development of optical connectors. He is an engineer of the Optical Network R&D Department in Yokohama Research Laboratories.



Yuuko Hasegawa

hasegawa-yuuko@sei.co.jp

Yuuko Hasegawa received a M.S. degree from Kyoto University in 2001. She joined Sumitomo Electric Industries, Ltd. in 2001, and has been engaged in research and development of optical connectors. She is an engineer of the Optical Network R&D Department in Yokohama Research Laboratories.



Tomohiko Ueda

ueda@yklab.sei.co.jp

Tomohiko Ueda received a B.E. degree from Tokyo University in 1987. He joined Sumitomo Electric Industries, Ltd. in 1987, and has been engaged in research and development of optical connectors. He is a senior engineer of the Optical Network R&D Department in Yokohama Research Laboratories.



Toshifumi Hosoya

hosoya@yklab.sei.co.jp

Toshifumi Hosoya received the M.S. degree in Reaction Chemistry from Tokyo University in 1985. He joined Sumitomo Electric Industries, Ltd. in 1985, and has been engaged in research and development of optical fibers and connectors. Mr. Hosoya is now a chief research associate of Optical Network R&D Department.

Development of 24-fiber Flat Ribbon Cable for Two-Dimensional Array MT Connector

*Kazuaki Hamada¹, Tomohiko Ueda¹,
Nobuhiro Akasaka¹, Toshifumi Hosoya¹, Yoshikyo Tamekuni²*

¹Yokohama R&D Laboratories, ²Communication Division
Sumitomo Electric Industries, Ltd
1, Taya-cho, Sakae-ku, Yokohama, 244-8588 Japan
+81-45-853-7164 · hamada-kazuaki@sei.co.jp

Abstract

In recent year, demands for high density and efficient interconnect cabling technique in high-speed and massive transmission system such as WDM are increasing with the progress of information technology. In order to meet these demands, we have developed two-dimensional array 24-fiber connector and 24-fiber flat ribbon cable which has ribbon stack structure for interconnection between network equipments. In this paper, we will report measured characteristics of 24-fiber flat cable with two-dimensional array connectors. We have successfully manufactured high performance cable which provides good characteristics in attenuation, temperature cycling test and mechanical test.

Keywords

Optical cable, Optical connector, Two-dimensional array, Stacked Ribbon, Jacket shrinkage, Bend radius

1. Introduction

In order to meet demands for high density and efficient interconnect cabling technique in high-speed and massive transmission system such as WDM, we have developed 24-fiber flat ribbon cable for interconnection between network equipments using two-dimensional array 24-fiber connectors.

2. Forms of 24-fiber Patch Cord

2.1 Two-dimensional array connector

Recently two-dimensional 24-fiber MT connector with the end face shown in figure 1 has developed in order to achieve high density interconnect cabling at limited cabling space. However, there are no dedicated cables for connecting to this 24-fiber connector. So we have been using two 12-fiber ribbons for connecting to one 24-fiber connector.

There are two drawbacks in this connecting form.

First problem is congested cabling at transmission systems. There are many ribbons between transmission equipments or boards because each

connector has two ribbons. Another problem is low mechanical strength of ribbon. Bare ribbon is fragile for crush.

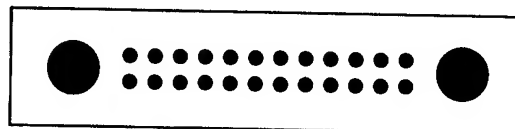


Figure 1. End face of 24-fiber MT ferrule

2.2 24-fiber Patch Cord Form

We have discussed about the structure of 24-fiber cable connected two-dimensional 24-fiber connector considering cabling forms and efficiency of connector assembly. (See figure 2)

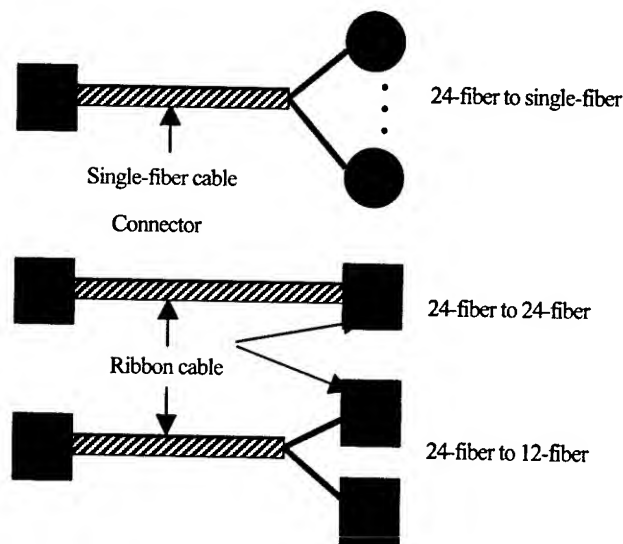


Figure 2. Example of 24-fiber Patch Cord Form

Round single-fiber cable and flat ribbon cable is known as the optical patch cord with connector. In case of "24-fiber to single-fiber" form, it is advisable to use single-fiber cable, because 12-fiber ribbonizing is

easier than making 12-fiber ribbon into twelve single-fibers and cover all fibers with protection tubes. In this patch cord form, we can use conventional 24-fiber round cable.

On the other hand, in case of "24-fiber to 24-fiber" form or "24-fiber to 12-fiber" form, it is better to use ribbon cable with two 12-fiber ribbons. And we have discussed about the structure of ribbon cable with two 12-fiber ribbons.

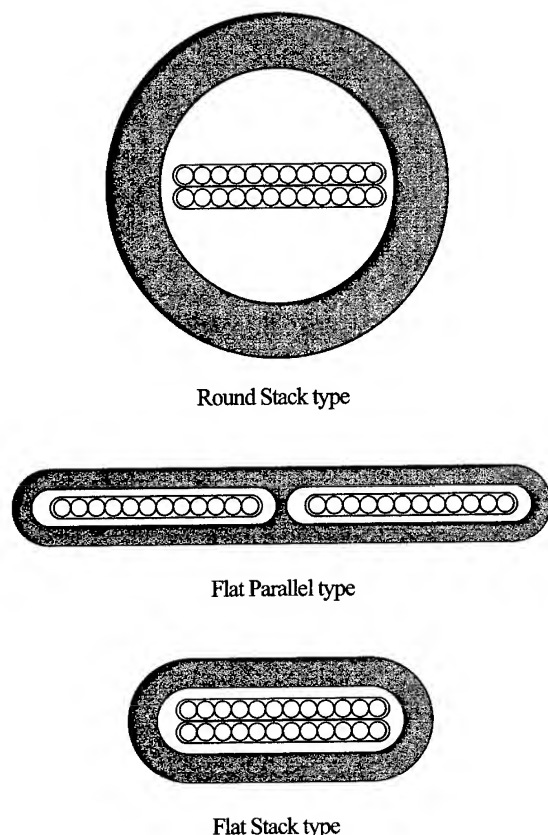


Figure 3. Draft of 24-fiber Ribbon Cable

Figure 3 shows three drafts of 24-fiber ribbon cable, and table 1 shows the comparison of cable structure and characteristics.

Round stack type is conventional style with stranded ribbons. Stranded ribbon structure provides good performance in cable bend because of fiber stress equalizing. However, it needs large inner space for ribbon stranding. As a result, large diameter is a drawback of this structure. In regard to cable manufacturing, ribbon stranding causes a limit of productivity.

Flat parallel type has no limitation in productivity and provides good performance in cable bend. However, its width is larger than the diameter of round stack type.

In regard to connector assembly, it is necessary to make ribbons in

parallel position into file position. The difficulty of this structure is ribbon crossing at cable end without ribbon damage or attenuation increase.

Flat stack type is superior to other type in terms of diameter minimizing. And it has no difficulty in connector assembly. However, this structure has limitation for cable bend because ribbons are not stranded.

Table 1. Comparison of Ribbon Cable Structure

	Round Stack	Flat Parallel	Flat Stack
OD (mm)	7.0	10.5 x 2.2	5.5 x 2.5
Ribbons	stranded	straight	straight
Bending	good	good	limited
Connector assembly	good	difficult	good
Productivity	limited	good	good

Consequently we have decided to consider concrete design of flat stack cable which is superior in terms of diameter minimizing and productivity. Then development of 24-fiber flat ribbon cable has done for ensuring good cable performance.

3. Design of 24-fiber Flat Ribbon Cable

3.1 Point of Development

We had two important considerations in this development. First point is an improvement of cable bend capacity in straight-stacked ribbon construction. Another point is restraint of jacket shrinkage which is common theme for interconnection cables.

Firstly, we describe about the idea of cable design for good performance in cable bend.

In case of loose jacket structure as figure 3, an excess length occurs on inside ribbon by cable bend, and inside ribbon winds. Then inside ribbon interferes with jacket inner surface and attenuation is increased. To prevent this ribbon winding, large space between ribbon and jacket is necessary. However, at least 6mm clearance is needed to ensure good attenuation at cable bend radius of 25mm. If the clearance is 6mm, cable thickness will be near the diameter of round stack type.

Then we have designed new flat ribbon cable which has tight jacket for restraint of ribbon winding by cable bending.

In designing of tight jacket structure, it is important to find an optimum combination of jacket thickness and material young's modulus. So we have simulated the state of ribbons with cable bend using CAE analysis for brush up our cable design.

Finally we have established the cable structure which allows small radius bend in cable handling or storage.

Second important consideration is restraint of jacket shrinkage under temperature cycling. Jacket shrinkage causes macro-bend of fiber, and it causes attenuation increase.

There are two types of material shrinkage. Material shrinkage under low temperature is according to coefficient of linear thermal expansion. This shrinkage rate is approximately 0.1% to 1.0%. Residual strain after material forming process causes large shrinkage under high temperature. This shrinkage rate is approximately 1.0% to 10.0% and it causes not only attenuation increase but also fiber damage in connector.

Annealing before connector assembly is effective means for relaxation of residual strain but it is effective for only near part of cable end. And annealing process increases the cable cost.

Because of these problems caused by jacket shrinkage, it is necessary to restrain the shrinkage radically. Then we have designed new jacket in which two tension-members are buried for the function of holding against compression.

3.2 Design of two-dimensional flat ribbon cable

Figure 4 shows the structure of 24-fiber flat ribbon cable. 12-fiber ribbon is general type of 0.3mm thickness. This 12-fiber ribbon is also used for conventional flat ribbon cable.

We have chosen a flame-retardant PVC which meets the Riser spec as a jacket material. Jacket is coated around two stacked ribbons tightly and two tension-members are buried in it for restraint of shrinkage. We used 0.4mm FRP as tension-member.

In conventional flat ribbon cable, aramid yarns are laid around a ribbon for get the tensile strength generally. On the hand, our 24-fiber flat ribbon cable does not need any aramid yarn because it has tension-member in the jacket.

Two notches above stacked ribbons are for taking ribbons out by ripping jacket. Using these notches, we can easily strip the jacket without ribbon damage. The above-mentioned CAE analysis confirmed that these notches have little influence for restraint of ribbon winding by cable bending.

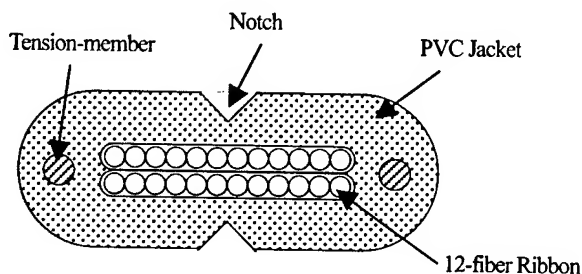


Figure 4. Design of 24-fiber Flat Ribbon Cable

Thus we have designed 24-fiber flat cable, and diameter of cable is 5.1mm width and 2.0mm thickness. This size is almost same as conventional 12-fiber ribbon cable with one 12-fiber ribbon. Fiber density of 24-fiber ribbon cable is 2.57fibers/mm², and 12-fiber ribbon cable is 1.13fibers/mm². Therefore this cable achieves high density and efficient interconnect cabling.

3.3 Design of connector assembly

Secondly we have discussed about connector assembly for 24-fiber ribbon cable. In case of conventional flat ribbon cable, spring back of MT connector occurring by connector joint is absorbed into the cable end because of loose jacket structure. Our 24-fiber ribbon cable has no clearance between ribbon and jacket because of tight jacket for good performance in cable bend. Therefore it is important consideration to develop the connector assembly form with tight jacket cable.

Because it was impossible to absorb a spring back of connector with tight jacket, we introduced protection tube to connector assembly. Two ribbons are covered with the protection tube after jacket removing at cable end. This protection tube is loose so that excess length of ribbons caused by connector spring back is absorbed into the tube.

In regard to protection tube structure, we have chosen flat shape because of prevention of crush by tube bend. And two tension-members are buried in tube same as 24-fiber flat ribbon cable. We have optimized the structure of protection tube and connector assembly with this tube.

Figure 5 shows the structure of protection tube and connector assembly form.

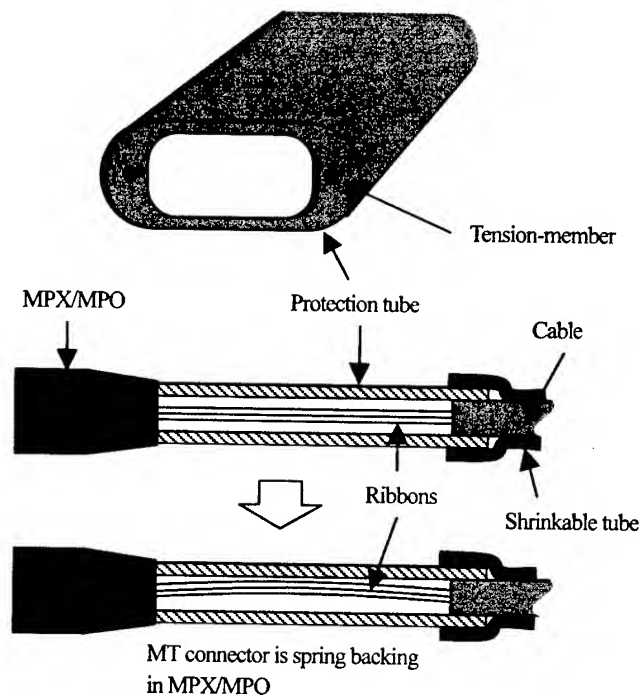


Figure 5. Design of Protection Tube and Connector Assembly

4. Result of Cable Testing

4.1 Cable Testing

According to the above-mentioned 24-fiber flat ribbon cable design, the trial cable was manufactured with twenty-four general single-mode fibers.

We have evaluated basic attenuations, temperature cycling performance, and mechanical characteristics (bend, crush, twist, tensile).

Examples of testing results are shown in table 2.

Table 2. 24-fiber Flat Ribbon Cable Performance

Test	Conditions	Result
Attenuation	@1550nm	Avg. 0.19dB/km Max 0.22dB/km
Temperature Cycling	-10°C to 60°C -40°C to 70°C @1550nm	Delta<0.02dB
Bend	R=25 x 10turn @1550nm	Delta<0.01dB
Crush	2000N/100mm @1550nm	Delta=0.00dB
Twist	2turn/300mm @1550nm	Delta=0.00dB
Tensile	400N @1550nm	Delta=0.00dB

The basic attenuations at 1550nm were measured on the condition that the cable was wound on the bobbin of 280mm diameter. We have confirmed good result as average attenuation of 0.19dB/km and maximum attenuation of 0.22dB/km.

The temperature cycling test has done on the condition that cable was wound freely in 280mm diameter. Delta attenuations at 1550nm were measured under -10°C to 60°C x 3 cycles and -40°C to 70°C x 3 cycles, and maximum delta attenuation was less than 0.02dB/km at any temperature.

We have confirmed good effect of tension-member buried in jacket.

The bend test has done on the condition of bend R=25mm x 10 turns. We have evaluated mechanical performance and delta attenuations at 1550nm. As a result, there were no damages on the cable jacket or ribbons and maximum delta attenuation was less than 0.01dB at R=25mm x 10 turns.

We have confirmed excellent effect of tight jacket structure.

The crush test has done on the condition that plate width was 100mm, plate edge was R=6 and maximum weight was 2000N. Delta attenuations at 1550nm were measured step by 100N. As a result, attenuations did not change at any weight and there were no damages on the cable jacket or ribbons.

The twist test has done on the condition that cable of 300mm was twisted at 1/2 turn, 1 turn and 2 turns x 10 times with 1.5kg tensile force.

Delta attenuations at 1550nm were measured. As a result, attenuations did not change at any twisting angle and there were no damages on the cable jacket or ribbons.

The tensile test has done on the condition that cable of 2m was stretched at tensile force of 400N. Delta attenuations at 1550nm were measured step by 100N. As a result, attenuations did not change at any tensile force and there were no damages on the cable jacket or ribbons.

4.2 Connector Testing with Cable

According to the above-mentioned connector assembly, the trial 24-fiber connectors were assembled with 24-fiber flat ribbon cable.

We have evaluated connecting attenuations, temperature cycling performance, and mechanical characteristics (tensile). Examples of testing results are shown in table 3.

Connecting attenuations were measured at 1310nm, and we have confirmed good result as average attenuation of 0.22dB and maximum attenuation of 0.78dB. (See figure 6)

In the temperature cycling test, delta attenuations at 1550nm were measured under -10°C to 60°C x 3 cycles and -40°C to 75°C. As a result, maximum delta attenuation was less than 0.10dB at any temperature.

We have confirmed good effect of new protection tube.

The tensile test has done according to GR-1435-CORE. Delta attenuations at 1310nm were measured at tensile force of 44N. As a result, residual attenuation was equal or less than 0.10dB and there were no damages on the connectors.

Table 3. 24-fiber Connector Performance with 24-fiber Flat Ribbon Cable

Test	Conditions	Result
Attenuation	@1310nm	Avg. 0.22dB Max 0.78dB
Temperature Cycling	-10°C to 60°C -40°C to 75°C @1550nm	Delta<0.10dB
Tensile	44N @1310nm	Delta<0.10dB

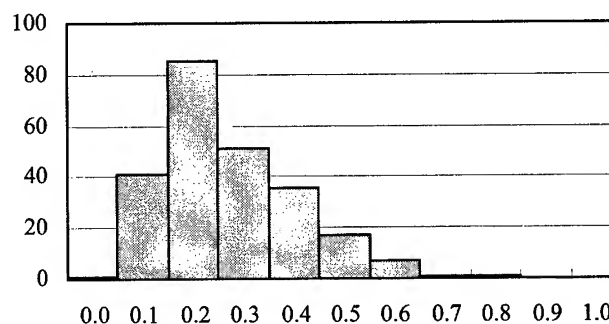


Figure 6. Histogram of Connecting Attenuation

5. Conclusions

We have designed 24-fiber flat ribbon cable which is suitable for "24-fiber to 24-fiber" form or "24-fiber to 12-fiber". To get good performance in cable bend and temperature cycling, we have developed tight jacket, tension-member buried in jacket and new type of protection tube for connector assembly. Consequently we have confirmed good performance in attenuations, temperature cycling test, and mechanical test to 24-fiber flat cable and two-dimensional 24-fiber connector.

6. References

[1] J. Register, M. Easton, "Optical Interconnect Cabling For Next Generation Central Office Switching" Proceedings of National Fiber Optic Engineers Conference (2001) pp.322-330

[2] T. Ohta, et al. "Development of Two-Dimensional Array MT Connector" Proceedings of the 49th International Wire and Cable Symposium, pp.187-193

AUTHORS



Kazuaki Hamada

Sumitomo Electric
Industries

1, Taya-cho, Sakae-ku
Yokohama, Japan

Kazuaki Hamada received a B.E. degree from Tsukuba University in 1991. He joined Sumitomo Electric Industries, Ltd. in 1991, and has been engaged in research and development of optical cable manufacturing. He is an engineer of Optical Network R&D Department in Yokohama R&D Laboratories.



Tomohiko Ueda

Sumitomo Electric
Industries

1, Taya-cho, Sakae-ku
Yokohama, Japan

Tomohiko Ueda received a B.E. degree from Tokyo University in 1987. He joined Sumitomo Electric Industries, Ltd. in 1987, and has been engaged in research and development of optical connectors. Mr. Ueda is an engineer of Optical Network R&D Department in Yokohama R&D Laboratories.



Nobuhiro Akasaka

Sumitomo Electric
Industries

1, Taya-cho, Sakae-ku
Yokohama, Japan

Nobuhiro Akasaka received his M.E. degree in chemical engineering from Tokyo University in 1983. He joined Sumitomo Electric Ind., Ltd. and he has been engaged in research and development of fiber optic cables. Mr. Akasaka is a Chief Research Associate of Optical Network R&D department in Yokohama Research Laboratories and a member of the IEICE Japan and the Material Life Society of Japan.



Toshifumi Hosoya

Sumitomo Electric
Industries

1, Taya-cho, Sakae-ku
Yokohama, Japan

Toshifumi Hosoya received the M.S. degree in Reaction Chemistry from Tokyo University in 1985. He joined Sumitomo Electric Industries, Ltd. in 1985, and has been engaged in research and development of optical fibers and connectors. Mr. Hosoya is now a chief research associate of Optical Network R&D Department.



Yoshikyo Tamekuni

Sumitomo Electric
Industries

1, Taya-cho, Sakae-ku
Yokohama, Japan

Yoshikyo Tamekuni received a B.E. degree from Science University of Tokyo in 1991. He joined Sumitomo Electric Industries, Ltd. in 1991, and has been engaged in research and development of optical connectors. Mr. Tamekuni is an engineer of Cable Connection & Fiber Splicing Products Department in Communications Division.

Development of Optical Fiber Attenuator using Fusion Splice Technology

Makiko Miura and Masakazu Nakano

Lucent Technologies Yazaki Ltd.

1157-106 Hotozawa, Gotemba-city, Shizuoka-Pref., 412-0046, Japan

+81-550-89-3592 · miura@lt-y.co.jp

Abstract

In Japan there is already considerable deployment of high bit rate DWDM systems in the long haul network. As such, with the continuing growth of Internet traffic, the metro network has recently become a significant bottleneck in end-to-end voice and data transmission. In order to resolve the kind of traffic demand emerging, service providers have begun installing WDM systems in the metro network. These systems need low-cost attenuators offering fine-grained, precise attenuation and low wavelength dependence loss to balance the transmitted power from channel to channel. These requirements make it difficult to use attenuators based on currently available technologies. In this paper, we report on the development of a technique for generating accurate optical fiber attenuators up to 5 dB using fusion splice technology using existing splicers. In laboratory tests, we have obtained $\pm 10\%$ attenuation tolerance with extremely low wavelength dependence loss from the O-band through the L-band.

Keywords

Optic fiber Attenuator; fusion splice; single splice; G.652 fiber.

1. Introduction

In order to achieve optimal performance, DWDM systems often require relatively uniform signal power across the entire operating wavelength band. This has traditionally meant large quantities of discrete attenuators must be installed to balance the transmitted signal power from channel to channel. In the case of long haul DWDM systems, the transmission light source powers is often relatively high and typical attenuator values range from 1 dB to 30 dB. The most common discrete attenuator is based on a small stub of fiber doped with metal ions to provide absorption [1][2][3][4], although other technologies are also used [5][6].

In Japan as elsewhere, as the long haul network capacity exploded through the rapid installation of new Non-Zero Dispersion Shifted Fiber (NZ-DSF) based trunk lines and DWDM transmission equipment, the metro network has become one of the throttles reducing the overall end-to-end voice and data transmission capacity. Furthermore, in Japan the growth of bandwidth demand continues to accelerate. Between 2000 and 2001, Japan had a 400 % increase in broadband Internet subscribers.

In order to address this bandwidth requirement, service providers have begun installing WDM systems in the metro network. However, some of these metro WDM systems, with their shorter

ranges and lower targeted deployment costs, utilize lower transmitted signal output power than do the long haul systems. For these systems, conventional attenuators are less than ideal because of their high cost, relatively coarse attenuation steps, and generally non-uniform wavelength dependence.

Recently the suppliers who want to make an attenuator to provide the customers can use the attenuators using core alignment single fusion splicers. The technique is based a controlled increase in the offset while the splice loss is monitored during splicing. It is easy to make an attenuator using this technique even though the loss is only monitored at one wavelength.

In this paper, we describe the development of this technique for generating fiber attenuation up to 5 dB using current standard fusion splicers. Optical and mechanical testing has confirmed the long term reliability and stability of these attenuating splices.

2. Fiber characteristics

Table 1 shows the optical and geometric characteristics of the fibers used in this study. Standard single mode fibers (G.652) typically use this attenuation jumper. Especially, Depressed Clad Single Mode fiber (DC-SM) has advantage for the micro and macro bending performance related on the Mode Field Diameter (MFD) of effective transmission wavelengths. However, mostly in Japan, the customers sometime need the same fiber type jumpers as transmission fibers such as G.653 Dispersion Shift Fiber (DSF) and G.655 NZ-DSF. Accordingly, we investigated 4 different fiber types in this study.

Table 1. Fiber characteristics using this study

Parameter		G.652		G.653	G.655
		Depressed	Matched		
MFD (μm)	1550nm	9.7 ± 0.6	10.4 *	8.0 ± 0.8	8.4 ± 0.6
	1310nm	8.5 ± 0.5	9.3 ± 0.5	6.5 *	7.0 *
Cladding diameter (μm)		125 ± 1.0	125 ± 1.0	125 ± 1.0	125 ± 1.0
Core/clad concentricity error (μm)		≤ 0.8	≤ 0.5	≤ 0.5	≤ 0.6
Cladding Non-circularity (%)		≤ 1.0	≤ 1.0	≤ 1.0	≤ 1.0

*Typical value

3. Theoretical model

3.1 Existing attenuation splice

There are a number of methods that have been previously developed for producing attenuating splices. One common technique is to set a lateral offset before applying the fusion arc (see Figure 1). The advantage of this method is that it is easy to control the arc duration for achievement of the targeted loss by power meter feed back. However, the wavelength dependent loss of this splice is generally high.

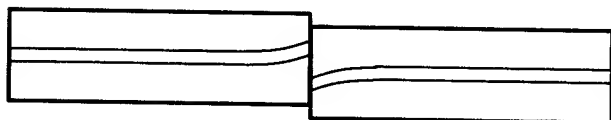


Figure 1. The method using fiber core offset

A simple relationship between the MFD offset and single-mode fiber splice loss can be expressed as: [7]

$$Loss_x (dB) = 4.343 \left(\frac{x^2}{w^2} \right) \quad (1)$$

where x is lateral offset (μm) and w is spliced fibers mode field radius. This formula can be applied the splice between same MFD fibers. Table 2 shows the estimated wavelength dependence splice loss based on the lateral offset using formula (1). In this result, we estimated for the DC-SM fiber splice loss from 1310 to 1625 nm (from O-band to L-band).

Table2. Estimation splice loss of DC-SM fiber using lateral offset method

(Unit: dB)

Target	1310 nm	1385 nm	1450 nm	1530 nm	1550 nm	1565 nm	1600 nm	1625 nm
0.5dB	0.66	0.61	0.56	0.51	0.50	0.49	0.47	0.46
1.0dB	1.32	1.21	1.13	1.02	1.00	0.98	0.94	0.91
2.0dB	2.64	2.42	2.25	2.05	2.00	1.97	1.88	1.83
5.0dB	6.60	6.06	5.63	5.11	5.00	4.92	4.70	4.57

This result indicates that the wavelength dependence splice loss in C and L-band are relatively small. However, in the O-band (1310 nm), E-band (1385 nm) and S-band (1450 nm) splice loss was usually higher than at the reference wavelength splice loss (1550 nm). Also tolerance of it is increased according to target splice

loss. The maximum splice loss difference from reference splice loss (1550 nm) in C through L-band was approximately 8 % (at 1625 nm) however in the O through L-band it was approximately 32 %. These values are not small enough to make these splices useful in many metro area WDM systems.

3.2 Developed technique

The technique we developed is based on MFD mismatch achieved through "passive" MFD deformation at the splice point [8]. It is generally known that an increase in the pre-fusion duration will result in a high splice loss. However it is very difficult to control the precise conditions before contact of the spliced fiber end faces. Accordingly, we used the cleaning arc stage to control the condition of the fiber ends. At this stage, the fiber MFD will change from its original size creating the MFD mismatch within a very short length.

Figure 3 shows the standard optical fiber splicing process using non-core alignment splicers. (it was one of the mass fusion splicer). The parts of hatching in this figure were applying the fusion arc on the splicing fibers and solid line shows the positions of the fiber end faces

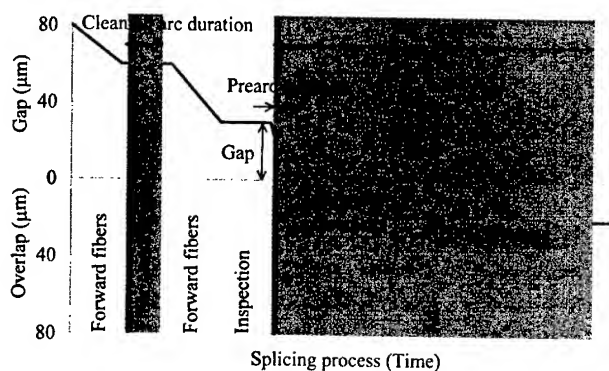


Figure 3. Fusion splice process

The attenuation splice technique we developed is based on controlling the characteristics of the fiber end faces by using a relatively high arc current and a long arc duration during the cleaning arc stage. There is a strong correlation between the preconditioning setting of the cleaning arc stage and splice loss. To control the prearc stage, we use a technique that is similar to the one used to obtain high splice loss. However when applying a high current arc before joining the splicing fibers to each other (as in the prearc method) it is difficult to control the precise overlap distance to get the target splice loss. If a high power arc is used before joining the fibers to each other for splicing, the fiber ends melt back from the initial gap set position. The result is that the gap position between the splicing fibers can easily change. This makes it difficult, if not impossible, to control the precise overlap distance using standard splicers. However, by using the cleaning

arc discharge during preconditioning, we can maintain accurate position control of the gap between the treated fibers before joining them together. Figure 4 shows the major difference between the fiber end face position obtained using the cleaning arc technique and that obtained using the prearc technique

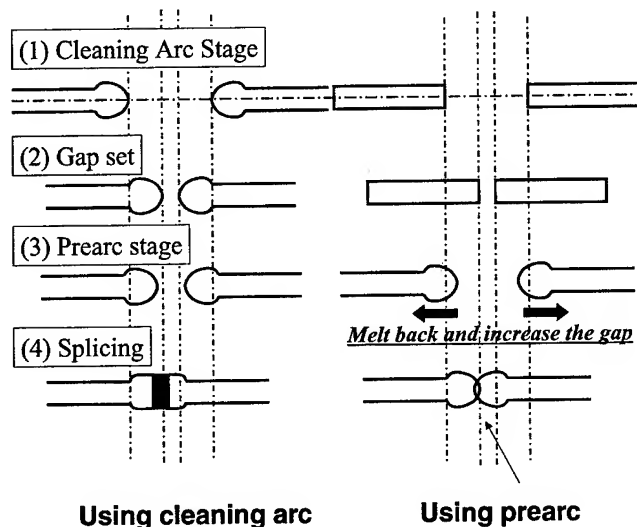


Figure 4. The difference of the fiber end face position

4. Evaluation result

4.1 Relationship between cleaning arc duration and splice loss

In order to increase the splice loss without splicing fibers core offset, we considered the deformation the fiber core before splicing using cleaning arc function, which is a feature found on all fusion arc splicers. Figure 5 show the relationship between cleaning arc duration and splice loss at 1310, 1550 and 1625 nm. As shown in the figures, it is easy to achieve the target splice loss by controlling the fusion arc duration of the cleaning arc stage and the wavelength dependence splice loss from 1310 to 1625nm is acceptable. This relation is close to the linear fitting for DC-SM and Matched clad Single Mode (MC-SM) fibers. For the G.653 and G.655 fibers, it is similar to the log fitting. It seems to be the important parameter of the original fiber MFD for deciding the cleaning arc setting.

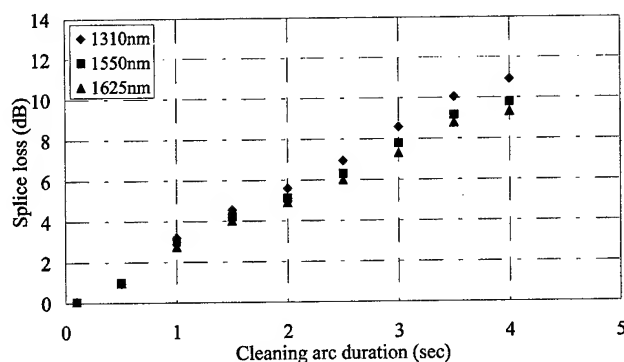


Figure 5-1. Depressed clad fiber (G.652)

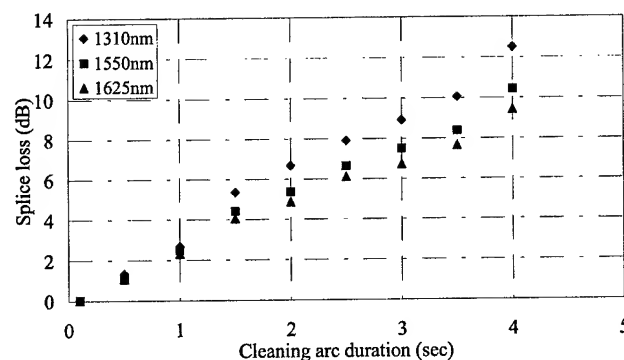


Figure 5-2. Matched clad fiber (G.652)

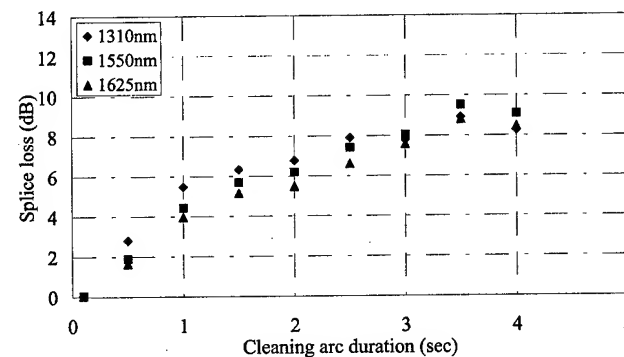


Figure 5-3. G.655 fiber

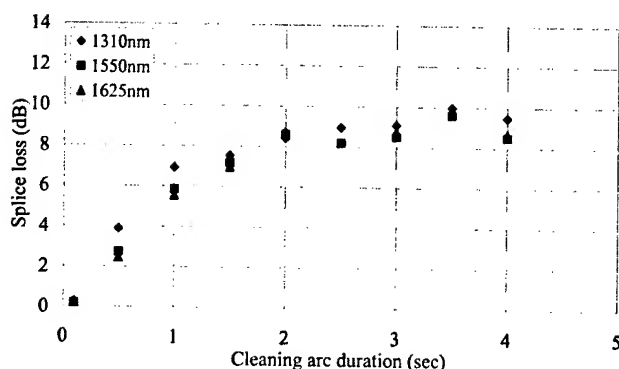


Figure 5-4. G.653 fiber

Focused on the wavelength dependency, the large MFD fiber such as MC-SM fiber has slightly wide splice losses in 1310 through the 1625 nm. However, it can be reducing the splice loss gap between the 1310 and 1625 nm by other splicing parameters such as fusion arc duration, fusion arc current, overlap distance etc.,

4.2 Actual result including wavelength dependence splice loss

Again of that the DC-SM fiber has a lot of advantages the attenuator jumpers such as the cost performance and macro bending performance, etc., Under this consideration, we focused on the DC-SM fiber attenuators and described the evaluation results of it in this section.

Table 3 shows the trial attenuators results of each target splice losses, which are 0.5, 1.0, 2.0 and 5.0 dB at 1550 nm, with several measurement wavelengths. These attenuators were made by optimized program for reducing the wavelength dependency and obtained the repeatability. These results indicated that all target splice losses have good repeatability and extremely low wavelength dependence splice loss for 1310 through 1625 nm.

Table 3-1. Target splice loss at 0.5 dB

(Unit: dB)

Items	1310 nm	1530 nm	1550 nm	1565 nm	1625 nm
Average	0.556	0.477	0.479	0.470	0.457
Median	0.555	0.473	0.474	0.473	0.452
Std dev	0.041	0.030	0.028	0.031	0.033
Max.	0.64	0.53	0.53	0.51	0.51
Min.	0.49	0.43	0.45	0.41	0.41
Count	21	21	21	21	21

Table 3-2. Target splice loss at 1.0 dB

(Unit: dB)

Items	1310 nm	1530 nm	1550 nm	1565 nm	1625 nm
Average	1.073	1.022	1.020	1.014	0.998
Median	1.059	1.030	1.028	1.025	0.994
Std dev	0.068	0.060	0.058	0.055	0.061
Max.	1.20	1.11	1.10	1.09	1.10
Min.	0.92	0.90	0.90	0.91	0.90
Count	21	21	21	21	21

Table 3-3. Target splice loss at 2.0 dB

(Unit: dB)

Items	1310 nm	1530 nm	1550 nm	1565 nm	1625 nm
Average	2.161	2.019	2.006	1.969	1.944
Median	2.107	1.989	1.975	1.979	1.945
Std dev	0.165	0.139	0.138	0.142	0.133
Max.	2.41	2.21	2.19	2.17	2.16
Min.	1.93	1.81	1.80	1.73	1.74
Count	15	15	15	15	15

Table 3-4. Target splice loss at 5.0 dB

(Unit: dB)

Items	1310 nm	1530 nm	1550 nm	1565 nm	1625 nm
Average	5.151	4.944	4.919	4.909	4.837
Median	5.086	4.937	4.922	4.930	4.882
Std dev	0.209	0.178	0.193	0.187	0.183
Max.	5.47	5.26	5.27	5.26	5.12
Min.	4.84	4.73	4.70	4.69	4.58
Count	14	14	14	14	14

Figure 6 shows the comparison of attenuator splice loss performance between theoretical splice losses using core offset technique and measured splice losses using our developed technique. The new technique has better wavelength dependency on all target splice losses especially 5 dB target splice loss.

This technique could be applying other fiber type attenuators and it seems to be getting high quality attenuator.

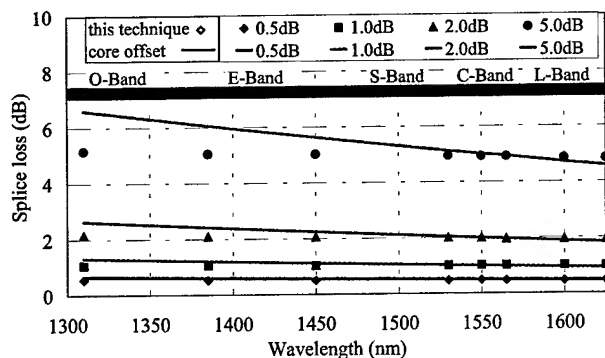


Figure 6. The wavelength dependence splice losses comparison between fiber core offset technique and our developed technique

5. Reliability test

This section described reliability tests results on 1.0 and 2.0 dB attenuators used developed technique. The evaluated attenuator type was the PVC buffered standard code jumper with SC connectors on both fiber ends. The splice point was protected by the heat shrinkable protection splint.

5.1 Thermal shock test

Figure 7 show the result of the thermal shock tests measured by 1550 nm followed by Bellcore GR-63 standard for Network Equipment-Building System Requirements: Physical Protection. Table 4 show the condition of thermal shock test on both high and low temperature. The results of three attenuators of each loss indicated that there are no loss change and no residual loss on both test conditions. Also the tested samples have no physical damage.

Table 4-1. High-temperature exposure and thermal shock test condition

Temperature (degree C)	Event	Duration Rate of change
23 to 70	Temperature transition	30 degree C/hr
70	Temperature soak	72 hr (minimum)
70 to 23	Temperature transition	Less than 5 minutes

Table 4-2. Low-temperature exposure and thermal shock test condition

Temperature (degree C)	Event	Duration Rate of change
23 to -40	Temperature transition	30 degree C/hr
-40	Temperature soak	72 hr (minimum)
-40 to 23	Temperature transition	Less than 5 minutes

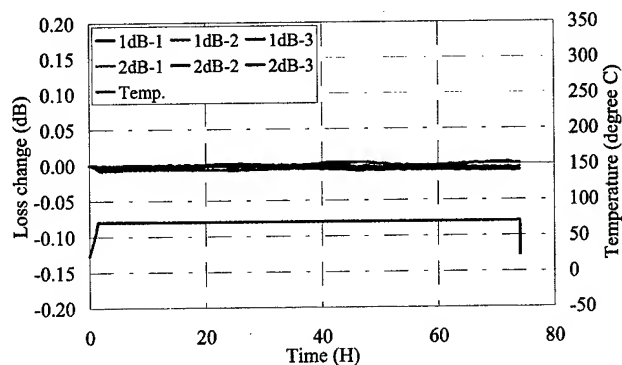


Figure 7-1. The result of high temperature thermal shock test at 1550 nm

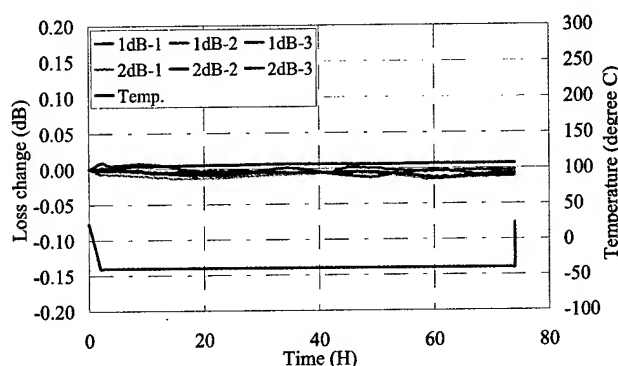


Figure 7-2. The result of low temperature thermal shock test at 1550 nm

5.2 Tensile strength test

This section referred to the investigation result of tensile strength performance of attenuation jumper codes. This test was followed number C6821 JIS standard; Test methods for mechanical characteristics of optical fibers; and details given in Table 5.

Table 6 shows the results of this test on un-aged samples and after thermal shock test samples. As shown in this result, the typical failure strength was approximately 40 N on both un-aged and aged samples. These values were about half strength as non-spliced normal optical fiber jumpers, because this has one splice point in the middle of it. The protection of splice point had very simple geometry (using standard heat shrinkable sprint on splice point). The tested samples typically broke at the edge of sprint protection tool. This performance could be satisfying the general using in the field condition such as in the optical cabinet. If the customer needs same strength characteristics as normal optical jumper code, it should be consider the protection method for increasing the failure strength.

Table 5. Tensile strength test condition

Items	Condition
Tensile speed	100mm/min
Sample length	500mm
Code type	PVC buffered fiber

Table 6. The result of tensile strength test (Average)

(Unit: N)

Items	Before test	After test	
		Low	High
1.0 dB	41.1	37.5	39.8
2.0 dB	41.9	36.2	39.4

6. Conclusions

We have developed a new technique for manufacturing high quality, precision attenuators ranging from 0 dB to 5 dB using standard arc fusion splicers. The key advantages of this technique are 1) the splice loss is very accurate (typical 0.03 dB at 1.0 dB attenuator), 2) the splice loss shows very low wavelength dependency (less than $\pm 10\%$ over 1.0 dB attenuator) and 3) no additional equipments (just using standard arc fusion splicer). And the splices have demonstrated a good level of temperature and mechanical stability.

We believe that this technique will be useful for producing high quality attenuators using any kind of fiber types.

7. Acknowledgments

The authors are thankful to Wayne Lewis of Lucent Technologies Yazaki for discussion and suggestion of technical issue.

8. References

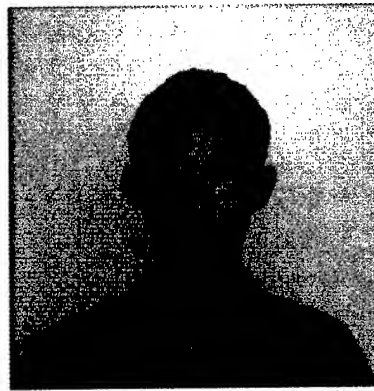
- [1] K. Kanayama, K. Takada, Y. Takeuchi and K. Kato, "Characteristics of SC Type Optical Attenuator using Metal Doped Fiber," *IEICE Japan, General Conference*, C-347 (1994)
- [2] Y. Ariga, Y. Morishita, M. Saijo, K. Sugi and K. Muta, "Optical Attenuator of Pig-tail Type using Metal Doped Optical Fiber," *IEICE Japan, General Conference*, C-3-112 (1997)
- [3] M. Saijo, Y. Morishita, Y. Ariga, K. Sugi and K. Muta, "Pig-tail Type Optical Attenuator using Metal-doped Optical Fiber," *46th IWCS*, 74-81 (1997)
- [4] E. Metsuyama, M. Watanabe, Y. Morishita and H. Noro, "Improved Performance of Attenuation Fibers," *IEICE Japan, General Conference*, C-3-50 (2000)
- [5] J. Kilmer and A. P. Sirti, "The Quest to Make Low Reflection Wideband Attenuators," *NFOEC*, 433-440 (1994)
- [6] S. Chia, "Cost-effective Single-Mode Wavelength Independent All-fiber Attenuator," *NFOEC*, 813-822 (1995)
- [7] S. C. Mettler, "Monte-Carlo Analysis of the Effect of Mode Field Diameter Mismatch on Single-mode Fiber Splices", *NFOEC* (1992)
- [8] Attenuation splice technique using Passive MFD deformation technology, Patent pending, M. Miura and M. Nakano

Authors



Makiko Miura

Makiko Miura received her B.E. degree from Akita University in 1997. She has been engaging in Optical Products Sales Department and her main work is sale the optical products and development of evaluation technology with fiber splicing.



Masakazu Nakano

M.Nakano has been engaging in Research & Development Department of Lucent Technologies Yazaki Ltd. in 1995. He was a Member of Technical Staff at OFS from 2001 to 2002. Then return to the Lucent Technologies Yazaki employee in 2002. His main work is development of evaluation technology with optical fiber, ribbon and apparatus in current company and he was occupied in splicing development team in Post draw R&D department at OFS.

Photodeposition of Bragg Gratings on Nano-Porous Silica Clad Optical Fibers

Dehipawalage Sunil and Harry D. Gafney

Department of Chemistry
City University of New York
Queens College
Flushing, NY 11367

Bolesh Skutnik

Fiber Optics Fabrication, Inc.
515 Shaker Road, Route 220
East Longmeadow, MA 01028

Abstract:

Recent experiments in our laboratories have led to holographic, photolithographic and laser writing techniques capable of patterning Bragg gratings in porous Vycor glass. Photodeposition of Bragg grating on optical fibers composed of fused silica core surrounded a nanoporous sol-gel derived silica has been examined. Gratings with line spacing of 10 μm have been achieved in the cladding of 180 μm diameter fibers, and the gratings have been used to inject light into and remove light from the core of the fiber. Equivalent photodeposition experiments have been carried out on square fibers prepared by coating inline a squared core with an equivalent sol-gel based silica. However, attempts to photodeposit a grating failed. Since adsorptivity depends on morphology, the morphologies of the claddings on the round and square fibers have been examined by optical and atomic force microscopy. Surface morphologies have been quantified in terms of surface roughness and correlated with the adsorptivity with respect to $\text{Fe}(\text{CO})_5$, the photoactive precursor. Surface roughness and adsorptivity are compared to that of commercially available Corning's code 7930 porous Vycor glass.

Introduction:

Photodeposition of metals and/or metal oxides in porous glasses and sol-gel derived xerogels increases the refractive index of the matrix. Consolidation occurs without loss of pattern resolution thereby creating gradient index structures useful as optical telecommunication and processing devices. One approach of current interest is the deposition of Bragg gratings consisting micron-spaced regions differing in refractive index and/or absorptivity. Such structures deposited in the cladding of an optical fiber, for example, could be used to switch light from one fiber to another. Previous experiments in our laboratories have examined the photodeposition of Bragg gratings in Corning's code 7930 porous Vycor glass.[1] Line spacings of *ca.* 5 μm are accessible by holographic, photolithographic and laser writing technique. Comparisons of optical performance reveal significant improvements with holographic deposition. Nevertheless, resolution of the deposited structure is independent of the deposition technique suggesting that resolution is limited by the scattering of the excitation light by the porous glass matrix [2]. These experiments were undertaken to examine the photodeposition of Bragg gratings in the cladding of optical fibers composed of fused silica core surrounded a nanoporous sol-gel derived silica. Data presented here show that well-resolved Bragg grating can be deposited in the cladding of 180 μm diameter fibers, and that these gratings can be used to insert and remove light from the

core of the fiber. Surprisingly, AFM analyses of the deposited structures reveal the photolyzed regions, even though heated to 1200°C surfaces, fail to consolidate in a manner analogous to the unexposed regions. The result is a series of steps similar to that found in gratings prepared mechanically.

To provide a means of optical coupling between fibers, photodeposition has also been examined on 160- μm square fibers. Although prepared in the same way as the round fibers, photodeposition of iron oxide via 488-nm photolysis of $\text{Fe}(\text{CO})_5$ physisorbed onto the square fiber failed to produce a grating, or a comparable change in refractive index. Since the amount of metal and/or metal oxide deposited as well as the resolution of the pattern depend on the morphology of the porous glass, the morphology and porosity of the different glass fibers have been characterized by optical and atomic force microscopy. Surface roughness indicates that the porous silica claddings on the square fibers are less porous than those on the round fibers thereby reducing the amount of $\text{Fe}(\text{CO})_5$ adsorbed and in turn the gradient index created photochemically.

Experimental:

Materials: $\text{Fe}(\text{CO})_5$ (Aldrich) was used as received since UV-visible and IR spectra agreed with published spectra. One inch samples of the round or square fibers were impregnated with $\text{Fe}(\text{CO})_5$ by previously described vapor deposition procedures.[3] All samples were exposed to $\text{Fe}(\text{CO})_5$ vapor for times ranging from 1-2 minutes to as long as 30 minutes.

The impregnated fiber samples were taped onto glass slides, which were then mounted on an optical stage driven by a computer controlled Aerotech DR 500 stepping motor. All samples were irradiated with 488-nm light in air with a Coherent Ar^+ laser focused through a Zeiss quartz microscope 10X objective at a power of 10W. The distance from the objective to the sample was adjusted so that the focal point of the objective was on the outer edge of the mounted fiber. The stepping motor moved the fiber across the excitation beam, and then stepped a specified distance and moved the fiber across the beam again. The individual exposure times, *i.e.*, the time required to move the fiber across the focused beam, are calculated to be 0.5 sec.

Samples were examined optically with a Zeiss microscope at a magnification of 400X. Fiber surfaces were imaged with a Digital Instruments Nanoscope IIIa AFM. Fibers were mounted on metal disks with double-sided tape and imaged using the constant tapping mode. Surface roughness was calculated with the supplied software. AFM images of Bragg gratings deposited on round and square optical fibers were

obtained by scanning the sample with a silicon probe with a spring constant of 20 N/m in tapping mode.

Results and Discussion:

$\text{Fe}(\text{CO})_5$ impregnation of 180- μm diameter fibers is evident as a change in color from colorless to light yellow. After a one minute exposure, however, the amount of complex adsorbed does increase linearly with time. At least visually through an optical microscope, fibers exposed for as long as five minutes appeared the same in color as those exposed to the vapor for one minute. As a result, samples exposed to the vapor as long as five minutes required the same time of exposure to the photolyzing beam as those that were exposed to the vapor for one minute. With samples containing the same amount of $\text{Fe}(\text{CO})_5$, deposition was examined as a function of exposure time by varying the rate at which the fiber was moved across the focused laser beam. Varying the rates from 100 to 1000 $\mu\text{m}/\text{sec}$ showed that a rate of 400 $\mu\text{m}/\text{sec}$ produced a series of exposed and unexposed regions that exhibited the highest relative overtone intensity when a He-Ne laser was passed through the grating. Consequently all samples described here were prepared by moving the fiber across the beam at a rate of 400 $\mu\text{m}/\text{sec}$. Figure 1 illustrate a grating photodeposited on a 180 μm diameter fiber. Since the core is consolidated, and there is no obvious difference in the light transmitted through the fiber, the photodeposited gratings are assumed to be only in the cladding and do not extend into the core of the fiber. The exposed regions appear as lines across the fiber, and an AFM image of the surface (Figure 2) confirms that the exposed regions do not consolidate to the same extent as the unexposed regions when the fiber is heated to 1200°C, which is sufficient to consolidate PVG, or base-catalyzed TMOS xerogels. This differs from the behavior found in PVG and in dried xerogels where heating to 1200°C consolidates the matrix and leads to a consolidated glass with a smooth surface. In fact, SIMS analysis of the gratings deposited in PVG show that consolidation leads to 0.5 nm thick layer of glass covering the photodeposited grating and the resulting structure having a smooth surface.

Although the grating is in the cladding of the fiber, impinging a He-Ne laser onto the grating results in injection into the fiber core. Visually, the amount of light injected into the core was independent of varying the angle of incidence of the He-Ne beam from *ca.* 30° to about 90°.

Equivalent experiments were carried out on 160 μm x 160 μm square fibers prepared in a manner equivalent to the round 180- μm diameter fibers except that in this case the porous silica was coated onto a square fused silica core. Although the porous silica claddings were prepared in the same manner, it was immediately obvious that the adsorptivity of the square fibers is significantly less than that of the round fibers. When exposed to $\text{Fe}(\text{CO})_5$ vapor, the round fibers developed a light yellow color within 1-2 minutes, whereas the square fibers failed to develop a color even after as much as 30 minutes of exposure. Extracting the square fibers with acetone or nitric acid, or cleaning in an ultrasonic cleaner with distilled water failed to improve the adsorptivity of the square fibers. AFM analyses of the square fibers reveal a surface different from that of the round fibers. Unlike the round fibers, as well as the surfaces of PVG and other base catalyzed xerogels [4], all of which possess a

surface made up of round silica nodules, the surfaces of the square fibers appear to be composed of elongated nodules with the elongation in the direction of the fiber axis. As a result, the surfaces of the square fibers are smoother as evidenced by a roughness parameters that is smaller than those obtained for the round fibers and PVG (Table I). Further experiments are needed to provide a rationale for why SiO_2 polymerization on the square cores fibers appears to occur in the direction of the fiber axis. One possibility is that the polymerization of the porous silica coating is being templated by the underlying core, but the mechanism of how this occurs on a fully consolidated SiO_2 core is not clear. Consistent with their low adsorptivity, however, attempts to photochemically create a Bragg grating on the square fibers failed. Even with square fibers exposed to $\text{Fe}(\text{CO})_5$ for as long as 30 minutes, extensive photolysis failed to create any change in refractive index that could be detected by either optical or atomic force microscopy, or by deflection of a He-Ne probe beam.

Conclusion:

Bragg gratings deposited in the cladding of round optical fibers composed of a silica core and a nanoporous silica cladding are capable of injecting light into, and removing light from the core of the fibers. The ability to deposit a diffraction grating on the cladding of a fiber depends on the roughness of the surface, which reflects the porosity of the nanoporous silica cladding. Porosity of the nanoporous silica cladding depends on the shape of the fiber core, with deposition onto square fibers resulting in a porous silica with reduced adsorptivity.

Acknowledgements:

Support of this research by the National Science Foundation (DMR-9314033 and CHE-0079040), the Department of Defense/Air Force Office of Scientific Research (F49620-94-1-0209), the New York State Science and Technology Foundation through the CUNY Ultrafast Photonics Materials and Applications Center for Advanced Technology, the Petroleum Research Fund administered by the American Chemical Society, and the Research Foundation of the City University of New York is gratefully acknowledged. Support of the research on the nanoporous silica clad fibers at Fiber Optic Fabrications, Inc. as well as portions of the research at Queens College were funded through SBIR contract DAAB07-96-C-D612 with the CECOM division of the US Army at Fort Monmouth, NJ, monitored by bridge scientist S. DiVita. HDG thanks Corning Inc. for samples of code 7930 porous Vycor glass.

References:

1. D.Sunil, A.W.McQuade, H.D.Gafney. *Applied Spectroscopy* (1998) **52**, 7, 1041.
2. D.Sunil, A.W. McQuade, H.D.Gafney. *Applied Spectroscopy* (2000) **54**, 6, 869.
3. Darsillo, M.S., Gafney, H.D., Paquette, M.S. J. Am. Chem. Soc. 1987, **109**, 3275.
4. Edgar A. Mendoza, Eugene Wolkow, D.Sunil, Peter Wong, Jonathon Sokolov, Miriam H.Rafailovich, Maten den Boer, and Harry D. Gafney. *Langmuir*. 1991, **7**, 3046.

Sample	Mean roughness
Fiber A1	80 nm
Fiber A2	105 nm
Fiber B1	70 nm
Fiber B2	43 nm
Sol-gel glass	285 nm
Porous Vycor Glass	400 nm

Fibers A1 & A2 are round fibers while B1 & B2 has rectangular shape.
Table I. Comparison of roughness of round and rectangular fibers.



Figure 1: Optical micrograph of a grating created on the side of a 180 μm diameter optical fiber with an *ca.* 70-80 μm porous cladding.

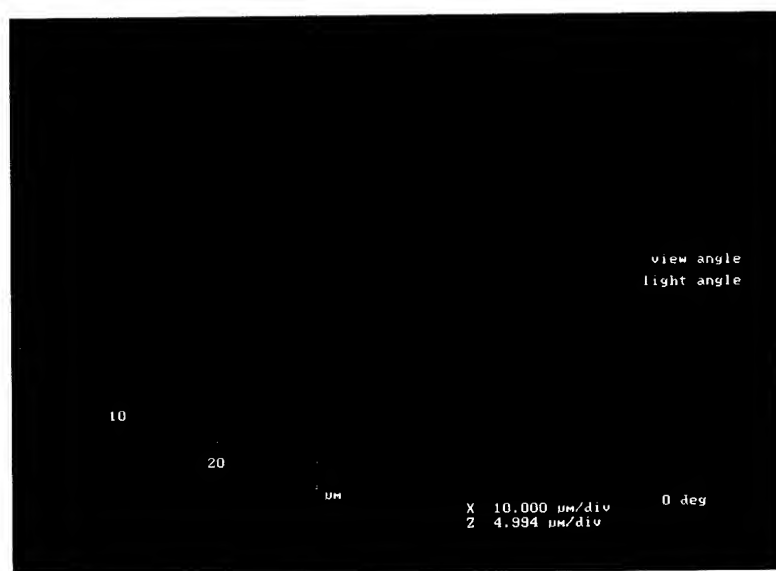


Figure 2: Atomic Force Micrograph of a grating written on a 180 μm diameter fiber.

Ring Network Architecture Using Wavelength Division Multiplexing Coupler

Takaaki AIHARA, Makoto KAWAKAMI, Yoshitaka ENOMOTO,

Kenichi NAKAZAWA, Takayuki TASHIRO, Kiminori SATO

NTT Access Service Systems Laboratories, Nippon Telegraph and Telephone Corporation
1-7-1 Hanabatake, Tsukuba, Ibaraki, 305-0805 Japan
+81-298-68-6310 · aihara@ansl.ntt.co.jp

Abstract

We propose a parallel architecture that will allow us to install cost-effective ring networks in metropolitan area networks (MAN), where the capacity demand for each building in the network varies greatly. This architecture involves connecting two types of transmission equipment to two fibers with a Wavelength Division Multiplexing (WDM) coupler. This approach is advantageous in terms of the effective use of both optical fiber and wavelength. Using this approach as a basis, we designed and manufactured a WDM coupler prototype and a distribution cabinet in which to install it, and obtained good levels of performance. This architecture was adopted in Tsukuba WAN, which is an ultra-high-speed network (Max. 570 Gbit/s) for connecting supercomputers.

Keywords

WDM coupler; Network architecture; Ring network; Optical fiber

1. Introduction

The explosive demand for broadband services has mainly been generated by the phenomenal growth of the Internet. We have developed technologies for reducing costs in optical access networks and systems [1], and installed a large amount of optical fiber cable to supply services immediately. However, there will be an optical fiber shortage because of the large number of optical fibers used for broadband services, and this has already occurred in some areas. It is therefore important to use optical fibers efficiently.

We have developed loop distribution and discrete distribution to enable us to use optical fiber efficiently in the access network architecture, namely an optical fiber network with a star configuration [2].

In contrast, networks that connect with a user's LAN, (MAN), employ an optical fiber network with a ring configuration to provide lower cost and greater reliability. It is important to use the optical fiber efficiently, and respond to demand flexibly in MAN. Recently, WDM has been deployed in MAN to reduce the optical fiber running costs. It is becoming obvious that we must reduce the running costs by reducing the number of optical fibers.

When demand is scattered and the individual capacity demands of the central office and user building vary greatly in MAN, a large

capacity network and a small capacity network are installed, especially when the network consists of a user building. User buildings need networks with a wider capacity range than the carrier's central offices, which were installed to meet the planned demand and network scale. When the network faces various capacity demands, network interfaces are installed to meet these demands. However, when expensive components are needed, such as DWDM, large and small capacity networks are installed individually.

In this paper, we first describe a network architecture for the effective use of optical fiber and communication signal wavelength in a MAN that consists of user buildings with a variety of demands. Based on the network architecture, we designed and manufactured a WDM coupler and a distribution cabinet in which to install it. Finally, we report on the ultra-high-speed network "Tsukuba WAN" that employs this architecture.

2. Network Architecture

2.1 Network Design

Figure 1 shows the two ring network architectures for a metropolitan area network, which incorporates large and small capacity networks. The ring network architecture is more reliable and less expensive than the star network architecture as regards physical network installation.

Figure 1(a) shows an "individual architecture". Two 2-fiber rings (one clockwise and one counter clockwise) connect each transmission equipment port. The transmission equipment for the large capacity network (TE-L) and that for the small capacity network (TE-S) are installed in the user site for the large capacity network (L-user). Only TE-S is installed in the user site for the small capacity network (S-user). The 2 fibers for TE-L pass the S-user as shown in Fig. 1(a). A total of 4 fibers are required in this conventional architecture.

Figure 1(b) shows our proposed "parallel architecture" [3]. The WDM couplers are installed between TE-L, TE-S and the 2 fibers in L-user. The WDM coupler divides and multiplexes TE-L and TE-S wavelengths. In S-user, they are installed between TE-S and an optical fiber so that they connect with the same port of each WDM coupler. The WDM coupler and parallel architecture enables us to install two networks with only 2 fibers.

2.2 Evaluation

Table 1 shows an evaluation of the individual and parallel network architectures. The cost involves a trade-off between the cost of the two fibers in the individual architecture and that of the WDM coupler in the parallel architecture. The parallel architecture is advantageous over long distances.

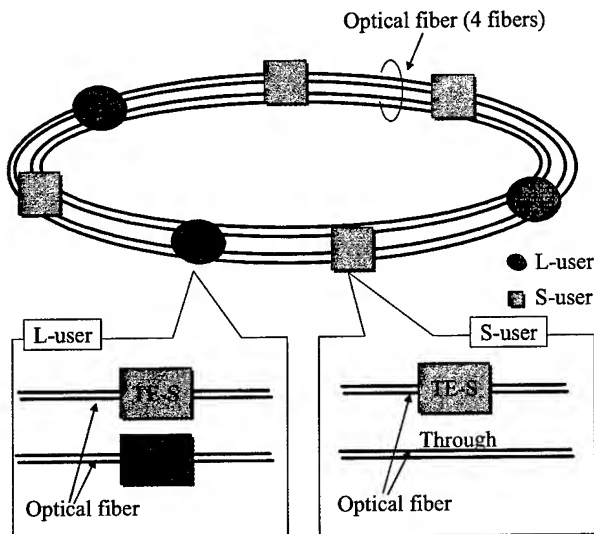
With both architectures it is easy to add TE-L to an S-building. However, when the optical fiber route design for TE-S is different from that for TE-L in the individual architecture, the optical fiber route must be changed in order to connect with an S-user.

Table 1. Evaluation of network architecture

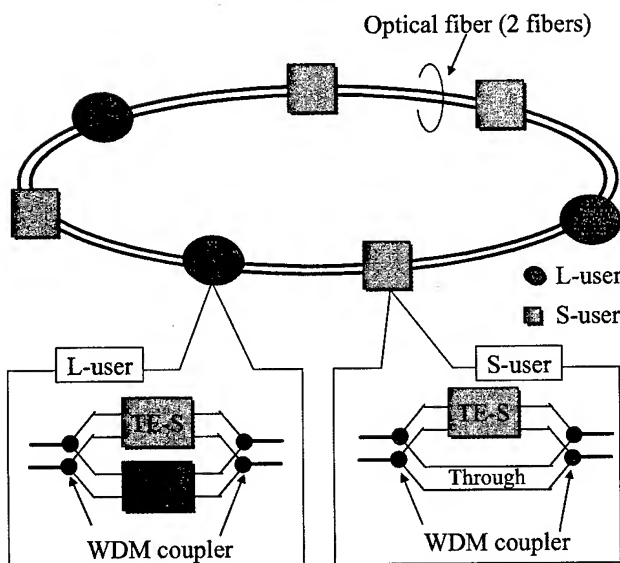
Item		Parallel	Individual
Cost	Optical fiber	$A \times B \times 2$	$A \times B \times 4$
	WDM coupler	$C \times D$	0
Flexibility	TE-L Addition	Easy	Same route: easy Another route: need to change route

Optical fiber: A yen / km
Distance: B km

WDM coupler: C yen / building
Number of users: D



(a) Individual architecture



(b) Parallel architecture

Figure 1. Network architecture

3. Distribution design at user site

The distribution design at a user site is important in terms of reducing optical loss, because a user site has many fiber connection points. Specifically, when the wavelength for TE-L passes the S-user in the parallel architecture, optical loss occurs when a signal passes through the WDM coupler and optical fiber at the user site.

Figure 2 shows the distribution design for user sites. We assume that TE-L and TE-S are installed in another building.

Figure 2 (a) shows the distribution design in the user site when the WDM coupler is installed in the same place as the TE-S. With L-user, the TE-L signal passes through user buildings 1, 2, 3 and the TE-L. There are certain fiber connection points with optical loss between buildings 1 and 3 and this optical loss must be minimized. With S-user, the TE-L signal passes through building 1 and is returned in user building 2. Optical loss occurs as the signal passes through the optical fiber cable between the buildings.

Figure 2 (b) shows the distribution design for a user site when a WDM coupler is installed in the cabinet in building 1, which is the nearest to WAN. With L-user, the TE-L signal passes through buildings 1 and 3. With S-user, the TE-L signal is returned to WAN in user building 1. This enables us to reduce optical loss without routing the signal through building 2.

When transmission equipment is installed in two or more user site buildings, it must be installed in the building nearest WAN in order to reduce optical loss. To reduce the optical loss for TE-L, it is necessary to minimize the optical loss when a TE-L signal passes through S-user. Moreover, to allow us to install the equipment simply in a building, we developed a distribution cabinet that can accommodate 4 WDM couplers.

4. WDM coupler for parallel architecture

4.1 WDM coupler design

Figure 3 shows the structure of our WDM coupler, which is constructed with three input-output ports, a, b, and c [3]. The communication signal wavelengths, λ -A and λ -B, input from port a are divided to λ -A and λ -B, and λ -A is output at port c, and λ -B

B is output at port b. Port a is connected to WAN, port b is connected to TE-S, and port c is connected to TE-L. We allocated the short wavelength band of the C-band, 1530-1543 nm, to TE-S, and the long wavelength band of the C- and L-band, 1547-1610 nm, to TE-L in order to use the wavelengths effectively. We therefore designed the port b outputs and inputs in the 1530-1543 nm band and the port c outputs and inputs in the 1547-1610 nm band.

Furthermore, a low insertion loss is required at a-c, because λ -A passes through port a-c in the S-building. We designed the WDM coupler with optical filters to reflect λ -A for a lower optical loss. Moreover, we designed the coupler to be compact to allow it to be installed in a distribution cabinet.

4.2 Characteristics of prototype WDM coupler

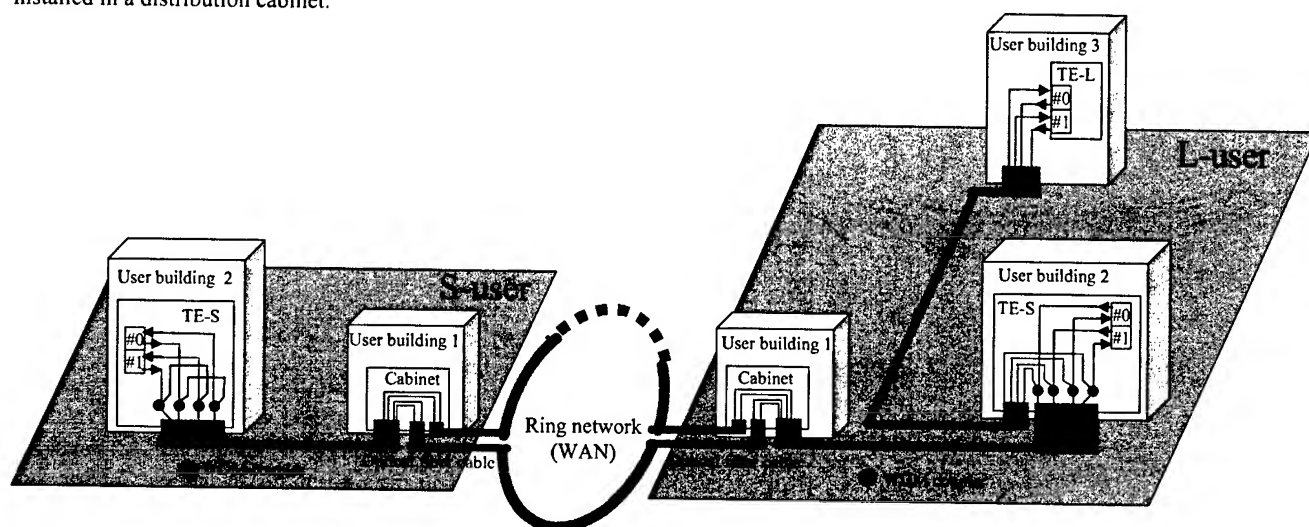
4.2.1 Optical characteristics

We manufactured a WDM coupler prototype that divided and multiplexed 1530-1543 nm signals for λ -A and 1547-1610 nm signals for λ -B.

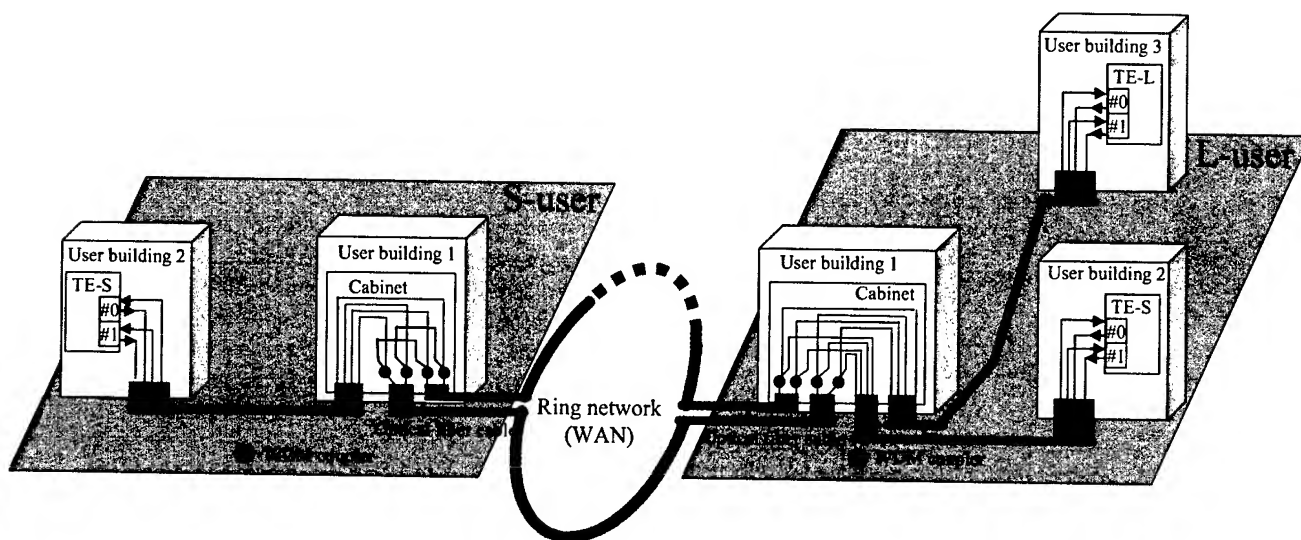
Figure 4 shows the insertion loss of the WDM coupler prototype. The insertion loss of each port was very low at less than 1 dB.

4.2.2 Appearance

Figure 5 is a photograph of our prototype WDM coupler. Its small size is aimed to be installed in a distribution cabinet.



(a) WDM coupler in transmission equipment



(b) WDM coupler in cabinet

Figure 2. Distribution design at user site

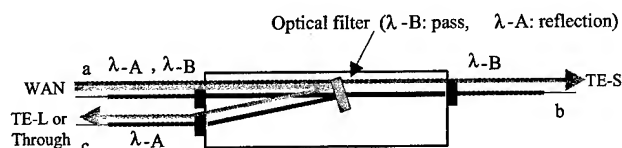


Figure 3. Configuration of WDM coupler

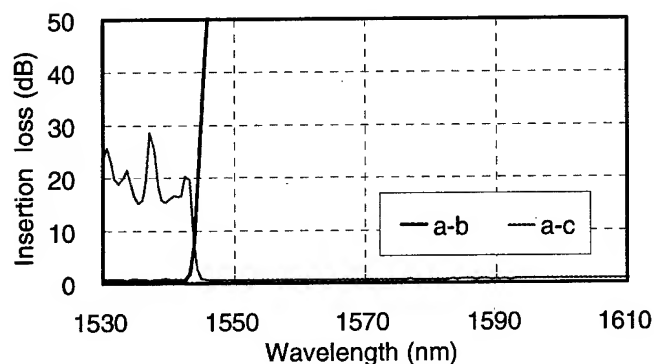


Figure 4. Prototype WDM coupler insertion loss

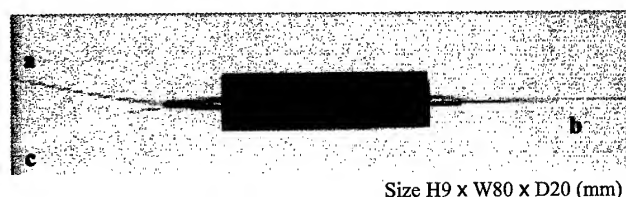


Figure 5. Photograph of prototype WDM coupler

4.3 Characteristics of prototype cabinet

Figure 6 shows the appearance of the cabinet in which the 4 WDM couplers are installed. Its size is small enough for it to be installed in the space for a main distribution frame (MDF). The cabinet can accommodate 4 WDM couplers in each tray.

Each WDM coupler is accommodated in the tray individually. A faulty WDM coupler can be replaced without touching any other WDM coupler that may be in use. The four trays are stacked and accommodated in the cabinet. The tray has three ports, a, b and c that employ an MU connector. This cabinet is equipped with a guide to prevent the optical fiber from bending with a small diameter and thus cause bending loss. This enables us to use the cabinet in the L-band.

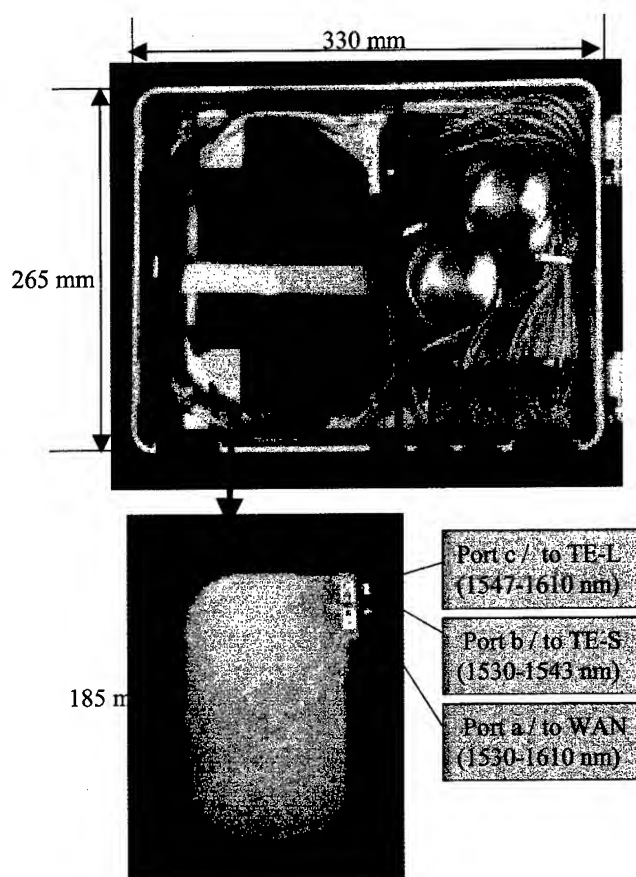


Figure 6. Appearance of cabinet containing 4 WDM couplers

5. Ultra-high-speed ring network "Tsukuba WAN" using parallel architecture

5.1 Background to Tsukuba Science City

Figure 7(a) shows the location of Tsukuba Science City. It lies 45 kilometers north of Tokyo, and is a unique area hosting a large number of research institutes. The most important feature of this area is that it hosts many research institutes, researchers and supercomputers [4]. To allow us to study ultra-high-speed access networks, meta-computing and interactive large-scale computer simulation, we need access to an ultra-high-speed network offering, for example, a rate of 10 Gbit/s per path.

5.2 Network requirements and design

Figure 7(b) shows the route of Tsukuba WAN. Ten research institutes are connected via Tsukuba WAN, and the total connected distance is 40 kilometers. Research institutes need highly reliable networks that operate in the 150 to 600 Mbit/s range, to provide such functions as data exchange. In contrast, supercomputer research institutes need even larger capacity

networks, for example 10 Gbit/s per path [5], and low latency networks to link with supercomputers in remote locations. Low network latency is required for currently used supercomputers.

To meet the first of the above demands, add drop multiplexers (ADM) have been employed to allow operation in the 150 to 600 Mbit/s range, and the total capacity of the ring network is 10 Gbit/s. An ADM functions with high reliability through the use of a unidirectional path switched ring (UPSR). If a failure occurs, the signal is switched to the other fiber.

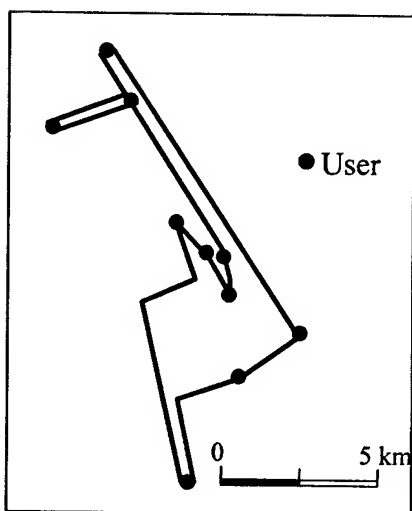
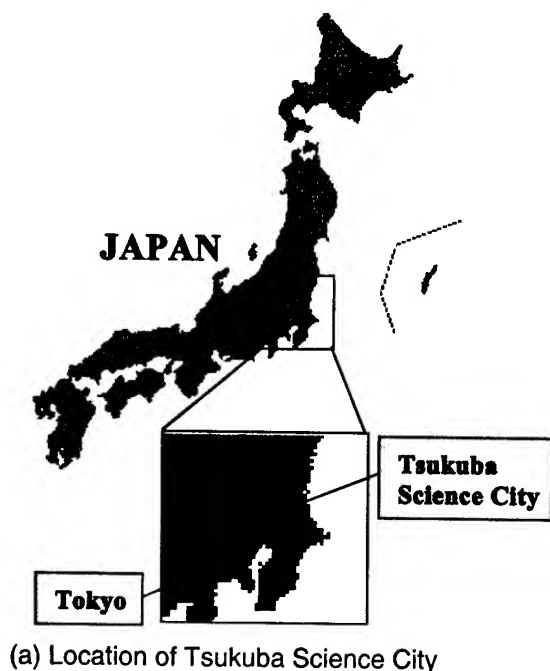


Figure 7. Location and Route of Tsukuba WAN

To meet the second demand, optical add drop multiplexers (OADM) have been employed that operate at 10 Gbit/s per path and realize low latency. An ADM has longer latency than an OADM, because an ADM processes the passing signal electrically in the same way as drop and add signals. The ADM network has two factors which give signals latency; one is optical fiber, the other is electrical processing. The latency is about 200 μ sec when the optical fiber length is 20 km and there are five ADMs between supercomputer research institutes. In contrast, an OADM allows a wavelength to pass without electrical processing at a building where no wavelength is dropped. We selected an OADM that can accommodate a maximum of 56 wavelengths to allow future extension.

In order to use wavelengths effectively, we allocated the 1530 to 1543 nm band to the ADM, and the 1547 to 1610 nm band to the OADM, which are connected with WDM couplers equipped with 2 fibers. The WDM coupler allocates the 1530 to 1543 nm band to the through port, port b, and the 1547 to 1610 nm band to the reflecting port, port c, which has a lower insertion loss than the through port. The optical loss of the OADM wavelength signal that passes through S-user is minimized.

The ultra-high-speed ring network "Tsukuba WAN" with a maximum capacity of 570 Gbit/s was installed with the above configuration, and began operation in April, 2002. It is providing satisfactory levels of performance.

6. Conclusion

We proposed a parallel architecture designed to provide cost-effective ring networks in metropolitan area networks, where the network capacity demand for individual buildings varies greatly. This architecture employs two pieces of transmission equipment connected to two fibers with a WDM coupler. It is advantageous in terms of the effective use of optical fiber and wavelength. To reduce optical loss at user sites, it is advantageous to accommodate an optical coupler in a cabinet installed in the nearest building to WAN. We designed and manufactured a WDM coupler prototype and a cabinet based on this architecture and obtained good levels of performance. We employed this parallel architecture using the WDM coupler for Tsukuba WAN, which has been operating satisfactorily.

7. Acknowledgments

The authors thank N. Sato and H. Takasugi for their encouragement.

8. References

- [1] Ryuichi Watanabe, Akira Hirooka, "Trends in Optical Access Networks and Related Technology", NTT REVIEW, Vol.12, No.2, pp. 65-72 (2000)
- [2] Kiminori Sato, Hidetoshi Takasugi, "Network Architecture Technology for a Highly Versatile and Economical Optical Access Network", NTT REVIEW Vol.12, No.2, pp. 85-89 (2000)

- [3] Takaaki Aihara, Makoto Kawakami, Yoshitaka Enomoto, Takayuki Tashiro, Kiminori Sato, "Ring Network Architecture Using Wavelength Division Multiplexing Coupler for Metropolitan Area Networks", OECC2002, pp. 562-563 (2002)
- [4] "Top 500 supercomputer sites (June 2002)", <http://www.top500.org> (2002)
- [5] Dona L. Crawford, Steven A. Gossage, John H. Naegle, Michael O. Vahle, "100 Gbps or Bust: Building Wide Area High Performance Networks", SC99, Invited Talks (1999)

Author



Takaaki AIHARA

NTT Access Network
Service Systems Laboratories

1-7-1 Hanabatake, Tsukuba,
Ibaraki, 305-0805, JAPAN

Takaaki AIHARA was born in 1971 and received B.E and M.E degrees in engineering from Tokyo Institute of Technology in 1994 and 1996, respectively. He joined NTT in 1996. Since then he has been engaged in optical access network research.

Improving geometric structure of coloring device in the fiber optics cabling process by numerical analysis of flow characteristics of coloring ink

Se myoung Yoon, Young Gyu Yang, June Sun Kim, In Sik Choi

CAE Team, Production Engineering Center, LG Cable Research&Development Center

555, Hoge-dong, Dongan-gu, Anyang-shi, Kyungki-do, Korea

+82-31-450-8250 · smyoon@cable.lg.co.kr

Abstract

In the fiber coloring process, the reduction of the eccentricity between the fiber and the coloring die is important to improve the speed and the quality of colored fiber. The eccentricity is related to the flow field of coloring ink in the die and it is strongly influenced by the geometric structures of the coloring die. A Numerical analysis by which we investigated the coloring ink flow according to the variation of the geometric structures of the coloring die was performed. The relations between the coloring ink flow pattern and the design variables of the die, i.e. the dimension of gap, approach angle, length of land and coloring speed were derived. From the results, a new coloring die which reduces the eccentric input of the fiber was designed and manufactured. Some experiments were performed and they show that the results of numerical analysis are valid. The numerical analysis was performed by FLUENT which is based on finite volume method.

Keywords

Fiber; coloring; eccentricity; self-centering-force; FLUENT

1. Introduction

The optical fiber coloring process is widely used to paint the fiber with several color of ink. In the process, the fiber passes through the tapered coloring die hole filled with coloring ink and experiences ink adhesion to the wall (figure 1). The colored fibers are combined and covered with tube to the optical fiber cable. In case of cable connection, each fiber is distinguished by its own color. The coloring speed and the uniformity of the ink adhesion determine the productivity of the coloring process. The former is related with the quantity of output and the latter is connected with the quality of output. The effective variables of coloring process are the process variables such as coloring speed, fiber tension, inverse tension, and the property variables such as density, viscosity, surface tension of coloring ink, and the flow variables such as pressure distribution of the ink which related geometric structure of coloring die. When we suppose the properties of the cured resin in the coated fiber is equal, the uniformity of ink adhesion is determined by the relative eccentricity between the coloring die and the passed fiber. In the inlet area, the fiber leans to the die wall because of initial vibration, this cause eccentric input of fiber and aggravates uniform adhesion of ink. In the worst case, the fiber is broken off or unstained in some area. Lots of scraps are produced because of inappropriate coloring process. After all, for low scraps and uniform coloring, it is important to reduce the eccentricity between die wall and fiber. By the way, A Self Centering Force

(S.C.F.) of fiber itself can reduce such eccentricity. In general, the wire shaped material which pass through the tapered die whose diameter decreasing toward moving direction experiences the S.C.F by which the material resists the eccentric input. In this article, we tried to clarify the mechanism of S.C.F and to design new coloring die which strengthen the S.C.F for high speed of coloring. We numerically analyse the internal flow pattern of coloring ink in the coloring die and examine the relationship between the S.C.F and the principal variable of the die geometry such as, approach angle, gap between fiber and die wall, land length. Some experiments carried out and compared to the numerical results. This shows a strong coincidence. The numerical analysis is performed by commercial CFD software FLUENT version 6.0.

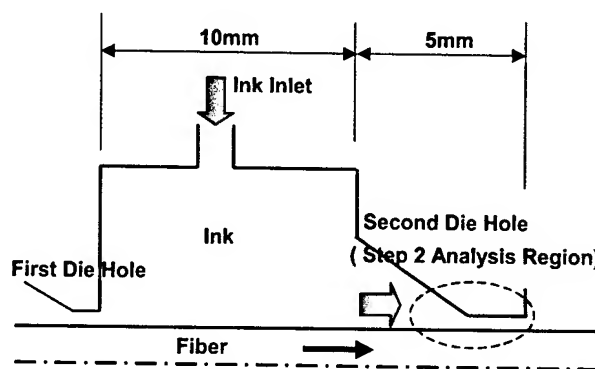


Figure 1. Geometry of Coloring Die
(Step 1 Analysis)

2. Problem Description

Analysis proceeded by 2-step. The step 1 is to analyse the entire flow pattern -pressure distribution and streamline- of the coloring ink as axisymmetric 2-D problem in case of concentric input of fiber to the whole die region. Then the step 2 analysis started to confine the discussion to the second die hole of coloring die and to analyse the effect of eccentricity as 3-D problem in case of eccentric fiber input. The step 2 analysis has also plane symmetric geometry but quantitative comparison of S.C.F for parametric change of variable requires 3-D modeling which is real situation. The entire geometry of the step 1 analysis is shown in figure 1. As we did not consider eccentric input of fiber, an axisymmetric 2-D

shape is drawn and the figure 1 represents the cutting section along with the axis. The coloring die looks like a tapered die with a small die hole attached to a cylindrically shaped body measured 10mm length. In the inlet, coloring ink inflows with the pressure of 1.5bar and the fiber passes through the ink region with constant speed. The internal flow of ink is assumed steady state and in this case the stagnated ink flow in the first die hole forms free surface by the balances of the drag inflow by the fiber speed and the pressure outflow by the die pressure. Thus the net ink flow out of the first die hole is zero. From the result, we regards the free surface of ink near the first die hole as a wall for the convenience of numerical analysis.

The model applied to Step 2 analysis is shown in figure 2. An approach region 400 μ m and a land length 200 μ m is modeled near the second die hole. A fiber enters eccentrically by amount of 'e' from the axis. By making use of symmetry, the tapered cone shaped die region is cut off. And the section is specified by a symmetry boundary condition. For the input pressure of coloring ink can be neglected with respect of the peak pressure in the die, we supposed the pressure of input ink to be atmosphere pressure.

As we only concern the pressure distribution and the flow pattern of coloring ink in case of steady state eccentric input of fiber, we neglect a unexpected variation of the gap between the fiber and the die wall which might be caused by invasion of dust, a sudden lump of the fiber diameter, or something other variations in modeling. In this analysis, we regard the process that the fiber enters into the coloring die with constant eccentricity from the axis as a similar situation of a translational motion of fiber wall with same speed of fiber input. We neglect the change of temperature during the coloring process because of small size of the die and relatively high speed of the fiber.[3]

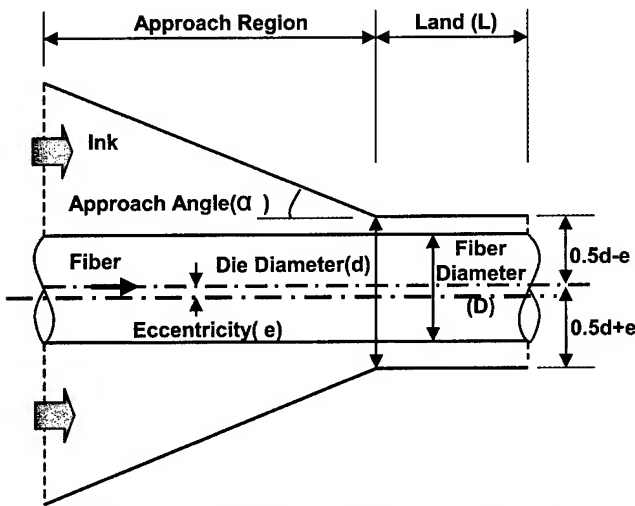


Figure 2. Geometry of Second Die Hole
(Step 2 Analysis)

2.1 Governing Equations

Under the above assumption, the governing equations and the boundary conditions that determine the flow in the coloring die can be presented as the following equations. The governing

equations are the well-known Navier-Stokes equation – a system of simultaneous nonlinear partial differential equations. The continuity equation and the momentum equations are given by (1), (2).

$$\nabla \cdot \vec{V} = 0 \quad (1)$$

$$\rho \frac{D\vec{V}}{Dt} = \rho \vec{g} - \nabla p + \mu \nabla^2 \vec{V} \quad (2)$$

2.2 Boundary Conditions

The boundary conditions are (3)–(6). In the Inlet (3) and outlet (4), the pressures are given. At the fiber wall (5), the fiber speed is given as a moving wall condition and at the die wall (6), no slip condition is given as a wall condition.

$$p(r, \theta, x=0) = p_i \quad \text{--- (ink inlet)} \quad (3)$$

$$p(r, \theta, x=L) = p_o \quad \text{--- (ink outlet)} \quad (4)$$

$$\vec{V}(r=r_{\text{fiber}}, \theta, x) = \vec{U} \quad \text{--- (fiber wall)} \quad (5)$$

$$\vec{V}(r=r_{\text{die}}, \theta, x) = \vec{0} \quad \text{--- (die wall)} \quad (6)$$

2.3 Solution Procedure

The density of ink is 998.2 kg/m³. And we suppose the coloring ink to a Newtonian fluid. So the viscosity of the ink is not changed by the shear rate.[1] Only by the temperature change the viscosity varies. Figure 3 shows that the viscosity of ink exponentially decreases with temperature increases. But the length of die is short enough to neglect temperature change during the passage and we set all the temperature of ink to 30°C.[2]

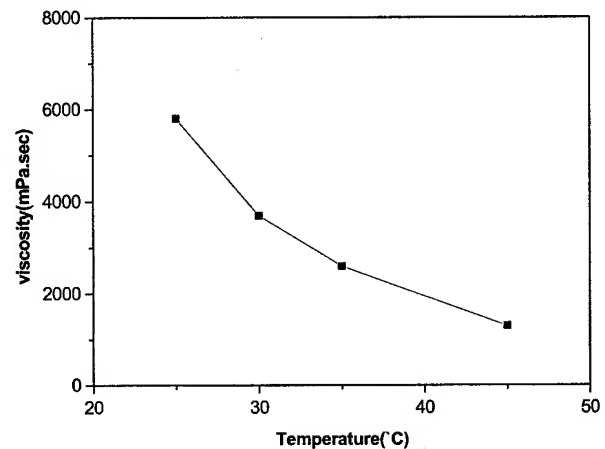
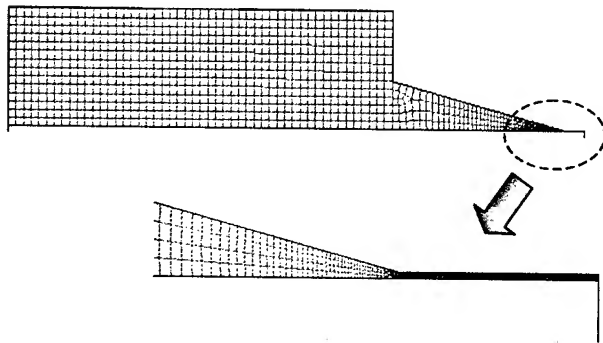


Figure 3. Viscosity Function of
Temperature

Under this condition, the Reynolds Number($Re = \rho VD/\mu$) is about 50 for the gap between the die and the fiber being $10\mu m$. So the entire flow of coloring ink can be regarded as laminar flow. The numerical analysis was performed by commercial CFD software FLUENT of version 6.0.[4]

The computational grid system used for step 1 analysis is (radial \times axial)(14×100) as figure 4. For step 2 analysis (radial \times axial \times azimuthal) ($10 \times 50 \times 100$) grid system is selected to generate 3-D mesh. The discretization is performed by use of 2nd upwind scheme. And the SIMPLE algorithm was used to couple pressure and velocity [5]. The drag coefficient of fiber wall was used for convergence criterion. After 200 iteration the drag coefficient converged for step 1 analysis and we continued to calculate for 600 iteration and the same method was used for step 2 analysis. The calculation time on HP Kayak workstation was around 5 minutes for step 1 analysis and one hour for step 2 analysis.



**Figure 4. Grid Generation
(Step 1 Analysis)**

3. Results and Discussions

The results of analysis proceeded by 2-step. The results for step 1 analysis is the simulation of entire flow pattern - the pressure distribution and streamline - of coloring ink. And the results for step 2 analysis is the simulation of the effect of eccentricity in case of eccentric fiber input to the second die hole of the coloring die.

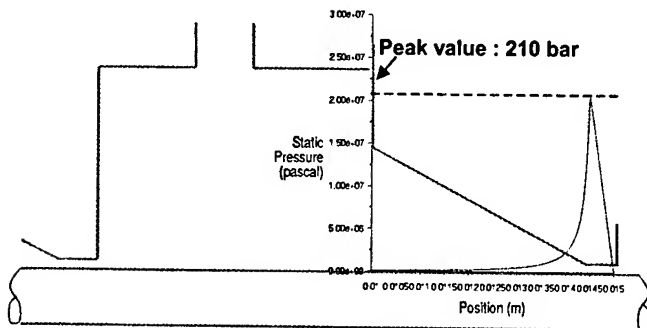


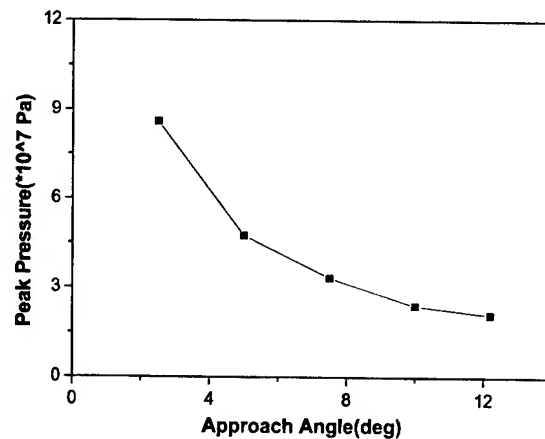
**Figure 5. Pressure Distribution on the
Fiber Wall (Step 1 Analysis)**

3.1 Results of Step 1 Analysis

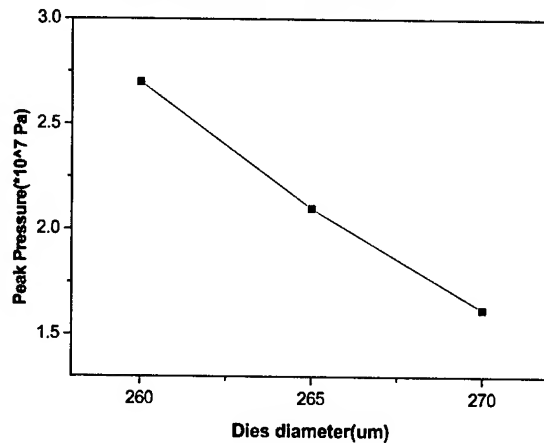
The simulation were carried out for the following condition of table 1. The pressure distribution on the fiber wall was presented by the figure 5.

**Table 1. Conditions for the Step 1 Analysis
and the Step 2 Analysis**

Parametric Variables	Step 1 analysis	Step 2 analysis
Inner diameter of die (d)	265 (μm)	265 (μm)
Fiber diameter (D)	245 (μm)	245 (μm)
Land length (L)	500 (μm)	200 (μm)
Approach angle (α)	12 (deg)	12 (deg)
Length eccentricity (e)	0 (μm)	5 (μm)
Coloring speed (v)	300 (mpm)	300 (mpm)



(a) Approach angle (α)



(b) Die Diameter (d)

**Figure 6. Peak Pressure vs Approach Angle
and Die Diameter (Step 1 Analysis)**

Except the approach region, the pressure of ink keeps constant 0 Pa(gauge pressure). The ink pressure of tapered approach region rapidly increases toward the moving direction for the reason that the passing fiber attaches the ink on the fiber wall.

As we go further down, the peak pressure(210bar) attained at the end point of the tapered die. Compared with peak pressure, the input pressure is assumed to be negligible. So we have carried out step 2 analysis for the condition that the input pressure is atmosphere pressure. The peak pressure linearly decreases along the land of the die to the atmosphere pressure. From all the result, the peak pressure is linearly proportional to the viscosity of the ink and have no relation to land length of the coloring die. As the approach angle increases the peak pressure decreases as is shown in Figure 6(a). This can be understood that the surface drag force of moving fiber is the net driving force that goes up the pressure of the tapered die, i.e., for the same length of tapered region, the smaller approach angle is the larger the drag force is per unit mass of fluid. As the diameter of coloring die increases the peak pressure exponentially decreases as shown in Figure 6(b).

It is evident that the gap between the die and the fiber increases as the diameter of die goes up for the same fiber diameter. So the peak pressure exponentially decreases as the diameter of the die increases.

3.2 Results of Step 2 Analysis

The Simulation was carried out for the condition of table 1. The pressure distribution of the land of die and the tapered region is given in the Figure 7. As shown in the figure 7, the pressure distributes symmetrically to the y-axis and high pressure is simulated at the bottle neck region. especially at upper bottle neck region is presented the maximum pressure (420 bar). The S.C.F. can be obtained by means of integrating the pressure on the fiber wall over the entire fiber surface. In this case we computed S.C.F. for the region of 600 μ m length from the end of die.

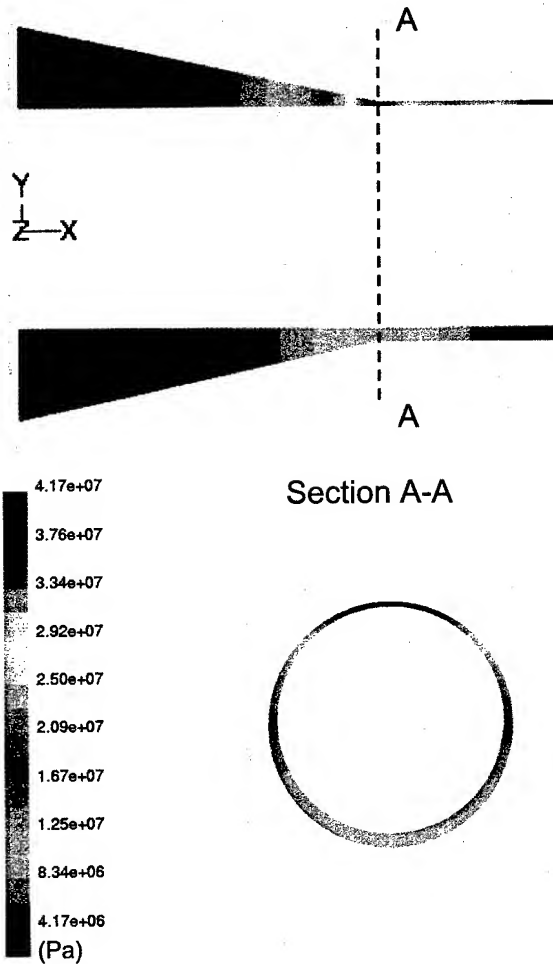
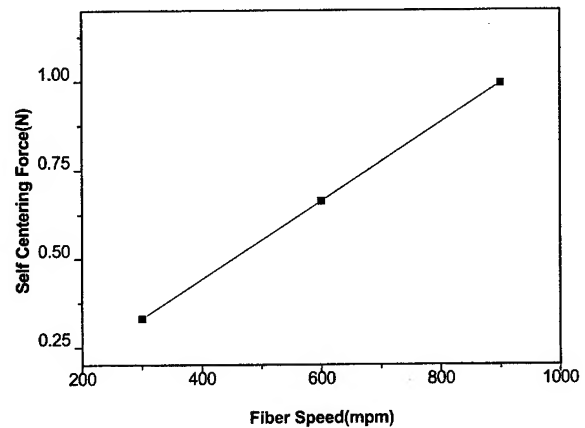
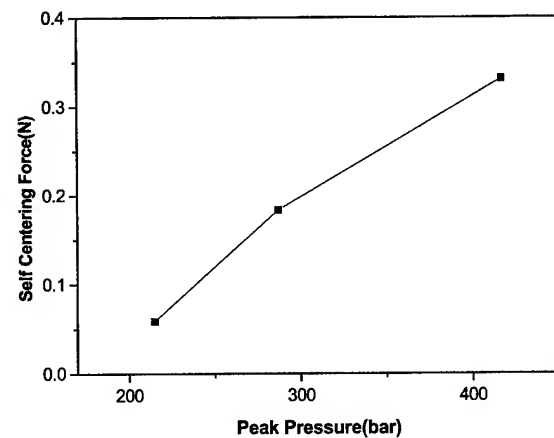


Figure 7. Pressure Distribution in the Second Die Hole (Step 2 Analysis)



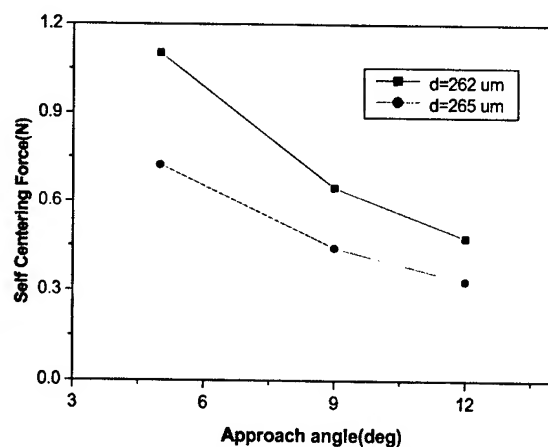
(a) Fiber Speed (v)



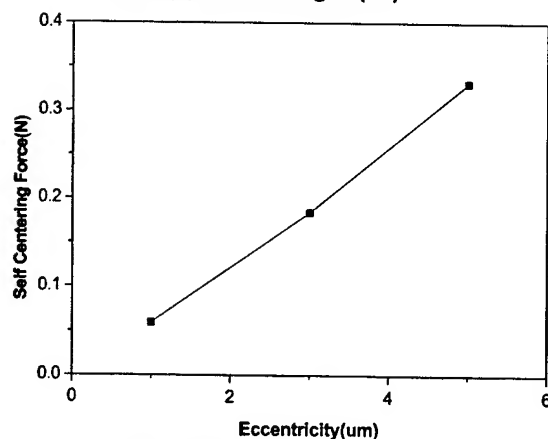
(b) Peak Pressure (bar)

Figure 8. Self Centering Force vs Fiber Speed and Peak Pressure (Step 2 Analysis)

The result shows that the S.C.F. acts against the fiber eccentricity and the magnitude of S.C.F. is 18 times as large as that of the drag force of the moving fiber. The accurate value of S.C.F. is 0.3313(N) toward $-y$ axis (the direction against eccentricity) and that of the drag force is 0.0182(N) toward $-x$ axis (the direction against fiber input). Figure 8 shows that The S.C.F. linearly increases with coloring speed. We see that The S.C.F. grows with the pressure in the region between coloring die and fiber. As it is evident from Figure 9, the S.C.F. exponentially increases by both decreasing the gap and increasing the approach angle. The S.C.F. is regulated by the mechanism of which The more eccentricity is, the bigger S.C.F. is. So the fiber becomes stable toward the concentric axis. Supposed that the eccentricity of input fiber is constant, the reduction of gap between fiber and die may cause the fiber being exposed to weakness of the dust input and sudden lump of fiber diameter. This is the reason why we are interested in the approach angle - the effective design variable.



(a) Approach angle (α)



(b) Eccentricity (e)

Figure 9. Self Centering Force vs Approach Angle and Eccentricity (Step 2 Analysis)

Table 2 gives the S.C.F. value to various kind of gap and approach angle. if we select the approach angle 5(deg), the S.C.F. value of the changed design grows up twice bigger than that of current design - approach angle 12(deg). We manufactured the draft design of type I, type II to coloring die and tested it in real plant situation. We found that the unstain area scrape of the design type II is twice as lower as that of the current type.

4. Conclusions

The flow characteristic of coloring ink in the coloring die is numerical analyzed by using FLUENT. From the results, we found that the pressure of ink in the coloring die is proportional to the coloring speed, the eccentricity and inversely proportional to the approach angle. The peak pressure of ink decreases as the gap between fiber and die increases and irrelevant of the land length. The S.C.F. exponentially increases with the gap, the eccentricity and exponentially decreases with the approach angle. From the result, a revised coloring die is manufactured. The concept of new design is to decrease the approach angle with the same the gap. Several test shows the scrape by unstained area to the revised die is twice as lower as that of the current die. and we found that the the eccentricity also can be controlled by raising the coloring speed.

Table 2. Compared Results between the S.C.F. of the Numerical Analysis and the Experimental Outputs

Design Type	Gap: (d-D)/2	Approach angle:(α)	S. C. F	Frequency of Unstained Fiber
Current type	10 (μ m)	12 (deg)	0.3313 (N)	3 ~ 4 (/day)
Type I	10 (μ m)	9 (deg)	0.4473 (N)	3 ~ 4 (/day)
Type II	10 (μ m)	5 (deg)	0.7222 (N)	1 ~ 2 (/day)
Type III	8.5(μ m)	5 (deg)	1.1032 (N)	Not Tested

5. References

- [1] Frank M. White, *Viscous fluid flow*, 2nd ed., McGraw-Hill, (1991).
- [2] W. M. Kays and M. E. Crawford, *Convective heat and Mass Transfer*, 3rd ed., Mc Graw-Hill, (1993).
- [3] Frank P. Incropera and David P. Dewitt, *Fundamentals of heat and mass transfer*, 4th ed., John Wiley & Sons Inc., (1996).
- [4] *FLUENT manual Volume 3,4*, Fluent Inc, (2002).
- [5] Klaus A. Hoffmann, *Computational fluid dynamics for engineers I, II*, Engineering Edu. Sys., (1993).



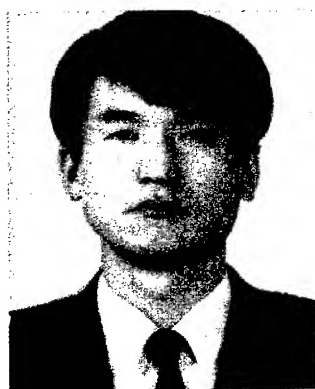
Se myoung Yoon

LG Cable Research&Development Center
Production Engineering Center
CAE Team
Associate Research Engineer



June Sun Kim

LG Cable Research&Development Center
Production Engineering Center
CAE Team
Senior Research Engineer



Young Gyu Yang

LG Cable Research&Development Center
Production Engineering Center
Equipment Research Team
Principal Research Engineer



In Sik Choi

LG Cable Research&Development Center
Production Engineering Center
Vice President

Forecasting Optical Network's Components Cost: A Simple Methodology

Edoardo Cottino, Roberto Leone, Giacomo Monari

Networks Technologies Dept., Sirti S.p.A.

Milan, Italy

+39-0295885144 · E.Cottino@Sirti.it, Ro.Leone@Sirti.it, G.Monari@Sirti.it

Abstract

When planning optical networks, complementary to an accurate cost model, there is also the need referring to reliable trends/curves showing optical equipment production costs evolution, versus their technological maturity. The resulting curves could be useful, for instance, in evaluating the right timing to begin the deployment of a planned network, or in estimating the total cost of the initial investment. The adopted prediction model is based on the combination of an extended *learning curve* model and a logistic *growth curve* model.

Cost curves were traced for some meaningful optical network components. The prediction procedures and computations are discussed taking into account the current photonics manufacturing environment. The conclusion is that only an improvement of the same factors (standardization, outsourcing and automation) characterizing the computer industry could really speed up a photonics products cost decrease.

Keywords

Optical components; cost evolution; learning curves.

1. The current photonics manufacturers scenario

Although the photonics sector is destined to become a major force in the world economy, and the market demand for photonics component and systems is potentially massive, it is our view that the current manufacturing approaches are too inefficient. It is true that optical communications components and systems markets experienced a phenomenal growth in the last few years, but this growth was mostly driven by the need of carriers to rapidly expand and upgrade their infrastructure to meet an explosive growth in bandwidth demand. We think that in these years photonics companies paid more attention to their capacity expansion rather than to processes optimization. This phase has been characterized by rapid building of manufacturing plants, widespread hiring of low-cost manufacturing personnel, and purchasing of basic, non-integrated tools. Process engineering innovations, automation, and standardization were largely absent from this type of expansion, since all of these factors have to take lower priority than "time to capacity". Time to capacity is such an essential competitive factor in the supply-constrained industry setting, that we believe it may cause manufacturers to side-step industrial engineering issues.

An analysis of the current photonics manufacturing industry can explain why some optimistic predictions about costs trends have been more times corrected. By means of a comparison with the silicon semiconductors industry we can derive some useful insights [1]:

- First of all we must observe that the photonics devices fabrication sector is severely fragmented: a multitude of technologies and competencies is involved. For example the know-how of an optical switch supplier must comprehend: semiconductors (encompassing both Si and III-V semiconductors), thin-film technology, wave-guide propagation, polarization, micro-optics, Micro-Electro-Mechanical systems (MEMS). Assembling modules and testing processes form the "back end".
- Another negative and common characteristic is the reluctance of photonics companies in outsourcing manufacturing technologies, with a consequent lack of scalability in the current manufacturing processes. To outsource processes means gradually to migrate toward higher value-added activities, to reach deeper, more proprietary technologies, to do innovative component design; to perform a proper module and system-level engineering.
- The automation level of the current manufacturing processes is still very far from the desired one. Despite the high-technology nature of the products, manufacturing of optical components is most often compared to "shoe making", in terms of labor intensity, lack of automation, and lack of process optimization¹. Assembling modules and final fiber attachment (also called "pig tailing") and testing are also notorious for their high manual labor intensities.
- Moreover standardization is not enough defined throughout the supply chain, except for SDH equipment that follows strict recommendations. For example, the form-factors of thin-film dies vary among different vendors. This is widely recognized as one of the main inhibitors of manufacturing scalability throughout the supply chain, pertaining not only to the components, but also to the modules and systems.

All these factors yield as a consequence that industrial photonics manufacturing processes are not well engineered and optimized. We can list here the effects of the above-mentioned factors:

1. Inefficiencies in the manufacturing processes: low productivity due to high production costs.
2. Inhibition of the growth of industrial infrastructures and development of an organic supply chain.
3. Retards in the harmonic maturation of the sector.

However we may say that things are gradually changing. We believe that the industry is transitioning from a supply-constrained

¹ This is why many customers are obliged to re-test products before installation or to use them under the guaranteed performance (as it often happens with WDM multiplexers).

situation to having a more balanced demand and supply situation². The photonics industry is now entering a harmonic demand-driven growth phase that will see the development of a mature supply chain. Industrial processes will be organized and optimized. A lot of benefits will come into the photonics business model, including:

- Rapid cost reduction, hence rapidly declining average selling prices;
- Improved manufacturing efficiency and scalability;
- Reduced labor intensity combined with increased capital intensity.

2. Generalities about cost predictions

In the past a realistic prediction of network equipment cost trends could be based on a limited but substantial body of "solid" information and statistical data referring to previous years. Today factors affecting evolutions and insufficient historical data make doing reasonable predictions to be extremely more difficult.

2.1 Features making predictions to be difficult

The present situation in the telecommunication environment is characterized by the presence of a number of evolutionary factors that currently contribute to make future introduction scenarios less "controllable", and thus less "predictable" than in the past. These factors are:

- Widespread liberalization and deregulation: the evolution from a "natural monopoly" "full competition" is a really common situation in many countries.
- Technical innovation: the optical components evolution is really dynamic, new technologies change the overall scenario in few years.
- Introduction of new broadband services

These factors affect all the optical communication market sectors and in particular the manufactory production costs.

2.1.1 Uncertainties lie also in time. Many prediction uncertainties lie in answering not only the "how much at that time?" question, but also the "when available at that cost?" matter. Indeed, components' cost actual decrease is often "smoother" when compared with the expected one (see Figure 1). Many grounds could be the cause of this: for instance, due to the recent net-economy uncertainties and financial weaknesses, many incoming network operators are relenting their investments towards all-optical networks. Moreover, despite of promises, due to some unexpected technological difficulties, the development of all-optical functionality and management capabilities, for WDM systems, seems to be late if referred to expectations. As a further consequence, components suppliers hesitate to improve their production processes and automation because they could be very expensive and wasteful if not properly targeted. All of this implies a slower unitary cost decrease.

² This modification could be considered as one of the "positive" effects of recent downturn in the economy

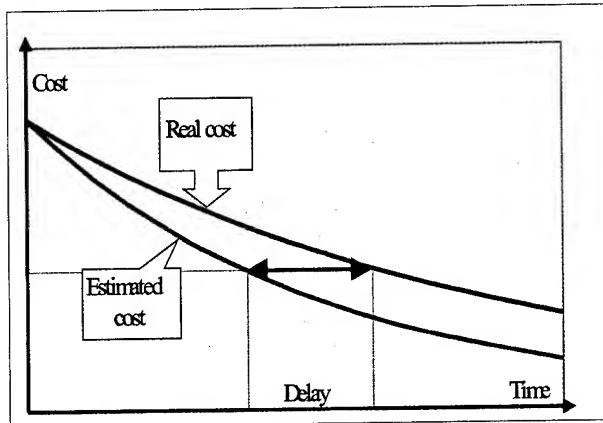


Figure 1. A delay of investments in technology, automation and production process could retard the component cost decrement.

2.1.2 Features facilitating predictions. Despite of the uncertainties factors described in the previous paragraphs, some other features could determine a certain cost decrease:

- Standardization
 - Components can be interchangeable with an equivalent one.
 - Modularity allows creating a multi-vendor network, by assembling components of different manufacturers (and choosing the most advantageous ones).
 - Severe requirements preventing failures permit to concentrate many devices into a unique equipment without loss in reliance.
 - "Ad hoc" studies for new networks aren't needed any more.
 - Competition between manufacturers increases.
- Large scale economies
 - Automated manufacturing processes allow a cost decrease and, overall, a more reliable product (e.g. the importance of the mechanical alignment in the optical switch is crucial).
 - Larger volume production justifies the implementation of new and specialized simulation, planning and CAD tools to improve components engineering.
- Learning curves
 - The accumulated experience leads to a year-by-year cost save for manufacturers.
- Monolithic approach
 - Several devices are integrated into a single component, thus saving space and redundant devices (like power suppliers or connectors).
- Component maturity
 - Even if the cost of a prototype is particularly more expensive of a consolidated one, we can expect that its cost will reduce faster in percent because the associated

technology is being introduced first and it isn't still inserted in a productive process (that determines the major cost reduction).

3. Approach adopted to perform predictions

3.1 Predictive model choice criteria

One possibility could be to forecast production costs directly by using a time series representing the production cost trend in the last period (usually one year) and then extrapolating it in the future. Other possibilities could also be to use different types of forecasting models, still based on data available, like:

- Simple or multiple regression models
- Smoothing models like Holt or Holt-Winters models
- ARIMA models
- Transfer models
- Kalman filter models
- Growth curve models

However these models could be properly used only when sufficient historical costs are available. We then adopted an alternative method that is based on a combination of an extended learning curve model and a growth curve model. The advantage of this choice³ is essentially the possibility of using it when only a few observations (see the following paragraph) are available and even if historical costs are partially or totally absent. For this reason, the method is particularly suitable for innovative components, or components not having a long production history, like those considered in this work.

The required considerations concern the maturity level of the component, the time it will remain on the market, the dependence between the annual cost decrease and the cumulated production experience. All these arguments are strictly correlated with standardization, scale economies, learning curves and technology maturity, all features we have previously seen.

The described advantage could be a limitation in the case we only dispose of historical costs. We removed this possible drawback by implementing a program that allows utilizing the model extrapolating the information needed from historical costs (see paragraph 3.3.3).

3.2 The costs forecasting formula

The function used to evaluate future costs is firstly based on Wright theory: "Each time the cumulated units production doubles, the unit cost decreases of a constant percentage" (Wright, Boston Consulting Group). It means that the unit costs decrease as an inverse function of the incremented productive experience.

That observation was then traduced into a time dependent function⁴:

³ The combination of these models was used to determine cost trends contained in the Project TITAN tool database. The model is also used by several other techno-economical network studies (Cobnet, Astra, Optimum and others).

⁴ The theory and the math behind that equation are explained in the Appendix of [17].

Predicted cost at time $t =$

$$f(t) = f(0) [n(0)^{-1} (1 + \exp[\ln(1/n(0)) - 2t \ln 9 / \Delta t])^{-1}]^{\log_2 K} \quad (1)$$

To use correctly the method, an appropriate knowledge of the coefficients' meaning is needed. Indeed the choice of their values determines the prediction.

- $n(0)$ = the relative proportion of produced components at time 0. It roughly synthesizes the maturity of the component at time 0, in fact a low value indicates that we are at the beginning of its production and, consequently, of its technology and standardization.
- Δt = the time it takes for the growth curve to go from 10% to 90% of the cumulated volume. A long time expresses that there aren't competitive alternatives to the component, but also that its technology evolution is slow enough to obstruct the advent of new components. A short time indicates a component that will be replaced early or that its high demand determines its strong commercialization at the beginning of the production with a fast market saturation.
- K = the learning curve coefficient (relative decrease in the cost by the double production). It is related to the production experience increase. It is indirectly influenced by the standardization because clear recommendations permit large-scale approaches and a more automated production.
- $f(0)$ = the initial component cost.

To clarify which is the real meaning of Δt , $n(0)$, the following graphical representation could be useful (see Figure 2, Source [2]).

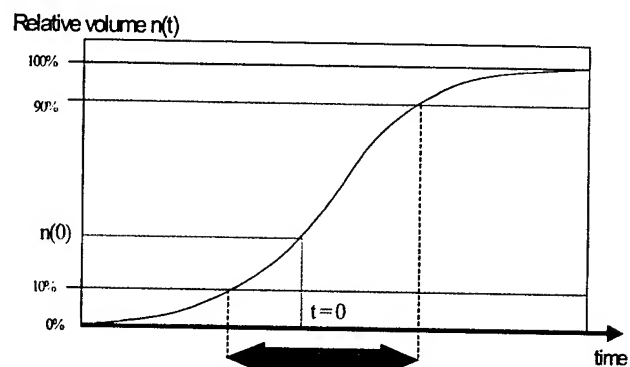


Figure 2. Δt , $n(0)$ graphical interpretation (Source [2])

3.3 How to determine the coefficients

3.3.1 Information sources. Where to look for the information used to evaluate the function's coefficients? Typical sources could be a lot of Internet sites concerning techno-economics of optical networks; some sites are reliable, others almost unknown, some with recent information, others with past, some provide predictions, others historical data. We can find this information under different formats, being either numbers or qualitative considerations: data mining, online surveys, web analysis, market researches. Further information could be gathered from company's databases and from optical networks specialized magazines.

3.3.2 Definition of the coefficients. The first step is to get a rich availability of information, either quantitative or just qualitative. Once this base has been built, mean / pondered values could be determined for the coefficients. We can generally say that market experts opinions are the main references to define Δt , $n(0)$, while vendors information is often used to determine K and $f(0)$.

3.3.3 Additional availability of historical data. As we explained in paragraph 3.1 the model we adopted can work without historical data, nonetheless more accurate results could be obtained by a coefficients definition that takes into account also historical information. In order to exploit a historical data availability, we implemented a program (in Visual Java language, it runs on Windows operation systems) that gets the coefficients starting from the component historical costs. A brief explanation of how the program works follows:

When the user inserts the past costs values with their referring year, the program calculates many predictions using equation (1). For all the previsions, the initial value $f(0)$ of (1) is the oldest value provided by the user. The program returns the coefficients of the equation that performs the best forecast of the other inserted costs. The result can be useful to evaluate unreliable coefficients or to be directly used in (1) to extend the forecast for future years.⁵

A following upgrade of the program allows to fix some coefficients, that we suppose right, to find the others in function of them and of the historical costs.

3.4 Costs trend calculation

To perform the computation of the cost trends and to plot them out, we implemented a simple MS Excel program, requiring the predictive formula coefficients and the initial cost as input. It calculates the (1) year by year, thus drawing the component cost curve for the next 10 years as output.

By changing one (or more than one) coefficient value at a time, the program allows the user to observe how this affects the cost forecast.

Such different cost forecasts can be simultaneously estimated and represented, thus allowing a comfortable comparison of several cost curves on the same graphic.

4. Forecasted equipment cost curves

4.1 Assumptions

We made the following assumptions:

- We considered production costs, not market pricing, because selling prices are generally personalized taking into account the importance of the customer and the volume of unit bought. Moreover sector growth or recession drastically influences them. Pure production costs are more appropriate for long period predictions.

⁵ It is worth noting that the calculated value of $n(0)$ refers to the year of the less recent cost inserted, assumed as initial value. The equation to be used to find the $n(t)$ (value of relative volume produced at time t) is: $n(t) = 1/(1 + \exp(\ln(n(0))^{-1} - 1) + 2(t/\Delta t) \ln 9)$. Differently the other coefficients, K and Δt , are time independent.

- To simplify the coefficient calculation, we catalog the several devices in different components families that use the same technology, so we can extend the coefficients value (except the initial cost $f(0)$) of the component to all the other components that belong to its family. For example if we characterize the coefficients for the SDH STM16 port, we can generalize assuming that the coefficients of all other SDH ports will inherit the same values.
- The lack of historical data for prototypal components forced us to make several hypotheses to determine their lifetime, cost, maturity. The hypotheses concern mainly the technology used, the possible component upgrades, the estimated volume for the next years and the trends of similar components.

4.2 Coefficients definition

Due to the fact that it was not possible to us⁶ to find out neither a large availability of information (see paragraph 3.3), nor additional historical costs (see paragraph 3.3.3), we couldn't perform any proper elaboration in order to derive likely coefficients. Then, we had to refer to already defined coefficients coming from some authoritative market research houses. Relying on these sources we tried to draw the prediction for some representative components.

4.3 SDH STM16 Card

For SDH cards we found the values reported in Table 1. Data are derived from [3] except the initial cost that is derived from [4], the value is expressed in KEuro units.

Table 1. SDH STM16 Card coefficients

Component	initial value	k	n(0)	deltaT
SDH STM16	35	0.14	1	1

Inserting the coefficients in the excel sheet that computes (1), the following forecast is obtained (see Figure 3).

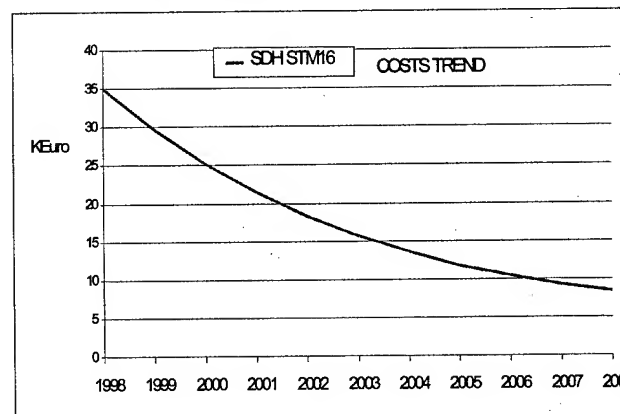


Figure 3: SDH STM16 card cost trend

The average cost decrement is about 14% per year. The component recommendations are clear and the technology is well known, but the SDH components prices are too high. Maybe the

⁶ but in the case reported in next paragraph 4.4

advent of 10-Gigabit Ethernet equipment as potential substitute could lead to a more marked cost decrement [5].

4.4 Gigabit Ethernet backbone switch port

For this opto-electronic device we calculated the model coefficients, listed in Table 2, applying the program explained in the paragraph 3.3.3. The cost values inserted to run the program derive from [6] as the initial value, the unit used is KEuro.

Table 2. 1GigabitEthernet port coefficients

Component	Initial cost	k	n(0)	deltaT
GbitEth port	2.5	0.72	2.00	9

Inserting the coefficients in the excel sheet and running (1), the following forecast is obtained (see Figure 4. Gigabit Ethernet port cost trend).

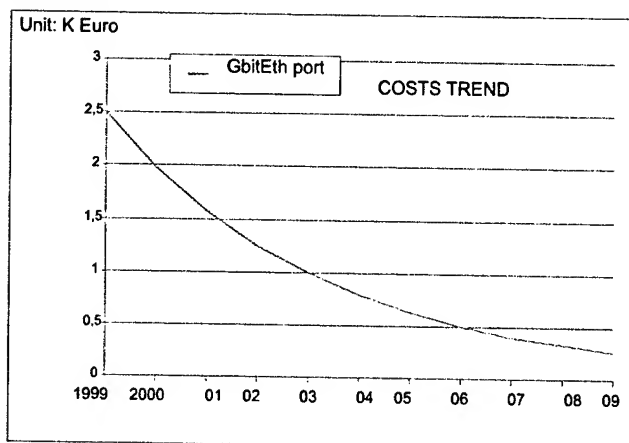


Figure 4. Gigabit Ethernet port cost trend

Gigabit Ethernet shifts Ethernet from a LAN-only technology to a LAN, MAN, and WAN technology. When 10-Gigabit Ethernet will be available and cost effective, DWDM will leverage 10-Gigabit Ethernet in optical networks as a more efficient and less expensive technology than SDH/SONET [7]. The annual cost decrease (about 20%) could be mainly induced by a concrete standardization and a competitive industrial segment where generally the leading actors are electronic manufacturers.

4.5 EDFA Optical Amplifier

For optical amplifier we found the values reported in Table 3. Data are derived from [3] and [2] except the initial cost that is the same one proposed by [8], in which the values are normalized by the cost of one kilometer of deployed fiber under standard conditions

Table 3: Optical Amplifier coefficients

Component	Initial value	k	n(0)	deltaT
40ch Amplifier	100	0.72	2.00	9

Inserting the coefficients in the excel sheet and running (1), the following forecast is obtained (see Figure 5).

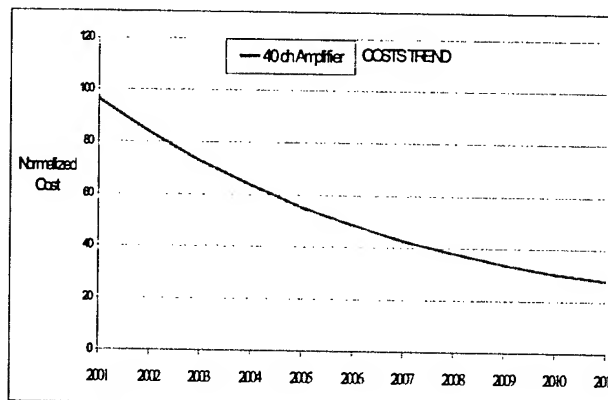


Figure 5. Optical Amplifier cost trend

The annual cost decrement is about 13% for the first years, then it slowly changes to 10%. The EDFA amplifiers are useful devices, but they operate on a bandwidth that today appears too limited (4 Thz) and their cost is still considerable. New Raman amplifiers are the most promising alternative; they have a flat gain over 200nm (about 20Thz). Consequently a more marked decrement (not foreseen by the curve above) could happen when Raman amplifiers will be widely commercialized. We are trying to improve the cost curve in this direction. (For further details see [9] and [10]).

4.6 WDM (De)Multiplexer

For WDM we found the values reported in Table 4. Data are derived from [2] except the initial cost that is the same one proposed by [8], in which the values are normalized by the cost of one kilometer of deployed fiber under standard conditions.

Table 4. WDM Coefficients

Component	Initial cost	k	n(0)	deltaT
WDM40ch	50	0.72	2.00	9

Inserting the coefficients in the excel sheet and running (1), the following forecast is obtained (see Figure 6)

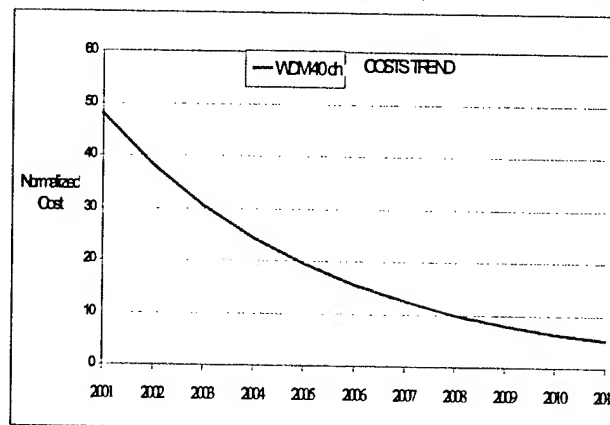


Figure 6. WDM cost trend

The annual cost decrease is about 20%. The cost save is mainly caused by the lithography process improvement used to produce the AWG (Arrayed Wave-guide Grating) that is the core element of WDM Mux/Demux (for further details see [11], [12]). Another cause could be the advent of new competitive products that allow the transmission of signals using closer wavelengths (the number of channels used by the multiplexers doubles each 10 months).

4.7 Optical Switch Connection Matrix

For OSM we found the values reported in Table 5. Coefficients are derived from [2] except the initial costs that we estimated for the year the component will be commercially available basing our analysis on the cost values proposed by [8]; the values are normalized by the cost of one kilometer of deployed fiber under standard conditions.

Table 5. Optical switch connection matrices coefficients

Component	Initial cost	k	n(0)	deltaT
Switch 1024x1024	209	0,75	0,001	10
Switch 256x256	261	0,75	0,001	10

We calculated when new space switches will be available by the following consideration: the MEMS switch capacity doubles roughly each 12 months, its max switching speed each 6 months (see Figure 7). The major obstacle to the capacity increment is the insertion loss, an imprecise misalignment could cause the waste of many dB of optical power. The wavelengths that pass through the matrix could be subject to different attenuation values. (Source: i.e.e.e. Communications).

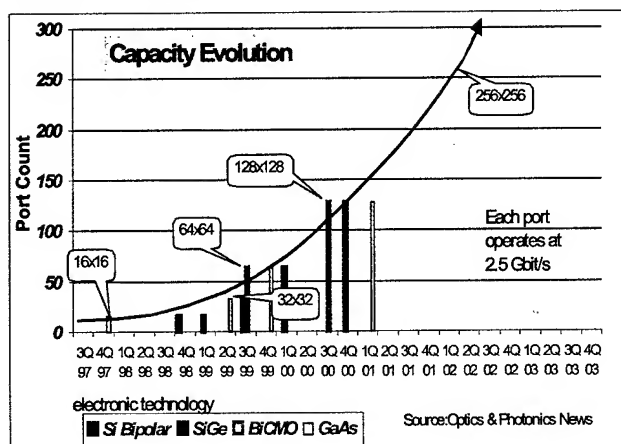


Figure 7. Optical switch matrix performance trend

The switches costs prediction is depicted in Figure 8. The values are calculated inserting the coefficients of Table 5 in the excel program. The initial costs are the same proposed by [8].

The predicted cost decrement is about 16% per year. The switch matrices are a representative example of optical devices, indeed their performance expectation is very high because they will be the core of optical cross connect, but, today, their price is too high and the capacity too low. The technologies used to produce them are essentially two: the arrayed waveguide grating (AWG) and the

MEMS technologies [13]. Even if the last one seems to prevail, this indecision determines a delay of performances and of investments in the automation of the productive processes.

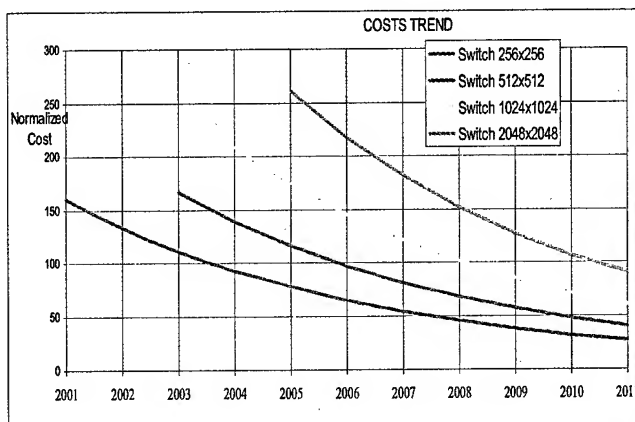


Figure 8. Optical switch cost trend

4.8 OXC

The Optical Cross Connect we consider is based on the block model, shown in [8], we reproduced it in Figure 9.

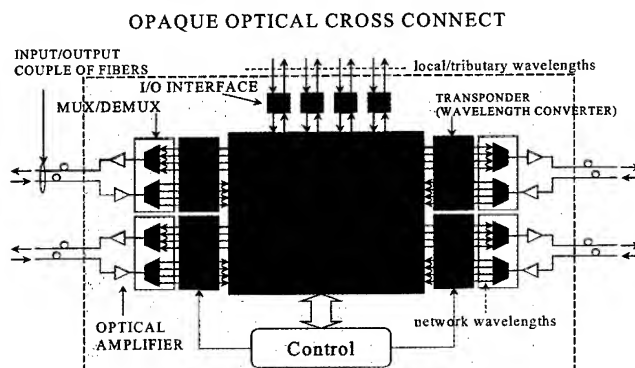


Figure 9. A simplified block model for a generic optical cross connects

A possible OXC could contain the devices listed in Table 6:

Table 6. Devices included in a possible OXC configuration

Switch matrix 256x256	1
Control plane & management	1
Mux/Demux 40 ch	6
Wavelength converters 40 ch	6
Optical Amplifier 40 ch	12
I/O Interface	16
I/O Couple of Fibers	6

Then the initial cost is:

$$C_{OXC-256 \times 256} = 6 (2 C_{OA} + C_{MUX/DMUX} + C_{WC}) + 16 C_{ITF} + C_{SM} + C_{PCM}$$

$$C_{OXC-256 \times 256} = (96 \times 12) + (48 \times 6) + (284 \times 6) + (57 \times 16) + (1500 \times 1) + (100 \times 1) = 5656$$

Values are relative to one kilometer of deployed fiber under standard conditions.

The forecasted cost curve for the OXC, obtained inserting the component coefficient in the excel program, is shown in Figure 10. The relative coefficients are derived from many sources ([3], [2], [4], i.e.e. Communications, Optical Network Magazine). The initial devices costs are the same ones proposed by [8] the values are normalized by the cost of one kilometer of deployed fiber under standard conditions.

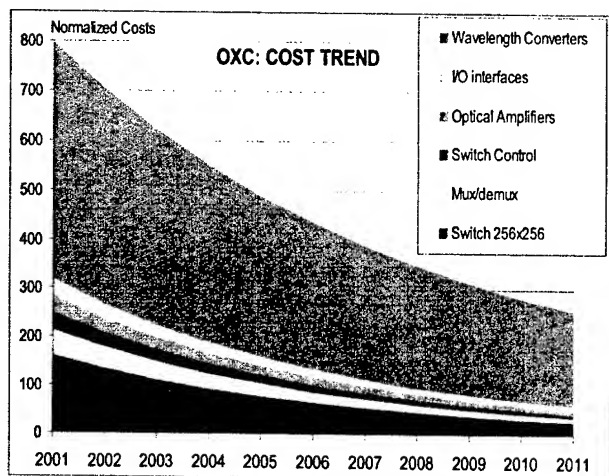


Figure 10. OXC cost trend

The OXC average cost decrement is about 13% per year, but some considerations are necessary:

The wavelength converters today available, that influence heavily the overall cost, shouldn't considerably reduce their cost quickly in the next few years. However new all optical wavelength converters, based on Mach-Zehnder principle, are really promising and they should be available in two or three years. They will consent to improve the current opaque OXC to a completely transparent one (independent to the bit-rate speed and to the kind of modulation). Today it is really difficult to predict their cost. (For further details see [14]).

The switch matrix will become less critic in future from a cost point of view.

The 40 channels amplifier cost will decrease slowly (but maybe it will be replaced by a more cost-effective Raman amplifier in the next three years scenario).

We are working on the prediction of the DXC future cost to compare it with the OXC.

5. Comparison with some other forecasts

A comparison of our results with some other predictions could be useful. In this section we illustrate and comment three components costs previsions found on the Internet.

After a first look at the forecasts the analogy with our predictions will appear to be remarkable, even if a more rigorous control of

the cost curves reveals little discrepancies. This similarity contributes to validate our results and, above all, it comforts us about the correctness of the methodology adopted to reach them.

5.1 General prices reduction (Source: RHK).

The Compound Semiconductor magazine shows the results of a RHK (Ryan Hankin Kent Inc, Telecommunications Industry Analysis) research about economics of photonic manufacturing: the products price reduction is about 25% per year.

Even if this prediction concerns component prices and not costs, we can compare its trend with the cost curves shown before. We predict a cost reduction of 20% per year also for WDM Mux/Demux, that is one of the most promising components from a cost point of view. This forecast is a bit more optimistic than ours. Anyway, in order to perform a more accurate comparison we should know the hypotheses used to obtain that value.

5.2 Price Evolution of the AWG (Source: [15])

A more precise forecast is presented in [15]. It predicts the price evolution of the AWG (it belongs to the WDM family) until 2003; we can confront the trend and not the absolute values. In Figure 11 we compare the price curve presented in that document with the one we derived inserting the WDM coefficients of Table 4, except the initial value that is the real price (not estimated) of the year 1999. All the values following the year 1999 are previsions. The curves are really close, only in the year 2003 we can see a divergence of 10% of the price that indicates our prediction as the more optimistic.

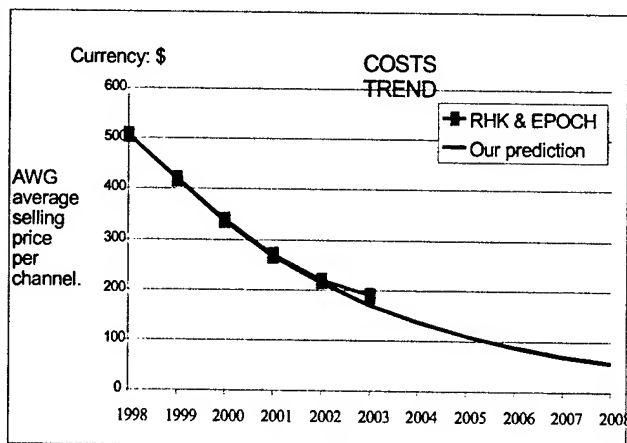


Figure 11. Comparison of AWG cost predictions

5.3 Comparison between SDH and Gigabit-Ethernet Cost Evolutions (Source: [16]).

10-Gigabit Ethernet Alliance presents a third forecast, it compares trends of SDH and Ethernet for the next 3 years (source: [16]). We reproduce it in Figure 12.

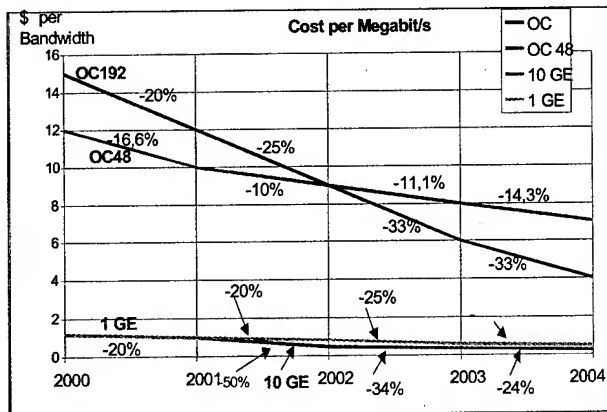


Figure 12. Ethernet – SONET interfaces comparison

Figure 12 underlines the huge difference of the bandwidth / cost ratio between SDH and Ethernet equipment. Here we try to qualitatively compare those forecast with ours. To draw our predictive curves we inserted in the excel program the same coefficients of paragraphs 4.3 and 4.4, except the initial values that are the same of GEA.

The trend of the OC 48 (equivalent to STM 16) is compatible with our forecast (see paragraph 4.3 and Figure 3), its decrease fluctuates from -10% to -16% per year. Instead we think the prediction concerning OC-192 device (equivalent to STM 64) is to far optimistic, even if we admit it is a less mature component and its cost curve will be steeper then the OC 48 curve (but it should not reach a -33% per year as the Figure 12 predicts from year 2002 to 2004).

For the 1Gigabit Ethernet interface the trend is almost the same of our prevision (see paragraph 4.4 and Figure 14), while, differently from what Figure 12 indicates, we suppose the 10GE will be commercially available only in 2002 and its decrease cost less effective.

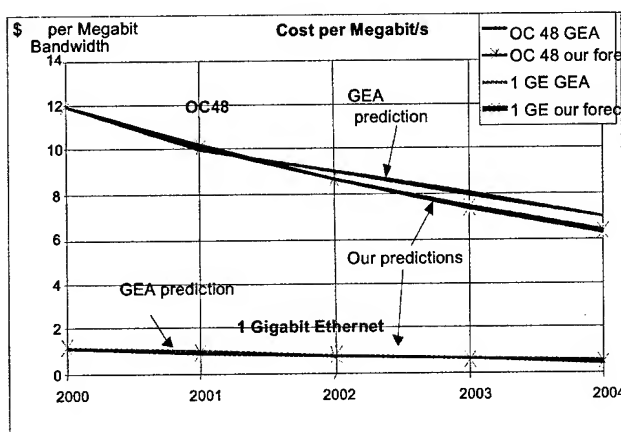


Figure 13. GEA and our forecasts comparison

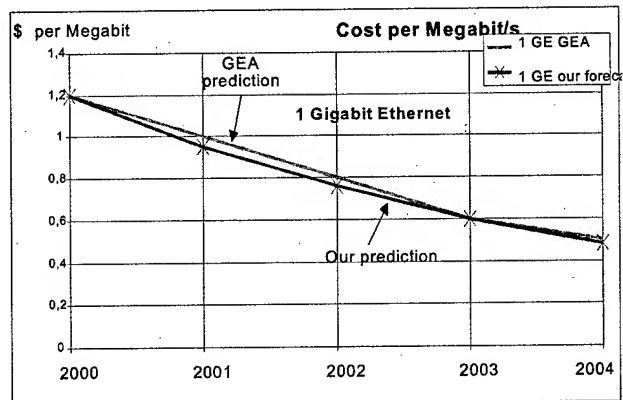


Figure 14. Focus on 1 Gigabit Ethernet forecasts

6. Uncertainties

The strength of the adopted method is the possibility to use it knowing only qualitatively information, even if historical data doesn't exist. However, to make the result reliable and complete, it would be opportune to start from a large availability of data. Moreover, we must say that the results could be completely wrong if the coefficients inserted in the formula are too much approximate or not correct ⁷.

Indeed, it was not simple to produce significant and complete characterizations of such new cost trends. One main reason was that it is still hard to collect concrete and reliable information. Moreover the documents, we are looking for, are often reserved because the selling prices are personalized for each customer.

Then, our policy was trying to identify at first simple and preliminary indicative trends. In this selection phase, the policy was trying to follow the most probable evolutionary trace. These basic curves could then be reproduced, with proper modifications, up to more realistic trends.

7. Applications

Once reliable cost forecasts have been calculated, the natural evolution of this study could be to analyze the most representative and likely network scenarios from the cost point of view. This will allow:

- to understand which ones will be really cost-effective,
- to determine which is the best trade-off between performance and cost today, the direction it will move to in future,
- to roughly predict the right timing to begin the deployment of a specific technology and the total amount of the initial investment.

⁷ Here we remind how we found some data, from different sources, not only different but even divergent in some cases.

8. Conclusions

The purpose of this work was to study and provide with evolutionary trends/curves for some meaningful optical-network equipment production costs, versus their technological maturity. The resulting curves could be useful, for instance, in evaluating the right timing to begin the deployment of a planned network or in estimating the total amount of the initial investment. The adopted prediction model is based on a combination of an extended "learning curve" model and of a logistic "growth curve" model, thus the unit production cost is traduced from an inverse function of the cumulated volume into a time dependent function. To perform computations and to plot graphics a simple Microsoft Excel program was used.

The prediction procedures and computations were placed into a critical insight concerning the current photonics manufacturing scenario. An analysis of photonics industry explained why some optimistic predictions about costs trends have been more times corrected in past. The conclusion was that only an improvement of the same factors (standardization, outsourcing, automation) characterizing the computer industry could really speed up a photonics products cost decrease.

9. Acknowledgments

The Authors wish to thank all the Participants of the IST Project LION for the fruitful collaboration.

10. References

- [1] E. Chen, D. Lu "The economics of photonics manufacturing", J.P.Morgan H&Q Equity Research, July 2001
- [2] COBNET WP0, "Cost-economic study of photonic CPNs", document DW123, 1998. Available at <http://www.intec.rug.ac.be/research/projects/horizon/searchData/cobnetd.htm>
- [3] Cselet "Astra 1.1, Ambiente di Studio Tecno-Economico della Rete di Accesso - manuale utente", 1996, handbook, reserved document.
- [4] A. R. Cantera, "Evolution towards an Optical Network Layer - project P615 volume 4", © 1998 EURESCOM. Available at www.eurescom.de
- [5] T. Chung (Bell Canada), J. Coulter (Bell Canada), J. Fitchett (Sentor Canadian Network Management), S. Mokbel (Onet Networking), B. Arnaud (CANARIE) "Architectural and Engineering Issues for Building an Optical Internet", Sept. 1998. Available at www.canet3.net/optical/pdf/architectural.pdf
- [6] Jean Michel Jouanigot, Olivier Martin "NT3 The LHC Networking Technology Tracking Team" - Cern document, 1999
- [7] S. Siwamogsatham, "10 Gigabit Ethernet", Netlab document, Nov. 1999. Available at [ftp://ftp.netlab.ohio-state.edu/pub/jain/courses/cis788-99/10gbe.pdf](http://ftp.netlab.ohio-state.edu/pub/jain/courses/cis788-99/10gbe.pdf)
- [8] LION Project (Layers Interworking in Optical Networks) "Cost Model for WP3 v1.70", internal document, September 2001
- [9] Y. Emori, S. Namiki "Demonstration of Broadband Raman Amplifier: a Promising Application of High-power Pumping Unit" Furukawa institute, 2000. Available at www.furukawa.co.jp/jiho/fj105/fj105_09.pdf
- [10] Peter Blixt, "Manufacturers get smarts with new strategies for amplifiers", Sept. 2000, FibreSystems Europe magazine. Available at <http://www.ericsson.com/microe/products/optoelectronics/pdf/articleamplifiers.pdf>
- [11] S. Kang, H. Choo, K. Yoo "Design and Fabrication of an 8-Channel InP Arrayed Waveguide Grating Demultiplexer Module with Wide Tuning Range", Korean Physical Society, March 2000. Available at www.photon.kyunghee.ac.kr/~khyoo/pubsub/0103jkps.pdf
- [12] T. Astle, A. Gilbert, A. Ahmad, S. Fox "Optical Components - The Planar Revolution?", Merryll Lynch & Co., May 2000. Available at www.lightwavemicro.com/PDFs/The_Planar_Rev.pdf
- [13] J. Lipton, P. Schwarzbach "Integrated Optics: Promise or Hype?", 2000. Available at <http://connected.jpqh.com/issue43/2.html>
- [14] E. Karasan, E. Ayanoglu (AT&T and Bell Labs researchers) "Performance of WDM transport Network", IEEE Journal, September 1998
- [15] Epoch partners "The Silicon Sizzle in Optics" Compound Semiconductor magazine, March 2001
- [16] Bruce Tolley, "10 Gigabit Ethernet: Technology and standard updates" - 10 Gigabit Ethernet Alliance, Cisco Systems, May 2001. Available at www.cisco.com/warp/public/784/packet/oct00/pdfs/standard_s.pdf
- [17] LION IST Project (Layers Interworking in Optical Networks) WP3, Deliverable D19, "Multi-layer resilient network planning and evaluation: intermediate results", internal deliverable, December 2001

Simulation of fiber drawing using metallic wire

Hiroki Ohara, Tetsuo Katsuta, Takeo Shigemoto, Zen Komiya

JSR Corporation, Tsukuba Research Laboratories
25 Miyukigaoka, Tsukuba, Ibaraki, 305-0841 Japan
+81-298-56-1218 · email address: hiroki_ohara@jsr.co.jp

Abstract

Optical fiber coatings are developed basically based on the flat film evaluations. Flat film is made by applying optical fiber coating on flat substrate, such as glass or PET film, and passing it under UV lamp. However, there are several differences between flat film and actual optical fiber drawing condition. For example, UV lamps for optical fiber drawing have far higher intensity than those for flat film curing. Draw speed is also difference. The condition gap between flat film and fiber drawing is deep. It is already reported that such difference can make the performance of cured coating on fiber different from that of flat film [1]. To remove or narrow this gap, we made a draw tower simulator using metallic wire for evaluation of optical fiber coating. By using metallic wire, draw speed can be changed without affecting temperature of the substrate on which UV curing coating is applied. The draw tower simulator is capable of not only single coating but also wet-on-wet type double layer coating. Evaluation of the cured coating can be made by several methods. For example, the Young's modulus of secondary coating is measured by tubular sample and the modulus of primary coating can be evaluated "pull-out-modulus" measurement as reported elsewhere [2]. In this paper, the drawing simulator and the several insights made by using this machine are presented.

Keywords

Optical fiber coating; Re-winder; Draw tower; Cure speed; Quartz tube; Simulator

1. Introduction

Recent sophisticated characteristics and high demand for optical fiber require coatings to have finely tuned performance and high productivity. Therefore it is indispensable to evaluate performance of the coating by method close to actual production condition. By putting metallic wire instead of glass on actual draw tower, simulation of fiber drawing was carried out [3]. However, better reproducibility and easier operation were desired. A new simulator that can simulate drawing conditions more stably and more conveniently was developed. In this paper, we describe a design of new simulator and some results obtained by using this simulator. Accuracy of cure speed measurement was compared with the metallic wire on draw tower. The new simulator was also used to evaluate darkening of quartz tube on UV lamp by volatiles of coating.

2. Experiments

1.1 Materials

The secondary coatings, S-1 ~ S-3, based on urethane acrylate with various photoinitiator packages were employed for cure speed study. Table 1 shows formulations of these coatings. Other secondary coatings, Q1 ~ Q5, were employed for the study on the volatility and quartz tube darkening. Table 2 shows formulations of these coatings.

Table 1. Formulation of S-1 ~ S-3

	S-1	S-2	S-3
Oligomer			
A	56	56	60
Monomer			
A	8	13	11
B	9	10	9
C	16	2	7
D	7	19	11
Photoinitiator			
A	0.5	1.2	-
B	2.5	-	3
C	0.5	-	-
Additive			
A	0.3	0.3	0.3
B	0.6	-	-

Table 2. Formulation of Q-1 ~ Q-5

	Q-1	Q-2	Q-3	Q-4	Q-5
Oligomer					
B	73	73	73	73	73
Monomer					
E Volatility=25%*	26	-	-	-	13
F Volatility=5%*	-	26	-	-	-
G Volatility=30%*	-	-	26	-	-
H Volatility=100%*	-	-	-	26	13
Photoinitiator					
A	2	2	2	2	2
B	0.9	0.9	0.9	0.9	0.9
Additive					
C	0.6	0.6	0.6	0.6	0.6

* Weight loss under 100 °C for an hour.

1.2 Cure speed measurement by flat film

Liquid coatings, S-1 ~ S-3, were drawn on a glass plate with 200 μm thickness using an applicator bar. These coatings were cured by using a UV conveyor at 3, 6, 15, 24 m/min under air. These conveyor speeds correspond 500, 250, 100, 63 mJ/cm² UV doses. Cure speed was measured by gel fraction or Young's modulus of the resultant films.

1.3 Measurement of gel fraction for cure speed (flat film)

Cured film was extracted with refluxing methylethylketone (MEK) for 12 hours and the resultant sample was dried under vacuum. Gel fraction was calculated from the amount of unextractables in the sample.

1.4 Measurement of Young's modulus for cure speed (flat film)

Young's modulus at 23 °C of film was measured by using a tensile machine. A specimen with 6 mm width and 25 mm length was pulled at tensile speed of 1 mm/min. The modulus was defined by 2.5%-secant modulus.

1.5 Cure speed measurement by metallic wire drawing

Drawing experiments were carried out by using metallic wire of 125 μm in diameter instead of optical fiber glass. Liquid coatings, S-1 ~ S-3, were applied on the wire with thickness of 40 μm and cured by one Fusion P200S/I600 lamp. The draw speed was varied from 200 ~ 1600 m/min.

1.6 Measurement of gel fraction and Young's modulus for cure speed (tubular sample)

A coated metallic wire was pulled to extend and became thinner. The coating was separated from metallic wire as a tubular sample. Measurements of gel fraction and Young's modulus were done by using this tubular sample.

1.7 Volatility measurement of liquid coating

TGA measurement was carried out to evaluate the volatility of the liquid coatings, Q-1 ~ Q-5. The sample was heated from room temperature to 100 °C at the rate of 10 °C/min and kept at 100 °C for an hour. Linear weight loss was observed at 100 °C. The weight loss at 100 °C was defined as volatility.

1.8 Evaluation of quartz tube darkening

Drawing experiments were carried out by using metallic wire. Liquid coatings, Q-1 ~ Q-5, were applied on the wire with thickness of 40 μm and cured by one Fusion P200S/I600 lamp at the draw speed of 100 m/min. Fiber length of each experiment was 8000 m.

2. Results and Discussion

2.1 Draw tower simulator

The schematic drawing of the drawing simulator is given in Figure 1. A commercially available re-winder was remodeled by adding coating dice, UV lamp, and diameter detector.

Configuration of metallic wire on actual draw tower is shown in Figure 2 in order to compare the configuration of the draw tower simulator.

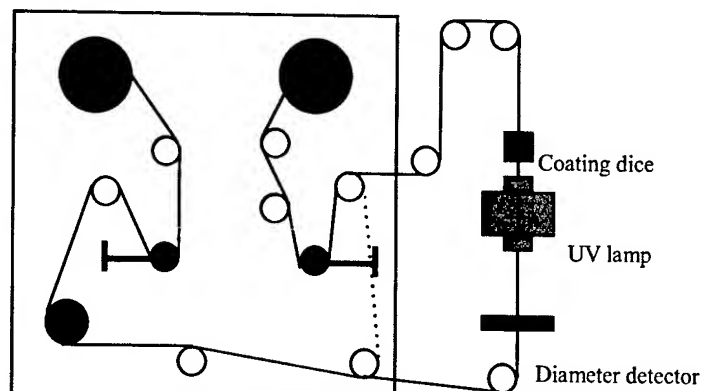


Figure 1. Configuration of draw tower simulator

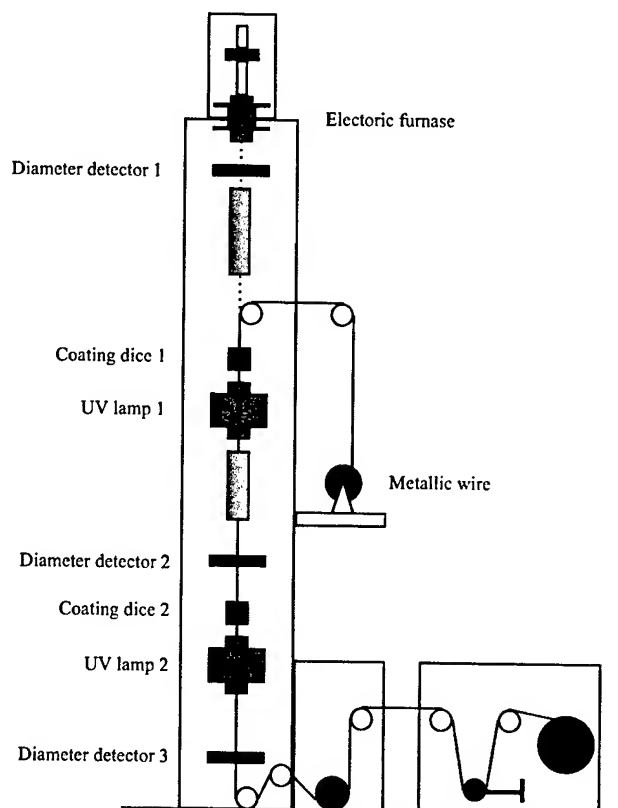


Figure 2 Draw tower simulation by actual draw tower

Comparison of the draw tower simulator and actual draw tower was carried out. Characteristics of the simulator and draw tower are summarized in Table 3. Figure 3 shows the diameter change of the wire after drawing without applying coating. The wire run by the draw tower decreased its diameter, which went down further at more than 1000 m/min of draw speed. The wire after

draw was pulled at constant force and the elongation was recorded. The elongation is plotted against the draw speed in Figure 4. Over 1000 m/min of draw speed, elongation of wire drawn by the draw tower decreased. In contrast, the wire drawn on the draw tower simulator did not become thinner and showed constant elongation after draw up to 1600 m/min. Since the simulator has pay off and take up controls, the tension is kept constant throughout the experiments. In case of the draw tower, the metallic wire was elongated by excessive tensile force especially at high draw speed. This difference turned out to be affecting the result of coating evaluation. Figure 5 compares the cure speed evaluation result of a certain coating by draw tower and the simulator. The gel fraction of this coating decreased linearly as the increase of draw speed. However, the gel fraction obtained by the draw tower went up at 1200 m/min of draw speed then again decreased linearly. The draw speed where gel fraction increased coincides with the speed where the elongation and diameter of metallic wire decreased. On the contrary, the gel fraction obtained from the draw tower simulator showed linear relationship up to 1600 m/min.

Table 3. Characteristics of draw tower simulator

	Draw tower simulator	Draw tower
Maximum draw speed (m/min)	1600	2000
Draw speed control	Automatic	Manual
Height (m)	2	18
Coating dice	1	2
Tension control	Pay off and take up	Take up only

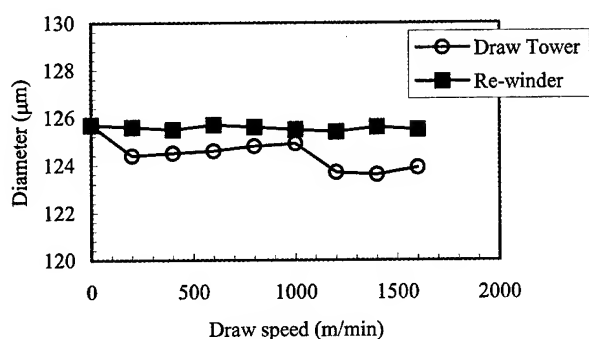


Figure 3. Changes in diameter of the metallic wire after drawn on the draw tower and the simulator

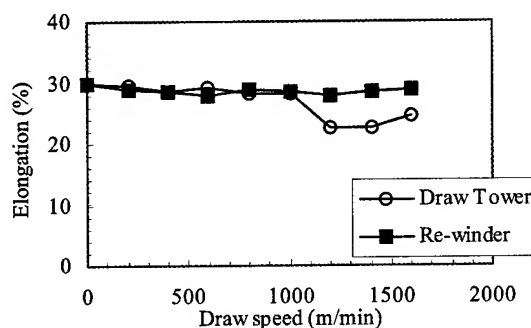


Figure 4. Changes in elongation of the metallic wire after drawn on the draw tower and the simulator

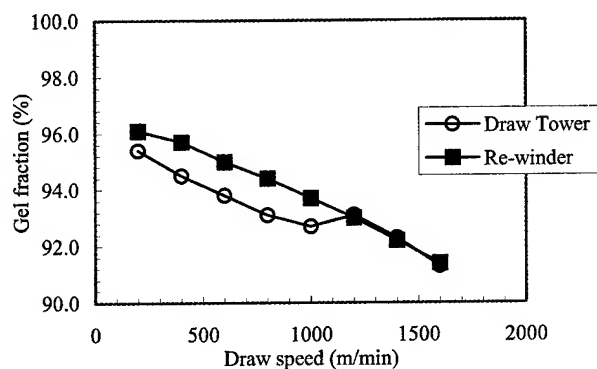


Figure 5. Comparison of draw tower and the simulator by gel fraction

2.2 Cure speed of flat film

Cure speed of coating is one of the important factors determining productivity of optical fiber. Cure speed has been estimated by using flat film. In this section, cure speeds based on flat film and by the draw tower simulator are compared. Cure speeds of three coatings, S1 ~ S3, evaluated by using flat film are plotted in Figures 6 and 7. When cure speed was compared by gel fraction, S-2 was fastest. S-1 and S-3 came second (Figure 6). In contrast, cure speed based on Young's modulus, S-1 and S-2 showed almost the same cure speed and S-3 became last (Figure 7).

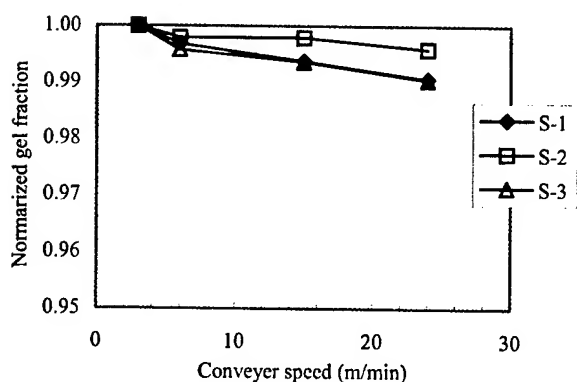


Figure 6. Cure speed by relative gel fraction of secondary coatings by using flat film

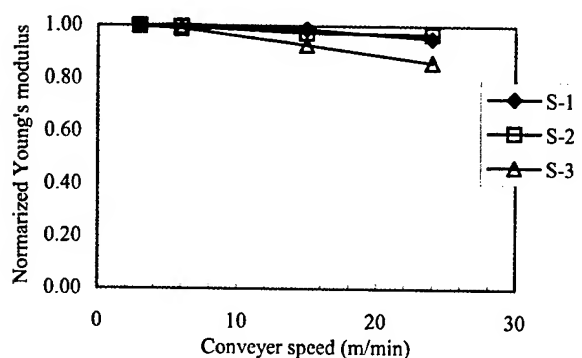


Figure 7. Cure speed by relative Young's modulus of secondary coatings by using flat film

2.3 Cure speed by the draw tower simulator

Cure speed of these coatings, S-1 ~ S-3, evaluated by using the draw tower simulator are plotted in Figures 8 and 9. S-2 shows the smallest decline in gel fraction and Young's modulus against draw speed among these coatings. S-3 shows the largest dip of gel fraction and Young's modulus against draw speed among these coatings. As indicated by the gel fraction of flat film, S-2 cures fastest among these three coatings. Although the slowest one was not clear by flat film evaluation, the draw tower simulator clearly indicated that S-3 was slowest in cure speed both by gel fraction and Young's modulus. The draw tower simulator is able to differentiate the cure speed more unambiguously than flat film evaluation.

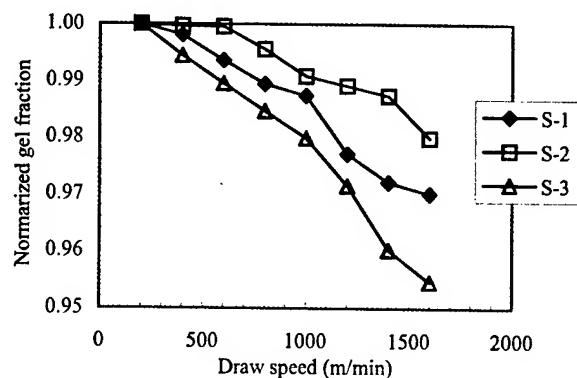


Figure 8. Cure speed by relative gel fraction of secondary coatings by using tubular specimen

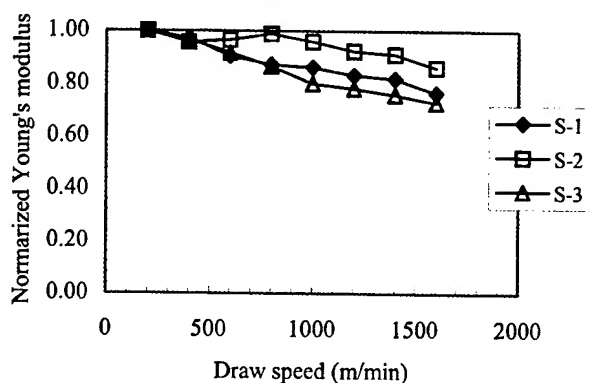


Figure 9. Cure speed by relative Young's modulus of secondary coatings by using tubular specimen

2.4 Volatility of coating and darkness of quartz tube

Recent technical development allows us to have a fat preform, which can draw more fiber at a run. Therefore the length of fiber is getting longer per drawing. The longer the fiber drawing becomes, the darker the quartz tube on the UV lamp becomes, because it was believed that volatile materials from the coating were darkening the tube. This can be a problem since at the end of the fiber drawing, the coating may not receive enough UV energy giving poorly cured UV coating layer on fiber. At first sight, the darkness of quartz tube seemed to be caused by volatile materials from coating generated during curing. To examine this speculation coatings with different volatility were compared. The volatility of the coatings, Q-1 ~ Q-5 is summarized in Table 4.

Table 4. Volatility of coatings

	Q-1	Q-2	Q-3	Q-4	Q-5
Volatility (%)*	6	3	8	23	15

* Weight loss under 100 °C for an hour.

The darkness of quartz tube was evaluated by comparing the transparency before and after drawing with a UV-Vis spectrometer. To obtain a quartz tube darkened sufficiently for quantitative comparison, an 8000 m of wire needed to run at slow

draw speed (100 m/min). Transmittance of the quartz tube after drawing is summarized in Table 5. Comparison of Tables 4 and 5 indicates that volatility does not necessarily correlate to the darkness of the quartz tube. The coating Q-4 showed the biggest weight loss. However, this coating gave the most transparent quartz tube among these coatings. Intuition tells us that the darkness of quartz tube seemed to be caused by volatile materials generated during curing. However, volatile materials do not always cause darkness to the quartz tube.

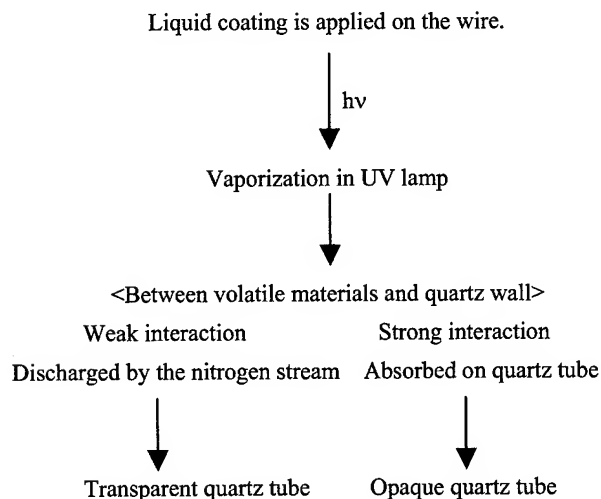
Table 5. Transmittance of quartz tube after drawing

Wavelength (nm)	Transmittance (%)*				
	Q-1	Q-2	Q-3	Q-4	Q-5
250	49	59	62	71	60
300	50	59	62	70	60
350	58	65	68	75	66
400	63	70	73	79	71
500	72	78	81	86	76

* Relative value to the tube before use

2.5 Mechanism of the quartz tube darkening

Though Q-3 and Q-4 had higher volatility than Q-1 and Q-2, the former gave more transparent quartz tube than the latter. The quartz tube darkening was influenced by the chemical structure of monomers, because these coatings have the same composition except for monomers. The monomers included in Q-1 and Q-2 consist of ethylene oxide, that is to say polar compounds. In contrast, the monomers included in Q-3 and Q-4 consists of hydrocarbon, that is to say non-polar compounds. The quartz tube darkening seemed to be influenced by the polarity of monomers. Mechanism of the quartz tube darkening suggested is illustrated in Scheme 1.



Scheme 1. Mechanism of darkness of quartz tube

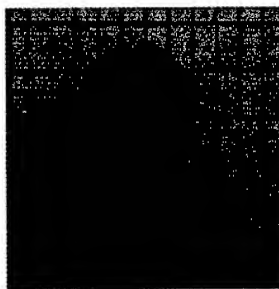
As illustrated above, volatilities (monomers) are vaporized in UV lamp by reaction heat and infrared rays from UV lamp. If volatile materials have weak interaction with glass wall, these are discharged outside and quartz tube remains transparent. However, if volatile materials have strong interaction, these are absorbed on quartz tube. The absorbed monomer degrades to dark color materials. The coating Q-5 has the intermediate formulation of Q-1 and Q-4. Its behavior in volatility and darkening of the quartz tube came in the middle of these two coatings. This result indicates that the volatility and darkening have a linear relationship to the amount of monomers. However, it should be emphasized again that the volatility and darkening do not have direct correlation.

3. Conclusions

The drawing simulator was developed by adding coating cup, UV lamp, and diameter detector to a re-winder. This draw tower simulator enable us to reproduce drawing conditions more easily and precisely than the draw tower with metallic wire. Tubular specimen prepared by this simulator could detect the subtle difference of cure speed that could not be detected by flat film experiments. Darkening quartz tube is one of the practical problems for fiber manufacturing. This draw tower simulator provided a quantitative evaluation method. To minimize the darkness of quartz tube, it is necessary to use not only less volatile materials but also materials that are not easily absorbed on quartz.

4. References

- [1] J. Yoshizawa, Y. Naito, T. Takase, Z. Komiya, T. Ukachi, *Proc. of 48th IWCS*, 680 (1999).
- [2] T. Katuta, H. Uchida, Y. Naito, Z. Komiya, T. Ukachi, *Proc. of 49th IWCS*, 460 (2000).
- [3] S. Morita, Y. Naito, Z. Komiya, T. Naganuma, A. Fujimori, T. Ukachi, *Proc. of 44th IWCS*, 513 (1995).



Hiroki Ohara

Tsukuba Research Laboratories, JSR Corp.

25 Miyukigaoka, Tsukuba, Ibaraki, 305-0841 Japan

Hiroki Ohara received his M. E. degree Industrial Science and Technology from Science University of Tokyo and joined JSR Corp. in 1997. He has been engaged in research and development of radiation curable materials for optical fiber coatings.

The study of UV foaming technology for ABF bundle

Selee Chang, Hwa Joong Kim, Jung-Hyun Oh, Daesung Lee, Eugene Kim,

LUVANTIX Co., Ltd.

Ansan, Kyonggi, Korea

+82-31-494-6100, csl@luvantix.com

Abstract

To carry fiber from one located to another in ABF (Air Blown Fiber) bundle installation, the fiber bundle needs to have special aerodynamic properties and light weight for long blown-distance. The thermal extrusion-foaming technology is commonly used to make lightweight and bumpy surfaced sheath for low friction in conventional ABF bundle production.

In this study, the photochemical (Ultra Violet) reaction is employed to foam gas bubbles trapped in the coating film for optical fiber bundle. The gas bubbles trapped in the film lower the density of the coating significantly down to one half of that of the solid film. Spontaneous UV curing of the coated resin and UV foaming of the gas bubbles in the cured film will not only lower the density of the bundle and but also increase the line speed in ABF bundle production at least to ten times compared to that of regular thermal extrusion and foaming system.

Keywords

ABF, air blown fiber, polymer sheath, optical fiber coating, UV cure, foaming, low friction, photo cure, photodecomposition, radical curing.

1. Introduction

Optical fiber cables are installed in much the same way as copper wire cables. The fiber cable is pulled into place through ducts and conduits using a rope attached to a cable end. The Cables experience very high tensile loadings during such installation, and consequently optical fiber cables need very considerable reinforcements to prevent the optical fibers from being damaged. These requirements increase the size, weight, cost of optical fiber cables and limitation in installation length. Air blown fiber system is an alternative approach to optical fiber installations method. It is known to blow optical fiber cables into ducts in order to install long, continuous lengths of optical fiber cables over long distance, such as to install optical fiber cables in so-called sub-ducts in kilometer lengths. In this method the fibers are installed along a previously installed duct using fluid drag of a gaseous medium, which passes through the duct in the desired direction of advance. This method uses distributed viscous drag forces to install a cable unit that is supported on a cushion of air.¹⁻²

The fiber bundle for ABF application should be designed to meet various physical requirements for long distance installation. The lightweight and low surface friction between the bundle and the duct are main concerns in optical fiber bundle design. The lightweight and low friction design will give longer installation distance and less tensile loading in optical fibers. In typically design, optical ribbon units consist of plurality of conventionally coated fibers are held together in lightweight polymer sheath which contain foamed bubbles to reduce weight and surface friction.

Commonly, foamed skin is made by thermal cure coating system. The coating consists of thermal cure polymer resins and heat blowing agents. By heat extrusion process, the polymer is cured to provide physical strength as sheath and the blowing agent is decomposed to foam gas bubbles. This extrusion and heat foaming processes limit the production speed to one tenth of conventional fiber optic industries standard.

UV cure technology has been successfully implemented to optical fiber coating and cabling processes for the high-speed production up to 2,500 meter/minute. By combining this UV cure polymer coating and UV decomposition technology, UV foaming process has been developed.¹⁻⁵ In this paper, several UV curable compositions (EFIRON®) including photo-reactive oligomers, monomers and photo-decomposition reagents, which fit for use in UV curing system as blowing agent, are studied for ABF application. This new development coating resin (EFIRON®) can be new material for polymer sheath to make lightweight air blown fiber bundle.

2. Basic principle

2.1 Photodecomposition & Radical Quenching

Most conventional thermal foaming processes can utilize chemical blowing agents (CBAs), also known as foaming agents. CBAs are added to the polymers during thermal processing to form minute gas cells throughout the film. The gas is liberated by chemical changes in the CBA. The foamed cellular structure reduces polymer film density, saves in materials costs, improves thermal insulating properties and increases the strength-to-weight ratio. The liberation of gas when heating chemical foaming agents occurs through series chemical reactions or decompositions. Different chemical foaming agents have different decomposition temperatures

depending on their chemical structures. The most used CBA for medium temperature polymer processing (325~430 °F) is azodicarbonamide. The some of blowing agents are decomposed into gaseous products when subjected to sufficient conditions, for example by raising temperature or even by sufficient photo energy radiation. Generally, materials which have functional groups such as photosensitive or chromospheres in their main backbone or photo-resist reagent in their compounds can be reacted and de-composed by photo-energy.³⁻⁴

-N=N-, -CH=N-, -CH=CH-, -C≡C-, -NH=NH-, -S-, -NH-, -O-, >C=O are typical photo sensitive functional groups, which absorb photo-energy easily. Therefore molecules including those functional groups can be decomposed by photo-energy and possibly be used as photo-induced blowing agents. To be used as a blowing agent, the molecule should be easily decomposed by UV radiation and generates gas like nitrogen or carbon dioxide. As one of examples, the molecules contain diazo group, which absorb strongly UV energy around 200 ~ 300nm wavelength range, decompose and generate nitrogen gas. In Figure 1, the chemical reaction route illustrates the generation of nitrogen gas by azo-group and some side-reactions.⁵⁻⁷

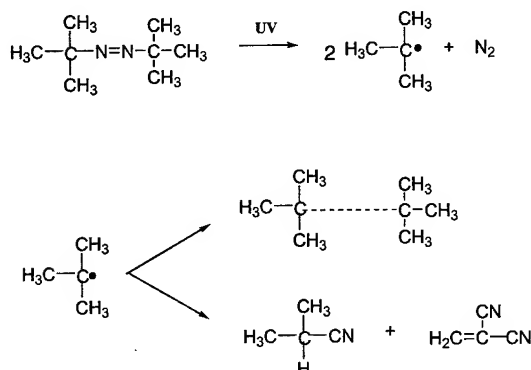


Fig 1. Azo compound decomposition by UV energy

Nitrogen gas generation synchronize with ultra violet cure of polymer compounds. Therefore the gas is trapped in cured solid coating film as like foam.

Unfortunately, azo blowing agents, which can be used in photo-induced foaming application, decompose into products, which adversely affect the photo-induced polymerization. For example, the decomposition products, especially radicals, undesirably react with monomers, oligomers and even with cured polymers, lowering the molecular weight, and causing brittleness in the final cured polymeric film. It would be desirable to have azo blowing agents, and/or a method of UV

curable foaming compositions wherein the agents would be versatile, and would have degradation products which would not react with the final polymeric film. This kind of azo compound can be prepared by various known methods like reacting a diazonium ion with an organometallic compound, or contacting an isocyanate-substituted aromatic compound with a tertiary alkyl primary amine compound; and then oxidizing urea compound.

Photo-intensifiers and metal complexes behave as catalyst when be added in photosensitive compounds. Photo-intensifiers contain aromatic ketone groups, for example benzophenone, acetophenone and acetoquinone take hydrogen molecules from photosensitive compounds and help the decomposition process by lowering decomposition energy.

2.2 UV curing system and formulation

Radiation Curing is the technology of utilizing short wavelength ultraviolet light (UV), or high-energy electrons from electron beam (EB) sources. UV curable coatings are formulated using selective materials that react to UV energy forms to yield very specific performance properties. UV cure process causes liquid coating to change into solid film virtually instantly. Curing is very fast and cool in relative terms, which allows applications to high-speed production and to heat sensitive substrates. Once cross-linked by UV curing, properly cured products exhibit both highly physical and chemical resistant properties.⁸⁻¹⁰

A radiation curable formulation consists of the flowing components;

1. Prepolymers, urethane based oligomers
2. Reactive diluents, monomer contain acrylates
3. Additives for leveling and storage stability
4. Photo-initiators (PI) for UV curing process

Obviously, for a UV curable formulation, it is necessary for a UV photo-initiating system to be present. This applies to both free radical and cationic curable systems.¹¹⁻¹³ Much of the selection of a photo initiator is connected with its effect on cure rate and degree of cure, thus frequent reference will be made to the assessment cure. Urethane based oligomers and special monomers should be selected to overcome the brittleness due to the azo side reaction and to give enough toughness so that the cured film protect the optical fiber from being damaged during the ABF installation.

3. Experiment and Result

The same amount of photoinitiator (PI), azo blowing agent and metal complex catalyst are mixed in a solvent and the

mixture is tested to illustrate the effect of the catalyst to UV absorption of PI and blowing agent (BA).

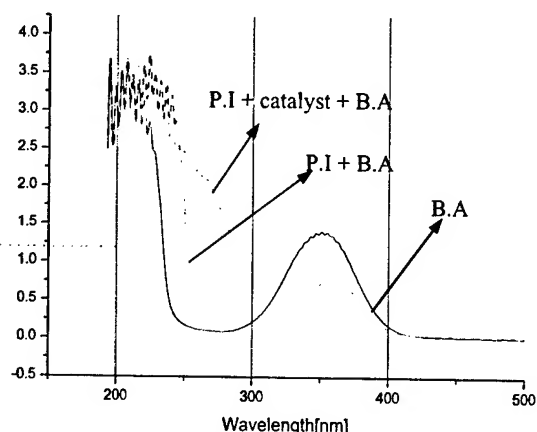


Fig.2 UV absorption of azo compounds

Figure 2 shows the ultra violet absorption of various mixtures of azo compound, photo initiator and metal complex catalyst. The total area under the graph represents the total absorption of photo-energy. The mixture of photo-initiator and photo-induced blowing agent shows higher absorbance due to the absorption of the blowing agent. The addition of metal complex catalyst into the previous mixture even enhances the absorption of UV energy. By implementing this UV-induced generation of gas and radical system into the UV cure coating formulation, the foam like film can be achieved by the conventional UV curing process

To find out the effect of azo compounds as blowing agent in UV curing compounds, diacrylate oligomers (Mw 4,500 ~ 5,000) and mono, di, multi functional acrylate monomers and photo-initiation compounds are mixed with photo-induced blowing agents and organometallic catalyst. The urethane diacrylate oligomers included polycarbonate groups are applied to these experimental compounds to increase the toughness and hardness of the cured film. Monomers having low acrylate contents are selected to decrease viscosity of coating solution and curing shrinkage. These monomers enhance the flexibility of UV cured film. Hydroxyl alkylphenone type photo-initiator is cooperated for D-bulb curing system.

Various UV curable coating formulations containing different amount of photo-induced blowing system are prepared as Table 1 below.

Table 1. UV curable formulation (wt %)

	A	B	C	D
Oligomer	73.3	72.8	72.3	71.8
Monomer	25			
Photoinitiator	1.0			
Blowing agent	0.5	1.0	1.5	2.0
Catalyst	0.2	0.2	0.2	0.2

Each coating materials A/B/C/D, as shown in Table 1, is cured with different UV power conditions from 300 mJ/cm², 100 mJ/cm², 70 mJ/cm² and to 50 mJ/cm². For UV curing, Fusion 600I/VPS model equipped with D 600 Watt bulb lamps is used to make specimens with variation of UV radiation power. The density of each cured film is measured to analyze the effect of radiation power and dose of the blowing agent. The test results are illustrated in Figure 3.

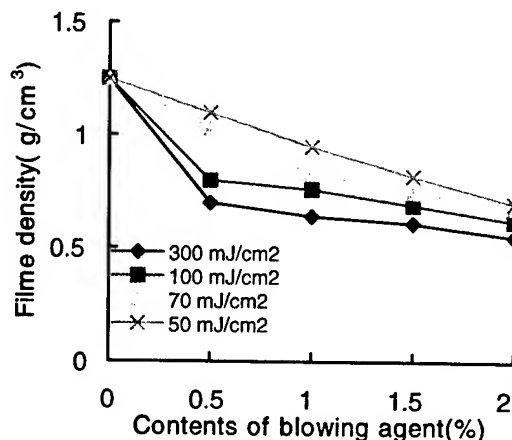


Fig. 3 Density of film with four different UV power

The density of the cured film decreases proportionally with increasing blowing agent content. But there is a limitation showing the saturation of blowing agent effect. The higher power level of radiation enhances the activation of the blowing agent even more, but there is also saturation point. This result implies the balance of dose of blowing agent and UV power level is critical to achieve the strong UV cured film with lower density and good toughness

Figure from 4.1 to 4.4 are the microscope pictures of UV cured film surface of the formulation D with various UV power levels. This sequenced pictures shows increasing in number of bubbles trapped in the cured film when the UV power level is increased.

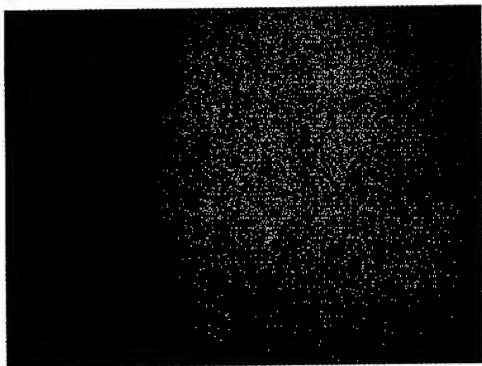


Fig. 4.1 Standard Film without the blowing agent

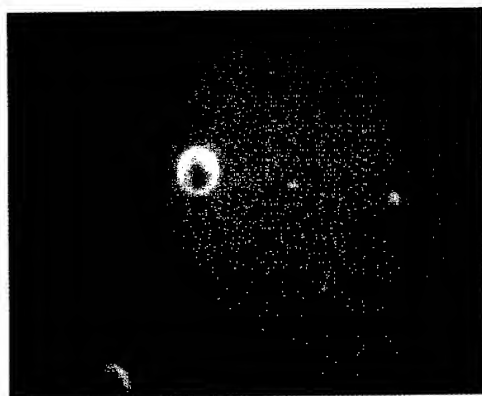


Fig. 4.2 Sample D with UV dose of 70 mJ/cm²



Fig. 4.3 Sample D with UV dose 100 mJ/cm²

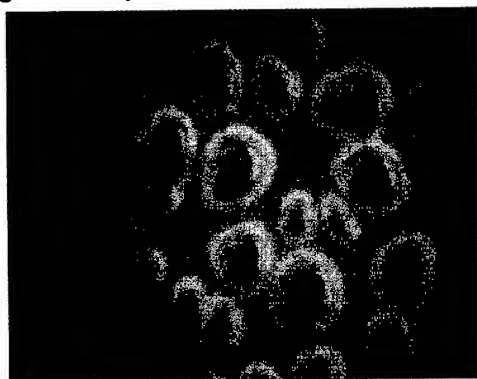


Fig. 4.4 Sample D with UV dose 300mJ/cm²

Figure 5.1 and 5.2 are the microscope picture of the cross sections of the cured film without the blowing agent and the cured film with the blowing agent at 300 mJ/cm² power level (Figure 4.4). The thickness of the Figure 5.2 is doubled compared to that of Figure 5.1. This increase in volume due to the gas trapped in the film lower the density of the film to half.

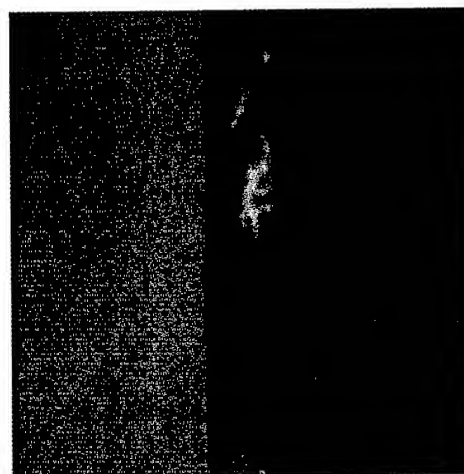


Fig. 5.1 The cross section of film (Fig 4.1)

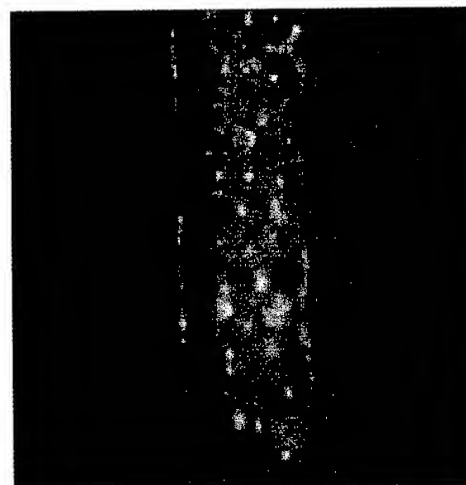


Fig. 5.2. The cross section of Fig. 4.4

Surface friction coefficient of the UV cured foam film is measured by UTM (Universal Testing Machine; Instron). The film is folded and 500g of weight is loaded over the folded film; and then the maximum loading is measured to move the upper film. Typically, the friction coefficient of matrix coating for optical fiber bundle is in the range of 0.6 ~ 1.0 kg_f. The friction coefficient of the UV cured foam film with 300mJ/cm² is measured to be 0.2kg_f, which is lowered by 1/3 ~ 1/5 compared to that of regular UV cured film. This low friction surface created by the UV induced bubbles lower the tensile loading of optical fiber in the ABF installation.

4. Conclusion

In this experiment, with implementation of UV induced blowing agent system into conventional UV curable optical fiber coating, the low density and low friction surface film can be achieved from UV cure process. The density of foam film is proportional to blowing reagent content and ultra violet energy with limitation of saturation point. Some of formulations show the decrease of density by 40% with only 100mJ/cm² UV power. Typically, UV systems in fiber bundle and optical fiber coating production lines are operated over the 400 mJ/cm² power level. Under these conditions, the density of foam film can be reached easily down to 0.50 g/cm³. Therefore, low-density polymer sheath for air blown fiber bundle can be made in conventional UV curing system of optical fiber coating industries using this new formulation. This new UV curable coating material trade-named EFIRON[®] makes it possible to produce ABF optical bundle faster and cheaper than conventional thermal process.

5. Reference

1. Philip A. Barker; Davis J. Stockton; Christopher Fisk; Peter D. Jenkins, US 5,555,335
2. William C. Fisher, Cuyahoga Falls; Paul C. Menmuir, Richfield, US 3,354,331 B1
3. Richard A. Wolf, Edwin J. Wilson, US 4,743,623
4. Deker, C. & Moussa, K. macromolecules, 22(1989) 4455
5. Sumiyishi, T., Schnabel, W., Henne, A. & Letheken, P. polymer, 23(1985) 141
6. Radiation Curing in polymer science and technology, Vol II. Photoinitiating system, Ed, J.P. Fouassier, J.F.Rabek.
7. S.K.L Li, J. P. S, Polymer chem., Ed, 18.2221 (1980)
8. W.Kawai, J.P.S, Polymer chem, Ed, 15, 1479 (1977)
9. D. J. Carlsson, J.P.S., Polymer, Chem. Ed., 16, 2353(1978)
10. Fowler, A New Synthesis of Unsymmetrical Azo Compound, 37 J. Org. Chem. 510 (1972)
11. Fouassier, J.P. In photopolymerization and photo imaging science and technology, ed.N.S Allen. Elsevier, London, UK, 1989,p.209
12. Schnabel, W.J. radiation curing, 13 (1986) 1.
13. Fouassier, J.P. Proc. Radiation Technologies, Florence, p .33, Radtech Europe Ed., Fribourg, 1989

Author

Selee Chang

Luvantix Co.,Ltd.

cs1@luvantix.com

Selee Chang is graduated the Hong-Ik University in Chemical Engineering in 1997. and joined with Luvantix Co.,Ltd. She is an engineer in optical fiber & material research & development division.



Hwa Joong Kim

Luvantix Co.,Ltd.

khi704@luvantix.com

Hwa Joong Kim received his B.S. and Ph.D. in Chemical engineering from Hong-Ik University in 2001. He joined with Luvantix Co.,Ltd in 2001, and works in optical fiber & material research & development division.



Jung Hyun Oh

Luvantix Co.,Ltd.

ojh@luvantix.com

Jung Hyun Oh is a general director in technical center. He received his B.S. and M.S. degree in Materials Science & Engineering from Cornell University in 1996.



Daesung Lee

Luvantix Co.,Ltd.

lds@luvantix.com

Daesung Lee is a project manager in optical fiber & material research & development division. He received his B.S. & M.S. in Chemical Science from Dan-Kuk University in 1992.



Prof. Eugene Kim

ekim@wow.hongik.ac.kr

Eugene Kim is a professor in of Hong-Ik University Seoul. He received B.S. in Chemistry from Seoul National University in 1985 and Ph.D. in Chemistry / Materials Science & Engineering from Cornell University in 1994. He joined with Luvantix Co.,Ltd in 2002 as a general director



Extrusion Line for Fine Wires with Highly Expanded Insulation

Pierre-Yves Bonvin

Product Manager, Maillefer SA

Route du Bois 37, 1024 Ecublens, Switzerland

Phone: +41 21 694 41 11 - e-mail: pierre-yves.bonvin@maillefer.net

Abstract

Maillefer has designed and developed a specialized insulation line for the processing of fine wires. It is the solution for cable suppliers who are willing to manufacture small diameter but highly expanded wire for the electronics industry. This line is able to process materials such as PE, PP, PVC, FEP, PFA. It is a versatile tool that has all the characteristics of producing high-level cable. The success of this project is due in part to the development of dedicated components. In addition, these components were integrated with a constant attention to line productivity. This development has resulted in an original and patented Capacitance / Diameter control that ensures production reliability.

Keywords

Micro wires, extrusion line, Extrucell™, highly expanded insulation, physical foaming, FEP foam, capacitance / diameter close loop control, LAN cat 6, LAN cat 7, LAN cat 8

1. Introduction

Continual size reductions of consumer electronic devices place pressure on cable suppliers to decrease wire dimensions. The reduced constructions are challenging, as the electrical performances requested do not follow the same trend. Higher data transfer is needed at ever-higher frequencies. The Bluetooth standard is a good example. The short distance "wireless" application works at very high frequencies, where each device is wired with its own miniature antenna.

Nowadays, applications like USB rev 2.0 follow a standard, which can still be met with solid insulation wires. In the future, the only way to reach the necessary electrical performances while keeping with the size constraints is through the use of expanded insulation. Cable suppliers generally exceed the standard minimums by providing cable to the market that has expanded insulation. In other standards, like the IEEE 1394 for high-performance serial bus cable, expanded insulation is the norm. The requested insulation dielectric is so low that high expansion is a must. Going to more demanding applications we find the field of measuring devices. Miniaturization and performance reach their heights here through the combination of very low dielectric material (PFA, FEP, etc.) and high expansion rates.

To enable cable manufacturers to meet the challenges, Maillefer has developed an insulation line for fine wires. This extrusion line is able to run solid or stranded conductors down to 0.2 mm. This versatile and flexible production tool processes expanded FEP, PE, or PP insulation with high productivity. New components were designed such as a three layer crosshead ECH 3/9 FEP with

manual centering for fluoropolymers, a dedicated nitrogen injection system, a driven preheater and a low tension capstan. With the target of delivering a process having high stability and high productivity, our process specialists have created an original Capacitance / Diameter control, which is adapted for fluoropolymers and tube tooling. The patented C/D uses the regulation of cone length to reduce the start-up time and scrap during production.

2. Technical specification of the line

The production of fine wires is challenging and pushes the standard extrusion technology to its limit. In order to propose a versatile solution, we designed a line able to produce fine wires as well as LAN and TEL wire: solid and stranded conductor wires from 0.2 mm to 0.6 mm; over insulation diameter from 0.5 mm to 3 mm; maximum speed of 1000 m/min. To realize this machine we had to develop and improve most of the components. When preparing the specification of this new insulation line, we identified three main areas:

1. Expanded resin processing
2. Wire pulling
3. Productivity

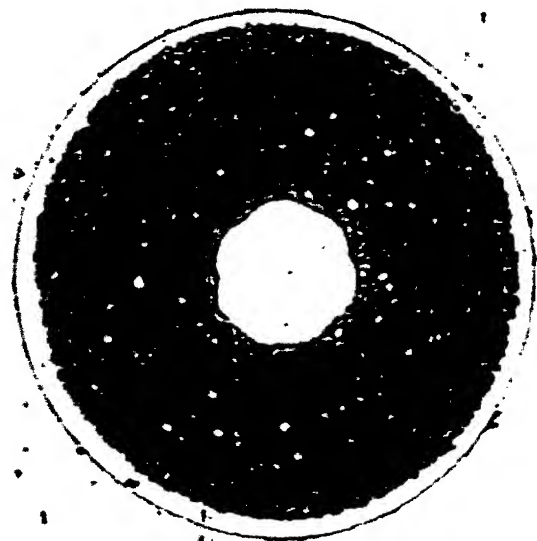
The first phase consisted in melting the resin and dissolving the nitrogen as homogeneously as possible. The challenge for the insulation was to reach high expansion with limited cell size and sufficient mechanical structure. The expansion target was 70% foaming for PE and FEP with an average cell structure below 20 microns. In our specification, the line had to process solid PE, PP, PVC, FEP, PFA and physically expand PE, PP, FEP with the possibility of extending it to foamed PFA.

Of course this development could not be done without calling upon the resin suppliers as partners. Sharing our goals with them, new resins were developed to reach the demanding target. Experimental resins were supplied and tested on this new line before being proposed to the market. The optimal processing parameters for each type of product are now known, which results in fast production start-ups.

The second challenge of the project after the extrusion process was wire pulling. All the line had to be designed to maintain the insulation quality furnished by the extrusion group: concentricity, ovality, skin smoothness, final elongation, and adhesion. The in-line tension had to be as low as possible and stable even at high speeds to maintain productivity.

For a high-tech line, productivity is finally the main issue. The line had to be able to work without a process specialist needed to fine tune and constantly modify the parameters. The process had to be as repetitive and stable as possible to avoid long start-ups

and scrap. The design of the line was made with this main concern and resulted with original solutions such as the C/D control for FEP foam.



Wire construction:

conductor: 0.26 mm
overall diam. FEP: 0.92 mm
outer skin FEP: 60 microns
capacitance: 65 pF/m
expansion: 58%

Wire quality:

diameter tolerance: ± 15 microns
capacitance tolerance: ± 1 pF/m
cell structure: max 30 microns
min 10 microns
average 17 microns
concentricity: 95%

Figure 1: FEP foam-skin Micro wire, ID 0.26 mm / OD 0.92 mm, average cell size 17 microns

3. Line description and new components

3.1 Extrusion group

The optimal size for the main extruder was a compromise between quality and productivity. The NMC 45-30D F extruder was selected due to its versatility and its outstanding linearity. Equipped with a bimetallic barrel and two screws for both fluoropolymers and standard resins (PE, PP, PVC) it is capable of high output for solid insulation in PE and FEP and high stability at low speed for highly expanded FEP and PE. The optimal position for the injection point for nitrogen was calculated and then measured for each process thanks too a special barrel with extra injection points all along its length. The key parameter for the selection of the injection point is the cell size. Two injection points separated by about 10 cm were selected for PE and FEP for the finest cell structure. A study on the heating / cooling phenomenon on the heating zones resulted in the installation of new cooling fans having a reduced cooling effect at the start-up of the fan for the small corrections. If the fans continue to run, then the cooling efficiency increases. This improved linearity between cooling and heating beneficially influences the stability in temperature, especially when working within the limits between cooling and heating.

The auxiliary extruder NMA 30-24D F was chosen to apply either PE or FEP layers using one of two dedicated screws. When producing FEP skin-foam-skin wires, the flow coming from the NMA 30-24D F is divided in two for the outer and the inner skin. On the other hand, the inner skin extruder NMA 20-24D offered sufficient output to apply the inner skin PE for the skin-foam-skin configuration.

Convinced by our preliminary study that the inner and outer layers were bringing added value for the productivity and the stability of the process for the FEP foam, the specification on the line included the development of a three-layer crosshead (skin-foam-skin) for FEP foam: ECH 3/9 FEP.

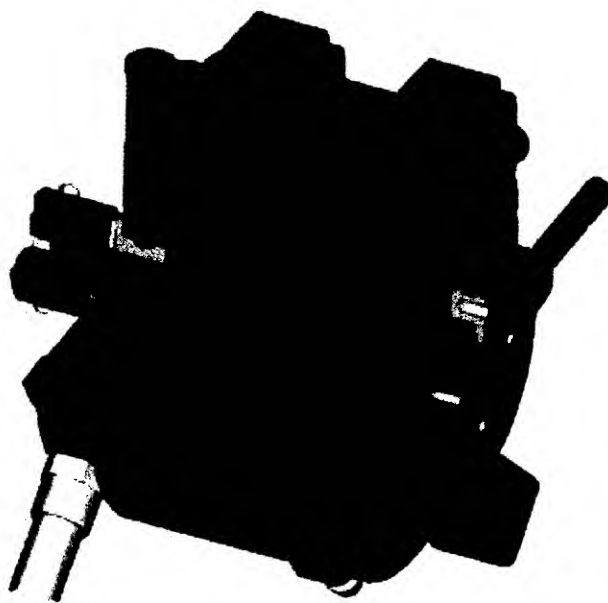


Figure 2: ECH 3/9 FEP head for FEP skin-foam-skin production

Designed and assembled by Maillefer, this manual centering head has the flexibility of working with one or two auxiliary extruders for the inner and outer layers. The head separates one flow into two layers when working with an individual machine. For high-level products, two auxiliary extruders can be used. In this case, the same head directly channels the individual layers from the two separate machines.

The anti-corrosive Inconel head has three individual heating zones:

- die zone where the die holder extends from the body
- distributor zone for the inner skin
- main body zone.

A special wire guide system is built into the vacuum pump connection for precise conductor centering. The head is designed for reduced maintenance and quick set-up times. Its asset for the production of fine wires is the reduced volume of the assembly. Measuring less than 112 mm for a diameter of 115 mm its limited temperature inertia reduces the transition-working mode at the start-up of the line.

A number of innovations have resulted from the improvement of the injection group system. The challenge was considerable: delivering nitrogen at a constant and stable flow of less than 1 l/h with a working temperature above 300°C at the injection point. To reach this result we had to improve the resistance to the external influences: air quality (oil, humidity) and pressure stability, nitrogen quality, power supply. The electro-valve, filters and high-resolution manometers were sized to provide a stable and uninterrupted supply of 0.8 l/h minimum. These innovations were also designed as a kit for the upgrade of existing units.

High temperatures and low outputs required special attention to injector design. The nozzle area can reach more than 200°C when working with FEP. Through the use of Maillefer's water-cooled injectors, nozzle temperatures were brought down to an ideal operating temperature of less than 40 °C. Stable outputs and long nozzle life were thus ensured. Avoiding dilation prevented leakage around the gem and mechanical strains on the nozzle. This solution was technically necessary for the FEP foam process, but promises to be economically interesting for the lifetime of the injectors supplied for the PE.

3.2 Wire pulling

The main difficulty in the production of fine wires was production start-up and tension control. All the components had to be able to run wires with a constant and stable tension between 2 and 4 N. For example, the selected pay-off was equipped with a high precision pneumatic dancer remotely controlled by the line supervisor. The AC motor allowed a wider range of speed with a guaranteed stability.

To keep the tension constant throughout the entire process, the specification of the line included a close loop control with load cell. It served to measure the tension on the preheater and to regulate the capstan motor. For this application, our partner developed a totally new preheater. It was able to control the inline tension of the wire while reducing the heat loss of the 0.2 mm wire from the ceramic pulleys as much as possible. The non-contact temperature measurement was placed as close as possible to the crosshead. Heat loss due to low wire mass was minimized. An optional hot air preheater was included in the design to avoid heat loss after the induction preheater.

Good electric insulators are generally also good thermal insulators. Because of the volume of captive nitrogen cells acting as a thermal insulator, the highly expanded products were difficult to cool. With an expansion of 70% and reduced mechanical strength, these products required high cooling efficiency combined with gentle handling. The cooling line was configured to enhance cooling efficiency while limiting elongation through wire drag in the cooling trough. An original combination of immersion, spray and V plates provided the optimal solution. The versatile cooling line could be easily modified from immersion to spray or no water-cooling depending on the process.

At production start-up, the fine wire must put in motion all the non-driven pulleys of the line and tolerate transitory tension unbalance. In order to facilitate the task and reduce in-line elongation, the multipass-cooling trough was modified with a second motor. As usual, a 3.8 Kw Ac motor was found on the master capstan equipped with a drum. At the other extremity, five multipass pulleys each made up of 3 grooves, rotated on a driven

shaft with ball bearings. The shaft was driven with a 0.75 Kw AC motor. This configuration succeeded in combating drag and resulted in smooth line start-ups with the benefit of low-tension during production.

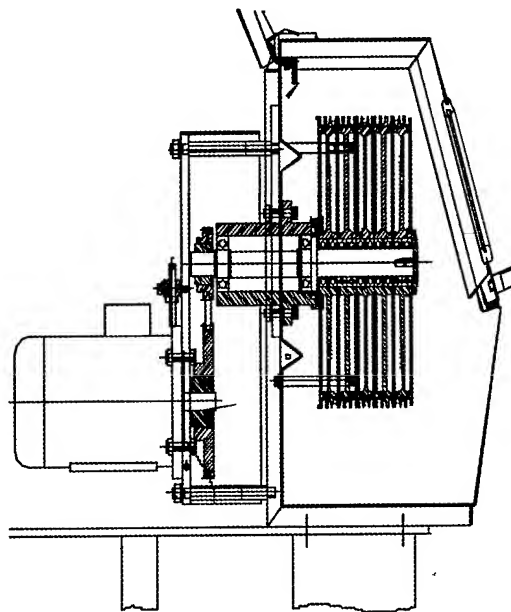


Figure 3: multipass trough OV 4-350 with driven pulleys

4. Process industrialization with a new patented C/D control

With all components and process parameters fine-tuned to the demanding requirements, our attention was brought upon the widely accepted model of C/D control.

A traditional C/D control found on high-speed insulation lines has three control loops. Two loops control capacitance by acting on the mobile trough position and the flow of nitrogen to the extruder. The third loop controls diameter by adjustments on either extruder speed or line speed. These three control loops are interdependent. The closed loop system takes into account the modification of one parameter to correct another as outlined in the following:

Standard diameter control:

- line speed or extruder speed

Standard capacitance control:

- injection pressure of the nitrogen
- mobile trough position for fine tuning.

During our study it became obvious that the standard C/D model was not well adapted to the FEP foam process. The limitations were shown to be:

- Mobile trough positioning offered too small a window for correcting capacitance ($\square 4$ pf/m for 0% to 50% and not effect beyond)
- Slight adjustments of injection pressure resulted large capacitance swings and long delays

We had also made the following observations:

- Expanded insulation applied with tube tooling is sensitive to the length of the extrusion cone
- Capacitance and diameter are modified by cone geometry
- At a given temperature, the expansion of the insulation is dependent on the:
 - injection pressure
 - cone length
 - position of the mobile trough

A new development for C/D regulation of FEP foam was required. The idea was to take into account the use of tube style tooling for the production of expanded insulation. This meant linking expansion variations to cone length. Cone length would therefore become a new process parameter.

New diameter control:

- line speed or main extruder speed

New capacitance control:

- cone geometry
- mobile trough position.

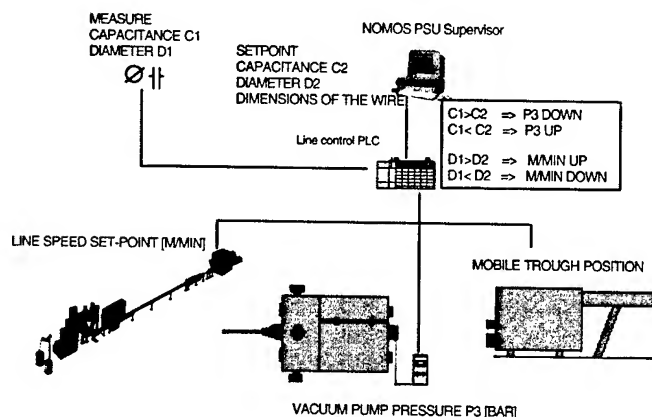


Figure 4: new C/D control for expanded layers applied with tube tooling

The feasibility of the new C/D control was demonstrated through a series of trials. The target was to characterize a new actuator to determine the correction window – capacitance variation versus cone length variation.

The work done shows that cone length control influences capacitance and diameter without interfering with other wire parameters. If the system is used within defined limits, then parameters such as ovality, concentricity and adhesion are not altered by the use of the cone length control. When crossing these limits we could detect an effect on the concentricity and on the cell's structure. The average cell size of 17 microns for an expansion of 55% is doubled when exceeding the limit. The concentricity value drops radically. With the help of these observations on the quality of the wire, we could easily define the working range of the new C/D cone control.

From this sequence of trials, a model was built to extract the best working conditions for the new C/D control. This basis allowed us to determine the critical working point for a precise process parameter. Whether the priority parameter during wire production is capacitance stability or cell structure, the optimal cone length shall be different.

The values mentioned above were the maximum correction variations we could reach without altering the minimum required quality of the wire. The correction window of 16 pf/m was wide enough to limit the cone's length variation to less than ± 10 mm. The stability of the NMC 45-30D extruder does not require a correction value of more than ± 5 pf/m. An adjustment of just a few millimeters of cone length was sufficient to balance a capacitance variation due to temperature instability or a compound batch change. The correction limit was fixed in order to stay within the predetermined quality border.

The large variations due to injection pressure in the extruder encouraged us to eliminate injection pressure from the new C/D control. The cone length control had a sufficient effect on the capacitance value without the disadvantage of latency time from injection pressure variation. When using injection pressure variation, the delay between the modification of the set point and the effect on the wire in relation to the extruder's speed reached 3 to 4 minutes. Cone length control had an immediate effect on the actual value of the capacitance. If a deviation was detected the algorithm immediately corrected the set-point value.

This patented C/D control has been tested mainly with FEP resin. However, the concept is not limited to fluoropolymers. We expect its use with most expanded layers that require tube tooling.

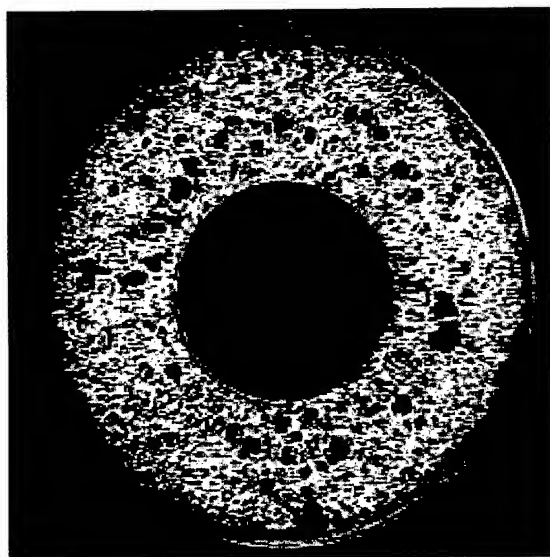
The new C/D control using cone length equips all our fluoropolymer insulation lines having the Extrucell™ process for high-pressure nitrogen injection. Maillefer currently has a patent pending for this new C/D concept, which applies to tube tooling extrusion in general. The reliability and the stability of capacitance are radically improved without altering other quality parameters.

Equipped with the new C/D control, the FEP foam process has come of age for mass production. Scrap reduction and tighter tolerances resulting from the robust and fine C/D control improves the productivity of insulation lines. Each minute of production saved increases manufacturer competitiveness. Having a properly adapted C/D control that responds quickly means faster start-ups to within tolerance and reduced risks of generating scrap during production runs.

5. Technological transfer for the LAN cable CAT 6 and CAT 7 production

The development project for the production of micro wire resulted in new components and process improvements listed in the previous pages. However, these innovations were not limited to the production of fine wires. They are now being benchmarked to other areas such as LAN cable. The main benefits found are the stability of the FEP foam process with the new C/D control; plus the improved cell structure of PE and FEP insulation gained through process fine-tuning and new components. One concern, the sufficient mechanical strength of the insulation, is not lost at

the price of higher expansion rates and a lower dielectric constant. The expanded wire is prepared to face the next process steps – pairing and assembly. The resulting cables achieve performances going up to category 8 LAN tested at 1.2 GHz.



Wire construction:

conductor: 0.568 mm
overall diameter : PE: 1.35 mm
inner skin PE: 15 microns
outer skin PE: 60 microns
capacitance: 92 pF/m
expansion: 70%

Wire quality:

diameter tolerance: ± 10 microns
capacitance tolerance: ± 1 pF/m
cell structure: max 60 microns
min 10 microns
average 30 microns
concentricity: 95%

Figure 5: SFTP LAN cable in PE expansion of 70%

6. Conclusion

The optimized process has resulted in high-level performances. Expansion rates of up to 70% were reached on AWG 32 conductors with a PE skin-foam-skin construction. A FEP foam-skin construction reached 58% expansion for AWG 27 conductor. That level of expansion has required an optimization of the cell's structure to maintain sufficient mechanical strength. An involved study was undertaken on cell growth versus various control parameters. As a result, a sample with an average cell structure of 17 microns was produced under industrial conditions, where the minimum cell measured 10 microns and the maximum 25 microns.

The results from process fine-tuning and the design of new high-quality components have exceeded expectations. Not only have the innovations of high expansion rates, low pulling tensions and high quality productivity been incorporated into a specific micro-wire line package, but they are being introduced across a series of LAN cable lines. Making fine micro-wire has also benefited developments within the area of Cat 8 LAN cable.

These capabilities have opened new processing windows for cable designers. The innovative tools, which include cool low-flow gas injection, low-tension dual driven capstan and a reliable C/D regulation using cone length, are all available now. Cable makers

have the means for moving the highly expanded small diameter wires from the design desk into a competitive manufacturing environment.

7. References

- [1] Bluetooth V1.0
- [2] Universal Serial Bus Specification
Revision 2.0; 2000
- [3] IEEE 1394-1995 High Performance Serial Bus Specification
- [4] Electronique; Mai 2001; N° 144
USB 2.0: Plus qu'une affaire de débit

About the author

Pierre-Yves Bonvin graduated from the Swiss Federal Institute of Technology in 1994 with an Engineering degree in Microtechnology. He joined Maillefer in 1994 as a commissioning engineer and was promoted in 1997 to project engineer. Since 1998 he has been Product Manager for insulation lines and is responsible of the process and product development team for copper telecommunications.

Pierre-Yves Bonvin
Maillefer S.A.
Route du Bois 37
1024 Ecublens, Switzerland
Phone: +41 21 694 41 11
Direct: +41 21 694 44 96
Mobile: +41 79 446 30 35
Fax: +41 21 694 44 74
pierre-yves.bonvin@maillefer.net



Development of Novel Crosslinkable Polyester Elastomers for Automotive Wire and Cable Applications

William Z. Wan and Anthony E. Listro

Judd Wire Inc.
Turners Falls, MA, USA
+1-413-863-4357 · wwan@juddwire.com

Shinya Nishikawa, Hiroshi Hayami, Satoshi Shukushima

Osaka Works, Sumitomo Electric Industries, Ltd.
Konohana, Osaka, Japan
+86-6-6466-5638 · nishikawa@okk.sei.co.jp

Abstract

The current technical trends for engine room wire harness require wires having high heat resistance and reduced wall thickness. These wires must possess excellent physical abuse characteristics, chemical resistance and hydrolysis resistance, and good flexibility. Judd Wire Inc. and the New Chemistry Research Department of Sumitomo Electric Industries, Ltd. have jointly developed two new and unique crosslinkable polyester elastomers to successfully meet the above tough requirements. One material is designed for use as an insulation system for thin wall automotive applications or as a jacketing material for heat resistant multi-conductor cables, and another has been developed as an insulation system for ultra thin wall wiring systems. Both of these materials exhibit excellent mechanical properties, very high heat resistance and chemical resistance. They are both crosslinkable and very flexible. During this product development, new hot water resistance and flexibility testing facilities and/or procedures were developed.

Keywords

Polyester, thermoset elastomer, ultra thin wall, cross-link, hot plate test, heat aging, hydrolysis, flexibility.

1. Introduction

Insulation materials used in engine harness wiring in automotive applications must utilize polymers excellent in certain key criteria. These include flexibility, physical abuse characteristics, such as cut through resistance and abrasion resistance, hot water resistance, heat resistance and flame retardancy. These characteristics are necessary from three standpoints: engine harness design, harness manufacturing and end-use application.

The engine harness designer has faced an increased challenge as the amount of electronics devices and sensors has increased. Meanwhile, the space in the engine compartment and instrument panel has decreased over the past several years as new car designs have increased the passenger volume and storage compartments. Electronics technology and consumer demand has made many electronic features common in today's automobiles. The reduced

space in the engine compartment has resulted in increased temperatures in this area of the vehicle. A continuous use temperature of 150°C is common in the engine compartment. Further, the increase use of electronics and decreased engine compartment size has led to the demand of high temperature wires having ultra thin wall thicknesses such as 0.25 mm or 0.20 mm wall thickness.

Since many wires are typically bundled together in a harness, engine wiring must be flexible in order to route the harness in place on the vehicle. The automotive industry does not have a standard method to measure and quantify flexibility of insulated wires. In addition to flexibility, the wire may be exposed to physical abuse such as cut-through or scrape abrasions during the harness manufacture processes and installation. Therefore, toughness of the insulation material is critical especially for an ultra thin wall insulation. Key criteria are measured by pinch resistance or by sandpaper (and scrape) abrasion resistance. Pinch resistance is specified by SAE and is conducted by determining the load to failure when placing the insulated wire between an anvil and a mandrel and then subjecting the insulated wire to a load rate of 2.3 kg/minute. Sandpaper abrasion is specified in SAE specifications and the insulated wire is subjected to sandpaper of a specified grit moving at a specified rate while under load and the length of sandpaper necessary to abrade the insulation is recorded. Scrape abrasion (specified in ISO 6722) is similar except the wire is subjected to a moving needle or blade under load.

Heat resistance, flame retardancy and hot water resistance are the three criteria that are most critical in the end use application of the wire. Heat resistance is determined by performing the 3000 hour aging test at the rated temperature. For example, if the continuous temperature rating is 150°C, then the insulated wire sample is exposed to 150°C for 3000 hours. The wire is then subjected to a mandrel wrap followed by a wet dielectric test. No cracking or dielectric failure is allowed. Flame retardancy is another key criteria for engine harness wire. The test consists of fixing the insulated cable at a 45° angle, holding a flame perpendicular to the

wire for 15 seconds and then removing the flame. The flame must then extinguish within 70 seconds and a minimum of 50 mm of insulation must remain at the top of the sample once the flame has extinguished. The hot water test is performed to determine the insulation materials ability to resist hydrolysis or electrochemical degradation. The insulated wire is subjected to a salt water bath containing 10 g/L of NaCl in water at 85°C. The wire is wrapped around a mandrel having a specified diameter and then placed in the water bath. A copper electrode is placed in the bath. A 48 V DC power source is then connected to the wire sample and the electrode. Two samples are tested. One sample is tested with the positive lead to the electrode and another sample is tested with the positive lead to the conductor of the wire sample. The power source is removed every 7 days and the insulation resistance is measured. The insulation volume resistivity (calculated from this measurement) shall not be less than 10^9 ohm-mm. This procedure is repeated for a total of five cycles, 35 days. A visual inspection of the sample is made after this exposure and no cracks in the insulation are allowed. Finally, a wet dielectric test is performed on the sample.

Thermoplastic elastomers are excellent candidates as a class of materials possessing desirable characteristics to meet the design, process and end-use characteristics outlined above. These materials offer the ability to be produced in ultra thin walls, excellent abrasion and cut-through resistance and when properly designed, outstanding heat age and hot water resistance, and a very attractive cost-performance balance. As a subset of this class of materials, polyester elastomers are most attractive polymers because they are excellent not only in flexibility but also in abrasion resistance and thermal aging resistance. These materials can be modified through the addition of special additives and are crosslinkable by electron beam irradiation, both of which improve their wet electrical properties and their ability to comfortably and consistently meet the stringent hot water resistance tests.

Polyester elastomers are block copolymers comprising a crystalline hard segment such as poly(butylene terephthalate), made up of repeating units derived from terephthalic acid and 1,4-butanediol, and a non-crystalline soft segment derived from polyether glycol or ϵ -caprolactone. The flexibility of these polymers can be tailored by varying the ratio of the hard to soft segments and the crystallinity of the hard segment.^[1]

Judd Wire Inc. and the New Chemistry Research Department of Sumitomo Electric Industries, Ltd. have jointly developed two novel modified crosslinkable polyester elastomers to meet the above tough requirements successfully. One material is designed as an insulation system for thin wall automotive applications or as a jacketing material for heat resistant multi-conductor cables, and another has been developed as an insulation system for ultra thin wall wiring systems. While both materials exhibit excellent flexibility, the former material is designed to be more flexible than the latter. Both of these materials exhibit excellent mechanical properties, very high heat resistance (above 150°C continuous operating temperature), hot

water resistance and chemical resistance, and are crosslinkable and very flexible.

2. Materials Development

2.1 Hot Water Resistance

As previously mentioned, polyester elastomers have many excellent physical properties. However, the polymer architecture must be carefully designed in order for the polymer to resist hydrolysis. If the polymer itself is improperly designed and/or formulated, these materials may be susceptible to hydrolysis if exposed to hot and humid environments. Simply stated, hydrolysis is depolymerization of the base resin. Since polyesters are condensation polymers, meaning that water is a by-product of the polymerization reaction, their molecular weight may significantly drop in the presence of heat and water. The performance of polyester elastomers in this regard varies greatly depending on the composition of the soft segment and the hard to soft segment ratio. Typically, the hydrolysis resistance of polyester elastomers for wire insulation and cable jackets for use in automotive applications are further improved from their base resins by properly formulating stabilizer(s) into the base resins therefore greatly improving their hydrolysis resistance.

2.1.1 Hot Water Resistance Test Facility Development/ Improvement

In automotive industry, insulated wire must meet the Hot Water Resistance Test (per Specification J1128 or J1678). This test is designed to determine the ability of the insulation to withstand a very corrosive environment and to determine the hydrolysis resistance of the material. This test method was utilized during the development of these new polyester elastomer materials. So far, a testing facility to perform this test is not commercially available. Per the specifications, this test takes up to takes 35 days to complete; to speed up our research, it was necessary to develop the a facility in which multiple specimens could be tested concurrently while still keeping accurate results.

A hot water resistance test facility was setup to test multiple specimens, which greatly expanded our testing capacity. The assembly was designed utilizing a parallel connection for the test specimens. Independent timers were employed to accurately record individual specimens' performance.

2.1.2 Hot Water Resistance Tests

- (1) Effect of test power polarity on hot water resistance results: Per the test procedures, there are two test polarity requirements: one is positive to the electrode (negative to wire sample), and another, negative to electrode (positive to wire sample); both tests are required. Both polarities were tested.
- (2) Hot water resistance screen tests: We made insulated wires using our compound candidates and then tested their hot water resistance per J1128/J1678 using our new test facility.
- (3) Improved hot water resistance: Formulation K69-1 was altered to create K69-2 by modifying the hydrolysis stabilizer package, then its hot water resistance was tested. The wire construction for both K69-1 and K69-2 was 0.35mm² conductor with a 0.2mm nominal wall thickness.

2.1.3 Results and Discussion

- (1) With the new test facility, the effect of test DC power polarity on hot water resistance test results is shown in

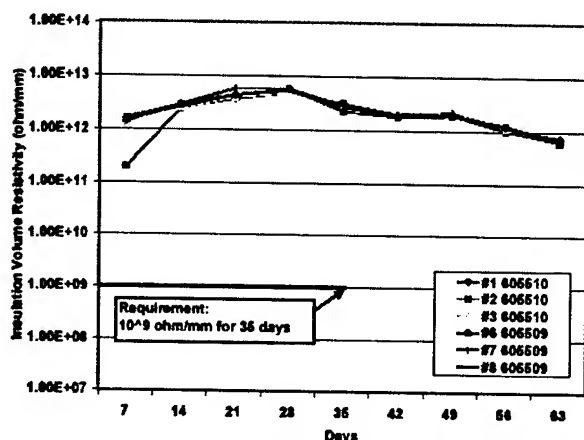


Figure 1a. Hot Water Resistance - Positive to the Wire Sample

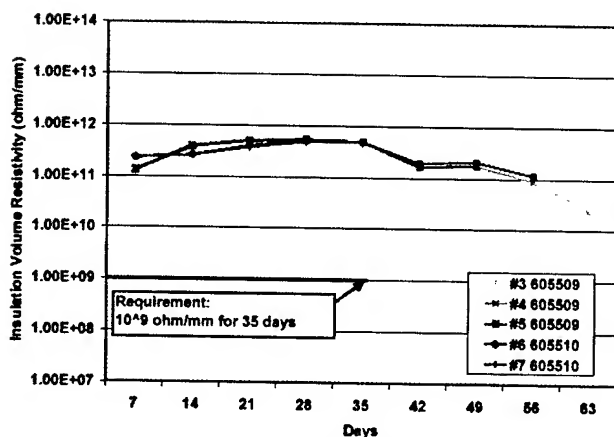


Figure 1b. Hot Water Resistance - Positive to the Electrode

Figures 1a and 1b. In this experiment, it was determined

that all of the tested specimens could last much longer in the hot water test when positive polarity was to the wire, compared to the ones with positive to the electrode. It is clear that positive to electrode is a much tougher test procedure for our polyester materials. In other words, as long as our polyesters could pass the tests with positive to electrode, they would well pass the resistance requirement with positive to the wire.

- (2) Hot water resistance screening: Two new compounds, X14 and K69-1 were effectively screened out. Their hot water resistance curves are shown Figure 2 and Figure 3, respectively. Obviously, both of them are well above the specification requirements. K69-1 performed slightly better than X-14 due to differences between these two insulations' base resins and/or formulations which were deliberately differentiated for different potential applications. The difference between the time that each material lasted in the

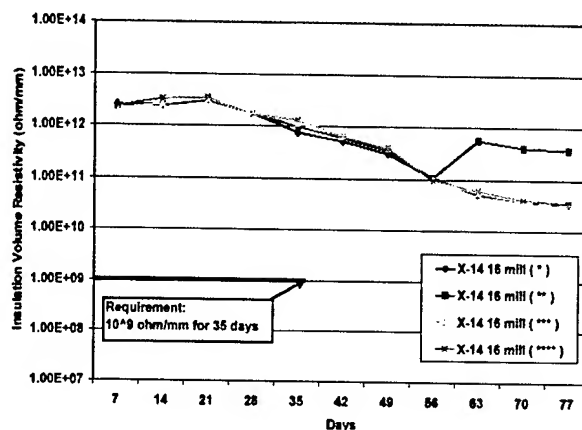


Figure 2. Hot Water Resistance Positive to the Electrode - X-14

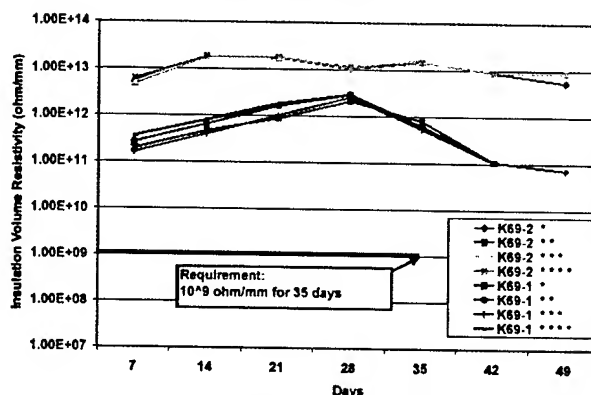


Figure 3. Hot Water Resistance Positive to the Electrode - K69-1 vs. K69-2

test before experiencing a failure is believed to be due to the influence of the wall thickness. The X14 sample had a wall thickness of 0.4 mm and the K69-1 sample had a wall thickness of 0.2 mm.

- (3) Figure 3 shows the hot water resistance improvement from K69-1 to K69-2 through our formulation change (modification of stabilizer package). This demonstrates that K69 type polyester was further improved to increase its hydrolysis resistance per final application requirements.

2.2 Wire Insulation and Bundle Flexibility

There is a popular flexibility test method for aerospace wires and cables per BSS7324. Its procedure I is for single wires, combining conductors and insulations, while the procedure II is specifically designed as a wire shop evaluation test (to inspect the deformation of jacket layer when using wires to make cables in the shop). There is also a "Fish-Scale" flexibility test used in the automotive industry. The "Fish-Scale" method involves tying a bundle of wires of a specified length together, placing them on two mandrels separated by a specified distance, and then measuring the force required to deflect the center of the wire bundle through the mandrels at a specified distance. This method is repeated using bundles of various wire counts. The data generated using this technique is utilized to precisely route the wire harness within a vehicle such that there is minimum movement of the harness in the vehicle. The BSS7324 procedures are designed for aerospace, and "fish-scale" method is a manual test where the results are not automatically recorded. For characterizing our very flexible polyester insulations due to their base resins intrinsic properties, formulations and processes, effective methods were selected, developed and/or modified to demonstrate the flexibility of both the crosslinked insulation itself and bundles of insulated wire samples.

2.2.1 Wire Insulation Flexibility: Stress-Strain Curve (DMA Method)

Stress-strain curves are common in materials engineering. Therefore, we employed this method to determine the intrinsic flexibility of K69-2 and X-14 polyester elastomers themselves. In other words, this is a measure of the flexibility of the material itself without the influence of conductors and the data are normalized to eliminate the effect of wall thickness. We selected a dynamic mechanical analyzer (DMA) since it produces a precise stress-strain relationship and a high resolution for tested materials.

Experiment:

Equipment: Dynamic Mechanical Analyzer, Model: DMA 2980

Samples: Stripped (tubular-shaped) wire insulations; wall thicknesses: 0.4 mm for X14, 0.2 mm for K69-2 and 0.25 mm for a commercial product.

Test Temperature: Room temperature (25 °C)

2.2.2 Wire/Cable Bundle Flexibility: Bundle Flexibility Test Method

In automotive harness applications, wires are very often used in bundles, instead of single wires. To simulate these situations, we decided to test bundles of finished wire to determine their

flexibility. A simple (user-friendly), meaningful and automated recording method was developed. An attachment was made for an Instron (a microprocessor controlled universal mechanical tester) that partially takes the idea from "Fish-Scale" method. This assembly is shown in Figures 4 and 5. In this assembly, two mandrels with $\frac{3}{4}$ inch (19 mm) diameter and a distance (center-to-center) of 4 inches (100 mm) were attached to a plate that was fixed to bottom of the Instron. The test bundle is held against and forced through these mandrels by a hook. The hook was attached to the upper jaw of the Instron and was placed at the center of the bundle. The test is conducted by starting the Instron, which automatically pulls the bundle upward bending the bundle. The Instron automatically records the pull force versus distance as the bundle moves through the mandrels. The maximum pull force is obtained from these results. Obviously, the stiffer a bundle is, a higher maximum pull force is obtained.

Since this method is to test a bundle, individual wire size, conductor, wall thickness and wire number involved in the bundle, will all affect the results.

Experiment:

Equipment: Instron (Model: 4467) with attachment (see Figure 5)

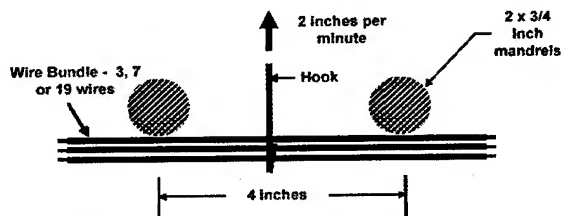


Figure 4. Schematic Diagram of Bundle Flexibility Test

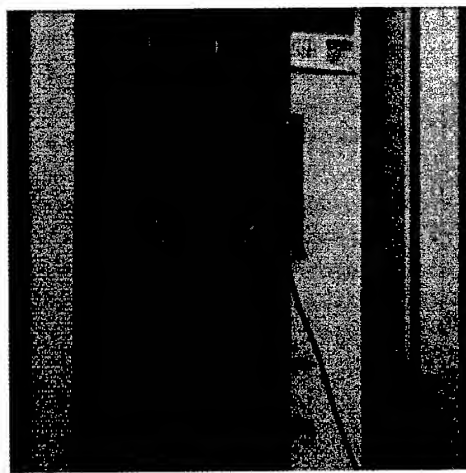


Figure 5. Picture of Bundle Flexibility Test Setup on Instron

Samples: X14 and K69-2 insulated wires and a comparative product

Wire Bundles: 3, 7 and 19 wires, respectively, all 25mm long with 0.5 mm² 7/0.316 conductor having a 0.25 mm wall thickness

Instron Pull Rate: 2 inch (50mm) /minute

2.2.3 Results and Discussion

- (1) The wire insulation stress-strain curves (DMA method) are shown in Figure 6. These curves clearly indicate that the insulation of the comparative product is very stiff, K69-2 is more flexible and X14 is most flexible. Stress-strain relationships eliminate, in theory, the wall thickness effects on the results. Therefore, we may directly compare the flexibility of different materials even if they have different wall thicknesses. There is no quantitative specification requirement for flexibility in the automotive industry even though wire users typically express a desire for wire flexibility. K69-2 and X-14 may well meet this requirement.

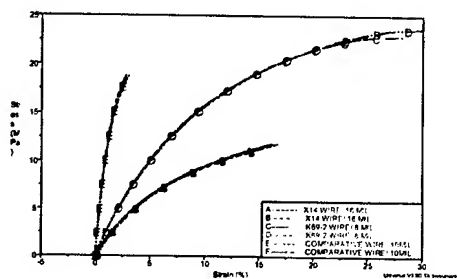


Figure 6. Stress - Strain Curve @ 25°C

- (2) The wire bundle flexibility test results are summarized in Figure 7. From the curves in Figure 7 it is observed:
 - (a) X14 or K69-2 is much more flexible than the current comparative product, though all of these three wires have exactly the same constructions.
 - (b) The force required to bend a bundle is not linear with respect to the bundle size. Up to a 19-wire bundle was tested. If bundles contain more wires, the difference between the maximum (pull) forces required to bend the comparative and Judd products will be further increased. In other words, when a bundle contains more wires, like a big harness, Judd products may bring more benefit for harness installation through their flexibility.
 - (c) An interesting phenomenon is that K69-2 insulated wire has slightly better bundle flexibility than X14, which has better intrinsic material flexibility. This may be caused by the difference in these materials surface texture and hardness.
- (1) The flexibility of Judd's polyester wire samples were compared with Judd's 150°C crosslinked polyethylene (XLPE), all having a nominal wall thickness of 0.4 mm; the

result is shown in Figure 8. Unexpectedly, it was found that the polyester material is much more flexible than XLPE.

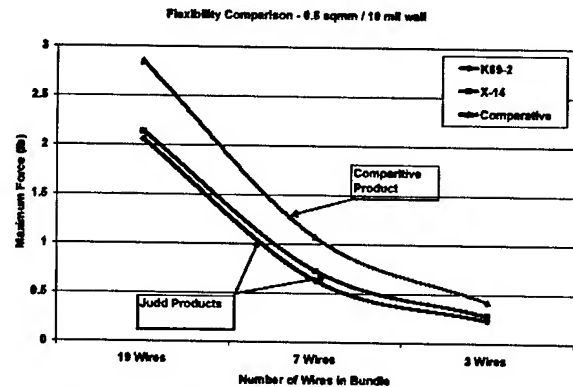


Figure 7. Results of Bundle Flexibility - Comparison of Polyester Materials Test

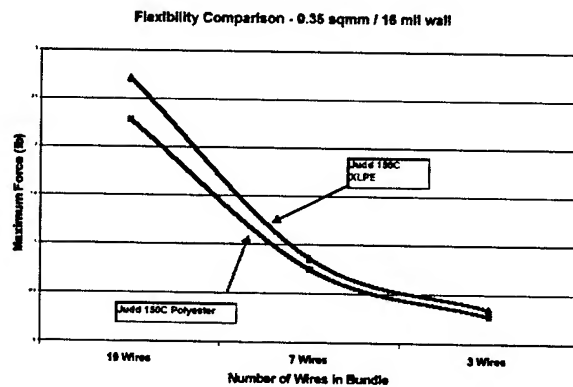


Figure 8. Results of Bundle Flexibility Test - Polyester versus 150°C XLPE

2.3 Heat Resistance

The heat resistance of insulated wires and jacketed cables is so important since every automotive wire or cable has a temperature requirement or continuous temperature rating per industry and application specifications. The demand for higher temperature wire and cable applications in the automotive industry has increased in the last decade. K69-2 and X-14 polyester elastomers were optimized through polymer chemistry and formulation to possess excellent heat (aging) resistance.

2.3.1 Heat Resistance Tests/Experiments

The following tests were completed to determine the heat resistance of K69-2 and X-14:

- (1) Long Term Aging: X14 and K69-2 were tested per Specification SAE J1678 at 150°C for 3,000 hours.
- (2) Short Term Aging: X14 and K69-2 were tested per Specification SAE J1678 at 175°C and 200°C for 240 hours.
- (3) The tensile strength and elongation (T&E) retention were tested at high temperatures.

2.3.2 Results and Discussion

The results of the long term and short term aging tests are shown in Table 1.

Table 1. Results of Aging Tests per J1678

		Long Term Aging (3000 hours)	Short Term Aging (240 hours)	
Insulation	Construction	150 C	175 C	200 C
X14	.35mm ² /4mm	3 of 3 Pass	n/a	3 of 3 Pass
X14	.35mm ² /4mm	3 of 3 Pass	3 of 3 Pass	3 of 3 Pass
K69-2	.35mm ² /2mm	3 of 3 Pass	3 of 3 Pass	3 of 3 Pass
K69-2	.5mm ² /2mm	3 of 3 Pass	n/a	3 of 3 Pass

indicate the likelihood that these materials are capable of qualifying at a continuous temperature rating much higher than 150°C rating.

- (c) Some data show higher than original tensile and elongation results were obtained after short term heat aging, this phenomenon is demonstrates that these materials are very heat resistant. and
- (d) K69-2 has a better retention than X-14 at 210°C.

2.4 Crosslinking Proof

Crosslinking of polymers sets up chemical links between their long molecular chains so as to form a three-dimensional network. Therefore, crosslinking significantly changes a polymer's thermal, chemical and physical properties. There are two types of crosslinking: chemical and irradiation. Judd employs electron beam irradiation for crosslinking. In the case of insulation materials for wire and cable, the beneficial results of irradiation crosslinking are: improved mechanical properties (such as tensile strength, cut-through resistance, pinch resistance, abrasion resistance), chemical resistance, and heat resistance. Crosslinking is a very important and efficient method to improve materials properties.

Though crosslinking may bring many benefits for materials performance, not all materials are crosslinkable. Some materials are even degraded by the irradiation process, which greatly reduces their performance. Judd/SEI polyester elastomers are designed to be crosslinkable through their chemical structures and formulations.

Table 2. Results of X14 and K69-2 Hi-T T&E Retention

Insulation	Construction	Original		165 C		180 C		210 C							
				168 hr		168 hr		16 hr				168 hr			
		TS	EI	TS	EI	TS	EI	TS	EI	TS	EI	TS	EI	TS	EI
		(MPa)	(%)	(MPa)	(%)	(MPa)	(%)	(MPa)	(%)	(MPa)	(%)	(MPa)	(%)	(MPa)	(%)
X14	.35mm ² /4mm	51.2	380	58.4	380	30.4	335	51.5	355	33.0	275	18.9	170		
	.8mm ² /4mm	50.4	380	55.5	385	30.3	325	43.8	435	33.6	280	n/a	n/a		
K69-2	.35mm ² /2mm	42.1	310	49.7	325	n/a	n/a	60.3	360	n/a	n/a	33.3	220		
	.5mm ² /2mm	26.5	305	n/a	n/a	n/a	n/a	44.6	385	n/a	n/a	28.9	235		

- (1) Long term aging: All tested specimens of X14 and K69-2 favorably passed all requirements following 3000 hour exposure at 150°C.
- (2) Short term aging. The aging results are summarized in Table 1. From the table, it is clear that both X14 and K69-2 may reach 200°C short term aging requirements per J1678.
- (3) Insulation tensile strength and elongation retention. The test results are summarized in Table 2. From the table, it is shown:
 - (a) K69-2 and X-14 polyester elastomers have very high original tensile strength (from 26.5 MPa to more than 51 MPa), and favorable elongation (>300% to near 400%).
 - (b) More importantly, they kept high tensile and elongation retention even at 210°C; these excellent retention results

2.4.1 Crosslinking Proof Test

There is a simple method to test the proof of crosslinking called the Hot Plate test per SAE J1678. In this method, an insulated wire sample is placed on a pre-heated plate at 250°C ± 25, with a mandrel under a force of 5 to 7 N for 5 to 6 seconds. This high temperature exposure is then followed by the Withstand Voltage test per J1678. The Hot Plate test is used to check if finished products are properly crosslinked. We utilized this method to test our finished wire samples. Every wire construction described in this paper were tested per this method. All specimens very easily passed this test since these materials are all properly crosslinked.

2.4.2 Discussion

Many excellent properties of these polyesters previously discussed are related to the fact that the material has been crosslinked. These include not only mechanical properties and chemical resistance, but also and especially, the heat resistance.

Judd/SEI polyesters not only have excellent both short term and long term heat resistance, but may also meet challenging severe short term temperature exposure, such as thermal shock, due to their crosslinked structures. Some non-crosslinked materials can reach high temperature rating, say 150°C, when used at below their melting points. If they, however, meet thermal shock that is higher than their melting points, they will be melt and fail in the application.

2.4.3 Pinch Resistance and Abrasion Resistance

The tensile strength and elongation data of K69-2 and X-14 described and discussed in section 2.3 Heat Resistance are an indication of the toughness of these materials. Other key properties related to the physical abuse characteristics of the materials, including pinch resistance and abrasion resistance were investigated.

2.5 Pinch Resistance and Abrasion Resistance Tests

(1) Pinch Resistance Test

Test procedure: Specification J1678 or J1128.

(2) Sandpaper Abrasion Resistance Test

Test procedure: Specification J1128.

(3) Scrape Abrasion Resistance Test

Test procedure: Specification ISO 6722

Different constructions insulated with X14 and K69-2 were tested.

2.5.1 Results and Discussion

(1) The test results of pinch resistance and abrasion resistance (both sandpaper and scrape methods) are summarized in Table 3.

(2) X14 and K69-2 exhibited excellent pinch resistance and abrasion resistance. For example, J1678 requires 0.5kg pinch resistance for 0.20mm insulation thickness, yet we reached 7.55 kg. Also, the requirement per J1128 for a 0.35 mm² having a 0.40mm nominal wall thickness is 2.7 kg for pinch resistance and

Table 3. Results of Pinch Resistance and Abrasion Resistance

Insulation	Construction (wire size/wall thickness)	Pinch Resistance (kg)	Sandpaper Abrasion Resistance Bracket A, 0.22kg (mm)	Scrape Abrasion Resistance (cycles)
X14	.35mm ² /.4mm	8.14	1011	913
X14	.8mm ² /.4mm	7.94	1359	1247
K69-2	.35mm ² /.2mm	7.55	228	158
K69-2	1.0mm ² /.4mm	7.63	2195	1448

250 mm for sandpaper abrasion resistance. Values of 8.14 kg for pinch and 1011mm for sandpaper abrasion were obtained on these wire samples - about 2 to 3 times higher than the specification requirements. These high pinch and abrasion resistance values and the high tensile strength and elongation previously discussed demonstrate the excellent physical abuse characteristics of these polyesters. While these materials maintain excellent flexibility

(they are elastomers), they are also tough (strong) in mechanical properties; this special combination is heavily related to the fact that these insulation systems are crosslinked.

2.6 Flame Resistance and Fluid Compatibility

Flame resistance (retardancy) is a must for automotive wire and cable. Fluid compatibility, a type of chemical resistance, is also important, especially for engine harness type of applications. Both of them have clear specification requirements, such as per J1678 or 1128.

2.6.1 Flame Resistance and Fluid Compatibility Tests

(1) Flame Resistance

Test procedure: J1678 or J1128.

Every wire construction described in this paper was tested per this method.

(2) Fluid Compatibility

Test procedure: J1678 or J1128. The outer diameter (OD) of the test specimen is measured. The procedure specifies that test specimens be separately immersed in the eight fluids and specified temperatures shown in Table 4. The immersion time is 20 hours for each fluid. After immersion, the OD of each specimen is measured and the percent swell (OD change) is calculated and must not exceed the specification requirements. The samples must then pass the mandrel wrap (no cracks) and withstand voltage tests.

Different constructions insulated with X14 and K69-2 were tested.

2.6.2 Results and Discussion

(1) Flame Resistance

All test specimen, insulated with either X14 or K69-2, favorably passed the flame resistance test. The burn times were from 3 to 22 seconds (maximum), with an average of about 10 seconds or less, while the SAE specifications allow up to 70 seconds.

The results indicate that K69-2 and X-14insulations posses excellent flame resistance.

(2) Fluid Compatibility

The test results are summarized in Table 4. All of the tested specimens had favorably passing results. The OD changes were from 0% (no change) to less than 25% (one-fourth of maximum) of the spec allowed changes. The samples passed the mandrel wrap and withstand voltage tests. The results show that K69-2 and X-14 polyesters have excellent compatibility with all of these fluids.

Table 4. Results of Fluid Compatibility per J1678 or J1128

Fluid	Test Temp. (°C)	OD Change Allowed (%)	Sample	Results		
				OD Change (%)	Met Mandrel Wrap & Dielectric Requirements	Final Result
Engine Oil (IRM-902)	3. 50±3	15	X14, .35mm ² /.4mm	0.5	Yes	Pass
			X14, .8mm ² /.4mm	0.8	Yes	Pass
			K69-2, .35mm ² /.2mm	-0.2	Yes	Pass
			K69-2, 1mm ² /.4mm	-0.5	Yes	Pass
Gasoline (Ref. Fuel C)	4. 23±5	15	X14, .35mm ² /.4mm	3.7	Yes	Pass
			X14, .8mm ² /.4mm	2.7	Yes	Pass
			K69-2, .35mm ² /.2mm	0.1	Yes	Pass
			K69-2, 1mm ² /.4mm	0.2	Yes	Pass
5. Ethanol (Ethanol + Ref. Fuel C)	6. 23±5	15	X14, .35mm ² /.4mm	0.2	Yes	Pass
			X14, .8mm ² /.4mm	1.1	Yes	Pass
			K69-2, .35mm ² /.2mm	0.9	Yes	Pass
			K69-2, 1mm ² /.4mm	-0.3	Yes	Pass
Diesel Fuel (IRM-903 + p-xylene)	7. 23±5	15	X14, .35mm ² /.4mm	0.3	Yes	Pass
			X14, .8mm ² /.4mm	0.3	Yes	Pass
			K69-2, .35mm ² /.2mm	0.0	Yes	Pass
			K69-2, 1mm ² /.4mm	0.3	Yes	Pass
Power Steering (IRM-903)	50±3	30	X14, .35mm ² /.4mm	0.8	Yes	Pass
			X14, .8mm ² /.4mm	0.1	Yes	Pass
			K69-2, .35mm ² /.2mm	0.7	Yes	Pass
			K69-2, 1mm ² /.4mm	0.3	Yes	Pass
Auto Trans (Citco Dextron III SAE J311)	50±3	25	X14, .35mm ² /.4mm	0.6	Yes	Pass
			X14, .8mm ² /.4mm	0.1	Yes	Pass
			K69-2, .35mm ² /.2mm	-0.2	Yes	Pass
			K69-2, 1mm ² /.4mm	-0.1	Yes	Pass
Engine Coolant (Water + Ethylene Glycol)	50±3	15	X14, .35mm ² /.4mm	0.6	Yes	Pass
			X14, .8mm ² /.4mm	-0.7	Yes	Pass
			K69-2, .35mm ² /.2mm	0.9	Yes	Pass
			K69-2, 1mm ² /.4mm	0.0	Yes	Pass
Battery Acid	8. 23±5	5	X14, .35mm ² /.4mm	- 0.3	Yes	Pass
			X14, .8mm ² /.4mm	0.5	Yes	Pass
			K69-2, .35mm ² /.2mm	0.1	Yes	Pass
			K69-2, 1mm ² /.4mm	-0.1	Yes	Pass

Note: immersion period is 20 hours for any fluids.

3. Conclusions

Judd Wire Inc. and the New Chemistry Research Department of Sumitomo Electric Industries, Ltd. have jointly and successfully developed two novel crosslinkable polyester elastomers, K69-2 and X-14. It has been demonstrated that these materials possess excellent flexibility, tensile strength, pinch resistance, abrasion resistance, chemical resistance and have a continuous temperature rating of at least 150°C. The maximum continuous temperature rating has not been determined and will be the topic of future development efforts. These materials are suitable for high temperature applications for automotive industry. K69-2 was found to meet the requirements of insulation systems for ultra thin wall automotive applications. X-14 was determined to be suitable as an insulation system for thin wall wiring systems or as a jacketing material for heat resistant multi-conductor cables in automotive applications.

During this investigation, Judd Wire Inc. also successfully developed hot water resistance and wire bundle flexibility testing facilities and procedures that may benefit the automotive wire and cable industry.

4. Acknowledgments

Sincere appreciation is given to Nathan Duda, Bill Shattuck, Polly Wozny and Don Smith, for their preparation of wire samples and assembly of our new test facilities, processes improvements, manufacturing scale up, numerous testing, and lab experiments. Thanks also go to Jun Yi and Michael Ryan, for their support during Judd's wire bundle flexibility testing facility development; all other Judd Wire coworkers, for their cooperation and supports; and other professionals, for their assistance to compounding scale up. Special thanks to the New Chemistry Research staff at Sumitomo Electric Industries' Osaka Works for the evaluation of the dozens of formulations leading to the successful development of K69-2 and X-14.

5. References

- [1] G. Holden, N.R. Legge, R. Quirk, H.E. Schroeder, *Thermoplastic Elastomers*, 2nd ed., Hanser, Cincinnati, USA, p. 192 (1996).

6. Authors

William Wan
Sr. R&D Engineer
Judd Wire Inc.
124 Turnpike Road
Turners Falls, MA 01376
124 Turnpike Road
Turners Falls, MA 01376



William Wan received his BS in Electrical Engineering and Polymeric Materials from Shanghai Jiao Tong University, Shanghai, China; MS in Polymer Chemistry from Wichita State University, KS, USA. He worked for Polymeric Materials Research Institute and Department of Applied Chemistry, Shanghai Jiao Tong University, as Instructor; at Manis Pty. Ltd., NSW, Australia, and FPD Technologies Inc., TX, USA as Process Engineer. Since 1999, William Wan has been working with Judd Wire Inc., MA, USA as Senior R&D Engineer. 20+ papers; 1 patent pending. CCS and ACS, Member; SPE, Senior Member.

Anthony E. Listro
Director of Engineering
Judd Wire Inc.
124 Turnpike Road
Turners Falls, MA 01376



Tony Listro earned his BS and MS degrees in Plastics Engineering from the University of Lowell, Lowell, MA and his MBA from the University of Massachusetts, Amherst, MA. He worked as a Research Engineer for Quantum Chemicals from 1989 to 1993. Since 1993 he has worked in various levels of responsibility in Judd Wire's Engineering Department. Tony is a senior member of SPE, and a member of the SAE Cable Task Force and SAE AE-8D. He has authored six technical journal articles and holds one US patent.

Automotive Applications of Bimetallic Wire

Brian Suwarow and Alan Gibson

Copperweld Bimetallic Products

Fayetteville, Tennessee

+1-931-433-7177 · bsuwarow@ltv-copperweld.com, afgibson@aol.com

Abstract

This paper explains copper clad steel and aluminum wire and identifies opportunities to take advantage of the unique combinations of properties available with clad wire in automotive applications. It explains how the use of small copper clad steel cables for low current and signal leads can reduce both weight and wiring harness bundle size, and how copper clad aluminum can reduce the weight of power cables. Examples of components that have been built to demonstrate these applications are discussed in detail.

Keywords

Bimetallic; Automotive; Cable; Wire; Weight Reduction; Wiring Harness; Copper Clad Aluminum; Copper Clad Steel

1. Introduction

Bimetallic wire was first produced in 1915 by pouring molten copper around a steel billet, and working the resulting bimetallic ingot into bimetallic wire. Over the last nearly ninety years, both the manufacturing process and the product it yields have evolved into forms that only slightly resemble the results of those early efforts.

Today, bimetallic wire is produced by mechanically cladding rod of one metal with the flat form of another. This process is shown in the photograph of the first step in copper clad aluminum production in Figure 1.



Figure 1. Copper Strip Being Formed Around Aluminum Rod in Preparation for Bonding

In the figure, copper strip is being continuously formed around a moving aluminum rod in preparation for bonding. In this case the diameter of the rod is about 20 millimeters, and the strip thickness is approximately one-half millimeter. Just after the point at which the photograph was taken, the materials to be bonded receive processing which produces metallurgically clean surfaces on both the rod and strip, permitting them to form a metallurgical bond during subsequent thermomechanical processing. This metallurgical bond renders the cladding and substrate inseparable.

The modern cladding process is robust and flexible. It has been applied successfully to a variety of both substrate and cladding metals. The flat stock over rod process permits the cladding thickness to be engineered by adjusting the thickness of the flat stock and/or the diameter of the rod being clad. The thickness ratio established in the initial cladding operation is always maintained, no matter how fine the wire is eventually drawn.

Clad products are fundamentally different from plated wire products. Plated wire products, such as tinned copper, are essentially a wire of one metal with a thin surface layer of a second metal. The physical and mechanical properties of the wire are those of the wire material, for example copper. The surface characteristics are those of the plated layer, for example tin. Clad products, in contrast, are true composite materials, with mechanical and physical properties that approximate the weighted average of the two metals combined. The surface characteristics are those of the cladding metal. Clad products are distinguished from plated products because the clad layer is much more massive than typical plated coatings, as shown in Figure 2.



Figure 2. Metallographic Cross Section of Copper Clad Steel Wire 1mm in Diameter

Bimetallic clad wire products and plated wire products are not normally considered to be substitutes for each other. Plating lends itself to more economical production of thin surface layers, and where such layers are adequate, plated products are the usual choice. Clad products are chosen where true composite properties are desired, or a more massive exterior layer is required to achieve the desired performance. For example, the relatively thick clad layer on copper clad aluminum permits that material to be used for center conductors in coaxial cable, achieving lighter weight and lower cost, while maintaining the same impedance as copper. This application is possible because the clad layer is engineered to be sufficiently thick that the skin effect of the high frequency signal causes the signal to remain entirely within the clad layer of copper.

The same massive copper layer makes copper clad aluminum suitable for the automotive applications that are the subject of this paper. Clad copper layers are able to mitigate the tendency of aluminum to develop increasingly high resistance in connections. Thinner plated layers would be unlikely to survive and maintain effectiveness through the mechanical damage involved in crimping and the severe vibration and temperature extremes inherent in automotive applications.

While several clad wire products are produced commercially, the combinations of greatest commercial importance are copper clad aluminum and copper clad steel. Copper clad aluminum is most often used today as a lighter, lower cost alternative to copper in high frequency applications. Copper clad steel is widely used where a conductor with greater strength is needed, and reduced conductivity can be accepted.

These two products have excellent potential for automotive applications in two areas:

- The use of smaller copper clad steel cables for signal and low current leads that are sized based on cable strength rather than current carrying capacity. This reduces weight and wiring harness bundle size, as well as improving harness flexibility and facilitating installation.
- The use of copper clad aluminum to reduce the weight of battery cables and other power leads.

These two applications are the subject of this paper.

2. Bimetallic Clad Wire Products Recommended for Automotive Applications

2.1 Copper Clad Steel

The copper clad steel product suggested for small automotive cables is SAE 1006 low carbon steel clad to 40% IACS

conductivity and hard drawn. The properties of this material are summarized in Table 1.

Table 1. Properties of 40% Copper Clad Steel

	Cu Thickness	Volume % Cu	Resistivity	Density	Tensile Strength
CCS	10% Ø	36%	.044Ωmm ² /m	8.2g/cm ³	780MPa
Cu	100%	100%	.017Ωmm ² /m	8.9g/cm ³	230MPa

AWG 26 (.13mm²) cables of this product have comparable breaking strength to AWG 20 (.50mm²) copper cables. AWG 24 (.22mm²) can also be used, achieving the same benefits to a lesser degree, but producing an even more rugged assembly. Small copper clad steel cables and the copper cables they usually replace are described in Table 2.

Table 2. Comparison of Copper Clad Steel (CCS) and Copper Automotive Cables

Cable	Diameter	Break Load	Weight	Ampacity*
.13mm ² CCS	1.0mm	13kgf	1.6kg/km	Not tested
.22mm ² CCS	1.1mm	22kgf	2.4kg/km	6.5
.35mm ² Cu	1.5mm	8.7kgf	3.8kg/km	14
.50mm ² Cu	1.7mm	14kgf	6.3kg/km	18

*Ampacity as determined by one automotive wiring harness manufacturer.

While .13mm² CCS was not included in the same group of tests, other tests have shown ampacities from 3 to 5 amps.

The values in Table 1 are for cables having PVC insulation in accordance with SAE specifications. Values will vary slightly depending upon the type and thickness of insulation, but the size and weight advantage of the small copper clad steel cables is clear.

2.2 Copper Clad Aluminum

The copper clad aluminum product suggested for automotive applications is clad to 10% copper by cross sectional area and hard drawn. The properties of this material are summarized in Table 3.

Table 3. Properties of 10% Copper Clad Aluminum

	Cu Thickness	Volume % Cu	Resistivity	Density	Tensile Strength
CCA	2.5% Ø	10%	.027Ωmm ² /m	3.3g/cm ³	250MPa
Cu	100%	100%	.017Ωmm ² /m	8.9g/cm ³	230MPa

These electrical properties permit copper clad aluminum cables in standard even gage number sizes to be substituted for copper cables of the next smaller even gage size without affecting electrical performance while achieving significant weight reductions. This is illustrated in Table 4.

Table 4. Comparison of Copper Clad Aluminum (CCA) and Copper Automotive Cables

Cable	Construction	Resistance	Conductor Weight	Ampacity
AWG 10 CCA	19/.57mm	5.6Ω/km	16kg/km	47
AWG 12 Cu	19/.46mm	5.9Ω/km	27kg/km	46

The ampacities in Table 4 are actual values determined by an automotive wiring harness manufacturer for PVC insulated cables. The other values are nominal. The general rule that a copper cable can be switched to a copper clad aluminum cable two gage numbers larger and obtain similar resistance and current carrying capacity at about a forty percent weight reduction applies to the entire range of cable sizes.

3. Manufacturing and Performance Considerations for Automotive Applications of Bimetallic Cable

3.1 The Use of Hard Drawn Wire

While copper cables are usually fabricated from annealed copper, hard drawn bimetallic cables are recommended. The term "hard drawn" simply means that the strands making up the cable are not annealed after drawing to final diameter. Omission of the annealing heat treatment to soften the strands leaves them in a work hardened condition with higher strength and less ability to accept deformation without fracturing. It is this tendency to fracture when severely deformed that leads to the misconception that hard drawn cable is not suitable for automotive applications. Hard drawn wire will break after only a few repetitions of sharp bending by hand, while annealed wire of any metal will survive this treatment much longer.

Sharp bending by hand, however, is not representative of actual service conditions. Such bending plastically deforms the wire. Plastic deformation work hardens the metal and reduces its ductility. Since the work hardening from the drawing operation is still present in hard drawn wire, it will break in after fewer bends than annealed wire. No wire, however, regardless of its metallurgy will tolerate more than a few dozen cycles of repeated plastic deformation. Metals cannot be used in service conditions that involve repeated plastic deformation.

Figure 3 is a schematic representation of the stress-strain curves for the same metal in both the annealed and hard drawn conditions. The hard drawn material has a higher yield strength, denoted by the point where the curve deviates from a straight line, a higher ultimate tensile strength, denoted by the peak of the curve, and a lower total elongation, shown by the overall length of the curve. The annealed material does tolerate greater plastic deformation, as shown by the longer length of the plastic section of the curve, indicated by a dotted line.

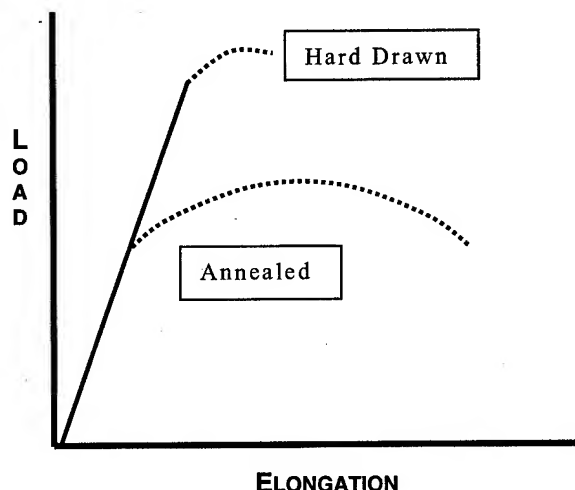


Figure 3. Schematic Stress-Strain Curves for Annealed and Hard Drawn Wire

These differences are important in the application of the materials. The work hardening behaviour of steel permits development of high strength with the use of low cost and easily drawn low carbon steel. The high yield strength of the copper clad steel permits small cables to have good buckling resistance and adequate column strength to accommodate typical insertion forces.

For copper clad aluminium, the use of hard drawn strands results in a more rugged cable with improved fatigue life. The fatigue life of a metal is generally proportional to its tensile strength. In the hard drawn condition, the tensile strength of copper clad aluminium is similar to or slightly higher than that of annealed copper, resulting in similar fatigue life.

The use of hard drawn wire has been validated in 20,000 cycle liftgate simulations and 80,000 cycle door simulations. In both cases, prototype harnesses containing both copper clad steel and copper clad aluminium went through flex testing simulating life of vehicle service without breaking any strand of any cable.

3.2 Cutting and Stripping Bimetallic Cable

Copper clad aluminum cables can be cut and stripped in the same manner as copper cables with no changes in operating practice. Due to the hardness of the steel, copper clad steel cables may require a change in cutting blade material, or more frequent blade replacement. Because of their strength, copper clad steel strands resist breakage during stripping, making the stripping operation more robust.

3.3 Joining Bimetallic Cable

The preferred joining technique for bimetallic wire is ultrasonic welding. This type of welding is routinely used during the manufacturing process. Both types of bimetallic wire also have excellent solderability. Silver brazing, however, cannot be used with copper clad aluminum because the temperatures involved are too high.

3.4 Crimp Terminations in Bimetallic Cable

Bimetallic cables of the type recommended for automotive use accept standard crimped terminals. Figure 4 is a cross section photomicrograph of a typical crimp. The strands deform in the

usual manner during crimping and the cladding on each strand remains intact.

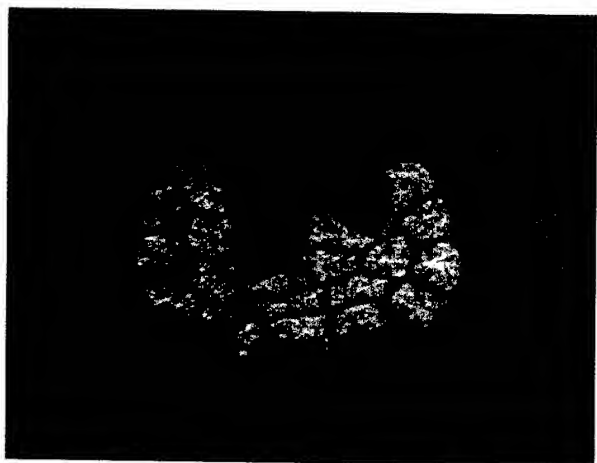


Figure 4. Cross Section of Crimp in 18 Gage Copper Clad Aluminum Cable

In Figure 4, both the terminal and the cladding on each strand are copper, so there is no difference in contrast in the photograph, and the sections of the clad layers that are adjacent to the terminal are not resolved. However, this area is especially important because it provides a copper surface at the point of interaction between the cable and the terminal. This means that the connections perform more like connections to copper cable rather than connections to aluminium cable.

The performance of the recommended cables during thermal and environmental cycling tests of crimped connections has been good. Failures have been rare. They have occurred only on certain combinations of cable construction and terminal material, with most combinations having a zero failure rate. When failures have occurred, they have been intermittent, with the majority of the crimps in any condition always having good performance. All the failures have been increases in resistance of the crimped connection to a level that was above the maximum allowed, but would still be functional. There have been no catastrophic failures. Crimp geometry may be a factor in the small number of failures that have been observed.

Copper clad aluminium cables resist the stress relaxation, connector loosening, and exponential resistance increases that are hazards for aluminium cables for several reasons. With no exposed aluminium in the connection, the tendency of aluminium to oxidize and develop high resistance crimps is eliminated. Without high resistance, excessive heating and associated thermal expansion and cable softening do not occur. The hard drawn strands with their higher yield strength can accommodate greater thermal stresses than annealed strands without suffering plastic deformation and permanent distortion.

3.5 Corrosion and Its Prevention

Whenever two metals are in contact in the presence of moisture, the more chemically active one of them is subject to accelerated corrosion due to galvanic action. This situation is aggravated by the presence of electrolytes such as dissolved salts. Road de-icing salts and airborne salt in marine environments have in the past caused severe corrosion to automobiles. Several metals are used in vehicle construction, and the industry has learned to manage

the corrosion hazards. The same care that prevents general body, chassis, and trim corrosion is applicable to wiring components.

At the cut ends (and only at the cut ends) of bimetallic cables, both metals are exposed and there is a hazard of galvanic corrosion. For successful application of bimetallic cables, the corrosion hazard must be controlled. Fortunately, it is easily controlled. Corrosion is a wet process and cannot happen without moisture, so the simple solution is, **KEEP IT DRY**. This means that all terminations in bimetallic cable outside the passenger compartment must be sealed. Conventional sealed connectors should be adequate. Where open connections are desired, such as for battery cables, they can be soldered or sealed with any of a variety of commercial products such as plastisols that provide a barrier coating. Properly installed heat shrinkable tubing also can provide an effective seal.

3.6 Ruggedness and General Durability

Both applications of bimetallic wire result in more durable components. For hard drawn copper clad aluminium cables, the specific strength is equal to or greater than copper, but the cables are larger than the copper cables they replace. With larger cables the stress levels are lower, and life should be longer.

Copper clad steel benefits from its very high strength level. The strands of copper clad steel cables are very difficult to break, even at the 0.16mm diameter used in .13mm² cable. Because it has a steel core, copper clad steel exhibits the endurance limit characteristic of ferrous metals.

4. Examples of Automotive Applications of Bimetallic Wire

4.1 Small Copper Clad Steel Cables

This application replaces a portion of the minimum size copper cables normally used in a wiring harness with smaller copper clad steel of equivalent strength. It reduces weight and bundle size and improves the overall flexibility of wiring harnesses and makes them easier to install and service. The effects of CCS on a harness can be seen by analyzing the hypothetical harness described in Table 5.

Table 5. Analysis of the Benefits of Substituting Copper Clad Steel (CCS) Cables

Cable	Number of Leads		
	Base Harness	With CCS 12 volts	With CCS 42 volts
26 gage CCS		216	410
22 gage Cu	360	144	0
20 gage Cu	150	150	100
18 gage Cu	72	72	72
16 gage Cu	18	18	18
Total Leads	600	600	600
% of Base Cross Section	100%	90%	80%
% of Base Weight	100%	86%	72%

The harness in Table 5 does not exist, but it is a model that can be used to analyze the effects of copper clad steel substitutions. The assumptions used in the table are very conservative in that they

assume extensive use of 22 gage copper cables, when often the smallest copper leads are 20 gage. Also, it assumes that 26 gage copper clad steel could handle the current and voltage drop requirements for 36% of the leads. In actual harnesses that have been analyzed, the electrical properties of 26 gage copper clad steel cables would permit them to be used for 40% to 60% of the leads. The final column in Table 5 considers the effect of the proposed change to 42-volt electrical systems. In this case, currents in power leads will be reduced and even more leads will be available for conversion to small copper clad steel cables.

The hypothetical benefits of small copper clad steel cables have been demonstrated in prototype wiring harnesses.

4.1.1 U. S. Mini-van Main Body Harness. The production supplier of this wiring harness built a fully functional prototype, substituting 26 gage (.13mm²) copper clad steel where appropriate. The overall weight of this harness was reduced from 15 to 12.7 kilograms, a 15% reduction. This includes all terminals, connectors, packaging, protective wrapping, and attached mounting brackets. The average cross sectional area reduction for the 30 branches of this harness was 20%, with the main trunk of the harness being reduced from three bundles to two. Flexibility was improved throughout the entire harness assembly.

4.2 Copper Clad Aluminum Power Cables

This application reduces weight by replacing copper power cables with appropriately upsized copper clad aluminum cables having similar electrical characteristics. The benefits of this substitution can be shown in the analysis of the cables used in a 2001 Lincoln Town Car. This analysis was done by the supplier of wiring harnesses for this vehicle and is shown in Table 6.

Table 6. Weight Reduction Possible by Substitution of Copper Clad Aluminum (CCA) for Copper Cables in 2001 Lincoln Town Car

Copper Weight	CCA Weight	Copper Insulation Weight	CCA Insulation Weight	Final Weight Savings
16.7kg	9.5kg	4.9kg	6.0kg	6.1kg

The 2001 Town Car contained 1800 meters of cable in ten sizes from 4 gage to 22 gage. There were also ten different insulation specifications, and a total of 27 different types of cable. The analysis in Table 6 is based on replacing the copper cables with copper clad aluminum cables ranging from 2 gage to 20 gage, and insulated to the same specification as the cables they replace. It thoroughly analyzes the weight effect of the fact that the larger copper clad aluminum cables require more insulating material.

4.2.1 Copper Clad Aluminum Battery Cables. Battery cables are the largest power cables in a vehicle and present one of the best opportunities for weight reduction through the use of copper clad aluminum. An especially good opportunity occurs with current vehicle designs that are more frequently relocating the battery to the rear of the vehicle. Table 7 shows the comparison of copper and copper clad aluminum cables proposed during the design of a 2004 large sedan having a rear battery

location. For cables the size and length of this type of battery cable, significant weight reductions are possible simply by changing the material of one component.

Table 7. Proposed Copper Clad Aluminum Battery Cable for 2004 Model Year Large Sedan

	Resistance (mΩ/m)	Cable Diameter (mm)	Cable Weight (kg/m)	Battery Cable Length	Battery Cable Weight
AWG 2 Copper	0.51	9.8	0.35	6.1m	2.1kg
AWG 1/0 10% CCA	0.54	12.2	0.23	6.1m	1.4kg

Cables based on the proposal in Table 7 have been validated in laboratory testing and installed on test vehicles.

4.3 Optimized Components Using Both Copper Clad Steel and Copper Clad Aluminum

The use of both types of bimetallic cables in the same harness uses the technology of bimetallic cable to greatest advantage. Harnesses with this design approach achieve maximum weight reduction and still can be smaller and more flexible.

An example of this type of harness is a functional prototype door harness for a large pickup truck. The supplier of the production harness built these prototypes to demonstrate the advantages and practicality of bimetallic cable. This small harness has 22 leads. Of these, 12 are power leads requiring copper clad aluminum, and 10 are low current leads using copper clad steel. The completed prototype harness weighs 0.9 kilograms, while the production harness weighs 1.4 kilograms. These weights are for complete harness assemblies with all terminals, connectors, tape wrap, and attached mounting brackets. In addition to being lighter, the bimetallic harnesses are noticeably more flexible.

5. The Brief History of Copper Clad Aluminum Wire in the Automotive Industry

While bimetallic wire is an established product manufactured and used in quantities measured in thousands of tons per month, it has been largely absent from automotive material applications. There is one bit of history, however, and it merits reviewing because it demonstrates the applicability of the product and provides some lessons on how it can best be used.

During the first period of downsizing and weight reduction in the 1970s, one manufacturer used copper clad aluminum battery cables in some models. This application was generally successful, but was not without problems. The cables failed at a rate that was considered a nuisance at the time, but would be unacceptable by today's quality standards. After a few years, the application was abandoned for the following reasons:

- Breakage
- Corrosion failures
- Cost

These were all valid issues at the time, but with current technology and understanding, they can all be addressed.

5.1 Preventing Breakage

Some of the cables required premature replacement because they fractured. The cables used at the time were not highly stranded. Individual strands were about 1.5mm in diameter, and they were annealed. Both factors made the cables subject to fatigue fractures caused by vibration. The larger strands are less flexible and any movement induces higher stresses. The higher the stress level, the shorter the fatigue life of any metal will be. Modern battery cables typically have strands no larger than 0.57mm diameter.

The second factor contributing to fatigue failures was the use of annealed strands. Annealing reduces the ultimate tensile strength and the fatigue life of all metals is proportional to their tensile strength. This effect is particularly severe for copper clad aluminum because fully annealed aluminum has very low tensile strength.

Modern cable constructions with smaller strands, and the elimination of the annealing operation have made today's copper clad aluminum cables resistant to fatigue failures. This durability has been demonstrated in several laboratory vibration and mechanical cycle tests. There has also been limited experience with these cables on test vehicles. In all of this testing, not one broken strand due to fatigue has been observed.



Figure 5. Copper Clad Aluminum Cable Connected to Alternator Terminal After 40 Cycle Proving Ground Corrosion Test

5.2 Avoiding Corrosion

The cables used 25 years ago were frequently terminated with open connections, making them susceptible to galvanic corrosion. It is not recommended to expose unprotected cut ends of

bimetallic wire to atmospheric conditions in any situation, but where the corrosion accelerating effects of electrolytes such as road salt and battery acid are present, it is particularly risky. Corrosion can be prevented with proper sealing techniques. Figure 5 shows an alternator cable termination that was sealed with heat shrink tubing. It is in excellent condition after 40 corrosion cycles at the proving ground of one of the domestic automotive companies, a very severe test. The cable marked "3" in the photograph is AWG 1 copper clad aluminum. Note the heat shrink tubing between the "3" and the terminal, and the absence of corrosion on the cable.

5.3 Costs Have Changed

Manufacturing technology and material prices have changed significantly in 25 years. Cost is no longer a barrier to the use of copper clad aluminum cables, as the next section will explain.

6. The Economics of Bimetallic Cables

No paper suggesting a materials change in a widespread application would be complete without a discussion of costs and the economics of the application.

The process of producing cables consists of the steps of producing wire rod, drawing to strand gage, stranding or bunching, and insulating. The cost of these manufacturing steps combined with the raw material cost determines the cost of the finished cable.

The costs of all the manufacturing steps after rod production are incurred on a length basis. Bimetallic wire processes at the same speed through these operations as copper. Therefore the manufacturing cost to produce a kilometer of bimetallic cable from clad rod is the essentially the same as the manufacturing cost to produce a kilometer of the same construction copper cable from copper rod.

Cost differences arise from differences in the cost of the rod. Bimetallic wire starts with lower cost raw materials, but the cladding process involves significant metallurgical processing and is expensive. Therefore, depending the copper price in effect at the time, bimetallic wire rod at a typical diameter of about 8mm may be more expensive than copper wire rod. However, because copper clad steel is used at smaller gages, and copper clad aluminum conductors are about 40% lighter than the copper conductors they replace, less raw material is required and the final costs of bimetallic and copper cables are similar. Of course the cost relationship is related to copper prices. Bimetallic cables are less sensitive to variations in copper price and can develop attractive cost advantages when copper prices are high in their historic range.

Generally, cost should not be a major consideration in the substitution of bimetallic cables for copper cables. It is appropriate to consider that the benefits of bimetallic cables can be achieved at no significant cost penalty.

7. Conclusions

Cables produced from bimetallic copper clad aluminum and copper clad steel wire offer unique opportunities to reduce the weight, size, and rigidity of automotive wiring components. Weight reduction of wiring components has the same beneficial

effects on vehicle performance and fuel economy as all weight reduction measures. Smaller and more flexible wiring facilitates installation and reduces assembly cost.

Both engineering analyses and prototype testing have validated the performance of these cables, including the superiority of cables made from hard drawn strands. The advantages of bimetallic cables present a rare opportunity make important improvements without incurring significant cost increases.

8. Acknowledgements

The authors would like to acknowledge the assistance of their Copperweld associates and express their appreciation for advice and contributions from the following organizations:

Alcoa Fujikura Limited

Cables Perti, s. a.

Champlain Cable

Contech Research Incorporated

Delphi Automotive Systems

Ford Advanced Vehicle Engineering

International Wire Group, Inc

Leoni Wiring Systems

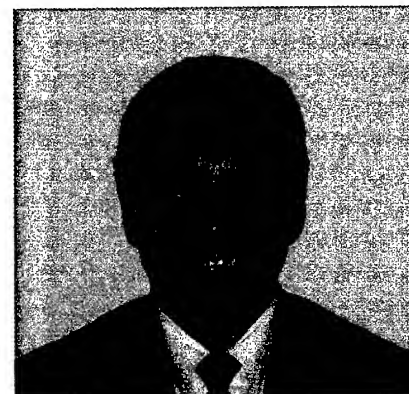
Yazaki North America

9. References

- [1] SAE Specifications J1127, J1128, and J1678, Society of Automotive Engineers, Inc.
- [2] W. Perrard and A. Gibson, "Reduction of Size, Weight, and Cost of Automotive Wiring Components Through the Use of Bimetallic Wire," SAE Paper 2000-01-0067, Society of Automotive Engineers, Inc.



Brian Suwarow is Sales Representative for Copperweld in Fayetteville, Tennessee. He is experienced in both operations and maintenance aspects of clad metal manufacturing. He has also worked in the engineering services industry. Brian majored in Public Relations at the University of South Alabama. His mailing address is: Copperweld, 254 Cotton Mill Road, Fayetteville, TN 37334



Alan Gibson works with Copperweld to develop new applications for bimetallic materials. He is a metallurgical engineer with over thirty years industry experience in manufacturing, marketing, and research and development. He holds twelve US patents on metallurgical products and processes and is the President of Palmate Technologies, Inc., a metals industry consulting company. His address is P. O. Box 1374, Beaufort, SC 29901.

Alternative Polyolefin Insulation Materials for Communication Cable Applications

Chun D. Lee and Tim S. Schloemer

Equistar Chemicals, LP, Cincinnati, OH 45249

Chun.Lee@EquistarChem.com

Abstract

High density polyethylene (HDPE) has predominantly been the polyolefin of choice for wire insulation in Tele-Communication and Data-Communication cable applications for years. The typical ranges of MI (Melt Index) and density are < 1.0 and 0.940 to 0.955 . The usage of HDPE can be attributed to the excellent processibility (> 2500 m/minutes), mechanical strength, electrical properties and long term durability. The processibility of HDPE derives from its rheologically broad molecular weight distribution. An alternative polyolefin to HDPE is in-situ reactor blended impact polypropylene copolymers (IPP). Compared to HDPE, IPP provides improved mechanical and electrical properties as well as heat resistance. However, the past usage of IPP has generally limited extrusion line speed (< 1700 m/minutes) and output due to the eccentricity of a wire.

A new commercially IPP (nIPP) has been developed for high line speed insulation extrusion applications. The processibility of this nIPP is now equivalent to that of HDPE. The nIPP has shown enhanced mechanical strength, improved low temperature performance, and reduced extrusion head pressures, compared to conventional IPP and HDPE. Possible reasons for improved performances of nIPP are discussed.

Keywords: High density PE, polypropylene, broad molecular weight, processibility, eccentricity, oscillatory melt fracture, viscoelastic melts, polydispersity, dynamic rheological data, GPC.

Introduction

It is well recognized that of the polyolefins commonly in use in the United States, high density polyethylene (HDPE) and impact polypropylene (IPP), HDPE has been predominately used as an insulating material for communication cables[1].

HDPE is a simple chemical structure, consisting of the monomer repeating unit of two carbons, ethylene. The crystalline architecture is made of lamella with chain folding. The crystallinity of HDPE is mainly controlled by an addition of high alpha-comonomer addition such as butene or hexene during the polymerization process. The mechanical strength of HDPE is mainly determined by the degree of crystallinity or density. The polymer provides exceptional mechanical strength and electrical properties as an insulation as well as processibility for a wire coating process. The excellent processibility of the HDPE results from its broad molecular weight distribution (MWD) [2].

Polypropylene (PP) has similar chemical structure to HDPE with an addition of one methyl group in the backbone structure. Thus, its monomer repeating unit of the polymer is propylene. The presence of the methyl group in the structure of PP results in a different crystalline structure, leading to different crystallization mechanism, compared to PE. The crystallinity of PP is determined by stereo-regularity, called "tacticity". The type of

catalyst employed for polymerization mainly controls the tacticity. Compared to HDPE, PP is much stiffer and has poorer impact properties, leading to a poor balance of stiffness and impact. In order to improve the balance of properties, in-situ rubbery material is produced in the reactor during polymerization process to produce impact modified PP (IPP). Generally, IPP has a narrower MWD than HDPE for insulating material in communication application.

Conventional IPP had been used for insulating materials for communication application in the past. However, the extrusion speed had been limited due to poor centering of the conductor (eccentricity). For an example, in the process of telecommunication singles, eccentricity can take place at line speeds as low as 150 m/min[3]. In many cases, maximum production rates are limited because of these eccentricity problems. In the insulation of data communication, eccentricity is more critical for a given line speed than telecom. Eccentricity problem sometimes leads to wall thickness variation that can cause decreased signal performance due to capacitance effects. The origin of eccentricity in the wire coating extrusion of conventional IPP might be related to oscillatory melt fracture originated from the structure of the material. Thus, absence of eccentricity is highly desirable for high speed IPP wire insulation process.

The presence of oscillatory melt fracture had been investigated in the capillary or die flow of molten IPP[4-5]. At low shear, a smooth cylindrical extrudate was observed. At high flow rates, a periodic oscillation began in the capillary inlet and the extrudate took on the shape of a regular helix, with the pitch increasing as the flow rate increased. Similarly, Bialas et al [6] have shown that this helical pattern is directly related to a swirling motion of the melt at the entrance to the capillary, term as the inlet melt fracture. The inlet melt fracture differs from typical land or exit fracture shown by HDPE and LLDPE [7]. This inlet melt fracture is thought to be a result of elastic failure of the viscoelastic melts, which is different from the typical land or exit melt fracture, originated from slip-stick mechanism.

In this report, we investigate the structural and morphological difference between HDPE and IPP. The difference leads to an understanding of the performance in communication application as an alternative insulating material. IPP showed a limitation in the usage of high speed extrusion due to the presence of oscillation flow which is related to wire eccentricity. A possible explanation for the origin of the limitation of IPP is given. A new IPP (nIPP) produced by the use of a new catalyst and a reactor condition is introduced. The difference in structure and property between IPP and nIPP is discussed.

Experimental

1. Material

The sample materials used for this investigation are commercial HDPE and two grades of impact polypropylene resins with

similar melt flow rates (MFR), One resin, denoted IPP is a conventional impact PP with a Ziegler catalyst and the other resin, denoted new IPP (nIPP) was produced with a high activity catalyst and reactor conditions. The basic data is given in Table 1.

2. Test methods

Molecular weight (M_w) and molecular weight distribution (MWD) were measured by a Waters Gel Permeation Chromatography (GPC) unit. Melting(T_m) and crystallization temperatures(T_c) were determined by a Perkin-Elmer DSC 4 calorimeter. Dynamic mechanical properties for solid state were determined with a Dupont 983 DMA for the measurement of E'' (loss modulus) as a function of temperature. Dynamic complex viscosity, η^* as a function of frequency and shear viscosity, η as a function of shear rate were measured by a Rheometrics ARES and Rosand Capillary rheometers at 210 °C. During the capillary measurements, a technique outlined by Cogswell[8] was employed to determine the entrance pressure drop (EPD in short) associated with changes in the velocity distribution near the die entrance of the capillary[9].

A Davis-Standard (L/D= 20, D= 64 mm) single screw extruder at 230 °C (die temperature) was employed with a specially designed wire coating die to determine extrusion head pressure (EHP) as a function of screw speed and critical screw speed for the occurrence of oscillatory melt fracture. Flexural Modulus, Low Temperature Brittleness (LTB) and Shore Hardness were also determined with injection molded specimens using the ASTM methods.

Results and discussion

1) Basic data and phase morphology

Table 1 shows the difference in basic properties between HDPE and IPP. Even though HDPE shows higher density(crystallinity), it shows lower LTB and T_m than IPP. The lower T_m with higher crystallinity for HDPE results from different crystal structure with molecular chain packing. IPP is a better choice for higher temperature applications. HDPE is a single-phase material whereas IPP is two phase in-situ in-reactor blended materials, consisting of homo PP as a matrix phase and rubber (22 wt%) as a disperse phase. The nIPP shows improved LTB, T_m and T_c compared to conventional IPP. The higher T_c for nIPP (than IPP) is benefit for quicker solidification process during wire coating run.

Table 1. Basic data for the resins

Resin	HDPE	IPP	nIPP
MI	0.7	-	-
MFR	1.3	2.5	2.6
Density	0.943	0.900	0.900
LTB(°C)	< -70	-35	-45
Rubber content	0	22	23
T_m (°C)	127.6	161.2	165.4
T_c (°C)	116.3	110.2	118.4

We carried out the DMA measurements in order to understand the phase difference between HDPE and IPP. Polymer phase miscibility can be detected by a single glass transition (T_g) whose temperature is intermediate between those corresponding to the individual polymers [10,11]. On the other hand, blends of completely immiscible polymers that segregate into distinct

phase show T_g identical in temperature to those of the unblended components. The DMA data (Figure 1) indicate that IPP shows multiple transition (no single T_g temperature) whereas HDPE shows only one α -transition at 45 °C due to the relaxation process of crystalline domain. We identified individual T_g s of IPP such as the T_g near 65 °C (α -relaxation due to PP crystalline domain), 5 °C (β -relaxation due to PP amorphous phase) and -40 °C (γ -relaxation due to rubber phase). Both(HDPE and IPP) show the transition at -120 °C due to a relaxation of methyl group. This DMA data shows that PP and rubber phase is immiscible. It is evident that HDPE shows different DMA data, compared to IPP. At present, we do not know the effect of these transitions and temperature on the electrical property of insulation for HDPE and IPP.

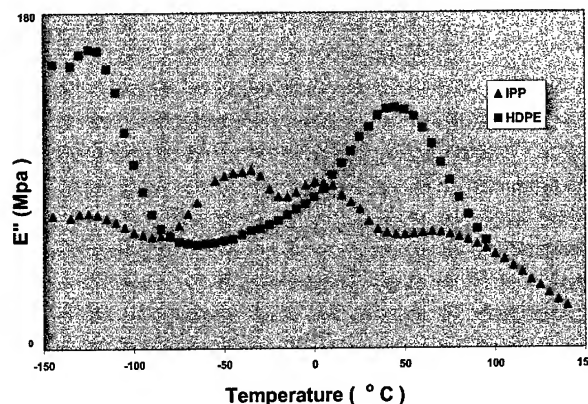


Figure 1. DMA E'' vs. temperature data for HDPE and IPP

2) Structure and rheology

Table 2 shows the results of GPC data and Figure 2 shows MWD curves for the materials. IPP shows higher M_w than HDPE. This GPC result is contrary with MFR data (lower MFR for HDPE means higher M_w material). The higher number of M_w for IPP results from one more carbon unit in the monomer repeating unit. This means that for a given equal length of chains, the M_w of IPP shows higher (approximately 1.5 to 2 times depending on) than that of HDPE. A direct comparison for GPC data between HDPE and PP is misleading in order to understand the GPC data. However, it is evident that HDPE shows broader MWD (as indicated by Polydispersity (Pd) in Table 2) than IPP. IPP showed slightly broader MWD with similar M_w than nIPP. If the MWD curve of IPP or nIPP is shifted to lower M_w with the normalization of the additional carbon in the repeating unit for the polymers, the broadness for HDPE results from an increased amount of low and high M_w species. IPP shows similar observation (more low and high M_w species for the MWD broadness), compared to nIPP. We will confirm this observation with the dynamic rheological data (see the next discussion).

Table 2. GPC structural data

Resin	HDPE	IPP	nIPP
$M_w \times 10^{-5}$	1.25	2.30	2.10
Pd (M_w / M_n)	11.4	6.1	3.8

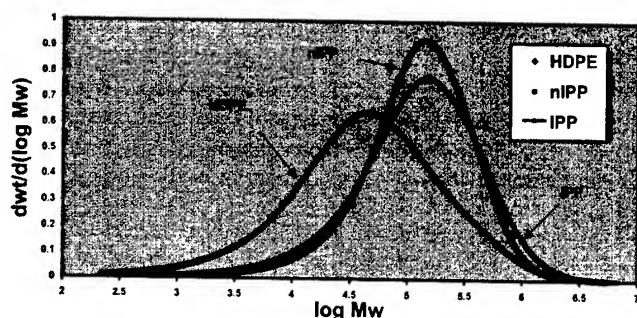


Figure 2 GPC data for the resins.

As shown in Figure 3, dynamic rheological data indicates that broader MWD for HDPE shows more shear-thinning behavior (higher viscosity at low frequency region and lower viscosity at higher frequency) as compared with IPP. A direct comparison in rheology between IPP with nIPP confirms the effect of MWD on shear thinning; the former resin showed more shear thinning than the latter. The more shear thinning results from the improved disentanglement process of long chain molecules with shear in the presence of more low M_w species. This understanding of dynamic rheological data is in line with the result of the GPC MWD curves.

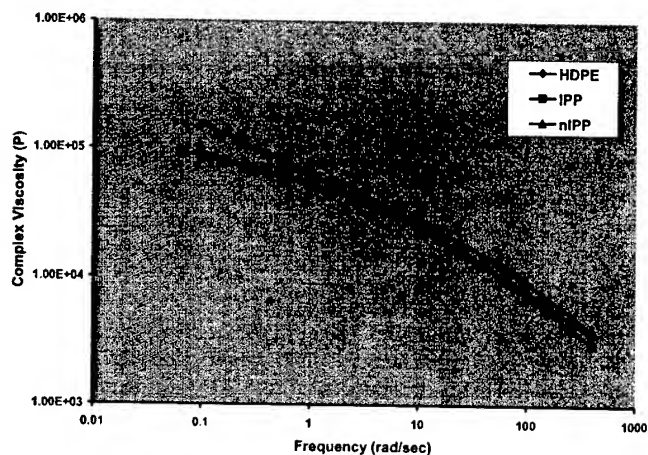


Figure 3. Dynamic rheological data

3) Mechanical and electrical properties

It is important to increase mechanical strength and to decrease dielectric constant of solid insulation as well as expanded insulation. Improved mechanical strength leads to enhanced crush resistance for insulation. During manufacturing process of data communication cables, the twisting process of the insulated pairs becomes tighter and even HDPE lacks the toughness to withstand the abuse that occurs during the twinning process. Greater insulation thickness helps compensate for the insulation deformation but at a higher cost. Similar principle can be applied to telecom insulation.

IPP shows improved flexural modulus and shore hardness (Table 3) compared to HDPE. This improved mechanical strength for IPP with lower density clearly indicates different crystalline morphology for the polymer. It is evident that nIPP shows even better strength than IPP. If the application requires some flexibility, HDPE is a better choice than IPP. Also, IPP and nIPP show lower dielectric constant than HDPE. The lower dielectric constant with enhanced mechanical strength for IPP and nIPP is advantageous over HDPE whenever capacitance effects can deteriorate electric properties of the final cable [12].

Table 3. Mechanical and electrical properties of the resins.

Resin	HDPE	IPP	nIPP
Flex Modulus(Kg/cm ²)	13000	18000	22800
Shore hardness	63	69	71
Dielectric constant	2.33	2.25	2.26

4) Extrusion test and high shear rheology

Extrusion head pressure (EHP) is dependent on the extrusion speed and the viscoelasticity of a melt. For safe operation, it is important to keep the head pressure low. Lab scale extrusion runs without running of conductor determined the head pressure. We observed a good correlation of EHP between lab extrusion and commercial high-speed wire coating [13].

Figure 4 shows the dependency of head pressure with screw speed. For a given screw speed, HDPE showed much higher EHP than IPP. Capillary viscosity (Figure 5) and entrance pressure drop (EPD) (Figure 6) indicates that higher EHP for HDPE compared to IPP related to the combined effects of higher viscosity at the extrusion shear rate (~ 1100 1/sec) and higher melt elasticity (as determined by EPD).

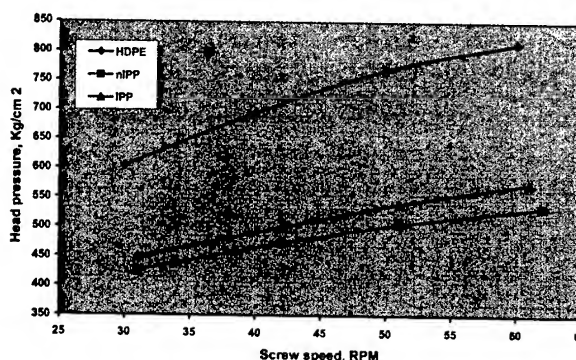


Figure 4. Extrusion screw speed vs. extrusion head pressure for the resins.

When polymer melt enters a die from an extruder barrel during a wire coating process, the velocity profile starts to develop and continuous to change until it reaches a certain distance beyond which flow is said to be fully developed. This transitional stage (being fully developed) results in pressure drop. For a given extrusion condition, the more elastic melt with similar shear stress resulted in the higher EPD [9]. In this sense, the shear

dependent EPD for PE is very similar to die swell which is the die exit behavior. In general, there is a good correlation between EPD and die swell for PE such that EPD and swell increased with increased shear rate or stress.

There is a good correlation in EHP between HDPE and IPP such that higher shear viscosity and EPD for the former resin showed higher EHP. Interestingly, there is poor relation in EHP between IPP and nIPP such that lower viscosity at extrusion shear and lower EPD for IPP showed higher EHP. The MI die swell measurements at 190 °C indicated that IPP showed much higher swell (181%) than nIPP (131%). We confirmed that IPP showed higher shear dependent die swell than nIPP. For a given MFR and viscosity, the EHP for IPP appears to be dependent on die swell.

It was discussed that the relaxation mechanism under chain deformation with entrance flow differs from die swell at die exit even though both parameters have been commonly used as a measure of melt elasticity [9]. Also, the effect of die swell on EHP in the wire coating process was discussed in the literature [13]. The poor correlation between EPD and die swell for IPP and nIPP may be related to the blend nature of immiscible two phase. More work is necessary to confirm this observation of the poor correlation in IPP.

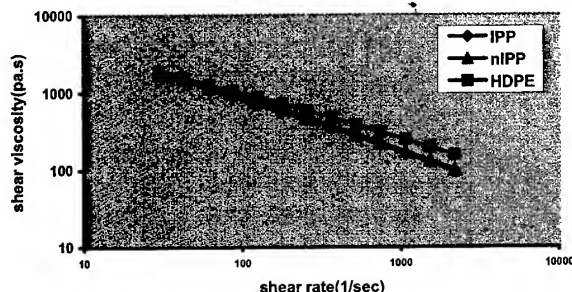


Figure 5. High shear capillary viscosity data

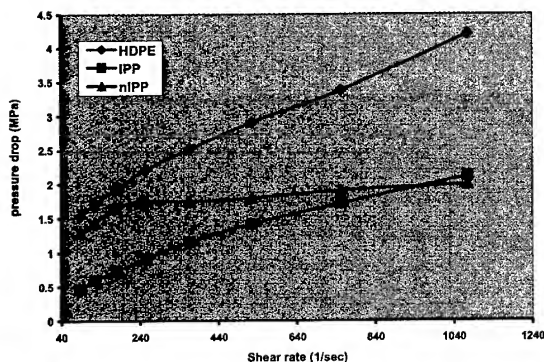


Figure 6. Entrance pressure drop for the resins

During the high speed insulating processes, an examination of a cross-section of insulated wire is used to determine the extent of eccentricity. A common misconception when using this test method is to assume that the center of a conductor is a continual distance from the center of the construction (Figure 7a). Upon closer examination during wire coating processing conditions that

favor oscillatory flow, the conductor is forming a helical pattern within the insulating medium (Figure 7b). In order to identify the root cause of the eccentricity, the extrusion without running of a conductor was performed with the same conditions as a function of screw speed. The extent of helical distortion increases with increased speed as shown in the extrudates (Figure 8). This helical flow is consistent with oscillatory melt fracture. The helical fracture is typical for PP which is related to the fracture at the die entrance (inlet fracture) [4]. IPP showed the occurrence of oscillatory melt fracture even at low screw (= 20 RPM) speed whereas HDPE and nIPP did not show any indication of the fracture above 60 RPM, which is limit of the extrusion

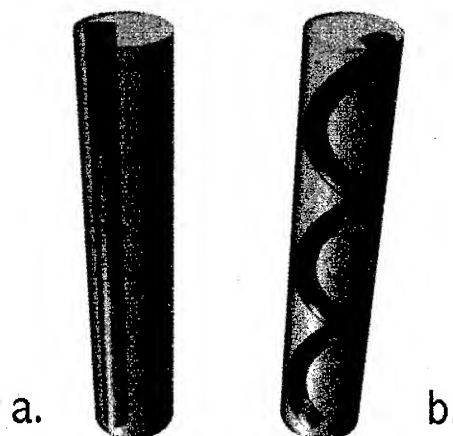


Figure 7. A schematic diagram for the eccentricity

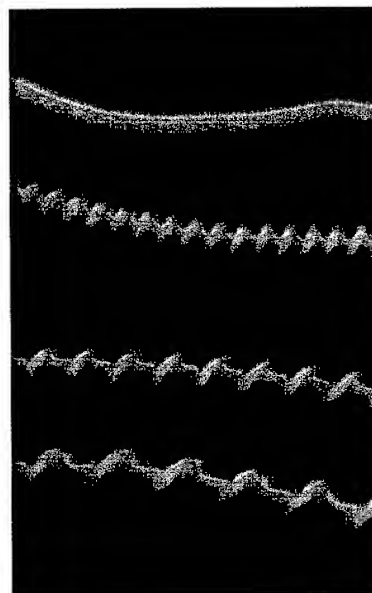


Figure 8. Extent of helically distorted extrudates with increased screw speeds: 10-20-30-47 RPM from top to bottom.

Conclusions

High density polyethylene (HDPE) has predominantly been the polyolefin of choice for wire insulation in Tele-Communication and Data-Communication cable applications for years. We

investigated conventional impact PP (IPP) as an alternative polyolefin. It was found that compared to HDPE, IPP showed structurally narrower MWD, better mechanical strength, high temperature resistance, better dielectric constant and reduced extrusion head pressure but poor low temperature brittleness and conductor eccentricity. The eccentricity of a wire appeared to be associated with the occurrence of oscillating melt fracture from the die entrance of molten IPP (inlet melt fracture). With the employment of a new catalyst and reactor conditions, a new IPP (nIPP) was produced with improved performance in LTB, mechanical strength and the elimination of melt fracture with high shear extrusion. The elimination of melt fracture from IPP appears to be related to the phase nature, leading to enhanced EPD at low shear and reduced die swell. Further investigation is necessary to identify the phase structure of nIPP, compared to IPP.

References

- [1]. Y.X. Zhang, IWCS Proceedings, p59(1990).
- [2]. B.H. Bersterd, J. Appl. polym. Sci., **28**, p2777 (1983).
- [3]. J.S. Borke, IWCS Proceedings (1999).
- [4]. T.F. Ballenger and J.L. White, J. Appl. Polym. Sci., 1949(1971).
- [5]. I.B. Kazatchkov et al., ANTEC Proceeding, p1180(1994).
- [6]. G.A. Bialas and J.L. White, Rubber Chem. Technol. 42, 675(1969).
- [7]. J.P. Tordeller, J. Appl. Polym. Sci., **7**, 215 (1963).
- [8]. F.N. Cogswell, Polymer Melt Rheology, George Godwin Limited (1981).
- [9]. C. D. Han, Polymer Processing, Academic Press (1976).
- [10]. A.R. Scholtz and R.M. Gendron, J. Macromol. Sci-Chem, **8**, 175(1974).
- [11]. J.R. Fried, F.E. Karasz, and W.J. MacKnight, Macromolecules, **11**, 150(1978).
- [12]. G.F. Kenney, Engineering Properties and Applications of Plastics, John Wiley & Sons, Inc., P229 (1957)].
- [13]. Rideal, G. R. and Padget, J.C., Polym. Eng. Sci., **57**, 1 (1976)

Authors



Chun D. Lee
Equistar Chemicals, LP
Equistar Technology Center
Cincinnati, OH 45249

Chun Lee received his Ph. D. degree in Polymer Science and Engineering from the Case Western Reserve U. in 1984. Chun joined the company in 1984 and is currently in the Product Development group within the Wire and Cable Group focusing on the Communications Market segment.



Tim S. Schloemer
Equistar Chemicals, LP
Equistar Technology Center
Cincinnati, OH 45249

Tim Schloemer received his Bachelor of Science degree in Materials Engineering from the University of Cincinnati in 1994. Tim joined the company in 1992 and is currently the Applications Specialist for the Wire and Cable Group providing technical support to the Communications Market segment.

Design of New Easy Processing High Modulus Compounds for Fiber Optic Cable Use

Geoffrey D. Brown

K. P. (Peter) Pang, Ph.D.

Scott H. Wasserman, Ph.D.

The Dow Chemical Company
1 Riverview Drive
Somerset, New Jersey 08873
+1-732-271-7958 · brownkd@dow.com

Abstract

Novel polyolefin compounds for fiber optic loose buffer tube and core tube applications feature an improved balance of high modulus and enhanced extrusion processing characteristics. One new higher modulus material with good toughness and improved buffer tube grease compatibility provides an advantaged balance of properties for the buffer tube application. Another new material incorporating high melt strength is a preferred material for core tube (central tube), slotted cores, and similar profile extrusion applications benefiting from improved dimensional control and reduced melt sag. Both materials also provide a low post extrusion shrinkage, which contributes to reducing optic fiber signal attenuation by minimizing excess fiber length associated with axial compression of the fiber core. Key application performances for these new materials will be outlined along with comparisons to materials currently in commercial use.

Keywords

Fiber, optic, cable, polyolefin, buffer, core, slotted, tube, MDPE, HDPE, PBT, polypropylene, polyethylene.

1. Introduction

The focus of early development efforts on optical fiber telecommunications cables was to enhance technical performance, especially the improvement of optic signal attenuation. Reduced signal attenuation would provide major cost and performance advantages by increasing the short spacing between optic signal amplifiers (also known as repeaters). In addition, optic fiber was expensive, so cable designs and manufacturing practices were also focused upon maximizing fiber yield and optimal mechanical protection. Dramatic technical evolution occurred, especially with regard to the development of improved optical fibers and fiber splices providing much better signal attenuation, but also with respect to cable designs and materials of construction. Signal attenuation performance was dramatically improved as a result of this rapid technical evolution, and the required optic signal amplifier spacing shifted from a few kilometers in the early 80's, to current capabilities of approximately 100 kilometers between amplifiers. In addition, there has been a dramatic decrease in the cost of the

optic fiber. As the market rapidly grew and suppliers substantially boosted production capabilities, optic cables became more of a commodity product, with an ever increasing emphasis on cost/performance optimization.

Innovations in polyolefin resin and formulation technologies, both by material suppliers and also via in-house efforts by the cable makers, complimented the evolution of improved optic cable designs. As material performance needs were identified, improved material candidates were developed through application of polymer science and formulation know-how. An early example of optic cable materials innovation was the 1987 commercialization of a special medium density polyethylene (MDPE) black jacketing compound (DHDA-8864 BK, available from The Dow Chemical Corporation) optimized for optic cable use. When evaluated versus conventional MDPE jacketing compounds, this material provided substantially improved signal attenuation performance during temperature cycling testing of optic cables. The compound provided this result via a novel polyethylene base resin that combined excellent low temperature modulus properties with a low post extrusion shrinkage characteristic to minimize the axial compressive stress exerted by the jacketing on the cable core. After many years, this low stress MDPE jacketing compound continues to be the preferred optic cable jacketing material in North America. There was also a series of HDPE black jacketing materials developments (1, 2, 3) that achieved low compressive stress by minimizing post extrusion shrinkage. This provides several jacketing material selection options to the cable designer and end users providing different balances of toughness, deformation (crush) resistance and flexibility.

Another example of optic cable materials evolution is the optimization of buffer tube materials within loose buffer tube cable designs. First generation products incorporated a dual layer polybutylene terephthalate (PBT)/nylon buffer tube construction. This was supplanted by use of dual layer PBT/polycarbonate and single layer PBT designs. More recently, there has been substantial use of lower cost polyolefin materials, both HDPE and nucleated impact modified polypropylene (IMPP) copolymers (4, 5) in single layer designs, particularly in North America. In comparison to the

PBT, both of these polyolefin materials provide some significant performance advantages including substantially improved flexibility, kink resistance and hydrolytic stability, along with a substantially reduced material cost. However, PBT provides substantially higher modulus/crush resistance and better compatibility (improved retention of modulus) with the hydrocarbon based water blocking greases used to fill the space inside the tubes around the fibers. Both impact modified polypropylene and PBT provide good fabricating characteristics including low post extrusion shrinkage (to minimize excess fiber length), good surface smoothness to minimize friction against the transmission fibers, and adequate cold bend and cold impact performance satisfying the range of outdoor installations. Compared to the IMPP, the HDPE shows advantage in buffer tube grease compatibility but exhibits a substantially increased level of post extrusion shrinkage characteristic that must be carefully accommodated in the buffer tube fabrication process. This example illustrates the complex balance between the cable design, materials selection and interactions, materials cost and a range of required technical performances. Commercial use is currently split between the HDPE and IMPP polyolefins and PBT, with PBT favored for applications requiring higher levels of crush resistance, particularly in the European market.

Also evolving in functional development was the design of water-blocking technology in the loose buffer designs, first via use of improved cable greases incorporating super absorbents. Cable manufacturers then developed dry core designs, with water-blocking provided by water swellable functionality incorporated into yarns, tapes, loose powders, and coatings such as those applied to the central strength member (6,7). The dry core design provided a craft friendly product substantially reducing installation costs while

sustaining the technical advantage of a strong water blocking capability.

Core tube (also known as central tube) designs represent another evolution in both cable design and compound technology. HDPE has traditionally been the material of choice for core tubes. Although the HDPE provided fabrication ease and relatively good grease compatibility, commercial use has evolved toward IMPP. The original incentive for the move to IMPP was to substantially boost the material melting temperature to avoid undesired fusing to the outer black jacketing during the subsequent jacketing extrusion process. However, when compared to the HDPE, the impact polypropylene also provided improvement to key modulus/crush resistance and post extrusion shrinkage performances. There was some sacrifice to extrusion fabrication ease and dimensional control due to the low melt strength and increased melt sag of conventional impact polypropylenes. For other profile extrusion shapes having increased dimensional control requirements, notable the various slotted core constructions, continuing use of polyethylene has been favored since conventional impact polypropylenes lack adequate melt strength. This situation offers a materials development opportunity for the core tube, slotted core and other optic cable profile extrusion applications. A new material would preferable have the desirable melting temperature and high modulus performance of conventional impact copolymer polypropylenes, but would incorporate substantially improved melt strength to enhance dimensional control in the profile extrusion

The technical evolution is a dynamic process, with cable suppliers constantly striving to reduce cable and installation costs and/or to enhance application performance. This creates a continuous demand for materials development yielding improved cost/performance in existing applications. There is also additional materials development opportunities to meet changing performance requirements as cable designs evolve.

Novel polyolefin materials providing substantial advantages to the buffer tube application and the core tube/slotted core profile extrusion will be introduced as the leading edge in the continuing cost/performance optimization of optic cable materials. A new family of polyolefin-based materials, called INSPIRE® Performance Polymers, has been developed by the Dow Chemical Company. The INSPIRE Performance Polymer family includes two technology platforms, one featuring enhanced melt strength for improved processing performance, and another featuring enhanced physical properties via increased stiffness and toughness in the solid state. As we discuss buffer tube and core tube/slotted core applications, developmental INSPIRE Performance Polymer products will be used to illustrate the ability to design molecular structure to deliver the desired properties for next generation products for both application areas.

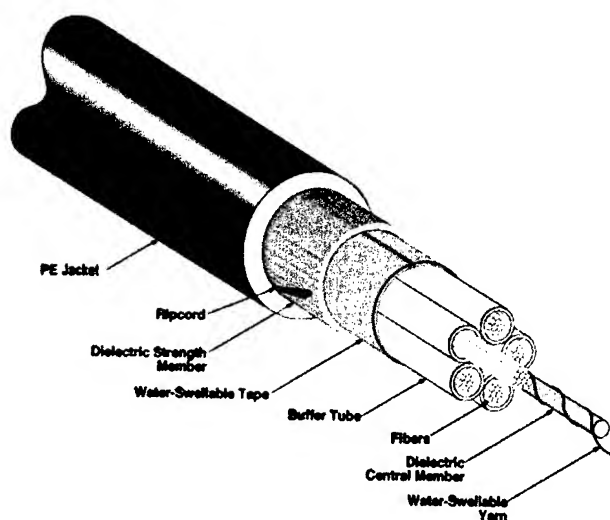


Figure 1. Loose buffer tube design.¹

¹ Copyright© Corning Cable Systems LLC, all rights reserved, reprinted with permission

2. Buffer Tube Application

The following performance attributes are typically required for materials used in loose buffer tube cable designs, primarily to minimize signal attenuation:

- **Balance of high stiffness and good impact strength.** Stiffness of buffer tube assures the protection of fiber optics by minimizing the mechanical stress asserted on them during bending of FOC. However, good impact strength is also important, particularly for cable installation and operation colder climates, as poor cold impact and cold bend toughness can lead to mechanical cracks of buffer tubes.
- **Compatibility with gel filling compound.** Due to the chemical composition of gel filling compounds, which are usually petroleum based, buffer tube materials will absorb the lower molecular weight species of such gels and result in deterioration of mechanical properties, especially modulus affecting tensile strength and crush resistance. Commercial buffer tube materials like impact modified polypropylene, due to its high permeability, can absorb significant amount of gel filling compounds during condition at 85°C for 45 days (according to Bellcore's GR-20-CORE specifications, section 6.3.4 on "cable material compatibility") (8). Deteriorated crush resistance can lead to signal attenuation when FOC is subjected to environmental stress during its operation.
- **Minimized excess fiber length (EFL).** Buffer tube materials must exhibit low shrinkage after fabrication in order to minimize EFL, which can expose fiber optics to environmental stresses during installation and operation.
- **Good surface smoothness.** Surface roughness of buffer tubes can also cause signal attenuation since fiber optics are subjected to friction against the tube when the cable is bent, or otherwise moved or mechanically deformed.
- **Good processability.** High production rates and uniform wall thickness of fabricated buffer tubes are optimal.

2.1 New Materials

As introduced earlier, polybutylene terephthalate (PBT) and HDPE

and impact modified polypropylene (IMPP) polyolefin materials represent the state-of-the-art materials technology for the loose buffer tube application. These polyolefin materials offer some significant advantages versus PBT, such as better impact strength and hydrolytic stability. However, these polyolefin materials have substantially lower crush resistance than the PBT due to their decreased modulus. In addition, due to its higher permeability, IMPP requires the use of specially formulated and more expensive gel filling compounds to minimize the amount of gel absorbed by the buffer tube material. Thus, the lower material cost of IMPP can be negated by the higher cost of gel filling compounds, such that the system cost (buffer tube plus gel) when using IMPP may not be very different in system cost than a PBT-based system for the FOC manufacturers.

Due to the advances in polymerization and material technologies, new PP materials are being introduced that offer a combination of good impact toughness with substantially higher modulus than IMPP. These materials, developed as part of the INSPIRE Performance Polymer platform by The Dow Chemical Corporation, offer high strength and toughness with the advantages of high modulus that is similar to PBT and improved toughness that is comparable to IMPP. Shown in Table 1 is a comparison of the material properties of INSPIRE PP1, PBT and IMPP. INSPIRE PP1 is a developmental material, not yet commercially available. The sample referred to as PBT in this comparison was Celanex 2001, available commercially from Ticona, and IMPP was Acctuf 3240, available commercially from BP Amoco.

2.2 Gel Compatibility

Due to a higher hydrocarbon permeability than PBT, the absorption of gel filling compounds by IMPP can severely affect its crush resistance after gel exposure at condition, 85 degrees C for 45 days, as specified in Bellcore's GR-2-CORE standard. This deterioration of crush strength can lead to signal attenuation when fiber optic cables are subjected to external stresses.

Two gel-based buffer tube filling compounds available commercially in North America from the Stewart Group were used in this study. LA444 is typically used for PBT and HDPE materials,

Table 1. Key Property Comparison for Buffer Tube Material Candidates.

Properties	Test Method	INSPIRE PP1	PBT	IMPP
Specific Gravity	ASTM D792	0.90	1.31	0.90
Melt Flow Rate, 2.16 kg at 230 °C, g/10 min	ASTM D1238	4.8	6.5	5.0
Flexural Modulus, at 23 °C, MPa	ASTM D790	1,731 - 2,172	2,276	1,310
Izod Impact Strength, at 23 °C, J/m	ASTM D256	64 - 214	55	approx. 200

while K550 is intended for IMPP. To model the crush resistance of buffer tube materials, coated wire samples, using a 14 gauge copper conductor, were used to compare different buffer tube compound materials. The wire samples had an outside diameter of ca. 3.3 mm (0.13") and a wall thickness of 0.76 mm (0.03"). Prior to aging buffer tubes in gel filling compounds, the copper conductor was removed from wire samples by drawing down the conductor. After aging, wire samples, with their surface cleaned of gel compound, were cooled down to room temperature (ca. 23°C). Drawn down 14 gauge copper conductor (with diameter of ca. 1.5 mm) was then inserted into wire samples for crush resistance testing.

As shown in Figure 2, crush resistance was tested by measuring the load required to crush through a wire sample. The jig had a width of about 1 mm and was traveling at 25 mm/min. The inserted copper conductor was intended to short-circuit the Instron machine as the jig came into contact with it, thus protecting the load cell. The reported value for each material was an average of five samples. Standard deviation of test results was about 10%.

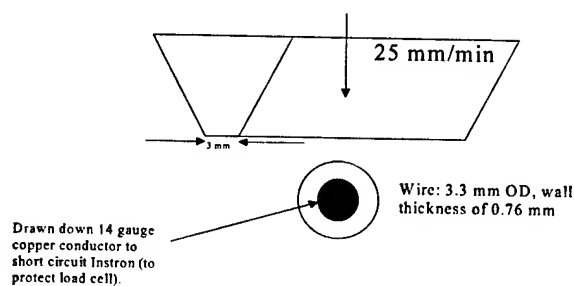


Figure 2. Crush resistance test.

As shown in Figure 3, INSPIRE PP1 had substantially higher crush resistance than IMPP after 45 days of aging in either the LA444 or K550 gels. The less aggressive K550 gel showed the expected advantage for the conventional IMPP. The high strength and toughness INSPIRE PP1 compound-based sample exhibited a substantial advantage in crush resistance versus the IMPP and achieved the targeted performance of providing improved crush resistance in combination with the lower cost LA444 gel versus the conventional IMPP with the K550 gel.

In addition to crush resistance, we can demonstrate the gel compatibility of buffer tube materials by measuring its modulus. The same extruded wire samples used for crush resistance were also

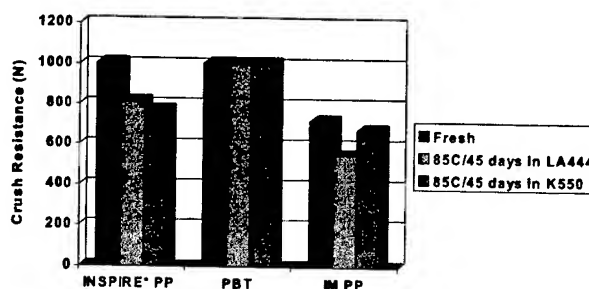


Figure 3. Gel compatibility comparison.

tested for 1% secant modulus (at 25 mm/min). As shown in Figure 4, the INSPIRE PP1 material had much higher modulus than IMPP when conditioned in either LA444 or K550 gel filling compounds.

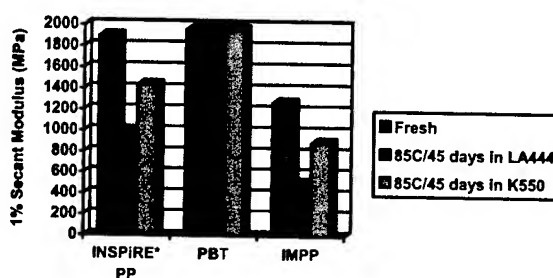


Figure 4. Gel absorption-stiffness comparison.

Results from these gel compatibility studies indicate that INSPIRE PP1-type compounds will maintain excellent crush resistance and stiffness after exposure to various gel filling compounds at 85 degrees C for 45 days. More importantly, INSPIRE PP materials can be used with less expensive gel filling compounds that are intended for PBT, thus offering substantial total system economic benefits for FOC manufacturers.

2.3 Other Physical Properties

In addition to improved performance in gel compatibility, INSPIRE PP1 also demonstrates comparable performance in post extrusion shrinkage and surface smoothness to PBT and IMPP, as shown in Table 2. Post extrusion shrinkage on wire samples was measured by conditioning wire samples in a convention air oven at 100

Table 2. Extrusion Fabrication Benchmarking Showing Good Surface Smoothness and Post Extrusion Shrinkage Performance

Buffer Tube Materials	Shrinkage after 24 hr at 100 °C (%)	Smoothness (micron)
INSPIRE PP1	1.37 ± 0.02	2.7 ± 0.6
PBT	1.52 ± 0.07	1.5 ± 0.5
IMPP	1.41 ± 0.02	3.6 ± 0.6

degrees C for 24 hr. Surface smoothness of wire samples was measured by SurfTest SV-400 profilometer.

3. Profile Extrusion-Type Applications

3.1 Core Tube Design

Figure 5 illustrates a typical core tube cable design. In this design, the transmission fibers are typically included as fiber bundles or ribbon cables positioned at the center of the cable core. They are surrounded by core tube containing cable grease for water blocking protection. The core tube contributes to crush resistance in combination with the outer jacketing and strength member reinforcement.

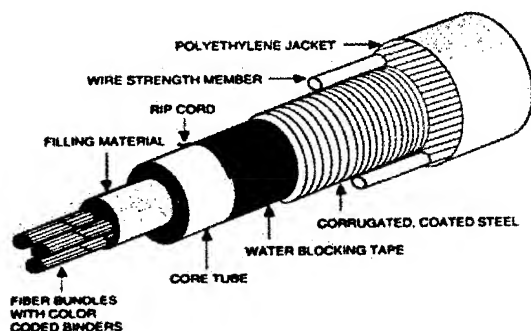


Figure 5. Core Tube Design.²

Many of the requirements for core tube are similar to those for the optic buffer tube application:

- **Good surface smoothness.** Important to minimize frictional force between fiber bundles or fiber ribbon cables components and the inner surface of the core tube, especially when cable is bent, or otherwise moved or mechanically deformed.
- **Low post extrusion shrinkage.** Core tube design provides some advantage in accommodating increased shrinkage versus buffer tube design.
- **Good crush and deformation resistance** contributing to the protection of fiber optics against mechanical stresses.
- **Good compatibility with core tube greases**, especially in terms of retention of modulus and crush resistance.
- **Good dimensional control** with minimal sag during extrusion and cooling
- **Good cold bend and cold impact properties** to provide good application toughness for installation and use in cold climates
- **High melting temperature** to minimize potential for melting/fusing during outer jacket extrusion

- **Good extrusion capability.** High speed capability with good surface smoothness and dimensional control.

High density polyethylene was originally used in the core tube application, but there was increasing use of IMPP copolymer starting in the early 1990s as a result of a number of technical considerations. These included an increased melting point which reduced the potential for any undesirable fusing of the core tube to the outer black jacket during the jacketing extrusion process, reduced post extrusion shrinkage for reduced EFL and signal attenuation and higher modulus/deformation resistance. These advantages overcame a trade-off in extrusion capability relating to the low melt strength of conventional IMPP material.

Novel INSPIRE materials having substantially improved melt strength and extrusion capabilities have been introduced. These high melt strength materials have been an excellent fit to applications such as blown film, foamed sheet and the optic cable core tube and slotted core extrusion profile applications. A high impact grade, D113.01 has been developed for use in optic cable applications. Figure 6 shows the enhanced melt strength for D113.01 versus a comparative conventional IMPP.

The melt strength data presented was generated using a capillary rheometer coupled to a Rheotens apparatus. Samples were equilibrated at 190°C and the melt extruded a 1.0 inch/minute piston speed. The Rheotens nip rolls are located 100 mm below the capillary die and are accelerated at a rate of 2.4 mm/sec². Tensile force is recorded as a function of nip roll take-off speed. The maximum tensile force attained is defined as the melt strength, recorded in centi-Newtons (cN). Drawability is defined as the speed at which the maximum tensile force was achieved.

The substantial improvement in melt strength provides the cable manufacturer a significant improvement in fabrication extrusion and dimensional control that is very advantageous.

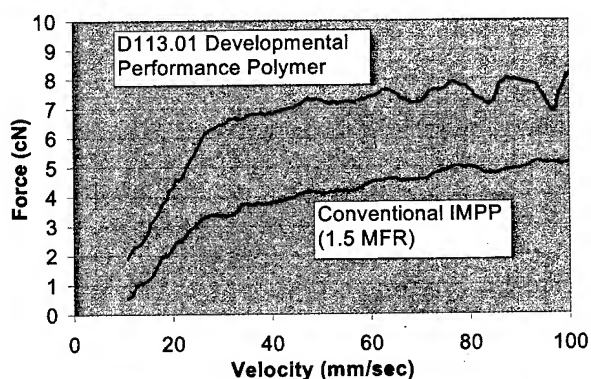


Figure 6. Melt strength comparison for D113.01 and conventional IMPP.

² Copyright© OFS Brightwave, all rights reserved, reprinted with permission

Table 3. Comparison of Critical Physical Properties for D113.01 and Conventional IMPP.

Properties	Test Method	Units	D 113.01	Conventional IMPP
Melt Flow Rate, 230°C/2.16 kg	ASTM D 1238	g/10 min	0.9	1.5
Specific Gravity	ASTM D 792	g/cm ³	0.90	0.90
Flexural Modulus; (0.05 in/min, 1% secant)	ASTM D 790A	psi	148,000	140,000
Tensile Strength @ Yield	ASTM D 638	MPa	19.5	22.0
Ultimate Elongation	ASTM D 638	%	>500	>500

Table 3 compares the D113.01, commercially available from the Dow Chemical Company, to a conventional IMPP previously used in core tube applications. This high melt strength product, D 113.01, is providing good commercial performance in core tube applications.

3.2 Slotted Core Design

Figure 6 illustrates a typical slotted core cable design. The performance requirements are very similar to those for core tube use, although the balance of properties is slightly shifted. The more complex slotted core shape includes radial fins providing the slots for holding the optic fibers.

The need to tightly control the shape of these fins increases the need for good melt strength during the profile extrusion process, as well as tight control of the elastic portion of the polymer rheology. In particular, there is a need for minimal sag of the fins during extrusion and subsequent cooling in the water troughs. On the other hand, the strength central member greatly reduces post extrusion shrinkage because it provides high compression resistance when the slotted core profile is extruded over it to form a composite structure. Hence, the performance balance favors high melt strength with minimal sag, with less concern about post extrusion shrinkage, and this has traditionally favored the continued use of polyethylene materials in this application. The new D113 high melt strength product is a strong candidate for this application by providing good dimensional control during extrusion of the slotted core profile while contributing increased deformation resistance to the finished product. Slotted core evaluations are being pending and

will be reported in the near future.

4. Conclusions

Novel developmental INSPIRE products featuring high melt strength or high strength and toughness offer good potential to advance overall cost/performance improvements in key optic cable applications. For buffer tube use, high modulus/high toughness materials bring substantially improved crush resistance and cable grease compatibility versus medium impact polypropylenes now in use. Enhanced compatibility with the less expensive buffer tube filling gels offer system cost advantages compared to existing PBT use, as well as advantages compared to conventional IMPP which require higher viscosity, and higher priced, gels.

For optic core tube (center tube) and slotted core applications, novel high melt strength polypropylenes offer good extrusion characteristics with minimal sag characteristics, while bringing the desirable high modulus and corresponding crush resistance of the polypropylene materials. These materials have also demonstrated the needed balance of other performance characteristics such as good surface smoothness, low post extrusion shrinkage contributing to excess fiber length and signal attenuation, and sufficient cold impact performance for outdoor installation and use in cold climates.

5. Acknowledgements

The authors gratefully acknowledge the assistance of Dow Chemical Company research and technical service personnel, principally Alan Whetten, Lisa Madenjian, and Marie Hare for their support throughout this work. The assistance by Brian Thiffault of the Stewart group in the evaluation of buffer tube filling gels is also appreciated.

6. References

- [1] Aldhouse S.T.E., McMahon D., Robinson J.E., "Problems and Opportunities in the Use of 'Short Relaxation' Linear Polymers in Telecommunication Cable Applications", Proceedings of Fourth International Conference; Plastics in Telecommunications, 1986, pp. 32.1-32.12.
- [2] Rogstedt L., Martinsson H.B., "A New Generation Polyethylene Resins For Cable Jacketing Applications, Proceedings of the 47th IWCS, 1999, pp. 126-131.

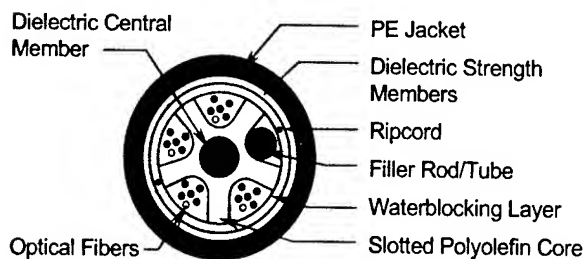


Figure 7. Slotted Core Design

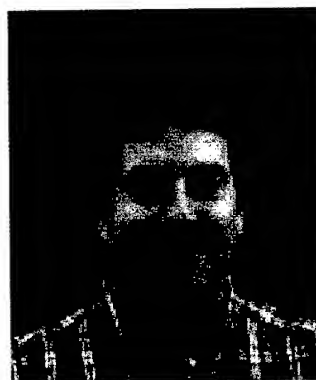
- [3] Chen T., Leech J. R., "Design of Polyethylene Cable Jacket Compounds of Superior Jacketing Performance", Proceedings of the 48th IWCS, 1999, pp. 807-814.
- [4] Adams M., Holder J., McNutt C., Tatat O., Yang M., "Buffer Tubes: The Next Generation", Proceedings of the 44th IWCS, 1995, pp. 16-21.
- [5] Yang H.M., Holder J.M., McNutt C.W., "Polypropylene-Polyethylene Copolymer Buffer Tubes for Optical Fiber Cables and Method for Making the Same", United States Patent #5,574,816, November 12, 1996.
- [6] Clyburn III C. E., Bringuier A. G., "A Dry Core Loose Tube Cable for Outside Environments", Proceedings of the 44th IWCS, 1995, pp. 29-36.
- [7] Gaillard P., McNutt C., Holder J., Bouvard A., and Tatat O., "Significant Improvement of Loose Tube Cable Splicability Based on New Cable Dry Design", Proceedings of the 45th IWCS, 1996, pp. 353-358.
- [8] Bellcore, "Generic Requirements for Optical Fiber and Optical Fiber Cable, GR-20-CORE", Issue 2, July 1998.



Dr. K. P. (Peter) Pang is a scientist in the Wire & Cable Compounds R & D of The Dow Chemical Company and is responsible for research and product development of buffer tube compounds for fiber optic cables, and insulation and semiconductive compounds for power cables. He earned his Chemical Engineering degrees from University of Wisconsin, Madison and Princeton University, and his MBA from Indiana University.



Mr. Geoffrey D. Brown is a scientist in the Telecommunications Wire and Cable Materials Research Group of The Dow Chemical Company. He earned his BS and MS in Mechanical Engineering at Bucknell University in Lewisburg, Pennsylvania. He has extensive wire and cable materials development experience across a broad range telecommunications and flame retardant wire and cable applications. Current assignments include project leader for development of INSPIRE performance products for telecom wire and cable applications.



Dr. Scott H. Wasserman is the Global Technology Leader - Telecommunications, in the Wire & Cable Compounds business of The Dow Chemical Company. He received his Ph.D. in Chemical engineering from Princeton University in 1993 and his BChE degree in Chemical Engineering from the University of Delaware in 1988. Dr. Wasserman's expertise includes the rheology of polyolefin melts and the design of polyolefin-based compounds for fiber optic cable components, wire and cable jackets, and solid and foamed insulation applications.

The Power of Performance Additives

W. Mark Stewart

PolyOne

6521 Davis Industrial Blvd.

Solon, Ohio 44139

Phone: 440-715-7000

Fax: 440-715-7070

Mark.Stewart@PolyOne.com

Abstract

This paper explores the incorporation time of Performance Additives (prepared rubber chemicals or pre-dispersions of rubber chemicals, and colorants) with dry powders. The value of Performance Additives in compounding and mixing will be demonstrated in formulations based on several different polymers. Some of the functions of these materials include reducing manufacturing time, improving the worker environment, driving consistency, and providing a safe means of handling difficult raw materials. "Right engineering" of a solution will be covered as we delve into the sometimes-overwhelming number of options available to compounders and plant chemists.

Keywords

Prepared chemicals; additives; concentrates; performance additives.

1. Introduction:

Performance Additives provide a variety of benefits, but the selection may seem overwhelming at times. To select the "best" one a clear definition of the desired outcome must be envisioned. A systematic approach is necessary. Common objectives include the following: Cleanliness, Dispersion, Color Control, Ease of Handling, Ease of Incorporation, Consistency, Better Throughput and / or Precise control of critical ingredients. Envision the result needed for a particular application in order to work toward the solution. An initial review of the available forms builds the foundation for this work.

2. The Power of Performance Additives

2.1 Additives Types

2.1.1 Pre-weighed Materials. Critical compound components, such as the cure system, are often pre-weighed. This technology may be simple as off-site hand weighed components. Low melt point bags are used and the unit is added directly into an internal mixer. This technology is no different than the compounding methods the industry has employed for years. The prime benefit of this approach is direct labor reduction.

When the multi-components are pre-blended on a large scale, improved uniformity can be expected. During the blending operation, oil may be added to reduce dust loss when the bag is broken in a mixer and pre-wet powders may incorporate faster.

When a specified system contains reactive components, the reactive material is separately weighed and packaged. This bag is

sealed and added to the balance of the system. Thus, the unit becomes a bag within a bag.

This technology provides the following benefits:

1. Improved product uniformity and process control
2. An "environmentally friendly" package
3. Labor reduction by eliminating a compounder
4. Reduced work, downgrading or scrap

2.1.2 Dust-suppressed powders. Dust-suppressed powders are materials that have been treated to make them less dusty. The most common treatment is wetting the powders with an oil or plasticizer. Several issues are important in fluid treatment. Fluid selection should be governed by the intended application. Obviously, a compatible fluid is required to achieve a reasonable incorporation time during mixing. Incompatible fluids may bleed and cause fabrication problems and an unacceptable final product. Regulatory considerations are also important if the final product is a medical device, FDA regulated or a NSF governed product. Complete powder treatment is needed for effective dust suppression. Over-treatment can lead to re-massing and handling problems. Commonly, fluid addition levels range from 4% to 20%. Since fluid application is performed in low to medium intensity mixers, the particle size and agglomeration of the original powder critically affects dispersion quality.

Moisture sensitive materials are afforded a degree of protection by oil treatment. Magnesium oxide and calcium oxide are commonly treated with oil. These products may have a bead-like appearance or if heavily treated to a paste consistency, they may be extruded into bar forms.

Dust suppression reduces direct material contact, inhalation hazards and in-process material loss to dust collectors. Plant effluent streams, such as packaging residue and contaminated clothing, are also reduced by treated powders.

Since fluid treatment may be performed in powder mixing equipment, an opportunity to manufacture powder blends is present. Critical compound components, such as cure systems, flame retardant systems and multi-pigment colorants, are often prepared as pre-blends. The main constraint for multi-component blends is chemically compatible, non-reactive components. These pre-blends are often customer specified, proprietary compositions.

Pre-blends reduce the number of weighings by compounders. Therefore, labor reduction may be possible in large plants. Large scale powder blending can improve blend composition uniformity. This often yields improved process and product

uniformity. Improved uniformity normally translates into improved quality and reduced manufacturing costs. These are measurable benefits.

2.1.3 Encapsulations. The processes used to encapsulate powders are very similar to fluid treatment processes. The major difference is the composition of the additive. The composition of the encapsulating material is dictated by the same concerns noted for dust-suppressed powders – compatibility and regulator constraints. Since these products are mixed in the same type of low to medium intensity equipment which is used for the previously described product form, the particle size and agglomeration of the basic powder component(s) is important.

Early encapsulated products were wax treated. This was common in the lead oxide market. Obviously, lead products are prime candidates for treatment due to their health hazards. However, waxes frequently exhibit compatibility problems with polymers. Therefore, mixing and bloom problems may be encountered. During mixing, waxes tend to coat the surfaces of mixing equipment and lubricate compounds. Thus, these materials reduce shear input and extend the mixing time. Since waxes are thermoplastic, they may cause re-massing of the treated powder, if the product is subjected to heat. Handling problems occur when this happens.

A number of year's ago, a polymer and fluid based encapsulation system was developed to address the above concerns. These are polymer bound powder products. Single component or customer specified, chemically compatible, non-reactive systems are available. These systems have overcome the deficiencies of wax or thermoplastic material encapsulations.

Polymer encapsulated powder products are completely dust-free and do not cling to packaging or handling equipment. Thus, in-process losses are substantially reduced and the product form is "environmentally friendly". Due to their polymer content, they are not thermoplastic. Therefore, re-massing is eliminated. Additionally, they have an affinity for compounds, not mixing equipment surfaces. Plate-out on the surfaces of mixing equipment is eliminated and mixing efficiency is maintained.

Properly handled, mixing times can be dramatically reduced and mill pan or internal mixer throat sweeps can be eliminated. These products have the appearance of finely ground rubber. Their small particle size facilitates distributive mixing. The rapid incorporation of Polymer encapsulated powders has facilitated changes in mixing procedures and resultant cost savings. Some have introduced cure components late in a single pass mix to eliminate two-pass mixing requirements. If the cure system has a very short scorch time, the compound may require some cooling before the curative(s) can be added. This may be achieved on the drop mill below the internal mixer. Compared with dry powders, some have seen incorporation times on a 2-roll mill reduced by over 50% with Polymer encapsulated powder substitution. These are measurable manufacturing cost reductions.

2.1.4 Absorbed "Liquids" - Dry Liquid Powders. A low melting solid or viscous liquid is difficult to handle and mix. Often, the material must be heated to handle, thus creating a

safety hazard. Liquid addition during mixing tends to lubricate compounds and reduce shear input. When liquids are added, they must be added slowly to maintain effective mixing. Such materials are often absorbed on high surface area carriers. The final product handles like an "oiled" powder. Carrier selection may be tailored to the final application. Products utilizing fumed silicas or diatomaceous earth can achieve 60 to 75% activity. Unfortunately, these carriers are prone to moisture pick up. Unless the carriers are dried prior to use, moisture is expected. For moisture sensitive materials or applications, calcined clays may be used. They are not as prone to moisture pick up. Due to their lower surface area, final products are typically 30% to 40% active. Some of the common material handled in this fashion are petroleum oils, ester plasticizers, low softening point resins (pine tar, rosin, coumarone-indene, phenolic, etc.), waxes, low molecular weight liquid elastomers, adhesion promoters, silane coupling agents, co-agents and peptizers.

Some of the benefits of the above technology include:

1. Improved handling
2. More accurate weighing and addition
3. Reduced packaging losses
4. Improved mixing

2.1.5 Partitioned "Solids". Lower melt point solids, such as tackifying resins, are often supplied in drums. Due to their low melt point, the material is one large mass. To handle these materials, they must be broken or crushed into small particles that can be weighed and mixed. Unless the particles are partitioned, they will re-mass. Partitioning agents are usually clay, precipitated silica or diatomaceous earth. The prime benefit of this form is improved handling which translates into reduced labor costs and decreased health and safety issues.

2.1.6 Polymer based Dispersions. The key factors that determine dispersion quality are the raw material quality, the dispersion formulation, processing equipment and mixing procedure. A polymer based binder system (continuous phase) should be of sufficient viscosity at processing temperature to ensure adequate shear input to attain good deagglomeration and uniform dispersion. The pre-dispersion must be soft enough at processing temperatures to attain good distributive mixing in the final compound. The binder system should also be non-reactive polymer that is compatible with the final compound and it's application. For these reasons, dispersions based on NR, SBR, NBR, EPR, EPDM, EPDM/EVA, CPE, CR, PVC, various other thermoplastic polymers, or customer specified polymer grade and/or source may be required. Single component dispersions are the most common, however, multi-component dispersions are produced to customer specification. These dispersions are limited to non-reactive compositions.

Some of the benefits obtained when powders are replaced with polymer based dispersions include:

1. Improved material handling
2. Reduced mixing time (Mixing is distributive rather than dispersive.)
3. Improved product & process uniformity when a multi-component dispersion is used

4. Reduced in-process material shrinkage
5. Lower scrap and/or downgraded product
6. Improved environmental conditions (Both direct contact & indirect contact are reduced.)

2.1.7 Paste Dispersions. Chemical or color paste dispersions are often used in very low viscosity compounds to achieve good dispersion and distributive mixing. The same constraints are present with paste dispersions as were noted for all previous systems. Fluid selection and multi-component limitations are important. Paste dispersions can range from fairly low viscosity products that are pumped and metered to products so viscous, they are extruded as bar forms.

Dispersion quality should be specified to ensure adequate quality for the final application. Generally, paste dispersion cost is directly related to the quality of dispersion specified. Paste dispersion quality or deagglomeration may be measured by the Hegman NS Grind test (ASTM D-1210). This simple test measures the maximum residual particle size and expresses it as a number between 0 (100 microns) to 8 (0 microns).

Among the benefits noted with the use of single or multi-component paste dispersions are the following:

1. Improved dispersion and faster distribution in low viscosity compounds
2. Improved uniformity with multi-component paste dispersions
3. Reduced re-work, downgrading and scrap

2.1.8 Color Dispersion. Colorants or pigments are frequently used in pre-dispersed forms for numerous reasons:

Handling, housekeeping and cross-contamination are major problems with dry pigments.

Color consistency is a major problem, since color and strength are often variable between pigment lots.

Generally, pigment strength is a function of surface area. Therefore, pigments become more efficient as their agglomerates are reduced in size. Pigment efficiency is a significant factor for high priced pigments.

Colorants requiring multi-pigment systems are difficult to formulate and adjust with changes in pigment lots.

Numerous types of pigments can be used to produce the same final color. However, the performance of these pigments in various environments and applications can vary greatly. Key considerations are the temperature range encounter during processing and service, light exposure, chemical environment and expected service life. Thus, selection of the proper and most cost effective pigment for each application is important for cost containment and product quality.

These are the prime factors leading to the use of pre-dispersed and color certified colorant systems. The actual dispersion forms are

fairly similar to those discussed for chemicals. The guiding principals are also very similar.

2.2 Experimental

Laboratory testing has been completed to evaluate the distributive mixing of 6 common rubber formula ingredients in 4 different performance additive forms in 3 different base polymer systems. Some of the results were expected; others were very surprising.

The procedure utilized a 2-roll mill with a friction ratio of 1.24 and a temperature of 52 C (125F). Two hundred grams of rubber were banded on the mill and brought to temperature. The rubber was then sheeted out at 4.76 mm (3/16 inch) thickness and then 3.2 grams of active material was placed in the center of the sheet. To assure uniformity of addition, the active was then rolled into the sheet. This material was placed end to end on the mill, the stopwatch was started, and it was allowed to band. The rubber was continuously worked to assure consistent, uniform observation. As soon as the active had visually disappeared, the stopwatch was stopped. This test was run in triplicate and the average time to visual disappearance was calculated.

The chemicals studied were Zinc Oxide, Sulfur, MBT, MBTS, TMTD and Magnesium Oxide. The forms included powder, EPDM/EVA binder, EPR or NBR binder, Bar and some proprietary encapsulation technology. EPDM, NBR and CR based formulations enabled incorporation times in various polymer systems to be studied.

TABLE I

CR Formulation	Parts
CR Polymer	100
ODPA	2
Stearic Acid	0.5
SRF Carbon Black (N762)	30
Total Parts:	132.5
EPDM Formulation	Parts
EPDM Polymer	100
N550 FEF Carbon Black	95
TMQ	2
Paraffinic Process Oil	90
Stearic Acid	1
Total Parts:	288
NBR Formulation	Parts
NBR Polymer	100
DOP	10
N-762 Carbon Black	75
TMQ	2
Total Parts:	187

The unaccelerated masterbatch (Table I) was mixed in the PolyOne Burton, Ohio facility. These batches were mixed on a Moriyama mixer. The Moriyama is a tilt-chamber, seal-less, tangential mixer that is used for small batch mixing. The material was packaged in an enclosed box with an approximate weight of 50 lbs. per box and shipped directly to Massillon from Burton. The testing was done using the same lot of each masterbatch.

2.3 Results & Discussion

In each of the Figures, there are "E", "N" and / or "C" types of concentrates. The "E" versions are specifically designed for EPDM type materials. The "N" versions are formulated to go into NBR type materials quickly, and the "C" versions are prepared for quick incorporation into CR base compounds.

2.3.1 MBTS - 2, 2' - dibenzothiazyl disulfide - Melting point of 180 C

This work shows the results for distributive mixing. Examining the data in Figure 1 reveals the following. When MBTS was incorporated into the compounds, EPDM accepted the MBTS more quickly than NBR, and NBR more quickly than CR.

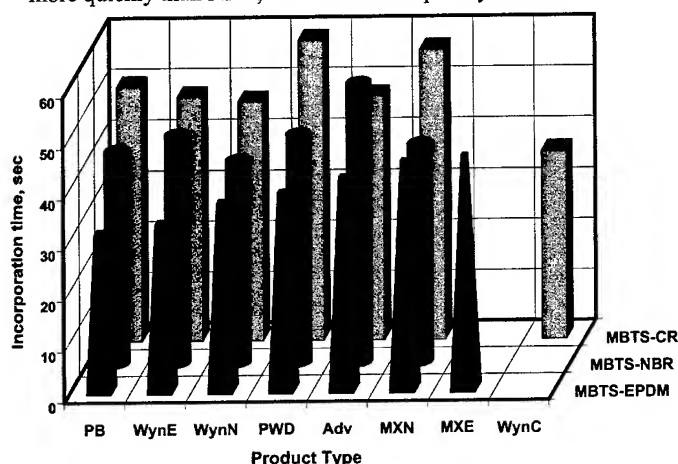


Figure 1. Incorporation Time for MBTS Dispersions

The seven materials shown in Figure 1 are:

1. PB - Polymer bound encapsulated powder, 80% MBTS
2. WynE - Proprietary chemical masterbatch dispersion, "E" type, 80% MBTS
3. WynN - Proprietary chemical masterbatch dispersion, "N" type, 80% MBTS
4. PWD - MBTS powder
5. Adv - An EPDM / EVA masterbatch, 75% MBTS
6. MXN - Commercially available masterbatch using a NBR binder, 75% MBTS
7. MXE - Commercially available masterbatch using a EPR binder, 75% MBTS
8. WynC - Proprietary chemical masterbatch dispersion, "C" type, 80% MBTS

MBTS is a commonly used thiazole type accelerator. Studying the incorporation of MBTS we see that an incompatible binder was worse than powder. In the EPDM compound, when NBR is used

as the binder (MXN), the MBTS concentrate does not distribute well into the EPDM, similar to EPDM concentrates (WynE and Adv) in NBR. Polymer bound encapsulated powder (PB) appears to be the best for quick incorporation of MBTS when the base polymer is EPDM.

In Nitrile, the EPDM/EVA based concentrate (Adv) took the longest to incorporate, 55 seconds. Actually, this phenomenon was noted in Production batches and was the impetus to begin this study. The EPDM based concentrates seemed to work well for the EPDM based compound, but were very difficult to incorporate into Nitrile compounds. Powder (PWD) took 45 seconds. Both a Nitrile based additive (MXN) and one compatibilized for NBR (WynN) were better than powder (PWD), but the best was the concentrate compatibilized for Nitrile (WynN) which distributed in 40 seconds.

Each concentrate tested was better than Powder (PWD), 59 seconds, going into CR. The best was the CR compatibilized material (WynC) which took only 37 seconds.

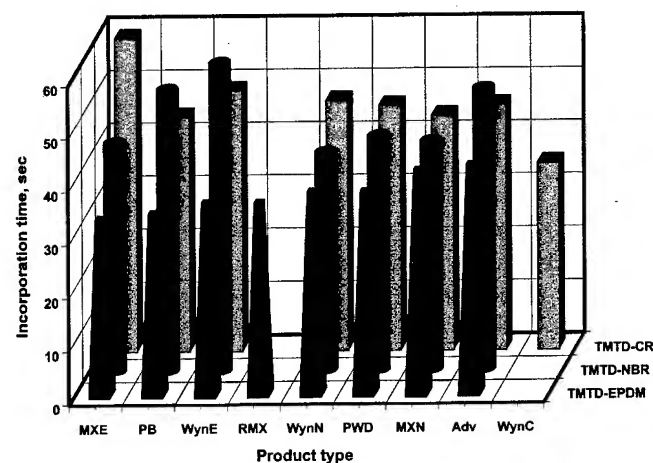


Figure 2. Incorporation Time for TMTD

2.3.2 TMTD - tetramethyl thiuram disulfide - Melting Point of 155 C

The nine materials shown in Figure 2 are:

1. MXE - Commercially available masterbatch using a EPR binder, 75% TMTD
2. PB - Polymer bound encapsulated powder, 80% TMTD
3. WynE - Proprietary chemical masterbatch dispersion, "E" type, 80% TMTD
4. RMX - Oil treated Powder, 90% TMTD
5. WynN - Proprietary chemical masterbatch dispersion, "N" type, 80% TMTD
6. PWD - TMTD powder
7. MXN - Commercially available masterbatch using a NBR binder, 75% TMTD
8. Adv - An EPDM / EVA masterbatch, 75% TMTD
9. WynC - Proprietary chemical masterbatch dispersion, "C" type, 80% TMTD

The quickest incorporation of TMTD into EPDM uses the EPR binder (MXE), then Polymer encapsulated powder (PB). Powder (PWD) incorporates in 44 seconds in the NBR compound. It is clearly evident that the wrong binder choice can significantly

delay incorporation. Note the Proprietary chemical dispersion "E" type optimized formulation (WynE) took 58 seconds, and the EPR based (MXE) took 55 seconds. The best was a formulation optimized for NBR (WynN), followed by an NBR binder (MXN). A consistent theme that this work shows is that concentrates made specifically for incorporation into CR binders outperform many "generic" types. The 35 seconds for WynC illustrates a 20% improvement over the next closest TMTD material (PB).

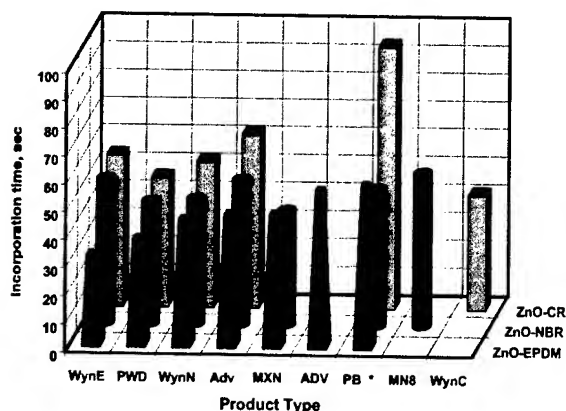


Figure 3. Incorporation Time for ZnO Dispersions

2.3.3 ZnO – Zinc Oxide

These nine materials in Figure 3 are:

1. WynE - Proprietary chemical masterbatch dispersion, "E" type, 85% ZnO
2. PWD - ZnO powder
3. WynN - Proprietary chemical masterbatch dispersion, "N" type, 85% ZnO
4. Adv - An EDPM / EVA masterbatch, 80% ZnO
5. MXN - Commercially available masterbatch using a NBR binder, 85% ZnO
6. ADV - An EDPM / EVA masterbatch, 85% ZnO
7. PB* - Polymer bound encapsulated powder, 85% ZnO-
*Note – this never fully incorporated, this is the time when no further visual improvement occurred.
8. MN8 - Commercially available masterbatch using a NBR binder, 80%
9. WynC - Proprietary chemical masterbatch dispersion, "C" type, 85% ZnO

The ZnO WynE distributed more quickly in EPDM than any of the other choices, with powder (PWD) being the second. Since Zinc Oxide can be difficult to disperse, speed of incorporation does not completely reflect final performance in a compound. In Nitrile compound, the Nitrile based dispersion (MXN) was the first to incorporate, followed by powder (PWD), then the WynN, a material compatibilized for Nitrile. For CR, the best was the material specifically created for CR incorporation (WynC), followed by powder (PWD).

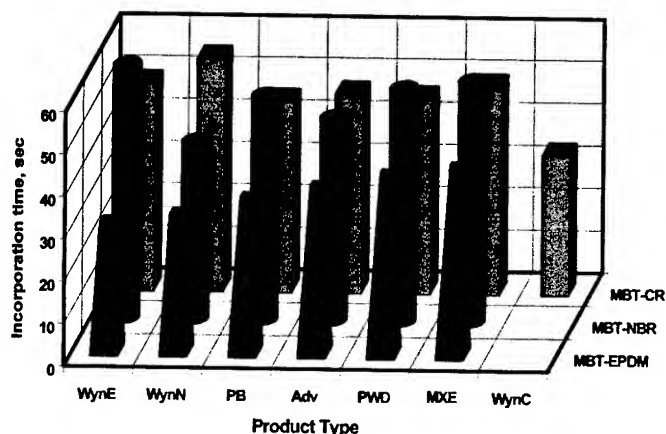


Figure 4. Incorporation Time for MBT Dispersions

2.3.4 MBT – 2 – mercapto benzothiazole – Melting point of 181 C.

The seven materials shown in Figure 4 are:

1. WynE - Proprietary chemical masterbatch dispersion, "E" type, 80% MBT
2. WynN - Proprietary chemical masterbatch dispersion, "N" type, 80% MBT
3. PB - Polymer bound encapsulated powder, 80% MBT
4. Adv - An EDPM / EVA masterbatch, 75% MBT
5. PWD - MBT powder
6. MXE - Commercially available masterbatch using a EPR binder, 75% MBT
7. WynC - Proprietary chemical masterbatch dispersion, "C" type, 80% MBT

MBT powder (PWD) incorporated into the EPDM in 43 seconds. The best was Proprietary chemical dispersion "E" type (WynE) at 31 seconds.

Powder (PWD) took 55 seconds to incorporate into NBR; it can be noted that the best was one created specifically for NBR compatibility (WynN), and it was 42 seconds. The longest was the binder developed for EPDM, (WynE), with 60 seconds. The incorporation time of MBT into NBR graphically illustrates the importance of binder/polymer compatibility.

Examining incorporation into the CR based material, MBT powder (PWD) dispersed in 46 seconds, while the worst was 55 seconds for the NBR optimized Proprietary chemical dispersion "N" type binder (WynN). By far the fastest was the material optimized for a CR binder (WynC), and it took only 33 seconds.

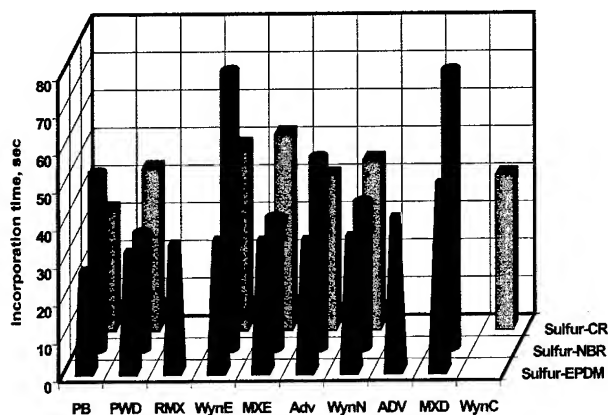


Figure 5. Incorporation Time for Sulfur Dispersions

2.3.5 Sulfur

The ten materials shown in Figure 5 are:

1. PB - Polymer bound encapsulated powder, 85% Sulfur
2. PWD - Sulfur powder, ½ % oil treatment for dedusting
3. RMX - Oil Treated Powder, 90% Sulfur
4. WynE - Proprietary chemical masterbatch dispersion, "E" type, 80% Sulfur
5. MXE - Commercially available masterbatch using a EPR binder, 75% Sulfur
6. Adv - An EDPM / EVA masterbatch, 75% Sulfur
7. WynN - Proprietary chemical masterbatch dispersion, "N" type, 80% Sulfur
8. ADV - An EDPM / EVA masterbatch, 80% Sulfur
9. MXD - Commercially available masterbatch using a EPDM binder, 80% Sulfur
10. WynC - Proprietary chemical masterbatch dispersion, "C" type, 80% Sulfur

Sulfur is used for many cure systems. Large quantities of both soluble and insoluble sulfur are consumed on an annual basis. This study used the soluble sulfur type, ½ % oil treated. Each of the concentrates were prepared using this sulfur type so valid comparisons could be made.

Although powder (PWD) disappeared into the EPDM quickly in 32 seconds, the polymer-encapsulated powder (PB) was still better with a time of 27 seconds.

Nitrile accepted the powder (PWD) quickly, outperforming all of the concentrates tested here. Recall that dispersion is not the reported criteria, only visual examination while on the 2-roll mill. When incorporating Sulfur into CR, the clear winner is the polymer-encapsulated powder (PB) with 32 seconds. Both the EPDM/ EVA (Adv) and the compatibilized concentrates for CR (WynC) went in faster than powder. Those compatibilized for other polymers, WynN, WynE and an EPR based concentrate (MXE) did not perform nearly as well.

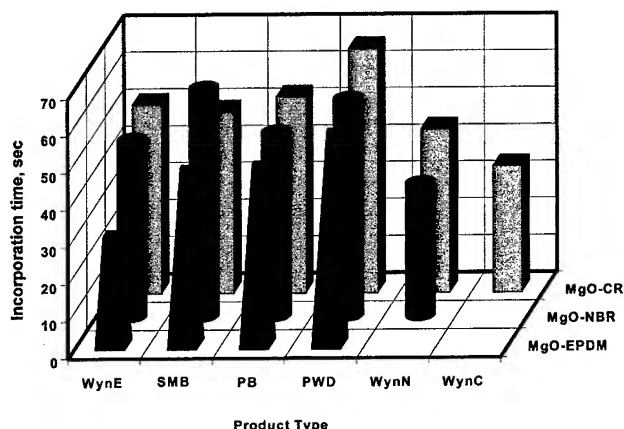


Figure 6. Incorporation Times for MgO Dispersions

2.3.6 Magnesium Oxide-

The six materials shown in Figure 6 are:

1. WynE - Proprietary chemical masterbatch dispersion, "E" type, 65% High Activity MgO
2. SMB - Extruded Bar, High Activity MgO, 70% MgO
3. PB - Polymer bound encapsulated powder, 70% MgO
4. PWD - High Activity MgO powder
5. WynN - Proprietary chemical masterbatch dispersion, "N" type, 65% High Activity MgO
6. WynC - Proprietary chemical masterbatch dispersion, "C" type, 65% High Activity MgO

For comparison, we tested the dispersability of Magnesium Oxide dispersions in various binders. All of the Magnesium oxides used in this study were of the high activity type. In order, the EPDM base polymer shows powdered MgO (PWD) taking the longest to incorporate at 58 seconds. The polymer encapsulated powder (PB) and extruded bar (SMB) were both quicker to incorporate than the powder (PWD). The best was a concentrate specifically designed for ease of incorporation into EPDM type material (WynE), which took only 30 seconds.

The Nitrile base polymer reveals the importance of binder compatibility. The longest incorporation time was 62 seconds (SMB), powder (PWD) was 59 seconds, but the best was a Magnesium Oxide material specifically compatibilized for NBR (WynN), incorporating in only 36 seconds. Binder compatibility can play a significant role in incorporation time.

Since MgO is an activator and an acid scavenger, it is most often used in CR polymers. For MgO to perform, it must be protected from moisture. All of the performance additive forms provide some degree of protection from moisture. Powder (PWD) was the most difficult to incorporate into the CR polymer, at 62 seconds. The polymer encapsulated powder (PB) took 53 seconds, the WynE, 51 seconds, the extruded bar (SMB) 49 seconds, the WynN 44 seconds, and again, a binder specifically compatibilized for CR type polymer (WynC) was a clear winner requiring only 34 seconds.

3. Conclusions

Binder selection and compatibilization can make a significant difference in the incorporation time in different polymer systems. The difference of a "universal" type binder versus custom designed binders in various polymer compound types was surprising.

Finding the best solution can be difficult. The answer lies in a well-defined problem. Is it lower total cost, excellent dispersion, ease of handling, worker safety, or some other issue that describes the desired outcome? The options available include: DeDust, Pre-Weigh, EPDM / EVA, Custom MB, Paste, and Easier to handle powder of a viscous liquid.

Dedusted powder would be the product of choice if reducing airborne contamination, or precise ratios of critical ingredients are important. A Pre-weigh takes this product form one step further and insures accurate weights of the pre-blended components, thus eliminating one more variable. If dispersion and quick incorporation is necessary, one may evaluate a "universal" EPDM/EVA type binder, but as shown in this paper, that is often not the "best" solution. Using a chemical or color concentrate dispersed in a known compatible binder will bring not only dispersion, but also quick incorporation. For truly critical dispersion requirements, a paste product may be the best option. Finally, if all that is needed is a better method of handling and

weighing, especially liquids and tackifiers, the free flowing liquid powder concentrates would do well.

Carefully consider the broad range of options to select the optimum solution.

Work is continuing on custom binders that will easily incorporate into given polymer types. Further work is planned to evaluate other variables in the incorporation and dispersion of Performance Additives and the quantification of their many benefits.

4. Acknowledgements

I would like to thank PolyOne for allowing me to present this work. I would also like to thank the following PolyOne associates for their contributions to the scope and content of this paper:

Paul R. Dean II, Sales Manager, Performance Additives, for his help in defining the overall concept and much of the background information.

Valentina Marsh, PhD, Senior Development Chemist and Mike Mikolay, Development Engineer, who are responsible for the development of several of the products discussed in this paper, and the definition and execution of the test methods used to generate the test data.

Robert Grizer, Development Technician, for his help in actually generating the test data.

Transmissions Parameter Deviations of a Data Channel Consisting of Cables and Connecting Hardware in Cascade

Lauri Halme, Adrian Boukalov, Rauno Kytönen, Juri Lisjutin, Mika Nupponen, Viktor Nässi, Kari Ranta, Erik Törnqvist

Helsinki University of Technology, Communications Laboratory
Otakaari 5A, Espoo, Finland
+358-9-4511 (Principle contact: lauri.halme@hut.fi)

Abstract

The tests made show that modelling and simulation of access data links and channels consisting of cascaded two-ports are possible by using advanced measuring technique and computing. Based on very careful scattering parameter measurements of cables and connecting hardware the transmission parameters and their deviations can be computed. Important results of the theory of inhomogeneous transmission lines are highlighted. The measurement and computing results correspond well to the theory of transmission lines. To achieve a forward echo noise attenuation of 30 dB same as the minimum equal level far-end crosstalk attenuation at the middle frequencies (300 MHz) of a Cat. 7 cable for a Class F data channel insertion loss deviation smaller than ± 0.25 dB is needed.

Keywords

Transmission and scattering parameters; operational attenuation or operational insertion loss deviations and forward echo attenuation; data access channel; cascaded two-ports; data cables and connectors or connecting hardware.

1. Introduction

Both coaxial and balanced cables have been used in information and telecommunications networks. Some parts of the wire-bound information and communication network (ICN), especially long-haul parts including both land and sea cables have been taken over by optical cable techniques, but for economical and practical reasons glass fiber has not found very much ground in private homes and SOHO (Small Offices Home Offices) environment. Also the development both in balanced and coaxial cable techniques has been extensive. Inspired by digital communication techniques both balanced and coaxial cables have widened their frequency range:

- Balanced pair upwards, towards and above 1 GHz
- Light coaxial pairs also downwards from 30 MHz

Features that will keep the metallic cable techniques attractive for the last 100 m of the access networks are the costs and the easiness of installation, especially now when their transmission capacity and electromagnetic screening problem have in principle been solved.

In new data networks the use of balanced pairs have become a standard technique which allows fast and economic constructions

and easy of changing network architecture. However, the optimum characteristics of the individual components and the channel are not known sufficiently well, which cause various problems.

It became clear at the meeting of ISO/IEC JTC1/SC25/WG3 "Customer Premises Cabling" in February 2001 in Nice that a more exact model for the IEC 1108 (2001) "copper pair" data channel than the present one is needed to decide on the cable and connecting hardware (connectors and fittings) specified electrical inhomogeneous transmission characteristic limits. E.g. better return loss values than 8 dB for the connecting hardware is needed because the 8 dB return loss in a junction leads to a through signal reflection loss of about ± 0.7 dB ILD (Insertion Loss Deviation) in the worst case. It is a common understanding that worst case models give too pessimistic (conservative) ILD values compared with the reality.

It was decided in Nice to freeze the limiting values of the data channel components until a sufficiently exact model is available. In this paper such a model is created, tested and verified and the first simulations done.

2. Calculations and Measurements of Cascaded Two-ports

In the measurements and calculations it more practical to use scattering parameters [1], [2] and [3] than parameters from classical two-port theory [4]. From that theory is the term "operational" (German: "Betriebs") meaning that the measurements and calculations are made in normalized operational conditions by using terminating resistance's equal to the nominal impedance of the data channel [5].

2.1 The Operational Scattering Matrix of a Two-port

The Operational Scattering Matrix of a Two-port is defined and measured between nominal impedances e.g. 100 ohms resistive. We get

$$S_n = \begin{vmatrix} S_{11_n} & S_{12_n} \\ S_{21_n} & S_{22_n} \end{vmatrix} \quad (1)$$

All the scattering parameters are complex $z = x + jy$

The goal is to calculate and measure the resulting operational scattering matrixes of the in cascade coupled two-ports (quadripoles or four-terminal network).

$$S = \begin{bmatrix} s_{11} & s_{12} \\ s_{21} & s_{22} \end{bmatrix}, \quad (2)$$

$s_{21} = s_{12}$ when the two-port is passive.

Complex Operational Attenuation and Complex Operational Insertion Loss Γ_B are defined to be synonyms in this paper. They are defined as the ratio of the incident fictive unreflected square root of power wave ($\sqrt{P_{i1}} = V_{i1}$) from the generator, internal impedance Z_{N1} , and the square root of power wave ($\sqrt{P_2} = V_{r2}$, when $E_2=0$) consumed by the load Z_{N2} expressed in decibels and radians. Its nominal impedances Z_{N1} and Z_{N2} terminate the two-port.

$$\Gamma_B = A_B + jB_B = \ln \frac{\sqrt{P_{i1}}}{\sqrt{P_2}} = 20 \lg \left| \frac{\sqrt{P_{i1}}}{\sqrt{P_2}} \right| + j \arg \frac{\sqrt{P_{i1}}}{\sqrt{P_2}} \quad (3)$$

$$= \ln \frac{1}{s_{21}} = 20 \lg \left| \frac{1}{s_{21}} \right| + j \arg \frac{1}{s_{21}} \quad (4)$$

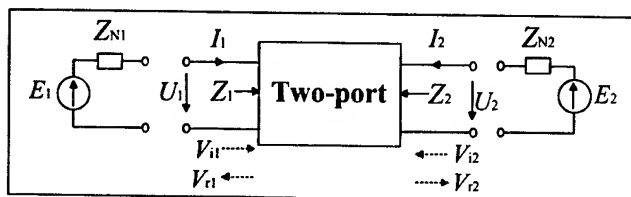


Figure 1. A two-port.

2.2 Transformation Matrix

A two-port "c" measured under the nominal conditions is inserted between two two-ports "a" and "b" which resulting scattering matrix also has been measured. The inserted two-port "c" is not more between the nominal impedances (Fig. 2), which changes its transmission parameters. This means e.g. that the sum of the operational attenuations or operational insertion losses of the

individual two-ports differs from the resulting operational attenuation when cascaded. This is called insertion loss deviation ILD.

The new incident and reflected square root of power waves are calculated as follow [1]:

$$\begin{bmatrix} V'_{i1} \\ V'_{r1} \end{bmatrix} = \mathbf{T} \begin{bmatrix} V'_{r2} \\ V'_{i2} \end{bmatrix} \quad (5)$$

where \mathbf{T} is defined as

$$\mathbf{T} = \frac{1}{s_{21}} \begin{bmatrix} 1 & -s_{22} \\ s_{11} & -\det S \end{bmatrix} \quad (6)$$

$$\mathbf{T} = (t_{ij}) \quad (7)$$

When reciprocity applies to the junction

$$\det \mathbf{T} = \frac{s_{12}}{s_{21}} \quad (8)$$

becomes unity.

The resulting two-ports in cascade has the transformation matrix

$$\mathbf{T} = \mathbf{T}_1 \mathbf{T}_2 \mathbf{T}_3, \quad (9)$$

And the resulting scattering matrix is

$$\mathbf{S} = \frac{1}{t_{11}} \begin{bmatrix} t_{21} & \det \mathbf{T} \\ 1 & -t_{12} \end{bmatrix} \quad (10)$$

$$\mathbf{S} = \begin{bmatrix} s_{11} & s_{12} \\ s_{21} & s_{22} \end{bmatrix} \quad (11)$$

The resulting operational insertion loss A_B and operational phase-shift B_B are according to Eq. (3)

$$A_B = 20 \cdot \lg \left| \frac{1}{s_{21}} \right| \quad [\text{dB}] \quad (12)$$

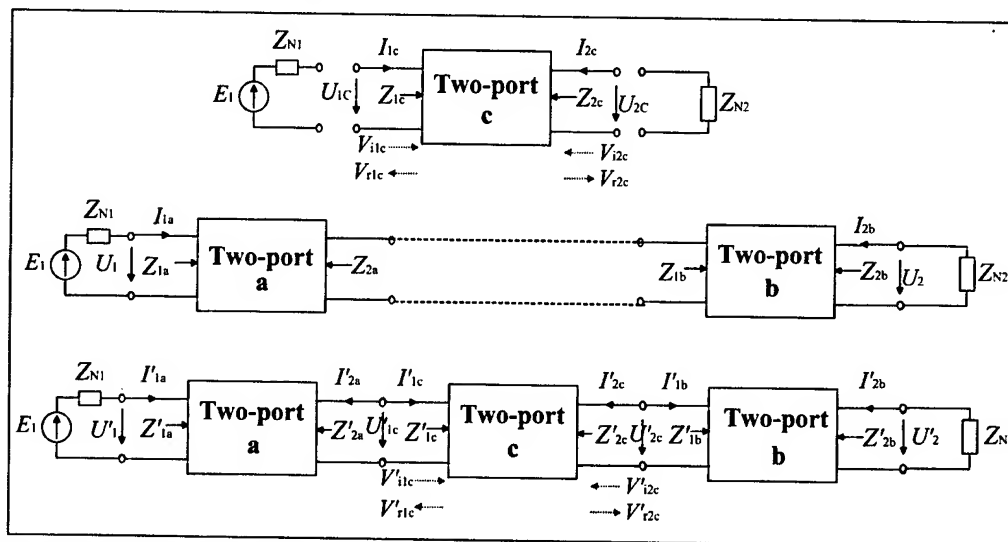


Figure 2. The insertion of a two-port into a network and the deviations caused to the operational parameters.

$$B_B = \arg \frac{1}{s_{21}} \quad [\text{rad}] \quad (13)$$

s_{11} and s_{22} are the operational reflection coefficients at the input and output of a two-port.

2.3 Comparison between Measurements and Calculations

To check the above theory in practice and the measurement accuracy and stability needed the scattering matrix of two Cat 7 cables (length a' 4 m) coupled together with a Cat 7 connector were measured. Then the mated connector was removed by cutting the cables 12 cm from the middle of the connector and the separate scattering matrixes of the three components were measured.

The most interesting test results are shown in Figs 3a-e. First in Figs. 3a-c the magnitude of the measured scattering parameters s_{21} , s_{12} , s_{11} and s_{22} of the three components, then in Figs 3d and 3e the measured and calculated scattering parameters for the three components in cascade.

The correspondence of measured and calculated scattering parameters is good and shows that the base for simulation has been achieved. The small differences in return losses are caused by the faults occurring in cutting and mounting the cables and connector for individual measurements. Especially the 0.1 dB fault in the measurement results of s_{12} and s_{21} is due to inaccuracy in the mounting of the connectors for the 100 MHz measurements.

The deviation in operational attenuation caused by reflection can clearly be seen from the ripple at the higher frequencies. Up to 100 MHz these so called insertion loss deviations ILD are small, in the order of ± 0.1 dB equivalent to a forward echo attenuation of 38 dB (Table 1), which very well corresponds to the return loss values of the individual and cascaded components. At higher frequencies ILD increases being ± 0.5 dB at 300 MHz. We will return to this in Chapters 3.4 and 4.

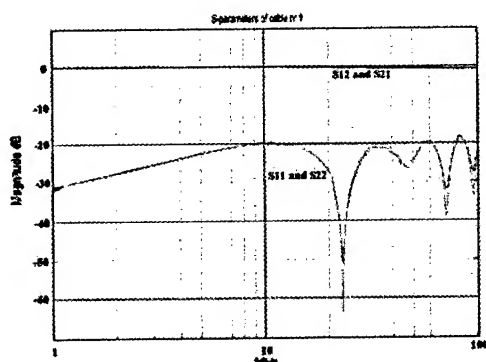


Figure 3a) Cable 1: Magnitude of the measured scattering parameters from 1 to 100 MHz

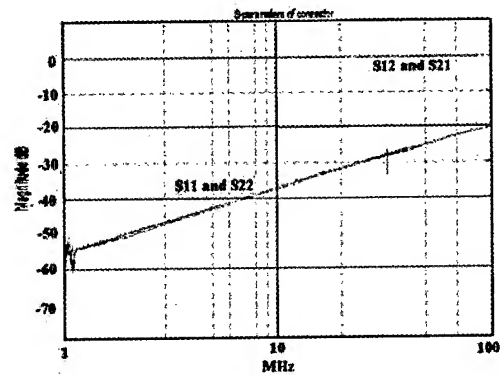


Figure 3b) Connector: Magnitude of scattering parameters in decibels from 1 to 100 MHz

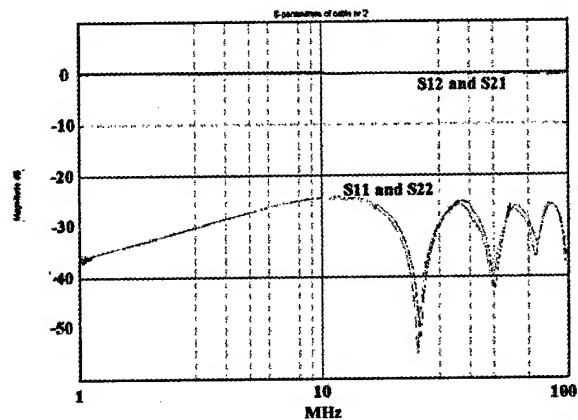


Figure 3c) Cable 2: Magnitude of measured scattering parameters in decibels from 1 to 100 MHz

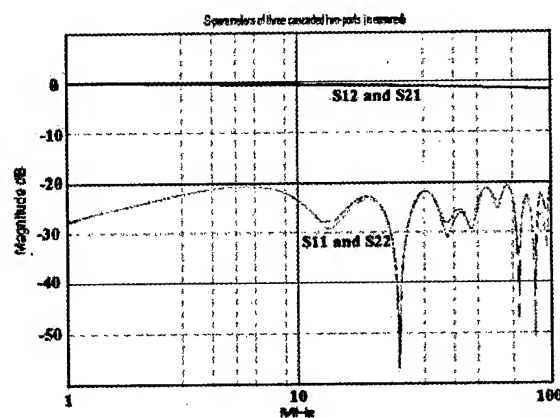


Figure 3d) Magnitude of the measured scattering parameters in decibels of cable 1, connector and cable 2 in cascade from 1 to 100 MHz

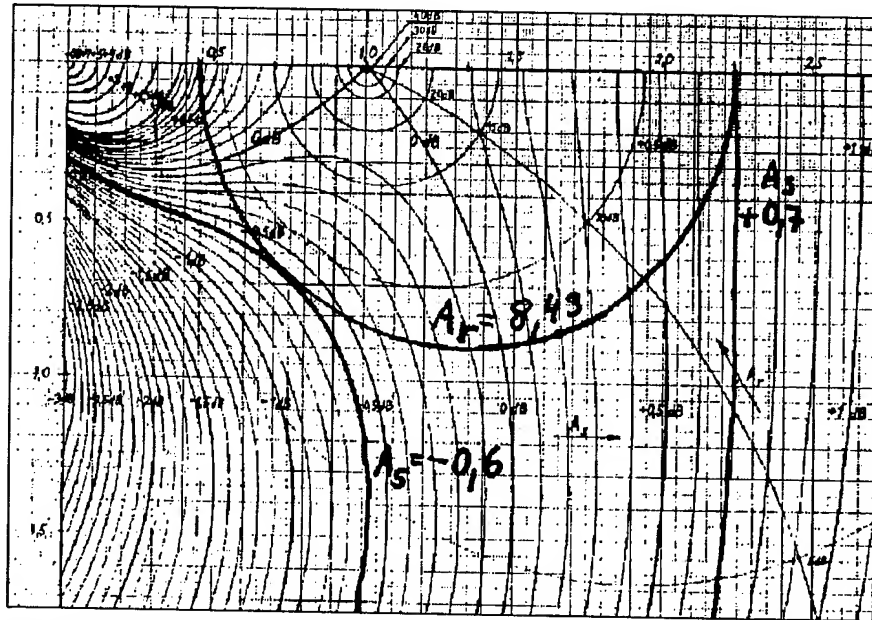


Figure 4. The locus diagram of the constant return loss (A_r) and of the constant reflection loss (A_s) in the complex plane [2] (page 136, figure 4.7 - 4) $A_r = \text{constant}$, $A_s = \text{constant}$

$$A_r = 20 \log \left| \frac{z_n + 1}{z_n - 1} \right|, \quad A_s = 20 \log \left| \frac{z_n + 1}{2\sqrt{z_n}} \right|, \quad z_n = \frac{Z_2}{Z_1} \quad (= \text{normalized impedance}) = r + jx$$

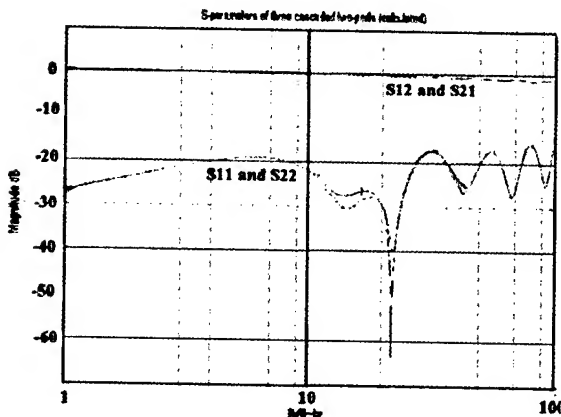


Figure 3e) Magnitude of the calculated scattering parameters in decibels of cable 1, connector and cable 2 in cascade from 1 to 100 MHz

3. Reflection Loss and Forward Echo Noise of Cascaded Two-Ports

Reflection happens both between cascaded two-ports and inside a two-port. Double reflections cause an echo wave travelling forward behind and below the signal resulting in a noise effect. Reflections cause also losses.

3.1 Return Loss and Reflection Loss

The complex return loss is defined as ratio of incident square root of power wave V_i and the reflected square root of power wave V_r expressed in dB and radian. It is well known that

$$\Gamma_r = A_r + jB_r = 20 \lg \left| \frac{V_i}{V_r} \right| + j \arg \frac{V_i}{V_r} \quad (14)$$

$$\frac{V_r}{V_i} = \frac{Z_2 - Z_1}{Z_2 + Z_1} \quad (15)$$

The complex reflection loss is defined as the ratio of the unreflected square root of power wave V_i and square root of power wave V_2 continuing after the reflection expressed in decibels and radian.

$$\Gamma_s = A_s + jB_s = 20 \lg \left| \frac{V_i}{V_2} \right| + j \arg \frac{V_i}{V_2} \quad (16)$$

$$\frac{V_i}{V_2} = \frac{Z_1 + Z_2}{2\sqrt{Z_1 Z_2}} \quad (17)$$

In Fig. 4 are shown the locus diagram of constant return loss (A_r) and of the constant reflection loss (A_s). The constant A_r curves are Apollonius circles. All normalized impedance values $z_n = r + jx$, which are inside a circle A_r , have a higher return loss than A_r . Observe that A_s can also be zero or negative.

3.2 Increase of attenuation due to inhomogeneities

From the input of a two-port measured structural return loss is a good measure for its expected transmission quality. In an evenly inhomogeneous cable the increase of attenuation due to structural reflections is [2][6]:

$$\overline{\Delta \alpha L} = \alpha L \left[\sqrt{|p|^2} \right]^2 \quad [\text{dB}] \quad (18)$$

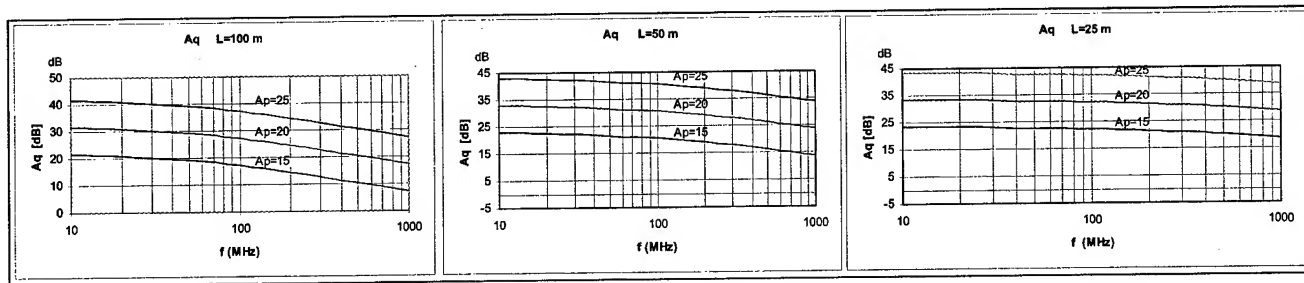


Figure 5. Relations between structural return loss A_p and forward echo attenuation A_q .

Where $\overline{p^2}$ is the variance of the, from the end of the cable measured, structural reflection coefficient p .

With a 1 % p the increase in attenuation is only 0.01 %, which means 0.005 dB in 50 dB, but if the variance is 10 % the increase in attenuation is 0.5 dB

3.3 Forward Echo Noise Caused by Regular Periodic Reflection in a Cable

As before a complex mathematical analysis [2] leads to simple results. The relation between the periodic structural return loss A_p and the forward echo noise attenuation A_q is:

$$A_q = 2A_p - 20 \lg K \quad (19)$$

$$K = \frac{2\alpha L - 1 + e^{-2\alpha L}}{(1 - e^{-2\alpha L})^2} \quad (20)$$

$$\approx 2\alpha L - 1 \quad (21)$$

The graphical presentation of the forward echo attenuation A_q in Eqs (19) and (20) for different lengths of Cat 5 to 7 data cables are shown in Figs 5. To keep the forward echo attenuation A_q resulting from structural periodic reflections above 25 dB up to a cable length of 100 m at a middle frequency of 150 MHz the periodic structural return loss A_p should be kept above 20 dB.

3.4 Forward Echo Noise Caused by Double Reflections

Forward echo noise is caused by double reflections. In Fig. 6a there are two reflection points on the transmission line "a" and "b". When the propagating signal wave V_s reaches point "b", a part of it reflects back. The reflection signal attenuates A dB on its way to reflection point "a" where it reflects back and attenuates again A dB etc. The strongest echo component is created by the first roundtrip attenuation. In other words, the maximum forward echo noise is the roundtrip attenuation below the propagating signal at point "b".

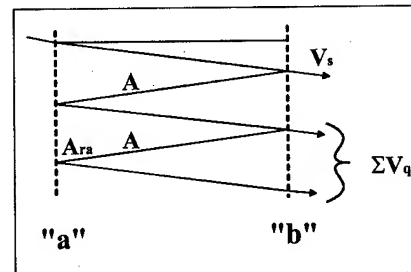


Figure 6. Forward echo waves ΣV_q caused by a double reflection "a" ↔ "b" in a transmission line.

In Fig. 8 is shown the magnitude of the measured scattering parameters of cable 1 up to 600 MHz. The widening ripple of s_{12} and s_{21} is the insertion loss deviation ILD caused mainly by reflections back and forth between the cable ends. E.g. at 300 MHz the round trip attenuation is approximately $(2 \times 3 + 8 + 8)$ dB = 22 dB corresponding to an ILD of ± 0.65 dB, which coincides with the test results of Fig. 8.

$$A_q = A_{rb} + A + A_{ra} + A \quad (22)$$

$$= 2A + A_{ra} + A_{rb} \quad (23)$$

The relations between forward echo coefficient q , forward echo attenuation A_q and insertion loss deviation ILD are

$$A_q = 20 \lg \left| \frac{1}{q} \right| \quad [\text{dB}] \quad (24)$$

$$\text{ILD} = 20 \lg |1 + q| \quad [\text{dB}] \quad (25)$$

The relation is given in Fig. 7 and Table 1.

Table 1. The relations between forward echo coefficient q , forward echo attenuation A_q and insertion loss deviation ILD.

q [%]	A_q [dB]	ILD [dB]
100	0	± 6
50	6	± 3.5
25	12	± 2
12	18	± 1
6	24	± 0.5
3	30	± 0.26
1.2	38	± 0.1

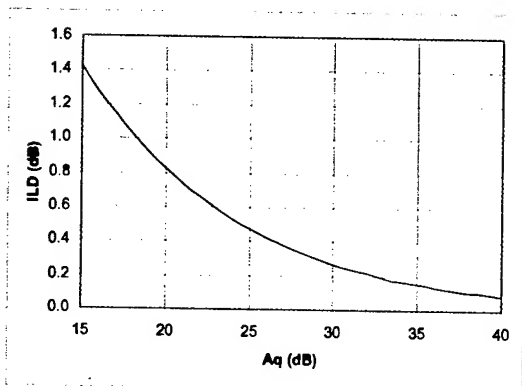


Figure 7. The relation between forward echo attenuation and insertion loss deviation ILD.

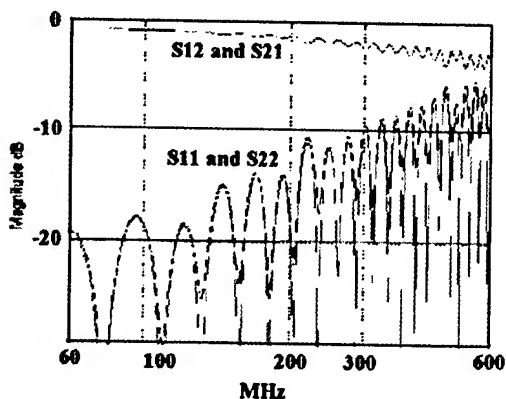


Figure 8. Cable 1: Magnitude of the measured scattering parameters in decibels from 60 to 600 MHz.

4. Simulation of a Data Channel of Cascaded Two-ports

A data channel consists of cascaded two-ports. With modern network analyzers (NWA) the scattering matrix under well-defined conditions can be measured. By being able to calculate the resulting scattering matrix of two-ports in cascade it is possible to both calculate and measure an individual data channel. By altering the scattering matrixes of the components it is possible to simulate data channels with other component limiting values.

Given are the scattering parameters s_{ijn} of four (4) connections (connecting hardware or connectors) and of three (3) cables. The corresponding to scattering matrixes are S_n

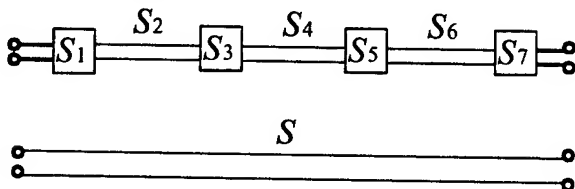


Figure 9. Scattering matrixes S_n of seven (7) cascaded two-ports and the resulting scattering matrix S .

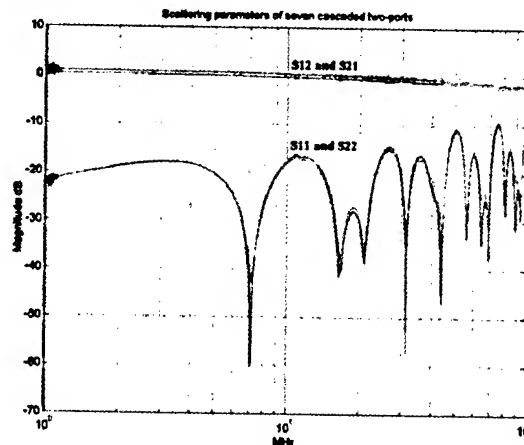


Figure 10. The calculated magnitude of scattering parameters of a cascaded data link of three cables connected and terminated with four connectors.

In Fig. 10 are the calculated scattering parameters of a cabling channel with three cables connected and terminated with four connectors. As scattering parameters of S_1 , S_3 , S_5 and S_7 of the four connectors are used the test results in Fig. 3b. As scattering parameters S_2 and S_6 are used the parameters of cable 1 in Fig. 3a and for S_4 the parameters of cable 2 in Fig. 3c.

The scattering parameters of s_{11} and s_{22} of cable 1 around 80 – 100 MHz are -20...-18 dB (Fig. 3a), for cable 2 -25...-26 dB (Fig. 3c) and for the connectors are -22...-20 dB (Fig. 3b). The calculated resulting parameters in scattering matrix S are for s_{11} and s_{22} -10...-8 dB and the ripple in s_{12} and s_{21} , being equal to the ILD, about ± 0.5 dB corresponding to a signal to ILD noise ratio of 24 dB.

5. Conclusions

The tools to model a physical data channel with measurements of individual components and then calculations to get the resulting transmission parameters have been developed. An experiment to model a physical data channel by measuring the scattering parameters of the cascaded components (cables and connecting hardware) and then calculating the resulting scattering parameters of the channel has been made. It is shown that especial care must be taken in measuring individual components especially connecting hardware or connectors. More simulation work is needed to find the minimum transmission characteristics to achieve acceptable physical data channel performance according to ISO/IEC 11801 and Publ. 15018 "SOHO" cabling.

6. Acknowledgments

The authors express appreciation to the work done in the Transmission line laboratory of Telecom Finland in the 1960's and 1970's and the support from its successor Sonera, Ballmann and Bedea and the management of the Communications Laboratory of HUT for the measuring equipment and advice.

Special thanks to The Siemon Co. for cables and connectors and the ISO/IEC JTC 1 SC25 customer cabling specialists encouragement and advice.

7. References

- [1] International Telephone and Telegraph Corporation, "Reference Data for Radio Engineers", 4. Edition, pp. 648-649, 1957.
- [2] L.K. Halme, "Johtotransmissio ja sähkömagneettinen suojaus (Transmission lines and electromagnetic screening, in Finnish)" Parts A and B, Otakustantamo 2nk Eddition Helsinki 1989.
- [3] F. F. Kuo "Network Analysis and Syntesis", John Wiley & Sons, Inc., New York, London 1962.
- [4] R. Feldtkeller, "Einführung in die Vierpoltheorie", S. Hirzel Verlag, Leipzig, 1948.
- [5] M. Bidlingmaier, A. Haag, K. Kuhnemann, "Einheiten-Grundbegriffe-Messverfahren der Nachrichten-Übertragungs-technik", Siemens Aktiengesellschaft München, 1973, 4. überarbeitete und erweiterte Auflage.
- [6] P. Mertz, K. Pfleger, "Irregularities in Broad-Band Wire Transmission Circuits", the Bell System Technical Journal, Vol. 14, No 4, Oct. 1937.

8. Biographies



Lauri Halme, Diploma Engineer (M.Sc. E.E.) 1962, Licentiate (D.Sc. E.E.) 1972, both in Electrical Engineering from the Helsinki University of Technology (HUT).

Dr. Halme was employed by Telecom Finland 1962 -1997. Initially, he worked as head of the transmission line laboratory group. From 1970 to 1976 he headed the planning and building of longhaul coaxial cable and radio networks. From 1976 to 1988 he was Executive Director of the Telecommunications Laboratories and Research Center. From 1988 to 1997, he worked in the Executive Staff of Telecom Finland as R&D Director responsible for standardization and research & development being active in

IEC (International Electrotechnical Commission) and establishment and development of ETSI (European Telecommunications Standards Institute) and EURESCOM (The Research body of European Telecommunication operators).

Since 1964 he has been Assistant and Specialist Lecturer on transmission lines and electromagnetic screening at the Helsinki University of Technology (HUT). After leaving Telecom Finland in 1997, he continues as Lecturer and Specialist at the Communications Laboratory, taking part in a project on the evolution paths of the Access network architectures to meet the future market needs.

Dr. Halme has delivered many papers at national and international professional conferences on transmission lines and EM screening and is the author of a book (in Finnish) on the same subjects. In 2000, Dr. Halme was granted by SESKO an Erkki Yrjölä Medal for outstanding services at electrotechnical standardization work.



Rauno Kytönen, Diploma Engineer (M.Sc. E.E.) 1968, in Electrical Engineering from the Helsinki University of Technology (HUT). Kytönen was employed by Telecom Finland (from 1997 Sonera) 1966 - 2001. Initially, he worked as Research Engineer of the Transmission Line Group of the Telephone Laboratories. From 1970 to 1989 he was Head of the Transmission Line Laboratory and from 1989 Research and Development Manager responsible for metallic cable measurement and development.

Since 1983 he has taken part in the communications cables standardization and research work of IEC being until 1999 the secretary of a working group, TC46/WG5, dealing EMC screening effectiveness of communications cables.

From 1966 he has been Assistant and Special Lecturer of Line Transmission and Electromagnetic Screening at HUT. After leaving Sonera he continues at the Communications Laboratory of HUT as Special Lecturer and researcher.

Adrian Boukalov, Juri Lisjutin, Mika Nupponen, Viktor Nässi, Kari Ranta and Erik Törnqvist are researcher and assistants at the Communications Laboratory of HUT.

Generic Cabling for Broadband Access Networks Using Application Independent Universal Cables

Paul E. Gregor, Pietro Sonza Reorda, Paul Schnee, Peter E. Zamzow

Nexans Deutschland Industries AG & Co KG
Moenchengladbach, Germany
+49-2166-27-2229 · paul.gregor@nexans.com

Abstract

At present the market requires reliable access cable networks which are able to transmit actual broadband systems on the one hand and to take over the coming transmission technologies in the near future on the other hand. Thus a new high grade cable design containing a sufficient headroom is necessary to be introduced.

Typically the first part of the access network consists of outdoor cables and the second part of the total transmission link however is normally executed with indoor cables which have to be flame retardant in case of fire and have to avoid undesired smoke release.

The challenge now is to introduce only one cable construction which is able to serve for both outdoor and indoor installations. The described cable concept meets this general requirement concerning installation of a new defined universal cabling concept.

At the same time the electrical quality of this cable construction offers the ability to take over the current available transmission systems and to incorporate arising new transmission techniques of the near future. In order to ensure highest broadband channel behavior for certain cases in the course of time optical fibre elements can be incorporated into the copper cable core and appropriate jointing technologies for both copper and fibre are proposed.

This introduced universal cable generation defines a highly advisable generic cabling for access links in city networks. It fulfills important criteria respecting mechanical and electrical behavior. Thus this cable concept constitutes an investment safe technology which avoids repeated cost intensive plant installations.

Relating the clear trend towards high grade digital transmission systems focus has also been taken upon the transmission behavior of the copper transmission circuits for xDSL-systems.

Transmission parameters like attenuation, crosstalk attenuation, longitudinal conversion loss, return loss, characteristic impedance will be examined.

Keywords

Access network, universal cable technology, cable jointing technique, xDSL-transmission

1. Introduction

The market challenge towards multimedia infrastructures for cabled broadband transmission links is increasing rapidly worldwide. This tendency influences dramatically the development of technical and economical suitable link

components for subscriber access networks within cities accordingly.

It is the basic intention to introduce a new cable generation which is able to serve for indoor and outdoor employment considering balanced copper stranding elements due to economical reasons.

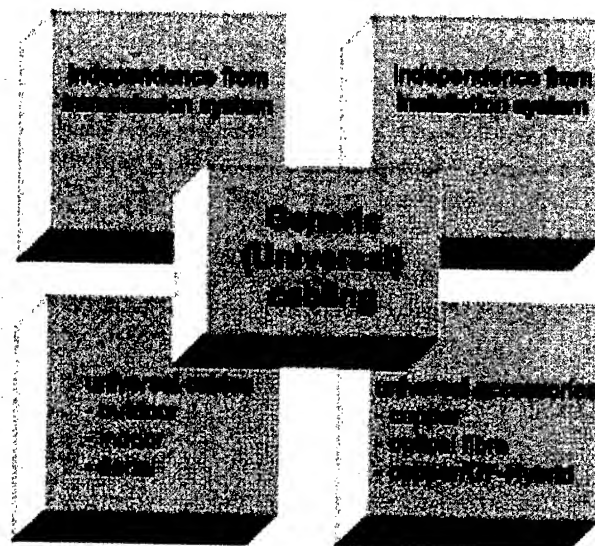


Figure 1. Generic (universal) cabling concept

In figure 1 the basic cabling concept is shown. It comprises the independency from cable transmission systems and installation environments on the one hand and the necessary link components, like cables and accessories to achieve this independency on the other hand.

Normally outdoor cables for access networks are not permitted to be installed within buildings since the cable cores of these constructions are filled with jelly compound. Such material is unsuitable to protect itself against fire attacks and it drops out at cable ends within distribution cabinets at higher temperatures unfortunately. Additionally typical outdoor cables with polyethylene sheathing are not flame retardant and thus unallowed for internal employment.

In order to avoid these disadvantages regarding mechanical properties and to meet the demands concerning transmission characteristics for higher digital applications adequate cables and components have to be introduced. Such high grade copper design techniques should consider a minimum frequency range of 600 MHz to meet the demands of current systems available on market. Reliable category 7 outdoor cables have to be introduced in order to close this bottle neck within copper cable transmission links.

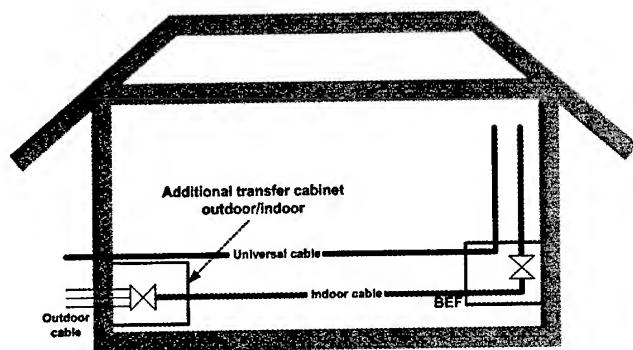


Figure 2. Universal and conventional cabling configuration for access networks

2. Achievements of low cost cabling using universal cables

As shown in figure 2 conventional outdoor cables are installed up to a typical building entrance facility (BEF) where such incoming cables are transferred to the ongoing typical flame retardant halogen free indoor cabling.

In bigger buildings often the BEF is located at the far end of that estate and thus a cost intensive additional space for distribution and branching of cables has to be erected.

In order to overcome this uneconomical situation only the described universal cabling concept meets the necessary requirements since those cables can serve for both outdoor and indoor use.

Depending from the local situation a cost reduction between 10-20 % compared to the conventional technologies is obtainable.

3. Construction of copper universal cables

3.1 General

Cable design at the time being requires more than ever a compromise between high grade broadband transmission characteristics on the one hand and favorable dimensions on the other hand, i.e. largest possible drive distances and smallest cable diameter.

3.2 Core make up and sheath design

Solid copper conductors with diameter of 0,6 mm are insulated with foam skin polyethylene of high grade materials and with highest possible concentricity ($\geq 96\%$) and homogeneity. Those insulated conductors are twisted together to form pairs or quads in a geometrical stable construction employing suitable pitch lengths. The pairs are covered by a combination of metallic and plastic foils in order to reach a high quality level relating transmission characteristics up to a frequency of 600 MHz.

The screened elements (Pairs in Metal Foil-PiMF) have been stranded together in concentric layers considering a wide range of

different numbers of pairs. Since the cable has to serve for both indoor and outdoor use longitudinal and transversal watertightness has to be obtained on the one hand and typical cable characteristics for indoor cables have to be reached on the other hand. No jelly compound is accepted respecting indoor installations. Therefore the interstices within the cable core are filled with swellable yarns in order to achieve reliable longitudinal watertight cables.

As a moisture barrier a laminated aluminium tape applied longitudinally has been selected in combination with a halogenfree flame retardant plastic compound which allows cable installations within buildings. Below the moisture barrier sheath a rip cord for fast sheath removal during mounting measures is applied longitudinally.

Various numbers of pairs have been stranded together based upon users demands. As a standard delivery program pair counts up to 50 elements have been produced. For certain projects copper /OF-hybrid solutions have been realized considering single mode fibres according to ITU G652. Special multimode fibres capable for higher data rates and link distances specially for GBit-Ethernet systems are employed too. In order to meet international provisions regarding fibre-to-the-home systems 24 fibres can be incorporated into the copper cable design.

Figure 3 shows a typical universal cable design using 10 pairs with conductor diameter of 0,6 mm and individual pair screening.

Type abbreviation: A-02YSTF(L)H 10x2x0,6 PiMF.



Figure 3. Typical universal copper cable design consisting of 10 pairs with individual screening

4. Transmission characteristics of cable delivery lengths

4.1 DC and VF characteristics

The tests have been carried out on delivery lengths of 1000m at a temperature of 20°C and a frequency of 800 Hz employing the MEA/KP5 automatic testing equipment. The results are shown in table 1 and compared to the requirements of specification IEC/PAS 62255-1 Edition 1.0 "Multi-pair cables used in high bit rate digital access telecommunication networks-Part 1: Outdoor cables"

Table 1. DC and VF characteristics of individual screened pairs of universal cables

Characteristic at 20°C	IEC/PAS 62255-1: IEC/PAS 61156-5: IEC 708-1:	Test result	IEC test method 61156-1
DC resistance	$\leq 130 \Omega/\text{Km}$	$\leq 123,3 \Omega/\text{Km}$	Clause 3.2.1

DC insulation resistance @ 100V, 60 sec.	$\geq 1.5 \text{ G}\Omega\text{xkm}$	$\geq 10 \text{ G}\Omega\text{xkm}$	Clause 3.2.4
DC resistance unbalance	$\leq 2 \%$	$\leq 0.3 \%$	Clause 3.2.2
Mutual capacitance @ 800 Hz	$\leq 40 \text{ nF/km}$	$\leq 34.5 \text{ nF/km}$	Clause 3.2.5
Capacitance unbalance to ground @ 800 Hz	$\leq 1600 \text{ pF/km}$	$\leq 640 \text{ pF/km}$	Clause 3.2.6
Dielectric strength, AC cond./cond. cond./screen	700 V, 1 min	Passed	Clause 3.2.3

4.2 High frequency characteristics

4.2.1 Insertion loss

The achieved insertion loss results have been registered within a frequency range of 1 MHz and 600 MHz employing a network analyzer of type HP 4396 A considering the test procedure given in IEC 61156-1 clause 3.3.2.

More than 1200 frequency points have been checked in order to detect undesired insertion loss peaks. For the selected frequency range favorable smooth curves have been recorded.

In comparison to the requirements of specification IEC/PAS 61156-5, category 7 the obtained results for insertion loss of universal cables exhibit an advantageous headroom of approximately 20% for a wide frequency range compared to the international specified level as shown in figure 4.

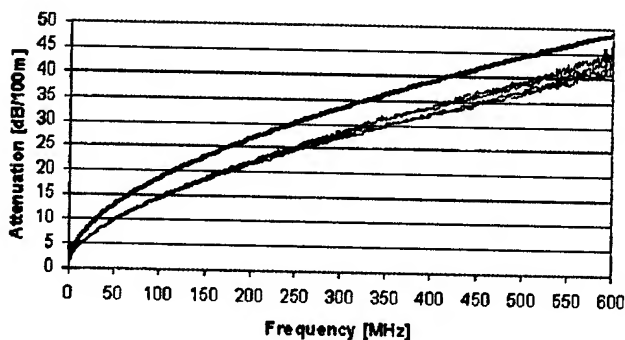


Figure 4. Insertion loss for pairs of copper universal cable

4.2.2 Velocity of propagation

The velocity of propagation has been verified according the test method described in IEC 61156-1 clause 3.3.1 up to a frequency of 600 MHz.

As recorded in figure 5 the velocity of propagation has been detected well above the specified value of at least 60 % with 0,79 c as an average value and 0,78 c as a minimum figure according to the test configuration in IEC/PAS 62255-1, clause 3.3.1.

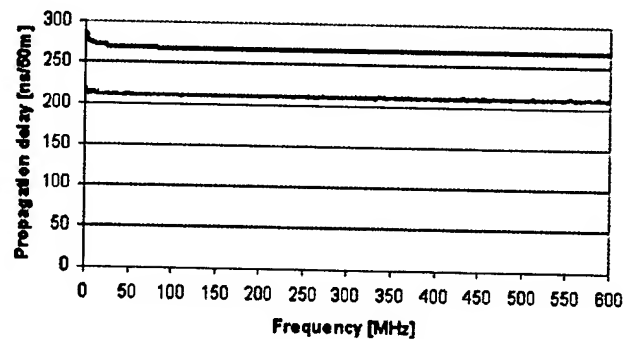


Figure 5. Velocity of propagation of copper universal cables

4.2.3 Near end crosstalk attenuation (NEXT)

The tests for NEXT have been executed from both sides of the delivery lengths within a frequency range from 1 MHz to 600 MHz employing the test method given in IEC 61156-1 clause 3.3.4. Due to the strong frequency dependency of NEXT characteristic a minimum of 1200 frequency points have been performed concerning combinations between neighbor quads. The pairs not under test have been terminated with the nominal characteristic impedance.

Figure 6 shows the measured NEXT values in relationship to the requirements of IEC/PAS 61156-5. These test results show the expected high quality level of these individual screened pairs with a remarkable head room of almost 10 dB for nearly the whole frequency range. Such a high NEXT-level can only be reached by using pairs with individual screening. It guarantees network carriers the capability and planning safety of operations for future upcoming transmission systems.

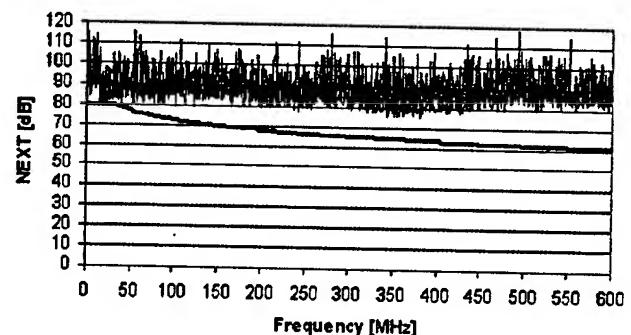


Figure 6. Near end crosstalk attenuation of adjacent pairs in universal cables

4.2.4 Far end crosstalk attenuation (FEXT)

The examinations have been carried out within a frequency range from 1MHz to 600 MHz considering the test procedure of IEC 61156-1 clause 3.3.5.

Figure 7 shows the plots of all possible combinations compared with the requirements of IEC/PAS 61156-5 resp. DIS ISO/IEC 11801 2nd edition.

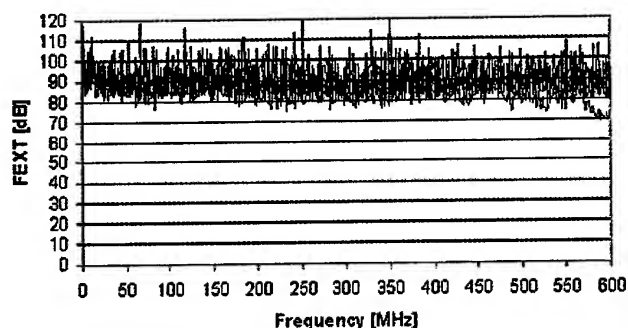


Figure 7. FEXT values of individual screened pairs in universal cables

Taking the calculated ELFEXT-values into account it can be summarized that the obtained level for PiMF-elements of universal cables meets clearly the above mentioned international specified requirements.

4.2.5 Return loss

In order to verify the transmission quality of the whole cabling the return loss property represents a reliable indicator for links and channels. Thus also cables as an important part of the transmission line have been examined up to a frequency of 600 MHz upon terminated screened pairs using IEC 61156-1, clause 3.3.7 as test procedure.

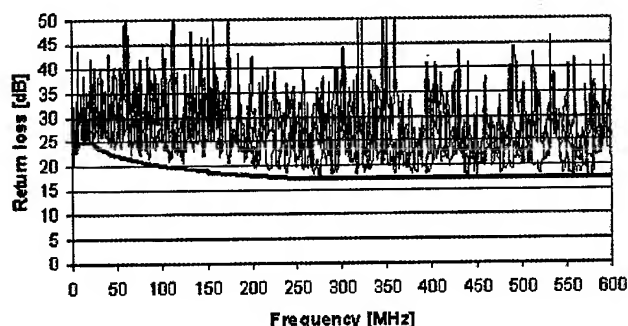


Figure 8. Return loss values of individual screened pairs in universal cables

Figure 8 shows the recorded curves comprising all possible combinations of the cable under test. In comparison to the requirements of IEC/PAS 61156-5 the reached return loss values meet the specification with a clear sufficient headroom.

4.2.6 Characteristic impedance

Examinations have been made in the frequency range from 1 MHz to 600 MHz employing the open/short circuit test method according IEC 61156-1 clause 3.3.6 The achieved characteristic impedance values have been detected at $130 \Omega \pm 25 \Omega$ for the frequency range between 200 MHz and 600 MHz, $130 \Omega \pm 22 \Omega$ between 100 MHz and 250 MHz and $130 \Omega \pm 15 \Omega$ regarding the range 4 MHz up to 100 MHz.

4.2.7 Longitudinal conversion loss (LCL)

The investigations have been executed upon the test procedure described in IEC/PAS 61156, clause 3.3.3 up to a frequency of 100 MHz achieving minimum LCL values of 40 dB.

4.3 Mechanical properties of universal cables

4.3.1 Longitudinal watertightness

Since an universal cable is also employed for outdoor applications regularly relevant cable properties have to be achieved accordingly, like transversal and longitudinal watertightness.

The latter has been verified based on the test method according IEC 60708 as shown in principle in figure 9. The test results meet the provisions described in the before mentioned specification.

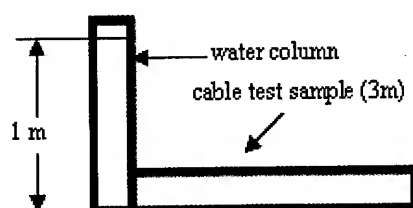


Figure 9. Longitudinal watertightness test

4.3.2 Transversal watertightness

For burial and duct installations transversal watertightness is important to be realized in order to ensure a life expectancy time of at least 20 years. This fundamental requirement has been reached by a reliable aluminum/polyolefin moisture barrier sheath to avoid vapour permeation into the non-jelly filled cable core. Compatible, completely water-tight jointing systems have also been designed for achieving homogeneous performances on the whole link.

4.3.3 Cable behavior under fire conditions

With respect to the intended indoor applications the cable design has to fulfill certain criteria regarding fire load.

Concerning flammability this universal cable has been examined according standards IEC 60332-3-24 and IEC 60332-3-10. Here the cable has been mounted vertically in a test chamber of 4 m high under conditions listed up in following table 2.

Property/Condition	required value
Cable diameter	22,3 mm
Ignition source, propane flow rate	39 l/h
Ignition source, air flow rate	600 l/h
Flame configuration, overall height	170-190 mm
Flame configuration, blue cone height	50-60 mm
Flame application time	70 sec

Table 2. Flame test conditions for universal cable Examination

The test results meet the international defined requirements considering a time of burning after removing the flame of 15 s and a damaged cable section of 120 mm.

4.3.4 Smoke density

As a further important indoor cable characteristic in case of fire load the smoke density has to be tested within a cube according to IEC 61034-2 procedure. As a favorable result the achieved light transmission decrease can be announced with 66 %.

5. Connecting hardware for cable links

This contribution describes a complete cabling concept consisting of cables and components like special jointing sleeves and adequate termination boxes.

5.1 Copper conductor connecting technology

A special insulation displacement connection technology (IDC) has been applied generally. Considering pairs with individual screening a metal separation is designed for the connection blocks as shown in figure 10 principle. Those compax modules enable the connection to be performed almost without untwisting the pairs or interrupting shielding continuity, hence maintaining the existing NEXT level of cables.

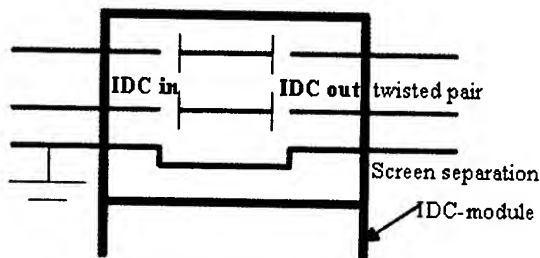


Figure 10. IDC-technique in principle

5.2 Jointing sleeve technique

The jointing sleeve component range is based on a modular concept and a fully mechanical, fully reversible watertight system. This allows easy upgrades to the network and fast accessibility to the splices at any time of copper conductors without the need for any special tools or spare parts.

Generally the design of these jointing sleeves consist of thermoplastic rectangular boxes suitable for buried, manhole and aerial, Telcordia GR771 compliant application. The closures are also pressurizable. All sealing components are reversible, reusable and designed for fast and simplified tool less installation procedures. External grounding can be assured by a copper plug.

Two optimized dimensions are available:

WTC 1: L 390 mm x W 178 mm x H 123,5 mm

WTC 2: L 500 mm x W 262 mm x H 179 mm

For the described cable design with individual screened pairs a WTC 1 joint sleeve has been equipped with a Faraday cage and screened copper splice modules. These IDC Compax components assure both pairs and individual screen continuity. All connections are then introduced into the Faraday cage. In figure 11 above an individual IDC Compax modul is drawn and in the

below part of the figure a complete mounted jointing sleeve is shown.

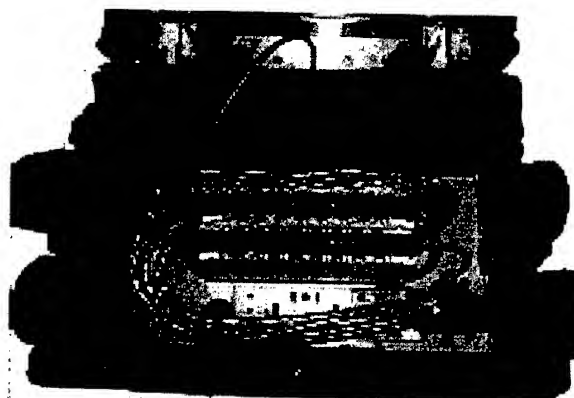
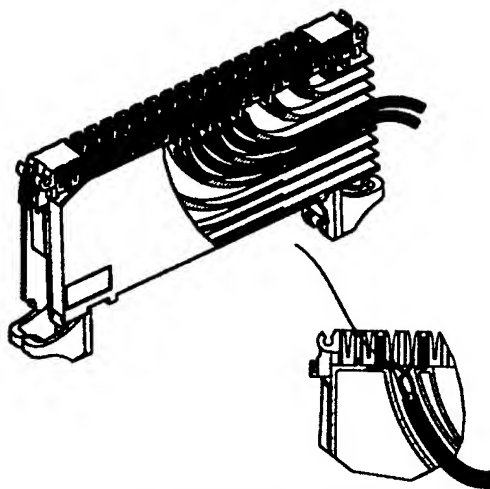


Figure 11. Completed jointing sleeve WTC1 with compax modules and 10 individual screened pairs

In case of copper/optical fibre cables the WTC 2-jointing sleeve type assures both copper and fibre interconnections management.

The incoming cables are anchored on the bottom of the closure, where the over-length of fibre tubes is stored. Cable guides assure the minimum bending radius of the fibre tubes which are then routed towards the top level of the closure where the splice modules for fibres are located. The compax-modules are located in the bottom level below the fibre splice section. Figure 12 exhibits such a copper/OF-hybrid jointing sleeve. FiberArt fibre management modules have been chosen due to their modularity, compactness, and ability to manage mechanically independent optical circuits.

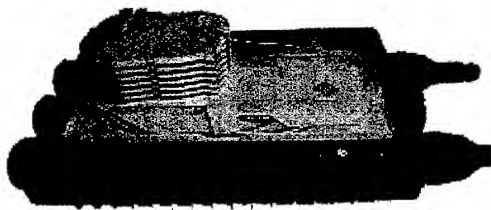


Figure 12. Copper/OF-jointing sleeve

Regarding the termination technology both the compax IDC blocks and optical fibre devices as described before are employed accordingly.

Tests which have been made upon transmission characteristics of cable links including jointing technique up to 600 MHz express very clear only a neglectable deterioration of the link quality caused by this jointing technique. This has been verified in particular respecting the return loss behavior however one has to take care for connections at the beginning of a transmission link.

Here the screening of transmission elements towards the connecting hardware have to be executed very accurate and the pair twisting should be maintained as far as possible. The influence of a connection within jointing sleeves after a cable section of more than 50 m is neglectable.

6.Channel characteristics using different transmission applications

6.1 Channel configuration consisting of universal cables and components

In order to detect the possible drive distance for transmission systems the channel length have been varied by switching together pairs of a universal cable length according to figure 13. This configuration has been chosen to simulate a certain noise level influencing the signal operation as it happens in practice.

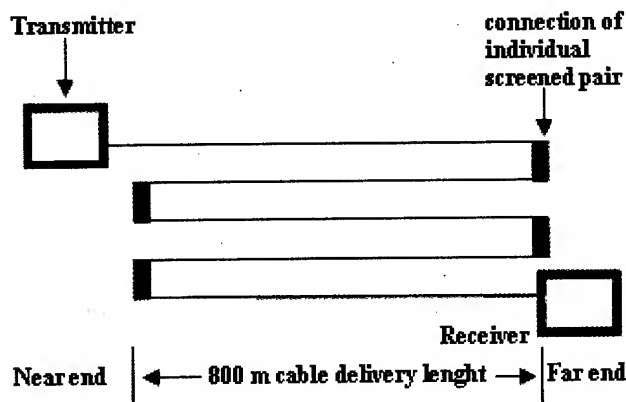


Figure 13. Channel configuration enabling variable lengths

6.2 Structure of channel configuration

Various transmission systems have been connected to the above described cable link in order to determine the overall capability of

the channel configuration to be used for future access network applications.

Figure 14 exhibits the link configuration prepared for the xDSL-transmission tests.

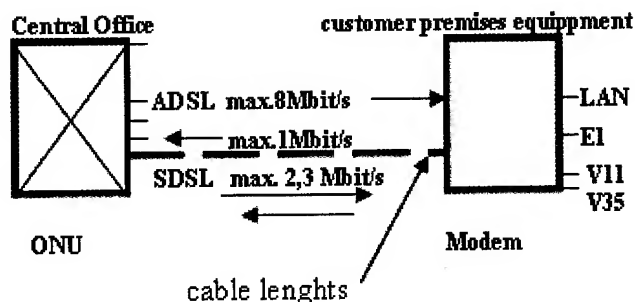


Figure 14. Channel structure for transmission of xDSL- systems

6.3 Correlation between data transmission rate and system drive length

The practical test configuration in laboratory is shown in figure 15.

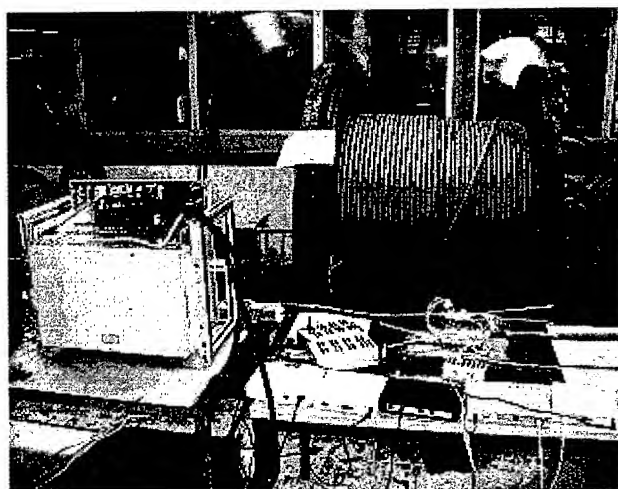


Figure 15. Test configuration in laboratory

The obtained results are shown in a graphical performance in figure 16 and 17. It should be pointed out that a one-pair SDSL-system and a one-pair ADSL system (frequency band above ISDN) has been taken under operation for the test. Regarding the noise margin the international specified value of 6 dB had been taken under consideration.

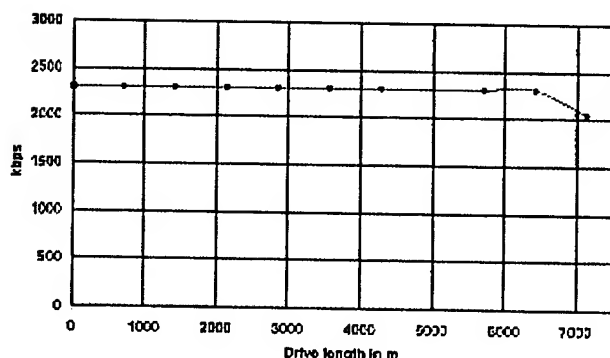


Figure 16. Correlation between data transmission rate and system drive length concerning SDSL-technique

Regarding the SDSL application a maximum data rate of 2,3 Mbit/s downstream and upstream has been put under operation.

The main result of these measurements are as follows: With respect to the investigated SDSL-operation a drive length of 6,43 km transmitting a data rate of 2,304 Mbit/s has been achieved. Above this drive length the data transfer rate was decreased by the transmission system as shown in figure 16.

It must be stated that the measured values are very close to the theoretical calculations.

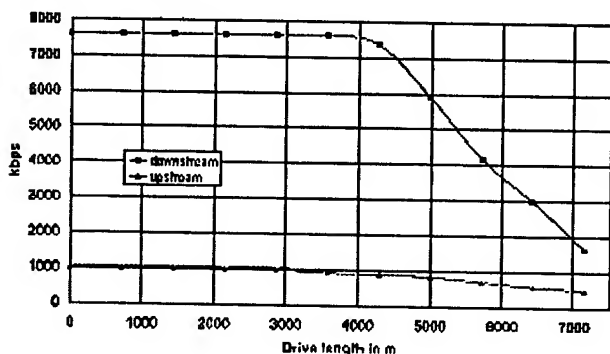


Figure 17. Correlation between data transmission rate and system drive length regarding an ADSL - operation/interleaved channel

Relating the ADSL-system a data stream of maximum 8 Mbit/s downstream and 1 Mbit/s upstream has been performed. In figure 17 the collected results for an ADSL-operation (ITU-T G992.1, Annex B) are drawn graphically. Up to a drive length of almost 4,0 km a maximum data rate of 7,6 Mbit/s downstream has been achieved. Above this distance the data transfer rate was decreased by the transmission system itself.

In figure 18 an overview considering the obtained results for xDSL-Systems together with the conventional PCM 30 and an Ethernet 10BaseT- technology are shown regarding relationship for drive length and data rate.

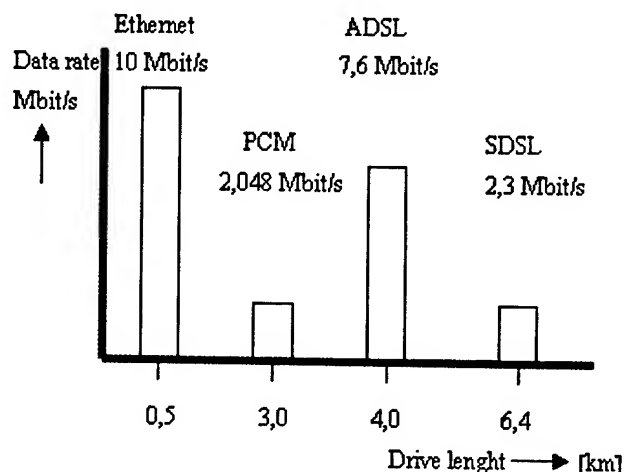


Figure 18. Comparison between transmission systems regarding data rate and drive distance

7. Conclusion

- Universal cables including adequate connecting hardware are necessary to erect a most economical generic cabling solution since this technology serves for both outdoor and indoor cable sections.
- Cost reduction for the total cable plant if no installation for an additional building entrance facility is needed.
- Time and space saving installation concept due to a non-erectable additional BEF and universal cable application.
- This universal cable design offers reliable and application independent broadband transmission compatibility including cable sharing by using individual screened pairs which guarantees planning security for a period of at least a decade.
- No electrical mismatching between indoor and outdoor cables since the cable design does not change between the burial and the indoor section of the total transmission link.
- Most recent connecting hardware integrated in special jointing sleeves and termination boxes do not influence the transmission quality of links and channels unfavorable since the pairs remain almost untwisted and the Faraday cage of the individual pair screening is applied continuously.
- The employed jointing sleeves and termination boxes can be applied to copper/OF-hybrid cable links enabling a rapid standard installation and upgrade of the hybrid cable networks.
- Electrical and mechanical stability of cable transmission characteristics after laying procedure have been achieved favourably independent from environmental conditions.

8. Acknowledgement

The authors would like to express their special thanks to the team of Nexans development department for their support and to Eberhard Marx from Marconi, Backnang.

9. References

1. IEC/PAS 62255-1 Multi-pair cables used in high bit rate digital access telecommunication networks – Part 1: Outdoor cables
2. DIS ISO/IEC 11801 2nd edition: Information technology- Generic cabling for customer premises
3. ISO/IEC CD 15018 Integrated cabling for residential and SOHO environment
4. Gregor, Tholen, Knop
Data cables and system components for the use up to 100 (300)MHz“ International Wire and Cable Symposium Proceedings 1994
5. Paul Gregor, Harald Bütthe, Peter Zamzow
“High grade copper/optical fibre hybrid cable technology for investment safe broadband access networks”
International Wire and Cable Symposium Proceedings 2001

10. Authors



Paul E. Gregor
Nexans Deutschland
Industries AG
Mönchengladbach,

Germany

Paul.Gregor@nexans.com

Paul E. Gregor was born in 1941. After study at Ingenieurschule Duisburg, Germany, he joined AEG Kabel, today Nexans Deutschland Industries, where he had been involved in development projects for special symmetrical and coaxial telecommunication cables. About for a decade he took over the responsibility as head of design department for cable design technology. At present he is responsible for the technical sales department and is acting as a member in national and international standardisation bodies, like DKE resp. ISO/IEC.



Pietro Sonza
Nexans France
pietro.sonza@nexans.com

Pietro Sonza Reorda was born in Italy in 1970 and graduated from the 'Politecnico di Torino' (Italy) and the 'University of Brighton' (UK). He had been working for Pirelli (in the UK) in manufacturing, and AMP (in Italy), where he initially took product and market responsibility for active and passive networking products for specialising in optical networks. In 1998 he took European responsibility of the wireless networking product line.

In 1999 he became product manager of Alcatel Passive Optical Components in France.

He now lives in Germany and is Product Manager for Outside Plant Interconnection Products for Nexans.



Peter E. Zamzow
Nexans Deutschland Industries
AG
Mönchengladbach,
Germany

Peter.Zamzow@nexans.com

Peter E. Zamzow (61) is director of the Nexans company. He completed his post-graduate studies in telecommunications in Munich and Graz as Dipl.-Ing. He joined AEG Kabel in 1970 and was engaged in development and production of telecommunication cables. In 1980 he became head of AEG Kabel fibre optic division and in 1982 he was nominated senior engineer and 1995 nominated technical director. From 1992 he was plant manager of the Alcatel Kabel Optical Fibre Cable Plant Mönchengladbach. Since July 1994 he was senior manager of the German CATV- product line. Since 1998 he was responsible for Sales and Marketing in Division Licences and Production Lines world-wide.

Since beginning of 2001 he is head of Research and Development of Nexans Germany.

Introduction of intelligence into telecom network flexibility points

Authors: Gilles Le Traon, Fabrice Fauchoux, Daniel Morellec

FRANCE TELECOM R&D

Technopole Anticipa

2, Avenue Pierre Marzin

22307 LANNION Cedex

FRANCE

Abstract

Automatic copper cross connect, installed in central office or remote cabinet automates initial service deployment and service migration. This system reduces space and permits in general to make remotely lines tests : loop qualification, single line test, loop back, monitoring,...

In July 2001, the first automatic Main Distribution Frame has been implemented in one central office of the access network of France Telecom at Rennes. The automated copper cross connect equipment, remotely controlled from the main central office, switches any customer to any services (POTS, T1/E1, XDSL, ISDN), providing rapidly services installation and reducing wiring errors. Cross connection process are controlled through software from remote location. This software manages the connections, is easy to use and permits to have a better database management compare to manual cross connect solution.

Results of this experimentation will be given in the paper and the analysis permits a better knowledge of technical networks evolution necessary for a future field deployment.

This field trial experimented in Rennes is issued from the studies of France Telecom R&D laboratories. All existing cross connect technology are evaluated as well as hardware, software and integration in the access networks.

In business access networks, we shown that automatic cross connect systems could be used to provide voice and data lines (xDSL, LAN,...) and to accommodate the rapid operations changes by an automatic wire replacing with a simple remote terminal operation.

The paper concludes on the interest of the automatic flexibility in access network providing easy and rapid new services installation for customers, reducing operating costs and increasing access network reliability.

Keywords

Automatic cross connect systems; access network; cabling systems;

1. Introduction

The flexibility points of a telecommunications wired network provide the physical links between a customer and the telecommunication service operator. From the creation of this network, all of these flexibility points are managed manually (installation, operation and maintenance). This management is heavy in terms of direct (travel, labor, equipment, logistics) and indirect (DB reliability, maintenance of quality of service, etc.) operating costs. The increase in network data rates, the

multiplication of xDSL type broadband transmission technologies and associated services significantly increase the number of interventions at the level of these flexibility points and require the order/delivery process to be optimized. To respond to the increasing demands of our customers, one solution is to management the crossconnection of the network flexibility points in a way that is automatic, reconfigurable and that can be controlled remotely. Equipment exists on the market and the evaluation and integration of this equipment is one activity of the France Telecom R&D laboratories at Lannion. This document describes the existing functionalities of the private and access network flexibility points, the different technologies and performances of automatic crossconnection and finally describes the methodology for introducing this type of system within the context of initial trials conducted by France Telecom in 2001 on a real site.

2. Network flexibility points: Which functionalities?

The classic construction of an access network and of a network terminal cabling is shown in figure 1 below. The flexibility points are located throughout the system, from the telephone exchange to the customers. Each customer is connected to the operator network by a set of telephone pairs that are interconnected at the level of the flexibility points. Each pair in the network is identified so as to determine the exact physical path between the telecommunication equipment in the central office and the geographic area of each customer. For the France Telecom access network, the main element of flexibility is the main distribution frame located at the central office, then there is the area remote cabinet, building distributor, the distribution point and finally the customer cabling system.

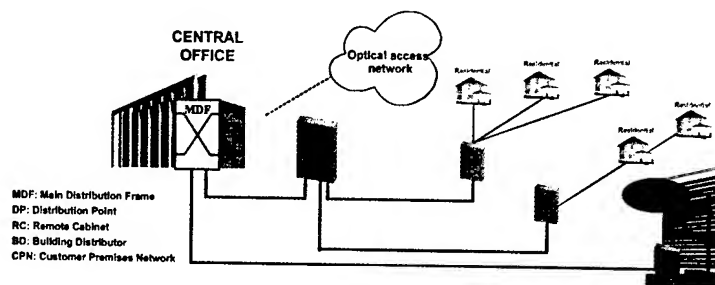


Figure 1: Block diagram of a telecommunications network

Connecting a customer to the various services provided by the operator requires physical operations at the level of the main distribution frame, the RC or BD and the DP depending on the case. The connection operations involve laying one or more jumpers (twisted copper pair) between different interconnection elements of the type cable terminals, management elements and connectors.

The flexibility points are the elements of transition between parts of the network that have different rates of occupation, thus enabling the network to be managed flexibly and particularly the cable and telecommunication equipment resources to be optimized.

The operating functionalities are:

- Creation or termination of lines
- Identification of lines and equipment
- Taking of measuring points for preventive and curative maintenance.
- The rapid movement of lines (line changes) during cable grouping operations or the change of generation of active equipment
- The evolution of services requiring crossconnection or interconnection of a customer line between different telecommunication equipment (e.g. Subscriber Connection Unit, DSLAM, subscriber multiplexers, .)

3. Why automate the flexibility points?

Flexibility in the network infrastructures (access and private domain) must make it possible to respond to changes linked not only to the diversification and multiplicity of the services offered, to the increased volatility and mobility of the customers, but also to the multiplicity of local loop telecommunications actors. Introducing automation at these flexibility points will enable new functionalities to be offered for tomorrow's networks. The increase in data rates on the networks associated with the multiplication of broadband technologies eventually deployed on all the network flexibility points (MDF, RC, BD, customer BD) will significantly increase the number of operations and require the optimization of the ordering/delivery processes.

With regard to the operator, the necessity of lowering network operating costs and optimizing Quality of service (QoS) also impels us to make the access network flexibility points more efficient. The technical management of documentation is currently manual and there is no consistency between physical links made in the field and the descriptive data. Automation would enable us to attain reliability levels for the databases. These databases are vital in the technical optimization of the network and concern the reduction of high indirect operating costs.

Functions of the automatic crossconnect equipment :

- Automatic crossconnect functions :
 - o Can be controlled locally and remotely
 - o Provides the automatic construction and deconstruction of metallic links

- o Enables equipment/network pairs to be identified, etc.

- o Retains the "jumper" performances (transmission characteristics)

- o Provides a flexible management identical to the function of the jumper

- Provide the crossconnect terminal with new functions

- o Enables the automatic management of the equipment (optimization of the busy rate of the equipment cards, etc.)

- o Gives access to all the pairs for testing (preventive, curative)

- o Provides remote supervision

- o Enables services to be provided rapidly to the customers.

- Interface with the order management processes

- o Allows interfacing with the descriptive databases

- o Enables the consistency of the databases to be verified

4. Technical solutions

There are several technologies: robotic technology crossconnect systems, relay and micro-relay crossconnect systems. The work of France Telecom R&D in evaluating the performance of these systems involves establishing specifications from a hardware (transmission parameters, EMC, environment, etc.) and software (HMI, control architecture) point of view, integrating them into the access and private networks as well as technical and economic studies on the subject.

The principles used on these different equipment types enable "any to any" flexibility via an assembly in a Clos interconnection crossconnect network by ensuring a very low blockage rate (in the order of 10^{-7}). These systems allow the physical interconnected links to be conserved in the event of power failure.

Table 1 below summarizes the main characteristics of the different technologies currently available on the market.

Technology	Advantages	Disadvantages
Pins	<ul style="list-style-type: none"> - very high density - proven technology - only the LAN crossconnect system uses pins 	<ul style="list-style-type: none"> - slow - sequential connections - noisy - low connection repeatability
Relays	<ul style="list-style-type: none"> - Rapidity - Simultaneous switchovers 	<ul style="list-style-type: none"> - low density - does not support LAN
Micro-relays	<ul style="list-style-type: none"> - High density - Rapidity - Simultaneous switchovers 	<ul style="list-style-type: none"> - Density lower than the automatic and pin crossconnect systems - No high capacity for the moment

Table 1: Comparison of automatic crossconnect technologies

The main advantage of the pin technology is its density, which enables the entire main distribution frame to be automated but its fault is its slowness of the connections and disconnections.

Relay technology is rapid but has the disadvantage of not being very dense. These systems are generally small capacity systems.

Micro-relay technology combines the rapidity of relays with (almost) the density of the pin system. There is however currently no high capacity system.

The choice of automatic crossconnect technology will be made according to the field used, the capacity of the flexibility points to automate and the applications required to be deployed in the network.

5. Methodology for integrating automatic systems: FT trials

In this section, we will be describing the methodology for integrating an item of automatic crossconnect equipment on an experimental site.

Indeed, initial testing on the automatic crossconnect system was undertaken in the access network in cooperation with France Telecom operating services. A main distribution frame (of class 4 type) fully switched over in July 2001 to the automatic management of the physical links, particularly simplifying the delivery of services to the customers served by this distribution frame. The system installed on the trial site automatically connects pairs through an automated system that retains a physical memory in the event of power failure. The manual operation of wiring is now replaced by running a command on an HMI controlled by teams whose purpose is specifically to control the activity of the distribution frames.

5.1 Different phases:

The trials were implemented in several phases over a period of 10 months, culminating in the start up of the automatic distribution frame in July 2001. To obtain this result, the actions were carried out sequentially in the following chronological order:

Phase 1: Choice of the site and inventory of fixtures

- Establishment of the detailed composition of the main distribution frame in terms of equipment and transport pairs. Gathering information from the different contributors to the project.

Phase 2: Technical preparation for the trials

- Study of the current cabling engineering rules for adapting the automatic distribution frame to the management of connections.
- Study of the control architecture and of the human/machine interface configuration.
- Definition of the specifications for the equipment order.

Phase 3: Installation of the equipment

- Upgrading the existing distribution frame, laying the cable trays, providing the power supply.
- Factory acceptance and validation of the system (distribution frame, HMI, control architecture).

- Cabling on the main distribution frame, installation and test of the control architecture.

Phase 4: Start up and training

- Switchover from manual to automatic management.
- Fault reporting and technological survey
- Informing and training the operators concerned (operation and maintenance)

5.2 Composition of the main distribution frame

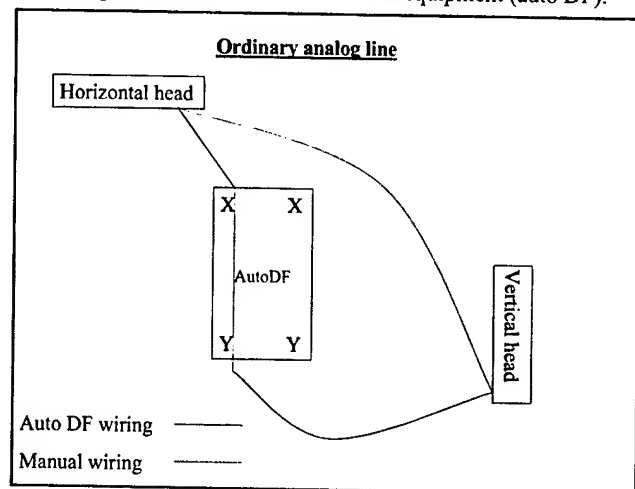
The inventory of fixtures for the distribution frame is the basic element for determining the capacity of the automatic crossconnect equipment to be installed. The composition of the exchange is given by a descriptive database that groups all the information on the physical line of the customer (telephone no., equipment no., transport pair no., distribution pair no., address, customer name, type of line).

The various elements installed number 3172 (number of pairs installed) and comprise analog, ISDN, small capacity multiplexer (PCM 2 and 11), ADSL, payphone, and leased link (HDSL) types.

5.3 Equipment hardware integration with respect to the existing distribution frame

The equipment was connected in parallel to the traditional wiring system and "isolated" on the equipment end by isolation systems integrated with the existing management elements of the equipment. This isolation was necessary owing to the factory pre-configuration of the automatic distribution frame.

There are different cabling rules according to the services. The equipment cabling had to be adapted to the traditional cabling, because the major constraint of this integration is the transparency of the automatic crossconnect system with respect to manual cabling. The block diagrams for the main services are shown in figure 2 below. The diagrams show the comparison between the connection principles of traditional cabling by "crosconnects" and the cabling of the automatic crossconnect equipment (auto DF).



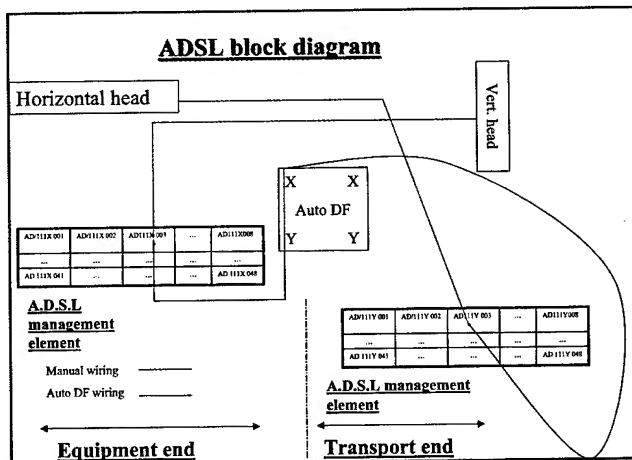
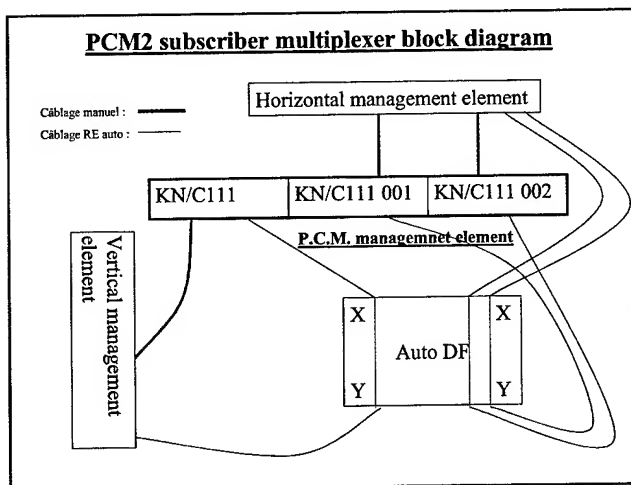
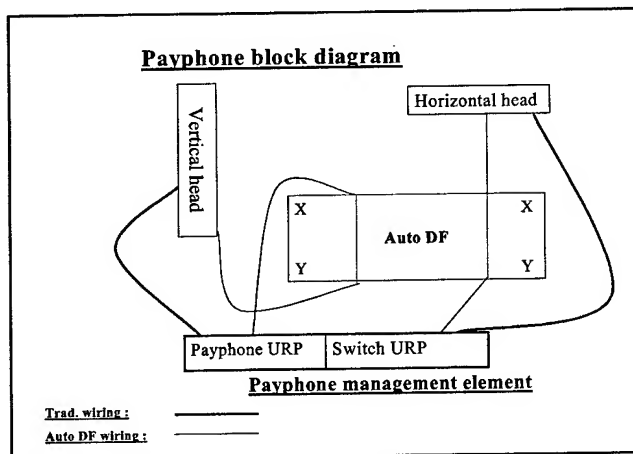


Figure 2.— Block diagrams of the auto DF according to the services

U.R.P.: Payphone connection unit

P.C.M.: Subscriber multiplexer (increases the transport pairs by multiplexing 2 or 11 subscribers on the same pair)

A.D.S.L.: Broadband system on copper support superposed on the telephone line

5.4 Description of the control architecture

The technician who operate in "activity control rooms" carried out the remote operation of the equipment tested. Their normal role includes receiving customer faults and organizing the work of the technicians intervening on the network. It was therefore necessary to install a control station in the "activity control rooms" of the France Telecom General Public Agency (responsible for domestic customers). A station was also installed in the Business Service Unit (responsible for professional customers). Finally, to cover failures during non-working hours, it was necessary to install a third workstation in the premises of the Local Maintenance Group (G.I.L.). Three control workstations were therefore necessary for the operation of the automatic DF (see figure 3).

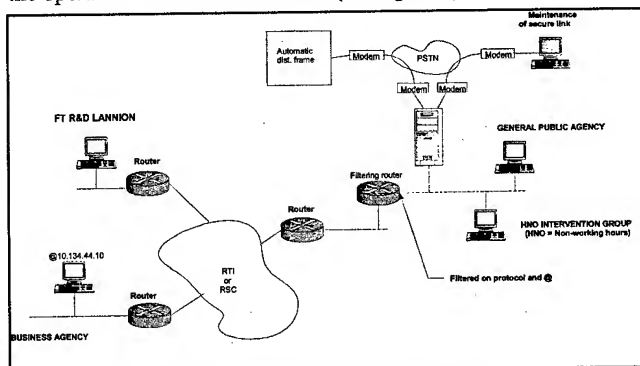


Figure 3 – Control architecture

5.5 Operating software

The human machine interface (HMI) of the system is the system control component. This software had to be customized at the level of the visual interface to enable it to be integrated into the France Telecom network with a maximum of transparency for the operators. We developed an organizational tree structure for the equipment ports according to the France Telecom notations used in our descriptive databases. Hence, we organized the following tree structure for the ordinary lines:

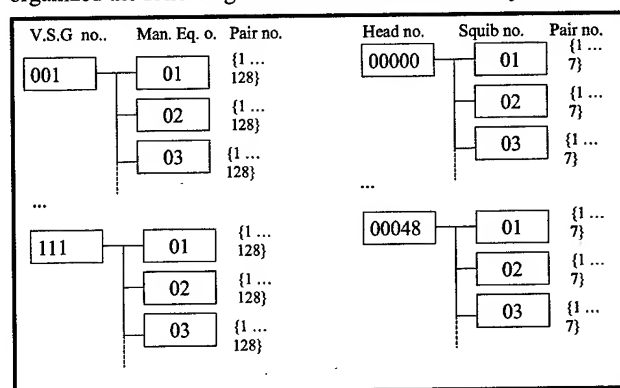


Figure 4 – Analog line tree structure

5.6 Principle of operation

A work order sheet is emitted for the creation, cancellation or change of telephone line. This is interpreted by an operator who enters the order on the remote management Human

Machine Interface. For a line change, the agent must then update the 42C database.

With the automation of the distribution frame, the same person carries out this procedure, whereas in the manual procedure two people are required to carry out the work. The first received the work order (W.O.) and then controlled the on-site intervention of a line operator to make the manual crossconnections then updated the 42C information when the intervention was completed.

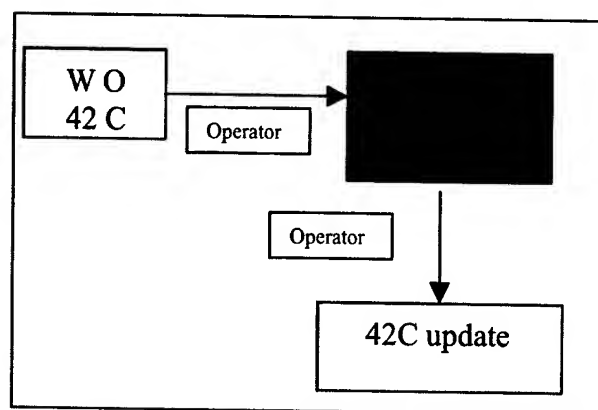


Figure 5 – Principle of operation of the automatic distribution frame for the trials

5.7 Report

The technical testing of the first automatic distribution frame in a class 4 revealed itself to be highly productive from the technical point of view and shows that the studies and integration that were conducted will enable other distribution frames of any size and composition to be automated more easily. A major evolution would be to fully automate the procedure described in section 5.6 by creating a direct interface between the France Telecom databases and the operating software of the automatic crossconnects. This would make the documentation fully reliable and reduce the operating costs of the automatic DF.

Upon completing this installation, it appears that it is technically possible to automate the telecom access network exchanges. However, the economic viability of these systems remains to be proved. The objectives of the France Telecom R&D research are the interconnection of these systems with the IS of France Telecom, and the study of the savings made by this system to characterize/test the subscriber lines. New ideas for services are also being studied.

6. Use of automatic crossconnect systems in customer terminal installations

The Telecom operator access network is not the only area in which these systems can be used. The multiplicity of communication services involves changes in our way of communicating that affect both the active equipment and the communication infrastructures of customer terminal installations.

6.1 LAN network distribution frames

Businesses have internal telephone and computer networks. Distribution frames are used for these two types of links in order to allocate resources to the personnel.

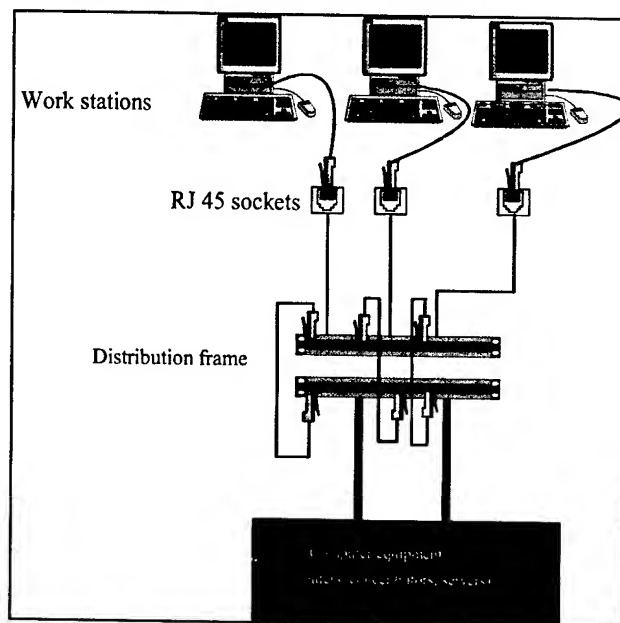


Figure 6: Example of a LAN system in a business

The automation of this type of distribution frame is currently being studied. Indeed, integrating this type of equipment adapted to the cabling of category type 5 or 6 would enable the administrators of these networks to:

- Make connection procedures more reliable and easier while reducing the costs associated with manual management.
- Limit any risk of connection error and computer hacking.
- Meet the temporary requirements of physical links in infrequently used rooms, meeting rooms, etc.
- Supply new services within the business (videoconferencing on demand, resource roaming, etc.).
- Crossconnection can be managed locally or remotely and does not require any special skills owing to the development of very user-friendly HMI.

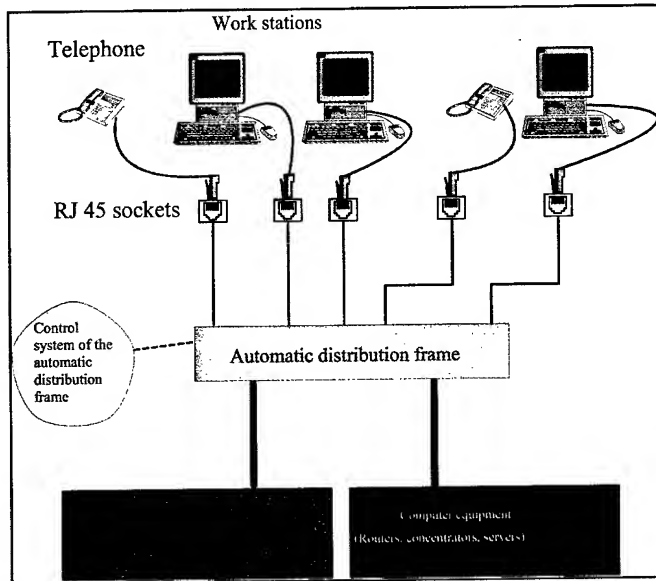


Figure 7: Principle of automation of LAN and telephone distribution frames

6.2 Distribution of broadband links on request in the private domain

Broadband needs are multiplying and 'border points' become potential market targets in this domain. In this case, it would appear to be necessary to be able to allocate broadband links dynamically to meet customer requirements. A manufacturer in the domain offers, for example, a system that can distribute ADSL links automatically for the hotel industry in an almost transparent manner for the administrator thanks to a voice server and interfacing with the management system of the establishment.

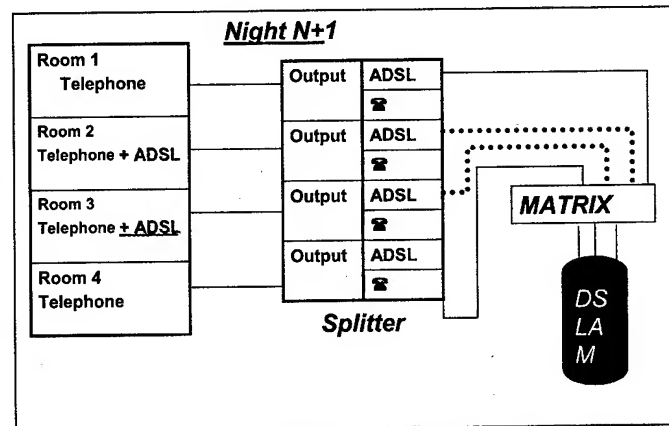
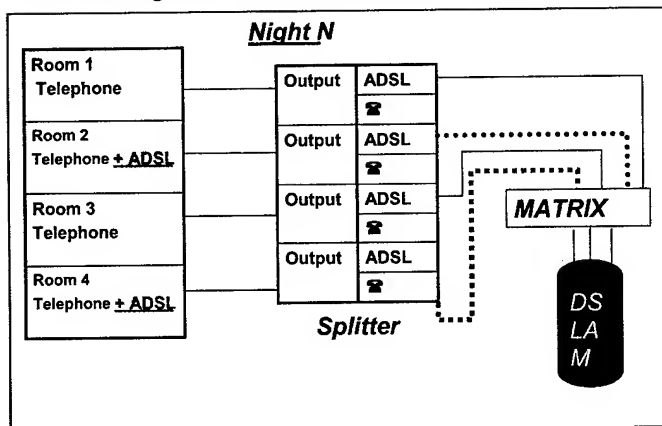


Figure 8: Example of ADSL link distribution in a hotel

For this type of request, the most suitable products are those that use relays or micro-relays, taking into account the frequency of movement and the requirement for simultaneous connections/disconnections.

7. Conclusion

The increase in data rates on telecommunication networks combined with the multiplication of broadband transmission technologies will require the processes and management of the network flexibility elements to be optimized over the coming years. The introduction of automatic crossconnection functions is an innovative solution that enables these requirements to be met. In this domain, technical solutions exist and the initial trials of automatic crossconnect equipment integration on a real site have demonstrated the technical potential of the products.

However, the economic viability of these systems remains to be proven and the new functionalities allowed by the automation are essential elements to justify the introduction of this equipment at the network flexibility points. The advantages associated with automation will enable, by sharing the broadband accesses, to meet the customer demands more satisfactorily and to increase the reliability of global management of the ordering/delivery processes for the different services offered to customers. In the private domain, the technical solutions enable administrators to make cabling more reliable, to free themselves from the management procedures of the cabling and thus to better respond to the needs of their customers.

8. Authors



Gilles Le Traon received his engineer degree from the Ecole Nationale d'Ingénieur de Brest (ENIB) in 1992. He joined the France Telecom R&D center in 1994. He works in the Local Loop Infrastructure Laboratory, as project manager in optical and copper main distribution frames evolutions.



Daniel Morellec began his career with France Telecom in 1978. He joined the France Telecom R&D center in 1989. He works in the local loop Infrastructure Laboratory. He is in charge of automatic cross connect systems tests and field trials



Fabrice Fauchoux received his engineer degree from the Ecole Nationale Supérieure de Sciences Appliquées et de Technologie (ENSSAT) in 2001. He joined the France Telecom R&D center in 2001 to work in the Local Loop Infrastructure Laboratory, on cabling systems architecture.

Cable for xDSL Technologies with Up to 25 Concentric Pairs in the Same Binder.

Ricardo Tadashi Tanaka, Antonio Carlos Silva, Renato Flávio Cruz

Furukawa Industrial S.A. Produtos Elétricos, Curitiba, Paraná, Brazil

Phone: +55 41 341-4062 E-mail: tanaka@furukawa.com.br

Abstract

The development and widespread use of services that need high speed in data transmission such as VoIP, teleconference, high speed internet are increasingly demanding better performance from the metallic telecommunications network. The new technologies such as DSL were developed in order to transmit broadband signals through the metallic network as HDSL, ADSL, RADSL, VDSL, etc. This technology was developed to be used in the currently metallic network (POTS), which, however, has limitations mainly due to noise and crosstalk from different transmission systems sharing several cooper pairs of the same cable at same time.

This paper presents the development of a new cooper pairs cable that provide superior performance in frequencies up to 40 MHz when compared to conventional cooper pairs cables.

Keywords

xDSL cable; concentric pairs; cooper pairs; ADSL emulator

1. Introduction

The bandwidth over metallic network is raising very fast. Several new services are available to the customer by using the copper wire telephone infrastructure. Digital subscriber line (HDSL, ADSL, RADSL, VDSL, etc) is a technology developed to supply broadband to the customers. The figure 1 shows a typical application of DSL technology over metallic network, providing multiple services in the last mile.

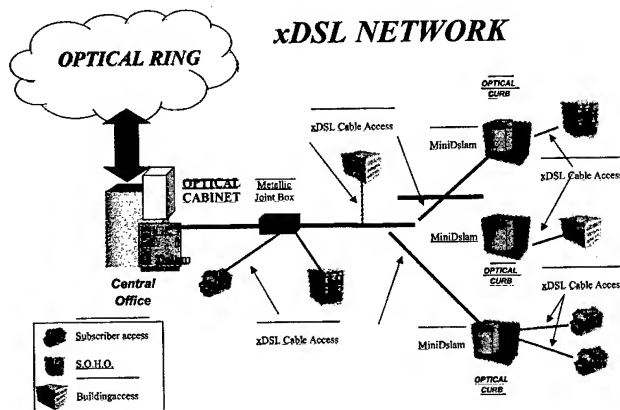


Figure 1 – Typical xDSL Network

In order to attend the growing demand for bandwidth in our country a new copper pairs cable has been developed taking into account the main electrical and transmission parameters like NEXT, FEXT, Return Loss, Impedance and other parameters that providing enhanced performance in xDSL system. The transmission parameters obtained in the cable was continuously compared with DSL standards in order to assure a superior performance when compared to conventional cooper pairs cables.

2. xDSL Technology

As well know, the xDSL technology was developed to be applied over standard telephone subscriber lines and frequencies involved in this transmission can reach up to 1 MHz for ADSL and 30 MHz for VDSL.

The figure 2 and figure 3 shows a typical ADSL and VDSL Power Spectral Density versus frequency.

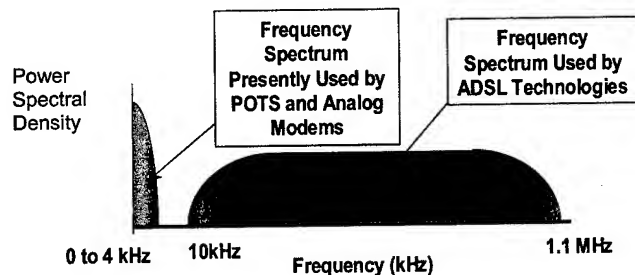


Figure 2 – ADSL Frequencies Range[1]

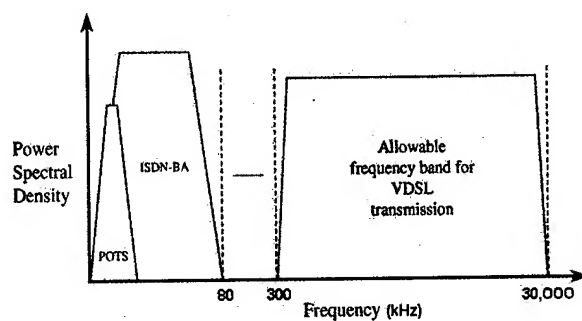


Figure 3 – VDSL Frequencies Range[2]

3. Cable Design

The concept of the new multipair cable design optimized for xDSL applications was developed following a main premise: a new cable design must keep the basic constructive characteristics of a standardized model of cable full compatible with the present cooper access network in Brazil. According to this premise, some requirements were defined and followed during the new cable development:

1. Characteristics like capacitance, impedance and core layup of the new cable must be equivalent of the standard cables;
2. The transmission parameters should be in accordance to current and future specifications for xDSL technologies. Along this line aim is to obtain a cable optimized for bandwidth performance up to 40MHz;
3. For the project calculation of high frequency parameters was used the H. Kaden method [3]. This method considers phenomenon like skin and proximity effect for determination of the dimensional of the insulated conductor from the attenuation and impedance desired. This method is widespread used for calculation of high bandwidth cables like LAN cables and presents good results when we compare the calculated and measured results;
4. The crosstalk level must be minimized. For optimize crosstalk level, the option was reduce the lay length of the pairs, in order to keep the standardized core layup;
5. The process control should be improved. An optimized xDSL cable needs more control than a telephonic cable in order to obtain a better performance at high frequencies.

3.1 Process Control

Furukawa has a large background in the production process and control of LAN metallic cables. For this reason, it was easy to change the set up of the telephone cables machines for producing xDSL cables.

Indeed, the process control used in this new cable design is far better than the control process used to manufacture a conventional telephone cable. The tolerances in the process parameters are much more tight. The main parameters are:

1. Concentricity of the insulation;
2. Cooper and insulation diameter;
3. The surface of the conductor should be as smooth as possible because a skin effect;
4. Tension of the pairs during the tensioning;
5. Dimensional stability of the pairs lay length

3.2 Cable Core Layup

The figure 04 shows a typical core layup of a standard cable. This core layup is the same of the new cable. Figure 05 and 06 shows the configuration of 100 and 200 pairs cables.

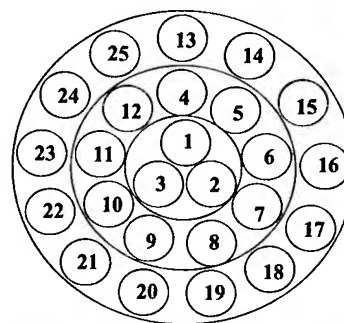


Figure 4 – 25 Concentric Pairs in the Same Unit

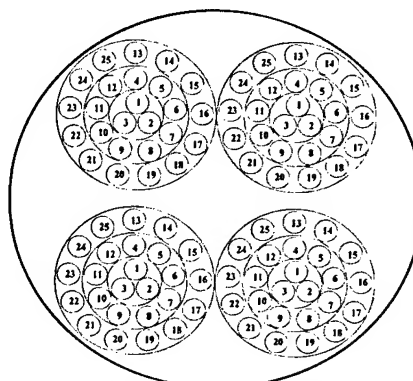


Figure 5 – 100 Pairs Core Layup (4 Units of 25 pairs)

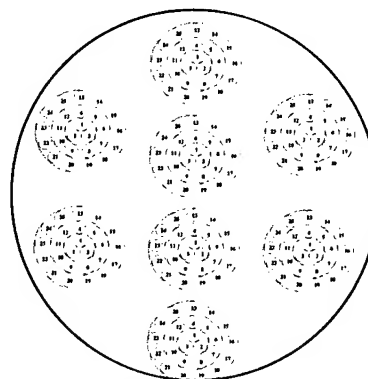


Figure 6 – 200 Pairs Core Layup (08 Units of 25 pairs)

3.3 Cable Construction Comparison

Table 1 shows the construction comparison between the new cable optimized for xDSL and a similar cable manufactured according to telephone industry Brazilian standard [4] which requirements are generally based on REA specification PE 22.

Table 1 – Construction Comparison between xDSL Cable and Standard cable

Construction	Standard Cable	New xDSL Cable
Conductors	0.5mm annealed cooper	0.5mm annealed cooper
Insulation	Solid Polyethylene with 0.16mm thickness	Solid Polyethylene with 0.19mm thickness
Pair Lay Length	Max. 150mm	Max. 50mm
Cable Core	Unfilled	Unfilled
Core Wrapping	Non-hygrosopic dielectric tape	Non-hygrosopic dielectric tape
Shield	Plastic coated Aluminum Tape	Plastic coated Aluminum Tape
Jacket	Black LDPE	Black LDPE

Both cables are used for distribution in exchange area and usually in duct or aerial lashed application. Pressurization is not applied in the distribution network, even with unfilled cables.

4. Results and Discussions

The table 2 describes the main electrical parameter obtained in the new cable. The measurements were performed in a 200 pairs cable with a length of 2000m. As showed in the table 2, parameters like capacitance and impedance of the new cable are the same of the standard cable in order to keep the compatibility with the current network. Other parameters like resistance and capacitance unbalance were narrowed for improving the performance of the digital transmission.

Table 2 – Electrical parameters

Parameter	Standard	xDSL
Conductor resistance max. (Ω/km) at 20°C	93	91
Resistance unbalance, max (%)	5	2
Capacitance Avg (nF/km)	50	50
Capacitance Unbalance pair to ground, max. (pF/km)	2,625	1,000
Capacitance Unbalance pair-pair, max. (pF/km)	181	100
Dielectric strength (V/3s)	3,000	1,500
Insulation resistance, min (M Ω .km)	15,000	20,000

4.1 Transmission Parameters

The transmission parameters were measured in the frequency range from 1 MHz up to 40 MHz. These measurements were performed in each group of 25 pairs of a 200 pairs cable. The results are shown below.

4.2.1 Attenuation

The figure 7 and table 3 shows the attenuation measurements up to 40MHz. We compared the performance of the new cable with the specified values according standard T1.417-2001 for a 24 AWG PIC air core[5]. The transmission attenuation of the new cable comply with the attenuation specified values.

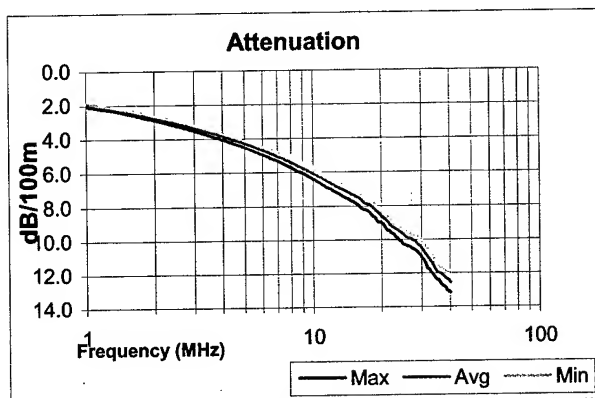


Figure 7 – Attenuation curve

Table 3 – Attenuation measurements

Frequency (MHz)	xDSL Max. (dB/100m)	Std T1.417-2001 (dB/100m)
0.77	1.6	1.7
1.03	1.9	2.0
6.18	4.7	5.0
10	6.1	6.4
15.4	7.4	8.0
19.6	8.5	9.1
29.3	10.4	11.4
34.3	11.7	12.5
40	12.6	13.7

4.2.2 Impedance

Measuring impedance uniformity provides a good idea of the cable's construction. Figure 8 shows the fitted impedance curve. The impedance curve presents variation from 95 to 108 Ω . As mentioned before, the new xDSL cable has been designed to be compatible with the current network, which have a typical impedance of 100 Ω . However, the new xDSL cable shows a better impedance uniformity than a standard cable.

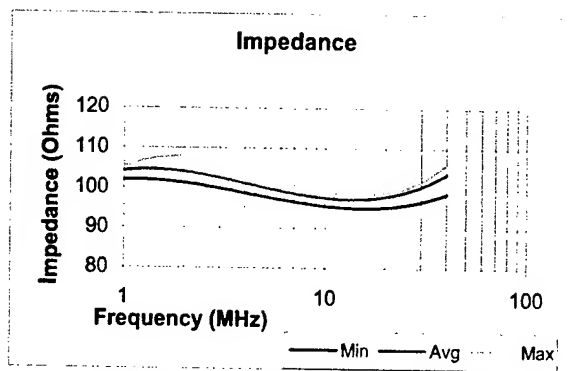


Figure 8 – Fitted impedance curve

4.2.3 Return Loss

As well as impedance uniformity, structural return loss (SRL) measurements provide a good evaluation of the consistency of the cable's construction, as SRL the deviation of impedance from a nominal value. The figure 9 shows the SRL results. In all range of frequencies, the worst case measured was 17dB, exceeding the minimum limits established for DSL technologies, like ADSL (10dB), SDSL (12dB) [5] and VDSL (12dB) [6]. Good return loss is the key to high frequency data rate performance, keeping bit error at an acceptable level within systems expectations. The new cable design exceeds the SRL limits and provide useful margin to accommodate return loss reduction by connectors and transmitting/receiving equipments

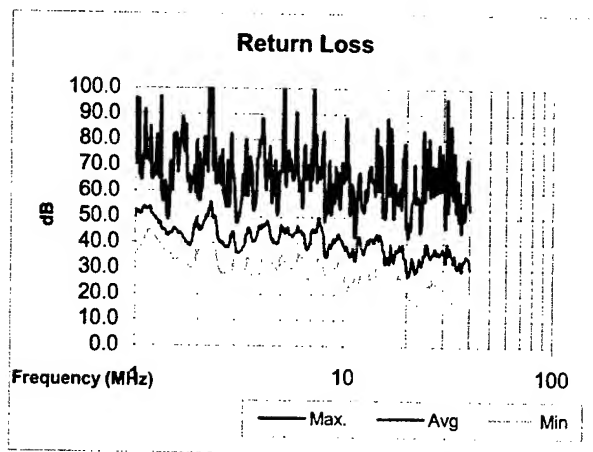


Figure 9 – Return Loss Curve

4.2.4 PS NEXT and PS ELFEXT

The Power Sum concept became very important when you need transmit DSL signals in several pairs of the same cable. Figures 10 and 11 shows the respective performance in PSNEXT and PSELFEXT of the new cable and the typical value for a 24 AWG PIC air core cable with 24 disturbers. The performance of the worst case of the new cable is about 10 dB better than the standard cable.

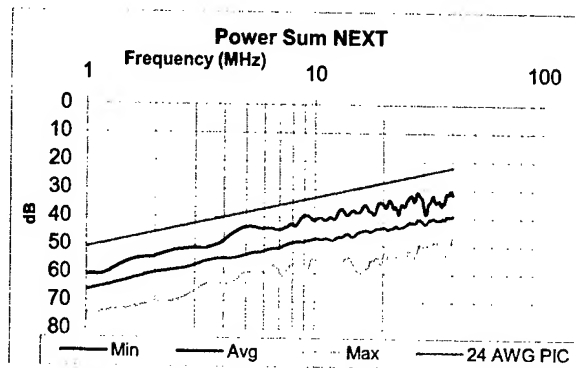


Figure 10 – Power Sum NEXT Curve

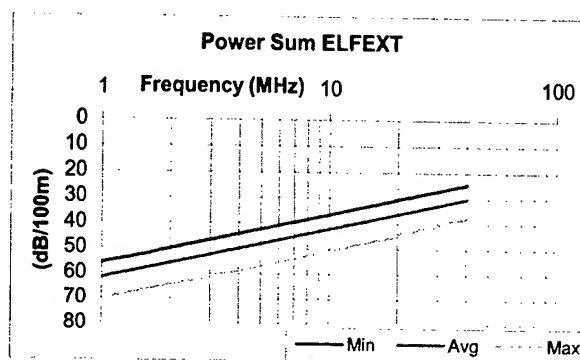


Figure 11 – Power Sum ELFEXT Curve

5. Tests with ADSL System Emulator

To evaluate and confirm the expected better performance of the new cable design, test loops were performed in accordance with customer's requirements. When and where appropriate, ANSI standard T1.417-2001 was used to complement the performance evaluation requirements. Figure 12 shows the resulting noise power spectrum density of the ADSL interferes used for testing.

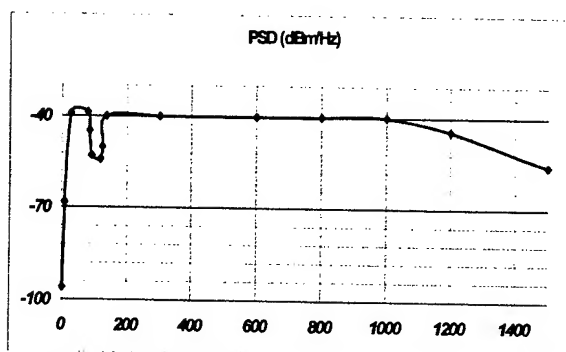


Figure 12 – Power Spectrum Density of ADSL Noise

The figure 13 shows the test set up used for measuring the performance of the ADSL system incorporating test loops with a test length of 6000m. The measurements were performed in

1000m steps along the total length of the test loop. In this test were used three cables of 100 pairs. Field terminations blocks type 110 IDC were used for access the ends of the cables. Patch cords cat. 5-e were used as jumper to connect cables and equipments. To obtain cable loops with more than 3000 meters, it was necessary to connect 2 units of 25 pairs of the same reel. The ADSL noise emulator was introduced in 24 pairs and in the 25th pair was monitored the bit rate and the SNR using an ADSL field tester.

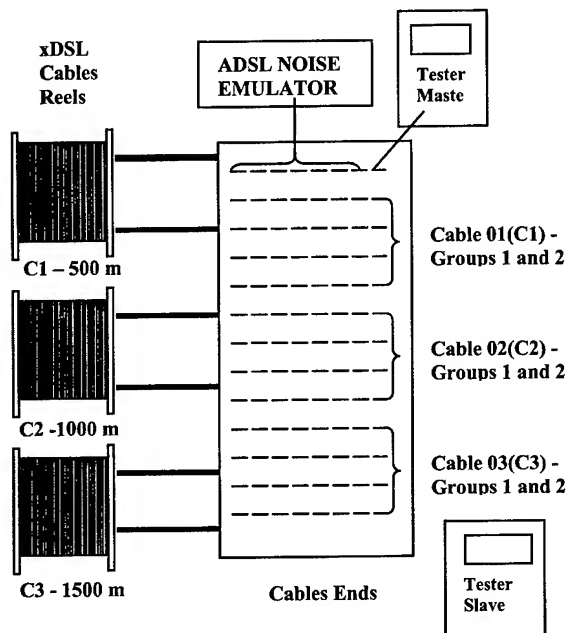


Figure 13 – Test Circuit

5.1 Results of the Tests with ADSL Signals

Figures 14 and 15 shows the SNR of a cable xDSL and a Standard cable respectively in a test with 24 noise sources in a length of 3000m. The cable xDSL has a SNR up to 10 dB better than a standard cable.

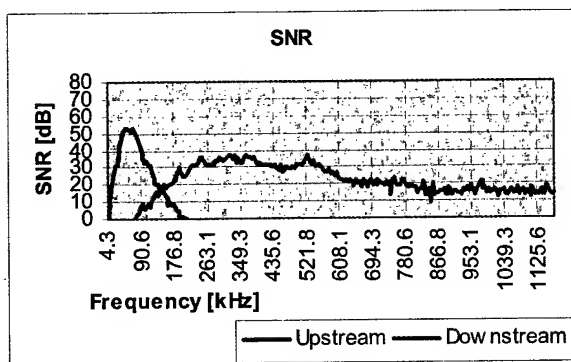


Fig. 14 – xDSL Cable SNR with 24 ADSL Disturbances and 3000m

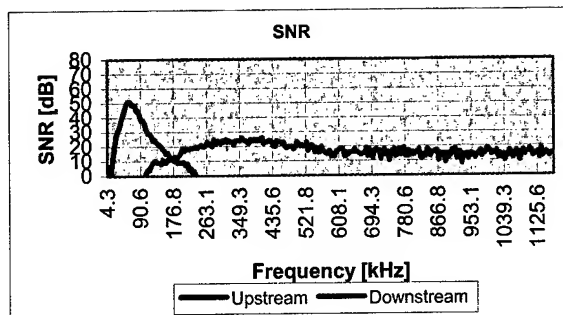


Fig. 15- Standard Cable SNR with 24 ADSL Disturbances and 3000m

Table 04 shows the bit rate of a standard and the new cable in a loop of 3000m and 24 ADSL disturbers. This table shows the bit rate of the new cable is about 2 times of a standard cable.

Table 04 – Bit rate in a 3000m link with 24 ADSL disturbers

Cable	Bit rate (kbps)		
	Up Stream	Down Stream	Total
xDSL	649	2251	2900
Standard	611	771	1382

Also was made tests along the total length. The performance of the new cable and standard cable was evaluated in links from 1000m up to 6000m in steps of 1000m with 24 ADSL noise disturber emulators. Figure 16 shows that the new cable can transmit 2Mbps (usually bit rate used by the carriers in Brazil) in lengths about 1000m more than a standard cable.

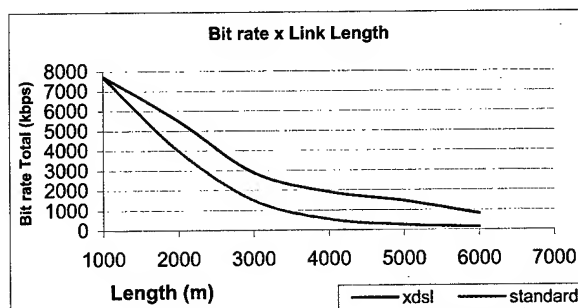


Figure 16 – Bit rate x Link Length

6. Conclusions

Due to the growing of the new technologies that demand more and more bandwidth of the metallic cables, is advisable that the new metallic networks should use the new cables optimized for this technologies. The new cable developed presents enhanced electrical and transmission characteristics in a range of frequencies up to 40 MHz for support the present and future technologies. In order to the new cable to have same main

construction and electrical characteristics of a standard cable, the installation of this cable became easy..

The tests made with the ADSL noise emulators prove the better performance in distance and bit rate of the new cable when compared with a standard Brazilian cable. The fact of the new cable to be much similar of a standard cable, becomes the cost of the new cable very competitive with a good relation cost x benefit.

7. Acknowledgement

The authors wish to acknowledge the support of many people in our own organization. Special thanks to Mr. Marlon Sassi de Lima who provides the setup loop test used for xDSL measurements.

8. References

- [1] ITU-T G.992.1 – Digital Transmission Systems – Digital Sections and Digital Line System – Access Networks
- [2] ETSI TS 101 207-1 V1.2.1 (1999 –10) – Transmission and Multiplexing (TM); Access Transmission Systems on Metallic Access Cables; Very High Speed Digital Subscriber Line (VDSL). Part 1: Fundamental Requirements
- [3] H. Kaden, “Wilbelstrome und Schirmung in der Nachrichtentechnik” springer-Verlag, Germany (1959)
- [4] NBR 9124:2000 - Cabo telefônico isolado com termoplástico, núcleo protegido por capa APL – Especificação. Plastic insulated, APL sheathed telephone cable - Specification
- [5] T1.417-2001 – Spectrum Management For Loop Transmission Sytems
- [6] ETSI TS 101 270-2 V1.1.1 (2001-02) – Transmission and Multiplexing (TM); Access Transmission Systems on Metallic Access Cables; Very High Speed Digital Subscriber Line (VDSL). Part 2: Transceiver specification

Authors



Ricardo Tadashi Tanaka received his B.S. degree as an Electrical Engineer from Center of Technological Education (CEFET) in 2000. He joined Furukawa Industrial S.A. in 1998 and since then he has been involved in design and development of telephone and LAN metallic cables. He is currently working at Cable Development Engineering.



Antonio Carlos da Silva received his B.S. degree as Mathematics from PUC in 1977. In the same year he joined Furukawa Industrial S.A. and since then he has been involved in optical and metallic cables design and installation techniques. He is currently working in Product Engineering.



Renato Flávio Cruz received his Chemical Engineer degree from Universidade Federal do Paraná (UFPr) in 1988. He joined Furukawa Industrial S.A. in February 1989 and since then he has been involved in research and development of products for telecommunication cables. He is now Manager for Development Cables Engineering.

Development of Optical Fibers and Copper Twisted Pairs Composite Cables for Both of FTTH and xDSL Broadband Networks

Shoji Matsumoto, Yukihiro Hamada, Fumihiko Shimizu

Nishi Nippon Electric Wire & Cable Co., Ltd.

Kasugaura, Oita, Japan

+81-97-537-5568 matumots@nnd.co.jp

Abstract

Cable network configuration was investigated and several types of composite cables consisting of optical fibers and copper twisted pairs were developed, in order to make more efficient and flexible both of the FTTH and xDSL broadband network services. The cables are the most suitable for the cable network configuration. The cable network configuration was investigated using three different case studies that were according to location and use. The suitable cable structures for each case were also considered, and several composite cables were developed, studying the important factors in each case. Furthermore, cable installation and the connection method for the composite cables were investigated.

Several composite cables were manufactured for the experiment and evaluated in each case. Excellent results on their characteristics were obtained. In addition, it was confirmed that composite cables can be installed and connected to others by using conventional methods and closures for both optical fibers and copper twisted pairs. Moreover, the newly developed composite drop cable can be draw into the building with only a single pipe, rather than the two necessities for optical fiber cable and copper twisted pairs. Hence, it was possible to provide various broadband networks easily, rapidly and economically by installing these newly developed cables. Additionally, by using these composite cables the load to be held up by the electric poles can be reduced and they visually improve the scenic outlook.

Keywords

Optical Cable; Composite cable; Broadband Internet Services; FTTH Service; xDSL Services;

1. Introduction

In recent years, the requirement for data communication speeds to increase has been on the rise due to further expansion of the broadband Internet use by general subscribers as well as commercial enterprises.[1] To keep up with broadband networks, the FTTH technology using optical fibers are used to apply. However, in the present transition period to the FTTH, not a few people are choosing xDSL services, using conventional copper twisted pairs cables, because of its low cost. In addition, it is easy to join xDSL services, because the conventional copper twisted pairs cables are already installed in existing buildings. Also, the area where the FTTH services can be provided is still quite small, and even in those areas xDSL services are usually available.[2]

On the other hand, it is difficult to replace copper twisted pairs cables with optical fiber cables for the FTTH services perfectly outside urban area. Moreover, in Japan, it is difficult to install another cables such as optical fibers, because the load to electric poles is very high and most building have only one pipe for cable installation. Also, the installation adds considerably to the cost.

Therefore, to resolve the above problems, new composite cables were developed.

2. Cable network configuration

First of all, cable network configuration according to the installation area was investigated, in order to provide various broadband network services efficiently and flexibly. As a result, three cases were posited and three types of composite cables that were most suitable for each case were designed. These three cases are shown in Figure 1. Case A is in the distribution area from the telecommunication center to the drop point, case B is in the drop area from the drop point to the Central Termination Frame (CTF) in buildings, and case C is in the indoor area from the CTF to subscriber.

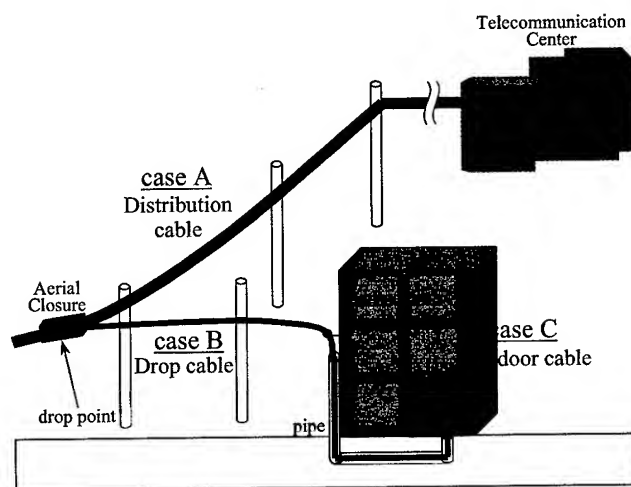


Figure 1. Model of cable network configuration

3. Cable structure design

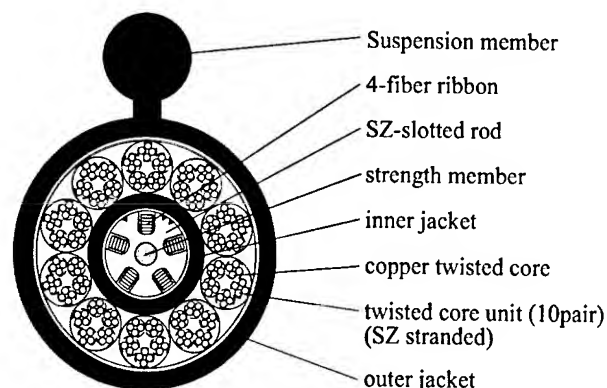
3.1 Distribution cable

Regarding case A, at first, the cable is installed from the telecommunication center to the drop point. If the cable is laid underground from the telecommunication center to the first electricity pole, we proposed that the distribution area is that from the point where the cable come above ground to the drop point.

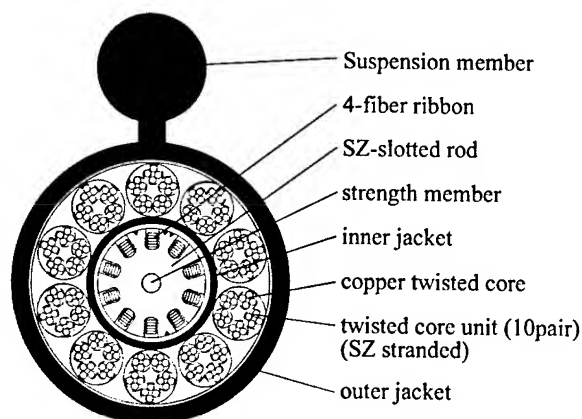
This cable, consisting of optical fiber and copper twisted pairs, must be able to be spliced and reconnected at any point along the cable. Therefore, we needed to design a cable which could easily facilitate mid span branching and which would keep slack length of both optical fibers and copper twisted pairs. Furthermore, we considered strength and ease of manufacturing the composite cable. We determined that the best composition for the cable was to have the optical fiber cable part stranded in SZ slotted core with 4-fiber ribbons, and the copper twisted pairs part SZ stranded outside of the optical fiber cable part. Also, the optical fiber cable part was sheathed by an inner jacket in the center of the composite cable.

Therefore, in the case of mid span branching or connecting only copper twisted pairs, these operations can be carried out without damaging the optical fiber. Also, this cable has a self-support structure feature for installation in an aerial environment.

Figure 2 shows the composite distribution cable. We choose the number of optical fibers and copper twisted pairs refer to conventional cables. For example, we show the composite cables that consist of 100 core fibers and 100 twisted pairs and of 200 core fibers and 100 twisted pairs.



(A1) 100 core fibers and 100 twisted pairs sample



(A2) 200 core fibers and 100 twisted pairs sample
Figure 2. Distribution cable structures

3.2 Drop cable

Next, about case B, the cable is installed from the drop point to the CTF in buildings. We proposed that the drop point is the connecting point of cables for draw cable into the building. Most of buildings have only one pipe for communication cable in Japan. This pipe is not so thick. Therefore, it is forced to install additional cable in same pipe or to add pipe for another cable. However, about the former, it is very difficult to lead another cable into same pipe for many bends are existed and a part of pipe is used flexible pipe. About the latter, it is too expensive to construct or bury another pipe.

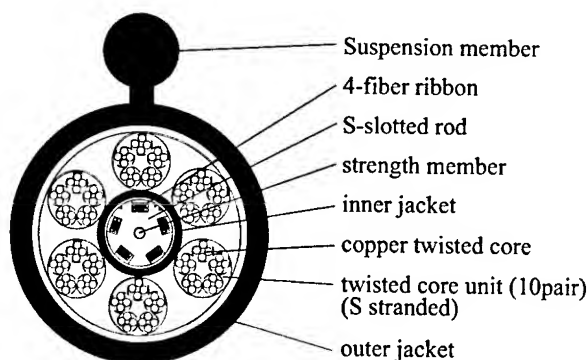
Therefore, composite cable has pretty advantage. The important property of this cable is down sizing in order to be able to install at existing pipe. Optical fiber cable part of this composite cable was

stranded in S slotted core with 4-fiber ribbons and copper twisted pairs were S stranded outside of the optical fiber cable part. Because this cable has no need to operate mid span branching. The optical fiber cable part was sheathed by an inner jacket in the center of the composite cable, too. Also, this cable is used only toward buildings at short distance. Therefore, we designed that this cable is more down sized by reducing the number of fibers and of twisted pairs. The cable for this case was self-support structure or simply circle structure. We can use different structure considering installation case.

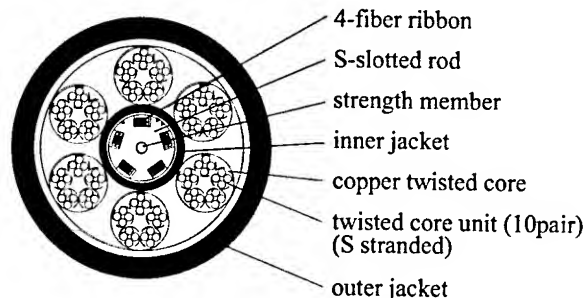
Figure 3 shows the composite drop cable. We choose the number of optical fibers and copper twisted pairs refer to the number of people requiring FTTH service and xDSL service in the building usual. For example, we show the composite cables that consist of 40 core fibers and 60 twisted pairs. Type B1 cable is self support structure and type B2 cable is simple circle structure.

Type B1 cable is installed directly in an aerial environment. Also, if the cable is installed from the outside of the building to the CTF in the building, suspension member of the composite cable must be separated off.

On the other hand, type B2 cable is installed by applying hanging method with the messenger wire in the aerial environment, such as from the drop point to the outside of building. Also, if the cable is installed from the outside of the building to the CTF in the building, the cable is lead in the pipe directly.



(B1) Self support structure
(40 core fibers and 60 twisted pairs sample)



(B2) Circle structure
(40 core fibers and 60 twisted pairs sample)
Figure 3. Drop cable structures

3.3 Indoor cable

For case C, the communication cable is installed from the CTF to the subscriber in the buildings. This cable is required to be able to provide both of the FTTH and xDSL services for each subscriber's requirement rapidly, then it should be compounded optical fiber cord and copper twisted pairs cord. The cable structure is flat molded for progressing mechanical characteristics under installation. Also, the sheath of this composite cable should be fire retardant polyethylene, because the fire retardant performance was demanded for indoor application. Furthermore, this composite cable has two notches on the both side of the sheath, for easy separating optical fiber cord and copper twisted pairs cord from the cable.

The required number of optical fibers for the FTTH is one or two, which is designed by FTTH service provider. Most of installed copper twisted pairs cord to the subscribers have one or two twisted pairs. Therefore, we designed this composite cable for various type combinations of the number of optical fibers and copper twisted pairs, in really same dimension of them as shown in Figure 4.

This time, the composite cable of two core fibers and two copper twisted pairs (C4) was manufactured, because this combination was considered the highest frequency of use.

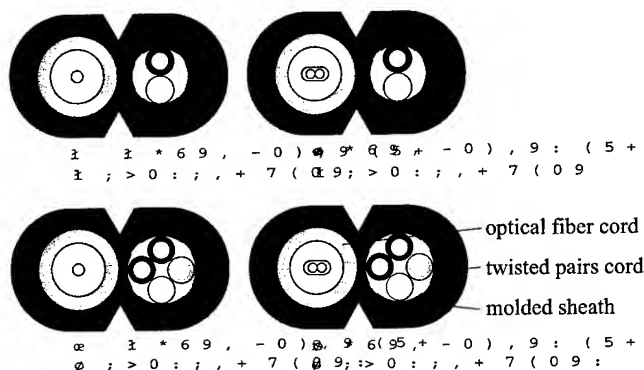


Figure 4. Indoor cable structures

4. Cable characteristics

In order to evaluate cable performance, composite cables of each structure were manufactured for the experiment and tested. Transmission, environmental and mechanical characteristics were evaluated.

4.1 Transmission characteristics

The transmission characteristics of each composite cable are shown in Table 1. All of optical transmission losses are excellent, because those values are less than 0.40dB/km at 1310nm and less than 0.25dB/km at 1550nm that are IEC standards. Also, all of characteristics of copper twisted pairs are excellent as shown in Table 1.

Table 1. Transmission characteristics of each composite cable

Items		Distribution cable	Drop cable	Indoor cable
Transmission loss	@1310nm	<0.40dB/km	<0.40dB/km	<0.40dB/km
	@1550nm	<0.25dB/km	<0.25dB/km	<0.25dB/km
Capacitance		35-45nF/km	35-45nF/km	35-45nF/km
Conductor Resistance		<147.5ohm/km	<147.5ohm/km	<147.5ohm/km
Insulation Resistance		>5000Mohm	>5000Mohm	>5000Mohm
FEXT		>42dB/km	>42dB/km	-

4.2 Environmental characteristics

Figure 5 and Figure 6 show the optical loss changing in temperature cycling test of each composite cable. The distribution and drop cables were measured in the range of -30 to 70 degrees centigrade according to outer environment, and the indoor cable was measured in the range of -20 to 60 degrees centigrade. The optical loss changing of all composite cables were excellent with less than 0.1dB/km, at the 1550nm measurement optical wavelength.

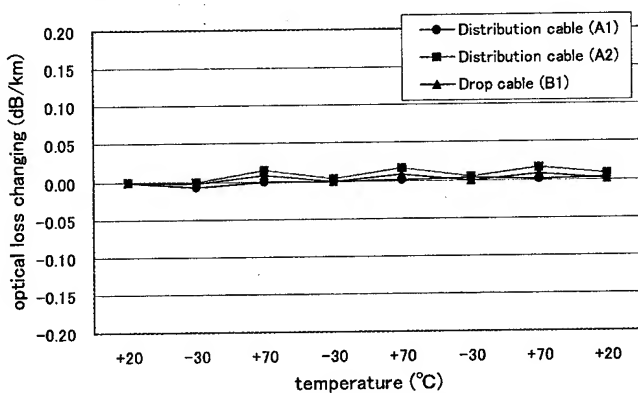


Figure 5. Temperature cycling characteristics of distribution cable and drop cable

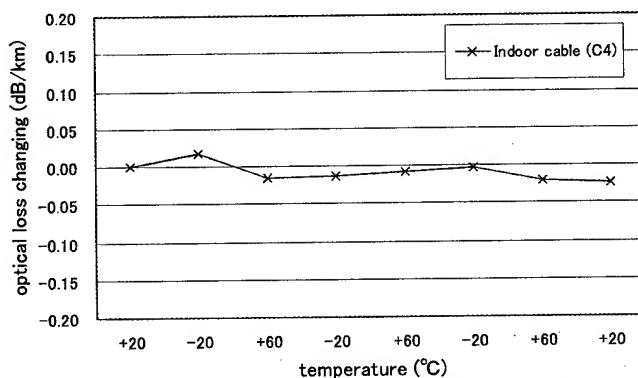


Figure 6. Temperature cycling characteristic of indoor cable

4.3 Mechanical characteristics

Table 2 shows the results of mechanical characteristics of each composite cable. The methods of examinations are based on the IEC60794-1. All of optical loss changings measured at the 1550nm measurement optical wavelength, were negligible.

Table 2. Test results of mechanical characteristics of each composite cable
(a) Distribution and Drop cables

Items	Conditions	Results			
		Distribution cables		Drop cables	
		A1	A2	B1	B2
Repeated bending	Cycle:10 (R=220mm for type A1) (R=270mm for type A2) (R=160mm for typeB)	No optical loss changing	No optical loss changing	No optical loss changing	No optical loss changing
Crush	1960N/100mm				
Tensile	10.78kN for type A1				
	13.72kN for type A2				
	6.86kN for type B1				
	2.94kN for type B2				
Squeezing	1.47kN R=250mm				
Torsion	±90deg/m twisting				
Impact	9.8N·m				

(b) Indoor cable

Items	Conditions	Results
Repeated bending	Cycle:10 R=20mm	No optical loss changing
Crush	980N/100mm	
Tensile	196N	
Squeezing	196N R=250mm	
Torsion	±90deg/m twisting	
Impact	4.9N·m	

5. Connection form design

Connection forms of each composite cable were also investigated to use the cable in field. The connection forms must be considered not only developed composite cables but also conventional optical fibers and copper twisted pairs cables. When twisted pairs are connected, they must not damage to the optical fibers. Furthermore, by applying conventional closure and connection

operation, development cost can be reduced and these composite cables are installed easily.

5.1 Connection form of drop cable

Figure 7 shows a example of connection form, by which the newly developed composite drop cable is connected to the conventional optical fiber distribution cable and copper twisted pairs cable. The upper portion in figure 7 is a conventional optical cable closure, and the lower portion is a conventional copper cable closure.

In the copper cable closure, the composite drop cable would be separated the optical cable part and copper twisted pairs. It is easy to pick up copper twisted pairs, for the optical fiber cable part is centered of the drop cable. Those copper twisted pairs are connected to the others of the conventional copper twisted pairs cable. The optical fiber cable part is led into the optical cable closure through the copper cable closure. In the optical cable closure, the optical fiber cable part and the conventional optical fiber distribution cable shall be connected each other. The optical fibers would not be damaged under connecting operation, for optical fiber cable part has inner jacket.

Therefore, the connecting operation for those cables can adopt the same as conventional one.

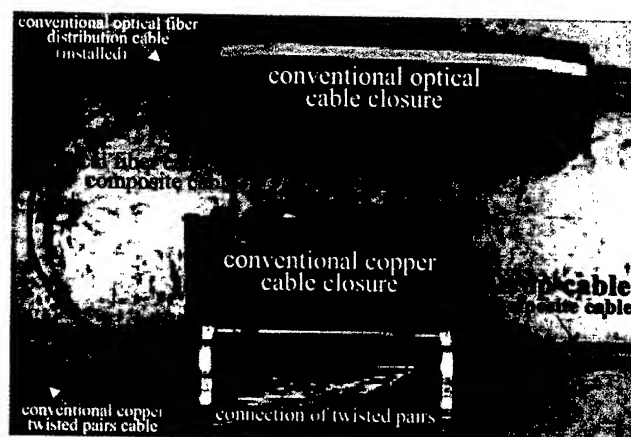


Figure 7. Connection form of drop cable

5.2 Connection form of distribution cable

Figure 8 shows example of connection form, by which the newly developed composite distribution cable is connected to the conventional optical fiber cable and copper twisted pairs cable in the conventional optical cable closure. The conventional optical cable closure would be attached to the composite distribution cable which is already installed. Then, the optical fiber cable and the copper twisted pairs cable are led into this closure for connecting.

The optical fibers and the copper twisted pairs can be picked up easily with keeping slack length from the composite distribution cable by removing outer jacket and inner jacket, because both of the optical fibers and the copper twisted pairs are SZ stranded. Therefore, any fibers and twisted pairs can be connected to other cables without cutting the distribution cable.

The copper twisted pairs can be connected in the space made by removing optical fiber trays. Then, the copper twisted pairs and the optical fibers can be connected by conventional operation. On

the other hand, the optical fibers and copper twisted pairs that are not necessary to connect, would be lead through out the closure.

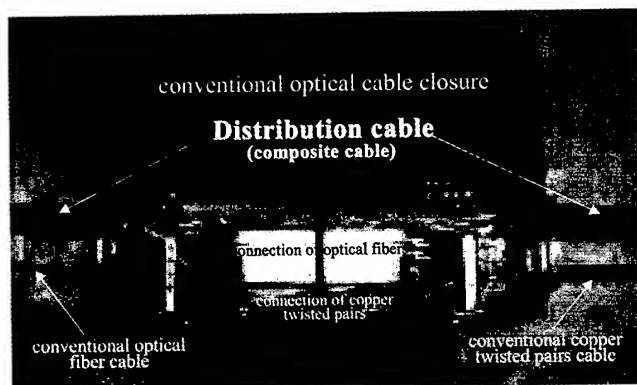


Figure 8. Connection of composite distribution cable with conventional cables

6. Conclusions

Cable network configuration was investigated. According to location and use, three different case studies were considered. The most suitable cable structures for these cases were also considered. Several composite cables consisting of optical fibers and copper twisted pairs were designed, manufactured for the experiment and tested in each case. As results, each composite cable has excellent transmission, environmental and mechanical characteristics.

Furthermore, connection forms of not only newly developed composite cables but also conventional optical fiber cables and copper twisted cables were investigated. The conventional optical cable closure and the copper cable closure were able to apply for various combinations connecting of these newly developed composite cables, conventional optical fibers cable and copper twisted pairs cables.

Therefore, these investigations and developed composite cables will be helpful to realize both FTTH and xDSL broadband Internet network services.

7. References

- [1] Y. Hamada et al., "A new optical cable attachable to drop wires" 49th IWCS, pp.8-12 (2000)
- [2] Y. Hamada et al., "Optical fiber and metal composite communication cable for the broadband Internet services" IEICE March 2002, B-10-33

Authors



Shoji Matsumoto was born in 1971. He received a M.E. degree in electronic engineering in 1995 from Oita University. He joined Nishi-Nippon Electric Wire & Cable Co., Ltd. in 1995. He has been engaged in development of optical fiber cable. He is a member of IEICE of Japan.



Yukihiro Hamada was born in 1970. He graduated in electric engineering from Oita National College of Technology in 1991. He joined Nishi-Nippon Electric Wire & Cable Co., Ltd. in 1991. He has been engaged in development of optical fiber cable. He is a member of IEICE of Japan.



Fumihiko Shimizu was born in 1959. He received a M.E. degree in information engineering in 1984 from Toyohashi University of Technology. He is a manager of Telecommunications Engineering Department, Nishi Nippon Electric Wire & Cable Co., Ltd. He has been engaged in development of optical fiber cables, optical connectors and their accessories. He is a member of IEICE of Japan.

Solutions for business building cabling infrastructures

A.C. Réau-Thomas, F. Fauchoux, E. Cressan

France Telecom R&D RTA/LLI

Avenue Pierre Marzin, 22307 Lannion Cedex (France)

Annececile.reau@rd.francetelecom.com

Fabrice.fauchoux@rd.francetelecom.com

Emmanuelle.cressan@rd.francetelecom.com

Abstract

There are many interesting solutions for the distribution of telecommunication services to business customers. Various copper and optical cabling system solutions exist to respond to the increased data rate in the business networks. Economically, the advantage of these solutions varies depending on different parameters such as customer type, initial investment, etc. However, the installation of optical media is becoming an increasing reality for medium and large professional customers.

This paper focuses on the issues involved for the cabling solution in a building. It explains the different cabling infrastructures suitable for services for small companies, in the first section, and for large companies in the second section.

For small companies, the cabling infrastructure generally uses copper cables. However, it is possible for customers to have services up to 2 Mbps. Two types of cabling infrastructures used with 2 scales of services: xDSL and ISDN/ HDB3 are described.

This paper presents the various existing cabling solutions to supply the business customer with broadband services (from 2 Mbps to 155 Mbps and greater). It highlights the problems of cabling: Which service? Which data rate? Which support? Which distance? Which engineering?

For the very high data rates, the optical support is inevitable. The paper presents the blowing method, which is a new optical cabling technology that offers the possibility of great flexibility for cabling. We will explain the benefits of using this technology, in particular the economic advantage. A detailed cost comparison will be produced for a flexible technology based on blowing and a more traditional optical solution.

In addition to the simple prolongation of large bandwidth services to the business customer, the paper presents the latest innovations to satisfy the needs of large companies: "secures" the flow of information. The realization of a "security cabling system" affects the infrastructures of the building and/or the network.

Keywords

Cabling system; copper cable; optical cable; microtubes;

1 Introduction

Operators can offer many broadband services to business customers thanks to a suitable cabling solution. Producing a cabling infrastructure depends on several parameters such as the building construction actors, engineering rules, etc.

During building construction, several actors are called upon between the telecommunication operator and final customer.

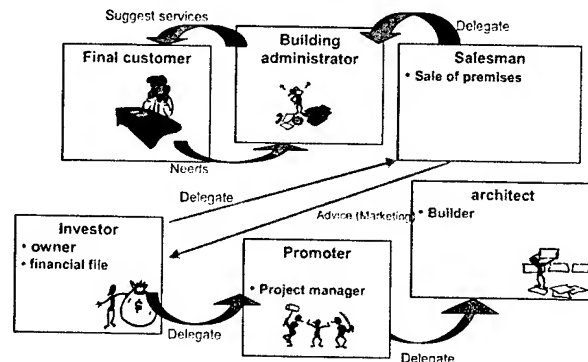


Figure 1: The actors

In France, cabling infrastructure belongs to the ILEC operator or to the building owner.

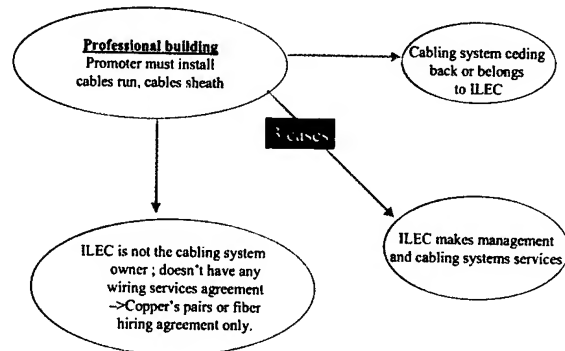


Figure 2: The rules

If operators want to distribute their telecommunication services well, they have to:

- Work on cabling infrastructure before the building conception
- Suggest suitable cabling infrastructure for the needs of final customers
- Suggest flexible and upgradeable cabling infrastructure with limited investment

There are many interesting solutions for the distribution of telecommunication services to business customers. Different copper and optical cabling system solutions exist to respond to the increased data rate in the business networks. Economically, the advantage of these solutions varies depending on different parameters such as customer type, initial investment, etc.

This paper focuses on the issues involved for a cabling solution in a building.. It explains different cabling infrastructures adapted to services for small companies, in the first section and large companies, in the second part.

2 Cabling solution for small company

2.1 Introduction

The broadband access network is now a reality for small companies. The most popular networks are xDSL (with ADSL as the most well known) and wireless local loop (WLL).

Due to the explosion of Internet services, small company cabling systems must support an increasingly high data rate. In this context, xDSL technologies have the advantage of meeting demand without any major investment by using the existing network, which generally comprises category 5 copper materials. Many solutions can be deployed to respond to the increase in data rate: new wire cabling system (copper cabling systems with category 5, multimedia cabling system, etc.) and no new wire products (HomePNA, PLT, etc.)

2.2 Backbone cabling subsystem

The building backbone cabling subsystem for small companies traditionally uses copper cables, whether or not the access network uses copper or optical cables.

The figure below shows the typical architecture for the delivery of services based on ADSL techniques.

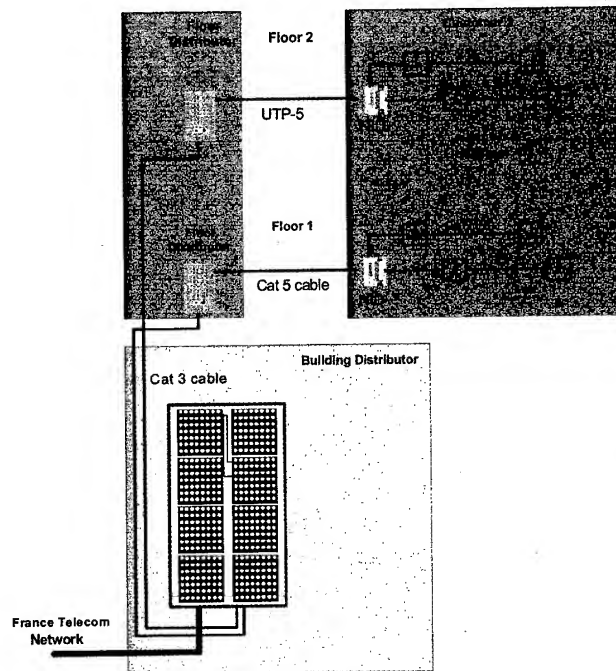


Figure 3: Typical existing backbone cabling system

2.3 Customer cabling subsystem

2.3.1 "New wire" solution

2.3.1.1 "Bottom-of-the-range" cabling system

The cabling system in figure 4 is the minimum technical cabling that is offered to customers.

It is defined for customers who initially require POTS services only.

The proposed cabling has a bus or Y (2 branches) topology, with a Network Interface Device (NID) which is the delivery point for France Télécom services. This architecture has 2 or 3 connectors called "T outlets" and a 4-pair cable with category 5 performance.

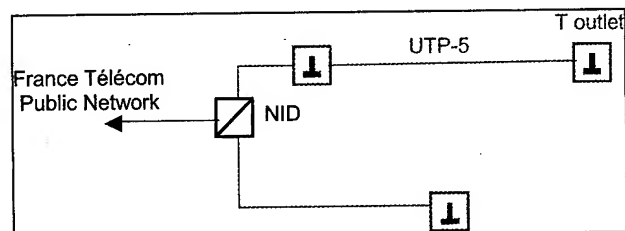


Figure 4: "Bottom-of-the-range" cabling

This cabling system is designed for one or two phone lines and is compatible with ISDN and ADSL "distributed

filters" solutions (see figure 5). For ISDN, the services are only available on the Network Termination (NT).

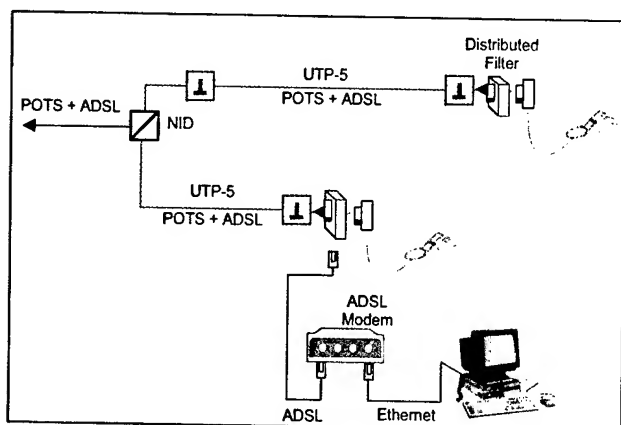


Figure 5: ADSL "distributed filters" solution

With the "distributed filters" solution, no changes to the existing Customer Premises Network (CPN) that comprises "bottom-of-the-range" cabling are required.

Both ADSL and POTS signals are transmitted on the same pair inside the rooms on all outlets. The low-pass filters (LPF) are distributed on the "T" outlets connected to analog phones. On the outlet dedicated to the ADSL signal, the ADSL modem is connected via an adapter. The PC terminal is connected to its ATM or Ethernet interface.

2.3.1.2 "Multimedia" cabling system

The solution described in figure 6 was defined to provide the customer with many broadband services and allowed a private network to be created: many terminal types can be connected to this cabling system.

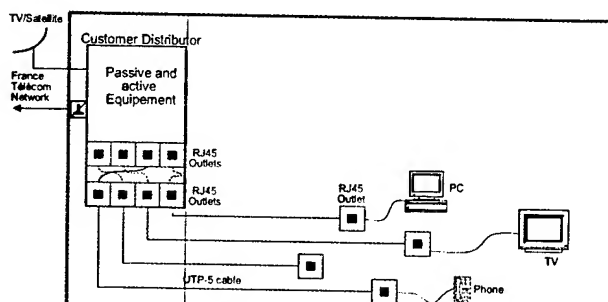


Figure 6: "Multimedia" solution

The "multimedia" cabling system is based on a star topology from the customer distributor to the category 5 RJ 45 type outlets. The installed cable is also a category 5 type so that the link can be qualified as class D, thus enabling frequencies up to 100 MHz to be used.

The end of the telecom network is located in the customer distributor featuring an RJ 45 panel.

This solution allows the customer to connect any type of terminal: telephone, PCs, television (via suitable modules), etc.

2.3.2 "No new wire " solutions: "Multi-terminals" options

The aim now is to give the customer the possibility of installing a network for use with several terminals (PC, phone, etc.) in existing building without dedicated wiring.

Several solutions exist and are described in the following options.

The technologies used are "HomePNA", "Powerline or PLT (Power Line Telecommunications)" and "wireless radio" solutions. These technologies, similar to the LAN ones, enable resources to be shared on the private network and infrastructure costs to be reduced.

2.3.2.1 "Privatize HomePNA" option

The principle is that one pair is re-used on the phone cable to connect 2 PC terminals equipped with Home PNA cards to share high data rate Internet access such as ADSL for example (see figure 7).

The HomePNA signals are compatible with POTS and ADSL signals.

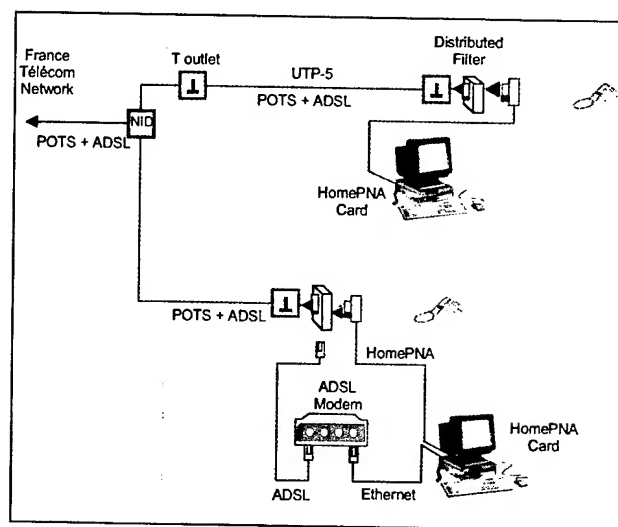


Figure 7: HomePNA solution

The frequency band used for HomePNA is between 1 MHz and 10 MHz above the ADSL band. The data rate is approximately 10 Mbit/s with a future evolution up to 32 Mbit/s with a range of 150 meters to 500 meters between two HomePNA cards.

2.3.2.2 "PLT" option

The principle of "Powerline" technology^[1] is also to share a high data rate network link between several home devices connected on the same low voltage network via a specific "Powerline" interface (see figure 8).

Several modulations are used by different industrials using a frequency band from 1.6 MHz to 30 MHz.

The data rates range from 100 Kbit/s up to few Mbit/s.

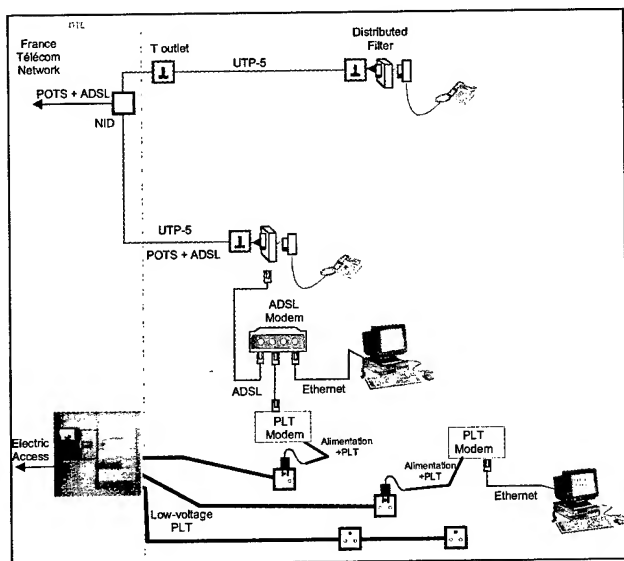


Figure 8: PLT solution

PLT architecture is used behind a high data rate access such as ADSL. On an Ethernet interface available on the ADSL modem, the connection is made on the low voltage network via the PLT modem. The other terminal is then connected with a PLT modem.

2.3.2.3 "Wireless Radio" option

The principle of the "Wireless radio" technology is also to share a high data rate network link between several home devices.

France Télécom now recognizes three wireless interface standards: HomeRF, IEEE802.11b and Bluetooth.

Data rates and ranges are dependent on the technology used:

- HomeRF: data rate from 600 Kbit/s to 1.6 Mbit/s on 45 meters maximum,
- IEEE802.11b (Wireless Ethernet): from 1 to 11 Mbit/s on 25 to 100 meters maximum,
- Bluetooth: 800 Kbit/s maximum on 5 to 15 meters.

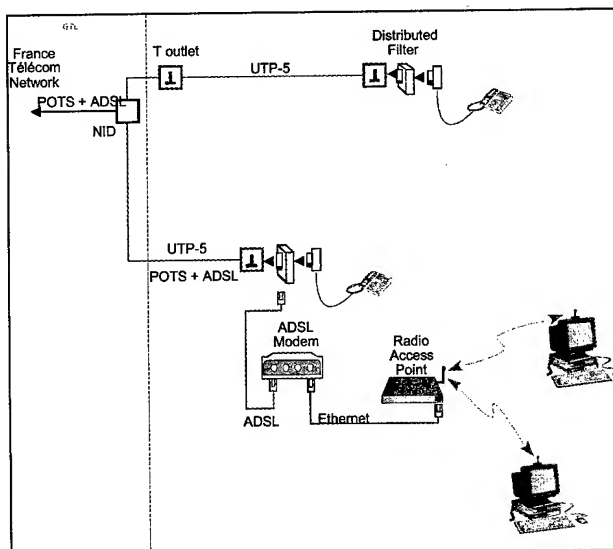


Figure 9: Wireless radio solution

For the "HomeRF" solution, with Internet access sharing software, the PC terminal with the physical connection to Internet uses server software to manage access sharing between the wireless "customers".

For "Bluetooth", each PC terminal connected to the Bluetooth network can be the master. The first terminal connected assumes this role.

For the "IEEE802.11b" wireless Ethernet solution, the wireless access point (radio modem) connected to the ADSL modem manages all the network accesses between terminals equipped with IEEE802.11b cards.

2.4 Comparison of performances and costs

- "new wire products"

	"Bottom of the range" cabling system	Multimedia cabling system
Services	Phone, ADSL	Phone, xDSL, LAN, TV
Estimated cost	First outlet: X \$ (25 one more) 10 outlets 5X \$	1 customer distributor + 10 outlets : 10X \$

Multimedia cabling system is a cheap solution to install a flexible cabling and create a mini-LAN for small company applications.

- "no new wire" products

Concerning the products used on the existing CPN ("no new wire" products), performances and costs are summarized in the following table:

	Home PNA	PLT	Radio		
			Home RF	IEEE802.11b	Bluetooth
Data rate	10 Mb/s	from 100 kb/s to 10 Mb/s	from 600 kb/s to 1,6 Mb/s	from 1 Mb/s to 11 Mb/s	800 kb/s
Range	500 m	100 m minimum	50 m	100 m maximum	5 to 15 m
Estimated cost of materials	X \$ (2 USB cards)	10X \$ (2 modems)	5X \$ (2 USB boxes)	20X \$ (1 access point + 1 PCMCIA card)	6X \$ (2 PCMCIA cards)

HomePNA products have the best quality/cost ratio, the only constraint is the availability of service at the phone outlet only (average of 2 or 3 in France).

PLT is not cheap at the moment since the products are only prototypes for most of the industrial providers.

Concerning wireless radio products, IEEE802.11b interfaces are business market oriented. This implies that the cost is somewhat too expensive, whereas HomeRF and Bluetooth products have good quality/cost ratio.

2.5 Conclusion

There are many interesting solutions for the distribution of narrowband and broadband services to small companies.

The solutions described below are currently being tested in our laboratory and in the field.

3 Cabling solution for high data rate business needs

3.1 Introduction

Beyond a critical size and depending on their activity, companies need very high data rate applications and secure services. This paper presents backbone cabling solutions to offer services up to 2 Mbps to the business customers in a building. Backbone cabling solutions extend the operator access network from the building cabinet to the floor customer cabinet [1].

Depending on the data rate, different media may be used (table 1). An existing backbone cabling in a building (made with coaxial or twisted pairs) may be re-used according to the type of applications, environment, data rate and distances. However, for high data rates, optical media is generally installed in the building backbone

cabling because it supports all applications over long distances in a difficult environment.

Media	Data rate (Mbit/s)	maximum Theoretical length (m)
Twisted pairs cat 5	2	300
	10	90
Coaxial pairs	34	190
	45	150
	155	90
Multimode fiber	100	2000
	155	2000
	1000	440
Monomode fiber	155	15000
	622	15000
	2500	15000

Table 1: Example of maximum theoretical length between the operator and the customer

In the first part of the section, optical building backbone cabling solutions are presented. Moreover, to satisfy the business requirements, cabling solutions that provide different levels of guaranty are described.

The second part focuses on an original laying technology, a flexible optical cabling system based on the blowing method. Latest developments are applied to improve performances and reduce the cabling cost. Experiments based on flexible optical cabling system were carried out in buildings in France. The experiments, configuration and first results are presented in the chapter 4.

3.2 Optical backbone cabling solutions

Several optical cabling solutions exist to supply broadband services to business customers in a building.

For example, figure 10 represents a cabling solution for the interconnection of distant private local networks.

The cabling system configuration and engineering rules are adapted to the building cabling infrastructures. In a multi-customer building, an operator cabinet is useful for installing operator equipment. In this way, the cabling solution may be shared between building customers, thus reducing costs.

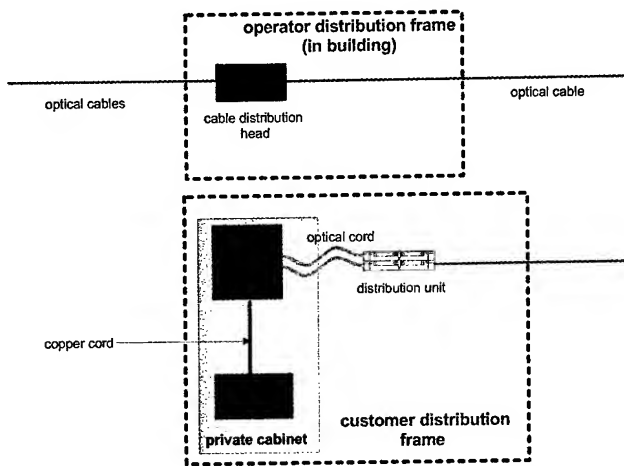


Figure 10: Cabling solution for interconnection service

Increasing numbers of business customers are interested in telecommunication service quality and, particularly in the supply of non-stop service in the event of a fault in the cabling.

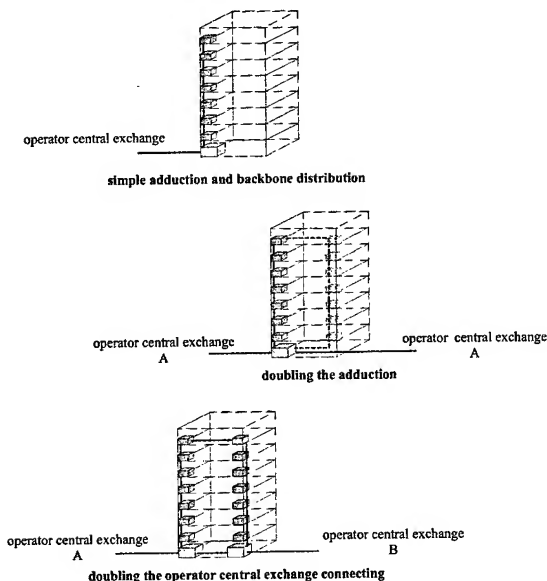


Figure 11: Secure cabling solutions

Several levels of guaranty are proposed (illustration in figure 11):

- simple adduction to the building cabinet and vertical distribution to the customer cabinet
- backing up the adduction from the same operator central exchange, backing up the vertical distribution

the highest level of guaranty with the back-up adduction from two different operator central exchanges, and backing up building cabling infrastructures.

3.3 Flexible optical cabling system

As an optical infrastructure of a building cabling network, a flexible cabling system is an interesting alternative to traditional cabling. Firstly, an empty tube network is laid along the traditional cable paths of the building. Then, the cable is blown with air in a tube on customer demand.

3.3.1 Blowing method

The laying method combines a blowing pulling force, by using a tight shuttle, with pushing assistance. Pulling force performances are especially limited for bends [2]. Additional pushing (under a critical sinusoidal force) effectively enhances laying distances. The pushing force reduces the forces against laying located at the start of the trajectory: the airtight cable entrance, the cable reel and the friction forces due to the cable mass dragging.

The blowing technique is achieved with a Microjet® tool [3] presented in figure 12. Microjet® is suitable for pushing small diameter cable from 1 mm to 4 mm.



Figure 12: Microjet®, a universal tool for blowing optical cables in a building network

3.3.2 Performances

In buildings, blowing performances are limited by the complex trajectories. A recent study on the configurations and cabling spaces has been conducted in business buildings in Paris. The results show that most business buildings are multi-customer constructions and two building configurations may be considered: a large part of small buildings and few large buildings whose principal dimensions are presented in table 2.

	Small buildings	Great buildings
Average floor surface (m ²)	540	1000
Average building height (m)	25	70
Maximum building height (m)	70	220

Table 2: Configurations of business buildings in Paris

The small building configurations in Paris correspond to the most common business building in small cities in France. For this typical case, the distribution cable path characteristics are resumed in table 3.

	Small buildings
Distance (m) between the building distribution cabinet and the vertical distribution	Average = 20 Maximum = 150
Vertical distribution distance (m)	Average = 25 Maximum = 70
Number of bends in backbone distribution	Average = 15 Maximum = 30
Distance (m) between vertical distribution and customer distribution cabinet	Average = 10

Table 3: Cable pathway characteristics

The building age impacts the cabling infrastructure facilities. The most complex trajectories are obtained in old buildings. The blowing method described above is suitable for laying the cable in complex trajectories. Performances are based on special cable and tube requirements. Blowing is achieved using a small diameter ($< 8\text{mm}$), antistatic tubes and light micro-cables with a very low friction coefficient (< 0.1). The pushing force delivered by the microjet® is necessary to enhance blowing performances within the building. In special cases, the blowing method may be used with an intermediate mechanical assistance.

3.3.3 Advantages

Owing to the blowing method described above, laying operations are achieved with low air consumption (a few tens of liters per minute for a 4 bar pressure) and energy. The installation unit is easily portable in the customer cabinet, an important functionality in very high buildings.

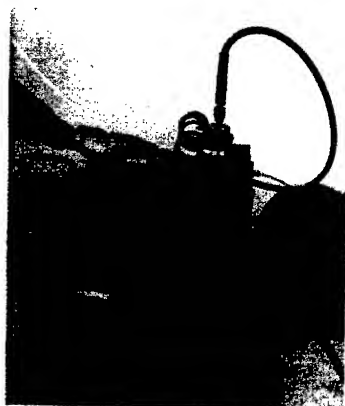


Figure 13: Portable blowing installation unit

Then, the flexible cabling system offers several advantages:

- Flexibility: reconfiguration of the tubes network may be made without fiber connecting operations or a traditional cable pulling.
- Upgradability: cable may be easily changed from multimode to monomode, for example.

Another main advantage of the system is the economical aspect, described in the following section.

3.3.4 Cost evaluation

The comparison is between a traditional cabling on demand and a flexible cabling system installed from the operator cabinet to the customer in a small building with an average configuration.

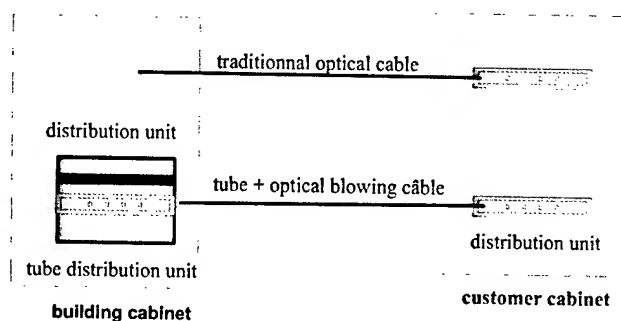


Figure 14: Compared cabling systems for an optical backbone solution

Cost evaluation includes cabling passive elements, laying and connecting operations and optical measurements.

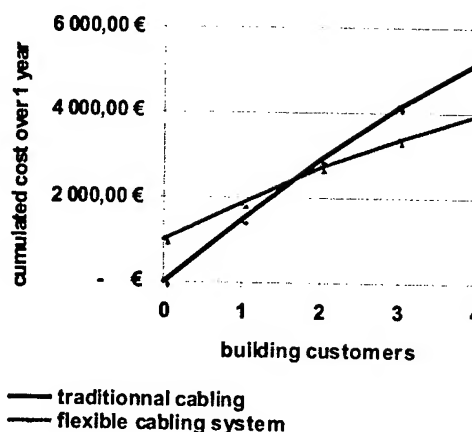


Figure 15: Comparison of total cost between cabling systems

Results are shown in figure 15. The graph represents the total cost of the optical cabling system against the business

customer connecting demand. The building is supposed to be fully occupied by four business customers during a one year period.

Whereas the flexible cabling system involves an initial investment, the solution is more economical than a traditional one from the second customer demand.

Then, the flexible cabling system deployment involves the operator firstly anticipating business customers needs in the buildings and secondly developing a commercial process adapted to construction promoters and building owners.

4 Cabling solutions experiments

This chapter describes several cabling solution experiments described above for low and high data rate applications successively.

4.1 Backbone cabling solution experiments

A first experiment of backbone cabling solution was conducted in a new business building of a large city in France. A flexible optical cabling system was laid to supply very high bit rate to the future business customers.

Building presents a horizontal configuration with a 7000 m² floor surface and 4 steps. In this configuration, the blowing installation unit was carried out to lay up to six optical fibers cable from the operator cabinet. The tubes installation was carried out easily and rapidly because it was performed during the building construction. Moreover, the small initial investment in tubes may be integrated easily into the construction cost.

The tube network was dimensioned to supply about six customer's cabinets with one tube for each customer. Broadband services (private local networks interconnecting, dedicated optical ring, etc.) will be soon proposed.



Figure 16: Connecting tubes for access to the customer cabinet

A second experiment was carried out in a multistory building in France. A backbone cabling solution using a flexible cabling system was installed to supply a high data rate shared Ethernet application up to 90 meters from the operator cabinet.

An large tube network was laid in the vertical path of the building to allow about one hundred customers. Installing a flexible cabling system in this building offers several advantages: limitation of subsequent operations, reduction of disturbance to customers, reactivity and upgradeable cabling. The blowing method was successfully tested for complex trajectories (average height about 100 meters and total average cabling distance about 200 meters with a large number of bends) installing the blowing unit on customer floor and so drawing down the optical cable.



Figure 17: Blowing optical cable operation from a customer cabinet

4.2 Cabling reference for a building complex

The infrastructures described below are defined and produced for new buildings.

This field trial (project for 2004), performed near Paris, concerns a large buildings complex with about 1000 apartments in quite small buildings, spread over about 12 hectares (see figure 18).

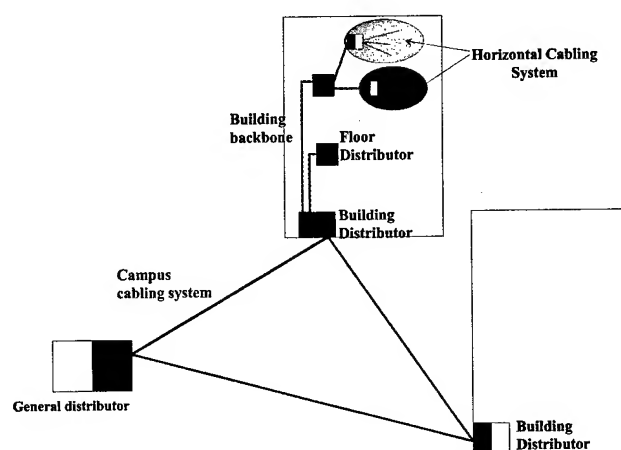


Figure 18: Schematic of buildings complex cabling system principle

The objective is to enhance the reputation of the property developer and the service providers, to propose alternative

solutions allowing for the future integration of broadband transmission systems and to perpetuate investments while reducing costs.

The infrastructures described in figures 19 and 20 take into account the different types of access network such as xDSL and FTTx currently deployed or used in field trials at France Télécom.

This infrastructure covers a high number of services to customers in both private and collective areas, taking into account individual services (POTS, audiovisuals, IP, etc.) and collective services (remote meter reading, Intranet, etc.).

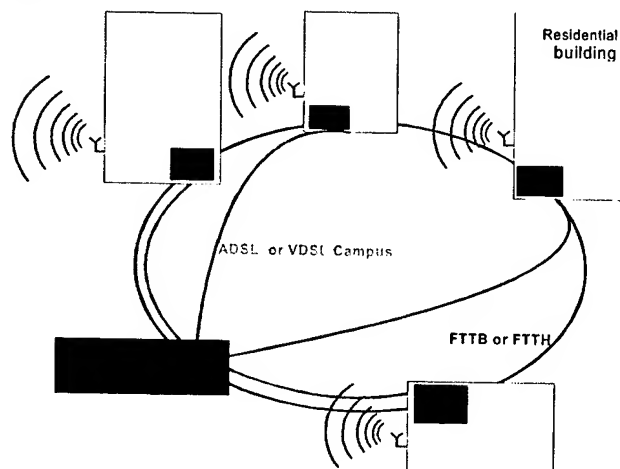


Figure 19: Campus cabling system infrastructure

The campus cabling system and the building backbone cabling system consists of two networks:

- one xDSL copper point to point network (made of classical cables used in the France Télécom public network)
- and one FTTx network/services (made of optical loops connecting the buildings).

Outdoor radio cover is provided to offer proximity services such as self-surveillance, etc. and Radio terminals can be used for internal building communications (Intranet, etc.).

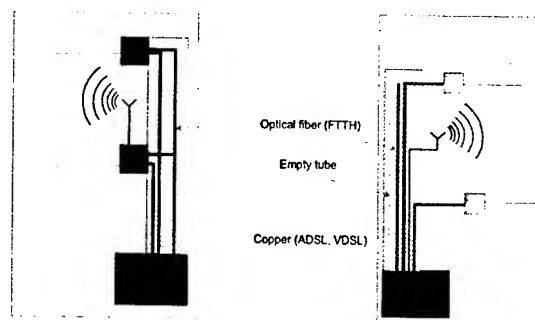


Figure 20: Building backbone infrastructure

In building, empty tubes are installed in order to be able to install optical cables and offer further services subsequently.

5 Conclusions

There are many interesting solutions for the distribution of narrowband and broadband service to business customers.

For "small" companies, the re-use of existing cabling systems such as Phoneline or Powerline is useful for connecting several terminals and for networking.

For new buildings, new cabling systems are created based on LAN cabling systems.

For "large" companies, different copper and optical cabling system solutions exist to respond to the increasing data rate in the customer LAN. Economically, the advantage of these solutions varies depending on different parameters such as customer type, initial investment, number of outlets needed, etc., but the installation of optical media is becoming an increasing reality.

For both "small" and "large" companies approaches, solutions are being tested and validation in field trials is in progress to define cabling systems for France Télécom customers.

6 References

- [1] E.Cressan, O.Bouffant and al, "Cabling systems for XDSL services in both residential and business buildings," *IWCS (November 2000)*.
- [2] A.C. Réau and al, "An economical optical cabling method for building networks", *EC (June 2000)*
- [3] G. Plumettaz, "A new universal tool for the placement of microcables in the local and business access network", *EC (June 1999)*.

7 Authors



customers.

Anne-Cécile Réau-Thomas was awarded a doctorate at the university of Rennes (Physics and Chemistry of Materials) in 1996. She joined the France Telecom R&D center in 1997 to work on cabling engineering and optical cable installation for business



Fabrice Fauchoux graduated from the University of Rennes in Electronics in 2001. He joined the France Telecom R&D center in 2001 to work in the Local Loop Infrastructure Laboratory, and on cabling systems architecture.



Emmanuelle Cressan was awarded a doctorate at the University of Rennes (Physics and Chemistry of Materials) in 1994. She joined the France Telecom R&D center in 1994 to work on optical cables. In 1998, she joined the Local Loop Infrastructure Laboratory to manage the studies relating to cabling systems for business customers., she has been manager of the ACC (All Cabling Concept) Research and Development Unit since 2001, working on copper cables and new high data rate applications on Customer Premises Cabling Systems.

Propagation Limits of Twisted Pair Cables

Juliusz Poltz, Joan Beckett

OptEM Engineering Inc.

Suite 453, 3553 – 31 Street NW

Calgary, AB, Canada · T2L 2K7

+1-403-289-0499 · jpoltz@optem.com · jbeckett@optem.com

Abstract

A series of shielded and unshielded pairs of assumed external dimensions are analyzed using a Computer Aided Engineering (CAE) software tool equipped with an electromagnetic field solver. After entering cable design data including materials, plating, stranding, twisting and wire naming, the tool processes geometrical information in order to calculate a realistic model of a twisted pair cable. The resulting model of the cable is subsequently analyzed numerically using a combination of finite element and boundary element methods. Based on a series of analyses, designs with the smallest attenuations are selected. These designs are then used to calculate optimal characteristic impedance of shielded and unshielded pairs. Eventually, a plot linking the frequency, attenuation level and wire size is produced. The discussed method offers a quick evaluation of limitations for twisted pair cable applications at high frequencies. The optimal design is used to study the impact of shrinking dimensions on attenuation.

Keywords

attenuation; characteristic impedance; simulation; modeling; skin effect; proximity effect; eddy currents; cable; optimization.

1. Introduction

In the continuously increasing demand for higher speed rate, combined with the physical limitations of lossy conductors, one has to wonder about the future of copper cables and their place in the next generation of communication networks. Although this question is left unanswered in this paper, a theoretical study of transmission limitations of unshielded and shielded copper cables based on targeted attenuation levels is discussed.

An analytical analysis of the electromagnetic behavior of a twisted pair cable at very high frequencies is not very practical due to the theoretical complexities of solving the equations. At high frequencies cable attenuation, dispersion and crosstalk affect the signal quality and system performance in a significant way [1, 2, 3]. To assess these effects in a timely and efficient way a CAE software tool equipped with a numerical EM field solver was used to model and analyze various cable geometries. The CAE software is called OptEM Cable Designer and was used extensively for this paper to model and analyze shielded and unshielded cable geometries. Modeling has proven its ability to predict cable performance with high accuracy [4,5].

A twisted pair cable (shielded or not) is difficult to model accurately despite its relatively simple geometric structure. Secondary effects that were originally neglected in theoretical studies of cables [1] have gained importance due to the increase in operating frequencies. Any accurate cable modeling and analysis must consider skin and proximity effects in wires, eddy currents in cable shields, and dielectric losses in insulation. Skin effect causes a reduction of inductance and a rapid increase of equivalent resistance. Conductor and shield losses were numerically analyzed much earlier for power cables [6,7,8,9] and a similar technique was adopted in OptEM Cable's EM field solver [10] which allows very accurate calculation of unit parameters of high frequency cables [4]. Once current distribution is considered, the losses and frequency dependence of unit parameters can be calculated. Unit parameters are then used to assemble cable models and predict attenuation, crosstalk and return loss [5].

Selected geometries of shielded and unshielded copper pair cables were modeled and numerically analyzed using OptEM Cable (Figure 1) [10].

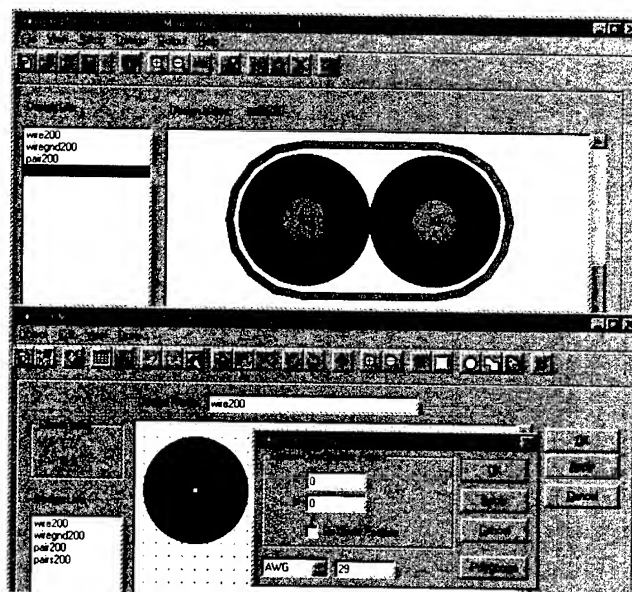


Figure 1. Sample of a shielded copper pair cable modeled in OptEM Cable Designer. The software assembles the cable pair geometry hierarchically using two instances of a single 29 gauge copper wire geometry.

For this paper over a hundred different cable geometries were modeled and analyzed by the software within a 72 hour period. The simulations were run on a PC workstation with an AMD K6 processor, 56 MB RAM and 16 GB disk. The software uses a combination of boundary element and finite element methods to solve Maxwell's equations in the frequency domain. Skin effect, proximity effect and the presence of lossy dielectrics and conductive shield is taken into account. The modeling technique which independently calculates magnetic and electric field distribution is valid providing that the energy propagates as a quasi-Transverse Electro Magnetic (quasi-TEM) wave. Since non-TEM propagation is possible only on conductors separated by a distance of at least half a wavelength, a simple comparison of typical cable dimensions was used to estimate the maximum frequency range for the software. The tool's ability to predict performance of twisted pair cables tested in laboratory conditions was reported in earlier studies presented at IWCS [4,5].

In this paper the focus of study is on transmission limitations of unshielded and shielded copper cables based on targeted attenuation levels. Frequency dependence of the inductance, resistance, conductance and capacitance with their influence on attenuation are the main issues discussed. The authors also offer their view on the concept of optimization of copper cables based on attenuation.

2. Minimum Attenuation of Shielded and Unshielded Pair

As we approach physical limits of propagating high frequency signals on copper cables, we must realize that some of the constraints currently placed on cable design need to be released in order to minimize attenuation. We decided to search for twisted pairs of specific external dimensions which would offer the smallest attenuation within a selected frequency range.

As part of our investigation we selected shielded and unshielded pairs built from insulated wires which had identical external dimensions with 0.1mm or 0.8mm insulation diameters. The conductors and shield were copper, and the polyethylene dielectric had relative permittivity of 2.26 and loss tangent of 0.0002. We simulated all cable configurations initially for frequencies 1 GHz, 4 GHz and 16 GHz. The optimal wire gauge and attenuation points concluded in the paper can deviate by changing dielectric properties, conductor materials and/or frequency range. But our intention was to provide some guidelines based on our detailed analysis rather than a universal solution.

We realized that the attenuation of the cable should grow proportionally to the square root of frequency if conductor losses (skin effect, proximity effect and eddy currents in the shield)

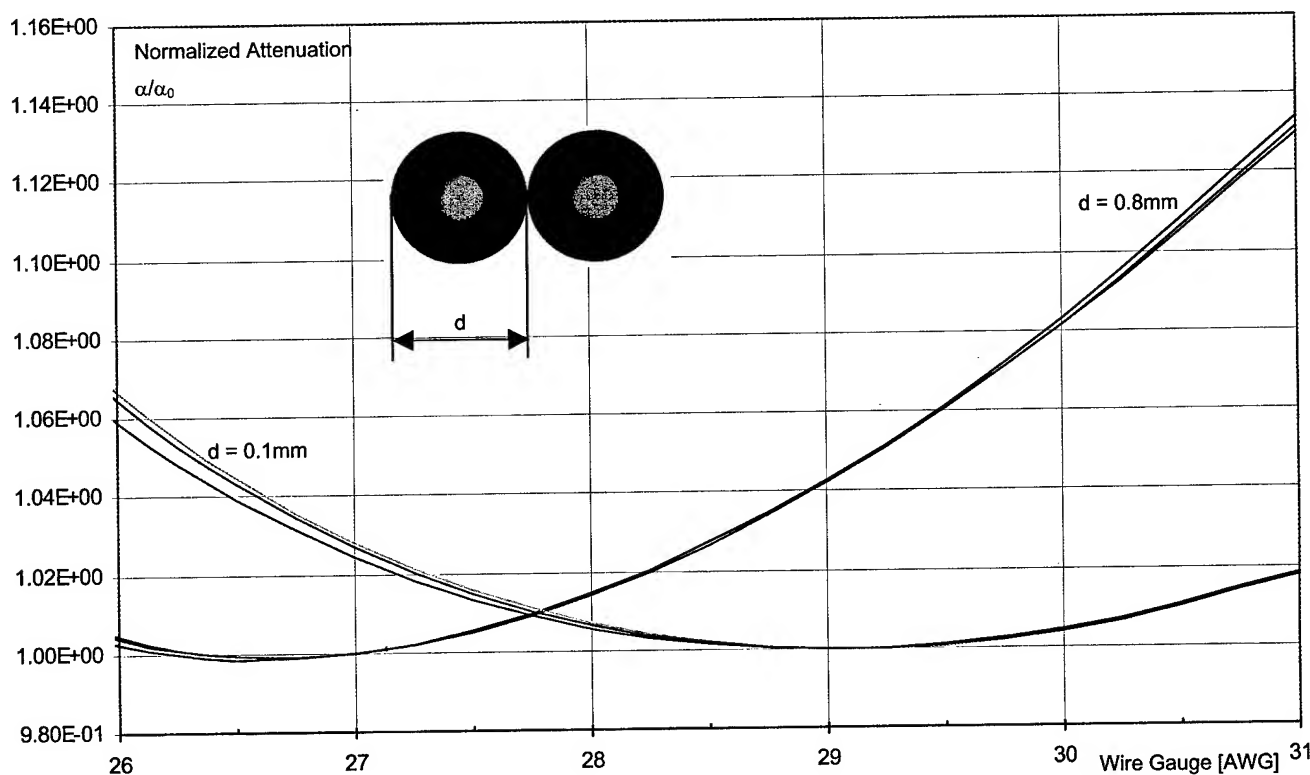


Figure 2. Normalized attenuation of an unshielded pair simulated at 1 GHz, 4 GHz, and 16 GHz, and for two insulation diameters as a function of wire gauge. α_0 is the minimum attenuation calculated for the selected frequency and insulation diameter.

dominate power dissipation in the cable. Once dielectric losses (based on constant loss tangent) start to dominate the dissipation, the attenuation would accelerate proportionally to the frequency. We were pleased to find out that the dielectric losses based on the 0.0002 loss tangent had marginal influence on the attenuation at the investigated spectrum 1 to 16 GHz.

Knowing that conductor losses dominate the dissipation, we expected that there must be an optimal wire gauge (for a given external dielectric diameter). For an unshielded pair, the smallest loss would result from a gradual reduction of proximity effect losses and increase of the skin effect losses as we increase wire gauge (reduce conductor diameter). Simulation results calculated for an unshielded pair are presented in Figure 2. To allow accurate plotting of attenuation calculated for frequency 1 GHz, 4 GHz and 16 GHz the vertical axis is scaled as normalized attenuation (ratio of calculated attenuation and the minimum value of attenuation calculated for the same frequency). We found out that the smallest attenuation for an unshielded pair built of wires 0.8mm (external insulation diameter) can be achieved with conductors 27 AWG. Whereas 0.1mm wires require 29 AWG copper conductors.

For a shielded pair, the distribution of losses is more complex. In a shielded pair, in addition to skin effect and proximity effect, there is also a gradual reduction of eddy current losses in the shield (when conductor diameter is reduced) which influences attenuation. For this investigation we used a shield thickness

exceeding 3 times the skin depth, effectively eliminating the external field. Since losses in a solid shield may be substantial, one can expect that the optimal configuration (smallest attenuation) for a shielded pair will be reached for a much higher AWG (smaller diameter) than the unshielded optimum. In addition, we found out that the optimal configuration of the shielded pair attenuates the signal twice as fast as the unshielded cable. Simulation results calculated for a shielded pair are presented in Figure 3.

Again the vertical axis is scaled as normalized attenuation (ratio of calculated attenuation and the minimum value of attenuation calculated for the same frequency). The smallest attenuation for a shielded pair built of wires 0.8mm (external insulation diameter) can be achieved with conductors 44 AWG. Whereas 0.1mm wires require 47 AWG copper conductors.

3. Optimal Characteristic Impedance

After we analyzed a number of geometries and found the optimal (smallest attenuation) cable configuration for an assigned external dimension, we found out that the characteristic impedance of the optimal designs within the same group is very similar. In other words, we found that an unshielded copper pair (with insulation $\epsilon_r=2.26$, $\tan(\delta) = 0.0002$) of characteristic impedance $Z=130 \Omega$ has the smallest attenuation within 1 to 16 GHz spectrum, whereas an optimal shielded pair would have characteristic

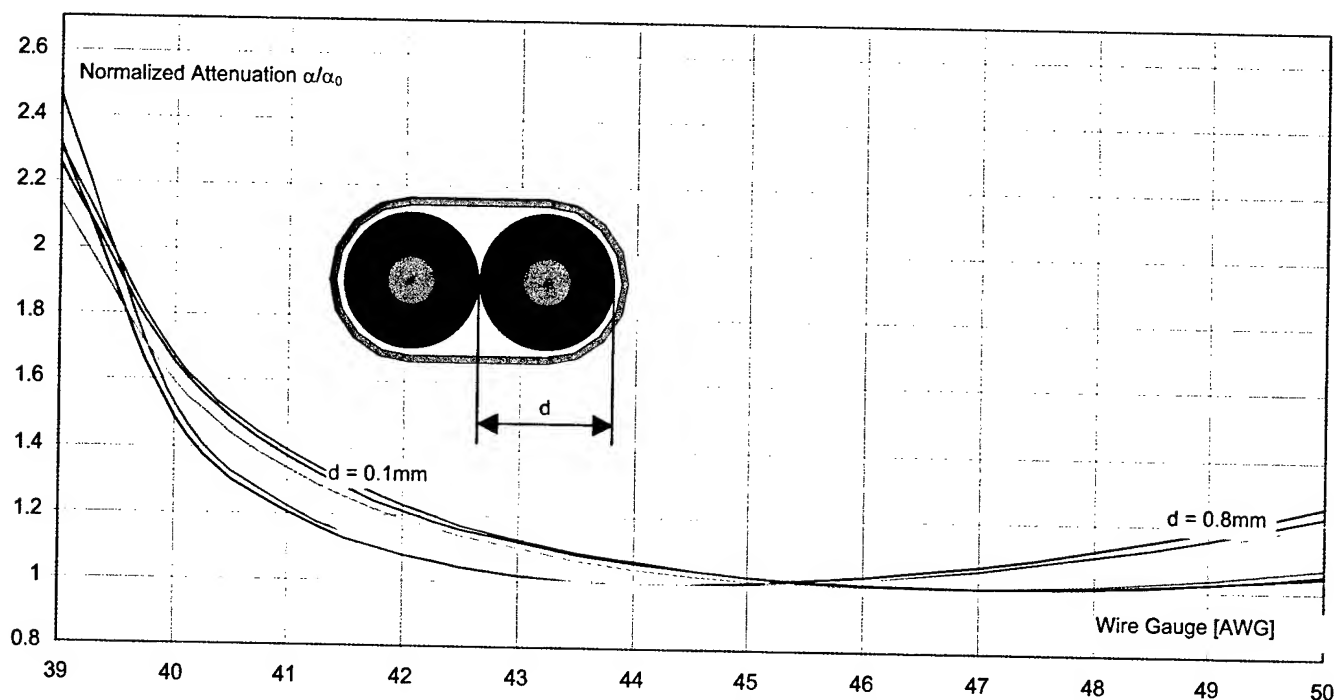


Figure 3. Normalized attenuation of a shielded pair simulated at 1 GHz, 4 GHz, and 16 GHz, and for two insulation diameters as a function of wire gauge. α_0 is the minimum attenuation calculated for the selected frequency and insulation diameter.

impedance $Z=96 \Omega$. The results are plotted in Figure 4.

We also found that the optimal characteristic impedance is frequency dependent and is gradually getting smaller with the increase of the frequency. However, the changes are not substantial and can be neglected within one decade of change in frequency.

4. Crosstalk Reduction

It is difficult to consider an optimal design of a cable without considering crosstalk. The oscillation of unit parameters of a twisted pair can be neglected for lower frequencies. However for very high frequencies the variation of unit parameters (mutual components) must be included in the cable model. Based on interaction with HF labs we know that OptEM Cable can predict very accurately crosstalk levels between pairs of different lay length at very high frequencies. However, we could not find any systematic way of dealing with crosstalk, yet.

In practice, when facing higher frequencies, the designer has two choices. He may apply shorter lay length or use a shield. Although both solutions will generally cause an increase of attenuation, the reduction of external dimension of the pair may be required to reduce the lay length without substantial increase of attenuation. Having this in mind we specifically optimized the design for fixed external dimensions of the cable. We plan to

incorporate crosstalk in our future search of an optimal copper cable configuration.

When analyzing a shielded pair we assumed a perfect screening. Typically, an effective screen will cause an increase of attenuation at high frequencies. It is very likely that the best performance of a twisted pair cable can be achieved with partial screening and twisting of pairs.

5. Attenuation Limits for Standard Shielded and Unshielded Pairs

Final results are assembled in Figure 5 representing relationships, which are dependent on both signal frequency and wire dimensions. Figure 5 is similar to a plot of equi-potential lines or projection of a 3D function on a plane. To help in visualization of current distribution in conductors, Figure 5 is divided into three regions by two parallel lines (a,b). One can draw conclusions about the need for a detailed analysis of the current distribution by locating frequency and conductor size area in one of the three regions in Figure 5. If the skin depth is in the range of the conductor cross-sectional dimensions then the current is distributed in a non-uniform way and a solution of the Helmholtz equation [4-9] is required for calculating equivalent circuit components.

For low frequencies (below a), the DC approximation of current distribution (uniform throughout the conductor cross section) is

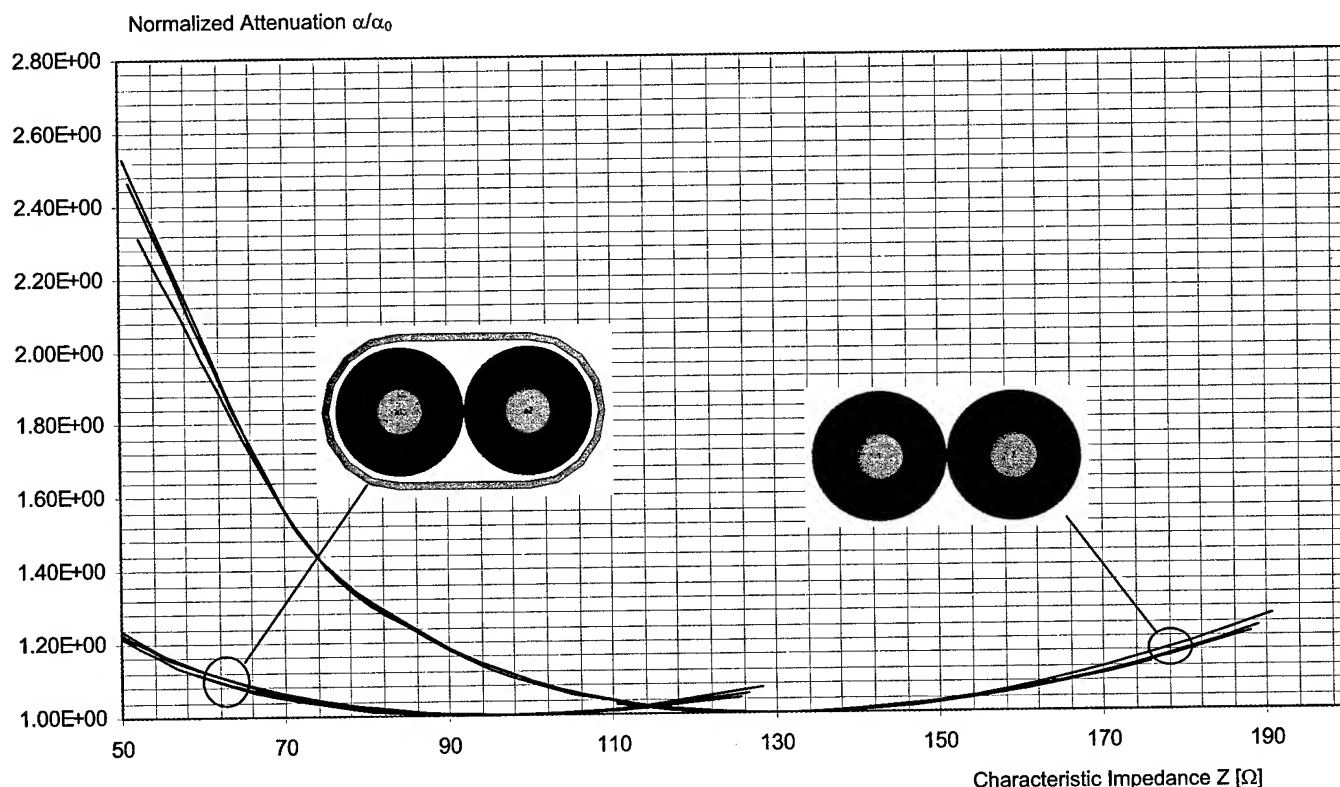


Figure 4. Optimal characteristic impedance of shielded and unshielded pair

accurate enough. The situation is similar for very high frequencies where the surface currents screen the interior of the conductors (well developed skin effect). Both cases can be handled by the Laplace equation, which is used by static field solvers. The important difference between the DC region and the region with well developed skin effect is the dependence of losses on the frequency in the latter case.

The transition between the low (DC) and high-frequency range can be described as the region of generally non-uniform current flow in the cross-section of the wire. To estimate the range of the non-uniform current region one must calculate the skin depth for different frequencies. Inductance is strongly dependent on frequency when the skin depth is within the conductor cross-sectional dimensions (non-uniform current region).

As we indicated earlier, the dielectric losses did not play a significant role in our studies. Line c in Figure 5 indicates the balance between conductor and dielectric losses. One can assume that a vast majority of high frequency cables operate within the

region of the well developed skin effect with dominant conductor losses (between line b and c).

After calculating wire diameters for designs with smallest attenuation, we were able to put together a table listing the highest frequency for which attenuation of 1dB/m and 8dB/m can be achieved for optimally constructed unshielded and shielded copper pairs (insulation $\epsilon_r=2.26$, $\tan(\delta) = 0.0002$). These results - plotted in Figure 5 - have, in general, slightly irregular behavior due to the nature of optimization and rounding to the nearest AWG values for calculated conductor diameter. We consider them to be the high frequency limits for constructing 1dB/m and 8dB/m cables of a given insulation diameter.

6. References

- [1] H. Kaden, "Wirbelströme und Schirmung in der Nachrichtentechnik", Springer-Verlag, Germany (1959).
- [2] H. Hughes, "Telecommunications Cables Design, Manufacture and Installation," John Wiley & Sons, New

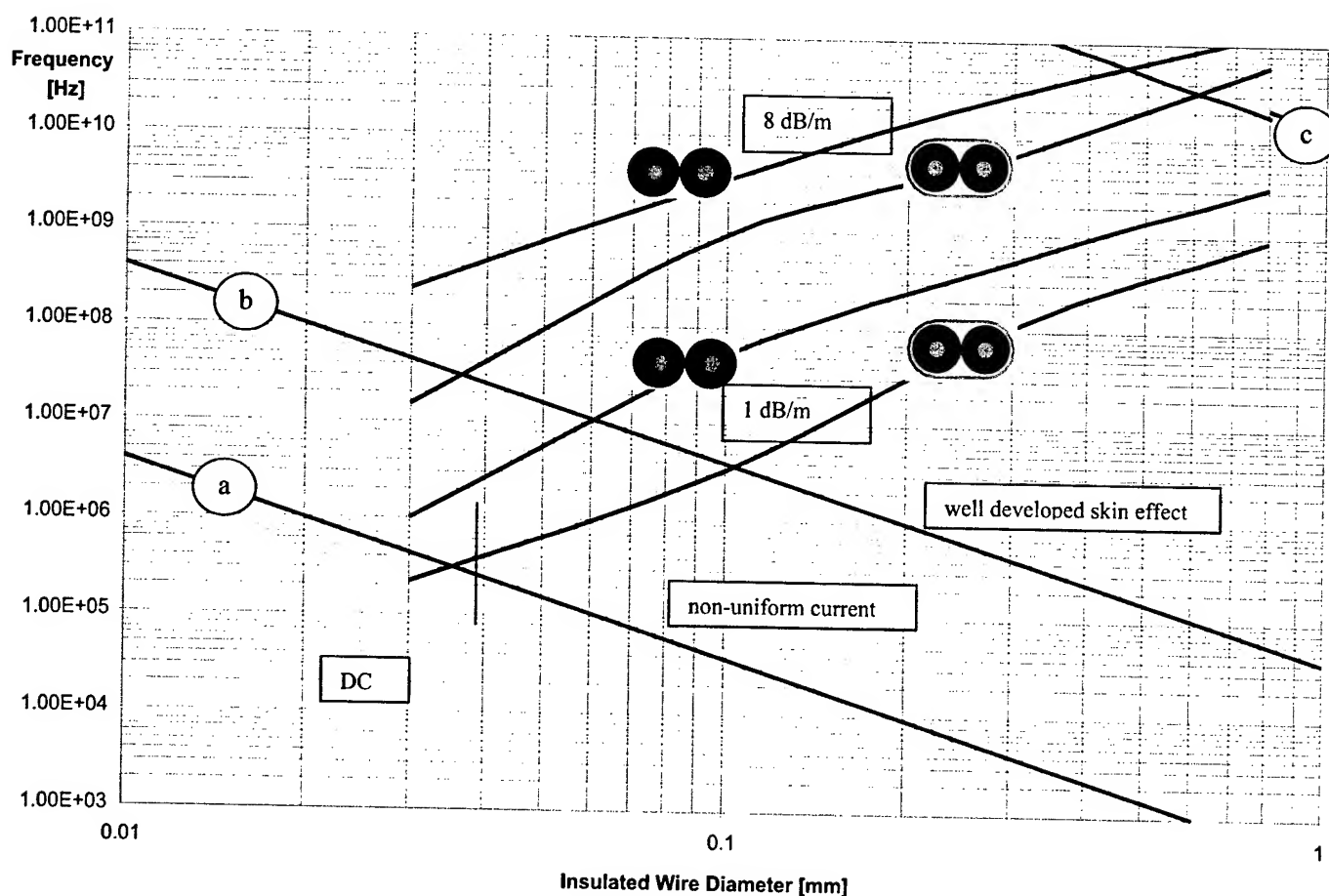


Figure 5. Different size copper pairs optimized for the smallest attenuation of 1 dB/m and 8dB/m for frequencies from 1 MHz to 100 GHz

York (1997).

- [3] C. Paul, "Analysis of Multiconductor Transmission Lines," John Wiley & Sons, New York (1994).

- [4] J. Poltz, D. Gleich, M. Josefsson and M. Lindström, "Electromagnetic Modeling of Twisted Pair," *Proceedings of the 49th International Wire and Cable Symposium*, Atlantic City, NJ, Nov. 13-16 2000, pp. 121-128 (2000).

- [5] J. Poltz, D. Gleich, M. Josefsson and M. Lindström, "Simulation and Measurement of Crosstalk in Twisted Pair Cables," *Proceedings of the 50th International Wire and Cable Symposium*, Lake Buena Vista, Florida, Nov. 12-15, 2001, pp. 577-585 (2001).

- [6] J. Poltz and S. Grzybowski, "Magnetic Field Outside the Three-Core Cable Considering the Cable Stranding", *IEEE Transactions on Power Apparatus and Systems*, Vol. PAS-98, No. 4, p. 1142, (July/August 1979).



Juliusz Poltz holds M.Sc. and Ph.D. degrees in both mathematics and electrical engineering from Universities in Poznan, Poland. He has published over 70 technical papers related to electromagnetic field analysis. In 1992 Dr. Poltz co-founded OptEM Engineering Inc. located in Calgary Canada. OptEM develops CAE software for interconnect modeling and analysis.

- [7] E. Kuffel and J. Poltz, "AC Losses in Crossbonded and Bonded at Both Ends High Voltage Cables", *IEEE Transactions on Power Apparatus and Systems*, Vol. PAS-100, No. 1, pp. 369-374, (January 1981).

- [8] J. Poltz, E. Kuffel, S. Grzybowski, and M.R. Raghuveer, "Models Adopted for the Calculation of Eddy-Current Losses in Pipe-Type Cables", *IEEE Transactions on Magnetics*, Vol. MAG-17, No. 6, P. 2592-2594, (1981).

- [9] J. Poltz, E. Kuffel, S. Grzybowski and M.R. Raghuveer, "Eddy-Current Losses in Pipe-Type Cable Systems", *IEEE Transactions on Power Apparatus and Systems*, Vol. PAS-101, No. 4, pp. 825-832, (April 1982).

- [10] "OptEM Cable Designer User's Manual," Version 5.3, OptEM Engineering Inc., Calgary, Alberta, (May 2002).



Joan Beckett received her B.Sc.E.E. in 1987 from the University of Manitoba, Winnipeg, Canada, and a General Management Certificate in 1999 from the University of Calgary, Calgary, Canada. In 1992 she co-founded OptEM Engineering Inc., a company specializing in the electromagnetic modeling and signal integrity analysis of electronic interconnects.

Performance Aspects of a Novel Two-Rod, Dielectric Sheath Design for Central Tube Cables

*Richard H. Norris, Peter A. Weimann and Howard M. Kemp**

OFS • Optical Fiber Cable Division • Norcross, GA 30071

*OFS • Optical Fiber Cable Division • Chester, NJ 07930

+1-770-798-4142 • rnorris@ofsoptics.com

Copyright © 2002

Fitel USA Corp.

All rights reserved

Abstract

Designs for dielectric cables include strength members comprised of multiple packages of glass and/or synthetic fibers, coupled together with varying amounts of crosslinked resin. These composite reinforcements cannot rival the mechanical properties per unit area nor the cost per unit length of their metallic counterparts. For these reasons, fabrication of dielectric cables that are cost-effective, compact, and sufficiently robust is a challenge for the cable designer.

This paper discusses the design and performance of a new central tube, dielectric cable sheath that employs two linearly applied composite rods. The new sheath design has been applied to a wide variety of core structures, including, tube-in-tube, filled ribbon and dry ribbon cores. The composite rods utilize novel coatings that provide optimized coupling between the rods and the cable jacket. This coupling is quantified through laboratory measurements of adhesion between rods and the cable jacket. Adhesion results are also compared with adhesion performance of rods that use other types of coatings.

Optimized coupling between the rods and the outer jacket results in excellent behavior in tensile, compressive and twisting deformations, as illustrated by cable-level mechanical tests. Most importantly, the new sheath design provides substantial improvements in installation performance. We report the results of a rigorous series of installation simulation tests, comparing results for this sheath design to alternate dielectric sheath designs.

Keywords

Outside Plant Cable; strength member; dielectric; fiber optic cable; coatings; fiber reinforced polymer rods (FRP); bending stiffness.

1. Introduction

In Outside Plant (OSP) fiber optic cable designs, product performance depends strongly on the cable strength system. The optical fibers housed within the cable are inherently fragile, and can fracture at low strains under tensile, compressive or torsional loading. In addition, optical fibers are subject to attenuation losses

when bent. Strength members protect the optical fibers from loads encountered during cable manufacturing, installation and service.

For over ten years, the performance and reliability of central tube cables with linear metallic sheaths [1] has been demonstrated in the field. In the linear metallic design, the central core tube is wrapped by corrugated electrolytically chrome-coated steel (ECCS) armor. Reinforcement is provided by two linearly applied steel music wires that are embedded in the jacket. The strength, robustness and affordability of this metallic cable design cannot be matched. However, metallic designs are not suitable in areas where high lightning activity is prevalent, or in regions where metal corrosion could be a problem. In these situations, a dielectric cable design is the better solution. Dielectric cables are typically reinforced with nonmetallic materials, such as rigid fiber-reinforced polymer (FRP) rods, fiberglass or aramid yarns, or semi-flexible glass rovings.

One well-known family of dielectric central tube cable designs utilizes helically applied reinforcements [2][3]. These constructions, commonly referred to as "crossply" designs, typically contain one or more layers of rigid FRP rods, as well as rovings or yarns. Dielectric crossply central tube cable designs are flexible and compact, and typically have very high fiber packing density. Therefore, crossply cables are especially ideal for cable routes that use small ducts, including new right-of-ways that use "microducts" [4]. However, crossply designs can have relatively high raw materials costs, due to the use of many individual small reinforcements. In addition, these designs typically rely on incompressible cable gels to provide compression resistance. Therefore, dielectric crossply sheaths may be inappropriate for new types of reduced-gel central core cable designs [5].

Dielectric central tube cables with linearly applied strength members tend to be less expensive than crossply cables, and are typically easier to manufacture. However, these benefits can come at the cost of increased cable size, as the reinforcements in linear dielectric central core cables are typically much larger than the reinforcements in crossply cables. In order to minimize cable size and cost, linear dielectric central core cables often contain a combination of rigid FRP rods, which provide tensile and compressive stiffness, and less expensive semi-flexible rovings,

which provide only tensile reinforcement. A common design uses six reinforcing members: two large rigid FRP rods, and four large semi-flexible rovings, which we will refer to as the "six-member design". Figure 1 is a schematic of the dielectric, two-rod/four-roving sheath design, detailing the individual components; a picture of a typical cable is shown in Figure 2. The two linear rigid glass/epoxy rods are diametrically opposite one another, and are located on the neutral axis of the cable. Rovings are located above and below the rods. In a typical six-member design, the reinforcements are designed to adhere strongly to the cable jacket, providing for a robust cable. Unfortunately, the high adhesion between the reinforcements and the jacket is also the source of undesirable preferential bend behavior. Six-member dielectric central tube cables can typically only be bent easily in the direction perpendicular to the two rigid FRP rods. Despite their robustness, these cables can be difficult to handle and install in the field.

In this paper, we present the development of a new two-rod, linear dielectric central-core sheath with substantially reduced preferential bending. Components of the new two-rod sheath are shown in the schematic in Figure 3, and a photograph of a ribbon cable with a two-rod sheath is presented in Figure 4. This cable sheath was originally introduced for a new tube-in-tube cable design [6]. After further optimization, the design is now commercially available for tube-in-tube, gel-filled, and totally dry [7] cable designs. An outdoor/indoor, riser-rated version of the sheath is available with both gel-filled and dry ribbon cores.

This paper describes the design of new reinforcements for this application, as well as prove-in testing of the new sheath in

laboratory and installation simulation tests. In section 2, we discuss development of reinforcements that bond to the cable jacket by "frictional adhesion". Section 3 reviews the cables available with the new two-rod sheath, and details the model two-rod and six-member cables manufactured for quantitative comparison of the two sheath designs. Section 4 provides a summary of experiments characterizing the tensile and bending performance of the two designs. Compared to the six-member design, the two-rod design has similar tensile performance. However, the new two-rod design exhibits significantly reduced preferential bending, due to the frictional adhesion between the rods and the cable jacket. Reduced preferential bending provides for improved field handling and installation performance, as discussed in Section 5. A detailed study presented in section 5 quantifies the excellent performance of the two-rod sheath in blowing installation. Additionally, a simple model presented in Section 5 describes how the improved performance of the two-rod cables can provide cable installers with significant savings in both time and cost.

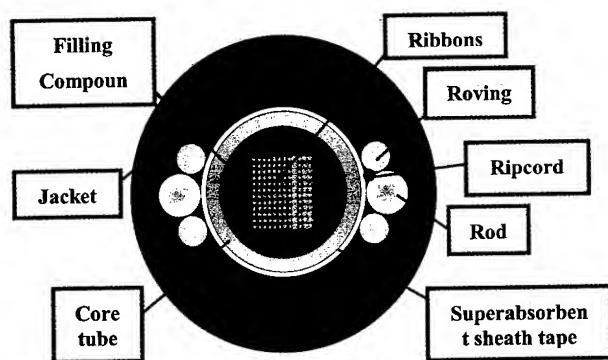


Figure 1 – Schematic of Six-Member Dielectric Central Tube Cable Design

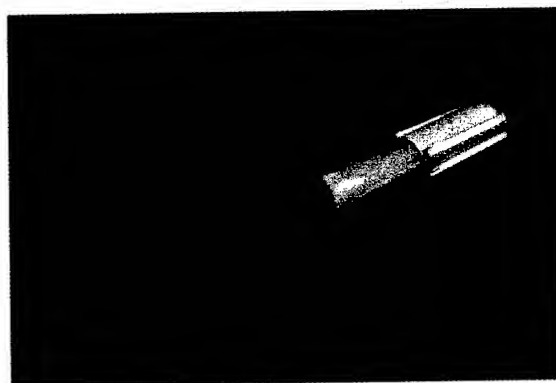


Figure 2 – Photograph of Six-Member Dielectric Central Tube Cable Design

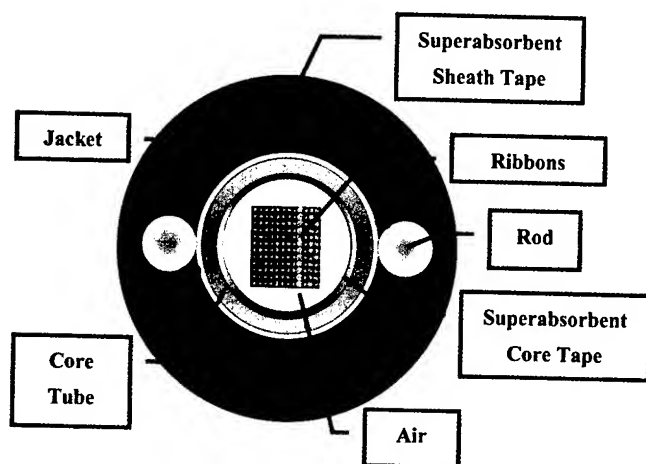


Figure 3 – Schematic of Two-Rod Dielectric Central Tube Cable Design

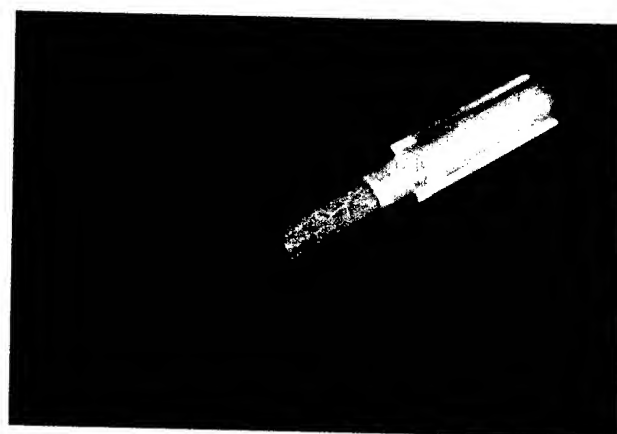


Figure 4 – Photograph of Two-Rod Dielectric Central Tube Cable Design

2. Reinforcement Design and Characterization

In order to develop a new linear dielectric sheath with reduced preferential bending, it was necessary to design and develop new cable reinforcements with sufficient tensile stiffness, compressive stiffness, and coupling to the cable jacket.

2.1 Design Goals for New Reinforcements

Although other components of a cable do have some load-carrying capacity, the strength members provide most of the tensile stiffness of a cable sheath. For a two-rod design rated at 2700N (600 lb.), each rod should be capable of carrying a minimum load of 1380N (310 lb.) at 0.5% strain, with a preferred nominal load at 0.5% strain of at least 1560N (350 lb.). In addition to having the necessary tensile and compressive stiffness, it is desirable for these FRP rods to be as compact as possible, to minimize the overall size of the cables.

In the standard six-member design, the FRP reinforcements are typically coated with a hot-melt adhesive. During jacketing extrusion, this coating melts and subsequently forms a strong adhesive bond with the jacket upon cooling. As a result, when a six-member dielectric cable is handled in the field, it exhibits a preferential bend. It is relatively easy to bend the cable in the plane perpendicular to the rigid FRP strength members. However, as shown below in Section 4.2, it is difficult to bend the cable in the plane parallel to the rigid rods.

To minimize preferential bend in an improved design, the rods must be able to relax locally when the cable is bent. However, the rods still must be able to couple sufficiently with the jacketing material and the rest of the cable to provide the necessary tensile performance. To balance these potentially conflicting needs, we set a goal of developing a new means of

coupling the reinforcements to the sheath through “frictional coupling”. Instead of forming an adhesive bond with the cable jacket, the desired reinforcements would couple to the jacket through a high coefficient of friction between the rod surface and the jacketing material. This would provide for reinforcement of the cable during application of tensile loads, while still allowing for local slippage of the rods in bending. In order to meet these goals, a new type of coating was needed: a material that does not melt when the jacketing material is extruded, but is still soft enough to exhibit high friction with the jacket.

2.2 Characterization of Candidate Reinforcements

Two different types of temperature-resistant materials were identified as candidates for the “frictional” coating: soft thermoplastics, and soft UV-cured materials. Samples of rigid rods coated with these types of materials were obtained from multiple manufacturers of rigid FRP reinforcements. Tests in our laboratory found that all of the materials met the minimum load-bearing target of 1380N (310 lb.) at 0.5% strain. All of the reinforcements had diameters smaller than 2.80 mm (0.110 in.).

In order to characterize adhesion of the rods to high-density polyethylene jacketing materials, we utilized a test method based on ASTM D1871, “Adhesion of Single-Filament Steel Wire to Rubber” [8]. Two 5.1 x 20.8 x 0.95 mm (2.0 x 8.0 x 0.38 in.) plaques of typical high-density polyethylene (HDPE) jacketing material are first prepared by compression molding. Then, multiple samples of a candidate FRP rod are compression-molded between the two plaques, such that a 5.1mm (2.0 in.) gauge length of each sample is encased in the plastic. Each sample is then individually pulled out of the plastic using a MTS ReNew electro-mechanical tensile testing machine, at a crosshead speed of 5.1 mm/min. (2.0 in./min.). For each

sample, adhesion is quantified as the maximum pull-out force recorded during the test. For each of the candidate rods described below, at least five samples were tested.

After initial screening, we chose to focus on four candidate rods: one with a soft thermoplastic coating, and three with soft UV-curable coatings. These rods will be referred to as rods "A" through "D". Results of adhesion tests at 23°C are summarized below in Table 1. A standard rigid FRP rod, coated with a typical hot-melt adhesive, was included as a control. This rod will be referred to as rod "E". Despite the differences in coating material, the adhesion of rods A, B and C is similar, while the adhesion of rod D is substantially higher. However, the adhesion of all of the candidate rods is much less than that of rod E, the control material. Each candidate in the A-D series was found to meet the design goal of coupling to the jacketing material through frictional adhesion.

Table 1 – Adhesion of reinforcements to HDPE at 23°C

Rod	Coating Type	Adhesion at 23°C, N (lb.)	Standard Deviation, N (lb.)
A	Soft thermoplastic	270 (61)	31 (7.0)
B	Soft UV-cured	270 (61)	30 (6.8)
C	Soft UV-cured	250 (57)	35 (7.9)
D	Soft UV-cured	630 (140)	78 (18)
E	Hot melt adhesive	1250 (280)	91 (21)

During field service, outside plant cables jacketed with carbon-black-filled polyethylene can frequently reach temperatures of 50°C (122°F) or higher. These high temperatures could conceivably affect coupling between the reinforcements and the cable jacket. With standard hot-melt adhesive coatings, a strong bond is maintained between the rod and jacketing material at any temperature below the melting point of the adhesive. For the new "frictional" coatings, the coupling between the cable jacket and the reinforcements is designed to be less than that provided by hot melt coatings. In order to characterize the performance of the new coatings at elevated temperatures, we repeated the adhesion test described above at a temperature of 55°C (131°F). For these experiments, the MTS ReNew electromechanical tensile testing machine was fitted with a forced-air environmental chamber equipped with a calibrated thermometer. Samples were allowed to condition at 55°C for 5 minutes before the test. Results of the tests for rods A-D are given below in Table 2.

For all of the candidate rods, adhesion to the jacketing material decreases at high temperature. However, upon heating to 55°C, the adhesion of rod "A", with the soft thermoplastic coating, is much less than the adhesion of any of the rods coated with soft

UV-curable materials. Since Rod D exhibits the highest adhesion to standard HDPE jacketing at elevated temperature, we selected this material as the best candidate for further development.

Table 2 – Adhesion of reinforcements to HDPE at 55°C

Rod	Coating Type	Adhesion at 55°C, N (lb.)	Standard Deviation, N (lb.)
A	Soft thermoplastic	64 (14)	9.8 (2.2)
B	Soft UV-cured	150 (34)	10 (2.3)
C	Soft UV-cured	210 (47)	38 (8.5)
D	Soft UV-cured	280 (64)	22 (4.9)

The balance of the paper focuses on characterization and proven of two-rod cables using rod D, including laboratory tests of cable mechanical properties and installation simulation tests. At each step, we compare performance this new two-rod cable design to that of the standard six-member linear dielectric design.

3. Cable Designs

The six-member linear dielectric design has been commercially available for over 10 years. Gel-filled ribbon cores are currently offered in two different sizes and accommodate fiber counts ranging from 12 to 216. The new two-rod linear dielectric sheath is available in three different cable sizes, also accommodating fiber counts from 12 to 216. The new sheath design is available with multiple core configurations: tube-in-tube [4] a gel-filled ribbon core, or a new dry ribbon core [7]. Both two-rod and six-member sheath designs have a tensile rating of 2700N. Table 3 summarizes the configurations and fiber counts of commercially available linear dielectric cables.

For quantitative comparisons of the performance of the new two-rod linear dielectric design to the six-member design, the study will focus on model, central tube cables with 216-fiber ribbon cores. A series of four prototype 18.5 mm (0.710 in.) 216-fiber ribbon cables were manufactured for qualification testing, as summarized in Table 4. These included one cable with "live" fibers for optical, mechanical, and installation-simulation testing, and three cables with "filler" fibers that were only used for limited mechanical and installation-simulation tests. Two of the cables had gel-filled cores, while the other two cables had a new totally dry central-core design that is described in a companion paper [7]. Taken together, these four cables allow examination of the effects of sheath design (two-rod vs. six-member) and cable weight (gel-filled vs. dry).

Table 3 – Construction and fiber counts of commercially available dielectric cables

Cable Construction	Dielectric Strength Member System	Fiber Count	Core OD mm (in)	Cable OD mm (in)
Dry 12-fiber ribbon core	Two rod	12 to 48	6.0 (0.236)	13.0 (0.510)
Tube-in-tube core (12 fiber tubes)	Two rods	12 to 48	6.0 (0.236)	13.0 (0.510)
Dry 12-fiber ribbon core	Two rods	60 to 144	7.9 (0.310)	15.5 (0.610)
Gel-filled 12-fiber ribbon core	Six members or two rods	12 to 144	7.9 (0.310)	15.5 (0.610)
Tube-in-tube core (12 fiber tubes)	Two rods	48 to 84	7.9 (0.310)	15.5 (0.610)
Dry 12-fiber ribbon core	Two rod	156 to 216	10.4 (0.410)	18.0 (0.710)
Gel-filled 12-fiber ribbon core	Six members or two rods	156 to 216	10.4 (0.410)	18.0 (0.710)
Tube-in-tube core (12 fiber tubes)	Two rods	96 to 144	10.4 (0.410)	18.0 (0.710)

Table 4 – Prototype cables manufactured for qualification testing

Cable	Cable Diameter, mm (in)	Reinforcement System	Core Design	Fiber Count	Fiber Type
1	18.0 (0.710)	Six-member	Gel-filled	216	Filler
2	18.0 (0.710)	Six-member	Dry	216	Filler
3	18.0 (0.710)	Two-rod	Gel-filled	216	Filler
4	18.0 (0.710)	Two-rod	Dry	216	Live

4. Cable Mechanical Performance

4.1 Tensile Performance

The Automated Long Gauge-Length Tensile Tester (ALTET) is a device developed in our laboratory for mechanical tests of long-length cable samples. In this device, 4.6 m (15.0 ft) lengths of cable are mounted horizontally, held by flexible wire mesh grips. Tensile force is supplied by a motor and screw jack system, and strain is measured by a pair of independently mounted optical encoders 1.80m (71 in.) apart in the center of the device. This apparatus allows for accurate testing of long lengths of cable independent of end effects, and as such is an excellent simulation of field loading conditions.

To illustrate the tensile performance of the new cable design, we compare the ALTET test performance of two 216-fiber cables: a grease-filled cable with a standard six-member sheath (Cable 1), and a dry cable with the new two-rod sheath (Cable 4). 4.6 m (15.0 ft) lengths of each cable were loaded at a speed of 0.43 m/minute (1.4 ft/minute). Strain vs. load curves for each cable are shown below in Figure 5. For clarity, only half of the actual data points collected are plotted in Figure 5. The tensile stiffness of each cable may be calculated by a linear regression fit to the data between 0.25% and 0.5% strain. Results of these fits are shown below in Table 5. The data indicate that the tensile stiffness of the two-rod cable is slightly less than that of the six-member design. However, based on the data, the stiffness of each cable is more than sufficient to carry a 2700N

(600 lb) load at 0.5% strain, as required by the Telcordia GR-20 standard [9] in North America

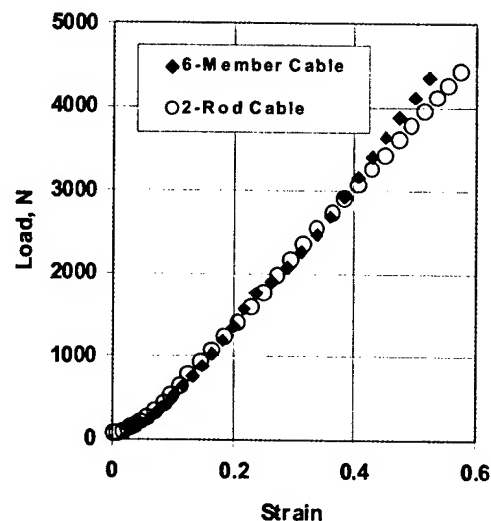
**Figure 5 – Load versus Strain Behavior in ALTET Tensile Testing of Cables**

Table 5. Tensile stiffness of representative 216-fiber dielectric cables

Cable Number	Cable Construction	Tensile Stiffness, N/% strain (lb./% strain)
1	Six-member, grease-filled	9700 (2200)
4	Two-rod, dry core	8200 (1800)

4.2 Bending Stiffness

A three-point bend test was used to compare the bending stiffness of the six-member and two-rod linear dielectric designs. The test was loosely modeled after ASTM D 790-98 "Flexural Properties of Unreinforced and Reinforced Plastics and Electrical Insulating Materials" [10]. A three-point flexure test jig was designed and machined for this application. As required in this specification, the jig bearing edges have radii less than or equal to 1.6 times the cable diameter. The fixture is adjustable, such that lengths of cable ranging from 2 to 24 inches may be tested.

A 29.7 cm (11.0 in.) sample length was used for these tests. For this length, a flexural deflection of approximately 50.8mm (2 in) will closely model the minimum bending radius of these cable designs. All testing was performed on a MTS ReNew electro-mechanical test system at room temperature, approximately 23°C (73°F). Special care was taken to assure the cable sample was completely straight before beginning each test. Samples were bent at a speed of 5 mm (0.2in) per minute, and each test was run long enough to allow for at least 50.8 mm (2 in.) displacement. Using an external displacement gauge, values of load and displacement were measured as the cable was bent. Tests were performed for cables with the flexural loading applied both perpendicular and parallel to the plane of the rods, as shown in Figure 6.

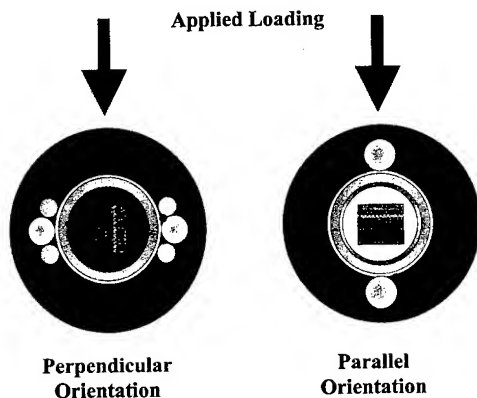


Figure 6 – Schematic of Sample Orientation in Bending Stiffness Tests

The general equation describing the small-strain deflection of a beam constructed from a linear elastic material [11] is:

$$B = \left[\frac{d^3}{48} \right] \left[\frac{F}{\Delta Y} \right] \quad (1)$$

where the variables are defined as :

$B \equiv$ bending stiffness (N·m² or lb-in²)

$D \equiv$ distance between supporting points (m or in)

$F \equiv$ Force needed to bend the cable over a distance ΔY (N or lb)

$\Delta Y \equiv$ displacement (m or ft)

For purposes of evaluating cable bending, this equation may be re-expressed in terms of specific variables:

$$EI = \left[\frac{l^3}{48} \right] \left[\frac{P}{y} \right] \quad (2)$$

where:

$EI \equiv$ bending stiffness (N·m² or lb-in²)

$l \equiv$ span length (between supporting points) (m or in)

$P \equiv$ Load needed to bend the cable over a distance y (N or lb)

$y \equiv$ displacement (m or ft)

Using the relationship in Equation 2, the bending stiffness may be determined from a tangential curve fit to a plot of load vs. displacement. This method provides a reasonable quantitative assessment of a cable's bending stiffness, especially for cables with a non-linear response. The bending stiffness, EI , was consequently calculated over a range of corresponding load (ΔP) and displacement (Δy) values.

Results of curve fits to flexural load-displacement curves are shown in Table 6. When the cables are loaded perpendicular to the plane of the strength members, there is no significant difference in the bending stiffness of the two designs. For bending parallel to the plane of the rods, the behavior of the two designs is quite different. The bending stiffness of the six-member cable in the "parallel" orientation is approximately 430% greater than the bending stiffness in the "perpendicular" orientation. As a result, the six-member design exhibits strong preferential bending behavior. In contrast, for the two-rod

Table 6 - Bending stiffness results

Cable Number	Cable Strength System	Rod orientation to applied loading	Bending Stiffness (N·m ² [lb-in ²])
2	Six Member	Perpendicular	1.02 (356)
4	Two Rod	Perpendicular	1.04 (364)
2	Six Member	Parallel	4.43 (1543)
4	Two Rod	Parallel	1.28 (446)

TABLE 8 – Summary of cable blowing tests

Cable Number	Reinforcement system	Core design	Ambient Temperature (°C [°F])	Initial Blowing Velocity (mpm[fpm])	Final Blowing Velocity (mpm[fpm])	Average Blowing Velocity (mpm[fpm])	Total Blowing Distance (m[ft])
1	Six-member	Gel filled	28 (82)	56.4 (185)	0	33.2 (109)	1160 (3804)
2	Six-member	Dry	26 (79)	57.9 (190)	0	42.4 (139)	1242 (4074)
3	Two-rod	Gel filled	21 (70)	59.4 (195)	54.9 (180)	56.7 (186)	1328 (4358)*
4	Two-rod	Dry	16 (61)	57.9 (190)	56.4 (185)	57.3 (188)	1328 (4358)*

* Full length of duct route

The average velocity of both two-rod cables was approximately 35% higher than that of the dry six-member cable, and about 80% higher than that of the gel-filled six-member cable.

5.2.2 Benefits for Cable Installers: Time Savings Resulting from Improved Blowing Performance

Actual blowing performance will depend on many factors, including ambient temperature and weather; topology of the duct system; condition of the duct system; and performance of the blowing equipment. However, deployment of the new two-rod design instead of the standard, gel-filled six-member design could provide installers significant savings in time and cost. Using the results of the blowing study described above in Section 6.2, we can construct a simple model that compares installation of the two designs for a long-haul route. As in the case of the installation study above, 216-fiber cables are installed in underground duct with an inner diameter of 31.8 mm (1 ¼ in.). The assumptions made in this model are summarized below in Table 9.

Table 9 – Blowing installation scenario assumptions

Length of route	150km (93.2 miles)
Length of cable per reel	6.0km (3.72 miles)
Frequency of manholes/handholes	One per kilometer
Length of work day	6 hours
Average installation velocity for six-member cable	31 m/min. (102 ft/min.)
Average installation velocity for two-rod cable	57 m/min. (187 ft/min.)

We also assume that the cables are being installed using “cascading” blowing equipment at each manhole or handhole. Through use of cascading equipment, the entire 6km length of each cable may be installed at once, without intermediate coiling or figure-eighting of the cable. This minimizes the overall time required to place cable along the route.

Given these assumptions, the time required to place the of the gel-filled six-member cables in the duct system will be 53.6 hours, or 8.9 working days. In contrast, placement of the two-rod cables would only require 29.2 hours, or 4.9 days. In this scenario, compared to the six-member design, installation of the two-rod cable takes 45% less time, saving four working days.

6. Conclusions

This paper describes the design and performance of a novel dielectric central-core cable sheath that employs two linearly applied FRP composite rods. The novel coating of the composite rods provides optimized frictional coupling between the rods and the cable jacket. The coating allows decoupling of the rods and jacket in bending or torsional deformations. However, once these types of loads are relieved, the coatings allow the rods to re-couple to the jacket.

The new sheath design has been applied to a variety of core structures, including tube-in-tube, filled ribbon and dry ribbon cores. These cables are available in fiber counts ranging from 12 to 216, utilizing 12-fiber tubes or 12-fiber ribbons. The new sheath design has a tensile rating of 2700N (600 lb.).

Coupling of the FRP rods to the cable jacket through frictional adhesion provides a robust cable sheath with minimal preferential bending. As a result, the installation and handling performance of the new two-rod linear dielectric design is superior to that of the industry-standard six-member linear dielectric design. The improved performance of the two-rod design in blowing can substantially reduce cable installation time and cost.

7. Acknowledgments

The authors would like to acknowledge the extensive contributions of Jennifer Meeks of OFS. Her testing of cables and materials was a critical part of the success of this development effort. In addition, the authors would like to thank Lisa Dixon of OFS providing the ALTET testing and data reduction. Finally, the authors would like to acknowledge the

valuable contributions of retired co-workers Richard Small, Phillip Thomas and Jim Clifford.

8. References

- [1] P.D. Patel, A.J. Panuska, "Lightweight Fiber Optic Cable", Proceedings of the Thirty-ninth International Wire and Cable Symposium, 158-165 (1990).
- [2] M.J. Buckler, M.R. Santana, S.C. Shores, "Design and Performance of an Optical Cable", Proceedings of the International Wire and Cable Symposium, 276-280 (1977)
- [3] P.F. Gagen, M.R. Santana, "Design and Performance of a Crossply Lightguide Cable Sheath", Proceedings of the International Wire and Cable Symposium, 391-395 (1979).
- [4] H.P. Debban, Jr., M. Rossi, P.A. Weimann, M. Kinard, C.S. Davis and J. Pedder, "Development of Lightweight Ribbon Cables for Blown Installation", Proceedings of the Fifty-First IWCS/FOCUS, (2002).
- [5] Lisa A. Dixon, Peter A. Weimann, Richard H. Norris, H. Paul Debban, Richard D. Small, "Crush and Bending Resistance in Next Generation Cable Designs" Proceedings of the Fifth International Wire and Cable Symposium, 422-431 (2001).
- [6] H.P. Debban, Jr., L.M. Bocanegra, C.S. Davis, R.D. Small, Jr., P.A. Weimann, M.R. Santana, "A New High-Density Central Cable Core Design", Proceedings of the Forty-Ninth International Wire and Cable Symposium, 1-7 (2000).
- [7] R.H. Norris and P.A. Weimann, "Dry Central Tube Cables for the Outside Plant Environment", Proceedings of the Fifty-First IWCS/FOCUS, (2002).
- [8] ASTM D 1871-98, "Adhesion of Single-Filament Steel Wire to Rubber", American Society for Testing and Materials, Philadelphia, PA
- [9] Telcordia GR-20-Core, "Generic Requirements for Optical Fiber and Fiber Optic Cable", Issue 2, July (1998).
- [10] ASTM D 790-98, "Flexural Properties of Unreinforced and Reinforced Plastics and Electrical Insulating Materials", American Society for Testing and Materials, Philadelphia, PA.
- [11] E.P. Popov, "Mechanics of Materials", Prentice-Hall, Inc, 99 (1952)



Richard H. Norris is a Member of the Technical Staff in the Outside Plant Cable Development Group, Optical Fiber Cable Division, OFS, Norcross, Georgia. Dr. Norris joined OFS (then Lucent Technologies) in 1997. He received a B.S. degree in Materials Engineering from North Carolina State University and M.S. and Ph.D. degrees in Metallurgical Engineering from the Georgia Institute of Technology. His primary duties include cable design, process development, tooling design and specialized cable and materials testing. He has published over 15 outside technical publications in varied technical areas and has been awarded six patents relating to optical fiber cable technology. He is also a registered Professional Engineer.



Peter A. Weimann is a Member of the Technical Staff in the Materials Technology Development Group, Optical Fiber Cable Division, OFS, Norcross, GA. His primary focus is materials development for outside plant fiber-optic cable products. He has been awarded seven U.S. patents relating to optical fiber cable technology. In 2001, he was a co-recipient of the Jack M. Spergel Memorial Award from the IWCS. He received his Ph.D. in Materials Science and Engineering from the University of Minnesota in 1998. His thesis research focused on structure-property relationships in polyolefins. He received a B.S.Eng. in Materials Science and Engineering, as well as a B.S.Econ. in Organizational Management, from the University of Pennsylvania in 1992



Howard M. Kemp is a Member of Technical Staff in the Outside Plant Cable Development Group, Optical Fiber Cable Division, OFS, Chester, NJ. Mr. Kemp began work at OFS (formerly Bell Laboratories) in 1978 where his current responsibilities include installation testing and development of installation and engineering guidelines for OFS outside plant cables. He received an Associate degree in EET from The Pennsylvania State University, a BSME degree from Fairleigh Dickinson University, and an MS Engineering degree from Stevens Institute of Technology.

Dry Central Tube Ribbon Cables for the Outside Plant Environment

Richard H. Norris and Peter A. Weimann
OFS • Optical Fiber Cable Division • Norcross, GA 30071
+1-770-798-4142 • rnorris@ofsoptics.com

Abstract

Historically, optical fiber cables for the Outside Plant (OSP) environment have employed filling compounds to immediately surround the fibers within the core tube or buffer tubes. The primary function of filling compound is to impede the migration of water within the interior of the cable. Additional benefits provided by filling compounds include increasing hydrostatic resistance to compressive forces and vibrational damping. The performance and reliability of filled cables has been demonstrated over the past 15 years.

However, during cable installation, filling compound is generally a nuisance. The most significant difficulty is removal of the filling compound and cleaning of the fiber units before splicing. This is a time-consuming process that increases expense and reduces productivity during installation operations. Filling compound can also contribute significantly to the total weight of cables, increasing the equipment and personnel required for long-haul installations. Filling compounds tend to be sticky or greasy, and therefore are a housekeeping annoyance to installers. In recent years, to overcome these drawbacks, many cable manufacturers have offered new designs that minimize the amount of filling compound, as reviewed briefly here.

The focus of this paper is the development of a family of new central tube ribbon cables that completely eliminate all filling compounds and/or oils within the central core tube. This new design family has been applied to fiber counts ranging from 12 to 216, in both metallic and dielectric sheaths. All of the cables in this family are fully compliant with the Telcordia GR-20 standard requirements for Outside Plant cables. Compared to conventional filled OSP cables, the new family of cables has equivalent or better optical, mechanical and environmental performance. We also summarize the results of a rigorous battery of installation simulation tests that show the performance of this family of cables is generally better than that of standard filled cables. Finally, we present time-study results that demonstrate that these new cables offer installers substantial time and cost savings during splicing operations.

Keywords: fiber optic cable, filling compound; waterswellable; superabsorbent.

1. Introduction

Ingress of water into fiber optic cables can be a serious threat to network reliability. If water penetration is not controlled, water can travel along the interior of cables to splice closures, potentially leading to damage to the telecommunications system and interruptions in service. Water may penetrate a cable sheath by two means: by diffusion through the cable jacketing, or as the result of damage to the cable.

In wet conditions, diffusion of water through the cable sheath could conceivably result in condensation of free water within the cable. However, a recent study [1] has shown that superabsorbent materials can prevent condensation of water that diffuses through the jacket. The study found that, in an undamaged dielectric cable, waterswellable superabsorbent materials limit condensation of water for at least 20 to 25 years at 23°C. Therefore, damage to the cable jacket is the most likely scenario by which water can enter the interior of a fiber optic cable. Jacket damage can occur as the result of dig-ups, accidental impacts, lightning strikes, or chewing rodents.

In the initial deployment of optical fiber networks, pressurized air core cables were introduced into outside plant applications. In these designs, ribbonized fibers were surrounded by poly(tetrafluoroethylene) tape within a polyethylene core tube, contained within a crossply metallic or dielectric sheath [2][3]. To block the migration of water, cable cores were pressurized with nitrogen gas. Because of the expense and difficulty of maintaining the required pressure, the air core design eventually gave way to new means of blocking water migration in cables: filling or flooding compounds. These compounds are typically petroleum-based gels that are used to fill void areas within the cable sheath, including the voids directly surrounding the optical fibers. The use of filling compounds in fiber optic cables has been an established practice for over 15 years.

However, there are several drawbacks to the use of filling compounds. Filling compounds increase cable weight, making installation and handling more difficult. These gels are also a housekeeping nuisance, as they can easily contaminate clothes, tools or

closures – essentially anything they contact. Special care must be taken to clean splicing machines and optical test sets contaminated by gel. Residues from gel can eventually lead to long-term reliability problems with these types of costly installation equipment.

Most significantly, filling compounds lead to increased installation costs for telecommunications service providers. During installation of filled cables, it is necessary to carefully remove all gels in order to prepare fibers for splicing. Skilled craftspeople are required to spend a great deal of their time cleaning gel, instead of focusing on splicing and testing of fibers. In addition, any gel residues remaining on fibers during fusion splicing will likely cause process errors and/or defects. As a result, removal of filling compound is a significant component of cable installation time and costs.

To address problems resulting from use of filling and flooding compounds, many manufacturers have introduced designs that minimize the use of gels. These include dry loose tube designs [4] and "tube in tube" central core designs [5][6][7]. However, these new designs still use filling compounds within the fiber-containing tubes, and as such still require installers to perform extensive cleaning. Recently, two types of dry, central core ribbon cables have been documented. A completely dry central-core design using a large number of superabsorbent yarns within the cable core has been described in the literature [8]. However, this design is apparently only available in dielectric sheaths. In an alternate cable design described in the literature, the core tube houses a specially designed water blocking laminated tape and uses intermittent resin plugs in the tube in order to fix the fibers in the cable [9].

In this paper, we describe the development of a complete new family of totally dry, central core ribbon cables in which a single piece of superabsorbent tape provides waterblocking. These cables, marketed under the trade name AccuRibbon® DC, are fully compliant with all requirements of Telcordia GR-20-CORE [10]. The family of cables is commercially available in both dielectric and armored metallic sheaths, in fiber counts ranging from 12 to 216. As discussed below, the complete elimination of filling compound provides substantial reductions in the time required for cable splicing operations. Therefore, this family of cables can afford service providers considerable installation cost savings.

2. Cable Design

2.1. Core Design

The optical fibers are arranged in 12-fiber ribbons within a central core tube. Ribbonized fibers provide inherently high fiber packing density in central core

constructions, and ribbons can be easily routed and managed in splice closures. In addition, ribbons allow for increased productivity through mass fusion splicing. However, the ribbons used in these new dry central-core cables may also be spliced and managed as subunits or single fibers. Breakout of these 12-fiber ribbons into robust subunits is straightforward, and separation of the ribbon into individual fibers is simple, as the matrix material is engineered to be removed from the fibers easily [11]. Depending upon fiber count, three different core tube sizes are employed, as shown in Table 1.

TABLE 1 –Dimensions and Fiber Counts of Core Tubes

Fiber Count	Ribbon Count	Core OD mm(in)
12 to 48	1 to 4	6.0 (0.236)
60 to 144	5 to 12	7.9 (0.310)
156 to 216	13 to 18	10.4 (0.410)

Figure 1 shows a schematic of a representative 144-fiber cable core. As seen in the schematic, the ribbons are wrapped by a single piece of an engineered superabsorbent tape, referred to as the core tape, which replaces the filling compound. As described below, the core tape acts to block water propagation along these cables, in compliance with Telcordia GR-20. The ribbons and superabsorbent tape are contained within a hollow impact-modified polypropylene central core tube.

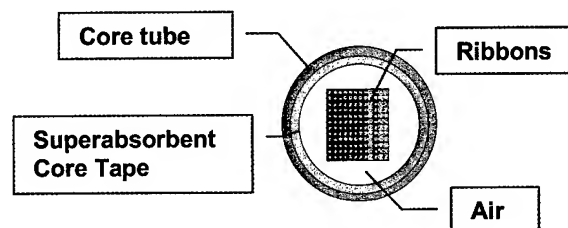


Figure 1 – Schematic of Core Design

The dimensions of the cable core tubes are similar to those of common filled central core cables. As is the case with filled central core cables, the cores are sized to provide for minimum fiber strain during installation and service. The cores are also engineered to have sufficient excess fiber length to ensure excellent optical performance under mechanical stress and at temperature extremes.

2.2. Sheath Design

These dry ribbon cables are available in both metallic and dielectric sheath configurations. The cables are available in three sizes, depending upon fiber count, as summarized below in Table 2. For a given fiber count, the metallic and dielectric cables have the same outer diameter. Figure 2 is a schematic of the metallic

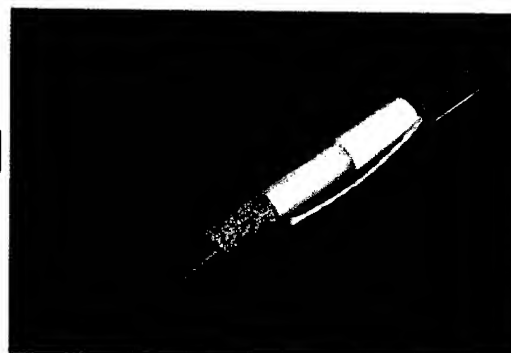
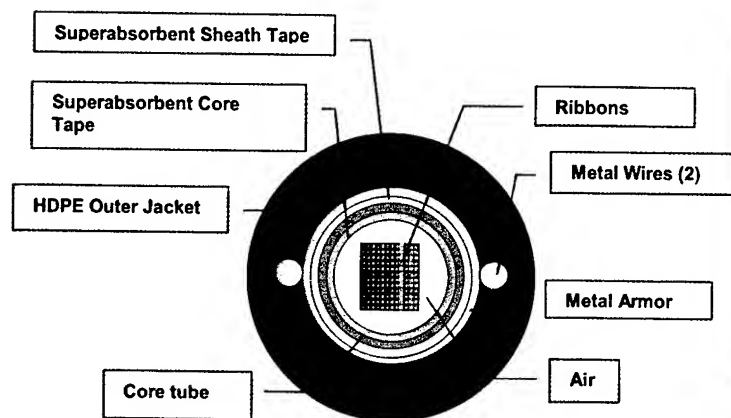
sheath design, detailing the individual components; a picture of a metallic cable is shown in Figure 3. The metallic sheath is a standard, proven design that has been utilized in multiple service conditions for many years. The strength system in the metallic sheath is comprised of a corrugated ECCS armor and two diametrically opposed linear steel wires. The dielectric sheath, as illustrated by the schematic in Figure 4 and the picture in Figure 5, is appropriate for use in areas where lightning or stray electrical currents may be a problem. Two diametrically opposed, linear glass/epoxy rods provide strength in the dielectric sheath. The rods are coated with a UV-cured "frictional coating" that provides ample mechanical coupling between the rods and jacket over a broad temperature range. Both dielectric and metallic strength systems provide a tensile rating of 2700N for all members of this cable family.

In each design, a standard superabsorbent waterblocking tape is used to wrap the core tube, to

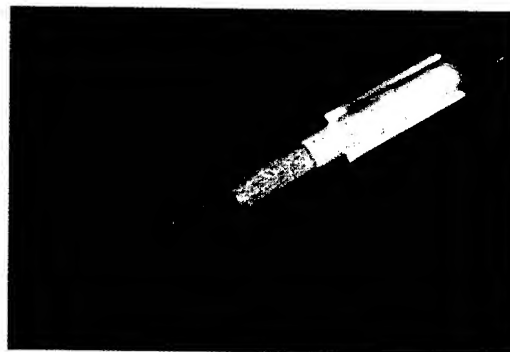
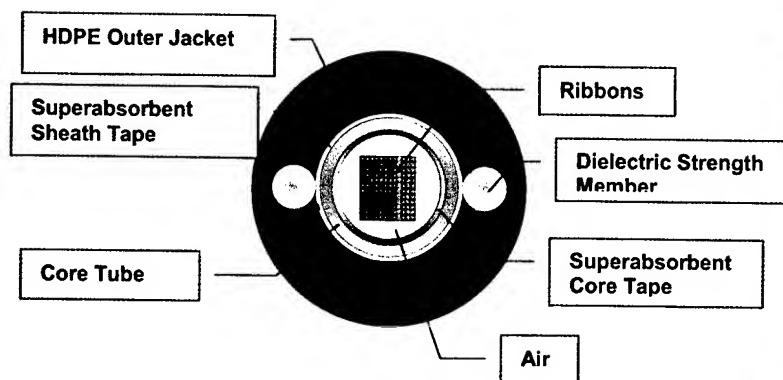
prevent water ingress between the jacket and core. All cables in the family are jacketed with high-density polyethylene. HDPE has been selected because of its hardness, ruggedness, and low coefficient of friction, all of which enhance the installation performance of these cables.

TABLE 2 – Dimensions and Fiber Counts of Cables

Fiber Count	Ribbon Count	Cable OD mm(in)
12 to 48	1 to 4	13.0 (0.510)
60 to 144	5 to 12	15.5 (0.610)
156 to 216	13 to 18	18.0 (0.710)



Figures 2 and 3 - Schematic of Metallic Dry Ribbon Design (left) and Picture of Cable (right).



Figures 4 and 5 – Schematic of Dielectric Dry Ribbon Design (left) and Picture of Cable (right).

Table 3. Results of extended water penetration tests on dry cable core tubes

Core Tube OD mm (in.)	Fiber Count	Number of Samples Tested	Results per FOTP-82
6.0 (0.236)	12	15	All samples pass
6.0 (0.236)	24	112	All samples pass
6.0 (0.236)	48	80	All samples pass
7.9 (0.310)	60	116	All samples pass
7.9 (0.310)	144	109	All samples pass
10.4 (0.410)	156	111	All samples pass
10.4 (0.410)	216	110	All samples pass

3. Design Qualification

All cables in the family have passed a complete series of qualification tests, including tests of optical performance under mechanical loads and at temperature extremes. In addition, these cables have been subjected to a rigorous battery of installation tests that simulate both standard and abusive installation practices. Performance of this family of cables is similar to or better than comparable filled cables. Details of the findings follow.

3.1. Telcordia Testing

The AccuRibbon® DC has been extensively tested in accordance with Telcordia GR-20, "Generic Requirements for Optical Fiber and Fiber Optic Cable - Issue 2" and has been found to be in conformance with the waterblocking, mechanical and environmental test requirements.

3.1.1. Water Penetration Performance

The waterblocking core tape in this new design family replaces filling compound. The core tape must block water penetration within the central core tube per Telcordia GR-20 and FOTP-82. All qualification cables that have been tested pass this standards requirement. However, since the core superabsorbent tape is required to block water penetration within a large void space in the cable core, an extended series of water penetration tests were performed on cable core tubes to verify the waterblocking performance. A pressure-head manifold was designed to allow testing of multiple core tube samples by continuous exposure of the samples to the equivalent of a 1-meter pressure head. Results of these tests are given above in Table 3.

3.1.2. Mechanical Testing

Numerous metallic and dielectric cables with the new dry core design have been qualified to the mechanical requirements of Telcordia GR-20. Below, in Table 4, results at 1550nm are presented for a typical,

representative cable, a 216-fiber dielectric cable with an 18.5 mm (0.710 inch) outer diameter. As shown in Table 4, for this cable, median and maximum added losses are both much less than is allowed under the GR-20 standard.

3.1.3. Environmental Testing

Numerous metallic and dielectric dry ribbon cables have also been qualified to the environmental performance requirements of Telcordia GR-20. To demonstrate this, results for a 48-fiber metallic cable with an outside diameter of 13.0 mm (0.510 inch) are used as an example of typical cable performance. Full test results, with maximum and median added loss results, are presented below in Table 5. Results of environmental cycling tests are illustrated in Figure 6, which plots the maximum added attenuation measured at each temperature during the test. Results of cable aging tests are illustrated in Figure 7, which also shows maximum added attenuation. As indicated by the data, this dry 48-fiber cable passes the requirements of these tests by a wide margin.

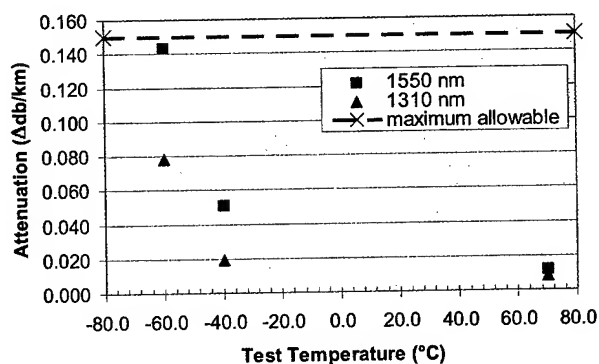


Figure 6 – Temperature Cycling Data

Table 4 – Telcordia Mechanical Testing Results

Cable Test	Test Level	Requirement: Maximum Δ Loss	Measured Maximum Δ Loss (dB)	Requirement: Median Δ Loss	Measured Median Δ Loss (dB)
Impact	4 kg	< 0.15	0.004	< 0.05	-0.008
Tensile Load & Bend	801 N	< 0.15	0.027	< 0.05	0.010
High Temperature Bend	60°C, 356 mm	< 0.15	0.011	< 0.05	-0.001
Low Temperature Bend	-30°C, 356mm	< 0.15	0.020	< 0.05	0.009
Compression	1112 N	< 0.15	0.011	< 0.05	0.001
Twist	2 m, 180°	< 0.15	0.022	< 0.05	0.008
Cyclic Flex	356 mm	< 0.15	0.004	< 0.15	-0.003

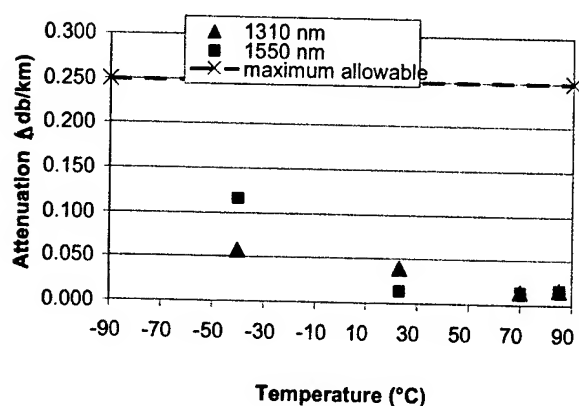


Figure 7 – Cable Aging Data

Measurements of added attenuation taken at -60°C during the environmental cycling test are also included in Table 5 and Figure 6. Although no requirements

currently exist for this temperature, the median loss is similar to that observed at -40°C, and the maximum loss is less than the maximum allowed by the standard at -40°C. This response is characteristically not observed in cables containing filling compound. At low temperatures, filling compounds typically become highly viscous, generally resulting in significant attenuation losses

3.2. Installation Simulation Testing

The installation performance of multiple dry ribbon cables has been evaluated at OFS' installation simulation test facility in Chester, NJ. The testing emulates both standard and abusive field installation practices. Although no standards body requires these tests, they do provide valuable information on the "real world" performance of these dry outside plant cables. Table 6 summarizes the tests performed.

Table 5 – Typical Environmental Maximum and Median Values

Test Temperature (°C)	Δ Loss (dB/km)			
	Temperature Cycling		Cable Aging	
	Median	Maximum	Median	Maximum
-60	0.007	0.143	—	—
-40	0.001	0.051	0.018	0.116
23	—	—	0.005	0.015
70	0.004	0.012	0.006	0.015
85	—	—	0.008	0.017

Table 6. Installation Simulation Tests

Test	Description
Initial attenuation measurement	Pre-test baseline
Pulling grip	Determine performance of pulling grips
Cable jettng	Determine cable jettability in underground duct
Underground placing	Determine cable behavior during underground placing
Tension/Bending	Pull cable around quadrant block and various sheaves
Capstan Assist	Determine performance on intermediate capstan assist winch
Aerial Coiling	Attenuation performance in coils
Direct Buried Plowing	Performance during plowing operation
Abusive Tests	Truck run-over, cable kinking
Final attenuation measurement	Comparison to baseline
Ultimate strength tests	Attenuation at ultimate tensile load
Sheath Dissection	Evaluate internal components for test-related damage
Ribbon Inspection	Evaluate ribbons for test-related damage

Table 7 displays results of installation simulation tests for three representative dry central-core ribbon cables: a 48-fiber, 13.0 mm (0.510 inch) outer diameter dielectric cable; a 60-fiber, 16.5 mm (0.610 in.) outer

diameter metallic cable; and a 216-fiber, 18.0 mm (0.710 inch) outer diameter metallic cable. The results are excellent, even in abusive tests performed beyond accepted practice.

Table 7 – Results of Installation Simulation Tests for Three Representative Dry Ribbon Cables

<i>Test</i>	<i>Maximum residual attenuation (dB)</i>		
	48-fiber dielectric	60-fiber metallic	216-fiber dielectric
Coiling tests			
Foldover method (18" dia)	0.07	-0.05	0.08
Tear drop method (24" dia)	0.10	0.13	-0.08
Garden hose (18" dia)	0.11	-0.04	0.12
Iterative capstan (10 pulls)			
Maximum Δ attenuation (dB/km)	0.01	0.02	0.01
Intermediate capstan			
7 wraps w/70ft slack	-0.01	0.07	0.07
2-2-3 wraps w/25ft slack	0.04	-0.03	-0.09
7 wraps, 1 at a time w/15ft slack	0.01	0.09	0.09
Tension & bending (non-abusive)			
600 lb @ 12 inch radius	0.04	0.06	-0.14
Tension & bending (abusive)			
600 lb @ 4 inch radius	0.05	0.04	0.04
Cable jettng – 3 loops attempted	<i>Maximum blowing distance (m[ft])</i>		
1" innerduct	4360(1330)	NA	NA
1¼" innerduct	4360(1330)	NA	4358 (1242)

**Table 8 – Performance Specification for
Dry Central Core Cables**

Tensile Strength:	2670 N (600 lb.)
Temperature Range:	
Operation:	-40°C to 70°C (-40°F to 158°F)
Installation:	-30°C to 60°C (-22°F to 140°F)
Storage/Shipping:	-40°C to 75°C (-40°F to 167°F)
Bending Diameter:	No load – 20 times cable diameter Loaded – 40 times cable diameter

3.3. Performance Specifications

The performance specifications for this family of dry ribbon cables are identical to those for similar filled central core cables. All cables in this new family meet the specification shown above in Table 8, as required by Telcordia GR-20 for the North American market.

4. Benefits for Service Providers

With complete elimination of filling compound, this family of dry ribbon cables has many attractive features that afford service providers significant savings in installation time and costs. Removal of filling compound allows rapid access to fibers and reduced splice preparation time. The design also provides substantial reductions in weight that result in installation advantages.

4.1 Weight

In typical central core cable designs with 216 fibers or less, the filling compound contributes approximately 10 to 20 percent of the total weight of the cable. Reducing the weight of cables through removal of the filling compound provides several benefits. Shipping is simplified, and cables are easier to handle and manipulate. Cost savings due to weight reduction can be realized in installation. Compared to similar filled cables, these dry ribbon cables can achieve longer distances in cable jetting, as described in a companion paper [12]. In addition, capstan-pull installation simulation tests have found that, compared to filled cables, reduced loads are required to install these dry cables in underground duct. Therefore, the reduced weight of the design can translate into longer cable pulls or blows, reducing the overall time and cost required for installation of a given cable route.

4.2 Reduced Splice Preparation Time

The most significant cost savings that a service provider may realize through deployment of these dry ribbon cables results from time savings during splice preparation. To quantify this, a trial splicing simulation has been performed, comparing a 108-fiber

metallic dry ribbon cable with a metallic, grease-filled, central core ribbon cable with an identical fiber count. The trial was performed by qualified installation trainers in a controlled environment. The time required to prepare the end of each cable for splicing was measured. Results of the trial are illustrated below in Figure 8. The full end preparation time for the dry ribbon cable was approximately 4¼ minutes, as compared to approximately 30¼ minutes for the filled cable. In this model experiment, use of the dry cable led to a time savings of over 85%. Looking at Figure 8, it can be seen that cleaning of ribbons and cleaning of tools and hands accounts for the majority of the time required for preparation of the filled cable.

Using the results of the time study described above, the cost savings due to deployment of these dry ribbon cables may be modeled for a typical long-haul installation scenario. The assumptions made in these calculations are shown in Table 9.

**Table 9 – Installation Scenario
Assumptions**

Fiber count	108
Length of route	160.9km (100 miles)
Length of cable per reel	6.4km (4 miles)
Length of work day	6 hours

Along the intended route, there would be a total of 25 splices, therefore a total of 50 cable ends to be prepared for splicing. Based on the model time study, the time savings resulting from use of the dry ribbon cable is assumed to be 26 minutes per cable end preparation. Therefore, the total time savings realized during installation of this route would be 22 hours, or 3.6 days. To put this into perspective, the *total* time required for cable end preparation with dry ribbon cables would be 3½ hours, roughly ½ work day. The total time required for end preparation of conventional grease-filled cables is 25 hours, approximately 4.2 workdays.

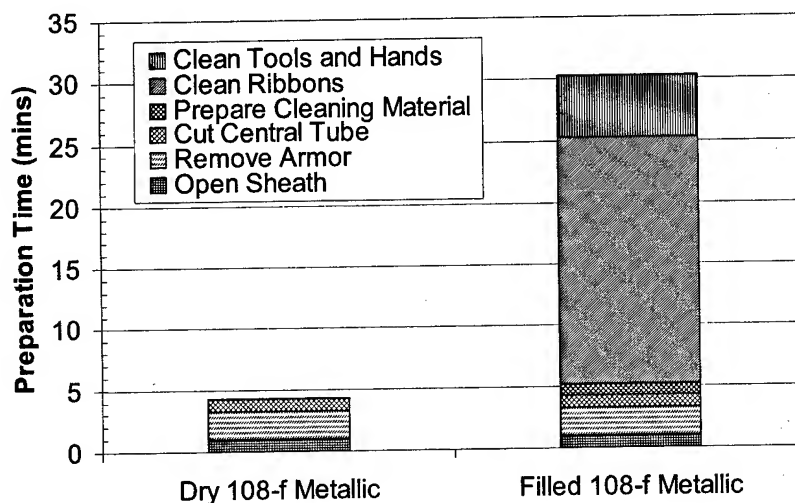


Figure 8 - Splice Preparation Comparison

4.3 Cleanliness

In addition to the time savings realized in cable end preparation, the removal of filling compound also provides significant housekeeping advantages in the field. Filling compounds are typically messy and sticky, and tend to contaminate splice trays, other areas of closures, tools, splicing equipment, test equipment, work areas and clothing. Specialized solvents are generally required for cleaning or removal of filling compounds. Contamination with gel can affect long-term reliability of splicing and test equipment. Removal of filling compounds eliminates all of these concerns. Also, during fusion splicing, residual filling compound on fibers can cause splicing defects that could require additional unwanted rework.

5. Conclusions

This paper describes the performance of a new family of totally dry, central core ribbon cables that contain no filling compounds or gels. The design is available in both metallic and dielectric sheaths, with fiber counts ranging from 12 to 216. All cables in the family are fully compliant with all requirements of Telcordia GR-20, including requirements for water penetration, mechanical performance, and environmental performance. A series of installation simulation tests has demonstrated that the field performance of these cables is equivalent to or better than that of comparable filled cables. The cables have been carefully engineered to eliminate the need for painstaking cleaning of ribbons. A time study has

demonstrated that, for these dry ribbon cables, end preparation for splicing can be accomplished much more quickly than with comparable filled cables. This allows telecommunications service providers significant savings in both installation time and expense.

6. Acknowledgements

The authors would like to acknowledge the extensive contributions of Jennifer Meeks of OFS. Her testing of cables and materials was a critical part of the success of this development effort. In addition, the authors would like to thank Mario Rossi of OFS for arranging the time study and analyzing its results. The authors would also like to thank Bill Allen, Howard Kemp, Trupti Marshall, and others at OFS for their assistance with qualification tests. Finally, the authors would like to acknowledge the valuable contributions of retired co-workers Richard Small, Phillip Thomas and Jim Clifford.

7. References

- [1.] C.R. Taylor, K. Konstandinidis, R.D. Small, Jr., R.H. Norris, M.R. Santana, R.P. DeFabritis, "Effects of Water Blocking Materials on Moisture Diffusion in Prototype Cable Structures", Fiftieth IWCS Proceedings, 518-525 (2001).
- [2.] M.J. Buckler, M.R. Santana, S.C. Shores, "Design and Performance of an Optical Cable", Proceedings of the International Wire and Cable Symposium, 276-280 (1977).

- [3.] P.F. Gagen, M.R. Santana, "Design and Performance of a Crossply Lightguide Cable Sheath", Proceedings of the International Wire and Cable Symposium, 391-395 (1979).
- [4.] C.E. Clyburn III, A.G. Bringuier, "A Dry Core Loose Tube Cable for Outside Environments", Proceedings of the Forty-Fourth International Wire and Cable Symposium, 29-36 (1995).
- [5.] P. Jamet, P. Trombert, N.LeCourtier, D. Bernier, M. Delpech, "Optimal High Fiber-Counts Microsheath Cables Fitting New Fiber Networks Requirements", Proceedings of the Fiftieth IWCS/FOCUS International Wire and Cable Symposium 650-657, (2001).
- [6.] S. Pastuszka, J.P. Bonicel, M.G.S. Emeterio, P. Gaillard, K. Nothofer, A. Weiss, "A New Type of High Fiber Count, Low Dimension Optical Cable with Simplified Installation Characteristics", Proceedings of the Forty-Eighth International Wire and Cable Symposium, 106-111 (1999).
- [7.] H. P. Debban Jr., L. M. Bocanegra, C. S. Davis, R. D. Small, Jr., P. A. Weimann, M. R. Santana, Lucent Technologies Inc., Norcross, GA, "A New High-Density Central Cable Core Design", Proceedings of the Forty-Ninth International Wire and Cable Symposium, 1-7 (2000).
- [8.] P.V. Vickie, S. Chastain, S. McCreary, "Innovative Dry Buffer Tube Design for Central Tube Ribbon Cable", Technical Proceedings of the National Fiber Optic Engineers Conference, Volume 1, 154-161 (2001).
- [9.] N. Okada, Y. Sato, H. Watanabe, K. Watanabe, M. Miyamoto, "Development of New Dry Tube Cable with Water Blocking Laminated Tape" Proceedings of the Forty-Ninth International Wire and Cable Symposium, pp. 164-168 (2000).
- [10.] Telcordia GR-20-Core, "Generic Requirements for Optical Fiber and Fiber Optic Cable", Issue 2, July (1998).
- [11.] K. Konstandinidis, N.W. Sollenberger, S. Siddiqui, K.W. Jackson, J.M. Turnipseed, T.W. Au, R.P. DeFabritis, C.R. Taylor, "UV Color Coatings and Matrix Material For Enhanced Fiber Optic Ribbon Products", Proceedings of the Forty-Sixth International Wire and Cable Symposium, 274-280, (1997).
- [12.] R.H. Norris, P.A. Weimann, "Performance Aspects of a Novel Two-Rod, Dielectric Sheath Design for Central Tube Cables" Proceedings of the Fifty-First International Wire and Cable Symposium, (2002).



Richard H. Norris is a Member of the Technical Staff in the Outside Plant Cable Development Group, Optical Fiber Cable Division, OFS, Norcross, Georgia. Dr. Norris joined OFS (then Lucent Technologies) in 1997. He received a B.S. degree in Materials Engineering from North Carolina State University and M.S. and Ph.D. degrees in Metallurgical Engineering from the Georgia Institute of Technology. His primary duties include cable design, process development, tooling design and specialized cable and materials testing. He has published over 15 outside technical publications in varied technical areas and has been awarded six patents relating to optical fiber cable technology. He is also a registered Professional Engineer.



Peter A. Weimann is a Member of the Technical Staff in the Materials Technology Development Group, Optical Fiber Cable Division, OFS, Norcross, GA. His primary focus is materials development for outside plant fiber-optic cable products. He has been awarded seven U.S. patents relating to optical fiber cable technology. In 2001, he was a co-recipient of the Jack M. Spergel Memorial Award from the IWCS. He received his Ph.D. in Materials Science and Engineering from the University of Minnesota in 1998. His thesis research focused on structure-property relationships in polyolefins. He received a B.S.Eng. in Materials Science and Engineering, as well as a B.S.Econ. in Organizational Management, from the University of Pennsylvania in 1992.

Fiber Optic Cables and Cable Modules with Balanced Mechanical Characteristics Based on Self-Reinforcing Polymers with Controlled Orientation

M.T. Heino, J.T. Ravela, P.E. Korhonen and E.P. Virolainen

NK Cables Ltd.
PO Box 419
FIN-00101 Helsinki
FINLAND

Abstract

New lightweight, buffered and stabilized non-metallic fiber optic cable designs for several end use applications have been studied. The development is based on the use of advanced plastic materials and multilayer extrusion for processing different thermoplastic materials simultaneously as described earlier [1]. The aim has been to make compact non-metallic cables or cable modules based on coextruded multilayer constructions.

The current non-metallic fiber optic cable designs are composed of several discrete elements set around the plastic buffer tubes such as reinforcing aramide fibers, composite strength members, water-blocking tapes, flooding compounds, binding yarns, outer jacket etc. We have developed novel cable concepts to simplify and find better possibilities for easier customizing of the cable designs. The idea is to use special thermoplastic polymers or compounds exhibiting appropriate functional properties such as high strength and stiffness, low moisture permeability, fire retardance, wear resistance etc. as thin layers coextruded in one processing step. Combination of these functional layers is made by co-extrusion, typically using a special cone extrusion technique.

The paper discusses basic physical properties like tensile strength, crush resistance, thermal stability and barrier properties for some different non-metallic cable designs. The aim was to utilize multilayer extrusion and control the fiber orientation of the stabilizing layer made of liquid crystalline polymer (LCP). These example cables can be used in access networks or as cable modules in central loose tube or stranded cables.

Keywords

Self-reinforcing polymers; Liquid Crystalline Polymers (LCP); Multilayer extrusion; Cone extruder; Helical orientation; Rotating tools; Non-metallic; Thermally stabilized; Lightweight cable

1. Introduction

The focus of this paper is on the development of small, non-metallic lightweight, high-fiber-density fiber optic cable constructions [1]. They seem to be attractive either to be used as cables as such or to serve as highly protective modules in bigger cables for special applications. One of the main targets was to create a small, blown-in-tube cable with relatively high fiber count, having proper flexibility but still maintaining the stiffness, thermal stability and resistance against harsh environmental conditions [2]. Other important characteristics, required increasingly for modern non-metallic cables, include e.g. low friction coefficient or other surface properties depending on the installation method to be used, flame retardance and resistance to moisture or chemicals. All these topics were investigated in this study. In particular, the aim was to study the feasibility to use extrudable reinforcing materials as part of a coextruded multilayer jacket to gain or improve these properties.

In such non-metallic fiber optic cables maybe the most challenging task is to create the required mechanical strength and thermal stability with an extrudable material. This is possible by using so called self-reinforcing polymers, in other words liquid crystalline polymers (LCP). These special polymers can be melted and extruded like thermoplastics, but due to their high molecular order they tend to form a composite-like fiber-reinforced structure when solidified. Thanks to this structure and the chemical composition LCPs show a range of attractive properties. High mechanical strength and stiffness, very low thermal expansion coefficient, good moisture barrier and resistance to chemicals, thermal stability etc. are attractive properties for fiber optic cables to create the mechanical, thermal and dimensional stability. However, processing and controlling of the properties of LCP is not easy, since the properties are highly anisotropic. Normal extrusion results in axial fiber orientation and high stiffness, but brittleness in bending. We have developed special processing techniques to control the fiber orientation and create more balanced physical properties for the LCP layer (lamellar layered structure, high degree of fibrillation, helical fiber orientation). This paper reports some of the results of our basic studies made to develop the non-metallic lightweight fiber optic cables and shows some examples of such cables with balanced properties.

2. About LCPs

Thermotropic main-chain liquid crystalline polymers (LCPs) are very special melt-processable polymeric materials. When melted they exist in so called liquid crystalline state, which means that the polymer chains are highly ordered already in the melt phase. By chemical nature they are typically polyesters or polyamides, but due to their rigid, mostly linear molecular chain structure and rather high degree of aromatic groups they differ a lot from conventional thermoplastic polymers. One of the most interesting features of LCPs is their special composite-like structure, which is the basis for their excellent mechanical properties even as thin layers. Due to this highly ordered internal structure these materials are also called self-reinforcing polymers. In addition to high mechanical strength and stiffness LCPs have several other attractive properties such as good dimensional stability (very low thermal expansion coefficient and shrinkage during solidification), good resistance to high temperatures, moisture penetration and several chemicals.

In addition melting of the material occurs rapidly, the melt viscosity is low and melt strength high giving good basis for different melt processing techniques. However, processing of these special materials is not straightforward. The good material properties are achieved by the highly ordered composite-like structure, which in turn is very dependant on the way of processing. During processing the LCP melt must be well oriented by high longitudinal or shear forces to be able to fibrillate the material. In normal extrusion drawing of the product easily creates highly fibrillated material, but due to the axial orientation, the material has very anisotropic properties (high strength and stiffness in axial direction, but poor bending properties). Controlling the fiber orientation is thus the key for balanced properties in extruded products [3,4].

For small lightweight fiber optic cables the properties of LCPs are promising, in particular to achieve the required mechanical and thermal stability.

3. Multilayer Extrusion

When processing LCP materials for cable manufacturing benefits of multi-layer extrusion are apparent. Supporting layers consisting of other thermoplastic polymers can be applied to allow the use of even very thin layers of LCP, where needed. Thicker layers of tough or more flexible materials around functional polymers like LCP or other special polymers may also help for example to compensate the brittleness of these special layers.

Coextrusion may basically ease the extrusion (draw-down process) of LCP, which normally exhibits very low melt viscosity. On the other hand, incorporating several different polymers in molten state to rather thin multilayer construction is very sensitive and may lead to several other difficulties. Hence, the materials to be combined must be compatible with each other in terms of

chemical nature, temperature range and melt rheology. In addition, the processing equipment shall be well designed to be able to make multilayer extrusion with such special polymers in a controlled way.

The main benefit of coextruded multilayer constructions is the possibility to combine different material properties into a compact product design and to make the whole cable in fewer process steps, in the extreme case all in one step.

3.1 Cone Extruder

Cone extrusion is an advanced extrusion method described in detail earlier [1,5,6]. It has been developed for optimal processing of thermoplastic materials, and therefore it differs from traditional screw extrusion significantly.

The main components of the cone extruder (Conex[®]) are a rotating conical screw with helical channels (rotor), two stationary cones (stators), one on either side of the rotor, and a simple die. Each rotor can produce two layers, and multilayers are achieved by adding more nested stator/rotor/stator combinations. The extruder used in this work has two rotors, which means that it can produce coextruded multilayer structures with 1 to 4 layers. All layers are seamless since the material flows symmetrically around the core, and the thickness of each layer can be controlled separately. The melt processing conditions are optimal for thermoplastics thanks to the special geometry of the extruder (effective melting, short residence time, low shear for melt). Moreover, the cone extruder generates, with its rotors, a helical flow field for the melt, which makes it easier to orientate fibrous polymers and control their mechanical properties [1,5,6].

As a versatile processing method, cone extrusion offers thus a major advantage for the manufacture of non-metallic fiber optic cables: a wide range of polymers with diverse functional properties can be processed simultaneously in a gentle way and combined in a single process step. Relatively wide variation in layer thicknesses is also possible which allows tailoring of the mechanical properties of the cables without significant effect on the final dimensions [1].

3.2 Helical Orientation with Rotating Tooling

Normal extrusion with LCP easily leads to axial (longitudinal) fiber orientation. The rotors of the cone extruder in turn create a helical flow field evidenced earlier with e.g. glass fiber reinforced thermoplastics [5,7]. This means that depending on the die geometry and take-up speed, the fiber-reinforced material has at least partially helical orientation (in the middle of product) at the end of the rotor, while the surfaces close to die walls very easily tend to orient axially. This is the case typically in cable extrusion. With higher take-up speeds the fibrillation of LCP can be further increased, which improves the mechanical properties of the LCP

layer. The axial fiber orientation results in high stiffness and tensile strength, but makes the tube very sensitive against bending and crush. To overcome this inconvenience, a rotating tip was introduced in this work to create helical orientation in the self-fibrillating polymer layer. This improved evidently the bending behavior of the cable generating not only helical orientation but also a lamellar layered structure in the innermost layer (LCP) of the sheath. This kind of gradual variation in the fiber orientation of the thin LCP layer results in balanced mechanical properties.

For thicker LCP layers and other applications efficient orientation of the whole layer may require also the use of a rotating die. When the tip and the die are rotated separately and independently it gives freedom to orient the whole multi-layer structure either in uniform helical angle, in different angles from inside out or in a cross-plyed manner.

4. Cable Constructions

The main focus of the work reported here was to study the feasibility of LCP as the stabilizing component for the non-metallic lightweight fiber optic cables. Particular attention was

paid to the control the extrusion conditions and especially the fiber orientation of the LCP layer. Therefore the cable constructions selected for this study were rather simple, consisting basically of three extruded layers. Based on this basic study, similar or slightly modified cable designs can be made with different material combinations depending on the needs of each application, as described earlier [1].

Figure 1 shows examples of the cable constructions made. The two upper cables show the difference in the internal orientation of the LCP layer in the test cables. The lowest drawing present an indoor/outdoor access cable with additional halogen-free flame-retardant (HFFR) jacket. The outer diameter of these small-size non-metallic multilayer cables typically range from 3 to 5 mm and fiber count from 6 to 48 fibers. The highest fiber density used here was 2.8 fibers per mm² of the cable's cross section.

These cables are thought to be suitable e.g. for access networks or LAN installations made by blowing into tubes or to be placed in ducts. Due to their good thermal stability and fair mechanical strength they are considered to withstand even the harsh Nordic climate and environment. Other possible applications of use and other evolved designs of the same principle are discussed below. The targeted properties are generally described in Table 1.

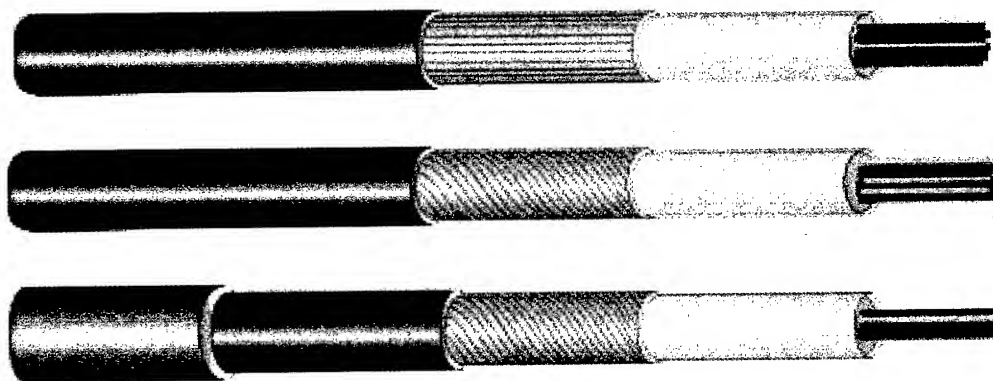


Figure 1. Schematic drawings of typical cable constructions.

Table 1. Targeted properties for the lightweight cables with 12 to 48 fibers [1].

Property	12/24 Fiber Cable	48 Fiber Cable	Criteria
Tensile strength	100 – 500 N	500 – 1000 N	allowed strain of the fibers up to 0.3%
Minimum bending radius	25 mm	40 mm	with no damage to the components
Temperature range	-40 – +70 °C	-40 – +70 °C	max. allowed attenuation increase < 0.05 dB/km
Crush resistance	500 – 1000 N/100mm	500 – 2000 N/100mm	with no damage to the components
Maximum weight	< 10 kg/km	< 25 kg/km	
Maximum diameter	< 4 mm	< 6 mm	

Table 2. Description of the test cables.

No.	Layer 1	Layer 2	Layer 3	d (mm)	Fiber count	Note
#0	PBT	PA	HDPE	3.8	12F	Reference (without LCP)
#1	PBT	LCP	PA	3.8	12F	Axial orientation
#2	PBT	LCP	PA	4.1	12F	<i>Helical orientation</i>
#3	PBT	LCP	PA	4.1	6F	<i>Helical orientation</i>
#4	PBT	LCP	PA	4.1	24F	Compact design, <i>Helical orientation</i>
#5	PBT	LCP	PA	4.7	48F	Compact design, Axial orientation
#6	PBT	LCP	PA	4.7	48F	Compact design, <i>Helical orientation</i>

Detailed descriptions of the cable designs studied are shown in Table 2. For this study, PBT loose tubes with optical fibers and filling gel were coated with a two-layer jacket. The LCP layer is naturally the most important and critical one in these constructions in terms of final cable properties and processing. The idea was to extrude thin layers (about 0.1-0.3 mm) of LCP together with slightly thicker jacket and to vary the orientation angle of the LCP fibrils. In this case, a special polyamide was selected as the outer layer to give a tough enough outer jacket complementing well the properties of the LCP. This kind of cables were considered to be the most suitable for evaluating the feasibility of self-reinforcing polymers and the effects of different fiber orientation angles on cable properties.

A reference cable (Sample #0) was made without LCP. All other versions contained the same materials (PBT//LCP/PA). Individual layer thicknesses were varied to some extent. The thickness of the LCP layer was varied within the range of 0.1-0.3 mm. The main aim was however to study the effects of different fiber orientation on the mechanical properties and temperature stability of the test cables. Therefore similar cables were made both using the rotating tooling and without it. In the previous case helical orientation field could be created in the thin LCP layer while the latter one showed purely axial fiber orientation, as indicated by the schematic drawings in Figure 1.

The reason to make the PBT loose tubes separately with a normal central loose tube line was that sufficient number of fiber pay-offs to run the cables with higher fiber counts (24/48F) were not available at the present Conex line. Therefore all different constructions studied here were decided to make in the same way. This gives, of course, an opportunity to have even five layer constructions. On the other hand due to the high fiber density, very small size and thin walls of the tubes one extra winding and stocking on a spool could be a risk to the final cable quality. The cone extruder itself is suitable for processing optical fibers and gel with four polymer layers in one step, thus giving better opportunities to vary the thickness and material of the innermost layer and to control e.g. excess fiber length [1].

5. Test Results

5.1 Test Procedures

Basic tests were made according to IEC 60794-1-2 to distinguish the effects of different process configurations and to verify the main properties of the test cables and their feasibility for the intended applications. Temperature cycling (Method F1), Tensile test (Method E1), Crush test (Method E3), Impact tests (Method E4) and Kink test (Method E10) were made on the test cables described in Table 2. Temperature cycle test was not made for cables 3 and 5 due to too small length of sample available.

The test criteria for particular cables are commonly described in the corresponding cable standards. In the case of completely new constructions there are no applicable standards available and the criteria are based on the use and installation circumstances of the cable. Here we compare the test results to the targeted properties of Table 1 and a new standard draft for small cables used in blowing installations [8]. Generally the tests were carried out by following changes in attenuation of the optical fibers and the appearance of any physical damages to the construction during the test. The basic idea was to study, how well this lightweight cable construction can protect the optical fibers in different installation environment. Generation of the LCP fiber orientation was analyzed with an optical microscope from the cable samples.

In addition, some special properties like surface friction coefficient, flame retardancy and moisture barrier efficiency were evaluated on some selected samples considering more specific applications of the lightweight cable.

One aspect became very clear when testing this type of cables: due to the small size of the cables and very high fiber density they were rather sensitive both in their optical and mechanical behavior even to small changes in dimensions and especially to variation of the excess fiber length (EFL). Similarly, due to the high strength, i.e. high Young's modulus of the LCP compared to that of the other polymer layers the mechanical performance of the cable changed rapidly according to the thickness and overall cross sectional variations of the LCP.

5.2 Mechanical Properties

Summary of the mechanical properties of the test cables is presented in Table 3. Results of the tensile tests are also shown in the form of force vs. elongation curves in Figure 2.

A reference cable manufactured of two tough engineering polymers (PBT, PA) with HDPE outer jacket was tested just for comparison of mechanical and thermal properties. All other test samples contained LCP layers, either axially or helically oriented. The reference cable like the other early stage samples had relatively modest fiber count and density. Samples from #4 to #6 were, like targeted, compact high-fiber-density cables.

The tensile force values of Table 3 and the curves in Figure 2 may give at first look somewhat confusing and unrealistic impression of the tensile characteristics of the cables. Owing to the small size (thin walls) of the multi-layer jacket even with lower fiber counts its strain resistance was close to that of the fibers, in some cases even smaller. Thus the high fiber count and low excess fiber length resulted in very low values of elongation at given force, when the fibers also started to carry the load soon after applying the force. This has to be considered when evaluating the curves in the Figure 2. As both the cable and fiber strain are shown this phenomena is however clearly visible.

To understand the reinforcing effect of the LCP in these multi-layer constructions better, the influence of the optical fibers can be calculated off. Therefore, the Force/Strain factors (i.e. an extra force needed to add the elongation by 0.1%) for the jackets were defined. This gave a more realistic and clearer picture of the tensile resistance of the multilayer jackets: starting from 18N/0.1% for the reference cable (# 0), rising to 40N/0.1% for the smaller cables (#2-4) and up to 50N/0.1% for the biggest cables (#5 and #6). The highest value 80N/0.1% was measured for Sample #3 having the thickest LCP layer (0.3 mm). These values were quite close to the predicted ones, calculated based on the Young's modulus of the combined multilayer structure consisting

of the known materials. Of course in real installation or under other tensile stress conditions the fibers and the sheath act together to resist the strain, which can be allowed if the strain limit defined for fibers (e.g. 0.3%) is not exceeded. This can be reached by adjusting a proper EFL for the cable. The orientation direction, axial or helical, had a negligible effect on the Tensile Force/Strain factor. This means that the helical orientation created to improve bending properties did not reduce the axial strength of the cables.

In evaluating the crush resistance of the cables the integrity of the components during and after the applied load were used as the main criterion. However, also attenuation was monitored and the reversibility of the attenuation was required. Generally the results met well the targeted values (Table 1 and [8]). Helical orientation seemed to improve the crush resistance to some extent. The high fiber density or high EFL did not increase fiber attenuation. In most cases, some of the sheath components broke or gave up and larger attenuation rise occurred only after that.

The destructive impact energies remained low through all samples tested. This was mainly due to the small size and layer thickness of the test cables and minimal amount of impact absorbing capacity in the cable construction itself, not so much to the materials used. However, no fiber breaks occurred. Helical orientation improved the impact resistance slightly by toughening the LCP layer, but its effect was rather small due to the extremely thin layer.

Minimum bending radius increased by the use of stiff self reinforcing polymer compared to the thermoplastic reference, which was of course expected. However, the use of helical orientation led to clear improvement in bending performance as targeted. The reduction of bending radius was from 40 mm (#1) to 25 mm (#2) for the smaller cable and from 50 mm (#5) to 35 mm (#6) for the bigger 48F cable.

Table 3. Mechanical properties of the test cables.

No.	Tensile force (N) at 0.4% cable strain	Crush resistance (N)	Impact strength (J)	Minimum bending radius (mm)	Temperature stability
#0	110	1500	>3	15	Fail
#1	180	1500	>3	40	Good
#2	180	2500	>4	25	Very good
#3	350	2500	>4	35	Not tested
#4	225	1700	>4	35	Good
#5	250	1500	>3	50	Not tested
#6	325	1500	>4	35	Very good

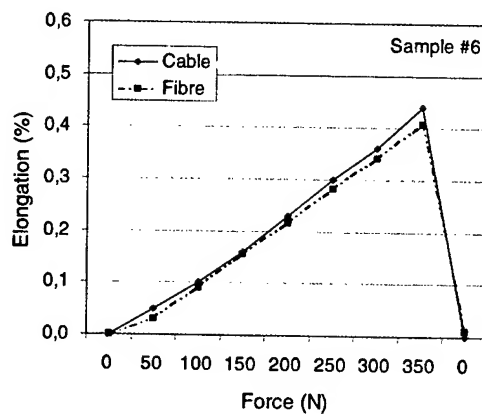
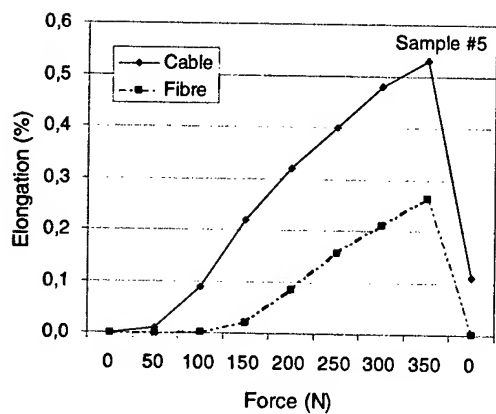
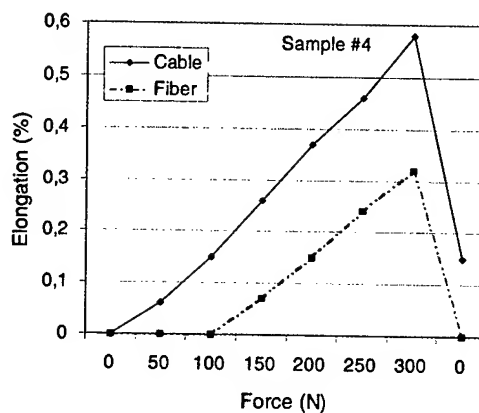
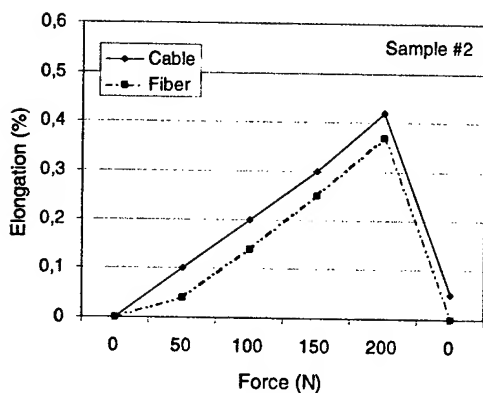
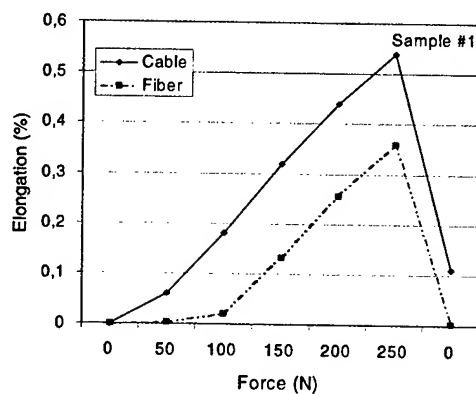
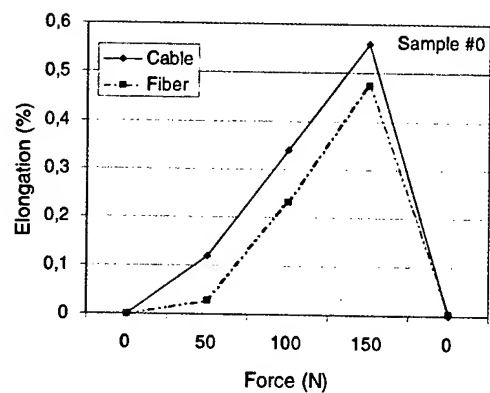


Figure 2. Cable and fiber elongation vs. tensile force for some test cables (see text and Table 2).

When comparing the reinforced cables (#1-#6) with the reference (#0) we can notice an evident rise of tensile properties by a factor from 2 up to 5 depending on the cross sectional area of LCP used (changes in total cross sectional area are considered). The effects on crush resistance and impact strength were minor. The minimum bending radius increased, but thanks to the controlled fiber orientation (Figure 3) it stayed however at a reasonable level (8 to 12 times the cable diameter) meeting the requirements. It should be noticed that the unreinforced reference sample did not meet the performance of a real cable, as will be discussed below.



Figure 3. Helical orientation of the LCP layer (optical micrograph, longitudinal cut).

5.3 Temperature Stability

Like in tensile tests the fiber density and EFL had a great impact also on the temperature stability of the cables. When the packing density is high i.e. the diameter of the fiber bundle close to the inside diameter of the tube and the EFL is positive, the fibers are forced to take a tortuous path inside the tube. This creates tight turns and small bending radii for the fibers. When the cable is brought to lower temperatures there always occurs unavoidable contraction, growth of EFL, further bending of the fibers and finally attenuation losses induced by macro-bending. The differences of the behavior of samples in Figure 4 can be mainly explained by different EFL level of the tested cables. As expected, the unstabilized reference cable (sample # 0) failed totally, owing to the relaxation and higher coefficient of thermal expansion of the normal engineering polymers. This happened even though the packing density was not very high (12F in a tube with 2mm inner diameter) and the EFL reasonably low (about 0.1%). In that respect the samples stabilized with LCP showed their superiority. Samples #1 and 2 with the same packing density withstood harsh temperature cycling between +80 and -60°C rather well. Even the compact cable with dense packing of 24 fibers and unnecessary high EFL (Sample #4) showed still tolerable results. In general the attenuation increase in the cables stabilized with LCP seems to correlate rather with high EFL than anything else. As a summary

we can say that LCP's capability to stabilize these lightweight, compact cables is far more remarkable than its reinforcing ability, not to neglect the latter either.

5.4 Moisture Barrier

The moisture barrier properties of the LCP material were studied separately on tube-like samples made especially for that test. The aim was to evaluate the moisture penetration rate of coextruded four-layer tubes consisting of PBT, LCP, adhesive polymer, and PA12 (outermost). Reference tubes were made, in which high-density polyethylene (HDPE) was used instead of LCP. HDPE is known as rather effective barrier against moisture penetration.

A test method for determining the water permeability of the cable sheath according to telecommunication cable specification KK 70-163 (NKF, internal method) was applied. In the test dry nitrogen gas was transferred through the cable sample immersed in a water bath. The moisture content was measured from outcoming nitrogen with a coulometric hygrometer and translated into the Water Vapor Permeation Rate (WVPR). Samples with a length of 2 m were kept in the water bath (60 °C) for 24 h according to the test procedure. Table 4 shows the results of two parallel measurements for each sample and the outer diameter and layer thicknesses of the corresponding tubes.

Since no moisture could penetrate the sample containing LCP during the normal test period (24 h), the test was extended first to 48 h and finally up to 168 h (one week). This result indicates that the LCP layer forms an effective moisture barrier and can give thus moisture protection to optical fibers in such non-metallic lightweight cables discussed above.

Table 4. Water vapor permeation rate (WVPR) results for four-layer test tubes.

Thickness of layers (mm)				d	WVPR
1. PA12	2. adh.	3.	4. PBT	(mm)	g/100m/week
0.45	0.17	0.21 HDPE	0.55	8.3	0.0017 0.0019
0.28	0.23	0.45 HDPE	0.40	9.6	0.0015 0.0015
0.32	0.22	0.41 LCP	0.44	7.1	0/0 (48h) 0 (168h)

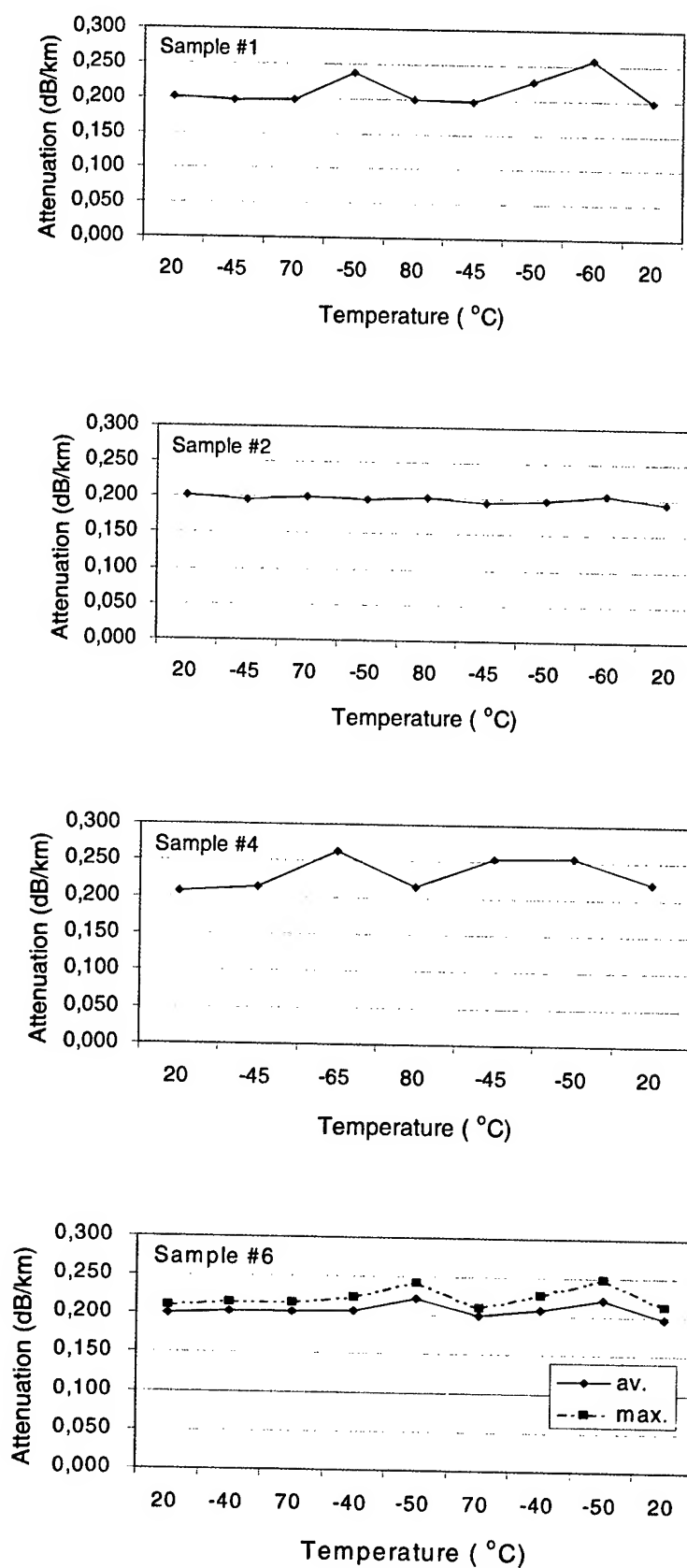


Figure 4. Attenuation vs. temperature during temperature cycling for test cables #1, 2, 4, and 6.

6. Other Cable Applications

Besides the described and tested designs intended mainly for applications in access networks the same principle of multilayer process with controlled orientation can be utilized for other applications as well. By changing the outer layer material to meet the designated use, several other installation objects and methods can be reached. Naturally, thanks to their compactness and small size most of the described cable designs can be used also as modules in bigger cables. Both central loose tube and stranded cables are possible whenever some of the above mentioned properties are needed in a non-metallic application. The basic structure, the lightweight cable, or module, gives also certain benefits in heavy and rough further cabling processes, like in optical ground wires and submarine cables, just to mention a few. No extra processing aids or reinforcements are needed because the structure itself is mechanically relatively strong and thermally stable. Likewise, additional protecting or buffering tapes or laminates can be replaced by a suitable polymeric layers in the multilayer extrusion itself.

7. Conclusions

Non-metallic, lightweight fiber optic cables with high fiber density have been developed based on coextruded multilayer constructions. In this study, particular attention was paid to the processing of the liquid crystalline polymer (LCP) which was used as the stabilizing layer for the cables. Rotating tools utilised with the cone extruder made it possible to control the orientation of the LCP fibers. As a result lamellar, well-fibrillated LCP layers were created with helical to axial orientation.

The compact cables with controlled orientation showed balanced mechanical properties and good temperature stability evidenced by tensile, crush, impact and bending tests, and temperature cycling. Since the LCP layers applied were rather thin, the tensile properties were not as high as targeted for the 48-fiber cables. Temperature stability, in turn, was good for both the 24- and 48-fiber cables with high fiber density. This allowed us to make these constructions even smaller than planned. As the properties of the studied test cables were well predictable, it seems possible to develop similar constructions with higher fiber counts (60F/72F) with cable outer diameters about 5 mm / 5.5 mm and to withstand tensions about 400N / 500N, respectively.

When comparing these compact cables with a conventional compact stranded loose tube cable presented earlier [9], the stranded cable has, of course, superior tensile strength due to a sizeable FRP strength member and the stranded structure itself. The benefits of the compact cables are however clear: about 50% reduction in diameter and weight, less processing steps and longer production lengths thanks to the smaller size.

The novel constructions have potential for several applications, also besides the aimed access and premises networks.

8. Acknowledgements

The authors wish to thank the innovative operators of the Conex line, Hannu Kleemola and Seppo Järvinen for all their help in the development work. In addition, we thank Johannes Ruotanen for his invaluable contribution in measuring and testing the cable samples.

9. References

- [1] M. Heino, J. Ravela, M. Suvanto, R. Phillips, and T. Vainio, "Novel Non-Metallic Multilayer Fiber Optic Cables Based on Cone Extrusion Process", *48th International Wire and Cable Symposium*, Atlantic City, USA, 385-392 (1999).
- [2] W. Griffioen, A. van Wingerden, and C. van't Hul, "Versatile Outside Plant Solution for Optical Access Networks", *48th International Wire and Cable Symposium*, Atlantic City, USA, 152-156 (1999).
- [3] C. Carfagna, ed., *Liquid Crystalline Polymers*, Elsevier Science Ltd., Oxford, England (1993).
- [4] M. Heino, "Blends of Thermotropic Main-Chain Liquid Crystalline Polymers and Thermoplastics", *Acta Polytechnica Scandinavica, Chemical Technology and Metallurgy Series No. 220* (1994).
- [5] K. Valta, S. Syrjälä, M. Karttunen, R. Phillips, and K. Kirjavainen, "Cone Extruder: Novel Method For Multilayer Extrusions", *Plastics, Rubber and Composites Processing and Applications*, 27 (9), 400-406 (1998).
- [6] U. Hochstrasser, R. Phillips, and C. Petit, "Conex: A Revolutionary Concept for Improved Multilayer Extrusion", *Wire Industry*, 66 (783), 187-190 (1999).
- [7] A. Sarioglu and J.-A.E. Månson, "Experimental Analysis of Fiber Orientation in Multilayer Tubes Extruded with a Conical Extruder", *Proceedings of PPS'18 Conference, The Polymer Processing Society*, Guimaraes, Portugal (June 2002).
- [8] IEC 60794-3-50 (Draft), Optical Fiber Cable, Part 3: Outdoor Cables, Section 50: "Family specification for miniaturised cables, fiber members and tube systems for installation by blowing", SC86A WG3 (Griffioen), (February, 2002).
- [9] M. Lahti, M. Heino, J. Ravela, and P. Lundström "High Speed Buffering Process of Compact Loose Tubes for Stranded Cables", *50th International Wire and Cable Symposium*, Orlando USA, 274-279 (2001).

Authors

Dr. Markku T. Heino

NK Cables
Draka Comteq
PO Box 419
FIN-00101 Helsinki
FINLAND
Tel. +358 10 5661
markku.heino@nkcables.fi



Markku Heino received the degree of M.Sc. in Chemical Engineering in 1990 and the degree of Dr. Tech. in Polymer Technology (Blends of Thermotropic Main-Chain Liquid Crystalline Polymers and Thermoplastics) in 1994 at Helsinki University of Technology, Finland. Before joining NK Cables (at that time Nokia Cables) in 1996 he worked as Research Scientist and Project Manager in the Laboratory of Polymer Technology at the HUT. Currently, as R&D Manager at NK Cables (Draka Comteq) his main responsibility is the Materials R&D.

Pertti E. Korhonen

NK Cables
Draka Comteq
PO Box 419
FIN-00101 Helsinki
FINLAND
Tel. +358 10 5661
pertti.korhonen@nkcables.fi



Pertti Korhonen has worked since sixties as Project Manager and Development Engineer at Nokia Cables (today NK Cables) for R&D, Production technology, Material and Process development. He has developed solutions e.g. for first high-speed telephone cable insulation lines, for our own factory and later for export of Nokia Machine Department (today Nextrom), as well as for rubber and plastic extrusion lines, process simulation programs of rubber crosslinking, super-steam crosslinking, etc. Now his main task is the Process development and test runs related to multilayer extrusion (Conex).

Jussi T. Ravela

NK Cables
Draka Comteq
PO Box 419
FIN-00101 Helsinki
FINLAND
Tel. +358 10 5661
jussi.ravela@nkcables.fi



Jussi Ravela received the degree of Engineer (B.Sc.) in 1973 from the Helsinki Polytechnic in Mechanical Engineering. He worked as Design Engineer at Nokia Cables, being engaged in the development of cable machinery, e.g. for manufacturing of optical fibers and their further processing. Since 1984 he worked in the area of Optical Fiber Cable Technology, first as a R&D Engineer then as a Design Manager focusing on materials, processing and cable designs. From year 2001 he has been working at NK Cables (Draka Comteq) as Technical Support Manager in Material Procurement, Supply Management.

Esa P. Virolainen

NK Cables
Draka Comteq
PO Box 269
FIN-90651 Oulu
FINLAND
Tel. +358 10 5661
esa.virolainen@nkcables.fi



Esa Virolainen received the degree of M.Sc. in Physical Chemistry in 2000 from the University of Oulu. He has worked since 1995 at NK Cables in the area of the Material Research and Information Processing. From June 2000 he has been working as a Chemist in the Material Laboratory at NK Cables, Oulu.

A NEW FILLING CONCEPT FOR IMPROVED OVERALL PERFORMANCE OF FIBER OPTIC CABLES

Börje Lindblom, Anders Björk and Måns Isacson

Ericsson Network Technologies AB, Hudiksvall, Sweden

Abstract

This paper demonstrates a new concept for optical cables with loose tubes, DryTech™. Instead of the traditionally used jelly as water blocking material, a foam-like thermoplastic elastomer (TPE-O) is used. The new concept gives a more user and environmental friendly cable, since the preparation and recycling of cables with the new concept is simpler and involves less use of solvents. Replacing jelly with TPE-O between the tubes also further supports the cable structure. This advantageous extra support can be used either to decrease the cable dimensions with maintained mechanical properties, or to enhance mechanical properties with maintained dimensions. In the work of developing the new concept, several cable designs have been evaluated. This includes cables for aerial, duct and direct burial installation. Field tests have been performed during the evaluation process. The conclusion from this work is that traditional jelly can be replaced with TPE-O as a filling compound for improved mechanical, manufacturing, handling and environmental properties.

Keywords

Optical cables, water blocking material, environmental friendly, mechanical properties, dry filling, loose tube design.

1. Introduction

In traditional concentric loose tube cables, filling compound (jelly) or swellable tape is used as longitudinal water blocking material. The jelly has an impact on the working and global environment. It is sticky and removing is easiest performed with some sort of solvent. Solvents evaporate and can be irritating when inhaled or in contact with the skin. Long term use can give more serious problems as for example eczema. For installers and test personnel who daily open and prepare cables it is of great interest to minimize the use of the solvent material and also the jelly. In material recycling of the cables the different materials have to be separated. Also in this process jelly filled cables must be cleaned with solvents.

In manufacturing of the cable types with jelly or swellable tape, the stranding and the sheathing are commonly performed in separate operations. One reason for this is that stranding is a relatively slow process and if an expensive multi operational line shall be economic it has to be relatively fast.

The stranding process is slower than the sheathing because that in a concentric loose tube cable the tubes have to be kept in place with yarn, spun with a relatively short pitch. Another reason that the traditional design is unsuitable for a multioperational line is the difficulty to stop the stranding process in order to change or splice yarns, tape etc. Stopping the process for these type of reasons is not an option if sheathing is performed in the same operation.

The main driving forces to develop a new dry filling concept were to get a more environmental and installation friendly cable and also to shorten the time to manufacture the products by performing the sheathing and stranding in the same process.

The conclusion from this work is that traditional jelly can be replaced with TPE-O as a filling compound for improved mechanical, manufacturing, handling and environmental properties.

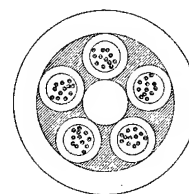


Figure 1. Schematic picture of cable. Dry filled area is hatched.

2. Materials and Process

2.1 Materials

2.1.1 TPE-O

The material used instead of jelly is a Thermo Plastic Elastomer - Olefin based (TPE-O). It is a low density compound with a density below 0.9 g/cm^3 . Significant for TPE is that the material contains hard segments (crystals) to "cross-link" the molecules and soft segments to make the material elastomeric. The hardness of the material increases with the number hard segments. The difference between an ordinary rubber material and the TPE is that the "hard segments" mechanically cross-links the TPE and therefore it can be melted and remelted. The following properties of the TPE-O further make it suitable as a dry filling material.

- *Foamability and high melt flow rate:* TPE-O has a molecule structure that makes it suitable to foam. It also easily fills the interstices in the cable because of its high melt flow rate, which gives the good water blocking characteristics.
- *Adhesion:* TPE-O is olefin based which gives good adhesion to other olefins. The material used in this dry filling concept has a lower melting point than the sheath material, polyethylene, which makes the two materials to weld, in the sheathing process. Consequently, the TPE-O will then easily be removed together with the cable sheath. The loose tubes are then exposed and ready for further preparation.
- *Mechanical properties:* Foamed TPE-O is relatively soft and distributes compressive loads, which protects the loose tubes. It is also easy to tear, which further simplifies the cable preparation (see section 4 below).
- *Environmental impact:* The material does not contain any hazardous substances. It can be compared to Polyethylene in respect of environmental impact.

2.1.2 Foaming agent

The foaming agent is a hydrocarbon gas encapsulated in small polymer spheres. When the temperature is increased the spheres soften and the gas expands with at maximum 40 times volume increase. This gives a controlled and predictable foaming process and a closed cell structure, which is important for the water blocking properties.

2.2 Process

With the new dry filling concept the stranding, filling and sheathing are made in the same operation. This can be performed since the filling material is used to keep the tubes in the SZ position and therefore no yarns etc are needed. The foaming agent is added to get the dry filling material to foam with a 50 % volume increase.

3. Developed Products

The new dry filling concept is used in loose tube cables, where the TPE-O has replaced jelly to fill the interstices between the tubes. It can also be used in dielectric cables for direct burial applications, in which the TPE-O is used between the inner and outer sheaths. In this design it replaces the traditional corrugated steel tape and protects the cable from radial crush and impact loads. The concept is also ideal in an aerial cable. Thinner tubes can be used with same mechanical characteristics as a standard cable, due to the TPE-O. As a consequence it is possible to have smaller cables with the same performance. Smaller dimensions and lighter cable weights gives less exposure to wind and ice loads. In developing the new concept the following constructions have been developed and evaluated:

- *Loose tube in one layer (Fig. 2a):* The duct cable with loose tube design contains up to 16 tubes in one layer stranded around a central strength member. All interstices in the cable core are filled with TPE-O and the cable is therefore longitudinally watertight.
- *Loose tube in two layers (Fig. 2b):* The duct cable with two layers loose tubes contains up to 16 tubes in the outer layer and 10 tubes in the inner. Using 12 fiber tubes the maximum fiber count is 312 fibers. A PE sheath separates the tube layers.
- *Loose tube with TPE-O armoring between inner and outer sheath (Fig. 2c):* In the direct burial cable, TPE-O is used in the interstices in cable core and as cushioning between inner and outer sheath. It is designed to be installed in macadam along railways. The cable is longitudinal watertight, also between inner and outer sheath. The material in the outer sheath is High Density Polyethylene.
- *Aerial loose tube with aramid yarn and TPE-O filling (Fig. 2d):* The aerial cable contains loose tubes and TPE-O in the cable core, surrounded by aramid yarns and an outer sheath of Polyethylene. The concept is ideal in an aerial cable. Thinner tubes can be used with the same mechanical characteristics as a standard cable, due to the enhanced mechanical properties with the TPE-O. As a consequence it is possible to have smaller cables with maintained mechanical performance. Smaller dimensions and lighter cable weight gives less exposure to wind and ice loads. Reduced tensile loads also results in reduced compressive loads in the cable fittings. Another advantage in an aerial cable is that the TPE-O locks the tubes in the SZ-shape, even when the cable is exposed to heavy loads.

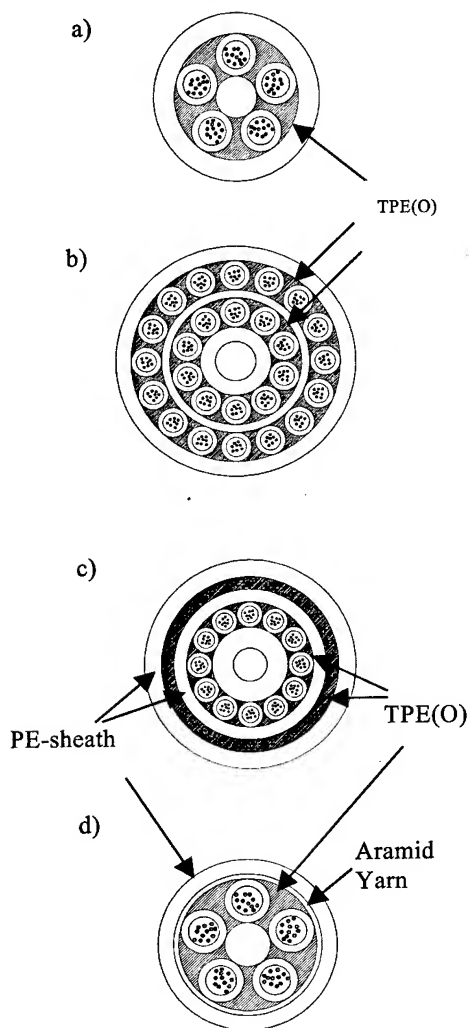


Figure 2; Developed cable constructions, a) One layer loose tube, b) Two layer loose tube, c) Loose tube with TPE-O armoring, d) Aerial

4. Tests and Results

4.1 General

All the developed cable constructions described in section 3, developed products, have been manufactured tested and installed. The tests have been general type testing including the tests described for the cables in the next section. All designs passed qualification, with respect to its design requirements. During these tests the enhanced mechanical performance was verified, when compared to traditionally jelly filled cables with similar design. In order to get a more precise estimate of how much more crush load a design with TPE-O can withstand, compared to the jelly filled, it was necessary to produce two nearly exact (only filling material differs) same designs. Otherwise the

number of fibers and tubes, sheath thickness etc can affect the results. The tests are described in the sections below.

4.2 Test Cables

Two 48 fiber loose tube test cables, same type as in Fig. 2a were produced. The only difference between the cables was that Cable no. 1 was filled with a Polybutene based jelly and Cable no. 2 with TPE-O.

The cables were developed to meet the requirements in accordance with table 1.

Table 1; Requirements for test cables

Tensile load (permanent)	[kN]	≥ 1.5
Tensile load (temporary)	[kN]	≥ 2.5
Crush resistance (100 mm plate)	[kN]	≥ 1.5
Impact resistance	[J]	≥ 25
Min bending radius	[mm]	≥ 150
Water penetration, 24 hours	[m]	≤ 3
Torsion	[°/m]	≥ 360
Repeated bend	[cycles]	1000
Temperature, operating	[°C]	-40 to +70

The cables were tested according to the international standard IEC 60794-1 and the European EN 187 000.

4.3 Crush test

In the crush test a plate with a diameter of 100 mm was used and the cables were exposed to increasing compressive loads until a significant attenuation could be observed. The test was repeated 20 times per cable and the attenuation at the wavelength 1550 nm was measured.

Cable no. 1 withstood an average load of 1.73 kN and Cable no. 2 an average load of 2.86 kN. Figure 3 shows the number of samples that failed at each load in the test.

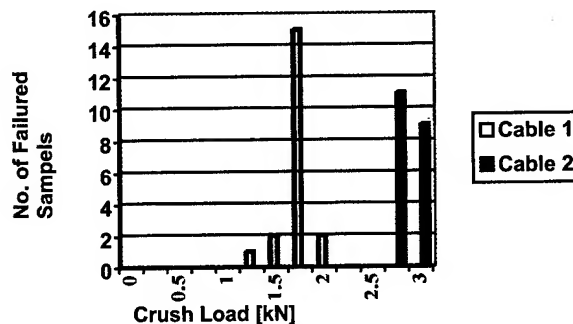


Figure 3; Number of failed samples versus crush load for the tested cables.

4.4 Other mechanical and environmental tests

The other tests performed on the cables are outlined in Table 1. These tests showed no significant difference between cable no. 1 and no. 2.

Table 2; Mechanical and environmental tests performed on the cables.

Parameter	Cable 1	Cable 2
Tensile load (permanent)	Passed	Passed
Tensile load (temporary)	Passed	Passed
Impact resistance	Passed	Passed
Min bending radius	Passed	Passed
Water penetration, 24 hours	Passed	Passed
Torsion	Passed	Passed
Repeated bend	Passed	Passed
Temperature, operating	Passed	Passed

4.5 Cable Handling

4.5.1 Preparation of cables with TPE-O filling

The cables with TPE-O filling is opened easily by cutting longitudinally on both sides of the cable and pulling the halves of the sheath apart. Figs 4 and 5 show how this has been performed on a one and a two layer loose tube design respectively. It can also be seen how the foamed TPE-O is still attached to the outer sheath and that the tubes are exposed and ready for further preparation.

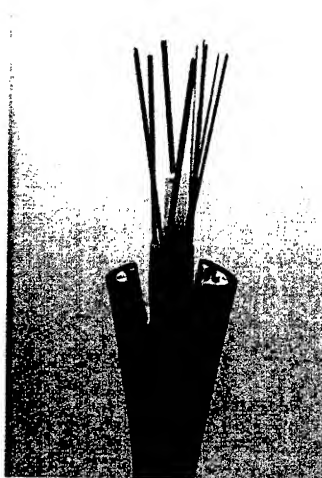


Figure 4; Opened one layer loose tube design



Figure 5; Opened two layer loose tube design

4.5.2 Comparison of preparation time

A test was performed to compare the time difference between preparing cables with traditional jelly and TPE-O, during field installation and splicing. The same cables (section 4.2) as for the mechanical and environmental tests were used. The test included removal of the outer sheath 1800 mm, and separation and cleaning of the tubes. Commercially available cable installation tools were used for the tests. The results are shown in Table 3, below.

Table 3; Measured preparation time for the different cable samples.

Cable type	Sample No.	Time
1	1	14.40 min
1	2	15.10 min
2	1	8.40 min
2	2	8.20 min

The test shows that there is a lot of time to be saved in preparation with the dry filling concept, compared to standard cables containing filling compound. The most time-consuming task for the traditional cable type is to remove the filling compound from the tubes. Cable 1 took in average 78 % more time to prepare. The relative impact on the total installation time depends clearly on the number of fibers to be spliced. For installation of low count fiber cables and in mid-span access operation (independent of fiber count in the cable) the time saving with the dry concept is significant.

5. Environmental Impact

5.1 Working environment

The working environment is improved both during manufacturing and installation when the dry filling concept is used, since the sticky jelly is difficult to handle and remove. The main advantage, with respect to working environment, with dry filling is that a minimum of solvent is needed to clean the cable in preparation, during installation or testing.

5.2 Environment

The environmental impact through pollution to the air will decrease, since the handling and use of solvent to remove the jelly is not necessary with the dry concept. There are several methods to take care of a used or scrapped optical cable. One alternative is energy recovery, i.e. combustion of the whole cable. In some combustion processes of hazardous waste an optical cable could be useful since the glass binds some hazardous chemical substances. Energy recovery works for all kind of optical cables, jelly filled and dry filled. Environmentally it is preferable with material recycling. Therefore the more of the cable that could be material recycled the better.

Today there are techniques to material recycle dry cable sheaths and energy recovers the rest of the cable. In the future it should be possible to material recycle more parts of the cable, for instance the strength member.

A requirement for material recycling is that the materials in a cable are easy to separate. In a dry filled cable it is easy to separate the materials and there is no need to clean the cable parts from sticky jelly. A jelly filled cable can be material recycled, but it is very costly and leads to environmental impact since the material must be cleaned with solvents.

6. Field Trials and Installations

In addition to the qualification program consisting of various standardized type tests, the new filling concept has also been tested and evaluated in field trials and "sharp" installations. The installations span over a wide range of field conditions from nearly arctic conditions in the north part of Sweden to very hot environments in Saudi Arabia. The main goals of these field trials have been to evaluate the handleability of the cables and to verify the new filling concept for different field conditions. The feed back from personnel working with the new concept in the field has been very positive in terms of handleability and working environment, as well as the overall performance of the cables. Examples of installations in terms of cable design, installation method, environment etc are presented in Table 4.

Table 4; Examples of installed cables/systems.

Country/ Year	Cable Design	Route length	Installation method	Network type
Sweden/ 1998	Loose tube TPE-O armoring. One layer, 24 SM- fibers. (Fig. 2a)	2 km	Direct burial	Transport
UK/2001	Loose tube 2-layer, 240 SM-fibers (Fig. 2b)	16 km	Pulling	Metro
Saudi Arabia/ 2001	Loose tube, TPE-O armoring 24 SM- fibers	90 km	Direct burial	Transport
UAE/ 2002	Loose tube One layer, 24 SM- fibers (Fig. 2a)	34 km	Pulling	Metro
New Zealand/ 2000	Loose tube 1-layer, 48 SM-fibers (Fig. 2a)	340 km	Pulling & Blowing	Transport

7. Conclusion

We have shown that traditional jelly can be replaced with TPE-O as a filling compound in loose tube cables for various applications. The new concept has proven superior to jelly filled cables in many respects because:

- It's more user and environmental friendly.
- Its faster to prepare for splicing, testing and mid-span access.
- Slippage between cable core and sheath is prevented and it locks SZ-laid tubes, with maintained pitch, even under high tensile loads. (These properties are especially important in aerial applications)
- It improves the crush resistance of the design (in average 60 % for the compared cables), which can be used to decrease the dimensions with maintained mechanical performance
- It allows the concentric loose tube cables to be stranded, filled and sheathed in the same process.

Therefore, the conclusion from this work is that: Traditional jelly can be replaced with TPE-O as a filling compound for improved mechanical, handling, manufacturing and environmental properties.

Acknowledgements

A special thanks to Bertil Olsson for his great contribution in developing the new concept. We also thank Anders T Ljung, Anders Lindroth and Maria Damberg for fruitful discussions and Per Ehrnholm for performing the testing of the cables.

AUTHORS



Börje Lindblom,
Ericsson Network Technologies AB,
S-824 82 Hudiksvall,
Sweden
borje.lindblom@eca.ericsson.se

Börje Lindblom received his degree in mechanical engineering in 1977 in Gävle. He joined Ericsson Network Technologies at 1977 and has worked with optical cable design and development since 1983



Anders Björk,
Ericsson Network Technologies AB,
S-824 82 Hudiksvall,
Sweden
Anders.bjork@eca.ericsson.se

Anders Björk, Manager of Product and Installation Solutions, joined Ericsson Network Technologies in 1989. He first did his technical work for his B.Sc. in Computer and Electronics, Gävle-Sandviken, Sweden. Since then he has been working with measuring techniques, type testing and development of fiber optic cables. During 1997 to 1998 he worked as Plant Manager for Opcom Cables in Kuala Lumpur, Malaysia. He is currently responsible for product and installation solutions.



Måns Isacsson,
Ericsson Network Technologies AB,
S-824 82 Hudiksvall,
Sweden
Mans.isacsson@eca.ericsson.se

Måns Isacsson, Manager of Optical Cable Development, received the degree of M. Sc. In Technical Physics in 1995 and the degree of Tech. Lic. in Fracture Mechanics in 1997, both from the Royal Institute of Technology, Sweden. He joined Ericsson Network Technologies in 1997. Previously he has been working with the mechanical aspects of Optical Fibers and the development of Fiber Optic Submarine Cable Systems.

Qualification of Loose Tube fiber Optic Cables with Reduced Weight and Diameter

Richard G. Gravely
OFS BrightWave Carrollton
Carrollton, GA

+1-770-838-5289 · richard.gravely@ofsbwc.com

Abstract

The telecom industry has expanded into multiple new applications and revenue generating opportunities that require, or would benefit from, low diameter optical cables. Not to mention that smaller cables are generally easier to handle and afford lower bending diameters for confined spaces. One such scenario where cable diameter is of primary consideration is duct applications where duct space is leased to the user. It is important to these customers to secure fiber optic cables with small diameters in an effort to reduce installation and ongoing system costs. The features of this novel construction are very attractive to the customer. Lower cable bend diameters allow more flexibility in cable slack storage locations and longer continuous lengths help reduce the number of splice locations within a route.

This presentation will cover the following qualification data:

- Qualification results showing compliance to Telcordia GR-20
- Qualification results showing compliance to RUS PE-90
- Qualification results showing performance of a field trial

The cable diameters have been reduced by 8 to 24% depending on cable construction. Graphs showing cable diameter and weight reductions will be presented.

Keywords

Telcordia GR-20, RUS PE-90, reduced diameter

1. Introduction

Reduced diameter cables are very attractive in many applications, especially in the local access, metro and trunk networks. Additionally, the possibility of using existing Rights of Way is also an important issue where lower diameter cables are especially attractive. For these, and other, applications, the cable must be highly robust and maintain environmental and mechanical performance levels suitable for outside plant use. For these reasons, the cable designs being introduced/discussed here have two primary design inputs for the North American Region:

- Reduced Diameter and Weight
- Telcordia GR-20 mechanical and environmental performance

Section 2 presents the characteristics and parameters that must be considered when designing a reduced diameter loose tube optical cable. Section 3 presents the configurations available in the reduced diameter loose tube cable. This section will illustrate the diameter and weight reductions when compared with traditionally designed and commercially available loose tube cables. Qualification test data per Telcordia GR-20 and RUS PE-90 will be presented in section 4 to illustrate full compliance to the NAR accepted industry standards. Section 5 presents information regarding a field trial installation in California. Section 6 discusses on going work and finally, section 7 presents our conclusions.

2. Design Considerations

The loose tube optical cable design is comprised of individual fibers that are contained within buffer tubes that are ROL stranded about a central strength element to form the core of the cable. Typically, sheath strength elements in the form of aramid or fiberglass yarns are helically applied about the core to provide additional tensile strength. Multiple sheathing configurations can then be applied to produce Single Jacket, Armored, LAP, etc. constructions. Generally speaking, sheath treatment parameters and dimensions have previously been minimized. For example, as process capabilities have improved, cable jacket thickness has been consistently reduced over the years to minimize material usage thus saving costs and reducing cable overall diameters. Additionally, corrugated steel armoring and LAP (Laminated Aluminum) dimensions have been minimized in an effort to reduce costs and cable diameters while maintaining functionality.

Essentially, the core of a loose tube cable is one of the primary sub-elements that can be manipulated to further reduce cable diameters. However, the core of the cable contains the optical fibers and great care must be taken when considering dimensional changes and/or material changes. The buffer tubes in traditional loose tube optical cables for the North American Region measure at either 2.5mm or 3.0mm outer diameter depending on the number of fibers that are contained therein. Material stability under mechanical and environmental influences is of utmost importance as the buffer tubes provide the first line of protection for the optical fibers.

The central strength element is also a consideration for dimensional reduction. The diameter of the central strength member is defined by the geometry of the buffer tubes, and the number of, stranded about it. Care must be taken in this

area to ensure that the central strength member is of sufficient size to maintain anti-buckling performance at low temperature extremes. The combination of reduced tube and central strength element dimensions must be carefully evaluated for mechanical stability. This has been achieved and a reduced diameter loose tube product line has been released that maintains GR-20 levels of mechanical and environmental performance.

3. Design Options

Currently, the reduced diameter loose tube cable is available in the following configurations to support duct, direct buried and self-supporting applications:

- All Dielectric Single Jacket
- Light Armored (Single Jacket, Single Armored)
- Armored (Double Jacket, Single Armor)
- ADSS Self-Supporting for short length drop applications

All cable constructions are designed to meet Telcordia GR-20 specifications. This design criteria has been established primarily to support existing NAR requirements. Design inputs for blown applications as well as regions outside the NAR region are currently under consideration for potential new product introductions that take advantage of requirements less stringent than those of GR-20.

The duct and direct buried configurations have also been tested per the RUS PE-90 specification and have subsequently been listed by the RUS.

The ADSS construction is designed for span lengths up to 300 feet under NESC Medium loading conditions. The ADSS cable is designed so that there is no axial fiber strain at the Maximum Rated Cable Load (MRCL) of 460 lbs. The ADSS cable can also be utilized in duct applications or aerial to duct transitions with a 600 lb rated short-term duct installation load. Upon release of the 600 lb load, any increase in attenuation of the fibers returns to zero.

There has been significant reduction of the cable diameter when manipulating the core configuration. The following table shows the diameter and weight reductions, in percentages, when compared to traditional loose tube configurations.

Table 1: Cable Diameter / Weight percent reduction compared to traditional construction.

	5 elements	6 elements
Single Jacket	11 / 18	12 / 24
Light Armor	10 / 12	12 / 19
Armored	8 / 13	10 / 17
ADSS	24 / 42	NA

The significant reduction in cable diameter and cable weight makes for easier handling. The diameter reduction allows longer continuous lengths on smaller reels, a significant advantage for customers. Many customers, or installation teams, have limitations on the size of a reel that can be handled. The large 96" (2.4m) reels are sometimes very difficult to handle and many installations require a

considerably smaller reel. It is our experience that a 60" (1.5m) reel size is a maximum reel size required by multiple customers. Based on this reel size limitation, the reduced diameter cables can offer longer continuous lengths per reel. This is a distinct advantage for minimizing splice points in a route. The following table shows the percentage increase in maximum continuous lengths of cables that can be wound on a US standard 60" reel.

Table 2: Percent increase in cable continuous length on 1.5m reel

	5 elements	6 elements
Single Jacket	26%	28%
Light Armor	23%	30%
Armored	19%	22%
ADSS	68%	NA

4. Qualification Results

All cables have been subjected to the mechanical and environmental test procedures and requirements of Telcordia GR-20. The cables designed for duct and direct buried have also been tested per RUS PE-90, the data package submitted, and subsequent official listing by the RUS.

All testing shows excellent performance verifying the robustness of the configurations. The ADSS product has been tested to ensure that there is no fiber strain at the MRCL. The following table summarizes the test results for each configuration.

Table 3. GR-20 & RUS PE-90 Qualification Results

Test Parameter	Requirement	Result
Jacket Adhesion	14.0 N/mm min. between outer jacket and steel armor	25.92 – 58.26 N/mm.
High & Low Temp. Bend	4 hours @ -30°C & +60°C, 20x OD bend	Max. change: 0.04 dB. No damage
Test Parameter	Requirement	Result
Impact Resistance	25 impacts, 30 cycles/min. Impact mass per cable OD	GR-20: Max. change: 0.02 dB. PE-90: Max change: 0.07 dB. No damage.
Compressive Strength	Non-Armored: Incidental load: 220N. Long term load: 110N. Armored: Incidental load: 440N. Long term load: 220N.	Max. change: 0.05dB at incidental load.
Tensile Strength	(a) Fiber strain less than 60% of proof strain (0.60%) @ rated install load (600lbs) (b) At load, 360° twist within 3 meters, no armor	(a) Max. fiber strain: 0.098%. (b) Max atten.

	zippering or jacket splitting. (c) At 30% of install load (180lbs), fiber strain < 20% of proof strain and fiber shall not exceed allowable attenuation change.	change: 0.03 dB. (c) Max fiber strain: 0%. Max atten. change: 0.0 dB.
Cable Twist	2 meter max. sample, 10 cycles, 180° CW twist, 360° CCW twist, 180° CW twist.	Max. atten. change: 0.02 dB. No mechanical damage.
Cyclic Flex	25 flex cycles, 20x OD, 30 cycles/min.	Max. atten. change: 0.02 dB. No mechanical damage.
Temp. Cycle	-40°C to +70°C extremes.	Avg: 0.04 dB. Max: 0.13 dB.
Aging	85°C, 168 hrs.	Avg: 0.03 dB. Max: 0.06 dB.
Buffer Tube Shrink-back	RUS PE-90. Shrinkback < 5%	All samples < 5%.
Buffer Tube cold bend	RUS PE-90. -20°C, Mandrel OD < 5x tube OD, 10 wraps	No damage.
Cold Impact	RUS PE-90. 4 N-m impact, -20°C.	No damage.

As the industry develops new lower cost materials and smaller dimensions for fiber optic cable, maintaining GR-20 and RUS PE-90 levels of mechanical and environmental performance becomes more difficult. Our ability to maintain sound compressive performance in the reduced diameter cables can be primarily contributed to the robustness of the PBT buffer tubes. Current alternative materials for buffer tubes, although generally a bit more flexible, experience difficulties maintaining mechanical crush resistance to the levels that can be achieved with PBT.

5. Field Trial

In January, 2002, a 144 fiber Single Jacket low diameter cable was installed in Oakland California. The low diameter cable was necessary to support installation of the cable within conduit measuring a ¾" (19mm) ID. At an 85% fill ratio, the customer required a cable diameter of 0.64" (16.25mm) or less. The product provided has a diameter of 13.4mm, which met the customer requirement and ultimately improved the installation performance by offering a fill ratio of 70%. A typical commercially available 144-fiber loose tube cable has a diameter of 0.74" (18.8mm).

A pulling grip was installed in the field and a 2500 ft (762 m) section of cable was easily installed within the ¾" conduit. The balance of the cable was installed in a 1-¼" conduit. The configuration of the route required considerable handling of the cable whereby the product was placed in a Figure-8 configuration for pulling in multiple sections. This was specifically required based on the pulling/installation configuration and not related to the cable product. The cable's flexibility and ease of handling made this operation user friendly and improved the speed and efficiency of installation. During the entire installation, the tensions measured never exceeded 200 lbs (890N). This can be attributed to the length of cable installation as well as the low fill ratio.

An additional benefit seen by the installation team was the reduction in volume of tube filling compound. There is less filling compound to clean which resulted in a slight improvement to fiber access time.

All fibers were measured optically after the installation with no change relative to the values measured at the factory.

6. On going work

1. These concepts are being applied to all other products within the loose tube portfolio.
2. We expect to expand upon these concepts to introduce application specific products. These application specific products, blown cables for example, will be designed to meet the conditions of the application. Where lower tensile strength cables can be employed or applications for temperature extremes that do not go to -40°C, products with further reduced diameters and weights can be established.
3. With decreased buffer tube sizing comes improved potential for a completely dry loose tube configuration. Work is being done to develop a water blocked buffer tube free of gels. Control of the buffering process and fiber to tube excess length are the primary considerations. The smaller tube design results in a smaller area requiring water blocking super absorbents.

7. Conclusion

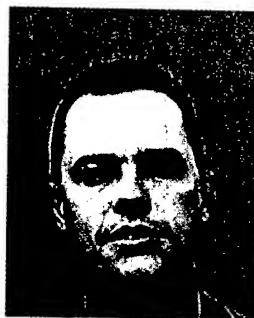
A reduced diameter loose tube product has been developed that maintains very high levels of mechanical and environmental performance. The product supports GR-20 and RUS PE-90 requirements while reducing product diameters from 8 to 24 percent depending on configuration. The bending performance of these products is rated at 10 times the cable diameter in static conditions and 15 times the cable diameter in dynamic conditions, producing some of the lowest bend diameters available for loose tube cables. The features of the product, lower diameter, improved flexibility, longer continuous lengths, easier handling, etc. make this product line an attractive solution for many applications. This has been achieved without reducing cable performance, making the product a simple transition for the user.

Continued work is ongoing to transfer this concept into all existing products. There is an effort to develop applications specific products that offer the customer an advantageous solution.

We are pursuing the potential to develop a completely dry loose tube cable in an effort to completely eliminate the need for solvents to clean the compounds. We believe that the reduction in tube diameter, and thus the reduction in free space, will allow the development of this product.

8. Author

Richard G. Gravely
One BrightWave Blvd.
Carrollton, GA 30117



Richard G. Gravely is the Product Manager for OFS BrightWave Carrollton in Carrollton Georgia. His responsibilities include product developments for optical fiber and apparatus. Richard received a B.S.E.E degree from North Carolina State University in 1991. From 1992 through 1995, Richard was a loose tube cable design engineer before coming to OFS BrightWave Carrollton. He has been serving as the Product Manager for the last 3 years.

Optical Fiber Connections Through Existing Sewers and Natural Gas Pipes

Dr. Jey K. Jeyapalan, P.E.

Engineering Consultant

New Milford, Connecticut, USA

1-860-354-7299 jkneyapalan@earthlink.net

ABSTRACT

Deployment of metro optical fiber networks requires extensive construction, usually involving excavation of city streets. These excavations cause pollution, traffic hold-ups, economic loss, and unsafe conditions to the inhabitants in every city. Even worse, the repair of the streets after excavation rarely left the streets in acceptable condition. These forced mayors to issue moratoriums on new open cut excavations involved in the last mile work. Leasing space inside of existing sewers, water pipes, and natural gas pipes by either private telcos or utility owned telcos has a rather interesting appeal in that owners of existing sewers and gas pipes get to generate a new revenue stream and telcos could install their optical fiber cables at an attractive cost. However, the fiber companies have to recognize that these utilities are the result of substantial public investment running into trillions of dollars combined with over 100 years of engineering advances and the owners of these pipes have to keep proper functioning of these pipes for originally intended functions first at heart at all times. If proper standard of care is not practiced, it is only a matter of time until major problems will manifest and the token pipe lease fee paid by a fiber installer to the owners of these pipes will amount to nothing compared to the cost the public will have to bear to return the sewers back to normal. This paper provides a detailed account of the track record in this field around the world of most deployments to date, and the engineering lessons learned. This paper also presents an account of progress made to date in standardization work for this new industry. This paper provides an overview of various technologies, and makes an open invitation to those qualified engineers and scientists in the global market to submit their valuable input toward preparing engineering guidelines with ASCE sponsorship and consensus standards within ASTM International.

Keywords: sewers; gas pipes; trenchless; optical fibers; robots; no-dig; last mile; liners

INTRODUCTION

More than 110 million North Americans are expected to telecommute to work by 2010. This will increase our productivity and quality of life significantly. This will also save energy, reduce pollution, and re-distribute the wealth and real estate values. For this to happen, we could turn to existing underground infrastructure to build our communication networks, so that we can avoid additional congestion underground. North America already has invested many trillions of dollars in the past century building over 2,000,000 km of sewers in the ground. An additional over 1,000,000 km of natural gas pipes come into our homes and businesses. Civil engineers have been responsible for planning, designing, constructing, operating, and maintaining this vast network of pipes below our feet. Civil engineers need to start

planning now toward working more closely with telecommunication engineers in making the information age come into full bloom so that any obstacles can be removed with the team approach. This will involve sharing the underground so that the same gas pipes and sewers are used for multiple functions. The absence of local optical fiber broadband loops in the last mile also impedes the optical Internet and indeed is a major contributing factor to the slowdown in the telecommunications industry. Copeland and Malik [7] reported that without widespread high-speed Internet access, the technology industry and the economy would remain stalled. Wall Street Journal also wrote several times on this subject and an example is in [46]. Kennedy [32] asserts that the utilities are well positioned to solve the last mile problems than any other players due to the fact that they have the ability and incentive to invest in a high-capital cost, low-return access network. Additional details on the win-win solutions from the business plans involving optical fiber deployment in existing sewers have been discussed in more detail in Jeyapalan [17 to 30].

INFORMATION SUPERHIGHWAYS TO WHERE?

The optical fiber industry has kept its pace of inventing better fibers and DWDM equipment. For example, Hecht [12] reports that Alcatel and NEC independently have squeezed more than 10 trillion bits per sec through a single strand of fiber. This capacity translates to carrying over 150 million telephone calls simultaneously in a strand that measures less than 7 microns in diameter or less than 7 % of the thickness of the human hair. Despite these major advances, an optical fiber network is only as fast as its weakest link. In recent years, and still today, many companies are laying optical fiber cable between continents, countries and cities. In America, over 400,000 km of fiber cables are in the ground. Even building owners have started laying fiber from their rooftop to basement; however, the missing link is still the last mile of route length as short as 10 m or as long as a few km. While the entire telecom is in chaos, everyone in this industry should ask the fundamental question: "where are the on and off ramps to the information superhighway most companies have been building for 2 decades in optical fiber cables?" The answer is "these do not exist to and from more than 97% of the commercial real estate all across America and the picture is even more dismal for multiple tenant units and single family homes. Naturally these information superhighways with their limited points of origin with a similar tale at the other end would remain empty with no one willing to pay the toll to the owners of such long haul networks. These limitations result in a mere 10% of the long haul fiber being lit. Given how we humans always take the path of least resistance have avoided bridging the last mile, which would be the hardest and the costliest, without ever realizing that without the ultimate on and off ramps, there would be no use for such long haul routes circling the continents. The so-called fiber

glut in the backbone and long haul fiber networks is mostly due to the lack of last mile fiber to provide the final link between the premises and the long haul carriers of data, voice, and video. It is important to recognize that the optical fiber technology still has to compete against other last mile technologies such as wireless, satellite, line of sight air fiber, various chipsets on copper plants, and other. If the optical fiber technology could be rolled out at a faster pace, with less hurdles in rights of way acquisition, and at a lower cost, then end to end optical fiber connectivity could win this race in the coming years in the last mile.

THIS IDEA HAS BEEN AROUND SINCE 1983

Using existing conduits for multiple uses is not a new concept. Early attempts were in Paris more than 100 years ago but poor results led to abandonment of the concept of installing multiple utilities in the same underground tunnels. The innovative idea of using existing fluid conduits for additional functions not originally intended, emerged again in 1983 when Jeyapalan et al. [14, 15, 16] designed 2 high pressure hydropower penstocks of size 2144 mm (84 inch) in diameter to hang from the roofs of 6.4m(21 ft) diameter outlet tunnels at Jennings Randolph and Gathright dams in West Virginia and Virginia. These large penstocks were designed in 304L stainless steel to survive the acidic water with a pH of 3 or less flowing through the outlet tunnels. A series of hydraulic model tests were performed initially at Sogreah, Grenoble, France and then for convenience these models were moved to Alden Research Laboratory in Holden, Massachusetts. In these physical model tests, we simulated the flow conditions in the tunnel under various operating curves of the reservoir and forces acting on the penstocks were measured to ensure that the penstocks and their supporting anchors could be designed to carry the anticipated loadings on the penstock and the tunnel linings during the design life of 50 years. The impact of penstocks occupying some portion of the waterway in the tunnels was also studied in the model tests to ensure that the installation of the penstocks did not affect the originally intended functions of the existing tunnels. There were numerous unprecedented design features that were included in these designs to provide the client the lowest possible water-to-wire cost per kilowatt of the hydropower generated, all due to the fact that the dam and the tunnels were already there. The above scheme was also chosen to prevent any disputes with environmentalists so that the project implementation could be achieved in the shortest possible time without any unnecessary delays.

OPTICAL FIBER IN JAPANESE SEWERS

Shortly thereafter, the first invention for using existing sewers for installing communication cables was developed by a group of engineers from the Water Research Center (WRc) in UK [42]. A patent was issued by the UK patent office on 16 May 1984. Subsequently, the US patent No: 4,647,251 was secured on March 3, 1987 and the assignee was Cabletime Installations Limited operating out of Washington, DC. [43] For reasons unknown even to the current employees of WRc, this patent was allowed to expire due to nonpayment of annual dues after WRc attempting to commercialize this invention for some years. Japanese assembled a robot in 1987, following an art somewhat similar to that disclosed in the UK invention, to install optical fibers initially in Tokyo sewers [34], and the Japanese applied for European,

Japanese, Korean, and US patents. The US patent No: 4,822,211 was issued on April 18, 1989 with Nippon Hume, Tokyo Metro Government, and Tokyo Metro Sewer Service Corporation as co-assignees [44] to protect the robot.

The primary reason for the Japanese engineers to install optical fiber in their sewers in Tokyo in 1987 was to control sewage treatment plants remote without having to employ human power at each of these locations as given in Shinoda [39]. Tokyo Metro Government and Tokyo Metro Sewer Service Corporation promoted this concept as their SOFT plan widely and a sampling of such efforts is evident in [37, 41]. Subsequently, the Japanese engineers formed JSOFTA and promoted this technology for additional functions as reported in Fujiyoshi and Yoshikazu [9] and JSOFTA [31]. JSOFTA was also instrumental in changing the Japanese public law in 1996 for the sewer owners to permit materials other than sewage in their sewer system paving the way for a wider deployment of fiber in the sewer [13]. Tokyo Metro [40] alone has more than 850 km of fiber in the sewer, with about 140 km installed by these robots, more than any other city in the world.

According to Nippon Hume [35], the original robots had options to either be self-driven or operated by winches. Given most of the sewers in Japan were made of centrifugally cast reinforced concrete pipe, drilling into the pipe wall required significant amount of power through the umbilical cable supplying water, air, electricity, and communication circuits. According to Nippon Hume [35], when the Tokyo Metro discovered that it was better to conserve power, self-driven robots were not the preferred option. Nippon Hume began to promote this robot system for sewer sizes 200 to 1200 mm widely as shown in Nippon Hume [36]. Recently, the Japanese Ministry of Construction has also published a goal of building 100,000 km of optical fiber networks in existing sewers all over Japan by year 2010 toward promoting the Multi-Media Society as given in [13]. In America, the Technology Network has called on the federal government to adopt a goal of 100 megabits per second to 100 million homes and small businesses by 2010.

BERLIN USING NIPPON HUME ROBOTS

BerliKomm owned by Berlin Water had an ambitious plan in 1997, in that it would provide each customer in Berlin with a broadband connection within 30 days of asking. Berlin water turned to 3 Japanese robots sold by Nippon Hume initially by setting up a new company named Robotic Cabling GmbH Kabelverlegung (RCC) owned with Marubeni and Nippon Hume and installed about 1500 m of optical fibers in its own combined sewers in Berlin in the winter of 1998. The Japanese robots used by Berlin water came in 3 sizes with various undercarriages for pipes of 250-350 mm, 400-450 mm, and 500-1200mm. The robot was steered by a control unit but was not driven by its own power. Instead, they were pulled using winches through the manholes. A special drill was used to cut a hole 6 mm dia. 15 mm deep for the J-hook anchor of the cable with its 2 part resin system that hardens in the hole after activating the plunger pin once deployed after placing the optical fiber cable in the J-hook. Berlin Water as of January 2000 solely owns this business entity and has replaced the Japanese robots with those manufactured in Germany by JT Elektronik GmbH where 2 robots could work in pipes of 200 to 1200 mm, provided the right undercarriage is used. According to

Beyer [4] and Nippon Hume [35] Berlin water returned the two units of second-generation robots back to Nippon Hume, but kept the third unit of the first generation. A change from the version of the Japanese robots Berlin used is that the 3 units assembled in Berlin could propel it once inside the sewers, in a way no different from the robots Japanese had in their first generation for Tokyo Metro, installing the cable at speeds as high as 200 m/day under optimal conditions as given in [3, 4]. The Berlin drill and dowel anchor robot has eliminated the use of the 2 part resin bonding the Japanese system uses.

TRACK RECORD IN SEWERS

When Alcatel and IK-T needed a technology partner in 1996 to develop a new optical fiber deployment robot, Ka-te was their choice. This author estimates Ka-te, Nippon Hume, and RCC Robots together did globally about 50% of the entire 1200 km of sewers carrying optical fiber cables based on what was given in GSTT [11]. The robots by Nippon Hume did work primarily in Tokyo, Berlin, and Copenhagen for a total length of over 180 km with some projects going back to 1988. RCC's technology has been used in Berlin in pipes owned by RCC's owner during the past 3 years for a total of over 20 km and over an estimated 7 km in North America, based on data the author has been able to obtain, primarily in point-to-point configurations connecting a few buildings. The connections to buildings have been primarily using HDD and if anything were to go wrong with the installed optical fiber cable, this author maintains that one has to start from scratch to do a whole new installation.

According to Nippon Hume, their installations using the drill and dowel system of over 10 years of age are still functioning in Tokyo sewers. However, the author has not been able to verify this independently from either CCTV records, his own inspections or by accounts of parties, who do not have a vested interest. The installations by RCC in Berlin sewers and Ka-te installations are being observed carefully for useful data.

MAN-ENTRY TECHNOLOGY

Man-entry sewers are those with a diameter larger than 700 mm. The sewer lengths in North America of sizes not larger than 700 mm exceed 90%. Even the sewers of sizes larger than 700 mm forming less than 10% of route lengths lie in the outer skirts of a major city, where the demand for last mile fiber is not there yet. This implies that the market for man-entry technology is rather small in North America at this time. Many methods could be used for putting fiber once human could enter the sewers. Using expansion wall anchors with FAST clips or CableRunner trays, for example, optical cables could be attached to the inside sewer wall, at a desired spacing. For fixing the expansion anchor, a hole must be drilled into the sewer wall, which would pose no major structural problems as long as there is adequate wall thickness in sewers with a 800mm dia. and above. The cables can be added in the future as demand for the fiber count increases. This technology has been in use for some years. In Tokyo alone, there is over 700 km of such fiber installations in man-entry sized sewers for the longest duration, more than any other city in the world. And in Vienna, there is over 300 km of man-entry fiber using CableRunner.

INVENTIONS FOR FIBER IN SEWERS

There are at least 5 robot companies namely: CableRunner, DTI-CableCat, Ka-te, Nippon Hume, and RCC. CableRunner uses a drill and dowel system in sewers of 250 to 700 mm in size. DTI-CableCat uses either a back-reamed anchor or an adhesive bed system in sewers of sizes 200 to 1200 mm, while Nippon-Hume and RCC use drill and dowel systems for the same sized sewers. Nippon-Hume uses a plunger pin stem for the anchor along with a 2 part resin system while RCC uses a frictional stem anchor. Ka-te uses a stainless steel clamp and conduit system for sewers of sizes 200 to 700 mm.

In the drill and dowel system, a drill hole is made into the wall of the sewer pipe within the upper part and the cable is attached using either an anchor or a cable tray. In the adhesive bed system, the sewer pipe surface is coated with a glue and either the cable is directly or attached or fitted into either trays or clips attached to the glue bed. In the clamp and conduit system, stainless steel rings are fitted inside the pipe where, the stainless steel conduits to house the optical fiber cables are clipped. Each method has its advantages and disadvantages and is likely to find work in its own market niche where the user will take some responsibility for using suitable engineering criteria to pick the best to fit their budget and the needs of the project.

In addition, there are liner systems vying to do some of this as part of routine sewer maintenance programs. There is a good chance that these liner companies will succeed if they are able to offer value-added relining systems for an attractive incremental fee to the city sewer agencies over the standard lining systems without cutting too much into the current functions of the sewers.

The author is also aware of a number of other new technologies for building optical fiber networks in sewers either under research & developments, applied for patents, or have approved patents in hand. For example, see US patent No: 6,301,414 issued on October 9, 2001 to a group of optical fiber experts from Alcatel [45]. DTI-CableCat has filed for patents to protect its adhesive bed-based non-invasive system and is in the middle of developing a robot shown in Figure 1.



Figure 1: DTI's Adhesive Bed Robot

Nippon Hume, Consec, TMG, and TMSSC have jointly applied for new patents to protect their new C and W anchors and new modular robots, shown in Figure 2, to work in various types of pipes. Nippon Hume also has applied for patents to protect their

inventions to pre-install optical cable ducts in new spun concrete pipe.

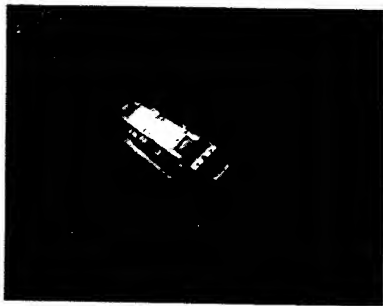


Figure 2: New Nippon Hume Robot

It is the author's understanding that Trolining has tried to sell its double wall HDPE liner system for municipal sewer relining since 1995, but has not found acceptance in North America with the exception of a few test sections. Trolining modifying its marketing program to the concept that their liner could house optical fiber cable has not produced any results either to date in the author's view, due to telecommunications companies desiring to build the last mile fiber at the lowest possible cost in sewers that require no double walled HDPE lining at this time. TMG, Corning Cable Systems MCS-Drain, shown in Figure 3, and Ashimori Industries' offering to use tensioning devices to span the optical fiber cable manhole to manhole to anchor them on the walls of the manhole are quite similar.

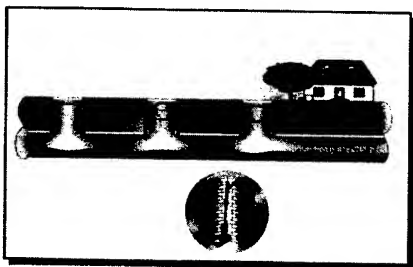


Figure 3: Corning's MCS Drain System

Brand-Rex [5] offers a technology to build optical fiber ducts as part of relining a sewer as shown in Figure 4.



Figure 4: Building Optical Fiber in Liners

OPTICAL FIBER IN NATURAL GAS PIPES

Sempre Fiber Links [38], Alcatel [33], and Gastec [10] are three companies offering new technologies to install optical fiber cables

in natural gas pipes. In Sempra's technology, special fittings are attached after tapping the gas main at two locations to form the entry and exit points for the optical fiber. The gas mains could be even as small as 25 mm in size and the fiber conduit will take up to no more than 10% of gas flow area. In the event a particular gas line cannot handle even a 10% reduction in capacity, additional pipe capacity will be added. A small HDPE conduit is threaded through the entrance fitting until it reaches the exit fitting. A special tool is used to grab hold of the threaded conduit and pull it out through the exit fitting. Once this housing conduit is placed in the gas main, the optical fiber cable is pushed through this conduit from one fitting to the next. The fittings and seals are designed to meet all gas pipeline safety requirements of the U.S. DOT, CFR 49, section 192 and any local regulations such as California PUC General Order 112-E. Sempra reports that a crew of 5 to 7 workers can install up to 600 m per day.

In the Alcatel system, a balloon device, shown in Figure 5, is used to pull a specially designed optical fiber cable through the Inlet port clear through the Outlet port shown using a gas pressure differential. The cable itself has a special metallic barrier, to prevent hydrogen gas migration to cause the optical fiber strands going blind. Again, the seals and the ports are designed to meet various safety regulations. More details could be found in Leppert et al. [33].



Figure 5: Alcatel's Balloon to Pull Optical Fiber in Gas Pipes

Gastec offers a solution where a specially designed shuttle pulls a cord from an inlet attached to the gas main all the way to the exit port using a gas pressure differential. This is done by creating an overpressure of about 150 mbar at the inlet side while a negative pressure is created by flaring off gas through a venting safety valve at the outlet side. If for some reason, shuttle gets stuck, the exact position will be known to the engineers from the transmitter signal built into the shuttle. An added benefit of fiber in gas deployment is that a few strands of the fiber could be used as a leak detection system by collecting spatial resolution data. When an engineer applies, Raman's law and Joule-Thompson's effects, the exact point along the pipe alignment where a leak appears can

be detected with a short response time to take appropriate remedial actions.

STANDARDIZATION

Efforts are underway to develop consensus standards within ASTM International by bringing industry experts together. ASTM International provides a legal, administrative, and publication forum within which producers, users, ultimate consumers, and representatives of government and academia can meet on a common ground to develop standards that best meet the needs of all concerned. The group that met during the past year unanimously agreed on the need to establish an ASTM standards development activity and approved the title: "New ASTM International Committee on Installing and Operating Optical Fiber Cables in Existing Sewer Systems." Over 250 stakeholders from 25 countries have joined together to form new ASTM Committee F36 on Technology and Underground Utilities. The group will create standards for the deployment of fiber-optic cables in underground utilities. Participants in the new committee include municipal authorities, building owners, robot-manufacturers, pipe manufacturers, optical-fiber cable manufacturers, telcos, and construction, architectural and engineering consultants, to name just a few.

Similar efforts are underway to develop engineering guidelines within ASCE for this 130,000-member organization of civil engineers to provide their input to the telecommunications industry in this new discipline. More than 25 authors have committed their time toward developing these guidelines for many months on this Task Committee on Installing and Operating Optical Fiber Networks in Existing Sewers.

As one example of the numerous questions and concerns raised by the possibility of placing fiber-optic cable in existing underground utility conduits, we'll look at the issues raised by sewer agency engineers, based on sound engineering principles, about allowing anything other than sewage in their sewers. The operation and maintenance of sewage conveyance systems need active preventive maintenance and sound pipeline engineering input. If proper standard of care is not practiced, it is only a matter of time until major problems will manifest and the sewer lease fee paid by a fiber installer to city hall will amount to nothing compared to the cost the public will have to bear to return the sewers back to normal. Historical lessons learned more than 100 years ago in the Paris sewer tunnels when engineers attempted to place more than one utility in the same space must be studied thoroughly so as not to repeat the same mistakes.

A new committee formed within the Collection Systems Committee (CSC) of the Water Environment Federation has conveyed most of these concerns among the sewer agencies in a letter to Committee F36 and have requested that these are addressed in the standards under development. Here is a sampling of their concerns:

- The extent to which hydraulic characteristics of the sewer would be altered when optical cables and the fasteners are introduced needs to be assessed by physical tests.
- These cables also would restrict many of the tools used for routine sewer monitoring, operation and maintenance.

- The corrosive effects of the sewage on the cables and fasteners and their longevity need to be addressed through extensive research.
- Debris, rags, and grease are likely to accumulate at a faster rate, causing blockage.
- Consensus standards need to address how to select suitable sewers, design, installation, operation, and maintenance considering the technology used for fiber installation, pipe wall material, size, applications, and how laterals are connected to the mainline sewers.
- Debris accumulates at the interior protrusions of the manholes when surcharged. How would this be handled if valuable telecom gear and customer connection gear were housed in these manholes?
- And most importantly, how would it affect the current functions of the sewer if additional fiber companies want to install their cables in the same sewers at a later time?
- The following attributes make one technology much different from another:
 - a. The size range of sewers each robot or other technique can work in,
 - b. The sewer wall materials in which these robots can be employed,
 - c. The composition and engineering properties of the deployment components,
 - d. The cost of the materials of deployment,
 - e. The cost of labor for each method,
 - f. The set up time for each technology,
 - g. The rate of production for each technology,
 - h. The ability of the optical cable owner to replace an installed cable,
 - i. The ability to use existing technology to clean the sewers,
 - j. The ability of the sewer owner to inspect the sewers using current technology,
 - k. The ability of the sewer owner or their contractor to maintain the sewers, and
 - l. Most importantly: How an engineer licensed to practice goes about choosing the suitable sewers.

SEWER SELECTION CRITERIA

As an example, let us address one of the most pressing issues in every sewer owners' heart at the present time. If we were to consider allowing optical fiber cables in existing sewers, what criteria should a fiber cable installer use to select the sewers that are suitable for optical fiber deployment? Operating an optical fiber network in the sewers poses its own challenges. Proper civil engineering input is essential for the selection of the suitable sewer system for deployment. The factors to consider in selecting the right sewer path are:

1. Access to the Sewer

The primary access to the sewer for fiber cable installation using either a robot or other means is through the manholes at both ends of the reach. It is desirable that the length of the reach is shorter than what is reachable by the umbilical cable needed for the supply of air, electricity, and communications circuits. If man-accessible pipes were chosen, then this limitation would not apply.

2. Hydraulics of the Sewer

Given the ubiquity of infiltration and inflow (I/I) problems, sewer designers have been able to count on only 85 percent of the actual flow area to convey the flow. The impact of optical fiber cables, their fasteners, and other deployment parts on flow characteristics need to be evaluated by running physical hydraulic studies with and without such components. Hydraulic studies of the flow conditions under the worst possible scenario based on past flow records in that sewer also needs to be done before the sewer is considered for optical fiber cable installation.

3. Structural Capacity of the Sewer

An evaluation of the structural capacity of the sewer to carry the soil load, groundwater load, and live load needs to be conducted. This is to ensure that the current condition of the sewer is adequate to house the optical fiber network.

4. Sewer Cleaning After Installation of Optical Fiber Cable

Sewers need to be cleaned periodically as part of their maintenance. Once optical fiber cables are installed in the sewer, special precautions must be taken in choosing and applying suitable cleaning methods that would not cause damage either to the sewer wall or the optical fiber cables.

5. Sewer Inspection After Installation of Optical Fiber Cable

Periodic maintenance of the sewer will also involve inspection of the internal condition of the sewer system once the optical fiber cables are installed. Special precautions need to be taken in choosing and applying suitable technology for sewer system inspection in order not to cause damage to either the sewer walls or the optical fiber cables.

6. Sewer Maintenance After Installation of Optical Fiber Cable

Sewers require periodic maintenance involving anything from point repairs, grouting and relining, to total replacement. The current condition of the sewer system and its need for repair or rehabilitation during the design life of the optical fiber network must be carefully evaluated.

7. Compatibility of the Sewer Wall

It is not possible to work with certain sewer wall materials depending on the fiber installation technology used, and so the materials will need to be evaluated.

8. Presence of Excessive Grease in the Sewer

Sections of pipe that have grease accumulations of more than a suitable thickness within one year of cleaning should not be considered candidates for fiber optic system installation until proper remedial action is taken.

9. Presence of Excessive Chemical Reagents in the Sewage

Sewage carries many chemical reagents and the compatibility of fiber deployment materials and components with all such chemicals needs to be tested.

10. Presence of Excessive Calcium Deposits on the Sewer Walls

Fiber optic systems should not be deployed in sewers with excessive calcium deposition.

11. Presence of Joint Separations/Offsets

Joint separations/offsets can lead to both infiltration and exfiltration. Structural damage to the sewer may result from pipe

bedding material being transported into the pipe. Enough care should be exercised when such sewers are encountered before these are chosen for optical fiber deployment.

12. Presence of Excessive Root Intrusion

Sewers should be free of excessive root intrusion to be eligible for installation of a fiber optic system.

13. Condition of the Manholes

Manholes should be in an acceptable physical condition for that sewer system to be used for fiber-optic cable installation.

14. Condition and Frequency of Lateral Connections

The condition of the lateral connections to the mainline sewer is important both to the hydraulic functioning of the sewer and to the installation and operation of the optical fiber network.

The selection criteria to use for natural gas mains would differ from the above and will be reported by the author in detail elsewhere.

CONCLUSIONS

1. The installation of optical fiber cables inside of sewers and gas pipes is a major break through in sharing the underground space to form utility corridors. Telecommunication companies need to address all the concerns associated with using existing pipes, before wide spread fiber deployment could proceed.
2. Working in the sewer will affect the health, safety, and welfare of the people we serve and any shortsighted approach to selecting the suitable sewers or gas pipes for installing and operating optical fiber cable, would expose all those in this new industry to an enormous liability. Developing sound engineering standards to guide this new industry falls well within this obligation.
3. The first mover advantage is there for certain companies. Once established as a leader, the odds are in favor for that company staying the leader. This is true provided the management of that company is nimble, is re-inventing itself with changing times and is continuing to add the best talent available in its workforce.
4. The factors which will continue to provide momentum for the market are:
 - Aging underground infrastructure
 - Doing more work with less funds
 - Protecting the environment
 - Increasing congestion in urban and suburban centers
 - Faster rate of technology transfer and information
 - Privatization of utility companies
5. More emphasis will be placed on evaluating the current condition of the entire pipeline network for cost effective spot maintenance and renovation strategies.
6. Not all sewers and gas pipes are amenable for installing optical fiber cables and companies which support strong engineering talent on their staff will focus their attention to those lines which would satisfy proper engineering criteria.
7. The deployment of optical fiber cables in existing pipelines offers a win-win situation for all parties involved if proper standard of care is afforded. However, working in sewers and natural gas pipes requires sound pipeline engineering input and anything less than that would be shortsighted. If

telecommunication companies did not follow proper engineering know-how, it would only be a matter of time before we will face major problems and the cost to return these sewers and gas lines to normal working order would be far greater than the lease revenue fiber installers are offering at the present time.

8. For telecom carriers and network service providers, it's a true, end-to-end last-mile optical fiber network, which they could control. For sewer and gas pipe owners, it's a unique and powerful economic development tool, providing added revenue from an existing infrastructure, and of course protection from most damage to roads and disruptions to traffic. And for building owners, it provides a major upgrade for their buildings for free, and that brings extra value to the buildings.
9. The author is spearheading a Task Committee within ASCE to develop Engineering Guidelines on Installing and Operating Optical Fiber Cables in Sewers. Likewise, he is leading standardization efforts within ASTM International. Anyone with information, data, or case histories that would help these committees carry out their mission is invited to present them to the author for possible inclusion.

REFERENCES

- [1] Alcatel, Ka-Te, and IK-T (1998) "FAST - Das schnelle Modulsystem für zukunftssichere Telekommunikations-Kabelnetze Informationschrift der Fa. Alcatel Kabel AG, Monchengladbach.
- [2] Berliner Wasser Betriebe (1997) Patent application on "Method and Device for Inserting, Positioning, and Fixing of Constructional Components Having Different Cross Sections." Applicant: Dr. Klaus Beyer, President of RCC.
- [3] Beyer, Klaus (2000) "Einbau Von Kommunikationskabeln in Abwasserkanalen," Proc. of the 6th International Pipeline Construction Show, Hamburg, Germany, June; pp. 370-379.
- [4] Beyer, Klaus (2001) "Personal Communications," Berlin, Feb.
- [5] Brand-Rex (2002) "Personal Communications," Fife, Jan.
- [6] CityNet Telecommunications, Inc. (2000) Personal communications, published articles, press releases, and their web site: www.citynettelecom.com
- [7] Copeland, M.V. and Mali, O. (2002), "Jilted by Broadband," paper in Red Herring, March.
- [8] Corning Cable Systems (2001) Technical Note on Data Superhighway in the Drain authored by Lothar Finzel.
- [9] Fujiyoshi, Yoshinobu, and Nomura, Yoshikazu (1996), "The Current Situation and Future of Sewer Optical Fiber Technology in Japan," Research Report by Japan Sewer Optical Fiber Technological Association.
- [10] Gastec (2002) "Personal Communications," Apeldoorn, Jan.
- [11] GSTT Nr. 12 (1999) "Leitungsverlegung in vorhandenen Netzen Teil 1: Kabelverlegung in Kanalnetzen, Dec.
- [12] Hecht, J. (2001), "Fiber Crosses The 10-Trillion-Bit Barrier," paper in MIT's Techreview, March.
- [13] Japan Sewage Works Association (1997), "Sewage Works in Japan-Sewerage and Optical Fiber Cable," authored by Yasuto Chiba.
- [14] Jeyapalan, J.K., Jaramillo, C.A., and Saleira, W. (1989), "Design Considerations for a Penstock Located in an Outlet Tunnel at the Jennings Randolph Dam in West Virginia," Proc. of WaterPower '89, ASCE Conference, pp. 426-436.
- [15] Jeyapalan, J.K., and Jaramillo, C.A. (1989), "Hydraulic Model Tests of Flow Around Penstock Suspended Inside the Tunnel for Design of Small Hydro," Proc. of WaterPower '89, ASCE Conference, pp. 577-587.
- [16] Jeyapalan, J.K., and Thiagaram, M. (1989), "An Evaluation of the Applicability and Cost of Polyester Resin and Cementitious Grouts for the Installation of Rock Anchors at Hydro Projects," Proc. of WaterPower '89, ASCE Conference, pp. 960-965.
- [17] Jeyapalan, J.K. (2001), "Fiber Optic Cables Inside of Sewers! Why Not?" paper at UCT, Houston, Texas.
- [18] Jeyapalan, J.K. (2001), "Optical Fiber in City Sewers-An Idea Whose Time Has Come" paper in Trenchless Technology Magazine, March.
- [19] Jeyapalan, J.K. (2001), "How Do You Install Fiber Optic Cables in Sewers?" Parts I and II in Publicworks.com, March.
- [20] Jeyapalan, J.K. (2001), "Fiber Cables in Sanitary Sewers," Civil Engineering News, March.
- [21] Jeyapalan, J.K. (2001), "A New No-Dig Industry Named Fiber Optic Cables in Sewers in Born," paper at NASTT, 10th annual conference, Nashville, Tennessee, April.
- [22] Jeyapalan, J.K. (2001), "Future Outlook for Trenchless Pipeline Rehabilitation Technologies," 2nd Asian Regional Civil Engineering Conference, Tokyo, Japan, April.
- [23] Jeyapalan, J.K. (2001), "Bridging the Last Mile With Fiber Optic Cables in Sewers," IWCS 50th anniversary conference in Orlando, Florida, November, pp 724-731.
- [24] Jeyapalan, J.K. (2002), "Optical Fiber Cables in Sewers 2002: What do we know? Where are we Heading?" paper in UCT, Jan. 14-17, Houston, Texas.
- [25] Jeyapalan, J.K. (2002), "Optical Fiber Cables in Sewers Part I- Sewer Selection Criteria," paper in Trenchless Technology Magazine, March.
- [26] Jeyapalan, J.K. (2002), "Optical Fiber Cables in Sewers Part II- Sewer Owner's Concerns," paper in Trenchless Technology Magazine, April.
- [27] Jeyapalan, J.K. (2002), "Optical Fiber Cables in Sewers in the USA," paper in No Dig International, April.

[28] Jeyapalan, J.K. (2002), "Optical Fiber Cables in Existing Sewers and Natural Gas Pipes," paper in No Dig conference of NASTT, Montreal, Canada, May.

[29] Jeyapalan, J.K. (2002), "Developing Standards for the Deployment of Optical Fiber Cable in Underground Utility Systems-Last Mile," ASTM International Standardization News, August.

[30] Jeyapalan, J.K. (2002), "Optical Fiber Cables in Existing Sewers and Natural Gas Pipes," paper in No Dig conference of ASTT, Sydney, Australia, August.

[31] JSOFTA (2001), "Sewer Optical Fiber Networks-Helping to Make Your Community More Advanced in Telecommunications," by Japan Sewer Optical Fiber Technological Association.

[32] Kennedy, M. (2002), "Utilities Go The Last Mile," paper in America's Telecommunications, January.

[33] Leppert, Hans-Detlef, Nothofer, Klaus, and Teschner, Wolfgang (2001), "Experience From The Field Installation of Optical Fiber Cables in Metro Gas Pipelines," IWCS 50th anniversary conference in Orlando, Florida, November, pp 747-752.

[34] Nakazato, T. (1997) "Sewer Optic Fibre Networks in Tokyo," WQI, Feb, pp. 16-18

[35] Nippon Hume Corporation-OFI Business Dept. (2001) "Personal Communications," Tokyo, Jan. to Dec.

[36] Nippon Hume Corporation-OFI Business Dept. (2001) "The World's First Robotic System for Laying Optical-Fiber Cable in Sewer Lines" August.

[37] Saeki, Kingo and Saito, Satoshi (1997) "Construction of the Optical Fiber Teleway Network Using Sewers," Research Report by Tokyo Metro Sewer Service Corporation.

[38] Sempra Fiber Links (2002) "Personal Communications," San Diego, Jan.

[39] Shinoda, Yasuhiro (1987), "Remote Control of Sewerage Facilities Using Sewer Optical Fiber Teleway," Research Report of Tokyo Metro Government.

[40] Tokyo Metro Government (2001) "Personal Communications," Tokyo, April - Dec.

[41] Tokyo Metro Government (2001) "SOFT Plan for Sewer Optical Fiber Teleway Network Plan," April.

[42] UK Patent GB 2129627, Granted on 16 May 1984 to Water Research Centre on Installation of Communication Cables; Inventors: John Gale, Ian Swallow, Martin George, Henry

Spooner, Steven Grosvenor, Timothy Henry, Reeve, John Ceerny, Nicholas Paul, Ouroussoff.

[43] US Patent No: 4,647,251, Granted on March 3, 1987 to Cabletime Installations on Installation of Communication Cables; Inventor: John Gale.

[44] US Patent No: 4,822,211, Granted on April 18, 1989 to Nippon Hume Corporation, Tokyo Metro Government, and Tokyo Metro Sewer Service Corporation on Method and Apparatus for Laying Cable in a Pipe; Inventors: Yasuhiro Shinoda, Yoshifumi Takahashi, Tsuneto Takaso, Akira Hagiwara, and Yoshiaki Ishii.

[45] US Patent No: 6,301,414, Granted on October 9, 2001 to Alcatel on Communication Cable Network in a Duct or Tube System Used Primarily for Other Purposes; Inventors: Wolfgang Liese, Alexander Weiss, Helmut Haag, and Bernd Menze.

[46] Wall Street Journal (2002), "Broadband Blues," Editorial on February 21.



Dr. Jey K. Jeyapalan, P.E.

9 Sundance Road
New Milford, Connecticut, USA 06776-3840

Dr. Jeyapalan graduated from the University of California at Berkeley and was a civil engineering professor for 10 years. Dr. Jeyapalan has been an international consultant for 30 years on design, engineering, construction, and standardization for a wide range of technology on last mile, optical fiber networks in pipelines, trenchless works, pipeline rehabilitation, and failure investigation. He has testified as an expert on numerous disputes, claims, mediations, arbitrations, and lawsuits on failures of pipelines for water, sewage, oil, gas, chemicals, desalination, and hydropower.

Armored Fiber Optical Cable for Sewer Applications

Kenneth E. Bow & Tsune Kawakita

The Dow Chemical Company

Midland, MI, USA

+1 (989) 638-3759 · kebow@dow.com

+1 (989) 638-0421 · kawakita@dow.com

Abstract

The use of various types of sewer pipes is an attractive alternative for the installation of fiber optical cables in the complex infrastructure of cities. A new development uses robots to attach the cable to the sewer wall. Armored cable is required for these installations to provide mechanical strength during installation and rodent and chemical protection after installation. This paper will provide data on the incorporation of either coated steel or coated stainless steel in a bonded sheath configuration as a chemical barrier to moisture, acids, bases, fuels and hydrogen sulfide that may be present in the sewer environment.

Keywords

Armor, Fiber Optical, Chemical Barrier, Cable, Sewer, Coated Steel, Coated Stainless Steel

1. Introduction

The challenge facing many telecommunication operators and cable installers is how to install cables in cities without disrupting normal activities. Digging is not only disruptive to neighborhoods and traffic flow, but oftentimes impractical because of the cost and time involved to get permits from civil authorities. Directional drilling brings other risks, the most important being the potential damage to the infrastructure of other utilities. Thus the use of sewer pipes is an attractive alternative to the complexities of installation in cities. The sewers provide convenient pathways to potential customers. There is another positive factor for the cities and other public entities in that, as owners of the sewers, they can reap additional revenue from their properties.

Laying of fiber optical cable inside small diameter sewer pipes is a relatively new advancement in the technology associated with deployment of fiber optical networks. The development of robotic methods has facilitated the growth in the use of sewer systems for fiber networks in city infrastructures. One method of installation uses the robot to install ring clamps every 1.5 meters.¹ The rings spring open and expand to tightly fit the interior of the pipe. The top of the ring has a series of clamps designed to hold conduit. The conduit is a stainless steel tube which is clipped in place by the robot. This conduit houses the fiber optical cable.

A newly developed method for sewer installation uses a robot to attach an armored fiber optical cable directly to the sewer pipe

using hangers. The robot simultaneously installs the hangers and the cable to the top of the sewer.² This method of installation is suitable for sanitary or storm sewers and requires the use of armored cable to provide mechanical, chemical and rodent protection for the fibers in the core of the cable. The purpose of this paper will be to describe the chemical resistance of a bonded or laminate sheath construction in a sewer environment. The use of sanitary sewers will require certain levels of chemical resistance including resistance to hydrogen sulfide, for example. The use of cables in storm sewers will require moisture resistance as well as resistance to fuels, such as diesel fuel, which may contaminate the water runoff.

Installation of cable in various types of sewers will also require the cable to provide mechanical protection and rodent resistance. The rodent resistance of cables armored with 0.15 mm (6 mil) coated steel or 0.125 mm (5 mil) coated stainless steel has been well documented.³ Likewise, the mechanical properties of armored cables have been well documented.⁴ The mechanical properties provided by the bonded sheath make it suitable for the robotic installation process in sewers.

Another beneficial aspect of the bonded sheath is a significant reduction in the thermal shrinkage and/or expansion of the jacket due to the fact the jacket is bonded to the armor. There is a possibility that some sewer lines may periodically receive discharges of high temperature effluent. The bonded sheath helps resist the potential for fiber stress induced by large temperature fluctuations.

When integrated into a bonded sheath construction, the coated steel or stainless steel prevents attacks by rodents from penetrating the cable core while providing the chemical moisture barrier. Cables armored with coated steel or coated stainless steel have been shown to be equally resistant to rodents in various tests using live rodents. The armor was not penetrated in any of the tests. A key feature of cables with bonded armors is the ability of the sealed overlap to prevent the rodent from prying it open. This prevents the rodent from entering the cable core without penetrating the armor. Thus, a properly sealed overlap prevents rodent entry while the bonded jacket also serves to improve rodent resistance by making it more difficult for the rodent to remove the cable jacket and cause damage over a larger area.

The corrosion resistance of coated steel and coated stainless steel are provided in different ways. For the coated steel the coatings have a chemical bond to the steel that is moisture resistant.⁵ The coatings control the rate of corrosion and prevent the corrosion mechanisms of differential aeration or differential concentration cells from working. Thus, coated steel provides excellent corrosion protection in a sewer environment because of its ability to control the rate of corrosion.

Coated stainless steel provides corrosion protection in a different way. The coatings also serve as an environmental barrier and to facilitate the formation of the bonded sheath while the stainless steel provides inherent corrosion resistance.⁶ Coated stainless is generally used in highly corrosive environments where there is the possibility of extensive rodent or insect damage.

2. Installation in Sewers

The first step before installation of the cable into sewers is to use a special vehicle to clean the sewer using high pressure water. After the cleaning step the sewer is inspected using a television camera. Areas that are found to be defective are then repaired. The optical fiber cable is laid into the sewer. A special robot is then used to fix the cable to the top of the sewer wall. The robot uses a special drilling tool to cut a hole 6 mm in diameter and 15 mm in depth into any type of pipe material. After this step, a specially designed corrosion resistant anchor/hook combination is lifted and pushed into the drilled hole. The anchors are spaced 1 meter apart. The cable fits into the hook portion of the anchor and is simultaneously installed as the robot moves along the sewer placing the anchors. The installed cable presents minimum obstacles to liquid flow in the sewer. The plastic construction of the anchor reduces the risk of corrosion. The sewer pipes can be continuously monitored for gas concentration during installation. In the case of pipes made of polyethylene, a special welding tool is used to fix the anchors to the pipe.

Along with the cable installation technology a special jointing technology has been developed to allow installation of the cable in potentially explosive atmospheres. The joint is installed on the wall of the manhole in a location that won't adversely affect working in the manhole. The joint is made from stainless steel to offer resistance to chemical attack. A gasket system protects the inside of the joint from all liquids. The cable is sealed against liquids where the cable enters the joint. The joint is designed to allow cable management as the need for additional fiber increases.

Several installations of fiber cable in sewers in cities in the USA, Canada and Germany have taken place. These installations vary in speed depending on the conditions of the sewer ranging from 200 - 400 m per 8-hour shift. The various advantages of sewer installations have been observed during these installations including no digging in the city infrastructure, no disruption to traffic or neighborhoods, relatively low cost and a rapid return on investment.

3. Chemical/Moisture Barrier Sheath

3.1 Concept

The technology to protect cable from chemicals and moisture consists of a sheath design based on the use of plastic coated metal

tapes bonded to a plastic jacket or oversheath. Such a construction is commonly referred to as bonded or laminate sheath. The tapes are applied longitudinally and frequently serve a dual function by providing mechanical protection as well as chemical and moisture protection. The bonded sheath cable may have several components. These are jacket, metallic tape as shield or armor and chemical-moisture barrier, sealed overlap, inner jacket, the cable core.

The bonded sheath derives its chemical and moisture resistant properties from the use of plastic coated metallic armoring tapes. The coatings on these tapes allow the tape to be heat bonded to the cable jacket while the jacket is being extruded during cable production. The forming of the coated tape longitudinally around the cable core results in an overlap. Sealing of this overlap with the coatings or a hot melt adhesive reduces the area through which chemicals and moisture can enter the core to a restricted path determined by the thickness of the overlap and the width of the overlap. The sealed overlap forms a "torturous path" for moisture and chemicals, thereby blocking their entrance into the cable. The sealing and bonding effectively incorporates the metallic component of the laminate into the cable sheath as an impervious barrier to chemical, moisture, and ions. In addition, the bonded jacket eliminates the moisture path between jacket and shield. Thus the combination of a bonded jacket and a sealed overlap results in essentially a metal lined plastic pipe which provides and excellent barrier to the ingress of chemicals and moisture.

3.2 Laminate Results:

3.2.1 Heat Seal Tests: As previously noted, the sealed overlap is the primary defense against chemicals. A laboratory test uses a heat sealer to prepare a sample that represents the sealed overlap. This sample is placed in a container of the chemical and then tested for heat seal strength after aging. The heat seal is accomplished with a bar heated to 300°F (150°C). The time for the seal is 2 seconds and the pressure is 40 psig. The heat seal represents the overlap of the cable. The dimensions of the sealed area are 25 mm x 25 mm (1 inch by 1 inch).

The results for the heat seal test with coated steel after aging in ASTM Fuel C at room temperature are shown in Table 1. The heat seal of the coated steel is basically unaffected by exposure to the chemical. This test is more severe than actual cable in that 4 edges are exposed to the chemical as opposed to only one edge in cable, i.e., the seam of the overlap.

Table 1. Heat Seal Adhesion Initial and After Aging in ASTM Fuel C

Time	Average Heat Seal Strength, N/km (lb/in)	
	Coated Steel	
Initial	29.7	(17.0)
7 days	32.2	(18.4)
28 days	27.5	(15.7)
63 days	28.5	(16.3)

Subsequent tests in other chemicals gave basically the same results. Therefore, additional data from heat seal tests will not be included in the paper.

3.2.2 Jacket Bond Tests: The jacket bond test is used in the laboratory to simulate the bond between a coated metal and a polymeric jacket or oversheath. The samples are prepared by laminating a premolded plaque of jacket to a sheet of the coated metal. Typically the work is done in a molding press set to 180°C. A film of polyester is inserted between the coated metal and jacket plaque at one end to allow a tab to be obtained. The plaque is cut into 25 mm (one inch) strips. For bond testing one tab of the strip is inserted into one jaw of a tensile tester and the other tab of the strip is inserted into the other jaw of the tensile tester. The coated metal is separated from the jacket at an angle of 180°. The force to separate the coated metal at 50 mm (2 inches)/min is recorded. The interface of separation of the components is also noted.

The results of the jacket bond test for coated steel in ASTM Fuel C are shown in Table 2. There is some reduction in bond strength, which follow changes in the interface of separation. Initially the separation is between the metal and the jacket (coating remains on the metal). After aging the interface changes to a cohesive mode where there was failure in the coating with separation from both interfaces. For a plastic to plastic bond, such behavior would be expected as the chemical penetrates (permeates) the jacket and eventually is stopped by the metallic barrier. A concentration of chemical in the interface could soften the plastic materials and lead to cohesive separation.

Table 2. Jacket Bond Adhesion Initial Values and After Aging in ASTM Fuel C at 23°C

Time	Jacket Bond Strength, N/m (lb/in) to LLDPE Resin	
	Coated Steel	
Initial	31.7	(18.1)M
7 days	41.1	(23.5)J
28 days	29.2	(16.7)C
63 days	24.7	(14.1)C

M = Denotes separation of the bond occurred at the metal-coating interface.

J = Denotes separation of the bond occurred at the jacket-coating interface.

C = Denotes separation occurred at both the metal-coating and the jacket-coating interfaces.

To simulate a sewer environment, another set of chemicals in liquid form were used to test for jacket bond. The potential exists for exposure of the cable to ground water that has been contaminated with acids, bases and fuels. For the acid a 0.1 normal hydrochloric acid was chosen and for the base a 0.1 normal sodium hydroxide was chosen. Spills or seepage from tanks or piping systems are the most frequent sources of fuels such as diesel fuel. A 100% solution was chosen. From the sanitary sewer point of view a potential contaminate would be hydrogen sulfide. A hydrogen sulfide water containing about 4% hydrogen sulfide was used for the tests.

The results are shown in Table 3. The jacket bond was unaffected by any of the chemicals through 60 days of aging. This indicates good resistance of the bonded sheath to various chemicals.

Table 3. Jacket Bond Strength of Coated Steel Laminate in Various Chemicals Versus Days of Aging at 23°C

Chemical	Jacket Bond Strength in N/cm (lb/in)					
	Initial		30		60	
Water	51.8	(29.6)	56.4	(32.2)	54.6	(31.2)
0.1N HCl	51.8	(29.6)	53.5	(30.5)	53.2	(30.9)
0.1N NaOH	51.8	(29.6)	53.8	(30.7)	53.6	(30.6)
Diesel Fuel	51.8	(29.6)	42.2	(24.4)	50.2	(28.7)
Hydrogen Sulfide	51.8	(29.6)	57.3	(32.7)	59.1	(33.7)

Note: All bond separations were at the metal-coating interface.

3.3 Chemical Resistance of Bonded Cable

Field experience has shown that the chemical/moisture barrier sheath is effective to protect cable in direct buried and duct applications in chemical plants and refineries.⁷ An instrument cable design using the bonded sheath concept dates from the mid-1970's for direct burial applications in chemical plants and refineries. A low density polyethylene jacket bonded to a copolymer coated, 8 mil aluminum tape formed the bonded sheath. Besides the benefit of chemical resistance, the sheath offered the additional benefits of improved mechanical properties and shielding against lightning.

Long-term tests simulating direct burial of this sheath design were run to test for chemical resistance.⁸ Samples of the cable were placed in barrels and covered with sand. The sand was then saturated with various chemicals. Make-up chemicals were added periodically and electrical continuity of the conductors was checked continuously. Tests of the physical properties of the cable materials were performed annually for two years.

The retention of adhesive seal strength in the overlap of the longitudinally folded tape was used as a measure of chemical and moisture resistance for the cables tested in simulated chemical environments. To measure seal strength, a section of sheath containing the overlap was removed from the cable. A die was used to produce a test specimen of the overlap approximately 6 mm wide and 150 mm long. The overlap was then separated for approximately 25 mm to allow it to be fitted into the upper and lower clamps of a tensile machine. The test was conducted at a rate of separation of 50 mm/min.

As shown in Table 4, the overlap seal strength was retained after two years of exposure to all chemicals tested. Thus the longitudinally-formed metallic tape with a sealed overlap functioned as a chemical barrier preventing penetration of chemicals into the cable core. Tensile tests of the inner jacket and conductor insulation showed that their physical properties were unchanged and industry specifications were met in all cases. The physical properties of the outer jacket were generally lower than the original values, but the jacket was still functional.

Similar results were obtained in another study using essentially the same procedure except cable samples were exposed for one year to sand saturated with sulfuric acid, ammonium hydroxide, sodium chloride solution (simulating sea water), benzene, wood

preservative (19% creosote oil), and water (complete submersion).⁹

TABLE 4. Seal Strength of Overlap of Bonded Sheath Cable Exposed for Two Years to Various Chemicals

Chemical	N/cm (lb/inch) 90° Peel Test			
	1 Year		2 Years	
Control	21.9	(12.50)	23.1	(13.20)
Mineral Spirits	24.0	(13.71)	21.5	(12.24)
ASTM #3 Oil	24.2	(13.81)	20.7	(11.80)
460 Solvent	26.7	(15.25)	21.9	(12.52)
Mixture*	31.1	(17.74)	19.3	(11.00)
Water	23.8	(13.60)	24.0	(13.67)

*50% mineral spirits, 25% 460 solvent, 25% ASTM #3 oil.

To simulate exposure of an actual fiber optical cable to some of the chemicals that might be encountered in a sewer environment, a test was devised for screening of cable specimens. The cable specimen was a commercial fiber optical cable which consisted of a core tube construction containing 12 fibers. The core was enclosed in aramid fibers then armored with corrugated coated steel. A final medium density polyethylene jacket completed the bonded sheath construction. The specimen was about 400 mm long. It was then bent into the shape of a "U" around a mandrel which was 6 times that of the overall diameter of the cable of 12 mm. The ends of the specimen were sealed with tape and the sample of cable was then immersed in various chemicals for 30 and 60 days at room temperature. Fluid level was brought to within 25 mm of the cable ends. After exposure the samples were removed from the specific chemical and the jacket bond determined in the circumferential direction according to ASTM D4565.

The results are shown in Table 5. For the specimens in water, 0.1 normal hydrochloric acid, 0.1 normal sodium hydroxide, diesel fuel and hydrogen sulfide water, there is essentially no change in initial bond strength. This indicates that the bonded sheath is maintaining its bond (and hence chemical resistance) in the presence of these particular chemicals. There appears to be good correlation between the laminate jacket bond data of Table 4 and the cable data of Table 5.

TABLE 5. Circumferential Jacket Bond Strength of Bonded Sheath Cable in Various Chemicals Versus Days of Aging at 23.°C

Chemical	Jacket Bond Strength in N/cm (lb/in)					
	Initial		30		60	
Water	33.4	(19.1)	34.3	(19.6)	32.3	(21.3)
0.1N HCl	33.4	(19.1)	36.8	(21.0)	31.5	(18.0)
0.1N NaOH	33.4	(19.1)	34.1	(19.5)	34.8	(19.9)
Diesel Fuel	33.4	(19.1)	33.8	(19.3)	28.6	(16.3)
Hydrogen Sulfide	33.4	(19.1)	28.9	(16.5)	36.4	(20.8)

Note: All bond separations were at the jacket-coating interface.

4. Conclusions

The bonded sheath with coated steel or coated stainless steel can provide sufficient chemical protection to fiber optical cable installed in sewers. The bonded, or laminate sheath incorporates a

longitudinally formed coated steel or stainless steel into an impervious chemical barrier with a sealed overlap that provides a tortuous path resistant to permeation of chemicals into the cable core. Data developed through aging studies show that the bonded sheath protects the fiber core from moisture, acids, bases, hydrogen sulfide and diesel fuel. These chemicals or others similar to them may be expected as contaminants in the effluent present in storm or sanitary sewers.

The cable can be installed directly into sewers using a robot. The robot cuts a hole in the top of the sewer for an anchor, then installs the anchor in the pipe and simultaneously places the cable into a cradle in the anchor. The robot can install cable at a rate of up to 800 m/day in two shifts. The installed cable presents minimal obstacles to liquid flow in the sewer. A special jointing technology seals the cable splices against liquids and allows for cable management as needed to meet network demand.

The bonded sheath with coated steel or stainless steel provides the cable with sufficient mechanical strength to preserve the integrity of the chemical barrier during installation. Bonding provides additional moisture and chemical protection by providing a water block in the armor-jacket interface that is not affected by bending, handling or aging.

The bonded sheath with coated steel or coated stainless steel provides rodent protection to the cable core. This metallic barrier to rodents is supplemented by the sealed overlap which prevents rodent entry through the overlap area and by the jacket bond which greatly restricts the ability of the rodent to strip the jacket from the cable.

5. Acknowledgements

Thanks to George Clingerman for performing the laboratory work and Trish Dufresne for preparation of the manuscript.

6. References

- [1] H. G. Haag, W. Liese, K. Nothefer, W. Teschner, A. Weiss, W. Stapel, "Experiences from Construction and Operation of Fiber Optic Cable Plants in Sewer Systems," *International Wire & Cable Symposium Proceedings 1999*, p. 126-183.
- [2] J. Nocery, "STAR Crossed," *Trenchless Technology International*, Feb. 2001.
- [3] W. F. Busch and K. E. Bow, "Armored Fiber Optical Cable for Subscriber Use," *Wire Journal International*, 1988.
- [4] W. F. Busch and K. E. Bow, "A Military Base Fiber Optic Cable Armored Sheath Design," *Proceedings of the Second International Government and Military Fiber Optic & Communications Exposition*, March 1988, MFOC '88, pp. 63-69.
- [5] K. E. Bow, "Corrosion Performance of Armored Cable with Coated Steel," Paper No. 63, Corrosion 89.
- [6] K. E. Bow, P.U. Bakru, P.L. Hagans, L. Shadoff, "Corrosion Performance of a Sheath with Plastic Coated Stainless Steel," for Fiber Optic Cable," *International Wire & Cable Proceedings 1985*, p. 61-73.
- [7] M.G. Bayer, K.E. Bow, J.H. Snow, and D.A. Voltz, *Chemical-Moisture Barrier Cable - Concept and Practice*, Record of Conference Paper, Industry Applications Society,

Petroleum and Chemical Industry Conference, 94-CH3451-2, (PCIC), Vancouver, BC Canada, September 12-14, 1994, pp. 183-190.

- [8] T. Gucwa, "Long Term Testing of Direct Burial Refinery Cable Taken After Two Years Exposure," Final Report – TSR 12-00050, September 13, 1978, Samuel Moore and Company, Aurora, OH.
- [9] L. Campbell, "Addendum Report 70-1015," September 29, 1971, Samuel Moore and Company, Aurora, OH.

7. Biographies



Kenneth E. Bow received a B.S. degree in electrical engineering from Michigan State University, East Lansing, MI, in 1962. Following graduation, he joined The Dow Chemical Company, Midland, MI, where he has been involved in the research and development of materials for the wire and cable industry for more than 35 years. He is currently the Chief Scientist for the development of polymer and coated metal products for wire and cable applications. His primary responsibilities are for the global development of products and

technology associated with cables using plastic-coated metallic shielding and armoring tapes. Ken is a senior member of the IEEE and the SPE. (E-mail: kebow@dow.com)



Tsune Kawakita received a B.S. degree in metallurgy and M.S. degree in material science and metallurgical engineering from Waseda University, Japan, in 1974. He continued his graduate studies in chemical engineering at University of British Columbia, Canada, under the Rotary International grant in 1975. Following the completion of the program, he joined The Dow Chemical Company, where he has been involved in various functions from engineering, environmental and health science, ceramics product development to technical service and development for the wire and cable industry. He is currently the Industry Leader for the Engineered Films and Laminates Business. His primary focuses are the development of new products for communication cables and the global market development support. (E-mail: kawakita@dow.com)

A New Fiber Optic Life for Old Ducts

W. Griffioen, W. Greven, T. Pothof

Draka Comteq - NKF Telecom

Zuidelijk Halfrond 11, 2801 DD Gouda, The Netherlands

+31-182-592490 · w.griffioen@nkf.nl

Abstract

Systems are described where loose bundles of 7 and 10 mm mini-tubes are jetted into ducts. In these mini-tubes, which can be coupled together into long routes including branches, micro-cables with up to 72 fibers each can be jetted in. These high performance mini-tubes allow jetting of the cables over 2500 m (8000') per single blow, thus offering the possibility to upgrade old ducts. Bundles of mini-tubes can also be installed in ducts occupied with one or more resident cables. Different trials and projects are described in this paper.

Keywords

Optical fiber; cable; duct; mini-tubes; jetting/blowing; additional jetting/blowing; resident cables; upgrading old ducts.

1. Introduction

Civil works are the largest cost contributors for fiber optic installations when existing ducts cannot be used anymore. Often new ducts have to be installed along existing ducts. The latter ducts may be of bad quality, not meeting requirements for long length fiber optic installation, or contain resident cables. Many duct routes have been built for copper telecom networks. Here short lengths of cables were pulled in with high forces and numerous splices were made to connect them.

Fiber optic cables are installed now over much longer lengths, on the order of 10 km between splices. Modern ducts are of improved quality resulting in lower coefficient of friction (COF) between cable and duct. Together with the development of the jetting (blowing) technique [1] this resulted in cost-efficient installation of fiber optic cables over the required lengths. Old ducts suffer from high COF, especially after long-term aging. They are often not able to withstand the air pressures needed for cable jetting. Moreover the sections are of short length. Numerous duct connections must be made to allow installation of long cable lengths. This is especially a problem when the ducts were cut immediately after entering the handhole, making it almost impossible to connect the ducts sufficiently pressure-resistant to allow jetting. All these problems are faced to a larger extent when resident cables occupy the ducts.

Installing loose bundles of mini-tubes (7 or 10 mm external diameter) [2] in old ducts are a way to overcome the above-mentioned problems. These mini-tubes are installed by jetting with, in most cases, low air pressures. In this way long continuous upgraded tube routes are obtained with low COF and high pressure-resistance. In each mini-tube cables with up to 72 fibers can be installed. It is also possible to install loose bundles of

mini-tubes in used ducts with traffic along resident cables. Tables are given for several combinations of additional tube jetting. Validity of this table has been obtained from trials and experiences with projects.

2. Mini-tubes Systems

Mini-tube systems consist of loose bundles of mini-tubes (outer diameter 7 and 10 mm), see Figure 1. These bundles can be jetted (synergy of pushing and blowing) in ducts such as used today for installation of fiber optic cables. Jetting lengths for tube bundles are typically 200 m (700') per bar air pressure. In good quality ducts more than 1500 m (5000') can be reached "in one blow" and less for ducts with resident cables. Bundles of mini-tubes can be coupled by means of simple connectors. Branching of one or more of the mini-tubes is possible by making a window-cut in the duct, cutting the mini-tube of choice and connecting it to a branching mini-tube. The ducts are recovered by using a (split) clip-on Y-connector, see Figure 2. This operation can be done without risk of damaging the other mini-tubes. Micro-cables with extremely high fiber-density (up to 72 fibers) can be jetted in these mini-tubes, each cable having its individual path through the network, without the need to make splices in the optical fibers.

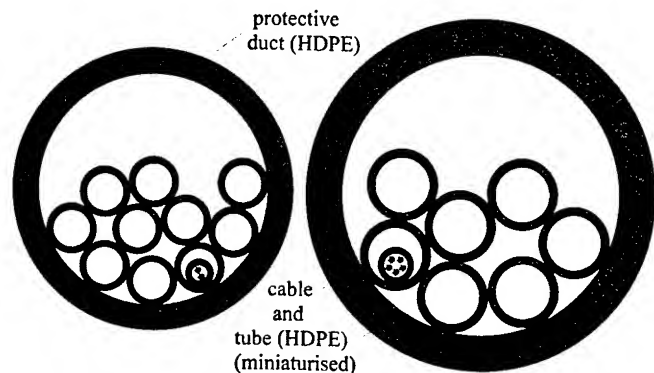


Figure 1. Typical bundles of mini-tubes with cables, left 40/33 mm (1 1/4") duct with 10 tubes of 7 mm and a 24-fiber cable, right 50/40 mm (1 1/2") duct with 7 tubes of 10 mm and a 72-fiber cable

Jetting technology allows installing lengths of the cables of up to 2500 m (8000') "in one blow". With cascaded jetting (tandem, see Figure 3) and buffering techniques (see Figure 5) more than 8 km (5 miles) splice-less cable lengths have been installed.

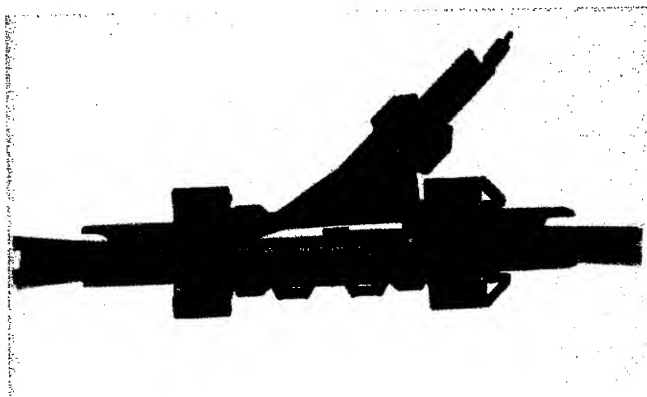


Figure 2. Y-connector to branch mini-tubes

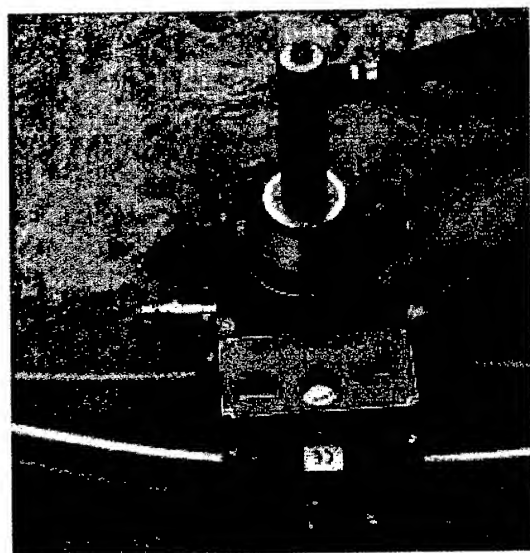


Figure 3. Jetting micro-cables in tandem

Some advantages of systems with loose bundles of mini-tubes are:

- Investments grow with demand.
- Installation of latest fiber optic technology.
- Midspan-access at any place and any time. Fibers with traffic not disturbed.
- Fast installation technology and short response time.
- Possibility of re-routing without lost fibers or splicing.
- Mini-tubes upgrade old ducts. Low coefficient of friction and high pressure-resistance improve jetting. Long continuous routes can be made.
- Mini-tubes easily jetted in ducts with resident cables.

The number of mini-tubes is advised to be such that half the space of the duct is filled, see Table 1. In this way the duct still gives the required mechanical protection (impact resistance) and Y-branching and jetting of the bundle are made easy.

Table 1. Recommended maximum number of tubes and fiber counts for different ducts

duct (mm)	10 mm tubes	max fibers	7 mm tubes	max fibers
63/50 (2")	10	720	20	480
50/40 (1½")	7	504	14	336
40/33 (1¼")	5	360	10	240
32/25 (1")	3	216	7	168
25/20 (¾")	1	72	3	72

3. Additional Jetting

When there is a demand for a new connection and the available ducts are used significant civil costs have to be made. Therefore one tries to use the free space in ducts already occupied with resident cables. Pushing and pulling with rodders can do this, but in many cases the lengths are short. Another technique, additional jetting of cables, can in many cases also be done, again only over short lengths. Even when the intermediate distance between handholes can be bridged these short lengths cause problems. Because fiber optic links require long splice-less lengths such installations are not economical. Additional installation of mini-tubes does not show this drawback when intermediate distances between handholes can be bridged. The tubes can simply be coupled and long continuous tube routes of high quality (low friction, high pressure resistance) are formed.

Additional jetting of mini-tubes appears at first sight comparable to additional jetting of cables: on the one hand the tubes are more lightweight, but on the other hand the wedging of the smaller tubes seems to be more severe. The latter turns out to be not true! When the diameter of the second cable becomes larger it comes out of the wedge first, but for still higher diameters the wedging effect increases again, especially close to the situation called jamming (see Appendix A). In many practical situations the wedge effect for mini-tubes is less than for cables. Moreover the tubes are much lighter so the jetting distances are much higher. Theoretical distances, confirmed at Draka Comteq's jetting test-site at Delfzijl (Netherlands), are given for 7 and 10 mm tubes in Tables 2 to 5.

Table 2. Jetting distances for 10 mm tubes in 40/33 mm (1¼") duct, different numbers and resident cables

cable 1 (mm)	1 tube	2 tubes	3 tubes	4 tubes
12 (0.47")	1200 (4000')	1100 (3600')	950 (3100')	800 (2600')
15 (0.59")	700 (2300')	600 (2000')	550 (1800')	
16.5 (0.65")	400 (1300')	400 (1300')		
18.5 (0.73")	200 (700')	200 (700')		

Table 3. Jetting distances for 10 mm tubes in 50/40 mm (1½") duct, different numbers and resident cables

cable 1 (mm)	1 tube	2 tubes	3 tubes	4 tubes	5 tubes	6 tubes
12 (0.47")	1600 (5200')	1500 (5000')	1300 (4300')	1150 (3800')	1000 (3300')	900 (3000')
15 (0.59")	1200 (4000')	1100 (3600')	1000 (3300')	850 (2800')		
16.5 (0.65")	800 (2600')	800 (2600')	750 (2500')	700 (2500')		
18.5 (0.73")	400 (1300')	400 (1300')	400 (1300')	400 (1300')		

Table 4. Jetting distances for 7 mm tubes in 40/33 mm (1¼") duct, different numbers and resident cables

cable 1 (mm)	1 tube	2 tubes	3 tubes	4 tubes	5 tubes	7 tubes
12 (0.47")	900 (3000')	1000 (3300')	1000 (3300')	1000 (3300')	900 (3000')	800 (2600')
15 (0.59")	350 (1200')	450 (1500')	500 (1600')	500 (1600')	500 (1600')	450 (1500')
16.5 (0.65")	250 (800')	250 (800')	300 (1000')	300 (1000')	300 (1000')	
18.5 (0.73")	200 (700')	200 (700')	200 (700')	200 (700')		

Table 5. Jetting distances for 7 mm tubes in 50/40 mm (1½") duct, different numbers and resident cables

cable 1 (mm)	2 tubes	5 tubes	7 tubes	9 tubes	10 tubes	12 tubes
12 (0.47")	1600 (5200')	1350 (4400')	1200 (4000')	1050 (3400')	950 (3100')	600 (2000')
15 (0.59")	700 (2300')	850 (2800')	750 (2500')	600 (2000')	550 (800')	400 (1300')
16.5 (0.65")	400 (1300')	500 (1600')	450 (1500')	400 (1300')	350 (1200')	
18.5 (0.73")	200 (700')	250 (800')	250 (800')			

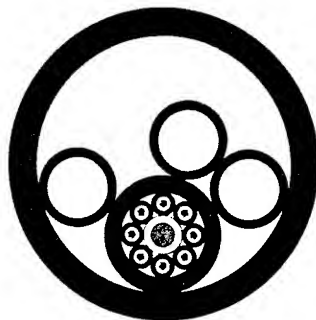


Figure 4. 40/33 mm (1¼") duct with 15 mm (0.59") resident cable and 3 tubes 10 mm

In Figure 4 an example is shown of a 40/33 mm (1¼") duct occupied with a 15 mm resident cable in which 3 additional 10 mm tubes were installed (possible over 550 m, see Table 2). Note that the partial filling of the duct with cable and tubes still guarantees resistance against impact. 10 mm corresponds to about the minimum wedge factor, see Figure 13. The 3 tubes can store 3 cables with up to 72 fibers, a total of 216 fibers. An additional cable with this fiber count would be very difficult to install.

4. Projects

4.1 San Diego

A reference project (i.e. with good quality ducts and no resident cables) is installation of 10 tubes of 10 mm in empty 60/50 mm (2") ducts between San Diego and Phoenix. Bundles were installed in lengths of about 1000 m (3000'), usually a few of those sections per day. Many splice-less lengths of 8 km (5 miles) of 60-fiber cable have been installed (one-day jobs), using tandem jetting and buffering (see Figures 3 and 5). Note that this installation was done with loops of cable-overlength stored in handholes about every 400 m (1300').



Figure 5. Jetting micro-cables with buffering

4.2 Upgraded Duct Trials and Projects

In Wuhan (China) a trial was done in thin-walled 32 mm (1") PVC duct. Here 7 tubes of 7 mm were installed over 500 m (1600') using only 2 bars. More pressure was not allowed. Expansion of the ducts and serious leaking already occurred. The newly installed mini-tubes eliminate these problems.

In Geneva the above ground part of the optical network of CERN needs extra fiber capacity (replacement) for new experiments. The 52 mm (1½") ducts are of such quality (high friction, probably

with leaks and immediate cut at handhole entrances) that burying new ducts was considered. Instead mini-tubes can be installed easily with handholes about every 500 m (1600'). After coupling of the tubes long spliceless cables can be jetted in.

4.3 San Jose

A short but challenging installation was done in San Jose, California. Here an installation was requested over 400 m (1300') in a 42/34 mm (1 1/4") duct with 2 resident cables (12 and 15 mm) with traffic. The civil and permitting costs that would be involved in digging up this portion of the route was prohibitive. Previous to our arrival several attempts, including the use of rodders, were done to install a third cable, all without success. Shown in Figure 6 is the duct with cables in the handhole. Note the damage to the duct, caused by the rodder (right in the picture). Some debris (only a small portion of the total encountered) can be seen at the end of the rodder, caused by scraping against the duct wall.

Because the duct was of poor quality it was decided to install only one 10 mm tube next to the cables (in good condition additional jetting of 2 tubes would be possible over 600 m (2000') in this geometry). During installation several additional problems were encountered. First the duct was leaking halfway. Next obstructions were present at three different locations in the duct, probably caused by debris from previous attempts with rodders. Finally also no aftercooler was present with the compressor, resulting in temperatures of about 60 degrees Celsius (140 degrees Fahrenheit) of the airflow, softening all materials. Nevertheless the tube could be installed and a 48-fibre cable was blown in immediately after. The whole project was finished in slightly more than two days, including splicing to other cables. The majority of time was spent cleaning from previous attempts. Actual installation of the guide tube and cable took only 1/2 day.

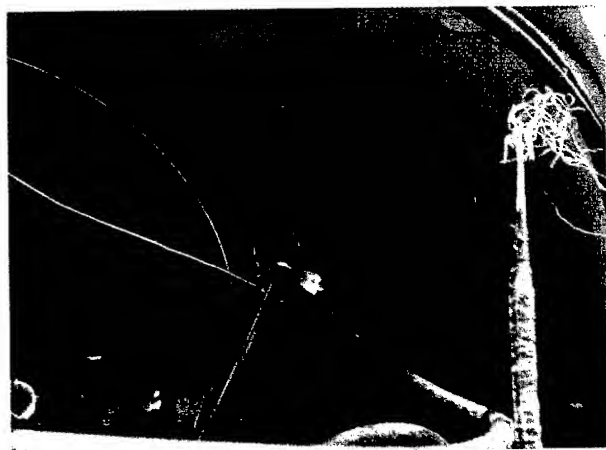


Figure 6. Duct occupied with 2 resident cables

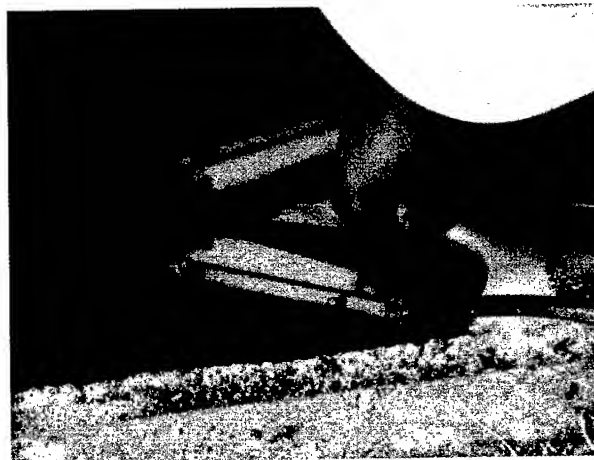


Figure 7. Mounting Y-piece for additional jetting with 2 resident cables and guide for the tube

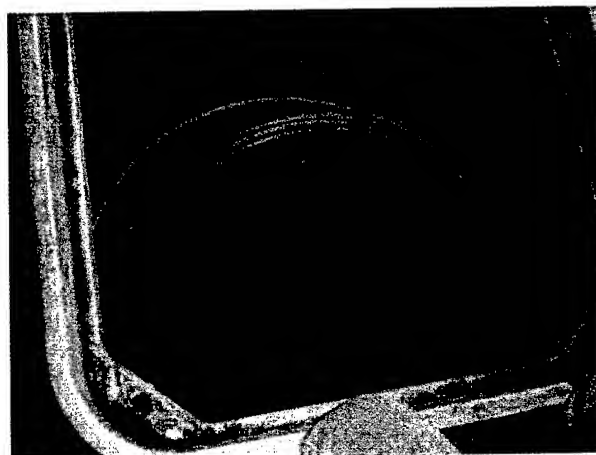


Figure 8. Installed additional tube and cable

4.4 Gothenburg

On a trajectory of about 3 km (2 miles) near Gothenburg, Sweden there was a demand for extra fiber capacity. Here a fiber optic cable with a diameter of 14 mm was already present in a 40/33 mm (1 1/4") duct. An initial attempt to install an additional 96-fibre cable with a diameter of 15 mm was not successful in that it only reached 150 m (500'). Instead 3 tubes of 10 mm were jetted in (see Figure 9). This was installed in slightly more than 2 days, with lengths per blow of up to 512 m (1680'). This length is somewhat less than expected. This might be caused by the fact that a lot of water was present in the duct, caused by the many duct openings resulting from the previous trials with cable.

In each of the 10 mm tubes a cable with up to 72 fibers can be jetted in easily (up to 2500 m or 8000' in one blow). One cable was successfully installed, without splice, jetted with one master and one tandem-jetting device.



Figure 9. Additional jetting of 3 tubes of 10 mm

4.5 Copenhagen

A trajectory of 1137 m (3730') of 32/27.2 mm (3/4") duct was occupied with a single resident 12 fiber cable with diameter of 10.9 mm over 755 m (2477'). Over a length of 32 m (105') even 2 resident cables were present. In the free duct section a bundle of 4 tubes of 10 mm was jetted in. In the section with single resident cable a bundle of 2 tubes of 10 mm was installed in a single blow. The same bundle was pushed in by hand over the remaining double occupied duct section. Next a 60-fiber cable was blown in over the entire length. The whole operation took half a day.



Figure 10. Additional jetting Copenhagen

4.6 Other Projects

In a trial in Chattanooga the water-jetting (floating) a bundle of 3 tubes of 10 mm over 1200 m (4000') in a 60/50 mm (2") duct with resident 288-fiber cable with a diameter of 20.4 mm was performed. Here also the same bundle was floated over 600 m (2000') in a 42/35 mm (1 1/4") duct with resident 96-fibre cable with diameter of 15.5 mm.

In Belgium a bundle of 3 tubes of 10 mm was successfully jetted over 1100 m (3600') into a 50/40 mm (1 1/2") duct with resident 48-fibre cable with diameter of 12 mm.

5. Conclusions

Systems with loose bundles of 7 and 10 mm mini-tubes can upgrade old duct routes. The mini-tubes can easily be coupled to longer lengths in which micro-cables with up to 72 fibers per tube can be installed with high performance. Bundles of mini-tubes can even be installed in occupied ducts, next to resident cables with traffic. Installation lengths per blow are, surprisingly, much longer for additional tubes than for cable. In addition to this benefit longer lengths are achieved by using coupling of the tubes.

6. Acknowledgments

Special thanks to all people participating in the trials and projects: Maja Keijzer, Cees van 't Hul, Ignaat Eijpe, Danny Bisessar, Frans Bakker, James Tualena, Frank de Bruin, Bert van der Tuuk, Kenneth Crowe, Nancy Li, Yang Zhanbing (Draka Comteq), Bill Bolle (Tier2), Michael van Moppes (Plumettaz), Luit de Jonge (CERN), Roland Ahl, Tobias Ahl, Per-Anders Andersson (Rala) and JJ Johnson (Triax communications).

7. References

- [1] W. Griffioen, "A new installation method for conventional fibre optic cables in conduits", *Proc. 37th IWCS* (1988), 172-178.
- [2] W. Griffioen, A. van Wingerden, C. van 't Hul, "Versatile outside plant solution for optical access networks", *Proc. 48th IWCS* (1999), 152-156.
- [3] P.B. Grimado and A.J. Colucci, "Placing fiber optic cables in multioccupied ducts", *IEEE Journal on Selected Areas in Communications*, Vol. sac-4, No. 5, August 1986.
- [4] J.M. Fee, M.J. Fee, "A study of tension and jamming when pulling cable around bends", *Proc. IEEE T&D Conference*, New Orleans, April 1999, 100-105.

Appendix A: Wedge Factor

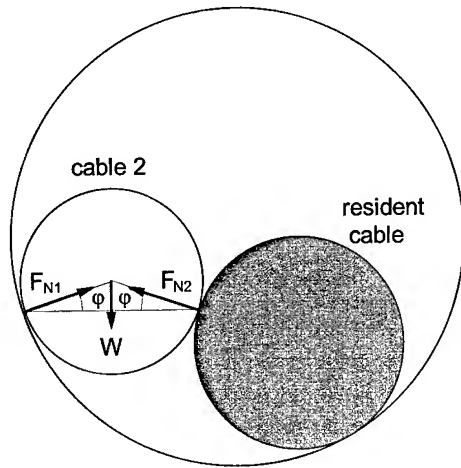


Figure 11. Forces on a second cable

When a second cable is installed in a duct next to a first (resident) cable it will experience higher friction forces because of the wedging effect. This effect is largest (worst case) in the situation that the weight W of the cable (or the resultant of the weight and other axial forces) is pointed symmetrically into the wedge, as indicated in Figure 11. From this Figure follows the wedge factor f_{wedge} , with which the friction force (proportional to the sum of the normal forces F_N acting on the cable) increases with respect to the situation of sliding over a flat surface:

$$f_{wedge} = \frac{1}{\sin(\varphi)} \quad (1)$$

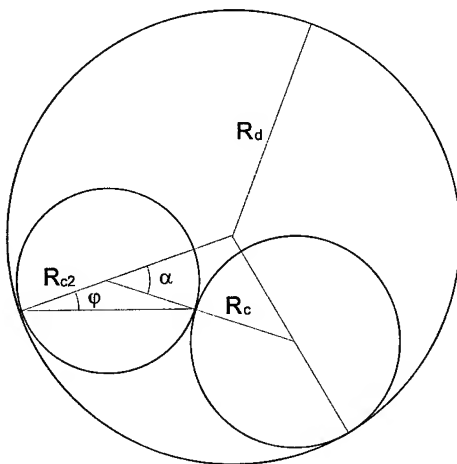


Figure 12. Parameters to calculate wedging

In Figure 12 parameters are given to further calculate the wedge factor, for clarity instead of the diameters D_d , D_c and D_{c2} for duct, first cable and second cable, respectively, the radii R_d , R_c and R_{c2} . The sum of the angles from the isosceles triangle with angles φ

and the middle of cable 2 is equal to $\pi - \alpha + 2\varphi$. This sum is for every triangle equal to π , hence follows:

$$\alpha = 2\varphi \quad (2)$$

For the triangle with angle α , center of duct and center of first cable it follows using modified "Pythagoras" for angle α (instead of a right angle):

$$(R_d - R_c)^2 = (R_c + R_{c2})^2 + (R_d - R_{c2})^2 - 2(R_c + R_{c2})(R_d - R_{c2})\cos(\alpha) \quad (3)$$

Together with equation (1), using $1 - \cos(2\varphi) = 2\sin^2(\varphi)$ and rewriting in diameters this leads to the simple expression:

$$f_{wedge} = \sqrt{\frac{(D_c + D_{c2})(D_d - D_{c2})}{D_{c2}(D_d - D_c - D_{c2})}} \quad (4)$$

This equation leads to the same results as the, much more intricate, set of equations in [3].

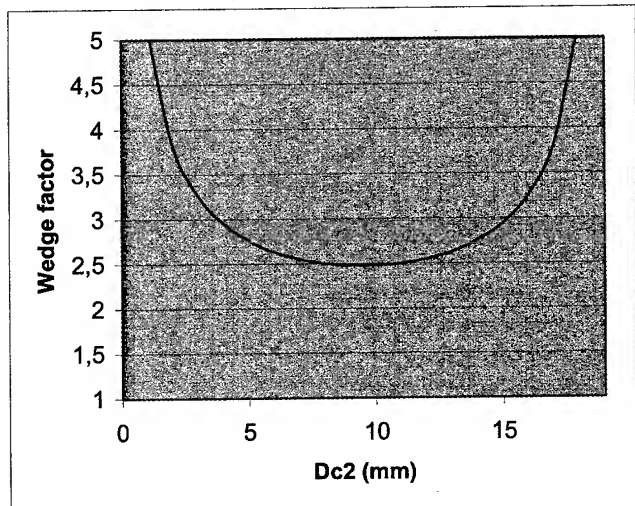


Figure 13. Wedge factor as a function of diameter D_{c2} of second cable for a 40/33 mm (1¼") duct with resident 15 mm cable

The minimum value for the wedging factor:

$$f_{wedge, \min} = \frac{D_d + D_c}{D_d - D_c} \quad (5)$$

is reached for an optimal diameter of the second cable:

$$D_{c2, \text{opt}} = \frac{1}{2}(D_d - D_c) \quad (6)$$

In Figure 13 an example is given of this wedging factor as a function of diameter of the second cable. Note the symmetry. The increase in wedge factor for higher diameters of the second cable can be understood by realizing that the walls in between which wedging occurs become parallel again for exact fitting of the second cable. This effect is also known as jamming, see e.g. [4].

Biographies



Willem Griffioen received an MS degree in Physics and Mathematics from Leiden University (Netherlands) in 1980 and worked there until 1984. He joined KPN Research, St. Paulusstraat 4, 2264 XZ Leidschendam, The Netherlands. Responsibilities R&D of Outside-Plant and Installation Techniques. He worked at Ericsson Cables, Hudiksvall (Sweden) and at Telia Research, Haninge (Sweden) in the scope of exchange/joint projects with KPN Research. He received his Ph.D. (Reliability of Optical Fibers) in 1995 from the Technical University of Eindhoven (Netherlands). Currently, since 1998, he is product manager at Draka Comteq - NKF Telecom, Zuidelijk Halfrond 11, 2801 DD Gouda, The Netherlands.



Willem Greven received his degree in advanced technical studies in Delfzijl in 1977. Since then he joined Draka Comteq - NKF Telecom, IJzerweg 2, 9936 BM Farmsum (Netherlands). He worked at departments of paper-insulated cables, plastics, was quality inspector, co-ordinator final inspection and unit-leader plastics. Since 1996 he joined the team that develops and introduces the JETnet system as senior projects & systems engineer. He made demonstrations and pilot projects of the system all over the world.



Thomas Pothof joined Draka Comteq - NKF Telecom, IJzerweg 2, 9936 BM Farmsum (Netherlands) in October 1968. He started at the department of paper-insulated cables. Then he worked for some years as quality inspector in the plastics department. Next he was one of the pioneers in the optical cable department, in the function of group leader. After introduction of self-steering teams he became materials planner of this department. In October 2000 he joined the JETnet team as projects & systems engineer.

Development of Lightweight Ribbon Cables for Blown Installation

H. Paul Debban, Jr., Mario S. Rossi, Peter A. Weimann, Michael Kinard, C. Shawn Davis

OFS Optical Cable Division
Norcross, GA, USA

+1-770-798-2039 debban@ofsoptics.com, msrossi@ofsoptics.com, pweimann@ofsoptics.com, mkinard@ofsoptics.com

Jason Pedder

OFS Optical Cable Division
Augsburg, Germany

+49-821-46049190 pedder@ofsoptics.com

Abstract

This paper describes the development and application of lightweight ribbon cables optimized for emerging cable architectures and installation techniques, primarily in the metro environment. The new cables are well suited for application in both micro duct systems and into new rights-of-way such as gas lines and sewer ducts.

Keywords

Ribbon; cable; sub-duct; blown cable; air-blowing installation; micro duct; miniaturized duct system.

1. Introduction

Telecommunications service providers face new challenges in the current economic environment. Demand for bandwidth continues to grow, while access to capital has become limited. Fiber is required in the metro and access markets in order to generate revenue from backbone networks that are already complete. Service providers need an economical alternative to the large-scale deployment of dark fiber to ensure that available capital generates maximum revenue. In addition, deployment of optical cables has become increasingly difficult, as governments are increasingly reluctant to allow the installation of new duct systems.

Solutions for these problems are emerging. New low-cost routes to the customer are being developed through existing infrastructure, such as roads, gas lines, and sewers [1][2][3]. Alternatively, miniaturized duct systems, usually called micro ducts, can maximize the usage of existing duct or increase the flexibility of new duct systems. Traditional cables are far from optimum for these new cable routes. In general, the new cable route solutions require smaller cables that make maximum use of resources.

Historically, ribbon cables have been ideal in applications where service providers want to maximize the number of fibers in limited duct space. Ribbon cables containing 432 or more fibers are commonly deployed in metro rings and long distance backbones.

The advantages of central-core ribbon design may also be realized in the design of small cables for metro applications. The inherently high packing density of ribbon units can be utilized to design very dense low fiber count cables. This paper presents the design of dielectric 48-fiber and 72-fiber ribbon cables with fiber packing densities greater than or equal to 1.6 fibers/mm². Figure 1, below, is

a photograph of the 48-fiber ribbon cable. These cables are appropriate for deployment in both micro duct systems and many new right-of-way systems, including gas lines and sewers.

The new cables will be ideal candidates for deployment in micro duct systems. Micro duct systems have been growing in popularity, primarily in Europe. The use of a micro duct system can reduce the initial capital investment required for a cable route, while leaving room for future capacity growth. We will compare the costs and cash flow of deploying the new small ribbon cables in a micro duct system to the costs associated with conventional cable installation.



Figure 1. Lightweight 48 Fiber Ribbon Cable

2. Economics of Lightweight Cables

2.1 New Right-Of-Ways

New right-of-ways, such as natural gas and sewer lines, provide an attractive alternative path for optical fiber cables compared to the installation of new duct systems. However, installation of optical cables cannot interfere with the primary functions of these utility systems. As such, sub-ducts installed in gas lines or sewers must necessarily be small. Therefore, small cables will be required in order to utilize the new cable paths.

2.2 Sub-Duct Systems

2.2.1 Economics of Miniaturized Duct Systems

Miniaturized duct systems are attractive in the current economic environment. For a given fiber capacity, a sub-duct cable system utilizing miniaturized ducts can be installed at a lower initial cost,

afford greater flexibility for future growth, and provide a greater return on investment in early years of system usage.

To study the economic return of a sub-duct cable system, we will compare the costs of two 288-fiber cable systems of identical length using a simplified model. One system will consist of a single 288-fiber cable. The second system will consist of four sub-ducts, with 72-fiber cables installed in each sub-duct over time.

To make the comparison, we will do the following:

- Calculate the normalized installation cost of the sub-duct systems and a high fiber count cable
- Compare the present economic value of the systems
- Compare revenue streams and return on investment

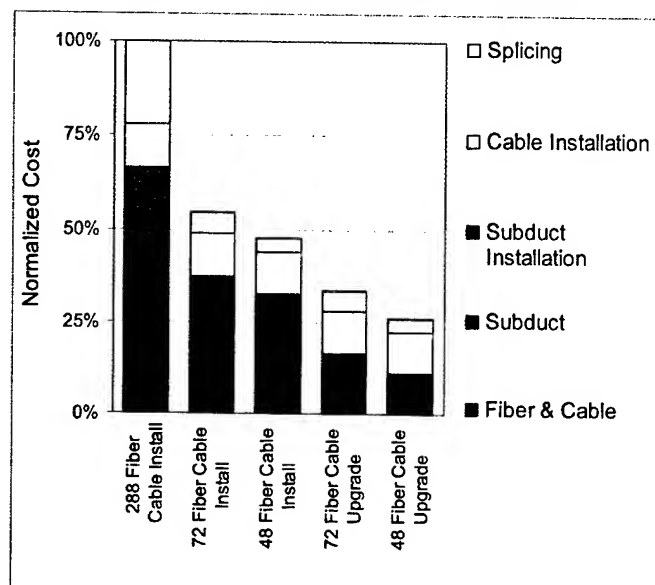


Figure 2. Installation Cost Comparison of Optical Fiber Cables

2.2.2 Initial Costs Figure 2 illustrates the costs of conventional high fiber count cables in comparison to the cost of installing sub-ducts and lightweight cables. An existing 32/40 mm (1.25 in.) cable duct was assumed. The duct has the capacity to hold five – 8/10 mm sub-ducts (48 fiber cables), four – 10/12 mm sub-ducts (72 fiber cables), or a single high fiber-count cable. Cable length was set to 1.5 km. A 288-fiber cable was used as a baseline to normalize costs. Typical North American costs for cabled fiber, cable installation, sub-duct installation, and splicing were used. The cabled cost per fiber was kept constant for all fiber counts. Comparative costs for 48 fiber cables are shown in Figure 2. For simplicity, only 72-fiber cables are used to compare costs in subsequent sections of this paper.

It is obvious that the cost of a lower fiber count cable is lower than the cost of a high fiber count cable. We calculate that the cost of a sub-duct system equipped with a single 72-fiber cable is approximately 54% of the cost of a 288-fiber cable. Three additional upgrades are required to bring the sub-duct system up

to the capacity of the 288-fiber cable. After all upgrades, the cost of a 288-fiber sub-duct cable system will be 155% of the cost of a 288-fiber cable installation. Figure 3 uses the normalized costs from Figure 2 to illustrate the *cumulative* cost of the two installation scenarios over time.

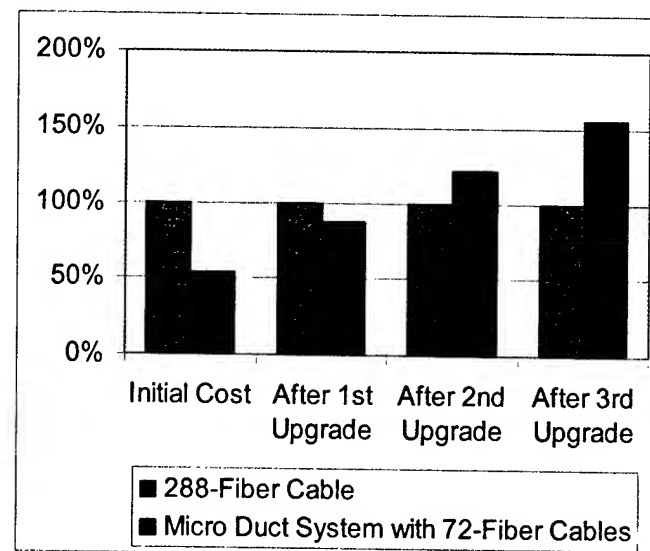


Figure 3. Cumulative Cost of Competing Conventional Cable and Micro Duct Systems

2.2.3 Present Economic Value We can compare the costs of the two systems taking into account the time value of money by looking at the present value of both scenarios illustrated in Figure 3. The equation for the present value of a future sum is given in equation (1).

$$\text{present value } P = F \times (1+i)^{-n} \quad (1)$$

where:

P is the Present value at time 0

F is the Future value at time *n*

i is the interest or discount rate

n is the time of a future value *F*

Note: $(1 + i)$ is raised to the *negative n* power

The relative present value of a micro duct cable system compared to the present value of a 288-fiber cable system using an interest rate of 7% is shown in Table 1. Table 2 illustrates results from calculations at 14%. Looking at the first column of data in Table 1, which uses an interest rate of 7% and an upgrade interval of 1 year, we find that the present value (cost) of the sub-duct cable system is 142% of the cost of the 288-fiber cable.

From Figure 2, we can see that sub-duct installation is a substantial portion of the initial cost of a micro duct cable system. If new duct is required for the route, we could eliminate the cost of a separate sub-duct installation step by using cable duct with integrated sub-duct. For example, when we look at the present value of a micro duct system without the cost of sub-duct installation at an upgrade period of one year, we find that the

present value of the micro cable system is 121% of the cost of the equivalent 288-fiber cable.

Table 1. Relative Present Value of 288 Fiber Cable Systems, 7% Interest Rate

Upgrade Period (years)	1	1.5	2	3	5
72 f Cables with sub-duct installation cost*	142%	137%	132%	122%	107%
72 Fiber Cables no sub-duct installation cost	121%	116%	111%	101%	87%

*System consisting of a single 288-fiber cable = 100%

Table 2. Relative Present Value of 288 Fiber Cable Systems, 14% Interest Rate

Upgrade Period (years)	1	1.5	2	3	5
72 f Cables with sub-duct installation cost	132%	123%	115%	103%	86%
72 Fiber Cables no sub-duct installation cost	111%	102%	94%	82%	65%

*System consisting of a single 288-fiber cable = 100%

In Table 1 and Table 2, the 100% base line is the cost of blowing a 288-fiber cable into an existing duct. The present value is the sum of present values for the four cable installations spaced out by the upgrade period. A 7% interest rate was used in Table 1 and a 14% rate was used in Table 2. By comparing the two tables, it is obvious that higher interest rates make the sub-duct solution more attractive.

2.2.4 Return on Investment As discussed in the previous section, *installed cost of a sub-duct system is usually higher than the installed cost of a high fiber count cable*, even when taking the time value of money into account. Why should a service provider consider the use of small cables in a sub-duct system instead of installing a high fiber count cable? The answer lies in return on investment (ROI), cash flow, and profit.

In Table 3 we extend our simplified model to compare economic return of a sub-duct system with the return on a conventional 288 fiber cable. Since actual revenue from a system is unknown, we have normalized all numbers. We assume that revenue from the comparable cable systems grows linearly as new cables are installed in the micro duct system. We keep the cost of all system components constant.

Table 3. Economic Return of Sub-Duct System

Time Period		0n	1n	2n	3n
Total Investment	288 Fiber Cable	1.0X	1.0X	1.0X	1.0X
	Micro Duct System 72 f cable	0.54X	0.88X	1.21X	1.55X
Revenue		1Y	2Y	3Y	4Y
Return $\left(\frac{\text{Revenue}}{\text{Investment}} \right)$	288 Fiber cable	1.0 (Y/X)	2.0 (Y/X)	3.0 (Y/X)	4.0 (Y/X)
	Micro Duct System 72 f cable	1.9 (Y/X)	2.3 (Y/X)	2.5 (Y/X)	2.6 (Y/X)

where:

- n is the time interval when upgrades are performed
- X is the investment required to install a 288 fiber cable
- Y is the revenue realized during the initial period 0n

From the table, we can see that the return (modeled as the Revenue divided by the Investment) for the micro duct system is greater than the return on the high fiber count cable until the third expansion. By using the micro duct cable system, we are realizing profits sooner than with the high fiber count system. These immediate profits are realized at the expense of potential future profits as the high fiber count cable reaches its forecast capacity.

2.2.5 Route Distance In the previous four sections, we compared the cost of high fiber count cable to a micro duct architecture assuming that the length of the cable route was identical. Another way to look at the micro duct system is to consider the distance of the routes that can be constructed using a given amount of capital. Compared to traditional installations, the lower initial cost of the micro duct system allows service providers to stretch scarce capital over more cable routes. Based on the simplified model, for the same amount of capital, a service provider may construct a route that is 85% longer using a micro duct architecture.

2.2.6 Conclusions from Economic Modeling The installation of small fiber count cables in sub-ducts and alternative rights-of-way makes economic sense in some circumstances. The following is a summary of the application of standard and lightweight cables:

High fiber count cables and/or heavy-duty cables should be used in the following circumstances:

- When the installation route requires the mechanical protection afforded by traditional cables
- When the capacity demand for a route is projected to grow rapidly

- When the cost of the fiber cable is not significant relative to the installation cost of the system
- When capital is readily available and borrowing costs are low
- Where access for future expansion is difficult (bridges, tunnels)
- When cost per fiber must be minimized

Lightweight cables in micro duct systems are attractive in the following situations:

- The service provider needs to maximize short term return on investment and profitability.
- The service provider needs to shorten planning horizons and maximize flexibility in order to react to growth. The micro duct and small cable system gives flexibility to deploy fibers where needed.
- The service provider anticipates that new fiber designs and technology will reduce the cost of future capacity.

From the economic modeling, we can see that the use of small cables in a sub-duct system can make economic sense.

3. Cable Design

3.1 Lightweight Cable Properties

3.1.1 Required Properties A new lightweight cable design must meet the following requirements in order to be useful in micro-duct installations:

- The cable must have the size, stiffness, and flexibility necessary for installation in a small diameter duct.
- The cable fiber count must be high enough to fit the metro route architecture.
- Sufficient mechanical protection and tensile strength are required for cable installation and for protection of the optical fibers.
- The cable must have acceptable attenuation performance in the expected operating temperature range.

3.1.2 Desired Properties In addition to the minimum requirements for a usable cable, other cable properties are desirable:

- The cable should be dielectric to minimize lightning damage and to provide a safe operating environment for technicians.
- Fibers within the cable should be easily identifiable.
- The cable should not exhibit preferential bending. Preferential bending can make the use of a passive intermediate storage device (fleeting) more difficult. [4]
- The cable should have sufficient tensile strength to be pulled for short distances.

- The cable should have sufficient robustness to be coiled inside a manhole without the protection of a duct.
- Other than tensile strength, the cable should have temperature and mechanical performance comparable to standard outside plant optical fiber cables.

3.2 Cable Description

3.2.1 Central Tube Cable Design Low fiber count central core ribbon cables are an appropriate solution for micro duct systems, due to the inherently high packing density of ribbon units. A central core design also provides for enhanced ruggedness in smaller cables. We can consider the entire cable structure as a robust, reinforced composite tube made up of multiple layers to provide crush resistance and cable flexibility.

In the 48-fiber cable, shown in Figure 4, a 4 mm diameter central tube contains eight 6-fiber ribbons. Six fiber ribbons were chosen to be compatible with a 12-fiber architecture. In the 72-fiber cable, shown in Figure 5, a 5 mm tube contains six 12-fiber ribbons.

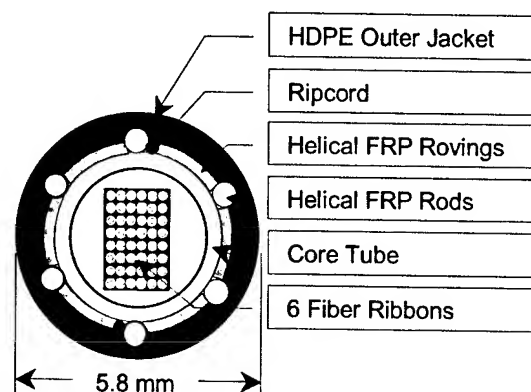


Figure 4. 48 Fiber Ribbon Cable

3.2.2 Ribbon Units Fiber ribbons are a convenient unit structure for small cables designed for simple, low-cost installation. The productivity of mass fusion splicing of ribbons can afford significant time savings during installation. However, the ribbon units in this lightweight cable are also engineered for use in architectures where single fiber management and splicing are desired. Single fiber access is easily accomplished, as the ribbon matrix can be flaked off the fibers without difficulty. [5] Compared to fiber bundles or loose fiber, ribbon units in a central core tube provide compact, easily identifiable fiber groups. In the central core, the ribbons are positioned in sequential order, and can be easily routed within splice trays.

3.2.3 Strength Member System The strength member system is designed as an integral part of the cable structure and is engineered for each core tube size. The strength members are helically wrapped around the core tube. This avoids asymmetrical bending stiffness that can lead to inconsistent coiling in a fleeting device [4]. A minimum of six FRP rods are used to avoid local

preferential bending in tight radius turns, which can occur when four or fewer rods are used. As illustrated in Figure 4 and Figure 5, the strength members completely girdle the core tube and are tightly encapsulated by the outer jacket, to reinforce the structure when the cable is subjected to crushing and impact loads.

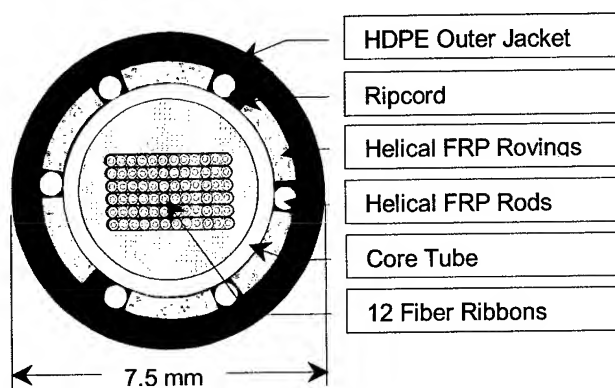


Figure 5. 72 Fiber Ribbon Cable

3.2.4 Outer Jacket Material High-density polyethylene was chosen to provide toughness for the thin jacket section and to provide a low coefficient of friction at high temperatures.

4. Cable Performance

The cable size, tensile strength, and fiber density of the 48 and 72 fiber cables are listed in Table 4.

Table 4. Cable Tensile Strength & Weight

Fiber Count	Fibers per Ribbon	Size (mm)	Fiber Density (Fibers/mm ²)	Weight (kg/km)	Tensile Strength	
					W ¹	N
48	6	5.8	1.8	31	2	600
72	12	7.5	1.6	49	2.7	1330

The operating temperature range of the cables is -40°C to +70°C. A representative sample of test results is presented in Section 5.

5. Test Results

5.1 Test Results Summary

The 48-fiber cable was tested using IEC test methods.

Except for tensile strength, the 72-fiber cable has been tested for conformance to *Bellcore² GR-20-CORE, Issue 2, 1998* [6] and *ICEA-S-87-640-1999, September 1999* [7].

All test measurements summarized in this paper were made at a wavelength of 1550 nm.

¹ A cable rated 1W is able to support 1 km of its own weight.

² Bellcore is now known as Telcordia Technologies.

Results are summarized using a box and whisker plot. The whisker represents the range of measurements. The box represents 50% of all points. The line in the white box represents the median value.

5.2 IEC Testing of the 48-Fiber Cable

5.2.1 Environmental Test Results The 48 fiber cable was tested per IEC 60794-1-F1. A summary of the added loss at the last three temperature measurements at -40°C, +70°C, and ambient conditions is shown in Figure 6. The slight elevation at -40°C is the result of elevation in corner fibers.

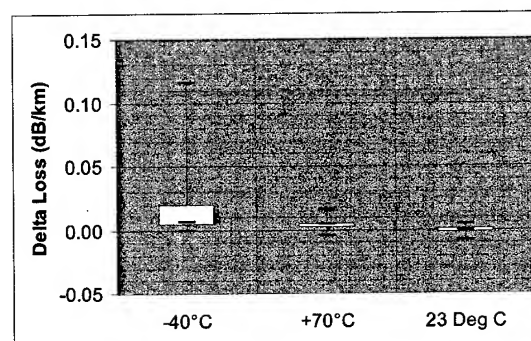


Figure 6. IEC 60794-1-F1 Temperature Cycling, Results for 48-Fiber Cable

5.2.2 Tensile Test Results The tensile performance of the 48-fiber cable was tested per IEC 60794-1-E1 at a tension of 2W, which for this cable is 600N. A summary of the added loss is shown in Figure 7.

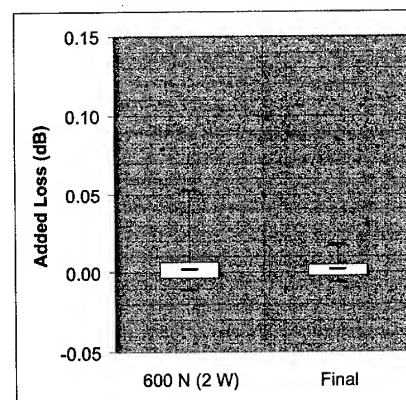


Figure 7. IEC 60794-1-E1 Tensile Performance 48-Fiber Cable

5.2.3 Compressive Strength The compressive strength was tested in two places using IEC60794-1-E3 with a load of 1112 N. The added loss was measured with the cable subjected to the long-term load. The Compressive Strength performance of the 72-fiber cable is summarized in Figure 8. The added loss returned to initial values after the test.

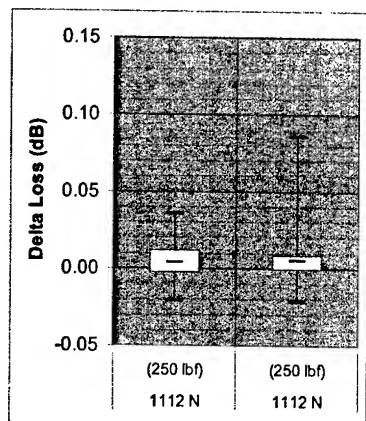


Figure 8. IEC 60794-1-E3 Crush, 48 Fiber Cable, Two Places

5.2.4 Bend Performance The cable was tested per the IEC 60794-1-E6 Repeated Bending test using a 107 mm mandrel. There was no measurable added loss at the end of the test.

The cable was also tested using procedure IEC-60794-1-E11. The cable was wrapped 5 times around a 203 mm mandrel. There was no significant added loss as shown in Figure 9

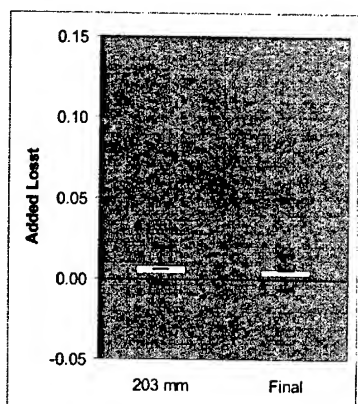


Figure 9. IEC 60794-1-E11 Bend 48 Fiber Cable, 203 mm Mandrel

5.3 Bellcore Testing of 72-Fiber Cable

5.3.1 Bellcore Test Results The 72-fiber cable was tested to the requirements of Bellcore GR-20-CORE, Issue 2 (1998). As described in the subsequent sections, the cable passed all Mechanical and Environmental Requirements except for tensile strength.

5.3.2 Environmental Test Results The 72 fiber cable was tested according to the Temperature Cycling and Cable Aging Tests in Bellcore GR-20. Results are illustrated in Figure 10 and Figure 11.

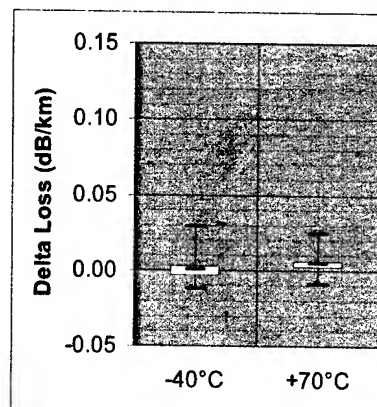


Figure 10. Bellcore GR-20 Temperature Cycling, 72-Fiber Cable

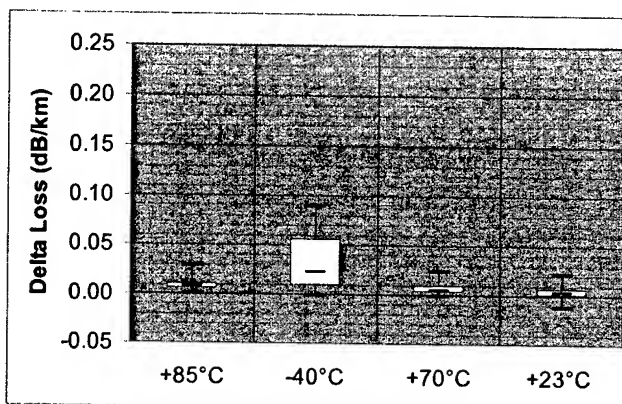


Figure 11. Bellcore GR-20 Cable Aging, 72-Fiber Cable

5.3.3 Tensile Performance The tensile performance of the 72 fibers cable is summarized in Figure 12.

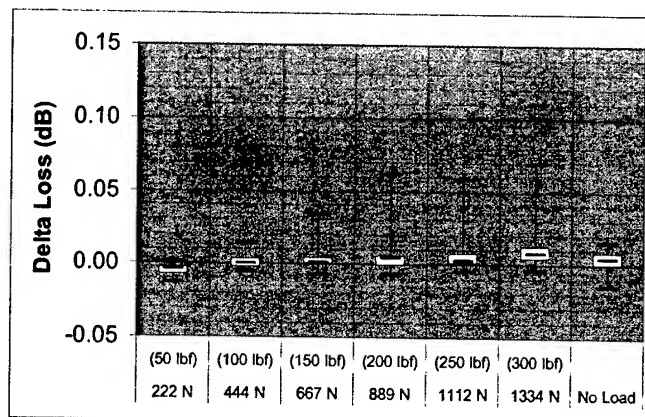


Figure 12. TIA/EIA-455-33A Tensile Load & Bend 72-Fiber Cable

5.3.4 Compressive Strength The compressive strength was tested in two places per Bellcore GR-20, Issue 2 with an incidental load of 220 N/cm, 2200 N total, for 1 minute and a long term load of 110 N/cm, 1100 N total, for 10 minutes. The added loss was measured with the cable subjected to the long-term compressive load. The final measurement after the total compressive load was increased to 440 N/cm and released. The Compressive Strength performance of the 72-fiber cable is summarized in Figure 13.

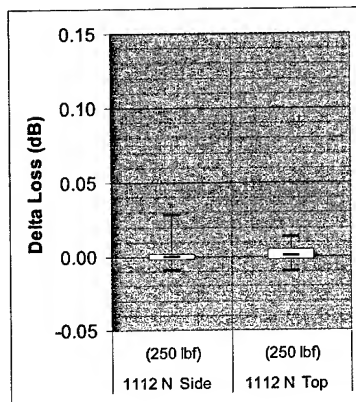


Figure 13. Bellcore GR-20 Compressive Strength Test, 72 Fiber Cable, Two Places

5.3.5 Low and High Temperature Cable Bend. The cable was wrapped 4 times around a 5 in. (127 mm) mandrel at temperatures of -30°C and +60°C per Bellcore GR-20 using FOTP-37. The low and high temperature bend performance of the 72-fiber cable is summarized in Figure 14.

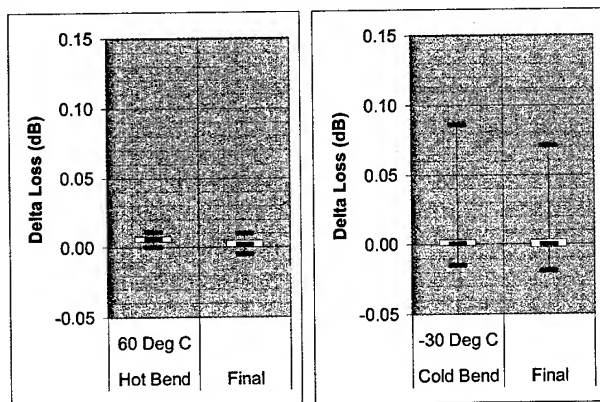


Figure 14. Bellcore GR-20, Low and High Temperature Cable Bend, 5 in (127 mm) Mandrel, 4 Turns, 72 Fiber Cable

5.4 Installation Performance

The 48-fiber cable was tested in a 700m duct trial system designed to simulate a congested inner city environment with numerous bends and rapid changes in elevation. The test route is illustrated in Figure 15. The target was to achieve a blowing distance of 500 m, which represented the maximum distance between access points anticipated by the customer in their network.

A series of trials were conducted comparing different micro-tubes and blowing installation equipment. One major point to note is that no lubricant was used for these trials.

The 500 m target was achieved in all combinations of equipment and tubes. A total distance of 700 m was blown in a time of 10 minutes and 35 seconds. This represented the maximum length of the available test route.

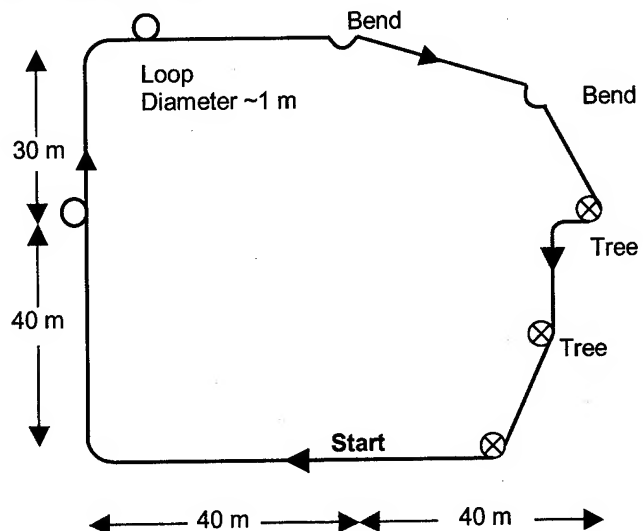


Figure 15. Cable Installation Test Route

The maximum installation distance that may be achieved is dependent upon a variety of factors. These include the blowing equipment, the compressor and the route configuration. Added to this are the different options open to installers with regard to selection of micro-duct designs, i.e. low friction liners incorporated within the tube or the use of lubricants prior to installation. Installation distances greater than 1000 m have been achieved with a maximum distance of 1400 m. This trial was into a duct with a low friction liner and no additional lubricant. Further trials are planned to determine the maximum installation distance that may be achieved.

6. Conclusions

Lightweight dielectric ribbon cables in 48 and 72-fiber versions have been developed. The cables were tested under criteria prevalent in both North America and Europe, and show excellent performance. Characteristic economics have been explored showing the advantages of using these small cable designs in the current economic situation.

7. Acknowledgments

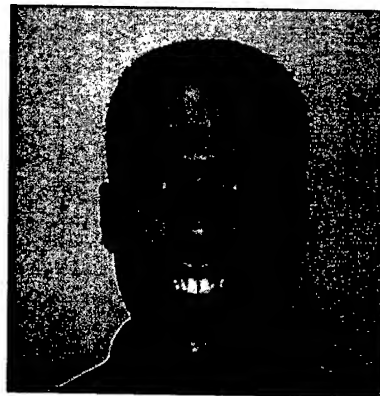
We would like to acknowledge the contribution of Bill Allen of the OFS Fiber Optic Cable Qualification Lab for his assistance in testing the cables.

We would also like to acknowledge the assistance of Czech Telecom, Emtelle UK Ltd., and CBS Products Ltd. for their support with installation trials.

8. References

- [1] J. P. Bonicel, H. Costa-Elias, P. Vertuaux, P. Gaillard, R. Newman, M. Rivard, "A Very Innovative Technology for Right of Way Application", *Proceedings of the 47th International Wire and Cable Symposium*, (1998), pp. 815-824.
- [2] P. E. Gregor, L. Kuhn, A. Weiss, "Optical Fiber Cable Links with Gas Pipelines as an Alternative Telecommunications Route Technology", *Proceedings of the 48th International Wire and Cable Symposium*, (1999), pp. 170-175.
- [3] J. K. Jeyapalan, "Bridging the Last Mile with Fiber Optic Cables in Sewers", *Proceedings of the 50th International Wire and Cable Symposium*, (2001), pp. 724-731.
- [4] M.V. Davies, C. J. Esbester, R. Suthall, P. Barker, D. F. Bastin, "Advances in Blown Cable Technology: The Development and Life Cycle Analysis of a High Density Fibre Cable," *Proc. 50th International Wire and Cable Symposium*, (2001), pp. 658-665.
- [5] K. Konstadinidis, N. W. Sollenberger, S. Siddiqui, K. W. Jackson, J. M. Turnipseed, T. W. Au, R. P. DeFabritis, C. R. Taylor, "UV Color Coatings and Matrix Material for Enhanced Fiber Optic Ribbon Products", *Proceedings of the 46th International Wire and Cable Symposium*, (1997), pp. 274-280.
- [6] Bellcore GR-20-CORE, "Generic Requirements for Optical Fiber and Fiber Optic Cable", Issue 2, July 1998.
- [7] ICEA-S-87-640-1999, "Optical Fiber Outside Plant Communications Cable", September 1999.

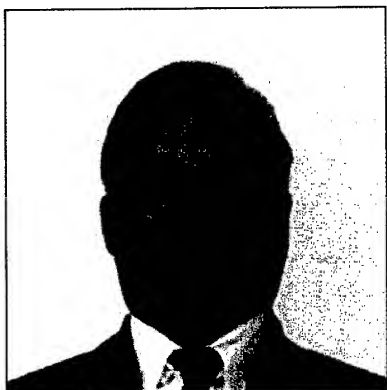
Authors



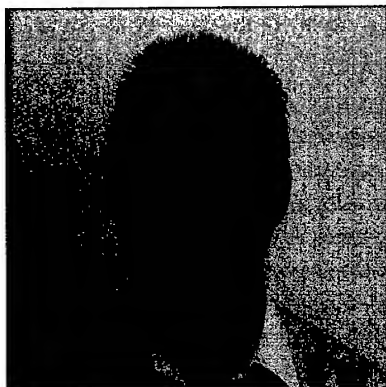
Shawn Davis is a Member of the Technical Staff in the Outside Plant Cable Development Group of the Optical Fiber Cable Division of OFS. Shawn graduated from the Georgia Institute of Technology in 1997 with a BSME. He continued his education part-time while working at Lucent and OFS, and 2002 he earned his Master's Degree in Mechanical Engineering from Georgia Tech specializing in Manufacturing.



H. Paul Debban is a Distinguished Member of Technical Staff in outside plant cable development with OFS, Norcross, Georgia. He holds a BSME from the University of Nebraska – Lincoln. He has more than 20 years experience in optical fiber cable manufacturing and design. In 2001, he was a co-recipient of the Jack M. Spergel Memorial Award from the IWCS.



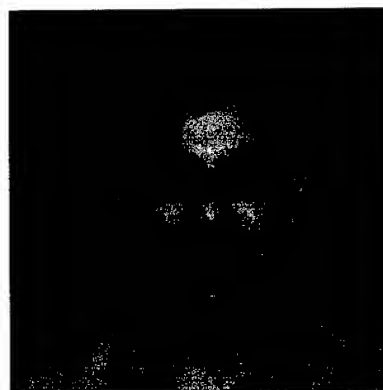
Michael D. Kinard is a Senior Development Engineer and Distinguished Member of Technical Staff with OFS, Norcross, GA. He holds a BSME from Old Dominion University and an MSME from Georgia Institute of Technology. He has worked in cable design and development for more than twenty years. He holds a number of patents in the cable design and processing area.



Jason Pedder is the Manager for Development Projects for OFS in Augsburg, Germany, where he is responsible for product development and R&D activities. He has been an active member of a number of standardization bodies, including BSI and IEC. He has a BSc in Mathematics with Computing and has worked in the optical cable manufacturing industry for 12 years in Engineering, Design and Development.



Mario S. Rossi has 20 years experience in the telecommunications industry, held several positions as Product Designer and Developer, Product Manager and Sales Manager of Central Office and Outside Plant products. Currently Optical Cable Applications Manager at the OFC facility at Norcross, GA, develops systems applications for optical networks. Mario is a graduate Mechanical Engineer from UFRJ (Universidade Federal do Rio de Janeiro), Brazil and Executive Marketing MBA.



Peter A. Weimann is a Member of the Technical Staff in the Materials Technology Development Group, Optical Fiber Cable Division, OFS, Norcross, GA. His primary focus is materials development for outside plant fiber-optic cable products. He has been awarded seven U.S. patents relating to optical fiber cable technology. In 2001, he was a co-recipient of the Jack M. Spergel Memorial Award from the IWCS. He received his Ph.D. in Materials Science and Engineering from the University of Minnesota in 1998. His thesis research focused on structure-property relationships in polyolefins. He received a B.S.Eng. in Materials Science and Engineering, as well as a B.S.Econ. in Organizational Management, from the University of Pennsylvania in 1992.

Design and High-Speed Processing of New Advanced Blown Fibre Units (EPFU's)

Tomas Jendel, Johan Jason, Bertil Arvidsson

Ericsson Network Technologies AB, Kabelvägen 1, SE-824 82 Hudiksvall, Sweden
+46 650 36843, tomas.jendel@eca.ericsson.se

Pasi Meriläinen, Pertti Salo, Jari-Pekka Tiesmäki

Nextrom Oy, Ensimmäinen savu, 01510 Vantaa, Finland
+358 9 50251, pasi.merilainen@nextrom.com

Abstract

Two concepts of EPFU, based on single fibers and ribbon technology respectively, are introduced and discussed from a general performance point of view. Unit design with respect to installation performance, mechanical properties and optical performance is emphasized.

A new, one-step manufacturing process with pertinent manufacturing equipment is furthermore introduced. Key requirements on the process, such as line speed, surface modification quality and stability are discussed.

Keywords

EPFU; blown fiber; ribbon; high-speed; process

1. Introduction

The optical access networks are by necessity getting closer and closer to the end customers as the bandwidth demands continue to increase. Only optical fibers can meet the bandwidth demands of the future, which means that cost-effective and flexible FTTx solutions are more and more important.

Air blown fibre solutions, consisting of small fibre units blown into pre-installed micro-ducts, play an increasingly important role in these solutions. Homes or offices can be connected to the network in any order and at any time when the demand occurs.

One of the most capable fibre units for air blown installation is the Enhanced Performance Fibre Unit (EPFU), developed by British Telecom (BT) during the 'eighties and 'nineties. These fiber units, typically consisting of 2-12 fibers, can be installed at lengths in excess of 1000m in standard 3.5/5.0mm micro ducts. The combination of the installation length, flexibility and cost-effectiveness of the air blown system, makes the use of EPFU in the optical access networks a powerful solution.

Aim and scope

This paper introduces two concepts of EPFU: the single-fiber EPFU for fiber counts up to 8 fibers, based on the concept proposed by BT [1], and the new ribbon EPFU for fiber counts up to 12 fibers. Both concepts are designed for single-mode (SM), multimode (MM) 50µm and 62.5µm fibers.

The first part of the paper deals with design considerations of the two EPFU concepts at hand. The second part of the paper concerns the manufacture of such EPFU's and in particular a new high-speed manufacturing process with pertinent manufacturing equipment is introduced.

A new family of flame retardant acrylates is also discussed. These materials have been developed by DSM Desotech and are partly tailor-made for the EPFU application.

2. EPFU design

2.1 Basic design

Modern EPFU's consist of a number of fibers or ribbons encapsulated in one or more layers of UV-curable acrylates. EPFU's based on acrylates are referred to as *Mark II* EPFU's in the BT terminology and the first versions appeared in the mid 'nineties. *Mark I* blown fiber units first appeared during the early 'eighties and were based on an extrusion process. The main advantages of using a unit design, as well as a process, based on UV-curable acrylates are:

- The fibers are better protected in acrylates. Optical and environmental performance is better compared to extrusion based units
- It is easier and faster to access the fibers during installation
- The units are very compact which means that the duct utilization can be optimized
- Processing in higher line speeds is possible which reduces manufacturing cost and increases capacity
- It is possible to modify the outer surface of the unit to enhance the blow performance – longer blowing distances are achievable

Figure 1 shows the cross-sections of the Mark II single-fiber EPFU and ribbon EPFU products.

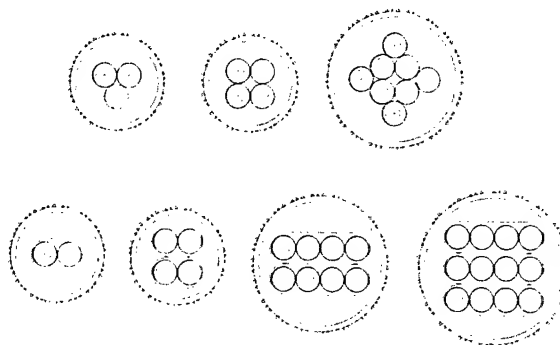


Figure 1. Mark II EPFU cross-sections

The top part of Figure 1 shows the 2f, 4f and 8f single-fiber EPFU (the 2f single-fiber EPFU includes a ripcord for breakout purposes). The bottom part of Figure 1 shows the 2f, 4f, 8f and 12f-ribbon EPFU. All ribbon EPFU units are built up from standard 2f or 4f-ribbons. The nominal outer diameter of the units are: 1.0mm for 2f and 4f units, 1.4mm for 8f units and 1.5mm for the 12f unit.

As can be seen in Figure 1, two acrylate layers are used both for the single-fiber concept and the ribbon concept. The inner layer (buffer layer) consists of a low modulus material, about 10MPa modulus, chosen to protect the fibers. Also, the inner layer must be chosen in a way that it ensures good breakout properties for fibers and ribbons. Since Ericsson ribbons have good fiber breakout performance, the user can decide whether the ribbon should be spliced/connectorized as it is or if the fibers should be accessed individually. The Ericsson Ribbonet™ FTTx system is based on ribbon splicing/connectorizing.

The outer layer consists of a material with a high modulus, 500-600MPa, to make the unit mechanically robust. With this two-layer design in mind it is reasonable to draw a parallel to the design of standard optical fibers and the ability to reduce the effects of both macrobend and microbend attenuation increases. Furthermore it is essential that the outer layer material can accommodate the small glass beads on the surface that are used to enhance the blow performance, see Section 2.2.

The outer layer acrylate is colored to distinguish different fiber types, i.e. yellow for SM, blue for MM50 and red for MM62.5.

2.2 Blow performance and installation

In this section the design of EPFU from a blow performance point of view is discussed. Installation of EPFU is carried out with a blowing tool connected to an air compressor. The unit is also typically pushed by a wheel as a complement to the air flow.

A good blow performance is mainly related to the following properties of the EPFU:

- Unit stiffness
- Unit weight per meter
- Unit memory
- Unit surface modification

Stiffness, weight and memory

Unit stiffness is specified with a minimum and maximum value. A low stiffness unit will tend to buckle whereas a high stiffness unit will have problems negotiating sharp bends along the installation route. The stiffness can be controlled by the modulus of the materials and also the corresponding layer thickness.

Since the unit is dragged forward by an air flow, a unit too heavy will have a negative impact on the blow performance. This means that the weight must also be specified and controlled.

Unit memory relates to the tendency of the unit to "remember" the shape of the reel or pan it is delivered on. This phenomenon can clearly have a negative impact on the blow performance. Controlling unit memory is, like the unit stiffness, also related to the modulus of the materials and the layer thickness. This is further discussed in Section 2.3.

Unit surface modification

The surface modification of the EPFU is critical to the blow performance. The modification proposed by BT consists of small glass spheres that are sprayed onto the surface of the uncured outer acrylate layer. When the layer is cured in the UV lamp, the glass beads are partially embedded in the outer layer. This is illustrated in Figure 2 and Figure 3.

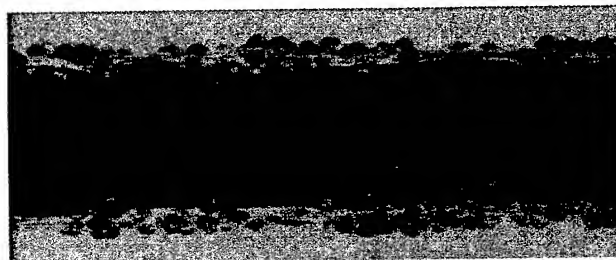


Figure 2. Sideview of MkII EPFU.



Figure 3. Cross-section of 4-fiber EPFU.

There are three reasons behind covering the surface with glass beads:

- 1) The coefficient of friction between the unit and the duct wall is reduced
- 2) The viscous drag force caused by the air flow is increased due to an increased surface roughness
- 3) Static effects between the EPFU and the duct wall are minimized due to the material properties of glass.

The effect on blow performance from different types of glass beads of different sizes have previously been investigated by BT [1].

Recent tests on EPFU's have indicated that a bead diameter of about 100µm is optimum. It is important that the beads do not penetrate the outer layer too much so that the acrylate layer comes into contact with the duct wall. Controlling bead penetration is also important from a mechanical point of view, see Section 2.3.

When it comes to the bead coverage, i.e. the amount of beads per surface unit, new tests have been performed in co-operation with BText Technologies. Figure 4 shows three 4-fiber single fiber EPFU prototypes with different degrees of bead coverage and surface roughness values. The units have been installed in

BTexact Technologies' blown fiber test route and the installation time needed to reach 1000m has been measured.

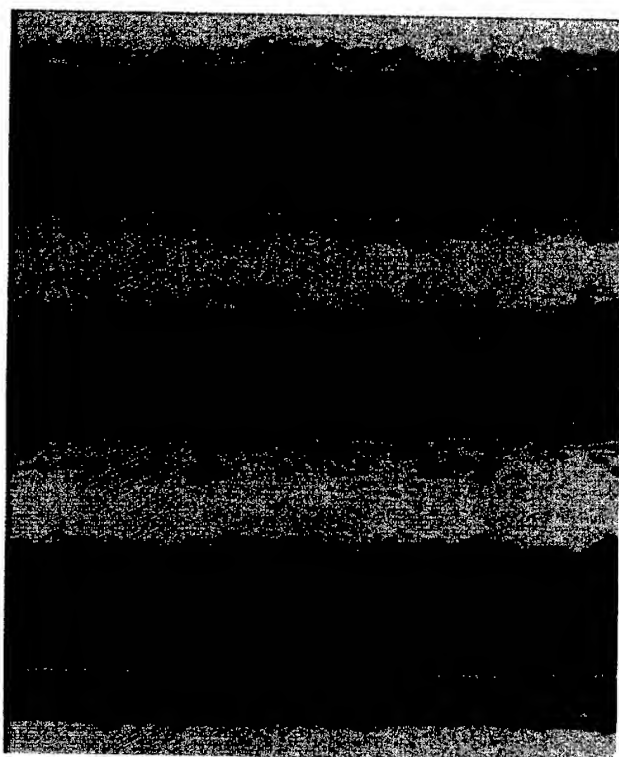


Figure 4. Prototype EPFU's with a different degree of bead coverage and Rz values. Samples are labeled A, B and C from the top and down.

The blow performance and corresponding unit Rz value is shown in Table 1 (the Rz value is the mean peak to valley height calculated according to the DIN standard). The installation time is normalized with the installation time of sample A.

Table 1. Blow performance comparison of three samples with different bead coverage degree and Rz values.

Sample	Rz [μm]	Normalized installation time compared to sample A to reach 1000m
A (top)	67	1.00
B (middle)	74	1.09
C (bottom)*	53	1.01

* The bead grade used in sample C contains a larger portion of smaller diameter glass beads compared to sample A and B.

As can be seen in Table 1, the installation time is rather independent of the bead coverage and the Rz value on the three samples. This is further supported by blow trials not reported in this example.

The surface modification by means of glass beads is thus summarized as:

- There shall be enough beads to ensure that the duct wall is not touched by the outer acrylate layer.
- The surface roughness value shall be maintained within specification for the same reason. This is controlled by the bead size and the bead penetration.
- Variations in the surface roughness value do not affect the blow performance significantly, at least not for the levels shown in Table 1.
- A very high degree of bead coverage does not necessarily optimize the blow performance. Also, too many beads may affect mechanical and optical properties of the unit.

2.3 Mechanical properties

It has already been mentioned in Section 2.1 that the EPFU's consists of two layers of acrylates for protection; a soft inner layer and a hard outer layer. The two-layer acrylate concept is very well suited to fulfill all mechanical demands.

Unit robustness

The unit shall be robust to protect the fibers during installation and during the operating life time when installed in the micro duct. The soft inner layer absorbs forces that originate from bends or pressures and the outer layer is hard and tough to prevent damage to the fibers and the inner layer.

Stripping and handling

The unit shall be easy to strip and handle during connectorizing and splicing. The inner acrylate material has been chosen to optimize fiber and ribbon breakout. It is also beneficial to have a soft layer inside a hard layer from a breakout point of view. The stripping of the single fiber concept follows the method outlined in the BT EPFU specification [2], see also Section 2.6.

Unit memory

The unit memory is controlled by optimizing the acrylate layers modulus and thickness. Generally speaking it is beneficial, from a memory point of view, if the materials are as close as possible in modulus. This optimization is a trade-off between fiber protection and unit memory.

Accommodation of glass beads and formation of cracks

The outer layer must be suited to accommodate glass beads and prevent the unit from breaking apart when subjected to bending forces.

Firstly it is important to control the bead penetration depth to avoid cracks forming down to the buffer layer when the unit is bent. The outer layer has a thickness of 80-90 μm and it has been found that a minimum distance of about 30-40 μm between the buffer layer and the glass beads is sufficient to prevent cracks forming during normal bending situations. This is illustrated in Figure 5.

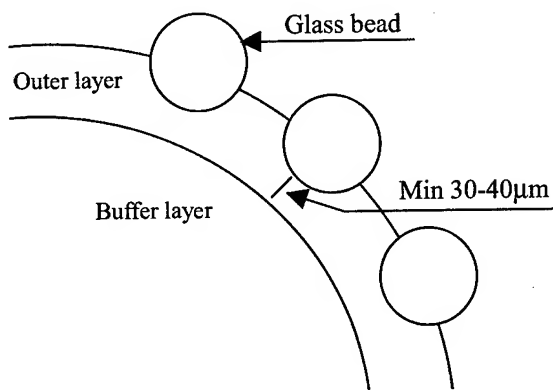


Figure 5. Minimum distance between buffer layer and glass bead to prevent crack formation.

Secondly it is important that the outer material has a high elongation, 30% or more [1], in order to reduce the risk of cracks forming between the beads and the surrounding acrylate.

2.4 Materials and flame retardancy

The materials used for the new EPFU product range are developed by DSM Desotech and are a part of a new family of developmental resins. Due to advances in chemistry, the materials have enhanced abilities compared to standard acrylates:

- All materials in the new family are easy to process, meaning that a good product quality can be maintained in high line speeds and at high material flows without using extreme acrylate and coater temperatures
- The materials are significantly cheaper compared to comparable acrylates due to the chemistry used
- The materials have, for acrylates, unique flame retardant abilities. The materials preliminary fulfill the UL94 V0 standard (UL94 Part 8.4.1, 3.5mm specimen thickness).

The materials have been partly tailor-made for the EPFU application, especially the high-elongation outer acrylate material.

2.5 Optical and environmental properties

EPFU's are typically used both in indoor and outdoor applications. This means that the unit design must take into account a wide operating temperature interval.

The two-layer acrylate concept described earlier is well suited to protect the fibers from harsh environments such as low (-40°C) and high ($+70^{\circ}\text{C}$) temperatures and moisture. Since there is no accepted international standard applicable for EPFU's, the Ericsson EPFU's are tested in accordance with the pertinent BT specifications [2], see Section 2.6.

The BT specifications include temperature cycling, water immersion and mechanical tests on the units.

2.6 Standards and specifications

Ongoing standardization work is represented by an IEC work proposal: *IEC 60794-3-50 Micro-cables, fiber units and mini-tube systems for installation by blowing technique* [3]. The proposal outlines tests and requirements on both tubes and fiber

members. The tests concerning the fiber units are: kink, bend, crush, tensile performance, temperature cycling, heat aging and water soak. Installation performance is not included in the proposal.

Until now, and until the IEC standard is widely accepted, the BT specification for EPFU's has been more or less acting as a standard.

3. EPFU processing

A completely new process and pertinent process equipment has been developed for manufacturing of the EPFU's described in Chapter 2. Here we will first focus on general process and equipment requirements in Section 3.1 and then turn to the actual implementation in the Nextrom OFC22 EPFU line in Section 3.2.

3.1 General process requirements

In the case of EPFU it is very important to reduce the manufacturing cost, since FTTx systems typically depend on a low total cost to be competitive. Modern production lines for fiber optical products are designed for high line-speeds, high capacity and minimum scrap and down-time to reduce the manufacturing cost. Advanced line control systems are used to control every detail of the process.

Some of the process requirements are general, like reducing down-time, guaranteeing product quality and maximizing capacity, while some requirements are unique to the EPFU product. We will here list the key requirements on the EPFU process and pertinent equipment that were used when the process and production line were developed:

- A one-step process. Additional operations increase the cost significantly. This means that both acrylate layers, and also the surface modification, must be applied in one process
- Single-fiber EPFU and ribbon EPFU produced in the same line. The dual concept of this product will lead to certain requirements for the production equipment, for instance a dual pay-off system and different die-sets for the coaters.
- Line speed $\geq 300\text{m/min}$
- Production lengths up to 25km in one set-up
- Fast and optimized ramps to reduce scrap
- Continuous acrylate feeding system to minimize down-time
- Operating friendly design.

The line speed is limited by the spray chamber used to modify the unit surface. When the line speed is too high, it may be difficult to obtain the bead coverage necessary for a good blow performance. At 300m/min the unit will only be inside the spray chamber for about 0.1s. The spray chamber, developed by BTexact Technologies, has been successful in achieving 300m/min with good quality and it is even possible that the line speed can be increased in the future.

Without the spray chamber active, line speeds of 600m/min or more are typically possible. This is interesting for future increases in line speed and when producing other products in the line.

3.2 Nextrom OFC22 EPFU line

The new EPFU line is based on long experience with ribbon lines, UV-curing and fiber handling technology. All requirements listed in Section 3.1 are fulfilled with the line. The process lay-out of the line is shown in Figure 6 and a picture of the same is shown in Figure 7.

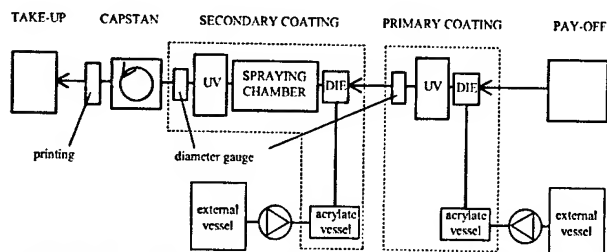


Figure 6. Process lay-out of OFC22 EPFU line.

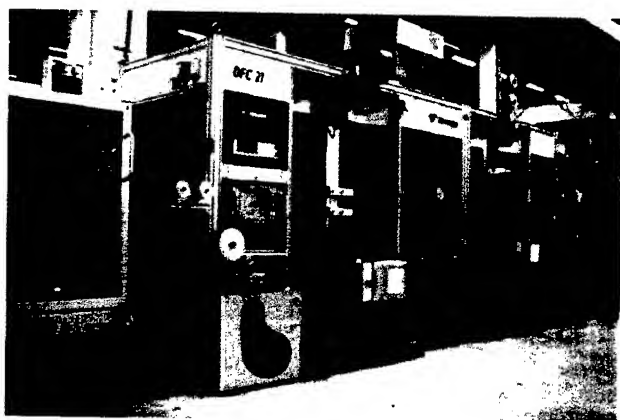


Figure 7. OFC22 EPFU line. Spray chamber not fitted at secondary coating stage in this picture.

General features

As can be seen in Figure 7, the line features two vertical coating stages, called primary and secondary coating, with independent, automated acrylate feeding systems. This line configuration, which is very similar to a standard ribbon line, makes the line easy to operate since no ladders or similar equipment is necessary for the operation. Also, the line will physically fit into average clean rooms since no tower structure is required. The function of the spray chamber also requires a vertical operating direction.

An integrated line computer with a dedicated control software controls all the relevant process parameters to maintain a high product quality. Control parameters include line speed and ramps, acrylate feeding controls, UV-system, fiber tension control etc.

Pay-offs

The line features a unique dual pay-off system to handle both the single-fiber and ribbon EPFU concepts, see Figure 8. The prototype EPFU line, shown in Figure 7, is equipped with three heavy pay-offs, suitable for ribbon reels, and four fiber pay-offs, suitable for standard fiber reels. The number of pay-offs can easily be increased for higher fiber count units since the line is of a modular design.

The pay-off tensions are individually controlled in order to optimize the excess lengths of both fibers and ribbons in the EPFU.

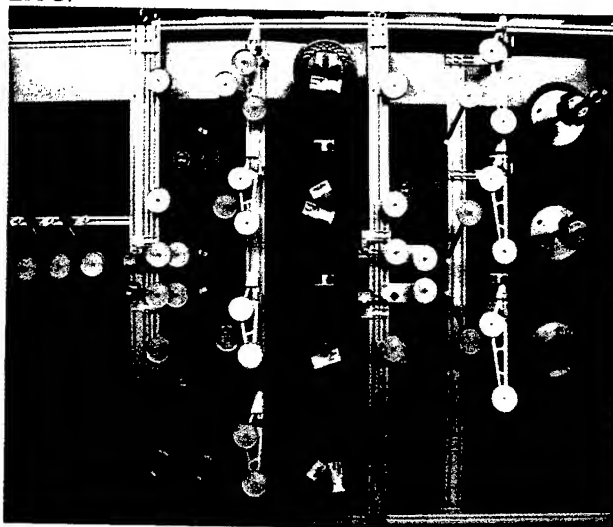


Figure 8. Dual pay-off system for fiber and ribbon reels.

Primary coating system

The primary coating, i.e. the buffer layer, is applied right after the pay-offs. The coaters are of a completely new design and are optimized for high-speed processing with large flows of material, see Figure 9.



Figure 9. EPFU coating system with coater table and coater.

All products within the EPFU product range have different guide dies at the inlet of the primary coater to build up the correct geometry of the unit. The circular exit die then determines the dimension of the buffer layer.

The 4- and 8-fiber single-fiber EPFU's feature a void in the middle of the unit, see Figure 1. This void has two purposes: 1) to avoid problems with trapped air in the center of the unit when the layer is cured in the UV-lamp and 2) to define and maintain the unit geometry.

The acrylate is fed from an electrically heated vessel inside the line via an electrically heated hose. The temperature of the acrylate is controlled by the line control software by means of a

temperature sensor just before the coater. The primary layer is cured in a 600W Fusion™ VPS lamp.

Secondary coating system

The secondary coating layer, i.e. the outer layer, is applied in a similar coater as the primary coating layer. In this case, however, the dies are all circular but with different dimensions corresponding to the fiber counts.

The surface of the unit is modified in the secondary coating stage by means of the spray chamber developed by BTexact Technologies. The small glass beads are sprayed onto the wet, uncured surface of the unit right after the outer layer has been applied. The main parameters to control are the degree of bead coverage and the bead penetration depth, see further Section 2.2. The outer layer with the glass beads on it is then cured in a 600W Fusion™ VPS lamp to create a solid surface modified for blow performance enhancement.

The exact design and function of the spray chamber cannot be published in this paper due to legal constraints.

Capstan and take-up

The capstan is creating a constant speed for the process. It is also working as a length calculation point. After the capstan the end product can be marked by an ink-jet printer for product identification. It is also possible to perform the marking during the panning operation (i.e. the coiling of EPFU into field use plastic pans).

Before the take-up, the product diameter is measured. An alarm can be set for diameter tolerance.

The fiber unit is then wound to a *FRT* take-up system which has been modified to handle extra heavy ribbon reels, corresponding to 25km of 4f EPFU, see Figure 10.

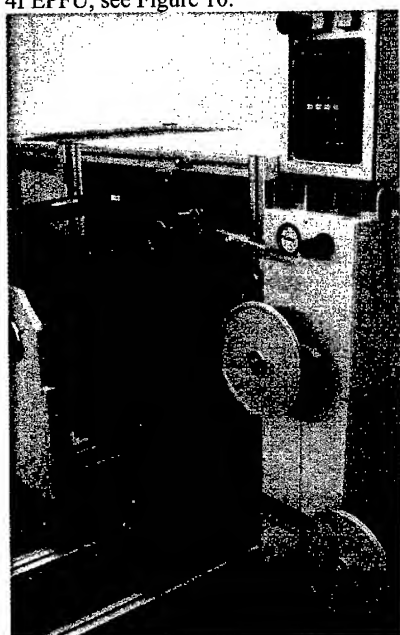


Figure 10. *FRT* take-up with a one loop dancer system modified for heavy ribbon reels.

The one loop dancer system provides easy setup and a wide range of tension settings for optimum product spooling.

Other features

There are also some other special line modifications that are related to the EPFU products. One example is the extra large diameter of the top and bottom pulleys after the primary and secondary coating systems. These large wheels are used to prevent the ribbons in the ribbon EPFU concept from travelling different distances. The effect is most notable for the 12-fiber unit, where the bottom ribbon tend to get buckled, with attenuation increases as a result, if the pulleys have too small diameters.

All pulleys and guide wheels have also been fitted with a special groove shape with a small radius in the bottom for stable processing.

Producing other products in the line

By changing coaters, materials and guide pulleys, the line can also be used to produce other products. Examples are standard ribbons, splittable ribbons and tight-coated fibers.

4. Conclusions

Two concepts of EPFU have been introduced and discussed from a general design and performance point of view. The single-fiber concept is based on the concept proposed by BT and consists of 2-, 4- and 8-fiber units. The new ribbon EPFU concept is unique in the way that the fibers can be accessed as ribbons or as single fibers depending on the application. Ribbon EPFU consists of 2-, 4-, 8- and 12-fiber units.

Key product performance areas like blow performance, mechanical robustness, mechanical handling and optical performance have been discussed. A family of developmental flame retardant acrylates has also been introduced into the EPFU product range.

A unique manufacturing process for both EPFU concepts has furthermore been introduced. Key features are a one-step process, high-line speed and a new production line capable of producing both concepts.

5. Acknowledgments

BTexact Technologies is acknowledged for providing access to the blow performance results and the development work of the spray chamber.

DSM Desotech is acknowledged for the development work with the new flame retardant EPFU materials.

6. References

- [1] P.A. Barker & R Lowe, "Blown Fibre – Second Generation Development," *Plastics in telecommunications*, (September 1995, London).
- [2] British Telecommunications, EPFU Specifications CW1572, CW1573 and CW 1574.
- [3] IEC Work Item Proposal 86A/755/NP, "IEC 60794-3-50 Micro-cables, fiber units and mini-tube systems for installation by blowing technique", (February 2002).

Biography



Tomas Jendel received a Licentiate degree in Vehicle Engineering from the Royal Institute of Technology in Stockholm in 2000. He is working with research and development of fiber optic products, mainly focusing on EPFU, tight-coated fibers and ribbon technology.



Johan Jason received a M.Sc. degree in Engineering Physics from Lund Institute of Technology, Sweden, in 1996. Currently he works with product and process development with special focus on ribbon and EPFU technology.



Bertil Arvidsson, manager of fiber technology at Ericsson Network Technologies AB and an Ericsson expert, has been involved in optical fibers for many years. He is active in IEC and CENELEC with the standardization of optical fibers and cables. Prior to joining Ericsson in 1990, he worked as a technical project manager in Sweden, the United States and Switzerland. Before that he was a university lecturer in theoretical physics. He has a doctor degree in Theoretical Physics from Uppsala, Sweden.



Pasi Meriläinen received his B.Sc. degree in Electrical Automation in 1998. He joined Nextrom in 1998 as a Process Engineer for optical fiber finishing lines. Currently he works as Product Engineer for optical fiber ribbon lines.



Pertti Salo joined Nextrom in 2001. He is currently working as Process Engineer for ribbon machinery. Mr. Salo received his B.Sc. degree in chemical engineering in 2000.



Jari-Pekka Tiesmäki was born in Espoo, Finland, in 1966. He received his B.Sc. degree in Electrical Automation in 1992. He joined Nextrom in 1994 where he first worked as Electrical Engineer of optical fiber cabling lines. Beginning in 1995 he worked as process specialist of optical fiber ribbon line. Currently he works as Product Manager of ribbon line.

Control of Loose Buffer Tube Properties with Advanced Techniques of Nonlinear Modelling

A. Bulsari

Nonlinear Solutions Oy, PL 953, 20101 Turku, Finland

and

M. Lahti and S. Sneek

Nextrom Oy, PL 44, 01511 Vantaa, Finland

Abstract

Several properties of loose buffer tubes or secondary coatings of optical fibers are important. Today, the producers resort to trial and error to arrive at process conditions which result in acceptable properties of the loose buffer tubes, because this task requires special know-how which is not very common. The producers normally find some acceptable conditions, but these can be far from the optimal conditions. It is still difficult to find the process conditions which will lead to narrowly specified properties. To make this task easier and more systematic, a lot of valuable infrastructure and knowledge has now been created. As suppliers of extrusion equipment for the loose buffer tubes, Nextrom has taken the responsibility to provide a high standard of support services to ensure that the user of their extrusion lines derive the best from the equipment.

Today, the user can key in the desired characteristics of the loose buffer tubes in terms of three properties, viz., excess fiber length, shrinkage, tensile modulus, and the process guidance system shows the process conditions which will result in the desired properties, if feasible. This, obviously, needs quantitative knowledge about the effects of process variables like line speed and cooling water temperature on the product properties. Advanced techniques of nonlinear modelling, which have come up in the last ten-twelve years, have been utilized to develop sophisticated nonlinear models of the loose buffer tube properties, for a variety of fiber/tube configurations.

This paper describes nonlinear models for three product properties of one fiber/tube configuration, along with how these models are utilized for control of the properties. As a conclusion, the task of determining good process conditions has been automated to a good extent, which makes a lot of valuable quantitative knowledge available to the users for their benefit.

Keywords

Loose buffer tube; PBT; excess fiber length; shrinkage; tensile modulus; nonlinear modelling.

1. Introduction

Every industrial sector faces competition and OFCs are no exception. Some compete by price, some by quality, some by their marketing prowess. Competitiveness on a sustainable basis comes usually from quality and production economics. Too many companies offer equipment that can produce the products, but few offer the added value in terms of optimized designs, and fewer offer packaged expertise and process know-how to get the most from the equipment. Nextrom wants its customers to derive the most from their equipment, and is in a position to provide relevant automation solutions in a compact form. These solutions are aimed at helping its customers improve the quality of the loose buffer tubes, and maximizing the line speeds while maintaining the desired characteristics of the buffer tubes.

Secondary coating is a plastics extrusion process, followed by controlled cooling and winding under tension (Figure 1). The properties of loose buffer tubes like excess fiber length depend to a large extent on the process variables and the material properties of the plastic. For a given product, the plastic material, the jelly, the external and internal diameters, and the number of optical fibers in it are fixed. The properties of the buffer tubes, then depend on the process variables, starting from tension on the optical fibers, extrusion variables, jelly temperature, cooling water temperature, line speed, capstan location, winding tension, etc.

A large part of technological development today is based on automation systems. Automation systems are getting more and more sophisticated, more and more intelligent all the while. These automation systems improve the quality of the products, make the processes smoother and often make the task of the production people easier. Electronics and computers have expedited the improvements in automation systems to a great extent particularly in the last decade. Today, computers do more and more of what used to be done by human beings. Automation is the future. Macroeconomic growth to a larger and larger extent will depend on the degree of automation. Better quality, better efficiency, higher productivity per employee in an industry means better competitiveness. Automation helps in all these aspects. We simply can't afford today not to continuously improve the degree of automation of our industries.

At the core of the automation systems is mathematics. Mathematical models determine to a great extent the efficiency of the automation systems. Today's process industries use a variety of quality assurance and quality control systems. Often they work quite well. The difficulty with them is that they are usually not updated often to reflect the present state of the process and the equipment. The models used are often linear, based on linear regression on a large number of variables. The models may sometimes exhibit misleading trends. The effects of process variables on the main variable of interest may not be predicted reliably.

The high-speed secondary coating line (Figure 1) is especially designed for loose tube production but it can be modified for fiber bundle or premises cable production thanks to its modularity. The line comprises multiple new innovations for high productivity and minimized scrap. Secondary coating is an important phase in the manufacturing process of fiber optic cables. The process is important in two ways. Stability and repeatability of the process together with high production speeds and flexibility of operation have been the key criteria in designing this line.

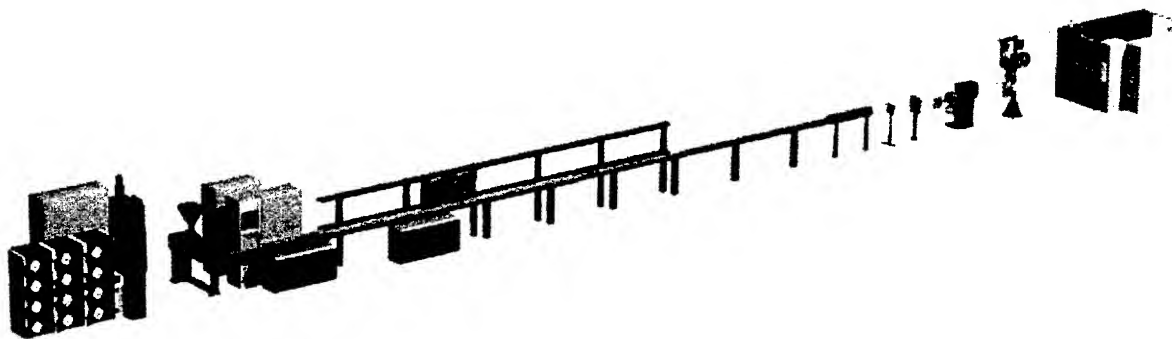


Figure 1. Extensive quantitative knowledge about the loose buffer tube production line makes it easier for the users to derive high line speeds while maintaining the properties within desired limits

2. Nonlinear modelling

There are hardly any processes in this world which are absolutely linear. It is therefore wise to treat the nonlinearities rather than ignore them. To treat the nonlinearities, one can use new techniques of nonlinear modelling, like artificial neural networks. The proponents of linear techniques draw on their simplicity and the possibility of adding nonlinear terms in linear regression. Often this is not done, and is not efficient even if it is done. Nature does not follow the simplicities that we try to fit it in, using linear techniques.

Neural networks, on the other hand, have the so-called universal approximation capability which make them suitable for most function approximation tasks we come across in process industries. The user does not need to know the type and severity of nonlinearities while developing the models.

2.1. Artificial neural networks

Artificial neural networks resemble structurally and to a smaller extent functionally the networks of neurons in biological systems. Like the networks of neurons in the brains, artificial neural networks also consist of neurons in layers directionally connected to others in the adjacent layers (see Figure 2).

There are many different types of neural networks, and some of them have practical uses in process industries [1]. Neural networks have been in use in process industries for about ten years. The multilayer perceptron, a kind of a feed-forward neural network, is the most common one. Most neural network applications in industries [2-10] are based on them. Nonlinear modelling can also be done in many other ways. Neural networks have been utilized for several purposes in plastics industries. Much of the work of the authors is confidential and is therefore not published.

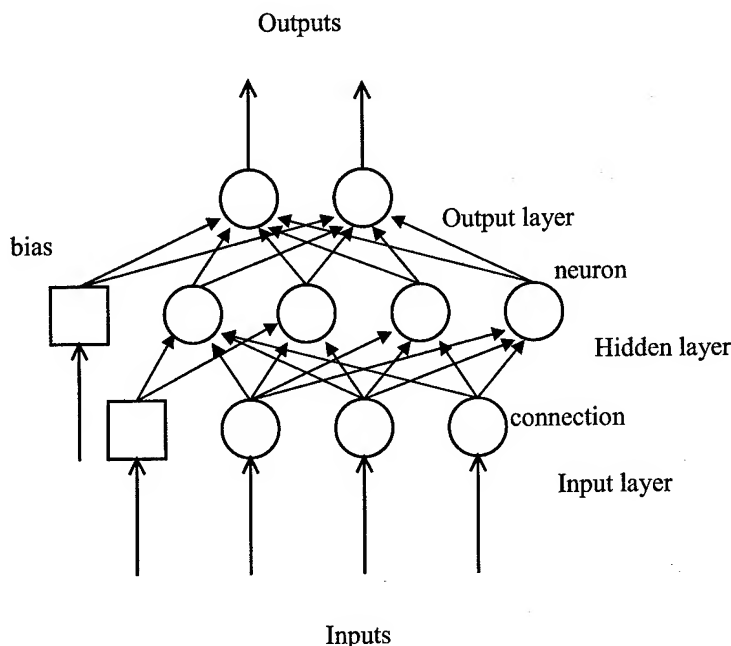


Figure 2. A typical feed-forward neural network

The output of each neuron i in a feed-forward neural network is given by

$$z_i = \sigma \left(\sum_{j=0}^N w_{ij} x_j \right)$$

where the activation function is usually the logistic sigmoid, given by

$$\sigma(a) = \frac{1}{1 + e^{-a}}$$

The incoming signals to the neuron are x_j , and w_{ij} are the weights for each connection from the incoming signals to the i^{th} neuron. The w_{i0} terms are called biases. This results in a set of algebraic equations which relate the input variables to the output variables. Thus, for each observation (a set of input and output variables), the outputs can be predicted from these equations based on a given set of weights. The training procedure aims at determining the weights which result in the smallest sum of squares of prediction errors.

There are a variety of training methods in use today. Back-propagation used to be the most common training method about ten years back. Today, most people use good optimization methods instead.

There is a lot to learn from ten years of experiences with nonlinear modelling in a wide range of process industries. The following factors seem to be common to most success stories:

- a problem fit for empirical modelling
- significant benefits from solving the problem
- expertise and years of experience of neural network modelling
- an understanding of process engineering and the materials
- powerful software tools
- a functional implementation of the models in easily usable form

2.2. Quality of the nonlinear models

A large number of people today claim to be able to develop neural network models. A large number of people can offer you impressive user interfaces that hide the details of the neural network models inside. However, not many people can solve real-world problems. Very few are able to produce industrially usable systems of good quality. Fewer are consistently successful in every project they agree to take. The result is that there is a wide variation in the quality of nonlinear models. How do you know which models are good and which models are not? In other words, what are the characteristics that you look for in a good nonlinear model? What kind of software tools and techniques help ensure a good quality?

2.3. Characteristics of good nonlinear models

The simple answer to the first question is that the proof of the pudding is in the eating: A good model has to work. There is of course more to it than that. A good model for industrial purposes has to be reliable. Accuracy is secondary. A good industrial model has to be robust. You want a model that can be updated relatively easily. You want the model to have some transparency, and the simpler the better. At the same time, a good model efficiently treats all the important nonlinearities. Reliability, robustness, simplicity, maintainability often come at the cost of accuracy and efficient treatment of nonlinearities. These conflicting demands make nonlinear modelling a harder task. That does not leave too many people who will offer you all these attributes. Most are satisfied with claiming accuracy. It is important to insist on highly reliable and robust models because several decisions might be made based on the answers from these models. Considering the possible effects these decisions can have, it becomes quite obvious that the models should be of as good quality as possible.

In other words, the quality of a nonlinear model is much more than accuracy, and there is a scarcity of quality of nonlinear modelling today. There are no simple ways of measuring reliability and robustness of nonlinear models. How does one ensure these and other features? Experience and expertise are essential for neural network model development. However, a good software tool goes a long way by offering you a variety of measures that tell you of possible undesirable features in the models.

2.4. Features of good nonlinear modelling software

Good nonlinear modelling software consists of facilities for (1) preprocessing of the data, (2) training, testing and validation of the models, and (3) a detailed analysis of the resulting models which can tell you something about the reliability and robustness of the models.

A good software package should let you divide your data set into training, test and validation sets of sizes you prefer, sequentially, blockwise or randomly. It should tell you how balanced the division is, and where the imbalances are. No division is perfectly balanced. A measure of the imbalance helps in comparing possible divisions of the data and interpretation of final results.

Training is an optimization task for which good optimization techniques should be used. Therefore, a good software should be based on good optimization techniques. In process industries, there is usually no good reason to use back propagation or one of its variations. The software should report several measures of the errors including variance, standard deviation or rms error, rms % error, etc. and also record each individual residual. It helps to know if some observations always have large prediction errors.

A good software tool should also let you see what each neuron in a neural network is doing. Often there are dead neurons, neurons performing the wrong task, or doing too little. Sometimes two neurons are found doing exactly the same task. It should record the

effects of each input variable, and some details of the nonlinearities present. A facility for sensitivity analysis is also useful. It is also useful to see the saturation levels of neural network models. This kind of analysis often exposes undesirable features in a neural network model.

3. Nonlinear models of three properties

In this work, feed-forward neural network models (Figure 2) were developed based on experimental data with process variables as inputs. The nonlinearities are visible in the neural network models (Figure 6). The neural networks used logistic sigmoid activation functions, and were found to work well. This is a typical situation where the conventional linear statistical techniques are not effective.

Levenberg-Marquardt method [11-13] was used to determine the free parameters of the models. Determining the free parameters of these models is essentially a least squares minimization problem, where the sum of squares of prediction errors is minimized. Back-propagation was a very popular technique in the earlier years, which is an approximation to the steepest descent method. However, today, almost all serious work is done with better optimization methods. The first order optimization methods use first derivatives to determine descent directions, often combined with a line search to determine the step length. The second order methods use a Taylor-series approximation to determine a better measure of the minimum assuming that the second order term of the Taylor series sufficiently represents the nonlinearity of the function to be minimized. The Marquardt method finds a direction between that of the steepest descent and a plain second order method which ensures that every iteration leads to an improvement in the function value until a local minimum is reached. There are variations of this method and improvements which reduce calculation time. Second order methods consume a lot of time in evaluation of second derivatives or their approximations.

3.1. Comparison between linear and nonlinear models

Often linear and nonlinear models have similar accuracies. Nonlinear models should be at least as accurate as linear models, but the improvement may be small in magnitude. Even in such cases, nonlinear models are usually better in many respects. However, for this data set, there is a visibly large difference between the linear and nonlinear models.

Figure 3 shows the results on modelling of excess fiber length on the total data set. The nonlinear model demonstrates a clear superiority over the linear model. The maximum error of the linear model, 0.1249 is almost twice the maximum error of the nonlinear model, 0.0696. The rms (root mean square) error of the linear model is 0.508 compared to 0.318 for the nonlinear model. The mean absolute errors show a similar difference.

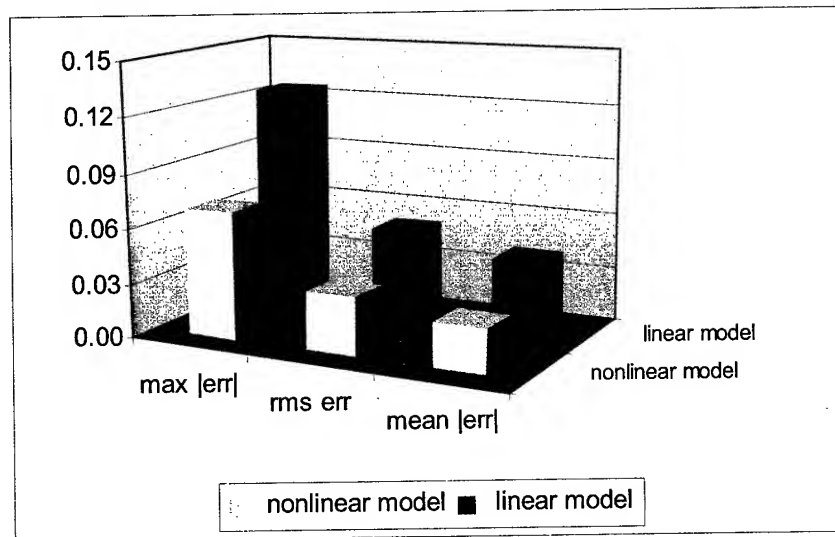


Figure 3. The nonlinear model for excess fiber length is significantly more accurate than the linear model

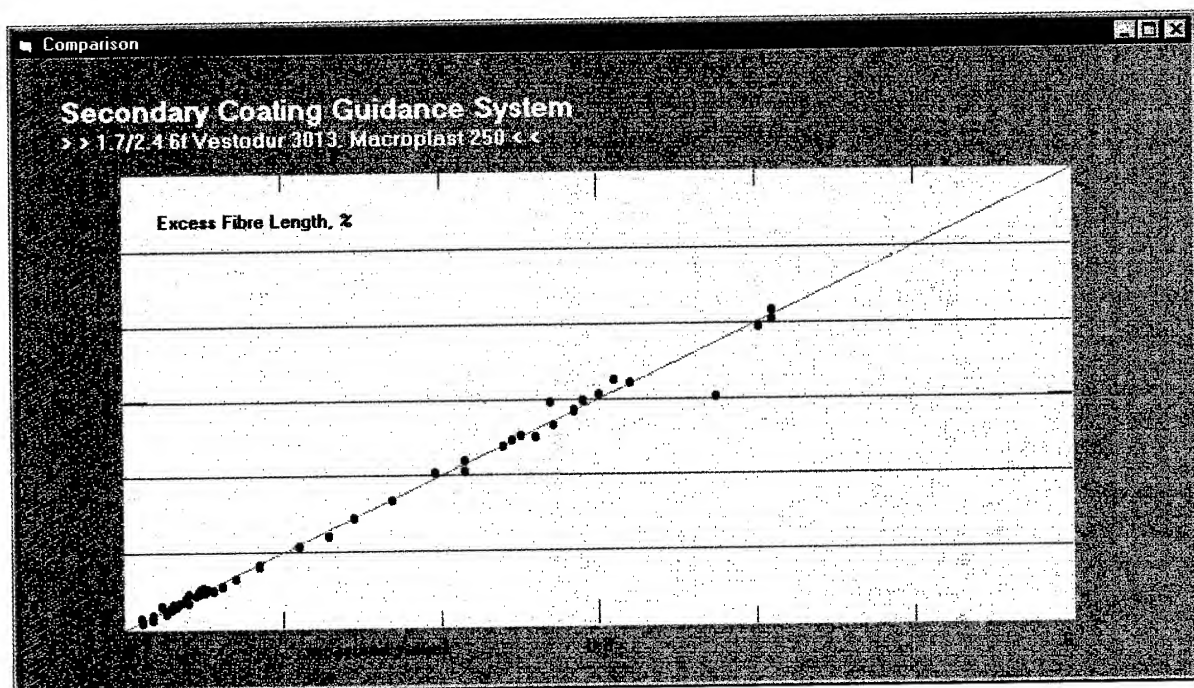


Figure 4. A comparison of measured values (horizontal axis) with predictions from the nonlinear model

4. Secondary Coating Guidance System

The nonlinear models can be cumbersome to use in the form of equations. For industrial use, it is important to make them easily accessible. A process guidance system has therefore been developed so that industries can utilize this technology without the need for nonlinear modelling experts. This system also allows us to see the characteristics of the models (Figure 4).

Several product properties of buffer tubes are important for the producers and the users. These properties include excess fiber

length, dimensional accuracy (diameter, circularity, concentricity) of the tubes, elasticity, etc. Excess fiber length was the first product property to be taken into account while developing the guidance system for secondary coating. Excess fiber length depends on several process variables, material characteristics of the tube material and the jelly, and the dimensions of the buffer tube (inner and outer diameters). Depending on the priorities and the needs of a given production unit, different input vectors can be implemented in the guidance system.

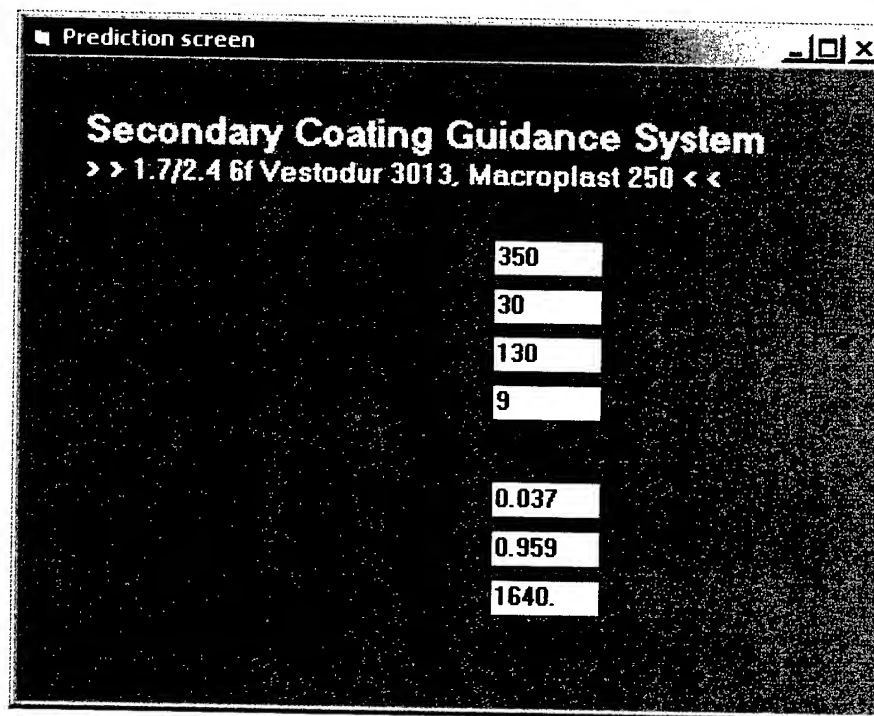


Figure 5. The prediction screen in the Secondary Coating Guidance System allows the user to calculate the properties after feeding in the process variables

In the examples shown in the successive figures, four input variables are considered: line speed, cooling water temperature, pay-off tension and capstan location. Figure 5 shows a simple calculation predicting excess fiber length, shrinkage and tensile modulus from these four variables. Excess length means excess fiber length measured within two hours after extrusion. Shrinkage means the change in the length of an unstressed tube caused by one-hour heat treatment in 80 °C.

It is easy to change the models, which may also have a different configuration. The system expects the models to be in files of a certain format. These files can be replaced to change the models. In future, the user will be able to pick the model of his choice at run time also.

Another window allows the user to see the effects of the input variables on the product property of interest. These plots also give a hint of how the performance can be improved. Figure 6 shows the effects of line speed and water temperature on excess fiber length.

The guidance system also allows the user to calculate suitable process variables within specified limits with a single click of a mouse, in less than a second.

In addition, there are features for determining the minimum or maximum of these properties in presence of box constraints. For example, it is possible to solve the following kind of optimization problems with the Secondary Coating Guidance System in a few

seconds. Sometimes, there is no feasible solution to the problem, in which case, it tries to find a good compromise.

Find line speed, payoff tension, cooling water temperature and capstan distance to

minimize *excess fiber length*

subject to

$300 < \text{line speed} < 500$

$60 < \text{payoff tension} < 150$

$20 < \text{cooling water temperature} < 60$

$7 < \text{capstan distance} < 13$

$\text{shrinkage} < 0.65$

$1450 < \text{tensile modulus}$

This feature can also be utilized to study the possible variations in properties in presence of uncertainties about the process variables.

5. Conclusions

Nonlinear models were found to be suitable for process guidance of secondary coating while linear techniques cannot perform the same tasks. This is a typical case where linear statistical techniques are not suitable. A process

guidance system has been developed which puts this new technology at the fingertips of the production engineers. This is demonstrated in the article with three properties of loose buffer tubes, viz., excess fiber length, shrinkage caused by heat treatment and tensile modulus.

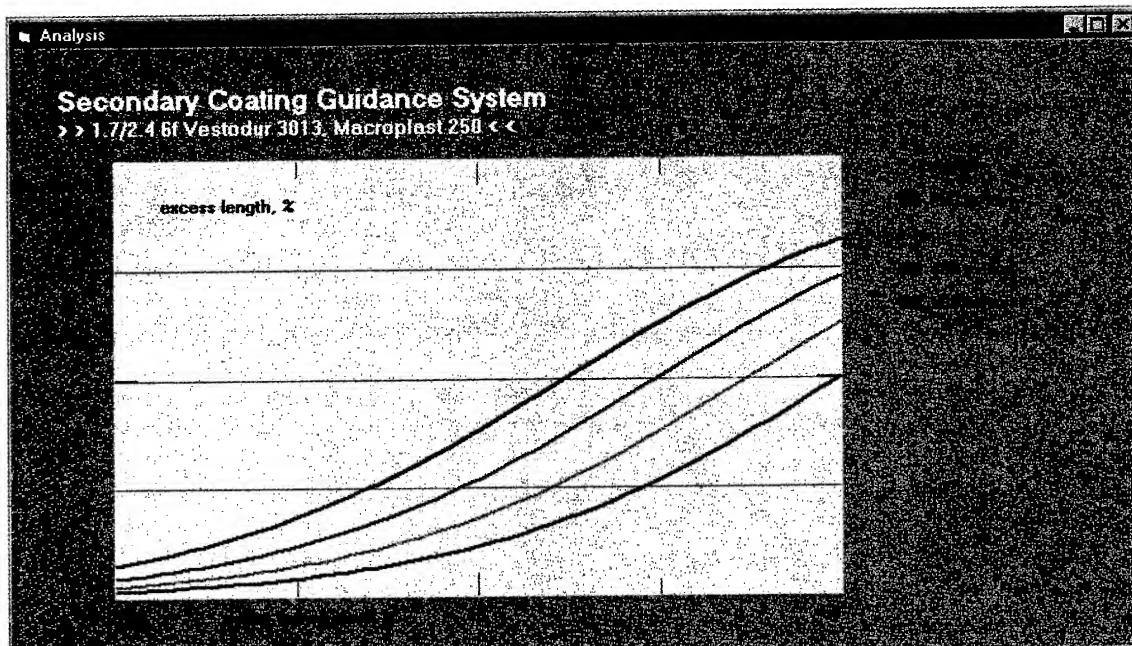


Figure 6. One window in the Secondary Coating Guidance System allows the user to see the effects of process variables like cooling water temperature on properties like excess fiber length

References

- [1] A. Bulsari (ed.), *Neural Networks for Chemical Engineers*, Elsevier, Amsterdam, Netherlands, 1995.
- [2] A. Bulsari and E. Hocksell, "Neural network systems for hardened components", *Steel Technology International*, 1996/97, 133-138.
- [3] A. Bulsari, "Quality of nonlinear modelling in process industries", Internal Report NLS/1998/2
- [4] A. Bulsari and M. Lahti, "Nonlinear modelling of secondary coating from expensive experimental data", *Proceedings of the International Wire and Cable Symposium, USA*, November 2001, 302-305
- [5] A. Bulsari and M. Lahti, "Nonlinear Models Guide Secondary Coating of OFCs", *Wire and Cable Technology International*, Vol. 29, No. 5 (September 2001) 40-43
- [6] A. Bulsari, J. Fredriksson and T. Lehtinen, "Neural networks for quality control in the wire rod industry", *Wire Industry*, Vol. 67 (March 2000) 253-258
- [7] A. Bulsari and P. Hooli, "More accurate alloying with neural networks", *Stainless Steel World*, Vol. 12 (November 2000) 54-57
- [8] A. Bulsari, J. Fredriksson and T. Lehtinen, "Uuden sukupolven laatuajärjestelmät sisältävät epälineaarisia malleja", *Vuoriteollisuus*, No. 1 (1999), 38-41
- [9] P. Myllykoski and A. Bulsari, "Selection of influential variables for modelling cold rolling of thin sheets", *Proceedings of the EANN '97*, 155-158
- [10] A. Bulsari and A. Käppi, "Prediction of compressive strength and compaction degree of concrete", *Proceedings of the EANN '98*, 181-184
- [11] P. E. Gill, W. Murray and M. H. Wright, *Practical Optimization*, Academic Press, London (1981) 136-140.
- [12] K. Levenberg, "A method for the solution of certain nonlinear problems in least squares", *Quart. Appl. Math.*, 2 (1944) 164-168.
- [13] D. W. Marquardt, "An algorithm for least-squares estimation of nonlinear parameters", *J. Soc. Indust. Appl. Math.*, 11 (June 1963) 431-441.

Authors

Dr. Abhay Bulsari

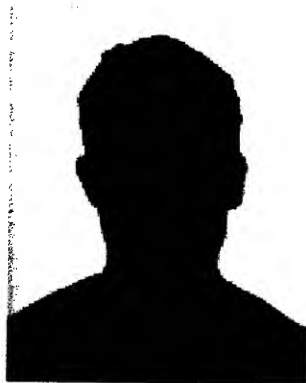
Nonlinear Solutions Oy
PL 953
FIN-20101 Turku
Finland
Tel. +358 2 2154721
abulsari@abo.fi



Dr. Bulsari has a doctorate in chemical engineering (University of Virginia, 1988) and has been working on nonlinear modelling since 1990. His company Nonlinear Solutions Oy has provided solutions to various industries based on nonlinear models of materials and processes. Dr. Bulsari has edited 6 books, authored over a hundred articles, and established the series of international conferences on Engineering Applications of Neural Networks in 1995.

Sami Sneek

Nextrom Oy
PL 44
FIN-01511 Vantaa
Finland
Tel. +358 9 50251
sami.sneek@nextrom.com



Sami Sneek received the degree of M. Sc. in chemical engineering in 2001. He joined Nextrom in 2001 and is currently involved with R&D of buffering process.

Dr. Mikko Lahti

Nextrom Oy
PL 44
FIN-01511 Vantaa
Finland
Tel. +358 9 50251
mikko.lahti@nextrom.com



Mikko Lahti received the degree of M. Sc. in Chemical Engineering in 1991 and the degree of Dr. Tech. in Polymer Technology in 1996. Before joining Nextrom in 1997 he worked as Research Scientist in European Joint Research Center in Milan. Currently, as Manager of Secondary coating lines, he is responsible for the development of the buffering process for fiber optic cables.

Raw Materials for Optical Fiber Manufacture

Art Shirley, Glenn Rush and Katy Lee

Optical Fiber Solutions, BOC Gases, 100 Mountain Ave.

Murray Hill, New Jersey 07974

+1-908-771-6104 · art.shirley@us.gases.boc.com

Abstract

The production of optical fibers requires rigorous materials handling to ensure the highest quality of the resulting products. The supply of the gases and chemicals depends greatly on the types and volumes of fibers produced.

Keywords

Fiber manufacture, fiber materials, gases, chemicals, purifiers, recycle, abatement.

1. Introduction

Optical fiber manufacture has undergone a profound transformation in the last few years, driving both fiber properties and fiber prices. Increasingly stringent performance requirements have resulted in tighter manufacturing tolerances, affecting both raw material specifications and supply modes. At the same time the telecom slump, initiated after record fiber production in 2001 and then diving towards a long "bottom" in 2002 and beyond, has resulted in depressed fiber demand as well as pricing that has squeezed margins and challenged the ability of some manufacturers to remain in business. For example, conventional single-mode fiber (CSF) prices have dropped below \$20/f-km and in some geographies have reached as low as \$15/f-km [1], which in many cases is perilously close to the cost of production of the fiber. At the same time much of the existing fiber manufacturing capacity has been idled or "throttled back", resulting in lower machine utilization and manufacturing efficiencies.

The key to remaining profitable in this scenario is cost reduction: reducing raw material and processing costs while increasing manufacturing yields. In the last two years there has been a steady movement of cable manufacturers who are integrating their operations into fiber manufacture, while at the same time many fiber manufacturers are starting to make their own preforms rather than simply drawing purchased preforms. Many of those manufacturers making preforms have opted to fabricate as much of the glass as possible, using combinations of internal and external deposition processes, rather than buying deposition tubes or jacket tubes from other glass makers. Each step of integration can provide significant cost savings; for example, if all the glass in a CSF was made by deposition using the typical raw materials, the raw material costs would only be \$3 – 6/f-km, depending on scale and location.

The quest for lower raw material costs is at odds, however, with the need for higher purities of gases and chemicals as required by most high-performance fibers. Higher purities often require additional

processing and special supply methods that can substantially increase costs.

The supply of gases and chemicals used in optical fiber production has numerous implications for the performance and application of the resulting fibers. This paper addresses some of the considerations in choosing supply modes for an optical fiber plant.

2. Preform Manufacture

Optical fiber is manufactured by a series of chemical reactions and material transformations done in three batch steps [2,3]:

1. Silica is deposited from the vapor phase to make core preforms. The deposited glass is doped with various chemicals for tailoring of the refractive index.
2. The core preforms are consolidated and/or overlaid with more glass to make draw preforms
3. The draw preform is heated in a furnace on top of a draw tower. Flowing glass forms the fiber, which is cooled in a heat transfer atmosphere, coated with a protective plastic and wound on a spool.

Commercial manufacture of optical fibers starts with the chemical vapor deposition (CVD) of SiO_2 formed by the reaction of SiCl_4 with O_2 in a process called flame hydrolysis. The reaction forms a "soot" that builds up in layers to form the core preform. Dopants such as GeCl_4 , POCl_3 , BCl_3 , SF_6 , CF_4 and C_2F_6 are added to the reactants to alter the reflective index across the diameter of the preform.

Although all preforms are made by CVD there are three distinct ways to accomplish this. The oldest is Modified Chemical Vapor Deposition (MCVD) which is practiced by several companies around the world. The CVD is done inside a rotating, ultra-pure silica tube mounted on a lathe, and heated by an oxygen-hydrogen flame that travels along the outer surface in a manner that controls the rate of deposition. The chlorides (using a helium or argon transfer gas) and oxygen are introduced at one end of the tube, and react under the heat of the flame.

Much of the SiO_2 in the resulting preform actually comes from the tube, so this process has a lower usage of SiCl_4 than other processes. Because the reaction is conducted inside a tube the reaction space is relatively easy to keep pure, and only requires that the reagents be of acceptable purity. Plasma Modified Chemical Vapor Deposition (PMCV) is a version using plasma as the heat source.

The Outside Vapor Deposition (OVD) process inverts the MCVD process by performing the deposition on the outside of a rod, which is removed prior to collapse of the preform. No H_2 is used in the OVD process; instead a hydrocarbon-oxygen flame provides the heat source for the reaction. Virtually all SiO_2 in the resulting preform is deposited, meaning that usage of $SiCl_4$ is comparably higher than in the MCVD process. The OVD process is highly productive, but has contamination issues requiring high purity reagents.

The Vertical Axis Deposition (VAD) process is also done by depositing glass as in the OVD process, except the entire preform is built up continuously from the end, and a set of two or more hydrogen-oxygen flames is used. The nozzles that produce these flames have elaborate annular designs with jets of argon to control the spreading of impinging streams of $SiCl_4$, O_2 , and H_2 , such that the deposition is controlled over a small area. VAD is a high-productivity process, since there are no tubes to limit preform length.

In each method the $SiCl_4$ and dopants are provided to the preform lathe via bubblers. In some cases the reactant gases are used as the vapor media; in others He may be used. Purity is of extreme importance since any impurity in the gas (especially water vapor) will end up in the reaction mix. Some manufacturers will place purifiers before the lathe to remove any unintentional water or metal contamination.

In order to improve productivity most manufacturers have automated the process through the use of sophisticated flow control equipment, including gas cabinets and liquid chemical dispensers, as well as process modeling.

3. Consolidation and Overcladding

Following deposition of the core glass the preform must be consolidated to remove internal voidage and moisture. The MCVD and OVD preforms require a collapse step to close the hole that remains at the preform center after the deposition stage. The OVD and VAD require a sintering step to vitrify the deposited soot. Following consolidation, additional cladding may be added in an overcladding step to build the preform to the desired diameter before drawing.

During the consolidation step, a helium/chlorine gas mixture is passed through the porous glass to remove impurities and reduce the water content of the glass to parts-per-billion levels. Helium is preferred in this step because its small atomic dimensions allow it to pass easily through the vitrified glass.

The waste stream from the consolidation furnaces may contain large amount of He, chlorine compounds, water, air components and soot, and must be scrubbed before being released to the atmosphere. The helium content from this stream can potentially be recovered for reuse in the consolidation furnace or in some other part of the fiber manufacturing process.

Overcladding is not typically required for preforms used to make multimode fibers, since the dimensions of the core are sufficiently large, but some preforms for single-mode fibers require additional cladding to provide sufficient mechanical strength. Overcladding is done by one of three methods: Sleeving, where a second silica tube is collapsed over the core preform; Soot deposition, where additional CVD is done to lay down the cladding, or; Plasma deposition, where silica powder is melted onto the core in a plasma torch. The plasma is generated by air in an induction coil, although it is initiated with Ar.

Before the preform is drawn it may be surface treated to remove irregularities and surface contamination, especially particles. This usually involves running the preform over another oxy-hydrogen burner to get small amounts of surface flow. Handles for the draw furnace are also attached at this time, requiring additional amounts of O_2 and H_2 .

The final preform, or any of the glass pieces used in its manufacture, may be washed with an etchant or solvents to remove surface imperfections. Large amounts of N_2 or compressed dry air (CDA) may be consumed in drying the surfaces.

4. Fiber Drawing

As producers of optical fibers strive for lower manufacturing costs and higher productivity from their factories, more focus has been placed on the fiber drawing step. The drawing of fiber requires expensive towers and process equipment that have significant impact on the final cost of the fiber.

While most of the expense in optical fiber production is incurred in preform manufacturing, the fiber drawing step may have the biggest impact on fiber yield. Preform damage, fiber breaks, off-specification fiber and low draw-tower utilization are just some of the contributors to reduced fiber yield and productivity. Adherence to certain best operating practices can do a lot to improve performance.

All fiber is produced from preforms by essentially the same process: a preform is placed in a furnace at the top of a draw tower, where the heat of the furnace partially melts the glass, forming a falling filament. As the filament falls it is cooled at first in the air surrounding the draw tower, and then by forced convection using N_2 or He. Before the fiber is taken up on a spool it is run through a series of coaters that apply urethane-acrylate resins, which are UV cured. The control of fiber diameter depends on the take-up speed of the spool, which in turns depends on how fast the preform is heated and how quickly the fiber is cooled. Coating applicators are also pressed by high drawing speeds, and pressurized N_2 or CO_2 are often used to dispense the resins.

4.1 Draw Furnace Purging

At the heart of fiber drawing is the draw furnace, where the precise positioning, heating and deformation of the preform produces the fiber. Industrial gases are used in a number of ways inside the

furnace to ensure that the resulting fiber is dimensionally consistent and without defects. This brochure describes the application of gases in the draw furnace and how fiber producers can benefit from their use.

Like other melt spinning processes, the drawing of optical fiber results from the precise control of the temperature and viscosity of the melt (in this case, the liquified surface of the preform) in conjunction with the tension on the solidified fiber. The draw speed, fiber diameter, preform feed rate and furnace temperature are variables in this process and are interrelated in very complicated ways.

In a typical drawing process, a preform is lowered at a fixed rate into the draw furnace at the top of the draw tower, and the furnace heat softens the outer surface of the bottom of the preform. This heat is typically provided by graphite elements (although zirconia is sometimes used) operating by induction or resistance heating. These devices are designed to achieve furnace temperatures up to 2400 °C and higher.

A "neck-down" region forms at the bottom of the preform as a transition region from solid to melt: Above the neck-down region the preform diameter is maintained, but along the neck-down region the preform thins to form the fiber.

At first gravity pulls the fiber away from the preform, but as the fiber hardens it is run through tensioning devices at the base of the tower to set the draw speed. Continuous feedback from diameter measurements at the bottom of the tower are used to set furnace parameters at the top, to ensure fiber specifications are maintained over the hundreds of kilometers of fiber that are made from the preform.

Furnace purging is required for two reasons: to protect the furnace elements from moisture and oxygen, and to protect the preform surface from particles and impurities. Purging also prevents the ingress of air (with its oxygen, moisture and particles) and sweeps impurities from the surface of the preform.

During operation graphite furnace elements should be protected by a gas purge consisting of an oxygen-free (less than 1 ppm oxygen) or a reducing atmosphere. This prevents carbon reactions and the formation of dangerous gases or particles.

Although the graphite is typically extremely pure, particles can be still be generated in normal operation. These particles can cause surface defects that contribute to breaks and low strength, so any furnace purge gas must be filtered.

Humidity has also been shown to decrease fiber strength so the purge gas must be very dry, typically less than 1 ppm moisture.

Although the majority of heat flux to the preform is the result of radiative transfer and not convective transfer, the composition and flow of the purge gas has an important affect on fiber quality. Purge gas flow can affect turbulence inside the furnace, which in turn can influence the variability of the fiber's diameter.

Most furnace manufacturers recommend nitrogen, helium or argon for an inert purge gas. The potential for nitrogen to react with carbon to form poisonous gases limits the temperatures to which it can be used to less than 1600° C, although this limit can be extended with controlled venting. Since higher draw speed require higher furnace temperatures, most fiber manufacturers do not use nitrogen.

Argon is non-reactive but may ionize at temperatures above 2000° C. Helium is acceptable at virtually any furnace temperature, but because of helium's expense argon is used by the majority of fiber makers.

However, helium can provide other benefits that may justify its use. Because of its higher thermal conductivity, helium actually heats faster than the preform it protects. This means that temperature profiles inside the furnace are less variable when helium is used instead of argon, particularly around the neck-down region. Circulation in the purge gas can also occur outside the neck-down region, which may contribute to higher temperature variability.

Localized turbulence in the purge gas is minimized when the temperature variability is reduced, which decreases fiber diameter variations and also reduces thermal stresses in the preform. Many commercial fiber specifications require $\pm 2 \mu\text{m}$ diameter control, while for higher speed production and higher fiber performance, a $\pm 1 \mu\text{m}$ range may be required. The use of helium in the furnace can help achieve these tighter tolerances.

Although purge gas usage will vary, depending on the draw process and furnace design, a set of best practices has developed through time that enable the manufacturer to achieve maximum efficiency with minimal cost. These best practices relate to three areas: application, control and composition.

In most instances, the purge gas is fed into the furnace in the same direction as the preform movement, producing downward laminar flow (helium, however, is sometimes introduced from the furnace bottom because of its tendency to rise). Countercurrent flow can be turbulent and does not help heat transfer inside the furnace. Downward flow, which causes the purge gas to exit the furnace along with the fiber, prevents entrained particles from entering with the ambient air, but requires rapid heat transfer to maintain fiber diameter control.

If the gas flow above the neck-down region becomes too rapid, cooling and breakage can result. Consequently, since purge gas flow is higher for larger diameter preforms, a minimum clearance must be maintained between the preform and the furnace walls.

The gas flow rate is typically controlled by mass flow controllers, although hand-controlled rotameters are sometimes used. Caution should be used to insure that the purge gas supply pressure is maintained constant, since minor fluctuations in this pressure can lead to large changes in the purge gas flow.

Iris at the top and bottom of the furnace can limit purge gas leakage, but also lead to increased velocities, which may introduce

turbulence. At the bottom of the furnace, a minimum iris opening of 5 mm is recommended.

Several manufacturers and furnace makers recommend helium-argon mixtures for fiber drawing. Although flows are highly dependent on furnace design and draw parameters, some typical parameters are shown in the graph below. As the preform size and draw speed increases, the purge gas flow also must increase, and more helium is used in the purge gas to the exclusion of argon.

Cost implications may result in the use of different gas mixtures in different regions of the furnace, or at different points in the draw cycle. Some manufacturers begin drawing with argon and slowly add helium to the purge gas as the draw cycle progresses. Others keep the purge gas composition constant but instead introduce gas mixtures with differing helium contents at the top and bottom of the furnace. In this case the gas containing more helium is added at the bottom while the more dilute helium stream is introduced from the top. To maintain a net downward flow the feed rate of gas at the top is about ten times that at the bottom.

This use of argon-helium mixture has even been envisaged as a process control method. One process puts a small argon stream in at the furnace exit to surround the fiber while adding a larger helium stream to surround the argon flow. Another process aims to manipulate the purge gas composition fed to the bottom as a means to control the preform surface temperature.

4.2 Fiber Cooling

Another key operational factor of which a manufacturer can take advantage is the use of gases to cool the fiber as it leaves the draw furnace. Efficient use of coolant gas requires the understanding of some basic physical concepts and the implementation of best operating practices

The fiber must cool in order to reach a safe temperature for the application of coatings and spooling of the fiber. At higher draw speeds forced convection with helium is used to enhance the cooling of the fiber as it falls. Depending on the draw tower design and height it may be possible to achieve speeds up to 5 m/s using N₂ or air, but at speeds above 10 m/s, helium is required. Because of the expense of helium it is desirable to recover and recycle this gas wherever it is used, and the draw step is a particularly attractive place to do this. Helium used for drawing need not be highly pure, but rather free from moisture and hydrocarbons.

The heat exchangers come in a variety of designs, depending on the fiber manufacturer and the draw tower vendor. Some are made as a single piece with variable apertures at top and bottom to allow the fiber to pass through the tube. Other designs split the exchanger into halves, which are hinged or pneumatically operated to allow the fiber to be started through the exchanger.

Draw towers are typically designed around a desired set of preform dimensions and draw speeds. The furnace power requirements and the height of the tower are then determined from heat transfer requirements, which in turn dictates the choice of the coolant gas

used in the heat exchanger. For modern, low-attenuation fibers it is desirable to use a dry gas as the coolant, with a dew point from -40 to -80 °C.

The heat transfer coefficient for a gas is generally proportional to the thermal conductivity of that gas. Consequently, helium is about 5 times more efficient than air for cooling. Other inert gases offer some improvement over air but only helium offers a substantial improvement in heat transfer properties, because of its high thermal conductivity.

Commercial draw towers are typically 20 to 25 meters tall. A 25-meter tower has about 12 meters for fiber cooling between the bottom of the furnace and the top of the coating cup. Using this length as the maximum available distance for convective cooling, along with typical values for the glass properties, one can calculate that the maximum fiber draw speed is approximately 10 m/s if air is used as the coolant gas. With helium used as the coolant gas, the draw speed can exceed 40 m/s. Many optical fiber plants use helium because it allows drawing at faster speeds using shorter towers, saving both capital and operating expenses.

Because of helium's low mass it will rise when dispersed into air. This means that when introduced into a cooling tube the helium will move up the tube, opposite to the fiber draw direction, and then exit the cooling tube at the top. This counter flow is essential for displacing the thin layer of warm gas that surrounds the falling, hot fiber. Testing or simulation can establish the critical flow rate of helium needed to displace the warm gas and bring cool helium into contact with the fiber. Flow rates of helium below this critical level will give little benefit for cooling, since the helium gas will not be able to reach the fiber.

Once the helium flow rate is above the critical rate, further increases in helium flow provide only slight improvement in the heat transfer properties. To avoid wasting helium the critical flow rate should be determined, and the actual flow rate set just above this level.

Industrial processes using helium can be prone to leaks, making helium an excellent choice for leak detection in pressure vessels and flow systems. Unfortunately, this also means that when helium is used as coolant gas extra steps must be taken to ensure that it is not escaping from the heat exchangers or the flow lines leading to the exchangers. Flow lines should be of metallic or impermeable plastic construction, and should be pressure-tested before being put into service.

Heat exchangers should be also leak-tested, but this is a more difficult procedure since the exchangers are meant to be open to the atmosphere. Optimal cooling will result when the majority of the helium fed to an exchanger exits the top of that exchanger, not from the bottom or (in the case of split-type exchangers) the sides. In many cases the best way to test for leakage is while fiber is being produced: tightening loose fittings or improving contact seals on split exchangers will show an immediate improvement in fiber cooling, as evidenced by lower coating temperatures or larger coated diameters.

To prevent leaks at the bottom of an exchanger, a flow of air or an inert gas such as nitrogen can be applied at the outlet of the exchanger to form a barrier or "curtain" that pushes the helium up and into the exchanger. Since at the outlet additional cooling is not needed the curtain gas doesn't need to have high heat transfer properties, but the flow rate of the curtain gas must be low enough so as not to induce vibration in the fiber.

The best way to prevent the wasting of helium is to recover and recycle it. Helium used in fiber drawing is especially suitable for recycle, since purity requirements for the draw step are not very stringent, and the only impurities that are found in recovered helium are air components and moisture. Any gas with helium content greater than 90%, having a low moisture dew point and being free of hydrocarbons, should be suitable for use in fiber cooling.

Some manufacturers will choose to blend helium with air or nitrogen in an effort to reduce helium usage. While this can occasionally be worthwhile in most cases it will only reduce the effectiveness of helium cooling and cause more helium to be wasted.

5. Purities of Gases and Chemicals

The need for low optical losses in fibers translates into very high purities for the gases and chemicals used during production. Gases such as He, Ar, H₂, O₂, N₂, Cl₂ and CO₂ are delivered at purities 99.9995% or greater and may require point-of-use purification, especially with respect to H₂O (< 1 ppm) and hydrocarbons (< 0.1 ppm). Furthermore, chemicals such as SiCl₄, GeCl₄, POCl₃ and BCl₃ are required to be 99.999 - 99.9999% pure with particular regard to transitional metals and hydroxyl ions.

Because purity is critical in the preform manufacture and the draw furnace, it is recommended to use gases from a liquid source, if possible, rather than compressed gas supply. Argon and helium should be produced cryogenically with total H, C and O bearing impurities of less than 4 ppm. Piping from gas storage to the furnace should be stainless steel or comparable materials, with special attention paid to the cleaning step prior to the piping being put into service. Particle filtration should also be utilized, with a specification of less than 50 particles/cubic foot of greater than 0.3 micron size, especially for draw furnaces.

Fiber producers utilize several analytical techniques for both quality control of raw materials as well as on-line process control. Gas chromatography and chemical assays are staples for acceptance testing of gas and chemical shipments, while on-line monitoring usually requires faster techniques such as hygrometry, thermal conductivity (for H₂ or He) and thermoparamagnetics (for O₂).

6. Supply of Gases and Chemicals

Modern optical fiber plants require large volumes of gases and chemicals, and the supply of these may vary depending on plant location and size. Table 1 contains typical consumption data for a plant making fiber from VAD-produced preforms.

Table 1. Typical Volumes of Gases and Chemicals for a VAD Plant

Product	Volume / mm fiber-km	Units
He	300,000	Nm ³
H ₂	1,600 - 2,400,000	Nm ³
O ₂	800 - 1,200,000	Nm ³
N ₂	2,000 - 3,200,000	Nm ³
Ar	800 - 1,200,000	Nm ³
SiCl ₄	500,000	kg
GeCl ₄	600	kg
Cl ₂	5,000	kg

For the air gases, O₂, N₂, and Ar, supply might come in the form of liquid deliveries for small producers (< 1.0 mm-fiber km/year), while large producers (>10 mm-fiber km/year) might utilize an on-site air separation plant. The relative amounts of O₂, N₂, and Ar from Table 1 do not match their respective concentrations in air, particularly so for Ar. This may require Ar to be made on site as well as delivered as liquid, and may make Ar recycle an attractive sourcing method.

For some smaller manufacturers it may be sensible to install a CDA system to provide dry gas, then adding a pressure swing adsorber to make N₂ for the other inert gas requirements.

In some geographies H₂ is delivered as a gas in tube trailers, but many fiber producers make it on-site by electrolysis or reforming, especially in geographies without large merchant H₂ sources. When produced on-site there may need to be additional purification for metals and moisture in order to meet process specifications. For tube trailer supply, the pressure reduction system requires stainless piping followed by particle filtration.

A fiber manufacturer who only draws fiber may have fairly modest requirements (20- 60 Nm³/hr) for H₂, while one making preforms and drawing can require substantial amounts (300- 1000 Nm³/hr). The former might choose compressed gas, liquid or small on-site plant for a supply method. The latter will likely require a large on-site or a pipeline supply scheme. Small on-site H₂ plants are typically electrolysis-based, while some very large on-sites could be reformer plants. The final decision as to production technology is not only a function of scale but also local dynamics of power costs and fuel sources.

Helium supply will vary from gas cylinder packs for small producers to liquid "dewars" for large producers. Helium demand for a fiber plant differs from other gases in that it is not a linear function of the amount of fiber produced. Helium usage is most sensitive to fiber drawing speeds, since the majority of He used in a fiber plant is used in the drawing step. The transport phenomena governing fiber drawing are complicated, but experience has

shown that He consumption increases with the square of the draw speed. Consequently, large volume fiber producers use more helium per fiber-km than small producers, and are more sensitive to He supply issues. He recovery and recycle can have strategic importance for large producers.

Helium is a by-product of natural gas production, and as such is a non-renewable resource. Increasing use of helium in a number of industrial processes, including optical fiber manufacture, has led to shortages and rising prices in many parts of the world. Great care should be taken for the effective use of helium in fiber production, requiring both knowledge of gas handling and the particular properties of helium, specifically its buoyancy and inertness.

Supply of SiCl_4 and other chlorine compounds is controlled by various HAZMAT regulations around the globe, such that these chemicals are usually sourced in the region they are produced. SiCl_4 is typically supplied in tonnage amounts by trailers such as the US-DOT MC 331, used for transporting a variety of chemical gases.

SiCl_4 used in MCVD manufacture is typically of higher purity (99.9999%, or "6N")) than that used for OVD or VAD (99.999%, or "5N")), and the 6N material is consumed in smaller quantities. The 5N material may be delivered in 20-tonne ISO shipping containers and decanted into on-site storage, while the 6N material is more often supplied in 200-liter drums which are fed directly to the supply manifold. Impurity introduction is often found in the switching of containers, which should be minimized.

High purity Cl_2 is often supplied in cylinders, which can make for logistical and operational headaches in addition to providing potential contamination points. For chlorine requirements in excess of 20 kg/hr it can be attractive to purchase industrial Cl_2 in rail cars and use on-site purification to make the final material. Not only does this greatly reduce material handling but the contamination risk is also mitigated.

7. Conclusions

The choice of gas and chemical supply can have significant impact on fiber manufacturing and fiber costs. Working with knowledgeable suppliers who can provide technical solutions to

these questions will lead to lower manufacturing costs and greater security of supply.

8. References

- [1] CRU Group, *Optical Fibre & Fibre Optic Cable Monitor*, (July 2002).
- [2] Ishwar D. Aggarwal, "Optical Waveguide Manufacturing," in: *Fiber Optics*, J. Daly, ed. (CRC Press, 1984).
- [3] H. Murata, *Handbook of Optical Fibers and Cables* (Marcel Dekker, 1996).



Art Shirley is the Director of Technology and Commercialization for BOC Gases' Fiber Optics Solutions team. He began his career with E. I. duPont after obtaining a Bachelor's degree in chemical engineering from the University of Oklahoma. In 1981 he entered Princeton University, completing a Ph.D. in 1985, and subsequently joined Arco Exploration and Production in the area of enhanced oil recovery research. He came to BOC in 1987, initially working on industrial gases production and separation technologies. He has published 17 technical papers and holds 16 U.S. patents, and is a member of the American Institute of Chemical Engineers and the Optical Society of America.

Novel Manufacturing Method of Graded Index Copolymer Optical Fiber Preform and Its Optical Characteristics

Jin-Sung Choi, Hansol Cho, Mu-Gyeom Kim, Byoung-Joo Ra, Joon-Yong Park, Jin-Taek Hwang, Jae-Geon Park, Seung-Hui Lee*, Moon-Hyun Do*, Jin-Han Kim, Eun-Gon Lee, Seung-Han Park**, and O-Ok Park**

E-polymer Laboratory, Samsung Advanced Institute of Technology
P.O. Box 111, Suwon 440-600, Korea

* R&D Group 1, Fiber/Cable PLC Team, Fiberoptics Div., Telecommunication Network Business, Samsung Electronics Co. LTD., #94-1, Imsoo-Dong, Gumi-City, Gyung-buk-Do 730-350 Korea

** Physics Department, Yonsei University 134 Shinchon-Dong, Sedaemoon-Gu, Seoul 120-749, Korea

*** Department of Chemical and Biomolecular Engineering, Korea Advanced Institute of Science and Technology 373-1, Kusong-Dong, Yusong-Gu 305-380, Daejeon, Korea

Abstract

In order to overcome a volume shrinkage problem of bulk radical polymerization of an acrylic monomer during the manufacturing of a preform with a radial gradient of refractive index for PMMA based graded-index polymer optical fiber, we design a novel cylindrical reactor with a three dimensional structure which can prevent the vacancy due to the volume shrinkage from propagating into the main reaction part of the reactor, namely, cavity-preventing type reactor and its novel processing method. Using the cavity-preventing reactor and several monomer-feeding routes, we can successfully fabricate a large sized graded-index preform. Especially, it is needless to adopt an additional monomer charging process by which the possibility of contamination is increased considerably.

Keywords

POF; cavity-preventing; graded-index; volume shrinkage

1. Introduction

Optical fibers primarily used for long-haul telecommunication network where the transmission distance, bandwidth, and long-term stability are of considerable importance. They are mostly the

step-index, single-mode optical fibers based on quartz glass [1]. They have a core diameter as small as 5 microns to 10 microns and, as a result, face serious challenges in terms of achieving proper alignment and connection.

On the other hand, multi-mode glass optical fibers of larger diameter than that of single-mode optical fibers may be used for relatively short distance data communications such as in local area networks (LANs). However, these multi-mode glass optical fibers, in addition to being fragile, also suffer from expensive costs relating to achieving proper end-face treatment, alignment, and connection as well as long-term bending stability. Accordingly, a metal cable, for example, a twisted pair or coaxial cable has been widely used for short distance communication applications within 200 meters such as in LANs in spite of their limitation of transmission capacity. However, as the demand for high bandwidth increases even in small office, home, and mobile environment, it has become increasingly important to develop low cost optical links that can be easily installed by common end-users.

To cope with these problems, the industry has expended great efforts and investments over the past 20 years towards development of polymer optical fibers (POF), which can be used in short distance communication applications within several decades of meter [2-3]. Since the diameter of POF can be as large as 0.5 to 1.0 mm which is 100 or more times larger than that of glass optical fibers due to its flexibility, its alignment, and connection are much easier issues than those of silica based optical fibers. Moreover, if polymer-based connectors were produced by compression molding, these connectors can be used for both alignment and connection and reduce total system costs. Generally, POF may have a step index (SI) structure, in which a refractive index changes stepwise in a radial direction, or a graded index (GI) structure, in which a refractive index changes gradually in a radial direction. Since a graded index polymer optical fiber (GI-POF) has a lower modal dispersion, it can have a larger transmission capacity than step index polymer optical fiber (SI-POF). Therefore, it is known that GI-POF is adequate for an use of a communication medium for short distance and high-speed

Temporary address of J. S. Choi, H. Cho, B.J. Ra, J. T. Hwang and S. H. Lee is 103-1, Moonji-Dong, Yusong-Gu, Daejeon 305-380, Korea to the end of this year.

J. S. Choi, +82-42-865-3831, jschoi@sait.samsung.co.kr

H. Cho, +82-42-865-3832, hansol@sait.samsung.co.kr

M. G. Kim, +82-31-280-6765, mugkim@sait.samsung.co.kr

B. J. Ra, +82-42-865-3831, bjra@sait.samsung.co.kr

J. Y. Park, +82-31-280-6731, joonypark@sait.samsung.co.kr

J. T. Hwang, +82-42-865-3830, jthwang@sait.samsung.co.kr

J. G. Park, +82-31-280-6721, jscrip@samsung.co.kr

S. H. Lee, +82-42-865-3834, pluronic@samsung.com

M. H. Do, +82-54-479-7162, mhdo@samsung.com

J. H. Kim, +82-54-479-7160, jinhan@samsung.com

E. G. Lee, +82-2-361-2617, gongon01@hanmail.net

S. H. Park, +82-2-361-2617, shpark@phy.yonsei.ac.kr

O. O. Park, +82-42-869-3913, oopark@kaist.ac.kr

communications such as high-bandwidth local area network (LAN), giga-bit home network, and IEEE1394b because of reduced costs derived from its larger diameter and large capacity of data transmission.

The conventional method for fabricating GI polymer optical fiber was first reported by researchers of Keio University in 1988 [5]. Since then, other related-techniques have been reported in a large number of papers [4-14].

2. Bulk Radical Polymerization

2.1 Batch Process for Gradient Refractive Index Preform

The methods for fabricating GI preform mentioned above are mainly classified into two methods as follows. The first method is a batch process wherein a preliminary cylindrical molding product, namely, a preform in which a refractive index changes in a radial direction, is fabricated, and then the resultant preform is heated and drawn to fabricate GI-POF [4-6, 10-12]. The second method is a continuous process wherein a polymer fiber is produced by extrusion process, and then the low molecular material contained in the fiber is extracted, or contrarily introduced in a radial direction to obtain GI polymer optical fiber [13-14].

It is known that the batch process is more beneficial for the production of GI-POF with a high optical quality because of being easier to control uniform refractive index profile and less to be contaminated, therefore, most of the related fabricating methods belongs to the batch process to fabricate GI preform.

The most well-known fabricating process for GI preform is an interfacial gel polymerization invented by professor Koike and his coworkers [5-8]. This batch process technique exploits the different reactivity of two monomers or different diffusivity of nonreactive additive, so-called dopant, to create a preform with continuously varying refractive index and followed by heat drawing, one can successfully fabricate a GI-POF having data transmission capacity of over 2.5 Gbit/s [9].

Van Duijnhoven and Bastiaansen reported another batch process to fabricate GI preform where very high rotation speed as high as about 20,000 rpm is imposed to the reactor [11]. This method uses the principle that if a mixture of monomers or polymer-dissolving monomers having different density and refractive index is polymerized under a very strong centrifugal field over $10,000 \times d^{0.5}$ rpm, where d is a diameter of a preform, concentration gradient is generated on account of a density gradient, and thereby, a refractive index gradient is generated.

2.2 Volume Shrinkage during Polymerization

Besides, none of the above-mentioned batch processes act against anything related to the problem inevitably caused by volume shrinkage during bulk radical polymerization common in the fabrication of GI preform. For example, the extent of volume shrinkage of polymerization from methylmethacrylate (MMA) to poly(methylmethacrylate) (PMMA) is over 20% (the density of

MMA at 25°C is 0.940 g/cm³ and that of PMMA is 1.179 g/cm³) [15]. Since the volume shrinkage occurs when monomers are polymerized (to produce a polymer), a preform for a POF fabricated under the rotation of a reactor has a hollow or a vacancy around its central axis of rotation to form a shape of a tube, so-called, cavity. Thus, it is required to fill the cavity with additional monomer, additive containing monomer, prepolymer (viscous mixture of polymer and monomer during the bulk radical polymerization) or polymer-dissolving monomers in order to fabricate a cavity-free preform.

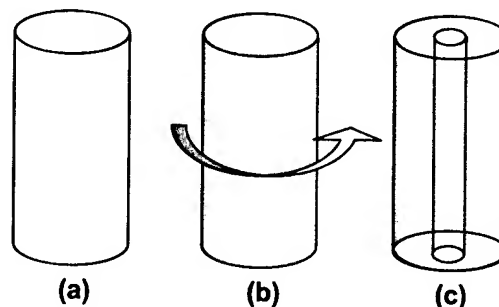


Figure 1. Volume shrinkage in the rotating reactor. A cylindrical reactor with a diameter of 4.1cm (a) filled with MMA (b), followed by rotation and polymerization result in a central cavity with a diameter of 1.8cm (c).

Figure 1 shows the typical case of volume shrinkage of rotating cylindrical reactor initially filled with MMA polymerized to be a PMMA tube with a cavity around the axis of rotation after completion of polymerization.

Accordingly, when a GI-POF is fabricated by using a cavity-filling type preform, the discontinuity of the refractive index profile increases in proportion to the size of a cavity, which can lead to a significant scattering loss in the interface. Therefore it reduces data transmission length so that GI-POF may not be useful. Furthermore, during the process of filling the cavity, contacting with minute dust, air or moisture may deteriorate the quality of the GI preform and GI-POF. Additional appliance and related cost are required in order to prevent this contact. When the large-sized preform is fabricated, the volume shrinkage problem becomes more significant and determinant.

Therefore, we have to make an effort to eliminate the contact of reactant in the reactor with the outer atmosphere as least as possible and investigate this complex and inevitable behaviors during bulk radical polymerization carefully.

2.3 Copolymerization for a GI Preform Fabrication

The batch processes for GI-POF fabrication can be divided into two methods with respect to how to develop the refractive index profile inside preform. One is the method utilizing the diffusivity of species having controllable refractive index and the other is compositional change of copolymer along a radial direction.

A lot of works manifest that GI-POF using dopant is superior to copolymer GI-POF in optical performance. For a copolymer GI-

POF, apart from the intrinsic absorption of light by polymer itself, an excess scattering loss due to density fluctuation of different monomeric unit is believed to increase total optical loss [6]. Therefore, it is reported that the total optical loss of copolymer GI-POF, even a partially fluorinated acrylic monomers used, is relatively higher than dopant GI-POF based on PMMA [16]. Furthermore, there is a difficulty to select the copolymer system where two monomers have to be miscible in the whole range of composition used.

On the other hand, copolymer GI-POF produced by suitable copolymer pair, for example trifluoroethyl methacrylate (TFEAM) and tetrafluoropropyl methacrylate (TFPMA) or MMA and benzyl methacrylate (BMA), has advantages over thermal stability and easiness to control the refractive index for a preform of large diameter compared with dopant GI-POF [18-20]. Among them, MMA and BMA copolymer is more excellent in their compositional randomness and more advantageous in raw material's cost [18]. Our novel method using patented cavity-preventing reactor utilizes the copolymer of MMA and BMA for fabricating a GI preform.

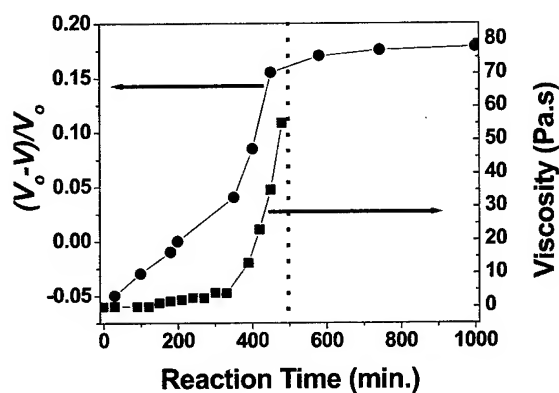


Figure 2. Volume shrinkage (●) and viscosity (■) as a function of reaction time for radical polymerization at 75°C. MMA/BMA = 9/1. An initiator (AIBN) of 0.03mol% and chain transfer agent (n-BuSH) of 0.3 wt% were used.

For a MMA and BMA copolymerization, we investigated the volume and viscosity changes as a function of reaction time (Figure 2). There was very rapid reduction of the volume in a short period of time. It is a typical behavior of so-called auto-acceleration [21]. During the autoacceleration, the viscosity was increased abruptly. This is a common nature of bulk radical polymerization and called as a glassification. From Figure 2, it was recognized that volume shrinkage takes place even after glassification. Although the volume shrinkage after glassification is not a matter for the small-scale reactor, it is very serious in a large-scale mass production.

Another problem is a matter of production rate. For an interfacial gel polymerization, the frontal propagation of gel region is very narrow and its propagation speed is very slow compared with

exothermic propagation [17]. Thus, interfacial gel polymerization takes more time to fabricate a larger preform. In addition to the slow fabrication time, GI preform using dopant usually shows a plateau of refractive index profile in its center region if its size is large and at elevated temperature [19-20].

As a matter of fact, we often encounter these unexpected problems in carrying out bulk radical polymerization in a mass production scale. These problems are generally dependent on the total volume of reaction. Therefore, we have to resolve these problems for producing GI-POF with larger size and faster production rate.

3. Cavity-Preventing Cylindrical Reactor

3.1 Cavity-Preventing 3-Dimensional Structure

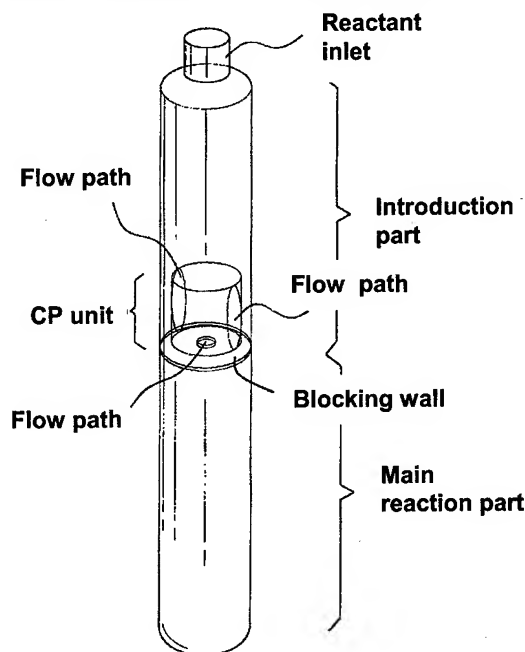


Figure 3. A perspective of a typical cavity-preventing type reactor according to the present work

Typical Cavity-preventing (CP) reactor is depicted in Figure 3. It is comprised of an introduction part and main reaction part with cavity-preventing structures. An introduction part has a reactant inlet through which a reactant is introduced into the whole reactor. A main reaction part is adjacent to the introduction part through a blocking wall. A flow path, through which the reaction part is connected with the introduction part, is located at the center of the blocking wall. One or more cavity-preventing structures exist between the flow path of the reaction part and the introduction part, and it has one or more flow paths through which the reactant flows from the introduction part to the reaction part, for preventing a cavity developed from the reactant inlet of the introduction part from extending to the reaction part during rotation of the reactor. The inner diameter and the length of main reaction part of CP reactor used in present work were 5.5cm and 70cm, respectively.

3.2 Fabrication of GI-POF

We have used two routes of reactant feeding and fabricating. The first one is shown in the Figure 4. The mixture of MMA and BMA was introduced in the reactor through an inlet. The mixture contained 0.03 mol% of azobisisobutyronitrile as a thermal initiator and 0.3 wt% of n-butyl mercaptan as a chain transfer agent. Here, we fed different reaction mixture in the main reaction part and introduction part, respectively. We fed a mixture containing higher BMA content into the introduction part so that the refractive index profile was generated by the difference between the BMA content of the reaction mixture in the main reaction part and that in the introduction part. The reactor was rotated by 1500 rpm vertically and heated at 75°C subsequently. After polymerization completed, the reactor was removed and the preform was drawn to a fiber with a diameter of 0.75mm by heat drawing (Method I). During the polymerization the vacant space in the introduction part was pressurized by inert gas upto 10 bar.

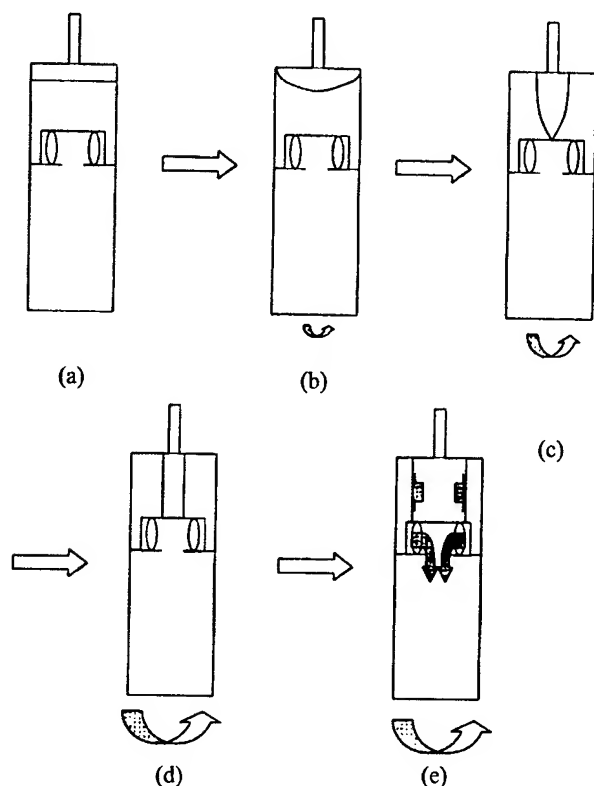


Figure 4. A diagram illustrating a series of process steps for fabricating a preform for a plastic optical fiber using the CP reactor.

Method II is different from method I in that a mixture of MMA prepolymer and BMA monomer is fed instead of monomers.

As shown in Figure 4 (d) and (e), the cavity generated during rotation in the introduction part did not propagate into the main reaction part by CP structure. However, the reactant could be flowed into the main reaction part so that the cavity did not appear

in the main reaction part. Only the cavity in the introduction part was left and increased in the whole polymerization period.

4. Optical Characteristics

4.1 GI profile of the Preforms

Table 1 shows the data of refractive index profile of GI preforms fabricated by our CP method. The refractive index profile of GI preform in the core region was usually approximated by the power law equation written as

$$n(r) = n_1 \left[1 - 2\Delta \left(\frac{r}{a} \right)^g \right]^{1/2} \quad (1)$$

$$\Delta = \frac{n_1^2 - n_2^2}{2n_1^2}$$

where n_1 and n_2 are the refractive indices of the core center and cladding, respectively, a the core radius, and g the index exponent. From the best fitting data of Δn and g values, it is proved that GI preforms were fabricated successfully.

Table 1. GI Preform Preparation*

Preform	Average core composition (BMA mol%)	Fabrication method	Δn	g
GI-1	15	I	0.0121	3.12
GI-2	15	II	0.0156	2.20
GI-3	20	I	0.0143	2.96
GI-4	20	II	0.0181	2.01

*Core diameter was about 37cm (preform diameter = 55cm).

4.2 Optical Properties of GI-POFs

Table 2. Optical Properties of GI-POF*

POF	Attenuation loss (dB/km) ¹	Bending loss increment (dB) ²	Bandwidth (GHz 100m) ³
GI-POF-1	210	0.5	1.56
GI-POF-2	198	0.2	2.56
GI-POF-3	226	0.5	1.58
GI-POF-4	201	0.2	2.02

*All GI preforms were heat-drawn to GI-POFs with a diameter of 0.75mm.

1. Measured by cut-back method at 650nm

2. Measured at 20mm 180-degree bending

3. Measured by pulse broadening method

Table 2 shows the attenuation, bending loss, and bandwidth data measured with our heat-drawn GI-POFs. The attenuation of all GI-POFs was around 200 dB/km or more and bandwidth was over 1.5 GHz · 100m.

5. Conclusions

Unlike market expectation of Europe and US, POF market in the eastern Asian countries, especially Korea, draw interests in the low-cost and high-bandwidth home network media. Because a lot of people reside in a high-rise apartment in the metropolitan area, the easiness of installation within walls or between stories in the apartment structure is most important factor as the introduction to transmission media market. In such an environment, the bending characteristic, mechanical strength, and the long-term reliability on small bending (under 2cm in diameter) of POF make it convenient medium for frequent installation and removal even by untrained workers.

Moreover, the high demand for faster speed of communication in Korea is so explosive that it is widely requested to utilize them as giga-bit speed transmission media for the end users. Considering these conditions, we believe that PMMA based GI-POF will be a strong candidate for high-bandwidth local area network (LAN), giga-bit home network, and IEEE1394b based systems.

In this paper, we reported a novel fabrication method for large GI-preform and the optical properties of GI-POF. We believe that our novel method can be used as a mass production method for copolymer GI-POF. In the technical session of IWCS, we will present the optical and reliability data of our GI-POF in detail.

6. Acknowledgments

E. G. Lee and S. H. Park appreciate for the partial support by grant No. R01-1999-00015 from the Basic Research Program of the Korea Science & Engineering Foundation.

7. References

- [1] G. Keiser, *Optical Fiber Communications*, 3rd ed., McGraw-Hill, (2000)
- [2] C. Emslie, "Review Polymer Optical Fibers," *J. Mat. Sci.*, 23(), 2281-2293 (1988).
- [3] J. Zubia and J. Arrue, "Plastic Optical Fibers: An Introduction to Their Technological Processes and Applications," *Opt. Fiber Tech.*, 7 101-140 (2001).
- [4] Y. Ohtsuka and Y. Koike, "Studies on the Light-Focusing Plastic Rod. 18: Control of Refractive Index Distribution of Plastic Radial Gradient-Index by Photocopolymerization," *Appl. Opt.*, 24, 4316-4320 (1985).
- [5] Y. Koike, Y. Takezawa, and Y. Ohtsuka, "New Interfacial-Gel Copolymerization Technique for Steric GRIN Polymer Optical Waveguides and Lens Arrays," *Appl. Opt.*, 27(3), 486-491 (1988).
- [6] Y. Koike, E. Nihei, N. Tanio, and Y. Ohtsuka, "Graded-Index Plastic Optical Fiber Composed of Methyl Methacrylate and Vinyl Phenylacetate Copolymers," *Appl. Opt.*, 29(18), 2686- (1990).
- [7] T. Ishigure, E. Nihei, and Y. Koike, "Graded-Index Polymer Optical Fiber for High Speed Data Communication," *Appl. Opt.*, 33(19), 4261-4266 (1994).
- [8] T. Ishigure, A. Horibe, E. Nihei, and Y. Koike, "High-Bandwidth, High Numerical Aperture Graded-Index Polymer Optical Fiber," *J. Lightwave Tech.*, 13(8), 1686-1691 (1995).
- [9] T. Ishigure, E. Nihei, S. Yamazaki, K. Kobayashi, and Y. Koike, "2.5Gbit/s 100m Data Transmission using Graded-Index Polymer Optical Fibers and High-Speed Laser Diode at 650nm Wavelength," *Electro. Lett.*, 31(6), 467-469 (1995)
- [10] J. H. Liu and H. T. Liu, "Preparation of Gradient Refractive Index Rods using Methyl Methacrylate and Benzyl Salicylate," *Macromol. Chem. Phys.*, 198(10) 3285-3292 (1997).
- [11] F. G. H. van Duijnhoven, and C. W. M. Bastiaansen, "Monomers and Polymers in a Centrifugal Field: A New Method to Produce Refractive-Index Gradients in Polymers," *Appl. Opt.*, 38(6), 1008-1014 (1999).
- [12] O. O. Park, S.H. Im, H. Cho, J. S. Choi, D. Y. Kim, J. G. Park, J. T. Hwang, E. G. Lee and S. H. Park, "A New Fabrication Method of a Graded Index Polymer Optical Fiber Preform," *Proc. POF 2001 Conf.*, Amsterdam, 341-347 (September, 2001).
- [13] B. C. Ho, J. H. Chen, W. C. Chen, Y. H. Chang, S. Y. Yang, J. J. Chen, and T. W. Tseng, "Graded-Index Polymer Fibers Prepared by Extrusion," *Polym. J.*, 27, 310- (1995).
- [14] C. W. Park, B. S. Lee, J. K. Walker, and W. Y. Choi, "A New Processing Method for the Fabrication of Cylindrical Object with Radially Varying Properties," *Ind. Eng. Chem. Res.*, 39, 79-83 (2000).
- [15] G. Odian, *Principles of Polymerization*, 3rd ed., John Wiley & Sons, Inc. New York, p. 210 (1991).
- [16] F. G. H. van Duijnhoven, "Gradient Refractive Index Polymers Produced in a Centrifugal Field," *Ph.D. Thesis*, Enidhoven University, Netherland (1999).
- [17] C. A. Spade and V. A. Volpert, "Mathematical Modeling of Interfacial Gel Polymerization for Weak and Strong Gel Effects," *Macromol. Theory Simul.*, 9(1), 26-46 (2000).
- [18] J. Park, K. Char, and C.W. Park, "A Study on the Miscibility of Selected Blends of Methyl Methacrylate-Benzyl Methacrylate Copolymers," *Ind. Eng. Chem. Res.*, 38(12), 4675-4681 (1999).
- [19] L. L. Blyler, Jr., T. Salamon, C. Ronaghan, and C. S. Koeppen, "Reliability of Graded-Index Plastic Optical Fibers," *Mat. Res. Soc. Symp. Proc.*, 531, 107-118 (1998).
- [20] I. Eiji, T. Masaki, S. Kayo, "Plastic Optical Fiber," *Densazairhou* (Japanese), 38(1), 58-61 (1999).
- [21] G. A. O'Neil, M. C. Winsnudel, and J. M. Torkelson, "A Critical Experimental Examination of the Gel Effect in Free Radical Polymerization: Do Entanglements Cause Autoacceleration?," *Macromolecules*, 29(23), 7477-7490 (1996).



Jin-Sung Choi received his B.S. and M.S. degrees in polymer engineering from Hanyang University, Seoul, Korea, in 1989 and 1991, respectively. He joined E-polymer laboratory of Samsung Advanced Institute of Technology (SAIT) from 1996.

Currently, he is a doctoral candidate of the department of chemical and biomolecular engineering at Korea Advanced Institute of Science and Technology (KAIST), Daejeon, Korea. He joined POF project of SAIT from 1999. His current research interest area is reaction chemistry of bulk radical polymerization associated with mass production of GI-POF.

devices and rheological evaluation of polymeric materials in confined geometries.



Jin-Taek Hwang received his B.S. degree in chemistry from Kyunghee University, Seoul, Korea in 1987 and M.S. and Ph.D. degrees in chemistry from KAIST in 1988 and 1991, respectively. From 1995, He joined E-polymer laboratory, SAIT. He started

POF project of SAIT from 1999. He is a project manager of POF project and a leader of polymer processing technology group of E-polymer laboratory, SAIT. His current research interest area is organic optical materials and their processing techniques including commercial manufacturing of GI-POF.



Hansol Cho received his B.S., M.S., and Ph.D. degrees in chemical engineering from KAIST, in 1992, 1994, and 1999, respectively. He joined POF project of SAIT from 2000. His current research interest area is an evolution of rheological and physical properties during bulk radical polymerization associated with mass production of GI-

POF.



Jae-Geun Park received his B.S. degree in chemistry education from Seoul National University in 1983 and M.S and Ph.D. degrees in chemistry from KAIST in 1984, and 1988, respectively. Now, he is a laboratory manager of E-polymer of SAIT. His current research interest area is organic-electronic materials and their processing

techniques.



Mu-Geom Kim received his B.S. degree in Physics from Hanyang University, Seoul, Korea in 1994, and M.S., Ph.D. degrees in Physics from KAIST, in 1996, and 2002, respectively. He joined POF project of SAIT from 2002. His current research interest area is the *in-situ* measurement of optical and environmental properties of GI POF.



Seung-Hui Lee received his B.S. and M.S. degrees in chemical engineering from Hanyang University in 1995 and 1997, respectively. He joined R&D 1 group in Fiberoptics Division of Samsung Electronics Co. Ltd. from 2001 and dispatched to POF project of SAIT in order to develop the commercial production skill of GI-POF.

His current research interest area is a preform manufacturing and fiber drawing associated with mass production of GI-POF.



Byoung-Joo Ra received his B.S. and M.S. degrees in fiber and polymer science from Seoul National University, Seoul, Korea, in 1996, and 1998, respectively. He joined POF project of SAIT from 2002. His current research area is to investigate the relationship between compositions and optical properties during bulk radical

polymerization associated with mass production of GI-POF.



Moon-Hyun Do received his B.S. and M.S. degree in material science from Chugnam National University, Daejeon, Korea in 1989 and Kyungbook National University, Daegu, Korea in 1998. Now, he is principal engineer of optical fiber & cable R&D 1 Group in Fiberoptics Division of Samsung Electronics Co. Ltd.



Joon-Yong Park received his B.S. in polymer processing from Hanyang University in 1991 and M.S. and Ph.D. in chemical engineering from KAIST in 1993 and 1997, respectively. He worked at National Institute of Standards and Technology(NIST) as a guest scientist in Polymer Division from 1997 to 1999. He joined E-Polymer Laboratory of

SAIT from 1999. His current research interest area is a nanofabrication of polymeric materials for electronic or optical



Jin-Han Kim received his B.S. and M.S. degrees from Pusan National University in 1982 and Kyungbook National University in 1990. Now, he is vice president of R&D Group 1 in Fiberoptics Division of Samsung Electronics Co. Ltd.



Eun-Gon Lee received his B.S. degree in Physics from Korea University in 2000. He is currently working toward M.S. degree in physics at Yonsei University. His main research interest is the optical characterization of SI and GI POF.



Seung-Han Park received his B.S. and M.S. degrees in physics from Yonsei University, Seoul, Korea, in 1982 and 1984, respectively, and Ph. D. degree from the optical sciences center at the University of Arizona, in 1988. After working as an assistant professor in the department of electrical engineering at the University of Pittsburgh, he joined the department of physics, Yonsei University, Seoul, Korea, in 1991, where he is currently a

professor. In 1997, he spent his sabbatical year as a visiting scientist at the CREOL, University of Central Florida. His current research interests are gradient index plastic optical fiber, near field optics, nonlinear optics, and phase shifting interferometry.



O-Ok Park received his B.S. degree in chemical engineering from Seoul National University in 1976, the M.S. degree in chemical engineering from KAIST in 1978, and the Ph.D. degree in chemical engineering from Stanford University, in 1985. He has been worked as a professor in chemical engineering of KAIST since 1985. Now he is a dean of student affairs. He has also started POF project with SAIT from 1999. His current research interest areas are polymer rheology, polymer nanocomposite, electroluminescence devices, control of nano-sized polymer structures and energy devices.

Environmental and Safety Considerations in Premises Cable

Hong Chen, Charles W. Jackson, Kaushik Chakrabarty, Wayne M. Newton, Samuel A. Aderogba, Paul E. Neveux, Jr.

Optical Connectivity Division, OFS
Norcross, Georgia
+1-770-798-2239 · hchen3@ofsoptics.com

Abstract

The need for environmental friendly premises cables, such as heavy metal-free PVC cables, has been increasing as more considerations are given to the "end-of-life" of these cables. For example, there have been efforts in both the US and Europe to create regulations controlling and/or eliminating the use of certain metals such as lead and cadmium in PVC applications.

To make "greener" cable products using PVC materials with lead and cadmium free stabilizers, the primary concern is whether the optical performance, long term reliability and fire safety of premises cables are compromised. All these issues were addressed in OFS effort to become ready to offer "heavy metal free" (HMF) premises cable products to the market. Various HMF PVC materials were evaluated in terms of thermal and UV stability. Cables were designed and tested to Telcordia GR-409, ICEA 596, or IECA 696.

Cables made from these new materials were also tested for fire performance. The results show that fire performance of HMF stabilized PVC cables is at least comparable to that of lead or cadmium stabilized PVC cables with the same designs.

Keywords

Premises cable; Environmental; Safety; Lead; Cadmium; PVC.

1. Introduction

In recent years, there has been an increase in the emphasis on environmental considerations of the materials used for a wide range of products, including fiber optical cables. Users, manufacturers and regulatory agencies realize that some safety and environmental issues need to be addressed as more cables are deployed into various service spaces. Traditionally, lead or cadmium compounds are added to PVC as stabilizers to make it more thermally and UV stable. Without stabilizers, PVC is difficult to process and would degrade when exposed to heat during processing. Lead and cadmium stabilizers are known to be very efficient thermal stabilizers. Lead is also present in some color concentrates used for cable products.

In the European Union, lead-containing products have been the subject of much discussion and legislation. In June 2000, the European Commission adopted a proposal for a Directive on Waste Electrical and Electronic Equipment (WEEE) and a proposal for a Directive on the restriction of the use of certain materials in electrical and electronic equipment. This proposal calls for the substitution of certain heavy metals including lead and cadmium, and brominated flame retardants in new electrical and electronic equipment from January 1, 2008 onwards.[1] Denmark even issued a ban on the import, sale and production of lead and products containing lead with a concentration of more than 50 parts per million.[2]

In the United States, the state of California has led the charge against lead, among other chemicals. In November of 1986, the voters of California passed the "Safe Drinking Water and Toxic Enforcement Act", or better known as Proposition 65. This legislation requires the governor of California to publish a list of cancer causing chemicals, or chemicals that can cause birth defects or reproductive harm.[3] The list of chemicals is determined by a panel that includes the EPA, the International Agency for Research on Cancer, the National Toxicology Program, the FDA and the National Institute for Occupational Health and Safety. Cadmium was added to this list as a reproductive toxin in 1987 and lead was added in 1992. The legislation also stipulates that all chemicals on the list are prohibited from being dumped in an area where they could pass or probably will pass into any source of drinking water.

OFS, formerly Lucent Technologies Optical Fiber Solutions Division, took a proactive approach to make more environmentally friendly cables starting two years ago, identified products that used leaded PVC materials and launched a series of projects to replace them with HMF materials.

Of primary concern for new materials qualification and heavy metal free cable production is whether the optical performance, long term reliability and fire safety of premises cables are compromised when PVC materials with lead and cadmium free

stabilizers are used. It was necessary to find out the effectiveness of the new stabilizing systems such as Ba/Zn or Ca/Zn in a PVC compound for them to be used in cables. Various grades of heavy metal free (HMF) PVC materials (PVC and low smoke PVC) were evaluated and compared with their lead or cadmium stabilized predecessors in terms of thermal stability and UV resistance. Cables were designed and tested to Telcordia GR-409, ICEA 596, or IECA 696. Fire tests were conducted based on the intended application of the cables.

This paper presents the comparative data on materials properties, optical performance and fire performance. The range of products included MINICORD® simplex and duplex cables, ACCUMAX® Riser and Plenum cables, and ACCUDRY® Indoor/Outdoor cables.*

2. Results and Discussions

2.1 Materials properties

2.1.1 Thermal stability

Traditionally, lead based compounds and/or barium-cadmium based compounds were used as heat stabilizers in PVC. Recently, lead and cadmium free stabilizer packages have become available. These are typically based on mixed metal salts of barium, calcium, zinc and magnesium, or are based on organo-tin compounds. In going from lead based to non-lead based heat stabilizers, it is important not to compromise the thermal stability of the PVC compounds.

Figure 1. Top NL-4, Bottom L-2, 1 hour travel at 230 °C



Figure 2. Top L-1, Bottom NL-2, 2 hour travel at 230 °C

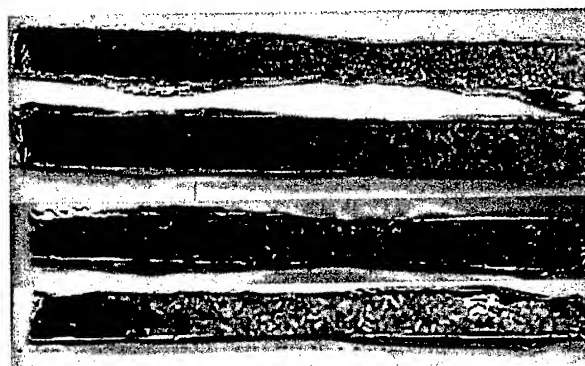


Figure 3. (Top to Bottom) L-1, NL-2, NL-1, NL-3, 2 hour travel at 205 °C

The thermal stability is usually determined using the Metrastat Oven Aging Test. PVC pellets are placed on a tray and pulled through a temperature-controlled oven at a controlled speed. In Figures 1-3, the pellets on left parts of the tray see the heat for a longer time than the right parts. The length of the tray over which the pellets are visually observed to discolor determines the thermal stability – the greater the discolored length, the less stable the compound.

PVC formulations with non-lead based stabilizers can be designed to match or even better the thermal stability of traditional lead based formulations. For example, the NL-4 formulation has the same Metrastat oven aging behavior as the L-2 formulation (see Fig. 1). NL-4 has non-lead based stabilizer package as compared to the lead based package in L-2; otherwise the formulations are identical. Non-lead compounds NL-2 & NL-3 have similar to slightly better thermal stability than the lead containing L-1, and non-lead NL-3 has significantly higher thermal stability than L-1 (see Figures 2 and 3).

The effect of heat combined with shear is studied using a Brabender Plasticorder. The PVC pellets are sheared using screws in a temperature-controlled chamber. The torque required to fuse and plasticate the pellets is monitored. After the plastication process is complete (flat torque in Figure 4), a rise in torque indicates degradation. The time over which the torque remains relatively constant is the dynamic thermal stability (DTS) time for the material. Long DTS times indicate greater thermal stability of the compound during extrusion processing. It is important to design non-lead based PVC to maintain sufficient high DTS for ease in processing. However, not all non-lead based PVCs are equivalent in this regard. For example: Non-lead NL-4 has the same DTS as the leaded L-2 (see Figure 4). Non-lead NL-3 has better DTS than L-1, but NL-2 has a lower DTS than L-1 (see Table 1).

Table 1. Dynamic Thermal Stability times for Lead-based and Non-lead Based Compounds

Material	DTS time (min)
L-1	30
NL-2	21
NL-3	35

* ACCUMAX, ACCUDRY, and MINICORD are registered trademarks of Fitel USA Corp.

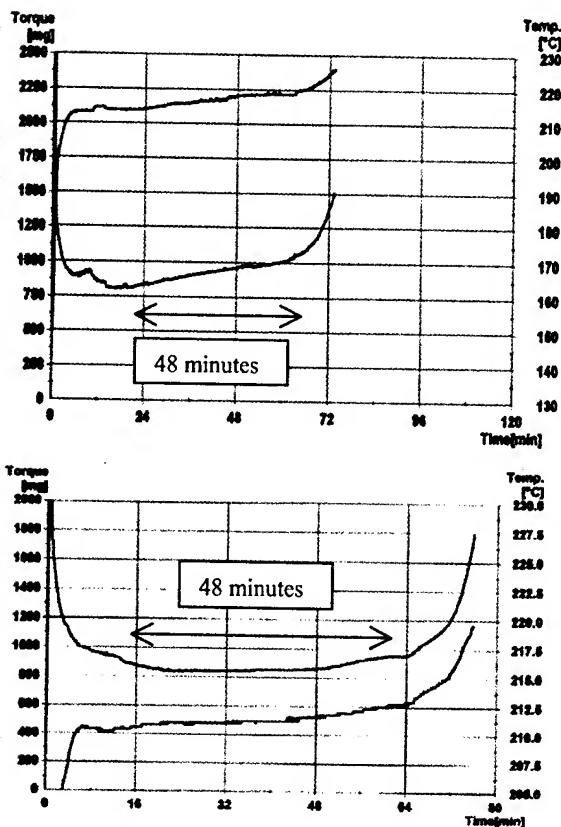


Figure 4. DTS time as measured in a Brabender Plasticorder (Top NL-4, Bottom L-2)

2.1.2 QUV tests

Cables with lead-based PVC jacket (L-2) and non-lead-based PVC jacket (NL-4) were subjected to QUV tests, in which the cables were exposed to high density fluorescent lights. The UV aging of the cables was performed on an Atlas UVCON, Model UC-1, ultra-violet/condensation screening device. The lamps were on continuously for 81 days with the humidity at ambient (uncontrolled) and the temperature between 55°C and 65°C. Four cable samples were tested: a 12 and a 48 fiber count cable with leaded PVC jackets, and their counterparts with non-lead PVC jackets. Cable samples were aged for 15, 34 and 81 days. The jackets were then removed and tensile tested on an Instron Model Model 5565 tensiometer.

Figures 5 and 6 show the results of tensile testing on the aged cable with leaded and non-leaded PVC jackets. As can be seen, no change in either the peak stress or the ultimate elongation could be seen after 81 days of aging. If UV degradation had occurred, the ultimate elongation would have decreased since the material would have become embrittled. For the peak stress, the standard deviation of the stress average after aging would increase since embrittlement would make the material sensitive to flaws. Note that the difference in the percent elongation at break for the 12 and 48 fiber cables is an artifact of testing. Because of the size difference in the samples, the samples were gripped differently. So, while the absolute percent elongation at break values are different, the relative changes between the two sizes are the same, i.e. no change. In conclusion, no UV degradation was observed with either the leaded or non-lead based cables.

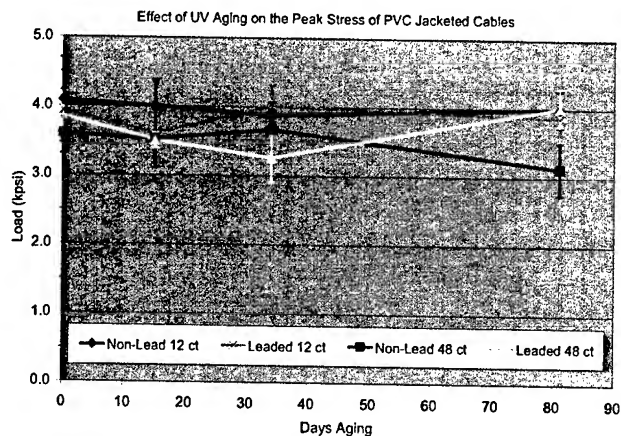


Figure 5. Effect of UV aging on peak stress

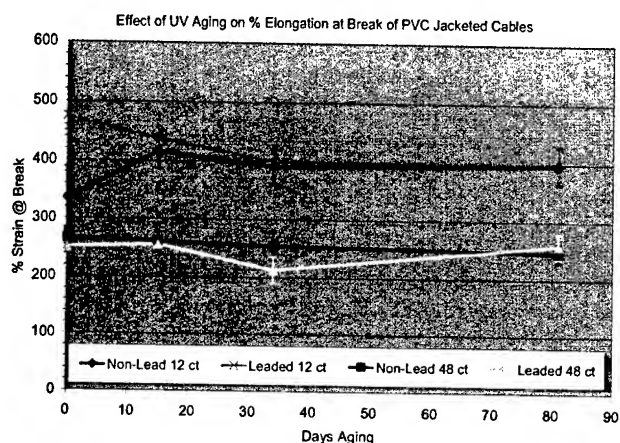


Figure 6. Effect of UV aging on %Elongation at break

2.2 Optical performance

2.2.1 MINICORD simplex and duplex cables

Added losses after 85°C aging per GR-409 on MINICORD simplex cables for 62.5 micron fibers buffered with nylon and jacketed with L-1 and NL-3 are presented in Table 2.

Table 2. Delta loss for MINICORD simplex and duplex cables

Temperature	Change in loss at 1300 nm in dB/km				
	Specified Maximum	Simplex		Duplex	
		L-1	NL-3	L-1	NL-3
0°C	0.6	0.21	0.14	0.17	0.45

As shown in the table, both the leaded and non-lead cables met the GR-409 requirements. NL-3 performs better than L-1 in simplex and worse than L-1 in duplex, although changes in strength members made at the same time confound the results.

2.2.2 ACCUMAX Building Cable – Riser rated

Here, cables were re-qualified using the non-leaded materials in buffering and jacketing. Added losses observed in ICEA-596 temperature cycling (-20°C to 70°C) were 0.014 dB in worst case for 62.5 micron fiber at 1300 nm, and 0.040 dB in worst case for

single-mode matched clad fibers, well below 0.4 dB/0.6 dB in the specification.

2.2.3 ACCUMAX Building Cable – Plenum rated

Here, (L-1) was replaced with (NL-3) as buffer, while the jacket material was changed from L-1 to NL-2. Again, environmental requirements during temperature cycling 0°C to 70°C were well within specified levels (0.264 dB/km vs. 0.4 dB/km at 1550 nm for single-mode matched clad fibers, and 0.215 dB/km vs. 0.4 dB/km at 1300 nm for 50 micron multi-mode fibers).

2.2.4 ACCUDRY Indoor/Outdoor cable – Riser rated

Here we replaced L-1 with NL-3 as buffering material. Added loss requirements on both 50 micron high bandwidth multi-mode and matched clad single mode fibers met requirements on temperature cycling per ICEA-696 (Table 3). Again, the leaded and non-leaded compounds had different rankings in the two comparisons.

Table 3. Environmental testing results for ACCUDRY Indoor/Outdoor cables

Loss Metric db/km	50 micron MM fiber		SM-MC fiber	
	L-1	NL-3	L-1	NL-3
Minimum	-0.032	-0.015	0.001	0.160
Maximum	0.197	0.133	0.024	0.232
Average	0.065	0.058	0.017	0.199
Spec Max	0.6 at 1300 nm		0.4 at 1550 nm	

2.3 Fire safety performance

All fire tests discussed in this paper were conducted by Underwriters Laboratory, Northbrook, IL.

2.3.1 MINICORD simplex, duplex and breakout cables

MINICORD simplex cable is comprised of a buffered fiber, aramid yarns and a PVC jacket. The PVC jacket material (L-1) used previously had lead stabilizer in its formulation. Three new materials (NL-1, NL-2 and NL-3) were evaluated as its potential replacement, and all three are lead and cadmium free. MINICORD cable prototypes were made with the new materials and subjected to UL 1666 riser test and UL 1685 smoke test. † Table 4 shows the comparison of fire performance between the leaded cable and the new simplex cables with lead/cadmium free jacket materials.

Table 4. UL 1666 and UL 1685 test results for MINICORD simplex cables

Cable Jacket	UL 1666 test		UL 1685 test	
	Flame Spread (ft)	Max. Temperature (F)	Total Smoke Release (m ²)	Peak Smoke Release Rate (m ² /s)
L-1	7-9	516	12.32	0.15

† UL is a registered trademark of Underwriters Laboratories, Inc.

NL-1	5-6	408	3.01	0.08
NL-2	4-3	389	3.50	0.05
NL-3	4-9	430	5.33	0.06
Spec max	12	850	95	0.25

* Test data are averages of two tests per cable. This applies to subsequent tables in this paper.

MINICORD duplex cables have the zipcord construction with two simplex cables attached using an interconnecting web. Table 5 shows the fire test results for duplex cables.

Table 5. UL 1666 and UL 1685 test results for MINICORD duplex cables

Cable	UL 1666 test		UL 1685 test	
	Flame Spread (ft)	Max. Temperature (F)	Total Smoke Release (m ²)	Peak Smoke Release Rate (m ² /s)
L-1	7-0	533	8.96	0.12
NL-1	6-0	428	7.23	0.07
NL-2	5-9	402	3.06	0.04
NL-3	4-3	394	6.41	0.05

As shown in the tables above, all simplex and duplex MINICORD cables passed UL 1666 and UL 1685 with comfortable margin, and therefore are OFNR rated as well as "LS" Marked (for low smoke performance). However, it can be seen that the non-lead cables performed better than the cables with leaded jacket in both UL 1666 and UL 1685 tests.

MINICORD breakout cables range from 4 to 72 fiber counts, and L-2 was used as the material for simplex, unit and outer jackets. Table 6 shows the fire test results comparison when the leaded material is replaced by the non-lead material (L-4).

Table 6. UL 1666 results for MINICORD breakout cables

Cable	Flame Spread (ft)	Max. Temperature (F)
4 -fiber with L-2	5-9	373
12 -fiber with L-2	7-9	483
4-fiber with NL-4	9-0	642
12-fiber with NL-4	9-0	636

As shown in the table, the non-lead cables did not perform as well as the leaded cables, but nonetheless meet the UL 1666 test requirements. Although the basic formulations for L-2 and NL-4 are similar, there had been other changes in addition to the stabilizer package change, which may have contributed to the difference in fire performance by the cables made with the non-lead based material.

2.3.2 ACCUMAX Building Cable – Riser rated

OFS ACCUMAX Building Cables are Riser rated, 2-72 fiber count cables. In the past, the cables were made with a leaded PVC

material. In an effort to remove lead from these cables, a new non-lead material was evaluated as a replacement in these cable constructions. Cables with different fiber counts, and with or without subunits were constructed and tested for fire resistance. Table 7 shows the UL 1666 test results for the cables with the leaded material (L-2) compared with those with the non-lead material (NL-4).

Table 7. UL 1666 results for ACCUMAX Riser Cables

Cable	Flame Spread (ft)	Max. Temperature (F)
6 -fiber with L-2	4-8	347
12 -fiber with L-2	5-8	392
72-fiber with L-2	5-3	366
6-fiber with NL-4	5-9	414
12-fiber with NL-4	5-6	415
72 fiber with NL-4	7-9	515

The results indicated that the leaded material had similar or slightly better fire performance than the non-lead material, especially in the case of the 72-fiber cable. However, the non-lead material can still provide adequate fire resistance as required by UL 1666 and National Electric Code.

2.3.3 ACCUMAX Building Cable – Plenum rated

ACCUMAX plenum cables were built with a leaded PVC material (L-1) for buffer and jacket. Three new materials (NL-1, NL-2 and NL-3) were evaluated as its potential replacement, and all three are lead and cadmium free. Table 8 shows the UL 910/NFPA 262 fire test results for various 72-fiber cables.

Table 8. UL 910/NFPA 262 results for ACCUMAX Plenum Cables

Cable Material		Flame Spread (ft)	Peak Optical Density	Average Optical Density
Buffer	Jacket			
L-1	L-1	4.5	0.34	0.12
NL-1	NL-1	3.0	0.46	0.19
NL-2	NL-2	2.3	0.23	0.10
NL-3	NL-3	1.5	0.28	0.11
NL-3	NL-2	2.1	0.26	0.11
UL 910 spec max		5.0	0.50	0.15

Among the three non-lead materials evaluated, NL-2 and NL-3, or the combination of these two materials yielded excellent fire performance as measured by the plenum fire test. On the other hand, NL-1 provided better flame performance than L-1, but the smoke performance was rather poor and failed the requirements by UL 910/NFPA 262 test. This also proves that the selection of appropriate materials for a certain application has much to do with cable constructions, as well as the synergies between different materials in the cable.

2.3.4 ACCUDRY Indoor/Outdoor cable – Riser rated

OFS also offers a line of ACCUDRY indoor/outdoor cables. One family of the cables is made with LSOH materials for customers with special considerations, while another family of the indoor/outdoor cables uses PVC material for buffer. Since the old PVC material has lead stabilizer in its formulation, a non-lead replacement for this application was developed.

Table 9. UL 1666 results for ACCUDRY Indoor/Outdoor cables

Cable	Flame Spread (ft)	Max. Temperature (F)
L-1	5-6	404
NL-3	4-3	382

Table 9 shows the UL 1666 test results for the 36-fiber indoor/outdoor cables made with leaded and non-lead buffer materials. It is shown that the cable with lead free materials performed slightly better than the previous version with leaded buffer material.

3. Conclusions

Throughout the work on the non-lead conversion of OFS premises cables, it has been shown that not all non-lead materials perform equally. Cable constructions and synergies among all materials in the cables need to be considered. Through careful screening and evaluation of materials, OFS has succeeded in choosing appropriate heavy metal free PVC materials to produce environmental-friendly premises cables with good thermal/UV stability, optical performance and fire performance.

4. Acknowledgments

We thank the Premises Cable Development team, the testing lab personnel at OFS, Dr. Priya Tabbador and Dr. Tom Chapin for their contributions to the development of non-lead premises cables. We also thank UL for conducting the fire tests.

5. References

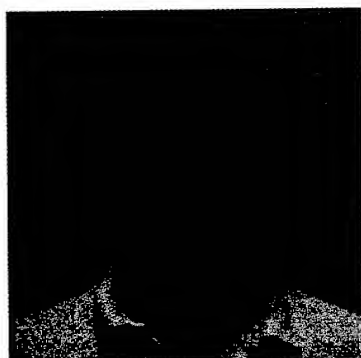
- [1] "Government Order Regarding the Prohibition of the Import, Sale, and Production of Lead and Products Containing Lead" Country of Denmark – Official Government Order. November 1, 1999.
- [2] "Government Order Regarding the Prohibition of the Import, Sale, and Production of Lead and Products Containing Lead", Country of Denmark – Official Government Order. November 1, 1999.
- [3] <http://www.oehha.ca.gov/prop65/>

6. Authors of the paper



Dr. Hong Chen

Member of Technical Staff. Responsible for materials evaluation and selection, cable safety standards and cable fire testing and listing. She has a Ph.D. in Chemistry from University of Cambridge, U.K. Previous experience included catalyst and polymer development, and R&D management in the chemical industry with 4 U.S. and foreign patents.



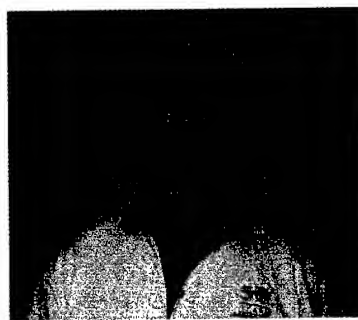
Dr. Charlie Jackson

Member of Technical Staff. Responsible for cable design and testing. He has a Ph.D. in Mechanical Engineering from Stanford University. Previous experience includes optical fiber processing and data analysis.



Dr. Kaushik Chakrabarty

Member of Technical Staff. Responsible for product development, materials evaluation and selection for fiber optic apparatus and fiber optic cables. He has a Ph.D. in Polymer Science from The University of Connecticut.



Mr. Wayne Newton

Distinguished Member of Technical Staff. Recently retired after 36 years with Western Electric, AT&T, Lucent Technologies and OFS. He had been responsible for Process Development Engineering. He holds a B.S. Degree in Electrical Engineering from Clemson University and an M.S. Degree in Industrial Engineering from Texas Tech University. He has 8 U.S. and 3 Foreign Patents in the Copper and Fiber Optic Cable field.



Mr. Samuel Aderogba

Member of Technical Staff. Responsible for cable design, process development, instrumentation, and optical measurement. He holds a B.Sc. and M.E. degrees in Mechanical Engineering from the University of Ibadan, and the Tennessee State University, respectively. He is a member of the American Society of Mechanical Engineers.



Dr. Paul E. Neveux, Jr.

Technical Manager for Premises Cable Design and Development. He has a Ph.D. in Inorganic Chemistry from University of North Carolina, Chapel Hill. He worked as Engineer and Supervisor at Sumitomo Electric Lightwave Corp. before joining Lucent Technologies, now OFS, working on copper and fiber optic cable materials development. He has 4 patents with 6 pending. He has served on TIA Standard committees, authoring two FOTP's.

Helium Recovery in Fiber Optic Production: Benefits and Application

Robert Busch/Lawrence Schottke/Frank Lauricella

Praxair, Inc.

Tonawanda, NY/Danbury, CT

+1-716-879-2569 · robert_busch@praxair.com

+1-716-879-7801 · lawrence_schottke@praxair.com

+1-203-837-2737 · frank_lauricella@praxair.com

Abstract

Helium is an essential component used in the manufacture of optical fiber and has proven substantial advantages over alternative gases. Due to the increased demand for helium combined with limited available new capacity, supply of this valuable gas has recently become tight. This situation has resulted in increasing helium prices as suppliers seek and develop new sources to meet demand.

In an effort to help encourage conservation and provide cost saving solutions to customers, Praxair has been very active for several years in bringing helium conservation and recovery technology to optical fiber producers and other large helium consumers.

The decisions made now may have a material impact on each fiber producer's ability to effectively control future costs and reap the benefits of uninterrupted production.

This paper serves to examine helium supply and demand drivers, advantages of using helium in fiber optics manufacturing, and important aspects of applied helium recovery technology, in order to assist the optical fiber producer in formulating a plan appropriate to their specific circumstances.

Keywords

Helium; recovery; fiber optic; fiber; draw tower; draw; cooling tube; cooling; utility; cost; consumption; consolidation; purification; recycle; supply; coolant.

1. Introduction

Due to its unique physical properties that enable improved product quality and increased production efficiency, helium is universally utilized in both the pre-form manufacturing and fiber draw processes. As fiber production becomes increasingly competitive, the need to reduce operating costs becomes more important to the success of each fiber manufacturer.

Over the past several years, utilization of helium has been increasing in areas as diverse as fiber production, lifting, welding, leak detection, electronics, MRIs, lasers, and others. As a result of the rising demand and limited new capacity, supply of this valuable gas has become tight. The outlook is for helium supply to remain tight in the future until new helium capacity is added to meet the expected growth in demand.

In an effort to help encourage conservation and provide cost saving solutions to customers, Praxair has been very active for several years in bringing helium conservation and recovery technology to optical fiber producers and other large helium consumers. A number of helium recovery strategies have been developed which, when combined to form a comprehensive plan, can reduce helium consumption and provide significant benefits. This plan, when implemented, can simultaneously reduce production costs, increase helium reliability, and conserve a valuable natural resource.

2. Helium Supply/Demand

2.1 Helium Supply

Virtually all natural gas deposits located throughout the world contain some helium. If the content level is high enough, it becomes economical to recover the helium from the natural gas. Typically, only natural gas containing more than 0.3 percent helium by volume can be processed economically for the extraction of helium.

There are relatively few known natural gas sources worldwide that contain helium at such levels. Major sources of worldwide helium include the Hugoton natural gas fields of Kansas, Oklahoma, and Texas and the Riley Ridge area of Wyoming. Since the 1920s, the Hugoton fields have served as the largest single source of helium in the world.

Other sources of helium exist throughout the world. LaBarge, WY and Ladder Creek, CO are two such active helium source locations in the US. Similarly, there are other worldwide sources in Algeria, Qatar, Russia and Poland. ⁽¹⁾

2.2 Helium Demand

Helium finds application in many different industries due to its unique chemical and thermodynamic properties. Helium and helium mixtures have long been used in the welding industry for MIG and TIG shielding gas. Laser welding, a newly developing technology, promises to carry helium forward as the gas of choice for both high and low tech welding applications.

Another large and growing application area for helium is the magnetic resonance imaging (MRI) market. Other application areas include diving gas, leak detection, balloons, NMRs, and of course fiber optics. In addition, exciting new application areas are currently being investigated. These developing applications

typically hinge on leveraging helium's unique thermodynamic characteristics to substantially improve the performance of an existing process.

Demand in these traditional helium applications is expected to grow in the range of 5% to 10% per year.

2.3 Future Outlook

As discussed, demand is expected to be robust in the coming years due to increased usage across many industries and applications. Worldwide production capacity of refined product is expected to increase at a rate comparable to the projected increase in demand. Therefore, the supply/demand situation is expected to remain relatively tight for the foreseeable future.

Increasing demand for helium, substantial new investment requirements associated with bringing new sources on-stream, and rising raw material costs from existing supply sources have resulted in a general rise in helium prices.

Praxair understands and appreciates the negative impact that higher prices can have on both small and large helium consumers. The outlook for a rise in helium pricing worldwide has added urgency to our push for helium conservation and recovery.

3. Helium Usage in Fiber Optics

3.1 Application Areas

3.1.1 Preform Manufacture. Helium is used in the preform manufacturing process in two general areas. First, helium is utilized as the carrier gas for material deposition during the preform lay-down process. Next, helium is used as a sweep gas for impurity removal during the consolidation step.

The vent streams from these processes contain significant amounts of helium. However, this helium is often mixed with other gasses used in the manufacturing process and contains difficult to handle trace impurities such as chlorine. The highly variable flow and compositional nature of these vent streams, combined with difficult to handle trace impurities, make helium recovery from these streams very expensive.

In both the lay-down and consolidation processes, purity of feed helium must be very high to prevent contamination of the final consolidated preform. This tight specification on helium purity is a significant cost contributor for a recovery system incorporating purification.

For these reasons, most recovery efforts in the fiber optic industry have concentrated on the draw cooling area of the manufacturing process. The remainder of discussion presented hereafter will deal exclusively with recovery from the draw tower area.

3.1.2 Helium- The Gas of Choice in the Draw Tower. As discussed above, the draw tower has historically been the area of focus for helium recovery in fiber optics. Pure helium is typically used in the draw tower heat exchangers to cool fiber exiting the

preform furnace prior to being fed to the coating operation. Helium is the gas of choice for this cooling application due to its extremely high thermal conductivity.

The use of helium facilitates rapid heat transfer from the molten fiber exiting the preform furnace to the inner surfaces of the cooling tube. This rapid heat transfer allows the length of the cooling tube(s) to be minimized and thus serves to minimize the overall height of the draw tower. This effect significantly reduces the overall cost of a new draw tower facility. For an existing draw tower facility, the use of pure helium as coolant gas allows operation at increased speed without modification of the cooling tube equipment.

Figure 1 shows the thermal conductivity for pure helium, nitrogen, and argon. This figure clearly demonstrates the superiority of helium for conductive heat transfer applications. No other gas or combination of gases provides the conductive heat transfer capabilities of pure helium.

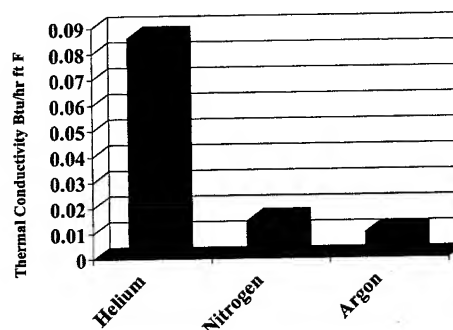


Figure 1. Conductivity of Gasses

Figure 2 shows how the thermal conductivity of a helium/air mixture drops as the air content rises.

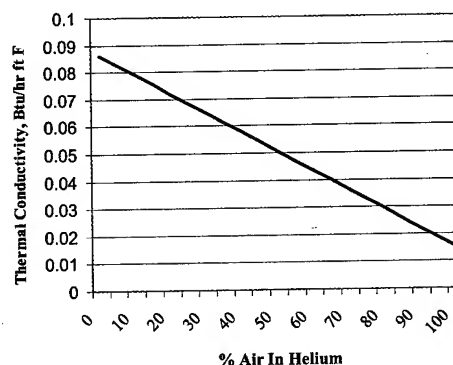


Figure 2. Conductivity of Helium/Air Mixtures

Evident from this figure is the fact that capital expended in achieving very high purity by use of purification is often not warranted or required for this application. In helium recycle type recovery systems, purification beyond particulate and moisture removal is typically not required. In these cases, the impurity level of the withdrawn gas (recycle stream) is carefully monitored and controlled to minimize infiltration of ambient air while maximizing recovery.

Since glass in the draw stage of the fiber manufacturing process is fairly insensitive to chemical change, the required purity of helium coolant is dictated only by heat transfer considerations. This fact is important in understanding and evaluating the different recovery system options that are available.

3.2 Helium Recovery Considerations

3.2.1 Customer Equipment. Experience has shown that recovery can not be successfully instituted without careful consideration of specific customer equipment and control methodology. While there is strong financial incentive to propose a recovery system design based merely on transmitted design and operational information, successful implementation of recovery hinges on the execution of one or more well planned on-site tests.

There is significant variation in the design and operation of draw tower cooling tube heat transfer equipment from customer to customer, site to site, and even tower to tower. Most differences are manifested in the following areas:

- Length
- Internal Diameter
- Coolant Distribution
- Inlet and Outlet Port Design
- Inlet and Outlet Port Location
- Number of Coolers
- Top and Bottom Tube Openings
- Jacketing Design
- Jacketing Coolant Type
- Jacketing Coolant Temperature

All of these factors impact helium recovery to some extent. Cooling tube design aspects with the greatest influence on potential recovery are the diameter of the top and bottom fiber openings, the coolant inlet port location(s), and the recovery port location(s). Limiting cooling tube top and bottom fiber opening area is essential in preventing excessive air infiltration and helium loss.

Proper selection of inlet and withdrawal ports is also extremely important for helium recovery. The optimum location of these ports is highly dependant on a number of factors including total helium flow rate, top and bottom fiber opening diameters, cooling tube internal diameter, and cooling tube length.

The reasons for these operational differences between cooling tube designs can be explained by examining the forces at work within the tube itself. Helium flow characteristics within a given cooling tube are dictated by a delicate balance of extremely small forces exerted on the coolant gas by the cooling tube and associated equipment. Figure 3 illustrates the forces that exist within the cooling tube. Because coolant flow rates and cooling tube internal pressures are typically very low, the forces acting upon the gas within the cooling tube are extremely small. The small forces at work on the coolant gas within the cooling tube cause the flow of gas to be sensitive to small changes in operating conditions.

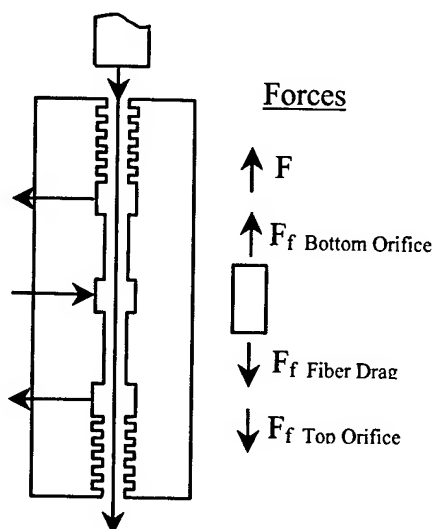


Figure 3. Forces at Work on Cooling Tube Gas

3.2.2 Helium Usage Rates. Next to equipment design, nothing has a greater impact on the ability to effectively recover helium from draw tower cooling tubes more than coolant flow rate. As helium flow rate is decreased, losses from the upper and lower fiber openings of a given cooling tube approach a fixed minimum value based on the opening size and cooling tube geometry. Thus, for applications with high total coolant flow, these fixed losses tend to be a low percentage of the total gas flow. In general, a high coolant flow rate enables high recovery.

For applications with low coolant flow rates, end losses can become very significant. In these applications, minimizing the top and bottom opening diameters is critically important. For low flow rate applications, openings are generally reduced to minimum practical values as dictated by equipment design and fiber vibration limitations.

In addition to affecting the efficiency of recovery, the flow rate of helium used by a given draw tower has a direct impact on recovery economics. A high initial helium usage rate can generally justify a high level of recovery system complexity and capital cost. Conversely, low helium usage rates make justification of cost effective helium recovery much more difficult. In these cases, recovery efficiency may be sacrificed to reduce capital cost in order to increase the overall attractiveness of draw tower recovery.

3.2.3 Available Space. Draw tower facilities are similar to many newer industrial settings. During design and construction of a draw facility, significant efforts are expended in maximizing space utilization in order to reduce capital requirements. As a result, there tends to be little available space for addition of ancillary systems. Single tower recovery systems are ideally suited to this type of environment. These systems are simple, small, and easy to install. A typical single tower system measures

just 0.5m x 0.7m x 0.3m, consumes less than 1 Kw of electricity, and is available in wall or floor-mount configurations.

3.2.4 Ease of Installation. Often overlooked and chronically underestimated are the issues of installation cost and logistics. Recovery systems are typically retrofitted into existing facilities that have been in operation for a significant period of time. Important issues in the following areas are often overlooked or underestimated:

- Equipment Size – Can the recovery equipment be moved around and through existing doorways and equipment?
- Equipment Weight – How will the recovery equipment be lifted into place? Are existing structures adequate for the additional weight?
- Electrical Requirements – How will the new equipment be powered? Is the supporting electrical system adequate?
- Supply and Return Piping System Design and Construction - Who will design and install new piping to and from the recovery system(s). Can this work be performed while the draws are in operation or will a shutdown be required?
- Control System Integration – Does the existing draw tower control system need to be modified to include signals from (or send control signals to) recovery system equipment?

3.2.5 Ease of Operation. Ideally, the addition of recovery to a draw tower operator's list of equipment he/she is responsible for should have very little impact on daily activities. Sophistication of recovery system equipment and controls chosen should reflect the type of equipment that a draw tower operator typically encounters. For instance, if helium flow to a cooler was manually adjusted with a rotameter and valve prior to helium recovery, good practice would dictate that manual control be considered for the recovery system also. Conversely, if helium flow was automatically adjusted prior to recovery, a recovery system should also employ continuous control in its design.

Recovery units are typically fairly simple systems constructed of high quality components reflective of the value of the gas being processed. Reliability of these systems is extremely important due to the relatively high cost of downtime.

Systems designed to recover helium from more than one source must be designed very carefully to insure that an upset at one source location does not affect any other. In addition, sufficient automatic controls and safeguards must be in place to insure that recovered helium, if contaminated by an upset at one source location, does not affect multiple draw lines downstream of the recovery system. This is as true for recovery systems that incorporate purification as it is for systems that do not.

3.2.6 Utility Costs. Recovery systems typically utilize electricity as their only major utility. Single draw recycle type recovery systems that do not need to rely on purification for purity control have very low power consumption. A typical 10-70 slpm

recycle type system can be plugged into a standard 110/220VAC outlet and will consume less than 1 Kw of electricity.

Purification based recovery systems have power consumptions that are significantly higher than recycle type systems. By necessity, these systems incorporate compression that dramatically increase energy usage. These units are typically 380/480VAC and require a dedicated electrical tie-in.

3.3 Recovery Technologies

3.3.1 Recycle Systems. The most widely applied type of recovery system to date is the single tower recycle system. Units of this type, based on Praxair's patented process and control technology², provide excellent recovery efficiency using a cost effective and easy to operate package. A flow diagram for this type of system is shown in Figure 4.

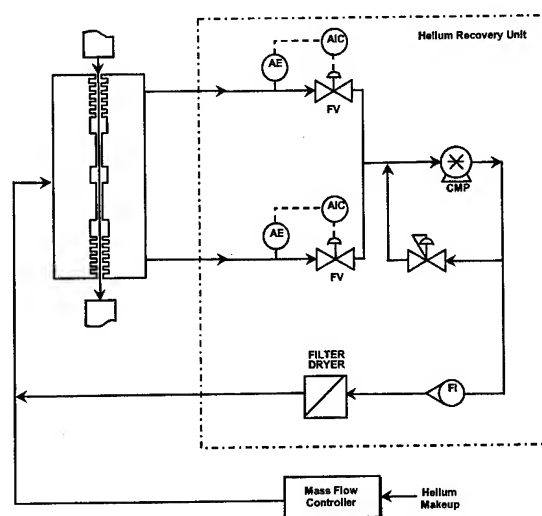


Figure 4. Single Tower Recycle System²

Helium from a single cooling tube is withdrawn from one or more taps. The recovered gas from each tap passes through a dedicated oxygen analyzer where the oxygen content of the stream is measured. This gas then passes through a control valve and to the suction of a vacuum pump. The oxygen content of the withdrawn gas is measured by the analyzer and controlled to a pre-determined set point by the automatic control valve. Discharge from the vacuum pump is filtered, dried, and sent back to the cooling tube as recycle gas.

This cycle is both simple and effective. In this system, the need for purification is eliminated by proper control of recovered gas purity. By utilizing active purity based control, excess air infiltration is eliminated while maintaining the optimum recovery. Effective recovery rates in excess of 90% have been demonstrated by this type of system

Utilities are minimized by the recycle system in that the vacuum pump needs only to supply sufficient driving force to the recovered gas to overcome system and control valve resistances.

Typical vacuum pump pressure rise is less than 1.0 bar. This pressure rise is far less than that required by recovery systems that rely on purification.

3.3.2 Purification Based Systems. An alternative to recycle-only type helium recovery systems is the purification based system. In this system, impure gas is withdrawn from the cooling tube at a fixed or variable flow rate. This gas is then compressed to approximately 10-15 barg and fed to a purification system where bulk removal of air impurities occurs. Purification can be provided using various technologies such as membranes, pressure swing adsorption (PSA), cryo-trap, etc. For purposes of this discussion, it is assumed that purification is accomplished with a membrane based system.

Low pressure product (95%-99% pure helium) from the membrane purifier is re-compressed in a second compressor, dried, and fed back to the customer's helium supply header. A flow diagram for this type of system is shown in Figure 5.

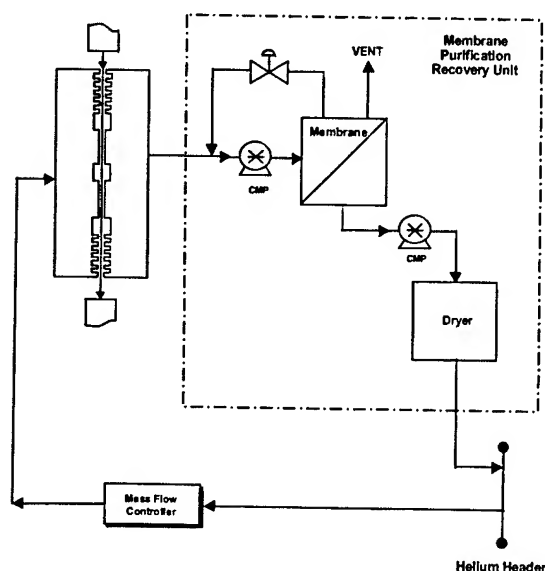


Figure 5. Purification Based Recovery System

For customers with low draw tower helium consumptions, single draw purification based recovery systems are usually not practical. For these customers, a central system recovering gas from multiple cooling tubes may be an attractive alternative. With a central system, however, significant time and attention must be focused on prevention of potential tower to tower interactions. All potential interactions between draw tower equipment that can affect operation must be identified and positively eliminated.

4. Recovery Plan Benefits

4.1 Cost Reduction

Helium, while not a major cost driver in fiber production, is an increasing variable cost to the producer. Marketplace factors promise to increase this cost in the future. A comprehensive

recovery plan can reduce a fiber producer's current cost of production and give a producer control over future costs.

4.2 Reliability and On-Site Storage

One ancillary benefit of reduced helium consumption is an increase in the effective on-site storage for a given facility. If helium consumption for a facility can be reduced by 50% by instituting a comprehensive helium recovery plan, the effective storage (number of production days worth of inventory) for the facility will be doubled.

An alternative to increasing a site's effective storage volume is a possible reduction in the number and size of helium containers used for on-site storage. Thus, helium recovery can, in some cases, enable a reduction in storage related equipment lease fees.

5. Conclusions

Helium recovery systems have been in use in the fiber optic industry for almost a decade. Interest in these systems continues to increase due to competitive pressures in the fiber industry and increasing helium prices worldwide.

These systems can provide benefit to all optical fiber manufacturers regardless of size, type of fiber produced, or volume of helium consumed.

6. References

- [1] Bureau of Land Management's website:
http://www.nm.blm.gov/www/amfo/helium_facts.html
(August 2002)
- [2] Thomas R. Schulte, United States Patent No. 5,377,491
"Coolant Recovery Process" (January, 1995)

Author Information:



Robert Busch

Praxair, Inc.
175 East Park Drive
Tonawanda NY 14150

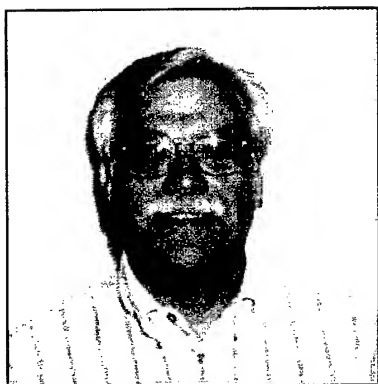
Mr. Busch is Team Leader for Praxair's Helium and Rare Gas Technology Group.



Lawrence Schottke

Praxair, Inc.
175 East Park Drive
Tonawanda NY 14150

Mr. Schottke is a Senior Applications Engineer specializing in gaseous & liquid helium distribution equipment and recovery system design.



Frank Lauricella

Praxair, Inc.
39 Old Ridgebury Road
Danbury, CT 06810

Mr. Lauricella is Director of Recovery and Business Development. His primary focus is on the increased application of helium recovery technology.

Automation of the buffer tube process using active systems

Werner Hoerschlaeger

Rosendahl Maschinen GmbH

A-8212 Pischelsdorf, Austria

+43 3113 5100-640 · w.hoerschlaeger@rosendahlaustria.com

Abstract

The actual trends in fiber optic cable manufacturing are all connected with the general optimization of each step of the production process. In order to improve the performance of the cable, to reduce the costs of the final product and to enhance the production range of the equipment, many technologies and devices have been invented to reduce optical loss, increase production speed and allow more flexibility in the manufacturing process. As fiber and cable continues its movement towards commodity production, continuous automated production methods, especially in the buffer tube process, will be required by the cable manufacturing industries to be competitive

New technological developments in equipment, from conception to design, are influenced by both physical and practical issues. These can range from production philosophies within the organization to physical limits such as processing lines speed for a typical modern buffer tube line.

A case study focusing on automated fiber launching demonstrates the importance of the utilization of active systems to provide the absolutely vital reliability of the production process. The equipment features maximum scrap reduction and highest efficiency considered over a longer period.

Keywords

Fiber, optical, fiber optics, buffering, loose tube, tight buffer, semi-tight buffer, simplex, premises cable, manufacturing, automation

1. Introduction

Most constructions of optical fiber cable (OFC) are based on a extruded plastic tube that contains 1 to 12 fibers. The fiber has some space to move to avoid attenuation increase if the cable is exposed to different temperatures or mechanical stress e.g. pulling or bending. To guarantee this property the ratio of length of the tube and the length of the fiber has to be kept very accurate for the finished product. This ratio - called excess fiber length (EFL) - is influenced by different parameters:

- Fiber tension
- Jelly viscosity
- Cooling water temperature (crystallization rate)
- tension of tube between mid span capstan and exit capstan
- take up tension
- line speed

Higher line speed itself has influence on crystallization rate caused

by less time for buffer tube material to cool down to the specific crystallization temperature. Additionally the tension increases in the cooling trough due to higher friction which results in tube elongation. Both results in high post shrinkage and therefore high EFL. Best results are obtained if the production speed of a loose tube or a tight buffer process is kept constant.

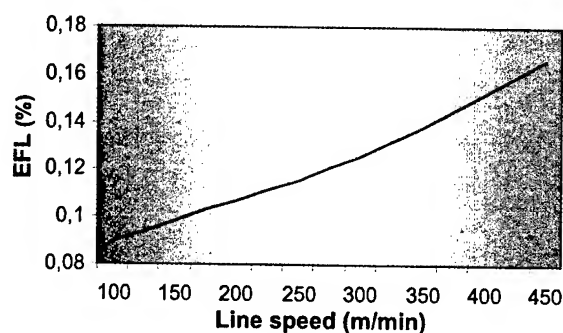


Figure 1. Effect of line speed on EFL.

As fiber cannot be joined like copper a new fiber has to be re launched into the running tube after a batch length is finished. The frequency depends on line speed and length of fiber. E.g. for fiber length of 2.2 km and a line speed of 300 m/min this would be about every 7 minutes where the operator has to re launch. The launching procedure is very critical and depends, especially at higher speeds, operator skill level, experience and attention.

Regardless of production speed, safety with respect to fiber handling is an issue. This issue becomes increasingly critical with higher production demands and increased line speeds. The operator is exposed to dangers like contamination with glass splinters or laceration. With the tensile strength of a fiber at 15 N, a 12 fiber bundle if wrapped around a finger pulls immediately with a force of 180 N (40 lb force) and this with line speed e.g. 300 m/min will result in injury. Or another alarming value is the pressure of a single fiber which increases to the amount of 20 times of the atmospheric pressure before the fiber breaks. You've experienced this if you have ever attempted to break a single fiber.

Summarizing there are several reasons why it is of interest to have fully automated systems for the production buffered tubes:

- to obtain a constant speed to get constant EFL
- to increase productivity of the line
- to decrease amount of fiber scrap and plastic scrap
- to minimize production safety issues

2. Automatic Fiber Launching, the missing Link

Many efforts were invested to automate the loose tube process. On the take up side, a dual reeler was developed to allow reel change without variation of the line speed. Two sets of pay offs are used to allow continuous production and minimal downtime due to setup. But still the operator has to wait for the end of the actual batch length that he can start the new one by manual launching.

Watching the operator you see that this procedure needs a lot of experience to launch the single fiber or the fiber bundle successfully. He holds the fibers in one hand against the back tension from the driven payoff dancers, with the other hand he feeds the end into the die of the crosshead or pre wetting unit, always taking care that there is a loop with enough fiber length which allows it to accelerate when the end of fiber is caught within the running tube. It is easy to imagine the scenarios for failure during the manual launching sequence. Included are a variety of reasons the operator may not be prepared to launch, ranging from working on other aspects of the line, product testing or to simply being absent from the line. The above description gives a general guideline to the requirements of an automatic launching system. They are:

- guiding of the fiber to the die of the crosshead
- active transport of the fiber to the tube
- highest dynamics to accelerate within the shortest time
- pulling capstan to decouple dancer load from fiber feed end
- complete release of the fiber after launching. Minimizing the influence on production quality and enabling preparation for launching the next fiber set

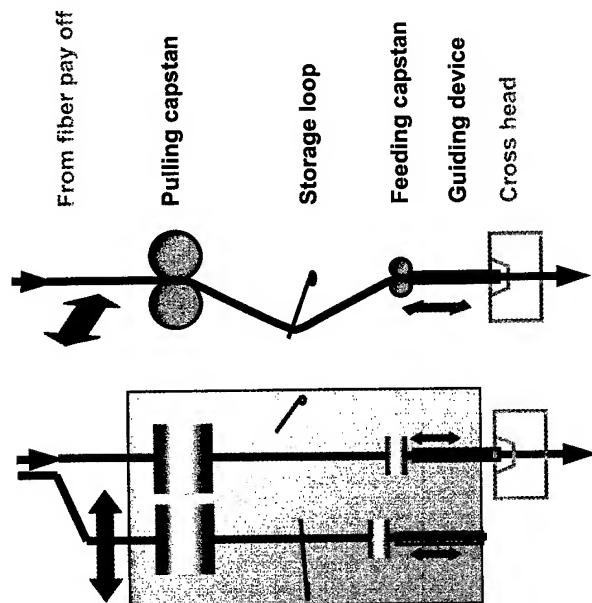


Figure 2. principal of an automatic launching system (Rosendahl patent pending)

To gain a fully automated fiber line with high productivity the following Equipment is necessary:

A **High dynamic fiber pay off** which is able to accelerate in shortest time to production speed. 2 Sets of pay offs are needed for continuous production.

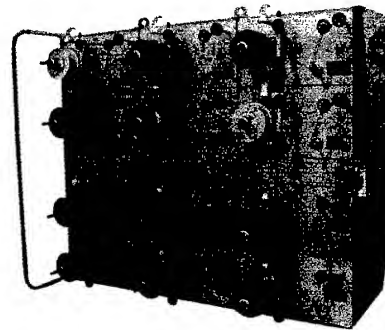


Figure 3. high dynamic fiber pay off

An **Active clamping and cutting device**, synchronized to the pay offs, that enables a fast stop from 500 m/min to zero within 1 second. That means less than 10 m fiber scrap at this high speed. Even that small amount will be rewound to the reel and may be used for the next launching. 2 Sets are needed for continuous production. Typical customer experiences show that fiber scrap is closer to 10x the scrap generated by an actively controlled system as described. In addition, any current systems employed have proven un-reliable at current high production speeds.

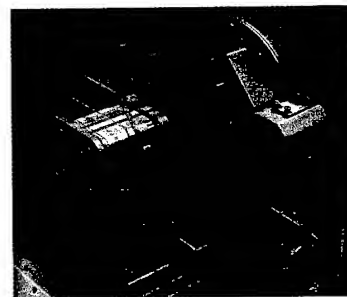


Figure 4. Active fiber clamping and cutting device

An **Automatic launching system** with an active feeding system which releases the fiber after launching may be set up with new fiber reel batch during production of the actual batch in production. This system is able to handle 1 to 12 fibers, including tight coated fiber for the continuous production of a simplex cable.



Figure 5. Automatic launching system

A **Dual reeler** with an optimized change over cycle time which is synchronized with the main line control system enables minimal scrap and total production flexibility. The short change over length of the finished cable coupled with a fast reaction of the dual reeler makes the need for an intermediate scrap reel. As is the norm for copper, the changeover scrap is put on top of the last reel, which can then be used for startup on the next process or can easily be pulled off the reel.

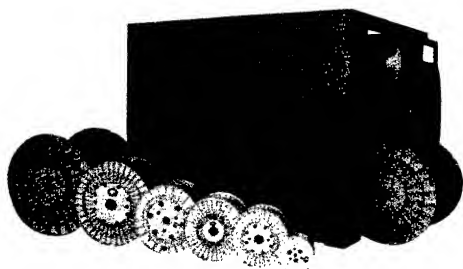


Figure 6. dual reeler

The **Line Control System** should have production batch control capabilities that allow for ease of operator setup and full automation of the changeover process from Fiber to Take-up.

3. Test results and Productivity of different Line Set Ups

The first test for an active launching system is the ability to demonstrate controlled acceleration. To show this case, equipment was installed in following way:

a fiber from a high dynamic pay off was threaded to the automatic launching system. From there it was guided to a running Belt-wheel capstan. This test actually demonstrated a worst case scenario as the fiber was 'snagged' by the belt with no slip, unlike the environment

with insertion into a tube, where slippage is present. In this case the dynamics and control of the system were tested to the extreme with respect to acceleration and synchronization with the line.

This test and demonstration was in effect, a prelude of results that could be expected for tight and semi tight buffer tube process. As expected, speeds in excess of 400 m/min were achieved to launch with the automatic launching system.

Figure 6., Table 1. to 5. show the comparison of the productivity of different line configurations on several products and fiber length

Line A)

A line with conventional pay off able to launch only at lower speed
A double reeler is used as take up

Line B)

Semi automatic line which is equipped with 2 sets of high dynamic pay offs and clamping/cutting devices. The launching process has to be done manually. A double reeler is used as take up.

Line C)

Automatic line for continuous production with 2 sets of high dynamic pay offs and clamping/cutting devices. A automatic launching system handles the launching process. A double reeler with short change over time in combination with the automatic launching make short scrap length possible which need no extra scrap reel. A sophisticated line control system execute a automatic batch control this includes reduction of color scrap length.

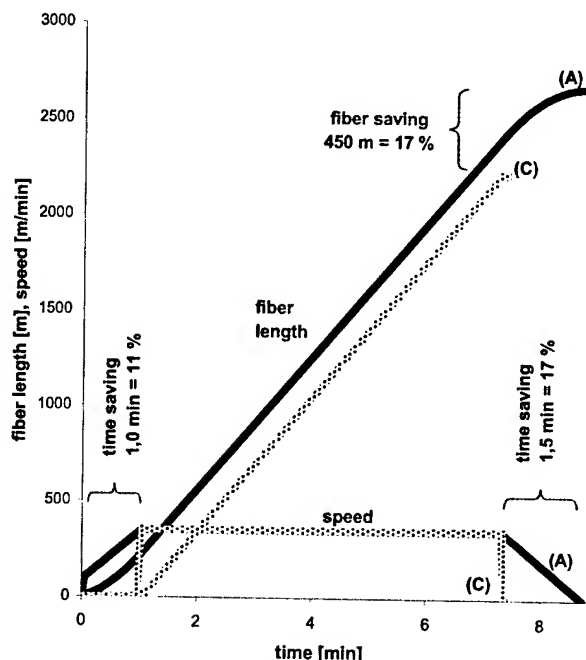


Figure 6. Ramping a line (A) compared to automatic launching system (C) / time and fiber saving at a 2000m production length

Table 1. Loose tube with 12 fibers, 300 m/min line speed, 6km batch length and 25km fiber length

Loose tube 1,5/2,5mm 12 fibers, 6km batch line speed 300 m/min 25 km fiber length		A) conventional line with ramping	B) semi automatic with manual launching	C) continuous production incl. automatic launching
preparation of line	min	3 *)	3 *)	1 **)
Launching	min	1	1	0,1
ramping (up + down)	min	2,5	0	0
threading new fiber	min	10	0	0
time for batch length	min	20	20	20
change over time	min	9 ***)	4	1,1
change over / 24h	1/24h	49,7	60,0	68,2
line not in production	min	447	240	75
productivity km / day	km/24h	298	360	409
length line ramping	km	124	0	0
Improvement	%	100	121	137

*) Preparation incl. threading of tube, color change and change of scrap reel

**) Reduced preparation time due to nearly no scrap which allow no use of scrap reel and reduced color change length optimized by line control system

***) There are 4 batch lengths on 1 fiber length. 1/4 of threading time was added to the change over time

Table 2. Semi tight coating, 300 m/min line speed, 8,8 km fiber length

Semi Tight Coating 0,3/0,9mm 1 fibers, 2km batch line speed 300 m/min 8,8 km fiber length		A) conventional line with ramping	B) semi automatic with manual launching	C) continuous production incl. automatic launching
preparation of line/ day	min	60	60	60
Launching	min	1	1	0,1
ramping (up + down)	min	2,5	0	0
threading new fiber	min	1	0	0
time for batch length	min	26,7	26,7	26,7
change over time	min	3,75	1	0,1
change over / day	1/24h	47,3	52,0	53,7
line not in production	min	237	112	65
productivity km / day	km/24h	361	398	412
length line ramping	km	118	0	0
Improvement	%	100	110	114

Table 3. Semi tight coating, 300 m/min line speed, 2,2 km fiber length

Semi Tight Coating 0,3/0,9mm 1 fibers, 2km batch line speed 300 m/min 2,2 km fiber length		A) conventional line with ramping	B) semi automatic with manual launching	C) continuous production incl. automatic launching
preparation of line/ day	min	60	60	60
launching	Min	1	1	0,1
ramping (up + down)	Min	2,5	0	0
threading new fiber	Min	1	0	0
time for batch length	Min	6,7	6,7	6,7
change over time	Min	4,5	1	0,1
change overs / day	1/24h	128,6	187,0	211,8
line not in production	Min	639	247	81
productivity km / day	km/24h	240	358	408
length line ramping	km	321	0	0
Improvement	%	100	149	170

Table 4. Semi tight coating, 400 m/min line speed, 2,2 km fiber length

Semi Tight Coating 0,3/0,9mm 1 fibers, 2km batch line speed 400 m/min 2,2 km fiber length		A) conventional line with ramping	B) semi automatic with manual launching	C) continuous production incl. automatic launching
preparation of line/ day	min	60	60	60
launching	min	1	1	0,1
ramping (up + down)	min	2,5	0	0
threading new fiber	min	1	0	0
time for batch length	min	5	5	5
change over time	min	4,5	1	0,1
change overs / day	1/24h	151,6	240,0	282,4
line not in production	min	742	300	88
productivity km / day	km/24h	279	456	541
length line ramping	km	379	0	0
Improvement	%	100	163	194

Aerospace/Automotive Session

Robert A. Pappas

Federal Aviation Administration
Atlantic City Int'l Airport, NJ
+1-609-485-6181 · rob.pappas@faa.gov

Abstract

Overview of the FAA Aging Electrical Systems Research Program and some lessons that are emerging concerning electrical systems maintenance and the need for the systems engineering process to consider electrical interconnect system design more carefully during original design and subsequent modifications, repairs, and upgrades.

Keywords: UL Standards, Safety, National Electrical Code (NEC), ANCE, CSA

Biography

Since joining the FAA three years ago, Mr. Pappas has managed the Aging Electrical Systems Research Program. This program supports a large number of projects aimed at the development of technologies to eliminate or mitigate the hazards associated with aircraft electrical interconnect systems. In partnership with the Naval Air Systems Command, the project has successfully managed the development of Arc Fault Circuit Breakers for use aboard aircraft. The program also conducts a number of projects aimed at the development of knowledge and data on various aspects of electrical interconnect systems aging and degradation.

Prior to joining the FAA, Mr. Pappas was employed by the Naval Air Systems Command for 13 years. While with the Navy, Mr. Pappas specialized in the system safety engineering for aerial target and unmanned air vehicle systems. He was Branch Manager for System Safety Engineering for eight years with responsibility for over a dozen fixed and rotary wing system safety programs.

Mr. Pappas has a BS degree in Industrial Engineering from Polytechnic Institute of New York, and an MS degree in Engineering Management from Widener University.

Aerospace/Automotive Session

Automotive Segment

Presentation followed by Panel Discussion Co-Hosted by SAE Cable Task Force



Moderator: *Larry Powell*

Delphi, Warren, OH

+1-330-373-3671 · Larry.Powell@delphiauto.com

Larry Powell is Senior Project Engineer, Delphi, with 23 years experience in wire and cable design.

In addition to his career at Delphi, Powell holds numerous positions with industry standards organizations and committees including the following:

Chairman, SAE Cable Task Force; Chairman, SAE US Advisory Group for ISO WG4, Low Tension Cable; Chairman, ISO WG4, Low Tension Cable; Chairman, SAE US Advisory Group for ISO SC3; US Delegate, ISO SC3, Electrical & Electronic Devices; Vice Chairman, SAE Electrical Distribution Systems Standards Committee; Member, SAE 42 Volt Advisory Committee; Member, SAE Wiring Systems Task Force; Member, SAE US Advisory Group for ISO WG 13, Environmental Conditions.

An original advisor for Wire & Cable Focus, Powell continues his role with IWCS/Focus as aerospace and automotive panel session moderator.

Invited Panel Participants:

Neng Kue, Yazaki North America

Noble Pepper, Dixie Wire, Div. AFL

Mark Sheppard, Exemplar Manufacturing

Vladimir Perlov, Delphi

Larry Matola, Delphi

Aerospace/Automotive Session

Automotive Flat Cable Designs



Vladimir Perlov

Delphi, Warren, OH

+1-330-373-5521 · Vladimir.Perlov@delphiauto.com

Abstract

Flat wire, Flexible Printed Circuit (FPC) and Flat Cable (FFC), provides innovative solutions to traditional wiring problems. Low profile, decreased weight and increased dimensional stability can enhance packaging and reliability. Patterned circuit arrangements on FPC allow for controlled EMC/RFI performance, opportunities for integration, and implementation of "smart" connectors and devices. FPC and FFC will help to facilitate overall Electrical/Electronic Distribution Systems (EEDS) architecture at Delphi. Unique Flat Wire connection systems, e.g. Dock & Lock, contribute to modularization of vehicle subsystems. Flat wire manufacturing and assembly processes are highly automatable which provides greater consistency and repeatability. An application specific design insures a better fit, minimizes assembly time and labor, and reduces the amount of assembly fixtures. Consistent with Delphi's vision, Flat Wire allows for an optimized E/E system that is smaller, lighter, smarter and more cost-efficient, while solving challenges in packaging, reliability and quality.

Keywords: FPC, FFC, EEDS, Flat Wire, Flat Cable, Automotive Harnesses

Biography

Vladimir Perlov, born in Moscow, former USSR, on August 18 1965. He graduated from the Moscow Institute of Technology with MS in mechanical engineering in 1987. At the end of the same year immigrated to USA.

Perlov held various engineering positions including the one in medical equipment field. From 1990 through 1995, he worked for a supplier of specialty products in the aerospace/military field, most of each were FPC based heaters, sensors and power and signal distribution devices.

Perlov joined Delphi in 1995 and held various positions related to adapting FPC technology to the automotive applications.

He is a member of the SAE wiring task force to create industry standards for Flat wire in automotive applications.

Aerospace/Automotive Session

Future Electrical Systems



Laurence Matola

Delphi, Warren, OH

+1-248-813-2440 · Laurence.Matola@delphiauto.com

Abstract

The automobile and light truck market is facing a potential revolution. From digital information and 42-volt power transmission to alternative power sources and "electronic" safety cocoons. The changes that have been forecast could change the way in which we interact with our vehicles and the way our vehicles interact with the surroundings.

This presentation will focus on the impact this revolution will have on the wire and cable found in four major areas of the vehicle. These areas are defined as infotainment, safety and chassis, powertrain and body. The topics covered will include what is the state of the design today, what standards exist, and what the next generation might look like.

Keywords: Automotive Harnesses, 42-volt, 42-volt Architecture, Automotive Cables

Biography

Laurence (Larry) Matola is a Staff Project engineer at Delphi (formally Delphi Automotive Systems) with over 28 years experience in the automotive electrical field. In his current assignment he is developing the physical layer specification for the Automotive MultiMedia Collaboration (AMI-C). The varied nature of automotive wiring systems has given Larry an extensive background in product design, component testing, and manufacturing.

He is a member of the US delegation to ISO's WG13, Chairman of the SAE Wiring Systems Task Force, and of the US technical advisory group to ISO WG14 and he has served on various Internal Delphi and GM Product Leadership committees. He was the primary contributor to vehicle wiring assembly guidelines (PQA) used at all GM North American Plants.

He has received several team recognition awards including the Delphi Packard Global Excellence Award.

Nanotechnology in Optical Networks and Components

Gernot S. Pomrenke

Air Force Office of Scientific Research

Arlington, Virginia

+1-703-696-8426 · gernot.pomrenke@afosr.af.mil

Abstract

Nanotechnology is a series of disciplines that work at the atomic and molecular level to create many types of structures or devices with improved or novel characteristics. In a recent national project, the National Nanotechnology Initiative (NNI), nanoscience and nanotechnology are showing a road full of opportunities and challenges ranging from fundamental discoveries to educational, societal, and business issues. The government's investment in the future of nanotechnology, is now supported by approximately \$600 million in fiscal year 2002, and serves as a major force in shaping the direction of the U.S. nanotechnology research and development activities (<http://nano.gov>). It emphasizes long-term, fundamental research aimed at discovering novel phenomena, processes, and tools; addressing NNI Grand Challenges; supporting new interdisciplinary centers and networks of excellence including shared user facilities; supporting research infrastructure; and addressing research and educational activities. Significant scientific developments have been an outcome to this initiative in such areas as quantum dots and wires, nanostructure assembly, molecular electronics, sensors and coatings.

Advances in understanding fundamental physics and engineering on the nanoscale are viewed as critical to the development of next generation devices and systems. Progress in nanotechnology is enabled by the remarkable success in semiconductor materials growth, nanoscale patterning, device fabrication, polymers and coating technology. It is now possible to fabricate, literally atom-by-atom, semiconductor materials that do not exist in nature and with properties that are near ideal for application in electronics, optics and magnetics. Nanotechnology as applied to optoelectronics offers an area ripe with opportunities and challenges. In one area the convergence of nanotechnology, material processing, tools, and applications is driving the realization of integrated photonics and the all photonics chip. Part of this approach is photonic crystals. Building these crystals requires creating periodic structures from dielectric materials that repeat themselves exactly and at regular intervals. If the matrix is made precisely the resulting structure may have a photonic bandgap (PBG), a range of forbidden frequencies within which a particular wavelength may be blocked, and the electromagnetic radiation is reflected. Photonic bandgap structures and the associated nanofabrication allows photonics to advance optoelectronic miniaturization, light localization, and highly integrated optical devices and components. Integrated 3-D photonic crystal structures form the basis for the fabrication of a photonic chip utilizing the important 1.5

micron wavelength associated with micro-photonic circuits, computers, optical interconnects, micronets, and communication systems.

These developments have been primarily in planar PBG technology, only modest efforts have been expended in implementing the PBG concept to the design, synthesis and fabrication of photonic crystal based optical fiber. Current optical fiber relies upon a transverse variation in index of refraction that varies slowly in comparison with photon wavelength. Also the glass absorption properties limit single mode propagation to a wavelength range that is very narrow compared to the fiber's inherent bandwidth. Furthermore, the integration of additional functions is currently restricted to a single task in a given length of fiber. Small amounts of PBG based fiber with wavelength independent single mode performance have been produced resulting in nano-scale control of the refractive index profile across the fiber's diameter. Although the lengths of fiber produced have been short and the design and modeling limited, it does show the potential benefits of nano-scale control of photons in fiber optics. Indications are that the fiber itself can be used as a sensor measuring, for example, pollutants in gases and liquids. Related areas of exploring nanoscale approaches to fiber communications include nanochannel glass, polymers, and special coating technologies.

Keywords

Nanotechnology, nanoscience, photonic, optical networks

Biography

Gernot S. Pomrenke joined the Air Force Office of Scientific Research (AFOSR) in July 2000 as Program Manager of the Optoelectronics and Nanotechnology Programs. His current interests include Nanophotonics and Chip Scale Optical Networks but also branch into Terahertz Technology and Quantum Computing. His duties include the position as Air Force Nanoscience & Technology Strategic Research Area (SRA) Representative and DoD representative to the national Subcommittee on Nanoscale Science, Engineering and Technology (NSET). Prior to arriving at AFOSR, Dr. Pomrenke was located at the National Science Foundation (NSF), and the Defense Advanced Projects Agency (DARPA) managing the Ultra Electronics Program. Prior positions, as active duty officer, were with AFOSR, AF Institute of Technology, U.S. Air Force Academy, Naval Research Lab, Fraunhofer Institute (IAF, Freiburg, Germany), Wright-Lab (WPAFB, OH), and Air Defense Command.

The Organization of Hierarchically Structured Functional Units and Domains in 3-D Composite Fibers and Films

Galen D. Stucky

Department of Chemistry and Biochemistry, Materials Department
University of California, Santa Barbara, California, 93106
+1-805-893-4872 · Stucky@chem.ucsb.edu

Abstract

Using biomaterials as a guide, we have explored various approaches to the continuous self-assembly and processing of hierarchically structured inorganic/organic composites with rare earth ions, organic dyes, and quantum dots organized into highly organized spatially defined domains built into silica, titania and other compositional media. These efforts have resulted in fibers with linear and nonlinear patterned mesostructures and with or without hollow micron sized channels; wave guides hierarchically structured from the nano through the photonic and micron length scales; and, in transparent films with built-in molecular optical switches and sensor functionality. The chemistry makes it possible to create Fabry-Perot or distributed feed back lasers, ring lasers and a single mode microcavity laser ($< 4\mu\text{m}$ diameter) that is completely constructed by self assembly without any additional processing, substrate or incorporation of mirrors. For the 1-d and 2-d laser configurations relatively low photon thresholds are possible due to the high homogeneity of the optical species that can be achieved within the composite structure.

Keywords

Synthesis and processing;; molecular assembly; biomimetics; hierarchical composite structuring; fibers; waveguides; films; lasers; multicompositional inorganic assembly.

1. Introduction

Synthesis with simultaneous process control of patterning and assembly on nano-, meso, submicron and micron length scales is of crucial importance for many applications, including sorption, separation, catalysis, and electro-optic device fabrication. Selectively utilizing the thermodynamics and kinetics of competing molecular assembly interactions can be particularly effective in collectively defining nano-, meso- and micron scale order. For example, it is now well established

that by using the isoelectric point (IP) and acid catalyzed assembly of silica into organized domains [2, 3] it is possible to simultaneously synthesize and process thin films [4, 5], fibers[6], spherical mesoporous walls encompassing liquids (by microemulsion or nanoemulsion templating) in oil or air[7], oriented monoliths[8], patterned waveguides using soft lithography techniques[9], two-dimensional configurations by ink-jet printing[10], and other 3D morphologies or patterning.

The current research is directed towards the development and optimization of new synthesis methodologies for the preparation of versatile, multi-structured, and multi-functional materials. The ability to obtain hierarchically structured composite materials with structural patterning on the nano-, meso, photonic, micron and larger length scales using molecular assembly has been established. Section 2 describes some of the recent results in this area.

The challenge now is to incorporate desired functionality into the structural components, and thus generate by molecular assembly integrated composite material systems made up of multicomponent functional units. Systems of interest have as electronic components variable band-gap nanoparticle arrays as well as low-concentration atomic (e.g. rare earth ion) or molecular (e.g. optical dye) species that are organized using meso- and micron-scale assembly. Section 3 briefly describes the design and selection of molecular components and processing conditions for the cooperative assembly and organization of electro-optic species into functional hierarchically ordered domains. These include optical waveguide and optical amplification materials that enable low-energy/photon or electron input, high sensitivities, low photon loss, and feedback, with potential applications as optical amplifiers, microlasers for bio- and chemical sensor applications, optical switches, displays, and optical limiters. This approach combines synthesis and processing with

patterning on multiple length scales using block copolymer self-assembly, sol-gel processing, and microlithography,

In Section 4, an example is given of how electronic confinement in quantum dots and semiconductor nanoparticles can be integrated by photon coupling within optical-sized cavities (photon storage and emission) which have incorporated waveguide structures (photon transport). These systems are molecularly assembled and defined across mesoscopic and photonic length-scales. Specifically we this includes (1) the molecular assembly of microcavity lasers, and (2) cooperatively assembled semiconductors (e.g. TiO_2) and rare earth emitters,

2. Background

2.1 Structured composite materials

The synthesis and processing of hierarchically structured materials[2, 3, 11, 12], is achieved by using weak hydrogen

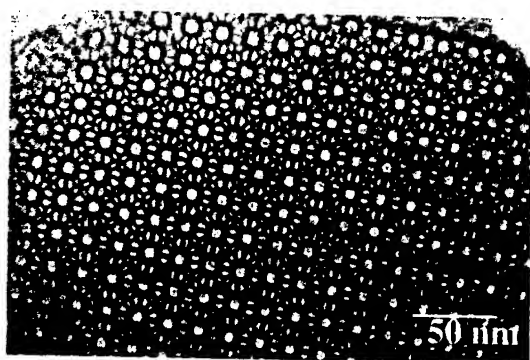


Figure 1. High-resolution electron microscopy image of cubic ($\text{Pm}3\text{n}$) mesoporous silica (SBA-1) showing periodic patterning of amorphous silica.

bonding interface interactions and careful control of the kinetics of the cooperative organization of organic molecules with inorganic molecular species into easily processible nanocomposite structures with highly ordered mesostructures (Figures 1 and 2) with different space group symmetries. For silica, this was initially achieved for the first time using cationic surfactants that interacted via hydrogen-bonding with cationic silica species at pH values below the isoelectric point of silica[2, 13]. More recently, it has subsequently been demonstrated that neutral triblock polymers, as well as diblock and star diblock copolymers, could be used at dilute

concentrations and at pH values below the aqueous isoelectric point of silica to make highly organized silica mesostructures[3].

With both types of organics, self-assembly takes place in the presence of hydrogen-bonding interactions between an organic functional group and the cationic silica species. This acid-synthesis approach has proven to be advantageous for a number of reasons, including the ease of processing, the high hydrothermal stability



Figure 2. Direct image of 3D cages and bimodal pore structure of SBA-1. Amorphous walls in silica SBA structures have a uniform thickness typically within the range of 40 - 60 Å

of the resulting products, and the high degree of mesoscale order (Figures 1, 2). The neutral poly(ethyleneoxide)-poly(propyleneoxide) poly(ethyleneoxide) (PEO-PPO-PEO) triblock copolymers are inexpensive and can be removed by simple aqueous or aqueous/ethanol wash for reuse. in further syntheses.

Molecular assembly can be particularly effective in defining nano- and mesoscale order. Process control of patterning and assembly on submicron and micron length scales is of crucial importance for many applications, including sorption, separation, catalysis, and above all for optical applications. The synthesis procedures described above lend themselves readily to multiphase media or shear processing, which gives great versatility for the creation of hierarchical or component systems on different length scales[9]. Combining this with the proposed studies on electro-optic response response is anticipated to provide a means to construct materials that are not only hierarchically structured, but that exhibit different functions related to the different length scales. Such materials will be used to form a basis for producing integrated systems with opto-electronic communication and environmental response functionalities on all system length scales.

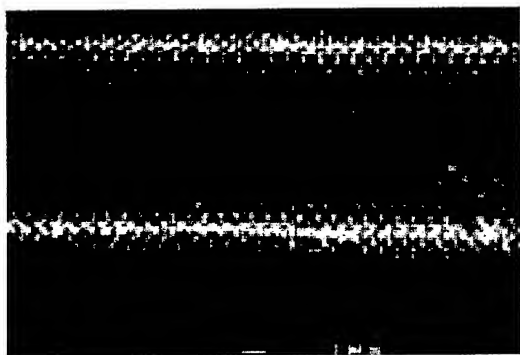


Figure 3. Optical wave guide hierarchically assembled on the photonic and meso length scales

form mesostructured fibers, one obtains well defined domains of helical pores near the capillary walls with straight channels parallel to capillary walls at the center of the fiber[16]. The fibers can be made hollow core, or with high-refractive-index coatings.

Waveguiding structures can also be prepared by patterning surfactant/silica precursor solution onto a low-refractive-index mesoporous silica thin-film support using soft-lithography methods, via confined space micromolding (MIMIC)[9]. This results in high-quality mesostructured line patterns (50 nm to 10 μm) with superior waveguiding properties (Figure 3).

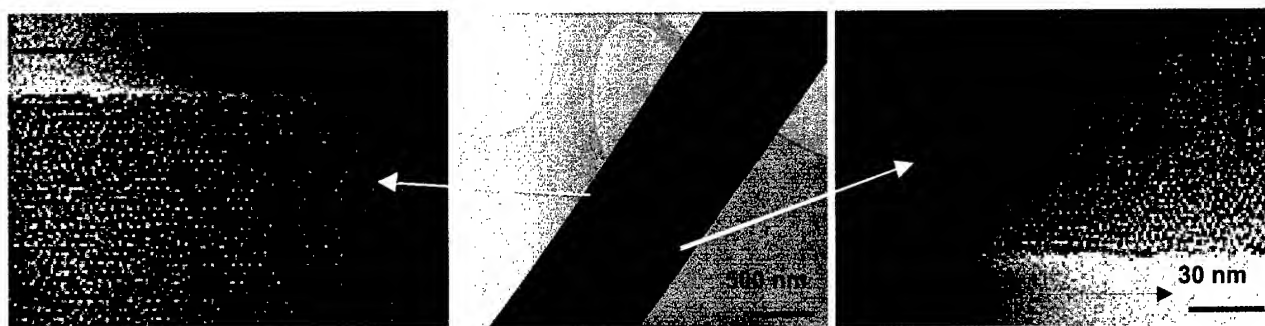


Figure 4. Hollow silica fiber with high surface area helical mesoporous ring structure[1].

Fiber morphologies are of interest for optical applications as waveguides and sensors. Among the first such structures synthesized were those either grown from a two-phase oil-water interface[6] or prepared by drawing a gel strand from a highly viscous amphiphilic block-copolymer/silica precursor solution[14]. The fibers have been shown to have superior optical transmission properties[15] and high degrees of mesoscopic ordering.

The fibers grown from an oil-water interface[15] have unusual anisotropic structures[1]. They can be made as hollow core fibers with ring-like cross-sections near the fiber surface that reflects the helical mesopore structure. The mesopore rings can penetrate radially far into, even completely through, the fiber to give a solid structure. The mesopores themselves are helical with a small translational component and highly ordered so that the normal {100} directions of the helices are also normal to the cylinder walls. This apparently reduces the surface energy that would result if they were simply straight and parallel to the fiber edges[1]. By using a capillary mold to

3. Optical functionalization

As-synthesized mesostructured materials, *i.e.*, materials in which the structure-directing surfactants/block copolymers remain an integral part of the final material, have recently been developed as hosts for the incorporation of opto-electronic guest molecular species, including organic dyes[17-19]. For amorphous sol-gel glasses, low-temperature dye doping was reported nearly two decades ago and on-going research has led to the introduction of doped sol-gel glasses into the commercial optical materials market. However, as we outline below, simultaneous silica/block-copolymer/dye co-assembly can produce materials with substantially improved optical and other material properties. For example, when amphiphilic (PEO-PPO-PEO) triblock copolymers are used to organize a polymerizing silica sol-gel system, structurally ordered silica/copolymer arrays result with uniform adjustable ordering length scales of $\sim 4\text{-}20$ nm. Such mesostructured materials possess nanoscale hydrophobic/hydrophilic regions and different local environments that are available to dye

species incorporated during synthesis. Such mesostructured block-copolymer/silica materials are composed of hydrophobic PPO block domains, hydrophilic PEO block domains, and the silica wall, with some extension of the hydrophilic PEO block into the silica wall. [20] The occlusion of a dye or capped quantum dot into preferentially one or maybe more of these regions is determined by physicochemical interactions, such as electrostatic forces, hydrogen bonding, and dispersion forces, and influenced by kinetic processes including competing assembly processes, silica polymerization, and mass transport.

Our initial studies have shown that for solid state/organic dye lasing, the mesostructured materials that we have made have stability and robustness (thermal, mechanical and optical), processibility, and low thresholds ($0.2 \text{ kW}\cdot\text{cm}^{-2}$) for optically induced lasing[21]. Such threshold figures are comparable to those of the best known organic- or polymer-based solid-state lasing systems. Along with their large organic/inorganic surface areas (to $1000 \text{ m}^2/\text{gm}$ or greater), which can be made selectively accessible through their monodispersed pore or pore/cage structures, their functionality and high degrees of orientational ordering[5, 17, 22, 23] make them attractive as possible hybrid inorganic/organic opto-electronic components. The aligned 3D organization and packaging of optically responsive organic phases is desirable for nonlinear optic applications, photovoltaics, sensors, and electro-optic modulation.

We have recently made significant progress in developing different processing strategies to achieve lasing using such mesostructured materials. One way is to pattern waveguide structures onto surfaces by using soft lithography methods[17]. This results in high-quality mesostructured line patterns that can be produced within hours (3–12 h). When the P123 is used as the PEO-PPO-PEO structure-directing block copolymer, the channels of the hexagonal $p6mm$ mesostructure are preferentially aligned parallel to the substrate and also along the direction of the capillary channels, giving fifth-order Bragg diffraction peaks. One of the laser dyes that we have used is rhodamine R6G, a member of the xanthene family for which the monomer-dimer-trimer equilibria are known, both in solution and when occluded in sol-gel glasses. When the R6G dye species in these waveguides are optically excited with second harmonic light from a Nd: YAG laser (532 nm, 10

Hz), the system exhibits amplified spontaneous emission (ASE). Above a critical threshold excitation power, this results in a gain-narrowing and super-linear output behavior, yielding a spectrum with a FWHM of 7-8 nm; approximately 60 nm of the photoluminescence spectra is generated below the threshold excitation power. Since this process does not provide any feedback, the light emitted at the end of the waveguides is usually not spatially and temporally coherent (referred to as "mirrorless lasing"). The threshold for ASE in these waveguides depends on the dye concentration, and we have thus far achieved thresholds as low as $\sim 6\text{-}8 \text{ kW}\cdot\text{cm}^{-2}$ at a dye concentration of 1.5 wt%. In contrast, the threshold for sol-gel glasses having the same dye content, but prepared without block copolymer, is more than an order of magnitude higher ($> 200 \text{ kW}\cdot\text{cm}^{-2}$).

Significantly, for all concentrations investigated, the quantum efficiencies of the mesostructured materials are higher by an order of magnitude or more than those of the dye-doped sol-gel glasses[24]. These results, along with the UV/Vis spectra, indicate that the R6G dye molecules are much better isolated and can be loaded at corresponding higher concentrations within the mesostructured PEO-PPO-PEO/silica composites. Higher quantum efficiencies are generally obtained, which accounts for the significantly lower thresholds for lasing.

We have determined in other ways that mesostructured silica/block-copolymer composites are well suited for lasing applications[21]. For example, feedback can be introduced by applying a metal coating to the ends of the waveguides. We have organized by molecular assembly other kinds of structures, which provide feedback and which is expected to also be important for direct use in optical and particularly sensor devices.

In one approach, a "micro-ring or μ -ring" laser design was obtained by coating optical fibers (40–125 μm diameter), first with a mesoporous thin film by dip-coating, followed by calcination[21]. Similarly to the multilayer waveguiding structure described above, the thin mesoporous film acts as a low-refractive-index support. In a further step, the lasing layer is then dip-coated on this support. When optically excited, a fraction of the emitted light is confined to the outer layer and travels around the μ -ring. At a certain threshold of the

pumping energy, the gain becomes greater than the loss and lasing is observed at the frequencies determined by the diameter of the optical fiber and the refractive index of the lasing layer. Preliminary studies of the modes show that they are further modulated by whispering gallery modes, which are modes traveling near the outer surface of the dye-doped layer that do not reach the mesoporous film/mesostructured film interface[25]. The threshold for lasing in these μ -ring configurations can be as low as $\sim 0.3 \text{ kW}\cdot\text{cm}^{-2}$ for a $40\text{-}\mu\text{m}$ fiber (Figure 5). We note that these values compare well with

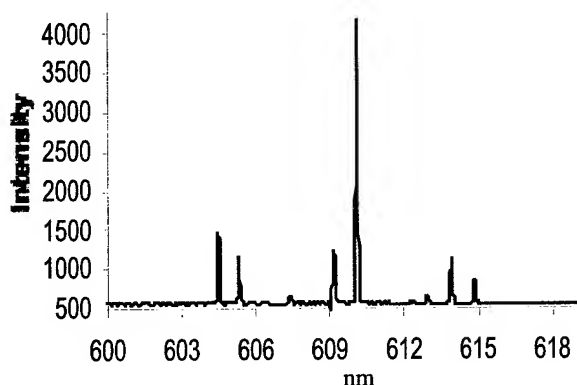


Figure 5. Microring lasing spectrum for $40 \mu\text{m}$ -diameter fiber. Threshold $\sim 0.3 \text{ kW}/\text{cm}^2$

semiconducting polymers, for which thresholds of $\sim 0.1\text{--}0.5 \text{ kW}\cdot\text{cm}^{-2}$ have been measured for the best compounds after nearly a decade of optimization. In short, the initial experiments that we have carried out are already approaching the currently lowest threshold limits known for organic lasing materials. We expect to push the limits to lower lasing thresholds by selection and adjustment of dye/block-copolymer/inorganic compositions and local structures. This will be combined with processing improvements, including use of smaller solid and hollow fibers in order to achieve single-mode operation and orientational ordering of dye species to further reduce the threshold. In addition, we are investigating the use of high concentrations of semiconductor quantum dots to achieve lasing.

It would be desirable to obtain coherent beam patterns not found in microcavity ring lasers, which emit in all directions. We have therefore extended our processing of optical mesostructured materials in conjunction with soft lithography techniques to fabricate distributed feedback lasers (DFB). In this context, we have recently successfully fabricated Bragg gratings, effectively a one-dimensional photonic lattice, on

top of waveguide structures to provide the feedback necessary for DFB. A promising example of such a mesostructured DFB composite is shown in Figure 6 and has been demonstrated to lase with two to three modes[26]. This is an important step toward the molecular assembly of integrated optical circuits and a key component of the proposed research.

We have found that the features described above make these materials excellent candidates for optical thin-film or fiber sensors. Formerly, sensing based on optical detection has been implemented in sol-gel glasses. Typically, these sensors are operated by measuring the transmission, emission, or lifetime of a complex or an organic dye embedded in a SiO_2 matrix. The response is altered through diffusion of the molecule to be sensed into the matrix towards the sensing dye/complex. Two important

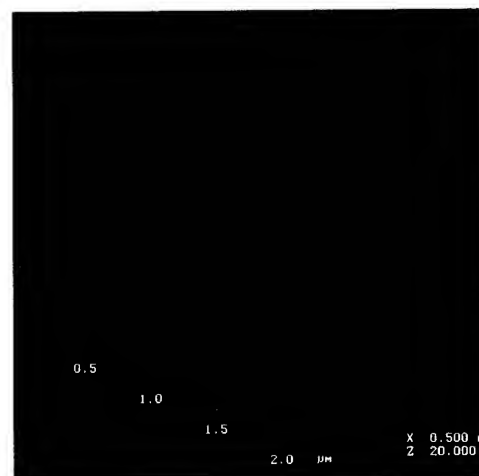


Figure 6. AFM of mesostructured Bragg grating on DFB laser

tasks in developing such a sensor are the occlusion of the dye/complex (physical occlusion versus covalent anchoring) and the diffusion times, which are determined by the glass microstructure. The first feature is important to leaching and hence to reliable long-term operation; the second determines the response times. In principle, the requirements of fast response and negligible leaching can be fulfilled advantageously in large-pore mesoporous materials by covalently anchoring an optically sensitive dye during synthesis followed by removal (e.g. by low temperature solvent extraction) of the block-copolymer species.

Based on these considerations, we are developing a number of optical sensors for pH, small-molecule, and biomolecular applications. We have been able to demonstrate, for example[27], the synthesis of an optical thin-film pH sensor with a fast response time. The pH-sensitive dye

fluoresceinisothiocyanate was derivatized with 3-amino-propyltriethoxysilane. This functionalization ensures that the dye is covalently anchored onto (or within) the SiO₂ wall during mesostructure synthesis. After thin-film synthesis employing the block copolymer F127, the ~900 nm thick films were dried at about 70 °C to enhance their robustness.

The sensor functions according to the intensity of emitted light associated with the anchored dye species. A plot of the emission spectra upon bringing the thin film into contact with solutions of different pH values is very similar to what is observed for fluorescein in solution: the integrated light emission increases with increasing pH. A typical plot of the emitted light intensity versus pH clearly demonstrates that the thin-film sensors act analogously to the dye in solution, except that the pK_a value is shifted from 6.4 in solution to ~7.3 in the thin films. In comparison to what is observed in solution, a broadening of the titration curve is evident. This is attributed to two factors. First, an inhomogeneous dye environment may contribute to this broadening. Second, fluorescein possesses three pK_a values (2.08, 4.31, 6.43), which are difficult to distinguish, even in solution. The response times of the thin films are on the order of 7 seconds for a 95% change in the emitted light intensity (Figure 7). Generally, in sol-gel glasses the response times are much slower, the only exception being small capillaries coated with sol-gel glasses[28]. This clearly demonstrates that these mesoporous, highly ordered, transparent, mechanically robust thin films are well suited for fast-response optical sensors. In this research we will extend our previous studies to ion sensors for bio-detection, small-molecule gaseous detection, and larger-molecule detection related to bio-sensing.

To evaluate and improve the performance of these materials as sensors, it is necessary to understand the origins of their sensitivity and response efficiency. Crucial factors influencing these properties are the local environments of the sensing species, the diffusivities of the target agents to the sensing sites, and the interactions between the target/sensing species themselves. For example, we have observed in preliminary measurements that the presence of the surfactant significantly lowers the diffusion of gas molecules, such as O₂, towards sensing complexes, such as trisbipyridylruthenium. In contrast, fast response times are observed in dye-functionalized mesoporous thin films, consistent with the

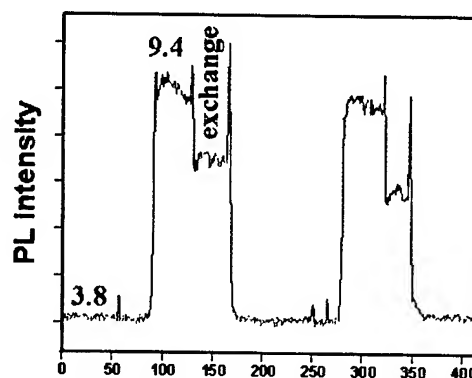


Figure 7. Time- and pH-dependent photo-luminescent response of a fluorescein-doped mesoporous thin film upon a change in solution pH.

reduced transport resistances experienced by diffusing target species in open pores to the active sensing sites.

The use of photochromic dyes, such as spiropyrans and spiroxazines, to induce optical switching through photoisomerism, is another excellent means of introducing sensing properties to SBA (Santa Barbara) mesostructured materials. They are sensitive probes of their local environments and can be used to assess the presence of co-adsorbed guest species. We have recently demonstrated that spiroxazines have particularly fast response times, which are comparable to those in solution and are stable over many months[29] (Figure 11). We believe that a promising approach to achieving substantial sensitivity enhancements for chemical sensing in these mesostructured sensor systems is to exploit the extraordinary signal amplification that can occur under conditions of lasing and/or amplified spontaneous emission.

4. Conclusions

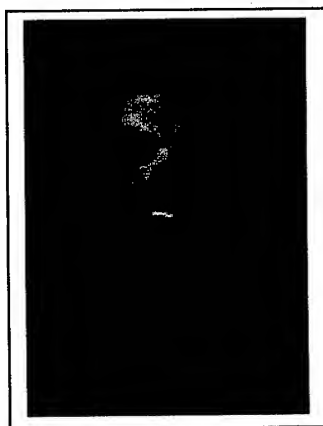
The projects described in this paper target understanding the molecular synthesis and 3D organization needed to structurally integrate hierarchical assembly with interacting electro-optic functionalities. The ultimate goal is the creation of opto-electronic communication and environmental response capabilities incorporated in a system on nano through micron length scales.

5. Acknowledgments

Special thanks to the National Science Foundation and the Army Research Office for their support of this research.

6. References

- [1] F. Marlow, et al., "Doped mesoporous silica fibers: the internal structure," *Microporous and Mesoporous Materials*, 39, 37-42, 2000.
- [2] Q. Huo, et al., "Generalized syntheses of periodic surfactant/inorganic composite materials," *Nature*, 368, 317-321, 1994.
- [3] D. Zhao, et al., "Triblock copolymer syntheses of mesoporous silica with periodic 50 to 300 Ångstrom pores," *Science*, 279, 548-552, 1998.
- [4] I. A. Aksay, et al., "Biomimetic pathways for assembling inorganic thin-films," *Science*, 273, 892-898, 1996.
- [5] S. H. Tolbert, et al., "A new phase of oriented mesoporous silicate thin films," *Chem. Mater.*, 9, 1962-1967, 1997.
- [6] Q. Huo, et al., "Room-temperature growth of mesoporous silica fibers: a new high-surface-area optical waveguide," *Adv. Mater.*, 9, 974-976, 1997.
- [7] S. Schacht, et al., "Oil-water interface templating of mesoporous macroscale structures," *Science*, 273, 768-771, 1996.
- [8] S. H. Tolbert, et al., "Magnetic field alignment of ordered silicate-surfactant composites and mesoporous silica," *Science*, 278, 264-268, 1997.
- [9] P. Yang, et al., "Patterning porous oxides within microchannel networks," *Adv. Mater.*, 13, 427-431, 2001.
- [10] H. Fan, et al., "Rapid prototyping of patterned functional nanostructures," *Nature*, 405, 56-60, 2000.
- [11] P. Yang, et al., "Hierarchically ordered oxides," *Science*, 282, 2244-2246, 1998.
- [12] P. Yang, et al., "Generalized syntheses of large-pore mesoporous metal oxides with semicrystalline frameworks," *Nature*, 396, 152-154, 1998.
- [13] Q. Huo, et al., "Organization of organic molecules with inorganic molecular species into nanocomposite biphasic arrays," *Chem. Mater.*, 6, 1176-1191, 1994.
- [14] P. Yang, et al., "Triblock-copolymer-directed syntheses of large-pore mesoporous silica fibers," *Chem. Mater.*, 10, 2033-2036, 1998.
- [15] F. Marlow, et al., "Doped mesoporous silica fibers: a new laser material," *Adv. Mater.*, 11, 632-636, 1999.
- [16] N. A. Melosh, et al., "Macroscopic shear alignment of bulk transparent mesostructured silica," *J. Am. Chem. Soc.*, 123, 1240-1241, 2001.
- [17] P. Yang, et al., "Mirrorless lasing from mesostructured waveguides patterned by soft lithography," *Science*, 287, 465-467, 2000.
- [18] G. Wirsberger, and G. D. Stucky, "Ordered mesostructured inorganic/organic arrays with optical functionality," *ChemPhysChem*, 1, 89-92, 2000.
- [19] H. S. Zhou, and I. Honma, "Dye-doped photosensitive mesostructure materials," *Adv. Mater.*, 11, 683-685, 1999.
- [20] N. A. Melosh, et al., "Molecular and mesoscopic structures of transparent block copolymer-silica monoliths," *Macromolecules*, 32, 4332-4342, 1999.
- [21] G. Wirsberger, and G. D. Stucky, "Microring lasing from dye-doped silica/block copolymer nanocomposites," *Chem. Mater.*, 12, 2525-2527, 2000.
- [22] H. Yang, et al., "Synthesis of oriented films of mesoporous silica on mica," *Nature*, 379, 703-705, 1996.
- [23] D. Zhao, et al., "Continuous mesoporous silica films with highly ordered large pore structures," *Adv. Mater.*, 10, 1380-1385, 1998.
- [24] G. Wirsberger, et al., "Patterned block-copolymer-silica mesostructures as host media for the laser dye Rhodamine 6G," *J. Phys. Chem. B*, 105, 6307-6313, 2001.
- [25] Y. Kawabe, et al., "Whispering-gallery-mode microring laser using a conjugated polymer," *Appl. Phys. Lett.*, 72, 141-143, 1998.
- [26] B. J. Scott, et al., "Dye-doped mesostructured silica as a distributed feedback laser fabricated by soft lithography," *Adv. Mater.*, 13, 1231-1234, 2001.
- [27] G. Wirsberger, et al., "pH sensing with mesoporous thin films," *Chem. Commun.*, 119-120, 2001.
- [28] C. Rottman, et al., "Doped sol-gel glasses as pH sensors," *Materials Lett.*, 13, 293-298, 1992.
- [29] G. Wirsberger, et al., "Fast response photochromic mesostructures," *Adv. Mater.*, 12, 1450-1454, 2000.



Galen Stucky
 Dept. Chemistry
 University of California
 Santa Barbara, CA
 stucky@chem.ucsb.edu
 Ph.D. Iowa State, Professor
 at U. Illinois Urbana, Group
 leader Sandia National Labs
 and du Pont Central
 Research. Today member of
 Biomolecular Science and
 Engineering Faculty,
 Materials and Chemistry
 Departments at UCSB.

Organic Nanostructured Materials for Photonics

Theodore Goodson III

Department of Chemistry, Wayne State University
Detroit, Michigan 48202
+1-313-577-6918 · tgoodson@chem.wayne.edu

Abstract

The dendritic architecture allows for the control of novel optical properties. Ultra-fast excited state dynamics of organic dendrimers have been studied with both polarized and depolarized femtosecond fluorescence spectroscopy. The dynamics of novel dendrimer-metal nanocomposite systems is also discussed as well as strong optical limiting behavior in these and other related systems. The inclusion of these materials in all optical signal processing by fiber optical design is also discussed.

Keywords

Dendrimer, quantum optics, optical fiber, nonlinear optics, telecommunications.

1. Introduction

As the search for better optical materials for photonic and telecommunication applications researchers have given an increasing amount of attention to the study of dendrimers, which are highly branched macromolecular systems.¹⁻⁵ Along with the synthesis and chemical properties, the photo-physics of these systems is attracting rising interest in connection with their applications as artificial antenna systems.^{2,3} However, the nature of electronic excitations and specific mechanisms of intramolecular energy transport in dendrimers are not well understood.³ In the A-DSB system the nitrogen branching centers⁶ can cause a disruption of π -electron conjugation of linear building blocks. In this case the optical excitation creates the electron-hole pairs localized on small segments.^{3,6-14} However, these localized electron-hole pairs can contribute either to *collective* optical excitations (excitons)³ or to the incoherent hopping^{6,7} due to inter-segment interactions. The goal of our research is to identify the mechanism of energy transfer and intermolecular interactions in these systems to find superior candidates for materials to be incorporated in to optical fibers for all optical applications.

2. Experimental Methods

The structure of the nitrogen-cored distyrylbenzene-stilbene (A-DSB) and the second generation dendrimer is shown in Fig.1. The linear absorption spectrum shows two prominent features with maxima at 410 nm and 320 nm. Synthesis and spectroscopic features of all the structures have been described elsewhere.^{6,14} Solutions in chloroform were used in this study. Femtosecond upconversion spectroscopy was employed to resolve temporally the polarized fluorescence. Optical arrangement for the upconversion experiments has been described previously.^{6-9,13-15} The laser had an average

pulse width of 100 fs tuned at 790-860 nm and a repetition rate of 82 MHz.

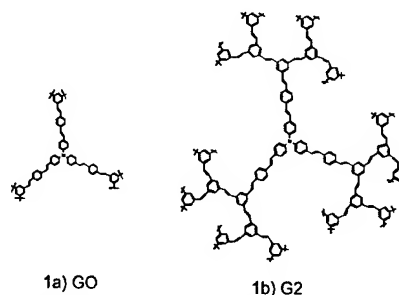


Figure 1: Molecular Structure of Organic DSB dendrimers used in the optical investigations.¹⁵

3. Results

The fluorescence isotropic decay of A-DSB on the picosecond time scale was found to be non-exponential and dependent on the emission wavelength (Fig. 2). The effect of fluorescence rise-time is clearly detected in the "red" regions of the fluorescence spectrum. This fluorescence time-behavior can be assigned either to intra-molecular interactions in the dendrimer (excimer formation, energy transfer) or to local relaxation processes in the chromophore (conformational changes, solvent rearrangement).¹⁵

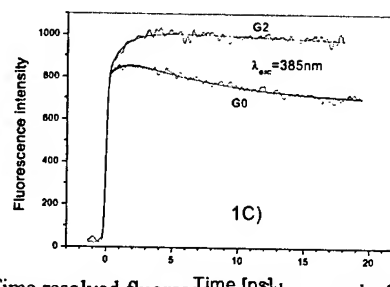


Figure 2: Time resolved fluorescence of the organic dendrimers (A-DSB) in solution at room temperature. The rise time in G2 gives the energy transfer time.¹⁵

The decay curves in Fig. 2 have been normalized by the peak absorption of the dendrimer core at 420nm. It is clearly seen from Fig. 2 that the fluorescence dynamics of G2 differ from those of G0 when fluorescence is excited at 385nm. Additional rise-time component in G2-dynamics can be attributed to the dendrons-to-core energy transfer process.¹⁵

To gain a further insight into energy transfer (energy migration) processes in A-DSB dendrimer molecules we investigated the fluorescence anisotropy dynamics in G0 and G2.^{6,15} The result for G2 is shown in Fig. 3. The Fluorescence anisotropy $r(t)$ was calculated from the decay curves for the intensities of fluorescence polarized parallel $I_{par}(t)$ and perpendicularly $I_{per}(t)$ to the polarization of the excitation light. It

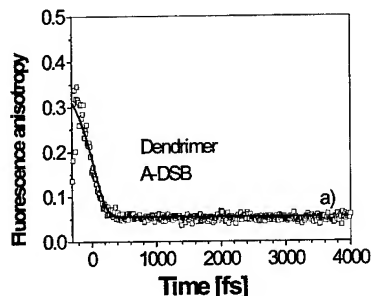


Figure 3: Anisotropy decay of A-DSB dendrimer at room temperature in solution.^{6,15}

is clearly seen in Fig.3 that the fluorescence anisotropy (FA) of A-DSB decays to a value close to zero in less than 200fs after excitation. The initial spike at about zero delay is comparable in duration with the time resolution of our system. Best fit of a difference signal with convolution with IRF gave the anisotropy decay time of $.57 \pm 7$ fs. The dendrimer core (G0) is a star-like molecule consisting of three DSB -segments bonded to a central nitrogen atom. The interaction between branches could lead either to the formation of coherent excitonic states¹⁰ or hopping-type¹¹ relaxation of excitations localized on one DSB-branch.

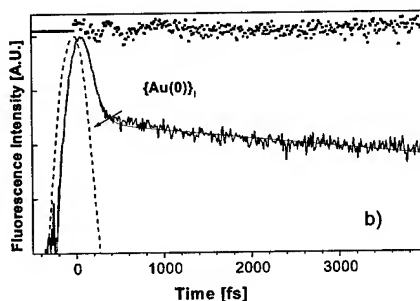


Figure 4: Dynamics of Dendrimer metal nanocomposites.⁹⁻¹¹

The dynamics of novel dendrimer nanocomposites systems have also been investigated. The PAMAM dendrimer with silver and gold transition metals have been investigated using time-resolve luminescence and the result for gold internal nanocomposite structure is shown in figure 4. The isotropic fluorescence decay was found to be much slower than the depolarization rate. The proposed mechanism of the emission decay is due to electron-electron and electron-surface scattering processes. We found that the emission decay was shorter than the relaxation associated with the phonon coupling process (~ 1 ps)⁹. Thus, electron-phonon

scattering is not likely to contribute the emission decay we observed for these novel metal dendrimer nano-composites.⁹⁻¹¹

With the novel optical properties of dendrimers as discussed above we have begun the fabrication of these structures in to novel fiber optical devices. The substantial increase in optical path length would suggest that the strong excitonic coupling could be extended over longer distances and consequently result in enhanced nonlinear optical as well as quantum optical effects. This type of architecture has also been used for the fabrication of electro-optical devices where impressive optical nonlinearities have been observed.

3.1 Conclusions

In conclusion organic dendrimers are strong candidates for new optical devices involving photonics and all optical communication applications. From the fast fluorescence depolarization results (within 200fs was found for A-DSB dendrimer) we have shown that the multi-chromophore architecture of these systems. These results demonstrate the ultra-fast transition dipole reorientation due to inter-segment interactions in dendrimer. The ultra-fast measurements with a novel dendrimer metal nanocomposite showed fast fluorescence decay related to the interaction of the PAMAM dendrimer and the metal centers.

4. Acknowledgments

This research was supported in part by the American Chemical Society Petroleum Research Fund, Air Force Office of Scientific Research, DARPA, National Science Foundation.

5. References

- [1] D.A. Tomalia, A.N. Naylor, W.A. Goddard III, *Angew.Chem.Int.Ed.Engl.* 29, 138 (1990).
- [2] J.M.J. Frechet, *Science* 263, 1710 (1994).
- [3] S. Tretiak, V. Chernyak, S. Mukamel, *J. Chem Phys.* 110, 8161 (1999).
- [4] Ispasoiu, R. G.; Balogh, L.; Varnavski, O. P.; Tomalia, D. A.; Goodson, T. J. *Am.Chem. Soc.* 2000, 122,11005-11006.
- [5] Ispasiou, R.G.; Goodson, T. *Opt. Commun.* 2000, 178, 371-376.
- [6] Varnavski, O.; Menkir, G.; Burn, P.; Goodson, T., *Appl. Phys. Letts.* 2000, 78, 1120-1122.
- [7] Varnavski, O.; Goodson T., *Chem. Phys. Letts.* 2000, 320, 688-696.
- [8] Varnavski, O.; Ispasoiu, R.G.; Narewal, M.; Fugaro, J.; Jin, Y.; Pass, H.; Goodson, T., *Macromolecules* 2000, 33, 4061-4068.
- [9] Goodson, T *Ultrafast Phenomena XII* 2000, 12, 613.
- [10] Screen, T.E.O.; Lawton, K.B.; Wilson, G.S.; Dolney, N.; Ispasoiu, R.; Goodson, T.; Martin, S.J.; Bradley, D.D.C.; Anderson, H.L., *J. Mater. Chem.* 2001, 11,312-320.
- [11] Varnavski, O.; Ispasoiu, R. G.; Balogh, L.; Tomalia, D.A.; Goodson, T. G., *J. Chem. Phys.* 2001, 114, 1962-1965.

- [12] Ispasoiu, R., G.; Lee, J.; Papadimitrakopoulos, F.; Goodson, T.; Chem. Phys. Letts. 2001, 340,7-12.
- [13] Varnavski, O., Tweig, R., Sukhomlinova, L., Bazan, G., Goodson, T., J. Am. Chem. Soc. 2002,124, 1736 -1743
- [14] Ispasoiu, R., and Goodson, T.; NanoLetters 2002, 2, 127-130.
- [15] Varnavski, O., Burn, O., Samual, I.D.F., Goodson, T., J. Chem. Phys., 2002, 116, 8893-8903.
- [16] Ranasinghe, M., Varnavski, O., Loise, J., Hartwig, J.F., Goodson, T. J. Am. Chem. Soc., Comm. 2002,124, 6520-6521 (2000).

Growth and Characterizations of Well-Aligned Carbon Nanotubes

Z. F. Ren^a, B. Kimball^b, Z. P. Huang^c, D. Z. Wang^a, Y. Tu^a, W. Z. Li^a, J. G. Wen^a, J. Y. Lao^a,
D. Steeves^b, M. Sennett^b, J. Rybczynski^d, M. Giersig^d, D. L. Carnahan^c, and K. Kempa^a

^aBoston College, Department of Physics, Chestnut Hill, MA 02467, +1-617-552-2832 . email: renzh@bc.edu

^bU.S. Army Soldier and Biological Chemical

Command, Natick Soldier Center, Materials Science Team, Natick, MA 01760

^cNanoLab, Inc., Brighton, MA 02135

^dHahn-Meitner-Institute, Berlin, Germany

Abstract

Aligned carbon nanotubes have been made by plasma enhanced chemical vapor deposition. Based on the technique used to prepare the catalyst dots, aligned arrays of carbon nanotubes could be made either without or with periodicity. In this paper, we report the development of carbon nanotubes arrays both without and with periodicity using cheap and scalable technologies. The periodic arrays show very interesting optical properties.

Keywords

Carbon nanotubes; alignment; plasma enhanced chemical vapor deposition; photonic crystal; honeycomb arrays.

1. Introduction

Large arrays of well-aligned carbon nanotubes are first made possible on substrates in 1998 by plasma enhanced chemical deposition (PECVD) [1,2] in which the diameter and length of each carbon nanotube are under control, but not the growth angle, location, nor the spacing between them. Soon after, the titled growth has been achieved by controlling the plasma direction using the same growth technique [3]. Almost at the same time, the control of location and spacing of the nanotubes have been accomplished using electron beam (e-beam) lithography to pattern the nickel dots first at where they are needed and then to grow the carbon nanotubes using the same growth technique [4,5]. However, e-beam is not possible to be commercialized for large scale. Therefore, alternative cheap and scalable technique is sought. Fortunately, the catalytic dots have been fabricated by electrochemistry and excellent aligned carbon nanotubes arrays have been grown [6]. Due to the nature of electrochemistry, the control on location of each nanotube is lacking. For applications that do not require the pre-determined location of each nanotube such as regular electron source, the arrays grown using the dots by electrochemistry is good enough. However, for applications that do require the pre-determined location of each nanotube such as microscopic probing tips, nanophotonics, etc., the control of location of each nanotube is crucial. Recently, we have been successful to grow large arrays of carbon nanotubes with diameter, length, location, and spacing under control by a simple and scalable technique, nanosphere lithography [7, 8]. Since the very first report on large arrays of well-aligned carbon nanotubes, numerous papers have used the same or a slightly modified technique to grow aligned carbon

nanotube arrays by either DC or microwave plasma CVD [9-19].

2. Experimental

The catalytic dots have been prepared by four techniques: magnetron sputtering, e-beam lithography, pulse current electrochemistry, and nanosphere lithography. The growth was accomplished by PECVD. The gases used are acetylene and ammonia that provides the carbon source and catalytic effect respectively. Scanning electron microscope (SEM) and transmission electron microscope (TEM) were used to characterize the arrays.

3. Results

3.1 Aligned growth of carbon nanotubes on sputtered Ni films

Fig. 1 shows the SEM images of the arrays of carbon nanotubes grown on glass substrates by plasma enhanced chemical vapor deposition [1]. They clearly show the excellent alignment with the glass substrate. In order to measure the alignment, diameter, and length of the carbon nanotubes, part of the sample was scraped as shown. For this particular sample, the tubes are about 20 μm long. For diameter estimate, higher magnification SEM exam was carried out.



Figure 1. SEM images of aligned carbon nanotubes. A) low magnification to show the alignment over large area, B) medium magnification to show the length of the nanotubes.

Fig. 2 shows SEM images of the aligned carbon nanotube arrays in higher magnifications. Clearly, nanotubes with different diameters have been produced. The diameters are controlled by the thickness of the catalytic Ni layer: the thinner the Ni, the smaller the nanotubes. For a thickness of 15 nm, nanotubes are about 50 nm in diameter as shown in Fig. 2A, whereas a 40 nm thick Ni yielded nanotubes of

about 250 nm in diameter as shown in Fig. 2B. Further reduction of Ni thickness has yielded nanotubes with diameters in the range of 10 – 25 nm, but without excellent alignment if the length is more than a few μm .



Figure 2. SEM images of carbon nanotube arrays grown with different thickness of Ni layers. A) 15 nm thick Ni, B) 40 nm thick Ni.

3.2 Aligned growth of carbon nanotubes on Ni dots made by e-beam lithography

For e-beam lithography, thin film nickel (Ni) patterns were fabricated on a p-type boron doped (100) silicon substrate. Ni layer of 15 nm was deposited by thermal evaporation. The patterned substrate was loaded into a PECVD system. The growth was carried out at the similar conditions as above.

Fig. 3 is a series of SEM micrographs showing the growth of single multiwall carbon nanotubes on each dot of an array of ~ 100 nm nickel dots. Figures 2a, 2c, 2e, and 2f were taken at an inclined angle, and Figures 2b and 2d are top views taken normal to the substrate. Figures 2a and 2b demonstrate selective growth of the carbon structures on the multiply repeated array patterns. The grown structures accurately reflect the spacing and periodicity of the lithographically patterned Ni dots. Figures 2c and 2d were taken at a higher magnification and show the repeated array pattern where the nanotubes are spaced either 2 μm apart (left) or 1 μm apart (right). Significant variation in the height (0.1 to 5 μm) of the grown bundles is observed, with no apparent relationship between height and spatial position. We note that even though the heights are different by more than a factor of 10, the base diameters are approximately uniform (~ 150 nm). Figure 2f shows the growth on a grid of Ni dots spaced 5 μm apart, indicating little dependence of growth on spacing (for spacings > 1 μm). The reason for such aligned growth of single carbon nanotubes in our system is due to the plasma, which is also used widely by others since our initial report [1].

Soon after, we were successful on obtaining patterns with more uniform length as shown in Fig. 4. Each nanotube has a sharp tip with radius of about 2-3 nm that may be very useful for high current field emission applications. Unfortunately, the nice patterns grown using e-beam lithography is only good for concept proving. In the next, we present a cheap way for fabricating arrays with spacing, but not location, controlled: electrochemistry.

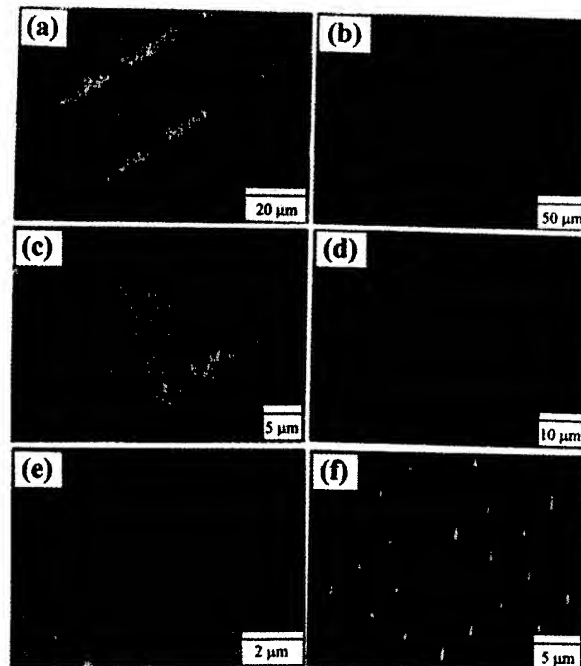


Figure 3. A series of SEM micrographs from different viewing angles showing growth of carbon nanotube obelisks on an array of submicron nickel dots. (a) An inclined view of a repeated array pattern. (b) A top (normal) view of a repeated array pattern. (c) An inclined view of one array pattern. (d) A top (normal) view of one array pattern. The initial Ni dots (and subsequently the grown carbon structures) are spaced either 2 μm apart (left) or 1 μm apart (right). (e) A magnified view along the edge of one pattern. A sharp, tapered tip is evident. (f) An inclined view of carbon obelisks grown on nickel dots separated by 5 μm .

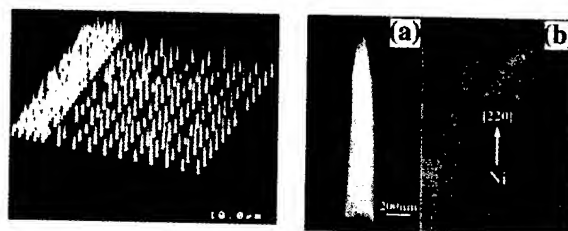


Figure 4. SEM and TEM images of carbon nanotube arrays.

3.3. Growth of aligned carbon nanotubes with spacing controlled by electrochemistry

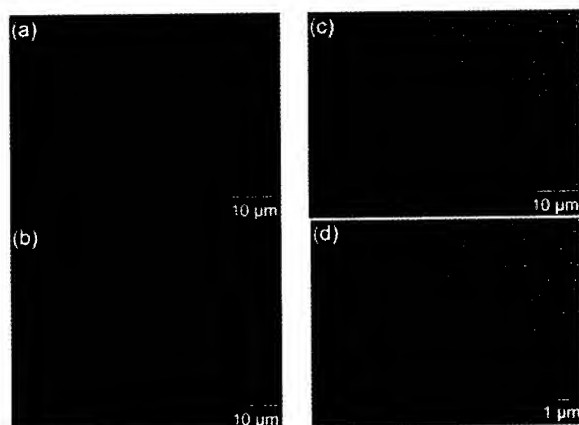


Figure 5. SEM images of Ni nanoparticles deposited electrochemically with site density of (a) $7.5 \times 10^5 \text{ cm}^{-2}$, (b) $2 \times 10^6 \text{ cm}^{-2}$, (c) $2 \times 10^7 \text{ cm}^{-2}$, and (d) $3 \times 10^8 \text{ cm}^{-2}$.

Fig. 5 shows the different nucleation site densities of the Ni nanoparticles from about $7.5 \times 10^5 \text{ cm}^{-2}$ to $3 \times 10^8 \text{ cm}^{-2}$ by electrochemistry. The white dots shown in the pictures were the Ni nanoparticles that had been confirmed by Energy Dispersive X-ray Spectroscopy (EDX). Most particles had diameter from 100 nm to 200 nm with some nanoparticles smaller than 50 nm. The Ni nanoparticles were randomly located on the surface of the substrate.

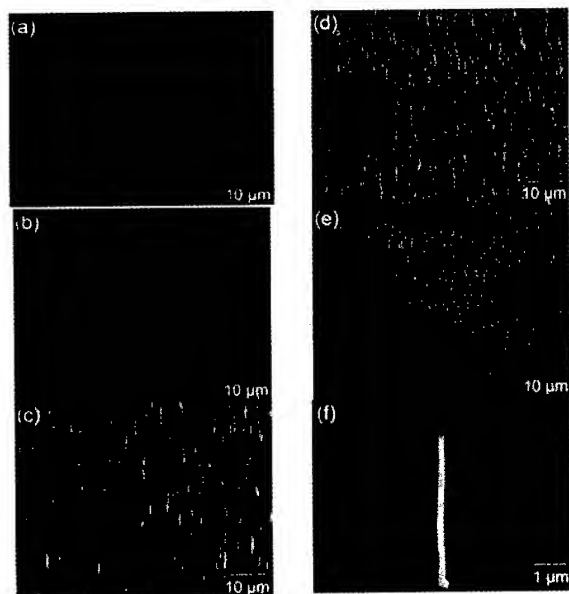


Figure 6. SEM images of aligned CNTs with site density of (a) $7.5 \times 10^5 \text{ cm}^{-2}$, (b) $2 \times 10^6 \text{ cm}^{-2}$, (c) $6 \times 10^6 \text{ cm}^{-2}$, (d) $2 \times 10^7 \text{ cm}^{-2}$, (e) $3 \times 10^8 \text{ cm}^{-2}$, and (f) a single standing CNT.

Fig. 6 (a) to (e) shows the different site densities of CNTs grown from the electrodeposited Ni nanoparticles. The CNTs site densities of the samples were about 7.5×10^5 , 2.0×10^6 , 6.0×10^6 , 2.0×10^7 , and $3 \times 10^8 \text{ cm}^{-2}$, respectively. Fig. 6 (f) provides a closer look at one of the well-aligned CNTs.

3.4. Growth of aligned carbon nanotube arrays with periodicity

Even though electrochemistry provided excellent control on site density, but could not produce Ni dots at the pre-determined locations. Fortunately, we have developed another technique, nanosphere lithography, to fulfill the goal. Fig. 7 shows the SEM images of the Ni dots made by nanolithography. Fig. 8 shows the nanotubes made from the dots shown in Fig. 7. Surprisingly, every sample is colorful (shown in Fig. 9) instead of being black as those without periodicity. The bright reflection of red, green, and blue light was recorded at three different angles from a white incident light, which demonstrates that such an array can be used as an optical filter.

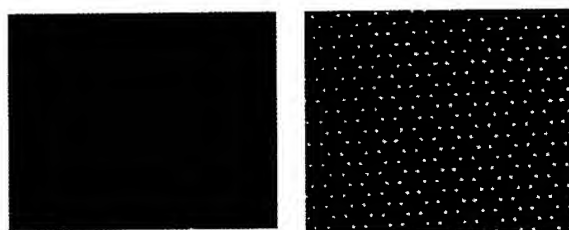


Figure 7. SEM images of Ni dots made by nanolithography in low (left) and medium (right) magnifications.

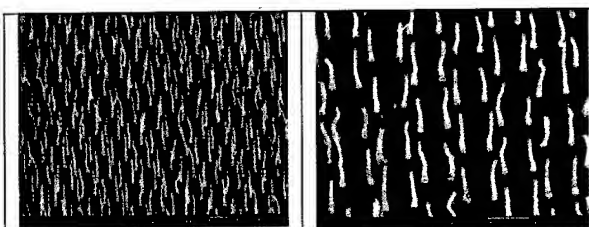


Figure 8. SEM images of low (left) and medium (right) magnifications of carbon nanotube arrays.

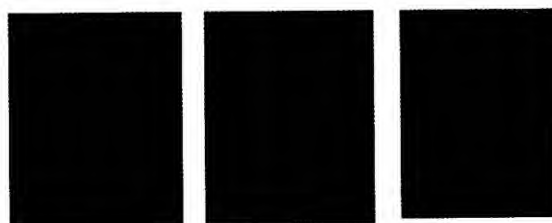


Figure 9. Bright diffraction colors of red, blue, and green.

In addition to these straightforward diffraction effects, our arrays of nanotubes can act also as 2D photonic band gap crystals. It has been shown [20], that periodic arrays of structures having dielectric constants (ϵ_a) different from the environment (ϵ_b), act on propagating photons not only by enforcing the Bragg scattering as discussed above, but also, in a complete analogy to the electron propagation in atomic crystals, lead to the opening of energy (frequency) gaps at the Bragg reflection points, i.e. at the Brillouin zone boundaries. If such gaps occur at all propagation directions of the photon (or electron), an absolute gap exists in the photonic spectrum, which in the case of the photonic crystal leads to a total reflection of light in this frequency band. It has been shown [21, 22] that a honeycomb array of rods, with large dielectric constant, embedded in a material with low dielectric constant, produces photonic band structure with absolute gaps at low fillings. This was later confirmed by an experiment in the microwave frequency range [23] in a perfect agreement with the theory. It was also shown, that a simple size scaling ($\omega \sim 1/a$) holds for the gaps, and therefore one can simply rescale the results of these papers to systems with different sizes, such as honeycomb arrays of nanotubes.

Even though our nanotubes have dielectric constant that is different from that of the nanorods considered in Refs. 21-23, we can still directly employ results of these references to our arrays of nanotubes, after proper dielectric constants scaling. First we note that in the theory of Refs. 22 and 23, all the relative sizes of the gaps $\delta_i = |\Delta\omega_i/\omega_i|$ are approximately proportional to the Fourier components of the perturbation (dielectric constant inhomogeneity), which in turn, for a system with $\epsilon_a > \epsilon_b$, are proportional to $p = 1/\epsilon_b - 1/\epsilon_a$. Therefore we find that $\delta_i \sim p$. Since this is the only dependency on ϵ_a and ϵ_b in the gap equations, the results for various gaps obtained in Refs. 21 and 22 can be simply scaled (by using p) to obtain corresponding results for systems with different dielectric constants. Using this, we immediately show that the honeycomb array of our nanotubes obtained by using nanospheres of diameter $0.5 \mu\text{m}$, should act as a 2D photonic band gap crystal with the gap at the radiation wavelength $\lambda \approx 0.5 \mu\text{m}$. Since our metallic nanotubes have $\epsilon_a < 0$ in the visible frequency range (their plasma frequency is at 6.5 eV), this yields $p > 1$, and therefore the gap size is expected to be $\delta_2 > 15\%$. Note, that since the dielectric constant of nanotubes has also an imaginary part (losses), the gap does not imply a perfect reflection. The experimental effort to demonstrate the photonic band gap in our nanotube arrays is in progress.

We note, that the nanotubes can be coated for better control of the photonic crystal parameters. They can also be used as structural templates, to obtain nonmetallic photonic arrays, including nonmetallic 2D band gap crystals.

4. Conclusions

Well-aligned carbon nanotube arrays without periodicity have been achieved on either Ni films made by magnetron sputtering or Ni dots made by electrochemical deposition, whereas the arrays with periodicity have been realized on either Ni dots made by e-beam lithography or on Ni dots

made by nanosphere lithography. Obviously, the electrochemical deposition is much better than magnetron sputtering, and the nanosphere lithography is much better than e-beam lithography in the sense of both the cost and scalability. The large periodic arrays not only reflect and diffract light to show colors but also potentially is excellent photonic band gap crystals.

5. Acknowledgments

This work is partially funded by US. Army Natick Soldier Systems Center under grants DAAD16-02-C-0037 and DAAD16-00-C-9227, Army Research Office under grant DAAD19-00-1-0001, DOE under grant DE-FG02-00ER45805, and NSF under grants DMR-9996289 and ECS-0103012.

6. References

- [1] Ren, Z. F., Huang, Z. P., Xu, J. W., Wang, J. H., Bush, P., Siegal, M. P., and Provencio, P. N., "Synthesis of Large Arrays of Well-Aligned Carbon Nanotubes on Glass", *Science* **282**, 1105 – 1107 (1998).
- [2] Huang, Z. P., Xu, J. W., Ren, Z. F., Wang, J. H., Siegal, M. P., and Provencio, P. N., "Growth of Large-Scale Well-Aligned Carbon Nanotubes by Plasma Enhanced Hot Filament Chemical Vapor Deposition", *Appl. Phys. Lett.* **73**, 3845–3847 (1998).
- [3] Ren, Z. F., Huang, Z. P., Xu, J. W., Wang, D. Z., Wang, J. H., Calvet, L., Chen, J., Klemic, J. F., and Reed, M. A., "Large Arrays of Well-Aligned Carbon Nanotubes", *AIP Conference Proc.* **486** (Electronic Properties of Novel Materials—Science and Technology of Molecular Nanostructures), 263 – 267 (1999).
- [4] Ren, Z. F., Huang, Z. P., Xu, J. W., Wang, D. Z., Wen, J. G., Wang, J. H., Calvet, L., Chen, J., Klemic, J. F., and Reed, M. A., "Growth of a Single Freestanding Multiwall Carbon Nanotube on Each Nanonickel Dot", *Appl. Phys. Lett.* **75**, 1086 – 1088 (1999).
- [5] Wen, J. G., Huang, Z. P., Wang, D. Z., Chen, J. H., Yang, S. X., Ren, Z. F., Wang, J. H., Calvet, L. E., Chen, J., Klemic, J. F., Reed, M. A., "Growth and characterization of aligned carbon nanotubes from patterned nickel nanodots and uniform thin films", *Journal of Materials Research* **16**, 3246–3253 (2001).
- [6] Tu, Y., Huang, Z. P., Wang, D. Z., Wen, J. G., Ren, Z. F., "Growth of Aligned Carbon Nanotubes with Controlled Site Density", *Appl. Phys. Lett.* **80**, 4018 – 4020 (2002).
- [7] Z. P. Huang, J. Rybczynski, M. Giersig, K. Kempa, D. Z. Wang, D. L. Carnahan, J. G. Wen, M. Sennett, and Z. F. Ren, "Growth of Large Array Carbon Nanotubes with Periodicity", *Appl. Phys. Lett.* (submitted).
- [8] K. Kempa, B. Kimball, J. Rybczynski, Z. P. Huang, P. F. Wu, D. Steeves, M. Sennett, M. Giersig, D. V. G. L. N. Rao, D. L. Carnahan, D. Z. Wang, J. Y. Lao, W. Z. Li, and Z. F. Ren, "Photonic crystals based on periodic arrays of aligned carbon nanotubes", *Science* (submitted).

- [9] Bower, C., Zhu, W., Jin, S. H., Zhou, O., "Plasma-induced alignment of carbon nanotubes", *Appl. Phys. Lett.* **77** (6): 830-832 (2000).
- [10] Cui H, Zhou O, Stoner BR, "Deposition of aligned bamboo-like carbon nanotubes via microwave plasma enhanced chemical vapor deposition", *J. of Appl. Phys.* **88** (10): 6072-6074 (2000).
- [11] Baylor LR, Merkulov VI, Ellis ED, Guillorn MA, Lowndes DH, Melechko AV, Simpson ML, Whealton, JH, "Field emission from isolated individual vertically aligned carbon nanocones", *J. of Appl. Phys.* **91** (7): 4602-4606 (2002).
- [12] Lee CJ, Lyu SC, Kim HW, Park CY, Yang CW, "Large-scale production of aligned carbon nanotubes by the vapor phase growth method", *Chem. Phys. Lett.* **359** (1-2): 109-114 (2002).
- [13] Merkulov VI, Melechko AV, Guillorn MA, Simpson ML, Lowndes DH, Whealton JH, Raridon RJ, "Controlled alignment of carbon nanofibers in a large-scale synthesis process", *Appl. Phys. Lett.* **80** (25): 4816-4818 (2002).
- [14] Wang SG, Wang JH, Qin Y, "Synthesis of carbon nanotubes by microwave plasma chemical vapor deposition at low temperature", *Acta Chimica Sinica* **60** (5): 957-960 (2002).
- [15] Kim J, No K, "Growth of carbon nanotubes on the glass substrate for flat panel display applications, *International J. of Modern Phys. B* **16** (6-7): 979-982 (2002).
- [16] Zhang WD, Wen Y, Tjiu WC, Xu GQ, Gan LM, "Growth of vertically aligned carbon-nanotube array on large area of quartz plates by chemical vapor deposition", *Appl. Phys. A-Mater. Sci. & Processing* **74** (3): 419-422 (2002).
- [17] Huczko A, "Synthesis of aligned carbon nanotubes", *Appl. Phys. A-Mater. Sci. & Processing* **74** (5): 617-638 (2002).
- [18] Teo KBK, Chhowalla M, Amaratunga GAJ, Milne WI, Pirio G, Legagneux P, Wyczisk F, Pribat D, Hasko DG, "Field emission from dense, sparse, and patterned arrays of carbon nanofibers", *Appl. Phys. Lett.* **80** (11): 2011-2013 (2002).
- [19] Chhowalla M, Teo KBK, Ducati C, Rupasinghe NL, Amaratunga GAJ, Ferrari AC, Roy D, Robertson J, Milne WI, "Growth process conditions of vertically aligned carbon nanotubes using plasma enhanced chemical vapor deposition, *J. of Appl. Phys.* **90** (10): 5308-5317 (2001).
- [20] E. Yablonovitch, "Inhibited Spontaneous Emission in Solid-State Physics and Electronics", *Phys. Rev. Lett.* **58**, 2059 (1987).
- [21] D. Cassagne, C. Jouanin, and D. Bertho, "Photonic band gaps in a two-dimensional graphite structure", *Phys. Rev. B* **52**, R2217 (1995).
- [22] D. Cassagne, C. Jouanin, and D. Bertho, "Hexagonal photonic-band-gap structures", *Phys. Rev. B* **53**, 7134-7142 (1996).
- [23] F. Gadot, A. Chelnokov, A. D. Lustrac, P. Crozat, J. M. Lourtioz, D. Cassagne, and C. Jouanin, "Experimental demonstration of complete band gap in graphite structure", *Appl. Phys. Lett.* **71**, 1780 (1997).

Have You Considered Atomic Layer Deposition?

Raj Solanki

Department of Electrical and Computer Engineering,
Oregon Graduate Institute
Beaverton, OR

+1-503 748 1168 solanki@ece.ogi.edu

Abstract

Atomic layer deposition (ALD) is a process that allows deposition of thin films in a highly controllable manner. It is ideally suited for producing conformal films with single atomic layer thickness control. This process was originally developed for fabrication of flat panel displays, however it currently used for a wide range of applications ranging from microelectronic devices to optical coatings. The basic ALD process is first described below and then some of the film properties produced by this technique are presented.

Keywords

ALD; thin films; optical coatings; nanowires.

1. Introduction

Atomic layer deposition is a monolayer stepwise growth process that exploits the binding energy difference between chemisorption and physical adsorption [1]. In this unique technique, self-limiting growth characteristic is due to the strong interaction between the initial layer of atoms or molecules of a reactive species and the surface leading to chemisorption. All subsequent layers will adhere to the surface less strongly (physisorbed). For these surface reactions, the temperature of the substrate is an important controlling parameter. If the substrate surface is heated sufficiently, then one can achieve a condition such that only the chemisorbed layer remains attached to the surface and the rest of the physisorbed layers can be flushed out with an inert gas. Hence the growth proceeds by exposing the substrate surface alternately to the precursors and following each reaction, the excess (physisorbed) species are removed with a nitrogen pulse. Therefore, unlike CVD, in ALD the precursors are introduced to the substrates separately. The reactant source pulses are separated by pulses of an inert gas. Under properly adjusted experimental conditions all the surface reactions are saturated, making the growth process self controlled. As a result, ALD is capable of depositing conformal films whose thickness can be determined accurately by the number of deposition cycles. The highly conformal and uniform films produced has led to application off this technique for coating porous alumina membranes, porous silicon, and powders of silicon and alumina [2,3]. In addition, the separate dosing of precursors eliminates detrimental gas-phase reactions. Also, in practice it has been observed that the temperatures needed for depositing films by ALD are lower than those required by other methods due to the growth process driven by surface chemistry.

The source for the reactant atoms or molecules in this process can be solid, liquid (with relatively high vapor pressure) or gas phase. The film grows stepwise, i.e., a single monolayer per pulse,

provided that at least one complete monolayer coverage of an element or a chemical compound is formed before the next pulse is allowed to react with the surface. Any excess incident atoms or molecules on the film will not stick if the substrate temperature

and the chemistry are properly chosen. Therefore, with proper optimization of the deposition parameters a self-limited, saturated monolayer coverage is obtained per cycle. The self-limited growth distinguishes ALD from other vapor phase deposition techniques, namely MBE and CVD. For this reason the name digital epitaxy has also been used to describe the monolayer per cycle growth.

The film thickness is expressed in terms of the number of cycles employed. Each cycle comprises a pulse of each source material. The source pulse is turned off for a sufficiently long time (a fraction of a second to several seconds) to allow the surface to approach thermodynamic equilibrium at the end of each reaction. This step entirely eliminates fluid dynamics (e.g., gas flow rates) from the growth process and allows uniform film growth over large substrates. To illustrate the pulsing sequence, one cycle for deposition of aluminum oxide using trimethyl aluminum (TMA) and water is shown in Fig. 1. The nitrogen pulse is the purge gas.

The layer-at-a-time deposition process ensures dense and pinhole-free films with exceptional thickness uniformity, even over irregularly shaped surfaces. The deposition of thin film covering all exposed parts of any three-dimensional structure is known as "conformal film growth." In addition, attributes related to the high-performance process characteristics such as accurate and simple film thickness control, sharp interfaces, uniformity over large areas, good reproducibility, multiple layer processing capability in a single run, and high film qualities can be achieved at relatively low growth temperatures.

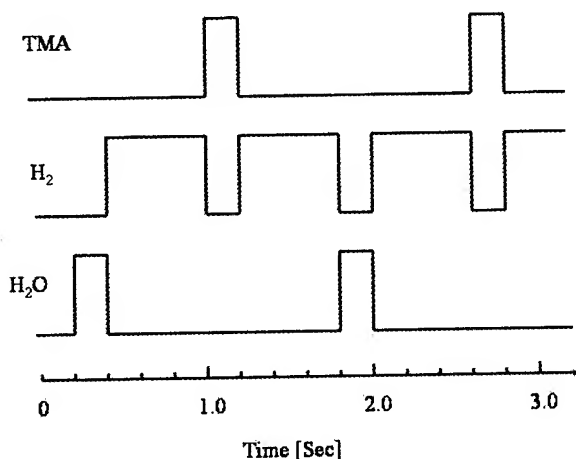


Figure 1. ALD pulse sequence for deposition of aluminum oxide

2. Applications of ALD

2.1 Flat panel displays

ALD was first developed in Finland by Suntola's group to fabricate thin film electroluminescent (TFEL) flat panel displays [4]. These displays have superior performance in terms of compact size, wide viewing angle, good image quality with high contrast and resolution, solid state ruggedness, and fast response time over a wide temperature range in comparison to the widely used liquid crystal based flat panel displays. Sizes ranging from giant screens to miniaturized active matrix head mounted EL displays are produced for both commercial and high performance military applications [5]. Full color displays are commercially available.

2.2 Microelectronic devices

2.2.1 Dielectric films

Exponential increase in the performance of ICs for multi-GHz speed devices is based on the down-scaling of devices and interconnects along with new chip architectures and design methods. Typical feature size requirements for a 16 Gb DRAM with a 100 nm poly-Si gate call for a 6 nm thick gate oxide and a 15 nm thick doped source/drain junction [6]. Replacement for gate SiO_2 has been under investigation in recent years as this material is fast approaching its thickness limit of approximately 2.5 nm (about 10 atomic layers) for sub 0.1 μm devices at which a large leakage current (1 A/cm^2) flows across the dielectric exhibiting direct tunneling effects.

High dielectric constant materials like $(\text{BaSr})\text{TiO}_3$, Ta_2O_5 , HfO_2 , ZrO_2 , and their nano-laminate (superlattice) structures have been investigated through the ALD approach. [7] The ALD process has produced films with large capacitances across the gate and at the same time reduced the tunneling or leakage current by at least six orders of magnitude. Electrical properties of three kinds of nanolaminates and their SiO_2 equivalent thickness based on dielectric constants are summarized in table 1.

Table 1 Electrical properties of ALD nanolaminates for gate oxide replacement [7]

Nanolaminate Matl/ ALD Growth Cycles	Equivalent Thickness	Dielectric Constant(k)	Leakage Current Amperes/ cm^2
$\text{Ta}_2\text{O}_5\text{-HfO}_2$ 2x(16+16) cycles	3.25 nm	12	2.0×10^{-7}
$\text{Ta}_2\text{O}_5\text{-ZrO}_2$ 2x(16+16) cycles	3.0 nm	13	4.2×10^{-7}
$\text{ZrO}_2\text{-HfO}_2$ 2x(12+13) cycles	3.2 nm	14	2.6×10^{-8}

The accuracy of controlled film growth on the atomic level using ALD approach allows optimization of the bulk and interfaces separately in nanoscale dimensions with perfect step coverage for ULSI fabrication. These nanolaminates are grown at 300 C in a single pump down run without any hydrogen incorporation in contrast to conventional SiO_2 gate oxides that require post-deposition heat treatments. An additional advantage of ALD processed high permittivity dielectric oxide films is that they are very effective diffusion barriers against gate electrode dopants such as boron, phosphorus or arsenic. The leakage current and breakdown voltages of the nanolaminates listed in table 1 are shown in Figures 2 and 3.

2.2.2 Metallic films

ALD has also been utilized to produce metallic films for microelectronic device interconnect applications. Interconnect technology has undergone a radical shift to copper metal with low dielectric insulator materials, which is expected to reduce signal delay time and simultaneously boost device speed by 4 times [8]. One of the biggest processing challenges is in the metal deposition step, as the copper must fill pre-defined sub-100 nm trenches and / or vias in the dielectric. This has been demonstrated, as shown in Figure 4, where a 20 nm thick copper film has been conformably deposited over a surface with high aspect ratio trenches [9].

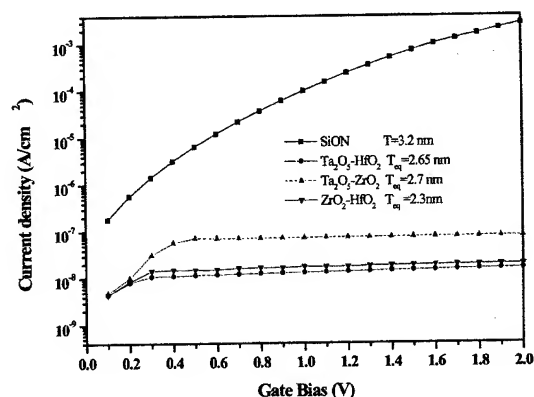


Figure 2. Comparison of leakage currents of SiON and three ALD grown nanolaminates

2.2.3 Optical coatings and interference filters

Planar Systems has been actively involved in developing ALD for thin film interference filters for wavelength division multiplexing and anti-reflective coatings. The as-deposited films are stress-free, and highly stoichiometric. Structurally, the films are amorphous, pin-hole free and have near theoretical film density. The refractive index across 8 inch wafer is accurate to fifth decimal point.

2.2.4 Nanowires

We have recently employed ALD to grow nanowires composed of ZnSe/CdSe superlattices. Growth of the nanowires was initiated using gold nanoparticles and vapor- liquid-solid mechanism.

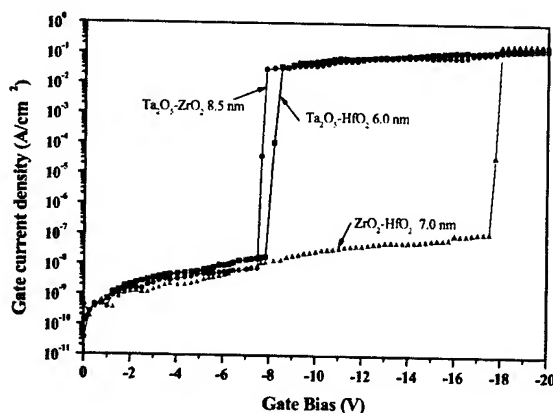


Figure 3. Electrical breakdown voltages of the three nanolaminates

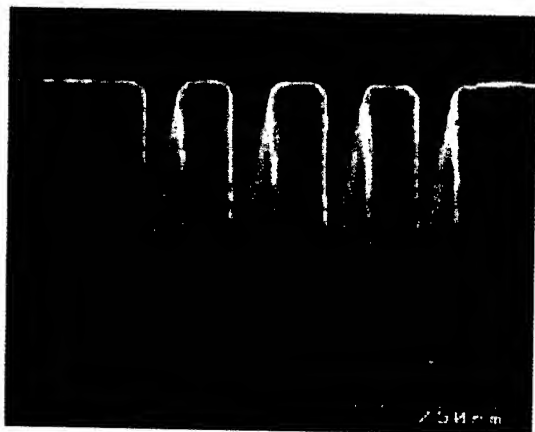


Figure 4. Conformal deposition of 20 nm thick copper film.

High resolution transmission electron microscopy analysis shows that these structures are single crystals and the phase of alternating layers of ZnSe and CdSe is face center cubic. A scanning electron micrograph of such a structure is shown below.

3. Conclusion

Atomic layer deposition is a highly versatile technique that can be used for deposition of a wide range of thin films with one atomic layer precision. This technique is relatively new and its full potential is yet to be realized, specially with regards to coating fiber optics.

4. Acknowledgments

The author would like to acknowledge the following PhD students who have worked on different aspects of ALD: W. Kong, S. Ahmed, J. Ferguson, H. Zhang, and W. He. Special thanks also go out to the following colleagues who provided valuable insight over the years: Drs B. Pathangey (Intel), R. Tuenge (Planar), S-S. Sun (Planar), Y. Ono (Sharp) and J. Conley (Sharp).

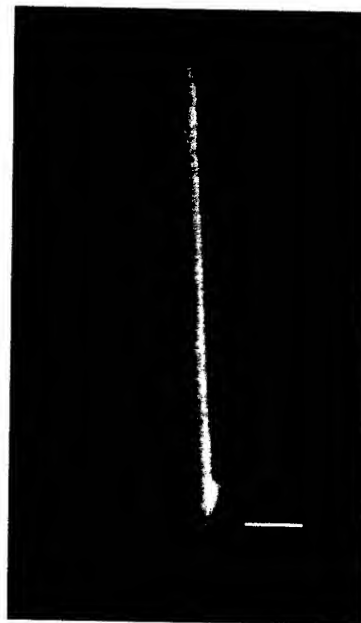


Figure 5. SEM view of a ZnSe/CdSe superlattice nanowire. The scale bar is 5 nm.

5. References

1. T. Suntola, "Atomic Layer Epitaxy", *Material Sci. Rep.* **4**, 261 (1989).
2. C. Dusco, N. Nguyen, Z. Horvath, I. Barsony, et al., "Deposition of Tin Oxide into Porous Silicon by Atomic layer Epitaxy", *J. Electrochem. Soc.* **143**, 683 (1996).
3. E. L. Lakomaa, "Atomic Layer Epitaxy (ALE) on Porous Substrates", *Appl. Surf. Sci.* **75**, 185 (1994).

4. T. Suntola and M. Antson, *U.S. Patent* 4058430 (1977).
5. C. N. King, "Electroluminescent Displays", *J. Vac. Sci. and Technol. A*, 14, 1729 (1996)
6. R. Djule, "Meeting the Ultra-Shallow Junction Challenge," *Semiconductor International* 4, 50 (1997).
7. H. Zhang, and R. Solanki, "Atomic Layer Deposition of High Dielectric Constant Nanolaminates" *J. Electrochem. Soc.* 148, 63 (2001).
8. K. Lee, "On-Chip Interconnects-Gigahertz and Beyond," *Solid State Technology* 2, 85 (1998).
9. B. Pathangey and R. Solanki, "Atomic Layer Deposition of copper seed layers", *Solid-State and Electrochem. Lett.* 3, 479 (2000).

6. Biography

Raj Solanki is Professor in the Department of Electrical and Computer Engineering at the Oregon Graduate Institute, where he started one of the first groups in US on ALD. His research includes electronic and optical devices.

Mailing address:
Department of Electrical and Computer Engineering
Oregon Graduate Institute
20,000 NW Walker Road
Beaverton, OR 97006

The Role of Nano-Structured Materials Enabling Miniaturization of Photomultipliers

Charles Beetz, Robert Boerstler, Robert Wright, James Agresta and David Winn

NanoSciences Corporation

Oxford, CT 06478

+1-203-267-4440 · cbeetz@nanosciences.com

Abstract

The next generation of photomultiplier receivers will be miniaturized for direct surface mount applications. Vacuum photomultiplier technology remains one of the most sensitive techniques for single photon detection with fast response time. In this paper we discuss the major problems confronting and review some of the approaches to miniaturization of photomultiplier technology for compatibility with direct surface mount technology to enable compact, very fast detection of low light level signals. Miniaturization and surface mount enables photomultipliers to become more compatible with fiber coupling enabling well-defined short circuit runs to signal processing circuitry. Miniaturization to a total dynode length ~ 0.1 or 0.01 cm while maintaining acceptable device performance is a challenge that is being met through the use of nano-structured materials in combination with micromachining technologies. The dramatic shortening of the electron trajectories enables response times on the order of 10 ps. Examples of the use of nano-structured materials for a new class of photocathode and active dynode materials are discussed.

Keywords

Photomultiplier tube, photocathode, dynode, nanowires, surface mount.

1. Introduction

A new approach for ultra high speed, large-area photodetectors, with wide dynamic range is presented. This paper explores the concept of applying vacuum microelectronics, vacuum photocathode and semiconductor micromachining technologies to obtain a monolithic, compact vacuum-microelectronic photodetector. The problems associated with this extreme miniaturization and solutions offered through employing nano-structured materials are discussed. The detector is a hybrid device that takes advantage of the robust gain mechanism of a dynode chain in a photomultiplier tube (PMT), the spatially constrained electron transit trajectories of a microchannel plate (MCP), the extreme compactness afforded by micromachining, and the wide range of detectable wavelengths and very low noise offered by vacuum photocathodes.

The vacuum-gap decouples the photon-electron conversion mechanism from the active output as in vacuum photodiodes (VPD), to obtain a very high-speed photodetector (>200 GHz cutoff) over a large area with the potential of spatial imaging capability. Several different detector formats are discussed: (1) a

2-D array of close packed micromachined multi-staged microdynodes arrays (both reflection and transmission), (2) miniature continuous dynode amplifiers, and (3) miniature Si-MCP amplifiers, inserted between a vacuum photocathode and an anode. The high frequency response of these miniaturized detectors is a direct result of the $>10\times$ decreased electron transit time of the integrated microdynode as contrasted to existing MCP PMT's¹ or compact PMT's².

Several approaches have been previously discussed for miniaturization of photomultiplier detectors through the use of micromachining techniques. Ehrfeld et al.³ discuss the use of LIGA processing to form miniature photolithographically formed discrete dynode multipliers. These devices are primarily lateral devices, that is the photocathode, dynode chain and anode all lie in the plane of the supporting substrate. Both single anode and multiple anode photomultipliers were proposed. This development introduced the concept of multiplexed manufacturing inherent in semiconductor device manufacturing methods. Later, Comby and co-workers⁴ proposed a miniature monolithic ceramic multiplier approach in which a dynode stack is build up from stacks of ceramic layers with varying size holes that are aligned over one another as illustrated in Figure 1. Comby et al. also included integral metal ceramic feed-throughs eliminating the traditional metal pins for electrical contacts. The importance of the Comby device was several fold, elimination of space consuming pins and sockets, elimination of the vacuum envelope and use of a low cost highly automated fabrication methodology. The devices produced were on the order of 20 mm x 20 mm x 10 mm with 16 pixels, each 0.6 mm in diameter. The photocathode was produced on the window and then transferred and sealed to the monolithic dynode stack in UHV conditions.

Over the past 10 years, very little progress has been made in reducing the size of the photomultiplier much beyond the monolithic ceramic multiplier. The smallest commercially available photomultipliers are the Hamamatsu metal package tubes. These devices are based on discrete metal dynodes arranged in a metal can package either square or round (TO-8) with pins that fit into a mating socket. A schematic diagram of a metal can miniature photomultiplier is shown in Figure 2. A key feature of this miniature photomultiplier is the method for mounting and locating the metal dynodes relative to each other. A special precision ball and socket locating mechanism at the corner of each dynode plate is responsible for determining both the lateral registration and the proper vertical separation between

dynodes. This family of photomultipliers is continuing to expand into new applications especially with the separately addressable anodes permitting spatially resolved imaging.

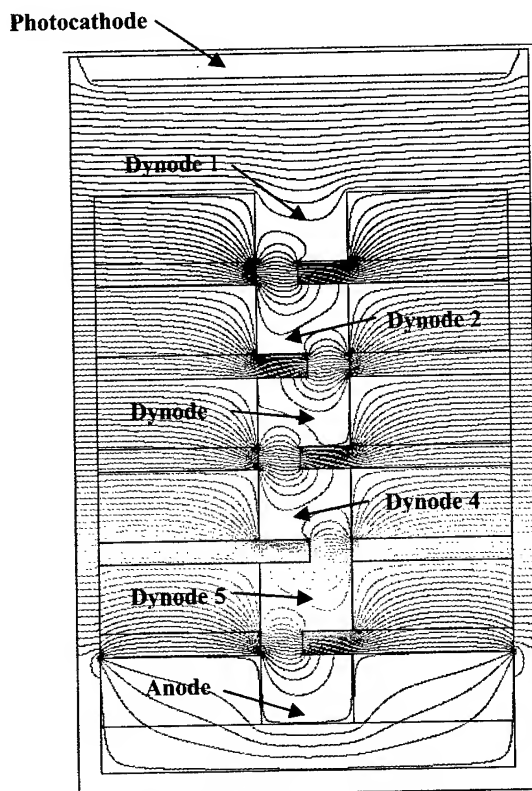


Figure 1. Equipotential plot for a Comby type monolithic ceramic photomultiplier.

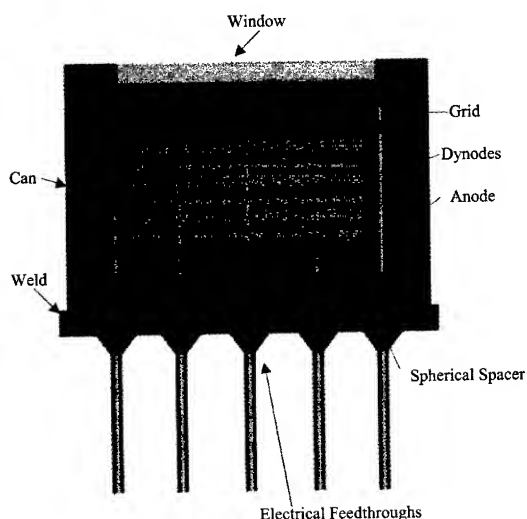


Figure 2. Schematic diagram of a miniature discrete dynode photomultiplier tube from Hamamatsu. Typical dimensions are 15 mm diameter by 10 mm in height, inter-dynode spacing ~ 650 micrometers.

2. Issues in Miniaturization of Electron Multipliers

There are several levels of problems to contend with when reducing the total electron travel distance in a photomultiplier to dimensions on the order of less than 1 mm. The first level is the geometrical shape of the dynode surface, the distance between dynodes, and the lateral location relative to the dynodes above and below and the tolerances required for maintaining efficient electron collection and secondary generation. The next level of problem focuses on issues of alignment of the dynodes and development of mechanisms for maintaining the alignment during mounting of the dynodes. Yet another level of problem focuses on elimination of potential sources of noise.

As the distance between dynodes decreases, the electric fields become larger. This is a result of the fact that the energy required for production of a secondary electron on the dynode surface is independent of the distance between dynodes and is principally controlled by the energy of the incident electron. In order to generate secondary electrons on the next dynode surface, the incident electron must be accelerated to a sufficient energy. Typical inter-stage voltages are on the order of 100 V, thus as the distance between dynodes decreases, the electric fields increase making control of electron trajectories more challenging. This requires precision alignment of the dynodes relative to one another. Small lateral misalignments between adjacent dynodes and loss of planar parallelism can severely impact secondary electron generation and multiplier electron collection efficiency. Another problem in miniaturization of electron multipliers is interstage capacitance, which tends to increase with smaller spacing between the dynode plates. This reduces the high frequency response capabilities of the tube. The following sections discuss alternative approaches⁵ for further miniaturization of photomultiplier detectors, and represent a progress report on ongoing technological developments in this area.

3. Nanostructured High Gain Dynodes and Photocathodes

Traditionally electron multiplier dynodes are produced from a variety of materials, examples are CuBe or stainless steel metal that has been either specially activated or coated with a high secondary electron yield material. These dynodes typically have secondary electron yields in the range 2 to 6 and therefore require 8 to 10 stages of multiplication in order to reach gains of 10^5 to 10^6 . The large number of stages could be significantly reduced if materials having larger secondary electron yields could be produced. Reducing the number of stages has several benefits such as faster response time; smaller transit time spread, and improved pulse height distribution.

Recently, it was discovered that dynode surfaces produced by deposition of a thin layer of MgO onto an array of vertically aligned carbon nanotubes (MgO/CNT) resulted in extraordinary

secondary electron yields.⁶ These surfaces exhibited secondary electron yields $> 10,000$. Secondary electron yields of this magnitude on dynode surfaces makes it possible to significantly reduce the number of dynodes in a photomultiplier. Depending on the application, either a single or a two-stage dynode is all that is necessary. Reduction of the number of dynodes from either 8 or 10 to 1 or 2 is a dramatic change. This significantly shortens the electron trajectory improving the tube response time enabling picosecond and possibly subpicosecond response times. The reduction of the number of dynodes also simplifies tube design and assembly.

Another material system that is under consideration as a high yield secondary electron yield coating is diamond thin films. Diamond thin film surfaces that have been treated with either hydrogen or oxygen and cesium have negative electron affinity and the secondary electron yields have been measured in excess of 130.⁷ Typical values of secondary yield typically achieved in photomultiplier tubes is ~ 25 -30. This enables a 4 stage tube with gain $\sim a \text{ few } \times 10^5$.

Another area where nanostructured materials will have a major impact on miniaturization of photomultipliers is in new photocathode materials. Nanoparticle-semiconductor composite thin films such as Ag-O-Cs, have shown enhanced photoemission.⁸ The enhanced photoemission is attributed to field induced variations in the energy band structure of the film due to nanoscale Ag particles embedded in the CsO matrix. The increase in quantum yield reported was 15.7% at 510 nm wavelength. Yet other material systems that show promise for extending the photoresponse into the 1.3 to 1.5 μm region are based on single wall carbon nanotubes where the band edge absorption is dependent on the nanotube diameter and can be tuned over the frequency range of interest.⁹ Studies of metal nanowire composite structures have also shown interesting tunable absorption properties that can be taken advantage of to engineer photoemissive coatings having selective optical responses.¹⁰ The enhanced plasmon excitation modes in nanoparticles and nanowires makes them interesting candidate materials for optical applications such as photocathodes.^{11,12,13,14}

The rapid developments taking place in nanostructured materials will have a significant impact on future photomultiplier technology. Nanostructured photocathodes with higher quantum efficiencies, narrow band tunable photoresponse and internal gain mechanisms will become possible.

4. Alternate Approaches for Miniature Photomultiplier Design and Fabrication

4.1 The Monolithic "Teacup Dynode"

As discussed earlier the monolithic ceramic multiplier was a first attempt to seriously reduce the size of a photomultiplier detector. In this section the ceramic multiplier concept is carried a step further in miniaturization in the form of a teacup shaped dynode produced by isotropic etching of glass wafers. Figure 1 shows a cross-section through a section of a monolithic teacup dynode based photomultiplier tube illustrating the potential distribution and

trajectories of electrons traveling from the photocathode to a spatially resolved anode. An illustration of a four-stage teacup dynode stack is shown in Figure 4, which also shows the means for alignment of the dynodes to maintain the proper offset for optimum secondary electron generation and collection.

The teacup dynode is produced by isotropic etching of a prescribed pattern of holes photolithographically produced in a mask on the glass wafer surface. The holes etch into spherical cavities as shown in Figure 5. Typical dimensions are 200 to 300 micrometers for the teacup entrance and 50 – 100 micrometers for the exit. The layers are each on the order of 200 to 300 micrometers in thickness, an eight stage dynode is ~ 1.6 to 2.4 mm in height depending on teacup size. The parallelness between stages is determined by the degree of parallelism between the two sides of the glass wafer and the lateral alignment is determined by photolithographically patterned holes for locating spheres as illustrated in Figure 4.

The sidewalls of the teacup structures are coated with a resistive film whose surface is treated to produce a high secondary electron yield. Electrical connection to each dynode is made by evaporation of a metal film onto the top flat surface of the glass substrate, overlapping the resistive film at the top edge of the teacup.

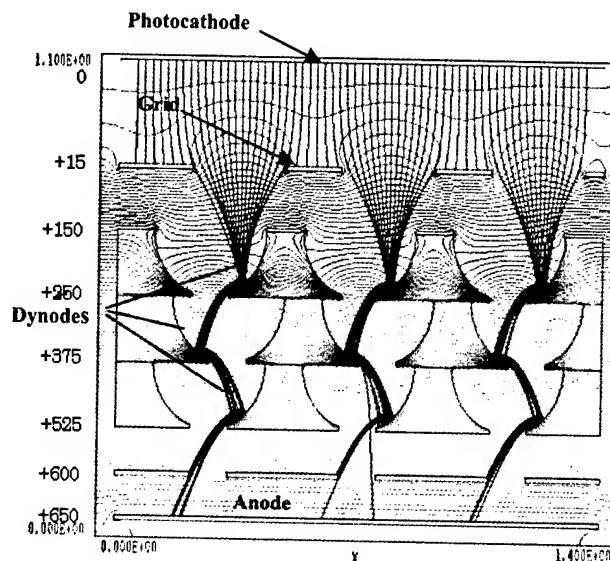


Figure 3. Cross-section view through a "teacup" dynode stack showing equipotential distribution and electron trajectories from electrons launched from a photocathode. Numbers on the left are the potentials on each stage of the dynode chain.

One of the major advantages of this approach for fabrication of a monolithic dynode structure is the flexibility offered by the photolithographic patterning process. The teacup dynodes can be arranged in a variety of patterns, square arrays, close packed arrays and linear arrays. The two dimensional array shown in

Figure 4 could easily be fabricated at a pitch of $275\text{ }\mu\text{m}$, a 100 by 100 pixel detector would have an active area of 2.75 mm^2 . The patterning process is not limited to spherical surfaces; it is also possible to produce straight or curved cylindrical surfaces. Figure 6 shows a simple linear array of half cylinders etched into quartz. These structures are part of a lateral monolithic dynode structure made by bonding two complementary glass plates, each with half of the dynodes, see Figures 7 and 8. Light enters through a window that seals the edge of the structure and strikes a reflection photocathode where photoelectrons are produced that are accelerated through the dynode structure. In this structure, placement of the dynodes is very critical and slight misalignments can result in low collection efficiencies. Also not shown are a series of electron lens structures necessary for focusing electrons.

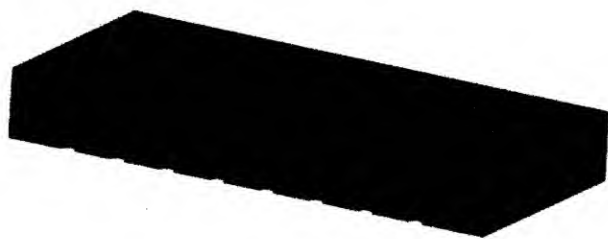


Figure 4. This schematic shows a top and cross-sectional view of a four-stage, 8x4 pixel micro-dynode array demonstrating arrangement of the dynodes. The layers are offset relative to each other to maximize secondary electron emission collisions as shown in Figure 3. Also shown on each side of the micro-dynodes are the spheres that are used to mechanically align the layers.

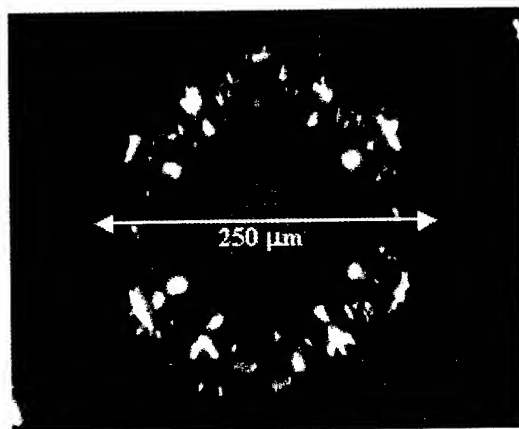


Figure 5. This optical photograph shows a top view looking down into a "bottomless teacup" micromachined into a quartz substrate by NanoSciences.

The gain performance of a linear array two-stage dynode stack of cylindrical dynodes similar to the illustration of Figure 4 is shown in Figure 9. In this example, the dynode cylindrical surfaces were coated with aluminium and the top surface of each dynode was coated with a thin layer of alumina produced by thermal oxidation

of the metal surface. The secondary electron yield of this surface is ~ 2.25 which is consistent with a gain of ~ 5 . This is similar to that reported by Comby et al for the monolithic ceramic electron multiplier.

The monolithic approach can now take advantage of ceramic chip packaging technologies to produce robust surface mount packages as illustrated in Figure 10. This type of packaging minimizes stray capacitance and places the detector output closer to the detection electronics. This arrangement permits convenient integration of the photomultiplier with high-speed pulse discriminators, amplifiers, ADC's and digital signal processors.

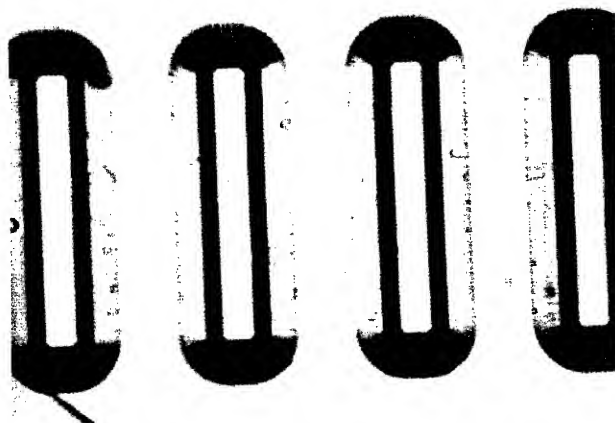


Figure 6. Optical micrograph of 4 half cylinders etched into a quartz wafer surface. The cylinders are $800\text{ }\mu\text{m}$ in length by $300\text{ }\mu\text{m}$ in diameter, the etched depth is half the diameter.

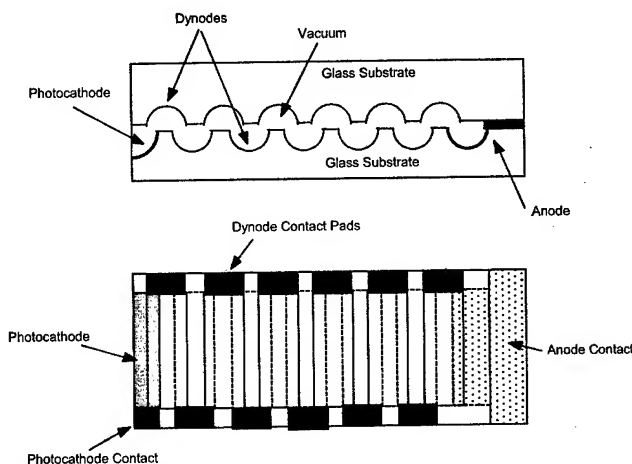


Figure 7 Schematic diagram of a lateral single pixel photomultiplier. Each dynode is a half cylinder

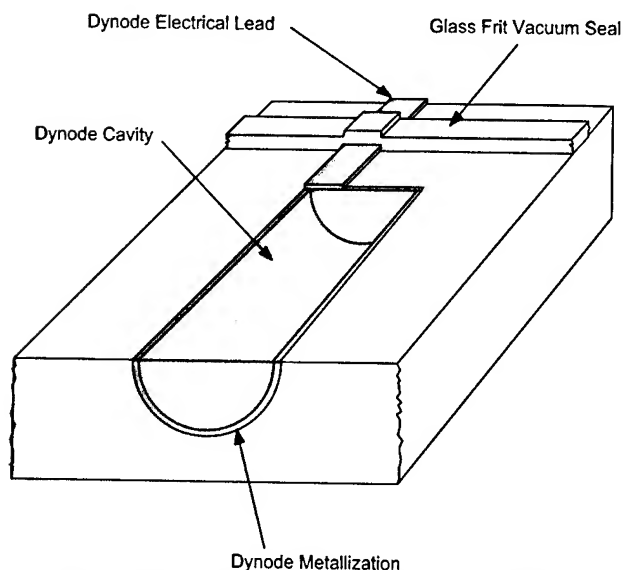


Figure 8. Illustration of dynode electrical connection and the patterned glass frit vacuum seal.

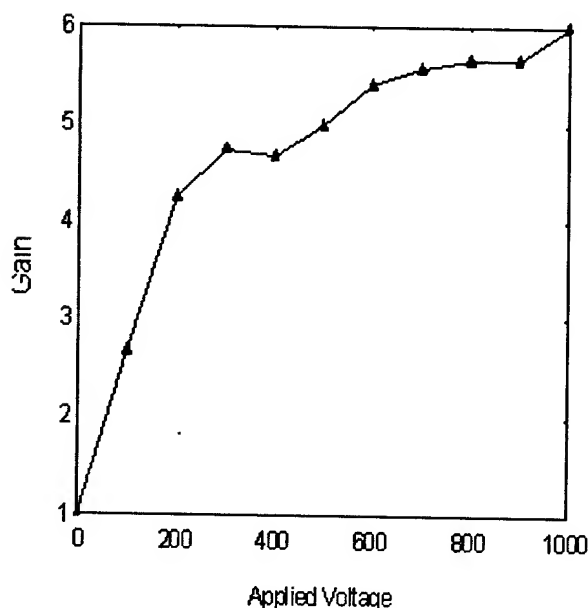


Figure 9. Measured gain for a two stage vertical stack of cylindrical dynodes.

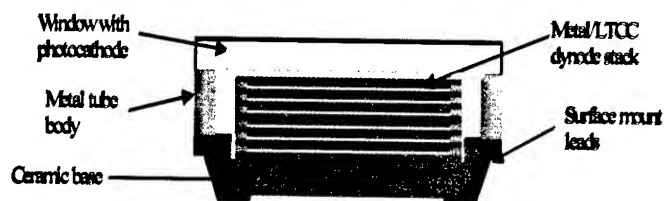


Figure 10. Illustration of a monolithic dynode stack packaged in a surface mount ceramic chip carrier enabling low profile and very compact photomultiplier detectors.

4.2 Microchannel Continuous Dynode Amplified Photomultipliers

The monolithic approach applied to the discrete dynode electron multipliers of the previous section can be extended to producing micro scale continuous dynode amplifiers. These structures are analogous to the macroscopic channeltron electron amplifiers and channel photomultipliers¹⁵ commonly employed in analytical applications such as mass spectroscopy and fluorescence detection where very sensitive low background detectors are needed. The previously described photolithographic patterning process can be employed to produce arbitrarily shaped cylindrical channels. Figure 11 shows a single channel micro scale electron amplifier. The channel diameter is 200 μm and is coated with a high resistivity film that forms the strip resistance for conducting charge back onto the dynode surface. The surface of the strip resistance film is coated with a higher secondary electron yield coating for producing electron gain. The measured gain for a single channel amplifier is shown in Figure 12. The gain increases with increasing bias voltage.

One of the significant advantages of this approach to electron amplification is that linear array detectors are as easy to produce as single channel devices. Figure 13 shows an etched array of a 1 x 50 linear array of 100 μm diameter channels each 5 mm in length. This type of linear array permits a high degree of spatial resolution. For example the array in Figure 13, has a pixel center-to-center distance of 125 μm yielding a total detector width of 6.25 mm.

The miniature continuous dynode electron amplifiers have an extremely flexible format and can be patterned in a wide variety of arrangements as illustrated in Figure 14 which shows a circular array of detectors arranged around the circumference of a circular opening, in this case the channel multipliers are designed to measure the uniformity of X-ray emission from a miniature cylindrical X-ray source. This device yields an angular distribution of X-ray flux with a single measurement. This type of device structure is also adaptable to three-dimensional stacking forming a monolithic stack of high sensitivity detectors.

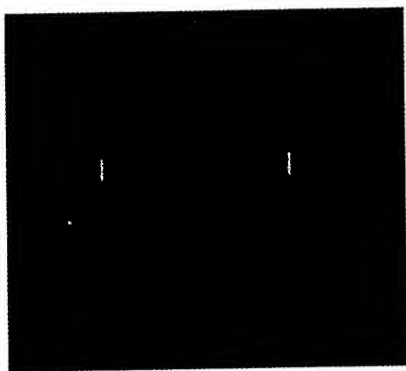


Figure 11. A prototype continuous dynode electron amplifier, the channel is 8 mm in length by 200 μm in diameter. The photocathode is deposited on the end of a cleaved optical fiber input. Two wires connecting through the side ports are used for biasing the channel and the wire opposite the photocathode is the anode.

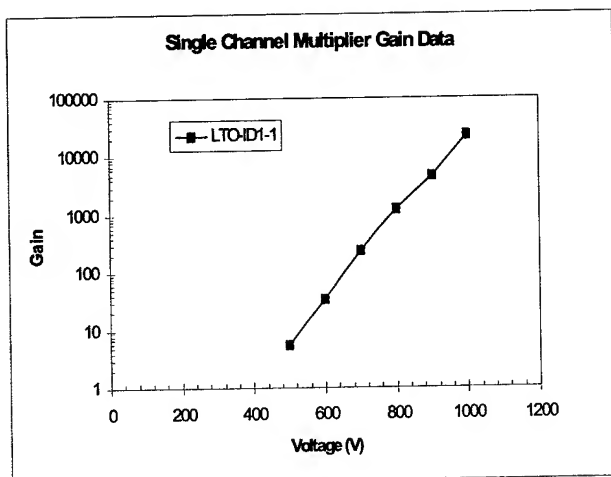


Figure 12. Electron gain measured on a microchannel electron amplifier. At 1000 V, the gain reaches 22,000.

4.3 Miniature Continuous Channel Amplified Photomultipliers

The previous section discussed microchannel amplifiers, in this section a slightly larger miniature microchannel amplified photomultiplier is presented. These tubes are intended to address applications where compact high sensitivity and high-speed detection are required. This family of photomultipliers is based on a novel channel amplifier that is micromachined in fused silica (Figures 15 and 16). The channel is 15 mm in length with a 0.5 mm I.D. The input cone can be coated with high secondary electron yield coatings such as the MgO/CNT, NEA diamond, or a reflection photocathode. The channel develops gain of 25×10^3 at 1000 V bias. The strip resistance and secondary electron layers are deposited by chemical vapor deposition at temperatures in excess of 700°C. The tube and its components are processed at

high temperatures for cleaning during preparation for photocathode deposition and tube sealing.

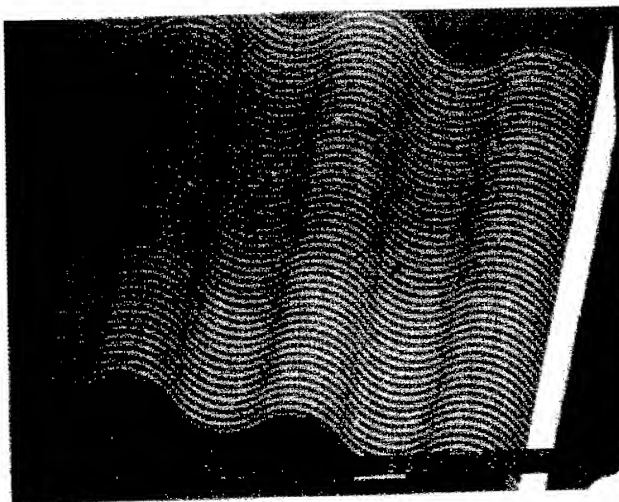


Figure 13. A linear array of 50 parallel "S" shaped channel amplifiers etched into a quartz wafer surface.

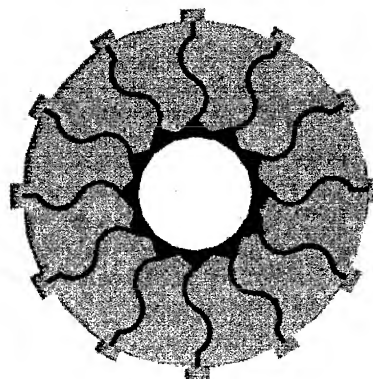


Figure 14. Illustration of the flexible formatting possible with the microchannel continuous dynode electron amplifier. In this figure 12 individual detectors are arrayed around the circumference of a circular cylinder on the interior. Each detector is biased separately and each anode is addressed independently enabling an angularly resolved measurement of X-rays emitted from a miniature X-ray source placed at the center of the interior cylinder.

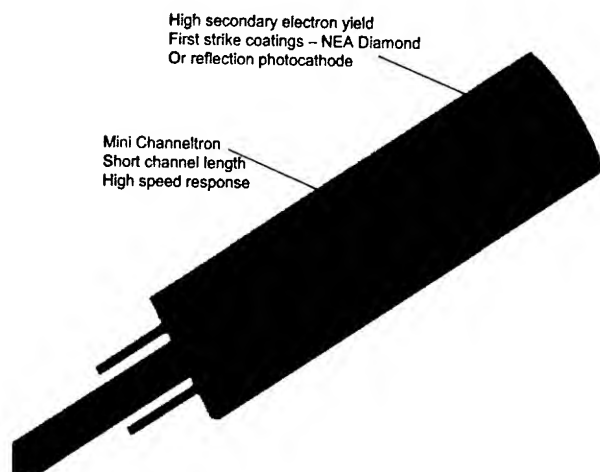


Figure 15. Cross-section view of a miniature channel amplified photomultiplier. The tube O.D. is 7.49 mm and the overall tube length is 28.1 mm.



Figure 16. Side view of the Pioneer I miniature channel amplifier photomultiplier showing the miniature channel amplifier.

4.4 Silicon Based Microchannel Plate Amplifiers

Glass microchannel plate amplifiers have played an important role in both particle and low level light detection. In this section a new microchannel plate amplifier structure based on micromachined silicon and its applications to miniaturization of photomultipliers is discussed. The silicon based microchannel plate (Si-MCP) is a relatively recent development,¹⁶ that has arisen out of a novel high rate anisotropic etching process.¹⁷ This process enables very high aspect ratio channels to be etched into the bulk of a silicon wafer. Some of the advantages of Si-MCP amplifiers are: (1) the channel structure and geometrical patterning can be controlled photolithographically, (2) the uniformity of the channel spacing results in a uniform dark background and a flat field response due to uniform illumination, there is no modulation due to the microstructure, (4) the structure is composed of materials that can be subjected to very high baking temperatures during photomultiplier processing and so out gassing is minimized, (5) the use of silicon as a substrate material also enables monolithic stacks of channels for "V" and "Z" channel geometries and (6) the micromachining approach and the use of semiconductor processing enables many

devices to be produced per wafer and many devices can be processed in parallel yielding a potentially interesting manufacturing cost structure. The Si-MCP has demonstrated performance characteristics similar to glass channel plates.^{18,19,20} The Si-MCP can enable miniature MCP amplified photomultipliers as illustrated in Figure 17. This is a prototype tube design presently under development. The next step in the development of this photomultiplier is the elimination of the pins and sockets. A plot of electron gain as a function of bias voltage applied to the Si-MCP is shown in Figure 18. Stacks of Si-MCP have shown electron gain as high as 10^6 .

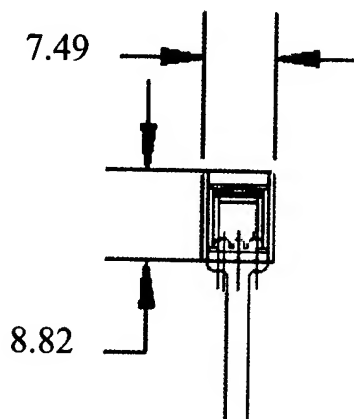


Figure 17. Illustration of the compact structure enabled through the use of a Si-MCP amplified photomultiplier tube. Dimensions are in mm.

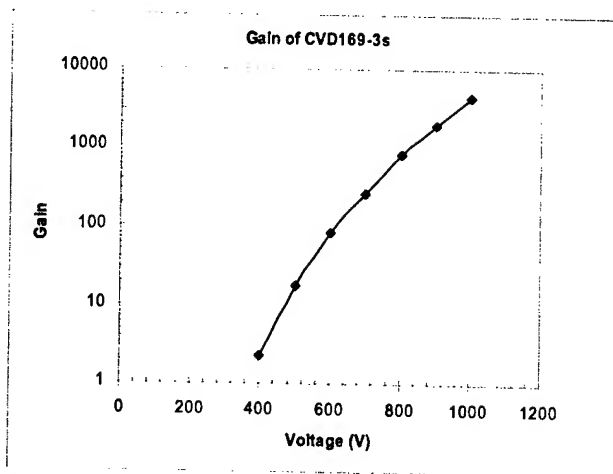


Figure 18. Gain measured as a function of voltage applied to a Si-MCP. The channel openings are ~6 mm spaced on 8 mm centers in a square array. The channel aspect ratio is ~40:1.

5. Conclusions

Recent trends in the development of miniature and micro-scale photomultipliers have been reviewed and some new approaches that are under development have been presented. Miniaturization of photomultipliers is reasonably straightforward, however, going beyond miniaturization requires the use of photolithographic patterning and micromachining to achieve the required precision and alignment necessary. Nanostructured materials also become critical to achieving microscale photomultipliers. New high gain dynode materials and nanostructured photocathodes will enable fewer stages of multiplication for comparable gain. This trend will enable micro-scale photomultipliers to compete more favorably with solid state detectors.

6. Acknowledgments

The authors would like to acknowledge support from Department of Energy Grant No. DE-FG02-02ER83523; NASA contract NAS5-00234; National Sciences Foundation Grant DMI-9901808; U. S. Army contract DAAB07-02-C-P005; and the Ballistic Missile Defense Organization contract DASG60-99-C-0077. The authors would like to thank John Bryan and Yosseph Habib for fabrication of some of the first microchannel amplifier substrates. The authors would also like to acknowledge interesting and insightful discussions with Mr. Charles Tomasetti, and Prof. Oswald Siegmund regarding vacuum photoelectric detectors.

7. References

- [1] K. Oba, H. Kume, K. Wakamori and K. Nakatsugawa, in Proceedings of the 9th Symposium on Photo-Electronic Image Devices held at Imperial College, London, 7-11 September 1987, p. 87, editor B. L. Morgan, published in Advances in Electronics and Electron Physics, editor Peter W. Hawkes, 74, (1988).
- [2] S. Suzuki, T. Nakaya, A. Suzuki, H. Suzuki, K. Yoshioka, and Y. Yoshizawa, IEEE Trans. Nuc. Sci. 40, 431 (1993).
- [3] W. Ehrfeld, H. Moser, and D. Munchmeyer, "Micro secondary electron multiplier," U. S. Patent 4,990,827, (1991).
- [4] G. Comby, F. Lehar, E. Chassaing, and G. Lorthioir, Nuc. Inst. Meth. Phys. Res. A 343, 263 (1994), *ibid*, A 387, 79, (1997).
- [5] C. P. Beetz, R. W. Boerstler, J. W. Steinbeck and D. R. Winn, U. S. Patent 6,384,519, (2002).
- [6] W. Yi, S. Yu, W. Lee, I.T. Han, T. Jeong, J. Lee, S. Jin, W. Choi, J. Heo, D. Jeon, and J. M. Kim, J. Appl. Phys. 89, 4091 (2001).
- [7] Q. F. Zhang, W. M. Liu, Z. Q. Xue, and J. L. Wu, J. Appl. Phys. 89, 2227 (2001).
- [8] J. E. Yater and A. Shih, J. Appl. Phys. 87, 8103 (2000).
- [9] M. J. O'Connell, S. M. Bachilo, C. B. Huffman, V. C. Moore, P. J. Boul, W. H. Noon, C. Kittrell, J. Ma, R. H. Hauge, R. B. Weisman and R. E. Smalley, Science 297, 593 (2002).
- [10] C. A. Foss, Jr., G. L. Hornyak, J. A. Stockert and C. R. Martin, J. Phys. Chem. 96, 7497 (1992).
- [11] R. A. Molina, D. Weinmann and R. A. Jalabert, Phys. Rev. B 65, 155427 (2002).
- [12] C. Sonnichsen, T. Franzl, T. Wilk, G. von Plessen and J. Feldmann, Phys. Rev. Lett. 88, 077402-1 (2002).
- [13] M. S. Sander, R. Gronsky, Y. M. Lin, M. S. Dresselhaus, J. Appl. Phys. 89 (2001).
- [14] J. J. Mock, J. Oldenburg, D. R. Smith, D. A. Schultz, and S. Schultz, Nano Lett. 2, 465 (2002).
- [15] B. Erjavec, Vacuum, 64, 15 (2002).
- [16] C. P. Beetz, R. W. Boerstler, J. W. Steinbeck and D. R. Winn, U. S. Patent 5,997,713 (1999).
- [17] C. P. Beetz, R. Boerstler, J. Steinbeck, B. Lemieux, and D. R. Winn, Nuc. Instr. Meth. Phys. Res A 442, 443 (2000).
- [18] A. W. Smith, C. P. Beetz, R. W. Boerstler, D. R. Winn, J. W. Steinbeck, Proc. SPIE, 4128, 14 (2000).
- [19] O. H. W. Siegmund, A. S. Tremsin, J. V. Vallerga, C. P. Beetz, R. W. Boerstler, J. Yang, M, and D. R. Winn, Proc. SPIE, 4497, August (2001).
- [20] Anton S. Tremsin, John V. Vallerga, Oswald H.W. Siegmund, Charles P. Beetz and Robert W. Boerstler, Proc. SPIE, 4497, August (2002).

8. Author Information

Charles P. Beetz

Dr. Beetz received a B.S. in mathematics and physics with distinction from Morehead State University, Morehead KY in 1970. He went on to complete M.S. and Ph.D degrees in solid state physics from Purdue University in 1973 and 1978 respectively. He was awarded the Lark-Horowitz prize in physics for outstanding thesis research. He joined the physics department at General Motors Research Labs in 1979. From 1979 to 1984 he was a Senior Research Scientist working in the areas of vapor phase growth of carbon fibres, diamond thin films and UHV single crystal film growth of refractory group IV elements and alloys. From 1984 to 1987 he was Assistant Head of Physics and was responsible for the Surface Physics, Molecular Physics, Magnetic Materials, and Metal Physics Groups. In 1987 he became a Principal Scientist of the research labs and Manager of Materials Physics. In 1988 he became a co-founder Advanced Technology Materials Inc. and was Director of Thin Film Research and Development. From 1991 to 1995 he was the Chief Scientist and Vice President of Research. In 1995 he co-founded NanoSystems, Inc. and was responsible for directing the companies new product development efforts. He is a co-inventor of NanoSystems microdynode photomultipliers and deep silicon etching processes. In 1999 he became CEO of NanoSciences Corp. He is responsible for directing the companies new miniature and micro photomultipliers, silicon based microchannel plate and microelectromechanical systems based electron multiplier product development efforts. He has over 80 publications and 14 issued U.S. patents.

Robert W. Boerstler

Mr. Boerstler is a Vice President and cofounder of NanoSciences Corp. and is responsible for all device fabrication of the company. Prior to NanoSystems, Mr. Boerstler was the Chief Process Engineer for Advanced Technology Materials, Danbury, CT, where he fabricated novel device structures in a wide range of materials systems including diamond, SiC, HTSC, Si, perovskite oxides and GaAs. Prior to joining ATMI in 1990, he was a Principal Investigator at Lockheed Sanders, where he investigated the materials and properties of the recently discovered High Temperature Superconducting Materials. He fabricated one micron and smaller "weak link" Superconducting Quantum Interference Devices (SQUIDS) and investigated their noise, magnetic, and microwave characteristics at varying temperatures. At Sanders he successfully initiated, developed, and transferred GaAs circuit microfabrication processes to pilot production manufacturing capability. He developed thin film ceramic processes to support component integration of these circuits into microwave modules. Before Lockheed in 1986, Mr. Boerstler was a semiconductor process engineer at General Instruments, where he was among the first to fabricate submicron gate structures in GaAs. He also has worked at Hughes Research Laboratory and is a U.S. Air Force veteran. Mr. Boerstler received B.A. from Wayne State University in 1976.

Robert L. Wright

Robert L. Wright is a Senior Process Engineer and one of the Principal Investigators at NanoSciences, Corporation. He is responsible for design and development of the mini photomultipliers, photocathode transfer processing and tube assembly. Prior to joining NanoSciences Mr. Wright was a Senior Project Engineer for Diamond Microelectronics Corporation of Boston, MA. Before that he was a Research Engineer for Advanced Technology Materials Inc., Danbury, CT. Mr. Wright was an Engine Systems Development Engineer for Textron Lycoming, Stratford, CT and a Systems and Operations Engineer for LEI, Vernon, CT. He graduated from Clarkson University, Potsdam, NY with his BS in Electrical and Computer Engineering in 1988 and his MS in Electrical and Computer Engineering in 1990.

James Agresta

Mr. James F. Agresta has been Facilities Manager for NanoSciences, Corporation since 1999. He is in charge of tooling development for mini and micro photomultiplier fabrication. He served as the Facilities Manager for IPEC- Precision, Bethel CT from 1996 until 1999. Prior to that he was the Project Manager for Grid Building Company, Orange, CT from 1976 until 1996. Mr. Agresta has extensive supervisory and practical experience in facility management. He has carpentry experience from Bargas Construction Company Trumbull CT and Carpentry Plus, Orange CT. Mr. Agresta trained at Housatonic Community College and Porter and Chester Institute.

David R. Winn

Dr. David Winn is one of the co-founders of NanoSciences, Corporation, Oxford, CT and is co-inventor of the company's nonvolatile memory and detector technologies. He received his BS from California Institute of Technology, Pasadena, CA, in 1969. His A.B. from Cornell University, Ithaca, New York in Physics in 1972 and his Ph.D. from the University of Wisconsin, Madison, Wisconsin, in 1979 in Experimental High Energy Physics with a minor in Mathematics and Nuclear Engineering. He was a Research Associate and Assistant Professor of Physics at Harvard University from 1979 to 1984. From 1984 through 1987 Dr. Winn was on the staff of Schlumberger Research, Ridgefield, CT as a Research Physicist than as a Program Leader of the Electron/Photon Physics Program and finally as Task Force Coordinator for Accelerator Technology. Dr. Winn has been an Associate Professor of Physics at Fairfield University Associate Professor of Physics, Fairfield University, Fairfield, CT, a Research Affiliate, Department of Physics, Yale University, New Haven, CT and a Research Professor of Physics, Department of Physics, Boston University from 1987 to the present. He is author and co-author of multiple research papers and articles.

Impact of preform fabrication and fiber draw on the optical properties of microstructured fibers

Ryan T. Bise, Dennis J. Trevor, Eric Monberg and Frank DiMarcello

OFS Laboratories

600-700 Mountain Avenue, Murray Hill, NJ 07928

+1-908-582-5829 · bise@ofsoptics.com

Abstract

We report recent results concerning the loss and transmission properties of both index guiding and photonic band gap microstructured fibers generated via a sol-gel method. The loss for an index guiding microstructured fiber at 1550 nm is 2 dB/km and shows an attenuation of 6 dB/km at 1385 nm, displaying the lowest level of hydroxyl in any microstructured fiber. Our results are compared to other recently published results.

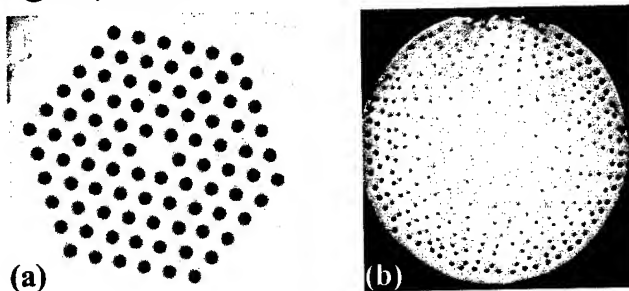
Keywords

Microstructured fiber, photonic band gap, attenuation, fabrication

1. Introduction

Microstructured optical fibers consist of an array of holes, embedded within a glass matrix, which extends longitudinally along the z-axis of the fiber, see Figures 1a and 1b. The ability to periodically place air holes within a silica matrix enables new designs, which utilize the large index contrast between air and silica to generate fibers with unique waveguiding properties. Highly nonlinear fibers for supercontinuum generation,[1] birefringent fibers,[2] endlessly single moded fibers,[3] dispersion shifted and dispersion compensating fibers[4] highlight the diverse range of properties afforded via microstructure fiber design. Furthermore, as these fibers have open air columns running along their length, it is possible to incorporate active materials within the holes to generate all fiber devices.[5] The aforementioned fibers are all index guiding structures, however, the ability to generate a regular periodic lattice with the large index contrast afforded by air and silica with a period close to optical transmission wavelengths allows one to guide light by the photonic band gap effect. Light is then localized within the core through a coherent scattering mechanism and consequently can propagate within a low index core region such as air[6] minimizing the effects of material absorption loss, scattering and nonlinearities and as a result, hollow core photonic band gap fibers are predicted to have significantly lower losses than standard silica fibers.[7]

While microstructured fibers show great potential in both transmission and device applications, until recently, these fibers have been plagued by high optical attenuation between 10-100 dB/km and have been restricted to short lengths of fiber on the order of a few hundred meters. Achieving low optical attenuation requires solving a number of challenges in fabrication, processing and draw. Preforms with uniform hole size and positions along the length are required and must be sufficiently large in size to



yield kilometer lengths of fiber. The surface of the air hole must be sufficiently smooth to minimize loss due to scattering at the

Figure 1. Cross-sectional view of sol-gel derived microstructured fibers with both a) closest packed and b) non-closest-packed air hole patterns. The dark regions are air holes while the bright regions are silica

air/glass interface. Processing steps which reduce the contamination due to OH at the surface of the air holes are required. Finally, it is essential that the air holes remain open during draw and furthermore that a uniform hole size and shape over kilometer lengths is obtained. Recently, tremendous progress has been made in the manufacturing of microstructured fibers with reported loss values in the 1-3 dB/km range[8-10] and uniform hole size distribution over km length scales indicating that microstructure fibers may indeed provide attractive solutions for both transmission and specialty fiber applications. In this paper, we discuss our progress towards producing low-loss uniform microstructured fiber on kilometer length scales for both index guiding and photonic band gap fibers and compare these with other recent results.

2. Design and manufacture of micro-structured fiber

To date, most microstructured fibers have been manufactured by a "stack-and-draw" method in which glass capillaries and or rods are stacked together to form a preform, which is then drawn down in a single or multiple steps to optical fiber dimensions. This method offers design freedom in the choice of the inner and outer diameters of the capillaries used and the placement of the air holes in the preform. While this method has been shown to be quite useful in generating a number of fibers with different optical properties such as high nonlinear fibers, endlessly single-moded fibers, and even photonic band gap fibers, this technique is

ultimately limited in design space to closest packed structures. Recently, a few publications have been made for the manufacturing of microstructured fibers via extrusion both for polymer fibers and for non-silica glasses. [11-13] The extrusion method offers additional flexibility in design, however, the polymeric or non-silica glass materials typically employed in extrusion suffer from high loss. Similar flexibility in design is achieved using a sol-gel casting method[14,15], as exhibited in the non-closest-packed fiber design is shown in Figure 1b which contains annular rings of air holes with an increasing number of air holes as the radius increases. With this approach a parabolic index profile for an inexpensive all-silica graded index fiber might be achieved.

One advantage of the casting technique is that after the green body is formed, water and transition metal contaminants as well as refractory particles can be removed through thermochemical processes prior to consolidating the body into glass and finally drawing into fiber. The stack and draw methods require handling of glass capillaries during the preform fabrication step, which serves as, a potential source for material contamination. Contaminants trapped within the glass preform are significantly more difficult to remove than from a porous body. Hence, fabrication techniques that involve a porous body provide a clear route towards a lower level of contamination for silica microstructured fibers.

2.1 Impact of hole placement on optical properties

The regularity of the air holes within a microstructured fiber is important both for index guiding as well as for photonic band gap fibers. The cladding consists of a regular array of air holes with bridging silica regions. These silica regions are typically weakly guiding and light propagating in these can be easily removed by bending of the fiber as is typical done in fiber attenuation measurements. However, if the air fraction is high, the silica regions are then small and not well coupled to each other. As a result, the light propagating in these silica regions of the cladding is difficult to remove by bending leading to potential errors in optical measurements. If the structure is mostly regular, with a few unintentional defects in the cladding, the light will tend to localize within these regions as shown in Figure 2. Coupling of these defect guides in the cladding with the core region increases the overall optical attenuation of the fiber. The six-fold symmetric core formed from the removal of one hole of a triangular lattice ideally exhibits no birefringence,[16] therefore maintaining a symmetric core along the length of the fiber should also reduce the polarization modal dispersion (PMD).

2.2 Lattice structure and Photonic band gap fibers

Photonic band gap fibers guide light through a coherent scattering process in which a regular periodic variation in the index of refraction causes particular frequencies of light, which satisfy the Bragg condition, to be localized within a defect region or core.

Due to the guiding mechanism, very regular extended periodic lattices are required in order to effectively transmit light with low

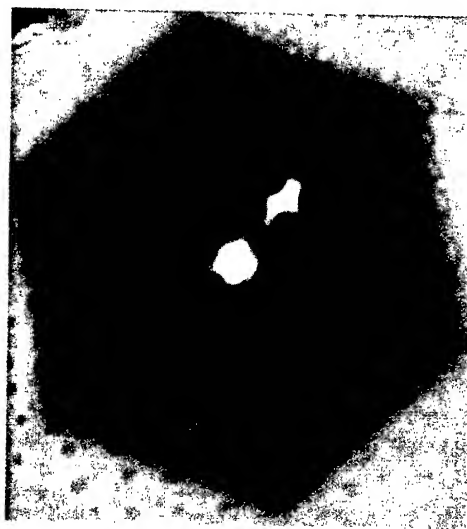


Figure 2. Cross section of an index guiding microstructured fiber with light coupled into the other end of the fiber. The bright region in the center of the fiber is light transmitted through the silica core of the fiber. Another bright section is observed in the cladding at a hole dislocation. A second region to the lower left of the picture shows green light at a position where the hole size is significantly smaller than the rest of the fiber.

optical attenuation.

Recently, we have demonstrated that solid silica core fibers surrounded by triangular lattice of air holes, such as the one shown in Figure 1a, demonstrate guidance by the photonic band gap effect when a high index liquid ($n_D = 1.8$) is inserted into the air holes. Shown in Figure 3 are the transmission spectra for two different sol-gel derived photonic band gap fibers, fiber 1A with 10 rows of holes and fiber 1B with 5 rows of holes. The lattice constant, Λ , or pitch of the air holes for fibers 1A and 1B is 4.3 and 5.2 μm respectively while the hole size is 2.4 μm for both fibers. The transmission spectra are displayed in normalized units with respect to the lattice constant. Despite the fact that fiber 1B has significantly fewer rows of holes, it has a significantly improved transmission spectrum compared to fiber A, with broader and flatter transmission windows, a sharp band edge as well higher order harmonic Bragg reflections at higher frequencies. The marked improvement in the photonic band gap transmission spectrum is a result of the increased uniformity both in the air hole size and spacing leading to a regular symmetric structure. Two-dimensional Fourier transforms of the transverse images of fiber 1A and 1B confirm that fiber 1B has a higher degree of order than fiber 1A. As the photonic band gap spectrum provides a direct link to the regularity of the structure as well as the uniformity of the hole size in the same manner as scattering or

image analysis, these spectra may provide an alternative noninvasive method for characterization of microstructured fibers.

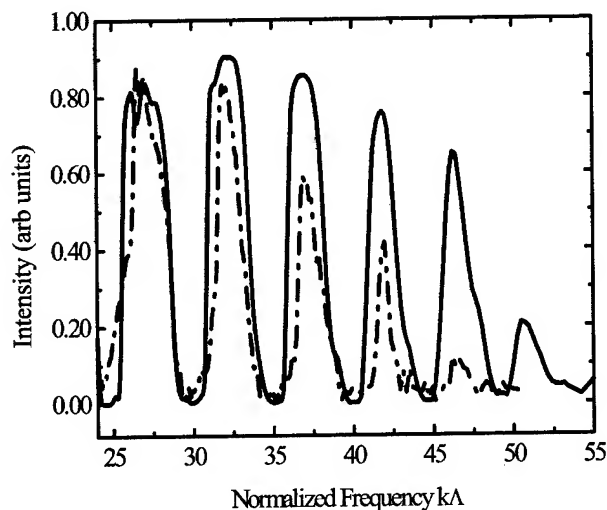


Figure 3. Normalized transmission spectrum for two photonic band gap fibers. Fiber 1A is shown with a dashed line while Fiber 1B is shown with a solid line. The details of the fiber parameters are discussed in the text.

Although photonic band gap fibers are anticipated to be low loss, the longest distance reported to date for such a fiber is 15 m, with a loss of 1 dB/m for an air-core photonic band gap fiber.[8] The loss for fiber B is estimated to be better than 1 dB/m, however, the length into which the liquid has been placed inside the fiber has been limited to lengths 2 m or less. The largest source of loss for photonic band gap fibers appears to be due to imperfections in the lattice structure. It is hoped that continued improvement in perfecting the fiber fabrication process will allow low loss hollow core transmission fibers to be produced.

3. Material contamination

As in all fibers, reduction of material contamination is essential to extend the transmission length of a fiber. While the manufacturing of high purity silica with low OH (e.g. AllWave fiber manufactured by OFS)[17] as well as low values for transition metal ions has become routine, obtaining the same levels of purity in microstructured fibers is complicated by the numerous air-glass interfaces near the core. Contamination can be particularly problematic for the stack and draw approach due to handling of capillaries during preform assembly. Despite this difficulty, stack and draw microstructured fibers have been reported with measured loss values between 1 to 2.6 dB/km at 1550nm. [8-10] Tajima *et al.* have attempted to characterize the leading contributions to the attenuation in microstructured fibers using equation 1,

$$\alpha = \frac{A}{\lambda^4} + \alpha_{abs} + B \quad (1),$$

where the total attenuation, α , is attributed to Rayleigh scattering with coefficient A , α_{abs} is the attenuation associated with material absorption and B is loss due to structural defects of the waveguides such as changes in hole size or lattice constant spacing. Equation 1 is oversimplified in that it does not explicitly take into account the affect of confinement loss[18] of the waveguide and its corresponding wavelength dependence. This equation also partially groups the expected excess scattering from the imperfect surfaces into the Rayleigh scattering coefficient since a lower order power of $1/\lambda$ is not included. However, this equation does provide a useful means of comparing the loss values for similar microstructured fibers. In Table 1 the attenuation at 1550 nm, 1385 nm, the Rayleigh scattering coefficient and the structural defect values are given for our microstructured fiber and for the three previously reported low loss microstructured fibers. Tajima *et al.* have achieved the lowest loss microstructured fiber by employing high purity capillaries made using VAD glass. The OH loss in the glass preform was less than 1 dB/km in the initial glass, but was greater than 30 dB/km in the final fiber indicating that subsequent processing steps including draw led to an increased level of contamination in the fiber. The microstructured fiber reported here has a loss of 2 dB/km at 1550m, twice that of Tajima *et al.*, however the OH for the sol-gel fiber is nearly 1/5 that of Tajima *et al.* demonstrating the lowest loss at 1385 nm of any microstructured fiber to date.

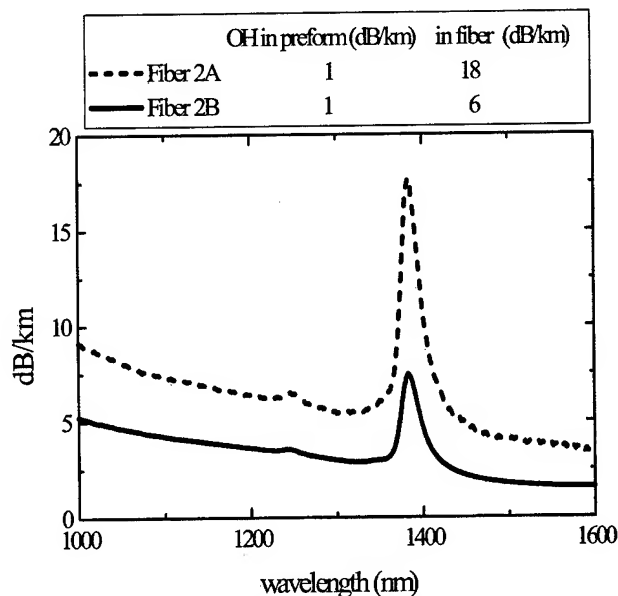


Figure 4 Attenuation of Fibers 2A and 2B. The 2B preform had additional purification.

In Figure 4, we show the optical loss of two different index guiding microstructured fibers as well as their OH concentrations in both the glass preform and the final fiber. Fiber 2A and 2B possess comparable hydroxyl concentration in the initial glass preform yet Fiber 2B displays an hydroxyl concentration which is a factor of three less than Fiber 2A. An additional processing step of heating the preform after attaching the handle was performed

for Fiber 2B to remove any water which may have entered the air holes and to remove any water from the air/glass interface.

Table 1. Contributions to loss for recently reported low-loss microstructured fibers

Ref.	Loss @1550 nm (dB/km)	A (dB/km/(μm) ⁴)	B (struct.defect) (dB/km)	Loss @1385 nm (dB/km)
[9]	1	2	0.6	30
[10]	1.3	1.9	1	>20 (est.)
This work	2	4.2	1	7
[8]	2.6	Not reported	Not reported	50

Table 1 shows that the present fiber possess a Rayleigh scattering coefficient twice as large as both Tajima *et al.* and Suzuki *et al.* and more than five times that of standard silica glass (0.8 dB/km/(μm)⁴). Tajima *et al.* have shown that polishing and etching the inside surface of the air holes in the preform significantly reduces the scattering loss of the fiber. Additional efforts to improve the surface finish of the air holes in the preform should reduce the loss of the fiber at 1550 nm by as much as 0.6 dB/km. The additional 1 dB/km loss assigned to the structural defect should be reduced with additional improvements in preform fabrication as well as improved control over the hole size during draw.

4. Fiber draw.

A uniform hole size along the entire fiber length is required to reduce excess fiber loss due to mode coupling or scattering. By varying the temperature during draw, the air hole size can be adjusted within the fiber. Figure 5 shows the air hole size in the fiber as measured with an optical microscope as a function of temperature showing an exponential decay in the hole size from 3.3 to 1.0 μm over a temperature range of about 40°C. Fitt *et al.* have examined the hole size as a function of draw speed, preform feed rate, and temperature.[19] The strong temperature dependence of the hole size is due to the dependence of the hole size on the relative ratio of the surface tension to the glass viscosity. Although the surface tension is relatively temperature independent, the viscosity, η , obeys, over a small temperature range an Arrhenius relationship, $\eta \propto \exp(E_a / RT)$, where E_a is the activation energy, R is the universal gas constant and T is the temperature. Our observed exponential decrease in hole size as a function of temperature is in agreement with the above theoretical calculations, indicating that the glass viscosity is the dominant term responsible for hole size in the final fiber.

The sensitivity of hole size upon furnace temperature allows a large dynamic range of hole sizes to be created from a single preform. However, it is imperative that the air hole size distribution be uniform within a given cross section as well as along the entire fiber length. The average hole size for the fiber in Figure 1a is 2.4 microns with a standard deviation of .03

microns We have been able to produce fibers which vary in hole size less than 5% over 2 km spans.

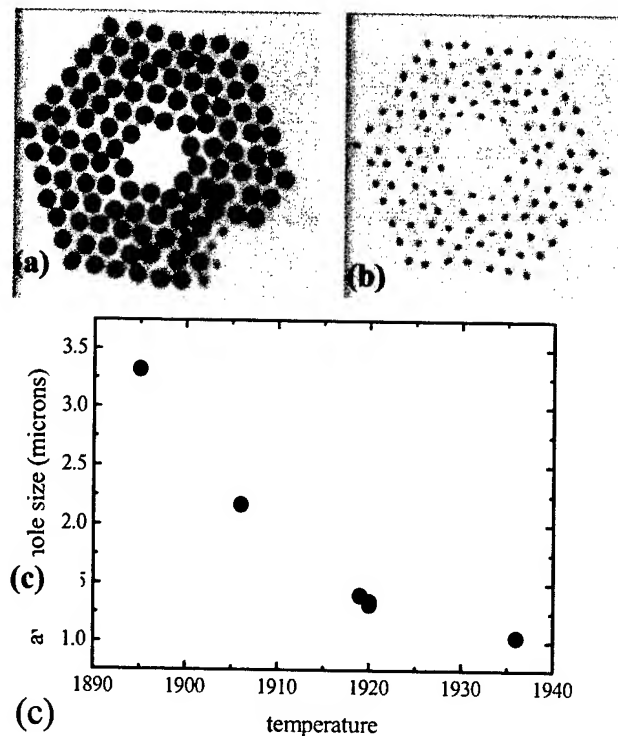


Figure 5. Temperature dependence of hole size on furnace temperature. Photos show cross section of fiber, which was drawn at a) 1906°C and b) 1936°C. c) Plot of the average hole size as a function furnace temperature.

5. Conclusion

In the past two years, researchers have quickly reduced the attenuation of microstructured fibers both by improving the structural quality of the fiber and adding additional processing steps to reduce the effects of material contamination and surface defects. Theoretical calculations suggest that for reasonable air fill fractions of 60% or less with 3 to 5 rows of air holes, the confinement losses of microstructured fibers can be reduced to values below 1 dB/km.[18,20] As the loss values for microstructured fibers begin to approach values below 1 dB/km, the unique waveguiding properties of microstructured fibers become significantly more attractive. Fibers reported here are rapidly approaching the world's best values for attenuation at 1550nm and have demonstrated the lowest level of hydroxyl for any microstructured fiber. Additional efforts to reduce surface defects and improve the structural uniformity of the fiber both in preform fabrication and during draw should lead to continued reduction in the loss both for index-guiding as well as photonic band gap fibers.

6. Acknowledgements

We would like to thank Bernie Zegarski, Mike McDonanld, and Mike McNamee for their assistance in fabrication, purification and draw of microstructured prforms. We would also like to thank David DiGiovanni for useful discussions.

7. References

- [1] J.K. Ranka, R.S. Windeler, and A.J. Stentz, "Optical properties of high-delta air-silica microstructure optical fibers," *Opt. Lett.*, 25 (11), 796-798 (2000).
- [2] A. Ortigosa-Blanch, J.C. Knight, W.J. Wadsworth, J. Arriaga, B.J. Mangan, T.A. Birks, and P.S.J. Russell, "Highly birefringent photonic crystal fibers," *Opt. Lett.*, 25 (18), 1325-1327 (2000).
- [3] T.A. Birks, J.C. Knight, and P.S. Russell, "Endlessly single-mode photonic crystal fiber," *Opt. Lett.*, 22 (13), 961-963 (1997).
- [4] J.C. Knight, J. Arriaga, T.A. Birks, A. Ortigosa-Blanch, W.J. Wadsworth, and P.S. Russell, "Anomalous dispersion in photonic crystal fiber," *IEEE Photonics Technol. Lett.*, 12 (7), 807-809 (2000).
- [5] C. Kerbage, R.S. Windeler, B.J. Eggleton, P. Mach, M. Dolinski, and J.A. Rogers, "Tunable devices based on dynamic positioning of micro-fluids in micro-structured optical fiber," *Opt. Comm.*, 204 (1-6), 179-184 (2002).
- [6] R.F. Cregan, B.J. Mangan, J.C. Knight, T.A. Birks, P.S. Russell, P.J. Roberts, and D.C. Allan, "Single-mode photonic band gap guidance of light in air," *Science*, 285 (5433), 1537-1539 (1999).
- [7] S.G. Johnson *et al.*, "Low-loss asymptotically single-mode propagation in large-core OmniGuide fibers," *Optics Express*, 9 (13), 748779 (2001).
- [8] J.A. West, N. Venkataramam, C.M. Smith, and M.T. Gallagher, "Photonic Crystal Fibers," presented at the Optical Communication, 2001. ECOC '01. 27th European Conference on Optical Communication, Amsterdam, (2001).
- [9] K. Tajima, K. Nakajima, K. Kurokawa, N. Yoshizawa, and M. Ohashi, "Low-loss photonic crystal fibers," presented at the Optical Fiber Communications, Anaheim, CA, (2002).
- [10] K. Suzuki, H. Kubota, S. Kawanishi, M. Tanaka, and M. Fujita, "Optical properties of a low-loss polarization-maintaining photonic crystal fiber," *Optics Express*, 9 (13), 676-680 (2001).
- [11] M.A. van Eijkelenborg *et al.*, "Microstructured polymer optical fibre," *Optics Express*, 9 (7), 319-327 (2001).
- [12] A. Argyros, I.M. Bassett, M.A. van Eijkelenborg, M.C.J. Large, J. Zagari, N.A.P. Nicorovici, R.C. McPhedran, and C.M. de Sterke, "Ring structures in microstructured polymer optical fibres," *Optics Express*, 9 (13), 813-820 (2001).
- [13] K.M. Kiang, K. Frampton, T.M. Monro, R. Moore, J. Tucknott, D.W. Hewak, D.J. Richardson, and H.N. Rutt, "Extruded singlemode non-silica glass holey optical fibres," *Electron. Lett.*, 38 (12), 546-547 (2002).
- [14] J.B. MacChesney, D.W. Johnson, Jr., S. Bhandarkar, M.P. Bohrer, J.W. Fleming, E.M. Monberg, and D.J. Trevor, "Optical fibers by a hybrid process using sol-gel silica overcladding tubes," *J. Non-Cryst. Solids*, 226 (3), 232-238 (1998).
- [15] R.T. Bise, R.S. Windeler, K.S. Kranz, C. Kerbage, B.J. Eggleton, and D.J. Trevor, "Tunable photonic band gap fiber," presented at the Optical Fiber Communications Conference, Anaheim, CA, (2002).
- [16] M.J. Steel, T.P. White, C.M. de Sterke, R.C. McPhedran, and L.C. Botten, "Symmetry and degeneracy in microstructured optical fibers," *Opt. Lett.*, 26, 488-490 (2001).
- [17] K.H. Chang, D. Kalish, T.J. Miller, and M. Pearsall, U.S. patent, 6,131,415 (1997).
- [18] T.P. White, R.C. McPhedran, C.M. de Sterke, L.C. Botten, and M.J. Steel, "Confinement losses in microstructured optical fibers," *Opt. Lett.*, 26 (21), 1660-1662 (2001).
- [19] A.D. Fitt, K. Furusawa, T.M. Monro, and C.P. Please, "Modeling the fabrication of hollow fibers: Capillary drawing," *J. Lighthwave Tech.*, 19 (12), 1924-1931 (2001).
- [20] M. Finazzi, T.M. Monro, and D.J. Richardson, "Confinement loss in highly nonlinear holey optical fibres," presented at the Optical Fiber Communications Conference, Anaheim 2002, (2002).

Ryan Bise received a B.S. in Chemistry from UCLA in 1995 and a Ph.D. in Physical Chemistry from UC Berkeley in 2000. As a Postdoctoral Member of the Technical Staff at Lucent Technologies in Murray Hill, NJ, he worked on the design, manufacture and characterization of sol-gel derived micorstructured fibers and continues this research effort as an employee of OFS Research in Murray Hill, NJ.

Dennis J. Trevor is technical manager of the Optical Materials Group of OFS Laboratories in Murray Hill, NJ, formerly part of Lucent Technologies Bell Laboratories. He received his undergraduate training at Illinois Institute of Technology and graduate training at the University of California, Berkeley.

Eric Monberg received his Ph.D. in Physical Chemistry from Michigan in 1977. His initial work at Bell Labs involved the development of the VGF process for the growth of low dislocation density III-V, compound semiconductors. In 1992 he began work on the implementation of a sol-gel process for the production of silica overcladding tubes for optical fiber manufacturing. For the last year he has been working in R&D of fiber drawing for OFS Research in Murray Hill, NJ.

Frank DiMarcello is a Technical Manager in the area of fiber draw at OFS Laboratories, Murray Hill, NJ. He received a B.S. in Geochemistry from Penn State in 1960, an M.S. in Ceramics from Rutgers in 1966, and has worked for Bell Laboratories, and OFS Laboratories for more than 42 years. He is currently involved in a variety of R&D projects related to optical fiber processing.

Giant Optical Transmission Through Nanometer-Scale Apertures

Tineke Thio

NEC Research Institute

Princeton, NJ

+1-609 951 2616 · tineke@research.nj.nec.com

Abstract

The extremely small optical transmission of a sub-wavelength aperture in a metal film limits the usefulness of near-field devices with super-resolution. But when the metal surface has periodic corrugations, a resonant interaction of the incident light with surface plasmon polaritons at the metal surface leads to extra-ordinary high transmission efficiencies. We review the physics of the surface plasmon enhanced transmission, and discuss possible applications.

Keywords

Surface plasmon polariton; light transmission; nano-apertures.

1. Introduction

The development of nanotechnology drives the need for controlling and positioning light on length scales less than 100nm. Since the length scale is far smaller than the optical wavelengths, far-field optics cannot be used because of the diffraction limit. A sub-wavelength spot of light is most commonly defined by a small aperture in an otherwise opaque metal film. The large disadvantage of such devices is their extremely low transmission efficiency.

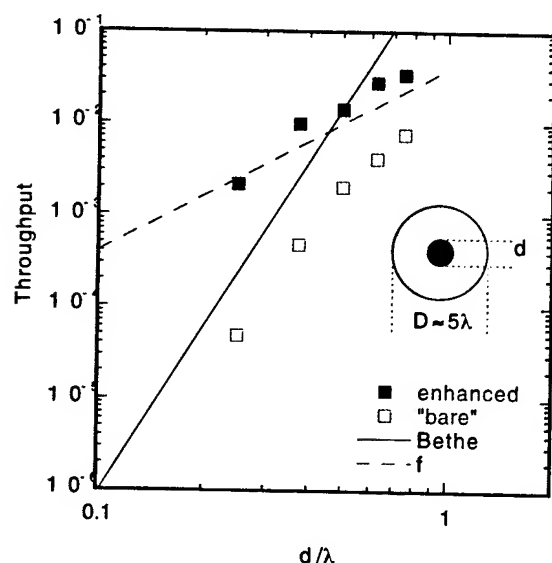


Figure 1. Throughput of a circular aperture in a metal film.

To illustrate the efficiency problem, let us consider the throughput of a laser beam (wavelength λ) which has been

focused to a spot of diameter $D \sim 5\lambda$ (see inset of Figure 1). When the aperture is large ($d > D$) the transmission is unity: $T=1$. For smaller apertures ($d < D$) the transmission simply follows the filling fraction $f=(d/D)^2$, given by the ratio of the areas of the aperture and the illuminating laser spot: $T=f \sim (d/\lambda)^2$ (dashed line in Figure 1). At this geometric (or macroscopic) limit, the intensity at the aperture output equals the intensity of the incident light: $I_{out}/I_{inc}=1$. But for apertures significantly smaller than the diffraction limit, the transmission drops much faster with decreasing hole size, and for the case of an ideal metal is predicted^{1,2} to follow $T \sim (d/\lambda)^6$ (solid line in Figure 1). Indeed our transmission measurements of cylindrical hole in silver films (open squares) bear this out.

We have recently shown³ that when the apertures are fabricated in a metal film of which the surface has a periodic corrugation, the transmission is enhanced to such an extent, that it can exceed the geometric limit: the solid square symbols in Figure 1 fall above the filling fraction line, meaning that the transmission coefficient, the ratio of the light intensity at the exit and entrance of the aperture, exceeds unity: $I_{out}/I_{inc}=T/f > 1$. This occurs despite the fact that the aperture is well in the sub-wavelength regime. The enhancement results from a resonant interaction of the incident light with surface plasmon polaritons, collective excitations at the metal surface.^{4,5}

We review here the physical principles of the surface plasmon enhancement, both in single aperture and arrays of apertures, and we discuss possible applications.

2. Surface Plasmon Resonance

Surface plasmon polaritons⁶ on a metal surface are collective excitations which can be thought of as surface charge density waves. Since they are longitudinal, they have TM polarisation, with the magnetic field in the plane of the surface. The surface plasmon dispersion relation follows

$$\frac{\hbar\omega}{c} = n_{eff} k \quad (1)$$

where $\hbar\omega$ is the photon energy, k the wavevector, c the speed of light, and the effective refractive index is given by

$$n_{eff} = \sqrt{\frac{\epsilon_m \epsilon_d}{\epsilon_m + \epsilon_d}}, \quad (2)$$

where ϵ_m and ϵ_d are the dielectric constants respectively of the metal and the adjacent dielectric medium.

The effective refractive index is slightly larger than $n_d = \sqrt{\epsilon_d}$, that is, the SP dispersion lies slightly below the light line (see solid line in Figure 2), reflecting the fact that a significant portion of the electromagnetic fields associated with the SP lie in the metal. Since the SP dispersion on a smooth metal surface lies entirely below the light line, an interaction between incident light and the SP on the metal surface is not allowed. However, it is allowed in the presence of periodic structure on the metal surface.⁷ This gives rise to zone folding, or grating coupling, indicated graphically in Figure 2 by the dashed lines showing the SP dispersion replicated at the first reciprocal lattice vector. There is a family of SP branches corresponding to higher-order zone folding, which are not shown in Figure 1 for clarity. The SP branches which now lie above the light line are accessible for interaction with incident light.⁵ A resonance is achieved whenever the energy and momentum conservation laws are obeyed.

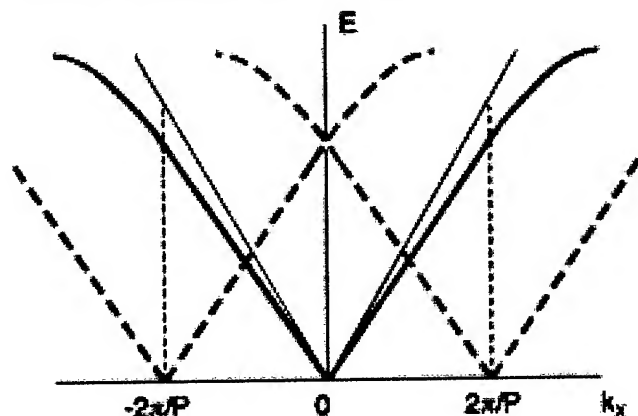


Figure 2. Surface plasmon dispersion relation at smooth surface (solid line) and corrugated surface (dashed lines)

The resonance leads to a large enhancement of the oscillating electric fields at the metal surface.^{8,9} Because of the very large intensities at the entrance of the apertures, the transmission through the apertures is enhanced significantly compared to that of the non-resonant case. The transmission through the aperture is still characteristic of a waveguide beyond cutoff, and falls exponentially with film thickness,¹⁰ but the prefactor to the exponential is considerably enhanced compared to the incident intensity.

The wavelengths of the resonance are tunable, since they depend on the geometry of the surface corrugation, on the angle of incidence of the exciting light, and on the dielectric constant of the medium over the metal surface. For normal incidence on a surface with a square-symmetry corrugation with a lattice constant P , the resonant wavelengths are given by⁵

$$\lambda_{SP} = \frac{P}{\sqrt{i^2 + j^2}} \sqrt{\frac{\epsilon_d \epsilon_m}{\epsilon_d + \epsilon_m}} \quad (3)$$

Here the integers (i,j) refer to the reciprocal lattice vectors associated with the SP branch.

3. Experimental Results

3.1 Aperture Arrays

Figure 3 shows the zero-order transmission spectrum of a square array of circular apertures, with $P=600\text{nm}$ and $d=150\text{nm}$, fabricated by focused-ion beam (FIB) milling of a 300nm thick silver film.⁴ A family of transmission peaks is clearly visible; the solid-line (red) markers at the top of the figure indicate the predicted positions of the surface plasmon resonances (no adjustable parameters), for both the metal-air interface, and the interface with the substrate, in this case quartz. The fact that both sets of surface plasmon resonances appear in the transmission spectrum indicates that the incident light also excites surface plasmon modes on the dark, unilluminated side of the metal film.⁵ The filling fraction for this sample is $f=5\%$, so a maximum transmission of $T=10\%$ corresponds to a transmission twice as high as the geometric limit, or $I_{out}/I_{inc}=2$. This result is the more astonishing, since for the longest-wavelength peak $d/\lambda=1/6$, where the Bethe-Bouwkamp theory^{1,2} would predict $I_{out}/I_{inc}=10^{-3}$.

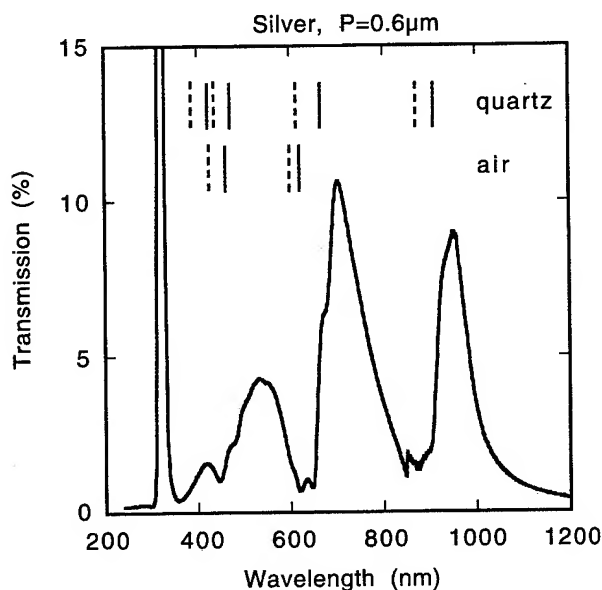


Figure 3. Zero-order transmission spectrum of silver film perforated with square array of circular apertures

The amplitude of the zero-order enhanced transmission is largest for the longest-wavelength resonance, $i+j=1$ and $\lambda=n_{eff}P$, which is beyond the diffraction limit ($\lambda=P$). In

general, for higher orders (shorter wavelength) the transmission maxima are lower, because a significant portion of the incident light is directed into diffracted orders. Indeed, whenever a diffracted order emerges tangent to the metal film, a resonance with the periodic structure at the surface causes it to usurp a large fraction of the energy. This effect, known as the Wood's anomaly,¹¹ results in deep minima in the zero-order transmitted light, at wavelengths indicated by the dashed (blue) markers in Figure 3. The surface plasmon maxima and the Wood's anomaly minima occur at very similar wavelengths because for a good metal such as silver n_{eff} is only slightly larger than n_d , the refractive index of the dielectric.

For a metal film lying on a dielectric substrate, in general the two sets of surface plasmon resonances from the two sides of the metal film occur at different wavelengths.⁵ However, when the refractive indices of the dielectrics on either side of the metal film are matched, either by applying an index-matching fluid on a supported metal film, or by making a free-standing perforated film, the an additional resonance between the surface plasmon modes on both sides of the metal film results in an additional transmission enhancement¹² of about a factor 10.

3.2 Single Apertures

Similar results are found even for the case of an isolated aperture in a metal film,^{3,13} as long as the metal surface surrounding the aperture has a periodic corrugation.

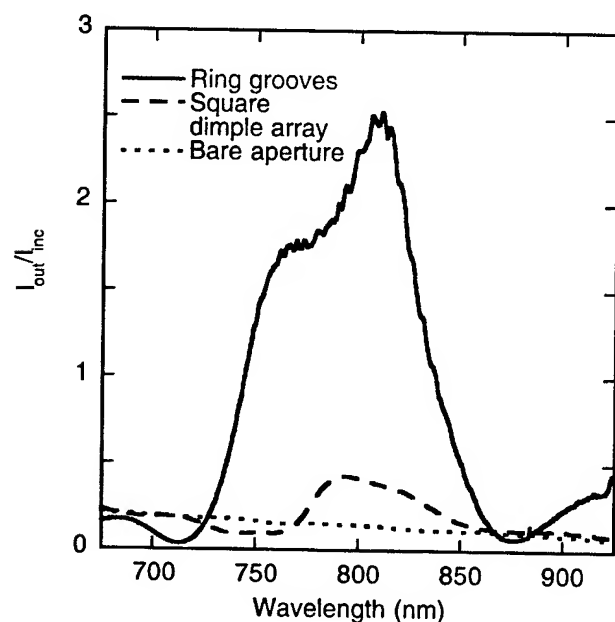


Figure 4. Transmission spectra of single aperture, enhanced and "bare"

Figure 4 shows the transmission spectra of a single aperture ($d=300\text{nm}$) in a silver film of which the surface has been patterned, either with a square array of indentations (dashed blue line), or with a series of concentric grooves around the

central aperture (solid red line). The depth of the indentations or grooves are shallow enough that no light passes through the metal film when the central aperture is absent. The square-symmetry surface corrugation clearly shows an enhancement compared to the transmission of a "bare" aperture in an otherwise smooth metal film (dotted line in Figure 4).

However, the ring grooves are much more efficient at generating the transmission enhancement. This is because the two-dimensional Huygens waves emanating from the central aperture have circular symmetry and therefore are much better matched to the surface plasmon modes on the ring structure than those of the square array of dimples, in which the surface plasmon modes are plane waves. Indeed, a systematic study³ has shown that the ring structure is the optimal geometry of surface corrugation for generating the maximum enhancement for a single aperture. The rings are equally spaced with a radial periodicity P , the optimal groove depth is 90nm , or about three times the skin depth of the metal (in this case silver). The width of the grooves should be about half the pitch, but sinusoidal or square-wave cross sections give similar results, implying that as long as the duty cycle is 50% the exact cross section is less important.

For the optimal geometry (See solid square symbols in Figure 1 and solid line in Figure 4) the maximum transmission coefficient can exceed the geometric limit by a factor of three.

4. Applications

The extremely high transmission efficiencies, and the tunability of the resonant wavelength, makes surface-plasmon enhanced transmission very promising for a number of applications.

High-efficiency near field devices have the potential to enable novel read-write heads for data storage devices with dramatically increased densities.¹⁴ The transmitted intensities possible match those required for writing data on phase-change media, or on magnetic media using heat-assisted magnetic recording (HAMR). For data densities about $1\text{TB}/\text{in}^2$, the spot size should be about 25nm . The near-field requirement that the distance between the aperture exit and the storage media must be comparable to the bit size is already fulfilled by current-technology fly heads, which can hover over the storage media at a 10nm distance.

In addition, near-field scanning optical microscopy (NSOM)¹⁵ can benefit greatly from surface-plasmon enhanced transmission through subwavelength apertures. The transmission enhancement factor F_{SP} , that is the ratio of the enhanced transmission to that of the "bare" aperture, scales as $F_{\text{SP}} \sim 1/d^2$, meaning that the largest enhancement effect is obtained for the smallest apertures where a transmission boost is most needed. The enhanced transmission makes possible the probing of processes which have so far eluded NSOM users because of the limited throughput of the near-field probes. Examples include very fast scanning rates, with video-rate

imaging being the benchmark target, and the probing of non-linear optical processes such as enhanced second-harmonic generation, and NSOM imaging of Raman scattering processes. The development of such probes would open up vast avenues for progress in the biological sciences.

Large-area arrays of apertures have the potential for applications as switches,¹⁶ for instance in integrated optics devices, or in display devices, especially for mobile applications. The proximity of the surface plasmon enhanced transmission peak to the Wood's anomaly minima makes it possible to control the transmission by varying the refractive index of the adjacent dielectric. We have demonstrated such a device using as the dielectric a liquid crystal which was used not as a birefringent but as a medium of which the effective refractive index can be varied by application of an external voltage. What makes surface enhanced transmission devices particularly attractive for mobile display devices is the large transmission efficiencies which in practice result in longer battery life.

5. Conclusions

One can boost the transmission of even very small, sub-wavelength apertures in metal films considerably by placing a surface corrugation in the vicinity of the aperture(s). This allows an interaction of the light incident on the metal surface with surface plasmon polaritons. When the interaction is resonant there is a large electric field enhancement at the surface, similar to that observed in surface-enhanced Raman scattering (SERS) which gives rise to a large enhancement in the transmission through the subwavelength aperture. The wavelength at which the resonance occurs is tunable: the surface corrugation fabricated with a pitch matching that of the desired laser wavelength. The rather large width (~60nm) of the resonances allows some room for spectroscopic

measurements. We expect this phenomenon to be important in a diverse variety of applications requiring high controllable transmission and very high resolution.

6. References

- ¹ H.A. Bethe, *Phys. Rev.* **66**, 163 (1944).
- ² C.J. Bouwkamp, *Rep. Prog. Phys.* **17**, 35 (1954).
- ³ T. Thio, K.M. Pellerin, R.A. Linke, H.J. Lezec, T.W. Ebbesen, *Opt. Lett.*, **26**, 1972 (2001).
- ⁴ T.W. Ebbesen, H.J. Lezec, H.F. Ghaemi, T. Thio, P.A. Wolff, *Nature* **391**, 667 (1998).
- ⁵ H.F. Ghaemi, Tineke Thio, D.E. Grupp, T.W. Ebbesen, H.J. Lezec, *Phys. Rev. B* **58**, 6779 (1998).
- ⁶ R.H. Ritchie, *Phys. Rev.* **106**, 874 (1957).
- ⁷ H. Raether, *Surface Plasmons on Smooth and Rough Surfaces and on Gratings*, Vol. 111 of Springer Tracts in Modern Physics, Springer-Verlag, Berlin, (1988).
- ⁸ L. Martín-Moreno, F.J. García-Vidal, H.J. Lezec, K.M. Pellerin, T. Thio, J.B. Pendry, and T.W. Ebbesen, *Phys. Rev. Lett.*, **86**, 1114 (2001).
- ⁹ U. Schröter and D. Heitmann, *Phys. Rev. B* **58**, 15419 (1998).
- ¹⁰ R.A. Linke, unpublished.
- ¹¹ R.W. Wood, *Phys. Rev.* **48**, 928 (1935).
- ¹² A. Krishnan, T. Thio, T.J. Kim, H.J. Lezec, T.W. Ebbesen, P.A. Wolff, J. Pendry, L. Martín-Moreno, F.J. García-Vidal, *Optics Communications* **200**, 1 (2001).
- ¹³ D.E. Grupp, H.J. Lezec, Tineke Thio and T.W. Ebbesen, *Adv. Mater.* **11**, 860 (1999).
- ¹⁴ T. Thio, H.J. Lezec, T.W. Ebbesen, K.M. Pellerin, G.D. Lewen, A. Nahata, and R.A. Linke, *Nanotechnology* **13**, 429 (2002).
- ¹⁵ B. Hecht, B. Sick, U.P. Wild, V. Deckert, R. Zenobi, O.J.F. Martin, D.W. Pohl, *J. Chem. Phys.* **112**, 7761 (2000).
- ¹⁶ T.J. Kim, T. Thio, T.W. Ebbesen, D.E. Grupp and H.J. Lezec, *Opt. Lett.* **24**, 256 (1999).



Tineke Thio
NEC Research Institute
4 Independence Way
Princeton NJ 08540, USA
tineke@research.nj.nec.com

<http://www.neci.nj.nec.com/homepages/thio/>

Tineke Thio obtained her physics degrees from MIT, where she did thesis and postdoctoral work on high-temperature superconductors. In 1990 she joined the NEC Research Institute where she is currently a Senior Research Scientist. Her varied interests have included deep defects in semiconductors, the metal-insulator transition, and extraordinary magnetoresistance in high-mobility semiconductors.

Polypropylene heterophasic copolymer for loose tube buffers

Bo Malm

Borealis Polymers Oy
PO Box 330, FIN-06101 Porvoo, Finland
+358 9 39 49 00
bo.malm@borealisgroup.com

Pekka Heikkilä

Borealis Polymers Oy
PO Box 330, FIN-0601 Porvoo, Finland
+358 9 39 49 00
pekka.heikkila@borealisgroup.com

Mikko Lahti

Nextrom Oy
P.O. Box 44, FIN-01511 Vantaa, Finland
+358 9 502 51
mikko.lahti@nextrom.com

Ruth C. Dammert

Borealis AB
SE-444 86 Stenungsund, Sweden
+46 303 86 000
ruth.dammert@borealisgroup.com

Abstract

Several different cable constructions exist to protect optical fibres from all kind of stresses during manufacturing, storage, transport, installation and operation. The loose tube cable design has become very popular as the buffer tube can easily be stripped for jointing.

A material suitable for loose tube buffers must fulfill several requirements. The buffer must hold its dimension, be tough, have good heat ageing properties and be flexible. Polybutylene terephthalate (PBT) and polyamide (PA) have traditionally been used in loose tube buffers. Polypropylene (PP) has many properties that are advantageous such as low density, flexibility at low temperatures, good processability, hydrolytical stability and low cost. Furthermore, PP is not sensitive to kinking. The most important aspect of the manufacturing process for loose buffers is the precise matching of the length of the buffer tube with the optical fibre. The tube is extruded around fibres and simultaneously filled with gel. This three-phase system has to be optimised.

This study was made in order to investigate which structure properties of heterophasic PP copolymers affect one of the main requirements for loose tube buffers, namely the excess fibre length (EFL) and shrinkage.

Keywords

Polypropylene; PP; heterophasic copolymers; loose tube buffers; excess fibre length; shrinkage.

1. Introduction

Polypropylene (PP), the most versatile commodity polymer, has been and remains the fastest growing major polymer. The consumption today is around 30 million tons globally and an estimated consumption of 40 million tons in 2005 [1]. PP homopolymers, random copolymers and heterophasic copolymers are known to give a broad range of material properties. Polypropylene (PP) has many properties that are advantageous such as low density ($<900\text{--}917\text{ kg/m}^3$, depending on comonomer content), flexibility at low temperatures, good processability, hydrolytical stability and low cost. Development of new highly efficient catalysts and new process technologies (e.g. Borstar[®] technology) has further enlarged the possibilities to produce higher value enhanced performance products that meet new market needs.

PP homopolymers are tailored by the tacticity, stereoregularity. They have high melting temperature of $160\text{--}166^\circ\text{C}$. The stiffness is

high but the impact properties are low. Random copolymers are statistical copolymers with one or several comonomers (generally ethylene). They have low melting temperature $130\text{--}150^\circ\text{C}$. The stiffness is low depending on the comonomer amount incorporated. The impact properties are low at temperatures below room temperature.

A good balance of stiffness and low temperature impact is the key for using and tailoring the properties of the heterophasic PP copolymers. A heterophasic PP copolymer is also known as 'impact PP copolymer' or 'PP block copolymer'. The heterophasic copolymers are PP reactor blends. The final product is a complex system consisting of a PP homopolymer or a random copolymer matrix with ethylene-propylene copolymers dispersed into it (see Figure 1, transmission electron microscopy (TEM) image). The properties are achieved with a polymer structure where an elastomeric phase, usually ethylene-propylene copolymer rubber, is dispersed uniformly within the PP homopolymer matrix [2].

The PP homopolymer matrix with high stereoregularity gives the stiffness of the copolymers. The matrix share can be in the range of 60–90 w% of the heterophasic copolymer. The matrix can also be tailored for high melt strength and right flowability.

The rubbery copolymer phase designed by the content, the composition and the dispersion gives the low temperature impact properties of the heterophasic copolymers.



Figure 1. Rubber particles distributed in a heterophasic PP copolymer (TEM image)

The trend of the market is to enhance the rigidity of material while retaining the impact properties. This can be done by adding different kinds of external nucleating agents. When using Borstar® PP technology it is possible to control crystallisation and maximise the stiffness properties and/or reduce the cycle times in processing due to fast crystallisation without these external nucleators.

Borstar® PP technology creates new possibilities for product differentiation in extrusion for film, pipe and cable applications, moulding for thin wall and transport packaging.

Several different cable constructions exist to protect optical fibres from all kind of stresses during manufacturing, storage, transport, installation and operation. Filled loose tube cables represent the largest category among fibre optic telecommunication cables [3]. A material suitable for loose tube buffers must fulfill several requirements. The buffer must hold its dimension, be tough, have good heat ageing properties and be flexible. Polybutylene terephthalate (PBT) and polyamide (PA) have traditionally been used in loose tube buffers. Recently studies of the use of polypropylene (PP) have been reported [4, 5, 6, 7, 8]. PP has many properties that are advantageous for buffer tubes, as mentioned above. Furthermore, PP is not sensitive to kinking. The most important aspect of the manufacturing process for loose buffers is the precise matching of the length of the buffer tube with the optical fibre. The tube is extruded around fibres and simultaneously filled with a gel. This three-phase system has to be optimised [3]. This study was made in order to investigate which structure properties of heterophasic PP copolymers affect one of the main requirements for loose tube buffers, namely the excess fibre length (EFL) and shrinkage.

2. Experimental

2.1 Materials

Table 1. Heterophasic PP copolymers studied

PP copolymer	MFR ₂ (230°C) g/10 min	Nucleation type	Ethylene content (w%)
BD1	7.1	No	7.8
BC2	3.5	Weak	8.8
BB6	1.5	No	9
BBp	1.4	Strong	4.6
BCp	3.5	Strong	4.8
BB3	4	Borstar	6.3
BB4	3	Borstar	8.3
BA4	4	Borstar	8.2

The heterophasic PP copolymers investigated in this study are shown in Table 1. The copolymers had different MFR, rubber content and nucleation type. All the copolymers have good stiffness of 1400 - 1500 MPa and good low temperature impact. The rubber content is indicated by the ethylene content (C2 in w%) in the polymer. The molar mass (Mw) of the rubber is usually measured by intrinsic viscosity (IV) in decaline. The similar copolymers, BCp, BB4 and BA4 have low Mw (IV = 2,5 dl/g) and BB3 has high Mw (IV = 3 dl/g). Nucleation indicated by 'weak' corresponds to a weak nucleating agent (as talc here). 'Strong' again relates to a strong nucleator (as Na-benzoate or Na-phenylenephosphate). Borstar corresponds to Borstar® PP technology mentioned above (without external nucleation agents).

PP buffering requires a special jelly composition. The thixotropic gel, which was used in this study, was chosen according to an earlier study where the jelly selection was optimized for high speed PP buffering [8].

2.2 Test Methods

MFR was measured according to ISO 1133 (at 230°C and 2.16 kg load). Ethylene content was determined by FTIR (Fourier Transform Infrared Spectroscopy) calibrated with PP materials that were previously measured by NMR (Nuclear Magnetic Resonance Spectrometer). DSC (Differential Scanning Calorimeter) measurements for crystallisation temperature were done by an internal method using a cooling speed of 80°C/min from a 210°C melt.

Excess fibre length (EFL) was measured from 40-meter samples instantaneously after the processing. 40-meter sample was placed on the table and 5-meter sample was cut out in the middle of the sample. The fibres were pulled out and the length of the fibres was compared to the length of the tube.

Some further investigations were carried out in order to verify the EFL behaviour as a function of time. The tube was stored at ambient temperature on the reel and the EFL was measured 24 hours after processing the sample. This measurement was then treated as the shrinkage of the buffer tube.

2.3 Experimental Set-Up

A high-speed secondary coating line was used in this study. Figure 2 presents the line configuration. It consists of a fibre pay-off, continuous jelly filling system, 60-mm extruder, cooling trough and automatic dual take-up. The cooling system is equipped with a middle capstan that is placed over the cooling trough. The location of the middle capstan can be optimised according to the process needs. The line speed was set to be 200 m/min.

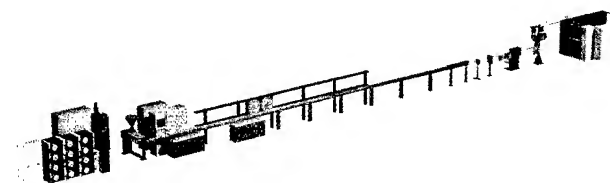


Figure 2. Secondary coating line

3. Results

3.1 MFR and nucleation

A too high or low MFR affects the melt strength and thus the extrudability of the buffer tubes. The PP copolymers BD1, BC2, BB6 and BBp with a MFR from 7 to 1,5 were used for this evaluation. The MFR 7 material BD1 gave lumpy, uneven tubes and the BB6 and BBp materials showed bad processability due to the low MFR. The best processability of the buffer tubes was reached for PP copolymers with MFR 3-5.

In addition the PP copolymers had to maintain fast crystallisation in order to obtain fast freezing of the tube without deformation. The fast freezing of the PP copolymers was tested by DSC with high cooling speed of 80°C/min. The results are seen in table 2.

Table 2. Freezing of the PP copolymer due to different crystallization techniques

PP copolymer	T _{cr} (°C) with -80°C/min	EFL (%)	Nucleation
BC2	103	0.1	Weak
Bp	113	0.07	Strong
BB3	112	0.05	Borstar
BB4	111	0.04	Borstar

The Borstar concept showed a similar freezing effect as a polymer with strong nucleating agent incorporated. The positive effect on excess fiber length was also seen.

3.2 Rubber Content and Composition

The rubber amount is the main parameter giving the low temperature impact properties of the heterophasic PP copolymers. In addition the content affects indirectly the shrinkage of the copolymer because only the crystalline matrix can shrink in the extrusion process. The more rubber incorporated in the copolymer the less matrix is present and thus less shrinkage is obtained. The rubber composition again affects the dispersion of the rubber particles in the PP matrix. A lower Mw of the rubber is an advantage in this high-speed application.

The following PP copolymers were tested, see table 3.

Table 3. The effect of rubber on EFL and shrinkage

PP copolymer	Rubber C2 (w%)	Rubber Mw	EFL (%)	Shrinkage (%)
BCp	4.8	Low	0.07	0.14
BB3	6.3	High	0.05	0.12
BB4	6.3	Low	0.04	0.09
BA4	8.2	Low	0.03	0.05

The results show that the higher rubber content (high C2 content) gave a shorter excess fiber length (EFL) but also less shrinkage (measured from buffer tubes on reel) than the materials with less rubber. A higher Mw of the rubber indicates to give more shrinkage.







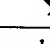
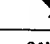
3.3 Matrix Stereoregularity

For high stiffness heterophasic PP copolymers the matrix is produced with a high isotacticity (stereoregularity). With higher tacticity the crystallinity is increased and thus also the shrinkage ability. Therefore the matrix for optimised PP copolymers for buffer tubes should be tailored for high enough stiffness but with low shrinkage. In Table 3 the PP copolymer BA4 was produced with lower tacticity compared to the BB4 material. The measured shrinkage was clearly decreased.

3.4 Effect of Process Parameters

The main process parameters as the pay-off tension, line speed, cooling water (trough) temperature and position of the middle capstan (DWC) were investigated in terms of excess fiber length (EFL). Table 4 presents the main effects of the process parameters on EFL and shrinkage.

Table 4. Effect of line parameters on EFL and on shrinkage

Process parameter	EFL	Shrinkage
Increase of:		
- Line speed		
- Capstan position		
- Water temperature		
- Fiber tension		

EFL and shrinkage are increased as a function of line speed. Rapid cooling under tension can create internal stress if the crystallisation process is not fast enough.

The capstan position plays an important role in PP buffering. The EFL range can be controlled from 0.05% to 0.30% by only changing the capstan position. When the middle capstan is too close to the cross head then the crystallization will dramatically affect on EFL. The tube crystallises on the middle capstan and it will lead to uncontrolled EFL and high shrink back characteristics.

Cooling water temperature has a strong effect on EFL, which is increased exponentially with temperature. When cooling water temperature is increased then the shrinkage is decreased.

The increase of the pay off tension decreases the EFL rather linearly which seems to correspond with the theoretical value of the fiber strain at the set tension. When the pay off tension is increased above 100 g, the decrease of the EFL will slow down. The phenomenon is typical also for PBT production. When the tube leaves the middle capstan, the high strain of the fibers will be released and then decreasing the EFL. The relaxation of the fiber strain starts to have an effect also on the tube. The strain is slightly decreasing the shrink back tendency of the tube.

4. Conclusions

The properties of great importance for loose tube buffers, namely shrinkage and processability, can clearly be improved by tailoring heterophasic PP copolymers.

Table 5 shows the lowest EFL and shrinkage that can be reached by tailoring heterophasic PP copolymers for this application. The matrix should be optimised for tacticity, MFR and right control of crystallisation.

Table 5. Effect of PP structure properties vs. buffer tube properties

PP parameter	High Processability	Low EFL	Low Shrinkage
Tacticity of matrix	Low	Low	Low
MFR	Optimum MFR 3-5		
Nucleation	Controlled crystallisation	Strong	Strong
Rubber content	Medium/High	Medium/High	Medium/High
Rubber Mw	Low	Low	Low

This control of crystallization can be obtained by strong nucleating agents or Borstar technology. The rubber content should be high enough for good impact properties and the rubber composition should be optimised for good dispersion of the rubber particles. The correct selection of polymer and gel together with optimised process parameters can guarantee a high-quality PP buffering process.

5. References

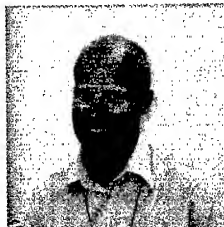
- [1] G. van Os, "The European Plastic Industry - A sunset industry," in *Polymers in Europe Quo Vadis, EPF, Special issue*, (July 2001).
- [2] E. P. Moore, Jr., *Polypropylene Handbook*, Hanser/Gardner Publications, 245-249 (1996).
- [3] O. S. Gebizlioglu, "Time- and Temperature-Dependent Material Behavior and Its Impact on Low-Temperature Performance of Fiber Optic Cables," *Mat. Res. Soc. Symp. Proc.* (Vol. 531), 333-345 (1998).
- [4] M. Adams, J. Holder, C. McNutt, O. Tatat and H. Yang, "Buffer Tubes - The Next Generation," *Proc. 44th International Wire & Cable Symp.* 16-21, (November 1995).
- [5] B. G. Risch, "Influence of Nucleating Agent and Melt Flow Index on Impact Polypropylene Fiber Optic Buffer Tubes," *56th Annual SPE ANTEC Conf. Proc.*, 1016-20 (1998).
- [6] B. G. Risch, J. Auton and O. Tatat, "Advanced Impact Polypropylene Buffering Material for Superior Long Term Hydrolytic and Thermo-oxidative Stability," *Proc. 47th International Wire & Cable Symp.* 698-704, (November 1998).
- [7] B. G. Risch, G. Dallas and M. Barber, "Materials Advances in Next Generation Loose Tube Cables," *Proc. 48th International Wire & Cable Symp.* 199-204, (November 1999).
- [8] M. I. Lahti, "High Speed Polypropylene Buffering," *Proc. 49th International Wire & Cable Symp.* 445-448, (November, 2000).

Borstar® is a registered trademark of Borealis A/S, Denmark

6. Authors



Bo Malm (bo.malm@borealisgroup.com) received his M.Sc. degree in organic chemistry in 1970 and Ph. Lic. in polymer chemistry in 1979 from University of Helsinki. He joined Borealis (Neste at that time) in 1982 and has mainly been involved in the Research and Technology department in developing new PP polymers.



Mikko Lahti (mikko.lahti@nextrom.com) received the degree of M. Sc. in Chemical Engineering in 1991 and the degree of Dr. Tech. in Polymer Technology in 1996. Before joining Nextrom in 1997 he worked as Research Scientist in European Joint Research Center in Milan. Currently, as Manager of Secondary coating lines, he is responsible for the development of the buffering process for fiber optic cables.



Pekka Heikkilä (pekka.heikkila@borealisgroup.com) received his M.Sc. degree in Materials engineering in 1988. Before joining Borealis in 1994 he worked in development projects with reinforced plastics for companies Exel and Neste Chemicals. At Borealis he has worked as Development and Technical Service engineer for polypropylene compounds and he is currently responsible for the sales of Borealis Wire and Cable products to Scandinavia and Baltic countries.



Ruth C. Dammert (ruth.dammert@borealisgroup.com) received her M.Sc. degree in organic chemistry from University of Helsinki, Finland, in 1986. After research work at Sandoz A.G., Basle, Switzerland, at University of Zürich, Switzerland and at University of Helsinki, Finland, she joined Borealis (Neste at that time) in 1989 and has since then mainly been involved in the development of materials for cable applications. She is currently application manager for Communication Cables at the Marketing and Development Centre Wire & Cable in Stenungsund.

Shrinkage of PBT, PP and PE in Central Tube Buffering Process

J. Kotala

Nextrom Oy, Ensimmäinen Savu, 01510 Vantaa, Finland

Tel. +358-9-50251, E-mail: juha.kotala@nextrom.com

Abstract

In this study the we were comparing the post shrinkage behavior of PBT, PP and HDPE. For that purpose we developed a central tube buffering process with minimized post shrinkage and possibility to control the fiber excess length from negative to very high positive values.

The condition for low post shrinkage is that the material is crystallizing in cooling trough as much as possible. This was realized by so called 'relaxation zone', where the tube was heated up by a hot water. At the same time the tube must be under no tension to enable the relaxation.

A series of ribbon buffering processes with excess lengths from zero to very high values were used to compare the three materials.

The line configuration and test results are presented and analyzed in this paper.

Keywords

Excess length; post shrinkage; relaxation.

Major reasons for post production shrinkage of loose buffer tubes are

1) Due to high processing speeds the crystallization is incomplete and will continue after the process.

2) Fast cooling under tension and the nonlinear cross sectional temperature distribution causes thermal stresses.

Annealing the tube in hot water in some stage of the process will enhance the crystallization speed and also releases the thermal stresses, thus minimizing the post shrinkage. Precondition is that this annealing happens under minimum tube tension. In this work we studied the effect of this annealing on PBT, PP and PE buffer tube process.

Another method used for minimizing the post shrinkage was compressing the buffer tube during the production.

Compressing between two haul-off is possible, if the fiber or ribbon bundle inside the tube has high enough tension to keep the tube straight.

1. Introduction

The line lay-out in figure 1 was set up in order to utilize the annealing and the compressing methods.

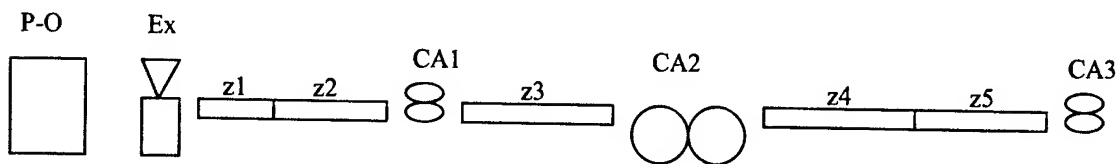


Figure 1: Line configuration
z1...z4, thermo controlled
z5 cold zone
z3 tension either speed difference or tension control
z4/z5 tension minimized

This lay-out was designed to fulfil the following assumptions:

1. The condition for low post shrinkage is that the material is crystallizing in cooling trough as much as possible. This was realized by so called 'relaxation zone', where the tube was heated up by a hot water, in order to enhance the crystallization. At the same time the tube must be under no tension to enable the relaxation. Furthermore the condition for zero post shrinkage is that the tube is compressed during the process. This was realized by the negative speed difference between the caterpillar CA1 and the dual wheel belt capstan CA2.
2. The condition for very high excess length value is that excessive length of fiber can be pulled into the buffer tube. This was realized by controlled stretching of the tube between the caterpillar CA1 and the dual wheel belt capstan CA2, which is pulling more fiber into the tube. In this case the relaxation must happen after the stretching.
3. The condition for negative fiber excess length is low crystallization after the locking point of the fibers (dual wheel belt capstan CA2) and high pay-off tension for the fibers (ribbons) before the locking point. In this case the relaxation must happen already before the first caterpillar CA1.

The relaxation of the tube is especially important in the high excess length process, where the tube is first stretched. Besides the material properties, also the process parameters are affecting shrink back. That's why we made tests with sheer tube to determine the plastic material properties, and then the whole process with 6x12-fiber ribbon buffering.

2. Relaxation of sheer tube

All three plastic grades (PBT, PP and PE) used here are commonly used in cable factories for loose tube buffering. To study the effect of the relaxation zone on these materials, we produced sheer tube. Stretching was done in zone three (z3 in fig. 1) and relaxation in zone four (z4).

Test conditions:

Line speed	70 m/min
Tube dimensions	5.0/3.4 mm

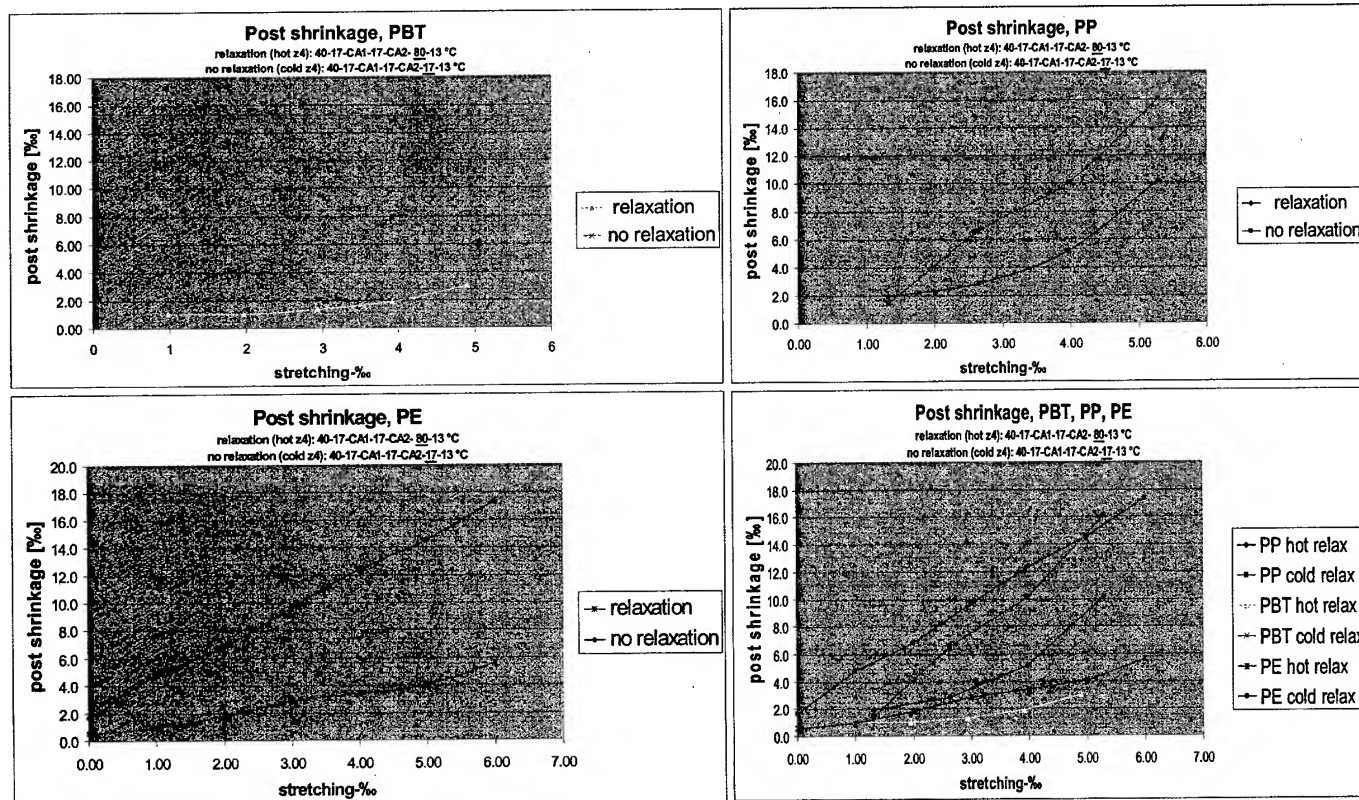


Figure 2: The effect of the relaxation on sheer tube

For PBT and PE the relaxation method seemed to have remarkable effect after stretching the tube. As expected for the PP tube the effect of the relaxation was not so drastic. A longer

dwelling time in relaxation trough might give lower shrinkage values for PP.

3. Ribbon buffering tests

For excess length and post shrinkage tests we produced 6x12-fiber ribbon in tube. id/od 5.0/7.5 mm. This relatively small number of ribbons was selected in order to save the scarce ribbon material, but the wall thickness was kept thick (1.25 mm) so the cross sectional area of the tube is equal to typical 12x12-fiber product.

Measurements

For each sample we measured the ribbon excess length (5 m sample), post shrinkage of the tube after 24 hours in room temperature (5 m sample) and tube shrinkage after one hour in 60 °C (average of three one meter samples cooled to room temperature after annealing).

Process parameters and test results

Three different methods were used to control the excess length

I) For high excess length values the tube was stretched between CA2 and CA1 (zone 3). Relaxation under minimum tension in zone 4.

II) Temperature difference on both sides of the locking point CA2 for fibers. Relaxation in zone 2. CA2-CA1 speed difference negative (compression of the tube).

III) High fiber/ribbon tension for zero or negative excess length. Relaxation in zone 2. CA2-CA1 speed difference negative (compression of the tube).

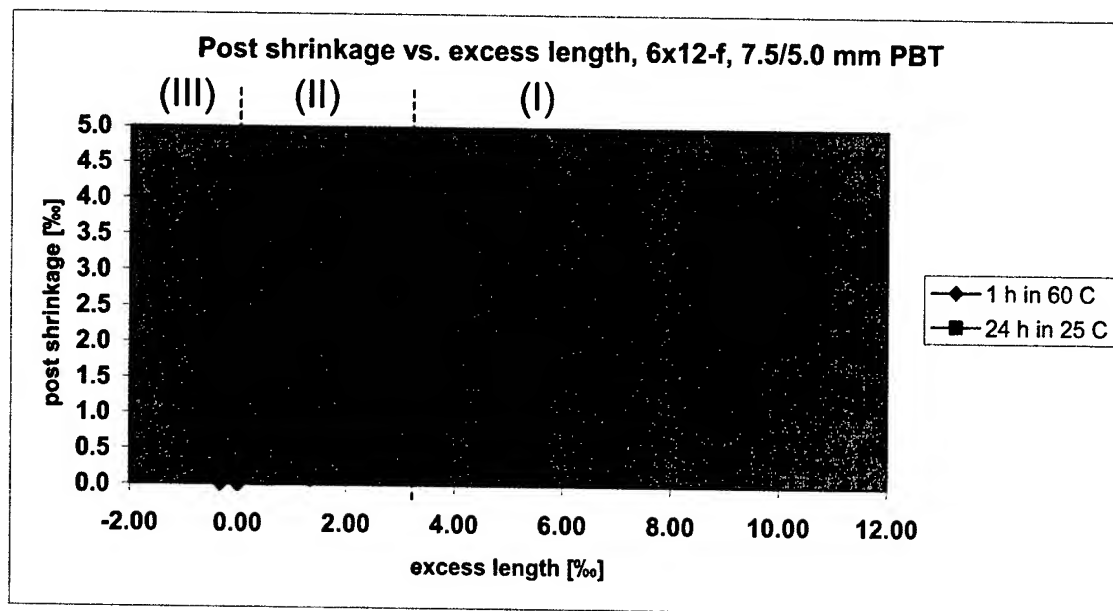


Figure 3.Excess length controlled mainly by

- (I) controlled stretching, relaxation in z4
- (II) thermal shrinkage, relaxation in z2
- (III) ribbon stack tension, relaxation in z2

Zero or negative post shrinkage in method (II) and (III) is possible, because in this process the tube was actually compressed between the CA1 and CA2, as can be seen from the negative speed difference. Compressing seemed to give even negative shrinkage values after 1 h annealing in 60 °C . Nevertheless this was not a stable condition,

because after 24 hours in room temperature the shrinkage was always positive, although the values were small.

The effect of the relaxation zone

To determine the effect of the relaxation zone, we produced a reference sample with each three methods mentioned above, but without relaxation.

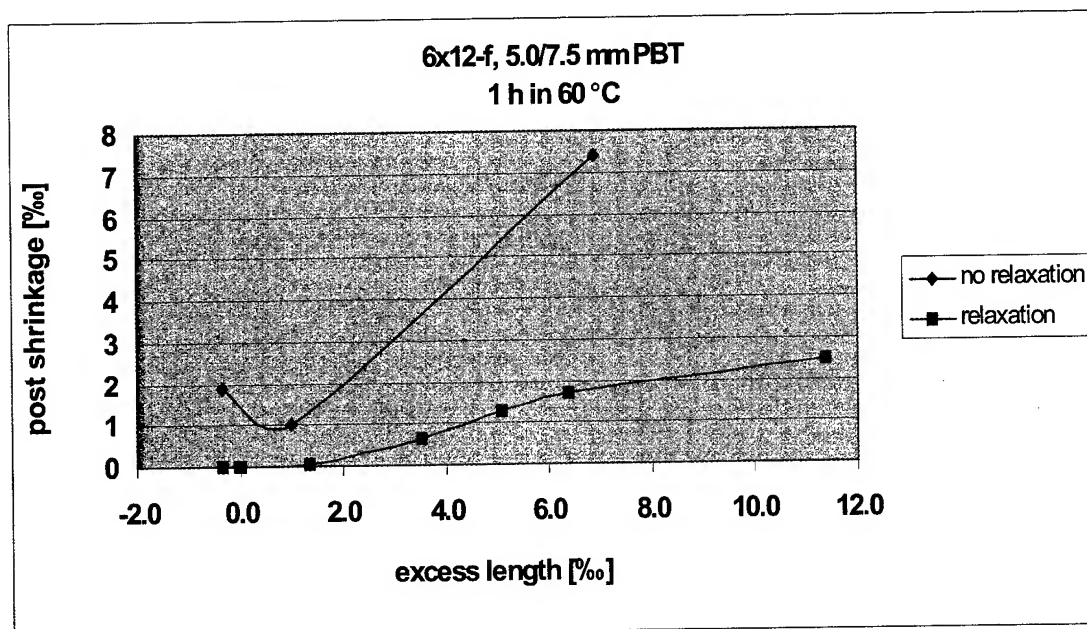


Figure 4: Effect of the relaxation on PBT tube

The results indicate that relaxation has remarkable affect on both post shrinkage and excess length itself. Especially by method (I)

(controlled stretching) the needed stretching force for desired excess length value is much smaller when relaxation is used.

3.1 Combined results for PBT, PP and PE buffering process

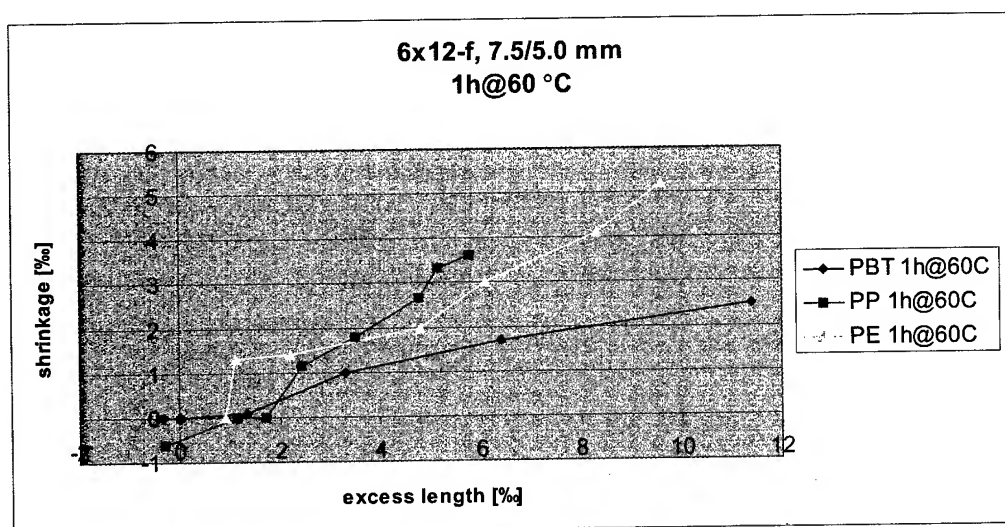


Figure 5a: Excess length vs. post shrinkage, annealing 1 h in 60 °C

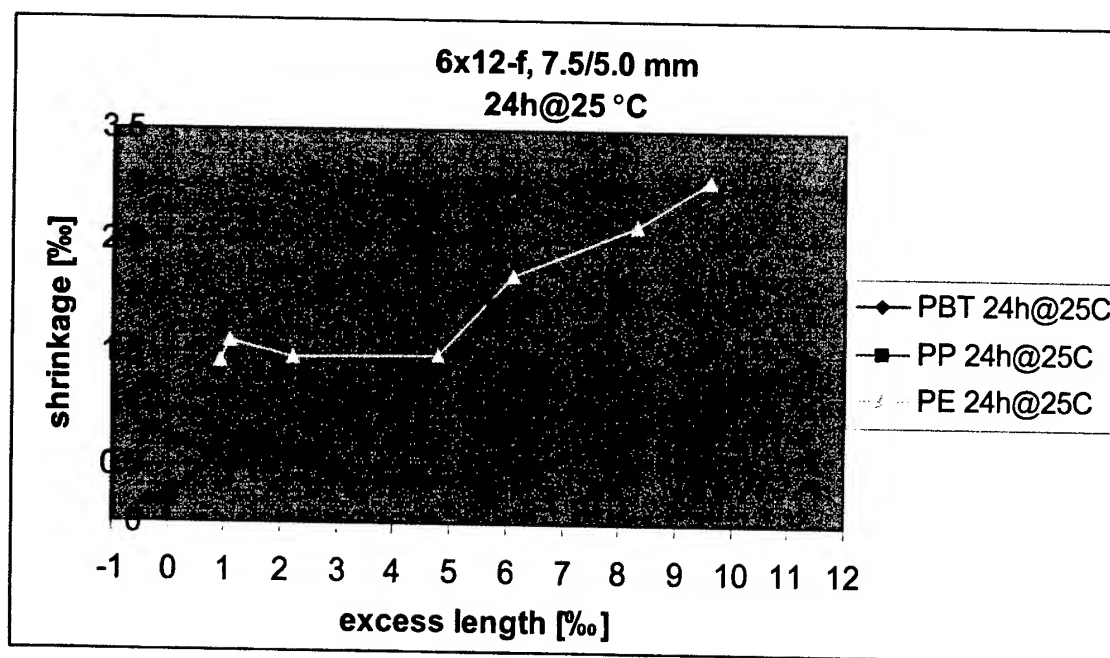


Figure 5b: Excess length vs. post shrinkage, 24 h in room temperature

4. Conclusions

Zero post shrinkage was achieved with small excess length value products. For very high excess length value products the post shrinkage was remarkable low with PBT. For PP the effect of relaxation is not very big. This results to higher shrink back values at high excess length process. Secondary effect is that it is not easy to reach very high excess length values with PP, because relaxation is not creating so much 'extra' excess length.

the tube proved to be right. Even better results with high excess length values might be possible by optimization of the cooling profile and the amount of compressing.

The assumptions about the enhanced crystallization and compressing



Juha Kotala
Nextrom Oy
P.O.Box 44
Fin-01511 Vantaa
Finland
e-mail: juha.kotala@nextrom.com

Juha Kotala obtained his bachelor's degree in telecommunications in 1981. Nextrom company he joined in 1986. For Fiber Optic Cable department he has worked since 1991 as a commissioning and process engineer, he also worked in Nextrom's Shanghai office as a technical manager for three years. Since 1998 he has worked as Product Manager of Central Tube Concept.

Investigation of Possibilities for the Proof Testing of Optical Fiber Immediately after Draw

Mika Lipponen

Optical Fiber, Nextrom Oy

Vantaa, Finland

+358-9-5025-3063 · mika.lipponen@nextrom.com

Harri Turunen

Optical Fiber, Nextrom (USA), Inc.

Duluth, Atlanta

+1-678-957-3517 · harri.turunen@nextrom.com

Abstract

In this paper, we investigate the limitations for the on-line proof testing of optical fiber. The strength of optical fiber is strongly dependent on stress corrosion. This chemical reaction does not occur immediately after the drawing process, and it takes several minutes before the strength of optical fiber is balanced to the normal level. This is primarily due to moisture, which diffuses from the ambient environment through the coating material to the surface of the glass.

Another interesting issue that is investigated in this study is the dwell time of the proof test. Due to the increased production speed that shortens the dwell time, the lifetime estimations calculated with the commonly used power law will be decreased. This can be compensated by raising the tension of the proof test.

Finally, we set up a test for an automatic break recovery system. The basic idea is to investigate the problems of threading fiber inside a tube during random fiber breaks when proof testing at full line speed.

Keywords

Proof test; mechanical strength; mechanical reliability; on-line proof testing; dwell time.

1. Introduction

The highly competitive optical fiber cable business forces cable machinery manufacturers to develop highly efficient equipment with the highest production capacity. With an on-line proof tester we can combine two separated processes, the fiber draw and the proof test. By using this approach the setup times can be reduced, and therefore remarkable economical benefits can be achieved.

There are some theoretical as well as practical problems concerning the on-line proof tester. The greatest problem has been the constraints on proof testing fiber immediately after the draw. The main issue is to maintain the mechanical reliability at the same high level as with proof testing fiber with a conventional proof tester. This is a combination of well-maintained proof tension and dwell time. Recovering from a random fiber break is the biggest challenge for the machinery. The on-line proof tester has to be able to handle fiber breaks at full line speed without disturbing the draw process. The reel change has to also be done without disturbing production.

2. Theory

2.1 The Effect of Water on the Strength

When drawing fiber, the preform has to be heated to approximately 2000°C. The fiber cools rapidly during the draw and remains dry. If the fracture strain of the fiber is measured immediately after the draw [1], an obvious decrease in strain during the time after draw is seen. The value of the fiber strength decreases in a similar way.

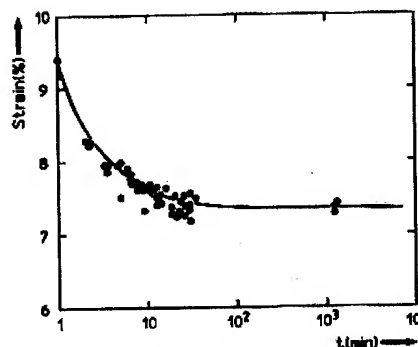


Figure 1. Fracture strain for dynamic fatigue measurements of fiber as a function of time t after drawing from the preform. [1]

This phenomenon is caused by stress corrosion, the effect of which begins immediately after stress is applied on the fiber, and moisture is diffused through the coating material to the surface of the glass. The water entry into a glass can promote structural relaxation, and this leads to strength reduction. Figure 1 shows that fracture strain balances in 50 minutes after the draw. This value is dependent on the coating material's permeability for water. The coating material's main functions are to protect the fiber from mechanical abrasion and to reduce microbending; however, it also works as a diffusion barrier against water.

Figure 2 shows the raw data for strength as a function of time after changing the ambient environment for the acrylate, polyimide, and silicone-coated fibers [2]. A two-point bend apparatus was used to measure the strength of fiber and it was operated with a constant faceplate velocity of 5000 $\mu\text{m/s}$. Twenty samples were broken at each humidity level. For all the coatings, moisture penetrates on a time scale of $\sim 10^2 - 10^3$ s [2]. It can be seen in Figure 1 that fracture strain balances simultaneously.

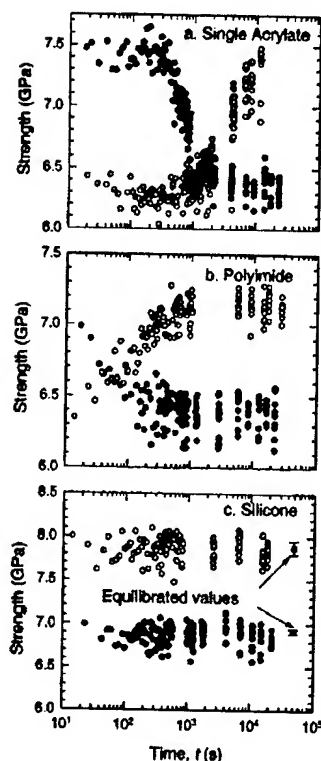


Figure 2. Strength as a function of time after suddenly changing the ambient humidity for the diffusion of moisture into (•) and out of (○) single-acrylate-coated fibers, polyimide fibers, and silicone-coated fibers [2]

If we consider proof testing fiber immediately after the draw, we have to take into account the fact that fiber is considerably dry (as in an inert environment), and the strength balances only after several minutes from the draw. In that case the proof test tension has to be multiple compared to a conventional proof tester, and that would cause the weak spot to fracture. Therefore, the chances of damaging the warm and soft coating are higher. The preferred manner would be to wait for some time after the draw and execute the proof test later.

2.2 The Effect of the Coating Material on Mechanical Properties of Optical Fiber

Earlier the theory determined the strength of fiber almost entirely based on the strength of the glass. Due to changes in dynamic fatigue test results, the behavior of the coating material in different strain rates has been studied. It has to be noted that 75 percent of the volume of fiber is coating material and only 25 percent is glass.

Standards (IEC 60793-1-30, TIA/EIA-455-31C) state that proof stress shall be applied uniformly through the cross-sectional area of the test sample [3, 4]. When the results of dynamic fatigue tests are examined, it is seen that contribution of the secondary coating can significantly affect the dynamic fatigue measurement of

optical fiber [5]. Test was performed using six different stress rates: 0.005 %, 0.025 %, 0.25 %, 2.5 %, 25 % and 100 % per minute of gage length.

The problem has been the so-called S-shape existence within the log-stress rate/log-break stress curve of the dynamic fatigue test. It has been proven that the strength of the fiber coating is strain rate dependent, and that the contribution of the secondary coating can significantly affect the dynamic fatigue measurement of optical fiber. The thicker the coating, the more load is exerted on the coating. The effect is also similar when using high strain speeds; the faster the strain rate, the more load the coating carries. [5]

Optical fiber manufactures commonly use the proof test tension of 0,69 GPa, which correlates to elongation of 1 %. Due to increased production speeds, the loading rate of the proof stress can be extremely high, around 150-250 GPa/s. In such a case the coating can carry a substantial part of the proof tension during the proof test and the risk of inadequate stress exertion to glass fiber could be possible. Therefore it is recommend that higher proof tension be used with an on-line proof tester than with a conventional proof tester.

Another remarkable issue is the temperature dependence of the viscoelastic properties of the coating [6]. When glass fiber is coated, it goes to the UV-curing unit, where the coating material is cured. The temperature of the coating can be over the T_g -temperature, and therefore the microstructure is relatively soft. When proof testing fiber immediately after curing, it may be possible to damage the fiber unless it is properly cooled.

2.3 Dwell Time Effect on Lifetime Estimations

Proof testing standards require that a specified tension or proof stress be applied sequentially along the full length of the fiber. Because the starting of the drawing process is slow, all possible interruptions during the draw have to be minimized. The on-line proof tester requires an automatic break recovery system, and because of that, the proof test area has to be level. There is no possibility to use any weight wheel, and so the fiber line goes trough from the breaking capstan to the drive capstan, and the proof tension is measured directly from the capstan. Therefore, the proof test time t_d becomes short, approximately 0,01 s to 0,04 s depending on the line speed. Kapron shows [7] that increasing the proof stress level increases fiber reliability. In addition, increasing the dwell time has a similar effect.

For example, if a crack of initial strength S before proof testing survives the proof test, it is reduced to the strength S_p after proof testing as given by [7]

$$S_p^{n-2} = S_i^{n-2} - \frac{\sigma_p^2 t_p}{B} \quad (1)$$

Here B is the crack strength preservation parameter or B-value; fibers with a higher value of this parameter will experience

relative less weakening. In the above equation the effective proof time is given by [7]

$$t_p = t_d + \frac{t_1 + t_2}{n+1} \quad (2)$$

where n is the stress corrosion susceptibility parameter or n -value. Note in Eq. (2) that the dwell time is the biggest contributor to the proof time. By Eq. (1) the weakening of a crack clearly increases with the dwell time [7]. If the dwell time is shortened, the lifetime estimations decrease.

Reliability in service is characterized by a lifetime or by a failure rate. For survival probability P , the fiber lifetime to failure is

$$t_f = \left\{ \left[\frac{\beta^{m_s}}{L} \ln \frac{1}{P} + (\sigma_p^* t_p)^{m_s} \right]^{\frac{1}{m_s}} - \sigma_p^* t_p \right\} \sigma_s^{-n} \quad (3)$$

Note that when the applied stress increases, the lifetime will decrease quite rapidly [7]. Following lifetime calculations are performed with parameters shown in Table 1. Figure 3 shows results from lifetime calculations, which were made with 0.69 GPa proof stress. It is easy to see that when the dwell time is reduced, the lifetime estimations drop. When proof stress is doubled and the dwell time is maintained the same, the lifetime rises to a similar level than with common dwell times (0.1 s, 0.5 s, 1 s, 2 s).

Table 1. Parameters for the lifetime calculations

$F = 10^{-6}, 10^{-5}, 10^{-4}, 10^{-3}$	$\sigma_p = 0.69 \text{ GPa}, 1.38 \text{ GPa}$
$L = 1000 \text{ km}$	$\sigma_a = 0.15 \times 0.69 \text{ GPa}$
$\ln \beta = 25.499$	$t_d = 0.01 \text{ s}, 0.02 \text{ s}, 0.03 \text{ s}, 0.04 \text{ s}$
$m_d = 2.359$	$t_1 = 0.005 \text{ s}$
$n = 20$	$t_u = 0.005 \text{ s}$

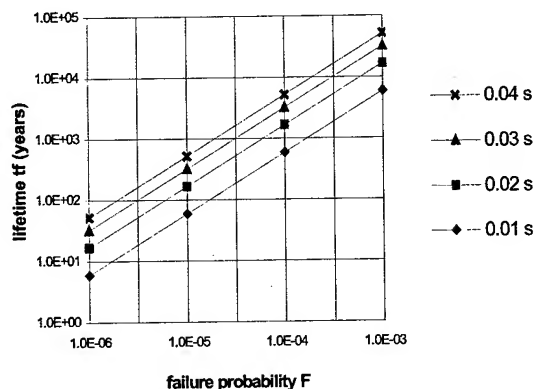


Figure 3. 1000 km Lifetime vs. failure probability for dwell times of 0.01 s, 0.02 s, 0.03 s, 0.04 s. Proof test stress 0.69 GPa.

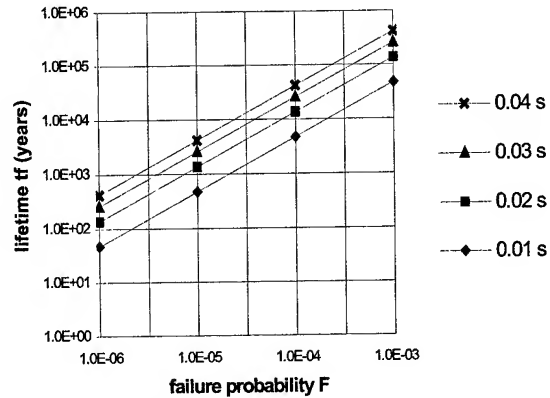


Figure 4. 1000 km Lifetime vs. failure probability for dwell times of 0.01, 0.02, 0.03, 0.04. Proof test stress 1.38 GPa.

Current industry standards use the power law form for lifetime prediction. It has to be taken into account that the power law theory has no physical significance and it gives an overly optimistic lifetime estimation compared to other forms based on chemical kinetics theories [8].

3. Possibilities for On-line Proof Tests

Based on the theoretical information presented above, three different approaches for on-line proof tests are suggested:

1. The moistening of the fiber with specified equipment immediately after the fiber comes out of the furnace. After UV-curing the fiber must be effectively cooled to room temperature, and after that the proof test can be executed.
2. Artificial aging before the proof test. This method utilizes an equipment that adjusts the pressure, temperature and moisture, and therefore accelerates the penetration of water through the coating to the surface of the glass. In addition, some chemicals can be used to activate the process. Before executing the proof test the fiber must be cooled to room temperature.
3. Using a very sophisticated accumulator between the drawing tower and the proof tester. This machine holds the fiber in ambient air for approximately 20-30 minutes regardless of the line speed. During this relaxation time the humidity and temperature of the fiber balances, and the proof test can be executed immediately afterwards.

4. Random Fiber Break

When proof testing fiber, there are occasional breaks depending on the quality of the drawing process. These occur approximately two or three times per 100 km (with good quality fiber) [9]. In a conventional proof tester fiber break causes a stop, and the operator has to thread the fiber again to the machine to continue the proof test. This interruption is not acceptable with on-line proof testing because ramping down the drawing process is a slow

process. The properties and functions of the on-line proof tester are described in patent FI108754.

There are also some patents concerning the so-called air-blown fiber, for example US4691896, US6022620, US5046815. Blown fiber is used when installing optical fiber to buildings or under ground piping. An airflow conveys the fiber inside the tube. On the surface of the fiber are small glass spheres, which help the transportation of the fiber. Some antistatic agents are also added to the airflow to minimize static electricity. In addition, the guiding duct can be made of an antistatic material (surface resistivity $\leq 10^6$ ohm).

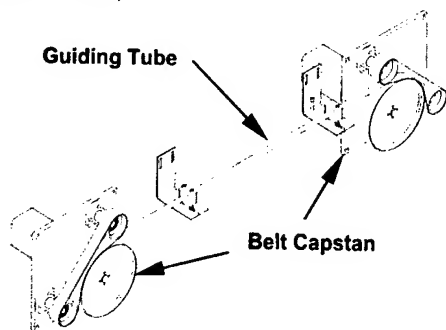


Figure 5. Test equipment

In the tests we focused on handling fiber breaks in the proof test region (test arrangement shown in Fig. 5). A guiding tube was located between the braking capstan and the drive capstan, and the proof tension was measured from the moving capstan with a load cell. Five different pipe materials were tested; glass acrylic, aluminum, inside polished steel, vinyl with carbon fiber and Teflon. The line speed was set to values from 250 m/min to 1750 m/min, and the break recovery probability was calculated from ten breaks per measured speed.

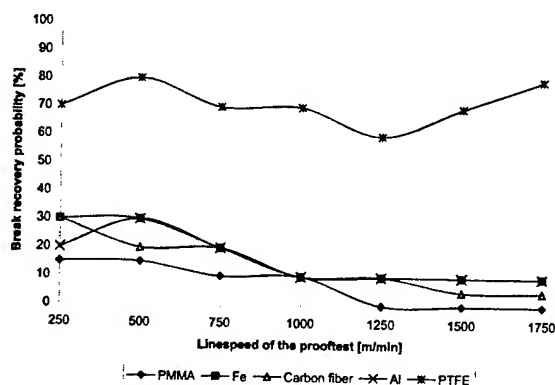


Figure 6. Break recovery result

As is clearly seen in Figure 6, Teflon is the best material; all the other materials induce reduction to the break recovery probability. This is caused by several different phenomena. First, Teflon is a quite effective insulator, and therefore it easily creates a strong surface electricity field around it. This field normally has the same polarity with the fiber. When we measured the surface

voltage of Teflon, the values ranged from +5 kV to +20 kV and varied excessively depending on the point of measurement on the tube. This charge works as an opposite force and helps to convey the fiber inside the tube. Second, the friction coefficient between the fiber and Teflon is extremely low, and therefore friction force breaks least compared to other materials. Third, the so-called "rubber band effect" at the proof test region interferes with the threading event. This is probably the reason why we did not manage to receive a 100 % probability.

4.1 The Elimination of Static Electricity

When the fiber is led through the belt capstan, the surface voltage rises from zero to approximately +1.4 kV to +1.6 kV. This value was measured with a non-contacting voltmeter, and the result must be regarded only as trend-setting. The high surface voltage is a result of frictional electricity, which is created when the rubber belt and the steely capstan wheel touch the fiber. When we calculated the effect of static electricity, it became clear that the electrical force can push the fiber against the inside of the tube much stronger than the gravity force.

Elimination of static electricity is crucial in order to convey the fiber inside the tube, and therefore static electricity has to be removed as soon as possible after the fiber comes out of the capstan. This is resolved by using ionizing air nozzles which blow ionized air into the guiding tube, or an ionizer which has corona points inside the guiding tube. In such a case it should be noted that the tube cannot be made of any conductive material, or otherwise it reduces the effect of the ionizer.

5. Conclusions

The strength of fiber balances after several minutes from the draw process. The moisture of the ambient environment penetrates through the coating, and because of that, the strength of fiber can be considerably higher immediately after the draw than approximately 20-30 minutes after the draw. In this work we have suggested three possibilities to overcome this phenomenon.

Because the strength of fiber is based on the crack growth of the weak spot, the dwell time of the proof have a strong effect on lifetime estimations. High production speed and the mechanical construction of the on-line proof tester forces the dwell time to become short. If the commonly used proof tension 0.69 GPa (100 kpsi) is used, it is possible that the weak spots of the fiber do not grow enough and the lifetime is low. If we increase proof tension and calculate the lifetime by the power law, lifetime estimations increase. Therefore, we suggest that higher proof tension be used with short dwell times.

Another remarkable issue is that the coating material's dynamic tensile modulus can change according to the stress rate. If high stress rates are used, it is possible that the coating carries a substantial part of the tension and the glass fiber does not experience full test tension. This can be, however, compensated

by using high test tension, but it might damage the coating material.

The automatic recovery from random fiber breaks essentially belongs to the properties of an on-line proof tester. This means that if fiber breaks in the proof test region, it must be possible to thread the free end of the fiber to the take-up reel for spooling at the full line speed without down ramping the draw process. In the test we threaded the fiber inside a guiding tube with different line speeds and tried to optimize the break recovery system. The results show that static electricity is the main problem when conveying fiber in the tube. In addition, the friction between fiber and the tube has to be as low as possible, and the so-called "rubber band effect" in fiber breaks makes treading challenging.

6. References

- [1] W. Griffioen, "Optical Fiber Mechanical Reliability," Leischendam, Nederland, p. 209 (1994).
- [2] J. Mrotek, M. Matthewson and C. Kurkjian, "Diffusion of Moisture Through Optical Fiber Coatings," in: Journal Of Lightwave Technology, 19(7), 988-993 (July, 2001).
- [3] TIA/EIA-455-31C, Proof Testing Optical Fibers by Tension, Telecommunications Industry Association (1999).
- [4] IEC 60793-1-30, Measurement methods and test procedures – Fibre proof test, International Electrotechnical Commission (2001).
- [5] B. Overton and G. Orcel, "The Effects of Coating Characteristics on the Determination of The Dynamic Fatigue Parameters for Optical Fibers," *PITVII*, 341-350 (1995).
- [6] S. Apone, L. Chiaro and G. Grego, "Viscoelastic properties of optical fibres coating", *PITVII*, 331-339 (1995).
- [7] F. Kapron, "The influence of proof test dwelltime on fiber reliability," Proceedings of 48th International Wire and Cable Symposium, 55-60 (1999).
- [8] J. L. Armstrong, M. J. Matthewson and C. R. Kurkjian, "Humidity Dependence of the Fatigue of High-Strength Fused Silica Optical Fibers," in: J. Am. Ceram. Soc. 83(12) 3100-108.
- [9] M. Lipponen, "Development of an on-line proof tester of optical fiber," The University of Oulu, Faculty of Technology, 2001. (Department of Mechanical Engineering, Master's Thesis)



Harri Turunen
Nextrom (USA) Inc.
1650 Satellite Blvd.
Duluth, GA 30097

Harri Turunen received his M.Sc. degree in Mechatronics and Space Technology in 1993. He joined Nextrom in 1992, where he was first involved in the R & D of heavy take-ups. In 1995 he joined the fiber optic group, and he now works as Manager of Rotating Machinery. Turunen received his Licentiate of Technology degree in 1999.



Mika Lipponen
Nextrom Oy
P.O. Box 44
Fin-01511 Vantaa
Finland

Mika Lipponen joined Nextrom in early 2001 as a master's thesis worker for developing optical fiber finishing processes. Today he holds the position of R & D Engineer for rotating machinery. Lipponen completed his M.Sc. degree in mechanical engineering at The University of Oulu, Faculty of Technology in 2001.

Stress and Index Variation for the Drawing Speed

Jae-Ho Lee, Sung-Koog Oh, Mun-Hyun Do, and Jin-Han Kim

R&D Group 1, Fiberoptics division, Telecommunication Network Business

Samsung Electronics Co. Ltd

#94-1, Imsoo-Dong, Gumi-City, Kyung-Buk, Korea

+82-54-479-7162 · j.lee@samsung.com

Abstract

Residual stresses and refractive indices of the depressed index clad fiber were measured for the various drawing speed, 20, 23.3, 26.7, and 30m/s and the stress-index relation are investigated. In the interface between the regions, residual stress has continuous change. For drawing speed, the absolute value of stress linearly increased in the core and cladding, that is, more compressive stress was applied after drawing process. And the increasing rate of refractive index also had linearity for drawing speed.

Keywords

Optical fiber, residual stress, refractive index, drawing process

1. Introduction

The internal stress in optical fiber, which affects mechanical and optical properties - attenuation, refractive index and reliability[1] comes from various manufacturing processes - deposition, collapsing, over cladding, drawing process. And the DIC (depressed index clad) fiber manufactured by MCVD process has three layers: core, cladding, and substrate (over cladding) tube. These three layers have the different thermal expansion coefficient and viscosity of glass materials. They cause the stress distribution.

After drawing process, the remained axial-stress of fiber is mainly made by the tension that is mechanically induced. The magnitude of stress induced by drawing tension, is different as glass material constitution. As material is the more viscous, induces the more stress. Generally the glass for which dopants such as Ge, B, P and F are added has lower viscosity value compared with pure silica glass. And as dopant concentration increased, viscosity decreased.[2] Mechanically induced stress is relaxed after time goes, but not removed.

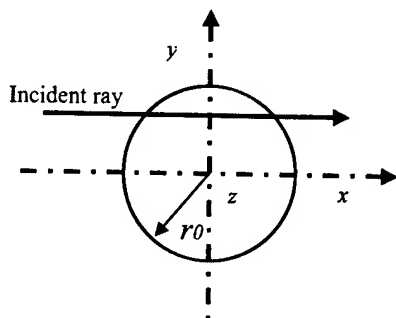


Fig. 1 Schematic diagram of Ray path

Index-stress relation has been investigated for developing the manufacturing method of fiber grating. It is known that releasing core-stress changes the refractive index. When mechanically induced stress is relaxed by annealing process, refractive index increase in pure-silica-core fiber.[3]

The purpose of this experiment is to investigate stress and index variation for drawing speed and obtain stress-index relation.

2. Theories and Experiments

2.1 Stress measurement[4]

The residual stress of the fiber (about axial direction) is originated from phase distribution caused by photoelastic effect first noted by Brewster: A phenomena that a fiber becomes birefringent through the non-isotropic stresses.

The photoelastic effect makes phase shift such that intensity difference of light is appeared. The phase profile is obtained by measuring the intensity difference. And phase profile can be converted to the stress profile.

When a plane wave incidents to the fiber in the direction x, there is the index difference induced by residual stress. (Fig.1) By stress-optic relation it can be expressed such that

$$n_z - n_y = C(\sigma_z - \sigma_y)$$

where C is called photoelastic coefficient or Brewster coefficient.

The phase shift by index difference between two components, retardation is as follows.

$$dR(y) = \frac{2\pi}{\lambda} (n_z - n_y) dx = \frac{2\pi C}{\lambda} (\sigma_z - \sigma_y) dx$$

where λ is a wavelength of incident light.

If the residual stress is uniform through axial direction i.e. independent of z, the integration of σ_y is disappeared in the cylindrical shape.

So the stress about axial-direction is obtained by Abel transformation

$$\sigma_z(r) = \frac{-\lambda}{2\pi^2 C} \int_r^{\infty} \frac{dR(y)/dy}{\sqrt{y^2 - r^2}} dy$$

2.2 Experimental Setup

Preform fabricated by MCVD was drawn at the speed from 20m/s to 30m/s. Drawing speed was controlled as 125 μm in fiber diameter. And another drawing condition is same for speed changes.

Refractive index of optical fiber was measured by FRIP. (Fiber Refractive Index Profiler S14, YORK Technology)

For measuring the residual stress, Fiber Stress Analyzer (made in FOSE, Korea) was used with 0.6 μm resolution. (Fig. 2)

As He-Ne laser (633nm) has narrow spectrum, it can be considered a single-wavelength light source. Light source transmits diffuser. Laser has spatial coherence like one point source, such that it is strongly diffracted and interfered. Diffuser controls the interference of the light and reduces unwanted effects. To obtain simple output function, quarter wave-plate is used. By using rotating polarizer, retardation is acquired. The light through the fiber is condensed and detected by CCD camera.

Without stress, the intensity of incident wave is detected as follows:

$$I = I_0 \sin^2(\theta/2).$$

where I_0 is background intensity and θ is rotating polarizer angle.

The change of intensity by photoelastic effect is retardation R .

$$I = I_0 \sin^2(\theta/2 + R)$$

Analyzer reduces background light transmitted rotating polarizer. Finally camera detects birefringent light by photoelastic effect.

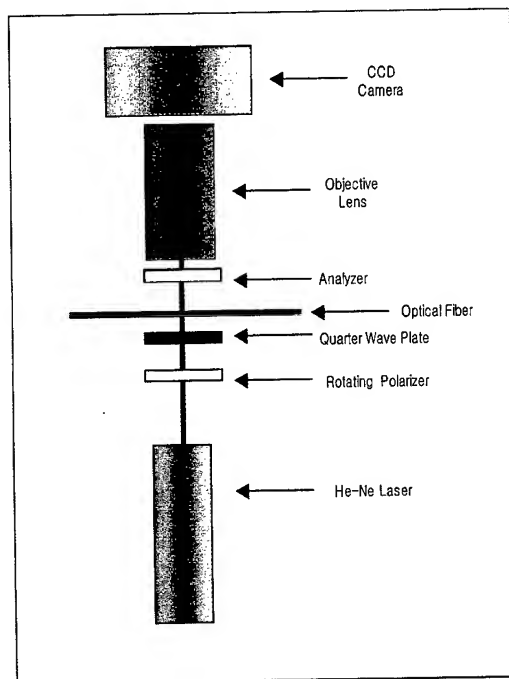


Fig. 2 Experimental setup for residual stress measurement

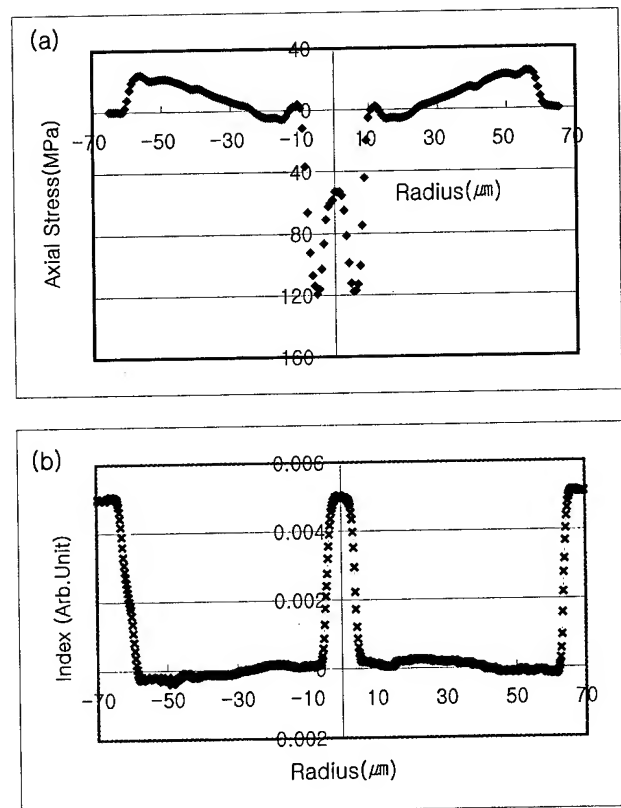


Fig. 3 (a) Stress profile and (b) refractive index profile in the fiber (30m/s drawing)

3. Results

3.1 Stress Distribution

The residual stress of DIC fiber manufactured by MCVD process is different for the regions: core, cladding and substrate tube.

Tensile stress was imposed in substrate tube. (Fig. 3 (a)) Near surface the stress is more tensile than interface between clad and substrate. And the magnitude of stress in substrate has a slope. This is caused by the difference of cooling rate. When the heated-fiber cools down below the glass transition temperature, the surface exposed atmosphere gets cool more rapidly than inner-part of substrate. In other words, inner-part has the time to anneal and relax the stress.

The compressive stress was inflicted the core and cladding. Because the cladding is more viscous than core, the core region was relatively tensile. And almost all stress applied the cladding.

Comparing with the refractive index profile (Fig. 3 (b)), the residual stress was smoothly changed though the refractive index had a step-functional shape in the interface of core and cladding, cladding and substrate tube. The maximum point of the compressive stress is located at the interface of core and cladding, that is, the distribution of stress is different from that of material concentrations. And the maximum point of compressive stress is

scarcely moved for drawing speed variation. It can be considered that there is the layer compensating the stress gap between two regions and maintaining core-cladding structure.

Residual stresses had linear dependency on drawing speed for the case that another drawing condition is same, and also had nearly same increasing rate in core and cladding although Ge concentration of core is higher than that of cladding.

3.2 Refractive index variation

Except the effect of matching oil outside fiber, fiber is roughly divided into two regions: high index (core) and low index (cladding and substrate). Because of background noise, it was hard to know the index change of substrate. It can be considered that substrate index is not varied for drawing speed. However, drawing speed affected the core index.

The refractive index (ΔN) was also changed for drawing speed. That is, residual stress affected the index variation and there was the linearity between stress and index. We confirmed that compressive stress causes the increase of refractive index. (Fig. 4)

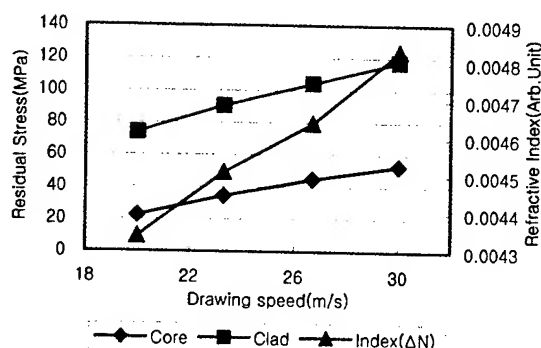


Fig.4 Property variation for drawing speed

4. Conclusions

The residual stress of core and clad is compressive, and substrate tensile. Stress was continuously changed and differed from index profile. It is inferred that the region exists for compensating the stress difference. For drawing speed, the absolute value of stress linearly increased in the core and cladding, that is, more compressive stress was applied after drawing process.

The increasing rate of refractive index also had linearity for drawing speed.

5. References

- [1] Y. Hibino, F. Hanawa, and M. Horiguchi, "Drawing-induced residual stress effects on optical characteristics in pure-silica-

core single-mode fibers," *J. Appl. Phys.*, 65(1), 30-34 (January, 1998).

- [2] A. K. Varshneya, *Fundamentals of Inorganic Glasses*, 1st ed., Academic Press, INC, p. 195 (1994).
- [3] T. Enomoto, M. Shigehara, S. Ishikawa, T. Danzuka, and H. Kanamori, "Long-period fiber grating in a pure-silica-core fiber written by residual stress relaxation," *OFC '98 Technical Digest*, ThG2, 277-278 (1998).
- [4] Y. Park, T. -J. Ahn, Y. H. Kim, W. -T. Han, U. -C. Paek, and D. Y. Kim, "Measurement of the residual stress and photoelastic coefficient of an optical fiber," *Photonics Conference 2000*, F2E7, 481-482 (2000).

6. Authors

Jae-Ho Lee



Jae-Ho Lee received a bachelor's degree in Physics from Yonsei University Korea in 1999 and master's degree in Materials Science from Korea Advanced Institute of Science and Technology in 2001. He researches the residual stress and polarization mode dispersion of optical fiber.

Sung-Koog Oh



Sung-Koog Oh received B.S, M.S and Ph.D in Physics from Chonnam National University Korea. He joined Samsung Electronics in 1998. Now he is senior engineer of optical fiber/cable R&D group in Fiberoptics Division.

Mun-Hyun Do



Mun-Hyun Do was born in 1963. He received a bachelor's degree in material science from Chungnam National University Korea in 1989 and master's degree from Kyungbuk National University in 1998. Now he is principal engineer of optical fiber/cable R&D Group in Fiberoptics Division of Samsung Electronics Co. Ltd.

Jin-Han Kim



Jin-Han Kim was born in 1957. He received a bachelor's degree from Pusan University Korea in 1982 and master's degree from Kyungbuk National University in 1990. Now, he is vice president of R&D Group 1 in Fiberoptics Division of Samsung Electronics Co. Ltd.

Feasible Operating Conditions in Optical Fiber Drawing

Xu Cheng, Yogesh Jaluria* and Constantine Polymeropoulos

Mechanical and Aerospace Engineering Department, Rutgers, The State University of New Jersey
Piscataway, New Jersey
(732) 445-3652 jaluria@jove.rutgers.edu

Abstract

The region of operating conditions, in which the drawing process for optical fiber manufacture is successful, is largely determined by the stresses acting on the fiber, flow of glass, and the stability of the process. This paper numerically investigates feasible operating conditions for fiber drawing. It is found that only certain ranges of furnace temperature and draw speed lead to successful fiber drawing. The length of the heated zone is another important parameter that can be varied to obtain a feasible drawing process. The physical behavior of the flow in the fiber close to the boundary of the domain is studied in detail to understand the basic underlying mechanisms. It is found that the numerical iteration to obtain the converged neck-down profile diverges rapidly when the draw temperature is lower than that needed for an acceptable process due to the lack of material flow. It is time-consuming and expensive to locate the exact boundary of the feasible domain. However, a rough estimate of the extent of the region can be more easily obtained.

Keywords

Optical Fiber; drawing; furnace; feasibility; viscous rupture

Introduction

One of the most widely used methods to draw optical fibers involves continuously feeding a silica glass preform into a cylindrical heating furnace, heating the glass above its softening point of around 1900 K, and pulling it into a fiber of diameter around 125 μm [1]. As the preform proceeds through the heating zone, it narrows down sharply and yields the "neck-down" region. The neck-down profile strongly depends on the fiber drawing conditions and significantly impacts the diameter uniformity [2], strength, and transmission loss of optical fibers [3].

The domain of operating conditions, in which the drawing process is successful, is important for the design and control of the process. Such a domain is determined by the stresses acting on the fiber and the stability of the process [4]. This paper presents a numerical study to investigate feasible conditions for fiber drawing. A cylindrical resistance graphite furnace, with low-speed aiding argon flow, is chosen. The inert gas flow in the furnace cavity keeps the graphite heating element from oxidation. A conjugate problem, with a free surface of glass, is considered. A complex thermal analysis, involving conduction, convection and radiation heat transfer, is necessary to simulate the optical fiber drawing process at high draw speeds. The flow and thermal transport in the two regions is solved to obtain the temperature, velocity, and tension in the glass. The zonal method is used to model the radiative heat transfer in the glass [5]. The

neck-down profile of the preform is iteratively determined by a force balance. It is shown that only certain ranges of furnace temperature and draw speed lead to feasible fiber drawing [4, 6]. The heat-zone length is another important parameter that can also be varied to obtain feasible drawing conditions.

The complexity of the physical processes and the strong variation of glass viscosity with temperature make it difficult to obtain iterative convergence of the numerical scheme. Several changes were made in the numerical methods employed earlier in order to locate the boundary of the feasible drawing domain. Through numerical experiments, it is possible to determine the dominating factors that affect the feasibility of the process and eventually lead to a rupture of the fiber. All these considerations indicate the importance of the phenomena at the boundary of the feasible domain.

Analysis and Numerical Algorithm

The transport phenomena for optical fiber drawing in a cylindrical graphite furnace are investigated for high-speed optical fiber drawing. A conjugate problem involving the glass and the purge gases is considered. Laminar flow is assumed due to the high viscosity of glass and low velocity in the gas flow. The transport in the two regions is coupled through the boundary conditions at the free surface. Conduction, convection and radiation are coupled in the heat transfer analysis.

The governing equations for axisymmetric conditions are obtained for both the glass and the purge gas. These equations involve the variable-property flow in glass, the free surface, whose profile is determined numerically, and radiative transport in the glass and the furnace. These equations are given in [7, 8], which may be consulted for details on the modeling of the process. The viscous dissipation and the radiative source terms are only kept for the glass due to their importance. For the convenient implementation of the finite difference method, the complicated domains for the glass and purge gas are transformed into cylindrical ones using Landau's transformation [9]. The boundary conditions for a free surface, arising from a force balance, are employed at the interface between the glass and the purge gas. A more detailed discussion on the governing equations and the boundary conditions can be found in [8, 9]. The draw tension is determined by considering the contribution of the viscous force, surface tension, inertia force and gravity.

The radiation transfer is a volume phenomenon in the semi-transparent glass and the zonal model is used to accurately compute the radiative source term [5]. In order to avoid computation of the direct exchange areas every time the neck-down profile is corrected, the optically thick approximation is

* Corresponding author

first used to generate the neck-down profile, and then this profile is used as the initial guess to generate the final neck-down profile with the zonal method. After a corrected profile has been obtained, the grids for both the radiation analysis and for the transport equations are re-adjusted, and the view factors and direct exchange areas are re-calculated. This strategy is based on the observation that the difference between the temperature variations predicted using the optically thick approximation and the zonal method is relatively small. After the neck-down profile is generated, the temperature and flow fields corresponding to the profile are calculated. Numerical experiments are necessary to obtain the optimum discretization schemes.

Results and Discussion

The velocity and temperature distributions in the fiber and the furnace are calculated. Several of these results have been presented earlier and are not repeated here. The focus is on the feasibility of the process. Several different wall temperature profiles, particularly cosinusoidal, parabolic and Gaussian are considered for a wide range of operating conditions.

A typical example of the numerical generation of neck-down profile with a cosinusoidal starting profile is shown in Fig. 1 from [4], using the optically thick approximation for glass. From the figure it is seen that during the first few iterations, the neck-down profile is quite unrealistic, with a flat region and an abrupt change in radius around where the starting profile ends. But after a few iterations the shape becomes smooth and monotonically decreasing, eventually reaching a steady, converged, profile, indicated by the invariance of the profile with further iterations. For convergent cases, perturbations to the initial profile and different starting shapes lead to the converged neck-down profile, indicating the robustness of the scheme and the stability of the drawing process. The force balance conditions are also closely satisfied if the iterations converged. However, convergence does not occur in every case, leading to a feasible domain.

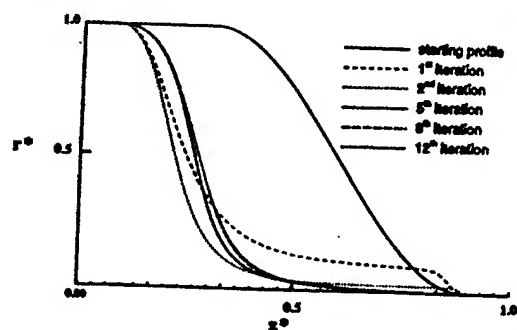


Figure 1. Iterative convergence of the neck-down profile. Here $r^* = r/R$ and $z^* = z/L$, R and L being the preform radius and furnace length, respectively.

It was found that, for given fiber and preform diameters and for a given draw speed, the fiber cannot be drawn at any arbitrary furnace wall temperature distribution. If the furnace temperature is not high enough, the iterative radius correction shows that the fiber breaks due to lack of material flow, a phenomenon that is known as viscous rupture [10]. Similarly, it can be shown that for a particular furnace temperature and fiber speed, the fiber can be drawn only if it is above a certain diameter. Also, for a

given preform and fiber size and with a given furnace temperature, there is a limit on the speed beyond which drawing is not possible, as this leads to rupture. Figure 2 (a) shows the different cases studied, including the cases where drawing is feasible and the cases when it is not. From this figure, a region can be identified beyond which drawing is not possible. For the region where drawing is feasible, the draw tension is calculated. The "iso-tension" contours are shown in Fig. 2 (b). As expected, the draw tension is low at higher temperatures and lower speeds, which explains the positive slope of the iso-tension contours. For a realistic fiber-drawing operation, these results are very important, since the operating parameters (such as furnace temperature and draw speed) can be identified so that a fiber of desired diameter can be drawn at the required tension. Thus, feasibility of the process is determined largely by material flow.

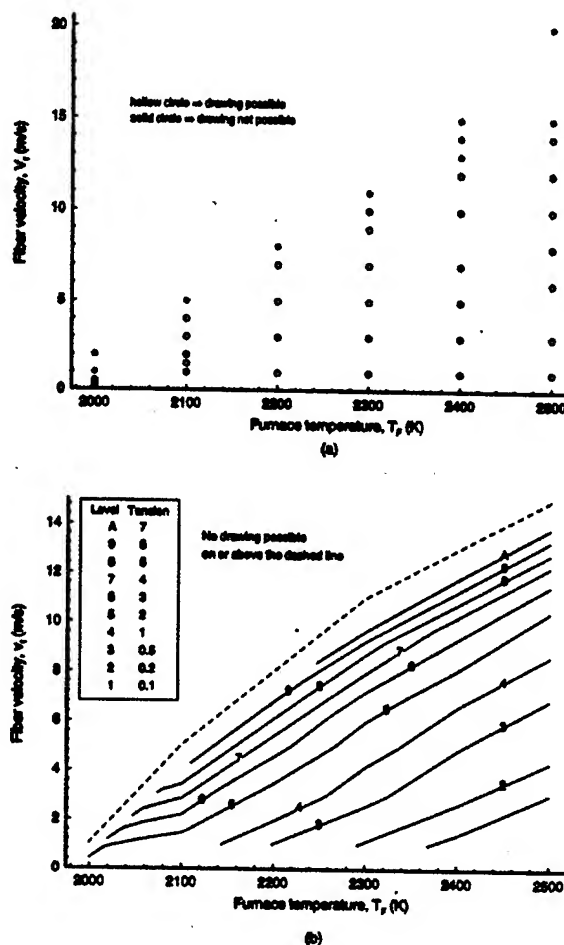


Figure 2. Feasibility domain and iso-tension contours.

The study was also extended to high draw speeds, which are of particular interest in industry today [11]. The furnace wall temperature distribution is assumed to be parabolic with a minimum temperature of 2000K at both ends. The maximum temperature, which is referred as the furnace temperature, is located at the mid-point of the furnace length and is changed to identify the feasible drawing conditions. The zonal method is used for radiation analysis in glass. Figure 3 shows the relation between the maximum allowable drawing speed and furnace temperature for successful drawing, from [12]. With an increase

in the furnace temperature, the maximum allowable drawing speed also increases, as expected. The feasible drawing conditions are given by the region below the curve.

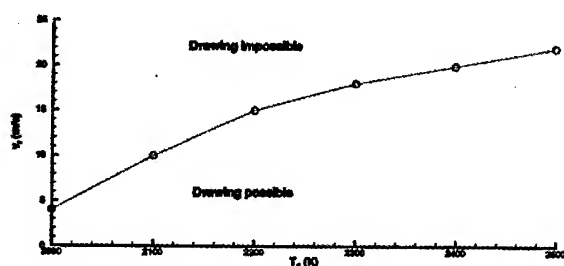


Figure 3. Feasible drawing conditions in terms of the furnace wall temperature and the fiber drawing speed.

Similarly, a proper design of the heat-zone can possibly alter the feasible range, particularly for high draw speeds or low furnace temperatures. The consideration that the preform/fiber temperature in the fiber drawing process should not drop below the softening point of the material gives rise to many of these constraints.

Attempts have been made here to identify the combination of heat-zone length, furnace temperature and draw speed for which fibers of a given size can be drawn from preforms of specified diameter. Two typical temperature distributions inside the draw furnace, parabolic and Gaussian profiles, are examined separately. The minimum temperature in the distribution is kept fixed, and the maximum temperature is varied and referred to as the furnace or draw temperature.

Fiber drawing for a parabolic temperature profile, as shown Fig. 4, is first studied. Both feasible and unfeasible cases are shown in Fig. 5 and Fig. 6. A feasible region can be easily identified based on a combination of heat-zone length, draw temperature and draw speed, beyond which the fiber drawing becomes not possible. Clearly, the maximum draw speed at a given furnace temperature could be restricted by the heating-zone length inside the furnace due to the requirement that the temperature in the

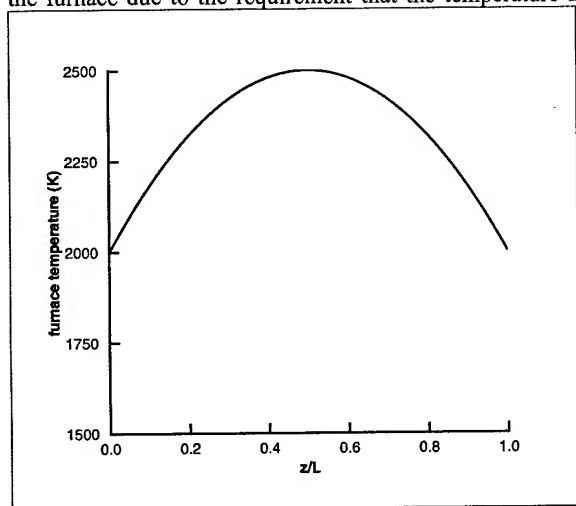


Figure 4. Temperature profiles specified on the furnace wall

neck-down region must exceed the softening temperature. Similarly, at a given draw speed, a longer heat zone could possibly allow lower furnace temperature in order to heat the glass up to the softening point. The latter is a good alternative since higher temperatures lead to higher concentration of defects and shorter lifespan of a graphite furnace [11]. It is also found from the numerical results that, as mentioned earlier, the lower bound of temperature and the upper bound of draw speed are all regulated by the viscous rupture, which is a direct result of high draw tension.

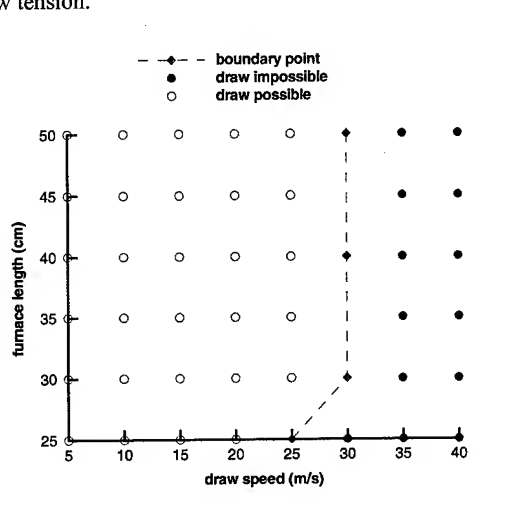


Figure 5. Feasible domain on a draw speed versus furnace length plane at a draw temperature of 2500 K

A Gaussian temperature distribution is next investigated to obtain the feasible domain. Either furnace length with respect to draw speed or furnace length with respect to draw temperature can be considered to determine feasible parameters for fiber drawing. Figure 7 shows the minimum draw temperatures possible for various heat-zone dimensions at different draw speeds. Compared to the results in Fig. 6, it is obvious that the

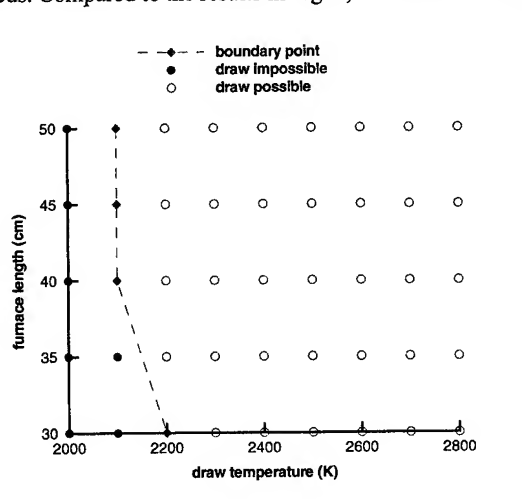


Figure 6. Feasible domain of draw temperature with respect to furnace length at a draw speed of 15 m/s

feasible boundary can be quite different due to the changes in the temperature distribution. It is also interesting to see that the boundary of the feasible domain shifts noticeably to the top right when draw speed increases. It indicates that either a higher draw temperature or a longer residence time is needed to make fiber drawing possible at higher draw speeds.

For a realistic fiber-drawing operation, these results are very important, since the parameters in a fiber drawing system, such as draw temperature, draw speed and heat-zone length, can be identified so that a fiber of desired diameter can be drawn at required quality. However, it must be pointed out that fiber drawing may never reach the boundaries due to the unacceptable draw tension in practice. Additionally, it is also possible to obtain similar feasibility results for different combinations of other physical and process variables. But, furnace temperature, draw speed and heat-zone size are investigated here because they are three of the major variables chosen in practical systems.

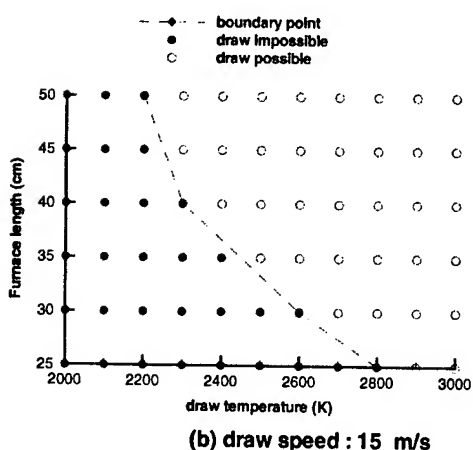
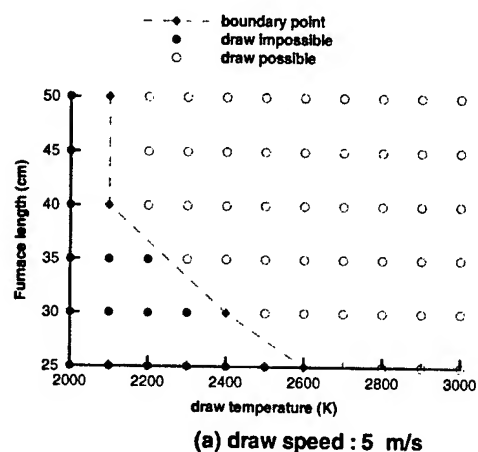


Figure 7. Comparison of feasible domains of draw temperature at (a) draw speed of 5 m/s and (b) draw speed of 15 m/s for a Gaussian distribution.

As the furnace temperature decreases or as the fiber speed increases in fiber drawing, the preform/fiber temperature inevitably drops below the softening point of the fiber materials and eventually makes drawing impossible. The behavior of numerical convergence and physical characteristics are of great interest when the drawing parameters are close to the boundary of the feasible domain. On one hand, it is important to know the dominating factors, which eventually cause the fiber to break. On the other hand, it is interesting to investigate the characteristics of the numerical algorithm and the iterative procedure in the search for the boundary of the feasible domain.

One typical case involving the draw temperature variation across the boundary of the acceptable domain is presented here. For a 30 cm furnace, the draw temperature is gradually increased, starting from an impossible drawing point of 2200 K, and finally reaching the feasible boundary at 2600 K. It can be sketched as a horizontal path in Fig. 7(b). The iterative evolution of neck-down profiles is shown in Fig. 8 at a draw temperature of 2200 K.

Several interesting observations can be seen clearly from these results. First, when the draw temperature is beyond the feasible drawing region, the neck-down profile becomes increasingly flat as the iterations proceed due to the lack of material flow. To satisfy the boundary condition of a fixed fiber diameter, it gives rise to an abrupt change in the fiber profile at the lower end of the furnace. Eventually the numerical procedure diverges. However, the rate of divergence is very different for various draw temperatures. The iteration diverges much faster at lower draw temperatures that are far away from the feasible boundary, but it diverges much more slowly at higher draw temperatures close to the feasible boundary. As an example, the abrupt change of radius profile at 2200 K becomes very obvious after only six neck-down corrections. However it takes more than eight corrections for 2300 K, and more than ten for 2400 K. Since one correction of the neck-down profile, using zonal method, requires an expense of 4000 iteration steps, the search for the feasible boundary, therefore becomes very expensive in terms of computational resources. In fact, it takes more than 50000 iteration steps to determine that the process is infeasible at 2500 K but feasible at 2600 K, as shown in Fig. 9. Once the boundary

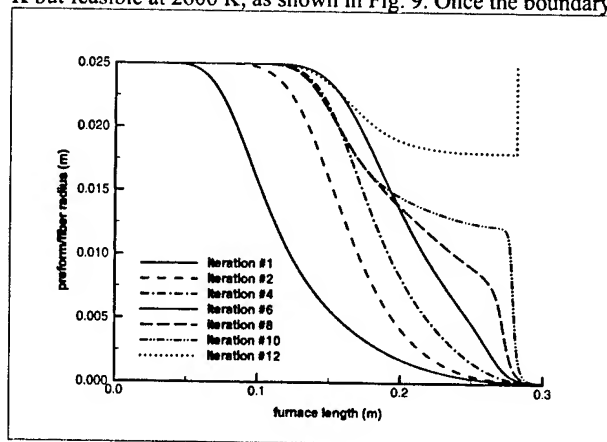


Figure 8. Neck-down profile corrections for an unfeasible fiber drawing circumstance at a furnace temperature of 2200 K and a draw speed of 15 m/s

point is reached, experience shows that the convergence of the numerical iteration process could be alternatively determined by the given number of iterations or neck-down corrections, instead of specified values of the convergence parameters. From numerical experiments, it is observed the difference caused by two control schemes is trivial, especially for feasible cases far away from the domain boundary.

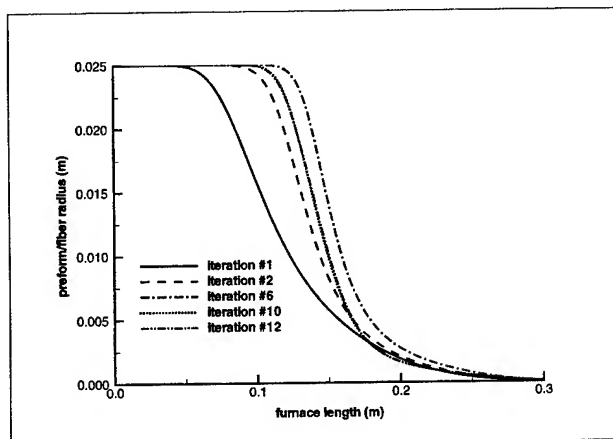


Figure 9. Neck-down profile corrections for a feasible fiber drawing circumstance at a furnace temperature of 2600 K and a draw speed of 15 m/s

CONCLUSIONS

In this paper, the feasible drawing domains are first considered for different temperature distributions of the draw furnace wall. It is seen that such domains are the direct results of the combinations of three important operating parameters, namely furnace temperature, draw speed and heating element length. The results show that the upper bound of draw speed and the lower bound of draw temperature could be changed by the heat-zone length at the given conditions. It is also found that the temperature distribution could alter the feasible domain significantly. The domain boundaries are determined by viscous rupture and flow instability.

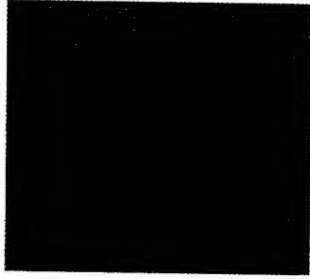
The physical behavior close to the boundary of a feasible domain is next studied. It is found the iteration diverges very rapidly when the draw temperature is lower and beyond the acceptable domain due to the lack of material flow. However the divergence rate becomes much smaller when the temperature gets close to the domain boundary. This observation implies that it is very expensive to locate the exact boundary of the feasible drawing domain. These results will be useful in the design and control of a successful optical fiber drawing process.

Acknowledgements

The authors acknowledge the financial support provided by the National Science Foundation, under Grant No. DMI-96-33194, and the computing facilities provided by the Pittsburgh Supercomputing Center, Under Grant No. CBT920017P, for this work. Helpful discussions with Professor G.H. Sigel and with Dr. S. Roy Choudhury are also acknowledged.

REFERENCES

- [1] U.C. Paek and R.B. Runk, "Physical Behavior of the Neck-down Region during Furnace Drawing of Silica Fibers," *Journal of Applied Physics*, 49, 4417-4422 (1978).
- [2] D.H. Smithgall, *The Bell System Technical Journal*, 58, 1425 (1979).
- [3] L.L. Blyler and J.C. Williams, "Optical Fiber Drawing and Coating," *AIChE Symposium Series*, 83(258), 27-28(1987).
- [4] S. Roy Choudhury and Y. Jaluria, "Practical Aspects in the Drawing of an Optical Fiber," *J. Mater. Res.*, 13, 483-493 (1998).
- [5] Z. Yin and Y. Jaluria, "Zonal Method to Model Radiative Transport in an Optical Fiber Drawing Furnace," *J. Heat Transfer*, 119, 597-603 (1997).
- [6] S. Roy Choudhury, Y. Jaluria and S.H.K. Lee, "Generation of Neck-Down Profile for Furnace Drawing of Optical Fiber," *Numerical Heat Transfer*, 35, 1-24 (1999).
- [7] X. Cheng "Design and Optimization of the Draw Furnace for High Speed Optical Fiber Drawing," *Ph.D. Thesis*, Rutgers University, New Brunswick, NJ (2002).
- [8] Z. Yin and Y. Jaluria, "Thermal Transport and Flow in High-speed Optical Fiber Drawing," *J. Heat Transfer*, 120, 916-930 (1998).
- [9] S.R. Choudhury and Y. Jaluria, "Thermal Transport Due to Material and Gas Flow in a Furnace for Drawing an Optical Fiber," *J. Mater. Res.*, 13(2), 494-503 (1998).
- [10] E.M. Dianov, V.V. Kashin, S.M. Perminov, V.N. Perminova, S.Ya Runanov, and S.M. Sysoev, "The Effects of Different Conditions on the Drawing of Fibers from Preforms," *Glass Tech.*, 29, 258-262 (1988).
- [11] Y. Jaluria, C.E. Polymeropoulos, and G.H. Sigel Jr., "Feasibility, Design and Optimization of The Optical Fiber Drawing Process," *NSF Grantees Conference*, Tampa, Florida (2000).
- [12] Z. Yin and Y. Jaluria, "Neck-down and Thermally Induced Defects in High Speed Optical Fiber Drawing," *J. Heat Transfer*, 122, 351-362 (2000).
- [13] X. Cheng and Y. Jaluria, "Thermal Design of Draw Furnace in High Speed Optical Fiber Manufacturing," *Proc. Int. Mech. Engg. Cong. Exp.*, Orlando, Florida (2000).
- [14] Cheng, X. and Jaluria Y., "Effect of Furnace Design on High Speed Optical Fiber Drawing," *Proc. 49th Int. Wire Cable Symp.*, Atlantic City, NJ, 2000.



C.E. Polymeropoulos

Department of Mechanical and Aerospace Engineering
Rutgers University
97 Brett Road, Piscataway, NJ 08854-8058

Dr. Polymeropoulos is a Professor of Mechanical Engineering at Rutgers and has been teaching and doing research in the general area of thermal processes.

The Use of A 3-D Computational Fluid Dynamics Simulation in the Design of an Optical Ribbon Coating Applicator

David W. Chiasson

Corning Cable Systems

Hickory, North Carolina

(828) 901-6237 · dave.chiasson@corning.com

Abstract

In this paper, a method is presented that utilizes computational fluid dynamics (CFD) as a tool for screening potential experimental parameters and their levels. The example used to demonstrate this method is a hypothetical coating applicator used in the manufacture of optical fiber ribbon. The objective of this work is to calculate the relative effect of various applicator geometric parameters and coating process parameters on the minimum coating thickness within the ribbon. Three geometric and two process parameters are investigated. These parameters are: applicator land length, taper angle, taper length, applicator wall temperature, and coating inlet pressure. Using two 8 run fully factorial experimental designs, it was determined that the levels chosen for the applicator temperature have the greatest effect on the minimum coating thickness.

Although the use of CFD provides insight into this coating example, it cannot replace proper experimental design and execution. The use of CFD allows a process designer to screen a number of potential experimental parameters without consuming any raw materials or process line time. The use of this tool is justified if the insight gained from CFD allows the process designer to reduce the cost of an experiment through the proper selection of parameters and their levels.

Keywords

Computational Fluid Dynamics, CFD; UV Coating; Coating Applicator, Optical Fiber Ribbon.

1. Introduction

In this paper, a 3-D computational fluid dynamics (CFD) model of a coating applicator is presented. The purpose of this applicator is to coat a group of individual optical fibers with a UV curable matrix material. Once the matrix material is cured, the final product is a flat optical fiber ribbon that allows for efficient fiber packing densities within optical fiber cables.

A number of factors affect the various properties of an optical fiber ribbon. To completely quantify the effects of all the possible factors on each of these properties would be very costly. To reduce the number of factors investigated during an experiment, a process designer will rely on their past experience with the process and their analytical skills to determine which factors and their respective levels might significantly affect the critical properties of the optical fiber ribbon. Once the designer has determined the property or properties of the ribbon to observe in

an experiment (i.e. the response of the experiment), the factors that will be investigated, and the levels of these factors, the designer can plan and execute the experiment. If the experience in the process is limited or if a new process is being considered, then one usually has to rely on screening experiments to determine the effect of particular factors on the property investigated.

The number of screening experiments and primary experiments required to achieve a particular objective can be time consuming and expensive. This is especially true if the expense includes various coating applicator designs, a significant amount of optical fiber, and/or a significant amount of raw material. To reduce the experimental expense and reduce the time required for implementing a design or process change, it is suggested that a series of CFD simulations be used as a means of screening possible experimental parameters and their levels. These simulations will allow the designer to determine which variables and their respective levels are significant and thus worth evaluating in a future experiment. These simulations will also allow the designer to gain insight into the process that would not be gained through rigorous experimental work [1]. For example, the use of CFD allows one to observe flow fields, pressure fields, temperature fields, etc, in greater detail than if these fields were obtained through experimental measurement.

Presented in this paper is a 3-D CFD simulation of a ribbon coating applicator. Although previous work has been presented on 2D simulations of fiber coating applicators [2,3,4] and a 2D simulation of a ribbon coating applicator [5], no work has been presented yet on a 3D simulation of a UV optical fiber ribbon coating applicator. The intention of the paper is to extend on the work conducted by Shen [5]. The example investigated is a hypothetical UV ribbon coating applicator proposed by the author. Using a 3D CFD simulation of this example, the effects of coating applicator design variables and coating process parameters on the minimum coating thickness are calculated.

2. Discussion

2.1 What is CFD?

Computational Fluid Dynamics (CFD) is the study of numerically generated fluid flow fields. It has been used extensively in the study of fluid dynamics for the following reasons:

1. It allows for one to observe fluid flow structures that would be difficult to measure [1] and
2. It allows the designer to gain an understanding of the fluid flow that may not be obvious through experimental observation [1].

CFD utilizes a method where the Navier-Stokes (N-S) equations for momentum and heat transfer are simplified so that a series of linear algebraic equations are obtained. These equations describe the desired properties at discrete points. The N-S equation for momentum and an example of a linearized or discretized form of the N-S equation are shown in the following two equations. This form of the discretized momentum equation is obtained with the use of a finite volume technique outlined by Patankar [1]. The values for a_x and b are constants that result from the derivation. The value of S is a source term and the surrounding values of velocity u_x and the previous value of velocity u_{old} indicate an iterative solution is required.

$$\rho \left[\frac{\partial u_i}{\partial t} + u_j u_{i,j} \right] = \rho g_i - p_{,i} + \mu u_{i,jj} \quad (1)$$

$$u_{i,new} = \frac{a_E u_E + a_W u_W + a_N u_N + a_S u_S + b + S + \rho \left[\frac{u_{i,old}}{\Delta t} \right] \Delta V}{\frac{\rho \Delta V}{\Delta t} + a_P} \quad (2)$$

The use of CFD is necessary because the N-S equation can only be solved for very simple geometries and not for the relatively complex geometry presented in this paper. Depending on the geometry of the flow field and the boundary conditions, these linear algebraic equations can be solved for fluid velocity, pressure, temperature, etc. This study utilizes a commercially available finite element CFD package. This CFD package has a feature that can calculate the shape of free surfaces and thus allow one to calculate the minimum coating thickness required in this study.

2.2 Dimensionless Numbers

What is proposed in this paper is the use of dimensionless numbers to evaluate this hypothetical UV coating applicator. These dimensionless numbers can simplify the problem by reducing the quantity of variables investigated. Below are the dimensionless numbers used in this investigation:

$$\text{Reynolds Number} = Re = \frac{\rho V L}{\mu} = \frac{\text{Inertial Forces}}{\text{Viscous Forces}} \quad (3)$$

$$\text{Capillary Number} = Ca = \frac{\mu V}{\gamma} = \frac{\text{Viscous Forces}}{\text{Surface Tension Forces}} \quad (4)$$

$$\text{Prandtl Number} = Pr = \frac{\mu C_p}{k_{\text{matrix}}} = \frac{\text{Molecular Diffusion}}{\text{Thermal Diffusion}} \quad (5)$$

$$\text{Brinkman Number} = Br = \frac{\mu V^2}{k_{\text{ink}} \Delta T} \quad (\text{Viscous Dissipation}) \quad (6)$$

$$\text{Dimensionless Pressure} = p^* = \frac{PL}{V\mu} \quad (7)$$

$$\text{Dimensionless Temperature} = T^* = \frac{T - T_0}{\Delta T} \quad (8)$$

A characteristic dimension (L) is also used in the creation of the applicator geometry. The fiber radius has the characteristic dimension of $L=R_f=1$ and any geometric length stated is in relation to this characteristic dimension. The process parameters and the material properties are incorporated into these dimensionless numbers. Please refer to the appendix for the description of the variables shown above.

2.3 The Sample Problem and Its Boundary Conditions and Assumptions.

The figure below is an illustration of a hypothetical 4-fiber ribbon coating applicator. This particular coating applicator consists of two matrix inlets located on the top and bottom of the applicator. As the fibers enter the applicator, matrix will contact the fibers and be conveyed through the internal geometry of the applicator. As the fibers and matrix leave the applicator, a free surface is formed where the matrix will draw down to its final uncured shape. Curing of the UV matrix material will take place in a subsequent process step.

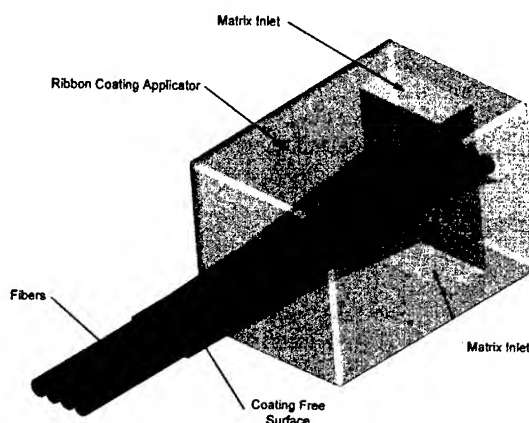


Figure 1. Proposed Ribbon Coating Applicator

The applicator internal geometry and the free surface are shown in the following figure.

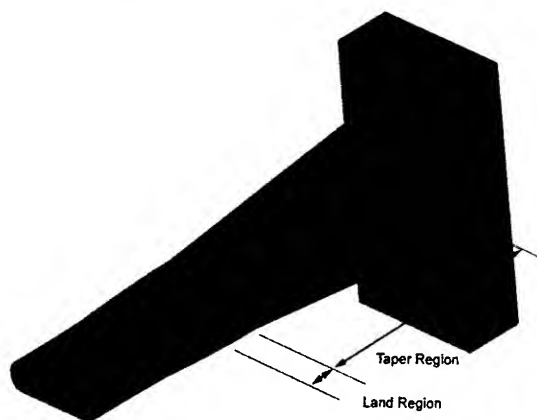


Figure 2. Flow Field with the Ribbon Coating Applicator.

The above geometry has two planes of symmetry. It is therefore decided to simulate only one quarter of this flow field. Utilizing these planes of symmetry will decrease the amount of redundancy in the solution and thus reduce the simulation set-up and run time. Below is the figure illustrating the proposed flow field. A further decision is made to eliminate the vertical matrix inlet channel. This decision is based on the assumption that this region will have relatively low coating velocities and have very little impact on the response investigated.

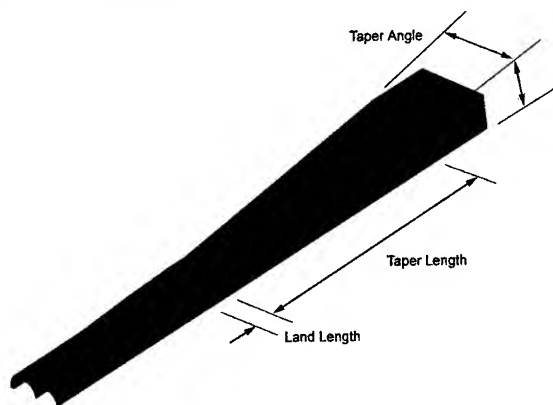


Figure 3. Proposed Flow Field for the Numerical Simulation.

It is also important to consider the proper application of boundary conditions for this particular geometry. The specifics of the problem investigated will be governed by the boundary conditions imposed on the equations of momentum and heat transfer. Below is a figure outlining the boundary conditions used for this problem.

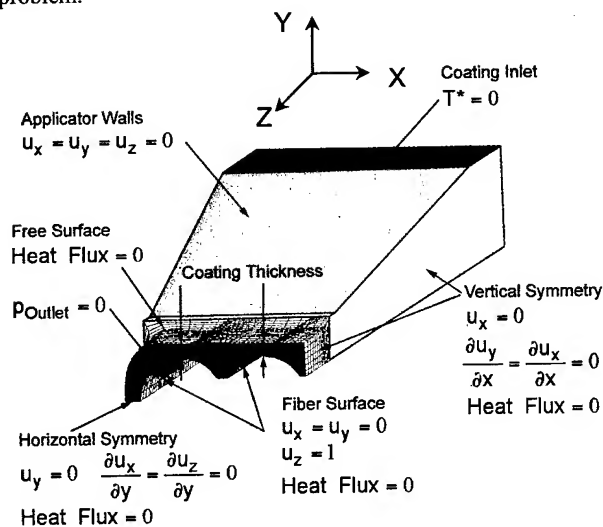


Figure 4. Boundary Conditions

The following assumptions are also incorporated into the CFD simulation: gravity is neglected, the upstream free surface is neglected, the coating flow is laminar, and the coating is Newtonian with a temperature dependant viscosity. Surface

tension and viscous heating effects are also incorporated into this simulation.

2.4 The Proposed Numerical Study

Table 1 lists the dimensionless numbers that are held fixed for the numerical study conducted.

Table 1. Fixed Dimensionless Parameters.

Parameter	Value
Re	0.1
Ca	20
Pr	20000
Br	7

In the numerical study, the minimum thickness of coating over the top of the fibers is calculated for various coating process and applicator geometric parameters. The minimum coating thickness is illustrated in the previous figure. The average of the two values calculated is the response used.

The numerical study is divided into 2 parts. The first part is an evaluation of three geometric parameters within the coating applicator. This part consists of an 8 run full factorial design in which the parameters and the levels shown in Table 2 are evaluated. These geometric parameters are illustrated in figure 3. The intent is to determine the most significant geometric parameter. The second part of this numerical study consists of another 8 run experimental design that will compare the effect of the most significant geometric parameter and the effects of the process parameters considered. The two process parameters and their levels are shown in Table 3.

Table 2. Dimensionless Parameters and The Associated Levels used for Part 1

Parameter	Level -1	Level +1
Land Length	$1 \cdot R_f$	$2 \cdot R_f$
Taper Angle (Degrees)	ϕ	2ϕ
Taper Length	$20 \cdot R_f$	$30 \cdot R_f$

Table 3. Dimensionless Parameters and The Associated Levels used for Part 2

Parameter	Level -1	Level +1
Geometric Parameter from Part 1	-1	+1
Applicator Wall Temperature, T^*	0	0.25
Coating Inlet Pressure, p^*	0	1

2.5 Results

Using the CFD package and appropriate convergence criteria, the solutions for the flow field, pressure field, temperature field, and the shape of the free surface are obtained. Below are the response graphs illustrating the effect of the land length, the taper angle, and the taper length on the average minimum coating thickness over the fibers. The values of dimensionless thickness are in

relation to the characteristic length used in this study. In this study, the radius of the fiber is given the characteristic length of 1. The linear and the curved lines shown in the following figures represent the linear best-fit line and the 95% confidence interval respectively.

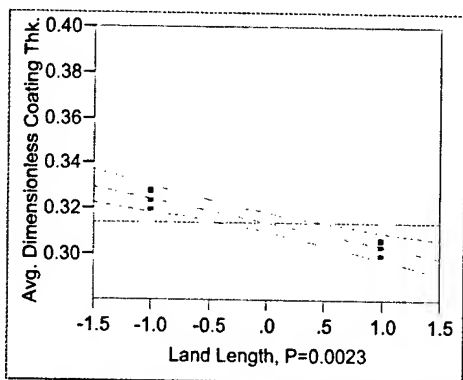


Figure 5. Effect Response for the Applicator Land Length.

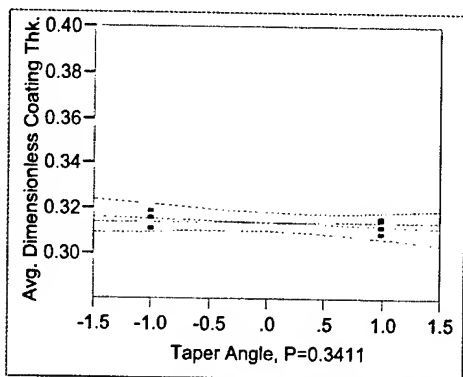


Figure 6. Effect Response for the Taper Angle

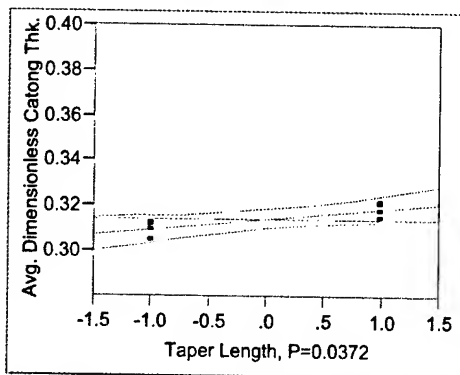


Figure 7. Effect Response for the Taper Length

Using a 99% confidence interval, it is evident the land length has an effect on the coating thickness that cannot be attributed to the noise generated in the simulation. The absolute value of this effect is 0.021. The effect of taper angle and the taper length cannot be segregated from the noise generated in the calculation. There were no interactions between any of the factors evaluated in first part of the numerical study. The results of this first 8 run design indicate that the taper length and the taper angle are

probably not worth evaluating in a future experiment using the geometry presented in this study.

In part 2 of the numerical study, the land length is investigated with two process parameters in a full factorial 8 run design. Below are the response graphs illustrating the effect of the land length, the applicator wall temperature, and the coating inlet pressure on the average minimum coating thickness over the fibers.

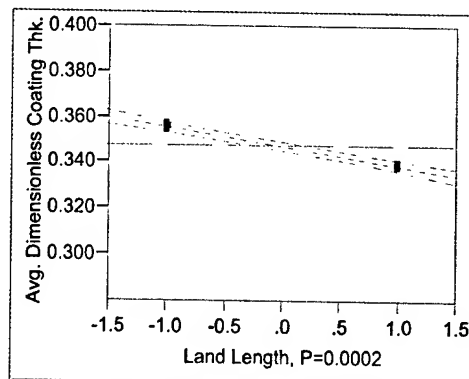


Figure 8. Effect Response for the Land Length.

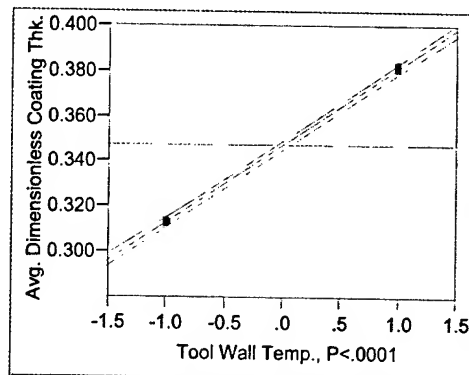


Figure 9. Effect Response for the Tool Wall Temperature.

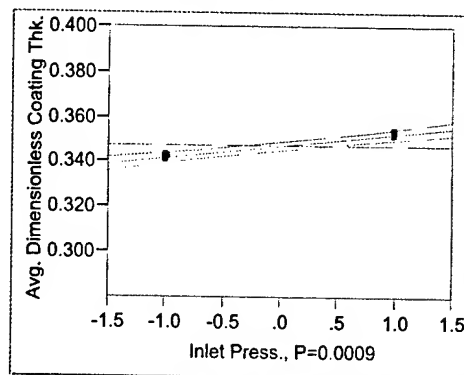


Figure 10. Effect Response for the Applicator Inlet Pressure.

Using a 99% confidence interval, each of the variables evaluated in part 2 has an effect on the minimum coating thickness that

cannot be attributed to the noise generated in the simulation. A summary of the effect values is shown in the following table.

Table 4. Effect Values for Part 2.

Parameter	Effect
Land Length	-0.017
Applicator Wall Temperature, T^*	0.068
Coating Inlet Pressure, p^*	0.011

It is interesting to observe that the tool wall temperature has the greatest effect on the response in this example. This effect has a calculated value of 0.068. No factor interactions exist.

3. Conclusions

In the optical fiber ribbon example presented, it is demonstrated that the use of a relatively simple 3D CFD simulation reduced the number of potential experimental variables from five to three. It was determined that the applicator temperature has the most significant influence on the minimum coating thickness.

One can gain valuable insight by utilizing CFD as a means of screening parameters in an experiment intended to quantify a process change or to quantify the performance of a new process. The insight gained from this exercise will reduce the cost of future experimental work through the proper selection of experimental factors and their levels.

4. Acknowledgments

I would like to thank Ming Li and Bill Jackman for their input into this paper.

5. References

- [1] S. V. Patankar, Numerical Heat Transfer and Fluid Flow, Hemisphere Publishing Corporation, New York, 1980.

- [2] C. D. Dimitropoulos, S. Chippada, E. W. Grald, and J. A. Kulkarni, "CFD Simulation of Optical Fiber Coating Flows", Proc. 49th IWCS, 89-96, (November, 2000).
- [3] K. Rattan and Y. Jaluria, "Simulation of Flow in Die and Applicator for Optical Fiber Manufacture", Proc. 48th IWCS, 700-707, (November, 1999)
- [4] S. Ravinutala, K. Rattan, C. Polymeropoulos, and Y. Jaluria, "Dynamic Menisci in a Pressurized Fiber Applicator", Proc. 49th IWCS, 474-478, (November, 2000)
- [5] S. Shen, "Computational Fluid Dynamics (CFD) Analysis of Ribbon Processing", Proc. 48th IWCS, 533-542, (November, 1999)

6. Appendix

6.1 Nomenclature

ρ = Density of the coating.
 V = Velocity of the fiber.
 L = Characteristic dimension.
 R_f = Radius of the fiber
 μ = Viscosity of the coating.
 γ = Surface tension of the coating.
 K = Thermal conductivity of the coating.
 T = Temperature.
 ΔT = Projected temperature difference within the coating.
 T_o = Reference temperature.
 C_p = Specific heat of the fluid.
 ϕ = Taper angle.

David Chiasson joined Corning Cable Systems' Canadian Cable Plant in 1989 after receiving his B.Sc. in Mechanical Engineering from the University of Alberta. In 1998, Dave obtained his M.Sc. from the University of Saskatchewan. Dave has since moved to the Corning Cable Systems Research, Development, and Engineering facility in Hickory, North Carolina where he currently is involved with the development of new UV coating processes.

Loss Performance of Standard Single Mode Fibre Cables In the Wavelength Region 1200-1750nm

Svend Hopland

Telenor Networks, Infrastructure Division
Oslo, NORWAY
+47 977 00805 · svend.hopland@telenor.com

Abstract

In this paper, we provide measurement results of installed standard single mode fibre cables, which reveal the wavelength dependence of the fibre loss from 1200 nm to 1750 nm. Old cables as well as new cables have been investigated. Values of measured fibre cable loss at different wavelengths are given, and characteristics of the observed loss behaviour are outlined. We also reveal the wavelength dependence of additional losses due to temperature, tension and crush for cable samples under test. The field measurements and the cable tests indicate that the average loss in recently installed cables should be less than approximately 0.40 dB/km in the entire wavelength range 1260 nm – 1675 nm.

Keywords

Fibre, cable, loss, installed.

1. Introduction

Today, it is foreseen that the whole wavelength range from 1260 nm up to nearly 1700 nm might be used for DWDM optical transmission at high bit rates up to at least 40 Gbits/s. This is recognised by the ITU-T by defining a continuous spectrum from 1260 nm to 1675 nm; consisting of the O-band: 1260-1360nm, the E-band: 1360-1460 nm, the S-band: 1460-1530 nm, the C-band: 1530-1565 nm, the L-band: 1565-1625 nm, and the U-band: 1625-1675 nm.

Optical fibre cables with standard G652-fibres have cut-off values of approximately 1260 nm, and are thus able to transmit such a large wavelength span. The fibres also have positive dispersion values from around 1300 nm and upwards, which is necessary to reduce non-linear effects at high bit rates. It is thus possible to use this fibre at the highest bit rates in a very broad wavelength range. The majority of installed cables up to now, at least as far as the traditional operators are concerned, have been G652-fibre cables.

It is thus of great importance to investigate and evaluate the possibility of using this wavelength span in existing cable network, including old cables as well as new cables.

Outside the traditional 1310 nm-band and 1550-band, limited attenuation data are available for installed fibre cables. Our earlier investigation of cable attenuation at 1625 nm [1], the upper limit of the L-band, has encouraged us to investigate even higher

wavelengths in the U-band. Also, cable attenuation values in the E-band and the S-band are of great interest both as transmission bands and as pump wavelengths for Raman amplification. In this paper, we present loss values of old and recently installed cables in the region 1200-1750 nm.

2. Measurements

2.1 Fibre and cable

The fibres used in our cables are Standard G652 with fibre cut-off values in the range 1190 nm-1330 nm. Our cables are specified for use at 1550 nm.

For the majority of our installed cables, the cable cores consist of fibres in stranded loose tubes, surrounded by different kinds of protection and tension members to form duct-, aerial- and underwater cables.

2.2 Measurement method

In the field measurements as well as the test measurements, we have used a white light source and a spectrum analyser to measure the spectral loss curve of individual fibres from 1200 nm to 1750 nm. The one end patch panel connector was directly connected to the light source while the other end patch panel connector was directly connected to the analyser. A short patch cord was used as the reference for the field measurements. Two-way OTDR measurements at 1310 nm, 1550 nm and 1625 nm was performed on the fibre lengths in order to control and compare with the spectral. Since the OTDR measurements could not include any splices close to the connectors, the spectrals tended to give slightly higher values than the corresponding OTDR value.

As a rule in the field we measured fibre lengths in the range 5-10 km in order to achieve optimum accuracy. Typically, 5-10 fibre splices were included in the measured path.

3. Results

3.1 Field measurements

The intrinsic fibre loss is expected to dominate the overall fibre cable loss. In particular, the OH⁻ hydroxyl absorption band around 1385 nm should be clearly visible throughout the E-band.

After installation, however, environmental factors such as temperature, crush and tension, or hydrogen intrusion, may cause additional attenuation in the fibre cable. Also, fibre splices including the bending of fibres in organizers will add to the path loss. Each of these added losses would have characteristic wavelength dependence.

Obviously, since a field spectral integrates all losses, it is not possible to separate in detail possible different loss contributions, but some clear tendencies should be evident.

3.1.1 Underwater cables.

In the late 1980's, Telenor installed underwater cables without hydrogen barrier, which resulted in some limited hydrogen ingress into the fibres. The hydrogen induced losses stabilized after a few years at low levels in the O-band (1310 nm) and C-band (1550 nm) [2]. In Fig. 1 is shown spectrals for an underwater cable installed in 1988. We observe the OH⁻ peak at 1385 nm as it appeared at that time, assuming no growth since installation. We also register the characteristic main molecular hydrogen peak at 1244 nm as well as two smaller H₂ related peaks at 1590 nm and 1700 nm, respectively. All these peaks will affect the different bands as outlined in more detail in Chapter 3.2. Since 1992, using hydrogen barriers, all H₂-induced peaks have been removed, and the spectrals are expected to be similar to spectrals in duct cables.

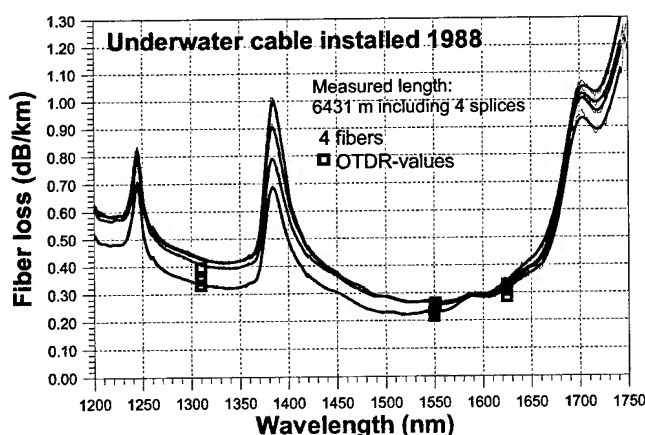


Figure 1. Spectrals from old underwater cable without hydrogen barrier.

3.1.2 Duct cables.

In Figure 2 are shown the spectrals from a duct cable installed in 1988. Again, we observe the rather high 1385 nm peak, while the rest of the spectrum has no evident features. The attenuation values are low even at wavelengths up to 1675 nm. This applies for Figure 1 as well as Figure 2.

In Figure 3 are shown spectrals from a duct cable installed in 1994. Now, the 1385 nm peaks have decreased markedly compared to Figure 1 and Figure 2. Attenuation values are low at wavelengths up to at least 1675 nm.

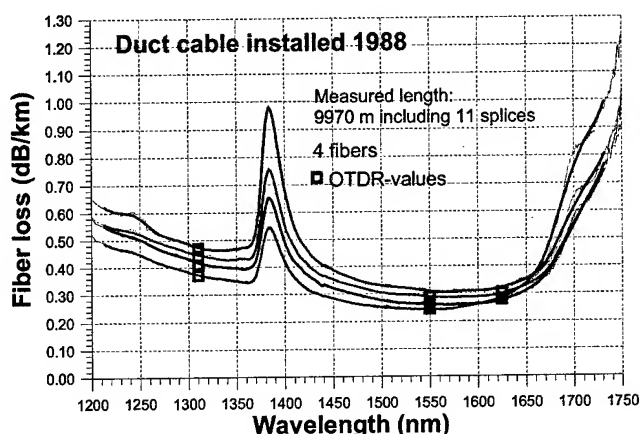


Figure 2. Spectrals from duct cable installed 1988.

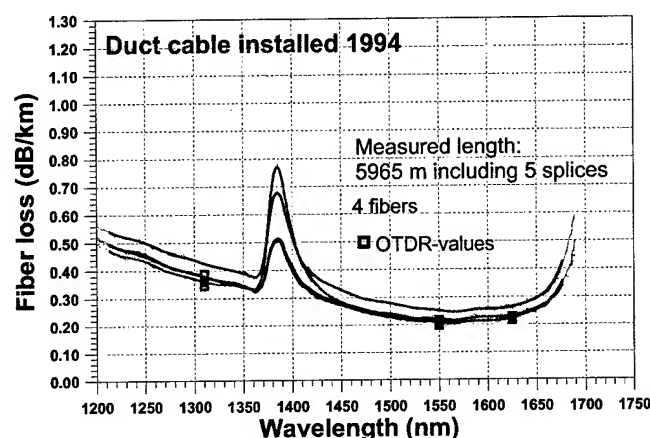


Figure 3. Spectrals from duct cable installed 1994.

In Figure 4 are shown spectrals from a duct cable installed in 2002. Now, the 1385 nm peaks are even lower, and the attenuation values are low up to approximately 1700 nm.

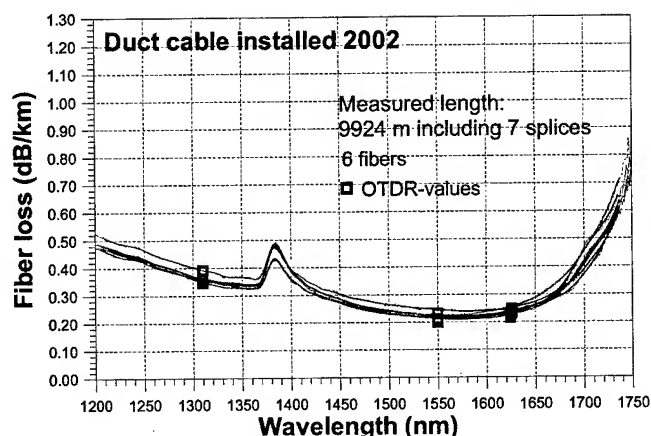


Figure 4. Spectrals from duct cable installed 2002.

3.2 Band affiliation

In order to study more closely attenuation behaviour, we have calculated the average spectral loss for the measured fibres in each cable, and plotted the average cable spectrals in the different bands.

3.2.1 The O-band.

In Figure 5 are shown the average cable spectrals in the O-band. For the duct cables the attenuation decreases throughout the band. We observe that the old duct cable installed 1988 has uniformly higher attenuation values than the duct cables installed after 1994. This is probably mainly due to the fact that in the late 1980's, splice losses were generally higher than in recent years. Also, fibre losses were slightly higher than today. These were observation made in an earlier work [1]. The total spectral average values for all duct cables installed after 1994 are calculated to 0.436 dB/km, 0.376 dB/km and 0.343 dB/km at 1260 nm, 1310 nm and 1360 nm, respectively. In comparison, the corresponding total average OTDR value at 1310 nm is 0.355 dB/km. For the old underwater cables the situation is a little different. Due to the main H_2 absorption at 1244 nm and the rather high OH^- absorption at 1385 nm, the attenuation values are slightly elevated near the band edges compared to the duct cables, while in the central region of the band, the spectrals are very similar to the duct cables.

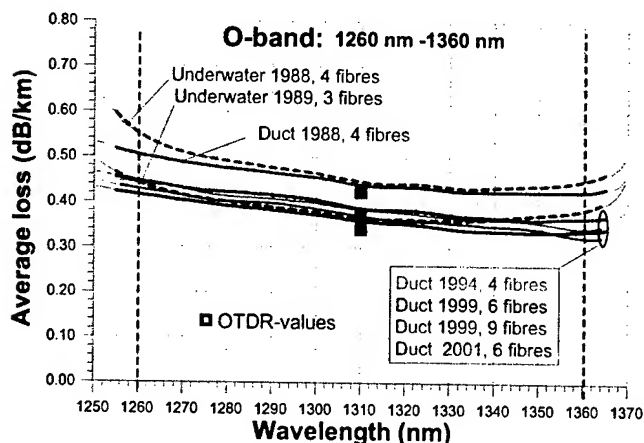


Figure 5. Average values of fibre cable losses in the O-band

3.2.2 The E-band.

In Figure 6 are shown the average cable spectrals in the E-band. Here, great differences among the cables are revealed. This is due to improvements of the fibre fabrication process resulting in lower intrinsic fibre loss. Through the years, fibre fabrication has become more refined with respect to the removal of the OH^- ion in the glass matrix, and the spectral value at 1385 nm has steadily decreased, as illustrated in Figure 7. We observe that the present peak value of approximately 0.40 dB/km is only slightly higher

than the average spectral value at 1310 nm in the middle of the O-band.

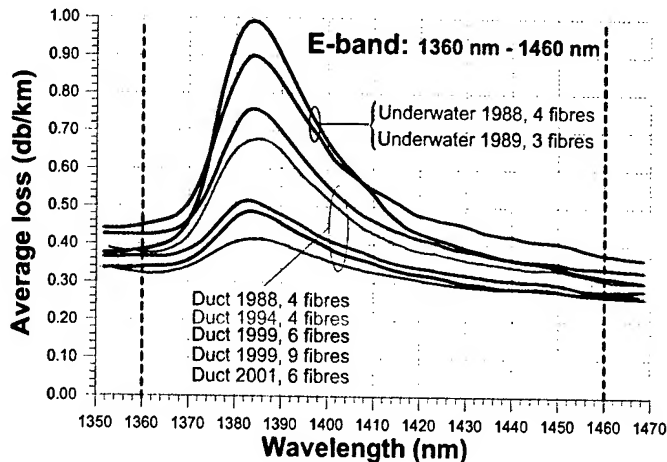


Figure 6. Average value of fibre cable losses in the E-band

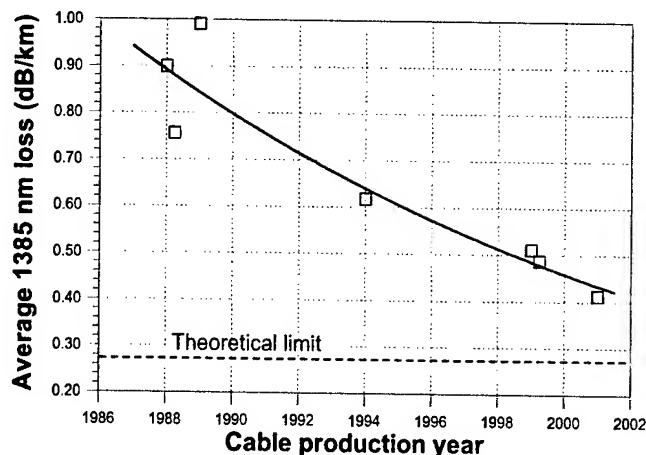


Figure 7. Historical development of fibre cable losses at 1385 nm

3.2.3 The S-, C-, L- and U-band.

In Figure 8 are shown the average cable spectrals in the S-, C-, L- and U-band. Again, the duct cable installed 1988 has uniformly higher attenuation values throughout all the bands than recently installed duct cables. Keeping in mind that the spectral dependence of splice losses tends to be more or less a constant value [1], we believe that the main reason for this are the higher splice losses observed in that time period.

In the S-band the attenuation values are steadily decreasing. The calculated total average spectral attenuation for recently installed duct cables is 0.273 dB/km and 0.228 dB/km at 1460 nm and 1530 nm, respectively.

In the C-band, the attenuation values are practically constant, and in the middle of the C-band at 1550 nm, the new duct cable spectral average value is 0.226 dB/km. In comparison, the average OTDR-value is 0.202 dB/km.

In the L-band, the attenuation values increase slowly, and at 1625 nm, the spectral average value is 0.240 dB/km. In comparison, the average OTDR-value is 0.216 dB/km.

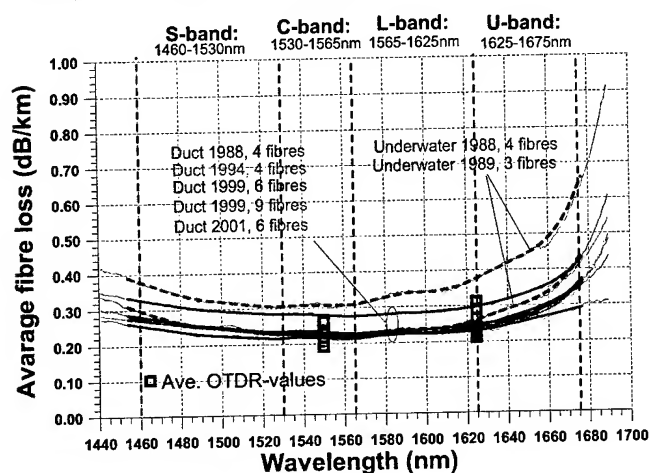


Figure 8. Average values of fibre cable losses in the S-, C-, L- and U-band

The spectral values as well as the OTDR-values in the C-band and in the L-band are in agreement with earlier observations [1].

Through the U-band, the attenuation values increase more rapidly. However, we observe that the recently installed duct cable spectral average at 1675 nm is as low as 0.342 dB/km, which is lower than the spectral average attenuation at 1310 nm.

For the old underwater cables the spectrals are different. Due to the high OH^- absorption at 1385 nm, the attenuation is elevated towards the S-band edge at 1460 nm, and due to the H_2 absorption at 1700 nm, the attenuation is elevated towards the U-band edge at 1675 nm as shown in Figure 8. We also know that the fibre attenuation is slightly higher than normal at 1550 nm as well as 1625 nm due to the molecular hydrogen induced loss [2].

The field spectral measurements have revealed the characteristics of the wavelength dependence on fibre cable attenuation of the OH^- absorption, which is present in all cables, and the H_2 absorption, which is present in old underwater cables. Also, higher splice losses in old cables seems to increase the attenuation more or less uniformly in all bands compared to new cables.

However, in new installed cables, there is no evidence that any substantial additional losses are present even at 1675 nm, the longest wavelength in the U-band.

3.3 Cable tests measurements

In order to characterize the wavelength dependence of additional losses due to temperature, crush and tension on the cable, duct cable samples were subjected to extensive testing, during which spectrals were recorded. In the following, the main results are presented.

3.3.1 Temperature test.

Figure 8 shows the spectrals of induced losses due to low temperatures in a new duct cable. The graph shows that the additional losses are less than the specified limit of 0.1 dB/km at temperatures less than -40°C , for wavelengths up to 1700 nm. Similar results were obtained for duct cables produced in 1994-95. We should note that our aerial cables have better temperature performance than our duct cables. Therefore, these results indicate that our cables are temperature resistant throughout the U-band, even if they are specified only for 1550 nm operation. In the field measurements, temperature induced losses are not present.

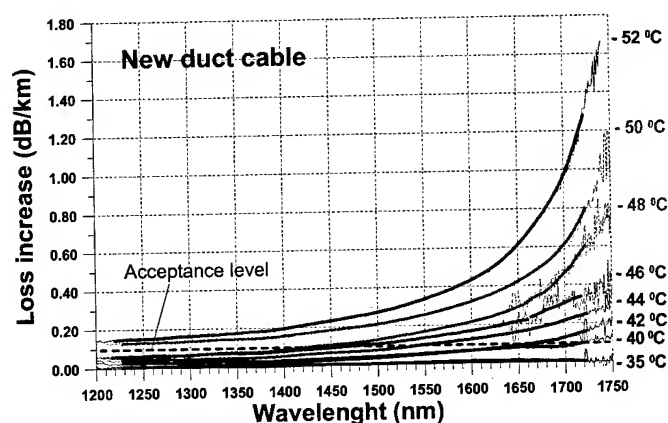


Figure 8. Temperature induced loss increase in new duct cable

3.3.2 Tension test.

In Figure 9 are shown additional losses due to fibre elongation at cable tensions well above the specified limit for a new duct cable. We note that significant induced losses are present at all wavelengths. Furthermore, they increase with increasing wavelength and elongation.

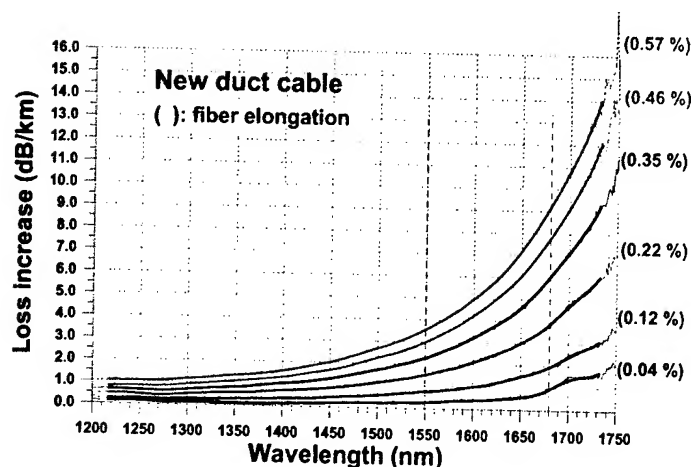


Figure 9. Loss increase due to fibre elongation during tension test

Typically, the additional loss at 1675 nm is more than 2 times the additional loss at 1550 nm. Similar wavelength dependence, only with different loss increase magnitude, has been observed on cables from other manufacturers.

Considering that it is not likely that longer lengths of cable will remain tensioned above the limit after installation, we believe that losses due to excess cable tension should not be a problem if the cables are installed properly. This assumption has been confirmed in the field measurements results, were additional losses of this character have not been visible in the OTDR curves nor in the spectrals.

3.3.3 Crush test.

In Figure 9 is shown the spectrals of loss increases at 15 min. hold time during mandrel/plate crush test for a new duct cable.

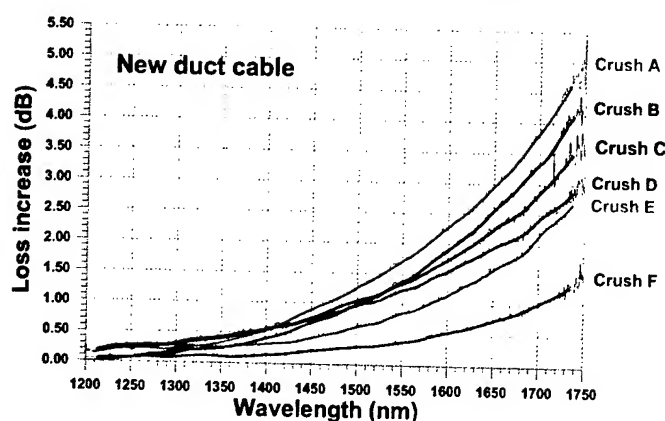


Figure 10. Mandrel-plate crush induced loss in new duct cable

The added loss increases with increasing wavelength. Typically, the added loss at 1675 nm is 2 times the added loss at 1550 nm. Also, the magnitude of the added loss shows a significant variation. However, it should be noted that less than 5-10 % of the crushes resulted in loss increases as shown. Thus the probability of loss increase is very low, and consequently a large number of crushes had to be performed in order to establish reliable statistics. The results are typical for new cables, while the statistics for older cables with other constructions may be poorer. Added losses of this type have not been visible in the field measurements on recently installed cables.

4. Conclusions

We have measured the attenuation spectrals for a number of installed fibre cables of different type and age.

In the O-band, we have found that the total spectral average values for duct cables installed after 1994 are 0.436 dB/km, 0.376 dB/km and 0.343 dB/km at 1260 nm, 1310 nm and 1360 nm, respectively.

In the E-band, the inherent fibre OH⁻ absorption, which is present in all our fibre cables, is totally dominant. However, the peak value at 1385 nm has decreased from nearly 1.0 dB/km in 1987 to 0.40 dB/km in 2002, due to improvements in the fibre fabrication process.

In the S-band, we have found the total average spectral attenuation for duct cables installed after 1994 to be 0.273 dB/km and 0.228 dB/km at 1460 nm and 1530 nm, respectively.

In the C-band, the attenuation values are practically constant, and in the middle of the C-band at 1550 nm, the post 1994 installed duct cable spectral average value is 0.226 dB/km.

In the L-band, the attenuation values increase, and at 1625 nm, the spectral average value is 0.240 dB/km for duct cables installed after 1994.

In the U-band, the attenuation values increase further, but not dramatically. The post 1994 installed duct cable spectral average value at 1675 nm is found to be 0.342 dB/km.

OTDR-values at 1310 nm, 1550 nm and 1625 nm are typically 0.02-0.03 dB/km lower than the corresponding spectral values.

Since each spectral include typically 4 end splices while the OTDR does not, the spectral values presented here, measured on lengths of 6-10km, are pessimistic when considering long link lengths of 100 km or more. In such a case we may assume that the spectral values would be lower and closer to the OTDR-values.

We have observed that duct cables installed before 1990, have uniformly higher attenuation values throughout all bands due to higher splice losses and slightly higher fibre losses as well.

In old underwater cables without hydrogen barrier, the attenuation values are slightly elevated at the O-band edges due to hydrogen and OH⁻ absorption. For the same reason, the attenuation values towards the S-band edge at 1440 nm and the U-band edge at 1675 nm are elevated compared to the duct cables. However, such edge effects are reduced in a practical link, where underwater cables usually form a small part of the total link.

We have revealed the characteristic wavelength dependence of additional losses due to temperature, tension and crush, which all increase with increasing wavelength. However, we have found that our cables are temperature resistant up to 1675 nm, even if they are specified only for 1550 nm operation. Furthermore, additional losses due to fibre tension are not dramatically higher at 1675 nm than at 1550 nm, and losses due to remaining excess cable tension should not be a problem if the cables are installed properly. Accordingly, added losses of this kind have not been observed in the measurement signatures. Likewise, additional losses due to mandrel/plate crush are of statistical nature with low probability, and are not dramatically higher at 1675 nm than at 1550 nm. Moreover, added losses of this type have not been visible in the field measurements on recently installed cables.

5. Acknowledgments

The author greatly appreciates the work of Idar Gangø, Telenor Networks, who has performed the field measurements and cable tests.

6. References

- [1] S. Hopland, "Investigation of 1625 nm Loss Performance of Fiberoptic Cables Intended for use at 1550 nm," *Proceedings International Wire & Cable Symposium 1999*.
- [2] S. Hopland, "Long Term Behaviour of Hydrogen Induced Losses in Installed Fiberoptic Submarine and Underwater Cables", *Proceedings International Wire & Cable Symposium 1997*.



Svend Hopland

Telenor Networks
1331 Fornebu
Norway

Svend Hopland graduated from the Norwegian Institute of Technology in 1985 with a PhD. on optical fibres. In 1986 he joined Telenor and is presently a senior engineer on fibre optic cables.

Transmission capacity and Interference analysis in ADSL system – Comparison between a standard copper cable and DSL cable.

Marcelo A. Andrade and Renata C. Federighi

Pirelli Telecomunicações Cabos e Sistemas do Brasil S.A., Av. Pirelli, 1100 – Sorocaba – SP –
Brazil – 18103-355, phone: +55 15 32359209, marcelo.andrade@pirelli.com.br

Oswaldo Tozze

Av. Nações Unidas, 4849 – SP – Brazil – 05477-000, phone: +55 11 30249737, otozze@telesp.com.br

Marco A. Garms

Av. Engenheiro Heitor Antônio Eiras Garcia, 943 – Apto. 62 – Bloco 7 – 05588-001, marcogarms@terra.com.br

Abstract

Copper cable pairs used to carry solely traffic consisting in voice analog electrical signals. However, with the appearance of the Internet, those same copper cables have been used for data traffic. With the increasing demand for data traffic, and increasingly higher data rates, there came into existence the digital subscriber line (DSL), which further increases the data rate to be supported by the old copper pair cable network. That technology makes use of digital signal processing, advanced algorithms, filters, analog/digital converters.

However, in order that such transmission rates may be reached, it is necessary to relay the service through short distances, in ideal transmission conditions. There is also the problem of signal interference between the conductor pairs, known as cross talk that limit the utilization of all pairs using digital transmission.

In order to solve these problems, was studied cables design and was developed a twisted conductor pair cable having improved electrical characteristics in ADSL Systems.

Keywords

DSL, ADSL, digital transmission, copper cable, twisted pair, cross talk, electrical noise.

1. Introduction

In the past, copper pair cables were used solely for traffic consisting in analog electrical signals (voice frequency). However, with the appearance of the Internet, those same copper cables have been used for digital signals (data traffic). With the increasing demand for data traffic, and increasingly higher data rates, there came into existence the digital subscriber line (DSL), which further increases the data rate to be supported by the old copper pair cable network.

That technology makes use of digital signal processing, advanced algorithms, filters, analog/digital converters, such as that in the ADSL (Asymmetric Digital Subscriber Line) type of transmission it is possible to reach rates up to 8 Mbps for downstream transmission and 640 kbps for upstream transmission, thus rendering the ADSL technology particularly appealing for downloading Internet files.

However, in order to reach such higher transmission rates, it is necessary to relay the service through distances of at least 2 km, in ideal transmission conditions. There is also the problem of signal interference between the conductor pairs, known as cross talk. There is a recommendation widely used by the telephony service operators, whereby only 8 of every 25 conductor pairs of a cable may be used for traffic of a digital system, in order to avoid cross talk.

In order to solve these problems, there has been developed a twisted conductor pair cable having improved electrical characteristics, whereby it is possible to reach across greater distances with the service, and also to use all the conductor pairs of a cable for digital transmission purposes in higher digital transmission rate.

So it was necessary to study the influences it of these services between itself and to determine the maximum occupation and reach in function of the types of cables and ADSL interference.

For this study, two types of cables have been used: a standard cable and the new developed cable of enhanced performance in ADSL.

2. Theory analysis

In order to solve the first basic problem, i.e., to allow an increase in the distance reached by the digital system, there has been made an option to reduce attenuation in the line without the need to alter the gauge of the metallic conductor. Any signal is subject to attenuation, i.e., loses power as it is carried along a line. The parameters that are responsible for this loss of power are the resistance of the conductors, the conductance (dielectric loss), the capacitance and the inductance.

Since attenuation is directly proportional to capacitance, in order to reduce attenuation in the line, the mutual capacitance of the conductor pairs was reduced, there being achieved thereby an attenuation reduced by 20% in average as compared to conventional cables, without the need to alter the diameter of the copper conductor. The reduction in capacitance could be achieved by increasing the insulation thickness, since the mutual capacitance inversely proportional to the distance between the pair conductors.

However, in order to achieve the desired levels of mutual capacitance, using only the insulation provided by a solid sheath of polyethylene for the conductor, it would be necessary to excessively increase the diameter of the insulated conductor, that in turn would cause an increase of diameter and weight of the overall cable assembly, which would be inconvenient from both in terms of cost and in terms of installation. Although inconvenient, this solution using solid polyethylene is technically feasible. However, in order to avoid the problems incurred by increased weight and diameter, an option was made to use a combination of cellular and solid insulation

The second basic problem in digital transmission is the maximum number of conductor pairs that simultaneously use the digital service within one same cable. An increasing number of conductor pairs carrying data will correspond to increasing cross talk.

Cross talk is the transfer of energy from a circuit (conductor pair) to another, causing loss of power of the signal being transmitted in the affected conductor pair.

In order to reduce the effect of cross talk, there are widely used twisted conductor pairs, since that when the conductor pairs are twisted with one another there occurs an effect of mutual cancellation of electromagnetic forces, causing a reduction in cross talk. Normally the conductor pairs of the cables are twisted with different pitches, a characteristic referred to as pitch series. This concept has been used with a special pitch series, shorter than usual, with pitches distinct from one another, following a geometric progression, according to studies that were conducted and results that were achieved empirically.

The ratio between the two twisting pitches follows a geometric progression:

$$a_n = a_1 \cdot q^{n-1} \quad (1)$$

There is not a satisfactory mathematical model for calculation of the impact of pitches upon cross talk, but it is known that shorter pitches provide better electrical performance. It is necessary to perform a cost/benefit analysis when deciding on a pitch series.

Therefore, the electrical performance results obtained in the tests performed in the sample are the consequence of the combination of two changes in cable design: an increase in the conductor insulation thickness together with the change of design of the series of pitches used for twisting the conductor pairs.

The thickness of the double insulation may vary, ranging from what would amount to a very small thickness value (almost null) of one of these (cellular insulation or solid insulation) to a very

large value of the other, including the possibility of very similar thickness values for both insulation. Nevertheless, in order that the result is satisfactory, it is necessary to shift the level of mutual capacitance which is used in prior art with a value of 51nF. This mutual capacitance shift should be at least about 20% less, which causes, for example for a cable configuration of dry core having insulated conductors made of solid polyethylene, that is necessary to increase by about 30% the insulation thickness leading the mutual capacitance to about 40 nF/km. Lower mutual capacitance values may be used provided that the cost/benefit relationship for the design is evaluated.

The first layer is made of cellular polyethylene, since this material has a low dielectric constant (ϵ_r). Over the layer of cellular material there is applied a layer of solid polyethylene, with much higher dielectric constant. This combination of dielectric constants is advantageous since thereby the resulting constant is lower than the constant in the case of solid polyethylene insulation, and therefore the diameter of the insulated conductor will be smaller. This is due to the fact that the capacitance is directly proportional to the dielectric constant, thus the same capacitance may be achieved without resorting to an excessive increase in diameter of the insulated conductor.

Once the diameter of the conductor has been determined, there should be calculated which will be the diameter of the assembly comprising the conductor and its thermoplastic insulation, also referred to as the insulated wire. This diameter is directly dependent on the mutual capacitance that is desired to be achieved in the cable.

Upon there having been determined the diameter of the insulated wire, it may be necessary to calculate the coaxial capacitance, since some machines control the diameter of the insulated wire by means of the coaxial capacitance.

$$C_{\text{coaxial}} = 2\pi \cdot \frac{\epsilon_0 \cdot \epsilon_r}{\ln \frac{\phi_v}{\phi_c}} \cdot 10^{-2} \quad (2)$$

C_{coaxial} = Coaxial capacitance (pF/m)

ϵ_0 = vacuum permittivity ($8,854 \cdot 10^{-12}$ F/m)

ϵ_r = Relative dielectric constant of the insulating material

ϕ_v = diameter of the insulated copper (mm)

ϕ_c = diameter of the conductor (mm)

Figure 1, 2 and 3 is a chart illustration comparing the improvement in attenuation at 20°C, FEXT (far end cross talk) and NEXT (Near end cross talk) according to frequency for a cable Fast Copper and reference.

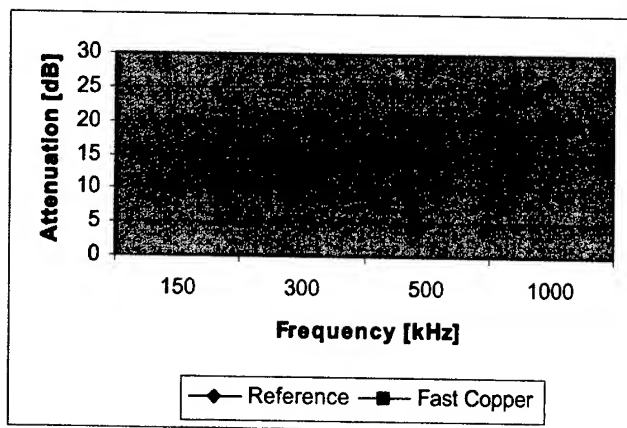


Figure 1 - Attenuation at 20°C according to frequency for a cable Fast Copper and reference.

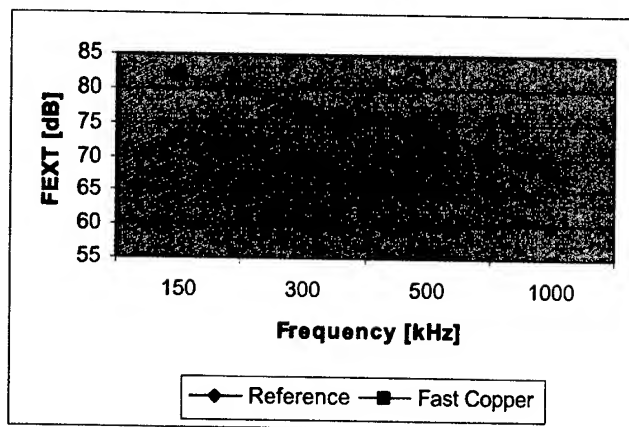


Figure 2 - FEXT (Far end cross talk) according to frequency for a cable Fast Copper and reference.

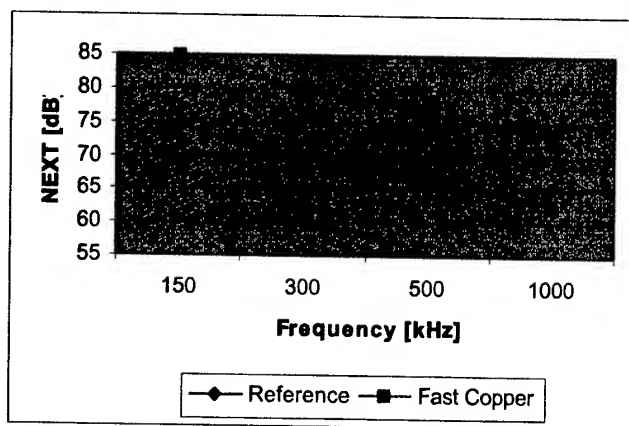


Figure 3 - NEXT (Near end cross talk) according to frequency for a cable Fast Copper and reference.

3. Experimental Analysis

To better evaluate the electrical performance of copper cables in the ADSL systems we have decided to realize tests using a DSLAM, modems and spectrum analyzer and broad band noise measurement used in ADSL systems.

3.1 Test Configuration

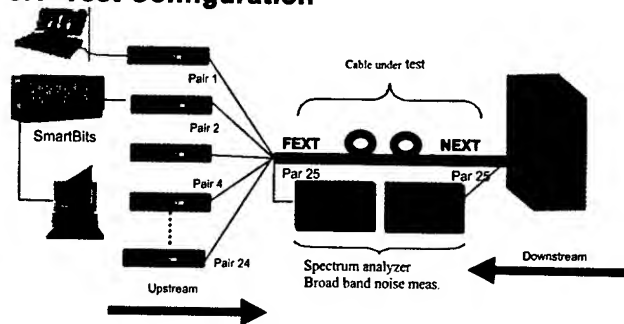


Figure 4. Test Configuration

3.2 Test Method

The tests had been carried through first in conventional copper cable sample CTP APL 40 x 100 pairs (Solid insulated copper cable - NBR9124 - Brazilian specification), which, for simplification, we will call reference sample. Later the same tests they had been carried through in other cables sample (Fast Copper 40 x 100 pairs), which we will call Fast Copper sample. Of this form the results could have been compared between them.

For accomplishment of the tests the following procedures had been adopted:

- With the configuration of test of figure 1, they had been carried through measured in sample length from 3km until a total of 5,5km for the sample reference and 6,5km for the sample Fast Copper. These had been the maximum values of distance that had synchronism between the modems.

- For 5,5km they had been used: a group of the handle of 3 km, four groups of the handle of 500m plus a pair of one of the groups in Loop. For 6,5km they had been used: two groups of the handle of 3km in Loop plus a group of the handle of 500m. For each sample we had one length of 3km and a sample length of 500m.

- For every length they had been monitored the traffics of data using the equipment SmartBits 2000, configured as protocol of tests for qualification of systems ADSL.

- The management of the DSLAM had measured the transmission rate of Upstream and Downstream. The data had been gotten using the management of one same modem, being that this always made the negotiation with the DSLAM after all to be synchronized.

- As the DSLAM was configured for opened profile, the speeds negotiated between modems ADSL and the DSLAM had been always the principles for each case.

In every sample we have connected the maximum number of ADSL modems and have observed the occupation capacity at the same group (25 pairs) of the sample.

3.3 Results

The results may be presented in three parts.

3.3.1 Attenuation and transmission rates.

In the table 1 and 2 are presented the results of electrical attenuation and the transmission rate (Up and Downstream).

Table 1 – Reference sample - Electrical attenuation and the transmission rate (Up and Downstream).

Sample Length [km]	Attenuation Up [dB]	Attenuation Down [dB]	Transmission rate Average [kbps]
3	31,5	49,5	6333
4	31,5	62,5	3088
4,5	31,5	68,0	1996
5	31,5	73,4	1166
5,5	31,5	80,0	592

Table 2 – Fast Copper sample - Electrical attenuation and transmission rate (Up and Downstream).

Sample Length [km]	Attenuation Up [dB]	Attenuation Down [dB]	Transmission rate Average [kbps]
3	28.1	43.6	7278
4	31.5	53.7	5326
4,5	31.5	59.9	3536
5	31.5	63.0	1734
5,5	31.5	67.0	1501
6	31.5	70.8	1312
6,5	31.5	75.5	970

At the figure 5 are presented the results of transmission rate (downstream) in function of sample length for both samples.

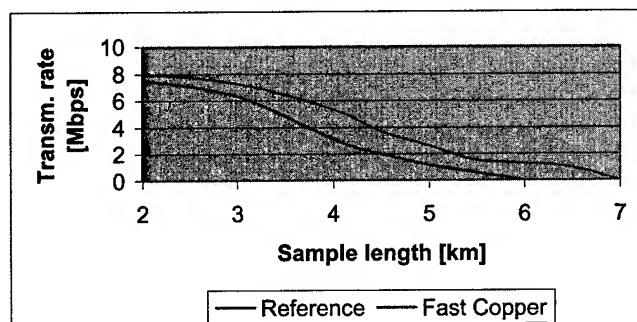


Figure 5 - Transmission rate downstream according to sample length.

3.3.2 NEXT and FEXT – Electrical noise.

Beyond the measures of attenuation and transmission rate the sample had been carried through also measurements of NEXT and FEXT in 25 pair.

Being overcome for base the measurements carried through with 4km in the samples reference and Fast Copper, it is possible to compare the noise with each insertion of modems through tables 3 and 4.

Table 3 – Reference sample – NEXT and FEXT according to ADSL modems number.

Reference sample		NEXT (dBm)	NEXT (mW)	FEXT (dBm)	FEXT (mW)
Pair	Number of DSL modem				
1	0	-55.8	0.0026	-59.4	0.0011
2	1	-59.6	0.0011	-59.8	0.0010
3	2	-38.2	0.1514	-58.4	0.0014
5	3	-37.8	0.1660	-58.4	0.0014
6	4	-37.2	0.1905	-58	0.0016
7	5	-37.4	0.1820	-58	0.0016
8	6	-36.4	0.2291	-57.6	0.0017
9	7	-36.2	0.2399	-57.4	0.0018
10	8	-35.6	0.2754	-57.2	0.0019
11	9	-35.4	0.2884	-57	0.0020
12	10	-35	0.3162	-56.4	0.0023
13	11	-34.6	0.3467	-56.2	0.0024
14	12	-34.5	0.3548	-55.6	0.0028
15	13	-34.4	0.3631	-56.2	0.0024
16	14	-34.3	0.3715	-55.6	0.0028
17	15	-34.2	0.3802	-55.6	0.0028
18	16	-32.5	0.5623	-55.5	0.0028
19	17	-32.4	0.5754	-55.4	0.0029
20	18	-32.1	0.6166	-55.2	0.0030

Table 4 – Fast Copper sample – NEXT and FEXT according to ADSL modems number.

Fast Copper sample		NEXT [dBm]	NEXT [mW]	FEXT [dBm]	FEXT [mW]
Pair	Number of DSL modem				
1	0	-60	0.0010	-60	0.0010
2	1	-52.2	0.0060	-60	0.0010
3	2	-48.5	0.0141	-60	0.0010
5	3	-47.2	0.0191	-60	0.0010
6	4	-46.8	0.0209	-60	0.0010
7	5	-46.6	0.0219	-60	0.0010
8	6	-46.2	0.0240	-60	0.0010
9	7	-45.3	0.0295	-60	0.0010
10	8	-45	0.0316	-60	0.0010
11	9	-43	0.0501	-59	0.0013
12	10	-42.8	0.0525	-58.7	0.0013
13	11	-42.4	0.0575	-59.4	0.0011
14	12	-42.5	0.0562	-59.2	0.0012
15	13	-42.3	0.0589	-59.2	0.0012
16	14	-42	0.0631	-59	0.0013
17	15	-42	0.0631	-59.2	0.0012
18	16	-41.8	0.0661	-59	0.0013
19	17	-40.5	0.0891	-58.8	0.0013
20	18	-40	0.1000	-56	0.0025

It can be observed for Figure 6 and 7 that a gain in the levels of noise of samples Fast Copper comparing with the sample reference.

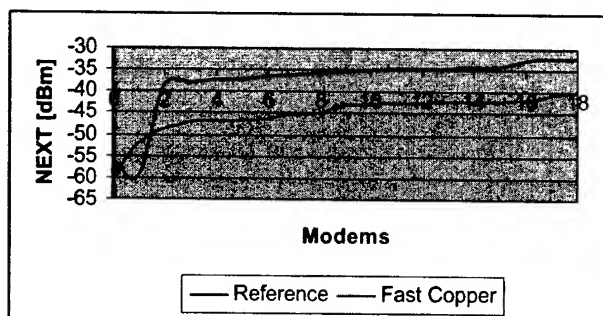


Figure 6 - NEXT according to ADSL modems count.

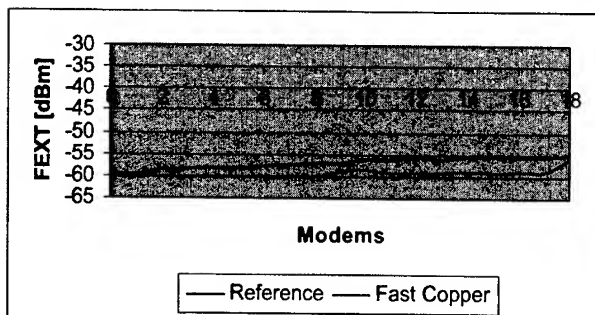


Figure 7 - FEXT according to ADSL modems count

This gain in average is of 7,6 dBm for NEXT and 2,3 dBm for FEXT. Moreover it can be observed that the power of noise NEXT and FEXT in gotten broad band in the adjacent pair was increasing to each synchronized modem, however had little variation in the transmission rate of system ADSL (figure 8).

3.3.3 Transmission rate after DSL modems insertion

In the figure 8 is presented the transmission rate in function of number of ADSL modems inserted. For both samples we can observe a small reduction of transmission rate.

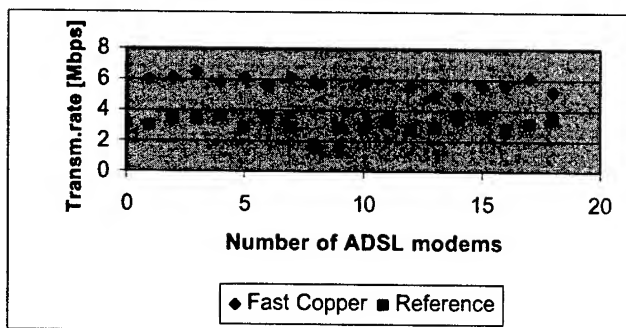


Figure 8 - Transmission rate according to ADSL modems number – sample length 4km

4. Conclusions

From the results of the electrical tests using insertion of ADSL modems and sample length can be concluded:

For ADSL insertion it is concluded that it inside the group did not have limitation of the percentage of occupation of a group of 25 pairs, independently of the length and the type of cable, even

so has observed a directly proportional increment of the level of noise with the increase of active canals and in the capacity of transmission of signals.

It was possible to also determine that the sample Fast Copper, when compared with the sample reference reaches distances of until 1km bigger, or that, for the same distance reaches 1 Mbps more than the transmission rate.

Concluding then in same condition the sample Fast Copper have higher electrical performance and supports a bigger insertion of electric losses.

5. Acknowledgments

The authors wish to thank everyone involved in the testing performed for this paper.

6. References

- [1] Renata C. Federighi and Marcelo A. Andrade, NT 1834 – Cabo Fast Copper – Ensaios, (2002)
- [2] Renata C. Federighi and Marcelo A. Andrade, ETP 0504 – Cabo para aplicação de tecnologia xDSL (2002).
- [3] DENNIS J. RAUSCHMAYER. ADSL/VDSL - Practical and Precise Study of Assymetric lines and Very High Speed Digital Subscribes. Mac Millian Technical Publishing, (1998).

Authors

M. A. Andrade

Pirelli Telecomunicações Cabos e Sistemas do Brasil
Av. Pirelli, 1100 – Sorocaba – SP – Brazil - 18103-355

Marcelo A. Andrade is graduated from Universidade Federal de Santa Catarina. He joined Pirelli in 1988 where he is in charge of Telecom Engineering and Quality

R.C.Federighi

Pirelli Telecomunicações Cabos e Sistemas do Brasil
Av. Pirelli, 1100– Sorocaba – SP – Brazil - 18103-355

Renata C. Federighi is graduated from Faculdade de Engenharia de Sorocaba. She joined Pirelli in 2000 where she is in charge of Telecom Product Engineering.

Osvaldo Tozze

Av. Nações Unidas, 4849
São Paulo - SP - Brazil – 05477-000

O.Tozze is graduated from Univ. Mackenzie de São Paulo.

Marco Antonio Garms

Av. Eng. Heitor Antônio Eiras Garcia, 943 – Apto. 62 – Bloco 7 - São Paulo - SP - Brazil - 05588-001

Marco A.Garms is graduated from Faculdade de Engenharia Industrial (FEI) and Instituto de Física of Universidade de São Paulo (USP).

Using flat steel wires as strength members in central core ribbon cables

Yongtong Guan

R&D Dept., Chengdu CCS Optical Fiber Cable Co. Ltd., An Affiliate of Corning
Hi-Tech Development Zone, Chengdu, Sichuan, P.R. China
+86 28 5182968-356, yongtong.guan@cdccs.com

Abstract

High fiber count ribbon cables are widely used in Access Networks. They are often laid inside of pre-installed pipes. These pipe resources are very precious in China, and telecommunication carriers are always trying to fill existing pipes with the highest fiber count cables. That means the outer diameter of the cable should be as small as possible. This paper presents a novel cable structure that uses two flat steel wires as strength members of the cable. This cable has a smaller outer diameter when compared to cables with two round steel wires as strength members, and has a lower risk of process upset than cable that are manufactured with four small round steel wires.

Keywords

Ribbon Cable; Flat; Steel wire; Strength member.

1. Introduction

Central core ribbon cables generally have a smaller outer diameter than stranded core cables. They normally have two steel wires that are placed 180 degree apart within the cable's jacket as strength members. (See figure 1.) This strength member configuration contributes to the cable's outer diameter, which may exceed the practical limit for some duct installation at higher fiber count cable designs. In China, the inner diameter of the pipe in which cables are laid is normally 90 mm, which normally houses three sub-pipes with inner diameters of 28 mm each. The outer diameter of cables should be limited to a certain value (approx. 20 mm), otherwise installation will be quite difficult. One method commonly used to reduce the outer diameter is to use four or more small round strength members (Figure 2) to replace two larger round strength members. Using this method, the outer diameter of cable is reduced by 1 mm at least, but cable manufacturing is more complicated since it needs more wire pay-off units and has a higher risk of process upsets.

To simplify the structure and production process, while keeping the same outer diameter and mechanical performance of the cable, we designed a new cable structure with two flat steel wires as strength members (Figure 3).

The cross section of the flat steel wire used in our new cable design is approximate a rectangle, which is 2mm long and 1mm wide. A reel of prototype cable has been manufactured with two flat steel wires as strength members. The production process is stable and the surface of the cable is smooth and round.

Cable testing has been completed that focused on the mechanical performance of the cable, including twist, cyclic flexing, tensile strength and toughness. The results show that the mechanical performance of the cable can meet the requirements and specifications of our customer.

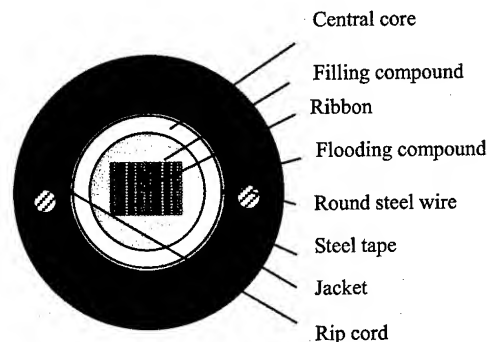


Figure 1. Cable with two $\Phi 1.5\text{mm}$ steel wires

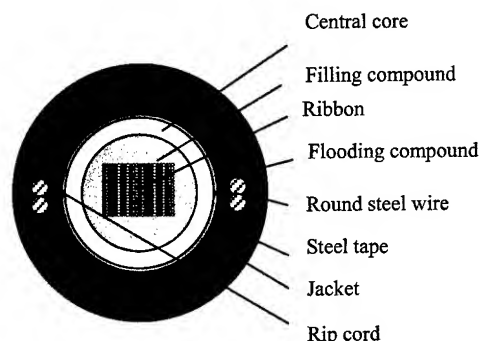


Figure 2. Cable with four $\Phi 1.0\text{mm}$ steel wires

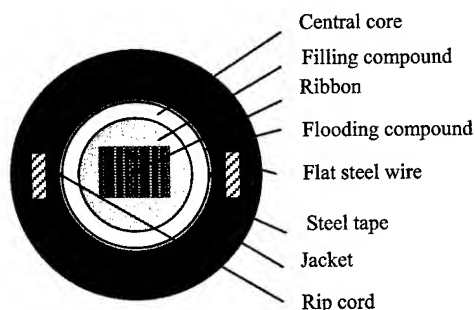


Figure 3. Cable with two flat steel wires

2. Cable Manufacturing

Flat steel wire is much different than round steel wire while being paid-off.

The flat steel wire pay-off units used in the cable manufacturing are the same as the round steel wire pay-off units, however, some new wire alignment equipments were designed and used to keep the wire from twisting. Special tools and apparatus also have been used to ensure the flat steel wires maintaining a stable position within the cable jacket.

A reel of cable was manufactured with two 1x2mm flat steel wires as strength members. The process is stable and the flat steel wires maintaining their proper positions in the cable jacket.

3. Test and Result

3.1 Mechanical Performance

In this new cable structure, we used flat steel wires to replace the traditional round steel wires as strength members, and made no other design changes. Because central core ribbon cable with round steel wires as strength members is a mature structure and they are widely used today, our tests on the new cable structure were focused on its mechanical performance which includes tensile strength, twist, cycle flexing, impacting, and toughness. Except for cable toughness, all tests are based on the requirements of IEC794-1: 1996 [1].

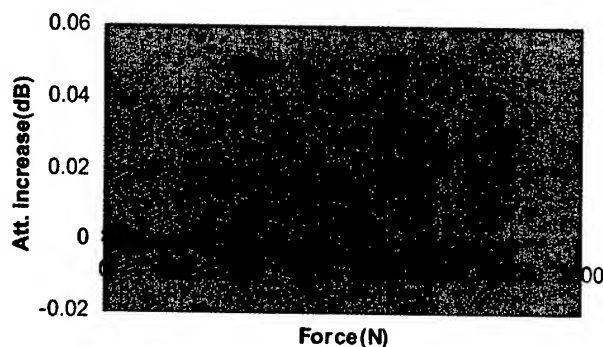


Figure 4. Att. increase in tensile test

3.1.1 Tensile Strength of Cable. Tensile tests of the cable have been completed. A length of cable sample was installed on the tensile strength testing machine, then specified incidental and long term tensile load was added on the cable. The attenuation increase and fiber strain of the cable was measured at the same time. The results showed that the attenuation increase of the cable does not exceed the specified value, and the measured fiber strain is lower than the required specification. No residual fiber strain was observed after the tensile force had been unloaded. Figure 4 shows the attenuation increase of the fibers, curve A represents the fiber with highest attenuation increase and curve B stands for the lowest. Table 1 shows the fiber strain in the test.

Table 1. Fiber strain in tensile strength testing

Tensile force	Long term load	Incidental load
Specified strain of cable (%)	$\leq 0.05\%$	$\leq 0.25\%$
Observed strain of cable (%)	0.012% ~ 0.020%	0.143% ~ 0.146%

3.1.2 Cable Twist. A one-meter sample of the cable was twisted ten times through $\pm 180^\circ$ on the twist testing machine while the attenuation increase was measured at the same time. No evidence of cracking or splitting of the cable jacket was observed after the test and the attenuation increase did not exceed the allowable value of the specification. The test results are shown in Table 2.

Table 2. Attenuation increase in cable twist, cyclic flexing and impacting

Test items	Specified Attenuation Increase (dB)	Observed Attenuation Increase (dB)
Twist	≤ 0.05	-0.01~0.01
Cyclic flexing	≤ 0.05	0.00~0.01
Impacting	≤ 0.05	0.00~0.01

3.1.3 Cable Cyclic Flexing. When the cable was taken up on the reel, the bending direction was perpendicular to a line connecting the two steel wires and parallel with the long side of flat steel wire. The bending direction in the test is in the same orientation.

Several meters long sample of cable was installed vertically on the cyclic flexing testing machine, then it was bended thirty times through $\pm 90^\circ$ under specified tension load, the attenuation increase of the cable was measured at the same time. The testing results showed that the cable can withstand mechanical flexing without exceeding the allowable attenuation increase and the outer cable jacket exhibits no evidence of cracking or splitting. The test results are shown in Table 2.

3.1.4 Cable Impact. While being tested, the sample of cable was laid on a flat and was impacted ten times by a one-kilogram weight which was one meter higher than the sample. Five different points of the cable were tested. Meanwhile, the attenuation increase was measured. The results showed that cable can withstand the specified impact force without exceeding the permissible attenuation increase, and the cable jacket exhibited no evidence of cracking or splitting. Table 2 shows the test results.

3.1.5 Cable Crushing. The specified long term and incidental compressive load was added on a ten-centimeter-long sample of cable and lasted for one minute respectively, three different section of cable were tested and the attenuation increase was measured at the same time. The results showed that the fibers subjected to long term and incidental compressive load did not exceed the allowable increase in attenuation. The results are shown in table 3.

Table 3. Attenuation increase in cable crushing

load	Specified Attenuation Increase (dB)	Observed Attenuation Increase (dB)
Incidental	≤0.05	0.00
Long term	≤0.05	-0.01~0.01

3.1.6 Cable Toughness. Toughness of the cable is related to the flexibility of the cable. If the cable is inflexible, installation of the cable will be difficult. We tested and compared the toughness of cable with two flat steel wires to cable with two round steel wires

The test method is shown in Figure 5. If a force F is added on the cable, it causes the cable to move a distance y. If the testing cable length is L, the toughness B of the cable can be calculated by the equation below.

$$B=L^3F/(3y) \quad [2]$$

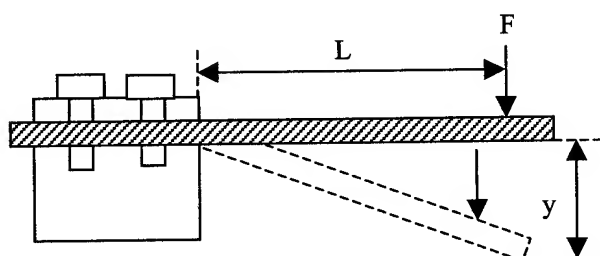


Figure 5. Test method for cable toughness

Table 4 shows the test results. The toughness of the cable is almost the same as the one using a traditional structure of two Φ1.5mm round steel wires as strength members.

Table 4. Comparison for cable toughness

Cable No.	Steel wire dimension (mm)	Steel wire number	Toughness (Nm ²)
1	1×2	2	1.63
2	Φ1.5	2	1.67

3.2 Temperature Behavior of Cable

3.2.1 Temperature Cycling Test of the Cable. The temperature cycling properties of the cable were tested. The attenuation increase of the fibers was measured at temperature extremes of -40°C and 70°C. The results are shown in table 5.

Table 5. Temperature cycling test of the cable

Temperature(°C)	-40	70	20
Specified Attenuation Increase @1310 (dB)	≤0.05	≤0.05	≤0.05
Specified Attenuation Increase @1550 (dB)	≤0.05	≤0.05	≤0.05

Observed Attenuation Increase@1310nm (dB)	-0.026 ~ 0.013	-0.007 ~ 0.041	-0.013 ~ 0.022
Observed Attenuation Increase@1550nm (dB)	-0.058 ~ 0.019	-0.048 ~ 0.039	-0.055 ~ 0.014

3.2.2 Temperature Cycling Test of the Cable with Coils.

When cable is installed, the excess cable is often coiled and stored. In order to simulate the installation of a cable with these coils, we wound a length of cable into circles with a diameter of approximately its minimum dynamic bending diameter, and then reperformed the temperature cycling testing. The test results showed that the attenuation increase did not exceed the allowable value, and no optical steps were observed in the test. Table 6 shows the results.

Table 6. Temperature cycling test of the cable with slack coils

Temperature(°C)	-40	70	20
Specified Attenuation Increase @1310 (dB)	≤0.05	≤0.05	≤0.05
Specified Attenuation Increase @1550 (dB)	≤0.05	≤0.05	≤0.05
Observed Attenuation Increase @1310nm (dB)	-0.038 ~ 0.021	-0.017 ~ 0.039	-0.011 ~ 0.025
Observed Attenuation Increase @1550nm (dB)	-0.027 ~ 0.016	-0.006 ~ 0.023	-0.033 ~ 0.017

4. Conclusions

Central core ribbon cable using two flat steel wires as strength members has the same outer diameter as similar cable using four round steel wires. The cable outer diameter of these two structures is smaller than cable with two round steel wires as strength members. Meanwhile, the production process of cable with two flat steel wires is simple, it requires only two wire pay-off units, minimizing the risk of process upset while being manufactured. Trials have been done with test results showing the two flat wires design meets or exceeds all IEC794-1 requirements while maintaining a cable flexibility similar to the two round wires design.

5. Acknowledgments

Special thanks to Ms. Rong Xia for the purchase of flat steel wire, Mr. Feng Yuan for all the tests made on the new structure cable, and also thanks all the kindly cooperation from different departments.

6. References

- [1] IEC794-1: 1996.
- [2] Hu Xianzhi, and Liu Zeheng, "Optical Fiber and Fiber Cables Engineering Test," (June, 2001).



Mr. Yongtong Guan, received his B.E. degree in Mechanical Engineering in Beijing Institute of Machinery Industry in 1995 and then joined Chengdu KV Engine Co., Ltd. as a process engineer. At the beginning of 2000, he joined Siemens Optical Fiber Cables Co., Ltd., and now is a R&D engineer in Chengdu CCS Optical Fiber Cable Co., Ltd.

Development of FR-PVC for Compact and High Performance UTP Cable

Do Hyun Park, Myeong Jin Ahn, Gun Joo Lee

Polymeric materials Technology Group, LG Cable Research & Development Center,
555, Hoggae-dong, Dongan-gu, Anyang-shi, Kyungki-do, Korea

+82-31-450-8333 · dhpark@cable.lg.co.kr

Abstract

In this work, it is revealed that the single layer insulated CMR 25P cable has better electrical property than that of the conventional double-layered cable. But single layer insulation structure has no flame retardation. To make this newly designed, high performance and compact cable, it is highly required to use very efficient FR-PVC sheath material.

Thus, the behavior of flame retardancy and smoke evolution of FR-PVC filled with various combinations of inorganic fillers is investigated to develop new cable construction for CMR 25P. Through the analyses on thermal stability and smoke density, it has been revealed that the flame retardation and smoke suppression of FR-PVC could be effectively enhanced by incorporation of zinc borate and molybdenum.

Using this newly developed FR-PVC sheath material, we can make newly designed CMR 25P cable that has only one insulation layer. This newly designed cable has superior electrical properties, fire performance and has more compact structure.

Keywords

Cable; FR-PVC, Electrical property; Flame-retardant; Smoke

1. Introduction

We designed new cable construction for CMR 25P, which is a revision of dual layered insulation. In conventional dual layered insulation, the inner insulation layer is made of non-flame retardant HDPE and the outer insulation layer is composed of flame retardant HDPE. But, the newly designed cable has only one layer of non-flame retardant HDPE insulation. With this newly designed cable, we can enjoy the merits such as advanced transmission property and more compact cable structure. But this cable design strongly needs to have very efficient flame retardant sheath material to compensate the role of flame retardant HDPE insulation layer. To achieve the requirement of flame retardant property of UL 1666 riser for newly designed cable, we have to develop high flame retardant PVC.

It is well known that the results of flame test were varied according to flame-retardant materials, cable constructions and were dependent closely on flame retardancy of sheath. Therefore, flame retarded FR-PVCs have been investigated to study the effects of inorganic fillers and plasticizers on the improvement of flame retardancy and the suppression of smoke density. Through the analyses on the behavior of combustion and smoke evolution, it has been revealed that the flame retardancy of PVC could be effectively enhanced by

incorporation of inorganic fillers and plasticizers. That is, there exist some synergistic interactions between inorganic fillers and plasticizers in developing the hard and compact charred layer that increases the resistance to flame stress and reduces the combustion rate. This argument was verified by the observation of fire performance using cone calorimetry. This compactly charred layer provides a good thermal and flame barrier and prevents non-flame retardant insulation from combustion.

Corrosiveness, smoke emission and the toxicity of combustion products have been important issues till now. Because we try to develop highly flame retardant PVC sheath of the newly designed compact and high performance UTP cable, the aim of this work is to study the behavior of flame retardancy and smoke evolution of FR-PVC filled with various combinations of inorganic fillers. The thermal stability and fire performances are quantitatively analyzed by oxygen indexer and cone calorimetry. To identify the flame retardant mechanism of these flame retardant systems, the combustion behavior was also investigated.

2. Experimental

2.1 Materials

2.1.1 Insulation

The polymers used in this study are ethylene-vinyl acetate copolymer (EVA) and high-density polyethylene (HDPE). Aluminum trihydrate ($\text{Al}(\text{OH})_3$, ATH) and bromine are used as the additives to increase the flame retardation.

2.1.2 Sheath

PVC is modified with plasticizer and flame retardant fillers. Used flame retardant plasticizers are such as brominated and phosphate plasticizer. The inorganic flame retardant fillers and fillers including ATH, hydrated magnesium carbonate, zinc borate ($2\text{ZnO} \cdot 3\text{B}_2\text{O}_3 \cdot 3.5\text{H}_2\text{O}$), molybdenum compound, antimony trioxide (Sb_2O_3) and calcium carbonate (CaCO_3) are used to increase the flame retardation and to reduce the evolution of smoke during the combustion. In this work, the FR-PVC is modified in three types. The mixtures of polymer and inorganic fillers were processed in a double roll plasticator at 130°C for 10 minutes. To get sheets for flame, mechanical and electrical test, the mixtures were pressed at 170°C for 5 minutes.

2.2 Electrical and mechanical properties

The electrical properties were measured at various frequencies using dielectric constant tester (ANDO electric Co.). A dumbbell type specimen with the width of 5.6 mm and the gauge length of 20 mm were prepared and tested at 200 mm/min by using Instron 6022 and the number of specimens is at least 5.

2.3 Fire test

The limited oxygen indices from burning samples were measured as the oxygen concentration (%) by Oxygen indexer (FTT Co.). Cone calorimeter (FTT Co.) was used to obtain heat release rate (HRR), rate of smoke release (RSR) and total smoke release (TSR) according to ASTM 1356-90 with a heat flux of 50 kW/m². This heat flux has been chosen because it corresponds to the evolved heat during a fire. The shape of burned samples were observed using microscopy.

3. Results and discussion

3.1 Electrical properties

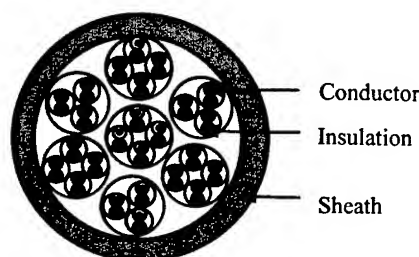


Figure 1. The schematic of CMR 25P

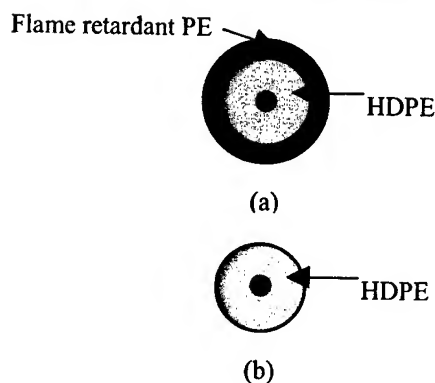


Figure 2. The schematic of insulation:
(a) Dual layer, (b) Single layer

Figure 1 shows the schematic of CMR 25P cable tested with newly developed flame-retardant (FR) materials. This cable is rated as UL riser. Figure 2 shows the schematic of the structures of HDPE insulation. Previous cable, which is shown in Figure 2(a), was consisted with dual layered insulation structure. FR-PE is skinnily extruded outside of the main HDPE insulation layer. But as shown in Figure 2(b), the newly developed cable has a only single

insulation layer. In this research, skinnily extruded FR-PE is removed to improve transmission property and to realize light weight and compact size. With a help of this design, thickness of insulation could be reduced from 0.234 mm to 0.217 mm. In addition, line speed is risen up to 10 % and the loss constant of PE is decreased up to 60%. Electrical properties, dielectric constant and $\tan\delta$ of insulation materials which are insulated around conductor in single or dual layer are listed in Table 1. In Table 1, FR-PE#1 and FR-PE#2 is based on HDPE and EVA respectively. Table 2 compares the electrical properties of dual layer insulation cable, FR-PE#1 formed second layer for Cable #1. Cable #3 and #4 are constructed with single insulated cables which are sheathed with various flame retardant PVC sheath. Newly developed cable is a designated as UL Category 5 cable.

Table 1. Electrical properties of insulation materials.

	Frequency	1 KHz	1 MHz
FR-PE#1	Dielectric Constant	2.6	2.57
	Tan δ	0.0025	0.0034
FR-PE#2	Dielectric Constant	4.4	3.94
	Tan δ	0.0161	0.0881
HDPE	Dielectric Constant	-	2.32
	Tan δ	-	0.00006

Table 2. Electrical properties of cables.

	Cable #1	Cable #3	Cable #4
Insulation	Dual layer	Single layer	
Attenuation (dB at 100 MHz)	Max. 18.2	Max. 17.5	Max. 17.5
SRL, at 20MHz	39.7	38.4	37.9
SRL, at 100MHz	28.03	27.01	26.57

As shown in Table 2, Cable #3 and #4 have lower value of attenuation at 100 MHz than that of Cable #1 due to the better electrical properties of insulation material, HDPE, which is insulated upon the conductor in single layer. Cable #1 having the dual insulation layer has higher value of attenuation. The improvement in transmission characteristics for newly developed cable was about 4% better than transmission for the conventional cable. This result is caused by higher dielectric constant and $\tan\delta$ of FR-PE #1 which is used as a second layer over the first insulation layer. Lower electrical properties of FR-PE #1 result from the fact that it is flame retardant polyethylene, which is modified with various flame retardants such as bromine and other halogen materials to improve flame retardancy. Comparing with the FR-PE's, the HDPE shows better electrical properties because it does not have any particular ingredients. In addition, the structural return loss (SRL) of cable #3 and #4 is similar to that of

cable #1. Generally, insulation roughness or irregularities, excessive eccentricity as well as variations in insulation diameter may increase SRL. With dual insulated conductors, the problem of achieving uniformity of insulation can be very serious because of the difficulty of forming a first layer that is substantially uniform and then forming a uniform second insulation layer. It is known as if the first layer is soft or compressible, the second layer can distort it, thereby increasing SRL to an undesirable level. If, in turn, second layer is compressible, it can be distorted by the helical member used to bundle the cable pairs, or during the twisting process. For this reason, though it has simpler structure, the cable with one-layer insulation shows better transmission characteristics than the cable that has two-layer insulation.

3.2 Fire performance

3.2.1. Sheath

In order that the developed cable, as depicted in Fig. 1, be suitable for use as a riser cable, it is necessary that the outer sheath be highly flame retardant. Mechanical and flame retardancy properties of FR-PE's modified with various flame retardants are listed in Table 3. Three kinds of FR-PVC's have similar mechanical properties such as tensile strength and elongation. Insulation materials such as polyolefins, unless specifically modified for flame retardation, are highly flammable materials. For this reason, to enhance flame resistance, the core that is formed by the several conductors need to be surrounded by a sheath of highly flame retardant polyvinyl chloride (FR-PVC) material. FR-PVC#1 comprises forty-one percent (41%) PVC resin; twenty-eight percent (28%) plasticizers including general phthalate, brominated phthalate; twenty-five percent (25%) flame retardants including alumina trihydrate and antimony trioxide; and six percent (6%) other additives including five percent (5%) stabilizers and one percent (1%) lubricants. FR-PVC#2 is modified with various halogen scavengers, such as zinc borate, and metal hydrate and calcium carbonate, which form rigid char when heated by fire, to increase the LOI. Its LOI is 40%. FR-PVC#3 comprises forty-two percent (42%) PVC resin; twenty-three percent (23%) plasticizers including phosphate phthalate and brominated phthalate; twenty-four percent (24%) flame retardants including alumina trihydrate, hydrated magnesium carbonate and antimony trioxide; eleven percent (11%) smoke suppressant including zinc borate and molybdenum; and other additives including stabilizers and lubricants. The LOI of FR-PVC#3 is similar to that of FR-PVC#2. A blend of flame retardant plasticizers, however, shows poor cold impact property, but the cable surrounded by this sheath material, FR-PVC#3, meets the cold bend test at -20°C .

Table 3 Mechanical and flame retardancy properties of PVC modified with various flame retardants.

	FR-PVC#1	FR-PVC#2	FR-PVC#3
Tensile Strength (kgf/mm^2)	2.0 ± 0.1	2.0 ± 0.08	2.1 ± 0.09
Elongation (%)	300 ± 8	260 ± 9	270 ± 8
Limited Oxygen Index (%)	35	40	40
Cold Impact ($^{\circ}\text{C}$)	-15	-10	-8

The residues of conventional FR-PVC#1 and newly developed FR-PVC#2 and #3 after burning are shown in Figure 3. For only ATH-filled polymer blends like FR-PVC#1, endothermic dehydration of ATH cools the plastic part and the water vapor dilutes evolved combustible gases. But as FR-PVC#2, the surface of blend modified with ATH and halogen scavengers, such as zinc borate, and calcium carbonate and particular metal hydrate, is covered with more compact charred layer. The various halogen-metal complexes form a surface shield layer on the surface of combusting plastic material preventing the further access of flame to fresh polymer. In case of FR-PVC#3, molybdenum acts as a combustion catalyst to increase hard charred layer, which is a good thermal barrier. That is, the interactions between antimony trioxide and molybdenum reinforce the protective shield under flame and thus the evolution of smoke is effectively suppressed. In addition, the effect of flame retardation is also increased.

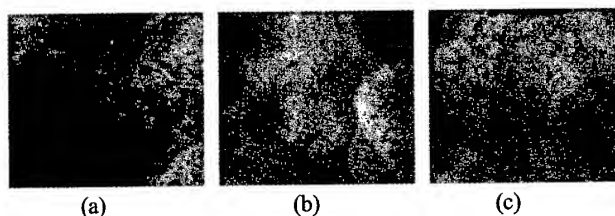


Figure 3. Micrographs of the surfaces of polymer blends modified with various flame retardant (after combustion):

(a) FR-PVC#1, (b) FR-PVC#2, (c) FR-PVC#3

3.2.2. Insulation

Figure 4 shows the difference in mechanical and flame retardation properties of FR-PE's modified with various flame retardants.

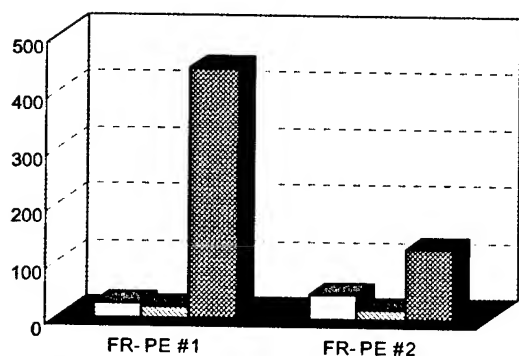


Figure 4. Mechanical and flame retardation properties of FR-PE modified with various flame retardants. ■ -Limited Oxygen Index (%), ■ -Tensile Strength (kgf/mm²), ■ -Elongation (%)

These FR-PE's are used as the second insulation layer over the first one. Halogen free flame retardant insulation material, FR-PE#2, is composed of polar polymer and halogen free flame retardants such as metal hydroxides. The base polymer of FR-PE#2 is ethylene vinyl acetate (EVA). LOI of FR-PE#2 is 42%. If FR-PE#2 is applied to the second insulation layer, good flame retardancy results, but there is much excess loss, which is shown in Table 1, at the highest frequency due to the high dielectric constants of metal hydroxides and polar polymer [1]. This cable meets the UL riser test. FR-PE#2 lacks certain mechanical properties such as elongation or flexibility because of the high filled inorganic fillers. To solve these problems, new type of flame retardant compound for the insulation was developed. In our study, a polymer alloy insulation material, FR-PE#1, that consists of a low dielectric constant polymer as shown in Table 1 and a flame retardant polymer is developed. FR-PE#1 is flame retardant insulation material that is composed of HDPE and halogen flame retardant such as bromine. Its Limited Oxygen Index (LOI) is 25.5%. High-density polyethylene is selected as the low dielectric constant ingredient. For the flame retardant ingredients, a bromine was selected because of its non-flammability, which prevents combustion of polyethylene.

3.2.3. Cone calorimeter by oxygen consumption

Figure 5 shows the curves of heat release rate (HRR) that is calculated from the amount of oxygen consumed during the combustion. Comparing with FR-PVC#1, as shown in Figure 5, by the addition of inorganic fillers such as zinc borate, calcium carbonate and particular metal hydrate, the maximum HRR peak of FR-PVC#2 is reduced to about 40 kW/m² and the second peak is also observed at low value. In case of FR-PVC#1 and #2, the curves proceed through three steps: at first stage, after ignition, the degradation of polymeric materials initiates and the values of HRR increases rapidly. However, at second step, the HRR is suppressed by the endothermic reaction of ATH and decreases by the formation of an expanded protective shield, which is induced by inorganic fillers those give the synergistic effect on the flame retardancy by

reacting with halogen as halogen scavenger. Finally, the HRR increases again which indicates the degradation of heat-protective shield formed on the surface. Thus, after second peak the heat is continuously released. In Figure 5, FR-PVC#3 exhibits better combustion behavior in the first stage of combustion than that of FR-PVC#2. These behaviors are quite different from the results of oxygen index. The oxygen indices of FR-PVC#2 and FR-PVC#3 are 40% and 40% respectively. The reason for this difference in HRR curve and LOI is that flame retardant system like phosphate ester and molybdenum filled in FR-PVC#3 forms very strong char during combustion. According to this phenomenon, the first peak is more delayed. Moreover, during combustion, the carbonized layer of that is not cracked. This also retards significantly further advancement of the combustion process. The latter is the main mechanism of smoke suppression. These results are shown in Figure 6.

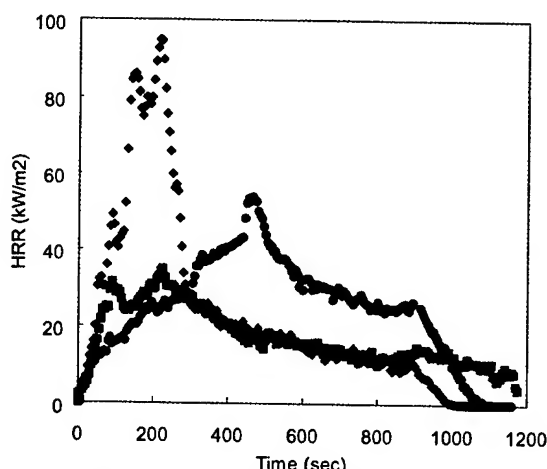


Figure 5. The curves of HRR with time (heat flux of 50 kW/m²):
◆:FR-PVC#1, ■:FR-PVC#2, ●:FR-PVC#3

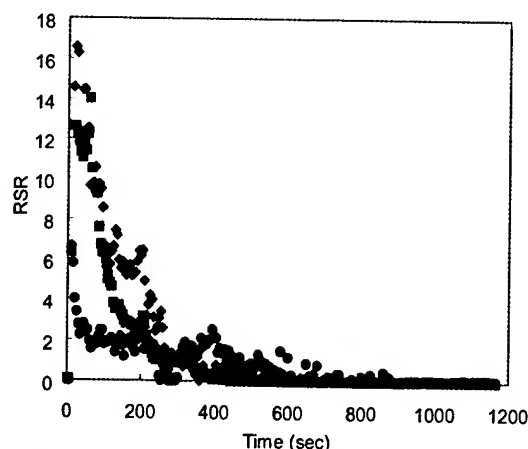


Figure 6. The curves of RSR with time (heat flux of 50 kW/m²):
◆ FR-PVC#1, ■ FR-PVC#2, ● FR-PVC#3

Table 4 Test results of UL 1666 Riser test

Structure of Insulation	Dual layer	Single layer		
	Cable #1	Cable #2	Cable #3	Cable #4
Maximum Damage Height (m)	1.5	3.66 ↑	1.5	0.9
Maximum Temperature (°C)	247	454 ↑	195	190
Cable Outer Diameter (mm)	29.4	28.4	28.4	28.4
Number of Length (EA)	20	21	21	21
Applied material	PVC#1	PVC#1	PVC#2	PVC#3

In the case of FR-PVC#1, the smoke is dominantly suppressed by the endothermic dehydration of ATH that release water vapor, cools the plastic part and dilutes evolved combustible gases.

Comparing with total smoke release (TSR) of FR-PVCs; FR-PV1# has 2050; FR-PVC#2 has 1530; FR-PVC#3 has 899, the interaction of the smoke suppressant such as zinc borate and ATH causes a considerable delay in reaching to maximum smoke evolution and significantly lowers the overall level of produced smoke. Therefore, it can be concluded that, when exposed to heat and flame, the interactions of molybdenum with zinc borate and ATH exhibit a synergistic effect on the depression of smoke evolution as well as the increase of flame retardancy [2]. In case of FR-PVC#3, the substitution of flame plasticizer like phosphate phthalate reduces smoke formation because it is acting mainly as the solid and liquid phase. Phosphorous compound is decomposed by heat and forms non-volatile phosphorous acid. Then, this acts as a coagulation agent of residues of carbon. As a result of this effect, soot particles and CO are reduced and the amount of initial smoke evolution is very low. This behavior is consistent with the shape of residue after combustion and smoke density and HRR. It can be concluded that both phosphorous ester and molybdenum exert the synergistic effect on the flame-retardant and smoke suppression.

3.2.3 Combustion properties

The riser test results of CMR 25P cables jacketed with various FR-PVC's and insulated with various insulation materials are shown in Table 3. The UL 1666 riser vertical shaft flame test is measured at two points; maximum temperature of 454°C; damage height of cable. Maximum damage height of Cable #1 having dual insulation layer and Cable #3 having non-flame single insulation layer in a UL 1666 riser is 1.5m and 1.5m respectively, and it is found that these cable have same flame retardancy. Generally, it can be regarded as the cable, which is surrounded with higher LOI jacket material, shows better result of flame retardation. In a real flame test, this result comes from developed FR-PVC forms a rigid char during combustion and prevents the heat and oxygen. This results in the improvement of flame retardancy of cable. If the sheathing material has low flame retardant or less solidification of carbonized layer such as Cable #2, it promotes the combustion of flammable insulation material of the cable. This makes the cable shows melt drip phenomena and burn it out. Cables jacketed with FR-PVC's having high LOI

up to 40% passed UL 1666 riser test, but the test results are quite different because of the different combustion behavior. At initial stage, the combustion behavior is similar for cable#3 and cable#4. However, in case of cable#3, the combustion of cable continuously proceeded because the inside insulation material of cable burns after the jacket material has been burned. From the test results for cables constructed with various FR-PVC's and insulation materials, it can be concluded that combustion characteristics of cable depend on the structure of cable. Also, it can be found that the flame retardancy of cable depends on the combustion behavior and formation material during the combustion of both sheath and insulation material.

4. Conclusions

In this work, the behavior of flame retardancy and smoke evolution of FR-PVC filled with various combinations of inorganic fillers is investigated to develop new cable construction for CMR 25P. Through the analyses on thermal stability and smoke density, it has been revealed that the flame retardation and smoke suppression of FR-PVC could be effectively enhanced by incorporation of zinc borate and molybdenum. There exist synergistic interactions between zinc borate and molybdenum in developing the hard and compact charred layer that increases the resistance to flame stress and reduces the combustion rate.

In addition, it can also be concluded that the electrical properties of two-layered insulation cable can be greatly enhanced if it is replaced by single layer insulation. With the use of single layer insulation and highly effective FR-PVC sheath material, the newly designed CMR 25P cable has high electrical property, flame-resistance and compactness.

References

- [1] A. Nakayama, International Wire and Cable Symposium, 726 (1996).
- [2] Morley J. C., Handbook of polyvinyl chloride formulating, edited by Edward J. Wickson, John Wiley & Sons, pp. 551 (1993).

Authors



Do Hyun Park
LG Cable R&D Center
Polymeric materials T/G
Senior Research Engineer



Myeong Jin Ahn
LG Cable R&D Center
Polymeric materials T/G
Senior Research Engineer



Gun Joo Lee
LG Cable R&D Center
Polymeric materials T/G
Principal Research Engineer

Mechanical Stress and Shield Structure Effect on Shield Performance for Screened Twisted-Pair Cables

S.-H. Chou, J.-C. Lin, J.-C. Lii, Y.-H. Huang, H.-P. Hsu, Y.-c. Lin and J.-Y. Liu

NOS, Telecommunication Laboratories, Chunghwa Telecom

Taoyuan, Taiwan, R.O.C.

886-3-424-5761 · SHC@CHT.COM.TW

Abstract

Shield structure effect and mechanical stress effect on shield performance for FTP cables and SFTP cables have been studied in this paper. Shield performance can be qualified by measuring shield transfer impedance. Although shield performance for ScTP cables is much dependent on cable manufacturers with different cable shield structure design, several conclusions can be drawn from this study. Based upon shield structure study, to solve electromagnetic interference problem, SFTP cable is recommended especially at high frequency. For FTP cable, helical Al/plastic laminate tape and stranded drain wire should not be used as shield construction. Under mechanical stress study, including ellipse test and figure eight test, figure eight test does some severe damage to Al foil for FTP cable; however, SFTP cable is available to suffering both mechanical stress tests up to 100 MHz.

Keywords

Ellipse test, EMI, Figure eight test, FTP cable, Mechanical stress effect, ScTP cable, SFTP cable, Shield structure effect, Transfer impedance, UTP cable

1. Introduction

High bandwidth applications usually require the need to provide excellent electromagnetic interference (EMI) protection [1-3]. EMI is presented everywhere, such as caused by power line, air conditioning system, mobile phone, and electric motor; the electromagnetic compatibility (EMC) behavior of cabling system therefore becomes important.

For a whole cabling system, cables are widely spread over the entire building and therefore are the most vulnerable and least controllable part [3]. The most effective cabling system against EMI is especially constructed from cables that utilize twisting, screening and grounding for additional crosstalk performance and effective EMI protection.

Balanced twisted pair cables, including unshielded twisted pair (UTP) cable and screened twisted pair (ScTP) cable, are popularly used for high bandwidth applications. UTP cable does not rely on physical shielding to block interference, but works on balancing technique [4]. Twisting is capable of canceling parts of EMI effective only up to 30 MHz [1,3]. Foil screen is ideally good efficiency against EMI over the frequency range up to 100 MHz or higher [1,3].

Basically, the shielding effectiveness depends on the material of the shield, its thickness, the type of EMI noise field, its frequency, the distance from the noise source to the shield, any shield discontinuity, and the grounding structure used [4]. However, the installation for a ScTP cable is more dedicate than that for a UTP cable. Full protection with the shield can only be achieved by well properly grounding the shields and shielding continuity [1,4]. If installed and/or terminated improperly, any shield will act as an antenna, radiating and receiving noise [2-4].

Shield performance has been quantified by measuring shield transfer impedance (TI) using the triaxial measurement technique [2,5]. Although the famous triaxial measurement technique was applicable to coaxial cable only, it has been used to characterize the shield performance of balanced twisted pair cable. The disadvantages of this technique are only on a very short length, 1 meter, and not applicable to unshielded cables [6].

Shield TI of a per unit length of cable (Z_T , in ohms/m or mohms/m) is determined by the ratio of the longitudinal voltage on the conductors enclosed by a shield to the surface currents on the outside of the shield as shown in Equation (1).

$$Z_T = V/(I \cdot L) \quad (1)$$

Where V is the potential difference built up between the conductors and the shield, I is the current induced by the external field on the shield, and L is the cable length. Lower TI values correlate to higher shield performance.

The correlation between TI performance and cable shield structures effect on the shield performance of ScTP cable will be discussed in this paper. Furthermore, the effect on mechanical stress test for ScTP cable will be also discussed in this paper in detail. The results could be helpful to the cabling designer to select the kind of ScTP cable and the cabling constructor to install the ScTP cabling system properly.

2. ScTP cable construction

Typically, ScTP cable includes an overall shield which may consist of a helical or longitudinal metal/plastic laminated tape, and/or braided non-insulated Sn-clad Cu conductors [7]. On the other hand, drain wire possibly included is in contact with the metal side of the tape. Different cable manufacturers supplied ScTP cables having different shield constructions.

In this study, several ScTP cables having different shield components were supplied from four cable manufacturers (identified as A, B, C, and D), providing 7 samples with different shield structures.

Four ScTP cables, named FTP cable, employ Al foil and drain wire, identified as A-1, B-1, C-1, and D. In detail for A-1, B-1 and C-1, a plastic coverage tape is used to isolate the foil tape from the four pairs. An overall Al/plastic laminate tape is applied longitudinally over the twisted pairs. A Sn-clad Cu wire behaved as a drain wire is located between coverage tape and foil tape and is in contact with the aluminum side of the Al/plastic laminate tape.

Compared with A-1, B-1 and C-1, D has several different shield attributes. Firstly, the Al/plastic laminate tape is applied helically over the twisted pairs. Secondly, the drain wire is located between foil tape and cable jacket, which means that aluminum side for Al/plastic laminate tape has the face to cable jacket. Further cable components description for four FTP samples is listed in Table 1.

Table 1. Cable components description for four FTP cables (unit: mm)

Sample	A-1	B-1	C-1	D
Conductor diameter	0.50	0.52	0.51	0.51
Coverage tape thickness	0.02	0.02	0.02	0.10
Drain wire type	Stranded	Solid	Solid	Solid
Drain wire diameter	0.45	0.45	0.48	0.50
Foil thickness (Al foil only)	0.055 (--)	0.065 (0.047)	0.070 (0.052)	0.025 (--)
Foil width	18	21	18	20
Cable jacket thickness	0.6	0.6	0.5	0.43
Cable diameter	5.7	6.0	6.0	5.7

The other three ScTP cables, named SFTP cable, use Al foil and Cu braid as shield components, identified as A-2, B-2, and C-2. A plastic coverage tape is also presented to isolate the foil tape from the four pairs first. Subsequently, an overall Al/plastic laminate tape is applied longitudinally over the twisted pairs and then Sn-clad Cu braid is used to wrap it up. However, a significant difference from A-1, B-1 and C-1 is that the aluminum side for Al/plastic laminate tape is opposite to Sn-clad Cu braid. Furthermore, except for B-2, the others provide no drain wire. The drain wire for B-2 is located between aluminum side for foil tape and Cu braid. Further cable components description for three SFTP cables is listed in Table 2.

In Table 1 and 2, for the term of foil thickness, (--) made as a sign means that it is not able to separate Al foil from the Al/plastic laminate tape and not able to measure the thickness for Al foil only.

Table 2. Cable components description for three SFTP cables (unit: mm)

Sample	A-2	B-2	C-2
Conductor diameter	0.50	0.50	0.52
Coverage tape thickness	0.02	0.02	0.02
Drain wire type	--	Solid	--
Drain wire diameter	--	0.5	--
Foil thickness (Al foil only)	0.055 (--)	0.045 (--)	0.050 (0.030)
Foil width	18	18	24
Braid	Diameter per strand	0.10	0.11
	# of strands per carrier	5	6
	# of carriers	16	16
Cable jacket thickness		0.4	0.6
Cable diameter		5.2	6.0

3. Experimental section

There are seven ScTP cables used to study cable shield performance. All cables are Cat 5 and with different shield structures as described in Sec. 2 (identified as A-1, A-2, B-1, B-2, C-1, C-2 and D). Although effective test length is 1 meter, the cable has to be cut into 1.13 meter in length to prepare the cable sample for TI measurement. For each cable, three samples were prepared for three test cables.

To prepare the cable sample and to install the cable under test into TI apparatus are very complicated and require professional craftsmanship. During the cable sample preparation, any damage for the sample, especially for shield discontinuity, will have a change for the worse in TI data.

All eight conductors for the balanced twisted pair cable should be shorted together to form a core and excited with a 50 ohm source, several resistors are therefore used to connect the cable under test and the TI fixture. The main purpose of connecting the resistors is to match the inner and outer impedances to the network analyzer subsystem. For cables A-2 and C-2 having no drain wire, three carriers from braid were wound together to form a pigtail and treated as a drain wire.

The shield performance measurement was performed by DCM CMS-2XLD TI measuring system, which is applicable for frequencies up to 100 MHz. The data for TI measurements would include twelve frequency points, 1, 10, 16, 20, 25, 31.25, 40, 50, 62.5, 70, 85 and 100 MHz. For a more accurate measurement, calibration is required before the measurements every day. All cable samples were measured for three times to ensure the accuracy of measurements.

For mechanical stress test, the sample was made to form an ellipse and then to form a figure eight. The detailed processes for each cable sample are described as follows:

- (1) To install the cable sample into TI apparatus and to measure the initial TI data for three times.

- (2) For the cable sample after measured initial TI data, to loop the sample into a 15 cm diameter loop, and then compress the coil into a 6.3 cm wide non-conductive trough to form an ellipse for 2 days.
- (3) After two days, to restore the original condition (uncoiled), and then install the cable sample into TI apparatus and test the ellipse TI data (ellipse test) for three times.
- (4) To loop the cable sample again, compress the coil to form an ellipse, and then rotate one end on the coiled ellipse by 180° to form a figure eight in the non-conductive trough for 2 days.
- (5) After two days, to restore the original condition, and then install the cable sample into transfer impedance apparatus and test the figure eight TI data (figure eight test) for three times.

Therefore, the TI data for the cable, including initial, after ellipse test and after figure eight test, will be measured in this study.

4. Results and Discussion

4.1 Shield Structure Effect

Initial TI data are illustrated graphically in Figures 1 ~ 4, which show the data that for the cable samples obtained by 12 frequencies as mentioned in Sec. 3. Figure 1 shows initial TI data for A-1 and A-2, Figure 2 is for B-1 and B-2, Figure 3 is for C-1 and C-2, and Figure 4 is for D.

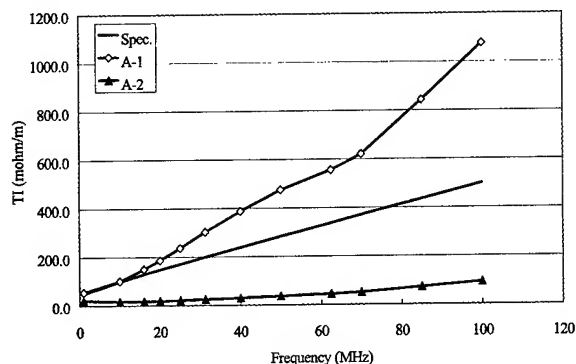


Figure 1. Initial transfer impedance data for cable A-1 and A-2, and specification data

In Figure 1 and 4, the curves without symbol represented the specification data [7]. On the other hand, The TI values for A-1, A-2, C-1 and D are the average values for three cable samples, whereas for the other cables, B-1, B-2 and C-2, the initial TI values are the average values only for two cable samples due to the appearance of strange data. Furthermore, it needs to be noted that there are completely different scales for TI data in these four figures.

Several features are shown in these figures for initial TI data. First of all, no matter what the manufacturer is, comparing to FTP cable, SFTP cable from the same manufacturer always has better shield performance. Secondly, as well known, the TI data normally increase with the testing frequencies as observed in Figure 1, 2 and 4, whereas B-1 and B-2 reveal different characteristics. Thirdly, the data of A-1 and D did not meet the TI requirements based upon TIA/EIA specification [7]. Finally, significant differences between the data for D and the specification data are shown in Figure 4.

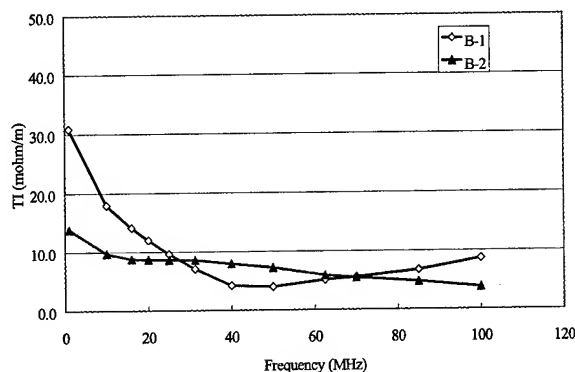


Figure 2. Initial transfer impedance data for cable B-1 and B-2

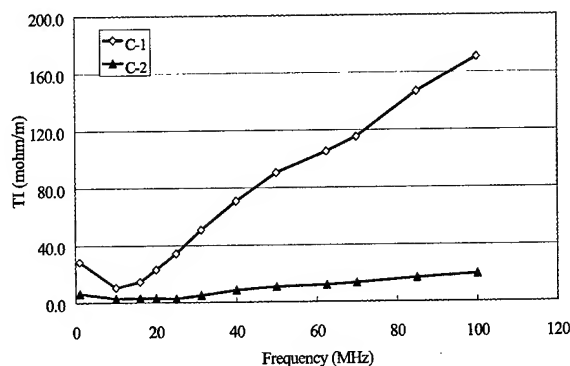


Figure 3. Initial transfer impedance data for cable C-1 and C-2

C-1 and C-2 are chosen as an example to discuss the difference in shield performance between FTP cable and SFTP cable. Shield components for C-1 include a longitudinal Al/plastic laminated tape and drain wire, whereas C-2 has a longitudinal Al/plastic laminated tape and Sn-clad Cu braid as shield components. As shown in Figure 3, the TI data for C-1 and C-2 are 101 mohm/m and 16 mohm/m at 10 MHz, respectively, whereas they are 1076 mohm/m and 93 mohm/m at 100 MHz, respectively. The data showed that

the difference in shield performance between C-1 and C-2 increases significantly at high frequency. The conclusion is that the existence of Cu braid can provide better shield performance in the entire frequency range, especially at high frequency.

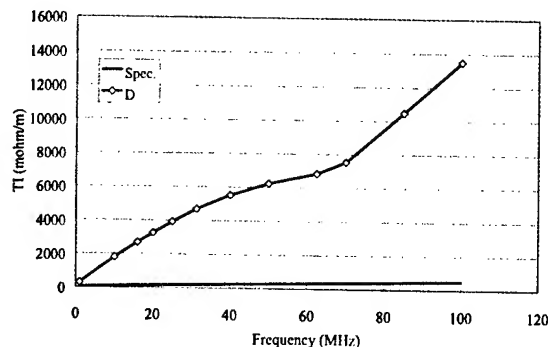


Figure 4. Initial transfer impedance data for cable D, and specification data

In Figure 2, for B-1 and B-2 supplied from the same manufacturer, the TI values at low frequency side (1 MHz) are somewhat high, comparing with the data at higher frequencies (100 MHz), which are significantly different from the other cables. However, based upon their shielding structure, it is still not easy to explain this behavior, which is not similar to the behavior of the cables supplied from A and C.

High TI data for A-1 are possibly explained that it has the drain wire with stranded type, which is different from the other FTP cables. As well known, solid wire and stranded wire provide different electronic characteristics.

Extremely high data for D, up to 13600 mohm/m at 100 MHz, are caused by special foil tape structure without doubt. Except for D with a helical tape structure, this tape is very thin, comparing to one for the other FTP cables. The result suggests that longitudinal tape can provide better shield performance. A helical and thin Al/plastic laminated tape is not recommended to be used as a cable screen. On the other hand, the drain wire is located between foil tape and cable jacket, which is different location from the other three FTP cables. Although they have different design attributed to individual concept, the drain wire is still in contact with the aluminum side. Further study is necessary.

4.2 Mechanical Stress Effect

A plot of TI change (mohm/m) vs log (testing frequency) is used to discuss mechanical stress effect on cable screen. The TI changes for seven cables are illustrated graphically in Figures 5 ~ 11. Again, there are different scales for TI change in these seven figures.

Figure 5, 6, 7 and 8 show the shield performance after mechanical stress test for four FTP cables, A-1, B-1, C-1 and D, respectively.

For each figure, the curve identified by "Ellipse-Initial" is initial data subtracted from the data for the cable after ellipse test. On the other hand, one identified by "Figure eight-Initial" is to take initial data away from the data for the cable after an ellipse test and then a figure eight test.

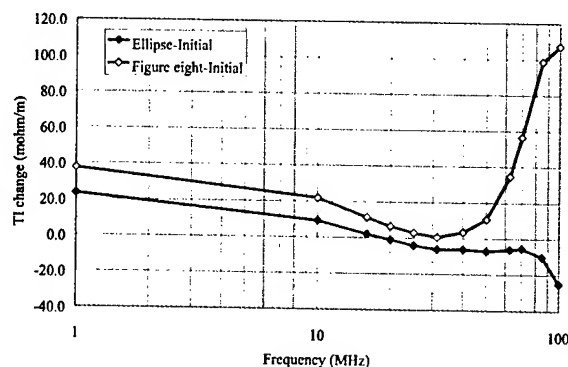


Figure 5. Transfer impedance data change after ellipse test and figure eight test for cable A-1

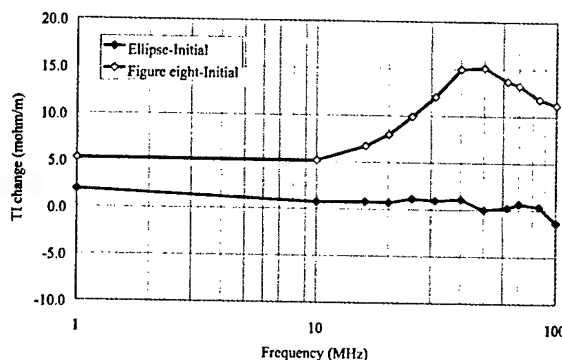


Figure 6. Transfer impedance data change after ellipse test and figure eight test for cable B-1

Although for these four cables their features are dependent on the cable's manufacturers, they still show somewhat similar characteristics. C-1 is chosen as an example to discuss mechanical stress effect on FTP cables in detail. There are several features in this figure. The TI difference between the data for the cable after ellipse test and initial data is very small at low frequency side, only 3.9 mohm/m at 31.25 MHz. On the other hand, the difference between the data for the cable after figure eight test and initial data is significantly high, 22.7 mohm/m at the same frequency. Furthermore, the TI change after figure eight test is much higher than that only after ellipse test, especially at high frequency. They approach to 32.8 mohm/m and 105.1 mohm/m relative to Ellipse-Initial and Figure eight-Initial, respectively, at 100 MHz.

The TI change for the other three cables undergoing ellipse test and figure 8 test shown in Figure 5, 7 and 8 is similar to C-1. However, it is worth pointing out that for B-1 after ellipse test the TI change is below 2 mohm/m in the whole frequency range. It is reasonable to assume that the TI data remain unchanged for B-1 after ellipse test. On the other hand, significant TI change is observed after figure eight test for B-1, similar to A-1, C-1 and D.

Based on the discussion, it is obvious to understand that ellipse test may not influence cable's shield performance for FTP cables; however, figure eight test may do some severe damage to the Al/plastic laminate tape, especially at high frequency region.

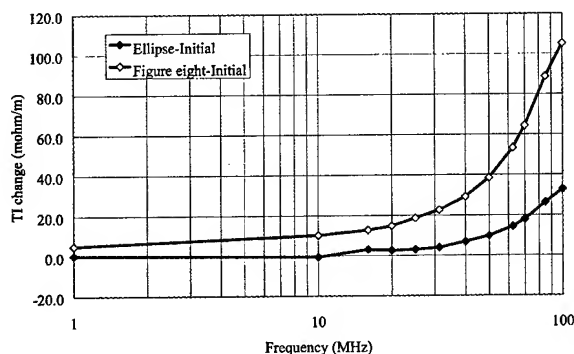


Figure 7. Transfer impedance data change after ellipse test and figure eight test for cable C-1

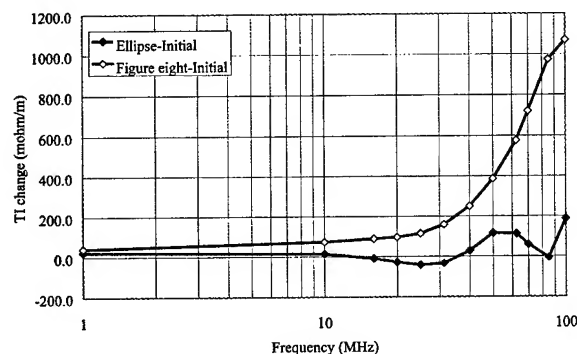


Figure 8. Transfer impedance data change after ellipse test and figure eight test for cable D

Figure 9, 10 and 11 present the shield performance after mechanical stress test for three SFTP cables, A-2, B-2 and C-2, respectively. They are very small scale for TI change compared to Figure 5 ~ 8. Furthermore, initial TI data for these three SFTP cables shown in Figure 1 ~ 3 are very low for entire frequency region.

As mentioned in DCM manual, low TI reading may be high error [5]. In these three figures, two conditions therefore should be

possibly assumed within experimental error and/or due to data fluctuation. One is negative TI change data for the cable after mechanical stress test, the other is less TI change for the cable after figure eight test than that for the cable only after ellipse test.

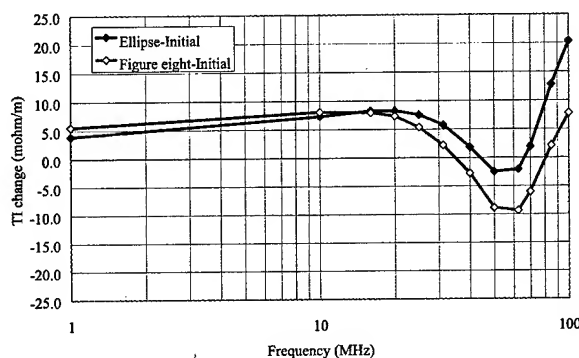


Figure 9. Transfer impedance data change after ellipse test and figure eight test for cable A-2

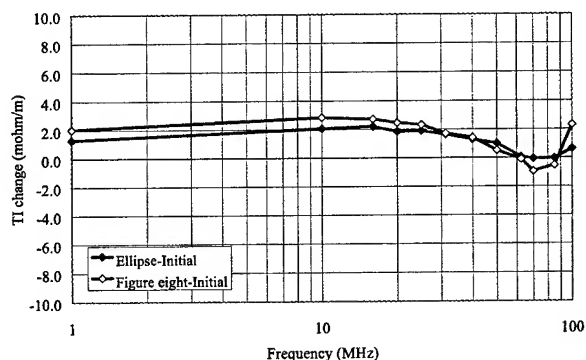


Figure 10. Transfer impedance data change after ellipse test and figure eight test for cable B-2

Compared with Figure 5 ~ 8, less TI change is observed in Figure 9 ~ 11. However, it is still able to discuss mechanical stress effect on SFTP cables. Regardless of Figure 9, 10 or 11, it is clear to see that significant TI change is observed for the cable only after ellipse test at low frequency side. Furthermore, the data indicate that the TI change from the data for the cable after ellipse test to initial data is similar to, even closed to, one from the data for the cable after figure eight test to initial data at low frequency side, especially for C-2 in Figure 11.

At high frequency side, it would like to explain that it is possibly an uncertainty region due to data fluctuation. The data for A-2 may be not enough to draw a conclusion. However, for B-2 and C-2, it seems reasonable to assume that TI data possibly remain unchanged at high frequency side, 100 MHz. It may reach the conclusion that SFTP cable is available to suffering mechanical stress, even for severe environment as figure eight test.

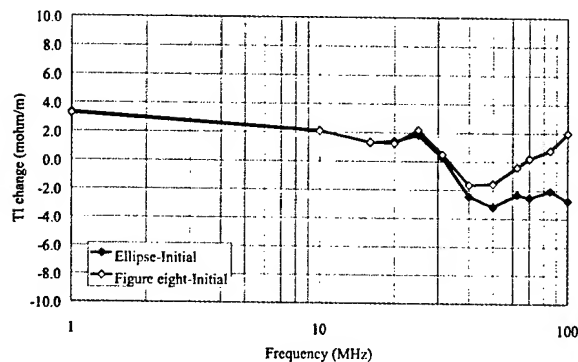


Figure 11. Transfer impedance data change after ellipse test and figure eight test for cable C-2

5. Conclusions

The shield performance of FTP cable and SFTP cable can be qualified by measuring shield transfer impedance. The data are dependent on the cable manufacturers due to different cable shield structure design. SFTP cable provides better shield performance than FTP cable, especially at high frequency side. Helical Al/plastic laminate tape and stranded drain wire are not recommended to be used. Under mechanical stress test, including ellipse test and figure eight test, FTP cables are generally more remarkably sensitive to mechanical stress test than SFTP cable. Ellipse test may not influence cable shield performance for FTP cable; however, figure eight test does some severe damage to Al foil, especially at high

frequency region. SFTP cable is available to suffering mechanical stress, including ellipse test and figure eight test, over the entire frequency range up to 100 MHz.

6. References

- [1] C. Hogg and M. Reichle, "EMC Test with Category 5 Unshielded (UTP) and Foil shielded (FTP) Twisted pair Cables," *MM Cables Communication Products, White Paper* (Jan. 1996)
- [2] V. A. Rybinski, "Shield Efficiency Test Method for Balanced Shielded Twisted-Pair Cable & Connecting Hardware," *International Wire & Cable Symposium Proceedings*, 277-286 (1996)
- [3] "Alcatel Cabling System," *Alcatel Company* (1999)
- [4] "UTP vs STP: A Comparison of Cables, Systems, and Performance Carrying High-Dta-Rate Signals," *Lucent Technologies* (1997)
- [5] "DCM CMS-2XLD User's Manual – Computerized Transfer Impedance Measuring System Triaxial Method, 2nd Ed., Rev. B," *DCM Company*
- [6] D. Prudhon and M. French, "EMC Compliance Testing of Link Termination in Local Area Networks," *International Wire & Cable Symposium Proceedings*, 107-110 (1997)
- [7] "Commercial Building Telecommunications Cabling Standard, Part 2: Balanced Twisted-Pair Cabling Components," *TIA/EIA-568-B.2* (May 2001)

Recycling of Polyethylene from The Discarded Copper Cable

*Fuminori Nakamijima, *, Eiji Konda*, Hiroshi Tajima*, Masami Hara*,*

Yutaka Suda, Hiroshi Hirukawa**, and Youichi Kajisa****

The Furukawa Electric Co., Ltd. ** Zaikoo Co., Ltd. *** Okano Electric Wire Co., Ltd.

Chiba, Japan

**Chiba, Japan

***Kanagawa, Japan

+81-436-1642 f-nakaji@ch.furukawa.co.jp

Abstract

Recycling of used products is desirable from the standpoint of global environmental preservation. As one recycling effort, we performed a feasibility study on recycling the polyethylene used as sheaths for communication metallic cables. We reused them for the same purpose.

We removed the polyethylene sheaths from discarded LAP (Laminated Aluminum Polyethylene) sheath cables and reprocessed them into pellets. After evaluating the reprocessed pellets for a number of physical properties, they proved to be perfectly reusable. We also tested the LAP sheath cables made from reprocessed polyethylene pellets, and confirmed that they fully satisfied the mechanical specifications required for general cables.

We also examined making plastic drums for communication cables with this type of used polyethylene insulation sheath. Plastic drums made of a blended material of polyethylene reprocessed from insulation coverings and virgin PP (polypropylene) were evaluated. As a result of the evaluation, though they were inferior to general-purpose plastic drums in their physical properties, they proved to be perfectly functional in the field.

Keywords

Recycle; discarded cable; Copper cable; Polyethylene sheath; Plastic drum

1. Introduction

Efforts to achieve industrial waste reduction and the recycling of used products have become important tasks among or social responsibility for global environment preservation. For more than thirty years, The Furukawa Electric Co., Ltd. has been manufacturing insulated and sheathed cables for communication. Eventually, after many years of use, these cables will become obsolete and will be discarded. Cables consist of metals such as copper and aluminum, along with plastic resin such as PE, which is used as an insulator jacket and an outer sheath. Of the materials involved, metals are comparatively easy to recycle, and have been consistently recycled, but the rotational recycling of plastic material has not been discussed much in the literature.

We studied the recycling of the PE used in LAP sheath cables, the composition of which is shown in Figure 1. These sheaths are generally discarded after they are used in aerial cables and underground cables. Studies to reuse the PE in used sheaths to create new sheaths, and to reuse PE used for insulation to create plastic drums for communication cables were conducted.

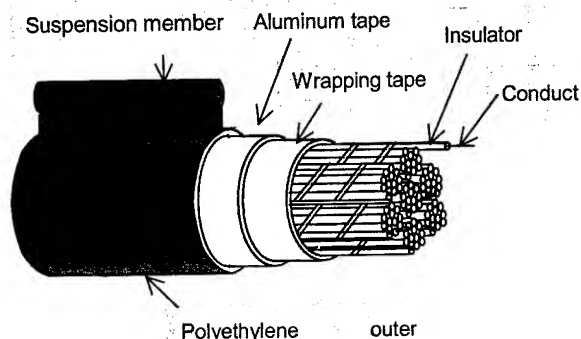


Figure 1. The Composition of discarded cable

2. Recycling Discarded Cable Sheaths

2.1. The Recycling Process of PE used for Sheaths

The recycling process of PE used for sheaths and insulators of discarded and recovered CCP (Color Coded Polyethylene) LAP cables is shown in Figure 2.

Discarded cables (1) are cut (2) using a cutter and cable sheaths (3) are removed from the cables. Then the Aluminum tape is separated

(4) from the cable sheaths, the sheath PE is ground up (5) using a grinder, and washed (6). Then ground sheath PE is made into pellets (7) using an extruding machine. The reprocessed pellets (8) are reused to make new cable sheaths (9).

2.2. Characteristics of Reprocessed Sheath PE

In order to verify the characteristics of reprocessed PE, we examined both the basic physical properties and the long-term features, and made cables using reprocessed PE and tested these cables. A Comparison of the test results against those of virgin pellets of low density polyethylene containing 2.6 % carbon is shown here.

2.2.1 Characteristics of Reprocessed Material

The physical properties of both pellets were evaluated by making them into sheets using press molding after roll milling. The physical properties of the sheets are shown in Tables 1, and Figures 3 and 4. The results show that reprocessed PE is by no means inferior to virgin pellets.

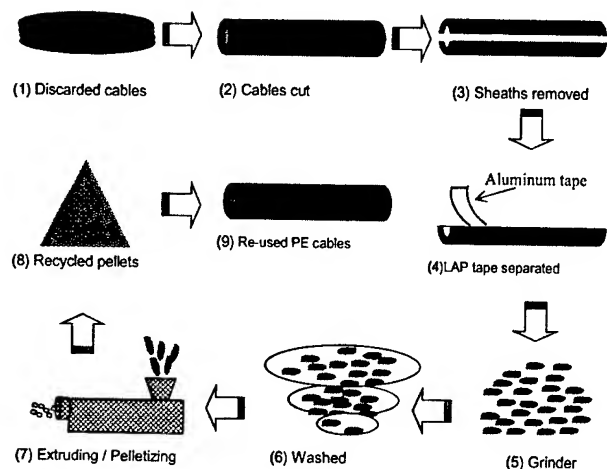


Figure 2. Recycling process of discarded cables

Table 1. Properties of reprocessed pellets

Item	Unit	Test Method	Reprocessed Pellets	Virgin Pellets
Density	g/cm ³	ISO 1183	0.937	0.934
Melt Flow	g/10min	ISO 1133	Max.	0.2
			Min.	0.17
			Avg.	0.18
Carbon Content	%	ASTM D1603	2.5	2.6
Brittleness at -70 degrees C	Broken/Tested	JIS K7216	0/5	0/5
Environmental Stress-cracking	Broken/Tested	ASTM D1693	0/10	0/10
Tensile Strength	MPa	ISO 527	Max.	20.4
			Min.	19.4
			Avg.	19.9
Elongation	%	ISO 527	Max.	700
			Min.	650
			Avg.	670

The sheaths of cables are exposed to various outdoor elements for many years, and gradual deterioration has always been a point of concern. The results proved, however, that there is no remarkable deterioration, and that PE from the sheaths of discarded cables can be used again.

2.3 Characteristics of Reprocessed Sheath Cables

Using reprocessed PE, we made a cable with 400 pairs of insulated conductors with a 0.4 mm outer diameter, the construction of which is illustrated in Figure 1. We then evaluated the physical properties of the sheath and the mechanical characteristics of the cable. The physical properties of the recycled sheath of the cable is shown in Table 2. Based on these tests, it was confirmed that the reprocessed sheath had the equivalent physical properties of a sheath conventionally used in a cable.

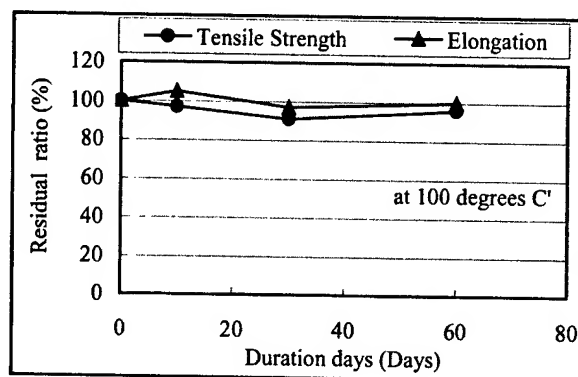


Figure 3. Reprocessed pellets durability for a heat aging

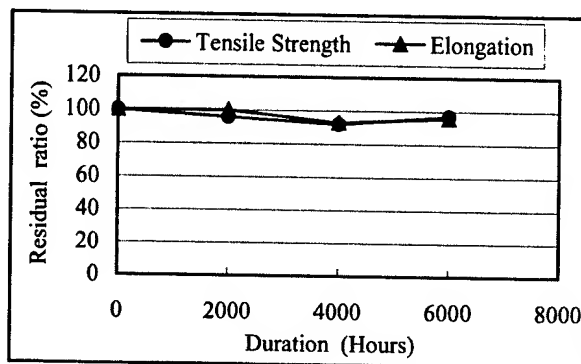


Figure 4. Reprocessed pellets durability for the UV light radiation

Table 2. Characteristics of a recycled cable sheath

Item	Unit	Recycled cable sheath
Density	g/cm ³	0.936
Melt Flow	g/10min	0.18
Tensile Strength	MPa	14.2
Elongation	%	520
Brittleness at -70 degrees C	Broken/Tested	0/5
Environmental Stress Clacking	Broken/Tested	0/10

3. Recycling Insulators into Plastic Drum Material

Insulated wires recovered from the discarded cable illustrated in Figure 1 are ground and copper nuggets and insulation PE are separated to reclaim the copper. While copper has a high monetary value, and is therefore often reclaimed, most insulation PE has been disposed of as industrial waste. For these experiments, we performed a feasibility study on the utilization of insulation PE as plastic drum material for communication cables.

3.1 Physical Properties of the Recovered Insulation PE

For general-purpose plastic drums, PP (polypropylene) is used. Therefore, we examined the basic physical properties of the discarded insulation material in comparison with PP. The results of the evaluation are shown in Table 3. They reveal that insulation PE is superior to sheath PE in the bending modulus (rigidity) and the heat deformation temperature (heat resistance), and, although the insulation PE is inferior to sheath PE in impact strength, it is superior to PP. From the above results, we concluded that insulation PE is preferable to outer sheath PE as plastic drum material.

Table 3. Comparison of material properties of sheath PE with insulation PE

Item	Unit	Outer Sheath PE	Insulation PE	PP
Izod Impact	kJ/m ²	70	20	4
Bending Modulus	MPa	300	600	1500
Deflection Temperature	Degree C	49	59	136

3.2 Material Composition Improvement

If insulation PE alone is used for plastic drums, products may fall behind conventional products in rigidity and heat resistance, so blending insulation PE with PP was studied to improve the quality. Results of this study are shown in Figure 5 thru Figure 7. We concluded that insulation PE and PP blended at a ratio of one to one has the characteristics best suited to plastic drums.

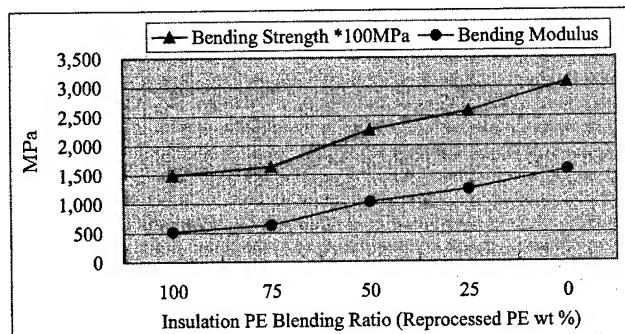


Figure 5. Relationship of insulation PE blending ratio and characteristics

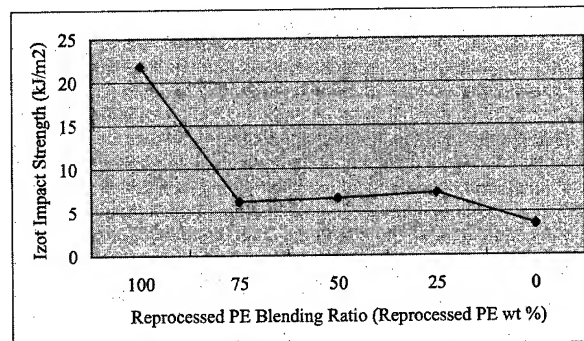


Figure 6. Relationship of Reprocessed PE blending ratio and Impact Strength

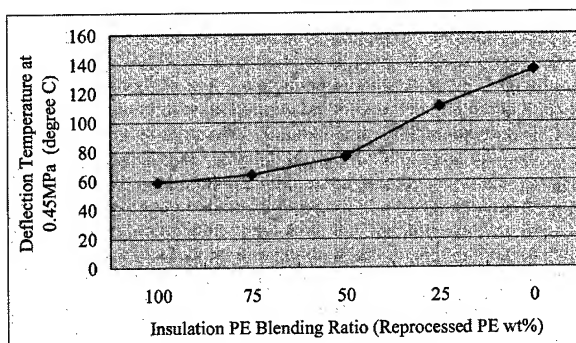


Figure 7. Relationship of insulation PE blending ratio and Deflection Temperature

3.3 Features of Ecoplastic Drums

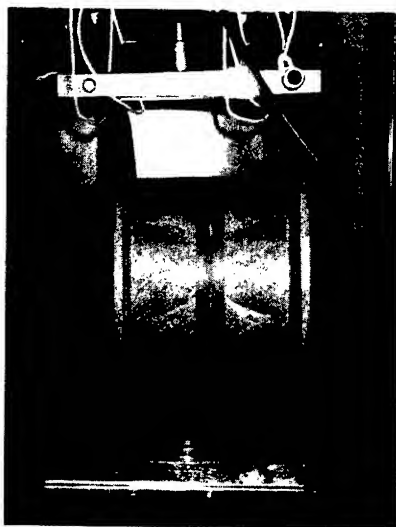
The facts obtained from confirming whether or not ecoplastic drums made from recovered insulation PE can actually be utilized are described below. The composition of the ecoplastic drums and conventional plastic drums evaluated are detailed in Table 4.

Table 4. Comparison of material properties of sheath PE with insulation PE

Material	Ecoplastic Drum	Conventional Plastic Drum
Reprocessed PE	50	-
PP	50	100

3.3.1 Compression Test

The compression test of a plastic drum is pictured in Figure 8, and Table 5 shows the results of this test. From this test, it became known that, when compared to conventional plastic drums, ecoplastic drums have only half the strength.



"Test Conditions"

Load Speed:

10 mm/min

Load Cell: 50 kN

Figure 8. Compression Test of a Plastic Drum

Table 5. Results of the compression test of plastic drums

Test Order	Ecoplastic Drum	Conventional Plastic Drum
First Test	11.3 kN	24.1 kN
Second Test	11.8 kN	23.4 kN

3.3.2 Cable Winding Test

To simulate using a drum in the field, the spreading of the drum flanges was measured by winding cables on the drum. Results are shown in Table 6.

3.3.3 Drop Strength Test

An ecoplastic drum packed in the same way as conventional drums was dropped from the bed of a truck, from a height of 1.2 meters, onto an asphalt paved road, to check damage to the drum. The results are shown in Table 6.

3.3.4 High Temperature Heating Test

An ecoplastic drum packed in the same way as conventional drums was stored at 70 °C for nine weeks. When the nine weeks elapsed it was left at the normal temperature for twenty-four hours. The spreading of the flanges was measured, and the results appear in Table 6.

Table 6. Results of the ecoplastic drum evaluation

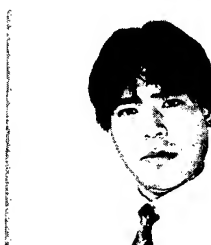
Items Evaluated	Conditions for Passing the test	Determination
Cable Winding	No breaking of coils, deformations, or damage could be noticed	good
Drop Test	sama as above	good
High Temperature Ageing	sama as above	good

4. Conclusion

We performed a number of feasibility studies on the ability to recycle the PE used in discarded communication metallic cables, which have often been disposed of as industrial waste. The physical properties of reclaimed PE used as sheaths for communication cables were studied. The ability to recycle the material and re-use it as sheath, as well as cable on which actual reprocessed pellets were used as sheath were evaluated. We came to the conclusion that reprocessed PE can be reused for cables.

In addition, PE that had been used as an insulator was studied for recycling use as plastic drum material, after blending it with PP. Tests were performed to check the capability of drums made of the blended material, to determine whether they could withstand actual handling in the field. These test have revealed that the drums made of blended material could indeed withstand these tasks, even though the physical strength of the material was about half that of conventional material (pure PP). From the above results, we conclude that the value of discarded communication copper cables can be increased and this sort of recycling can contribute positively to environmental preservation in the future.

Authors



Fuminori Nakajima

The Furukawa Electric Co., Ltd.
6, Yawata kaigan-dori Ichihara,
Chiba, 290-8555 JAPAN
f-nakaji@ch.furukawa.co.jp

He received his M.E. degree in Material Engineering from Nagaoka University of Technology in 1992. He joined The Furukawa Electric Co., Ltd. in 1992 and has been engaged in research and development of the materials for optical fiber cables. He is now an assistant manager of engineering dep., OPTCOM division.



Eiji Konda

The Furukawa Electric Co., Ltd.
6, Yawatakaigann-dori Ichihara, Chiba,
290-8555 JAPAN
konda@ch.furukawa.co.jp

He joined The Furukawa Electric Co., Ltd. in 1977 and has been engaged in research and development of materials and optical fiber cables. He is now an optical fiber cable development and design engineer of engineering dep., OPTCOM division.



Yutaka Suda

The Furukawa Electric Co., Ltd.
6, Yawatakaigann-dori Ichihara, Chiba,
290-8555 JAPAN

He joined The Furukawa Electric Co., Ltd. in 1970 and has been engaged in research and development of materials. He is now process engineer of copper telecommunication cable in production engineering section of dep., OPTCOM division.



Masami Hara

The Furukawa Electric Co., Ltd.
6, Yawatakaigann-dori Ichihara,
Chiba, 290-8555 JAPAN
hara@ch.furukawa.co.jp

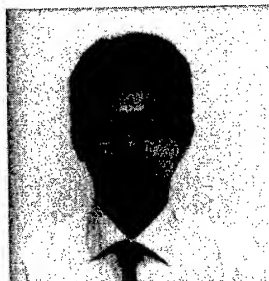
He received his M.E. degree in Physics from Osaka University in 1987. He joined The Furukawa Electric Co., Ltd. and has been engaged in research and development of optical cable. He is now a manager of engineering dep., OPTCOM division



Youichi Kajisa

Okano Electric Wire Co., Ltd
5-28, Fukaminishi, Yamato,
Kanagawa, 242-8501 JAPAN
kajisa@okano-cable.co.jp

He received his B.E. degree in Department of Electrical Engineering from Kyushu Toukai University in 1989. He joined Okano Electric Wire Co., Ltd., He has been engaged in development and manufacturing of telecommunication cables.



Hiroshi Tajima

The Furukawa Electric Co., Ltd
6-1, Marunouchi 2-
Chome, Chiyoda-ku, Tokyo, 100-
8322 JAPAN
tajihiro@ho.furukawa.co.jp

He received his B.E. degree in Department of electrical engineering from Yamanashi University in 1991. He joined The Furukawa Electric Co., Ltd and has been engaged in manufacturing and assembling optical fiber connector and cable component. He is now an assistant manager of engineering dep., OPTCOM division.



Hiroshi Hirukawa

Zaikoo Co., Ltd
6, Yawatakaigann-dori Ichihara,
Chiba, 290-8555 JAPAN

He received his M.E. degree in Polymer Chemistry from Yamagata University in 1974. He joined The Furukawa Electric Co., Ltd. and has been engaged in research and development of power cable materials. He is now a director of development division in Zaikoo Co., Ltd.

Structure-Property Relationships of Higher Performance Wire & Cable Jacketing Compounds

Day-Chyuan Lee

The Dow Chemical Company
1 Riverview Drive
Somerset, NJ 08873
+1-732-271-2021 · leedc@dow.com

Abstract

Polyethylene compounds have been successfully extruded for many years as jackets for telecommunications and power cable applications. The wire and cable industry has long recognized that the inclusion of a polyethylene jacket in the overall cable design represents a cost-effective way to extend the cable life and end-use performance. However, increasing competitiveness in the cable industry requires that the cable maker continue to search for jacketing materials with enhanced performance and/or value-added functionality, which can further reduce the total cable system cost. As part of The Dow Chemical Company, our Wire & Cable Compounds business has many new capabilities to design the chain architecture of polyethylene for enhanced jacketing performance. The ability to manufacture such compounds in all regions of the world adds to our ability to provide customers with the best balance of cost and performance.

Keywords

Polyethylene; jacket; bimodal; tie chain; processability; shrinkage, ESCR; new opportunities.

1. Introduction

The primary role of a jacket is to protect the cable core. The jacket compound used must meet very strict material requirements, including good tensile and flexure properties, abrasion resistance, environmental stress crack resistance (ESCR), low brittleness temperature, weatherability, and compatibility with other components in the cable design. Processability and post-extrusion shrinkage are also an integral part of the selection process. The jacketing operation must be performed at competitive line speeds using standard extrusion equipment offered commercially in the market place.

Polyethylene has been the preferred jacketing material for the cable industry since the 1940s. Continuous advancement in polyethylene manufacturing technologies, including catalysis and reaction processes with state-of-the-art compounding, have allowed polyethylene to become the most cost effective means to achieve the primary performance requirements in jacketing applications. For additional performance enhancement, components such as additives, functional fillers or polymers are very often compounded into polyethylene during the manufacturing process, as illustrated in Figure 1.

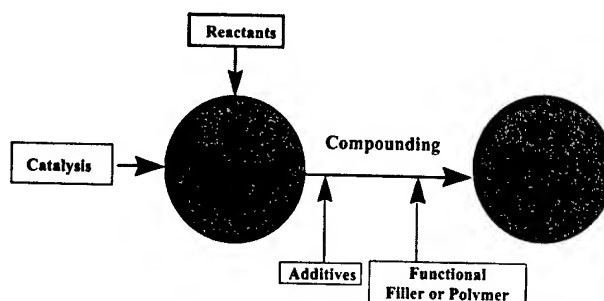


Figure 1. Jacketing compounds manufacturing

The majority of telecom jacketing applications use black jackets, but a few selected cable users in Europe and North America specify a fully colored jacket. Carbon black or color concentrate is compounded into the jacket compounds to satisfy these market segments. Carbon black and/or UV-stabilizers are common additives to enhance the weatherability of polyethylene jacket. Antioxidants are used in all jacket applications to ensure the stability of the jacket compounds during storage and extrusion. Other additives, functional fillers or polymers can be added to meet specific requirements of other unique jacket applications.

Current polyethylene jacketing grades range from low density PE (LDPE), made by a conventional high pressure process, to linear low density (LLDPE), medium density (MDPE), and high density (HDPE) PE made by a low pressure process. The base resin is selected to offer unique performance characteristics for a wide variety of jacketing applications [1-4]. LDPE typically has excellent processability and flexibility, but has been gradually replaced by linear polymer due to poorer LDPE physical properties. Polyethylene is conventionally specified according to its melt index (MI), and density. For identification purpose, ASTM [5] also classifies density and MI into various types and categories. The structure-property relationship for the majority of polyethylene made by conventional technologies can be described in terms of qualitative relationships or functions of density and MI. The direction of improved performance in relation to MI and density is indicated in Figure 2.

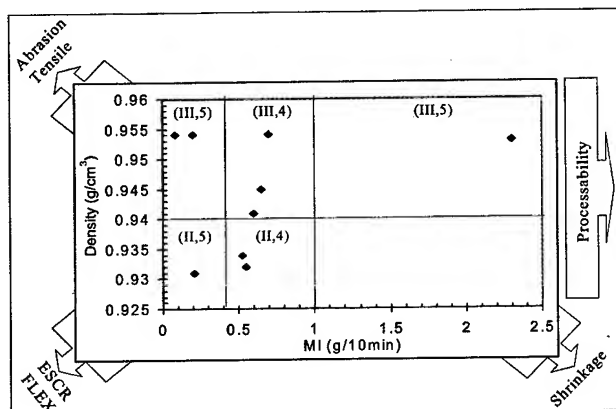


Figure 2. Jacket grades with ASTM classification and direction of improved performances

Recent polyethylene technology advancements such as the development of dual reactor manufacturing processes (gas, slurry, and/or solution phase) and single-site constrained geometry catalyst [6] provide new opportunities for the development of higher performance wire and cable jacketing compounds. Dual reactor manufacturing processes provide the flexibility to engineer resin structure via in-reactor blending of two structurally different polyethylenes at the molecular level. Constrained-geometry catalyst provides the precision to control the molecular structure of polyethylene. More control of the reaction process allows modeling to more accurately predict the structure-property performance, and to break many of the rules and restrictions of conventional technologies. The ability to manufacture such compounds in all regions of the world adds to our ability to provide customers with cost effective, high-performance products.

2. Experimental

2.1 Material

Sample involved in this study includes the commercial unimodal HDPE Jacket DGDA-7580 NT abbreviated as UNI and two developmental bimodal products abbreviated as BI-A and BI-B.

2.2 Solution Characterization

Molecular weight and its distribution (MWD) were determined by size exclusion chromatography (SEC) with a Waters 150C GPC. The SEC was operated at 140 °C with 1,2,4-trichlorobenzene as the solvent and mobile phase. Polydisperse polyethylene standards (with known MW statistics and intrinsic viscosity) were used for calibration to obtain the molecular weight, and MWD.

Short chain branching distribution (SCB) or composition distribution for polyethylene was determined using analytical temperature rising elution fractionation (TREF), in which a single beam infrared concentration detector monitors effluent concentration as a function of fractionation temperature (inversely related to SCB content). The solvent used was also 1,2,4-trichlorobenzene. Calibration standards and data reduction software converted the measurement to composition distribution statistics.

2.3 Melt State Characterization

Capillary viscometry was used to measure steady shear flow at 190 °C. Dynamic rheological measurements (oscillatory shear) were run in parallel plate mode and covered frequencies from 0.1 to 100 sec⁻¹ at 190 °C to characterize the viscoelastic behavior of a polymer melt. Controlled rate experiments to calculate the storage and loss moduli (and dynamic viscosity) were used to determine the relaxation time spectrum of the polyethylene via commercial software [7].

2.4 Wire Extrusion

Wire extrusion experiments were conducted on a 2.5" Davis-Standard line with a 20/40/60/20 stacked screen pack and a sleeve die with 4:1 drawdown over 14 AWG Cu. Line speed was set at 200 feet/min. Pressure readings at breaker plate were used to rank jacket processability.

2.5 Shrinkage

Shrinkage tests were performed on 30-cm long wire samples, which were aged overnight at ambient temperature followed by aging at 100°C for 24 hours on a bed of talc. Changes in plastic wire length relative to conductor length were taken as a measure of the shrinkage.

2.6 ASTM Testing

Flow Index was determined according to ASTM D1238. Density was determined per ASTM D1505. Tensile properties were measured according to ASTM D-638. Flexural modulus was determined per ASTM D-790. Brittleness temperature was determined according to ASTM D746. ESCR tests were conducted per ASTM D-1693 using 10% Igepal solution at 50°C, with Fo as the time for zero cracks. PENT test for tensile load test with single-edge notched specimen under plane strain condition was conducted per ASTM F-1473. Abrasion tests were done using a DOW internal method similar to the standard Taber test.

3. Results and Discussions

3.1 Material Characterization

The results from size exclusion chromatography and rheological measurements are shown in Table 1.

Table 1. Characterization Data

	UNI	BI-A	BI-B
FI (g/10min)	8.55	8.25	13.13
MFR	153.50	96.83	82.06
Density (g/cm ³)	0.946	0.949	0.947
Mn (g/mol)	5,992	11,702	12,034
Mw(g/mol)	220,354	268,045	226,066
Mz(g/mol)	1,343,081	1,245,610	1,004,188
Mw/Mn	37	22.9	18.8
RSI	74.9	22.5	17.5

The molar mass distribution curves presented in Figure 3 show bimodality for sample produced from a dual reactor. The high molecular weight tail observed in the unimodal sample contributed to its longer relaxation time and higher Z-average molecular weight.

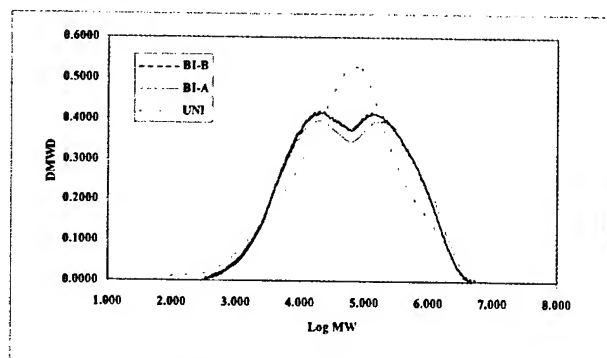


Figure 3. Molecular weight distributions

The short chain branching distributions are shown in Figure 4. Branching frequency is inversely proportional to polyethylene crystallinity or density. The shift in the peak position reflects the slight differences in density of the compounds.

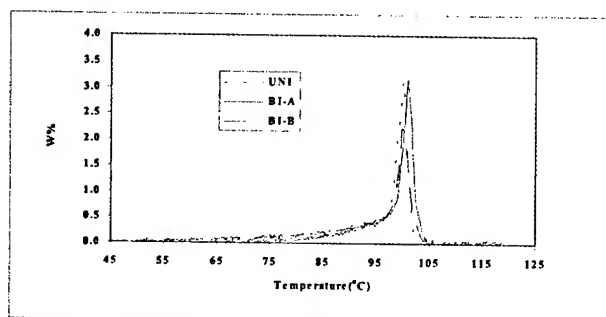


Figure 4. Short chain branching distributions

The shear viscosity curves are compared in Figure 5. The shear viscosity of bimodal samples is slightly lower than that of unimodal polyethylene at the same shear rate.

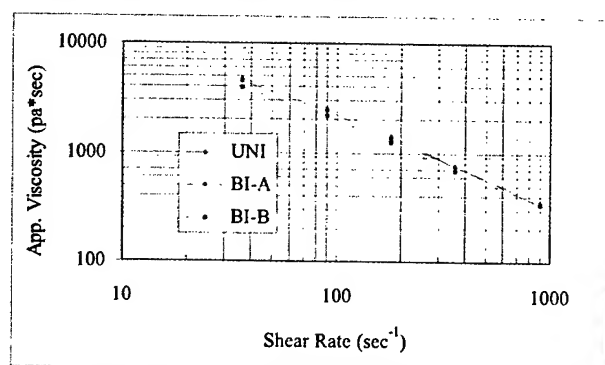


Figure 5. Shear Viscosity Comparison

3.2 Wire Extrusion

Extrusion performance has been summarized in Table 2. Compared to the unimodal resin, bimodal resins have lower shrinkage and

lower head pressure during extrusion. The improved processability allows the cable manufacturers more latitude in their process without impacting the material performance. Reduced shrinkage helps to maintain low signal attenuation in the cable manufacturing process, which is critical to the fiber optical application. Typically, when exposed to the thermal cycling, the shrinkage in a jacket can cause stresses and deformation that lead to the unwanted increase in cable attenuation. Jacket made from material with reduced tendency towards shrinkage in the laboratory will most likely also have reduced tendency for shrinkage when manufactured by the cable maker under a more severe processing condition.

Table 2. Extrusion Performance Comparison

			UNI	BI-A	BI-B
Head Pressure	Dow	psi	3980	3580	3310
RPM	Dow		46.6	46.5	42.6
AMP	Dow		47.5	49.2	46.4
MELT TEMP	Dow	°F	503	510	500
SHRINKAGE	Dow	%	1.30%	1.10%	1.00%

3.3 Mechanical Properties

Mechanical properties are summarized in Table 3.

Table 3. Mechanical Property Comparison

			UNI	BI-A	BI-B
Tensile Strength	D638	Psi	3015.7	3199.7	2977.3
Flexural Modulus	D790	Psi	11393	134429	122472
ESCR, 10% "Igepal", F0	D1693	Days	30	30	30
PENT	F1473	Hours	>100	>6000	>3000
Abrasion Resistance	Dow	Mg/100 cycle	11.2	9.6	12.0
Brittleness Temperature	D746	°C	-70	-70	-70

All polyethylene samples show low brittleness temperature performance as expected. Tensile strength, flexural modulus, and abrasion resistance performance are comparable, with the subtle differences accounted for by typical MI and density differences. Good mechanical properties ensure the ability of the jacket to withstand the rigors of installation conditions and to protect other internal cable components such as insulation and buffer or core tubes, etc.

Both ESCR and PENT measure Slow Crack Growth (SCG) rate. PENT is an accelerated test method for measuring SCG for predicting the service lifetime, while ESCR is a slower test. As shown in Table 3, all samples passed 30 days of ESCR evaluation, however, the SCG rate for bimodal polyethylene is much slower than that of unimodal polyethylene as indicated by PENT method.

The SCG rate is determined by the solid state morphology of a shaped polyethylene article. Polyethylene resins are semi-crystalline such that lamella crystals are bound together by the tie chains. As the polymer crystallizes, different parts of a particular molecule can become parts of different lamellae, and molecules that have parts of their chain in two or more lamellae are tie molecules as illustrated in Figure 5.

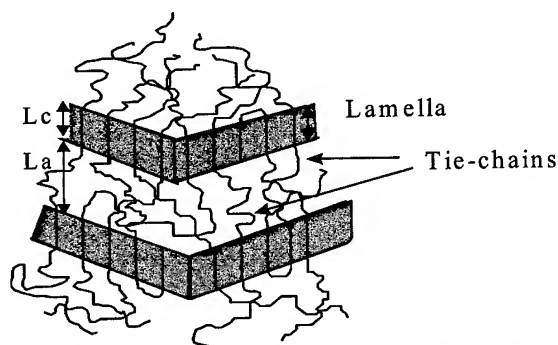


Figure 5: A schematic of the semi-crystalline structure of polyethylene.

Depending on the length (or molecular weight) of the tie molecule and the thickness of the lamellae it forms, a "network" of crystallites may be connected together with a single polymer molecule. When stress is applied, the tie molecules pull on the crystals, and attempt to "disentangle" the tie molecule from the crystallites. The crystallites act as anchors during the motion of the tie molecules. The disentangling rate of the tie molecules depends on the density of the tie molecule since the average stress experienced by a tie molecule is inversely proportional to density. The disentangling rate also depends on the length of the crystals. The stronger the crystal, the greater the restriction on the movement of the tie molecules.

The density of the tie molecules is dependent on MW and crystal size. The fraction of molecules forming tie chains can be calculated by using the scheme outlined by Huang and Brown [9]. They start with a one-dimensional view of polyethylene structure. They assume that lamella crystallites are infinitely long and run parallel to each other. L_c is the thickness of the lamella crystal and L_a is the interlamella spacing. The formation of a tie chain requires that a polyethylene molecule traverse two crystalline and one amorphous region. The distance traversed is then at least $2L_c + L_a$. If one assumes that the distance traversed by a molecule can be calculated by the random walk model, then the following equations can be used to calculate the probability of forming a tie chain or tie molecule.

$$P = \int_L^\infty r^2 \exp(-b^2 r^2) dr / 3 \int_0^\infty r^2 \exp(-b^2 r^2) dr \quad (1)$$

where L equals $2L_c + L_a$ and the factor 3 in the denominator of equation 1 is based on the geometry of a lamella crystal, since a tie molecule forms along one of the crystal dimensions. The thickness of the amorphous region between the crystallites can be calculated as:

$$l_a = l_c (1-X)/X, \quad (2)$$

where X is the crystallinity fraction.

$$b^2 = \frac{3}{2 \langle r^2 \rangle^2} \text{ in which } \langle r^2 \rangle^2 \text{ is the mean square value of}$$

the end-to-end distance of the random coil. For linear, monodisperse polyethylene in the equilibrium melt state, the mean square end-to-end distance for long chains is given as (Flory (1989) [9]):

$$\langle r^2 \rangle^2 = C_\infty n l^2 \quad (3)$$

where $C_\infty = 6.8$ is related to the stiffness of the chain, n is the number of carbon atoms ($= MW/14$) and $l = 1.53 \text{ \AA}$ is the bond length between adjacent carbon atoms.

The tie chain fraction can, therefore, be calculated if the lamella thickness, crystallinity and molecular weight are known. Hosoda et. al. [10] calculated tie chain probability as a function of crystallinity based on the morphological data obtained from butene-LLDPE crossfractions. Key features of tie chain probability are shown in Figure 6.

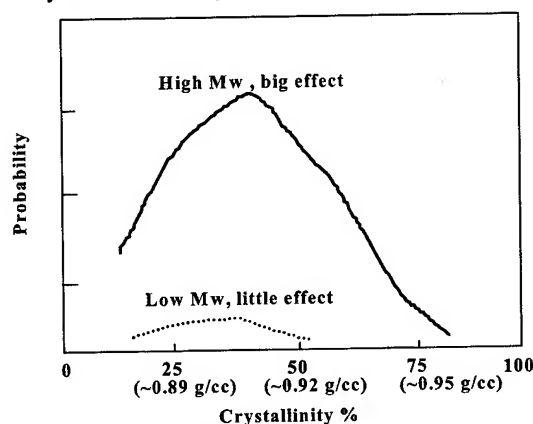


Figure 6. Probability of the tie molecule as a function of the crystallinity and molecular weight

The overall density and short chain branching distribution for unimodal and bimodal resin are very similar as indicated in Figure 4. However, in the dual reactor manufacturing process the tie chain probability can be easily optimized by incorporation more tie chain into the high molecular portions of the molecular weight distribution as pictorially demonstrated in Figure 7.

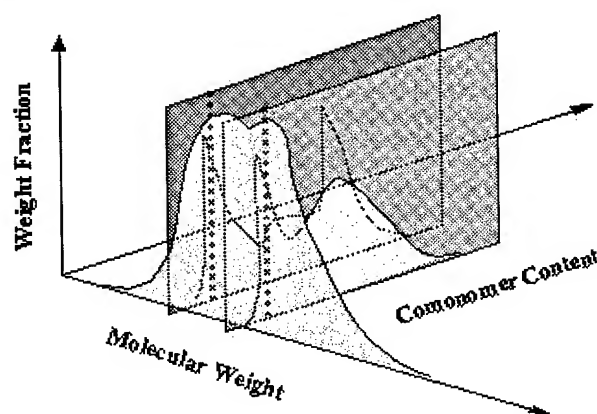


Figure 7. Optimization of tie chain along with polyethylene MWD

As a result of tie chain optimization, the crack resistance of bimodal resin can be superior to that of unimodal resin as indicated in Table 3 (i.e. PENT). In the conventional polyethylene manufacturing process, it is very difficult to adjust the molecular weight distribution and short chain branching distribution independently.

It is demonstrated that by optimizing the polyethylene chain architecture, the jacketing performance can be substantially improved relative to the typical linear structure-property relationships for conventional polyethylene technology. This is represented pictorially in Figure 8.

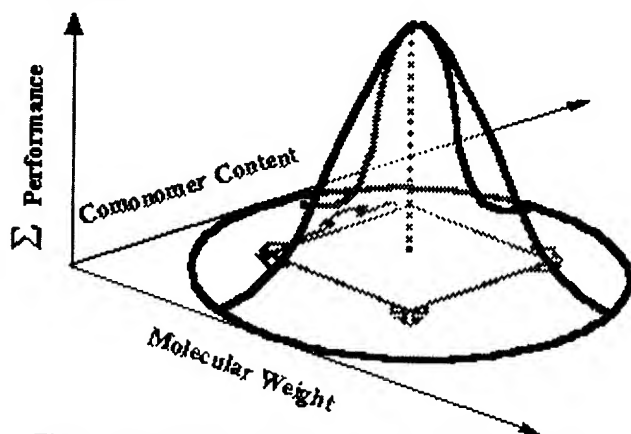


Figure 8. Breaking performance rules by resin structure and property optimization

4. Conclusions

Polyethylene continues to deliver cost effective performance in wire and cable jacketing applications. End use performance of the jacket is determined by its ordered solid state morphology as developed in the phase transformation from melt to solid. This morphology is controlled by the chain architecture of polyethylene. Polyethylenes are product-by-process materials. Their intrinsic molecular structure is determined by the catalysts and/or initiators, reactants, process configuration, and process conditions used in resin manufacture. Advancement in catalyst and process provides flexibility to control the molecular structure of polyolefines and to break many of the rules and restrictions of conventional technologies to make polyethylene-jacketing compounds more robust.

The use of the dual reactor provides flexibility to broaden molecular weight distribution and optimize the short chain distribution, which results in improved processability, shrinkage and slow crack resistance. Improved processability allows the cable manufacturers more latitude in their process without impacting the material performance. Reduced shrinkage helps to maintain low signal attenuation in the cable manufacturing process, which is critical to the fiber optic application. Reduced slow crack growth rate provides more insurance that the jacketing will not crack during reel storage or during the service, which is especially critical in thick-wall applications.

The ability to manufacture such state-of-the-art compounds in all regions of the world creates additional opportunities to develop jacket compounds with the best balance of cost and performance.

5. Acknowledgments

The author thanks S. Betso, S. R. Ellebracht, J. R. Leech, and S. H. Wasserman for their helpful discussions in related subject matters.

6. References

- [1] C. J. Kmiec and J.R. Leech, *International Wire and Cable Symposium Proceedings*, 177, (1996)
- [2] T. Chen and J.R. Leech, *International Wire and Cable Symposium Proceedings*, 807, (1999)
- [3] Y. Gau, C. J. Kmiec and T. J. Person, *Jicable 99*, B10.4, 638 (1999)
- [4] M. J. Sandelin, U. W. Gedde, H-F. Martinsson, and R. C. Dammert, *International Wire and Cable Symposium Proceedings*, 311, (2001)
- [5] "Standard Specification for Polyethylene Plastics Extrusion Materials for Wire and Cable", ASTM D-1248
- [6] K. W. Swogger, *MetCon '96*, June 12-13, 1996 Houston, TX USA
- [7] S. H. Wasserman, *International Wire and Cable Symposium Proceedings*, 190, (1999)
- [8] Y. Huang and N. Brown, *J. Polym. Sci., Polym. Phys.*, 29, 129 (1991).
- [9] P. J. Flory, *Statistical Mechanics of Chain Molecules*, Oxford University Press, New York (1989).
- [10] S. Hosoda and A. Uemura, *polym. J.*, 24, 939 (1992).



Day-Chyuan Lee (leedc@dow.com) received his Ph.D. in 1985 from State University of New York at Stony Brook then worked in two postdoctoral positions: University of Wisconsin (1985-1987) and Exxon Research and Engineering (1987-1988).

At Dow, Day-Chyuan worked in Blown Film, Material Science, and is now with Wire and Cable Compounds business for the product development involving either bimodal or metallocene polyethylene.

Benefits of Chlorinated Flame Retardants for Wire & Cable

Ronald L. Markezich

Occidental Chemical Corporation

P.O.Box 344

Niagara Falls, NY 14302-0344

+1-716-278-7885 · ronald_l._markezich@oxy.com

Abstract

This paper examines the factors that influence the formation of smoke in flame retardant systems. The flame retardant used, the resin and choice of the additive package can have a major impact on smoke generation when the material is burned.

The selection of the halogenated additive has the most major effect on smoke. The chlorinated flame retardant used, an alicyclic material, is superior to the brominated additives in char promotion during the burning process. That is a larger amount of the polymeric material is converted to non-volatile material and remains in the solid phase rather than being converted to soot-like material commonly described as smoke. In the same polymer system at comparable flame retardance performance, the chlorinated additive always yields more char, and therefore less smoke.

Keywords

Fire; flame; chlorine; chlorinated; bromine; brominated; wire; cable; testing; electronic; electric; dioxin; smoke; nbs; LOI; char; testing.

Introduction

Improved smoke performance has been achieved in flame retardant wire and cable materials by careful attention to the selection of the halogenated additive and also by the use of a small amount of an iron compound and the incorporation into the formulation of a surface modified talc. The chlorinated alicyclic flame retardant has proven superior to brominated additives in their ability to achieve less smoke generation. This is related to their mode of flame retardant activity where the ability to promote char leads to reduced smoke compositions. The halogenated additives used in the investigations are representative of those found in typical formulations.

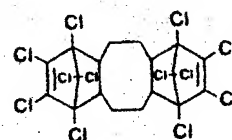
The halogenated flame retardants used are listed in Figure 1. CA-1 is the only chlorinated flame retardant used in the industry. Two of the most common brominated flame retardants used for wire and cable are BA-1 and BA-2.

While smoke generation is of major interest, the formation of hydrogen halides from materials containing halogenated additives during combustion is also of importance. The analyses of combustion gases during NBS chamber testing was carried out to determine the volatile hydrogen halides evolved. Our data shows quite low levels of the halogenated additives being converted to volatile halides, especially if compared to the PVC formulations.

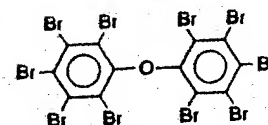
Besides discussing the different halogenated additives, this paper will also discuss different polyolefins used in flame retardant wire and cable formulation and smoke data in each.

Halogenated Additives

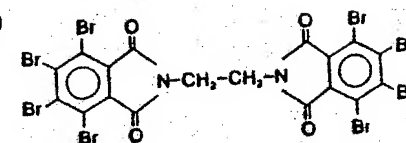
CA-1 (a)



BA-1 (b)



BA-2 (c)



- (a) Bis (hexachlorocyclopentadieno) cyclooctane
- (b) Decabromodiphenyl oxide
- (c) Ethylene bis(tetrabromophthalimide)

Figure 1. Halogenated Flame Retardant Additives

Results

Table 1 shows typical FR-EVA formulations using the chlorinated flame retardant CA-1. These formulations have a LOI of 27 and will pass the UL-44 VW-1 test.

Table 1. FR-EVA formulation using CA-1 at the flame retardant

Formulation (Weight %)	1	2
EVA	47.9	47.9
CA-1	25.0	18.0
Sb203	5.0	9.0
Translink-37 (Clay)	20.0	23.0
Agerite Resin D (Anti-oxidant)	0.7	0.7
Luperox 500R (Peroxide)	1.4	1.4
Oxygen Index (%)	27	27
UL 44 VW - 1 Flame Test	pass	pass
Tensile Strength (Mpa)	12.7	14.0
(PSI)	1846	2034
Elongation (%)	298	262

It has generally been accepted that flame retardant formulations for wire and cable materials generate greatly increased levels of smoke when undergoing forced combustion. While historically this is true, formulations are available using traditionally used additives that approach the smoke generation properties of unmodified polymers. This is illustrated in Figure 2 for a crosslinked polyethylene formulation. Proper selection of the halogenated additive and the use of selected formulation technology achieved this result. The unmodified sample in this case contains fiberglass to inhibit the dripping characteristics of polyethylene, which yield difficult-to-interpret results in the NBS Chamber. The FR-low smoke formulation is shown in Table 3.

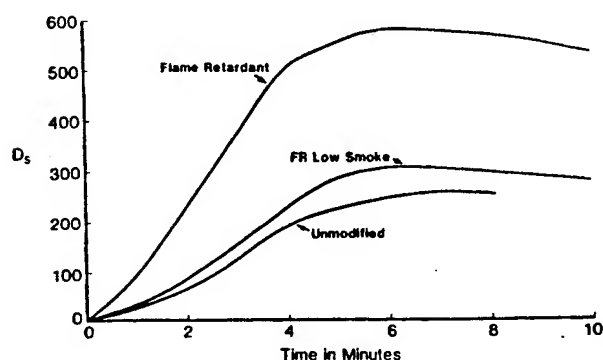


Figure 2. NBS Smoke Generation XLPE Compositions. Comparison of Performance Flame Retardant, Low Smoke, unmodified XLPE

The importance of the selection of the halogenated additive is illustrated in Table 2 for an ethylene-vinyl acetate copolymer (EVA) and an ethylene-propylene-diene terpolymer (EPDM) formulation. The formulation containing the chlorinated additive exhibits significantly lower smoke generation than those that contain the brominated additives.

Table 2. NBS smoke generation for FR-polyolefins brominated flame retardants versus chlorinated flame retardants

Polymer	Halogenated Additive	Ds @ 4 Min.	Dmax
EVA	CA-1	430	484
	BA-1	584	601
	BA-2	624	627
EPDM	CA-1	321	441
	BA-1	643	713
	BA-2	586	641

A generalized low smoke flame retardant polyolefin is shown in Table 3. The difference between these two formulations in the use of a surface treated talc and the addition of ~0.1 % of an iron compound such as ferric oxide.

Table 3. Low smoke FR-polyolefins formulations for W&C

Component	Weight %
Polyolefin	45-60
Halogenated Additive	15-25
Antimony Oxide	5-10
Iron Compound (Ferric Oxide)	~ 0.1
Surface Treated Talc	5-25

Table 4 gives the NBS smoke data for FR-polyethylene and FR-EVA using the low smoke technology. The Ds @ 4 minutes for the formulations using the chlorinated flame retardant CA-1 is 230 and 216. The values using the brominated flame retardants are greater than 500 at 4 minutes, this is also using the low smoke technology. While the Ds at 4 minutes for the CA-1 formulations dropped over 200 when using the low smoke technology, the brominated flame retardants only dropped about a 100, and the Ds at 4 minutes are still above 500.

**Table 4. Low smoke FR-polyolefins
Br FR versus Cl FR**

<u>Polymer</u>	<u>FR</u>	<u>Ds @ 4 Min.</u>	<u>Dmax</u>
PE	CA-1	230	310
	BA-1	597	658
	BA-2	501	535
EVA	CA-1	216	343
	BA-1	679	740
	BA-2	507	606

Table 5 shows typical FR-EPDM formulations using the different flame retardants. The low smoke formulations are shown in Table 6. There are only minor changes in the formulations. The most important is the use of a zinc stearate coated talc and the addition of 0.05 of an iron compound, such as ferric oxide.

**Table 5. Typical FR EPDM formulations
each contains 13.9% FR**

<u>Component</u>	<u>CA-1</u>	<u>BA-1</u>	<u>BA-2</u>
EPDM	38.2	38.2	38.2
Sb203	5.1	5.1	5.1
Polyethylene	8.4	8.4	8.4
Others (zinc oxide, Stabilizer, Paraffin wax, Antioxidant, Coupling agent, Peroxide)	9.1	9.1	9.1
Clay	25.3	25.3	25.3

**Table 6. Typical FR low smoke EPDM formulations
each contains 13.9% FR**

<u>Component</u>	<u>CA-1</u>	<u>BA-1</u>	<u>BA-2</u>
EPDM	38.2	38.2	38.2
Sb203	5.1	5.1	5.1
Polyethylene	8.4	8.4	8.4
Others (zinc oxide, Stabilizer, Paraffin wax, Antioxidant, Coupling agent, Peroxide)	9.1	9.1	9.1
Talc (Zinc Stearate Coated)	25.3	25.3	25.3
Iron Compound	0.05	0.05	0.05

The NBS smoke numbers for the formulations in Table 6 are listed in Table 7. The Ds @ 4 minutes for the chlorinated formulation containing CA-1 is 295 while the brominated flame retardants give values about 500. BA-1 gives a Ds @ 4 minutes of 686 while the formulation using BA-2 has a value 548.

**Table 7. Low smoke FR-EPDM formulations
Br FR versus Cl FR (NBS data)**

<u>Polymer</u>	<u>FR</u>	<u>Ds @ 4 Min.</u>	<u>Dmax</u>
EPDM	CA-1	295	385
	BA-1	686	713
	BA-2	548	606

Table 8 is the summary of the four different resins evaluated in our study. The NBS @ 4 minutes is compared for the normal formulation using CA-1 and the low smoke formulations using CA-1 with the low smoke technology.

**Table 8. Smoke generation from FR-polyolefins (NBS)
Ds @ 4 minutes**

<u>Polymer</u>	<u>CA-1</u>	<u>CA-1 Low Smoke</u>
	<u>FR</u>	<u>LS-FR</u>
XLPE	525	230
EVA	430	216
EPDM	321	295
EEA	510	151

Table 9 gives the results of the tests for dioxin formation in different resins.

Table 9. Results of dioxin testing in CA-1 formulations

DIOXIN FORMATION

CA-1 Formulations Tested for

Dioxin Formulation:

- Polypropylene
- Nylon
- HIPS

No Regulated Chlorodibenzodioxins or Furans Were Detected

Figure 3 shows the summary of the smoke generation for FR-polyolefin compositions comparing brominated flame retardants to chlorinated flame retardants, using both low FR formulations and FR-low smoke formulations. In all cases, Cl based flame retardants give less smoke than the Br based flame retardants.

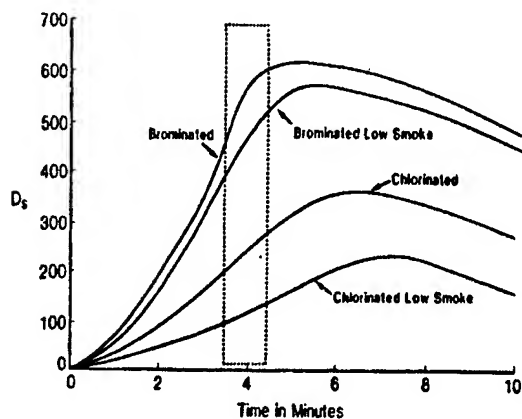


Figure 3. Smoke generation FR polyolefin compositions. Summary low smoke formulations versus normal FR formulations and Br versus Cl formulations

Figure 4 shows the corrosivity of HBr and HCl are similar. HCl is no worse than HBr. HBr will corrode as much as HCl.

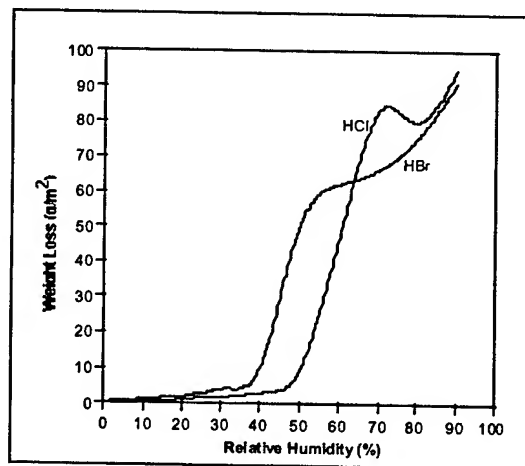


Figure 4. Corrosivity of HBr versus HCl

Figure 5 shows halogen halide generation in some FR-wire and cable formulations. Using CA-1 only 0.5 of the CA-1 comes off as HCl. With BA-1 at the flame retardant, 4% of the BA-1 comes off as HBr. In PVC, and of the Cl comes off as HCl when that sample is burned.

The samples were burned in NBS smoke chamber under flaming combustion conditions. Smoke was monitored continuously during the test. The chamber was modified by installation of a teflon tube through the box wall, which allowed sampling from the geometric center of the box. Samples were withdrawn at the desired time, generally at Dmax and after 20 minutes of test. The sample was drawn into a one-liter syringe and evacuated into a 500 ml. water trap to retain all volatile halides. The halide was determined by use of a Diomex Model 10 Ion Chromatograph in multiple analyses.

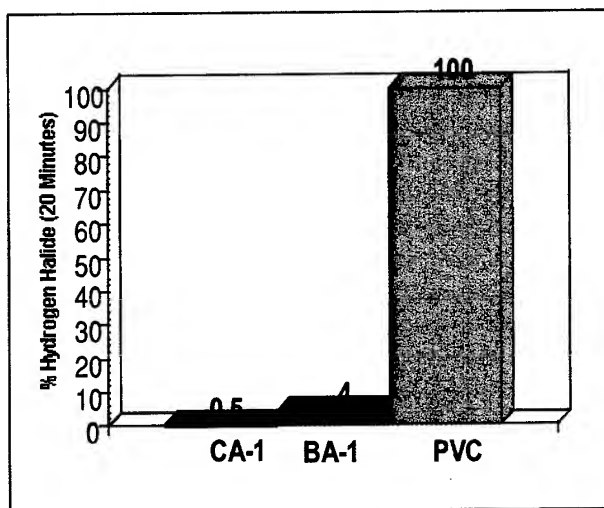


Figure 5. HX Liberation/ Comparison Chlorinated to Brominated Flame Retardants

Conclusions

- Chlorinated flame retardants generate less smoke than brominated flame retardants.
- Corrosiveness between HBr and HCl is similar.
- In flame retardant wire and cable formulations using CA-1 and BA-1, both produce similar levels of HCl or HBr when burned.
- FR-Polyolefins using the chlorinated flame retardant can generate less smoke by using a talc (zinc stearate coated) and a iron compound)

Author



Dr. Markezich is Technical Service Manager for Flame Retardants at Occidental Chemical. He has been at Oxychem for 22 years, specializing in flame retardants, and has published many articles in the flame retardant area. He received his PhD in Organic Chemical from the University of Wisconsin in Madison in 1972. After doing post-doctoral research at Stanford University he joined General Electric Company in its corporate research and development center in Schenectady, NY. Five years later he moved to the Plastics Division/Lexan Products. In 1980 he joined Oxychem. He has over 15 US patents and over 40 publication

Acknowledgments

Special thanks to the IWCS staff for making this template available for this year's publication. Additionally Sheridan Printing Co., Inc. is acknowledged for their assistance in producing the template

In Situ Cathodic Protection of Existing Lead-Sheathed Cables

Y.T Horng^{1,2}, J.H. Wang¹, H.P. Hsu¹, Y.-c. Lin¹, L.J. Liu¹, H.C. Shih²

¹ Network Operation Tech. Lab. Telecommunication Labs. Chunghwa Telecom Co., Ltd.

Yang-Mei, Taoyuan, Taiwan, P.O.C.

+001-886-3-424-4453, hyt751173@cht.com.tw

² Department of Material Science and Engineering, National Tsing Hua University,

Hsinchu, Taiwan, R.O.C

+001-886-3-5715131-3845, hcshih@mse.nthu.edu.tw

Abstract

Numerous lead-sheathed cables serve as the primary carriers of communication signals over twenty years at an outside plant in Taiwan. Corrosion of externally unprotected lead-sheathed cables in aggressive flooded manhole environments has long been a serious problem. Corrosion of lead-sheathed cables in manhole's environments causes a reduction of lead sleeve thickness in the cable sheaths, and when the reduction equals the extreme value of the lead sleeve thickness, failure occurs. Repair and replacement costs are expensive. At the request of the Chunghwa Telecommunication Company (CHT), a non-destructive method of applying zinc sacrificial anode cathodic protection (CP) to in-situ lead-sheathed cables has been undertaken. In addition to the reliability, such factors as the manhole's environmental hazard of lead were also analyzed.

Keywords

Lead-sheathed cable; cathodic protection.

1. Introduction

The underground communication cable system consists of various cables, closures, and supporting hardware in nonmetallic conduits and pre-cast concrete manholes. The currently underground communication cable system at CHT in Taiwan is composed of lead-sheathed and fiber optic cables. Although new installations are mostly fiber optic cables, the lead-sheathed cables are still the primary carriers of communication signals at CHT. These cables were covered with lead and lead sleeves covered the connections of wire pairs or coaxial tubes at the junction of two cables. Most of lead-sheathed cables were installed at least twenty years ago. The underground communication cable system has over ten thousand manholes and hand-holes. At each manhole, all the lead-sheathed cables are bonded to a copper grounding. Most of manholes are frequently flooded and both the cables and their connectors are always immersed in the underground water. The lead and lead sleeves in the manhole that corroded mainly by the stray DC at mass rapid transit system and electric rail transportation system. The other corrosion factors include galvanic action effect [1], differential aeration cell reaction, corrosive chemicals and bacteria that can lead to failures [2]. Despite lead is highly corrosion resistant, lead-sheathed cables also corrode at stray DC pickup point and in some strongly corrosive manholes water even after long time of service,

corrosion phenomenon began to occur in lead sleeve from near the mass rapid transit system in 1998 and is shown in Fig.1. Corrosion of lead sleeve causes a reduction of its wall thickness in the cable sheaths. Corrosion would have resulted in the thinning of lead sheath in localized area, when the reduction equals the extreme value of original wall thickness, failure occurs [3-5]. The frequency of the failures accelerated, and at this point, it was decided to install a zinc sacrificial anode to protect lead-sheathed cables from corrosion by cathodic protection. Zinc has long been a widely used as a sacrificial galvanic anode for the protection of pipelines, conduits and other buried structures.

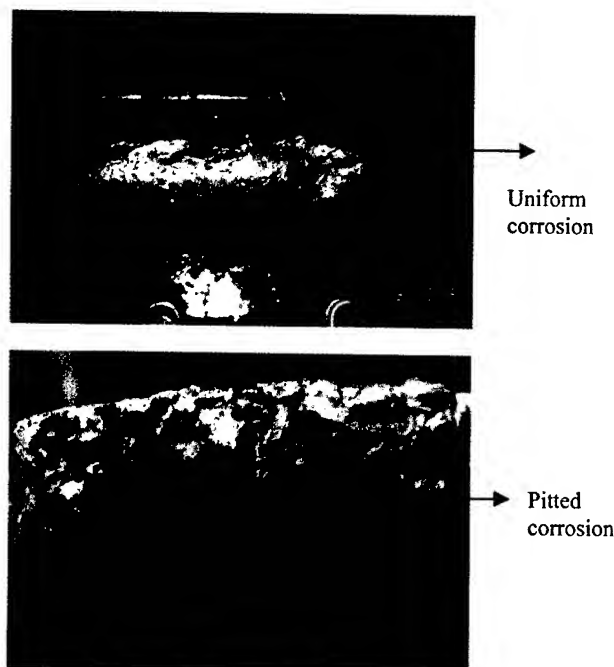
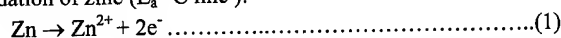


Fig.1 Uniform and pitted corrosion of lead sleeve near a mass rapid transit system from CHT lead-sheathed cable in the manhole.

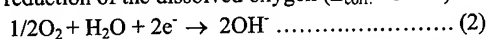
2. Experimental

Although there are different anode materials used for underground applications of cathodic protection, each material has unique characteristics that influence its performance in a given

environment. These performance characteristics vary from one environment to the next and must be examined for each application [6]. The principle of cathodic protection can be explained by the electrochemical polarization, as shown in Fig. 2 [7]. As can be seen from Fig. 2, the natural open circuit potential of sacrificed anode has lower value than that of the protected anode (E_a), in Fig. 2, where E_{corr} = corrosion potential, E_a = equilibrium potential, E_h = polarization potential, I_{corr} = corrosion current, I_{app} = applied current, I_h = polarization current. For zinc as a sacrificial anode, the primary anodic reaction is normally the oxidation of zinc (E_a -C line):



In an aerated manhole's environment, the cathodic reaction is controlled by reduction of the dissolved oxygen (E_{corr} -C line):



The open circuit potential (OCP, E_{corr}) of zinc sacrificial anode is more negative than that of lead sleeve for cathodic protection. According to the Nernst equation of the equilibrium potential of lead (E_{Pb}) in aqueous solution:

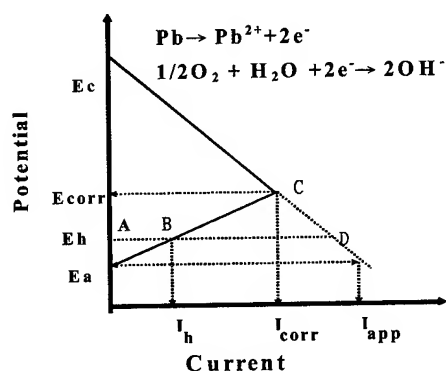


Fig.2. The polarization diagram of cathodic protection.

$$E_{Pb} = E_{Pb}^0 + (RT/nF) \ln [M^{2+}] \dots\dots\dots (3)$$

Where

E_{Pb} : equilibrium potential $E_{Pb}^0 = -0.124\text{V}$

R: gas constant n: number of oxidation state

F: Faraday constant $RT/F = 0.0257\text{ V at } 25^\circ\text{C}$

$[M^{2+}]$: metallic ion concentration (activity)

A value $E_{Pb} \leq -0.545\text{ V}$ is currently being considered as the maximum allowable potential for lead sleeves is shown in Fig. 3. According to the Pourbaix diagram of lead, it is seen that lead will become thermodynamically unstable at about -2.4 V and begin to corrode by the formation of lead hydride [8].

The zinc anode composition used in this paper is given in Table 1. The zinc anode specimens were prepared in dimension of $10 \times 3.5 \times 3.0$. The test conditions are given in Table 2. At each manhole, the zinc anode with a copper wire was soldered onto the lead sheath to provide an electrical connection. The zinc anode then fixed with a cable tie. The lead sheath without zinc anode protection in each manhole was compared. A small-scale field trial of the zinc sacrificial anode protection was undertaken.

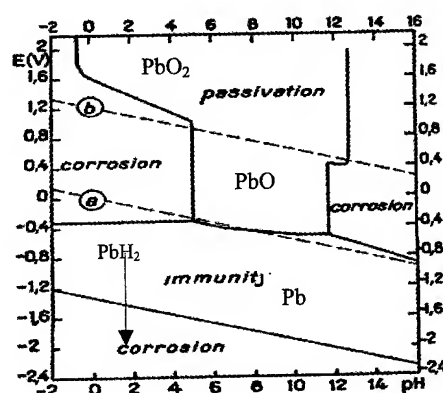


Fig.3. The Pourbaix diagram for lead [8].

Table 1. Zinc anode composition (wt%)

Element	Wt %
Zn	Bal.
Al	0.01
Fe	0.02
Sn	0.007

Table 2. Test conditions of field and simulated hazard manholes environments

Solution	pH	Corrosion potential (mV vs. SCE)
Underground water	6.9	-640
Salt water (NaCl)	6.7	-850
Strong acid (HCl)	1.2	-855

The field experimental setup is shown in Fig. 4. The cables are internally pressurized with air at 14.7 psi. Pressure transducers are used to detect the perforation of the sheaths by corrosion and other damages as well.



Fig.4. The setup of a zinc-sacrificed anode soldered onto the lead sheath.

The anode potential was measured using a multimeter (DM1250, registered trade name, Taiwan) and a saturated calomel electrode

(SCE) was located directly over the anode. In the laboratory, the potentiodynamic polarization experiments were carried out using a computerized corrosion measurement system (Model 273A, EG&G Princeton Applied Research, U.S.A.) and the scan rate was set at 1 mV/sec. In addition, impedance measurements were performed with an EG&G 273A potentiostat outfitted with option 92 and a Schlumberger 1255 frequency response analyzer (FRA). Sinusoidal potentials of 10 mV around the open-circuit potential; ranging in frequency from 100 kHz – 0.01 Hz, were applied to the working electrode.

3. Results and Discussion

3.1 AC impedance measurement

Because most manholes are frequently subject to flooding, the lead-sheathed cables are always submerged in the underground water. In order to simulate the corrosion behavior of bare lead-sheathed cable (without CP) in the manhole's water, ac impedance measurements in terms of Bode plot in various environments is shown in Fig. 5, in which the impedance of lead-sheathed is $\sim 5 \times 10^5 \text{ ohm.cm}^2$ in manhole's water; $\sim 1 \times 10^4 \text{ ohm.cm}^2$ in the salty water simulating the manhole's environment near the coastal area; and $\sim 4 \times 10^3 \text{ ohm.cm}^2$ in the strong acid of HCl, (pH=1.2). Such results indicated that the corrosion rate of lead-sheathed cable without CP increased significantly in the presence of strong corrosive chemicals in the manhole.

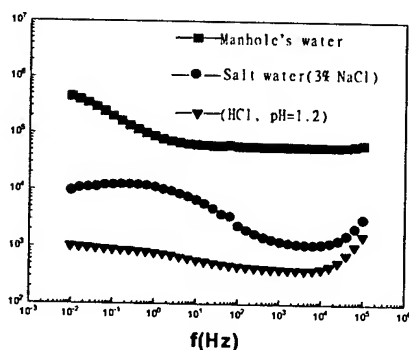


Fig.5. AC impedance measurement of lead-sheathed cable without CP in the CHT manhole water and simulated severe environments.

Fig.6 shows the Bode plot of the lead-sheathed cable with and without CP in the salty water and hydrochloric acid. The corrosion impedance of cable-sheathed cable with CP ($\sim 5 \times 10^4$) in the strong acid solution is ~ 50 times higher than that of lead-sheathed cable without CP ($\sim 1 \times 10^3$). The CP effect for the lead-sheathed cable in the strong acid is more obvious than in the salty water. Judging from the appearance of lead-sheathed cable without CP after immersed in the hydrochloric acid for 100h indicates that a severe corrosion problem took place, as shown in Fig.7.

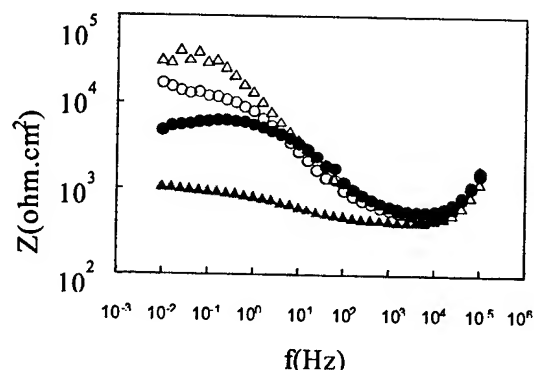


Fig.6. AC impedance measurement of lead-sheathed cable with/without CP protection tested in salt water and in hydrochloric acid solution.

●: without CP in salty water ○: with CP in salty water
▲: without CP in HCl (aq) △: with CP in HCl (aq)

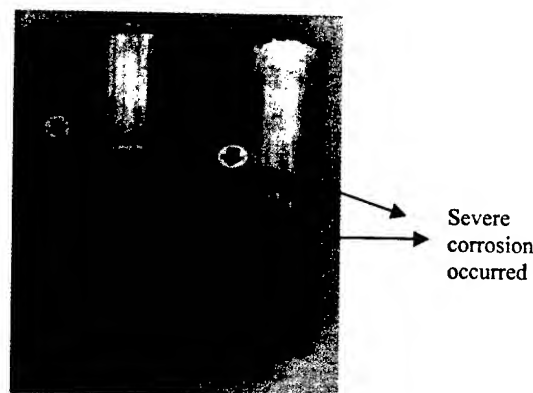


Fig.7. Visual examination of lead-sheathed cable with CP (left) and without CP (right) after immersing in the hydrochloric acid for 100 hours.

3.2 Potentiodynamic polarization

Fig.8 shows the results of the polarization curve of lead-sheathed cable tested in various conditions. The corrosion current density of the lead-sheathed cable in hydrochloric acid is $33.06 \mu\text{A/cm}^2$ and is $0.28 \mu\text{A/cm}^2$ in the manhole's water. For result of lead-sheathed cable in the salty water, a rapid increase in current density after breakdown of the passivity by Cl^- occurring locally rather than generally on the surface of lead-sheathed. This behavior can be explained from the polarization curve of noble metal formed pit corrosion in the chloride containing solution [9].

3.3 Potential measurement

3.3.1 Laboratory tests

CP investigations and major results are based primarily on the corrosion potential monitoring. A value $E_a \leq -0.545 \text{ V (vs. SCE)}$

is currently being considered as the maximum allowable potential for lead sleeves. The corrosion potential for the lead-sheathed cable tested in different conditions in the laboratory is shown in Fig.9. The lead-sheathed cable potentials initially decreases to values below -545 mV cathodic protection level after approximately 6 days until a steady state potential was achieved when immersed in salty water and in hydrochloric acid. The stable E_{corr} potentials for the lead-sheathed cables are -0.75 V, -0.93 V and -0.97 V, respectively, when they were separately immersed in the manholes water, salty water and hydrochloric acid.

The lead-sheathed cable has a higher potential in the initial stage (6 days) in the manhole's water may be caused by the anodic polarization of the sacrificed zinc anode. The reason for having lower potential of lead-sheathed cable in the salty water and hydrochloric acid mainly owing to both solvents with lower electric resistance, and lower the degree of polarization of the sacrificed anode.

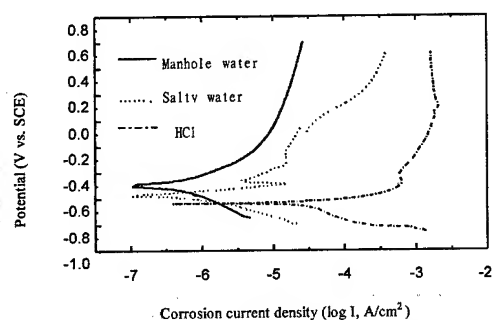


Fig.8. Polarization curve of lead-sheathed cable tested in the CHT manhole water, salt water and hydrochloric acid solution.

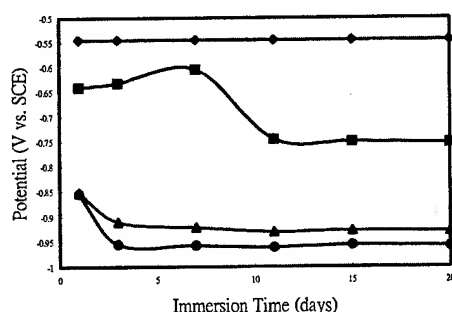


Fig.9. Potential (vs. SCE) variation of lead-sheathed cable with CP in the laboratory test.

- ◆: Cathodic potential of Pb (-0.545 V)
- : Manhole water (-0.75 V)
- ▲: Salty water (-0.93 V)
- : Hydrochloric acid ($\text{pH}=1.2$, -0.97 V)

3.3.2 in-situ tests

A number of well-controlled laboratory tests has been conducted to determine the effects of CP on the lead-sheathed cable. On the other hand, a small-scale field trial of the proposed CP system was undertaken. One of the early tests was set up at number AC20

manhole, Taipei. In situ corrosion potential for the lead-sheathed cable with and without CP after they were immersed in the field manhole's environment and compared with in the laboratory test change with time, as shown in Fig.10.

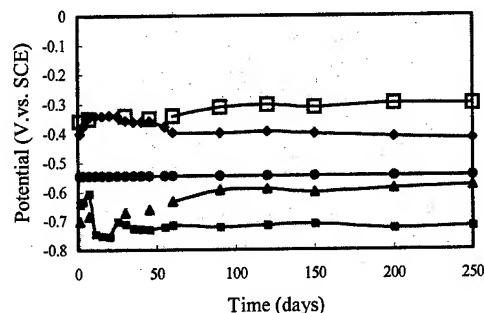


Fig.10. Corrosion potential vs. time for the field test and laboratory test in manhole water.

- : Lab. test with CP ◆: Lab. test without CP
- : Field test without CP ▲: Field test with CP
- : CP potential of Pb

Fig.10 shows that the zinc-sacrificed CP system was effective in protecting lead-sheathed cable from corrosion wherever in laboratory or in field test. The potential differences in the lead-sheathed cable without zinc sacrificed CP system wherever in laboratory or in field test at least is 300 mV higher than that of the one with CP system. The zinc-sacrificed anode CP system can lead the lead-sheathed cable to the immunity domain. The corrosion potential of lead-sheathed cable in the manhole has a tendency to positive direction was also observed. This phenomenon could be explained from the effect of coverage material on the lead-sheathed cable composing of mud, oil, bonding metal etc.

4. Conclusions

- Because of easy installation and low cost for maintenance of the existing lead-sheathed cable, the zinc-sacrificed anode cathodic protection system has been extensively used in manhole environments of the telecommunication.
- Based on the laboratory and field tests, the zinc-sacrificed anode cathodic protection system can lead the lead-sheathed cable to the immunity domain. The zinc-sacrificed cathodic protection system has been proved to be effective in protecting lead-sheathed cable from corrosion.
- The reliability of the communication network in the manhole system at CHT based on the lead-sheathed cables can be significantly enhanced by restoring the zinc-sacrificed anode cathodic protection system.

5. Acknowledgments

The authors gratefully acknowledge the installation of CP system by CHT outside plant engineering department.

6. References

- [1] J.F. Smith, "Corrosion of Lead and Lead Alloy", Material Handbook, Corrosion 9th ed., ASTM International, Ohio (1988).
- [2] J. W. Costerton and J. Boivin, "Microbially Influenced Corrosion and Biodeterioration", p.5-89(1990).
- [3] R.U. Lee, "Statistical Analysis of Corrosion Failures of Lead-Sheathed Cables", Mater. Perform. p.20-23(1992).
- [4] G. Haynes and Robert Baboian, "Field Corrosion Testing and Performance of Cable Shielding Materials in Sols", Mater. Perform. p.45-48 (1991).
- [5] B.M. Green, "In Situ Cathodic Protection of Existing Ductile Iron Pipes", Mater. Perform., pp.45-48 (1991).
- [6] D.H. Kroon and C.F. Schrieber, "Performance of Impressed Current Anodes for Cathodic Protection Underground", CORROSION/84, Paper No. 44, National Association of Corrosion Engineers, Houston, TX, 1984.
- [7] H.H. Uhlig and R.W. Revie, "Corrosion and Corrosion Control", 3rd ed., chap.2, John Wiley & Sons, Inc., New York (1985).
- [8] M. Pourbaix, Atlas of Electrochemical Equilibrium in Aqueous Solutions (Houston, TX: NACE, 1974).

- [9] H. H. Uhlig and R.W.Revie, "Corrosion and corrosion Control", 3rd ed., Chap.5, p.74, John Wiley & Sons, Inc., New York (1985).

Author



Chunghwa Telecom Co., Ltd.

P.O.Box 6-48, Yang-Mei, Taoyuan, Taiwan

Hyt751173@cht.com.tw

He received his MS degree in Chemistry from National Taiwan Normal University in 1983. He is now a doctoral candidate of Materials Science and Engineering of Tsing Hua University. He joined T.L. in 1983 and presently worked as a research scientist and a member of Network Operation Tech. Lab., in T.L.

Input Impedance of Irregular Cascaded Systems

^{^1} **Muhammed M Al-Asadi, ¹Alistair P. Duffy, *Kenneth G Hodge, *Arthur J Willis**
& ***David A Jackson**

¹ De Montfort University, The Gateway, Leicester LE1
9BH, UK

*Brand-Rex Ltd, Glenrothes, Fife KY6 2RS, Scotland,
UK

[^]Principle Author +44 – 7968 - 077195 · alasadi@dmu.ac.uk

Abstract

In this paper, we report and describe the derivation of an analytical approach for the calculation of the input impedance of a non-identical cascaded network of 'n' discrete components based on knowing the propagation constant and the characteristic impedance of each component. These parameters may be obtained analytically or experimentally in a complex form. The developed equation allows the study of the effects of network irregularity, load impedance mismatching and the mismatching of the impedance of cascaded segments of the whole network. It is then applied to calculate the impedance of a multi-segment communication channel at a range of frequencies and validated against a standard equation.

Keywords

Cascaded Networks; Communication Channels; Communication Cables; Characteristic.

1. Introduction

Many constraints may be added to designers and engineers working on high frequency circuits, such as VLSI circuits [1] and communication channels, with the increasing demand for high frequency communication channels to cope with very high data rate transfer, and high frequency circuits. Hence, the effect of impedance mismatches between elements of the cascaded network and the mismatching of the channel termination on the performance of such networks and circuits needs to be investigated.

Communication channels may include very long cables, in which case the impedance of the cable measured at any point along the cable is not constant and depends on local variations of dimensions, such as tolerance in copper diameter and dielectric thickness, and material properties. Figure 1 illustrates the measured characteristic impedance along a cable as a function of the distance between the near end of the cable and the point of measurement. Measurement of the characteristic impedance of three different cables of 10 m length are shown. This longitudinal variation has a great effect on the overall system parameters, including the input impedance and hence on the overall performance of the cascaded system or channel. In addition to that, the use of connectors of different impedance values and different propagation constant produces an unethical performance of the communication system.

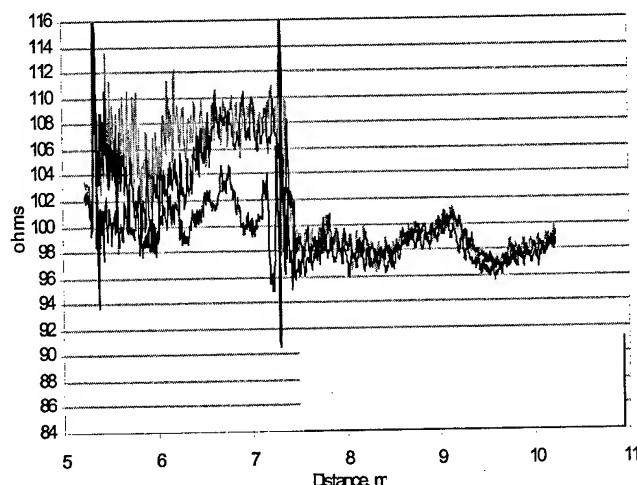


Figure 1. Measured Characteristic impedance of 3 different cables of 10 m length.

Previous work [2] presented the calculation of the overall return loss of a communication channel consisting of many cascaded segments and the calculation of the overall attenuation losses of cascaded systems [3]. In this paper, the work has been extended to develop a similar approach for the prediction of the input impedance, Z_{in} , of a network containing any number of elements, n . The developed equation is also a function of the impedance of every element, Z_o , the physical length of the element, l , the propagation constant, γ and the frequency of the transmitted signal, f .

As the developed equation relies only on the impedance and propagation constant values of the cascaded network elements, it can be used for analysis of channels containing any type of cables such as, STP, UTP and FTP cables. Since the new equation predicts the overall input impedance of any cascaded system, it can also be used for the prediction of the overall return loss and structural return loss of such cascaded system when connected to a source with known source impedance. The developed equation is then used for the prediction of the input impedance and the return loss of different cascaded systems. Results obtained are compared with those obtained using a traditional (but more cumbersome) analytical solution. These comparisons confirm the validity of the derived equations. The next section discusses the traditional approach of calculating the overall input impedance of cascaded systems.

2. Traditional Approach

A regular (perfect) cable of impedance, Z_{o1} , may be terminated at the far end with a load of impedance, Z_l , as shown in Figure 2, where l_1 and γ_1 are the physical length in meter and the propagation constant of the cable respectively.

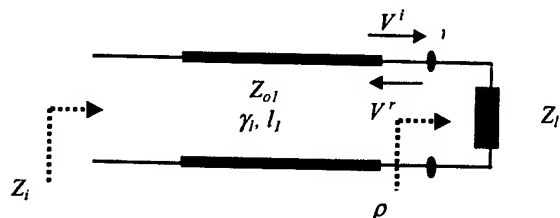


Figure 2. Schematic diagram of a single cable of impedance Z_{o1} terminated with load Z_l

For such a simple channel the input impedance, Z_i , of the channel is given using a traditional approach as described in [4] as:

$$Z_i = Z_{o1} \left[\frac{Z_l \cosh(\gamma_1 l_1) + Z_{o1} \sinh(\gamma_1 l_1)}{Z_{o1} \cosh(\gamma_1 l_1) + Z_l \sinh(\gamma_1 l_1)} \right] \quad (1)$$

The input impedance of Figure 1 can also be obtained in term of the reflection coefficient, $\rho = (V^r/V^i)$, at the load end as:

$$Z_i = Z_{o1} \left[\frac{1 + \rho \cdot e^{-2\gamma_1 l_1}}{1 - \rho \cdot e^{-2\gamma_1 l_1}} \right] \quad (2)$$

where V^r and V^i are the reflected and the incident voltages at the load end respectively. In this case the reflection coefficient can be obtained as function of both load impedance and cable impedance as:

$$\rho = \frac{Z_l - Z_{o1}}{Z_l + Z_{o1}} \quad (3)$$

The reflection coefficient given in equation 3 can either be measured or calculated using the complex form of the impedance values. For simple and regular communication channels, this operation is straightforward. The difficulty arises when a number of other elements such as connectors and more than one cable of different characteristic impedance, as illustrated in figure 1, are present in the network. It will also be more difficult if one or more

of those connectors and cables is suffering irregularity or deformation as a result of, tolerance in dimensions, production process or bad handling effect [5]. In this case the new developed approach described in this paper is more appropriate for the calculation of the input impedance of such system.

3. New Approach Derivation

A general cascaded system containing, n , elements can be illustrated using the two port network principles, as shown in Figure 3.

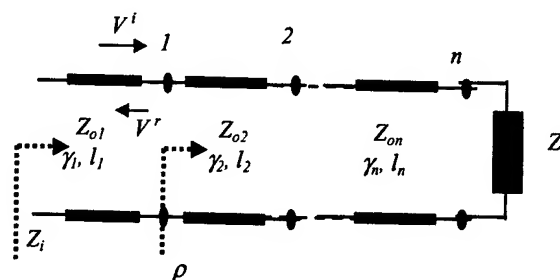


Figure 3. Schematic diagram of a cascaded network containing n segments and terminated with load.

The input impedance of such circuit can be obtained using equation 1. In this case, looking to the right side of the network input impedance at the connection $(n-1)$ between the load and the segment connected to the load can be obtained. This value should be considered as a load connected to the rest of the circuit at connection node $(n-2)$. Repeating this process for as many segments as included in the network, the overall input impedance of the cascaded system can be obtained.

Another approach is to measure the reflection coefficient at the connection point (1) between the 1st and the 2nd segments of the network. The obtained value can then be used to calculate the input impedance of the network using equation 2. Due to many difficulties that may interfere with the measurement process and the measuring devices, we propose our approach to calculate the reflection coefficient as function of impedance and propagation coefficient values of all cascaded segments of the network.

Following a similar approach described in [2] and [3] and using the relations between incident, transmitted and reflected voltages at the connection between segments along the network, the reflection coefficient at the connection between both 1st and 2nd segments of the network can be obtained as in equation 4.

Substituting equation 4 in equation 2, the overall input impedance of the whole network can then be given as in equation 5.

$$\rho = \frac{Z_{o2} - Z_{o1}}{Z_{o2} + Z_{o1}} + \sum_{k=2}^n \left[\prod_{i=2}^k \left(\frac{2 \cdot Z_{oi}}{Z_{oi} + Z_{oi-1}} \cdot \frac{2 \cdot Z_{oi-1}}{Z_{oi} + Z_{oi-1}} \right) \right] \cdot e^{-2 \left\{ \sum_{j=2}^k \gamma_j l_j \right\}} \cdot \frac{Z_{o_{k+1}} - Z_{ok}}{Z_{o_{k+1}} + Z_{ok}} \quad (4)$$

$$Z_i = Z_{o1} \left[\frac{1 + \left\{ \frac{Z_{o2} - Z_{o1}}{Z_{o2} + Z_{o1}} + \sum_{k=2}^n \left[\prod_{i=2}^k \left(\frac{2 \cdot Z_{oi}}{Z_{oi} + Z_{oi-1}} \cdot \frac{2 \cdot Z_{oi-1}}{Z_{oi} + Z_{oi-1}} \right) \right] \cdot e^{-2 \left\{ \sum_{j=2}^k \gamma_j l_j \right\}} \cdot \frac{Z_{o_{k+1}} - Z_{ok}}{Z_{o_{k+1}} + Z_{ok}} \right\} \cdot e^{-2\gamma_1 l_1}}{1 - \left\{ \frac{Z_{o2} - Z_{o1}}{Z_{o2} + Z_{o1}} + \sum_{k=2}^n \left[\prod_{i=2}^k \left(\frac{2 \cdot Z_{oi}}{Z_{oi} + Z_{oi-1}} \cdot \frac{2 \cdot Z_{oi-1}}{Z_{oi} + Z_{oi-1}} \right) \right] \cdot e^{-2 \left\{ \sum_{j=2}^k \gamma_j l_j \right\}} \cdot \frac{Z_{o_{k+1}} - Z_{ok}}{Z_{o_{k+1}} + Z_{ok}} \right\} \cdot e^{-2\gamma_1 l_1}} \right] \quad (5)$$

where, Z_{ok} is the impedance of the k^{th} segment and, where $k = n$, $Z_{o_{k+1}}$ is the load impedance, Z_l . It should be mentioned here that replacing the load impedance by an open circuit or short circuit, the reflection coefficient of equation 4 can be obtained, and hence the input impedance of the system under such termination conditions can be obtained. Using both calculated values of the input impedance under short and open circuit conditions, the input impedance of the network under a matching load condition can also be obtained using the following equation:

$$Z_i = \sqrt{Z_{ioc} \cdot Z_{isc}} \quad (6)$$

where, Z_{ioc} and Z_{isc} are the input impedance values of the overall network obtained under open circuit and short circuit load termination respectively.

4. Equation Validation

To validate the developed equation, the input impedance of seven segments communication channel connected as; {connector 1 (1cm), patch cable 1 (1m), connector 2 (1 cm), horizontal cable (10m), connector 3 (1cm), patch cable 2 (1m), and connector 4 (1cm)} is calculated. All the segments have the same dimensions and hence resulting in similar characteristic impedance. The network is connected to matching source impedance and terminated with matching load. The dimensions of the cascaded cables are:

$D = 0.94 \text{ mm}$ is the distance between the centres of the cable conductors.

$r = 0.53 \text{ mm}$ is the radius of each cable conductor.

These cable dimensions resulted in an impedance value of 96.7Ω . The input impedance of this network was also calculated using the traditional approach of equation 1. Both amplitude and phase of the impedance values are plotted in figures 4 and 5 respectively as function of the frequency of operation f . Both figures illustrate an excellent agreement between both sets of results obtained using the traditional approach and the new developed approach.

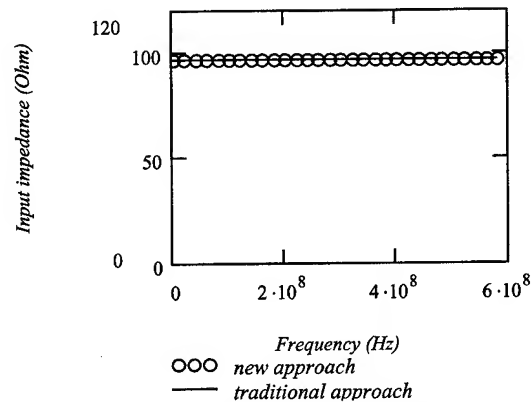


Figure 4. Input impedance of 7 segments network validated against the traditional approach of equation 1.

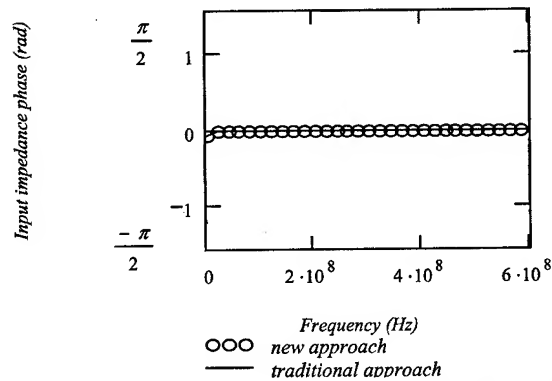


Figure 5. Phase of the impedance illustrated in figure 4

5. Application and Results

To illustrate the performance of the new equation, it is used for the calculation of the input impedance of irregular 7-segment system discussed earlier. To simplify the calculations, circular cross section connectors are used. Dimensions of each connector are; $D = 0.85 \text{ mm}$ and $r = 0.46 \text{ mm}$, while dimensions of each patch and horizontal cable are; $D = 0.87 \text{ mm}$ and $r = 0.55 \text{ mm}$ is the radius of each cable conductor. The length of each conductor is 1 cm , the length of each patch cable is 1 m and the length of the horizontal cable is 10 m .

The lay length of each cable is 20 mm and is taken into account for the calculation of the input impedance. Those dimensions resulted in impedance of 100.7 Ω of each connector and 84.93 Ω of each cable. The system is connected to a source of 100 Ω impedance and terminated with similar load impedance. Both amplitude and phase of the input impedance of overall system is calculated and plotted as function of the frequency of operation as illustrated in figure 6 and 7 respectively.

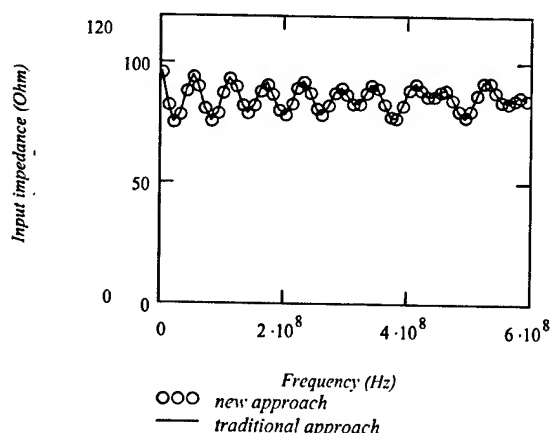


Figure 6. Impedance amplitude of a 7 segment irregular system calculated using both traditional and new approach.

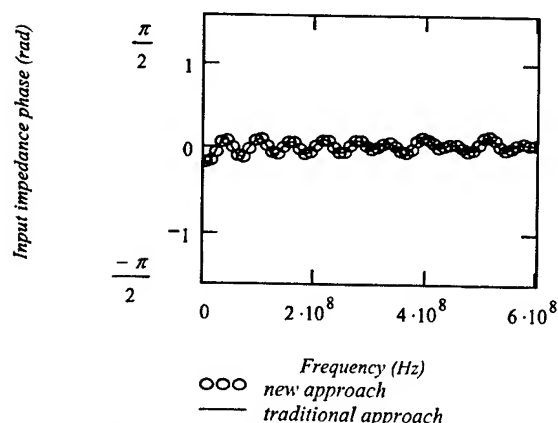


Figure 7. Phase of the impedance illustrated in figure 6.

Further validation can be achieved by using the new equation for the calculation of the input impedance using open circuit terminations. Both traditional and new approaches are used to validate the developed equation. Again amplitude and phase of the input impedance are calculated and plotted as function of the frequency of operation as illustrated in figures 8 and 9 respectively.

Furthermore, the new equation is used for the calculation of the input impedance of irregular system of a 100 m horizontal cable, using both equation 6 where short and open circuit terminations are used and using a matched load termination. Results are obtained for the same dimensions described earlier. Amplitude and phase are both calculated and plotted as illustrated in figures 10 and 11 respectively.

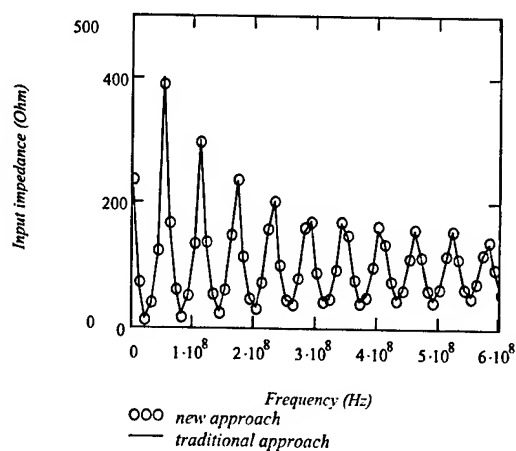


Figure 8. Reproduction of figure 6 for an open circuit termination.

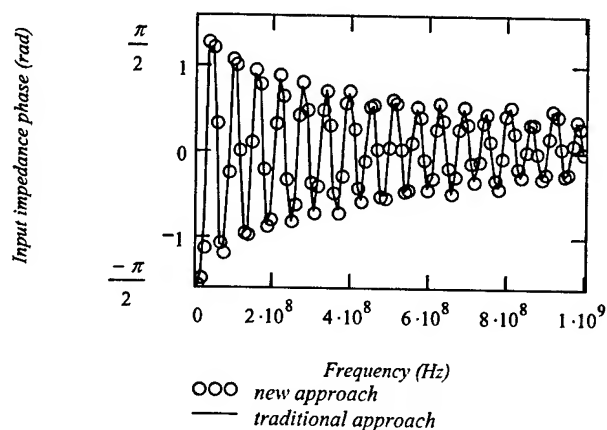


Figure 9. Phase of the impedance illustrated in figure 8.

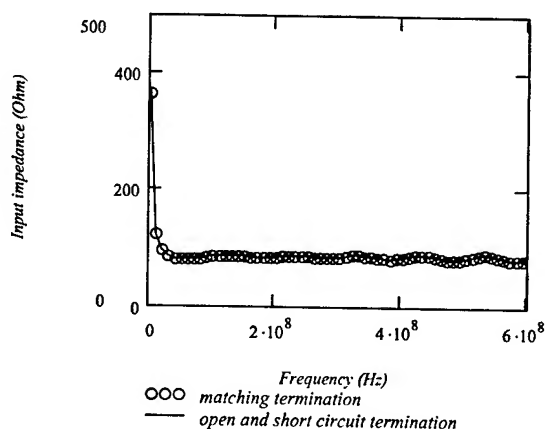


Figure 10. Amplitude of the input impedance where a 100-m cable is used obtained using the new equation and using matching and open and short circuit terminations.

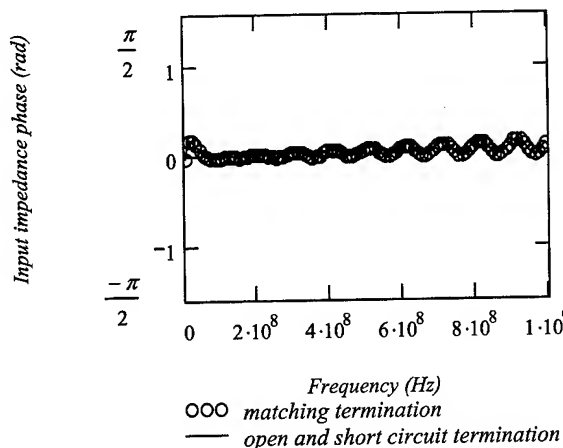


Figure 11. Phase of the impedance illustrated in figure 10.

Results obtained here illustrate the need to the development of such effective approach rather than using an iterative approach that can be computationally costly as the number of segments in the cascaded system is getting bigger. It should also be mentioned here that the input impedance obtained here can be used for the calculation of the return loss of the system using equation 28 of reference [2].

6. Conclusions

The calculation of the input impedance of any cascaded network, such as communication channel, can be achieved using an efficient and very simple equation presented here. The developed equation allows the direct calculation of input impedance without requiring the iterative calculations of current traditional equation (1). The new equation (4) can readily provide the reflection at any interface along the cascaded network. The performance of the new equation is illustrated by applying it to different illustrative channels with different terminations, different dimensions and different length of the horizontal cable. Excellent agreement was achieved between results obtained using the traditionally used approach and the new developed equation. The new equation performs equally well with any number of segments and at any frequency of operation. It also performs well for any load termination and can be applied to any structured cabling installation containing UTP, FTP and STP cables.

7. References

- [1] I. T. Sylla, M. Slamani, B. Kaminska, F. M. Hossien and P. Vincent, "Impedance Mismatch and Lumped Capacitance Effects in High Frequency Testing," *the 16th IEEE VLSI Test Symp. Proc.*, 239-244 (1998).
- [2] M. M. Al-Asadi, A. P. Duffy, K. G. Hodge and A.J. Willis "Return Loss Prediction for Cascaded Systems," *Proc. 49th IWCS Symposium*, 578-585 (November, 2000).

- [3] M. M. Al-Asadi, A. P. Duffy, K. G. Hodge, A.J. Willis and D. A. Jackson "Transmission Parameters of Cascaded Systems," *Proc. 50th IWCS Symposium*, 160-168 (November, 2001).
- [4] S. Ramo, J. R. Whinnery and T. Van Douzer, *Fields and waves in communication electronics*, 2nd ed., Wiley, Amsterdam, (1984).
- [5] M. M. Al-Asadi, A. P. Duffy, K. G. Hodge and A.J. Willis "Modelling as a tool for analysing handling effects in structured wire cabling," *Proc. 10th IEE International Conference on Emc, Warwick, UK*, 131-136 (September, 1997).

Authors Biographies



Dr. Mohammed Al-Asadi received his BSc. degree from the University of Basra, Iraq and an MPhil degree from the University of Nottingham, UK, both in Electronic and Electrical Engineering in 1988 and 1992 respectively. Between 1993 and 1996 he was working on a research project at the University of Nottingham, developing a program to incorporate charge particle motion in electromagnetic fields with transmission line modelling method.

In 1996 he joined De Montfort University in Leicester, UK, where he is working as a Research Fellow and where he obtained his PhD degree. His research involves the investigation of high frequency performance of structured wire cabling in communication systems. He is the author and co-author of many journal and conference papers. His research interests include EMC, communication cables, electron beam, field-particle interaction devices, numerical methods and simulation of electromagnetic fields. He is currently working on the Bit Rate Error Correction in wireless mobile communication.

David A. Jackson holds a BSc(Hons) in Electrical and Electronic Engineering from Abertay University, Dundee, Scotland. His career has been dominated by the design of test systems, initially as a Research and Development engineer working on test facilities for microprocessor systems. He has spent over 16 years in the cable industry designing and implementing radio frequency test methods.



For biographies of **A. P. Duffy**, **K. G. Hodge** and **A. J. Willis**, please see paper "Technology Forecasting Techniques in Communications" presented in this symposium.

Development of Novel High Efficient SiC Particle Removing System Based on Thermophoretic Effect

Alexei Malinin^(a), Timo Mattila^(a) and Markku Rajala^(b)

Photonium Oy

^(a)Sorronrinne 9, Lohja, FIN-08500, Finland
+358-19-357381 · photonium@photonium.fi

Liekki Oy

^(b)Sorronrinne 9, Lohja, FIN-08500, Finland
+358-19-357391 · liekki@liekki.com

Abstract

In this work, the mechanism of SiC particle deposition from Ar gas flowing over a fiber during drawing process onto a vertical surface by thermophoresis is investigated. Thermophoresis can be effective in moving submicron SiC particles in the range of 10-100 nm, and plays a significant role in moving these particles away from a heated surface. Thermophoretic velocity can be increased by incorporation of "blades" cooled by cooling medium. The data obtained are used in developing of novel high efficient particle removing system.

Keywords

Thermophoresis; optical fiber; SiC particles.

1. Introduction

Thermophoresis is known as a phenomenon in which small particles suspended in a gas migrate from the hot to the cold zones of the gas. This thermophoretic force is a result of greater momentum transfer from the gas molecules on the hot side of the particles compared to the cold side.

The deposition of submicron particles from an aerosol flow onto surface due to thermophoresis has gained importance for many engineering applications.

Aerosol particles flowing over surfaces tend to deposit under the influence of diffusion, gravity and other forces. In a non-uniform temperature field the particles experience thermophoretic force directed against the temperature gradient. As a result, the particles are deposited from hotter gas to colder surfaces. Contamination can arise from the furnace environment. In fiber drawing application the actual composition and formation mechanism of the particles is unknown. However it is known that both graphite and silica have a finite vapor pressure at fiber draw temperature, over 2000 C°, and species of carbon and silicon oxide (SiO) are evaporated from the element and preform surfaces. Thermodynamical calculations show that a number of different species can be born from these compounds depending on the temperature, time and mixing. It is assumed that at least a fraction of these particles is silicon carbide (SiC), which can cause fiber strength decrease and shorten the graphite parts lifetimes. Most

probably the particles are formed as condensation nuclei and then they grow due to coagulation to sizes 0.1 µm or greater. The growth is speeded up by the high concentration of ultra fine particles. If all evaporated carbon would end up as SiC and 1 µm particle size, the concentration would be 1 000 000 particles/cubic feet, i.e. much higher than typical clean room specification.

2. Theoretical

There have been many attempts to devise a suitable theory, which describes thermophoresis, but as yet a complete solution has not been found.

Molecular motion in a temperature gradient is considered. The movements will be more vigorous at higher temperatures. When a particle is placed in this gradient, the momentum transferred to one side of the particle exceeds that transferred to the other side, leading to a net force results. To determine this net force, it is necessary to know exactly the velocity distribution of the molecules at the particle surface. Among other things this depends on the ratio of particle size and pressure of the medium, the Knudsen number ($Kn=2\lambda/d$, where λ is mean free pass, d is particle diameter), because the particle itself can have very little or a significantly great influence on the velocity distribution of nearby molecules. A complete theory must take this varying influence into account. At present it is most convenient to consider several size ranges (or Knudsen numbers) when one is attempting to predict the magnitude of the thermal force.

In our case the particle is much smaller than the mean free path of the gas molecules. This represents the condition where $Kn \gg 1$ and is called the free molecule region.

In the free molecule region, molecules colliding with a particle will travel an average many particle diameters away from the particle before colliding with another molecule. Thus it is extremely unlikely that the molecule and particle will ever meet again or that the molecule will affect other molecules, which may collide with the particle. Therefore, the effect of the collision of the molecule with the particle is immediately lost, and the particle itself exerts virtually no influence on the velocities of the surrounding gas molecules [1].

Derjaguin and Bakanov [2] found the following expression for the thermal force on particle when $Kn \gg 1$:

$$F_T = -\frac{1}{2} \pi \mu v \frac{d^2}{\lambda} \frac{\nabla T}{T}, \quad (1)$$

where μ is gas viscosity, v is kinetic viscosity, ∇T is temperature gradient.

The thermophoretic velocity can be determine [1] by utilizing Stokes law and by assuming that the Cunningham correction factor is applicable for cases where $Kn \gg 1$. In this case thermophoretic velocity can be determine as

$$g_T = 0.55 v \frac{\nabla T}{T} \quad (2)$$

3. Experimental

3.1 Temperature measurements and thermophoretic velocity

For experiment we use fiber draw furnace with induction heating and extension tube (length 100 cm, internal diameter 8 cm). During operation furnace purged by Ar gas with three different gas flows: 7 l/min, 11 l/min and 15 l/min. Temperature inside hot zone was 2200 °C. Gas temperature was measured near axis and at the edge of extension with different distance from the hot zone of the furnace by using Pt/Rd(13%) thermocouple (Figure 1).

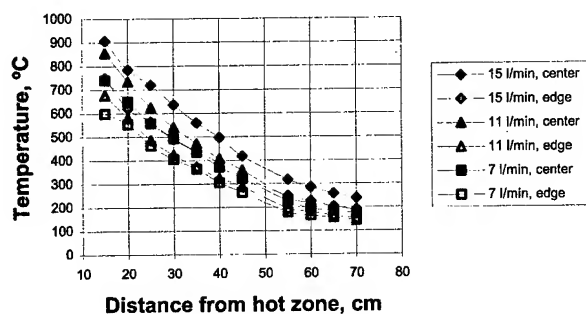


Figure 1. Gas temperature at different distances from the hot zone

Figure 1 shows that temperature inside extension tube strongly depends from distance from hot zone and gas flow. With lower Ar gas flow temperature is lower.

Considering as the initial temperature of the fiber that at the end of neckdown, where it reaches its final diameter (commonly taken to be glass softening point around 1600 °C) [3-5], and utilizing Eq. 2, thermophoretic velocity can be calculated. Results of calculation of

the thermophoretic velocity at different distances from hot zone for different gas flow presented in Figure 2.

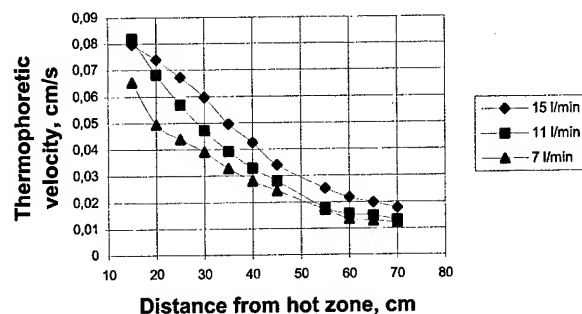


Figure 2. Thermophoretic velocity at different distances from the hot zone

It can be seen that the thermophoretic velocity decrease with increasing distance from the hot zone and decreasing Ar gas flow. Therefore, for developing particle removing system necessary to consider the upper region of the extension tube, where the thermophoresis is more effective.

3.2 Particle removing system

The data obtained were used in the developing of novel high efficient particle removing system.

Particle removing system consists of tube and "blades" inside tube. Distance from fiber to "blades" is 2 cm. "Blades" cooled by a cooling medium with controlled temperature.

Structure of the fiber draw furnace with particle removing system is shown in Figure 3. The particle removing system is placed between the fiber draw furnace and extension tube.

SiC particle, which are born during fiber drawing flow down from fiber draw furnace through particle removing system. Inside particle removing system SiC particles move in direction from fiber to cooling "blades" due to the thermophoretic force. And finally they are deposited on it.

Comparison of the values of thermophoretic velocity at different distances from the hot zone with and without particle removing system for 15 l/min Ar gas flow is shown in Figure 4.

Thermophoretic velocity inside particle removing system in the upper part is almost four times higher compared to thermophoretic velocity inside extension tube. In the lower part it decrease due to changing temperature gradient and becomes comparable to thermophoretic velocity inside extension tube.

These results illustrate the idea that thermophoresis can be effective in moving submicron SiC particles away from a heated surface of a fiber.

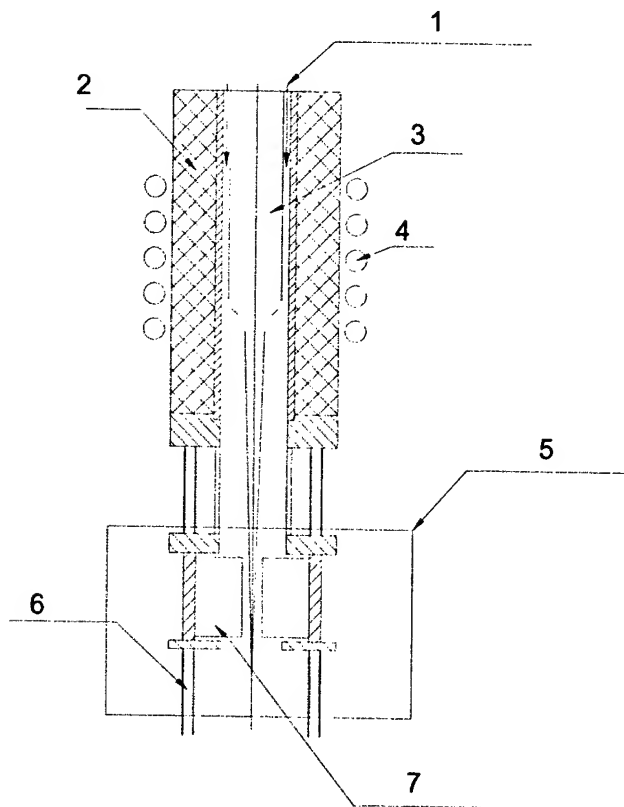


Figure 3. Structure of the fiber draw furnace with particle removing system (1 - Ar gas flow, 2 - heating element, 3 - preform, 4 - coil, 5 - particle removing system, 6 - extension tube, 7 - "blades")

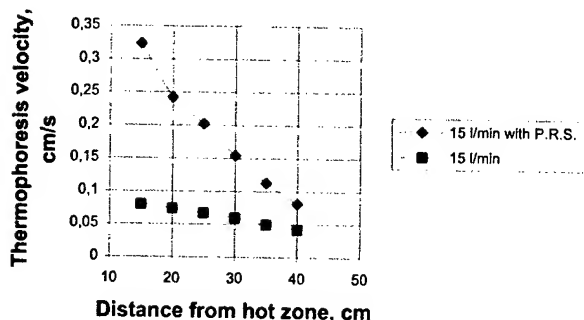


Figure 4. Thermophoretic velocity at different distances from the hot zone with and without particle removing system. Ar gas flow is 15 l/min

It is interesting to estimate parameters of the "blade" for effective thermophoresis. First of all "blade" temperature has great effect on the process, as can be seen from Figure 2. We calculated thermophoretic velocity for different "blade" temperatures and distance from hot zone (Figure 5). The curve slope is decreased for low temperature and "blade" cooling down lower 400 °C is non-effective due to small increase in thermophoretic velocity.

Another "blade" parameter is length along extension axis. It can be estimated from condition that particle should reach "blade" due to radial thermophoretic movement during moving along extension axis with Ar flow.

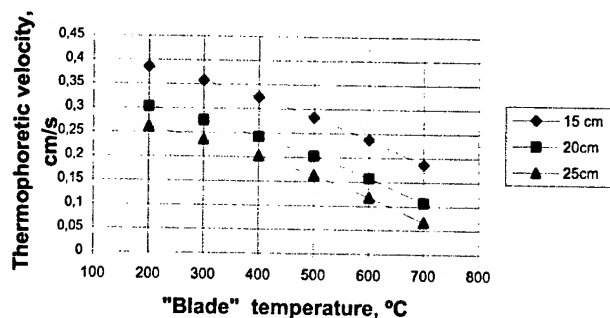


Figure 5. Temperature dependence of the thermophoretic velocity on "blade" temperature at different distances from the hot zone. Ar gas flow is 15 l/min

Length of the "blades" L can be found from the following expression

$$L = R \frac{V_G}{g_T}, \quad (3)$$

where R is distance between fiber and "blade", V_G is a gas velocity, calculated from gas flow rate.

4. Conclusions

In this work, the mechanism of SiC particle deposition from Ar gas flowing over a fiber during drawing process onto a vertical surface by thermophoresis is investigated. Thermophoresis can be effective in moving submicron SiC particles in the range of 10-100 nm, and plays a significant role in moving these particles away from a heated surface. The results show that thermophoretic velocity can be increased by incorporation of "blades" cooled by cooling medium. Geometry of "blades" can be estimated from obtained results. The data obtained are used in developing of novel high efficient particle removing system.

5. Acknowledgments

The authors are grateful to Mr. Taneli Tuurnala at Photonium Oy for helpful discussions and suggestions and Mr. Rami Niemi at Photonium Oy for assistance in carrying out the temperature measurements.

6. References

- [1] P. C. Reist, "Aerosol Science and Technology," McGraw-Hill, Inc., 2nd ed., 379 (1993).
- [2] B. V. Derjaguin and S.P. Bakanov, *Kolloidn. Zh.*, 21, p. 377 (1959).
- [3] S. S. Kyriacou, "Cooling Rates of Optical Fibers", *New Brunswick Rutgers, The State University of New Jersey*, p. 88 (1990).
- [4] T. Vaskopoulos, C. Polymeropoulos and A. Zebib, "Cooling of Optical Fiber in Aiding and Opposing Forced Gas Flow", *International Journal of Heat and Mass Transfer*, 38, pp.1933-1944, (1995).
- [5] S. R. Choudhury, Y. Jaluria, T. Vaskopoulos and C. E. Vaskopoulos, "Forced Convective Cooling of Optical Fiber During Drawing Process", *Journal of Heat Transfer*, 116, pp. 790-794, (August 1994)



Alexei Malinin received the M.Sc. and Ph.D. degrees from the Moscow Aviation Institute in 1985 and 1990, respectively. He worked on development of fabrication processes of components for integrated electronic devices in the Moscow Aviation Institute (1985-1992, 1994-1995), electrical characterization and physical properties of semiconductor

crystals at the Research Center for Interface Quantum Electronics in the Hokkaido University (1992-1994), in the fields of plasma enhanced chemical vapor deposition and reactive ion etching of semiconductor and dielectric films and fabrication of low

dimensional silicon structures for optoelectronics application at the Electron Physics Laboratory in the Helsinki University of Technology (1995-2002).

Since February 2002, he has been with Photonium Oy, where he is currently a senior research scientist. Dr. Malinin is a co-author of more than 30 scientific publications and 6 patents.



Timo Mattila received M.Sc. degree in mechanical engineering in 1997 from the Helsinki University of Technology and his BSc. degree in 1991 from Institute of Technology in Helsinki. From 1996 to 2001 he hold various positions in Nextrom Oy, Vantaa, Finland (earlier Nokia Maillefer Oy) beeing in charge of development of optical fiber processing equipment. From June 2001 Mattila has hold a

position of Chief Technology Officer (CTO) in Photonium Oy, equipment and process supplier for photonics industry.



Markku Rajala received his M.Sc. degree in physics at Tampere University of Technology. He was a research engineer at Nokia Machinery (1984-1987), R&D Manager (1987-1990) at Nokia Cables (SM Fiber and OVD process development), Founder and Maneger of the Ceramics and Glass Research Laboratory in UIAH (1990-1996), Managing

Director (1996-2000) at ABR Innova Oy (Fiber optic equipment and commissioning). He is currently CEO and CTO in Liekki Oy.

Markku Rajala has more than 30 relevant publications and 10 patents in fiber optics, ceramics materials and high-temperature applications.

Development of Optical Drop and Indoor Cable of high fiber density

Tetsuya YASUTOMI, Fumihori NAKAJIMA, Masanori HATTORI,

and Masami HARA

OPTCOM division, The Furukawa Electric Co., Ltd.

6 Yawatakaigan-dori, Ichihara, Chiba, Japan

+81-436-42-1642 · tomy@ch.furukawa.co.jp

Abstract

We have developed new type of optical fiber drop cables and intra-building cables that replaces slotted core cables. They are laid in multistory residences and small buildings.

Due to the fact that this cable is small in diameter, it can be laid in narrow spaces that were heretofore impossible to run cables through. Construction is very simple, which contributes to lowering the overall cost. Furthermore, it is possible to manufacture cables in a single process, thereby lowering processing costs.

The mid-span branching capabilities are far superior to the old type of cables, as well. In testing this type of cable for transmission loss, temperature tolerance, mechanical abilities, mid-span branching capabilities, and installation flexibility, we obtained positive results in every category, confirming that this cable is extremely practical.

Keywords

Fiber; cable.

1. Introduction

As the construction of optical networks advances, more optical fiber cable and optical fiber cords are being used. In years past in Japan, drop cables and distribution cables in buildings have utilized the slotted core feeder cables [1] to distribute the cable vertically to cabinets with cable connectors on each floor of the structure. These connection cabinets also contain the distribution cables that connect horizontally to the various units on each floor.

However, the large external diameter of slotted core feeder cables can make them unwieldy. They pose problems in small and medium buildings and often, especially in places where the ductwork is already in place, it is not possible to install these cables at all. For this reason, we have developed a new type of optical fiber cable, which is much narrower in diameter, and can be used for drop cables and intra-building cables.

2. Cable design

2.1 Cross Section Construction

Cables are constructed using the same configuration that has been adopted for indoor and drop cables. Inside a cross section of the cable, optical fiber units consisting of several 4-fiber ribbons or 8-fiber single strands are encapsulated.

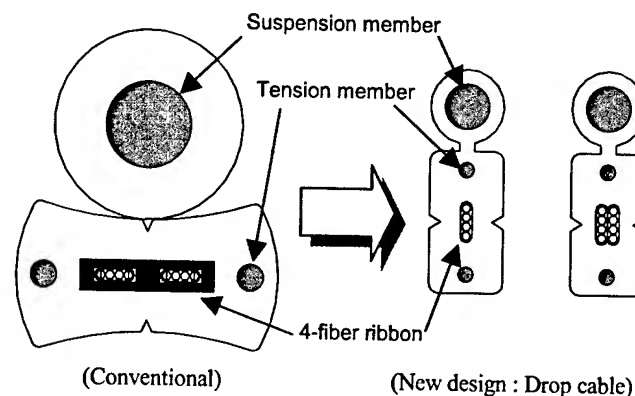


Figure 1. Aerial Drop Cables

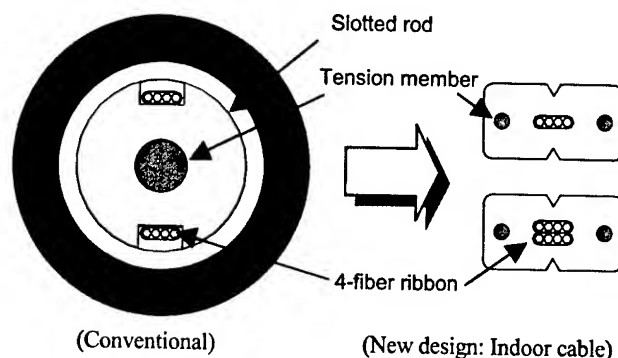
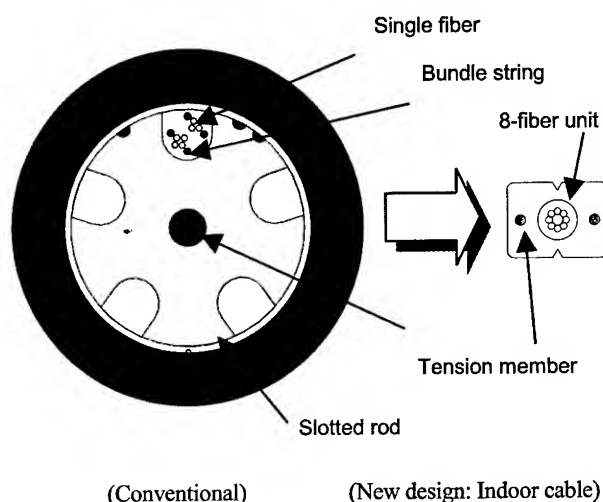


Figure 2. Underground Drop Cables and Intra-building Cables (4-Fiber Ribbon Type)



**Figure 3. Intra-building Cables
(Single Fiber Unit Type)**

2.2 Study of Construction Methods

The newly designed 8-fiber type is different from current indoor cables in that the cable's center and the center of the optical fiber inside the cable don't correspond, since the fibers are encapsulated in two layers. For this reason, the strain on the optical fiber is increased when the cable is bent, and this leads to problems with reliability. This is why we conducted a study on the strain and permissible failure ratios of optical fiber. defects

2.2.1 4-Fiber Ribbon, 2 Layer Type

We calculated and measured when the cable-bending radius was equal to 30mm. (1) is the formula used, and Figure 4 is a chart with the results of the calculations.

Strain = (The actual measurement of the distance between the center of the bent cable and the center of fiber) / (fixed bending radius) (1)

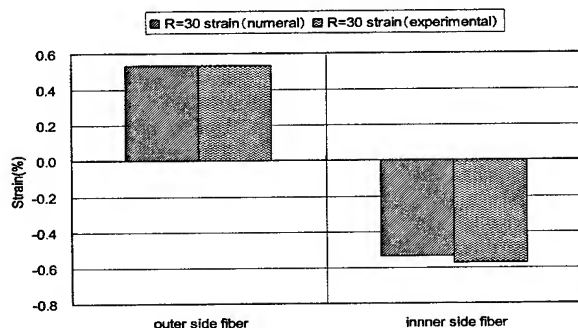


Figure 4. Fiber Strain from Cable Bending

The failure ratio per single optical fiber on the outside of the center of cable was calculated using formula (2), when the cable was left in a bent status at a given radius for 20 years. The formula used is labeled (2), and Figure 5 is a chart with the results of the calculations. The results revealed that permissible failure ratio, $1.8 \times 10^{-5}/\text{km}$ per fiber can be met if the fixed bending radius is greater than 60 mm.

$$\lambda = \alpha \cdot N_p \frac{B_p / E^2}{(B / E^2)^B} \times \frac{(\epsilon^n \times t_s)^\beta}{\epsilon_p^{n_p} \times t_p} \quad (2)$$

Table 1. Numerical Parameters

Symbol	Explanation	Value
λ	failure rate	-
N_p	fiber breaking ratio at screening test	0.002
α	$m / (n_p - 2)$	0.14
m	Weibull distribution constant	-
β	$(n_p - 2) / (n - 2)$	1
B_p	fatigue index at screening test	$\frac{B_p / E^2}{(B / E^2)^B} = 1$
n_p	fatigue coefficient at screening test	
B	fatigue index in service environment	
E	Young's modulus of fiber elasticity	
ϵ_p	screening strain	1.1%
t_s	service period	20 years
t_p	screening period	1 sec
ϵ	fiber strain at fixed bending	Equation (1)

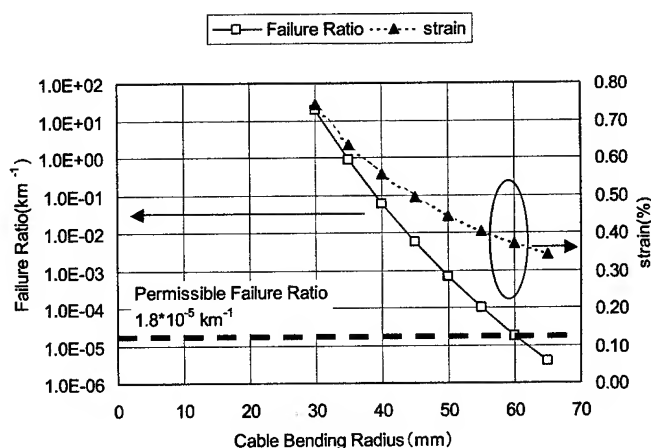


Figure 5. Failure Ratio and Fiber Strain when Cable Is Bent

2.2.2 8-single Strand Unit Type

Fiber strain of a bent cable with a 30 mm radius was calculated using this formula (1) and then actually measured. Figure 6 is a chart with the results of the calculations. The number of actual compress strains is slightly less than the number of calculated strains, but both the calculated and the measured tensile strains were the same.

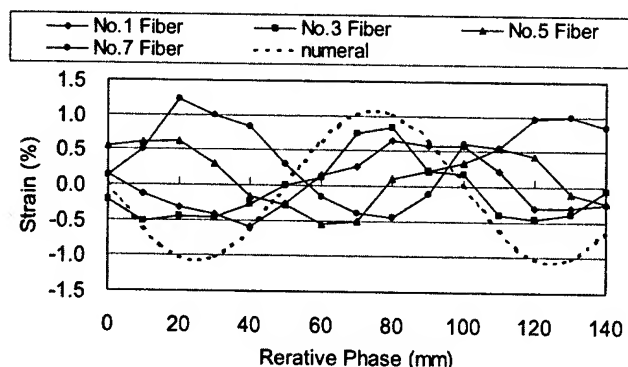


Figure 6. Fiber Strains when Cables are Bent

The failure ratio per optical fiber strand on the outside from the center of the cable after 20 years was calculated using formula (2), where the cable was left in a bent status at a given radius for 20 years. As indicated in Fig 7, it was assumed that 2/3 of a given distance affected by tensile strain was loaded with the maximum strain $\times 0.477$ (0--1/6 cycle, average of 2/6--1/2 cycle) and the remaining 1/3 was loaded with the maximum strain $\times 0.955$ (average of 1/6--2/6 cycle). Fig 8 is a chart of the calculated results. The results revealed that the permissible failure ratio, $1.8 \times 10^{-5}/\text{km}$ per strand can be met if fixed bending radius is greater than 95 mm.

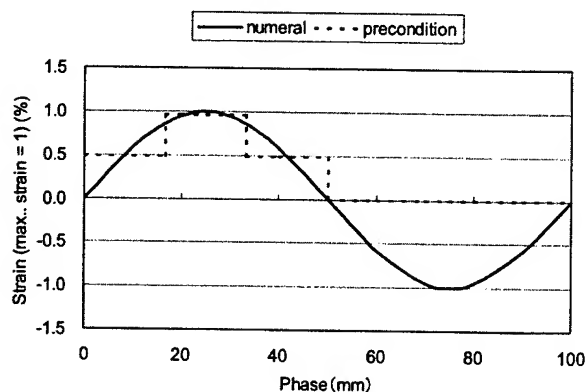


Figure 7. Preconditions for Calculations

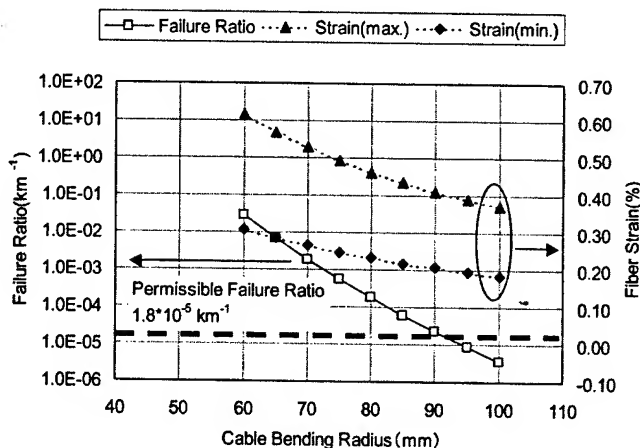


Figure 8. Failure Ratios and Fiber Strains when a Cable is Bent

3. Cable performance

Temperature characteristics, mechanical characteristics, and branching capabilities beyond the mid-span of the optical fiber were evaluated. Results of the tests were satisfactory. We also evaluated optical fiber cable with regard to their suitability in ducts. Optical fiber cables were found to be even better suited to ducts than conventional slotted construction.

3.1 Temperature Characteristics

Trial cables were tested for heat cycling between -30 degrees and 70 degrees and fluctuations of transmission losses are shown in Table 2.

Table 2. Temperature Characteristics (@1.55μm)

Cable Type	Increase in Maximum Transmission Loss (dB/km)	
	-30 degree	70 degree
8-fiber Drop(ribbon)	0.01	0.00
4-fiber Drop(ribbon)	0.01	0.00
8-fiber Indoor(ribbon)	0.01	0.00
4-fiber Indoor(ribbon)	0.00	0.00
8-fiber Indoor(unit)	0.03	0.00

3.2 Temperature Characteristics at Fixed Bending

Trial cables were coiled ten times with a 30 mm radius and tested for heat cycling between -30 degrees and 70 degrees and fluctuations of transmission losses are shown in Table 3. No remarkable increase in loss was observed in the temperature range.

Table 3. Temperature Characteristics at Fixed Bending (@1.55 μ m)

Cable Type	Increase in Maximum Transmission Loss (dB)	
	-30 degree	70 degree
8-fiber Drop (ribbon)	0.00	0.00
4-fiber Drop (ribbon)	0.00	0.00
8-fiber Indoor (ribbon)	0.00	0.00
4-fiber Indoor (ribbon)	0.00	0.00
8-fiber Indoor (unit)	0.00	0.00

3.3 Mechanical Characteristics

Table 4 lists the results of mechanical tests of trial cables. Results were satisfactory in various tests.

Table 4. Results of mechanical test (@1.55 μ m)

Item	Condition	Result
Bending	R = 30 mm	< 0.01 dB
Lateral pressure	2940 N/ 100 mm	< 0.01 dB
Squeezing	R = 300 mm 980 N 90 deg.	< 0.01 dB
Impact	0.6 kg \times 1 m	< 0.01 dB
Twist	\pm 180 deg. / m	< 0.01 dB
Tensile	1960N (Drop) 392N (Indoor)	< 0.01 dB

3.4 Laying Optical Fiber Cables in a Duct

For laying optical fiber cables in a building, we experimented with laying optical fiber cables in a duct to check the maximum number of cables that can be laid in a 25 meter long duct with a 16 mm inner diameter. We bent the duct 90 degrees with a 114 mm radius at 3 points for testing. The duct is illustrated in Fig 9 and test results are listed in Table 5. The experiment proved that the number of optical fiber cables that can be laid in a duct is greater than the number that can be laid in conventional slotted core cables.

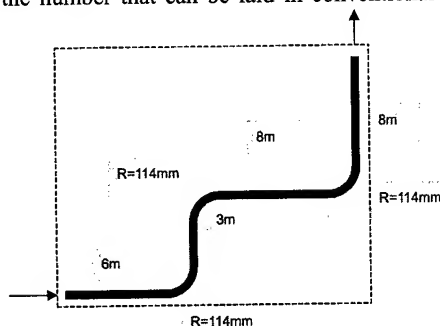


Figure 9. Duct model

Table 5. Results of duct installation tests (@1.55 μ m)

	Number of Max. Installation	Loss increase (dB)
Conventional Slotted core cable	1	0.00
8-fiber Drop (ribbon)	4	0.00
4-fiber Drop (ribbon)	4	0.00
8-fiber Indoor (ribbon)	7	0.00
4-fiber Indoor (ribbon)	7	0.00
8-fiber Indoor (unit)	6	0.00

3.5 Duct Squeezing Test

For laying optical fiber cables in a building, squeezing tests were performed loading 200N on a 16 meter long duct with a 16 mm inner diameter. The duct was bent 90 degrees with a 114 mm radius at 3 points for testing. The duct model is illustrated in Fig 10 and test results are listed in Table 6. These tests revealed that optical fiber cables have good squeezing characteristics.

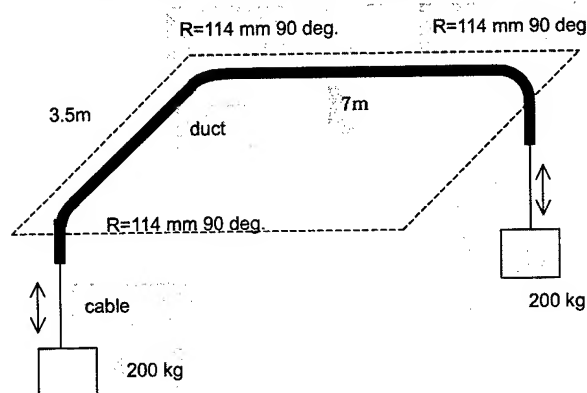


Figure 10. Duct model

Table 6. Results of duct squeezing tests (@1.55 μ m)

	Damage of sheath	Loss increase (dB)
Conventional Slotted core cable	No	0.00
8-fiber Drop (ribbon)	No	0.00
4-fiber Drop (ribbon)	No	0.00
8-fiber Indoor (ribbon)	No	0.00
4-fiber Indoor (ribbon)	No	0.00
8-fiber Indoor (unit)	No	0.00

4. Conclusions

A new small diameter and light optical fiber cable was developed for use as drop cable and distribution cable to and from multistory residences and small buildings. The features of the new type of cable are:

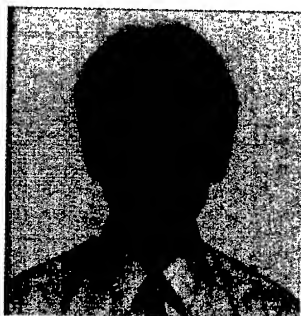
- Because this cable is small in diameter, it can be laid in narrow spaces.
- Its simple structure enables a reduction in material costs as well as processing costs, as it can be made in a single process.
- The trial cable has demonstrated good mechanical properties in many parameters.

We confirmed that the cable can be put in actual use.

5. References

- [1] R Takaoka *et al.*, "Development of Single Optical Fiber Stranded Premises Cable", *Proc. of IEICE General Conf.*, B-10-33, (1997).
- [2] Y. Mitsunaga *et al.*, "Strength Assurance of Optical Fiber Based on Screening Test", *Trans. of IECEJ*, Vol. J66-B, No. 7, 829-836 (Jul, 1983), (in Japanese).

Authors



Tetsuya Yasutomi

The Furukawa Electric
Co., Ltd.
6 Yawatakaigan-dori,
Ichihara, Chiba, Japan
tomy@ch.furukawa.co.jp

He received his M.E. degree in Metallurgy Engineering from University of Tokyo in 1998. He joined The Furukawa Electric co., ltd. in 1998 and has been engaged in research and development of optical fiber cables. He is now a research engineer of engineering dept., OPTCOM division.

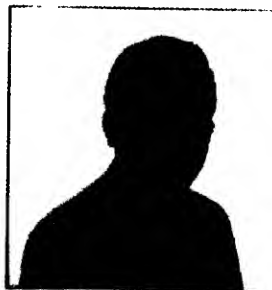


Fuminori Nakajima

The Furukawa Electric
Co., Ltd.

6 Yawatakaigan-dori,
Ichihara, Chiba, Japan
f-nakaji@ch.furukawa.co.jp

He received his M.E. degree in Material Engineering from Nagoya University of Technology in 1992. He joined The Furukawa Electric co., ltd. in 1992 and has been engaged in research and development of materials for optical fiber cables. He is now an assistant manager of engineering dept., OPTCOM division.



Masanori Hattori

The Furukawa Electric
Co., Ltd.

2-6-1 marunouchi,
Chiyoda-ku, Tokyo, Japan
hat@ho.furukawa.co.jp

He received his M.E. degree in Applied Material Science from Muroran Institute of Technology in 1991. He joined The Furukawa Electric co., ltd. in 1991 and has been engaged in research and development of optical fiber cables. He is now an assistant manager of engineering dept., OPTCOM division.



Masami Hara

The Furukawa Electric
Co., Ltd.

1-14-25 higashisakura,
Higashi-ku, Nagoya, Aichi, Japan
hara.masami@furukawa.co.jp

He received his M.E. degree in Physics from Osaka University in 1987. He joined The Furukawa Electric co., ltd. in 1987 and has been engaged in research and development of optical fiber cables. He is now a manager of engineering dept., OPTCOM division.

Development of MT Ferrule for Low-Loss 24MPO Connector

Katsuki Suematsu, Masao Shinoda, Yoshimi Ono

Fitel Photonics Laboratory, R&D Division, THE FURUKAWA ELECTRIC CO., LTD.

6, Yawata-kaigandori, Ichihara, Chiba 290-8555 Japan

+81-436-42-1725 · katsu@ch.furukawa.co.jp

Abstract

In this paper, we describe a design and characteristics of the newly developed two-dimensional array 24-fiber MT (Mechanically Transferable) ferrule. We have developed the ferrule that has higher accurate holes' position than conventional. We have evaluated characteristics of 24-fiber MPO (Multi-fiber Push-On)[1][2][3] connector utilized this ferrule by single-mode fiber with angled polish. And we have succeeded in the low-loss type [4] 24-fiber MPO connector that has more excellent optical characteristics than conventional.

Keywords

Two-dimensional array MT ferrule; MPO connector; High-density; Low-loss

1. Introduction

In recently, with the expansion of optical interconnect network, parallel optical interconnection technologies have been required in high speed and high-density data-transmission systems. In these systems, the high-density optical connecting techniques with very low insertion loss are required. Moreover easy connecting and disconnecting functions is also required. Therefore, in order to advance the optical network, the high-density, the low-loss and easy connecting techniques are necessary.

On the other hand, as the MPO connector is easy to connect-disconnect the ribbon fibers, they are widely used in communication markets. And there are some variations of fiber number up to 24-fiber in size of standard MT.

Under such recent situation, we have reported about development of 8-fiber low-loss MT ferrule and low-loss 8-fiber MPO connector in this society last year [4]. This time, we aimed higher density connection and developed two-dimensional array type 24-fiber ferrule for low-loss type 24MPO connector.

In this paper, we describe a design and characteristics of the newly developed two-dimensional array 24MT ferrule for low-loss 24MPO connector.

2. Design

2.1 Target characteristics

The target performance for low-loss 24MPO connector is established that optical performance in the insertion loss becomes less than 0.5dB in random mating. However, it is difficult to achieve

high performance connector only by ferrule design. Therefore, we used the high accurate fiber (diameter is 0.125 ± 0.00025 mm, core concentricity error is less than 0.25 μ m) and the definite accurate alignment pin (0.6985 ± 0.0001 mm), and evaluated the low-loss 24MPO connector.

2.2 Structure of 24MPO connector

As shown in figure 1, low-loss 24MPO connector is designed on the basis of MPO connector according to IEC 1754-7 type connector for optical fiber ribbons. 24MPO connector accommodates one 24MT ferrule, which has two alignment holes and 24 fiber holes. An end-face of connector is angle polished at 8-degrees with protrusion of fibers. An angled end face of optical fiber prevents light's reflection, so return loss of connector get better. And fiber protrusion enables physical contacts between fibers. Therefore, it's possible to be low insertion loss connections without index matching material.

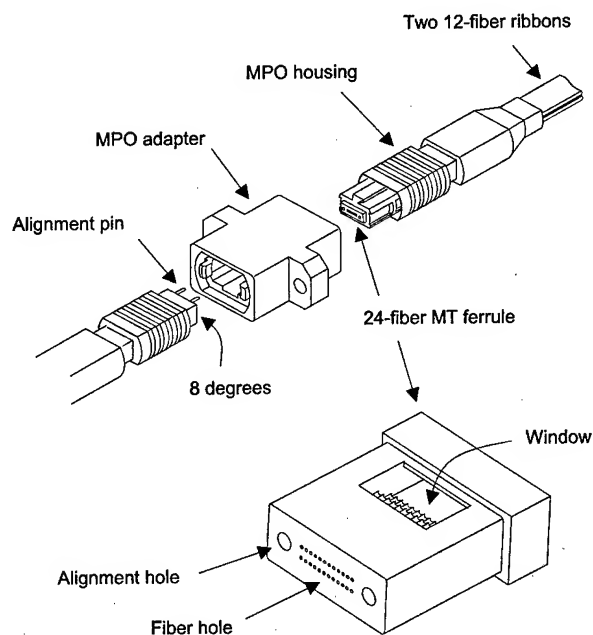


Figure 1. 24MPO Connector, 24MT Ferrule

For high-density connection and utilizing the standard MPO housing, outer dimension of 24-fiber MT ferrule is the same as standard MT ferrule. As shown in figure 2, it's 2.5mm in height and

6.4mm in width on the end-face of MT ferrule. Fiber-holes of 24MT are located in 12 columns by 2 rows, 0.25mm pitch between columns and 0.5mm pitch between rows.

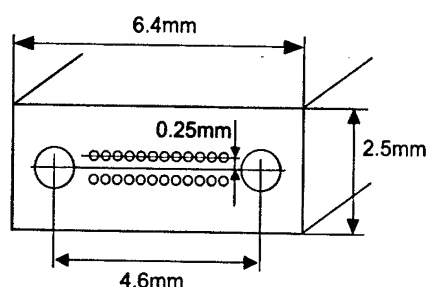


Figure 2. End-face of 24MT Ferrule

2.3 Cause of connector insertion loss

In general, the main cause of connector insertion loss is the position error of fiber core. Here, we quote from a citation paper [4] that is reported last year, and in order to make explanation intelligible, a figure of 8MT is used.

Insertion loss L is caused by the position error of fiber core defined as following equation.

$$L = 4.34 (R / w)^2 \text{ [dB]} \quad [5]$$

R [μm] is position error between each fiber core and w [μm] is mode field radius. And this R happens by following matters:

- 1) Clearance between alignment pins and alignment holes of MT ferrule (E1 in Figure 3)
- 2) Clearance between fibers and fiber holes of MT ferrule (E2 in Figure 3)
- 3) Fiber hole position error (E3 in Figure 3)
- 4) Fiber hole tilt against alignment hole (E4 in Figure 4)
- 5) Bend caused by shrinking the adhesive resin (E5 in Figure 5)

To achieve low insertion loss, we improved the precision of mold pins and V-groove molds to reduce the value of E1, E2, and E3. And we changed the ferrule's window size to reduce the value of E5.

In addition, because of clearance between alignment pins and alignment holes of MT ferrule, two angled MT ferrules are slipped when they are mated each other. This causes position error for center of mated MT ferrules as shown in figure 6.

Therefore, in order to design the MT ferrule for low-loss MPO connector, it is necessary to control the position of fiber holes more closely and to consider these causes against y-offset

$$\text{y-offset} = E1/2 + E4 + E5$$

We have investigated these values minutely and determined y-offset value.

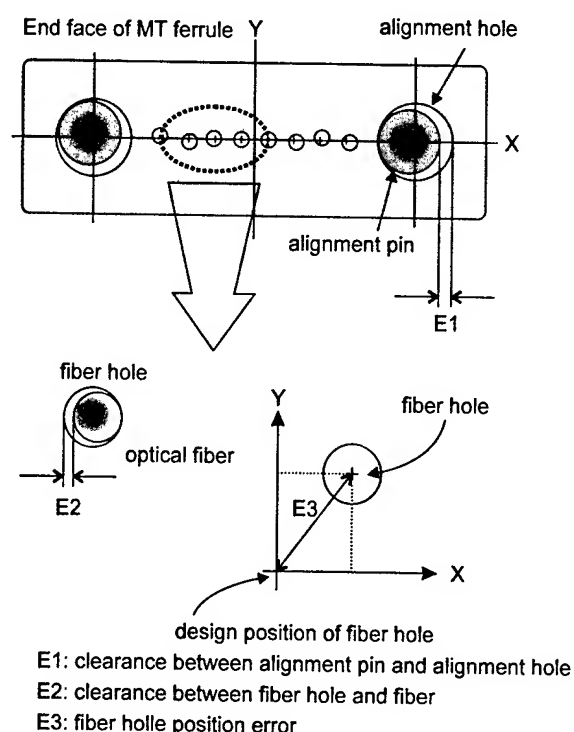


Figure 3. Causes of position error of fiber core

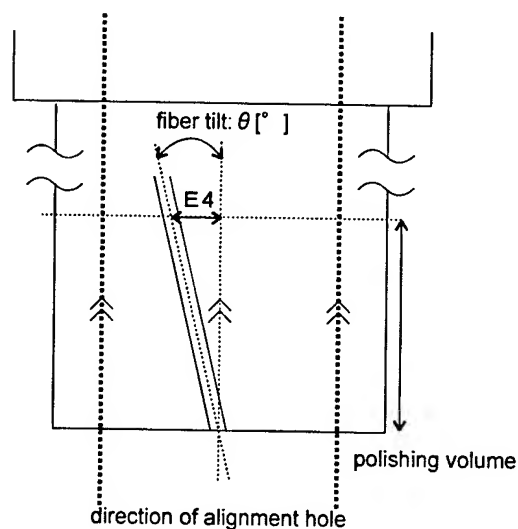


Figure 4. Fiber hole tilt

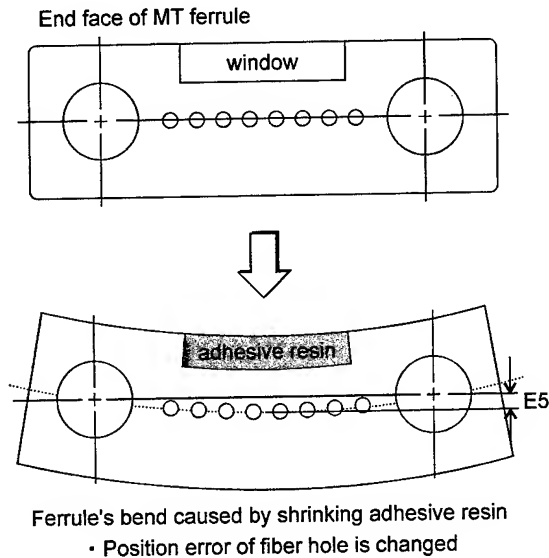


Figure 5. Bend by curing adhesive resin

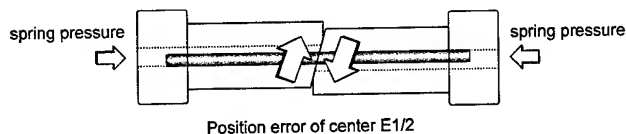


Figure 6. Position error by slipping

2.4 Difference between 8MT and 24MT ferrule

This time we applied the technology mentioned above of the low-loss 8MT ferrule for the 24MT ferrule. And moreover, we investigated realization of higher accurate ferrule. Two-dimensional array 24MT ferrule has two rows. So we improved the specific points of this 24MT ferrule as follows.

- 1) Improvement of fiber hole parallelism accuracy more than that of one row MT ferrule

As shown figure 7, when two-dimensional MT (24MT:two row) ferrules are angled (8-degree) polished, lower fiber hole position is more polished in depth than the fiber hole of one row MT ferrule. So fiber holes of the 24MT ferrule have to be improved parallelism accuracy more than one row MT ferrule.

- 2) Parallel arrangement of the upper and lower fiber holes

We improved accuracy of the distance between upper and lower fiber holes from the ferrule end-face to in depth of the ferrule.

- 3) Parallel arrangement of fiber holes and alignment holes

We improved accuracy of the distance between two alignment holes and fibers holes.

Figure 8 shows improvement of item 2), 3).

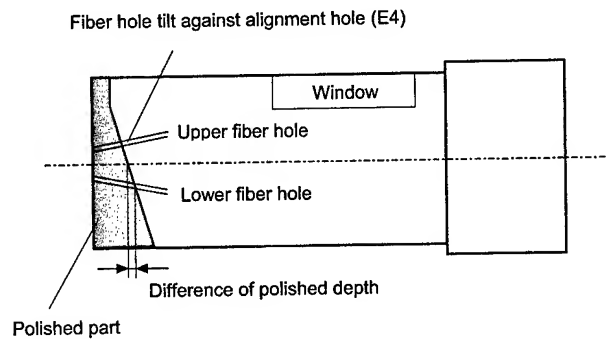


Figure 7. Polished 24MT ferrule

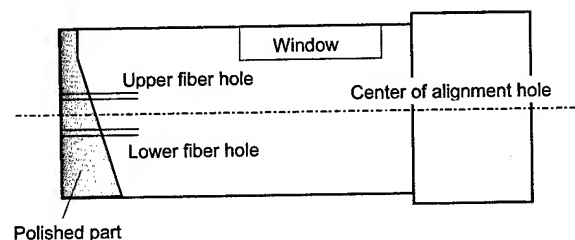


Figure 8. Parallel arrangement hole

2.5 Improvement of Metal Mold

In order to decrease the fiber holes tilt against alignment holes, we have improved metal mold of the 24MT ferrule. Figure 9 shows the structure of the 24MT ferrule. In the conventional metal mold, accurate alignment of pins was done at only end-face of ferrule. But this time, in order to make each holes parallel more accurately, the forming pins were aligned with the pin holder, and the pin holder was aligned with the cavity parts.

In the conventional structure we had another problem of holes' accuracy. As shown in figure 10, the fiber holes were located as an upper-and-lower interval might become narrow in the center at the inside of ferrule. We presumed that this depended on which resin flows. In general, as shown in figure 10, MT ferrule has fiber guide holes linking with fiber holes. In the conventional ferrule, diameter of fiber guide is the same as fiber columns pitch, so resin is not easy to be flowed into space between upper pins and lower pins during molding. Therefore the pins are pressed by resin from outside and bent.

In order to solve this problem, we have built a new structure fiber guide holes and pins as shown in figure 11. The fiber guide holes diameter is changed to less than fiber hole pitch, so resin is easy to be flowed in space between upper pins and lower pins through the gap between pins in row.

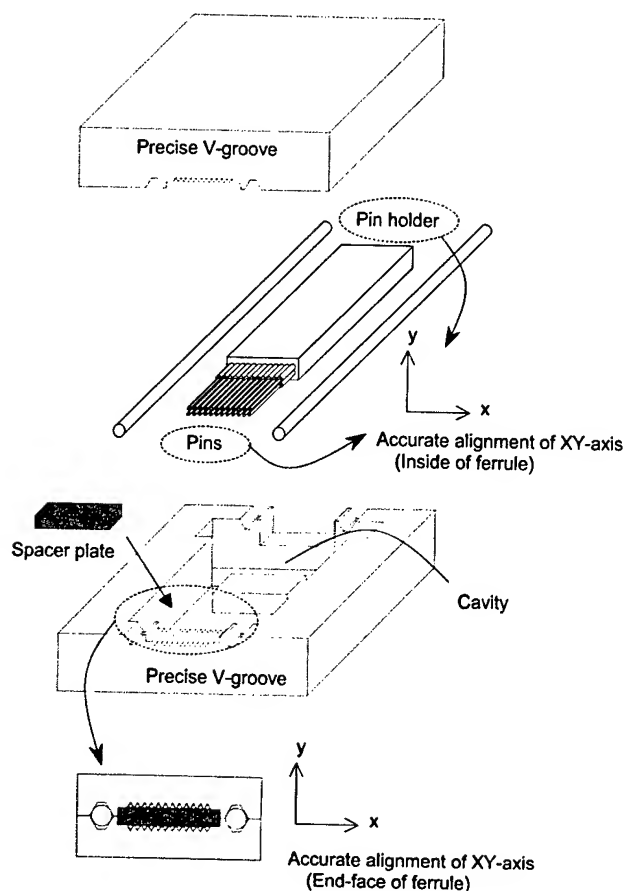


Figure 9. Structure of metal mold

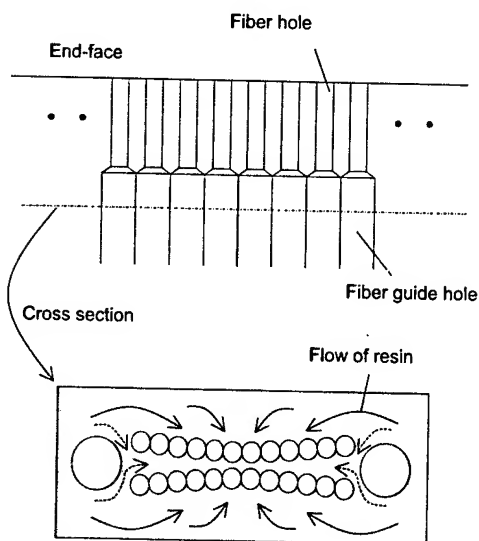


Figure 10. Conventional pins

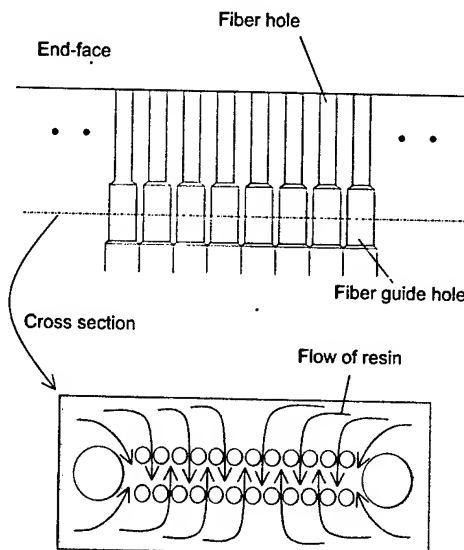


Figure 11. Improved pins

2.6 Molding

MT ferrule for low-loss MPO connector is manufactured by high-accuracy transfer molding technique. Figure 12 shows the transfer molding operations. First, the clamping device of the molding machine works to clamp tightly the mold. Second, the molding resin in tablet form pre-heated at high frequency is charged into the pot (see (1)). In (2), the plunger is inserted into the pot and presses the resin and then the cavity section is filled. After being pressed and heated for a certain time, the mold is opened, and the molded product is ejected from the cavity as shown in (3).

In the case of thermosetting plastics, because the curing temperature of the resin is very important factor to consider the characteristics of the molded product, we have optimized some molding conditions that include temperature of a mold, heating time and molding pressure. And we improved some parts of the mold to reduce the bend caused by shrinking the adhesive resin and fiber hole tilt.

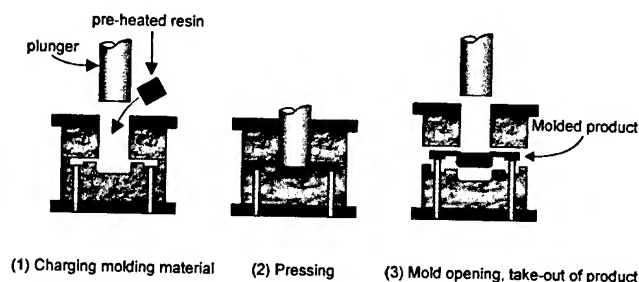


Figure 12. Transfer mold process

3. Characteristics

3.1 Position error of fiber holes

Since we improved the fiber holes tilt against alignment holes, we evaluated fiber hole position error (E3, E4) on both the end-face of ferrule and the inside of ferrule. Figures 13,14 show the results of position error measurement for conventional 24MT ferrule and low-loss 24MT ferrule. When position error is evaluated on the inside of ferrule, polishing value is 400 μ m which may be ground at assembling connector.

As the results show, average and deviation of the position error for low-loss 24MT ferrule are obviously much less than that of conventional one.

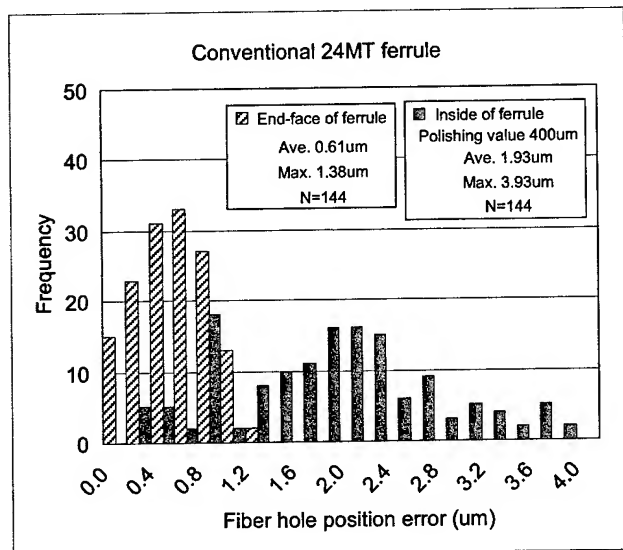


Figure 13. Distribution of Fiber hole position error of Conventional 24MT ferrule

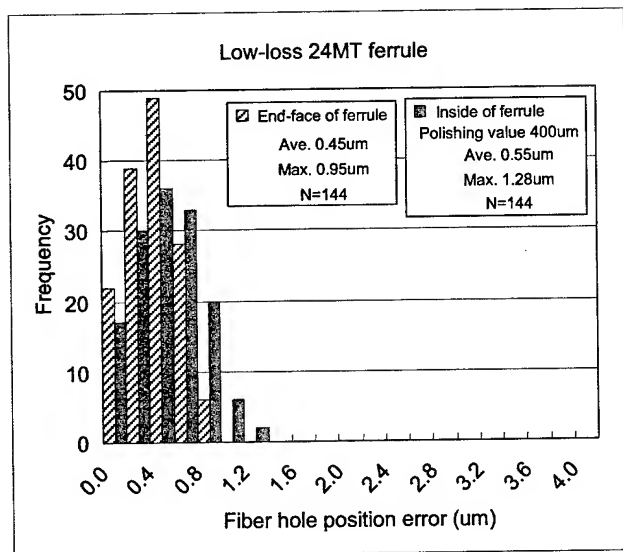


Figure 14. Distribution of Fiber hole position error of Low-loss 24MT ferrule

3.2 Optical characteristics

We have evaluated the insertion loss of low-loss 24MPO connectors with 1,310nm light source. To evaluate more precisely, we used the single mode optical fiber whose diameter is 0.125 \pm 0.00025 mm and core concentricity is 0.25 μ m or less and alignment pins whose diameter is 0.6985 \pm 0.0001mm. Figures 15,16 show the insertion loss of conventional 24MPO connector and low-loss 24MPO connectors. Newly developed low-loss 24MT ferrule were satisfied our target value of 0.5dB or less in random mating.

As the results show, the insertion loss for low-loss 24MPO connectors is obviously much less than that of conventional 24MPO connectors.

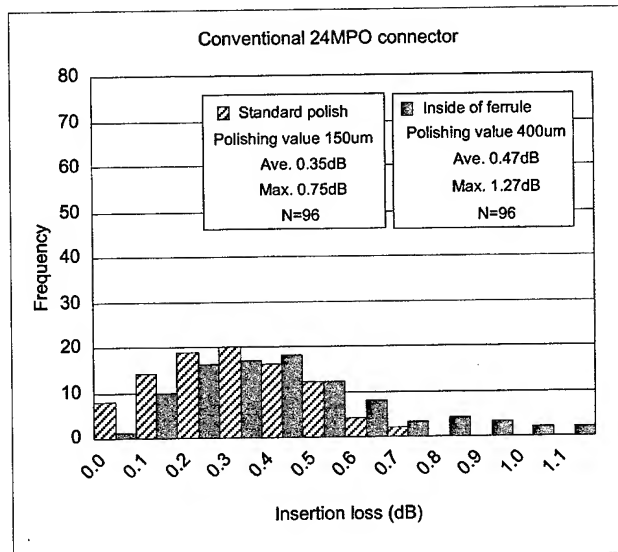


Figure 15. Distribution of Conventional 24MPO connector

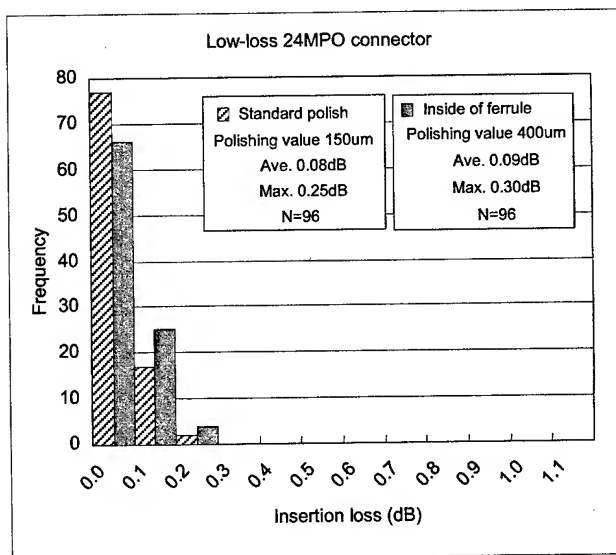


Figure 16. Distribution of Low-loss 24MPO connector

3.3 Reliability Test

We evaluated environmental and mechanical performance for low-loss 24MPO connectors. Reliability test results have been reported in our paper [4] of conventional 24MPO connector. Equally, sufficient characteristics are obtained as shown in table 1.

Table 1. Reliability test results

Item	Test condition	Loss change
Thermal cycle	-40~85deg.·8h/cycle· 14day	≤0.2dB
Humidity	+65deg.·95%·14day	≤0.2dB
Vibration	10~55Hz 2h	≤0.2dB
Straight pull	2.2N·5sec	≤0.3dB
Durability	200times	≤0.3dB

4. Conclusions

We have succeeded in developing higher accurate two-dimensional 24-fiber MT ferrule for the high-density low-loss MPO connectors. We have improved molding technique and obtained the excellent ferrule that has highly accurate parallel fiber holes against the alignment holes. Then, these low-loss 24MPO connectors utilized this ferrule proved to have low-insertion-loss characteristics less than 0.3dB. And we also obtained good reliability.

5. References

- [1] Nagasawa, Yokoyama, Ashiya, and Satake, "A High-Performance Single-Mode Multifiber Connector Using Oblique and Direct Contact Between Multiple Fibers Arranged in Plastic Ferrule", IEEE Photon. Techno. Lett., Vol.3, No.10, pp.937-939, 1991.
- [2] Shimoji, "MPO Optical Backplane Connector", IEICE Trans. Commun., Vol.E-80B, No.4, pp.535-539, 1997.
- [3] Suematsu, Shimoji, Iijima, and Hirao, "Development of Two-Dimensional Array 24-Fiber MPO Connector", Euro Cable, IOS Press, AKM, pp.278-285, 2000.
- [4] Tsukamoto, Hirao, Yamakawa, and Kamiko, "Low-loss MPO Connector", IWCS Proceedings of 50th, pp.379-383, 2001.
- [5] JIS C5962 p.19.

Authors



Katsuki Suematsu

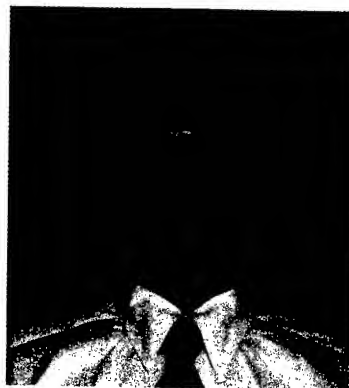
The Furukawa Electric Co.,
Ltd.

6 Yawatakaigan-dori,
Ichihara, Chiba, 290-8555
Japan

katsu@ch.furukawa.co.jp

Katsuki Suematsu was born
in Saitama, Japan, in 1970.

He received the B. E. degree in applied electric engineering from Waseda University, Japan in 1993. He joined the Furukawa Electric Company, in 1993 and has been engaged in manufacturing and assembling optical fiber connector components. He is now a research engineer of Photonics laboratory



Masao Shinoda

The Furukawa Electric Co.,
Ltd.

6 Yawatakaigan-dori,
Ichihara, Chiba, 290-8555
Japan

shinoda@ch.furukawa.co.jp

Masao Shinoda was born in
Chiba, Japan, in 1974. He

received the B. E. degree in applied electronic engineering from Shibaura Institute of Technology, Tokyo, Japan, in 1998. He joined the Furukawa Electric Company, in 1998. Since then he has been engaged in R&D on optical component.



Yoshimi Ono

The Furukawa Electric Co.,
Ltd.

6 Yawatakaigan-dori,
Ichihara, Chiba, 290-8555
Japan

y-ono@ch.furukawa.co.jp

Yoshimi Ono was born in
Chiba, Japan, in 1970. He
received the M.E. degree in applied mechanical engineering from Aoyama Gakuin University, Tokyo, Japan, in 1995. He joined the Furukawa Electric Company, in 1995.

Fiber Optic/Carbon Nanotube Skin Friction Sensing Device

Alexander K. Sang*, Michael F. Gunther*, Dr. Paige Stevenson*, David L. Carnahan**

*Luna Innovations Incorporated
2851 Commerce St.
Blacksburg, VA 24060
540-552-5128
sanga@lunainnovations.com

**NanoLab, Inc.
PO Box 615
Watertown, MA 02172
617-787-9822
dcarnahan@nano-lab.com

Abstract

This work establishes the feasibility of producing a nanotube/fiber optic-based device for measuring aerodynamic flow parameters for use in advanced aeronautic systems and machine design. The utilization of the special electronic properties of carbon nanotubes in combination with fiber optic sensor technology offers a unique means to measure skin friction to unprecedented resolution and accuracy. These measurements provide important insight into validating new aircraft design and evaluating performance shortfalls on existing aircraft. Current methods of directly and accurately measuring skin friction in airflows do not allow for point measurements. Most techniques are indirect and rely on relatively cumbersome methods of inferring shear loads from other measurements. The capability to directly measure skin friction is of significant immediate interest to aeronautical researchers and wind tunnel technicians.

Keywords

Fiber optics; Nanotube; Skin friction; Fabry-Perot; Aeronautics; Shear stress

1. Introduction

The accurate measurement of wall shear stress is important from several points of view. This information provides key input to understanding the basic fluid physics involved. The local skin friction (or wall shear) plays a central role in the correlation of all turbulent boundary layer flows. Skin friction data is critical to assessing the performance of the device by determining drag, transition, and any local regions of flow separation. Knowledge of wall property variations provides feedback to the design engineer leading to improvements in the design of the device itself for increased performance and efficiency. Providing single point measurements of skin friction and temperature in one combined sensor represents a significant step in the instrumentation for future aircraft design.

The development of an ultra-small (~130 – 250 micron) skin-friction/temperature sensing device, which combines leading-edge carbon nanotube and fiber-optic technologies, enables sensors smaller than ever before possible that will accurately measure wall properties. The mechanical model illustrates the flow field will cause substantial deflection of the nanotubes, and an electromagnetic model demonstrates that the nanotubes will interact with the evanescent field immediately outside an air-glass interface to produce a phase shift in the E-M wave when the nanotubes are deflected. The ability to directly measure viscosity in air and liquid flows would be of great benefit in the chemical, refining, and material processing industries. Fiber optic sensor technology is improving

measurement instrumentation by providing robust, small size, lightweight, highly reliable and multiplexed devices that are immune to electromagnetic interference (EMI).

2. Fiber Optic Sensing

The transducing mechanism used by the presented prototype sensors is based on the extrinsic Fabry-Perot interferometer (EFPI). EFPI-based sensors use a distance measurement technique based on the formation of a low-finesse Fabry-Perot cavity between the polished end face of a fiber and a reflective surface, shown schematically in Figure 1. Light is passed through the fiber, where a portion of the light is reflected off the fiber/air interface (R_1). The remaining light propagates through the air gap between the fiber and the reflective surface and is reflected back into the fiber (R_2). These two light waves interfere constructively or destructively based on the path length difference traversed by each. The interaction between the two light waves in the Fabry-Perot cavity is *modulated* by the path length. The resulting light signal then travels back through the fiber to a detector where the signal is *demodulated* to produce a distance measurement. Several different demodulation methods exist to convert the return signal into a distance measurement.

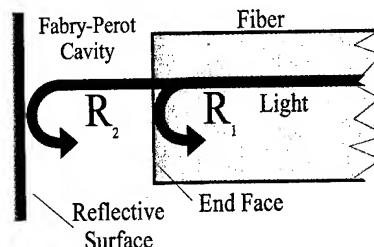


Figure 1. Extrinsic Fabry-Perot interferometer concept.

3. Nanotube Preparation and Purification

Some nanotubes were produced at Luna Innovations, and others were purchased from commercial suppliers. Luna utilized the carbon-arc technique, shown in Figure 2, to prepare a batch series of nanotubes, varying several reaction parameters such as catalyst identity, concentration, current, and voltage to increase the yield of carbon nanotubes. From run-to-run, the appearance and density of the soot varied considerably, ranging from large flaky particles to fine granular soot. From our experience the texture of the soot can be a qualitative measure of nanotube formation. Best nanotube formation was achieved at higher pressures with Ni-Y as catalyst. Nanotubes produced in this way have the same characteristics as those produced by laser-ablation techniques with Co-Ni as catalyst.

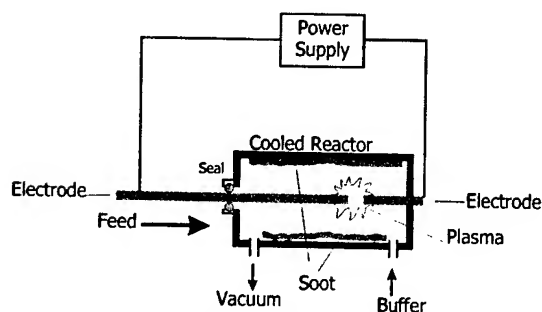


Figure 2. A typical Kratschmer-Huffman generator.

The higher pressures are believed to help the formation of single-walled carbon nanotubes [1,2]. Separation of the nanotubes from the remaining non-tube carbon and catalyst particles was accomplished through published acid-digestion methods[3].

3.1 Nanotube functionalization

Processed nanotubes were successfully functionalized with thiol-groups and attached to gold surfaces. Processed nanotubes from acid-digestion procedures (possessing residual carboxylic acid groups) were functionalized and attached to gold surfaces according to Figure 3. Gold surfaces were prepared by thermally evaporating gold on a silicon substrate to several precise depths.

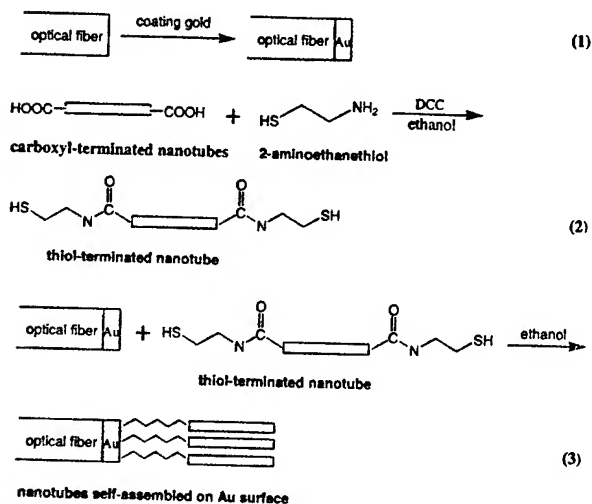


Figure 3. Procedure for nanotube functionalization and attachment to gold surface.

By varying several parameters—catalyst identity, concentration, and pressure, etc.—we were able to increase the yield of bundles of single-walled carbon nanotubes produced via the arc-discharge process. SEM images indicate most favorable nanotube formation at higher pressures (1000 torr) with Ni-Yi as catalyst. We were able to purify and process these nanotube samples via published techniques to give carboxylic-acid terminated nanotubes suitable for further functionalization. These processed nanotubes were thiol-

derivatized and attached to surfaces by self-assembled processes

An alternate mode of nanotube attachment to fiber for nanotube arrays was also investigated. Highly ordered nanotube arrays can be grown on various substrates: silicon, molybdenum, and glass. A nanotube array was grown on a 30-micron silicon wafer, consisting of a forest of individual multi-walled nanotubes approximately 20 nm in diameter, 5 microns in length, and an average spacing between two nanotubes of 20-50 nm. An SEM image of a nanotube array is shown in Figure 4.

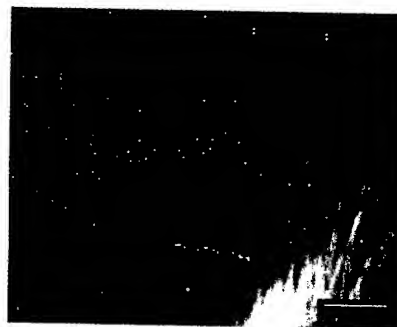


Figure 4. Ordered nanotube array courtesy of Nano-Lab.

The nanotube-substrate bond is strong, as shown by the nanotube array's ability to withstand prolonged sonication times. This mode of attachment ensures that the nanotubes will survive vigorous environmental conditions. The silicon wafer would be directly attached to the end of the optical fiber, or the nanotubes could be grown directly on the optical fiber sensor surface.

Although the sensors prepared using the proven gold-coupling chemistry may find alternate applications, nanotube arrays were determined to provide the best source of nanotubes for the demanding conditions governing this investigation. The move from the gold-coupling chemistry was made for several reasons: (1) the thiol-gold bond is a labile physical bond, strongly influenced by environmental conditions, (2) in the self-assembly process, there is no way to experimentally control the surface area coverage, and (3) the nanotubes have a broad length distribution, the acid-digestion procedures used for nanotube functionalization could not provide sufficiently uniform lengths.

Nanotube arrays are highly ordered nanotubes grown in the CVD process on a substrate sputtered by catalyst particles. The nanotubes contained in the array have very controlled aspect ratios—nanotube length, diameter, and spacing between tubes—and are suitable for device fabrication and testing. The nanotube arrays can be mounted to the ends of the fibers or grown directly on the fiber tips in a bulk process, creating the most efficient and economical sensor possible.

3.2 Modeling of nanotubes

The propagation of electromagnetic waves in aligned carbon nanotube structures was investigated. The carbon nanotubes chosen for the initial model are those supplied in the purchased nanotube array. These tubes are highly conductive along the direction of the tubes and have an outer diameter of about 20 nanometers and lengths of up to 5 microns. The average spacing between neighboring tubes is approximately 20 to 50 nanometers. A medium loaded with such nanotubes is modeled as a region with anisotropic conductivity. First, propagation of uniform plane waves in an infinite medium with anisotropic conductivity was investigated. Two limiting cases are considered; (1) perpendicular polarization for which the electric field vector is normal to the direction of the tubes, and (2) parallel polarization where the electric field is aligned with the tubes. The latter case, in which the anisotropic behavior of nanotubes influences the propagation properties significantly, is of more practical interest and will be addressed in greater detail.

The reflection of a plane-wave from the boundary between a nanotube-loaded region and a homogeneous and isotropic medium was modeled. The tubes are assumed to have an arbitrary direction, making an angle with the direction of propagation of the incident wave. This situation may be realized by subjecting the nanotubes to an external disturbance that would cause bending of the tubes. The results from numerical modeling predict that measurable changes in phase angle and magnitude of the reflection coefficient occur due to bending of nanotubes.

Alternatively, using the model equations information on the phase and magnitude of the reflection coefficient may be used to obtain a measure of the bend angle and in turn quantify the external disturbance that has caused the bending of nanotubes.

3.3 Sensor testing

To demonstrate feasibility of the sensors, we performed laboratory scale tests, which mimic device response, and performed an extensive modeling study to evaluate nanotube deformation in real-flow environments. This modeling analysis, never before attempted with nanotube-containing systems, represents a significant contribution to the knowledge base of nanotube properties.

3.3.1 Optical Test Results. A method was designed to demonstrate the effect of the nanotubes in the electromagnetic field of a fiber surface. Figure 5 shows a schematic diagram of the test arrangement. Light from a diode laser at a wavelength of 850 nm was directed into a singlemode optical fiber, which had been polished to a 45-degree angle on the remote end. An air gap was present immediately outside the 45-degree surface, establishing a total internal reflection condition so that the beam was reflected through 90 degrees, as shown in the figure. This reflected beam then propagates to the edge of the fiber, where a second air-glass interface created a reflected beam that propagates back toward the 45 degree angled surface, where it is reflected once more through 90 degrees and travels backwards through the fiber (2). At the 45-degree surface, a

small amount of light is scattered and guided backward through the fiber, establishing a second reflection and therefore a Fabry-Perot interferometer (1). The two optical reflected beams, (1) and (2), are combined where they interfere, creating the Fabry-Perot interference pattern.

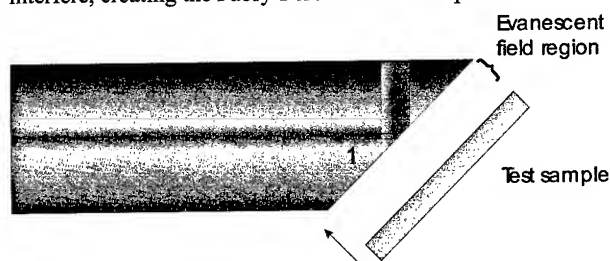


Figure 5. Test set up for evaluation of nanotube effects on optical signal.

Since there is no optical coating on the 45-degree polished surface, the phase and amplitude of the reflected beams may be influenced by introducing other materials into the evanescent field region, immediately outside the angled surface. The evanescent field will have an exponentially decaying nature, and will exist for all practical purposes only a micron or two away from the surface. This is the region where the interaction will take place. Introduction of a nanotube sample into the evanescent field would show a phase shift in the two reflected optical beams. Since beam (2) sees the 45 degree surface twice, while beam (1) sees it only once, the relative phases of the two beams will be altered by the presence of the nanotubes, appearing as a change in the Fabry-Perot fringe pattern in the signal conditioning unit.

3.3.2 Nanotube deflection. This skin friction-measuring device must be useful in varying shear environments. A simple design model was chosen for initial calculations and based principally on the deflection of nano-tubes 5 microns tall. The deflection of the nanotubes causes a change in the electromagnetic environment at the reflecting surface that correlates to the shear environment experienced by the nanotubes. Nanotube dimensions for this study are described in Figure 6.

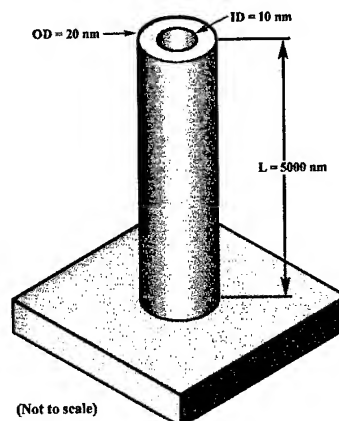


Figure 6. A singular nanotube.

A numerical flow study around a single nanotube was performed to determine the nature and magnitude of the

pressure and shear forces expected. Flow characteristics typical of subsonic flight, air at room temperature and pressure at a velocity of 300 ft/s in a 1/2 inch turbulent boundary layer, were used. The velocity profile of a boundary layer is illustrated schematically in Figure 7. In this study, the boundary layer was 2,540 times the length of the nanotube, placing the nanotube in a region within the turbulent boundary layer known as the laminar sub-layer (See Figure 8). The laminar sublayer is still 7 times the nanotube length.

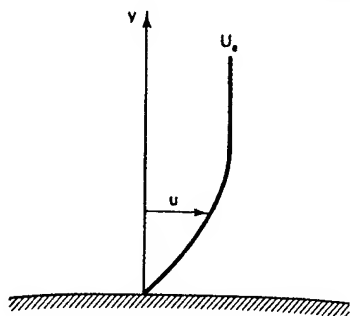


Figure 7. Boundary Layer Velocity Profile.

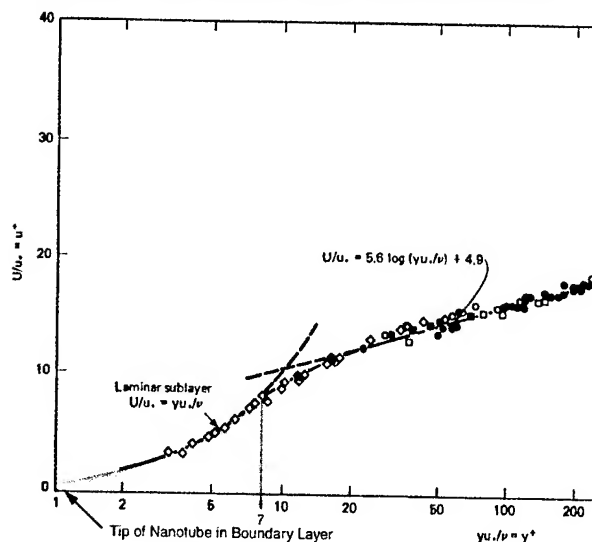


Figure 8. Universal wall plot for turbulent boundary layers on smooth, solid surfaces [4].

In order to properly capture the flow field, the defined domain included the entire laminar sublayer. The domain parameters were non-dimensionalized using the edge velocity of the laminar sub-layer, the nanotube diameter and density at standard temperature and pressure. Analyses were performed using ANSYS, a commercial, finite element/computational fluid dynamics code. A total of 12,000 elements were used to characterize the region with a greater element density concentrated around the nanotube. Figure 9 and Figure 10 are vector plots of the velocity field resulting from this study.

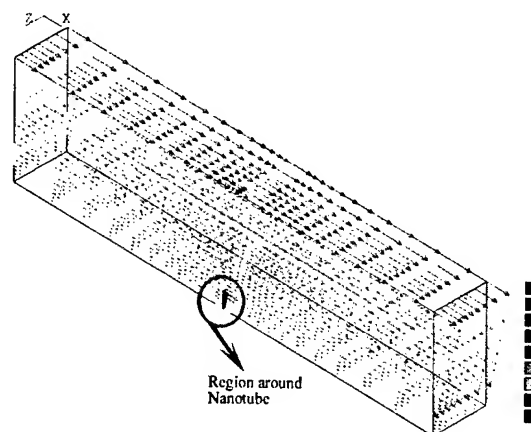


Figure 9. Velocity profile in the domain of study.

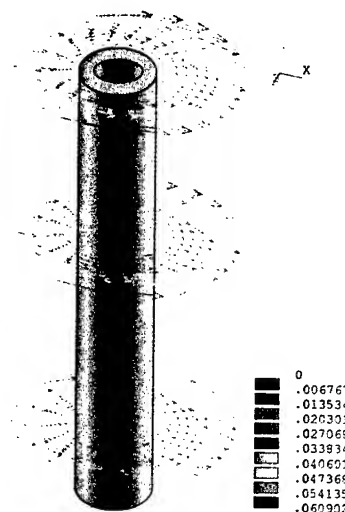


Figure 10. Close-up of the velocity profile around the nanotube.

4. Conclusions

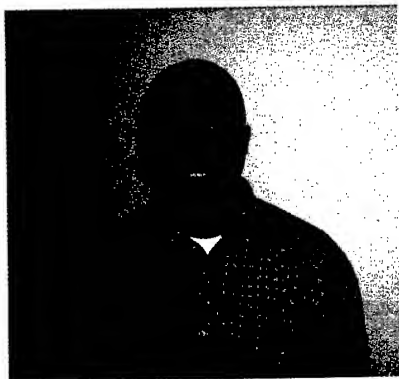
For preliminary analysis, the shear and pressure forces on the nanotube were integrated, and applied to the structure using Euler-Bernoulli beam theory to determine the corresponding deflection of the nanotube. In all cases, significant deflection resulted. Future studies will investigate flow in a structured array of nanotubes under similar flow conditions. This will allow for the reduction in drag in the interior nanotubes due to blockage. A large-strain theory will be used to determine tube deflection.

5. Acknowledgments

Special thanks to NASA LaRC, Contract# NAS1-02063 for funding this work. And Drs. Steve Stevenson and Joseph Schetz are acknowledged for their assistance.

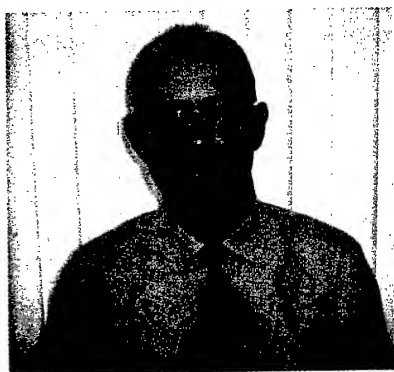
6. References

- [1] Shi, Z.; Lian, Y.; Liao, F.H.; Zhou, X.; Gu, Z.; Zhang, Y.; Iijima, S.; Li, H.; Yue, K.T.; Zhang, S-L. *Journal of Physics and Chemistry of Solids*. **2000**, *61*, 1031-1036.
- [2] Shi, Z.; Lian, Y.; Zhou, X.; Gu, Z. Production of single-walled carbon nanotubes at high pressure. *J.Phys. Chem. B*. **1999**, *103*, 8698-8701.
- [3] Liu et al, Fullerene Pipes. *Science* **1998**, *280*, 1253-1256.
- [4] Schetz, J., *Boundary Layer Analysis*, Prentice Hall, Englewood Cliffs, NJ, pp. 7, 205-212, 1993



Alexander K. Sang

Luna Innovations, 2851 Commerce St., Blacksburg, VA 24060
Alex joined Luna Innovations in 2001 from the Virginia Tech Aerospace Department where he spent the previous year working as a Research Associate. He has a BS and MS in Aerospace Engineering from Virginia Tech. He is a Research Engineer in the Physical Sensors Group.



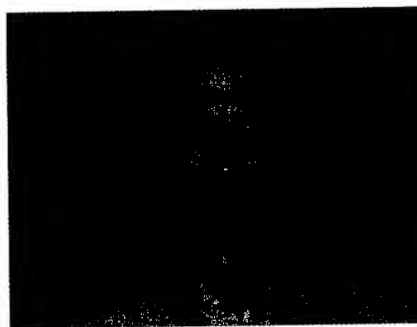
Michael F. Gunther

Luna Innovations, 2851 Commerce St., Blacksburg, VA 24060
Mike Gunther has more than 20 years experience in materials research systems engineering and sensor instrumentation development. As co-founder of Luna Innovations and Director of the Physical Sensor Group, he has been involved in numerous research programs. He is a co-inventor of the EFPI sensor and has authored and co-authored numerous papers in the field of fiber sensing and is named on several other patents.



Dr. Paige Stevenson

Luna Innovations, 2851 Commerce St., Blacksburg, VA 24060
Paige joined Luna in 1999 from Virginia Tech, where she obtained her Organic Chemistry Ph.D. in 1998. While at VT, Paige developed a strong background in polymer/ organic synthesis, kinetics, and mechanistic studies, using electrochemical and photochemical techniques. Currently she is exploring the chemical reactivity and functionalization of TNT metallofullerenes and nanotubes.



David L. Carnahan

NanoLab, Inc., PO Box 615, Watertown, MA 02172
David Carnahan received his BS and MS in Ceramics Engineering from Alfred University. His strength is in the processing and product development of advanced materials, including piezoelectrics, superconductors, composites, and carbon nanotubes. He co-founded NanoLab in Jan. 2000, to develop carbon nanotube products and devices.

Fiber Bragg Grating Sensors for Detection of Acoustic Wave Emission and Seismic Activities

Y. Zhang, R. Pastor^a, J. Ju, and H.L. Cui

^aDepartment of Physics & Engineering Physics, Stevens Institute of Technology
Hoboken, NJ 07030

+1-201-216-5637 ? hcu@stevens-tech.edu

^bU.S. Army CECOM-RDEC, Fort Monmouth, NJ 07703

Abstract

A systematic study of acoustic emission detection and seismic activity sensing using fiber Bragg grating sensors has been carried out recently in our laboratory. In this, we attempt to use the fiber Bragg grating to sense the dynamic strain created by a passing ultrasonic wave signal. Our goal here is to see if such a sensor is possible, and if so, what the detection sensitivity and limitations will be. To answer these questions, we carried out several experiments involving the detection of simulated acoustic emission events. In the first experiment, we attach fiber Bragg grating to the surface of a piezoceramic resonator which is driven by a signal generator. We were able to detect the resulting surface vibration of the resonator up to 2.1 MHz. In the second experiment, we attach a fiber Bragg grating to the surface of an aluminum plate. We excite an acoustic wave using an ultrasonic transducer located at various positions of the aluminum plate. In this way, we demonstrated that the fiber Bragg grating sensor is capable of picking up the signal coming from a distance (up to 30 cm) for up to 2.5 MHz. In a third experiment, we use the same fiber Bragg grating on aluminum plate set up, but set up an acoustic signal by either a gentle knock on the plate by a pin, or by breaking a pencil lead on the plate. We were able to detect acoustic emission set up by pencil lead breaking up to a frequency of 100 kHz. Higher frequency components were not detected mainly due to the limitations of the available electronic equipment at this time (high frequency bandpass filters and amplifiers). In yet another experiment we use the fiber Bragg grating to detect low-frequency seismic activities set up by vehicular traffic. In all the above-mentioned experiments we use a matching Bragg grating to demodulate the detected optical signal and use a dual channel scheme for electronic data acquisition and processing (a signal channel and a reference channel). Our experimental results have shown great promise of the fiber Bragg grating as a highly sensitive and accurate detector of vibrations of high and low frequencies. Furthermore, with WDM technology, multiple sensors can be deployed with little or no complication or new requirement.

Keywords Fiber Bragg grating; Acoustic Wave Emission; Structural Health Monitoring; Seismic Activity Monitoring.

1. Introduction

We have recently embarked on an experimental program of using optical fiber Bragg gratings to detect acoustic emission (AE) signals. As is well-

known, when cracks initiate and develop in a structure due to fatigue and loading⁴, there are always associated bursts of acoustic energy in the form of ultrasonic waves emanating from the cracks and propagating through the structure. Thus, detection of AE signals can give early indication and warning of structural failure. To date, most AE detection apparatus are based on application of ultrasonic transducers, which is not easily integrated into the structure itself for *in situ* detection and monitoring. On the other hand, fiber Bragg gratings are easily embedded in the structure without affecting the structural integrity of the structure itself, or surface-mounted nonintrusively. Furthermore, fiber gratings are ideal for multiple-sensor applications as many of these gratings can be employed either in series or in parallel. In this aspect, many of the multiplexing technologies developed in the telecommunication industry can be directly applied. These include time division multiplexing and wavelength division multiplexing. Thus, it is reasonable to envision in the near future of embedding hundreds of fiber Bragg gratings on an airplane wing to continuously monitor the structural integrity of the wing in flight. To be sure, there is a multitude of technical challenges that must be overcome to make this a reality. First, the detection sensitivity must be very high. This is especially important since AE events are usually buried in a noisy environment, which is especially true in aerospace applications. Secondly, detection speed must be high enough to capture instantaneously most of the frequency contents of an AE signal. Thirdly, one must develop a sophisticated computer-based real-time

data acquisition, processing, and analysis system in order for the AE sensors to be truly effective. These challenges must be overcome through systematic experimentation in conjunction with simulation and modeling. In this report, we present our recent work in trying to answer some of the questions and overcome some of the obstacles on the road to fiber Bragg grating based AE detection⁵.

2. Principle of Detection

Our detection system is based on a sensor/demodulator grating pair with the demodulator grating being mechanically tunable. Both gratings have nominally the same center wavelength (1300 nm) under unloaded conditions. Here, we take advantage of the sharp spectral mismatch of the two narrow-band gratings with identical spectral widths (with full width at half maximum being 0.3 nm.) Our optical signal processing scheme (see Figure 1) is designed for very fast dynamic strain signals (up to a few MHz) and very small amplitude (approaching a fraction of 1 μ strain).

Light from a broadband light source (a SLED from OptoSpeed, with center frequency at 1300 nm and a bandwidth of 40 nm) is launched into a single mode fiber, which goes into port 1 of 2 x 2 3dB coupler. It exits port 2, which is connected to the sensing fiber Bragg grating. The reflected light from the fiber Bragg grating enters another

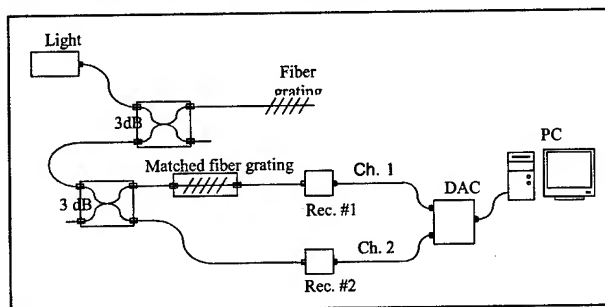


Figure 1 Block Diagram of the experimental setup.

3dB 2 x 2 coupler. One of the two exit ports of the couplers is connected with the demodulating fiber Bragg grating and to the photoreceiver. The

other exit port is connected to an identical photoreceiver as the reference leg. The output signals from the two photoreceivers go through band-pass filters and amplifiers and are collected by a PC running LabVIEW, which takes the ratios of the two signals and record and plot the result in real time (the data acquisition board from National Instrument has a sampling rate of 4MHz per channel for 2 analog input channels).

In the following, we briefly discuss the physics underlying our detection scheme. Consider an originally uniform fiber optic Bragg grating of period Λ_0 and average refractive index n_0 placed in a z -dependent longitudinal strain field, $\epsilon(z)$. Because of this, both the period of the Bragg grating and the refractive index will become z -dependent, with the former given by the expression

$$\Lambda(z) = \Lambda_0[1 + \epsilon(z)]$$

and the latter given by

$$n(z) = n_0 \{1 - 1/2 n_0^2 [p_{12} - \nu(p_{11} + p_{12})\epsilon(z)]\}$$

where p_{11} and p_{12} are the photoelastic constants for the fiber and ν is the Poisson's ratio. It then follows that the peak reflection wavelength of the Bragg grating $\lambda = 2n\Lambda$ also becomes z -dependent

$$\lambda(z) = \lambda_0 (1 + \{1 - 1/2 n_0^2 [p_{12} - \nu(p_{11} + p_{12})]\}\epsilon(z))$$

where λ_0 is the grating peak reflection wavelength without strain. To use this formula for the present case of silica glass fiber, we can write the above equation as

$$\lambda = \lambda_0 (1 + p\epsilon)$$

where the constant $p = 0.78$ for silica fibers. Thus the variation of the peak reflection wavelength of the fiber Bragg grating with respect to strain is given by

$$d\lambda / d\epsilon = 0.78\lambda_0$$

Working at 1300 nm, for example, we have

$$d\lambda / d\varepsilon = 1.014 \text{ pm} / \mu\varepsilon$$

i.e., for every microstrain, there is a shift of 1.014 pm of the peak reflection wavelength of the fiber Bragg grating.

The parameters relevant to the present experiments are: peak reflection wavelength of both the sensing Bragg grating and the demodulating Bragg grating $\lambda_{s0} = \lambda_{d0} = 1300 \text{ nm}$, they both have full width at half maximum (FWHM) of 0.3 nm, and peak reflectivity $R_{s0} = R_{d0} \approx 0.9$, which depend on the grating length L , the index modulation Δn , and the grating period Λ_0

$$R = \tanh^2 \left(0.8\pi\Delta n \frac{L}{\Lambda_0} \right).$$

Let I_0 be the intensity of the light source (which for the broad-band light source can be considered constant near 1300 nm), T the transmission factor which accounts for the losses due to couplers, splices, connectors, etc, the integrated intensity of light at the photodetector with the demodulating Bragg grating is given by

$$I_{\text{signal}} = I_0 T \int d\lambda R_s(\lambda) [1 - R_d(\lambda)],$$

while the integrated light intensity at the reference photodetector is

$$I_{\text{reference}} = I_0 T \int d\lambda R_s(\lambda).$$

If we choose Gaussian beam profile for the reflected light of both the sensing and the demodulating Bragg gratings,

$$R_s(\lambda) = R_{s0} \exp\left(-\left(\frac{\lambda - \lambda_s}{\Delta\lambda_s}\right)^2\right),$$

$$R_d(\lambda) = R_{d0} \exp\left(-\left(\frac{\lambda - \lambda_d}{\Delta\lambda_d}\right)^2\right),$$

The light intensities at the photodetectors can now be calculated, if we know the reflection peak wavelength and the width of the reflection peak.

The latter may be related to the FWHM of the reflection profile.

3. Experimental Results

3.1 Piezoceramic Resonators

To establish the detection sensitivity and speed of the fiber Bragg grating sensors, we performed a series of experiments with the sensors using controlled generation of ultrasonic signal. The latter was accomplished employing PZT acoustic resonators driven by a pulse generator (Ritec RAM-10000). The fiber gratings are glued to the side surface of the acoustic resonator, so that when the resonator is set into vibration in its thickness-extension mode, the fiber grating is stretched and shortened periodically at the frequency of the acoustic resonator. A super-radiant luminescent light source was employed to send light (centered at 1300 nm, with a spectral width of 30 nm, and a peak power of 1.3 mW) down the fiber. A high-speed photodetector converts the light signal back to electrical signal, which is displayed on a digital oscilloscope.

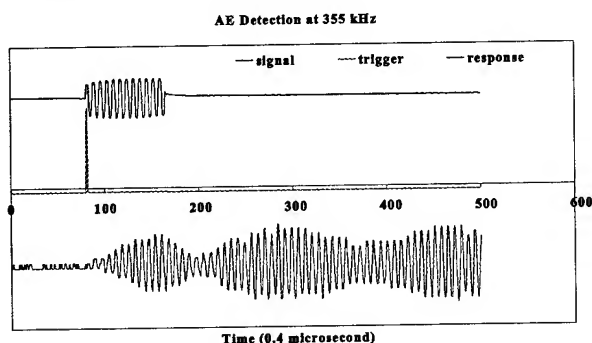
As the PZT resonators have resonant frequencies ranging from 200 kHz to 2 MHz, we were able to investigate the response of our fiber Bragg grating sensors to AE signals over the entire frequency domain mentioned above. However, the frequency response is not uniform across the frequency domain, as different resonators have quite different resonant frequency and displacement characteristics. Most of our data were taken near resonance, for the response falls sharply away from resonance. For demodulating the optical response signal, we used a tunable matching fiber Bragg grating. We found that this demodulator is very sensitive to small optical intensity change at extremely high speed.

To investigate the full range of parameter space, several PZT resonators of different thickness (thus different resonant frequencies) were

employed. Likewise, fiber Bragg gratings of various gage lengths were used.

Experimental data were taken in the form of photoreceiver voltage response to the light signal. In this, only the AC component is recorded (the DC voltage, of the order of several volts, carries no direct information on the AE signal.) The data taking commences when a trigger signal is received from the pulse generator, which is clocked to coincide with the onset of the sinusoidal wave train. Typically, about 10 cycles of sinusoidal voltage wave is applied, with typical amplitude of 10 to 100 volts. Figure 2 shows a typical waveform of the signal, the trigger, and the response, at a frequency of 355 kHz.

Figure 2 Pulse signal, trigger, and response at 355 kHz.



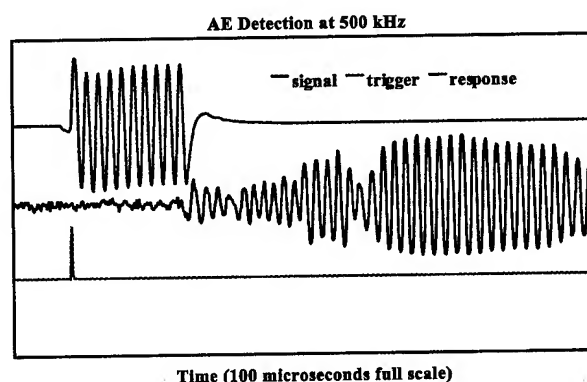
3.2 Experiments with ultrasonic transducer and aluminum plate

In a second experiment we replaced the PZT resonators with an aluminum plate of dimension $24\text{ cm} \times 12\text{ cm} \times \text{cm}$. We bonded a fiber Bragg grating sensor on the top surface of the aluminum plate. A sound wave is launched into the plate by an ultrasonic transducer in contact with the top surface of the plate. The rest of the experimental setup is the same as described earlier in conjunction with the PZT resonator experiments. The ultrasonic transducer is driven by the Ritec RAM10000 pulse generator. In order to determine the sensitivity of the fiber Bragg grating sensor we varied the distance between the fiber Bragg grating sensor and the ultrasonic

transducer. Furthermore, in order to assess the directional dependency of the detection

sensitivity we also varied the direction of propagation of the sound wave relative to the direction of the fiber Bragg grating. Specifically, measurements were made along three straight lines connecting the fiber Bragg grating and the ultrasonic transducer. Line a is perpendicular to the direction of the fiber Bragg grating; line b is at 45-degree angle with respect to the direction of the grating; line c is parallel to the direction of the grating.

The output signal from the photodetector is amplified by a preamplifier (40 dB gain) followed by an amplifier (20 dB gain). Clear signals can be



detected at the maximum separation allowed by **Figure 3** Detection of acoustic emission signal at 500 kHz. The fiber Bragg grating detection is at a distance of 5 cm from the ultrasonic transducer.

the aluminum configuration (~ 30 cm). We used transducers of various center frequencies (up to 5 MHz) but most concentrated in the spectral region from 300 kHz to 1 MHz.

In Figure 3, we show a typical waveform of acoustic signal produced at 500 kHz and its corresponding response from the fiber Bragg grating sensor.

3.3 Experiments with pencil lead breaking and aluminum plate

In a last set of experiments we attempted to detect acoustic emission signal generated by breaking a pencil lead on the aluminum plate described in Section 5. We were able to detect the AE signal's frequency components up to 30 kHz, mainly limited by available electronic filters and amplifiers beyond that. We were able to detect AE signal generated by pencil lead breaking

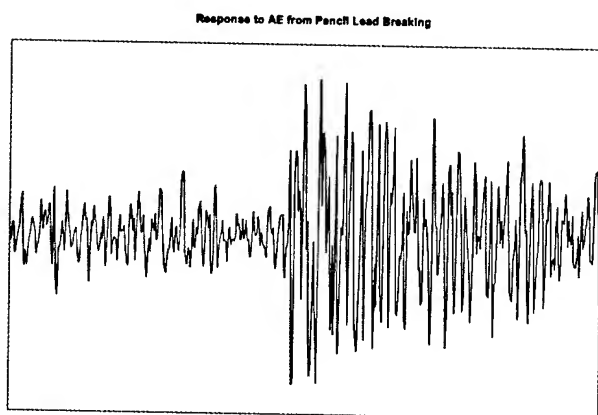


Figure 4 Fiber Bragg grating detector response to a pencil lead breaking event. The bandpass filter is set at 30 kHz.

on the aluminum plate on which the fiber Bragg grating detector was bonded. A typical photodetector response is shown in Figure 4. In obtaining this result, the electronic bandpass filter's center frequency was set at 30 kHz, and the total electronic gain was 80 dB.

4. Conclusions

We have performed a series of experiments to test the feasibility and limitation of using optical fiber Bragg gratings to detect acoustic emissions. These experiments differ mainly from one another in the way the acoustic emission signal

was generated. In the first experiment, it was generated by piezoceramic resonators; in the second experiment, it was generated by ultrasonic transducers; and in the third experiment, it was generated by pencil lead breaking. Our experiments show that dynamical strain of a fraction of 1 μ strain and frequency of the order of 1 MHz is detectable with our fiber optic Bragg grating sensor.

In conclusion, we have obtained very promising experimental evidence that fiber Bragg gratings may be used to detect acoustic emission events. This detection method is very sensitive, highly reliable, and can be easily adapted to structural monitoring. As this study is still preliminary, we hope to report more in-depth investigation of AE detection using fiber Bragg gratings in the near future.

5. Acknowledgments

This work was supported by the Office of Naval Research and U.S. Army CECOM.

6. References

1. K.O. Hill, Y. Fujii, D.C. Johnson, and B.S. Kawasaki, *App. Phys. Lett.*, **32**, 647 (1978).
2. G. Meltz, W.W. Morey, and W.H. Glenn, *Opt. Lett.* **14**, 823 (1989).
3. G. Meltz, W.W. Morey, and J.R. Dumphy, *SPIE* **1587**, 350 (1991).
4. R.K. Miller and P. McIntire, "Nondestructive Testing Handbook", vol. 5, Acoustic Emission Testing, American Society for Nondestructive Testing, Columbus, OH, 1992.
5. I.M. Perez, H.L. Cui, and E. Udd, *SPIE International Conference on Smart Structures*, Newport Beach, CA, March 1999.
6. A.W. Snyder and J.D. Love, "Optical Waveguide Theory", Chapman and Hall, New York, 1983.
7. Channel Industries, Inc., product information: www.piezoceramics.com.

Understanding Multimode Bandwidth and Differential Mode Delay Measurements and Their Applications

Paul F. Kolesar

OFS

Holmdel, NJ

+1-732-888-7181 · pkolesar@ofs optics.com

David J. Mazzaresse

OFS

Sturbridge, MA

+1-508-347-8583 · dmazzaresse@ofs optics.com

Abstract

Multimode fibers optimized for 850 nm transmission are increasingly referenced and used by applications, cabling, and fiber standards. Such fibers enable the lowest total system cost for interconnects between 150 to 600 meters by using low-cost 850 nm VCSEL transceivers at speeds up to 10 Gb/s. The fiber measurement technology used to guarantee operation evolved over time to address higher transmission rates. We describe and compare three key fiber measurements: Overfilled Bandwidth (OFLBW), Restricted Mode Launch Bandwidth (RMLBW) and Differential Mode Delay (DMD). Multimode fiber properties such as mode groups, modal delays and bandwidth are explored, as well as the interaction between optical fiber and sources such as Light Emitting Diodes (LEDs) and Vertical Cavity Surface Emitting Lasers (VCSELs). We touch on system properties such as mode power distribution, encircled flux, and Effective Modal Bandwidth (EMB). Finally, we show that the evolution from OFLBW to DMD has been a result of the requirement to measure more precisely the fiber properties that directly affect transmission when used with devices such as VCSELs. This paper draws on data from Telecommunications Industry Association (TIA) working group FO2.2.1 with reference to specific documents that standardize the relevant measurement procedures, fiber and source specifications, and applications within the US and International standards bodies.

Keywords

Multimode fiber; differential mode delay (DMD); overfilled bandwidth; restricted mode launch bandwidth; effective modal bandwidth (EMB); encircled flux; mode power distribution; 850 nm transmission; VCSEL; 10 Gb/s; TIA FO2.2.

1. Introduction

The advent of Gigabit Ethernet in the late 1990's ushered in the age of 850 nm VCSELs to replace slower LEDs as the transmitter of choice on multimode fiber datacom links. VCSELs excite fiber very differently than LEDs and precipitated new performance measurements that better qualify fiber to support these laser-based systems. Early attempts have evolved into sophisticated measurements that reveal a detailed picture of the modal propagation properties of fiber and expand its application capability.

2. Multimoded Transmission

Light travels through multimode fiber in modes. A multimode fiber, by definition, is a fiber where more than one mode travels and typically the number of individual modes is on the order of 100 to 1000. Each mode is an independent, self-supporting, electromagnetic field that propagates axially along an optical fiber independent of all other modes. Modes are identified in $LP_{n,m}$ nomenclature in accordance with a convention for describing field shape of linearly polarized modes. In accordance with this nomenclature, "n" is the azimuthal mode number and "m" is the radial mode number.

Graded index multimode fibers used in transmission systems typically have index profiles described by equation (1). The exponent α is tuned to make modes arrive at nearly the same time at a particular wavelength.

$$n(r) = n_1 \left(1 - 2\Delta \left(\frac{r}{a} \right)^\alpha \right)^{0.5} \quad (1)$$

n_1 is the index in the center of the core

Δ is the index difference between the core and the clad

r is the radial position

a is the core radius

α is the grading parameter typically between 1.7 and

2.1

For α values near 2, the index profile becomes parabolic.

The number of modes that propagate in a multimode fiber are given by equation (2) below [2]:

$$M = \left(\frac{\alpha}{\alpha + 2} \right) \Delta \left(\frac{2\pi n_1 a}{\lambda} \right)^2 \quad (2)$$

M is the number of modes

λ is the wavelength of light propagating in the fiber

Mode groups consist of multiple modes, for all but the single-member fundamental mode group, of the same axial phase velocity. As such, the hundreds of individual modes actually propagate in relatively few mode groups. For example, in a 50 μm fiber with a 0.20 numerical aperture, only 19 mode groups exist, of which the lower 17 propagate. Higher order mode groups consist of more modes than do those of lower order.

Depending on the index profile of the fiber and the wavelength of light, modes groups may travel at different velocities. The difference in travel time is called the differential mode delay (DMD). Multimode fibers are designed to minimize this delay difference so that light pulses remain compact for as long as possible permitting differentiation of subsequent pulses when they exit the fiber. DMD causes the transmitted pulse to spread out, or disperse, in time as shown in Figure 1.

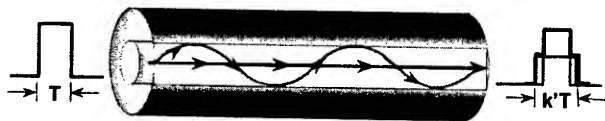


Figure 1. Modal Dispersion

In a graded index fiber, the modes that travel nearest the center of the core are subject to a higher effective index than are those that travel the longer paths through the outer portions of the core. When the profile is optimized, the varying index equalizes the travel time of all mode groups, and DMD is minimized.

Modal bandwidth is one measure that characterizes the effect of pulse broadening in a fiber. The longer the fiber is the more the pulse broadens and the lower the bandwidth will be. This length dependence is captured in the unit of measure, which is MHz·km.

Modal bandwidth can depend strongly on the power distribution among the modes, as the output signal shape is the sum of the arrival time of each mode group weighted by the fraction of the signal energy it carries. Thus different weights can lead to different pulse shapes and bandwidths.

DMD can also be used to quantify a fiber's modal bandwidth. By bounding the difference in propagation times between all modes carrying significant signal energy, a lower bandwidth limit is established for launches that are confined to the bounded modes.

In addition to modal dispersion just discussed, the signal also broadens due to chromatic dispersion. Chromatic dispersion occurs because the index of refraction of glass changes with wavelength, and therefore the various spectral components of the signal travel at different velocities. The modal and chromatic bandwidths combine quadratically to give the fiber's system bandwidth as shown in equation (3). System link models account for the effects of both modal and chromatic dispersion.

$$BW = \frac{1}{\sqrt{\left(\frac{1}{BW_{modal}}\right)^2 + \left(\frac{1}{BW_{chromatic}}\right)^2}} \quad (3)$$

Various types of sources have different spectral widths and therefore induce different amounts of chromatic dispersion. Typical LEDs have broad spectra around 50 nm (rms) wide, while lasers have relatively narrow spectra around 1 nm wide. Thus LEDs cause much greater chromatic dispersion. Practical LED transmitters cannot modulate at gigabit data rates; therefore

systems employ lasers at speeds where the LED's chromatic bandwidth would otherwise become the limiting factor.

3. Measurement of Modal Bandwidth

Fiber based datacom systems have evolved from 10 Mb/s to 10 Gb/s. The modal excitation of the fiber changed markedly as LEDs gave way to lasers. Since modal bandwidth is highly dependent on the mode power distribution, the industry developed new bandwidth measurements better suited to the sources.

There are two domains in which bandwidth can be measured. One way, shown in Figure 2, is in the time-domain. Here a pulse of light is launched into one end of the fiber and the temporal response of the output is measured. Conversion into the frequency domain reveals the bandwidth from the transfer function $H(f)$, defined as the earliest frequency at which the amplitude drops 3 dB below the amplitude at zero frequency.

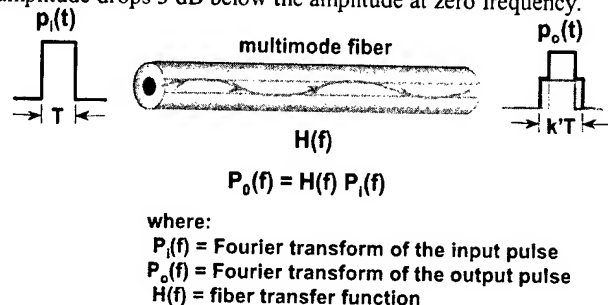


Figure 2. Time-Domain Measurement

The second method, shown in Figure 3, describes the frequency-domain method of measuring bandwidth. A source is modulated over a band of frequencies while monitoring the output power, P_o . The bandwidth is defined as the earliest frequency where the optical power drops by 3 dB.

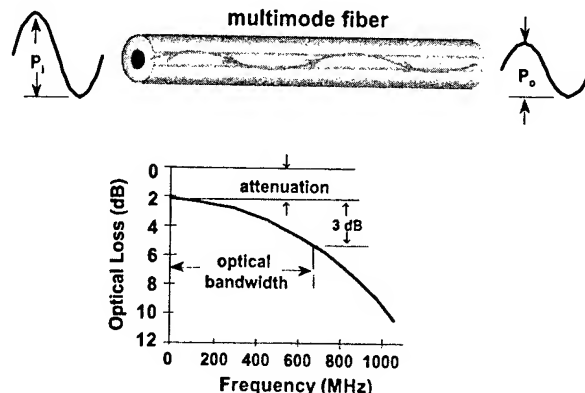


Figure 3. Frequency-Domain Measurement

Both the time-domain and frequency-domain methods give comparable results. The critical feature of either method for extracting meaningful bandwidth data is the launch condition. To provide bandwidth values that accurately predict performance, the launch condition must be similar to that of the system transmitter.

The type of transmitter employed for multimode fiber datacom systems depends on the data rate. LEDs are used up to 100 Mb/s. Between 100 and 622 Mb/s, systems employ both LEDs and 850 nm VCSELs. Above 622 Mb/s LEDs give way entirely to VCSELs.

An overfilled launch condition emulates the modal excitation of LEDs. The launch places equal power into each mode by uniformly illuminating the fiber by a source of higher numerical aperture and larger area than the fiber being measured, essentially flooding the core with light. The so-called overfilled bandwidth (OFLBW) is the original measurement condition standardized in the 80's and is useful for LED-based systems at data rates up to 622 Mb/s.

Bandwidth measurements for systems above 622 Mb/s require a launch condition emulating VCSELs. These devices have a lower numerical aperture and smaller area than LEDs. VCSELs launch into only a portion of the modes and their mode power distribution (MPD) can be highly non-uniform and highly variable, leading to large bandwidth variability [11]. Figure 4 depicts the mode power distributions of two LEDs and seventeen 1 Gb/s 850 nm lasers used in a Telecommunication Industry Association (TIA) study. While both LEDs closely approximate an overfilled MPD, the large variation amongst laser sources is easily seen. Thus finding a single launch condition representative of such sources proves elusive.

The restricted modal launch bandwidth (RMLBW) measurement developed for 62.5 μm fiber in the late 90's was an attempt to emulate these sources [3]. The specific launch condition, prescribed in TIA FOTP-204 [5], was found to correlate on 62.5 μm fiber to a subset of possible VCSEL launches as defined by limits on the encircled flux (EF) of the transmitter as measured by TIA FOTP-203 [4]. However, these corresponding EF specifications were not adopted by any application standard.

To address the needs of 10 Gb/s VCSEL applications, TIA FO2.2 examined alternate ways to characterize fiber bandwidth. Data on various individual launch conditions were compared to a method of extracting bandwidth from a DMD measurement. Part of the results of that study is shown in Figure 5. The minimum effective modal bandwidth (EMB) requirement for fibers to support the 300-m link length for 10-Gigabit Ethernet is 2000 MHz·km. Plotted on the left are the EMBs of twenty-one 10 Gb/s VCSELs when launched into one of the fibers in the study. Five of these sources produced EMB below the minimum requirement indicating the fiber should not be considered compliant. On the right are the bandwidth predictions from DMD and four other launch conditions. Only the DMD method predicted performance below the requirement and rejected this fiber. FO2.2 concluded that DMD provided the most reliable results and standardized the method in TIA FOTP-220 [6].

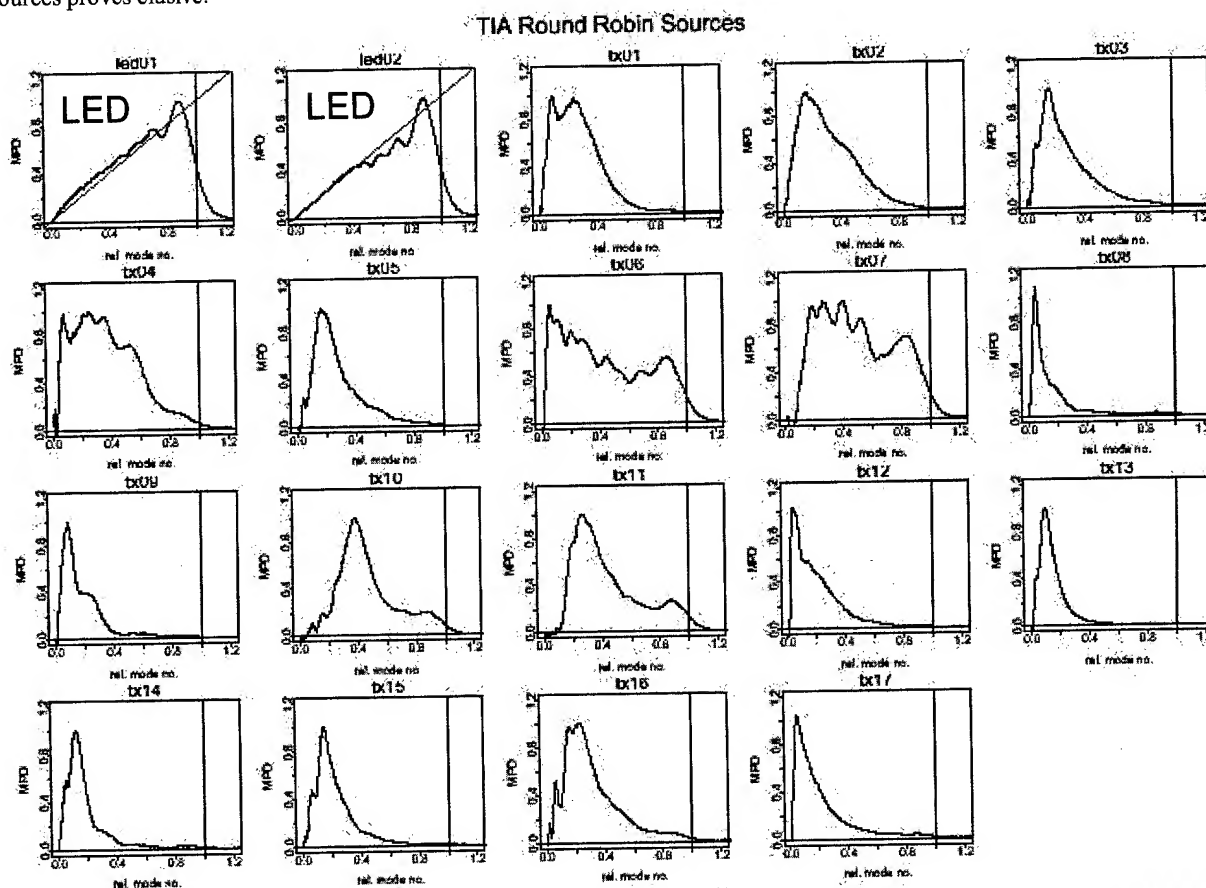


Figure 4. Mode Power Distribution of 1-Gb/s Sources

A. J. RIZZO April 1999

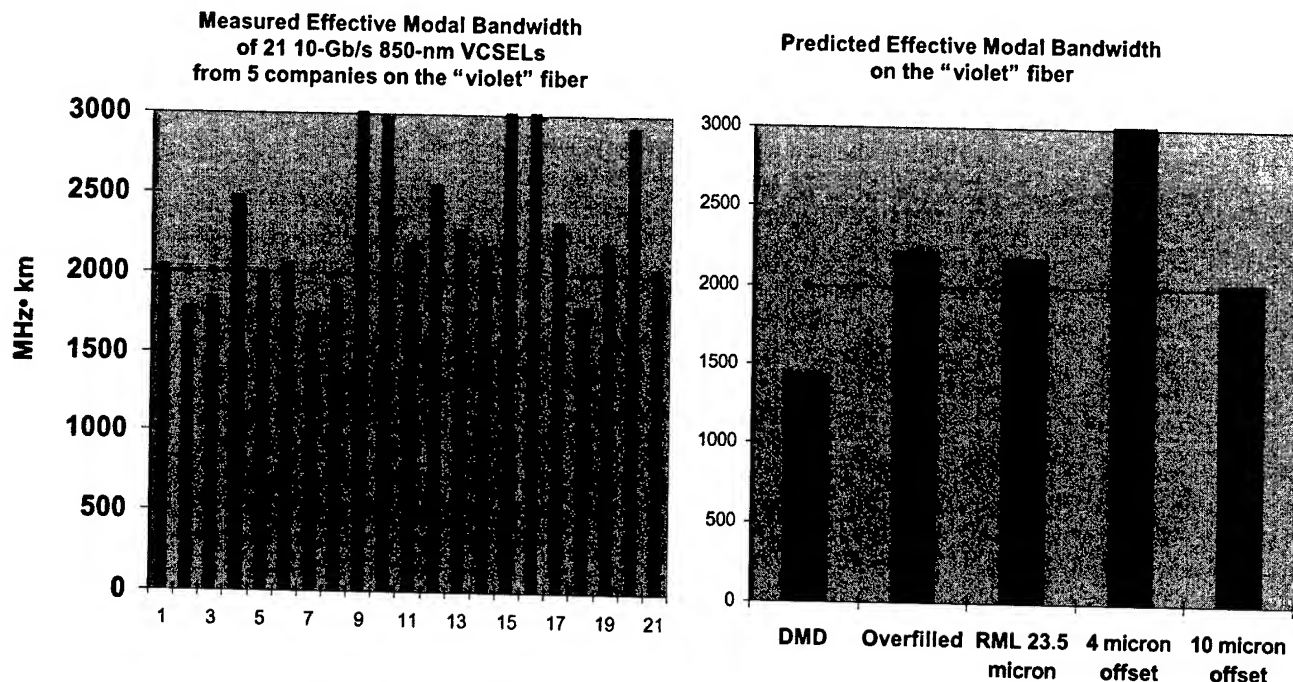
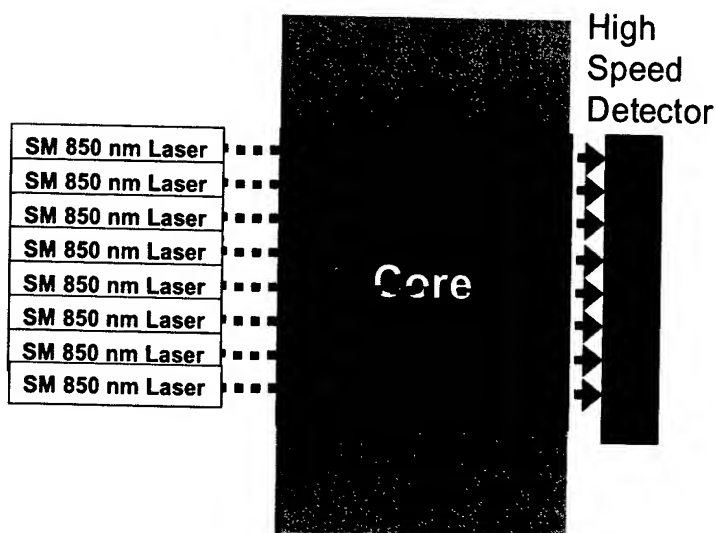


Figure 5. Predictive Capability of Various TIA Proposals

While DMD had been used as a process control technique for many years, the standardized method of FOTP-220 required refinement of this process [12, 13]. One of the major improvements developed by OFS (then Bell Labs) in the standardized DMD measurement was the use of a singlemode launch condition, which enabled resolution of low-order mode behavior previously invisible to the commonly used process control implementation of the measurement. Low-order mode behavior becomes critically important for 10 Gb/s VCSELs as they can couple efficiently into these modes.

The DMD technique is depicted in Figure 6. A singlemode 850 nm probe is scanned at small radial increments across the core of the multimode fiber under test. At each position the temporal response to a short impulse is recorded. After removal of the reference pulse temporal width, the DMD temporal width is determined at the 25% threshold level between the first leading edge and the last trailing edge of all traces encompassed between specified radial positions. In Figure 6 these radial positions encompass the entire scanned range.

DMD Scanning Process



DMD Scan Example

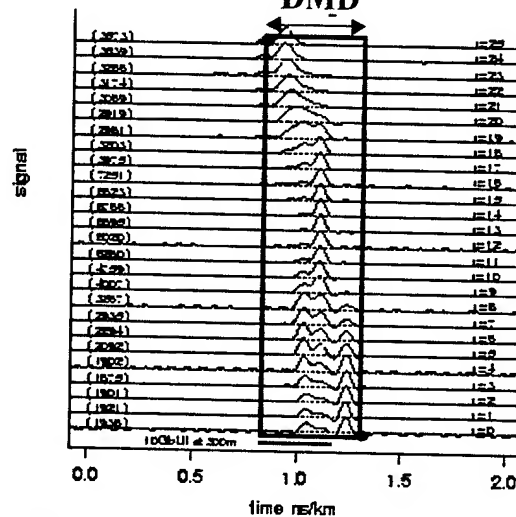


Figure 6. DMD Measurement Process

a.j.rilger 22Jan00

Equation 4 provides a handy approximation of the mode group of maximal excitation, m , as a function of radial scan position [1].

$$\frac{m}{M_{\max}} = \left(\frac{r}{a} \right)^2 \quad (4)$$

Figure 7 illustrates the mode-group resolution capabilities of the DMD method. The fiber measured therein is nearly optimized at 1300 nm, so the 850 nm DMD scan shows a fairly regular separation of the mode groups except near 18 μm offset where, for this fiber, a few mode groups have nearly equal delay. The fundamental mode is clearly seen dominating the scans below $r = 4 \mu\text{m}$. Individual members of the collections of few low-order mode groups peak and fade as the scan advances through 10 μm . Larger collections of mode groups contribute to the signal throughout the mid- and high-order as the scan advances further.

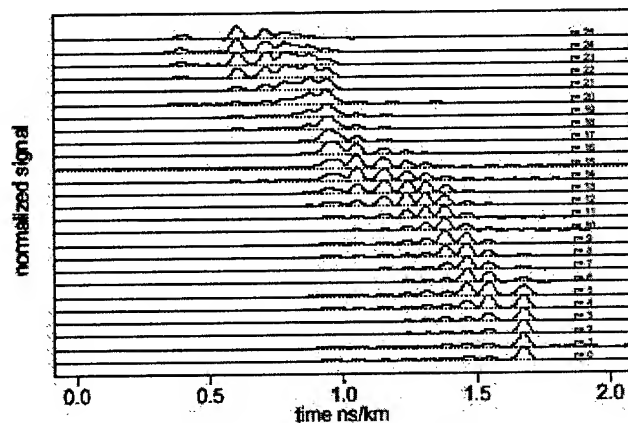


Figure 7. DMD Resolution

4. Establishment of Specifications for 10 Gb/s Operation

TIA FO2.2 realized during the work on 1 Gb/s applications that to create the most cost-effective solution the industry would need to agree on mutually compatible specifications for the transmitters and fibers. So proposals included both fiber specifications and transmitter launch conditions.

OFS proposed a 10 Gb/s fiber specification using DMD to constrain the modal delays to values less than the bit period for those modes carrying significant power. This concept is based on the observation that if all modes excited by the DMD measurement over appropriate radii lie within a period of time related to the bit interval, then the fiber should provide sufficient bandwidth no matter what subset of modes is excited within those radii. Transmitters would be required to launch into modes corresponding to the prescribed radii.

Out of the 1 Gigabit effort emerged a new measurement procedure, FOTP-203, for qualifying the transmitter launch condition. FOTP-203 prescribes a method of measuring the near field intensity, $I(r)$, of the power coupled into a multimode fiber

by a transmitter. The near field is converted into an encircled flux distribution by circular integration as shown in equation 5.

$$EF(r) = \int_0^r I(r) 2\pi r dr \quad (5)$$

Using the EF metric, boundaries on launch conditions may be established that provide allowances for fiber manufacturing. Fiber manufacturers requested that the sources not place too much power in the very lowest-order modes or in the very highest-order modes.

FO2.2 extensively modeled and simulated the system using modal theory that accounted for laser-fiber interactions and the effects of mode mixing at offset connections [8, 9, 10]. Figure 8 displays a block diagram of the simulation. The specifications that emerged are documented in the 50- μm fiber detailed specification, TIA-492AAAC and are repeated here in Tables 1 and 2 [7].

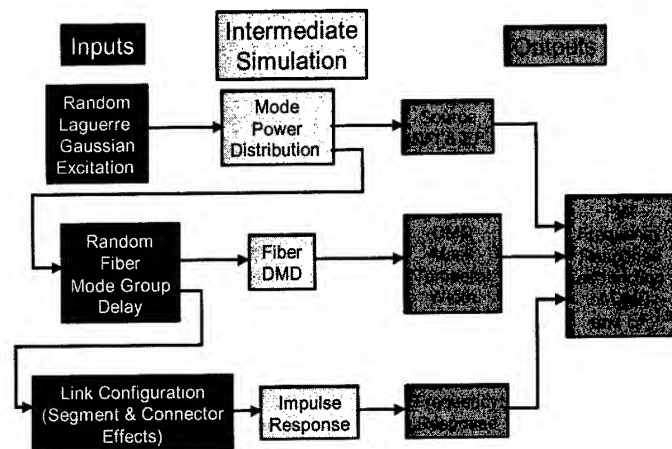


Figure 8. Simulation Block Diagram

Table 1. DMD Specifications for 2000 MHz-km EMB

Fiber shall meet at least one of the following six DMD templates		
Template number	Inner mask DMD for $R_{\text{INNER}} = 5 \mu\text{m}$ to $R_{\text{OUTER}} = 18 \mu\text{m}$ (ps/m)	Outer mask DMD for $R_{\text{INNER}} = 0 \mu\text{m}$ to $R_{\text{OUTER}} = 23 \mu\text{m}$ (ps/m)
1	≤ 0.23	≤ 0.70
2	≤ 0.24	≤ 0.60
3	≤ 0.25	≤ 0.50
4	≤ 0.26	≤ 0.40
5	≤ 0.27	≤ 0.35
6	≤ 0.33	≤ 0.33

Table 2. Transmitter Specifications into 50- μm Fiber

Encircled Flux at 4.5 μm radius $\leq 30\%$ (limits low-order mode excitation)
Encircled Flux at 19 μm radius $\geq 86\%$ (limits high-order mode excitation)
Center wavelength (λ_c): $840 \leq \lambda_c \leq 860$ nm (operate near nominal measurement wavelength)

The collection of DMD templates provides an allowance for fiber manufacturing based on simulation results, which showed that constraints on the modes carrying little energy could be relaxed as constraints on modes carrying the bulk of power are tightened. The inner mask is permitted to float temporally within the outer mask. This concept is depicted in Figure 9.

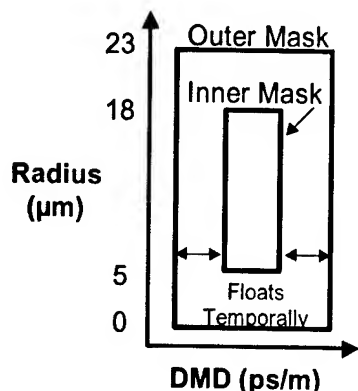


Figure 9. Inner Mask Floats within Outer Mask

The interlocking radial correspondence between the transmitter EF specification and the fiber DMD specification is depicted in Figure 10.

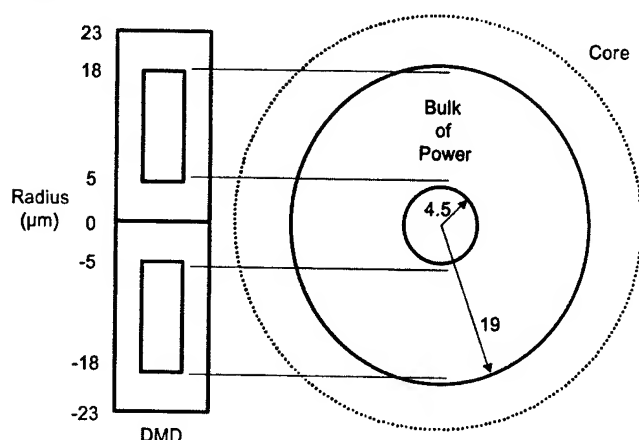


Figure 10. DMD to EF Correspondence

The bulk of the mode power distribution lies within the tightly constrained radial extent of the inner mask. The region

measured by the DMD probe actually extends beyond the radial prescriptions of the masks because the singlemode probe has significant radius. At 850 nm, the mode field diameter of the singlemode probe fiber is approximately 5 μm .

5. Standards and Industry Adoption

TIA FO2.2 worked closely with application standards bodies during the development of these fiber and transmitter specifications that enable 10 Gb/s serial transmission to 300 meters using 850 nm VCSELs. This coincided with the development of 10-Gigabit Ethernet by IEEE 802.3, 10-Gigabit Fibre Channel by ANSI NCITS T11.2, and OC-192 VSR-4 by the Optical Internetworking Forum (OIF). Each of these applications adopted both the new fiber specifications and compatible transmitter launch conditions [14, 15, 16]. This suite provides solutions spanning the LAN (Local Area Network), SAN (Storage Area Network), and CO (Central Office) markets.

The cabling industry also embraced the new fiber detailed specifications by referencing it within addenda to structured cabling standards like TIA 568B [17].

Equivalent international standards are emerging within the International Electrotechnical Commission (IEC) and International Organization for Standardization (ISO). IEC PAS 60793-1-49 mirrors TIA's DMD test procedure, FOTP-220 [18]. Draft IEC 60793-2-10 Edition 2 contains the fiber specifications from TIA 492AAAC [19]. And ISO/IEC 11801 2nd Edition assigns these new fiber specifications to a new multimode fiber level of performance called OM3 [20].

Figure 11 diagrams the relational interdependence between all of these standards. The measurement standards provide the foundation upon which the fiber specifications rest. Cabling standards reference the fiber specifications, which in turn support the applications standards.

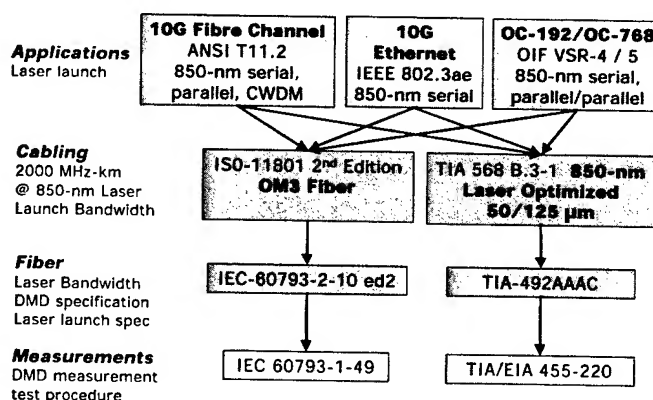


Figure 11. Standards Interdependence

Today, major fiber manufacturers sell the new high-performance 50- μm fiber verified using the DMD test procedure, and several cable manufacturers offer this fiber within new cables. Already 850 nm VCSEL-based transceivers with compatible launch conditions appear in 10 Gb/s Ethernet products, and these are

offered at the lowest prices among the transceiver alternatives by wide margin [21].

End-users find this new fiber solution attractive not only to ensure easy migration to 10 Gb/s applications, but to also support existing applications to extended reaches. Table 3 lists the distances supported by OFS for its TIA-492AAAC compliant fibers based on worst-case analysis using the IEEE 802.3 link model.

Table 3. Supportable Distance (m) Comparison

Application	LaserWave™ 300	Standard 62.5 μm
Ethernet	1500	2000
Fast Ethernet	2000	2000
Gigabit Ethernet	1000	275
10 Gig Ethernet	300	33
1 Gig Fibre Channel	900	300
2 Gig Fibre Channel	550	150
4 Gig Fibre Channel	300	70
10 Gig Fibre Channel	300	33
Token Ring	1500	2000
FDDI	2000	2000
155 Mb/s ATM	2000	2000
622 Mb/s ATM	300	300
10 Gig OIF	300	25

Supporting a 300-m minimum distance across all applications listed in Table 3 addresses over 92% of customer's in-building backbone needs according to a survey conducted by the IEEE shown in Figure 12, and positions the fiber as a universal media.

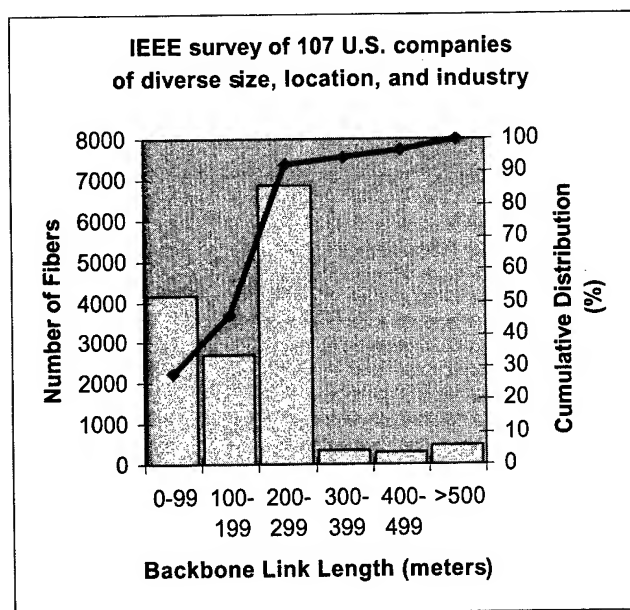


Figure 12. In-Building Backbone Distances

6. Conclusions

Through refined measurements of fiber modal propagation properties, the fiber industry in cooperation with the transceiver industry has succeeded in providing a robust solution for the cost-sensitive short-reach market that supports low-cost serial transmission on advanced multimode fiber. Broad industry acceptance, standards backing, and support for major LAN, SAN and CO applications assure end-users that 850 nm laser-optimized 50 μm fiber is a wise choice for datacom services.

7. Acknowledgments

The authors would like to extend special thanks to A. John Ritger of OFS, Norcross GA and Steven Golowich of Lucent Technologies Bell Laboratories, Holmdel NJ for their invaluable contributions towards the success of the DMD-based fiber performance specification.

8. References

- [1] Robert Olshanksy and Susan M. Oaks, Differential Mode attenuation Measurements in Optical Fibers Applied Optics 17, 1830 (1978).
- [2] D. Gloge and E.A. J. Marcatili, Multimode Theory of Graded Core Fibers, Bell System Technical Journal Vol 52(9) pp 1563 – 1578, (1973).
- [3] TIA TSB62-20, "Enhanced Bandwidth Performance over Laser-Based, Multimode Fiber Local Area Networks" (February 2001).
- [4] FOTP-203 (TIA-455-203), "Launched Power Distribution Measurement for Graded Index Multimode Fiber Transmitters" (June 2001).
- [5] FOTP-204 (TIA-455-204), "Measurement of Bandwidth on Multimode Fiber" (December 2000).
- [6] FOTP-220 (TIA-455-220) "Differential Mode Delay Measurement of Multimode Fiber in the Time Domain" (December 2001).
- [7] TIA-492AAAC "Detailed Specification for 850 nm Laser-Optimized 50- μm Core Diameter/125- μm Cladding Diameter Class Ia Graded-Index Multimode Optical Fiber" (March 2002).
- [8] S. E. Golowich, P. F. Kolesar, A. J. Ritger, and P. Pepeljugoski, "Modeling and Simulations for 10 Gb Multimode Optical Fiber Link Component Specifications", OFC 2001, paper WDD57.
- [9] M. Wegmuller, S. Golowich, G. Giaretta, and M. Nuss, "Evolution of the Beam Diameter in a Multimode Fiber Link Through Offset Connectors", *IEEE Photonics Technology Lett.*, Vol. 13, No. 6, p574 (June 2001).
- [10] P. Pepeljugoski, S. E. Golowich, "Measurements and simulations of intersymbol interference penalty in new high

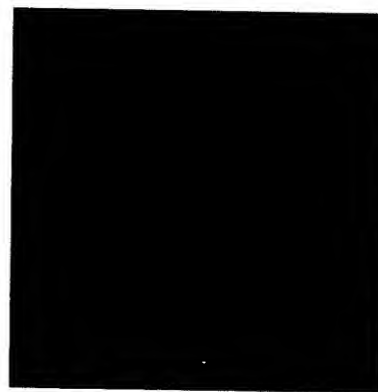
speed 50 μ m multimode fiber links operating at 10 Gb/s", OFC 2001, paper WDD40.

- [11] A. J. Ritger, "Use of Differential Mode Delay in Qualifying Multi-Mode Optical Fiber for 10 Gbps Operation", OFMC (2001).
- [12] M. J. Buckler, J. W. Shiever, F. P. Partus, "Optimization of Multimode Fiber Bandwidth via Differential Group Delay Analysis", Conference Digest ECOC '80, p33, York (1980).
- [13] D. Marcuse, *Optical Fiber Measurements*, Academic Press, New York, p288 (1981).
- [14] IEEE 802.3 "Supplement to Carrier Sense Multiple Access with Collision Detection (CSMA/CD) Access Method & Physical Layer Specifications – Media Access Control (MAC) Parameters, Physical Layer, and Management Parameters for 10 Gb/s Operation" (June 2002).
- [15] 10 Gigabit Fibre Channel (10GFC), NCITS xxx-200x, T11 Project 1413-D, Rev. 3.0 (April 10, 2002).



Paul F. Kolesar is a Distinguished Member of Technical Staff at OFS, 791 Holmdel-Keyport Rd., Holmdel, NJ. He actively contributes to the development of industry standards on fiber optics and originated the concept of 850 nm laser-optimized multimode fiber. He holds issued and pending patents on optical patch-panel design and high-speed multimode transmission and an MSEE degree from Fairleigh Dickinson University.

- [16] OIF-VSR4-04.0 "Serial Shortwave VSR Interface for Multimode Fiber", Optical Internetworking Forum (January 2001).
- [17] ANSI/TIA/EIA-568-B.3-1-2002 "Optical Fiber Cabling Components Addendum 1 – Additional Transmission Performance Specifications for 50/125 μ m Optical Fiber Cables" (April 2002).
- [18] IEC PAS 60793-1-49: "Optical fibre - Part 1-49 : Measurement methods and test procedures – Differential Mode Delay" (May 2002).
- [19] IEC 60793-2-10 Ed. 2.0: Part 2-10: "Product specifications – Sectional specification for category A1 multimode fibres", Committee Draft (May 2002).
- [20] ISO/IEC 11801 2nd Edition: IT – Cabling for customer premises (2002).
- [21] http://www.foundrynetworks.com/about/newsevents/release/s/pr5_16_01.html



David J. Mazzaresse is the technical Manager of the Preform and Measurements D&E at OFS, 50 Hall Rd., Sturbridge, MA. He has lead the development of various multimode, singlemode and specialty products over the past 9 years. He holds a PhD in Chemical Engineering and an MS in Electrical Engineering from the University of Massachusetts at Amherst.

Stability of Low Water Peak SMF against Hydrogen Aging

**Fumiyoshi Ohkubo, Hajime Igarashi, Hideyuki Wakiyasu, Kazuaki Negishi,
Takashi Hasegawa, and Kazuya Kuwahara**

Fiber Optics Division, Sumitomo Electric Industries, LTD.

1, Taya-cho, Sakae-ku, Yokohama, 244-8588 Japan

Phone#: +81-45-853-7267, Fax#: +81-45-851-0935, Email address: ohkubo-fumiyoshi@sei.co.jp

Abstract

In this paper, we describe the stability performance against Hydrogen aging with several types of Low Water Peak Single-Mode Optical Fiber (LWP-SMF). Long-term reliability over 25 years of each fiber is revealed through our experiments by using much severe condition than that of IEC 60793-2-50 test procedure.

Keywords

Low Water Peak SMF, Hydrogen aging test, CWDM, Hydrogen reaction, Molecular hydrogen diffusion

1. Introduction

Application of Wavelength Division Multiplexing (WDM) technology has been expanded not only to long haul networks, but also to metro area networks. For increasing the network capacity with further transmission distance, Dense WDM (DWDM) system has been evolved with more complicated and expensive components, especially for the long haul networks. On the other hands, Coarse WDM (CWDM) system has been newly developed as an indispensable technology for inexpensive metro area networks. CWDM systems require broad-range operating band because the systems utilize optical signals having broader channel spacing (typically 20 nm) without the use of high-end optical components such as wavelength-locked LDs. A newly developed LWP-SMF "PureBand™" has been designed suitable for the CWDM systems. Due to its broad-range low attenuation characteristics including Water Peak, the fiber can be available about 30 % wider operation band than a standard single-mode optical fiber as shown in Figure.1.

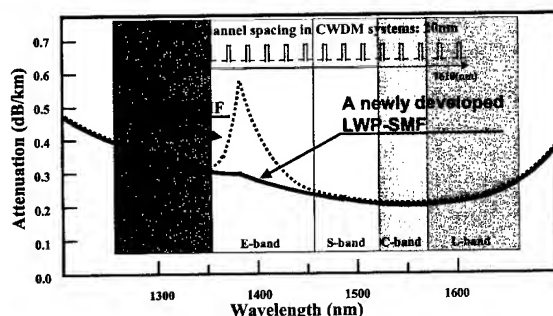


Figure 1. Spectral attenuation of the newly developed LWP-SMF

The newly developed LWP-SMF, which is manufactured by using VAD technology, was also designed to achieve stabilized attenuation characteristics against Hydrogen. In order to assure the long-term reliability of field installed optical fiber cables, it is necessary to investigate induced attenuation due to hydrogen.

2. Test Methods of Hydrogen Aging

A lot of accelerated hydrogen aging studies [1,2] have been conducted on the hydrogen reaction between hydrogen molecules and defects at high temperatures in the past. On the other hands, some recent studies [3,4] indicated, accelerated hydrogen aging tests at high temperature couldn't simulate the actual attenuation increase under field installed cable condition. The actual field installed cable condition of 4×10^{-4} atmosphere of hydrogen for the duration of 25 years is equivalent to the 0.01 atmosphere test for 367 days at room temperature or to the 1.0 atmosphere test for 4 days at room temperature [5]. We discuss the test condition under 0.01 and 1.0 atmospheres of hydrogen at room temperature below.

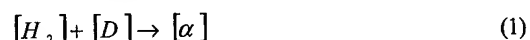
2.1 0.01 atmospheres of hydrogen condition

The test procedure described in IEC 60793-2-50 Ed. 1.0 requires to "Expose a fiber specimen to 0.01 atmospheres of hydrogen at room temperature and continue exposure until 1240 nm attenuation changes by 0.03 dB/km or more." This accelerated hydrogen aging can estimate the attenuation increase of the actual field installed cable after several years.

2.2 1.0 atmospheres of hydrogen condition

This accelerated aging under high hydrogen pressure at room temperature can simulate the actual reaction in a shorter period of time as described below.

The model of hydrogen reaction between hydrogen molecules and defects can be expressed as



where $[H_2]$ is hydrogen concentration, $[D]$ is defect concentration and $[\alpha]$ is concentration of reaction products.

The hydrogen aging loss is directly proportional to the concentration of reaction products.

In this case, the equation is

$$\frac{d[\alpha]}{dt} = k[H_2] \cdot [D] = A \cdot \exp\left(-\frac{E_a}{RT}\right) \cdot [\alpha' - \alpha] \cdot P_{H_2} \quad (2)$$

where α' is initial concentration of defects and P_{H_2} is hydrogen partial pressure.

We find

$$[\alpha] = \alpha' [1 - \exp(-k \cdot P_{H_2} \cdot t)] \quad (3)$$

$$k = A \cdot \exp\left(-\frac{E_a}{RT}\right) \quad (4)$$

where A is frequency factor, E_a is activation energy, R is gas constant, T is absolute temperature.

Assuming that the activation energy has a certain distribution, the equation 3 and equation 4 become

$$[\alpha] = \sum_{i=1}^n \alpha'_i [1 - \exp(-k_i \cdot P_{H_2} \cdot t)] \quad (5)$$

$$k_i = A \cdot \exp\left(-\frac{E_i}{RT}\right) \quad (6)$$

These equations indicate that the reaction products can be created by plural types of chemical reaction with different reaction velocity. In our experience, the attenuation increase both at 1380 nm and at 1430 nm at room temperature are can be expressed by equation 5 and equation 6 with

$$i = 1-3 \text{ (for attenuation increase at 1380 nm)} \quad (7)$$

$$i = 1-2 \text{ (for attenuation increase at 1430 nm)} \quad (8)$$

If temperature is invariant, this reaction model can be effective for the estimation of hydrogen attenuation increase as a general accelerated aging test, because the chemical reaction can be explained by hydrogen partial pressure and duration time according to equation 3.

In order to estimate the hydrogen attenuation increase of long period of time over 25 years, we adopted the test method with 1.0 atmosphere of hydrogen at room temperature for 4 days and beyond (up to 4 weeks).

3. Experiments

3.1 Sample fibers

In this study, we have tested kinds of LWP-SMFs identified as Fiber A, B, and C that is the newly developed LWP-SMF. We also tested Standard Single-Mode Optical Fibers (Standard SMFs) identified as Fiber D, E for references.

Two km length of each fiber specimen was looped 280 mm in diameter with tension free and was exposed to hydrogen in a test chamber. Hydrogen aging loss of each specimen was measured under the test condition of 1.0 atmosphere of hydrogen at room temperature.

Table 1. List of the sample fibers

ID	Classification
Fiber A	Low Water Peak Single-Mode Optical Fiber
Fiber B	
Fiber C	
Fiber D	Standard Single-Mode Optical Fiber
Fiber E	

3.2 Results and discussions

Figure 2, 3, and 4 show the spectral attenuation changes of LWP-SMFs (Fiber A, B, and C in Table 1) after exposure to 1.0 atmosphere of hydrogen at room temperature.

The attenuation increases at 1240 nm are observed in these Figures caused by molecular hydrogen diffusion and are reversible after about 1 month storage in the normal air environment. The attenuation increases in the 1400 nm band can be also found in these Figures and they are permanent loss even if hydrogen molecules are removed from the environment. These permanent attenuation increases occur due to chemical reactions mentioned in clause 2.2.

In the Figure 2, the attenuation increases in the 1400 nm band of the Fiber A can be found after 4 days exposure and reached to 0.34 dB/km at 1380 nm which is the same level as initial attenuation at 1380 nm of typical Standard SMF. After 4 weeks exposure, it seems to be that the hydrogen reaction reaches to saturation, and the attenuation at 1380 nm is 0.35 dB/km.

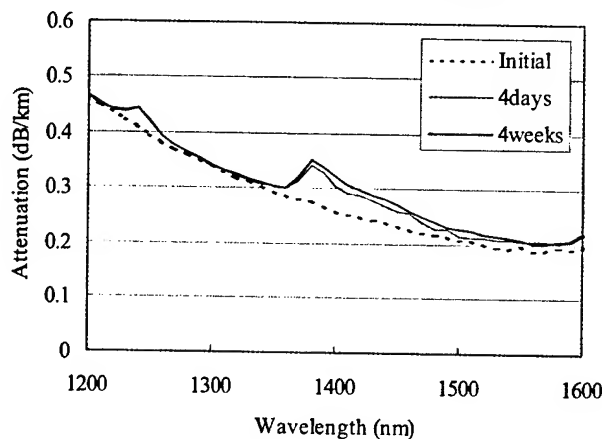


Figure 2. Spectral attenuation changes after exposures to 1.0 atmosphere of hydrogen at room temperature (Fiber A)

In the Figure 3, the induced attenuation due to hydrogen reaction at 1380 nm after 4 days exposure of the Fiber B is 0.01 dB/km. The attenuation increase, however, tends to increase up to 4 weeks. The attenuation at 1380nm reaches to 0.34 dB/km after 4

weeks exposure. The attenuation at 1430 nm can be also found in this figure and reaches to 0.30 dB/km after 4 weeks exposure.

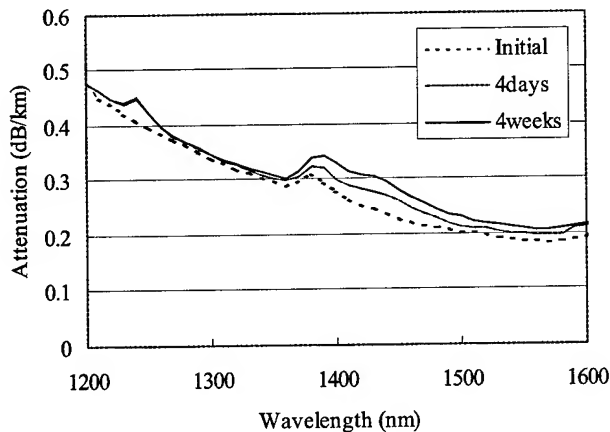


Figure 3. Spectral attenuation changes after exposures to 1.0 atmosphere of hydrogen at room temperature (Fiber B)

Figure 4 indicates that the stability performance against hydrogen of Fiber C is more stable than other LWP-SMFs (Fiber A and B). The attenuation at 1380 nm and 1430 nm after 4 weeks exposure reaches to saturation with 0.29 dB/km and 0.25 dB/, respectively.

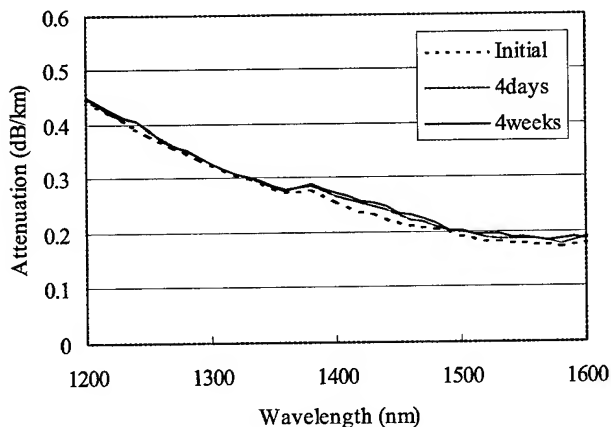


Figure 4. Spectral attenuation changes after exposures to 1.0 atmosphere of hydrogen at room temperature (Fiber C)

Figure 5 shows the induced attenuation due to hydrogen aging of all of the sampled fibers. The aging condition is after 4 weeks exposure to 1.0 atmospheres of hydrogen at room temperature. The attenuation at 1380 nm of the Fiber A (LWP-SMF) and the Fiber D, E (Standard SMFs) are particularly remarkable. The

induced attenuation at 1430 nm is also noted. They have long tails on the longer wavelength side and the affected the attenuation in the 1550 nm operation window and beyond. Although the attenuation at 1380 nm of the Fiber B relatively maintains low, the attenuation at 1430 nm is striking. These attenuation increases may affect serious problems to the Raman amplification and also CWDM system for entire life of service. On the other hands, it is obvious that the attenuation in the 1400 nm band of Fiber C (the newly developed LWP-SMF) still remain stable compare to others.

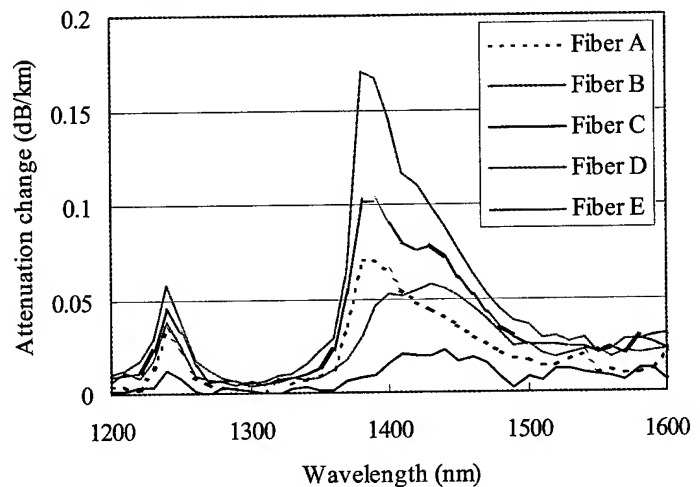


Figure 5. Induced attenuation variations after exposures to 1.0 atmosphere of hydrogen at room temperature after 4 weeks

4. Conclusions

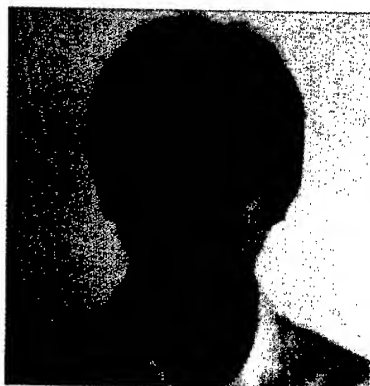
Accelerated aging test under 1.0 atmosphere of hydrogen at room temperature have been conducted with kinds of LWP-SMFs and Standard SMFs. Through these experiments, the excellent stability performance against hydrogen aging of PureBand™, the newly developed LWP-SMF, is clarified. Due to its stability and low water peak characteristics, the fiber provides superior attenuation performance throughout entire operation wavelength range for CWDM systems with long-term reliability over 25 years

5. References

- [1] M. Ogai, et al, "Absorption Peak at 1.52 μ m in Silica Fiber", *ECOC'86 Technical Digest*, pp.7-10,(1986)
- [2] M. G. Blankenship, et al, "Short-Term Transient Attenuation in Single-Mode Optical Fibers Due to Hydrogen", *OFC/IOOC'87 Technical Digest*, paper WA3, (1987)
- [3] K. H. Chang, et al, "New Hydrogen Aging Loss Mechanism in the 1400 nm Window," *OFC/IOOC '99 Technical Digest* paper PD22, (1999).

- [4] T. Voots , et al, "Hydrogen Aging of Optical Fiber at Low Partial-Pressure," *Proceedings NFOEC 2000*, 473-479, (2000).
- [5] Tests for optical Fibers," *Proceedings IWCS2001*, 219-223,(2001)

Authors



Fumiyoshi Ohkubo

Fumiyoshi Ohkubo received his B.S. and M.S. degrees in Mechanical Engineering and Material Science from Yokohama National University in 1993 and 1995, respectively. He spent seven years as an engineer of Fiber Optics in Sumitomo Electric Industries, Ltd. His current responsibilities include technical support for optical fiber to cable manufacture and end user customers.



Hajime Igarashi

Hajime Igarashi received his B.S. degree in Electric Engineering from Waseda University in 1988. In 1988, he joined Sumitomo Electric Industries, Ltd. and has been engaged in Fiber Optics Engineering Department. Currently, he is a senior engineer in the area of optical fiber engineering and customer's support.



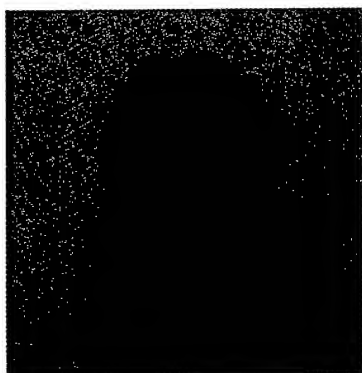
Hideyuki Wakiyasu

Hideyuki Wakiyasu received his B.S. and M.S. degree in Chemical Engineering from Kyoto University 1991 and 1993, respectively. In 1993, he joined Sumitomo electric Industries, Ltd. and has worked on the manufacturing engineer of optical fiber. He is now a senior engineer of the Fiber Optics Engineering Department



Kazuaki Negishi

Kazuaki Negishi received his B.S. and M.S. degree in Electrical and Computer Engineering from Yokohama National University in 1998 and 2000, respectively. In 2000, he joined Sumitomo electric Industries, Ltd. In his current position, he works on the Fiber Optics Engineering Department.



Takashi Hasegawa

Takashi Hasegawa joined Sumitomo Electric Industries, Ltd. in 1995 after receiving his B.S. degree in Applied Physics from The University of Tokyo. Currently, he is an engineer of the Optical Fibers Manufacturing Department.



Kazuya Kuwahara

Kazuya Kuwahara received his B.S. degree in Applied Physics and M.S. degree in Energy Science from Tokyo Institute of Technology in 1991 and 1993, respectively. In 1993, he joined Sumitomo electric Industries, Ltd. and has worked on the research and development of optical fiber. Currently, he is a senior engineer of the Optical Fibers R&D Department.

Multi- and Single Mode Fiber in One for Higher Bandwidth Applications

Andrew KACZMARSKI*, Mohamed TANANA**

*Pirelli Telecom Cables & Systems Australia P/L
Liverpool, NSW, Australia
+61 2 9600 0475 andrew.kaczmarski@au.pirelli.com

**CISCO Systems
North Sydney, NSW, Australia
+61 2 8448 7100 mtanana@cisco.com

Abstract

In this study, a newly developed waveguide characterized as both a multimode and singlemode fibre has been connected to several of the latest CISCO transmission equipments to investigate the number of errors and the maximum distance in comparison to the latest edition of ISO/IEC 11801:2002 standard. In order to meet the rapidly increasing demand for broadband services in Local Area, Access and Metropolitan Networks, we have proposed a newly developed universal optical fiber.

Fast growth and continuously expanding needs of the information technology set expects increasing flexibility and productivity from the telecommunication cable industry. At this moment there are, typically, three types of fibers utilised in these applications, 9/125 μm single mode as well as 50/125 and 62.5/125 μm multimode. In particular for fiber optic cable production, this means at least three different products which complicate manufacturing, distribution, installation and final optical system commission.

Keywords

Single Mode (SM); Multi Mode (MM) optical fiber; Gigabit Ethernet; Optical fiber cable network; Wide Passband; SDH; Access networks; Fiber To The Home (FTTH).

1. Introduction

Copper Cabling, Cat5E or Cat6, is still the basic choice for distribution cabling in Local Area Networks (LAN) due to its relatively low cost and ease of installation. However, the growing use of graphics in emails, web traffic within the LAN, and resource hungry software applications, is driving an increasing demand for more bandwidth, which in turn is driving a migration to fiber for backbones and fiber to the desk cabling. MM fiber (mainly 62.5/125 μm or OM1 -

optical multi mode as it is now referred to in ISO/IEC 11801:2002 standard), is still the fiber of choice for most LANs. Although, the same drivers that are driving the migration to optic from copper are also driving a shift from 62.5/125 μm MM to higher bandwidth 50/125 μm MM and also to Single Mode fibres.

Since the basic element in optical cables is glass fiber, the traditional range is now facing new challenges such as uniform high-speed production and advanced transmission equipment applications.

It wasn't very long ago that we were all happy with 10/100 Mbps to the desk. We are now in a fairly quick migration phase to Gigabit Ethernet with 10-Gigabit Ethernet waiting in the wings. As we move through these stages, using fibre for at least part of the network becomes mandatory as copper will not provide the bandwidth or distance needed.

2. High performance fiber and the latest transmission equipment

The universal multi / single mode fibre (FineLight™) has undergone extensive mechanical and optical testing using the latest electronic equipment at speeds up to 1000 Mbps (Gigabit Ethernet) at 850 nm operating as a Multimode fibre and at 1300 nm operating as a Singlemode fibre. The universal fibre also operates as a single mode fibre at both 1310 nm and 1550 nm in full compliance with ITU-T G.652. Testing has been undertaken to confirm Singlemode operation to at least 2.5 Gbps (SDH). The results demonstrate a significantly better performance than the minimum requirement of the standard parameters.

That patented fiber is available in many cable construction types, from Simplex and Duplex patch cords to Indoor/Outdoor Tight Buffered Riser cables featuring a LSOHFR (low smoke zero halogen flame retardant) sheath, to Jelly Filled Outdoor Loose Tube cables for all external applications. Composite cables are now a thing of the past, as individual fibers within a multi fiber cable can be used as

either Multimode or Singlemode, giving greater flexibility than a standard MM / SM composite cable.

3. Experiments

The universal fiber has been used in an experimental setup to generate bi-directional transmission using latest generation CISCO switches, connected as shown in Fig. 1

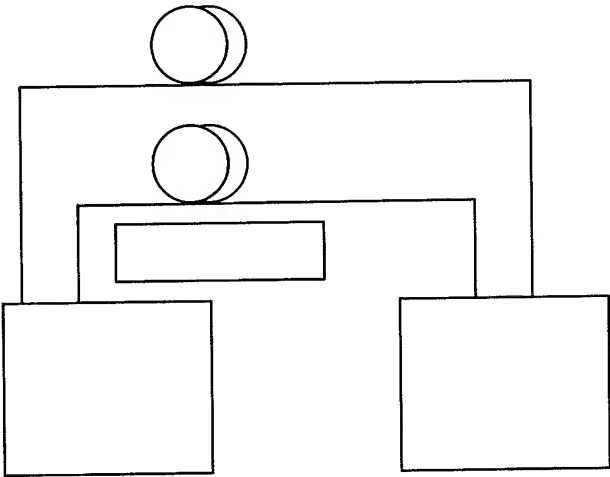


Figure 1. Schematic diagram of test setup

3.1 Technical data of new fiber

Glass geometry	
Cladding diameter	$\mu\text{m } 125.0 \pm 1.0$
Cladding non circularity	$\% \leq 2.0$
Core/cladding concentricity error	$\mu\text{m} \leq 0.8$
Coating geometry	
Outer coating diameter	$\mu\text{m } 245 \pm 10$
Coating/cladding concentricity error	$\mu\text{m} \leq 12.5$
Attenuation coefficients	
@850 nm	$\text{dB/km} \leq 2.20$
@1310 nm	$\text{dB/km} \leq 0.40$
@1385 nm (water peak)	$\text{dB/km} \leq 2.10$
@1550 nm	$\text{dB/km} \leq 0.30$
Macrobending attenuation	
100 turn, 60 mm diameter at 1550 nm	$\text{dB} \leq 0.1$
Dispersion coefficients	
In the range 1285 –1330 nm	$\text{ps}/(\text{nm.km}) \leq 3.5$

@1550 nm	$\text{ps}/(\text{nm.km}) \leq 18$
Zero dispersion wavelength (λ_0)	nm 1300 to 1324
Slope S_0 at λ_0	$\text{ps}/(\text{nm}^2.\text{km}) \leq 0.092$
Mode Field Diameter	
@1310 nm	$\mu\text{m } 9.2 \pm 0.4$
Cable cut-off wavelength (λ_{cc})	$\text{nm} \leq 1260$
Bandwidth @850 nm	
FineLight™Base	$\text{MHz.km} \geq 600$
FineLight™Giga	$\text{MHz.km} \geq 1000$

3.2 Test network

In this study, several latest generation CISCO transmission equipments have been inter-connected with Universal fiber to investigate the number of errors and the maximum distance in comparison to ISO/IEC 11801:2002 and other relevant standards. 2.5 Gbps SDH, 1000BASE-SX and 1000BASE-LX transmission applications have also been tested. Details of the test set up are shown in Fig.2.

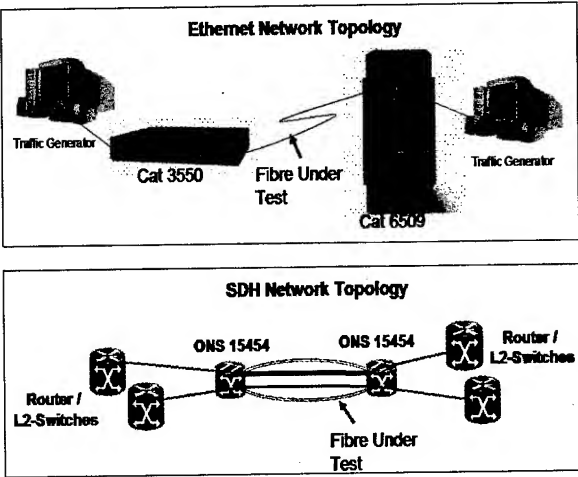


Figure 2. Detailed diagram of test setup

3.3 Theoretical bandwidth calculation

The theoretical bandwidth was calculated before the experimental trial.

Table 1 shows theoretical MM bandwidth (BW) of the new fiber.

With the assumption about linearity of the material dispersion across the optical fiber cable length, the following non-linear calculation applies for the final bandwidth:

$$BW_F [\text{MHz.km}] = (dL_{IN}/dL_{OUT})^{\gamma} \times BW_{IN}$$

Where:

L_{IN} – input length [km]

L_{OUT} – output length [km]

γ – bandwidth to length exponent coefficient

BW_{IN} – input bandwidth [MHz.km]

Table 1. MM Bandwidth of Fiber [MHz.km]

Input BW MHz.km	Gamma	Input Length h [km]	Output Length [km]	Final BW [MHz]
600	0.5	1	0.8	671
600	0.7	1	0.8	701
600	1	1	0.8	750

Table 2 shows theoretical SM bandwidth (BW) of the new fiber.

The standard single mode fiber bandwidth is calculated as the following:

$$BW = 44 \times 10^4 / (DW \times Dw \times L)$$

Where

DW – source spectral width

Dw – pulse broadening due to chromatic dispersion,

L – cable length

44×10^4 – empirically derived constant

Delta (chroma) – dispersion at the wavelength

Table 2. SM Bandwidth at 1550 nm of Fiber [MHz.km]

Delta Wave-length [nm]	D (wave-length) [ps/nm.km]	Length h [km]	Delta (chroma) [ps]	BW (chroma) [MHz]
2	18	25	383	489
2	18	5	77	2444
0.8	18	12	73	2546

3.4 Test methodology

The test generated bi-directional pings to observe interface statistics and Bit Error Rate (BER) of better than 10^{-12} has been demonstrated. A randomly selected sample of FineLight™ Base, as the lowest performing fibre (from a bandwidth perspective) in the range, has been used to simulate the worst condition from the bandwidth point of view. SC single mode bare fiber adapters have been used to connect fibre to equipment.

4. Experimental Results

Table 3 summarizes the results of the maximum length of the new fiber over which transmission was achieved with BER < 10^{-12} as measured on the CISCO Catalyst switches. The results achieved were without the use of any mode conditioning patchcord.

Table 3. Length [m] vs. transmission type

Switch	Max distance [m]	ISO/IEC 11801:2002
1000BASE-SX	800	550
1000BASE-LX	800	550

5. Discussion

The new fiber is capable of:

- Good bandwidth as a Multi Mode fiber, at current protocols using relatively inexpensive laser opto - electronics at 850 nm
- Insertion loss @ 850 nm is generally lower due to less dopant content than standard multi-mode fiber.
- Ability to switch to a Single Mode system utilising 1310 and 1550 nm window without the need to replace installed cables.
- Offers "decision deferring" benefits, in that the same cable can be used as both a Multimode and Single Mode cable, without having to install new fiber
- Offers "cost deferring" benefits, in that inexpensive Multimode fiber electronics can be utilised at the start and then upgrade to the higher performing Singlemode electronics as the price comes down or the need arises

6. Conclusions

The new developed Universal fiber (FineLight™) has brought a breakthrough in optical design. The FineLight™ fiber is a world first in that it operates at three windows (850, 1310 and 1550 nm), or in other words it can be used as both a Multimode (MM) and a Singlemode (SM) fiber. New Universal fiber is able to withstand emerging higher demands and to achieve stable performance in a wide range of the latest transmission equipment including Gigabit Ethernet and SDH.

7. Acknowledgments

The authors thank L. Roberts and S. Mennie of Pirelli Telecom Cables & Systems Australia, and W. Nixon of Cisco System, for support, discussion, and encouragement.

8. References

- [1] A. Kaczmariski and R. Beattie, "Merging your modes for cost and convenience," *Cabling Install. & Mainten. Mag.*, p. 52-54 (April/May, 2002).
- [2] A. Kaczmariski, "New generation multimode fibre," *Cabling Install. & Mainten. Mag.*, p. 60-62 (Dec/Jan, 2002).
- [3] A. Kaczmariski, "Cat6 caters for the future," *Cabling Install. & Mainten. Mag.*, p. 52-55 (Feb/March, 2002).
- [4] A. Kaczmariski, "High bit-rate fiber that can go anywhere," *Cabling Install. & Mainten. Mag.*, p. 42-43 (Dec/Jan, 2001).
- [5] A. Kaczmariski, "Monitoring trial on all-dielectric, self supporting, optical cables for power line use in Australia," *19th Australian Conference on Optical Fibre Technology (ACOFT, 1994)*.
- [6] A. Kaczmariski, "Optical fibre cable for overhead power lines," *Electrical Engineer Mag.*, (April, 1995).
- [7] F.I. Pomarico, M. Artiglia, E. Besozzi, S. Cozza, "BER measurements using 850-nm VCSEL on optimizes SMF with ultra-low inter modal dispersion at short wavelengths," *7th European Conference on Network & Optical Communication*, (June 18-21, 2002).



Andrew Kaczmariski is a technical product manager at Pirelli Telecom Cables & Systems Australia, Sydney. He received a B.S and M.S. degree in Electronics Engineering from Technical University of Gdansk, Poland in 1985. Worked within the Cable Industry for 9 years and has been with Pirelli for 2.5 years. In this period he has covered all aspects of optical and copper fiber cable design and has a broad experience of product management. Andrew has contributed over years to various technical standards (AS/NZS 3080, AS 1049, ACA

TS008 and the AS 3086 series of standards). He is the CT/1 Standard Australia Committee Member and IEEE member. Andrew is the author or co-author of several patents. Received "2002 Pirelli Inventions Award" for patent applications.



Mohamed Tanana is a System Engineer with Cisco System's Australia Operations. Currently working in the Service provider Team providing advanced next generation solutions to tier 1 service Providers.

1.25 Gb/s enhanced transmission performance on standard Single-Mode Fiber optimized for operating at 850-nm using single-mode VCSEL

Francesco Ivan Pomarico,

Massimo Artiglia

Fiber Optics Labs, Pirelli Cables and Systems Telecom SpA
Viale Sarca 222, Milano -20126-ITALY
+39 02 6442.7899 ivan.pomarico@pirelli.com

Abstract

Enhanced transmission performance at 850 nm on a novel fiber [1], compliant with Single Mode Fiber as described in ITU-T Rec. G.652, using recently developed single mode vertical-cavity surface-emitting laser (VCSEL), is demonstrated experimentally and briefly discussed in terms of coupled power and bit error rate (BER) measurements. Finally experimental power penalties, chiefly due to intersymbol interference (ISI), are presented for single mode VCSEL transmitting on different DMD samples of novel fiber.

Keywords

Fiber, singlemode fibre, multimode fibre, vertical cavity surface emitting laser, single mode VCSEL, Gigabit Ethernet, modal bandwidth.

1. Introduction

To support the steady growth of corporate Intranets and Internet traffic, many building backbone links in local area networks (LAN) are typically based on optical fibers. Also last mile links in access network are following this trend (FTTx). Usually the majority of LAN links are multimode fiber (MMF), however, some single mode fiber (SMF) is also present. Generally speaking, SMF, compliant to ITU-T G.652, is preferred to MMF when the current demand for bit rate and distance exceeds actual MMF capability, while mixed cables of MMF and dark SMF are sometimes deployed when future bit rate demand is of concern. These links typically operate at 850 nm to take advantage of low cost opto-electronic components, such as LEDs. However LEDs suffer from serious bandwidth and power limitations, which make them unsuitable to high speed transmission. Currently, the most utilized light source in high-bit-rate short haul optical data link is the 850 nm vertical-cavity surface-emitting laser (VCSEL), with its low cost and higher bandwidth compared with LED. However, most of the installed MMF are not suitable to support gigabit applications (i.e. GbE, Fiber Channel, etc..) and new types of MMF optimized for laser launch are been developed and marketed [6]. As far as SMF is concerned, at 850 nm SMF generally supports few modes and suffer from serious limits to the

bandwidth due to the rather high inter modal dispersion. This is the main reason why SMF has not been considered in practice for FTTx and LAN applications, despite the great interest shown in the past years [2-5]. To get around the outlined drawbacks of SMF and MMF, and to ensure the maximum flexibility and scalability of network, a SMF having high bandwidth at short wavelength (SX), 850 nm, and maintaining SMF optical properties in second and third operating windows (i.e. 1300 nm and 1550 nm) has been recently presented [1]. In particular, [1] demonstrated feasibility of error free Gigabit Ethernet (1.25 Gbit/s) transmission at 850 nm over up to two kilometers of this novel SMF and STM1/OC3 (155 Mb/s) over up to 7.4 km using commercially available multimode VCSEL.

In this paper we point out advantages of using this novel fiber especially with the recently developed 850nm single mode VCSEL, in terms of coupled power and BER performances. Moreover, intersymbol interference penalties were measured for this novel system, showing good agreement to Gigabit Ethernet model prediction.

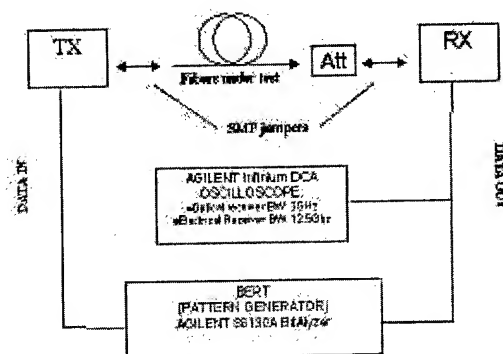


Figure 1: Schematic diagram of experimental setup

2. Experimental setup

The experimental setup used to carry out the transmission experiment is schematically shown in Fig.1. An 850-nm transmitter driven by a pattern generator is coupled to the fiber under test and an 850nm precision variable attenuator is positioned before the receiver to vary the received optical power. The received optical

power is measured by means of a power meter. Fiber spans are coupled to the transmitter and receiver by means of two conventional single mode jumpers with SC connectors, while the SC connectorized fibers under test are connected each other using commercial SC adapters.

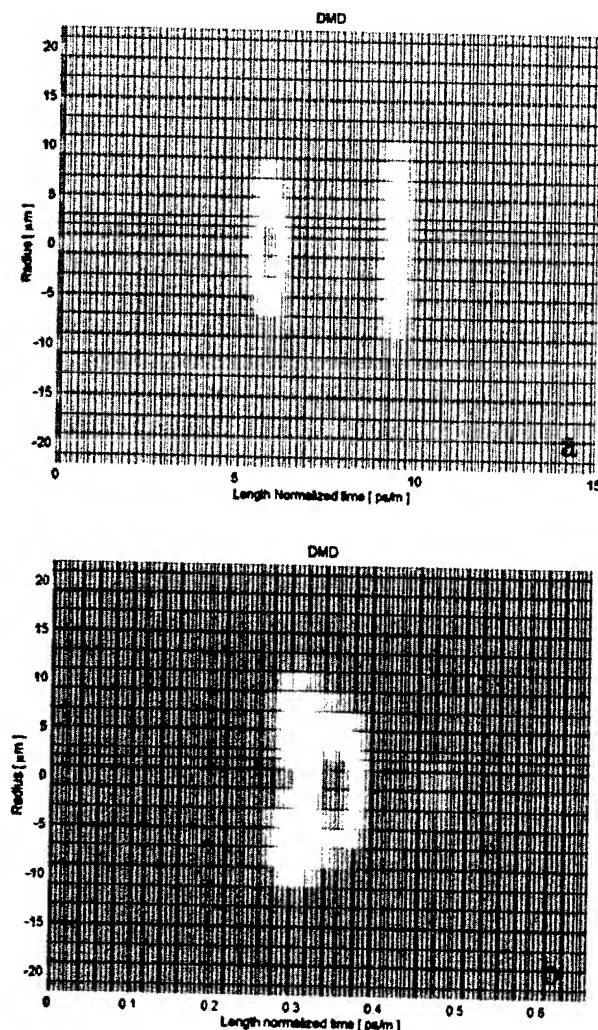


Figure 2 : Differential Mode Delay measurement at 850-nm for a) SMF (DMD of about 3 ps/m) and for b) SX optimized SMF (DMD of about 0.1 ps/m).

A sample of single mode VCSEL, in TO package, having a spectral width of less than 1-nm and operating at the nominal wavelength of 850-nm, has been utilized for the experiment. The data sequence is generated using a PRBS ($2^{23}-1$ word length), which directly drives the single mode VCSEL. A 3 GHz bit error rate test set (BERT) compares the electrical signal taken at the receiver output with the original sequence. Electrical signals are observed by means of a sampling oscilloscope equipped with a 12.5 GHz electrical receiver. An optical receiver of a commercial transceiver, compliant with IEEE802.3z/D2 Gigabit Ethernet (1000BASE-SX)

specification is utilized to receive the optical signal at GbE bit rate of 1250 Mb/s.

3. Fiber Description

In the wavelength region around 850-nm, G.652 fibers (optimized for operation around of 1310-nm) usually propagate few modes (linear polarized mode LP_{01} , LP_{11} , LP_{02} etc...). Two-mode (LP_{01} and LP_{11}) fiber systems based on inter modal delay equalization have been widely studied [7,8] in order to address several different applications. Refractive index profiles have been suggested to achieve zero-modal dispersion at 1300-nm [9] or in 800-900-nm wavelength range [10]. The refractive index profile of this novel fiber allows to obtain very good modal equalization around 850-nm and to guarantee excellent transmission performance with good manufacturing reproducibility. The manufactured fibers show typical inter-modal delay at 850-nm of less than 0.3 ps/m over a wide wavelength range, which inherently guarantees a -3dB worst case modal bandwidth higher than 1000 MHz.km. Since VCSEL is a laser source with spectral width generally less than 1-nm, chromatic dispersion is of low concern compared to inter modal dispersion in few kilometer systems at the considered bit rates. To evaluate inter-modal dispersion, differential mode delay (DMD) of a typical SMF and of the new SX optimized SMF has been measured. Results are shown in figure 2. In the DMD measurement procedure (FOTP-220 or IEC 60793-1-49), the fibre core is scanned at the entrance using a small spot size and very short pulse, while the corresponding output pulses are registered consecutively. In this way the modal delay structure of the fibre is found. Compared to the well-known bandwidth test methods, the DMD test method is capable of giving much more detailed information on the propagation characteristics of the different modes in multimode region of SMF.

DMD of a typical SMF at 850nm is reported in figure 2a. The modal structure of the fiber is clearly visible and the length normalized delay is of the order of 3 ps/m. In figure 2b DMD for a short wavelength optimized SMF is reported, showing a DMD of the order of 0.1 ps/m. As can be seen the propagating modes appear confused in a single spot. The measured loss of the fiber around 850-nm is less than 2 dB/km, typically 1.8 dB/km at 850-nm.

4. Single-mode vs. Multi-mode VCSEL

In [10], benefits of single mode VCSEL with respect to multimode VCSEL have been experimentally demonstrated and widely discussed. In particular authors of [10] analyzed important quantities like eye opening, on/off ratio and BER at different lateral offsets of laser device, pointing out better performance of single-mode compared to multi-mode VCSELs. Moreover, single-mode VCSEL can be coupled more efficiently than multi-mode VCSEL or LED to any optical fiber (i.e. MMF or SMF) without optics or with simple ball lens, due to its tighter circular beam shape. In our experiment, we used a single mode VCSEL coupling about -5dBm to SX optimized SMF. Generally speaking, single mode VCSEL can couple up to -3dBm on 9/125 micron diameter fiber, improving by about 10 dB the typical power coupled by an

“out of the shelf” multimode VCSEL. For all these reasons, single-mode VCSELs are very attractive laser sources for short haul systems and of course can match very well with SX optimized SMF. This feature greatly reduces any power budget limitation in short haul systems.

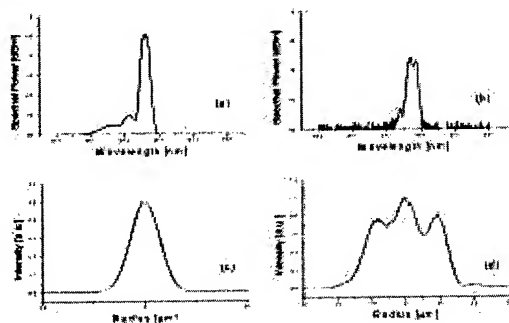


Figure 3 Examples of measured emitted spectrum for (a) single mode and (b) multimode VCSEL and typical spatial intensity distribution for (c) single mode and (d) multimode VCSEL

Figure 3a and 3b show the measured emitted spectrum for the single mode utilized for the system measurements and of a typical multimode VCSEL, while figure 3c and 3d show typical spatial intensity distribution of a single mode and a multimode VCSEL. This feature and the higher peak power account for the easier coupling of single mode VCSEL with any optical fiber, especially with a 9 micron core diameter fiber (i.e. SMF or the newly developed SX opt. SMF).

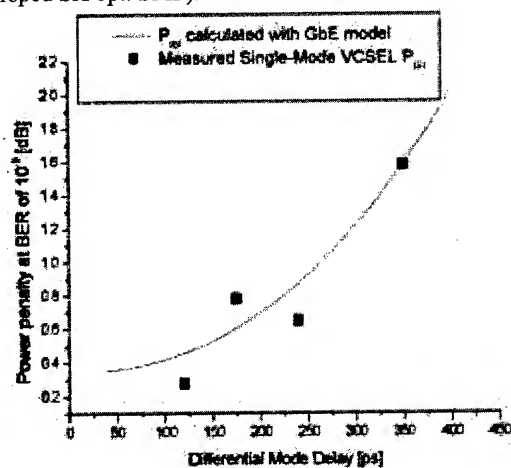


Figure 4: Penalties versus differential mode delay. Theoretical prediction (solid line) and measured penalty (filled squares).

5. Experimental results

We have measured power penalty of several SX optimized SMFs, having different DMD figures, using one sample of 850nm single mode VCSEL. The results are shown in figure 4 (filled squares).

The potential of this new fiber in terms of BER versus distance has been already demonstrated in a previous paper [1]. In order to get better insight in to our experimental data, we used the theory of Gigabit Ethernet model [12], adopted by IEC (series 61280) to draw a theoretical curve of power penalty versus measured DMD of the selected fibres, as shown by the solid line in figure 4.

The gigabit Ethernet model accounts for power penalties due to noise and dispersion [12]. In the present paper a rough evaluation of intersymbol interference power penalty (P_{ISI}), using formula of [12], is used and compared to experimental measured power penalty at a BER of 10⁻⁹. It is assumed that P_{ISI} is generally the most important penalty factor compared to other penalties affecting the link, such as mode partition noise (MPN), extinction ratio (ER) and relative intensity noise (RIN). P_{ISI} is evaluated using:

$$P_{ISI} = \frac{1}{1 - 1.425 \cdot \exp \left[-1.28 \left(\frac{T}{T_c} \right)^2 \right]} \quad (1)$$

where T is the bit time and T_c is the approximate 10-90% composite channel exit response time, given by

$$T_c = \sqrt{\left(\frac{0.48}{BW_m} \right)^2 + \left(\frac{0.48}{BW_{cd}} \right)^2 + T_s^2 + \left(\frac{0.35}{BW_r} \right)^2} \quad (2)$$

where BW_m is the modal bandwidth, here assumed equal to the worst case -3dB bandwidth and related to DMD by

$$BW_m = 1/(3 \cdot DMD) \quad (3)$$

BW_{cd} is the bandwidth due to chromatic dispersion, calculated using (16-17) of [12] and measured values for dispersion, dispersion slope and zero dispersion wavelength of the samples. T_s is the 10-90% laser rise time, here assumed to be ~390 ps, in accordance with our experimental data, while BW_r is the receiver bandwidth (about 1000MHz for the used receiver). Measured power penalties are reported versus DMD values of the used fiber spans. All the analyzed links have length comprised between 500 m and 1 km. Although some penalty factors of GbE model has been neglected and the power penalties has been related only to worst case modal bandwidth (i.e. DMD), yet agreement between measured data and theory is rather good, meaning that the major penalty in the optical system under test is chiefly due to modal dispersion.

As can be seen, measured penalty is well below 1 dB for DMD lower than 300 ps, this ensures that fiber, having a DMD specification lower than 0.3 ns/km, could operate with very good performance over distances typical of LAN applications and more (i.e. up to 1 km). The presented results are only preliminary, being based on laboratory setup and not on a fully engineered system

optimized for field operation. For this reason it has not been possible to carried out a meaningful comparison with multimode VCSEL. Further work is under way to settle validity of GbE model to this novel system configuration.

6. Conclusions

VCSELs technology is rapidly evolving towards higher performances at lower prices. This new technology matches very well with the recently presented SMF optimized for short wavelength operation [1], allowing to obtain the very high network flexibility and scalability in LAN and FTTx applications. In this paper the SX optimized SMF has been tested at G E speed using recently developed single mode VCSELs, which already showed improved BER performances [11] at moderate bit rates on standard MMFs. Using single mode VCSELs, very good power coupling efficiency has been demonstrated (-5dBm), with a consequent 10 dB improvement of power budget with respect to multimode VCSEL. Moreover power penalty, chiefly due to ISI, has been measured and compared with theory of Gigabit Ethernet model. Good agreement was found. The measured penalty of 1km long fibers, having DMD lower than 300 ps, is well below 1 dB, ensuring that SX optimized SMF performance at Gigabit Ethernet speed could exceed distances typical of LAN applications (i.e. up to 1 km).

7. Acknowledgments

The authors are greatly indebted to R. Stefanutto and G. Rossi for providing numerous electrical and optical components used in the measurements. Helpful discussions with S. Cozza and A. Rampulla are also gratefully acknowledged.

8. References

- [1] F. I. Pomarico, M. Artiglia, E. Besozzi, S. Cozza "BER measurements using 850 nm VCSEL on optimized SMF with ultra-low inter modal dispersion at short wavelengths", NOC 2002, 18-21 June, Darmstadt - Germany.
- [2] T. Nance and Shenk, "Lightguide applications in the loop" AT&T Tech J., vol 66 no 1 (1987) pp.108-115.
- [3] G. Morgensen et al., "RACE project R1030, ACCESS- A system study of the broad-band subscriber loop" J. Lightwave Technol., vol LT-7, no. 11, (1989) pp 1715-1726.
- [4] C. Gartside, III, A. Panuska and P. Patel, "Single-mode cable for long-haul, trunk, and loop networks", AT&T Tech. J., vol. 66, no.1, (1987), pp.84-94.
- [5] R. Ries, "Signal Transmission with optical carriers in multimode range of single mode fibres", Electron. Lett., Vol. 23, No. 2 (Jan. 1987), pp.71-72.
- [6] R. Michalzik, G. Giaretta, A.J. Ritger and Q. L. Williams, "10 Gb/s VCSEL based data transmission over 1.6 km of new

generation 850 nm multimode fiber", IEEE J. Sel. Top. Quantum Electron., vol. 5, (1999), pp 503-511.

- [7] K. Suto and E. Yoneda, T. Hayakawa and T. Tuchiya, "0.78-mm Digital Transmission Characteristics Using 1.3-mm Optimized Single-Mode Fiber for a Subscriber Loop", Elec. and Comm. in Japan, Part 1, Vol. 75, No.2 (1992), pp.38-47.
- [8] K. Kitayama, Y. Kato, S. Seikai, N. Uchida and M. Akiyama, "Transmission Bandwidth of the Two -Mode Fiber Link", IEEE J. of Quantum Electron., VOL. QE-18, No 11, (November 1982), pp.1871-1876.
- [9] L.G. Cohen, W. L. Mammel, C. Lin, and W.G. French, "Propagation characteristics of double-mode fibers," Bell Syst. Tech. J., vol. 59, (1980), pp. 1061-1072.
- [10] V. A. Bhagavatula, J.C. Lapp, A. J. Morrow, and J. E. Ritter, "Segmented-Core Fiber for Long-Haul and Local-Area-Network Applications", J. of Lightwave Techn., vol. 6, No. 10, (Oct. 1988), pp. 1466-1469.
- [11] S. W. Z. Mahmoud, D. Wiedenmann, M.Kicherer, H. Unold, R. Jäger, R. Michalzik and K.J. Ebeling, "Spatial investigation of Transverse Mode Turn-On Dynamics in VCSELs", IEEE Photonics Technology Letters, VOL. 13, NO. 11, November 2001.
- [12] MARK C. NOWELL, DAVID G. CUNNINGHAM, DELON C. (DEL) HANSON and LEONID G. KAZOVSKY, "Evaluation of Gb/s laser based fibre LAN links:Review of the Gigabit Ethernet model", Optical and Quantum Electronics 32: 169-192, 2000.



Francesco Ivan Pomarico was born in Paderno D. (MI), Italy on January 8, 1972. He received is master degree in Physics from University of Milan in 1997 (Summa cum Laude). After a brief experience in IT industry, he joint Pirelli in 2000 and is currently engaged in research on optical fiber design for data communication, especially

for LAN and FTTx applications. He is inventor of one patent and author in technical papers and technical presentations for the market.

Massimo Artiglia was born in Turin, Italy on May 27, 1953. He received is master degree in Physics from University of Turin (Summa cum Laude). He has been working on optical communications since 1985 at CSELT, R&D center of Telecom Italia, and joint Pirelli in 2000 where he is supervising the new product development group at R&D optical fiber, Fiber Optics Labs. He is involved in various standardization committees in ITU-T and IEC and is a member of OSA. He is author or coauthor or more than 80 technical papers and is inventor or co inventor of various patents.

The Study of Optimized Design Optical Fibers for WDM Transmission Systems

**Kazumasa Ohsono¹ Yao Bing¹ Tatsuya Shirosawa¹
Tomomi Onose² Tetsuya Sukegawa³**

1. The 4th Dept. Optoelectronic System Laboratory, Hitachi Cable, Ltd.
2. Optical Fiber & Device Dept. 3. Optical Fiber Design Dept., Hitachi Cable Ltd.
Hitaka-cho, Hitachi-shi, Ibaraki-ken, 319-1414 Japan
Phone; +81-294-25-3837· email; ohsono.kazumasa@hitachi-cable.co.jp

Abstract

We have developed two new types of single-mode fiber for the next generation WDM transmission systems. The both fibers have wide non-zero dispersion operation wavelength band over S, C and L bands. One type is LEF (Large Effective area non-zero dispersion Fiber) with an effective area of 63.8 m^2 . The other one is LSF (Low dispersion Slope non-zero dispersion Fiber) with dispersion slope of $0.013 \text{ ps/nm}^2/\text{km}$. We have ascertained that LEF had an advantage of Tbit/s transmission for long haul systems and also LSF had an advantage of Tbit/s transmission for metro ring systems, respectively, by using numerical transmission simulation.

Keywords

Large effective area fiber; low dispersion slope fiber; 40Gbit/s transmission; dispersion compensation

1. Introduction

The demand for data communication is growing rapidly due to the increasing popularity of the Internet and other factors. In about 1998 years, the transmission capacity per fiber increased to 10(20) Gbit/s per wavelength by wavelength Division Multiplexing (WDM) technique[1]. Moreover, in recent system, the overall transmission capacity exceeds 1Tbit/s per fiber by the improvement of the WDM techniques [2] [3]. In order to increase the transmission capacity, increasing the number of signal wavelengths, expanding the signal wavelength band and the high speed signal in the fiber are required. Those techniques cause increasing optical channel cross-talk and decreasing the allowable group velocity dispersion (GVD) tolerance. In order to increase the transmission capacity, the nonlinearities and the dispersion characteristics of transmission fiber have to be considered. The most practical way to solve the nonlinearities is to enlarge

effective area (A_{eff}). And also the most practical way to solve the dispersion is dispersion management of system and to optimize the dispersion characteristics (cumulative-dispersion & dispersion slope) of fibers respectively [4] [5]. In this paper, we challenged to enlarge the A_{eff} and to optimize dispersion characteristics, namely lowering dispersion slope. Unfortunately, enlarging the A_{eff} and lowering dispersion slope is antithetical relation. Therefore we have investigated two types of fiber. These fibers are classified with non-zero dispersion fiber (NZDF) of ITU-T Rec. G655. One type is LEF and the other one is LSF. We describe LEF and LSF with analyzing the optimum characteristics for WDM transmission systems. As our achievement, LEF with effective area of 63.8 m^2 and LSF with dispersion slope of $0.013 \text{ ps/nm}^2/\text{km}$ have developed. We have validated the both fibers are useful for new generation WDM transmission systems.

2. Design and Simulation of Metro ring network system and Terrestrial long haul transmission system with LSF & LEF

2.1 Model of metro ring network and terrestrial long haul transmission system

In order to increase the transmission capacity, increasing the number of wavelengths, expanding the transmission wavelength and the high speed signal transmission line are required. To realize such a higher transmission capacity, the NZDF, which has wide non-zero dispersion operation band over S, C and L bands, has been proposed [6][7]. We selected two kind of NZDF for modeling a metro ring network system and a terrestrial long haul transmission system. One type is LEF with an A_{eff} of 65 m^2 . The other one is LSF with a dispersion slope of $0.02 \text{ ps/nm}^2/\text{km}$. We simulated both fibers (LSF LEF) transmission characteristic, using Sprit-Step-Fourier change method [8]. Figure 1 shows the block diagram of both systems (LSF system & LEF system), used

for the simulation. The transmission parameter of each composition modules and the optical fibers are shown in table 1. The transmission distance of metro ring network system is 200 km and terrestrial long haul transmission distance is 1200 km. The bit rate per channel of the simulation is 10 Gbit/s and 40 Gbit/s. NZDF used in the transmission line are LEF and LSF respectively. The setting of the simulation model of this examination is excluding the wavelength dependence of the dispersion compensation characteristic and the full compensation of the accumulated dispersion of each wavelength by fiber bragg grating (FBG). We evaluated a transmission characteristic by Q value. The criterion Q value in all signal wavelengths is equal to or more than 16 dB.

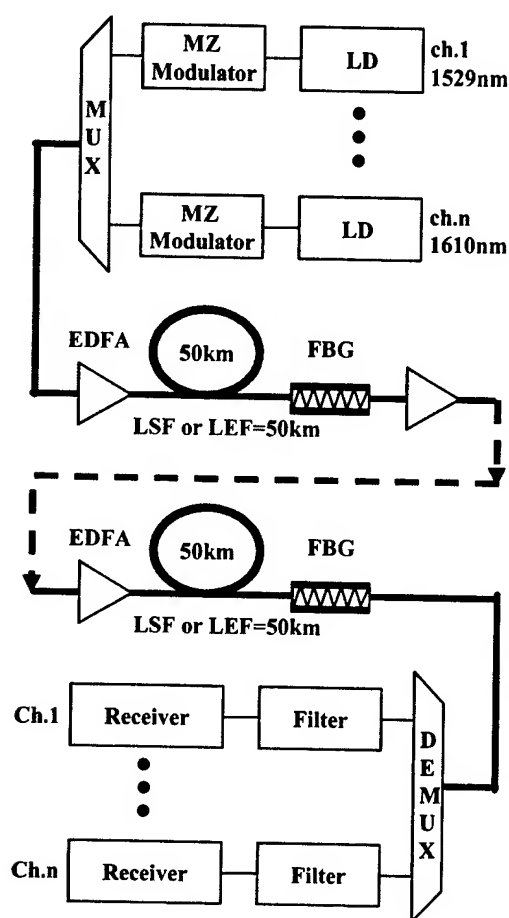


Fig.1 Block diagram of the DWDM system

Table.1 Transmission parameter of each composition modules and optical fibers

Bit rate [Gbit/s]	10	40
Channel spacing [GHz]	100	125
Number of channels	108	80
Bit format	NRZ,RZ-Gaussian	
Number of bits	2^7-1 PRBS	
Pulse width [ps]	20	
Transmission distance [km]	200,1200	
Filter width[nm]	0.25	
Filter factor	1024	
Repeater spacing[km]	50	
EDFA gain[dB]	10	
EDFA bandwidth[nm]	1530-1565(C), 1565-1625(L)	
EDFA NF[dB]	4.5	
Fiber character @1550nm	LEF	LSF
Dispersion [ps/nm/km]	8	2,4,6,8,-6
Dispersion slope [ps/nm ² /km]	0.06	0.02,-0.02
Fiber loss [dB/km]	0.2	0.2
Joint loss [dB/km]	-	-
Kerr coefficient: n_2 [m ² /W]	2.5	2.5
A_{eff} [m ²]	65	45,40
Fiber length [km]	50	50

2.2 Simulation of metro ring network system

The large capacity of transmission is indispensable for metro ring network systems. In addition, we also think that a cost of system construction shall be reduced. Thus, we examined by two different points of view. The one point is the system without the dispersion compensation. The other point is the repeater spacing. The both points are useful to decrease a cost of systems.

In a 104-ch \times 10 Gb/s metro ring network system over 200 km without dispersion compensation, we have compared the Q value of LSF (CD=2, 4 ps/nm/km, e.g. LSF_2, LSF_4) and LEF (CD=8 ps/nm/km, e.g. LEF_8). Figure 2 shows relation between repeater output power into fibers and Q value when bit format is at 100 GHz spacing NRZ signal. When the dispersion of LSF is 2 or 4 ps/nm/km (at 1550nm) and input signal power is -5 dBm, Q value is more than 16 dB. On the other hand, the Q value of LEF is far less than 16 dB. Therefore, LSF is very useful for a 104-ch \times 10 Gbit/s metro ring network system over 200 km because LSF is able to realize low cost system without the dispersion compensation.

In an 80-ch \times 40 Gb/s metro ring network system over 200 km, we have also compared the Q value of LSF (CD=2, 4, 6, 8 ps/nm/km, e.g. LSF_2, LSF_4, LSF_6, & LSF_8) and LEF (CD=8 ps/nm/km, e.g. LEF_8). Figure 3 shows relation between repeater output power into fibers and Q value when bit format is at 125 GHz spacing RZ signal. In all LSF, the repeater output power is limited up to about 5dBm. However LEF has higher tolerance input power than that of LSF. As shown in Figure 3, the tolerance of LEF is 4 dB more than that of LSF. As a result, LEF is able to expand the repeater spacing to 70 km. Expanding repeater spacing leads decreasing the number of repeater and reducing the constructing cost of system.

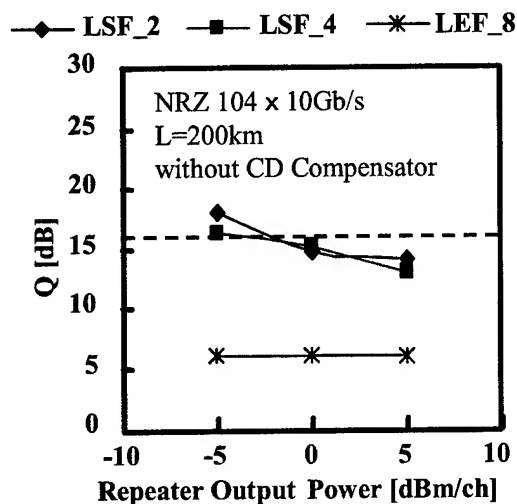


Fig.2 Relation between Repeater Output Power and Q value in a 104-ch 10Gbit/s over 200 km

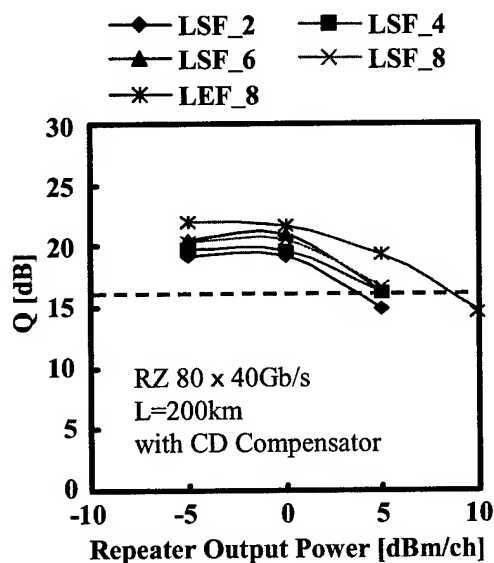


Fig.3 Relation between Repeater Output Power and Q value in a 80-ch 40Gbit/s over 200 km

2.3 Simulation of terrestrial long haul transmission system

Recent laboratory experiments have demonstrated that distributed Raman amplification and forward error correction (FEC) are key technologies for WDM terrestrial transmission [9] [10]. However we think that a cost of system constructing shall not be expensive. Therefore, we have examined the simple construction system. We first proved that the system without dispersion compensation was impossible because the accumulated dispersion could not be ignored. In a 104-ch \times 10 Gb/s terrestrial long haul system over 1200 km, we have compared the Q value of LSF (CD=6 ps/nm/km) and LEF (CD=8 ps/nm/km). Figure 4 shows relation between repeater output power into fibers and Q value when bit format is at 100 GHz spacing RZ signal. The repeater output power limitation of LSF is about 5 dBm. However, the repeater output limitation of LEF_8 is about 10 dBm. LEF has higher tolerance input power than that of LSF. The tolerance of LEF is 5 dB more than that of LSF. Therefore, LEF is able to expand the repeater spacing to 75 km. Thanks to decreasing the number of repeater, the constructing cost of system is reduced.

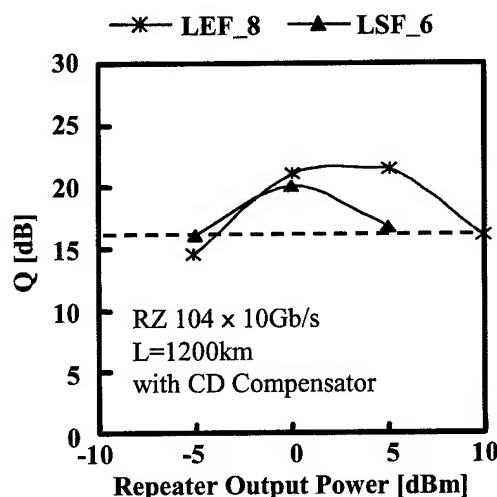


Fig.4 Relation between Repeater Output Power and Q value in a 104-ch 10Gbit/s over 1200 km

3. LSF design & performance

3.1 Fiber design

We have tried to optimize the refractive index profile of LSF. Figure 5 shows the profile model used in simulation. Considering dispersion slope, macro bending loss and the fabricating processes, we adopted the tetra clad structure with a deep depressed clad which has a -0.30 % refractive index. We have calculated the center core diameter to gratify targeting dispersion and slope value under setting the tetra cladding structure. We determined that core radius to achieve the dispersion of 3 ps/nm/km, the dispersion slope of 0.02 ps/nm²/km and the macro bending loss of less than 2dB/m at 1550 nm respectively.

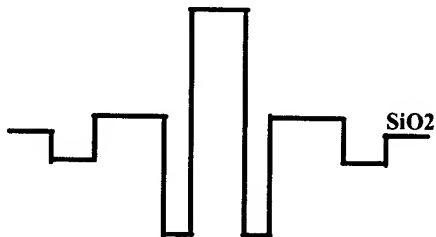


Fig.5 Refractive Index Profile Model of LSF

3.2 Fiber fabrication and performance

We fabricated LSF using the MCVD method. LSF has very complicated refractive index profile with a deep depressed clad. Figure 6 shows the relation between chromatic dispersion and the wavelength for the LSF. The chromatic dispersion is in the range from 1.7 to 3.8 ps/nm/km in S, C, and L bands. The dispersion slope at 1550nm is 0.013 ps/nm²/km. As we have shown in the simulation, this chromatic dispersion characteristic realizes 10 Gbit/s 104-ch WDM 200 km transmission for metro ring network system without dispersion compensation. Figure 7 shows the spectral attenuation of LSF. In the S, C, L band area, the attenuation is very low level at less than 0.25 dB/km. The summary characteristics are shown in Table 2. The macro bending loss at 20 mm diameter mandrel is 2 dB/m at 1550 nm. This macro bending characteristic has enough bending resistance to fabricate a practical ribbon slotted cables. We have validated that the LSF is useful to realize low cost and high capacity metro ring network systems.

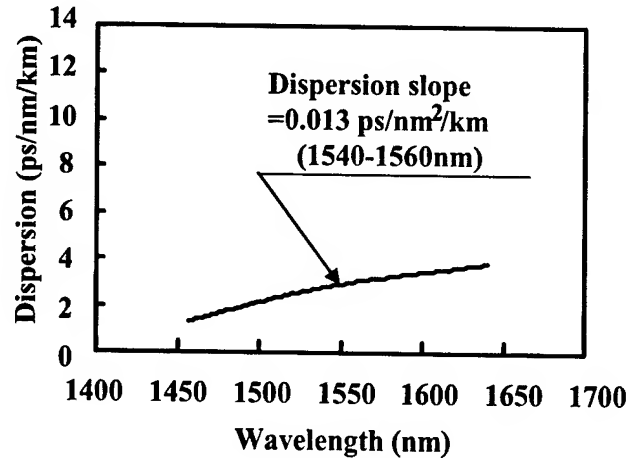


Fig.6 Relation between Chromatic Dispersion and Wavelength

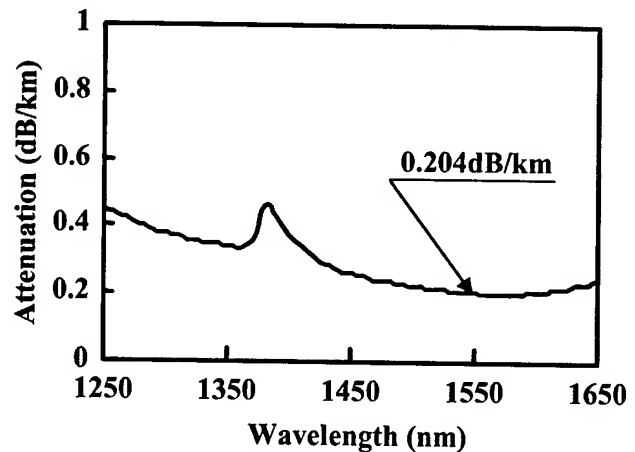


Fig.7 Spectral Attenuation of LSF

Table2. Typical characteristics of LSF

Dispersion	3.04 ps/nm/km
Dispersion slope	0.013 ps/nm ² /km
Attenuation	0.204 dB/km
PMD	0.04 ps/km ^{1/2}
MFD	7.5 μm
A _{eff}	43.6 μm ²
n ₂ /A _{eff}	6.7 × 10 ⁻¹⁸ cm ² /w/nm ²
Macro Bend Loss*	2 dB/m

*Bend diameter=20mm

4. LEF design & performance

4.1 Fiber design

We have tried to optimize the refractive index profile of LEF too. Figure 8 shows the profile model used in simulation. Considering A_{eff} , macro bending loss and productivity, we adopted the tetra clad structure with a shallow depressed clad which had a 0.02 % refractive index. We calculated the refractive index of center core to satisfy the dispersion of 8 ps/nm/km, the A_{eff} of 65 μ^2 and the macro bending loss (bending diameter, 20mm) of less than 2 dB/m at 1550 nm respectively. This macro bending characteristic has enough bending resistance to fabricate a practical ribbon slotted cables.

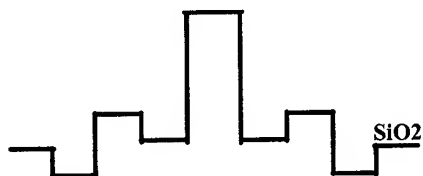


Fig.8 Refractive Index Profile Model of LEF

4.2 Fiber fabrication and performance

We used Vapor-phase axial deposition (VAD) method to fabricate LEF because VAD works better in mass production compared with other method. Figure 9 shows the relation between chromatic dispersion and the wavelength of the LEF. The chromatic dispersion is in the range from 3 to 11 ps/nm/km in S, C, and L bands. The dispersion slope at 1550 nm is 0.057 ps/nm²/km. As we have shown in the simulation, this chromatic dispersion characteristic makes 10 Gbit/s 104-ch WDM 1200 km transmission for metro ring network system. Figure 10 shows the spectral attenuation of LEF. In the S, C, and L band area, the attenuation is very low level at less than 0.23 dB/km. The summary characteristics are shown in Table 3. A_{eff} is 63.8 μ^2 . Consequently, the n_2/A_{eff} of LEF is 15 % smaller than that for conventional NZDF. The macro bending loss at 20 mm diameter mandrel is 1.5 dB/m. This macro bending characteristic is equal to LSF and has enough bending resistance to fabricate a practical ribbon slotted cables. We have validated that the LEF is useful to realize high performance terrestrial long haul transmission systems.

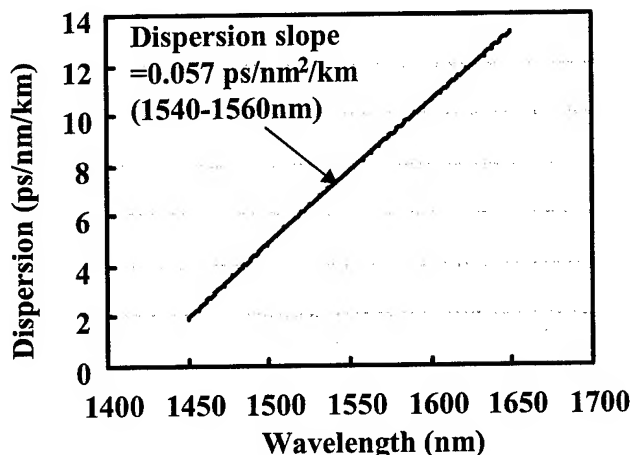


Fig.9 Relation between Chromatic Dispersion and Wavelength

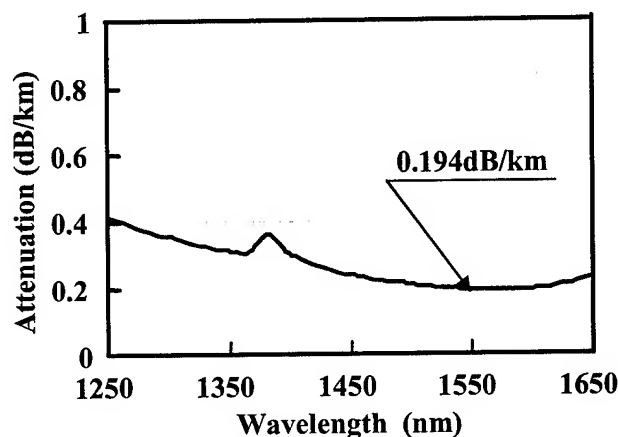


Fig.10 Spectral Attenuation of LEF

Table3. Typical characteristics of LEF

Dispersion	7.74 ps/nm/km
Dispersion slope	0.057 ps/nm ² /km
Attenuation	0.194 dB/km
PMD	0.04 ps/km ^{1/2}
MFD	9.3 μ m
A_{eff}	63.8 μ^2
n_2/A_{eff}	4.6×10^{-18} cm ² /w/nm ²
Macro Bend Loss*	1.5 dB/m

*Bend diameter=20mm

7. Conclusion

We have investigated the optimum NZDF for metro ring network systems and terrestrial long haul transmission systems. As conclusion, we have developed LSF and LEF. LSF has small dispersion slope of $0.013 \text{ ps/nm}^2/\text{km}$, dispersion of 3 ps/nm/km and A_{eff} of $43.6 \mu\text{m}^2$ respectively. Thus, we confirmed that LSF was a good fiber to be adapted to a $104\text{-ch} \times 10 \text{ Gb/s}$ metro ring network system over 200km without dispersion compensation. LEF has a large A_{eff} of $63.8 \mu\text{m}^2$, dispersion of 7.74 ps/nm/km and dispersion slope of $0.057 \text{ ps/nm}^2/\text{km}$ respectively. LEF has higher tolerance input power than LSF. Therefore, LEF is able to expand the repeater spacing comparing to that of LSF. Thus, in a $104\text{-ch} \times 10 \text{ Gb/s}$ terrestrial long haul system over 1200 km, LEF enable the system construction with a reduced cost.

8. References

- [1] G.E.Keiser, Optical Fiber Technol.,vol5, (1999) pp.3-39
- [2] Akiba, "Optical Submarine Cable Network", IEICE 00, March 2000
- [3] L.E.Nelson, OECC 2002, 11D1-1 (2002)
- [4] K.Ohsono,et al., IWCS 2001,12-3 (2001)
- [5] T.Tanaka, et al., OECC 2000,11A1-5 (2000)
- [6] T.Ooishi,et. al., OECC 2000,12B3-4 (2000)
- [7] S.Matsuo, et al., OECC 2002,11D1-2 (2002)
- [8] G.P.Agrawal, "Nonlinear Fiber Optice,2nd.,Academic Press, (1989)
- [9] A.Gnauck, et al., OFC'2002, paper FC2 (2002)
- [10] B.Zhu, et al., OFC'2002, paper FC8 (2002)

Author



Kazumasa Ohsono

The Dept.4 Optoelectronic System Laboratory, Hitachi Cable, Ltd.
Hitaka-cho, Hitachi-shi, Ibaraki-ken, 319-1414 Japan

Phone; +81-294-25-3837 email: ohsono.kazumasa@hitachi-cable.co.jp
Mr. Ohsono received his B.E. degree in Mechanical Engineering from the Science University of Tokyo in 1982 and joined Hitachi cable, Ltd. He has been engaged in research and development of optical fibers. He is now a senior researcher in Optoelectronic System Laboratory and a member of the IEICE of Japan.



Yoa Bing

The Dept.4 Optoelectronic System Laboratory, Hitachi Cable, Ltd.
Hitaka-cho, Hitachi-shi, Ibaraki-ken, 319-1414 Japan

Phone; +81-294-25-3837 email; @hitachi-cable.co.jp
Dr. Yao was born in 1969. He received M.E. and Ph.D. degrees in electrical engineering from Yamanashi University in 1997 and 2002 respectively. He joined Hitachi Cable, Ltd. in 2001 and he is now engaged in research of an optical fiber communication system and a member of the IEICE of Japan.



Tatsuya Shirosawa

The Dept.4 Optoelectronic System Laboratory, Hitachi Cable, Ltd.
Hitaka-cho, Hitachi-shi, Ibaraki-ken, 319-1414 Japan

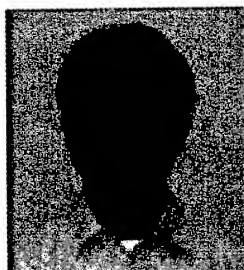
Phone; +81-294-25-3837· email; shirosaw.tatsuya@hitachi-cable.co.jp
Mr. Shirosawa was born in 1977. He received his B.E. and M.E degrees in Mechanical Engineering from Tohoku University in 1999 and 2001 respectively. He joined Hitachi cable, Ltd. He has been engaged in research and development of optical fibers.



Tetsuya Sukegawa

The Optical Fiber Design Department, Hitachi Cable, Ltd.
Isagosawa-cho, Hitachi-shi, Ibaraki-ken, 319-1418 Japan

Phone; +81-294-42-5971, E-mail; sukegawa.tetsuya@hitachi-cable.co.jp
Mr. Sukegawa received B.E. and M.E. degree in Electronic and Information Engineering from Tokyo University of Agriculture and Technology in 1997 and 1999 respectively. He joined Hitachi Cable, Ltd. in 1999 and has been engaged in the design and development of optical fiber and cables and telecommunications cables. He is now an engineer in the Optical Fiber Design Department.



Tomomi Onose

The Optical Fiber Section, Optical Fiber & Device Department, Hitachi Cable, Ltd. Isagozawa-cho, Hitachi-shi, Ibaraki-ken, 319-1418 Japan

Phone; +81-294-42-5043 email: onose.tomomi@hitachi-cable.co.jp

Mr. Onose received his B.E. and M.E degree in Electrical Engineering from Ibaraki University in 1994 and 1996 respectively. He joined Hitachi cable, Ltd. He has been engaged in development of optical fiber cables. He is now an engineer in the Optical Fiber & Device Department.

Holmium doped chalcohalide glasses for U-band (1.62~1.65 μ m) amplification

Se Ho Park, Jin Seong Yang, Mun Hyun Do, Jin Han Kim

R&D Group 1, Fiber-Optics Division, Telecommunication Network Business, Samsung Electronics Co. Ltd.,
Imsu-dong 94-1, Gumi, Gyung-Buk, Republic of Korea (South)
+82-54-479-7162 · seho35@samsung.com

Abstract

Chalcohalide glasses ($70\text{Ge}_{0.25}\text{As}_{0.10}\text{S}_{0.65}-15\text{GaS}_{3/2}-15\text{CsBr}$) doped with Ho^{3+} emitted 1.64 μm fluorescence with a long lifetime ($\tau_m \sim 3.3\text{ms}$), which can provide the efficient signal-gains in U-band (1.62~1.65 μm) for the future wide-band WDM network. Co-doping and up-conversion process were also discussed for the efficient depopulation of the lower metastable $^5\text{I}_7$ level. The cross-relaxation mechanism responsible for the fluorescence quenching along Ho^{3+} concentration was elucidated based on the energy transfer theory. The optimum of the Ho^{3+} concentration for the efficient optical amplification in U-band was estimated about 0.20% in mole.

Keywords

Optical Amplifier; Wavelength-Division-Multiplexing; Rare-Earth; Chalcohalide Glass

1. Introduction

The evolution of fiber-optic networks has expanded the transmission capacity over several tera-bit per second. All these progresses were carried out by the deployment of the all-optical transmission circuits and the wavelength division multiplexing (WDM) techniques. In all-optical networks, optical amplifier is essential to the long-distance transmission without any delay times via O-E-O regeneration. Some metro-networks use the optical amplifiers for the purpose of the pre- or power-boost amplification, etc. The optical amplifier increases basically the small signal power and compensates the attenuation loss. Typical Erbium doped fiber amplifier provides the optical gain of 17~27dB in C-band (1.53~1.56 μm wavelength), where the attenuation loss of silica fiber is minimum. Recently, semiconductor optical amplifier (SOA) has been deployed in the low-cost market such as metro-networks rather than the EDFA [1]. Raman fiber amplifier also gives the backward distributed gains, which offers the feasibility of the optical power management so as to reduce the noise figure efficiently [2]. Fluoride- and tellurite-based fiber amplifiers have the merit of wide-band operations [3]. Wideband capability of the optical amplifier is very important, because the capacity of the WDM system is limited by the gain bandwidth and the output-power of the optical amplifier. In other words, the detrimental non-linear noises such as cross-phase modulation (XPM) and four-wave mixing (FWM) in the long-distance transmission grow up as dense as the channel numbers in C-band [4]. Otherwise, total capacity of the WDM network can be expanded by the use of the alternative windows such as S

(1.45~1.52 μm), L (1.57~1.61 μm) and U (1.62~1.65 μm) band, rather than increasing the channel density in C-band [3].

Hybrid of the gain-shifted EDFA with the conventional EDFA, for examples, increased the optical gain bandwidth from 30 to 70nm. A hybrid amplifier including a Thulium doped fiber amplifier was demonstrated to amplify the S-band signals simultaneously with C- and L-band [3]. SOA and fiber Raman amplifiers have been also investigated for attain the optical gain in these alternative bands [5,6]. Since both amplifiers are tunable of the gain bandwidth, it is probable to deploy them in the metro-network. But, the output power of SOA and fiber Raman amplifier are not sufficient for the long-distance transmission applications. The noise figure of SOA is 7~11 dB, relatively higher than rare earth doped fiber amplifiers. Against these odds, rare-earth doped fiber amplifiers remain good candidates for the alternative band transmission. However, the long time stability of the non-silica based fiber amplifiers should be enhanced for the practical field deployment.

Ultra long-wavelength (1.62~1.65 μm) band transmission technology is primarily considered in the coarse-WDM networks, which can span relatively short distance transmission systems such as metro/access networks. Since the bending loss and the residual dispersion of U-band is the highest compared with the other transmission bands, the maximum arrival distance of U-band transmission was usually less than 100km. But, the commercial next generation fibers having lower dispersion slope are recently developed, so as to extend the maximum arrival distance compatible with ultra-long haul and long-haul networks even in U-band transmission [7]. Hence, it would be fair to concern the future U-band WDM transmission even in long-distance networks. This paper will investigate and discuss the possibility of the optical amplification of U-band signals, based on the rare earth doped glasses and fiber materials.

1.66 μm fluorescence near U-band was firstly observed from $^3\text{F}_4, ^3\text{F}_3 \rightarrow ^3\text{H}_4$ transition of Praseodymium doped in selenide glasses [8]. Since both $^3\text{F}_4$ and $^3\text{F}_3$ levels are thermally coupled, the broad fluorescence spectrum was observed when 1.48 μm pump laser excited the specimen (Fig.1(a)). The selenide glasses have small phonon-vibration energies less than 180 cm^{-1} so that their multiphonon relaxation rate from $^3\text{F}_3$ to $^3\text{F}_2$ level is one of the lowest among the well-known non-oxide glasses. About 50% quantum yield of fluorescence emission was measured from selenide glasses, the value of which is appreciable for the practical operation of the U-band amplifier. Other non-oxide host composition such as sulfide and fluoride glasses doped with Praseodymium, but were disable to

provide the optical amplification in U-band, since their quantum yields are too low ($\leq 10\%$). Nevertheless of these merits, the refractive indices of selenide glasses induce the very high insertion/coupling loss with conventional silica fiber. Therefore, it is very difficult to realize the optical amplification in U-band by using the selenide glasses as fiber host materials.

Holmium is one of the best candidates to be applied for rare earth doped fiber amplifier in U-band. The fluorescence from $\text{Ho}^{3+}:^5\text{I}_5 \rightarrow ^5\text{I}_7$ transition was previously observed at $1.65\mu\text{m}$ in various non-oxide glass systems [9]. The multi-phonon relaxation rate from $\text{Ho}^{3+}:^5\text{I}_5$ level is known to be relatively lower than that of $\text{Pr}^{3+}:^3\text{F}_3$. As shown in Fig.1(b), the optical amplification is carried out via the four-level process, which demands the lower threshold of the pump power to obtain the optical gain. However, pump wavelength should be 900nm rather than the wavelength of the commercially available laser diode such as 808 , 980 and 1480nm . Additionally, the lifetime of the lower metastable level, $^5\text{I}_7$ is too long to extinct immediately to the ground level, which may cause the early saturation of the output power. Co-doping of Terbium with Holmium would help to depopulate $\text{Ho}^{3+}:^5\text{I}_7$ level via the energy transfer from $\text{Ho}^{3+}:^5\text{I}_7$ level to $\text{Tb}^{3+}:^7\text{F}_2$ level (Fig.2(a)). Co-doping of Europium with Holmium also probably works for the depopulation of $\text{Ho}^{3+}:^5\text{I}_7$ level via the energy transfer from $\text{Ho}^{3+}:^5\text{I}_7$ level to $\text{Eu}^{3+}:^7\text{F}_6$ level (Fig.2(b)). These co-doping effects are expected to increase the saturation of the output power. But, the contributions to the optical gain have not been confidently examined yet from the co-doping effects of other rare earth ions.

Chalcohalide glass compositions have the priority of the low phonon energy and the low refractive index of $1.5\sim 1.8$, compared with common sulfide glasses such as Ge-As-S, Ge-Ga-S and La-Ga-S, etc. Host composition of $\text{GeS}_2\text{-AsS}_{3/2}\text{-GaS}_{3/2}\text{-CsBr}$ system was at first investigated by Shin et al [10]. Most impressive results of them were found in the excess concentration region of CsBr to $\text{GaS}_{3/2}$. Below the critical concentration, the fluorescence lifetime and the quantum yield of the $\text{Dy}^{3+}:^6\text{F}_{11}$ level was the same order of common sulfide glasses, i.e., $100\sim 200\mu\text{s}$. Above the excess concentration of CsBr to $\text{GaS}_{3/2}$, the fluorescence lifetime eventually jumped up to $1800\mu\text{s}$, which is the theoretically expected maximum of the quantum yield. Concerning this result including the other evidences, the local environment of Dysprosium ion is to change from the sulfur ligand to bromine ligand over the critical concentration of CsBr. However, the drastic change of the glass structure has never been reported before in the chalcohalide glass systems except for the alkali-halide additives. We will discuss, in this paper, the formation of the $\text{CsGaBrS}_{3/2}:\text{Eu}^{3+}$ meta-compound structure to percolate in the excess concentration region of CsBr to $\text{GaS}_{3/2}$. The same reaction is also expected to occur in the $\text{GeS}_2\text{-AsS}_{3/2}\text{-GaS}_{3/2}\text{-CsBr}:\text{Ho}^{3+}$ system, which can provide the highest efficiency of the optical gain in U-band.

2. Experimental Procedures

The chalcohalide glass composition was selected from the $\text{GeS}_2\text{-AsS}_{3/2}\text{-GaS}_{3/2}\text{-CsBr}:\text{Ho}^{3+}$ system. The concentration of CsBr

changed from 0 to 17% in mole where as $\text{GaS}_{3/2}$ was fixed in 15% in mole. $0.03\sim 0.25$ mole % of Ho^{3+} was added into host compositions. Pure powders of low materials (Ge, As, Ga, S, CsBr, Ho) were batches into a quartz ampoule inside the inert atmosphere (Argon). The batch inside the sealed ampoule was melted in rocking furnace at 950°C for 12 hours. Then, rapidly cooled melt by the quenching water inside the ampoule was annealed at 330°C for 2 hours and cooled down to room temperature slowly. Specimen was spliced into a disk shape and the surface of it was carefully polished.

Pump source was a tunable Ti-Sapphire solid-state laser with 900nm wavelength, pump beam was incident to the specimen and the fluorescence was collected from 90° of the incident angle. An InSb infrared detector and a grating mono-chromator were used for measuring the fluorescence spectrum. A digital oscilloscope recorded the transient decay curve of the fluorescence for the measurement of the fluorescence lifetime. Phonon-sideband spectrum was carried out by the excitation of Eu^{3+} doped in the chalcohalide glass with a Rhodamine-6G dye laser ($\lambda\sim 580\text{nm}$) and a cryogenic cavity (20K).

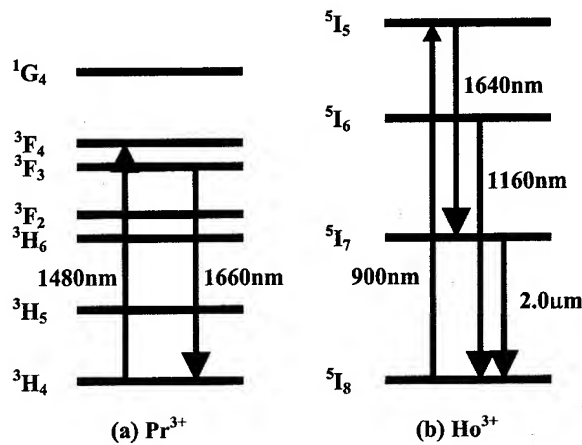


Fig.1 Energy level diagram and the possible radiative transitions of (a) Pr^{3+} and (b) Ho^{3+} ions

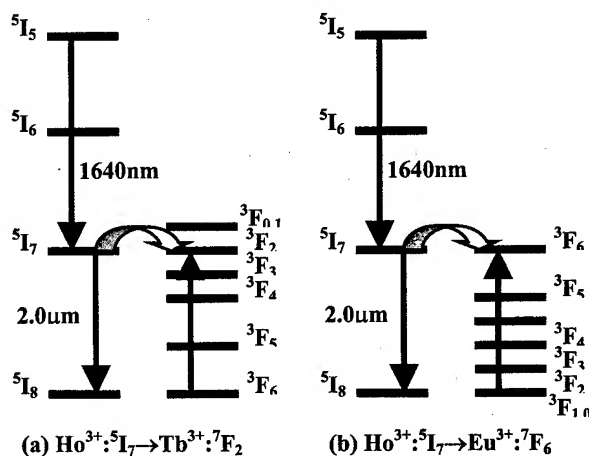


Fig.2 Energy transfer processes from $\text{Ho}^{3+}:^5\text{I}_7$ level to (a) $\text{Tb}^{3+}:^7\text{F}_2$ level; (b) to $\text{Eu}^{3+}:^7\text{F}_6$ level

3. Results and Discussion

3.1 Criteria of CsBr Concentration

Fig. 1 illustrates the energy levels and possible radiative transitions inside a Ho^{3+} ion. It shows that $1.64\mu\text{m}$ amplification occurs via a pseudo four-level system. Therefore, the population inversion of $^5\text{I}_5$ level to $^5\text{I}_7$ level is essential for the net optical gain in U-band. As shown in Fig.3, the fluorescence intensity of $2.0\mu\text{m}$ wavelength region decreased, as CsBr concentration increased from 5 to 15% in mole. The ratio of $1.64\mu\text{m}$ to $2.0\mu\text{m}$ emission also increased ~ 3.4 times. Since the fluorescence intensity is proportional to the excited-state population, the population inversion of $^5\text{I}_5$ level to $^5\text{I}_7$ is readily expected from the fluorescence spectrum. It is considerable that inversion of the ratio occurs across the critical concentration of $\text{CsBr}:\text{GaS}_{3/2}=1:1$. This exactly coincides with the previous results from $\text{GeS}_2\text{-AsS}_{3/2}\text{-GaS}_{3/2}\text{-CsBr}:\text{Dy}^{3+}$ [10]. The fluorescence lifetime also showed clearly the discontinuity around the critical concentration of CsBr as shown in Fig.4. Therefore, the local environment of rare earth ion is definitely to change from sulfide ligand to bromine ligand with the excess CsBr concentration to $\text{GaS}_{3/2}$. Blue shift of the fluorescence peak from 1.65 to $1.64\mu\text{m}$ indicates the formation of the ionic local environment near Ho^{3+} (Fig.3). It is also preferable for the optical gain in U-band, since the fluorescence peak moves to shorter wavelength region near U-band.

The phonon side band spectrum of $\text{GeS}_2\text{-AsS}_{3/2}\text{-GaS}_{3/2}\text{-CsBr}:\text{Eu}^{3+}$ glasses showed the primary coupling mode of the electron-phonon pair engaged to Eu^{3+} ion center is about $82, 162\text{ cm}^{-1}$ (Fig.5). It is different that the primary mode was found in $244, 340\text{ cm}^{-1}$ from Raman scattering experiments (Fig.6). The Raman scattering is related to the total contribution of host vibration mode, but the phonon side band corresponds with only local vibration mode near Eu^{3+} . We also found the Europium is stable in $2+$ oxidation state rather than $3+$ in sulfide glasses. But, it is found that both Eu^{2+} and Eu^{3+} ions co-exist only in chalcogenide glass with the excess CsBr concentration. It clearly evidenced that the ligand of rare earth ion changed from sulfur to bromine as the CsBr concentration over $\text{GaS}_{3/2}$.

3.2 Optimization Ho^{3+} Concentration

Typical fluorescence decay curve of $^5\text{I}_5 \rightarrow ^5\text{I}_7$ transition is non-linear as shown in Fig. 7. Especially, it is well de-convoluted with double exponential decay curves. The mean value of fluorescence lifetime (τ_m) was estimated by following equation and plotted in Fig.8;

$$\frac{1}{\tau_m} = \frac{a_1}{\tau_1} + \frac{a_2}{\tau_2}$$

Where the a_1 and a_2 is the pre-exponent, and τ_1 and τ_2 is the exponent coefficient in fast and slow part, respectively. The fluorescence lifetime decreased significantly as Ho^{3+} concentration increased over 0.20% in mole. This lifetime quenching can be elucidated by the cross-relaxation mechanism of $^5\text{I}_5 \rightarrow ^5\text{I}_7 \Rightarrow ^5\text{I}_8 \rightarrow ^5\text{I}_7$ as shown in Fig.9. Since the emission and the absorption spectra do not overlap, it is thought to be a phonon-

assisted energy transfer. However, due to the lack of associated phonon mode in chalcogenide glasses, the phonon assisted cross-relaxation occurs in higher Ho^{3+} concentration region, compared with the cases of common sulfide glasses. It means that highly concentrated chalcogenide glass fiber can operate with relatively small length, which of the attenuation loss due to Rayleigh scattering is minimized.

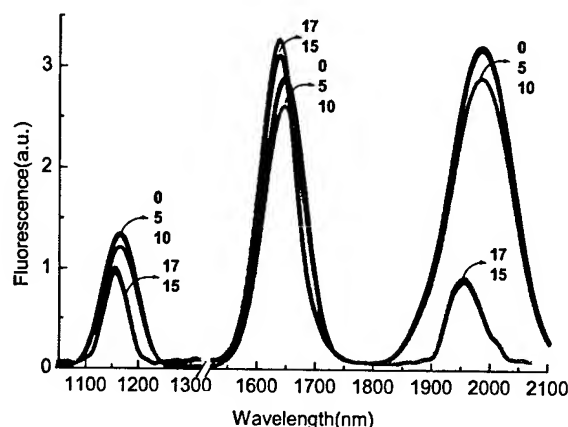


Fig.3 Fluorescence spectrum of $\text{Ho}^{3+}:$ $^5\text{I}_6 \rightarrow ^5\text{I}_8$ transition at $1.16\mu\text{m}$, $^5\text{I}_5 \rightarrow ^5\text{I}_7$ at $1.64\mu\text{m}$, and $^5\text{I}_7 \rightarrow ^5\text{I}_8$ at $2.0\mu\text{m}$ from 0.08% of Ho^{3+} doped in $(80+\text{X})\text{Ge}_{0.25}\text{As}_{0.10}\text{S}_{0.65}\text{-}15\text{GaS}_{3/2}\text{-XCsBr}$ glasses, where $\text{X} = 0, 5, 10, 15, 17$ in mole, respectively.

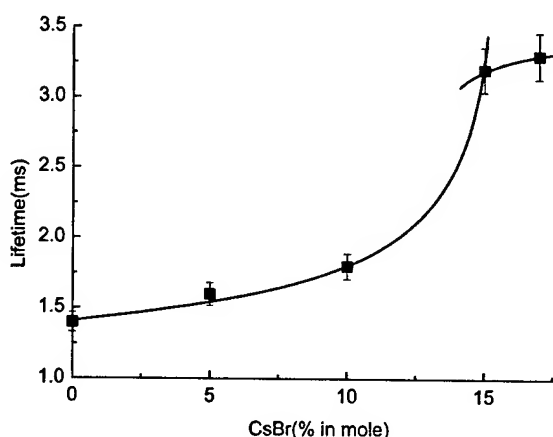


Fig.4 Fluorescence lifetime of $\text{Ho}^{3+}:$ $^5\text{I}_5 \rightarrow ^5\text{I}_7$ transition at $1.65\mu\text{m}$ from 0.08% of Ho^{3+} doped in $(80+\text{X})\text{Ge}_{0.25}\text{As}_{0.10}\text{S}_{0.65}\text{-}15\text{GaS}_{3/2}\text{-XCsBr}$ glasses, where $\text{X} = 0, 5, 10, 15, 17$ in mole, respectively.

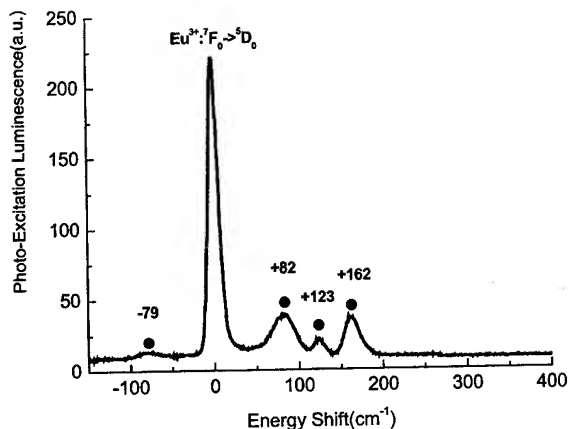


Fig.5 Phonon side band spectrum near $\text{Eu}^{3+}:\text{}^3\text{F}_0 \rightarrow \text{}^5\text{D}_0$ transition of $80\text{Ge}_{0.25}\text{As}_{0.10}\text{S}_{0.65}\text{-}15\text{GaS}_{3/2}\text{-}15\text{CsBr:Eu}^{3+}$ glasses.

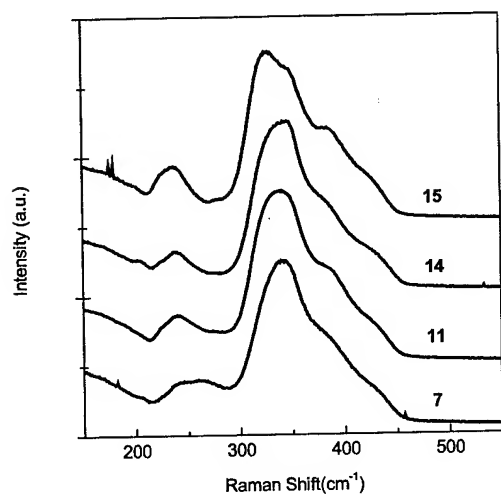


Fig.6 Raman Scattering spectrum of $(80+X)\text{Ge}_{0.25}\text{As}_{0.10}\text{S}_{0.65}\text{-}15\text{GaS}_{3/2}\text{-XC sBr:Eu}^{3+}$ glasses., where $X = 7, 11, 14, 15$

3.3 Pump Scheme

Since the lifetime of $^5\text{I}_7$ level is very long about 10~15ms, the blue (490nm) and red (650nm) up-converted fluorescence were well observed, which resulted from the pump excited state absorption as shown in Fig.10(a). Alternatively, if the second pump of 1.16 μm wavelength excites Ho^{3+} , then it would efficiently depopulate $^5\text{I}_7$ level and increase the saturation of the output power, as shown in Fig.10(b). Since the cut-off wavelength is longer than conventional 900nm pump wavelength, it has the additional merit to design the low loss fiber and the large overlap between the pump and the signal photons.

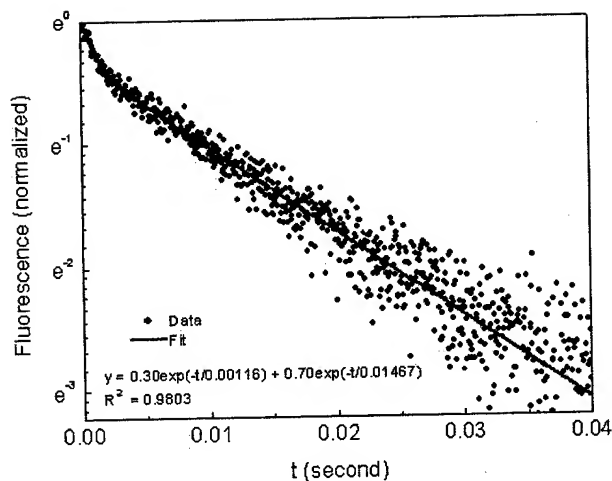


Fig.7 1.64 μm fluorescence decay curve of $^5\text{I}_5 \rightarrow ^5\text{I}_7$ transition from chalcohalide glasses doped with 0.2% of Ho^{3+} ; double exponential decay, $y = 0.30\exp(-t/0.00116) + 0.70\exp(-t/0.01467)$

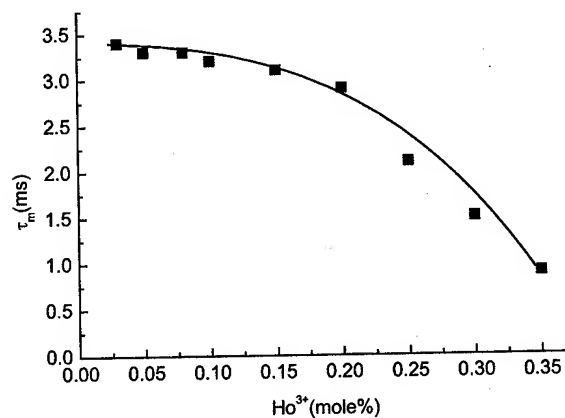


Fig.8 1.64 μm fluorescence lifetime of $^5\text{I}_5 \rightarrow ^5\text{I}_7$ transition from chalcohalide glasses doped with Ho^{3+}

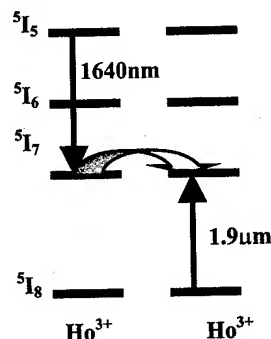


Fig.9 The cross-relaxation process between Ho^{3+} ion pair

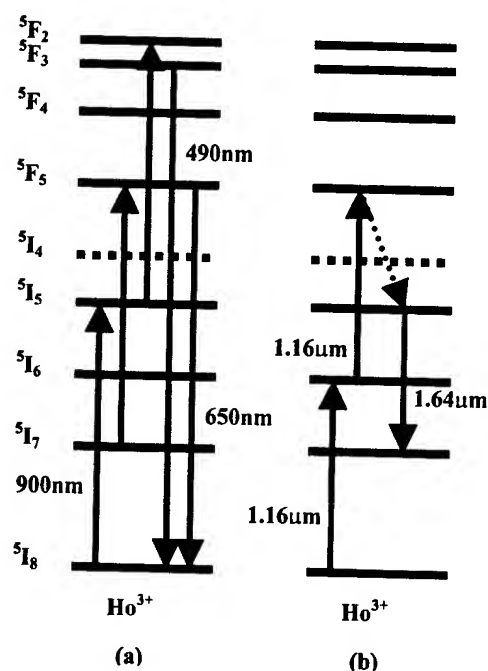


Fig.10 Up-converted fluorescence emission by (a) the pump excited state absorption by first wavelength of 900nm; (b) by the second wavelength of 1160nm

4. Conclusions

It was found that chalcogenide glasses ($70\text{Ge}_{0.25}\text{As}_{0.10}\text{S}_{0.65}-15\text{GaS}_{3/2}-15\text{CsBr}$) doped with Ho^{3+} emitted $1.64\mu\text{m}$ fluorescence with the spontaneous population inversion of $^5\text{I}_5$ level to $^5\text{I}_7$ level. The fluorescence lifetime ($\tau_m \sim 3.3\text{ms}$) of $^5\text{I}_5$ level is long enough to obtain continuous optical gain. However, the detrimental cross relaxation mechanism limited Ho^{3+} concentration below 0.20% in mole, which reduce the fluorescence lifetime of $^5\text{I}_5$ level and the population inversion. Based on the overall performance predicted from the measured optical characteristics, chalcogenide glasses with excess CsBr concentration to $\text{GaS}_{3/2}$ showed highest potential to provide the host materials to obtain efficient optical gain in U-band ($1.62\sim 1.65\mu\text{m}$). Blue shifted spectrum and higher critical concentration of Ho^{3+} are advantageous for the development of the practical optical amplifier.

5. Acknowledgment

We appreciate Prof. J. Heo (Pohang University of Science and Technology) for the critical review and advise on this paper.

6. References

- [1] H. K. Kim et al., "SOA-based transmission of 10Gb/s WDM signal over 500 km of NZDSF using wavelength modulation," OAA-01 PD2
- [2] R. Ludwig, U. Feiste, C. Schmidt, C. Schubert, J. Berger, E. Hilliger, M. Kroh, T. Yamamoto, C. M. Weinert, H. G. Weber,

"Enabling Transmission at 160 Gbit/s," OFC-02, TuA1, pp1-2 (2002)

- [3] H. Masuda, A. Mori, K. Shikano, K. Oikawa, K. Kato and M. Shimizu, "Ultra-wide-band hybrid tellurite/silica fiber Raman amplifier," OFC-02, ThB6, pp388-390
- [4] Z. Pan, Q. Yu, and A. E. Willner, "Fast XPM-induced polarization-state fluctuations in WDM systems and their mitigation," OFC-02, ThA7, pp379-380 (2002)
- [5] Y. Chen, R. Pavlik, C. Visone, F. Pan, E. Gonzales, A. Turkin, L. Lunardi, D. Al-Salamah, S. Lumish, "40nm Broadband SOA-Raman Hybrid Amplifier," OFC-02, ThB7, pp390-391
- [6] J. Bromage, H.J. Thiele and L.E. Nelson, "Raman Amplification in the S-band," OFC-02, ThB3, pp383-385 (2002)
- [7] G. C. Luther, "New fibers for ultra-high-capacity transmission systems," OFC-02, WA1, pp171-173
- [8] Y. G. Choi, K. H. Kim, B. J. Park and J. Heo, "1.6um Emission from Pr^{3+} : ($^3\text{F}_3, ^3\text{F}_4$) \rightarrow $^3\text{H}_4$ transition in Pr^{3+} - and $\text{Pr}^{3+}/\text{Er}^{3+}$ -doped selenide glasses," App. Phys. Lett. 78(9), p1249-1251(2001)
- [9] M. Shojiya, Y. Kawamoto, K. Kadono, "Judd-Ofelt parameters and multiphonon relaxation of Ho^{3+} ions in ZnCl_2 -based glass," J. App. Phys. 89(9), p4944-4950 (2001)
- [10] Y. B. Shin, C. K. Yang, J. Heo, "Optimization of Dy^{3+} -doped Ge-Ga-As-S-CsBr glass composition and its 1.31um emission properties," J. Non-Cryst. Solid 298, p153-159 (2002)

7. Authors



Se Ho Park, Se Ho Park was born in 1973. He received a bachelor's degree in materials science and engineering from Pohang University of Science and Technology (POSTECH), Korea in 1995, master's degree also from POSTECH in 1997, PhD. degree also from POSTECH in 2001. He is now senior engineer of optical fiber and cable R&D Group 1 in Fiberoptics Division of Samsung Electronics Co. Ltd.



Jin-Seong Yang, Jin-Seong Yang was born in 1966. He received a bachelor's degree in physics from Sogang University, Korea, in 1988 and master's degree also from Sogang University in 1990. Now he is a senior engineer of optical fiber & cable R&D Group 1 in Fiberoptics Division of Samsung Electronics Co. Ltd.



Mun-Hyun Do, Mun-Hyun Do was born in 1963. He received a bachelor's degree in material science from Chungnam University, Korea in 1989 and master's degree from Kyungbuk National University in 1998. Now he is principal engineer of optical fiber & cable R&D Group 1 in Fiberoptics Division of Samsung Electronics Co. Ltd.



Jin-Han Kim, Jin-Han Kim was born in 1957. He received a bachelor's degree from Pusan University, Korea in 1982 and master's degree from Kyungbuk National University in 1990. Now, he is vice president of R&D Group 1 in Fiberoptics Division of Samsung Electronics Co. Ltd..

A New Method for Validating the Performance of Aerial Drop Cables Under Ice Loads

Jonathan G. Fitz, Michael T. Petryszak and Dr. Jin Liu

Pirelli Communications Cables and Systems

Lexington, SC 29072

+1-803-951-4037 · jon.fitz@us.pirelli.com

Abstract

In this paper, we describe a method for simulating ice loads on self-supporting aerial drop cables. The importance of such testing is reviewed for those unfamiliar with aerial cable testing. Sample cases are given for traditional ADSS cables, which are well understood. Then, it is shown how established models may be difficult to apply to new designs. New test methods are considered and a brief examination of their feasibility leads to the use of a particular method. This method is then demonstrated, as well as some actual test results. The results are compared with theoretical values and found to be in agreement. The paper concludes with a discussion of the advantages and limitations of the test method.

Keywords

FTTH; FTTx; FTT.

1. Introduction

Many aerial cables are subject to ice loading at some time during their service life. Accumulated ice increases the weight of an installed span. This, in turn, increases the span tension. In many cases, this tension increase is quite large. Some aerial cables are lashed to a messenger for support. The messenger is usually quite large relative to the tensile support it must provide. In these cases ice loads are more problematic for the supporting structures (e.g. poles or towers) than the cable. However, if the cable is self-supporting, the ice loads pose a risk to the cable itself. Inadequate self-supporting cable designs can result in high optical attenuation or even cable breakage. Thus, aerial self-supporting cables must be designed to withstand typical ice loads, not just installation tensions.

2. Ice Load Calculations

ADSS (All-Dielectric Self-Supporting) optical fiber cables provide a convenient illustration of how ice loads are calculated. ADSS cables have been extensively studied and widely deployed. It is generally accepted that ADSS designs are well understood and field proven. Thus, they make a good starting point from which to approach new self-supporting designs.

It should be noted that this paper will not address the mathematical principles behind sag and tension calculations. If the reader is interested in a complete treatment of this topic, he or she is urged to do a literature search for papers specific to this topic. The existing

work constitutes a formidable bibliography and can easily be found by reviewing IWCS (or other) proceedings from previous years.

A typical sag and tension table is provided in Table 1. This table is derived from the specific properties of a single design. Thus, it cannot be used for cables with differing longitudinal stiffness, diameter or weight. The results have also been calculated for a particular ice accumulation. Results are usually calculated for 0.5, 0.25 or 0 inches (12.7, 6.4, or 0 mm) of radial ice accumulation in the United States (this example is for 0.5"). The appropriate ice value is specified by the NESC (National Electrical Safety Code) according to geographic location. The NESC also specifies wind loads.

Each result has also been calculated for a particular quantity of installed sag. This value is expressed as a percentage of the horizontal span length. In everyday terms, a 100 foot span with 1 percent installed sag would have one foot less vertical clearance at the lowest point than at the ends. Smaller sag values produce higher tensions in both the initial and ice-loaded spans.

**Table 1. Sample Sag and Tension Values
for an ADSS Cable**

Span	Installed Sag	Installed Tension	Sag Under Ice Load	Tension Under Ice Load
500' (152m)	1%	643 lbs. (2,864 N)	4.0%	1,680 lbs. (7,484N)
500' (152m)	3%	214 lbs. (953N)	5.0%	1,336 lbs. (5,951 N)

It can easily be seen that the tension under ice load is always substantially higher than the installed tension. Thus, it is clear that a self-supporting cable must be designed for ice (and/or wind) loads, and not just installation conditions. On the other hand, the cable cannot be grossly over-designed. This would waste costly material (typically aramid in the case of ADSS) and make it difficult to offer the cable at a competitive price. A careful balance must be struck between economy and reliability. This is a routine practice for ADSS cables, since their design rules are well established. However, this optimization becomes more difficult when a fundamentally new design is involved.

3. Differences Between Aerial Drops and ADSS Cables

It is important to recognize that conventional ADSS cables are designed for a fundamentally different application than Aerial Drop cables. The application differences require different cable features in order to be craft-friendly and cost-effective.

Not all of the differences between the designs will affect performance under ice loads. This discussion will address only those differences that might affect the cable during ice loading. This should help clarify why the authors found it necessary to experimentally validate the cable design with a new test method.

Aerial Drops tend to be smaller than ADSS cables. This is beneficial because it reduces the weight of accumulated ice and consequently, the maximum tension. However, the incremental tension created by the ice tends to be more dramatic as a percentage of installed tension. The tension of a Drop Cable under ice loads can easily be ten or more times (1000%) the installed tension.

In order to maintain a small size, Aerial Drops generally do not contain a stranded core. Thus, the fiber is not isolated from strain during ice loads. It is important to accurately quantify the fiber strain under maximum load.

Sheer economics require that Aerial Drop cables be designed as efficiently as possible. Any wasted material is multiplied over and over, yet the cost of each drop must be recovered from a single customer. Although an individual drop failure will not affect many people, a design flaw could result in widespread outages. Perhaps more than any other self-supporting design, Aerial Drop cables are pushed to their design limits.

4. Problems with Conventional Tensile Tests

Each of the above issues can be addressed easily enough through a test that simulates ice loads. Ice loads are normally simulated on ADSS cables through the use of a large tensile test apparatus. However, this approach may not be applicable to Aerial Drops due to differences in construction.

Drop cable runs tend to be very short. As with any aerial cable, it is necessary to terminate the span and access the fibers at each end. Thus, fiber access and span termination must be accomplished quickly and easily. In response to this requirement, the development team created a drop cable in which the strength element and fibers were in separate sub-units. This allowed both sub-units to be quickly accessed with a common wire stripper.

As can be seen in Figure 1, the strength elements and fibers in the drop cable are not concentric as they are in the conventional ADSS cable. This creates a fundamental change in the way that ice loads are transferred. With the ADSS cable, suspension hardware is applied directly over an intact jacket. Tensile loads are transferred to the fiber core unit only through shear forces, which must be passed through the aramid yarns. Thus, it is impossible to elongate the core without first straining the part of the cable which has the

highest longitudinal stiffness. If the jacket slips relative to the tensile yarns, it produces an obvious failure at the suspension hardware. Neither of these conditions applies to the drop cable shown in Figure 1. The strains experienced by the fiber sub-unit

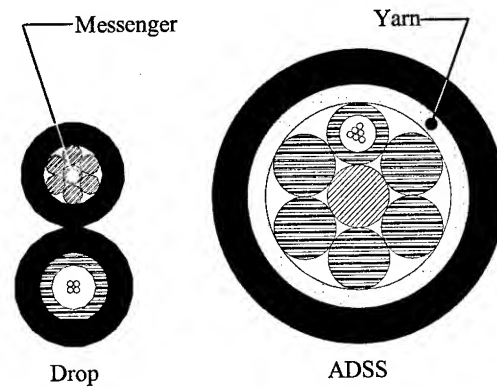


Figure 1. Cross-Sectional View of ADSS and Aerial Drop Cables

and strength member might not be identical. Moreover, the suspension hardware is attached directly to the exposed messenger. As can be seen in Figure 2, the jacket is removed in order to attach the hardware. Thus, the jacket could slip relative to the messenger without hardware failure. This jacket provides the only connection between the fiber sub-unit and the messenger.

These differences combine to raise questions that go beyond simple tension calculations. Conventional ADSS cables are

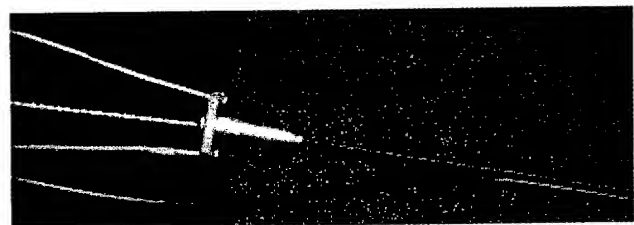


Figure 2. Drop Cable with Suspension Hardware

generally tested with field hardware on a tensile apparatus. The effect of pulling on the grips is equivalent to the application of a distributed load. It is difficult to be sure whether or not that same principle can be applied to a fundamentally new design. There is at least a possibility that it does not. These concerns can be addressed only if the new design is tested in a direct fashion. The tension must be increased by the application of a distributed load on the jacket until equivalence is established.

One final problem with conventional tensile tests is that they do not always inspire the confidence of customers. A relatively small weight of ice can produce surprisingly high tensions. Most people find the relationship to be counter-intuitive. Tensile testing a cable on the basis of theoretical load calculations is

bound to raise concerns with some customers. Although these concerns may not be scientific, they do need to be addressed.

5. Problems with Ice Testing

It might seem that the best way to test a cable under ice loads would be to use actual ice. To be sure, this would allow the cable to be observed under the actual conditions that are of concern. However, there are real drawbacks to this approach.

The first problem is time. Although many locales have freezing weather, it is not year-round and often occurs only at night. Waiting for the appropriate weather could greatly extend a product development cycle.

Although they are used for many low-temperature tests, environmental chambers are not practical for ice load testing. Span lengths can easily exceed 100 or even 150 feet. Few (if any) facilities of such size are available, and their cost of operation would certainly be prohibitive.

However, the most important limitation to actual ice testing is quality control. The test results can't be used to validate a performance model unless the ice is applied consistently and to a controlled diameter. Although qualitative observations can be made with uncontrolled ice loads, it will not permit the sort of fine-tuning that is possible with quantitative analysis.

6. Alternative Test Methods

It was clear to the development team that an alternative test method was needed in order to facilitate the validation of new Aerial Drop cables. In the long run, the team fully intended to return to conventional tensile testing. However, as mentioned above, this would first have to be validated by a test method in which test tensions were created by the application of a distributed load.

6.1 Discrete Loads

Initial proposals focused on the use of many small weights. These could be spread out evenly over the length of the span under test. Strictly speaking, this wasn't a distributed load. But, the idea was that a good approximation could be achieved if the number of weights was great enough.

There were two primary objections to this approach. First, the weights would have to be attached in such a way that the mechanical properties of the jacket would be substantially unchanged. Second, hanging a multitude of little weights would be time-consuming and tedious. However, for some time it seemed as though this was the only practical alternative.

6.2 True Distributed Loads

The development team continued discussions about what material might be attached to a cable in a continuous length. This would provide a true distributed load and might be applied with relative ease. However, the challenge was identifying a material with the appropriate weight per unit of length. Almost any flexible

material could be attached, but identifying a single candidate with the appropriate weight to length ratio proved more frustrating than expected.

There were also concerns that it would be difficult to attach the weight to the cable. It might be difficult to attach the full weight to the cable smoothly and continuously while the cable was suspended. But, the test would be greatly complicated if the weight were attached before the span was put up. In particular, this would make it hard to precisely control installed sag.

Finally, one team member devised a solution. In hindsight it seems quite obvious, and in fact, similar work has been done with aerial-lashed cables [1]. But, at the time it was a much-needed breakthrough. Flexible plastic tubing could be carefully selected on the basis of inside diameter and tubing weight. The tubing could easily be attached to an installed span while empty. Then, the tubing could be completely filled with water to achieve the final loading.

7. Simulated Ice Load Testing

7.1 Calculating Ice Weight

As mentioned above, the cable design under evaluation was not round. It was decided that the largest dimension should be used for the calculation of radial ice loads. Obviously, this would significantly increase the calculated ice load. However, it is believed that this approach most closely simulates real ice accumulation. The total weight of ice was based on an NESC heavy ice load.

7.2 Tubing Selection

The estimated ice weight provided a target for the combined weight of tubing and water. The next step was to select tubing of appropriate density and dimensions. Water and most polymers have densities close to that of ice. So, the ideal tubing diameter would tend to be close to that of the final ice diameter. The final selection could be made using one of two strategies.

The combination of tubing material and diameter could be fine-tuned to exactly match the weight of ice. This would be more complicated, but would allow the cable to be tested exactly at the specification limits.

Alternately, commonly available tubing materials and sizes could be evaluated to identify the closest match that is heavier than the expected ice load. Theoretical calculations could be made for an ice load equal to the selected tubing/water combination. Exact comparisons could then be made between theoretical and experimental values. By exceeding the NESC requirements, this approach would also ensure that the cable was conservatively rated.

It is common practice to conservatively rate cables on the basis of conventional tensile tests. The development team thought this approach should be used on the distributed load test, as well. For this reason, the team used the second, more conservative approach to tubing selection.

7.3 Span Installation

Two utility poles were installed 155 feet apart on roughly level terrain. Industry standard "J-hooks" were installed at a height of 6 feet (183 cm) on the pole. The test span was installed and adjusted to achieve an installed sag of one percent (approximately 18.5 inches). Baseline attenuation measurements were made before and after the initial installation. The jacket was inspected for any unusual features or damage. Markings were made on the exposed messenger in order to monitor jacket slippage. The marks were placed at the point where the jacket had been stripped back to install the suspension hardware.

7.4 Tubing Attachment and Filling

Three lengths of 1.25" (31.75 mm) OD tubing were joined with barbed hose connectors. Starting at one end, the tubing was attached to the flat side of the cable with duct tape. This approach was favored over aerial lashing because it reduced the likelihood that contact stresses would influence optical attenuation. Any twists that were trapped in the span as part of the installation process were allowed to remain. This created a few places where the cable was not perfectly flat. However, it is expected that some twisting will occur in field installations.

The tubing was allowed to extend beyond the cable on each end. The excess hose was attached to the utility poles so as to neutralize its effect upon the span under test. One end of the tubing was turned up and fitted with a large funnel, which made it easier to fill with water. A photo of one end of the experimental setup is shown in Figure 3. Optical attenuation measurements were made once again to ensure that the cable was not damaged by the attachment of the tubing.



Figure 3. View of the Experimental Setup

The tubing was then filled with water from above with the aid of some stairs, the funnel and two plastic carboys. The tubing was filled only until the water level reached the suspension hardware.



Figure 4. Inspection of the Span during Simulated Ice Load

7.5 Inspection and Measurements

The jacket was inspected for slippage and any unusual features (Figure 4). Attenuation measurements were made while the cable was fully loaded. The fully loaded sag was recorded.

The cable was allowed to remain fully loaded until it was certain that the cable was in a steady-state condition. The water was then drained from the hose, and the hose was removed. The cable was inspected for damage and the attenuation was measured in the unloaded state. The unloaded sag was recorded.

8. Results

Optical attenuation results at 1550 were comparable to results obtained during a conventional tensile test (and in compliance with the product specifications). There was no slippage of the jacket relative to the messenger. Theoretical calculations predicted a loaded sag value of 63.6 inches (161.5 cm). The actual sag value was 63.875 inches (162.2 cm), which represents an error of only 0.4%. A photo of the "ice" loaded sag measurement is shown in Figure 5. Note that the measurement is made at the bottom of the cable, not the attached tubing.

9. Conclusions

The new test method is a relatively straightforward way to simulate distributed ice loads on aerial cables. The test results validated the theoretical models used for the cable in question. The test also showed that there were no problems with the transfer of a distributed load through the jacket to the messenger. Thus, this test showed that conventional tensile testing could be used as an equivalent method for this particular cable design.

9.1 Advantages

The new test method is far more convenient than actual ice loading and can be set up in a relatively short period of time. It allows direct observation of the test cable under conditions that closely approximate real installations. Once a new design has been validated, conventional tensile testing can be used with increased confidence.

This method can also be used for long-term tests without tying up expensive tensile test equipment. Constant-load testing can be done without the need for complex controls. Thus, creep tests can be done more easily.

This test method can be particularly helpful when demonstrating cable performance to non-technical people. The hose and water have a specific gravity close to that of ice. The similarities between a water-filled hose and an ice cylinder of roughly similar cross-section are fairly obvious. This allows observers to "see" the cable tested under realistic conditions that do not rely upon a complete understanding of the underlying physical principles. This is particularly helpful for illustrating how span tensions can be so high when the ice itself weighs only a fraction of the resulting tension.

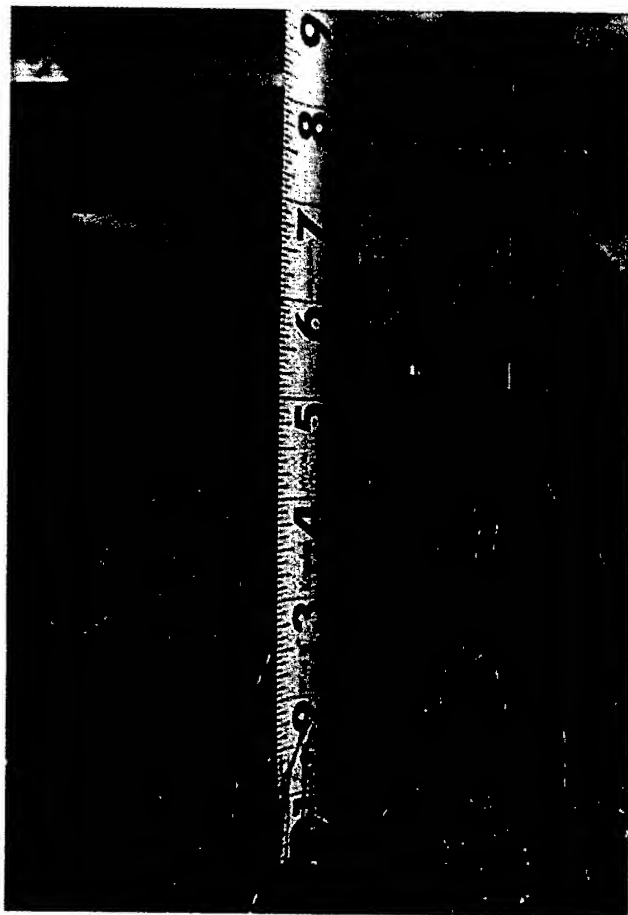


Figure 5. Sag Measurement during Simulated Ice Load

Jon Fitz received his B.S and M.S. (1990) degrees in Mechanical Engineering from the University of South Carolina. Since then, he has worked at Pirelli in a wide range of positions. He currently supports Pirelli's Fiber-to-the-Home activities, in addition to providing organizational support in the area of optical transmission components and systems.

Mike Petryszak received his BS in Mechanical Engineering from the University of South Florida in 1991. He Joined Pirelli cables in 1993 and is currently the Product Development Manager for North America.

9.2 Limitations

The accuracy of the test as conducted was limited by the available facilities. The ground was not completely level and precise measurements were obviously not realistic on a grassy surface. The support poles shifted slightly under load, further limiting the accuracy of sag measurements.

This test does not account for the effects of temperature upon cable materials. For example, the cable jacket is much softer at 30°C than at -10°C. It is expected that the jacket would be less likely to slip at lower temperatures. So, the test as performed is thought to be conservative. Nonetheless, temperature is an uncontrolled variable that can be significant.

It is not always possible to find a hose with a diameter and density that provides an exact match for the intended ice load. Thus, the test often cannot be used to provide design verification exactly at the specification limit. However, it is always possible to perform theoretical calculations using the distributed load that is available. Thus, the design model itself can still be validated. It is recommended that this always be done at a load that exceeds the specification limits.

The mechanical properties of the water filled hose are obviously not the same as ice. This is a minor issue for the cable alone. However, it would complicate the testing of cables in combination with special hardware. For example, splice closures and "snow-shoes" introduce concentrated loads that will behave differently under real ice loads.

9.3 Suggested Improvements

Testing could be done more conveniently on a site built especially for this purpose. A continuous, level concrete pad would simplify sag measurements. The utility poles would shift less if set in concrete. This also would improve sag measurements.

10. Acknowledgments

Thanks to all the members of Pirelli Lexington's Product Development group for making ideas into reality.

11. References

- [1] D. W. Chiasson, I. J. Greveling and C. Roy, "A Study of Aerially Supported Fiber Optic Cables," NFOEC 1992 Proceedings, pp. 475-481.

Jin Liu received his B.S. in Mathematics & Mechanics from the Beijing University of Aeronautics and Astronautics in 1982. He received his M.S. and Ph.D. in Mechanical Engineering from University of South Carolina in 1993 and 1997, respectively. Jin joined Pirelli in 1987 as a Development Engineer and currently holds the position of Senior Development Engineer. His primary focus is on outside plant ribbon cable products and premises cable products.

Optical Ground Wires with Improved Lightning Resistance

Lluís-R. Sales Casals¹, Josep Martin-Regalado¹, Alessandro Ginocchio²

¹ Pirelli Telecom Cables y Sistemas España S.L.
Rambla Pirelli, 2

08800 Vilanova i la Geltru, Spain
Tel. +34 93 811 60 26 - lluis.sales@pirelli.com, josep.martin@pirelli.com

² Pirelli Cavi e Sistemi Telecom SpA
Viale Sarca, 222
20126 Milano, Italy

Tel. +39 02 64 42 27 98 - alessandro.ginocchio@pirelli.com

Abstract

The present paper investigates the effects of the lightning waveforms described in IEC 60794-4-1 [10] on various OPGW designs. Increasing the charge transfer level of the continuing current component, the most damaging one, the residual breaking strength of the cable decreases. The damage on the cable for charge transfer larger than 100 C seems to be strongly dependent on the cable diameter more than on wire diameter. The results of this experimental work show that we have to consider both mechanical and lightning resistance together with Keraunic levels³ of the area of installation, in order to design reliable and cost effective OPGWs.

Keywords

OPGW; lightning; lightning resistance improvement

1. Introduction

The primary function of overhead ground wires is to protect a transmission line from damages and outages caused by lightning. Since early eighties, Power Utilities began to substitute the traditional large metallic cross-section ground wires installed on very high voltage overhead lines with composite Optical Ground Wires (OPGW), in order to assure both lightning protection and data transmission (generally relevant to the operation of the overhead power transmission systems). Short circuit currents required for such high voltage systems were generally high and thus metallic cross section, diameter and weight of these ground wires were relatively large.

During the last decade, the use of OPGWs has experienced a fast growth due to the liberalization of the Telecom market, allowing the Power Utilities to exploit all their existing rights of way in order to build their own long distance telecom transmission networks.

Nowadays the evolution of the Telecom market is pushing the Utilities to spread the telecom networks along power distribution lines where lower short circuit requirements allow in theory to install smaller and lighter ground wires. Such ground wires are obviously more vulnerable to

lightning strikes, consequently OPGWs may have their strands broken and the optical core severely damaged when struck by high-energy lightning.

However, Telecom transmission systems should present a very high degree of reliability and therefore, when a conventional ground wire has to be replaced by an OPGW, care must be taken to design and install an OPGW capable of withstanding lightning throughout its lifetime. A safe design trade off must be found taking into consideration OPGW diameter, weight, short circuit current, mechanical and lightning resistance, lightning frequency and statistical distribution of charge levels in the area of installation.

It is worth to mention that a natural lightning has three main components: a high-current, short duration initial stroke, followed by a low level continuing current component and, finally, by a fast-front subsequent stroke [1-3]. As a first approximation it can be assumed that 10% of all lightning events are positive and 90% are negative. Positive lightning flashes have a total charge transfer typically one order of magnitude larger than negative flashes (max. 300 C vs. 40 C of negative flashes for 95% of all lightning events) [1]. Positive flashes up to 600 C have been also reported during winter lightning [4], however it is known that winter lightning is an anomalous event in the world, which means it is very rare. Charges associated with typical negative lightning strokes are instead in the range from 5 to 40 C (95% of all events) [5,6]. It is widely accepted that the melting damage observed in the field is usually associated with the continuing current component of lightning. Previous works on lightning testing to OPGW have analyzed lightning damage of the continuing current component to the optical ground wire by the use of battery banks [7,8]. Alternative lightning test methods based on welding arc machine have also been studied [9].

The present work, after preliminary trials carried out using different waveforms in order to confirm the most damaging component of the lightning current, investigates the effects of the lightning phenomenon on various OPGW designs, characterized respectively by high short-circuit currents (large diameter OPGWs) and by low short-circuit currents

³ Keraunic level: number of thunderstorm days occurring per year at a given location.

(low diameter OPGWs). In particular, this paper investigates the effects of the lightning waveforms based on IEC 60794-4-1 [10] on 48 fibers OPGW cables with different armors (in terms of wire materials, wire diameter, cable diameter, wire numbers, etc.) and/or inner optical core designs. The prototype cables have been manufactured and tested at Kinectrics International Inc. (formerly Ontario Hydro Research)⁴, applying to the OPGW samples each separate component of the lightning current and the combination of them. The results obtained show that OPGW with diameters larger than 12.0 mm show a relatively good optical and mechanical behavior against lightning for charge transfers up to 200 C (which cover more than 99% of all events).

2. Experimental Setup

The purpose of a lightning arc test is to simulate the damage caused by natural lightning. A possible lightning arc test is described in Annex F of [10]. The lightning test waveform is specified as derived from a US military aviation specification [11]. Like natural lightning, the standard recommends a combination wave. Component A is a current pulse of high magnitude and short duration, simulating the initial stroke. Component C is a low-level DC pulse, simulating the continuing current. Component D is similar to Component A in magnitude but is shorter in duration and simulates the subsequent stroke. In addition to these, Component B, a medium-level current pulse not associated with natural lightning, is intended to sustain the arc between Components A and C during the test. The parameters for each component are described in Table 1.

Table 1. Parameters of the four components according to IEC

	I_{peak} [kA]	I_{mean} [kA]	I^2t [kA ² s]	Length [ms]	Front [s]	Charge [C]
A	120 10%	-	2 10%	0.5	25	-
B	-	2 10%	-	5.0	-	10 10%
C	-	to be agreed	-	to be agreed	-	to be agreed
D	100 10%	-	0.25 10%	0.5	-	-

The test circuit for the Component A involves a capacitor bank feeding through a low-inductance cable to the arc head, which clamps to the test cable. The test circuit for the Component B involves a 30 000 F capacitor bank charged to 400 V and discharging through 0.015 resistor used to indicate the current level. The arc head for A and B components is designed to withstand both the heating and mechanical forces imposed by the current. For Component C, the continuing current is supplied by a battery bank and limited by a resistor. Because of the lower power and longer duration of the Component C test, the arc tends to wander and even self-extinguish before the end of the test time. In order to achieve a stable arc, the arc head is designed to be magnetically balanced with four symmetrical returning paths

with respect to the electrode. Such an arc head does not completely eliminate arc root wandering or early extinguishing, but greatly reduces its likelihood. Figure 1 shows typical current waveforms applied on the cables according to [10].

Since one of the goals of this investigation is to assess the contribution of Components A, B, C and D on the damage caused by the complete combination wave, a series of tests involving the various waveform components, separate and in combination, were performed. The basic test program involved four waveforms, each to be applied to two samples of each type of cable: A alone, B alone, C alone and the combined waveform A + B C D, where the sign "+" means that A component is performed separately from B C D components, which were done consecutively. There were two C nominal levels: C1 with 100C charge transference (200A x 500ms) and C2 with 200C charge transference (400A x 500ms). All waveforms had negative polarity. The setup for the tests involved OPGW cable samples of approximately 12 m long tensioned to 13 3% of cable RTS. A 3 mm tungsten rod electrode was located 5 1 cm from the tested samples and a thin fuse wire was used to initialize the stroke. Before each strike, the cable in the arc-head region was locally heated to 40 5 °C with a heat gun to simulate solar heating on a warm day. After testing, visual inspection was conducted to determine the number of broken strands. All samples were submitted to tensile test to determine the rate of residual strength after lightning.

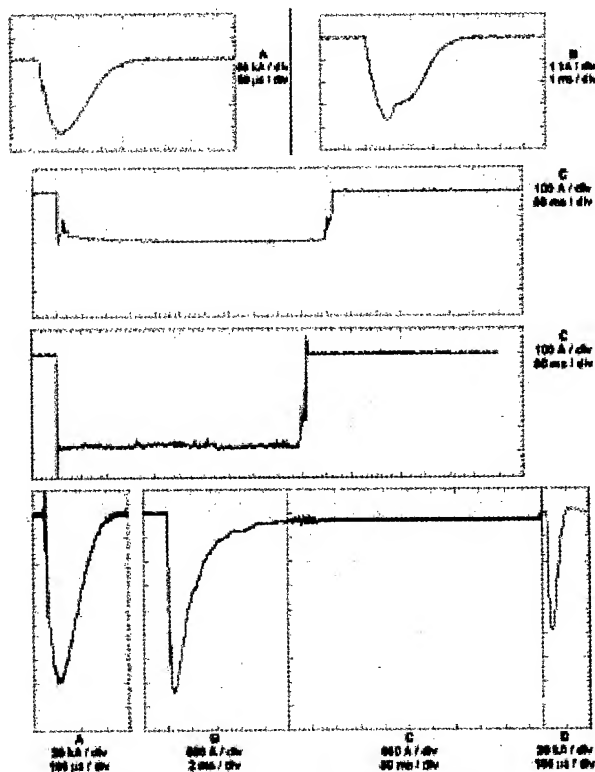


Figure 1. Waveform samples performed on OPGW S2

⁴ Kinectrics International Inc., 800 Kipling Avenue – Toronto, Ontario M8Z 6C4, Canada. Tel. +1 416 207 67 41 (www.kinectrics.com)

Three types of single armor OPGW cables samples (S1 to S3) were fully tested according to the previous testing schedule. Seven additional cables (S4 to S10) were tested for different severity levels of the continuous C component alone. Table 2 shows the cable structures of the OPGW submitted to testing which are schematically shown in Figure 2.

Table 2. OPGW structure of the cables tested.
SSCT stands for Stainless Steel Central tube; AL stands for Aluminum tube; SSST stands for Stainless Steel Stranded Tube, AS stands for Aluminum clad Steel, and AA stands for Aluminum Alloy.

#	OPGW	Type	Armour # x wire [mm]	Cable [mm]	RTS [KgF]	UTS [KgF]
S1	88A21z	SSCT	(4 AS+3AA) x 2.60	8.8	3076	3814
S2	32C50s	AL	15 AS x 2.20	13.2	7150	9368
S3	50H71z	AL	12 ACS x 3.0	15.0	10 726	12746
S4	27C36z	AL	(6 AS+7AA) x 2.40	12.7	4414	5341
S5	51E67z	AL	14 AS x 2.70	15.1	10240	12513
S6	30B50z	AL	13 AS x 2.44	13.0	7615	8992
S7	80A21z	SSCT	9 AS x 2.00	8.0	3547	4235
S8	88A26z	SSCT	8 AS x 2.40	8.8	4526	5680
S9	99A34z	SSCT	7 AS x 3.00	10.0	5963	7035
S10	51D57Ds	SSST	1 AS x 3.45 5 AS x 3.30 + SST 15 AA x 2.52	15.1	8848	10520

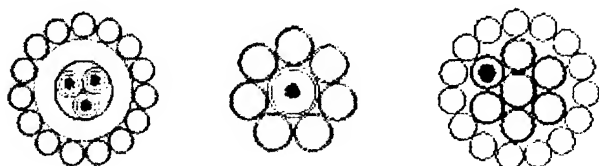


Figure 2. OPGW structures: with Aluminium tube (left), Stainless Steel Central Tube (center), and Stainless Steel Stranded Tube (right)

3. Results

Table 3 summarizes the results for OPGW S1 (88A21z). Component A causes minimal damage over a broad patch and no wires are broken. The residual breaking strength is that of the untested cable. Component B causes also minimal damage on the samples but the breaking strength decreases by 10%. As expected, Component C causes the most damage. For 100 C charge transference, the residual-breaking load is reduced by 40% and steel tube and fiber optics are damaged. For 200 C, the sample is severely damaged (all wires and central steel tube are broken). The results for the combination wave show that the damage of B and C components are cumulative. Figure 3 (left column) shows the cable samples after each lightning component is applied.

Tables 4 and 5 summarize the results for OPGW S2 and S3, respectively; Figure 3 (right column) shows the damage on the samples for OPGW S2. At C₁ level, the residual breaking strength is reduced to 47% of its original value for OPGW S2 and to 65% for OPGW S3. Such a

difference can be explained in terms of the large diameter wires of OPGW S3 relative to those of OPGW S2 together with a higher cable diameter. The combined waveform with C₁ causes no or very little additional damage to the samples. Comparing the rate of residual strength to the number of broken wires it is worth noting that it is not necessary for strands to be visibly broken for them to be structurally weak. For example, OPGW S2 at the combination level with C₂ shows a breaking strength of 34% with 2 broken wires and 44% with no broken wire for almost the same charge transference level.

Regarding the reliability of the optical system results are quite similar to those of OPGW S1 up to 100 C except that, for OPGWs S2 and S3, the optical unit (aluminum tube) is never damaged. The reason might be that aluminum has a much larger thermal and electrical conductivity than stainless steel and, therefore, the aluminum tube properly absorbs the arc energy and current of the flash, thus reducing the damage and protecting optical fibers.

Table 3. Charge transference in Coulombs, Number of Broken Wires, and Rate of Residual Strength (rate of ultimate tensile strength before and after testing) for OPGW S1 (88A21z). (*) SS means that stainless steel tube containing the fibers was severely damaged by lightning arc.

Component	1st shot			2nd shot		
	Charge	NBW	RRS	Charge	NBW	RRS
A	-	0	100%	-	0	100%
B	-12.5	0	86%	-11.1	0	93%
C ₁	-89	4	60%	-102	3+SS	64%
A+BC ₁ D	-109	4+SS	41%	-117	4+SS	48%
C ₂	-187	7+SS	0%	-192	6+SS	21%
A+BC ₂ D	-162	7+SS	0%	-	-	-

Table 4. Charge transference in Coulombs, Number of Broken Wires, and Rate of Residual Strength for OPGW S2 (32C50s).

Component	1st shot			2nd shot		
	Charge	NBW	RRS	Charge	NBW	RRS
A	-	0	100%	-	0	100%
B	-8.9	0	93%	-8.8	0	92%
C ₁	-95	3	46%	-94	7	47%
A+BC ₁ D	-110	2	64%	-110	1	60%
C ₂	-170	7	39%	-186	1	53%
A+BC ₂ D	-221	2	34%	-234	0	44%

Table 5. Charge transference in Coulombs, Number of Broken Wires, and Rate of Residual Strength for OPGW S3 (50H71z).

Component	1st shot			2nd shot		
	Charge	NBW	RRS	Charge	NBW	RRS
A	-	0	100%	-	0	99%
B	-8.8	0	96%	-9.2	0	99%
C ₁	-97	1	60%	-99	1	65%
A+BC ₁ D	-104	1	60%	-123	1	49%
C ₂	-192	2	52%	-189	3	59%
A+BC ₂ D	-209	1	58%	-210	1	50%

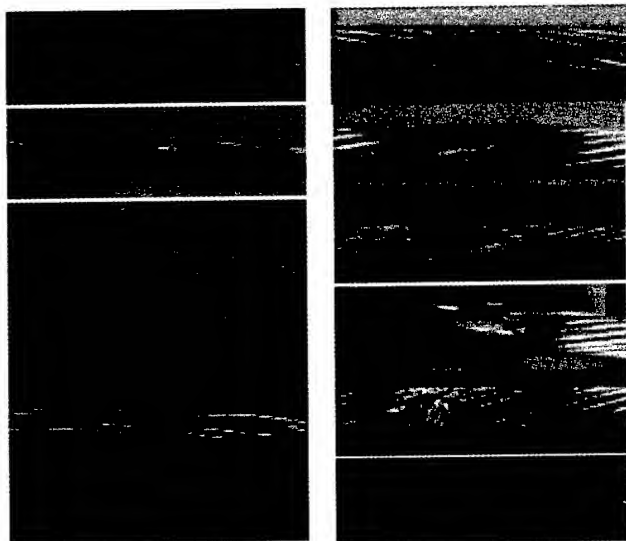


Figure 3. Lightning damage of different waveforms on OPGW S1 (left column) and S2 (right column). From top to bottom, components A, B, C₁, C₂, A+BC₁D and A+BC₂D

This statement can be supported by analysing the damage by charge transference levels of 200C on these two cables which show a quite large residual strength after testing compared to that of OPGW S1. This result can be a direct consequence of the combined effect of the charge transference level, the optical unit material and the dimension of the arc root relative to the cable diameter. When the arc root and cable diameters are similar (10mm) all the thermal energy supplied by the arc starts to fuse the upper strands (those closer to the electrode). Since the magnetically balanced electrode stabilizes the arc, further penetration of the arc root to the bottom strands occur causing the complete destruction of the armour. However, for large cable diameters, only the upper strand section is damaged. In addition, the aluminium tube looks to block the pass of the arc root to the bottom section of the armour thus limiting the damage to approximately half of the wires of the armour. The resulting residual strength is then in the vicinity of 50%.

In order to verify these statements a new series of lightning tests were carried out on OPGWs S4 to S10. Along this series, only the C-component waveform was performed but changing the charge transference level from 50 to 200C. Results are summarized in Table 6.

The optical unit was never damaged for OPGWs S4 to S6. OPGW S4 (27C32z) shows barely the same rate of residual strength (60-50%) for charge transfer levels going from 50 to 213C although the visual damage on wires is larger for increasing charge transfer. Similar results are observed for OPGW S5, a larger diameter cable with 2.70 AS wires.

Comparing the results for OPGWs S3 and S5 (similar cable diameters) it is observed that similar residual strengths are left independent of the diameter of the wires of the armor. This is in agreement with the idea that, for

large charge transfer levels, the damage caused by lightning is related to the dimension of the arc root relative to the cable dimension and less dependent on wire diameter.

Results for OPGW S7 to S9 correspond to lightning strikes on central steel tube structure. The stainless steel tube for these three cables is the same but the difference is the number and diameter of the wires of the armor. OPGW S7 shows a residual strength as low as 22% at 110C. In addition, the stainless steel tube is severely damaged at 155C. Same behavior is observed for OPGW S8, but the residual breaking strength is 34% and the steel tube results damaged at 208 C. However, for OPGW S9, with larger diameter wires and thus larger cable diameter (10 mm), the stainless steel tube is not damaged although the rate of residual strength is closed to 30% for 204 C. These results indicate that, provided the stainless steel tube is the same, the larger the diameter of the wires (thus the cable diameter) improves the protection of the OPGW against lightning strikes of higher charge transfer. It is worth noting that the complete damage observed at 187C for the central stainless steel tube S1 could be a direct consequence of using a mixed armour made of aluminum alloy and aluminium clad steel wires in the armor.

Finally, the last rows of Table 5 show the results for a double layer OPGW with a stranded steel tube. The cable has a central metallic element of AS 3.45mm, an inner armor made of 5 AS wires 3.30mm and the stainless steel tube, and an outer armor of 15 AA wires of 2.52mm diameter. For this cable, tests were done trying to perform the lightning strikes in a position close to the stainless steel tube since this is the most severe condition that can occur in the field from the point of view of reliability of the telecommunication system. Results show that the stainless steel tube was never damaged in all the range of charge transference levels (50-200C) whereas the rate of residual strength follows the trend of OPGW S3, an Aluminum tube OPGW with single layer and same outer diameter.

Table 6. Charge transference in Coulombs, Number of Broken Wires, and Rate of Residual Strength for C-component lightning tests on OPGWs S4 to S10. AS and AA references the material of the wire broken. (*) SS means that stainless steel tube containing the fibers was severely damaged by lightning arc.

OPGW	1st shot			2nd shot		
	Charge	NBW	RRS	Charge	NBW	RRS
27C32z S4	53	1AS+1AA	62%	49	1AS	61%
	101	1AA+2AS	61%	101	3AA+2AS	45%
	153	3AA+2AS	59%	213	3AA+2AS	56%
51E67z S5	92	0	55%	111	3	59%
	149	2	58%	152	3	57%
	185	4	43%	187	4	57%
30B50z S6	51	1	70%	54	1	68%
80A21z S7	47	2	51%	49	3	53%
	91	3	47%	102	4	44%
	110	5	22%	155	5+SS (*)	30%
	153	4	36%	-	-	-
88A26z S8	53	2	56%	52	0	61%
	106	1	48%	102	1	43%
	167	3	40%	140	2	41%
	225	5	34%	208	4+SS (*)	40%
99A34z S9	52	1	64%	55	1	65%
	110	2	56%	106	2	56%
	138	1	53%	141	2	45%
	211	3	40%	204	4	29%
51D57Ds S10	48	1 AA	77%	54	3 AA	74%
	98	2 AA	50%	90	2 AA	78%
	158	6 AA	55%	140	6 AA	52%
	213	5 AA	72%	194	7 AA	52%

To summarize the above experimental results, Figure 4 shows the worst values of the rate of residual strength vs. the charge transfer for the cables tested. Despite the scattering of the results due basically to the behavior of the arc root on the test samples, a general trend can be clearly observed. OPGW cables with diameter larger than 12.0mm show (in average) a decreasing rate of residual strength up to 50% RTS at 200C (solid line), whilst cables with diameter lower than 10 mm show a 30% RST at 200C (dotted line) and, more importantly, the optical unit is damaged for three of the four cables tested for charge transfer values above 100 C.

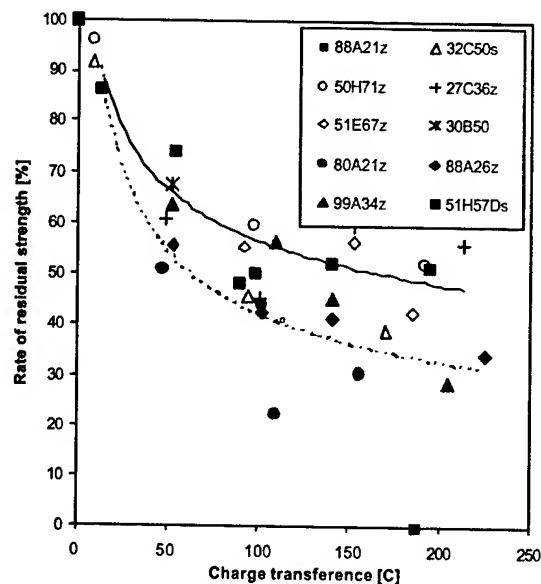


Figure 4. Rate of residual strength vs. charge transference for different OPGW cables. The solid/dotted line is the interpolating curve for cables above/below 12mm diameter.

4. Conclusions

This paper analyzes the effects of different components of the lightning waveforms according to [10] on different OPGW cable structures.

As far as the different components are concerned, it is shown that Component A (so D) alone causes no damage to the cable. The artificial B-component alone causes little damage to the samples. Component C, the continuing current, causes the larger damage. Therefore, combining component C with AB and D has no significant effect, and so it is unnecessary.

As regards the lightning damage from C component alone, it is shown that it increases progressively with increasing charge transfer level. Test levels up to 50C (covering 95% of all negative lightning events) lead to one to three broken strands, similar to lightning damage observed in field. OPGW cables with diameter larger than 12.0 mm show a rate of residual strength around 50% at 200C and no damage to the optical unit. Small diameter cables (<10 mm) with central stainless-steel optical unit show rates of residual strength around 30% of its original value at 200 C, and the optical unit is severely damaged for diameters below 9.0 mm at this charge transfer level. These results indicate that central stainless-steel tube designs with single armor have to be used only in areas with medium-low Keraunic levels. Whenever possible, it is safe to use OPGW with outer diameter larger than 12 mm, but with approximately the same weight of the original ground wires, in order to avoid heavy additional loads to the towers of the overhead lines.

The above results show that safe and cost effective design criteria can nowadays be defined for various OPGW

applications, considering both mechanical and lightning resistance together with the Keraunic level of the area of installation.

5. References

- [1] M. Darveniza, F. Popolansky, E.R. Whitehead, "Lightning protection of UHV Transmission lines", *Electra*, No. 41, July 1975, pp. 39-69.
- [2] R. B. Anderson, A.J. Erikson, "Lightning parameters for engineering applications" *Electra*, No. 69, March 1980, pp. 65-102
- [3] W. A. Chisholm, T.A. Short, P. Chowdhuri, R. Bratton. "Lighting Parameters for OPGW", OPGW Input, IEEE 1997
- [4] T. Shinada, "Research on the protection of overhead ground wires against lightning", IEEE/PES 1994 Winter Meeting, New York.
- [5] M.A. Uman. *The lightning discharge* (New York: Academic Press), 1987
- [6] K. Berger, R.B. Anderson and H. Kroninger, "Parameters of lightning flashes", *Electra* 40, 101-119.
- [7] W. Zischank, J. Wiesigner. "Damages to Optical Ground Wires caused by lightning", 10th International Symposium on high Voltage Engineering (ISH'97), August 1997, Montreal, Canada.
- [8] J.P. Bonicel, O. Tatat, U. Jansen, G. Couvrie, "Lightning strike resistance of OPGW", International Wire & Cable Symposium Proceedings 1995.
- [9] W.A. Chisholm, C. Pon, "Development of realistic lightning arc tests for optical fiber ground wires", internal report.
- [10] IEC Standard 60794-4-1:1999, "Aerial Optical cables for high voltage power lines".
- [11] MIL-STD 1757 "Aerospace Standar on 4Component Lightning Wave", June 1980

Authors



Lluís-Ramon Sales Casals was born in Berga in 1967. He graduated in Technical Telecommunication Engineering and Superior Telecommunication Engineering by Universitat Politècnica de Catalunya (UPC). He joined Cables Pirelli, S.A. in 1991 where he has been engaged in Quality control of optical fiber cables, Product Development of Optical & Energy cables and since 2001 he is the Engineering & Quality Manager of Pirelli Telecom Cables y Sistemas de España, S.A. He is an active member of IEEE Fiber Optics Working Group.



Josep Martin-Regalado was born in Barcelona in 1970. He got the M.Sc. in Physics at the Universitat de Barcelona, and the Ph. D. degree in Laser Physics in 1997 at the Universitat de les Illes Balears. He joined Pirelli Cables y Sistemas de España, S.A in 1998 where he is Project Manager of the Development Dept. He is also responsible of the testing laboratory of OPGW cables.



Alessandro Ginocchio was born in Milano in 1947. He graduated in Electrical Engineering from Politecnico di Milano in 1972 and joined Pirelli in 1974, where he was engaged in the research and development on submarine cables. Since 1987 he has been responsible for the technological development of optical fiber cables.

A Downsized Non-Metallic Drop Cable for FTTH

Kazunaga Kobayashi, Masahiro Kusakari, Shimei Tanaka, Keiji Oohashi

Fujikura Ltd.

1440 Mutsuzaki, Sakura-shi, Chiba-ken, Japan

+81-43-484-3945 kkobayashi@s.fujikura.co.jp

Abstract

We have newly developed downsized non-metallic self-supported aerial drop cable for FTTH. The new 8-figured drop cable of only 2x5 mm outer diameter is unique structure. Optical fiber element, which has optical fiber and two non-metallic strength members, and metallic supporting wire are arranged and sheathed with flame-retardant polyolefin material.

We adopted two types of strength members, one is glass FRP and the other is high strength plastic filament.

These non-metallic drop cables have many advantages, that is, lower construction cost, easy installation, excellent mechanical and optical characteristics, and excellent reliability. It is no doubt that the simple and inexpensive FTTH networks can be constructed by using these drop cables.

Keywords

Optical; Drop; Wire; Cable; Non-metallic

1. Introduction

In recent years, the demand for FTTH network is rapidly increasing in Japan. In order to construct FTTH network economically, it is necessary to reduce both the components cost and the construction cost of the networks. From the viewpoint of drop cable design, the cable structure should be designed considering easy installation, low-priced structure, and excellent reliability.

Figure 1 shows the current aerial drop cable in Japan. Optical fiber, two metallic strength members, and supporting wire are arranged and sheathed with PVC or flame-retardant polyolefin material. The cable has several features. First, it is very thin and inexpensive structure. Second, the cable has excellent in mechanical and optical reliability, even the divergence part of the cable, because rigid metallic wires are used as the strength member of the optical fiber element. Third, the cable can be easily installed in the closure, because the fiber can be easily taken out and the supporting wire can be easily separated from the cable.

However, when this cable is installed, the extra work is required to prevent the surfer surge, that is, cutting the cable at an outside termination box and connecting it to an indoor cable.

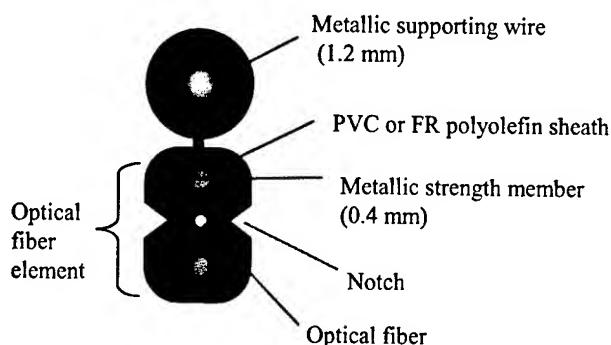


Figure 1 The current optical drop cable in Japan

To improve this problem, we developed aerial drop cable with non-metallic strength members for the reduction in the construction time and the components.

2. Design of the new non-metallic aerial drop cable

2.1 Basic cable structure

The basic structure of the new drop cable is designed by following the current type cable structure. That is thin 8-figured structure which consists of optical fiber element and supporting wire part.

2.2 Cable dimension and supporting wire size

We carefully examined the outer diameter and the supporting wire size so that the cable elongation might not exceed the safe range even in hard environmental condition, such as strong wind with high or low temperature. We designed the cable of 2x5 mm in outer diameter. And we adopted a steel wire of 1.2 mm diameter for the cable.

2.3 Optical fiber

We developed one fiber type and two fibers type cables, in order to adjust to the media converter of various types.

2.4 Study of the non-metallic strength member

We investigated the structure of the non-metallic strength member. We made four types of cables with various non-metallic strength members for trial. Figure 2 shows the structure of these cables. In

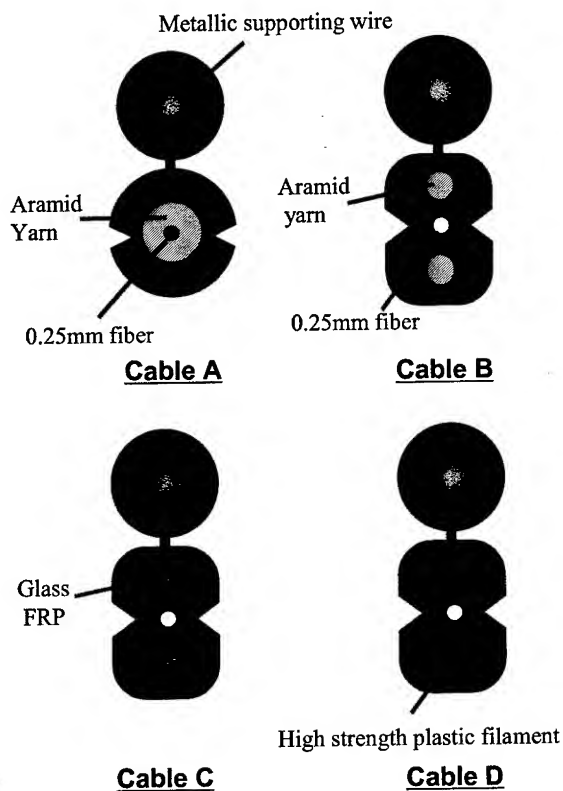


Figure 2 The prototype cable structure

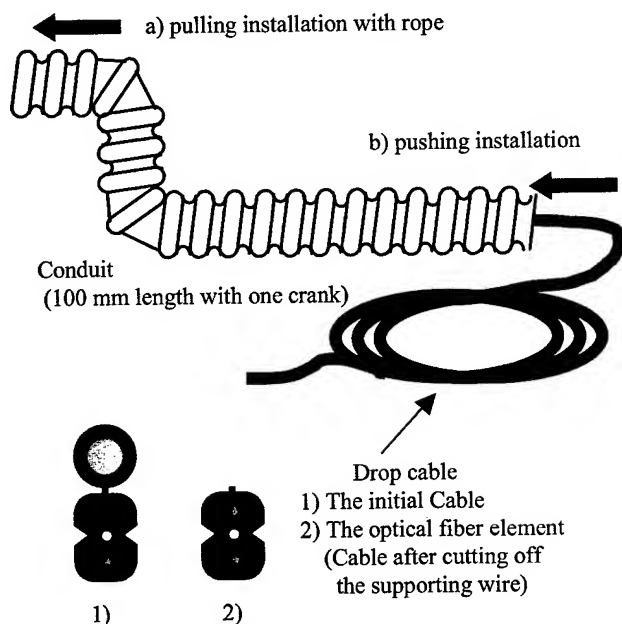


Figure 3 Illustrates of the installation test procedure

Cable A, aramid yarn surrounds the optical fiber. In Cable B, two bundles of aramid yarn are placed both side of the optical fiber in the sheath material. In Cable C, two glass FRP rods are placed both side of the optical fiber in the sheath material. In Cable D,

two hard plastic filaments are placed both side of the optical fiber in the sheath material.

These cables were subjected conduit installation test. Figure 3 illustrates the test procedure, and Table 1 shows the test result. These cables were pushed or pulled into the conduit. All the cables were easily installed into the conduit. However, as for the optical fiber element installation, only the hard plastic and the FRP type cables (Cable C, D) were able to be pushed into the conduit smoothly.

Then we evaluated the lateral pressure characteristics of the cables. Figure 4 shows the result of the test. The Cable B, C and D show almost no loss increase, up to 1960N. These test results indicate that stiff strength member is desirable for cable installation.

So, we developed two types of non-metallic drop cables, one is the cable with glass FRP as the strength member (FRP type cable), and the other is the cable with high strength plastic filament (PF type cable).

Table 1 The installation test result

	The initial cable		The optical fiber element (the cable after the supporting wire is	
	Pushing	Pulling	Pushing	Pulling
Cable A	Pass	Pass	Failure	Pass
Cable B	Pass	Pass	Failure	Pass
Cable C	Pass	Pass	Pass	Pass
Cable D	Pass	Pass	Pass	Pass

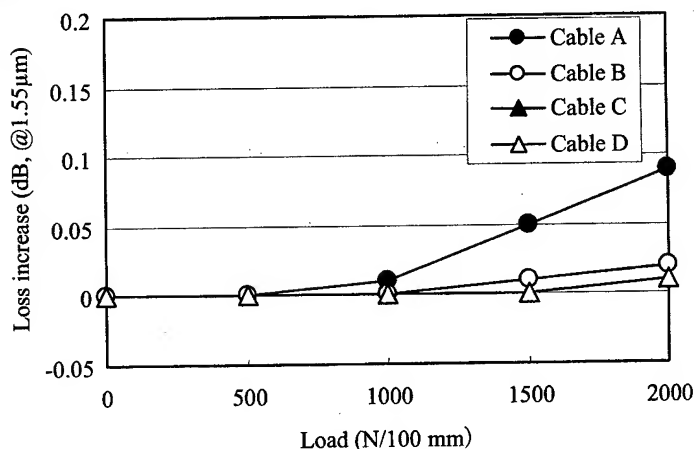


Figure 4 Lateral pressure characteristics of the trial cables

2-5 Structure of the newly developed cables

Figure 5 shows the cross section of the newly developed aerial drop cables. Primary coated optical fiber(s), two non-metallic strength members, and supporting wire are arranged and sheathed with flame-retardant polyolefin material. In order to keep reliability on optical characteristics, the strength member should be adhered to the sheath.

In this case we have applied adhesives to the FRP while the plastic filament uses its unique star cross-sectional shape to adhere itself with sheath material.

Table 2 shows the main characteristics of these cables. The outer diameter of the cables are about 2x5 mm. The maximum tensile road of the cable is 700N. As for the maximum tensile road of the optical fiber element, the PF type cable has about two thirds of the FRP type cable. But the PF cable is more flexible and tough than the FRP cable. So, these cables can be properly used according to the environment.

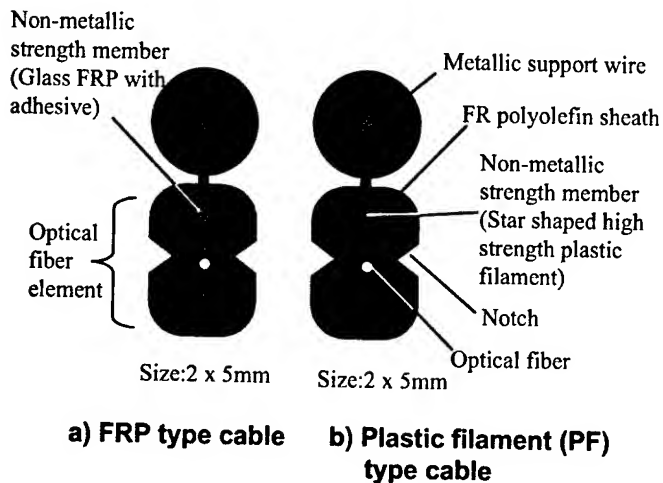


Figure 5 The cross section of the newly developed drop cables

Table 2 Main characteristics of the cables

	FRP type	PF type
outer diameter	2x5 mm	2x5 mm
Maximum tensile road (Supporting wire)	700N	700N
Maximum tensile road (Optical fiber element)	40N	25N
Minimum bend radius (Optical fiber element)	40mm	30mm

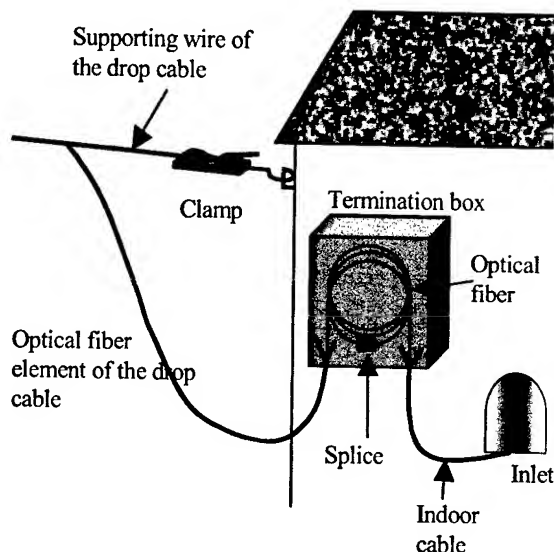
3. Advantages of the new drop cable

a) Reduction of component and construction work

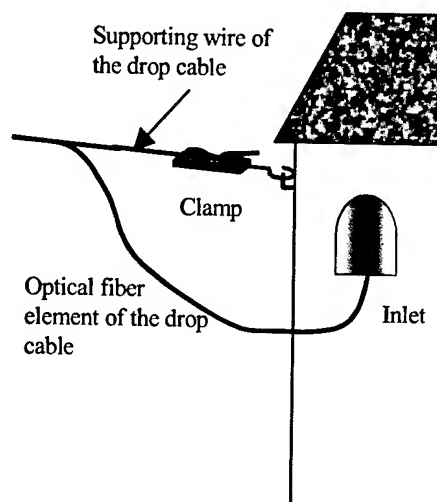
Figure 6 shows the example of wiring for the drop cable in outdoor.

The current cable should be terminated and connected to indoor cable at an outside termination box to prevent the thunder surge (6-a).

On the other hand, the newly developed non-metallic drop cable can be installed from the drop point into the house without termination box (6-b). So, we can achieve the reduction in the construction time and components by using this cable.



a) Current type (metallic type) cable



b) Newly developed (non-metallic type) cable

b) Easy separation

Figure 6 The example of wiring for the drop cable in outdoor

The optical fiber element can be easily separated from the supporting wire, because the cable has 8-figured structure with thin bridge part. In addition, the optical fiber can be easily taken out, because the optical fiber element has notches on the sheath above the fiber.

So, we can easily connect this cable to the feeder cable or media converter.

c) Easy fixing

Thin supporting wire can be applied for the cable because the cable has thinner structure. The supporting wire is steel wire of 1.2mm in diameter. Such size of wire can be easily bent by hand. So, we can use the clamp, supporting-wire-winding-type clamp shown in figure 7, for cable fixing. By using this inexpensive clamp, we can fix the supporting wire very easy, that is, we can bend and wind the wire onto the clamp by hand.

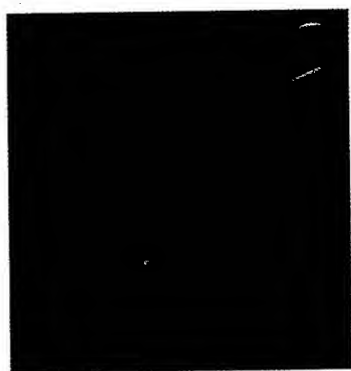


Figure 7 Supporting-wire-winding-type clamp

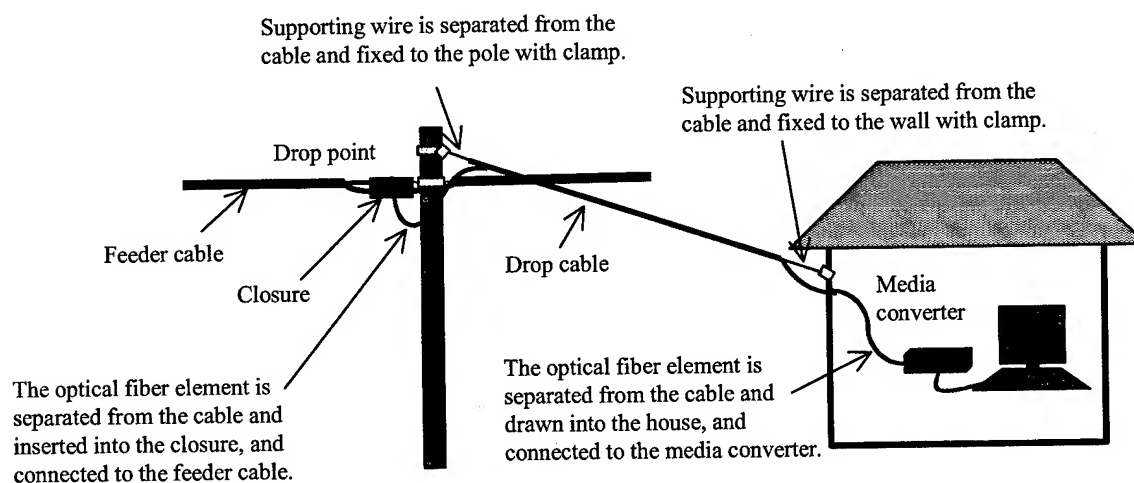


Figure 8 Outdoor distribution model

d) Excellent environment and mechanical stability

The optical fiber element has two rigid strength members, which are adhered enough to the sheath.

The optical characteristics of the divergence part will be kept even in the low temperature, because of these strength members. In addition, the divergence part has sufficient strength in handling such as cable installation work at the drop closure.

4. Outdoor distribution model

Figure 8 shows a typical distribution model of FTTH system by using the newly developed cable.

At the drop point, the drop cable is separated to supporting wire and optical fiber element. The supporting wire is fixed to the pole with the supporting-wire-twisting-type clamp. The optical fiber element is inserted into the closure and fastened. Then the optical fiber is spliced to the feeder cable. At the other side of the cable, the supporting wire is cut off and fixed to the wall of the house. And the cable is drawn into the house and connected to the media converter.

5. Characteristics of the trial cable

5-1 Optical loss after cabling

Table 3 shows the optical losses of these cables after cabling. All the cables were no loss increase after cabling.

Table 3 Optical loss after cabling

	FRP Type	PF Type
Attenuation (dB/km, @1.55 μ m)	0.20	0.20

5-2 Mechanical test

We examined the mechanical characteristics of the cables such as lateral pressure, bending, impact, twisting, and squeezing test. The test conditions and the results are summarized in Table 4. Almost no loss increases were observed in all of these tests.

Table 4 Mechanical properties of the drop cables

Test item	Test condition	Result	
		FRP type	PF type
Lateral pressure	Length=100mm Load=1960N	<0.05 dB	<0.05 dB
Bending	R=30mm 90°	<0.05 dB	<0.05 dB
Impact	0.3kg x 1m 1 time	<0.05 dB	<0.05 dB
Twist	90° 1 cycle	<0.05 dB	<0.05 dB
Squeezing	R=250mm Load=700N 4 cycles	<0.05 dB	<0.05 dB

5-3 Reliability test

We then examined the attenuation temperature characteristic after cabling. The cable winding on a drum of about 500m length was tested in a chamber. Figure 9 shows the test result. Almost no loss increases were observed in the range of -30/+70 degree C.

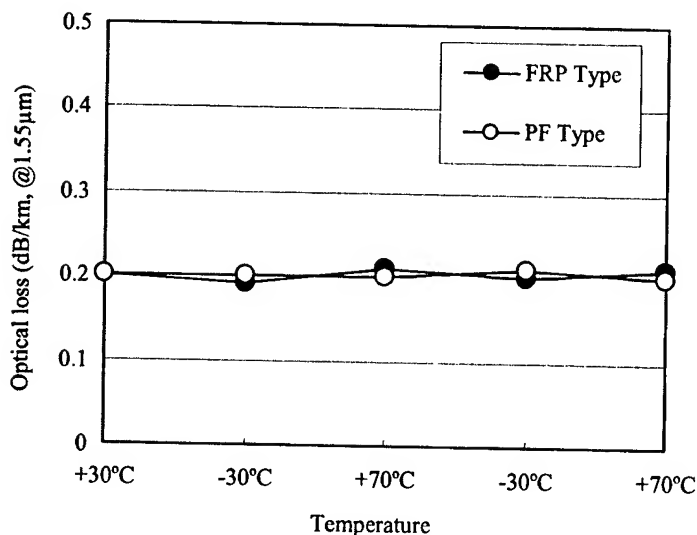


Figure 9 Temperature characteristics of the newly developed cables

We also examined the cable field test. Figure 10 shows the illustration of the field test method. About 30m of cable was installed from an outside pole into a house. Table 5 shows the test result. Almost no loss increase was observed for 8 months.

Therefore, it is confirmed that the cable has excellent reliability.

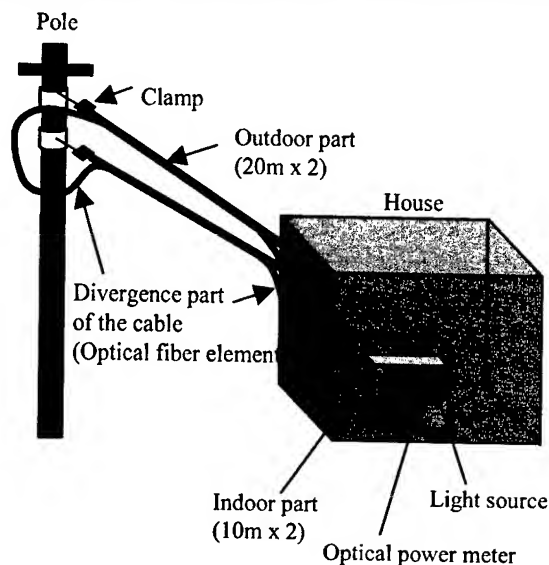


Figure 10 Illustration of the field test

Table 5 The test condition and the test result of the field test

Test condition	
-Outdoor part length	About 40m(20m x 2)
-Indoor part length	About 20m(10m x 2)
-Total cable length	About 60m
-Initial tension of the outdoor part	About 90N
-Test term	8 month (Summer to Spring)
-Field temperature	-5°C to +34°C

Test result		
	FRP Type	PF Type
Loss increase during the test (@1.55μm)	<0.05 dB	<0.05 dB

5-4 Flame test

We examined the flame test of the cables in accordance with IEC 332-3-C. Table 6 shows the test result. All the cables met the test requirements.

Table 6 Flame test results

FRP Type Cable	PF Type Cable
Pass	Pass

6. Conclusion

We have newly developed two types of thin non-metallic self-supported aerial drop cable for FTTH. One is the cable with glass FRP and the other is the cable with unique star shaped plastic filament. These cables have excellent optical and mechanical characteristics. These cables also have advantage in installing work. Because, by using these cables, the number of procedures and components can be reduced.

So, it is no doubt that the simple and inexpensive FTTH networks can be constructed by using these drop cables.

References

- [1] S. Furukawa, et al., "An economical and practical optical fiber distribution system for residential premises," IWCS, pp.842-851, 1997
- [2] K. Kobayashi, et al., "A self-supported aerial drop cable for FATTH," NFOEC 2000 Technical Proceedings Volume 1, pp.634-643, 2000
- [3] Y. Murakami, et al., "Design and characteristics of aerial optical drop cable with electric power wires," Trans. IEICE VOL. E-83-B, pp.38-46, 2000

Authors

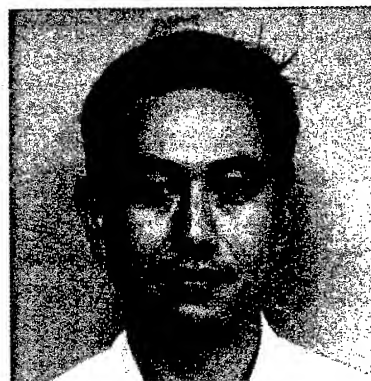


Kazunaga Kobayashi

Research and development department
Telecommunication cable division
Fujikura Ltd.

1440 Mutsuzaki, Sakura-shi, Chiba-ken, 285 Japan

Kazunaga Kobayashi was born in 1961. He joined Fujikura Ltd. after his graduation from Gunma University with a M.E. degree in 1985 and has been engaged in research and development of optical fiber cables. He is now an engineer in the Telecommunication cable Department and member of the IEICE of Japan.



Masahiro Kusakari

Research and development department
Telecommunication cable division
Fujikura Ltd.

1440 Mutsuzaki, Sakura-shi, Chiba-ken, 285 Japan

Masahiro Kusakari was born in 1965. He joined Fujikura Ltd. after his graduation from Nagasaki University with a B.E. degree in 1990 and has been engaged in research and development of optical fiber cables. He is now an engineer in the Telecommunication cable Department and member of the IEICE of Japan.



Shimei Tanaka

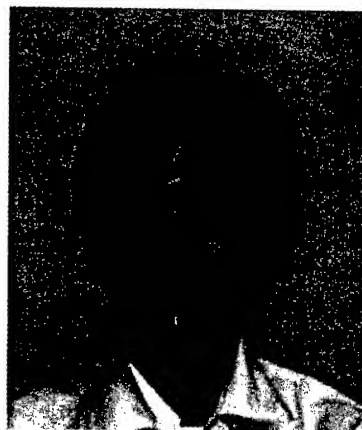
Research and development department

Telecommunication cable division

Fujikura Ltd.

1440 Mutsuzaki, Sakura-shi, Chiba-ken, 285 Japan

Shimei Tanaka was born in 1975. He joined Fujikura Ltd. after his graduation from Chiba University with a M.E. degree in 2000 and has been engaged in research and development of optical fiber cables. He is now an engineer in the Telecommunication cable Department and member of the IEICE of Japan.



Keiji Oohashi

Research and development department

Telecommunication cable division

Fujikura Ltd.

1440 Mutsuzaki, Sakura-shi, Chiba-ken, 285 Japan

He was born in 1956. He graduated from the Tokyo Institute of Technology in 1980 with a B.C. degree in chemistry. After eight years of work as an engineer in the field of materials for motor vehicles, he joined Fujikura LTD. in 1988. He has been engaged in research and development for optical fibers and optical fiber coatings. He is now a general manager of the Research and Development Department Telecommunication Cable Division and a member of the IEICE of Japan.

Development of Optical Fiber Composite Polyvinylchloride Insulated Drop Wire

Fumiki Hosoi, Fuminori Nakajima, Masami Hara,

**Shinichi Hirukawa, *Hirotaka Tanaka*

THE FURUKAWA ELECTRIC CO.,LTD.

Ichihara, Chiba, Japan

Phone: +81-436-42-1771

*KYUSHU ELECTRIC POWER CO.,INC

* Chuo-ku, Fukuoka, Japan

E-mail: fumiki@ch.furukawa.co.jp

Abstract

A study was conducted on the optical fiber composite polyvinylchloride-insulated drop wire (hereinafter called the OPDV), which is a combination of an optical drop wire. G-FRP was used in making an optical unit tension member for the OPDV. Under the title project, a type of tension member using yarns and another type combining yarns with G-FRP were developed to obtain satisfactory handling characteristics. As a result, an optical unit for the OPDV having satisfactory mechanical properties and handling characteristics was successfully developed.

Keywords

OPDV; Optical drop wire; G-FRP

- The strength necessary for cabling and ease of handling
- Flame retardant quality

Flame retardant quality is necessary, considering use in and around the house.

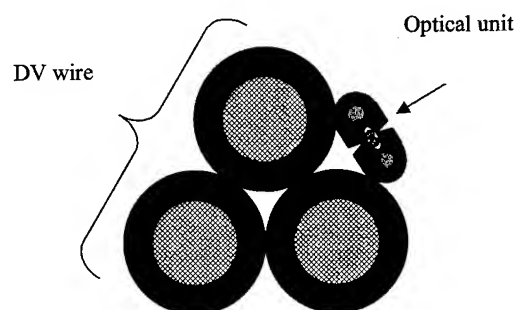


Fig.1 Structure of OPDV

1. Introduction

The widespread acceptance of optical communication by households in general requires optical fiber dropping to houses at low cost. It is necessary for this purpose to study optical cables and other wiring materials and also methods of cabling. Combining a DV wire (polyvinylchloride-insulated drop wire) for electric wiring to houses with optical fibers is effective for using the DV wire as an optical fiber tension member and for reducing the number of cables to be laid. The structure of the OPDV is shown in figure 1. Optical fiber units suited to combination with DV wire were studied for the development of an optical drop wire. G-FRP had been used for an optical unit tension member. An increase in its diameter increases the allowable bending diameter, which in turn causes an increase in the allowable cable bending radius and makes cable handling more difficult. To find a solution to this problem, the structure of optical units for the new OPDV was studied under this project.

2. Requirement for OPDV optical unit

The following conditions were taken into consideration as requirements for an OPDV optical unit.

- Non-metallic structure

The cable itself must be non-metallic to protect the optical devices in the house from the ill effects of the electric current induced by the DV wires.

3. OPDV optical unit design

G-FRP rods about 0.7 to 1.0 mm in diameter had been used to meet the tensile strength required in actually cabling OPDV optical units. FRP rods in this range of diameters need an allowable bending diameter of 50 mm or more so that accidental bending of an OPDV optical unit into too small a diameter during cabling could break the FRP. A solution to this problem demands FRP rods of smaller diameter, but the optical unit wouldn't be able to resist the tension caused by cabling.

3.1 Study on yarn type OPDV optical unit structure

To find a solution to the above problem, a structure using yarns was examined instead of rods as a tension member. Different from G-FRP, the yarn type is free from breakage by bending and permits adjustment of yarn content percentage as desired to satisfy the tensile strength conditions.

3.1.1 Effect of cable jacket materials

The shrinkage of the cable jacket is a matter of concern in using the yarn type. Yarns have tensile strength in the direction in which they are pulled, but cannot withhold the shrinkage of the cable

jacket because of no resistance to its shrinkage due to temperature change, for example. The cable jacket, when it shrinks, becomes wavy, causing the cores to bend and increases loss. This raises the necessity of finding ways of suppressing cable jacket shrinkage.

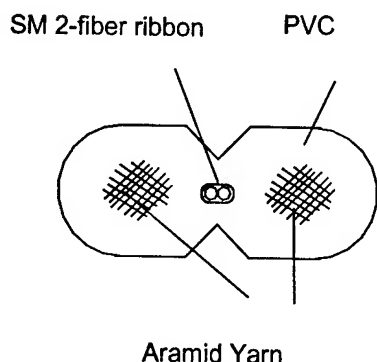


Fig.2 The Yarn Type OPDV Optical Unit

(a) Jacketing material and cross section dependence

One of the causes of elongation or contraction of the cable jacket is temperature change. The harder the jacketing material, the greater will be the force generated therein and the greater will be the force that bends the optical fiber. A large optical unit cross section tends similarly to increase the elongation or contraction of the cable jacket. That is, the force causing elongation or contraction of the cable covering is related to the cross sectional area of the optical unit. This suggests a possibility of aptly controlling the elongation and contraction of the cable jacket by adjusting the hardness of the covering material and the cross sectional area of the optical unit. Samples having different degrees of material hardness and different optical unit cross sectional areas were fabricated. The hardness of the materials used in making the samples is shown in Table 1.

Table 1 Hardness of Optical Unit Jacket Materials

Material	Hardness (Shore A)	100% modulus (kg/mm ²)
A	87	1.15
B	81	0.8

The sample optical units were made of the above materials and to be different in cross sectional area. The temperature characteristics of the samples exposed to high temperature are shown in figure 3. It is seen from figure 3 that loss increased at 70°C. No marked increase of loss was observed at -30°C. These

changes in loss are assumed due to the shrinkage of the cable jacket at high temperature as described before. A comparison of materials A and B regarding increase of loss showed that the sample A with a small optical unit cross sectional area had better characteristics than the sample B, while those with a large optical unit cross sectional area were otherwise. The results shown in figure 3 do not tell any mutual relationship between material hardness and increase of loss. In terms of cross sectional area versus increase of loss, materials A and B showed a mutual relationship completely contrary, and the dependence of increase of loss on cross sectional area is uncertain. The shrinkage of the cable jacket exposed to high temperature, which causes increase of loss, is assumed not so much affected by such factors as material hardness and optical unit cross sectional area. Dominant factors other than these are believed to exist.

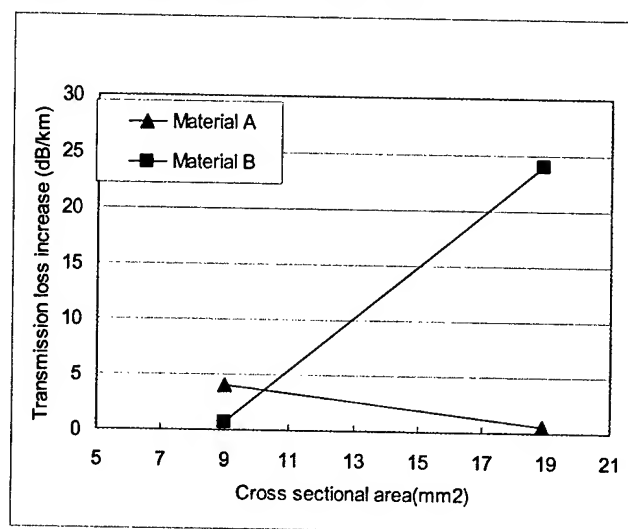


Fig.3 Transmission Loss Increase at 70°C of Yarn Type Optical Units (@1.55µm)

(b) Effect of processing distortion

The main cause of increase of loss from exposure to high temperature is assumed due to processing distortion during optical unit production. Processing distortion means the distortion that remains in the jacketing material after its sheathing. This distortion causes shrinkage of the cable jacket when it is subjected to high temperature hysteresis after its manufacture. The shrinkage of the cable jacket is considered one of the causes of worse temperature characteristics. The increase of loss shown in figure 3 remained even after the temperature was lowered back to 20°C from 70°C. A cable jacket affected by processing distortion will not return to its original state once it shrinks under high temperature hysteresis. This conforms to the above results. It was examined, therefore, how increase of loss would change after exposure to high temperature while changing the processing distortion caused during optical unit production. The results are shown in figure 4.

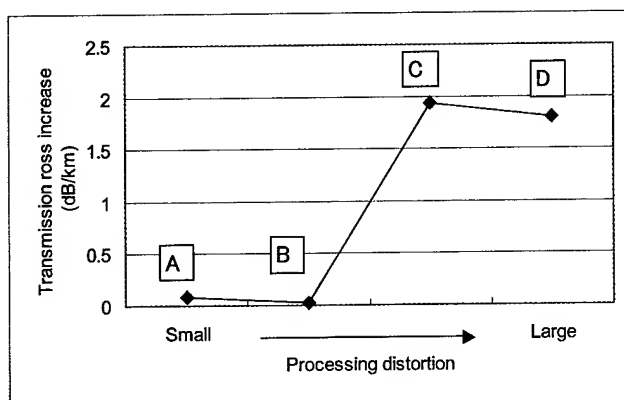


Fig.4 Processing Distortion versus Increase of Transmission Loss at 70°C (@1.55μm)

Processing distortion grows in the order of A, B, C, and D as shown in figure 4. It is seen from the results shown that the smaller the processing distortion of the optical unit, the less will be the increase of loss under exposure to high temperature. The results indicated that the processing distortion of the cable jacket was the main cause of increase of loss when it is exposed to high temperature. Optical units were designed on the basis of these observations.

3.1.2 yarn type characteristics

The yarn-type optical unit prototype designed and fabricated on the basis of the above studies are shown in Table 2. The following are the specs for the upper portion of your paper:

It was found from the results shown in Table 2 that all characteristics except the squeeze characteristics were satisfactory. The squeeze test is intended for evaluating optical units in actual cabling in which the cable jacket might be squeezed when the optical units are gripped by hand. Increase of loss was confirmed by this evaluation test. The assumed cause is this: Fibers have no resistance to shrinkage and do not adhere to the cable jacket so that a manual squeeze of the cable jacket caused it to elongate and form wrinkles, which in turn caused the optical fiber to bend. It was confirmed that, considering not only the temperature characteristics but also the external forces which would be applied during cabling, yarns alone would be insufficient.

Table 2 Yarn Type Characteristics (@1.55μm)

Item	Conditions	Results
Transmission loss	1.55μm	≤0.22dB/km
	1.31μm	≤0.33dB/km
Temperature cycling	-30 to 70°C	≤ 0.02dB/km
Bending	R=30mm	≤ 0.02dB
Lateral pressure	980N/50mm	≤ 0.02dB
Torsion	±180°	≤ 0.02dB
Impact	300g ×1m	≤ 0.02dB
Squeeze	Cable jacket squeezed by hand	2.4dB or more
Flame retardation	JIS C 3005	Passed (Inclined test)

3.2 Study on yarn + G-FRP-type OPDV optical unit structure

This type was developed to compensate for the weak points of the yarn type after examining it. The structure is shown in figure 5.

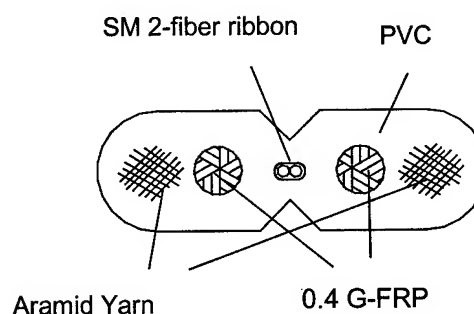


Fig. 5 Fiber + G-FRP Type OPDV Optical Unit

This design employs a small-diameter G-FRP to make it resistant to elongation and contraction of the cable jacket. The small diameter G-FRP permits a smaller allowable bending radius so that FRP bends can be prevented during cabling. Yarns are added to the small-diameter G-FRP because the latter alone is inadequate to withstand the tensile forces applied during cabling.

The results of design and prototype fabrication are shown in Table 3. Satisfactory characteristics were confirmed as shown in the table. The squeeze characteristics that posed a problem with the yarn type did not show an increase of loss because the elongation and contraction of the cable jacket were suppressed by the G-FRP. The combined yarn and G-FRP type controls cable jacket elongation and contraction by the resistance effect of G-FRP and does not increase loss from exposure to high temperature without reducing the processing distortion of the cable covering as in using the yarn type. This means that a broader range of manufacturing conditions can be applied to production.

Table3 Yarn + G-FRP Type Characteristics (@1.55 μ m)

Item	Conditions	Results
Transmission loss	1.55 μ m	≤ 0.22 dB/km
	1.31 μ m	≤ 0.33 dB/km
Temperature cycling	-30 to 70°C	≤ 0.02 dB/km
Bending	R=30mm	≤ 0.02 dB
Lateral pressure	980N/50mm	≤ 0.02 dB
Torsion	$\pm 180^\circ$	≤ 0.02 dB
Impact	300g \times 1m	≤ 0.02 dB
Squeeze	Cable jacket squeezed by hand	≤ 0.02 dB
Flame retardation	JIS C 3005	Passed (Inclined test)

4. Conclusion

A study was conducted on the optical fiber composite polyvinylchloride-insulated drop wire, which is a combination of an optical drop wire. G-FRP was used in making an optical unit

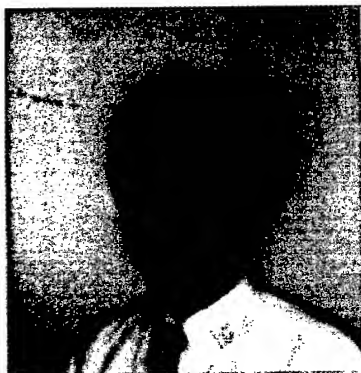
tension member for the OPDV. Under the title project, a type of tension member using yarns and another type combining yarns with G-FRP were developed to obtain satisfactory handling characteristics.

The yarn type was designed to reduce processing distortion of the cable jacket to control its elongation and contraction under exposure to high temperature. As a result, the yarn type could control variation of loss due to temperature change, but in a squeeze test in which cabling was simulated, the cable jacket developed elongation or contraction, causing the optical fiber to bend and increase loss.

As a solution to this problem, the composite type of yarns and G-FRP was developed. Because G-FRP has a resistant effect, the composite type can suppress the elongation and contraction of the cable jacket due to squeezes during cabling and temperature change. Therefore, this type showed satisfactory results in all mechanical characteristics, including characteristics of squeezing by hand.

5. References

- [1] Japanese Standards Association, "Test methods for rubber or plastic insulated wires and cables JIS C 3005", pp24-25, 1993
- [2] F. Hosoi, et al. "Halogen-free, flame-retardant optical fiber cable for the MT- RJ optical connector", Proc. of EC 2000,
- [3] F. Hosoi, et al. "Development of halogen-free flame- retardant optical fiber cables", Proc. of 49th IWCS, pp427 - 432, 2000



Fumiki Hosoi
THE FURUKAWA
ELECTRIC
CO., LTD

Fumiki Hosoi received his M.E. degree in Physics engineering from Tokyo University in 1995. He joined The Furukawa Electric Co., Ltd and has been engaged in research and development of the optical fiber cables.



Fuminori Nakajima
THE FURUKAWA
ELECTRIC
CO., LTD

Fuminori Nakajima received his M.E. degree in Material Engineering from Nagaoka University of Technology in 1992. He joined The Furukawa Electric Co., Ltd. in 1992 and has been engaged in research and development of the optical fiber cables.



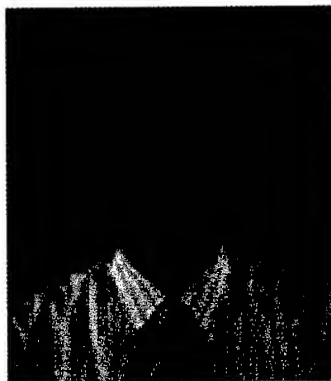
Masami Hara
THE FURUKAWA
ELECTRIC
CO., LTD

Masami Hara received his M.E. degree in Physics from Osaka University in 1987. He joined The Furukawa Electric Co., Ltd and has been engaged in research and development of optical fiber cable.



Hirotaka Tanaka
KYUSHU
ELECTRIC
POWER
CO., INC

Hirotaka Tanaka was born in 1964. He graduated in electric engineering from Kurume National College in 1985. He joined Kyushu Electric Power Co., INC. in 1985. He has been in charge of development of Integrated Automatic Distribution System.



Shinichi Hirukawa
KYUSHU
ELECTRIC
POWER
CO., INC

Shinichi Hirukawa was born in 1967. He graduated in Kanoya Technical High School in 1985. He joined Kyushu Electric Power Co., INC. in 1985.

Results of Qualification of ADSS Cable with Reduced Weight and Diameter

Alessandro Nunes

OFS

Campinas, São Paulo, Brazil

+55-19-3707-6825 · nunesa@ofsoptics.com

Abstract

For ADSS cable weight and diameter are very important characteristics because they directly impact on the mechanical tension induced on the supporting structure (pole or tower).

The cable diameter itself has to be as small as possible because it has a quadratic influence on the tension when ice and/or wind are considered.

Current design technique uses aramid as the cable strength element but it has limitations when very high spans or very adverse environmental conditions are an issue.

This paper presents the results of qualification of new a All Dielectric Self-Supported (ADSS) loose tube cable design technique that provides a reduction in cable weight and cable diameter and, consequently, a reduction of the load induced on the supporting structure, like poles and towers

Keywords

Optical Cable; ADSS; self-supported; aerial cable; PBO; aramid.

1. Introduction

One key point for a new long distance network is where the cable will be installed. The main possibilities are along highways, railways, gas and oil ducts, undersea or on overhead lines. Recently, some companies outside of the telecom sector have found they can increase their revenues charging telecom companies for the use of the right of way (ROW) of their infrastructure. Some of these companies decided to be players in this profitable market, deploying their own cables and becoming carriers carriers.

A solution for the utilities companies in this market is to install ADSS cables on their overhead lines. Initially, it has been a challenge for the fiber optic cable industry to design cables strong enough to support the installation on long spans usually found in the field. The stronger cables had higher weight and diameter placing a higher weight load on the supporting cables and towers.

It has been a constant goal of the optical fiber cable industry to develop ADSS cable designs with reduced weight and diameter in order to increase the maximum installation span and make possible the usage of this type of cable on Extra High Voltage (EHV) overhead lines.

The ADSS structure would also be effective in extreme environmental situations like hurricanes and/or temperatures

variations coming from negative values up to positive values including the area salencies.

The concept of cables with this new techniques begin present here, concluding that PBO (poly-para-phenylene-oxazole) is an effective alternative to the current design technique using aramid yarn. For a span of 1000 meters, the MWT (maximum working tension) of the cable with PBO is 9% smaller than when aramid is used. The thinner yarn layer obtained using PBO also gives more stability to the production process.

2. Mechanical cable strain

Aerial cables are routinely subjected to harsh environments: high winds, ice storms and lightning. OFS loose tube cable products are free of fiber tensile strain while the cable is within its operating constraints. Operating constraints differ for different products and applications. For standard loose tube cables, these constraints typically are a maximum rated cable load of 600 pounds and a temperature range of -40°C to +70°C. For all-dielectric self-supporting aerial cable, there will be no fiber tensile strain up to the maximum rated cable load as dictated by the worst case loading condition and under the conditions as listed on sag and tension charts. Cables can be custom designed to meet special customer applications.

There are situations where aerial cables are the only solution; as over river crossings, mountain slopes, or across a highway. There are two techniques to design the cable in accordance with field conditions; (1) the current technique, which uses aramid yarn, a dielectric material with very high modulus and low specific weight that has proven to be an excellent structure and (2) a novel technique that substitutes the aramid yarns with another synthetic fiber with higher modulus.

3. Prototypes

3.1 Features

We are presenting the characteristics of cables with PBO and aramid with 6 % of sag at EDS (every day stress) condition; Four prototypes were produced to confirm the theoretical calculations: 2 cables for 500 max span and 2 cables for 600 m max span. Two of the prototypes used the current technique and two used the novel technique.

Table 1. Characteristics of cables using the current technique

Characteristics	P1	P2
Span (m)	500	600
Diameter (mm)	15.1	16.2
Weight (kg/km)	202.0	236.5
Maximum working tension (kgf)*	1030	1450
Modulus (kgf)	250,634	265,366
LEC ($10^{-6} 1/^{\circ}\text{C}$)	0.22	0.34

*Without fiber strain

Table 2. Characteristics of cables using the novel technique

Characteristics	P3	P4
Span (m)	500	600
Diameter (mm)	13.6	13.9
Weight (kg/km)	170.0	176.5
Maximum working tension (kgf)*	860	1070
Modulus (kgf)	215,810	274,374
LEC ($10^{-6} 1/^{\circ}\text{C}$)	-0.82	-0.18

*Without fiber strain

4. Tests Results

We are showing here the results of qualification tests of prototypes:

4.1 Tensile Strength Test

The intent of this test is to verify the ability of cable to satisfactorily perform while undergoing tensile loading encountered during operation. The cable is designed to withstand rigorous tensile loading levels.

The cable is subjected to a first tensile loading of 15 % of MWT Load and the increase to a loading up to 150% of its maximum allowable tensile load. The load is applied in 45 %, 75 %, 105 % and 112% of MWT Load cable.

Cable Test Length:

220 meters

Table 3. Tensile Loading Test for 500 m span - aramid

% MWT	Load (kgf)	Elongation (mm/mm)
15	150.0	0.00
45	485.5	0.25
75	810.9	2.45
105	1081.2	3.47
112	1135.3	3.70
150	1621.8	5.38

Table 4. Tensile Loading Test for 600 m span - aramid

% MWT	Load (kgf)	Elongation (mm/mm)
15	150.0	0.00
45	227.0	0.26
75	681.0	1.74
105	1135.0	3.18
112	1589.0	4.58
150	1695.0	4.93

Table 5. Tensile Loading Test for 500 m span - PBO

% MWT	Load (kgf)	Elongation (mm/mm)
15	139.0	0.00
45	418.0	1.29
75	697.0	2.46
105	976.0	3.62
112	1041.0	3.86
150	1395.0	5.29

Table 4. Tensile Loading Test for 600 m span - PBO

% MWT	Load (kgf)	Elongation (mm/mm)
15	160.5	0
45	481.5	1.4
75	802.5	2.55
105	1123.5	3.78
112	1198.4	4.04
150	1605.0	5.49

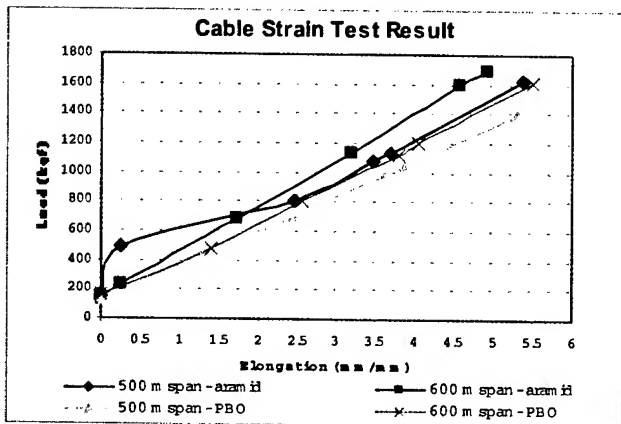


Figure 1. Prototypes cable strain

Comment:

None of the cables exhibited any fiber strain or change in attenuation up to the maximum rated tension.

4.2 Creep Test

Creep is the slow, continued lengthening under a constant load and the intent of this test is to measure the cable creep under the MWT load.

During 240 hours under the MWT load the cable elongation needs to measure in each 5 minutes during the first hour and in each 15 minutes during the next seven hours. In the rest of time three measure during 24 hours. The creep projection curve must have at least a correlation factor of 90 % (R^2) to a trust interval of 95 %.

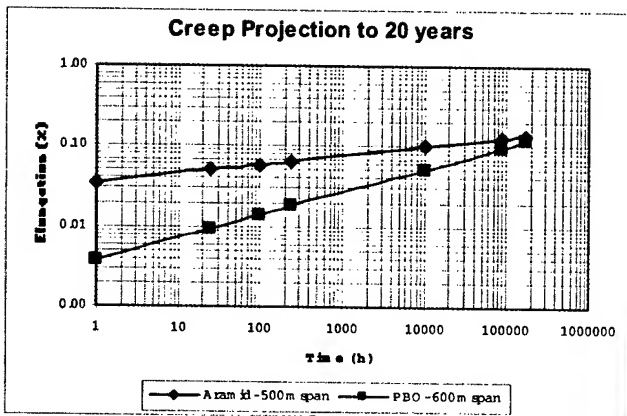


Figure 2. Creep Projection

Comment:

In the time the PBO comportment is different than aramid, but the projection of creep during 20 years are very similar.

We obtained the following correlation factors:

- ✓ 500 m span prototype – aramid: $R^2=0.9669$;
- ✓ 600 m span prototype – PBO: $R^2=0.9764$.

4.3 Cable Aeolian Vibration Test

The intent of this test is to assess the fatigue performance of cable and the optical characteristics of the fibers under typical aeolian vibrations. Aeolian vibrations are caused by gentle, steady wind blowing across a cable and are generally of low amplitude and high frequency. Amplitudes are typically considerably less than the cable diameter and frequencies are in the order of 10 to 100 Hz, depending on wind speed and cable diameter. The cable is subjected to a minimum of 100 million vibration cycles, under the MWT and amplitude equal to one-half the diameter of the cable.

Cable Test Length:

25 meters

Comment:

No broken fibers as a result of test, no changes on attenuation level and no damage to sheath, core components or hardware was observed.

Table 5. Cable Aeolian Vibration Test

Cable	Status
500 m span with aramid	Passed
600 m span with aramid	Passed
500 m span with PBO	Passed
600 m span with PBO	Passed

4.4 Temperature Cycling Test

The intent of the Temperature Cycling Test is to ensure that our cables maintain mechanical and optical integrity when exposed to temperature extremes during storage, installation, and operation.

The reel of cable is placed in an environmental chamber and preconditioned at 23°C. During the Temperature Cycling Test the cable is subjected to 4 cycles of exposure to 48 hours at -20°C and 24 hours at 65°C. Attenuation measurements are made on the fibers at both temperature extremes during the second cycle.

Comment:

No changes on attenuation level.

Table 6. Temperature Cycling Test

Cable	Status
500 m span with aramid	Passed
600 m span with aramid	Passed
500 m span with PBO	Passed
600 m span with PBO	Passed

4.5 Breaking Strength Test

The intent of this test is checking the breaking cable strength without the creep influence.

Table 7. Breaking Strength Test

Cable	Load (kgf)
500 m span with aramid	3653
600 m span with PBO	2800

Comment:

No damages in cable sheath were observed and the practical cable breaking elongation is 1 %.

5. Conclusion

Worldwide usage and applications of ADSS cables continues to increase. Improvements into cable design and response to customer requirements is essential to compete in the fiber optic cable market. Improved strength material with PBO is available to address issues regarding flexibility and handling for the user. PBO proved that it is

a good alternative for long spans applications and extreme environmental conditions.

After final qualification tests proved the PBO technical reliability.

6. References

- [1] Giacaglia, Vallente, Marcello, "Novel ADSS Cable Design Technique for a Reduction Weight and Reduced Cable Diameter" *Proceedings of the 50th IWCS, (November 2001)*.

Author



Alessandro Nunes received a Bachelor's degree in Electrical Engineering from Sorocaba University in 1998 and a MBA degree in Based Value Management from Getulio Vargas University in 2001. He is now the Product Manager of OFS cable Brazil plant.

Suggestion of ADSS cable standardization including installation procedure

Kyung-Tae Park*, Jung-Jin Hwang, Mun-Hyun Do and Jin-Han Kim

R&D Group 1, Fiberoptics division, Telecommunication Network Business

Samsung Electronics Co. Ltd

#94-1, Imsoo-Dong, Gumi-City, Kyung-Buk, Korea.

+82-54-479-7164 pkt1013@samsung.com

1. Abstract

ADSS cable has many strong points compare to OPGW, and a long history of applications in electric power line.

Many cable manufacturers are announcing & launching special ADSS cable which applicable up to 500kV power line. However, utility company still complains about tracking problem even in lower voltage. This cross point is happened when disregard various installation circumstance.

To solve the inveterate problem, tracking, this paper will define what parameters should be considered during cable design, suggest how to approach the solution regarding to cable itself and installation engineering. To assure a long period service life of ADSS cable in extremely high voltage circumstance, following "ADSS cable characteristics" should be well defined with a exact information of "Design parameters during ADSS cable installation". With these cable & site information, it is possible to pass judgment that "ADSS cable installation parameter" is correct or not compare to "Criterion"

Important ADSS cable characteristics

Elastic constant, creep (initial & final), MACT, Ultimate tensile strength.

Design Parameters during ADSS cable installation

Tower & Insulator type (tension or suspension), conductor, weather, span, voltage etc.

ADSS cable installation parameter

Sagging tension, install position

Criterion

- Distance between conductor & ADSS at tower (D @ tower) by wind
- Length from dead-end to a crossing point between conductor & ADSS (L @ cross) by wind both case of initial & final sag situation.
- Check D @ tower and L @ cross is within recommended distance

Voltage	100kV	200kV	300kV	400kV	500kV
D @ Tower	0.75m	1.5m	2.2m	3m	3.7m
L @ Cross (both initial & final sag)	15m	25m	40m	55m	70m

- Ice loaded final sag should satisfy ground clearance.

Keywords

ADSS, Tracking, Installation position,

2. Introduction

There are 2 grades of ADSS cable classified in "Class A & B" electrically according to IEEE P1222 which distinguished TRPE (tracking resistance polyethylene) from normal PE for outer jacket. IEEE P1222 test method is generally accepted to define whether the ADSS cable is applicable up to 25kV space potential or not in terms of the cable jacket damage caused by tracking

However there is a difference between IEEE P1222 test method and real installation circumstance as show in Fig.1

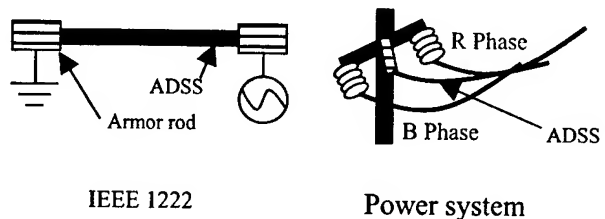


Figure 1. Compare IEEE P1222 test method to power system

For example, in case of suspension insulator, when wind blowing, ADSS is crossing with conductor "R" phase around mid span but at tower is closing to different "B" phase. This situation accelerates tracking current than in case of same phase.

Let's express the power system as a equivalent circuits to show the situation simply.

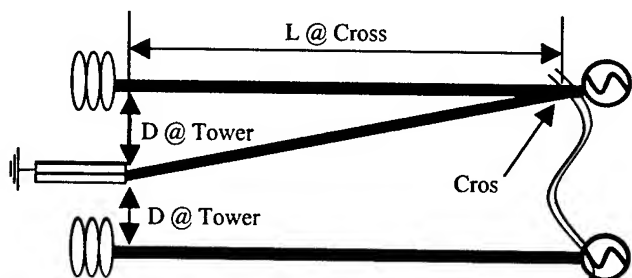


Figure 2. Equivalent circuit of power system

As shown in Figure 2., there are some important design factors, voltage, L @ cross, and D @ tower. The flashover between ADSS and conductor around cross point is intensified and moved to tower as the surface resistance of ADSS is lowered. That means to prevent ADSS jacket melting at armor-rod the length, L @ cross, has more safety factor than 25mm/kV. And it is also necessary to specify the length D @ tower.

3. ADSS cable Installation

During ADSS installation, there are lots of consideration factors. In this section authors confined topics only ADSS cable installation position.

3.1 Ground Clearance

Normally, ADSS cable has lower elastic constant and lighter mass than conductor. Therefore, the sag of ADSS cable is increasing dramatically in case of supposing a ice load in final tension. So, ADSS install position should be provide the ground clearance considering the ice loaded final sag.

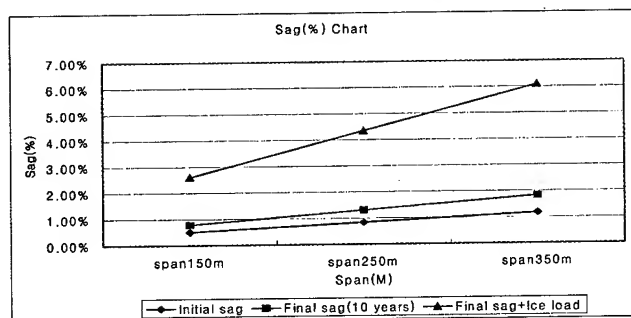


Figure 3. Ground clearance

As shown in Figure 3., ice loaded final sag should be studied in cold regions. That means ADSS install position will be higher in cold weather regions than near the equator.

3.2 Install position

During the site survey, ADSS cable installation position should be selected and verified whether the position satisfy the criterion or not. The necessary information is summarized bellows. First, as shown in table.1, conductor & ADSS characteristics are needed

Table.1 Characteristics of cable

Items	Electric wire	ADSS cable
Outer diameter (mm)	21.0	15.0
Unit weight (kg/km)	974.0	178.0
Elastic modulus (kN/mm ²)	80.4	85.0
Coefficient of thermal expansion (1/°C)	1.5E-5	6.7E-7
Supporting area (mm ²)	261.5	28.8
Initial tension (kN)	16.0	8.0
Final tension (kN)	14.0	6.2

Tower information like as, the co-ordinate of conductors and ground-wire installation position, insulator length are needed. The zero point of co-ordinate is center of tower at ground. And identify tower types whether suspension or tension tower as shown table. 2 .

Table.2 Tower information

Items	Example
Tower type	Suspension
Co-ordinate of conductor (m)	(-2.2, 16), (-2.0, 13), (-2.3, 10) (2.2, 16), (2.0, 13), (2.3, 10)
Co-ordinate of ground-wire (m)	(-2.1, 19), (2.1, 19)
Voltage (kV)	220
Insulator length (m)	1.82
Maximum wind speed (m/s)	42.
Span (m)	400
Allowed ADSS install position (m)	(0, 11.5)

Other information like as wind speed, span and allowed ADSS cable installation position is also needed.

Then, calculate the L @ cross, D @ tower with computer added program to verify the ADSS install position could secure long term period service life without tracking problems in case of both initial and final tension.

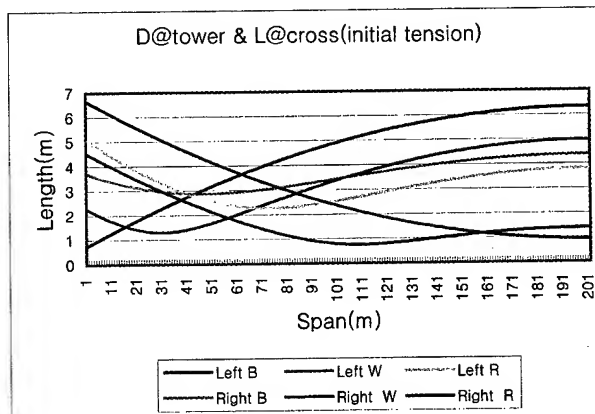


Figure 4. D @ tower & L @ cross (initial tension)

Figure. 4, 5 show the 2D co-ordinate that means along the ADSS cable axis calculate the distance between conductor and ADSS cable on same span. In figure 4 and 5, the equation is solved at maximum wind speed, however at low wind speed, the criterion is sometimes violated. ADSS cable creep characteristic is sometimes critical in compact size tower application. Therefore, final tension situation should always be calculated and verified.

In this example the D @ tower is not meet the request. If the criterion is violated, find another installation position or re-design ADSS cable for satisfying criterion.

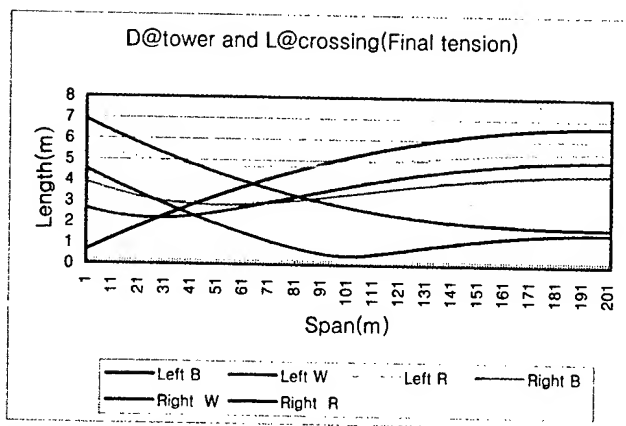


Figure 5. D @ tower & L @ cross (final tension)

4. Conclusion

We set up a miniature test experiment that can produce same space electric field intensity as power system. Therefore we can tested tracking phenomena by changing ADSS installation position according to simulation results with input parameters.(ADSS, conductor, wind speed, ionic concentration, insulator type, phase, creep). Test results show that tracking problem seems a little overstated exclude where coastal region and very contaminated area. However, test results also show that even though TRPE jacketed ADSS, disregarding proper install position & sagging tension, ADSS cable jacket was punched at armor rod at lower voltage in short time.

To prevent the tracking problem, authors suggest a ADSS cable installation procedure. And suggest what parameters should be standardized.

1. References

- [1] Neil R. Haigh, Simon M. Rowland, Arif J. Taha, and Chris N. Carter, "A fully instrumented installation and trial of a novel ADSS cable for very high voltage overhead power lines", 45th Proc International Wire and Cable Symposium(1996) 60-66.
- [2] A.J. Peacock, J.C.G. Wheeter, "Development of aerial fiber optic cables for operation on 400kV power line", IEE Proc. Vol.139, no.6, (1992) 304-314
- [3] Ulrich H.P. Oestreich, Hani M. Nassar, "Self-supporting dielectric fiber optic cables in high voltage lines", 37th Proc. International Wire and Cable Symposium(1988) 79-82.
- [4] K.T Park, J.H Kim, "ADSS cable design for no voltage limits: 48th Proc. International Wire and Cable Symposium(1999)

AUTHORS

Kyung-Tae Park
Engineering and R&D Group 1.
Optical Communication Products Division.
Telecommunication Network Business.
SAMSUNG Electronics Co., Ltd



Kyung-Tae Park was born in 1967. He received a bachelor's degree from Kwangwoon University Korea in 1992 and master's degree from Kwangwoon University in 1994. Now, he is a researcher of Engineering and R&D Group 1 in Optical Communication Product Division.

Jung-Jin Hwang
Engineering and R&D Group 1.
Optical Communication Products Division.
Telecommunication Network Business..
SAMSUNG Electronics Co., Ltd



Mun-Hyun Do
Engineering and R&D Group 1.
Optical Communication Products Division.
Telecommunication Network Business..
SAMSUNG Electronics Co., Ltd



Jin-Han Kim
Engineering and R&D Group 1.
Optical Communication Products Division.
Telecommunication Network Business..
SAMSUNG Electronics Co., Ltd



ADSS Cables with Extended Operating Lifetime

Reinhard Engel, Sabine Will

Coming Cable Systems, RD&E
96465 Neustadt, Germany

David Wartschinski

Technische Universität Ilmenau
98684 Ilmenau, Germany

Abstract

Aerial cables are a fast, elegant and economical solution when electrical power grids have to be upgraded to communication networks. Self-supporting aerial cables can be spanned between the poles under lifeline conditions with only minor safety precautions.

In addition to normal environmental stress, ADSS cables are subject to thermal electrical corrosion known as dry band arcing. This corrosion can be very aggressive and shortens the cable lifetime considerably by eroding the cable jacket.

In the continuous search for more track resistant jacket materials, filled Polyethylene compounds have been developed that prolong the operating lifetime of ADSS cables without giving up the well-known and proven properties of standard PE jackets. A new version of the filled PE jacket is able to extend the operating lifetime of ADSS cables up to nine times compared to an ADSS cable with a standard PE jacket.

The test methods that have been used to characterize the tracking resistance of the new jacket material are described in the IEC 587, IEC 112 and IEC 61302 standards and in the not approved standard proposal IEEE P1222. Compared to commercially available PE compounds, this newly designed material shows a significantly improved performance in these material tests.

In order to confirm the material properties under real life conditions, cable samples were produced and tested in the recently introduced lifetime test chamber [1]. The lifetime test results confirm the trend realized in the material tests and show a satisfying reliability over the requested lifetime span. In addition to the line voltage, environmental conditions like dust, humidity and temperature cycles strongly influence the operating lifetime of ADSS cables. When forecasting cable lifetime, these factors must be taken into account.

Keywords

jacket material; ADSS; aerial cable; lifetime; lifetime forecast; sheath erosion; high voltage; tracking; dry band arcing.

1. Introduction

Because of their nonconductive properties, self-supporting dielectric aerial cables can be installed in the vicinity of high voltage lines. This is of great importance for countries with a

starshaped electrical power distribution system. Switching off a power line for cable installation would result in an interruption of power supply in complete areas or cities for hours or days.

The disadvantage of installing ADSS cables parallel to the phase wires of a power line is the partial coupling of high voltage to the cable, which has to be grounded at the poles due to safety reasons. Depending on the conductivity of the cable surface, a more or less strong current flows along the cable from the center of the span to the poles. Surface current causes tracking and erosion at the jacket surface and can destroy the ADSS cable within a few weeks or months.

Since the beginning of ADSS cable development, the extension of the cable lifetime under high voltage conditions to more than 15 years has been the main objective. The measures to achieve this target include installation at the lowest possible space potential level, the reduction of surface currents by means of conductive elements in parallel to the cable and providing the cables with tracking resistant jacket materials. For a worldwide application under sometimes unclear environmental conditions, the tracking resistance of the jacket has a significant importance. In addition to the stress caused by surface currents, these cables are subject to regional varying and unavoidable damaging influences like UV sunlight, heat, mechanical strain and durable contamination layers.

Only a sufficient safety margin of the jacket material can provide the robustness for solution which is applicable in the most areas of the world.

2. Jacket Damage

The destruction of the jacket of ADSS cables appears in a series of symptoms. Depending on the kind of jacket material and stress, one can find conductive tracks, pinholes or plane erosions shaped as rings or irregular spots.

The first phase of jacket damage is always the loss of the hydrophobic property of the jacket surface. In a clean environment, it shows up as a tarnished structure after a good wetting. In polluted environments, the hydrophobic surface is covered by dust, soot or salt, soaking rain and dew, and forms a closed layer with good electrical conductivity. In this way, the prerequisites for the generation of electrical surface discharges are provided.

As the cable surface dries after wetting, ring-shaped dry areas are formed, which are bridged by electrical discharges driven by the voltage drop along the cable [2]. At first, the hot foot-spots of the discharges are sliding over the surface and deepen the roughness. With increasing effective duration, deeper structures are formed in which the foot-spots can settle and burn holes or tracks into the surface.

By analyzing this destructive process, two material properties which determine the lifetime of the cable jacket can clearly be distinguished. First, the ability to sustain the surface water repellent, which prevents the forming of dry areas. Second, the resistance to the thermal load generated by the hot foot-spots.

3. Test Procedures

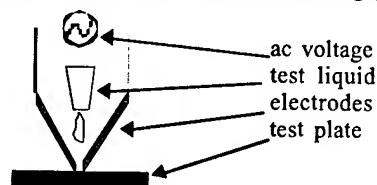
Being located in the electrical field of high voltage lines, the ADSS cables are subject to similar electrical stress, such as insulators and cable terminations, which are used to separate live devices of different electrical potential. The constantly applied operating voltage and conductive surface layer leads to a leakage current and partial discharges on the surface, and finally to erosion and conductive tracking traces. Due to the comparable stress of ADSS cables and insulators, the cable jacket materials are qualified with the same tests that are used for the qualification of insulating materials. In addition to the pure material tests, new procedures have been developed which consider the complete cable under realistic environmental conditions.

Table 1: Evolution from jacket material test to cable lifetime forecast

Test	Specimen	Conditions
IEC 60112	plate	moist surface, pin surface electrodes
IEC 60587	plate	moist surface, line surface electrodes
IEC 61302	tube	periodic dipping, ring electrodes at tube ends
IEEE P1222 (Draft)	cable	homogeneous salt fog, mechanical load, low ohmic electrical load
COLIT (Corning Lifetime Test)	cable	periodic wetting and drying, mechanical load, capacitive and induced electrical load

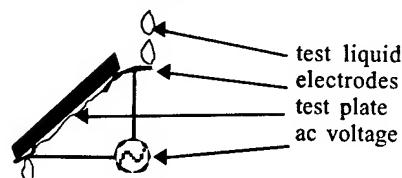
IEC 60112: Method for determining the comparative and the proof tracking indices of solid insulating materials under moist conditions. This test is limited to a voltage of up to 600V and a 4 mm distance between the electrode tips. It simulates a moderate strain and can differentiate between materials with normal resistance to electrical erosion.

Figure 1 — Set Up for Tracking Testing (IEC 60112)



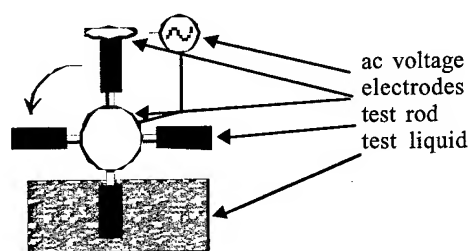
IEC 60587: Test methods for evaluating resistance to tracking and erosion of electrical insulating materials used under severe ambient conditions. Method 1 is suitable to distinguish between materials with a high resistance to electrical erosion. The test voltages applied are 2500 V, 3500 V and 4500 V. For materials with a moderate resistance to electrical erosion, method 2 gives a better resolution. Here the voltage starts at 1000 V and is increased in steps of 250 V.

Figure 2 — Set Up for Tracking and Erosion Testing (IEC 60587)



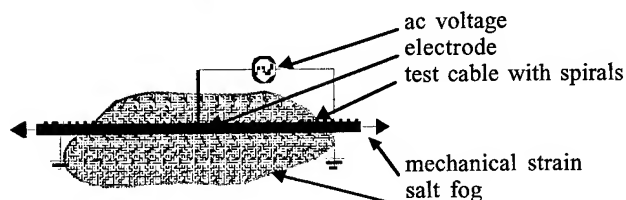
IEC 61302: Rotating wheel test to evaluate the resistance to tracking and erosion. Before the test voltage is connected to the electrodes attached to a cylindrical material specimen, the surface of the specimen is dipped into salt water and subsequently dried for a few minutes. This supports the generating of dry zones and accelerates the dry band arcing. The erosion and tracking results in this test are better related to the effects on ADSS cables in the field than the simple surface electrode test results.

Figure 3 —Rotating Wheel Set Up for Tracking and Erosion Evaluation (IEC61302)



IEEE P1222 (Draft): Test to evaluate the resistance of the cable sheath to erosion and tracking under combined electrical and mechanical stresses. In this test arrangement, the typical installation of ADSS cables with suspension spirals is considered. The test specimen is a piece of aerial cable taken from a production run, which is tensioned mechanically in addition to the electrical strain. After the 1000 hours of test run, strong jacket erosions can be found next to the grounded suspension spirals. Compared to field-installed ADSS cables, the concentration of erosion to the vicinity of the spirals is very strong and caused by the continuous salt fog and the high voltage connected directly to the cable jacket.

Figure 4 —Arrangement for Tracking and Erosion Test under Combined Mechanical and Electrical Stresses (IEEE P1222 Draft)

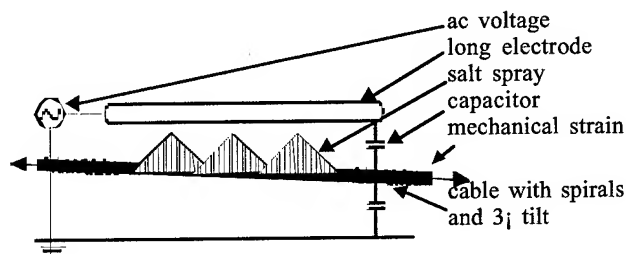


COLIT: The Corning Lifetime Test has been designed to evaluate the operational lifetime of ADSS cables under a realistic combination of simultaneous electrical, mechanical and climatic stresses. The erosion is accelerated by generating sequences of wetting and drying on the cable surface. For wetting, a salty water fog is sprayed on the cable. After a few minutes, the wetting is stopped until the cable surface has dried completely. Then the cable is sprayed again.

The test voltage is in the range of the line voltage and coupled to the cable specimen by capacitors and by a long electrode through the air.

This test not only delivers comparisons between the performance of different kinds of aerial cables, but also forecasts the operational lifetime, if the local electric and climatic conditions are well known.

Figure 5 —Arrangement for Operational Lifetime Test under Combined Mechanical Climatic and Electric Stresses (COLIT)



4. Results and Discussion

According to the recommendations of IEEE P1222 draft 1995, a class A jacket material can be used if the space potential for the ADSS cable is below 12 kV. This is typically a Polyethylene which contains carbon black and antioxidants for stabilization against UV light and oxygen decomposition.

For use in space potentials above 12 kV, LSOH jacket materials are preferred, which are filled with a high portion of metal hydroxids for flame resistance and are therefore able to better withstand the electrical arc erosion.

Both jacket materials were compared with a new tracking resistant polyethylene TR-PE. This material has been optimized for tracking resistance by a well balanced ratio of LLDPE basic polymer, modified metal hydroxid and a combination of stabilizers.

To compare the three materials for tracking resistance according to IEC 60112, we choose the test fluid B, which leads to a more aggressive surface contamination and results in a more clear

differentiation then fluid A. The surface of the plate specimen was cleaned by wiping it off, to preserve the hydrophobic properties.

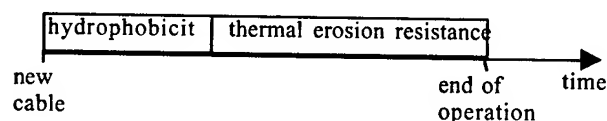
It could be shown that this test is not suitable for materials with a high erosion resistance. While jacket PE fails at test voltages above 525 V, the two materials LSOH and TR-PE pass the maximum voltage of 600 V and cannot be distinguished. As a result of this test, we only can state that the filled polyethylenes show a better resistance to electrical surface tracking than unfilled PE.

Line electrodes are used to test the resistance of jacket materials against tracking and erosion according to IEC 60587. The start and end points of the surface discharges are movable and by wandering them around, plane erosions can result. In addition, the surface of the plate specimens were roughened, which destroys the water repellence. Therefore the erosion starts immediately after the beginning of the test. Robust materials are tested for 6 hours at voltages of 2.5 kV, 3.5 kV or 4.5 kV. For less erosion resistant materials, the voltage can be increased by steps of 250 V, starting at 1000 V with a step duration of one hour.

Both test variations show the same result. The material LSOH has the best resistance to electrical erosion. TE-PE comes out a little weaker, and weakest is the unfilled PE. This ranking corresponds to the content of metal hydroxids which are added for their effect of hampering the combustion. Looking only at erosion, it must be stated that the resistance of PE increases with the content of hydroxid fillers. This view does not consider the fact that erosion can start only after the water repellence of the jacket surface is vanished and a closed conductive water film covers the cable [3].

To describe the complete aging process in electrical fields, both components of the lifecycle have to be looked at: hydrophobicity and velocity of electrical erosion. As erosion cannot start before hydrophobicity has reached a sufficient low level, both lifetime factors can be added in time. This explains why a material with a weaker erosion resistance can have a longer operating lifetime than a high track resistive material if it has a stronger and more long term hydrophobicity.

Figure 6: Factors of ADSS cable jackets «operational lifetime



The test of erosion and tracking in the standard draft IEEE P1222 is a modification of the test for electrical insulators under humid and polluted conditions [4]. By means of surface

electrodes, the voltage is directly applied to the cable surface. The constant moistening and the strong surface currents of several hundred mA lead to a uniform erosion of the cable surface. This erosion increases in the vicinity of the electrodes since this is where most of the surface discharges are ending (which start at the edges of the electrodes). The hot footspots of these arcs cause a stronger thermal strain next to the electrodes.

In this test, the TR-PE cable jackets show a significantly better erosion resistance than LSOH cable jackets, which can be explained by the influence of the durable hydrophobicity of TR-PE, caused by its lower content of fillers. During the hydrophobic phase, drops of salt water are formed, which prevent continuous ohmic paths along the surface. The hot discharging footspots cannot land on the jacket and cannot burn the surface, but are for a considerable test period located on the electrodes.

By using the COLIT (Coming Lifetime Test) [1], the more qualitative ranking of the three materials we have achieved in the standard tests can now be rated by figures. For the environment we chose the typical central European coastal conditions: spraying water with a low salt content, frequent rainfalls, a low grade of industrial and agricultural pollution and alternating wet and dry phases.

The result under these conditions proves a significant lifetime increase of filled PE jackets compared to the MDPE jacket. Despite their stable water-repellent surface, MDPE jackets reach only one third of the operating lifetime of the highly filled LSOH jackets. The most resistant jacket material is the medium filled TR-PE, which survives three times longer than LSOH and nine times longer than MDPE.

If we assume a lifetime of three years for a MDPE jacket installed in a 220 kV line, we can expect a threetimes longer lifetime for a LSOH jacket under the same conditions, and a nine times extended operating lifetime for a TR-PE jacket.

Latest investigations show that the results gained under central European conditions are not valid for other regional climates, especially not in desert areas. If, by the lack of rain, surface depositions of dust and salt are built up, the water-repellent operational phase will be considerably shortened. In addition, chemical interactions between the jacket material and the dust layer can accelerate the surface destruction during arcing considerably.

Table 2: Resistance to Tracking and Erosion of ADSS Cable Jacket Materials in Material and Cable Tests.

Test Material	IEC 60112	IEC 60587	IEEE P1222 (Draft)	COLIT lifetime/y
MDPE	++	+		3 ^{*)}
LSOH	+++	+++	++	9 ^{*)}
TR-PE	+++	++	+++	27 ^{*)}

+ normal, ++ good, +++ excellent *) central European conditions

5. Conclusions

A newly developed jacket material extends the operating lifetime of All Dielectric Aerial Cables significantly. It shows excellent tracking resistance in the standardized material tests. For the coastal conditions of Central Europe, the lifetime forecasts in the environmental cable test chamber confirm the expected improvements.

6. Acknowledgements

This work was supported with intensive and creative collaboration by Professor Dr. Porzel, Dr. Neudert and Dieter Franke from the Fakultät für Elektrotechnik und Informationstechnik at the Ilmenau Technical University in Germany.

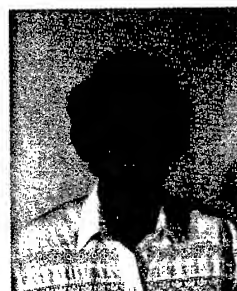
7. References

- [1] R. Engel, S. Will, D. Wartschinski, Lifetime Prediction of ADSS-Cables in High Voltage Lines, IWCS Proc., 49, pp. 70- 473, (2000)
- [2] S. M. Rowland, I. V. Nichols, The effects of dry-band arc current on aging of self-supporting optical cables in high fields, IEE Proc.-Sci. Meas. Technol., 143, pp. 10-14, (1996)
- [3] R. Bräsch, J. Lambrecht et al., The behaviour of medium voltage cable terminations at artificial pollution, 14th International Conference and Exhibition on Electrical Distribution CIGRE, (1997)
- [4] EN 60507, Artificial Pollution Tests on High-Voltage Insulators to Be Used on A.C. Systems



Reinhard M. Engel
Corning Cable Systems
Special Communication Cables
RD&E
Austraße 101
96465 Neustadt
Germany
reinhard.engel@corning.com

Reinhard Engel received his Ph.D. in 1985 from the University of Kaiserslautern. He has been developing optical cables and accessories for 20 years. Presently, he is managing the dielectric aerial cable development activities for Corning Cable Systems in Neustadt.



Sabine M. Will
Corning Cable Systems
Special Communication Cables
RD&E
Austraße 101
96465 Neustadt
Germany
sabine.will@coming.com

Sabine Will joined Siemens AG in 1970 and has been engaged in research and development of materials for copper and optical fiber cables. She is now project leader for dielectric aerial cables at Corning Cable Systems in Neustadt.



David Wartschinski
TU-Ilmenau
Fachgebiet Hochspannungstechnik
Kirchhoffstrasse 1
98684 Ilmenau/Th. r.
Germany
David.Wartschinski@E-Technik.TU-Ilmenau.DE

D. Wartschinski received his degree as an Diplom-Ingenieur from the Technische Universität Ilmenau in 1993. He has been working since 1994 on several research projects in the High Voltage Engineering department and is now member of a joint research project with Corning Cable Systems on aerial cables lifetime.

NEXT Characteristics for the Pitch of Twisted Pair Cable

Y. Shimoshio*, K. Kimura**, H. Koga*, N. Yamamoto*, and Tuyoshi Ideguchi***

*Dept. of Information and Communication Eng.

Kumamoto National College of Technology

2659-2 Suya, Nishigoshi, Kumamoto, 861-1102 Japan

+81-96-242-6059 · yshimo@tc.knct.ac.jp, koga@tc.knct.ac.jp

**Tsushin Kogyo Co. Ltd.

1735-2 Matoba, Kawagoe, Saitama Japan

+81-492-31-1232 · kkimura@tsuko.co.jp

***Dept. of Space and Earth Information Eng., Kyusyu Tokai University

9-1-1 Toroku, Kumamoto 862-8652, Japan

+81-96-386-2660 · tideguti@ktmail.tokai-u.ac.jp

Abstract

In a cable factory, sometimes an undesired cable which does not satisfy the NEXT specification is produced. One experimental fact has been found from the measurement about the undesired cable. It shows that the measured NEXT margin to the specification is inversely proportional to the least common multiple length of each pitch of the measured two twisted-wires. The goal of this research is to know why it occurs. But unfortunately we could not do that by now. In the process of doing this research, several fundamental NEXT characteristics about the pitch are obtained. In this paper, we describe these results. The NEXT characteristics is analyzed for the pitch combination and pitch length. The last short section length at the cable end, which is shorter than the L.C.M. length of each pitch of the two twisted-wires, affects the NEXT characteristics. The NEXT is also significantly influenced by the initial angle of each twisted-wires at starting point of the cable.

Keywords

NEXT, Twisted Pair Cable, Pitch, Least Common Multiple, Four-port Chain Matrix

1. Introduction

A twisted pair cable is widely used and it is recently developing for high frequency up to GHz band. One of the important characteristics of the twisted pair cable is the NEXT(near end crosstalk). In a cable factory, sometimes an undesired cable which does not satisfy the NEXT specification as shown in Figure 1. In Figure 1, the NEXT overs the limit at 40MHz. By analyzing the NEXT data about all of two twisted-wires of twenty four twisted-wires which are bundled in one cable, we have found an experimental fact as shown in Figure 2. In Figure 2, each point represents the NEXT margin to the specification and they are collected from the measured data at various frequencies from 1MHz to 100MHz. Figure 2 shows that the measured NEXT margin to the specification is inversely proportional to

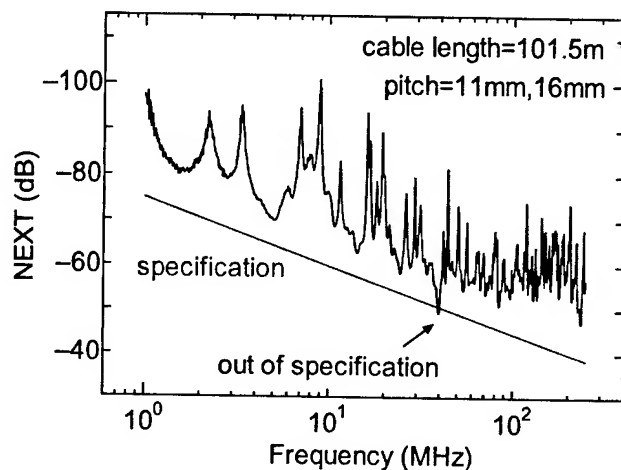
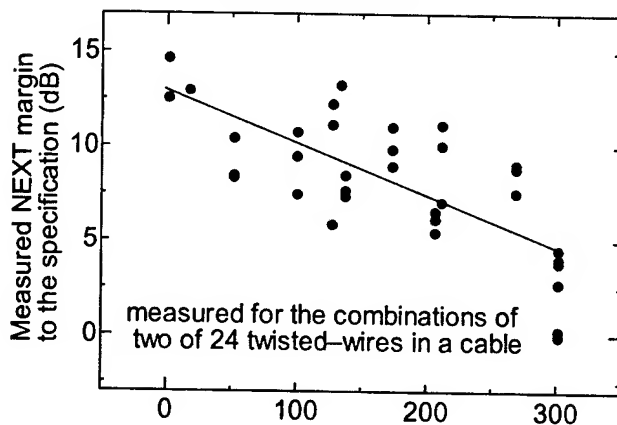


Figure 1. Example of NEXT characteristic not up to the specification.



The least common multiple length of each pitch of the measured two twisted-wires(mm)

Figure 2. Measured NEXT margin to the specification is proportional to the L.C.M. length of each pitch of the measured two twisted-wires.

the least common multiple length(L.C.M.) of each pitch of two twisted-wires. It means that we have to select the pitch which has small L.C.M. value. The longer L.C.M. pitch length may increase the NEXT at lower frequency. In this paper, we have tried to find the mechanism of this phenomena theoretically, but we could not do that by now. In the process of finding the mechanism, we obtained several fundamental NEXT characteristics. This paper describes those results.

The NEXT characteristics are analyzed for different pitch length and combination. The NEXT characteristics are analyzed for the relative position of each of twisted-wires along the wire and also for the last short section, which is shorter length than the L.C.M length of each pitch, of the cable end. They significantly influence to the NEXT characteristics.

2. Theory

2.1 Geometry of a Pair of Twisted-wires

Figure 3.(a) and (b) show the geometry of a twisted pair cable which is analyzed in this paper. As shown in them, the twisted pair cable consists of two twisted-wires on the ground. Each of wire11-wire12 and wire21-wire22 has different pitch, pitch1 and pitch2, respectively. The "pitch" means the length of one twist. Since the height of the wires from the ground is assumed to be sufficiently high in the analysis described later, the twisted pair cable can be considered as an unshielded twisted pair cable. As shown in Figure 3.(a) the cable which is L meter in length is divided into n pieces of short segment which have the same length of $dx(m)$. In each section, each of four wires are treated as a straight wire for simplicity in calculating the per unit length parameter. In Figure 3.(b) two angles, $\theta_{1,i}$ and $\theta_{2,i}$, vary from 0 to 2π in each pitch, pitch1 and pitch2, respectively. The angle $\theta_{0,i}$ is also prepared to consider a group pitch which means the twist of two twisted wires, but it is not used in this paper so that $\theta_{0,i}$ is always 0. Figure 1.(c) shows an equivalent circuit using the per unit length parameter[1] for the i -th segment of Figure 3.(a).

In Figure 3, the following symbols are used and the specified values are used in the calculation.

$r_{11,i}, r_{12,i}, r_{21,i}$, and $r_{22,i} = 0.25mm$: radius of each wire.

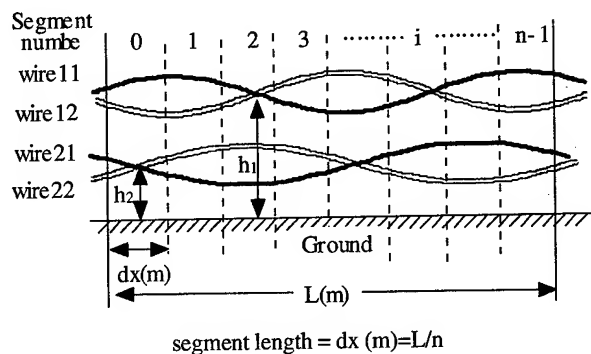
$b_{11,i}, b_{12,i}, b_{21,i}$, and $b_{22,i} = 0.5mm$: spacing between wire and the center of each twisted-wires, respectively.

$d_1, d_2 (m)$: projected distance on the ground from the center of each twisted-wires to the center of two twisted-wires.

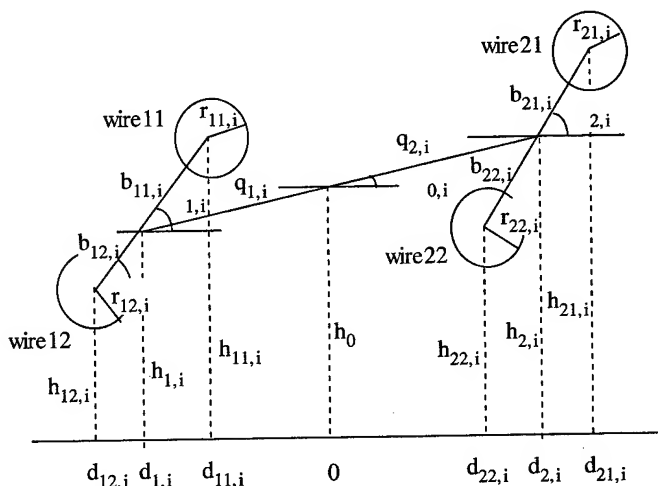
$h_0 = 0.3m$:height of the center of two twisted-wires.

$h_{1,i} = h_0 + q_{1,i} \sin(\theta_{0,i} + \pi)$ and $h_{2,i} = h_0 + q_{2,i} \sin \theta_{0,i} (m)$: height from the ground to each center of wire11-wire12 and wire21-wire22, respectively. $q_1, q_2 = 2mm$ and $\theta_{0,i} = 0$.

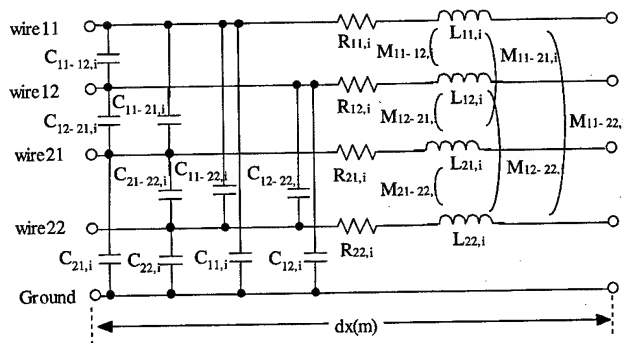
$h_{11,i} = h_{1,i} + b_{11,i} \sin \theta_{1,i}$, $h_{12,i} = h_{1,i} + b_{12,i} \sin(\theta_{1,i} + \pi)$,



(a)Side view of a twisted pair cable which are divided into n -pieces of short segments.



(b)Longitudinal view of a twisted pair cable



(c)Equivalent circuit for the i -th segment of Fig.1(a)

Figure 3. Geometry and equivalent circuit of a pair of twisted-wires which is analyzed.

$h_{21,i} = h_{2,i} + b_{21,i} \sin \theta_{2,i}$, and $h_{22,i} = h_{2,i} + b_{22,i} \sin(\theta_{1,i} + \pi)$ (m)
: height to each wires from the ground.

$d_{11,i} = d_{1,i} + b_{11,i} \cos \theta_{1,i}$, $d_{12,i} = d_{1,i} + b_{12,i} \cos(\theta_{1,i} + \pi)$,

$d_{21,i} = d_{2,i} + b_{21,i} \cos \theta_{2,i}$, and $d_{22,i} = d_{2,i} + b_{22,i} \cos(\theta_{2,i} + \pi)$ (m)

: distance from each wire to the center of each twisted-wires.

2.2 Four-port Chain Matrix for Short Segment

As each segment in Figure 3.(a) is represented by a four-port chain matrix of Eq. (1), whole of the twisted pair cable can be represented by a multiplication of n pieces of four-port chain matrix. R , L , and C in Eq. (1) are the per unit length parameters.

$$m_i = \begin{bmatrix} \mathbf{E}_4 & (\mathbf{R} + j\omega\mathbf{L}_i) \cdot dx \\ j\omega\mathbf{C}_i \cdot dx & \mathbf{E}_4 \end{bmatrix} \quad (1)$$

where,

$$\mathbf{E}_4 = \begin{bmatrix} 1 & 0 & 0 & 0 \\ 0 & 1 & 0 & 0 \\ 0 & 0 & 1 & 0 \\ 0 & 0 & 0 & 1 \end{bmatrix}, \quad \mathbf{R} = \begin{bmatrix} R_{11} & 0 & 0 & 0 \\ 0 & R_{12} & 0 & 0 \\ 0 & 0 & R_{21} & 0 \\ 0 & 0 & 0 & R_{22} \end{bmatrix},$$

$$R_{jk} = \frac{1}{4\pi r_{jk}^2 \sigma} \left\{ 1 + \sqrt{3^6 + (4\pi r_{jk}^2 \sigma \mu f)^3} \right\} \quad (\Omega/\text{m}) \quad [2],$$

$\sigma = 58 \times 10^6$:conductivity of copper (S/m),

$\mu = 4\pi \times 10^{-7}$:permeability of copper (H/m),

$$\mathbf{L}_i = \begin{bmatrix} L_{11,i} & M_{11-12,i} & M_{11-21,i} & M_{11-22,i} \\ M_{11-12,i} & L_{12,i} & M_{12-21,i} & M_{12-22,i} \\ M_{11-21,i} & M_{12-21,i} & L_{21,i} & M_{21-22,i} \\ M_{11-22,i} & M_{12-22,i} & M_{21-22,i} & L_{22,i} \end{bmatrix},$$

$\mathbf{C}_i = \mu_0 \cdot \epsilon_0 \cdot \epsilon_r \cdot \mathbf{L}_i^{-1}$ (F/m),

$\mu_0 = 4\pi \times 10^{-7}$:permeability of vacuum(H/m),

$\epsilon_0 = 8.85 \times 10^{-12}$:dielectric constant of vacuum(F/m),

$\epsilon_r = 2.4$:relative dielectric constant of material surrounding

wire (assumed value),

$$L_{jk,i} = \frac{\mu_0}{2\pi} \ln \frac{2h_{jk,i}}{r_{jk,i}} \text{ :self inductance (H/m), and}$$

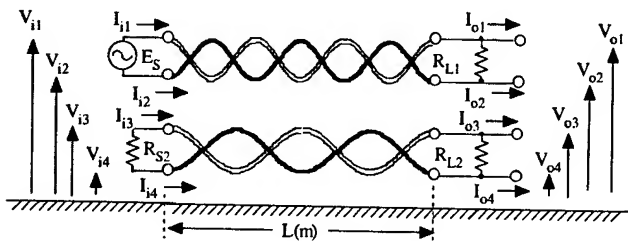


Figure 4. Analyzed circuit including terminal conditions.

$$M_{jk-lm,i} = \frac{\mu_0}{2\pi} \ln \sqrt{\frac{(h_{jk,i} + h_{lm,i})^2 + (d_{jk,i} - d_{lm,i})^2}{(h_{jk,i} - h_{lm,i})^2 + (d_{jk,i} - d_{lm,i})^2}}$$

:mutual inductance (H/m).

2.3 Calculation Method of NEXT

The analyzed circuit including terminal conditions is shown in Figure 4. In Figure 4, the input voltages V_i and input currents I_i are related with output voltages V_o and output currents I_o by Eq. (2). The source and load circuits are also represented by a four-port chain matrix, R_L and R_S , respectively in Eq. (2).

$$\begin{bmatrix} \mathbf{V}_i \\ \mathbf{I}_i \end{bmatrix} = \begin{bmatrix} \mathbf{A} & \mathbf{B} \\ \mathbf{C} & \mathbf{D} \end{bmatrix} = \mathbf{M}_S \cdot \sum_{i=0}^{n-1} m_i \cdot \mathbf{M}_L \begin{bmatrix} \mathbf{V}_o \\ \mathbf{I}_o \end{bmatrix} \quad (2)$$

where,

$$\mathbf{V}_i = \begin{bmatrix} V_{i1} \\ V_{i2} \\ V_{i3} \\ V_{i4} \end{bmatrix}, \quad \mathbf{V}_o = \begin{bmatrix} V_{o1} \\ V_{o2} \\ V_{o3} \\ V_{o4} \end{bmatrix}, \quad \mathbf{I}_i = \begin{bmatrix} I_{i1} \\ I_{i2} \\ I_{i3} \\ I_{i4} \end{bmatrix}, \quad \mathbf{I}_o = \begin{bmatrix} I_{o1} \\ I_{o2} \\ I_{o3} \\ I_{o4} \end{bmatrix},$$

$$\mathbf{M}_L = \begin{bmatrix} \mathbf{E}_4 & \mathbf{0}_4 \\ \mathbf{R}_L & \mathbf{E}_4 \end{bmatrix}, \quad \mathbf{M}_S = \begin{bmatrix} \mathbf{E}_4 & \mathbf{0}_4 \\ \mathbf{R}_S & \mathbf{E}_4 \end{bmatrix},$$

$$\mathbf{0}_4 = \begin{bmatrix} 0 & 0 & 0 & 0 \\ 0 & 0 & 0 & 0 \\ 0 & 0 & 0 & 0 \\ 0 & 0 & 0 & 0 \end{bmatrix}, \quad \mathbf{R}_S = \begin{bmatrix} 0 & 0 & 0 & 0 \\ 0 & 0 & 0 & 0 \\ 0 & 0 & 1/R_{S2} & -1/R_{S2} \\ 0 & 0 & -1/R_{S2} & 1/R_{S2} \end{bmatrix},$$

and

$$\mathbf{R}_L = \begin{bmatrix} 1/R_{L1} & -1/R_{L1} & 0 & 0 \\ -1/R_{L1} & 1/R_{L1} & 0 & 0 \\ 0 & 0 & 1/R_{L2} & -1/R_{L2} \\ 0 & 0 & -1/R_{L2} & 1/R_{L2} \end{bmatrix}.$$

In Figure 4, since all of the load currents are equal to zero, Eq. (3) is derived from Eq. (2).

$$\mathbf{V}_i = \mathbf{A}\mathbf{V}_o, \quad \mathbf{I}_i = \mathbf{C}\mathbf{V}_o \rightarrow \mathbf{V}_i = \mathbf{A}\mathbf{C}^{-1}\mathbf{I}_i \quad (3)$$

The input currents I_{i3} and I_{i4} are zero, too. Thus, the source voltages V_{i3} and V_{i4} can be obtained from Eq. (3) by giving the source voltages V_{i1} and V_{i2} , where $V_{i1} = V_{i2} = 1$ (V) for common mode driving and $V_{i1} = -0.5$ (V) and $V_{i2} = 0.5$ (V) for differential mode driving[3]. The NEXT is defined by equation (4).

$$\text{NEXT} = 20 \log \frac{V_{i3} - V_{i4}}{V_{i1} - V_{i2}} \quad (4)$$

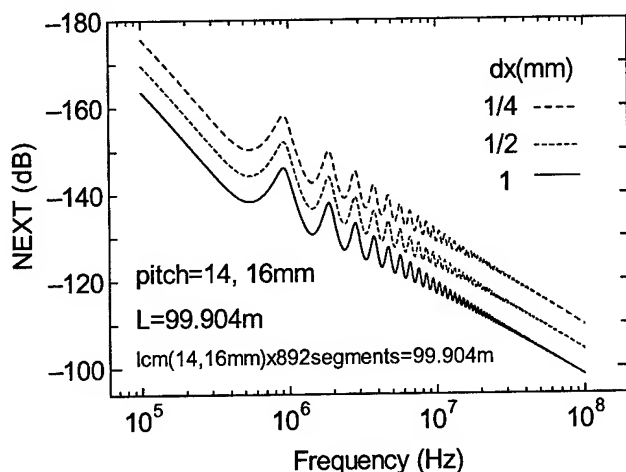


Figure 5. NEXT decreases as the segment length becomes short.

3. Calculated Results and Discussion

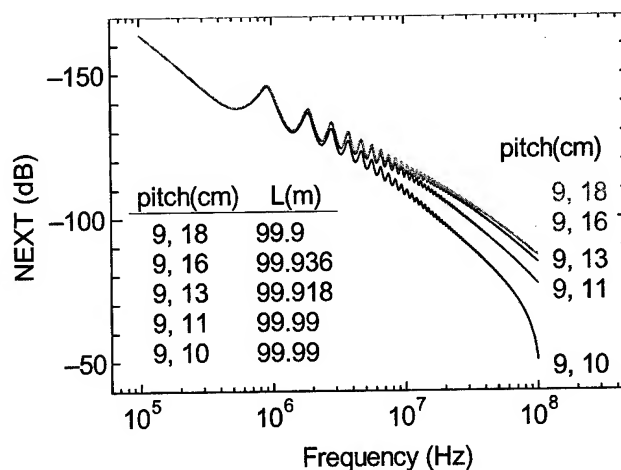
3.1 Calculated Data is the Relative Value

Figure 5 shows the NEXT characteristics when the segment length, $dx(m)$, changes. The NEXT decreases 6dB as the segment length become half. As the wires in the segment are treated as straight wire, the NEXT decreases according to the segment length. It means that all of the calculated NEXT characteristics in this paper show the relative NEXT value. The segment length of 0.5mm is used in other calculations of this paper.

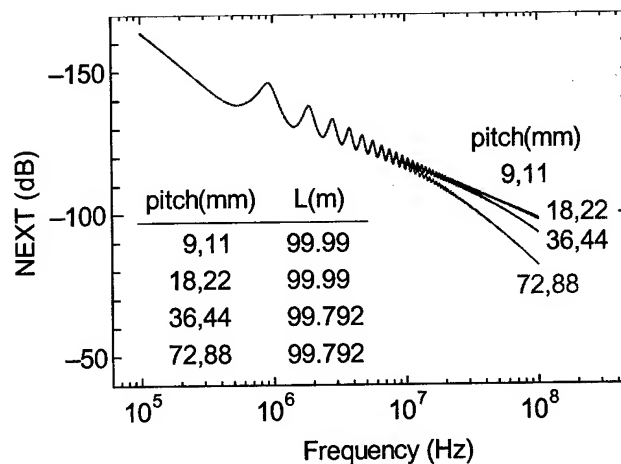
3.2 NEXT Decreases as the Pitch Ratio Increases

Figure 6(a) shows the NEXT characteristics as the pitch ratio changes. The result shows that the NEXT is improved as the pitch ratio increases. In Figure 6(a), each cable length has different length because the calculation is done for the cable of which the length is the multiplication of L.C.M. of each pitch. For example, the cable length of 99.9 meter for the pitches, 9mm and 18mm, is 5555 times of the L.C.M. length of 9mm and 18mm. As described later, the last short part of the cable which the length is shorter than the L.C.M. length of each pitch cause big difference in the NEXT characteristics. Thus we used the length of multiplication of L.C.M. of each pitch as the cable length.

Figure 6(b) shows the NEXT characteristics as the pitch length changes. The NEXT is improved as the pitch length becomes short. From Figure 6, it can be seen that the pitch length should be sufficiently short and the pitch ratio also should be large to get a good NEXT characteristic.



(a) NEXT decreases at high frequency as the pitch ratio increases.

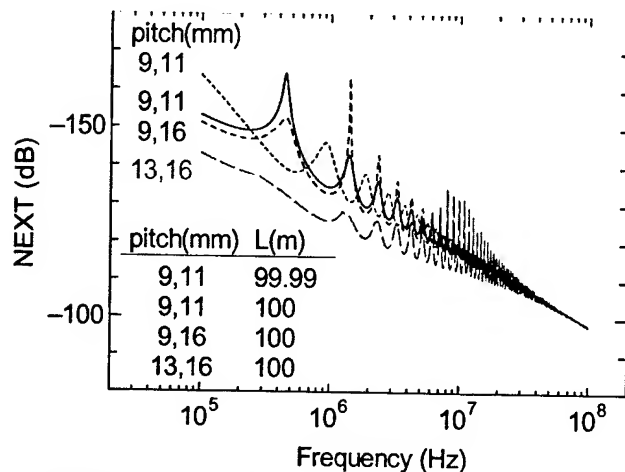


(b) NEXT decreases at high frequency as the pitch length becomes short.

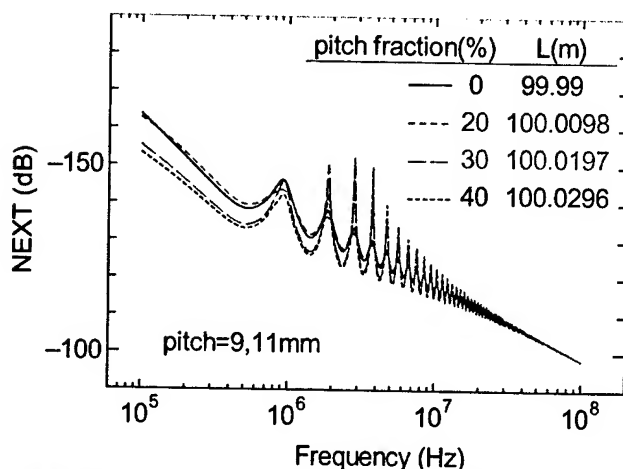
Figure 6. NEXT characteristics for the combination of pitches and the pitch length.

3.3 NEXT is Influenced by the Last Short Section Length of the Cable

Figure 7.(a) shows the NEXT characteristics as the pitch combination changes for the fixed cable length. The dot curve for the 99.99 meter cable which has the pitches of 9mm and 11mm is shown for comparison. The NEXT characteristics shown in Figure 7.(a) significantly change as the pitch combination changes. Because the cable length is fixed to 100 meter, there is a short section which has shorter length than the L.C.M. length of each pitch at the last part of the cable. Figure 7(b) shows the NEXT characteristics as the last short section length changes. The short section length is represented



(a) NEXT change as the pitch combination changes where the cable length is fixed.



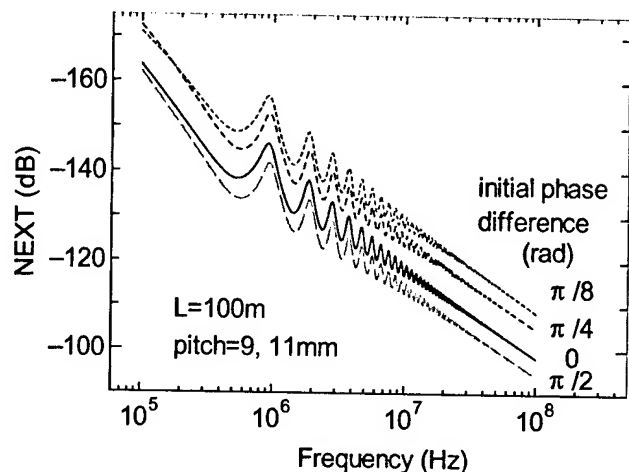
(b) NEXT change as the percentage of the pitch length to L.C.M. length changes.

Figure 7. NEXT varies by the last short section length of the cable which is shorter than L.C.M length of each pitch.

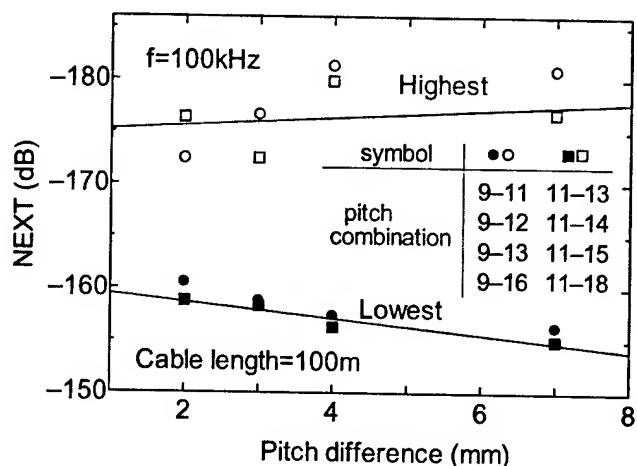
by the percentage of the pitch length to the L.C.M length of each pitch. This result means that the measured data would be significantly influenced by the slight cable length difference.

3.4 NEXT Change as the Initial Phase Difference between Two Twisted-wires Changes

Figure 8 shows the NEXT characteristics as the initial phase difference between two twisted-wires varies. The initial phase means the angle of two wires of a twisted-wires to the horizontal direction at the beginning of cable. There are two initial phases, $\theta_{1,i}$ and $\theta_{2,i}$, which are shown in Figure 3. In Figure 8(a), as the initial phase



(a) NEXT varies by the initial phase difference ($\theta_{1,i}$, $\theta_{2,i}$) between two twisted-wires.



(b) Maximum and minimum NEXT at 100kHz for the difference of pitch.

Figure 8. NEXT varies as the relative position between the two twisted-wires position changes.

varies from 0 to $\pi/2$ for the twisted-wires of 9mm pitch and the initial phase is 0 for the twisted-wires of 11mm pitch, the phase difference changes from 0 to $\pi/2$, too. In other words, the initial phase difference is equivalent with the relative position between two twisted-wires along the wire. Figure 8(b) shows the NEXT changes at 100kHz which are calculated in the same way of Figure 8(a) for various pitch combinations. It shows that the NEXT at 100kHz vary as the pitch difference changes. The highest NEXT value increases as the pitch difference increases and the lowest NEXT value slightly changes. As the cable is cut at anywhere, the initial phase difference always occurs and the NEXT also changes. Figure 8(b) shows that the bigger pitch difference causes the bigger changes in NEXT according to the initial phase difference.

4. Conclusions

We have found the relationship that the NEXT margin of the twisted-wires to the specification is inversely proportional to the L.C.M. length of each pitch of the twisted-wires. Unfortunately, we could not confirm the relation between the phenomena and the pitch of the twisted wires. In the process of this analysis, several NEXT characteristics are obtained by the calculation using the four-port chain matrix. Those are

(1) The pitch length should be sufficiently short and the pitch ratio also should be large enough to make a twisted-pair cable which has a good NEXT characteristic. But it is not clear what value is enough for it in this paper.

(2) The last short section length at the cable end, which is shorter than L.C.M. length of each pitch, affects the NEXT characteristic. and

(3) The initial angle between two twisted-wires at the starting point of the cable affects the NEXT characteristic. The bigger pitch difference causes the bigger changes in NEXT according to the initial phase difference.

In this paper, we have just shown the calculated results without experiment because it is difficult to make the ideal cable. Now we have a plan to confirm this calculation by FDTD analysis. Also, we are still trying to find the reason why the NEXT margin is proportional to the pitch by considering the group pitch. The future work is to find the pitch design method for the high speed LAN cable with sufficient NEXT characteristics.

References

- [1] C. R. Paul., *Introduction to Electromagnetic Compatibility*, John Willey, chap.4 (1992).
- [2] R. Croze. and L.Simon., *Transmission Telephonique*, Gakkensya, p. 31 (translated into Japanese, 1969).
- [3] N. Yamamoto, Y. Shimoshio, H. Koga, and M. Tokuda, "Electromagnetic Noise Characteristics between Two Unshielded Twisted-Wire Pair for the Number of Twist", *IEICE Technical Journal*, EMCJ2000-10, pp.1-6(May, 2000)(in Japanese).



Yoshifumi

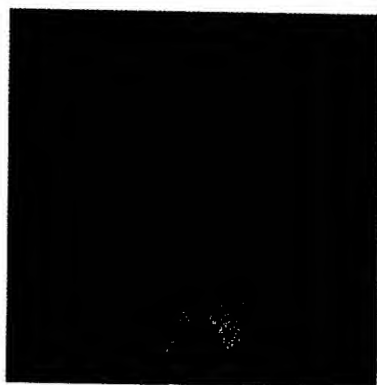
Shimoshio received the B.E. degree in Telecommunications from University of Electro-Communications, Tokyo, Japan in 1975 and Dr. E. from Kyusyu Institute of Technology, Kitakyusyu, Japan in 1999. In 1975, he joined

the Dept. of Radio Communications of KNCT (Kumamoto National College of Technology, Kumamoto), Japan, where he is currently a Professor in the Department of Information and Communication Engineering. He is a member of the IEEE.

Dept. of Information and Communication Eng.

Kumamoto National College of Technology

2659-2 Suya, Nishigoshi, Kumamoto, 861-1102 Japan



Ken Kimura

received the B.E. degree in Electric and Communication Engineering from Toyo University, Tokyo, Japan in 1966. He joined Tsushin Kogyo Electric Wire & Cable Co., Ltd in 1966. He had been engaged in development on

electric and telecommunication cables. He has currently developed category 5 and category 6 information and communication cables. He is a member of the IEICE, and also a member of the IEEE.

Tsushin Kogyo Co. Ltd.

1735-2 Matoba, Kawagoe, Sitama Japan



Hiroaki Koga

received the B.E. and M.E. degrees in Electric Engineering from Kagoshima University, Kagoshima, Japan in 1968 and 1970 respectively, and Dr. E. from Tohoku University, Sendai, Japan in 1988. He joined Electrical Commu-

nications Laboratories of Nippon Telegraph & Telephone Corporation (NTT) until 1991 and In 1992 he is engaged in the Dept. of Information and communication Engineering of KNCT, where he is currently a Professor.



Naoki Yamamoto

received the B.E. and M.E. degrees in Information Engineering from Toyohashi Institute of Technology, Toyohashi, Japan in 1991 and 1993 respectively, and Dr. E. from Kyusyu Institute of Technology, Kitakyusyu, Japan in 2001. In 1993, he joined the Department

of Information and Communication Engineering of KNCT, Japan, where he is currently an Associate Professor. He is a member of the IEICE.



Tuyoshi Ideguchi

received the B.E. degree in Communication Engineering from Kyushu University, Fukuoka, Japan, in 1971 and the Dr. E. degree in 1994, from Tohoku University, Sendai, Japan. He joined Electrical Communication Laboratories, NTT

in 1971. He had been engaged in research and development on electromagnetic compatibility technique for tele-communication systems. He is currently professor in the department of Space and Earth Information Technique of Kyushu Tokai University, Kumamoto, Japan. His current research interests are electromagnetic compatibility for information systems and Kansei information engineering for multimedia technologies. Dr. Ideguchi is a member of the IEICE, and also a senior member of the IEEE.

Dept. of Space and Earth Information Eng.

Kyusyu Tokai University

9-1-1 Toroku, Kumamoto 862-8652, Japan

Thermoplastic Foam Extrusion with Physical Blowing Agents

Thomas Reiner, Horst Scheid

SIEBE Engineering GmbH

Neustadt/Wied, Germany

+49 2683/3003 0 · siebe@siebe.de

Abstract

Consumer and business desire for high communication increases the market for high frequency cables in computer networks, CATV and GSM-systems. The optimization of electrical and mechanical characteristics of cable insulation by usage of foam techniques requires a good understanding of thermodynamical effects and their influence on the production process.

This paper introduces to physical basics of manufacturing foamed polymers. Regarding cable insulation, polymer and gas selection is discussed, the technical demands are shown and an explanation of foam growth and stabilization is given.

Using two cable types as example, an efficient way of checking foam equipment and/or production processes is presented. Therefore, a newly developed software is used, which calculates or simulates thermal and electrical behaviour of the foam with material and processing parameters as input.

Keywords: foam, RF-cable, data cable, extrusion, blowing agents, gas injection, quality prediction

1. Foaming methods in polymer extrusion

1.1 Physical foaming versus chemical foaming

Chemical Blowing Agents (CBA) are added to the polymer, either as admixture or as powder to mix with the polymer before the extrusion process begins, or they are already contained in the polymer. The amount of the admixed CBAs determines the degree of foaming but also the melt temperature does because the strength of decomposition process depends on the temperature. If added substances are between 1% and 5% of the total weight and those mixtures make foaming degrees up to 60 % possible [1].

In any case, they decompose thermally while giving some chemical by-products that can affect other additives like flame retardants, stabilizers or colorants. By-products act as nucleation particles but can also be a problem for the electrical characteristics, when the polymer is used as insulation layer in cable manufacturing. At higher concentrations, CBAs can cause deposits on screen and screw, mainly with exothermic powders. This gives from time to time a wash-out with process destabilisation. With CBAs, it is also difficult to foam high temperature polymers like FEP or PFA. In addition, the maximum void ratio is limited to 50-60%. Here, alternatives are physical foam techniques.

With physical blowing agents, void ratio can be much higher (e.g. 80% in cable insulation processes) and chemical by-products are

only the nucleation residues. The void ratio is no longer affected by processing temperature profile. On the other hand, there is more investment because of gas injection equipment than with conventional extruders.

1.2 Physical blowing agents

In physical foaming processes liquids or gases are injected into the extruder and dissolve in the plastic material under influence of heat and pressure.

Some important properties of gases used for physical foaming are listed in table 1 to give a comparison between (H)CFCs, organic and anorganic types.

Gas Formula	T _c [°C]	P _c [MPa]	Molar mass [g/mol]	bp [°C at 1013mbar]	Permeation in PE [10 ⁻¹² mol/m ² sPa]	Solubility [cc/gN ₂]
	-122	4.91	399	-186	220-1100	2
	197	3.37	72.2	28.0	n.a.	~1000
	31	7.38	44.0	-78.4	2900-3800	~10
	-147	3.39	28.0	-195.8	30-225	(=)1
	198	4.37	137.4	238	n.a.	n.a.
	96	4.93	86.5	-40.8	50-60	30
	374	22.0	18.0	100.0	n.a.	n.a.
	-268	0.23	4.0	-269.0	1300-2000	0.25

Table 1. Gases for physical foaming with some relevant properties(n.a.: data not available)

1.3 Additive nucleated (heterogeneous) foaming

In most present applications a nucleation substance (sometimes called "kicker") is added to the polymer, in order to start the foaming process. These nucleation substances can work in an active or passive manner. Passive means, that only a matter powder (e. g. talc, SiO₂ or TiO₂) is used. Active nucleation substances work equivalently to CBAs, so a small intrinsic foaming ratio (around 5-10%) already exists without adding extra gas to the melt.

1.4 Self nucleated (homogeneous) foaming

With a characteristic adjustment of production line parameters a fine cell-structured foaming of the melted polymer is obtained without nucleating agent. This process is physically described as a self nucleation, that makes an energy transition from a thermodynamic unstable state to a thermodynamic stable region by using the differential energy to create cell sites. A simple self nucleation example is heating up very clean water. Temperature grows up to more than 100°C (at 1013 mbar), resulting in a non-stable state of the liquid. As a little distorsion happens, the water starts boiling while lowering temperature to 100°C.

2. Description of the foaming process

General requirements to all blowing agents are :

- good solubility (high foaming power)
- rapid diffusibility
- stability and inertness in the applied temperature range
- high evaporation rate of during expansion
- easy handling (no poison, not combustible)
- low electrical attenuation in cable production
- low ODP values (Ozone Depletion Potential bzw. Global Warming Potential according to the agreements of Montreal 1982, Rio de Janeiro 1992 and Kyoto 1997).

To understand the foaming process it is helpful to subdivide the total process into single processes and to analyze them :

2.1 Polymer

On principle, almost polymer can be foamed. Criteria for choice are the electrical properties and the rheological characteristics. Considering the molecular structure, foaming poly-crystalline materials is more difficult than amorphous materials like PS.

The reason for this fact shows picture 1.

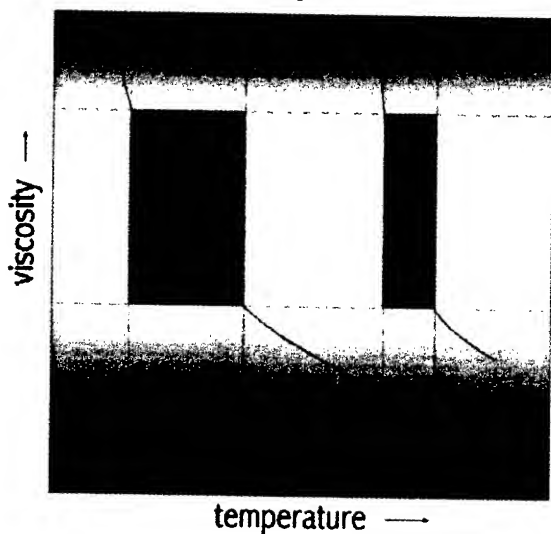


Figure 1. Processing window for foams of amorphous and poly-crystalline polymer

For poly-crystalline polymers, the process temperature range is smaller, that means, the production of fine cell-structured foams requires an more exact process control. Table 2 gives some values for crystallinity and temperature variations for a selection of polymers.

Polymer	crystallinity [%]	Processing window [K]
	0	30
	40-50	10
	50-65	5

Table 2: Crystallinity and processing range of some polymers

The relative permittivity is an important electrical parameter. The solid values are in the range of about 2.1 (PS) to 6.0 (PVDF). Because the communication cable engineering requires smaller values cables are manufactured in bamboo technique or produced with polymer foam. By this means, cables can be produced with relative permittivities to 1.3 (equation 1 for foamed polymer), depending on the void ratio (see picture 2).

$$\epsilon_r = \frac{\epsilon_{r_s}}{2} \left\{ (1 + S_{mf}) \cdot \left[(1 - sg) + \frac{sg}{\epsilon_{r_s}} \right] + \frac{(1 - S_{mf})}{(1 - sg) + \epsilon_{r_s} \cdot sg} \right\} \quad (1)$$

ϵ_{r_F} : relative permittivity of the polymer foam

ϵ_{r_P} : relative permittivity of the solid polymer

S_{mf} : a foam model factor

sg : the void ratio as volume / volume_{foam}

foam parameters (HDPE)

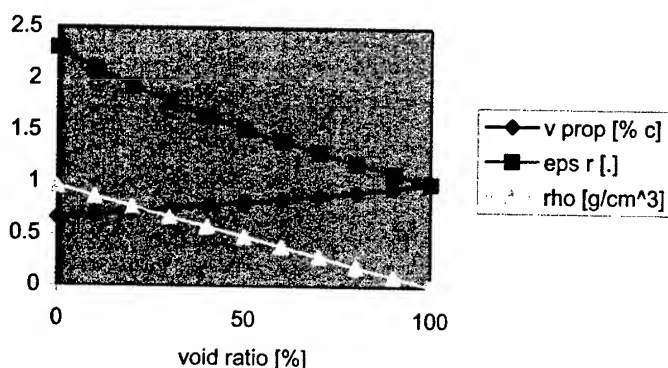


Figure 2. Change of relative permittivity, density and propagation speed, depending on the linear foaming degree (for HD-PE)

Permittivity is directly coupled to signal propagation speed

$$v_p = \frac{c}{\sqrt{\epsilon_r \mu_r}} \cdot 100 = \frac{c \cdot 100}{\sqrt{\epsilon_0 \epsilon_r \mu_0 \mu_r}} \quad (2)$$

For cable insulation, another very important aspect is the electrical damping, particularly in radio frequency applications. The value is calculated from an equivalent circuit with the telegraphic equation (3) [2] and is a function of resistivity, dissipation (loss) factor and dielectric constant.

$$\frac{\partial^2 u}{\partial x^2} = L' C' \frac{\partial^2 u}{\partial t^2} + (R' C' + L' G') \frac{\partial u}{\partial t} + R' G' u \quad (3)$$

R : ohmic resistivity
L : cable inductivity
C : cable capacitance
G : leakage resistivity
u : voltage at the circuit input

The electrical loss factor $\tan \delta$ can be written using the complex permittivity :

$$\tan \delta = \frac{\epsilon_r''}{\epsilon_r'} \quad (4)$$

It gives the relationship between regainable energy and energy dissipation by oscillation processes in alternating electrical fields and should be as small as possible. The reason for dissipation are polarization processes. The frequency dependence is given as [3]

$$\tilde{\epsilon}_r = \epsilon_r' + i\epsilon_r'' = 1 + \frac{e_0^2 (N_e / V)}{e_0 m_e (\omega_0^2 - \omega^2 + i\gamma\omega) - \left(e_0^2 \frac{N_e}{3V} \right)} \quad (5)$$

γ : damping constant
 N_e/V : electron density
 m_e : electron mass

Polymer	ϵ_r []	$\tan \delta$ [] at 1MHz	Heat Transfer Capability [W/m-K]	Heat Capacitance [Ws/g-K]
	2.27	$1 \cdot 10^{-4}$	0.22	1.7
	3.1	0.06	0.15	0.9
	2.25	0.005	0.4	1.8
	5.7	n.a.	0.19	1.4

Table 3. A selection of polymers to compare electrical and thermal properties [4]

The loss behaviour is basically governed by 3 processes :

- a low frequency dipole effect in the microwave range by frozen orientation polarization in the amorphous phase below the glass transition temperature (sometimes called Wagner range)
- an intermediate frequency in the deep infrared, where molecules are polarized by the local field (so-called Debye range)

- a high frequency effect above 10^{14} Hz (ultra violet), where polarisation is coupled to atoms and their electrons (intra atomic range)

In addition, there is a temperature dependence, that follows a 1/T-law in case of weak dipole coupling. But for the application described here, this effect can be neglected.

Typical values for $\tan \delta$ are between 10^{-4} for non-polar polymers and 0.06 for polar materials and the term $\epsilon_r \tan \delta$ will be further reduced by the foam (Table 3).

Because the cable application determines frequency , the term $\epsilon_r \tan \delta$ can be chosen depending on the frequency range. For this reason, solid PVC can be used for low-frequency applications without problems, but in high-frequency applications a small loss factor and a foam-reduced small relative permittivity are necessary. Picture 3 shows for a given geometry of a RF cable different polymer selections and different foam percentages to show the high influence in the range of GSM applications.

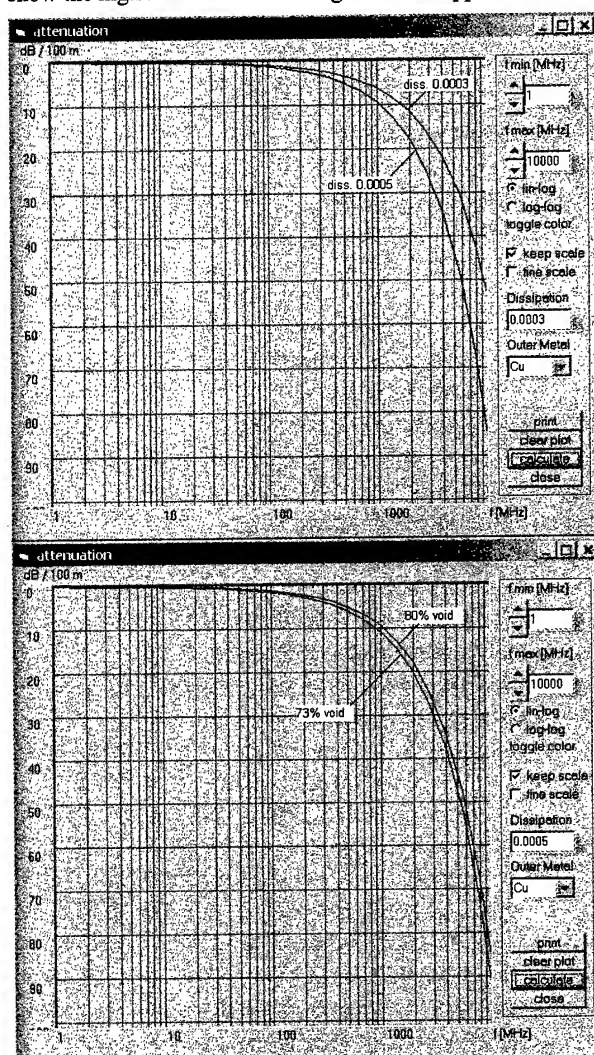


Figure 3. Attenuation calculation for an 1 5/8 inch RF cable. Upper diagram – influence of polymer $\tan \delta$, lower diagram – damping for different void ratio

An additional criterion for the polymer selection are the admixed nucleation substances. If an active nucleation substance is used for direct gassing, the amount is 10 times smaller than by mixes for chemical foaming. Passive kickers are in use much more for high temperature applications. In both of cases about 0.1-0.5 % in weight is sufficient for beginning tests. If the base polymer matrix does not contain nucleation substances, kicker as powder or granules can be added to the polymer before the melt process begins. For high-frequency applications it is important to know, that most additives are polar and reduce electrical quality.

2.2 Gases

According to the above mentioned requirements inert gases have the best properties for physical blowing agents. In most cases nitrogen is in use. The meaning of CFCs decreases in spite of its high solubility because of the ozone layer depletion. Water steam as blowing agents can't be used in the cable manufacturing because of bad electrical properties, Pentan and Butan are combustible. Carbon dioxide is not simple to handle but the higher solubility in comparison to nitrogen promotes the use of carbon dioxide. Noble gases are inert, but have a lower solubility than N_2 or CO_2 and are more expensive so noble gases are only applied in special applications.

2.3 Foaming agent injection

When using a direct gassed process, gas is injected under high pressure into the barrel, the injection position is typically at 18-20D using a 30-33D screw.

Under typical extrusion conditions ($T > 120^\circ C$, $p > 10 MPa$), nearly all inert gases are overcritical (sometimes called "supercritical"). Water, CFCs and organic gases can switch from undercritical to overcritical while changing process temperature or pressure. This phase transition should be avoided because flow measurement at the critical point using parameters like cp or density is not well defined.

Solubility can be described with Henry's law

$$c_A = p_i \cdot S(T) = p_i \cdot S_0 e^{\frac{\Delta H}{RT}} \quad (6)$$

- c_A : blowing agent mass concentration
 p_i : partial pressure
 S_0 : gas solubility coefficient at 0 K
 ΔH : molar solubility enthalpy of the gas
 R : gas constant (from gas law $pV=nRT$)

In amorphous polymers below glass transition or in heterogeneous nucleated systems, additional microvoids can be described by adding a second term (Langmuir isotherm) for gas sorption in these 'holes', modifying equation (6) to [11]

$$c = p_i \cdot (1 - X) \cdot S_0 e^{\frac{\Delta H}{RT}} + c_H \cdot \frac{b \cdot p_i}{1 + b p_i} \quad (6')$$

- c_H : Langmuir saturation constant
 b : Langmuir affinity

To increase solubility of the blowing agent in the melt, it is necessary to have a minimum barrel pressure at the end of the

screw of 100 to 150 bar, a higher pressure level (200-250 bar) gives more spare in process stability and is recommended while using self nucleation techniques.

The polymer system is also influenced by additives such as flame retardants, stabilizers or colorants that can change surface tension and energy and affects so gas solubility and mixing.

Very important is the dosing and injection equipment, because a constant gas flow is the main condition for stable foam production within small tolerances. (In terms of chemical foaming, this means equipment for exact amount of CBA per mass polymer). This can be demonstrated with a simple calculation : Production of a data cable (inner conductor 0.4 mm, foamed isolation OD 0.9 mm) with a void ratio of 60% at a production speed of 600 m/min needs a gas amount of about 0.12 l/min (l is the normalized volume in liters at 1013 mbar and $0^\circ C$). Using nitrogen in a direct gassing process at an injection pressure of 300 bar results in a volume of 0.4 cm^3 that has to be dosed linear during one minute. Assuming an equipment with an internal volume of 100 cm^3 , in case of a pressure variation of only 1 bar inside the barrel the injection system needs approximately one minute to find a new stable working point ! So the main aspects for the dosing/injection system are

- reproducible gas flow measurement
- constant pressure from the point of flow measurement of 1 bar or better
- short reaction times in case of working point interferences

SIEBE developed a new gas injection system, that has in addition a simple user interface, optional automatic parameter changes through the lines process control and a maintenance free gas injector on the barrel that enables foam production as well as solid production without assembling or disassembling any parts.

2.4 Gas dissolution, Mixing

One of the basic steps after the injection is homogenising the gas solution inside the barrel. The efficiency of the mixing process is in first order related to the geometry of the screw and the mixing elements. But it is important not to think in terms of mechanical mixing - the process is not based on a 2-phase (emulsion) system, but on a single-phase (solution) system with a solubility gradient. Too long mixing elements or static mixers with high shear rates can even deteriorate a homogenous solution. Therefore, Siebe designed different screw types with integrated mixing elements to get the fast required dissolution and the constant homogeneity needed.

To describe the diffusion process of the blowing agent in the melt, physical gas properties (e.g. solubility, diffusion rate) and extrusion parameters (e.g. melt temperature, barrel residence time) are important, see also Equ. (4)

Diffusion can be described with Fick's law [6]

$$\frac{\partial c_A}{\partial t} = D(T) \frac{\partial^2 c_A}{\partial x^2} = D_0 e^{\frac{-E_D}{RT}} \frac{\partial^2 c_A}{\partial x^2} \quad (7)$$

- t : time
 D_0 : binary diffusion coefficient of gas in polymer at 0 K
 x : diffusion distance
 E_D : molar activation energy of the diffusion

Unfortunately, the knowledge about S_0 and D_0 is poor, because permeation measurements give only the product of both. Another problem is, that equations (6) to (7) can only be used, if solubility is low. At high solubility values, the polymer matrix is no longer independent from gas amount and diffusion, even more when gas mixtures are used.

2.5 Melt Transport and Cooling

Once the foaming agent is fully dissolved into the melt, temperature and viscosity must be optimized to have best conditions for cell formation. If temperature is too high and/or viscosity is too low, cell membranes will undergo a minimum thickness and bubbles collapse. With too low temperature and/or too high viscosity, bubbles cannot expand because of a high surface energy (see below).

Using (H)CFCs is normally no problem in respect to saturation level. But with other gases, solubility is much lower and so, melt can be near the critical saturation. This causes an effect that should not be neglected: Even if static system pressure overrides the steam pressure of the blowing agent, local oversaturation and uncontrolled cell growth may happen because of dynamic pressure drops. This is possible on every place, where high shear rates reduce local pressure below critical saturation pressure.

Typical places for high shear rates are all points along the flow channel, where the cross section area has large changes (e.g. screen plate). Siebe makes screw- and flowchannel designs that are highly optimized for reduced differential changes in channel cross section. Measurements have shown that flow field are best with maximum angles below 45° . With higher slopes, uncontrolled local bubbles can establish. These bubbles grow and are transported from a critical size with the melt stream. If in high saturated solutions (for high void applications) pressure loss between screw and die can cause a light oversaturation, bubbles grow and destabilize the melt flow resulting in defects of the finished foam structure.

As the gas acts as a solvent in the polymer, the viscosity of the polymer reduces significantly (not depending on the gas process, e.g. chemical or physical foaming), so the user can either reduce temperature or pressure while maintaining flowability or getting higher throughput at same temperature/pressure level. In most cable extrusion applications, choice is lowering temperature, where up several K per % gas (in weight) is achievable, depending on polymer and gas type. An example is shown on figure 4 for a CO_2 laden polypropylene [clarant]. A phenomenological description assuming a linear behaviour for small gas amounts (<3%) is given in [9]:

$$T_g = T_{g0} - f_R \cdot a \quad (8)$$

- T_g : glass transition temperature of gas laden melt
 T_{g0} : glass transition temperature of pure melt
 f_R : reduction factor
 a : gas amount in % of weight

Measured values of T_g are in the range of 440 for R134a to 847 for CO_2 , so with carbonic dioxide, 1% of gas corresponds to around 8K in temperature.

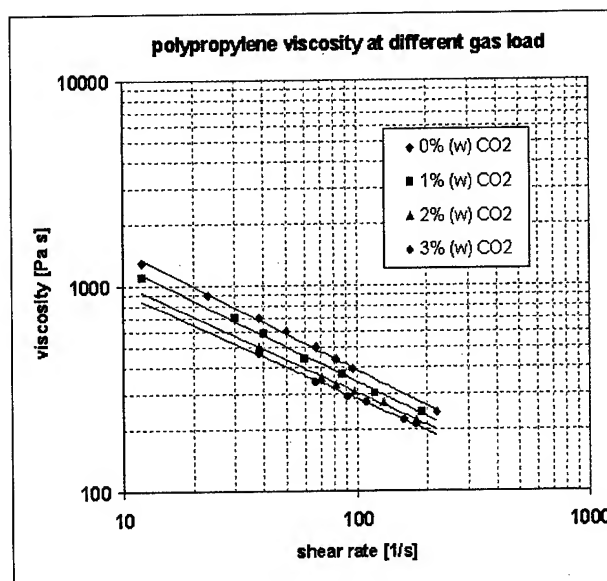


Figure 4: Polypropylene viscosity reduction as function of added gas amount (data from [18])

2.6 Nucleation

As the inner pressure of the dissolved gas gets higher than the outer pressure, the formation of cells can start. Normally, cell growth needs nucleation centres (e.g. solid particles or micro-cracks), where gas molecules collect. Pressure drop can occur as well at the cross head in extrusion as at injection moulding machines by shrinkage or opening the mould.

This pressure drop causes an oversaturation of gas in the melt, that is in physical terms a thermodynamic instability. As an unstable system tries everytime to stabilize, a certain amount of gas separates from the polymer. The gas molecules collect at certain hot spots, building so called "microbubbles". The physical description of this nucleation and the following step of cell growth is still a point of discussion. So the following short description represents only one possible model:

As already mentioned, nucleation can be separated into homogeneous and heterogeneous. Homogeneous (or spontaneous) nucleation can only happen with extreme oversaturation (see line 3 in picture 6). Heterogeneous nucleation on the other hand needs some boundary surface, where local void creation energy is reduced. This reduction is a function of surface roughness (described with a conicity angle ϕ) and the angle δ between bubble surface and boundary surface.

The relationship is expressed as [8]

$$\frac{A_{he}}{A_{ho}} = \frac{1}{4} \left[2 + 2 \cos(\delta + \phi) + \cos \delta \cdot (1 - \cos^2(\delta + \phi)) \right] \quad (9)$$

- A : Number of nucleation sites,
 he : heterogeneous,
 ho : homogeneous

This formula shows, that heterogeneous cell site creation is much easier than homogeneous. From a view of an operator it means, that the simplest way to foam a polymer is to use nucleation particles, that are small in size and have highest possible roughness. As a simple model, the number of nucleation sites can be calculated considering the nucleation particles as spheres with radius based on nucleation agent density and amount. Figure 5 shows theoretical plots for two particle sizes as a function of nucleation agent amount in a HDPE melt. To show relationship to real systems, measured data (talc and Hydrocerol, a sodiumbicarbonate system) are added. There is a good compliance of calculated and measured values. The reduction of cells at higher amounts of Hydrocerol is a beginning of overnucleation, where cell coalescence bubble collapse occur.

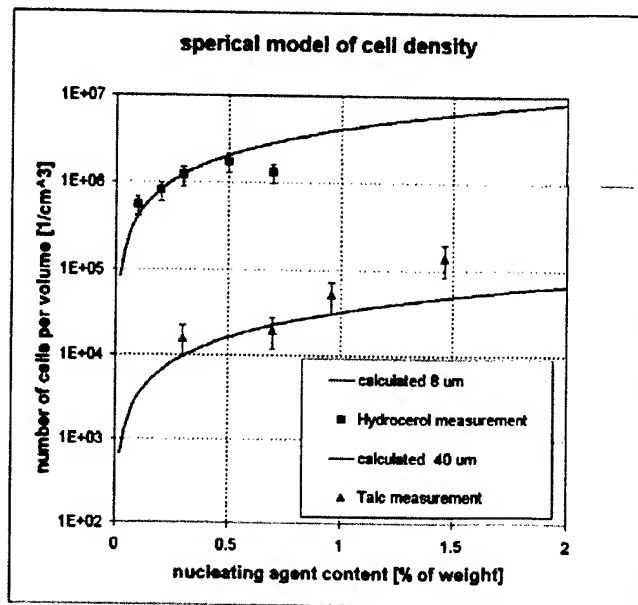


Figure 5: Number of nucleation sites as function of the nucleation agent amount. Solid lines are calculated values. Discrete data are measured cell densities in PE foam with different nucleating agents [10]

After adding the gas, the melt is oversaturated in terms of normal pressure (picture 6, zone I). Injecting more gas is only possible to a maximum point that depends on material and machine parameters (line 3). When the melt goes through the die, system pressure is lower than the blowing agents steam pressure – a (real) oversaturation occurs and bubbles grow.

At very high gas concentration, nucleation is the main process, at reduced concentration more and more gas separates from the melt by diffusing to existing cells. At the saturation point (line 1) nucleation and diffusion stop. The larger and faster a pressure drop is, the larger the number of cells is, because diffusion time (or diffusion length) is reduced.

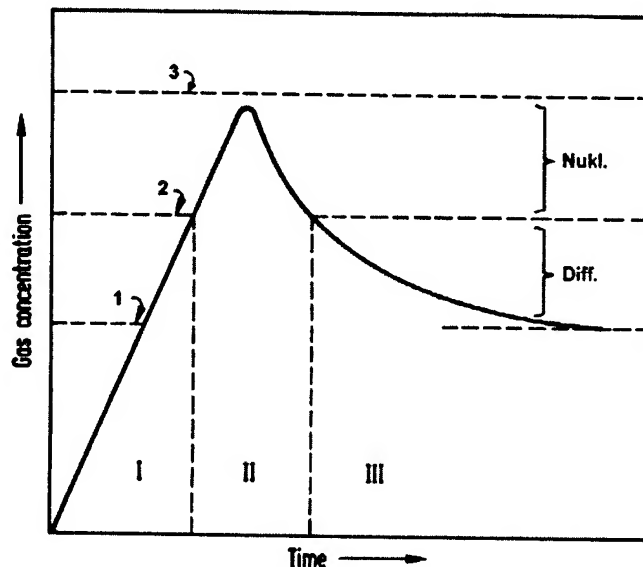


Figure 6. Cell nucleation and growth as a function of gas concentration

2.7 Cell Growth and Stabilization

Using concepts of statistical thermodynamics, free energy is used to describe phase transition and stabilisation of cells. Thermodynamic condition for cell stability is a reduction of free energy with increasing bubble radius ($d\Delta G/dr < 0$). In an early stage, ΔG grows with increasing radius (Picture 7, $r < r^*$). This means, that such microbubbles are unstable and can vanish. Once the microbubble overcomes the maximum ΔG^* , it stabilizes and at radius r^* , ΔG becomes negative and a stable cell grows.

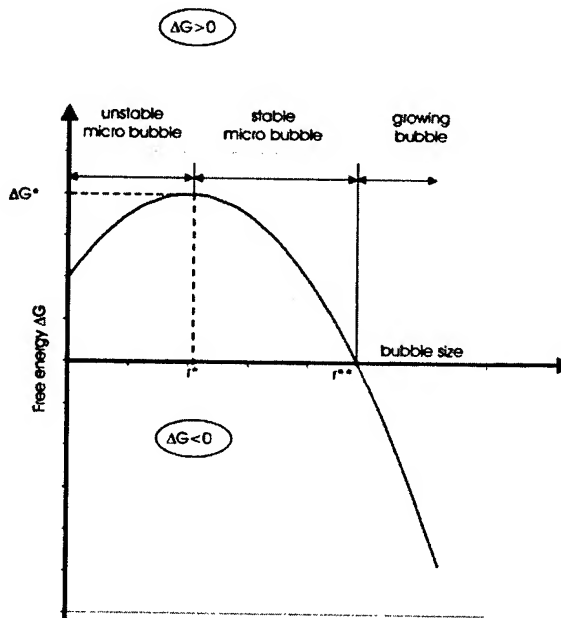


Figure 7: Change of free energy at the nucleation/growth of a cell

The existing microbubbles expand, til they reach an equilibrium between pressure inside the cell and steam pressure. In the simplified model of perfect spherical bubbles, free surface energy ΔG has to be equal to volume creation energy:

$$\Delta G = \sigma dA = p dV$$

$$\Rightarrow 4\pi\sigma d(r^2) = \frac{4}{3}\pi p d(r^3) \quad (10)$$

σ : melt surface tension
 A, V, r : surface area, volume and radius of the cell
 p : inner pressure of cell

Equation (10) shows another fact : at constant surface tension, the inner cell pressure reduces with increasing diameter. If bubbles with very different radius contact, the membrane between can burst and the gas of the small cell (r_a) enters the bigger one (r_b)

$$\Delta p_{a,b} = 3\sigma \left(\frac{1}{r_a} - \frac{1}{r_b} \right) \quad (11)$$

Even with stable membrane, there is some diffusion towards the lower pressure. This means, that in high void applications, a too long time between the initial foam growth and lowering temperature below mechanical stability let the foam structure tend to create large cells. This effect is shown in figure 8, based on same spherical model as it was used in chapter 2.6. The model assumes an isotropic and homogeneous distribution of cells in the polymer matrix. The measured data in the Hydrocerol system differ at higher nucleating agent amount from calculated values. As it is a high void foam, at a certain point more nucleation sites reduce the distance between cells under some critical value, resulting in increasing cell coalescence. With talc, the number of cells per volume is less, so this effect is not seen within the considered range.

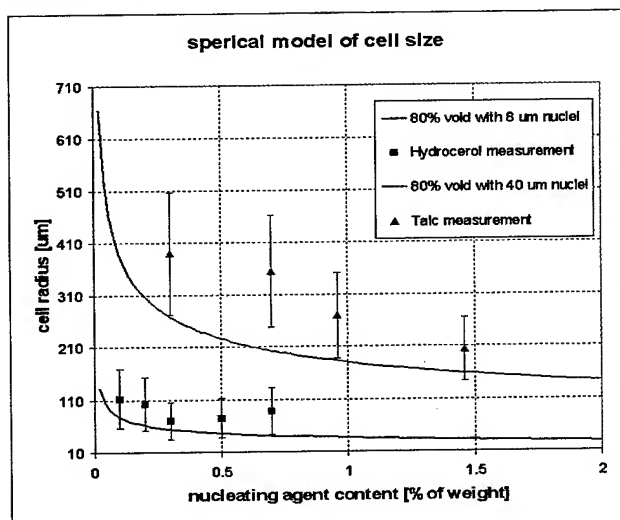


Figure 8: Calculated and measured cell size in a high void PE foam. Calculation is based on a spherical model, measured data from [10]

Applications with large cell size and/or low viscosity should also be considered under buoyancy effects [7] :

$$\frac{ds}{dt} = \frac{2r^2g}{9\eta} (\rho_s - \rho_g) \quad (12)$$

s : way of a cell through the melt
 g : gravitational acceleration
 ρ_x : density, S : melt, G : gas
 η : melt viscosity

By cooling down at the appropriate time, membrane bursts and buoyancy can be suppressed. This time depends on the diffusion speed and can be found in cable or profile extrusion processes as the maximum diameter of the foam cone after the die. The time reduces with cell radius, because diffusion length reduces as well.

If cell size is stabilized below 20 to 50 micrometers, foam is sometimes named "microfoam" or "microcellular foam". Another definition is a minimum number of nucleation centres in the order of 10^{10} per cm^3 . The physical background is the same as in larger cell size foam, the difference is the better optical/mechanical structure and the smooth surface feeling because of small cells and typically high nucleation site number.

3 Production of foamed cable insulation

Regarding to the mentioned facts about physical foaming a complex model for planning a foaming production line has been developed. The software uses polymer data and the spherical model to predict gas amount and to simulate thermal behaviour. According to this model numerical calculations by Siebe showed good approximations with real observations. As example, two typical cable types should be used.

3.1 Parameter calculation with CoaxCalc

As a first example, a CAT 7 data cable is used. The base parameters there are the values for cable geometry and the specifications:

Outer diameter inner conductor	0.60 mm
Outer diameter insulation	1.43 mm
Capacitance per unit length	100.3 pF/m
Impedance	110 Ω

Table 4: Typical parameters of a CAT 7 cable insulation

An HD-PE acts as the base matrix, a LD-PE inner skin with a wall thickness of 20 μm is assigned for the adhesion. Outer skin (LD-PE or PP) is used for color coding and additional mechanical stability. The production speed should be 1000m/min. With these data a lot of production parameters can already be calculated, for example void ratio (around 55%), gas amount (around 0.4 norm

liters/min), insulation diameter without gas (around 1.1 mm) or the dimensions of wire guide and die. If the characteristics of the used extruders are known, turn speeds are calculated from mass output (figure 9).

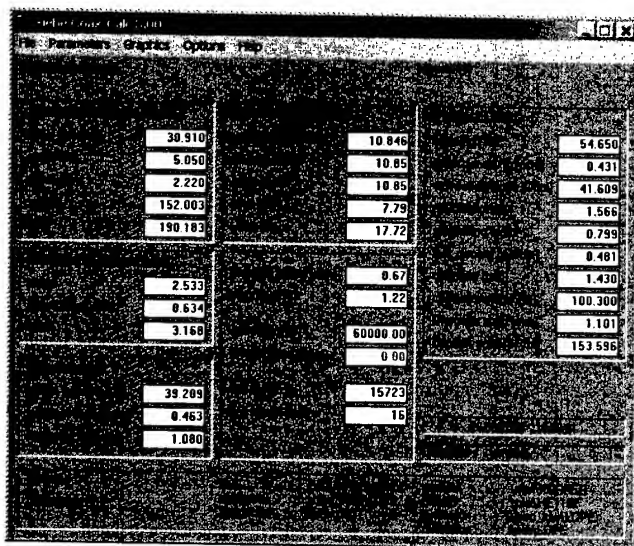


Figure 9: Calculated production data for a CAT 7 cable at 1000m/min (with a 65mm SIEBE gas screw)

Here can be seen the necessity of a high accurate gas injection system. As gas injection of N₂ happens at around 500 bar, the gas volume (0.46 liters/minute at norm condition) at the injection point is 0.92 cm³ (picture 10). This amount has to be dosed during one minute with variations less than 1%.

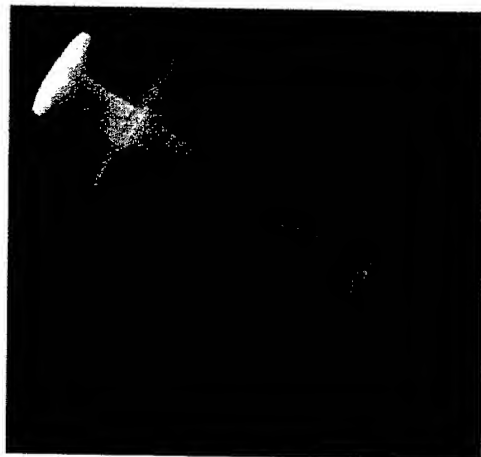


Figure 10: Gas volume at 500 bar for a CAT 7 foam insulation at 1000 m/min for 1 minute of production

All calculated data (like gas amount, turn speeds, solid values) are in good agreement with measured values during production.

3.2 Thermal Simulation of Cooling down along the Trough

If more parameters of the used polymers (as heat capacity, thermal conductivity) are available it is possible to simulate the thermal conditions of the cable along the water cooling. For

demonstration, a 1 5/8 inch RF cable is used. Production parameters should be 8.5 m/min, using around 6 norm liters/min of CO₂ to achieve 80% void.

It is very important to know the core temperature of the cable along the cooling trough, because the complete insulation needs at least to undergo the polymer melt temperature before the cable can be redirected. Otherwise mechanical damage would result as ovality and / or eccentricity. The cooling down can be simulated by using the same physical models as in electrodynamics : temperature difference corresponds to voltage, energy transport corresponds to current and the material layer heat transfer value corresponds to a true resistance [12]. The insulation is divided into concentric layers (see picture 11), where heat transfer is calculated from layer to layer at every length cross section.

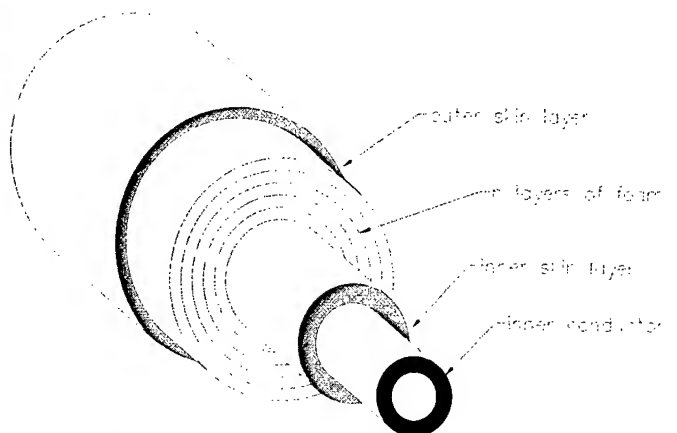


Figure 11: Physical separation of cable cross section into concentric layers

Using the well known formula for heat content

$$Q = c_m m \Delta T \quad (13)$$

Q : heat content

c_m : specific heat

m : mass

ΔT : temperature difference

and heat transfer

$$\Phi = \frac{dQ}{dt} = \frac{\lambda A \Delta T}{l} \quad (14)$$

A : transfer cross section

	17.3 mm
	41.0 mm
	78 pF/m
	50 Ω

Table 9: Typical parameters of a 1 5/8" GMS RF cable insulation

L : transfer length
 λ : heat transmission coefficient

simulation gives a prediction of the temperature behaviour inside the foam including a minimum cooling trough length at the predefined speed (see picture 12).

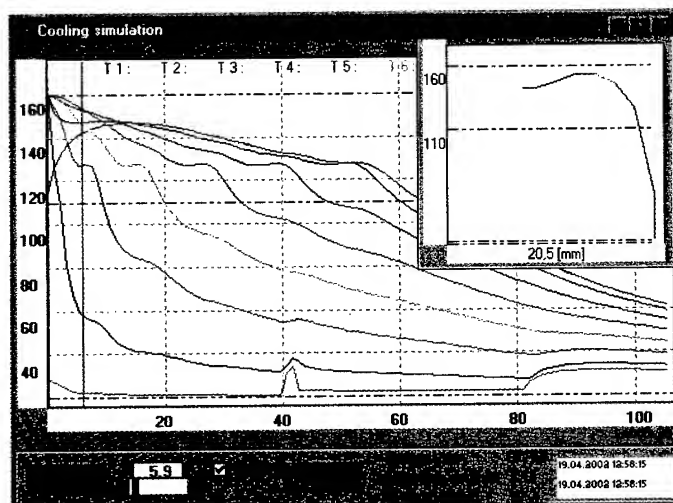


Figure 12: Simulated temperature of a foam insulated cable calculated as 9 layers

As verification the simulated inner conductor temperature has been compared with those measured in existing lines at the end of the cooling trough. A good correspondence of typically 2-3°C was found in every case. Using this tool, the limitations of production speed versus cooling distance can easily be shown. There are high standards in the automatic control technology too. A very precise temperature control has to keep the extruder exactly at the setpoint, the accuracy for gas flow control is already mentioned before. Dependent on the line concept the screw turn speed or head pressure must be kept constant by the automatic control system. In the same manner the control for rotational speed must guarantee a no-labile melt flow.

4. Conclusions

Even if the theoretical description of foam creation is not complete, there is a lot of practical experience, so the application engineer can select the right method and equipment for the foaming process.

Using the above-described results and software, we developed machinery that combines the advantages of all insulation processes to one line. Without any changes, the same line permits solid production, chemical foaming and physical foaming in configurations as nitrogen carbonic dioxide.

5. References

- [1] Helberg, Löw, Riedel, "Chemisches Verschäumen", Kunststoffe 6 (1985)

- [2] Herter, Lörcher, Nachrichtentechnik, Hanser (1994)
 [3] Schäfer et al., Novel approach to the analysis of broadband dielectric spectra, Physical review letters 76, Number 12 (1996)
 [4] BASF, „Kunststoff im Gespräch“, BASF lectures (1981)
 [5] Campus 4.0, Plastics Supplier database, <http://www.campusplastics.com>
 [6] Rao, Formeln der Kunststofftechnik, Hanser (1989)
 [7] Pahl et al, Praktische Rheologie der Kunststoffe und Elastomere, VDI (1995)
 [8] Clariant, Masterbatches direct gassing brochure, MB 1066/d 9.00 (2001)
 [9] Kropp, Extrusion thermoplastischer Schäume mit alternativen Treibmitteln, Dissertation, RWTH Aachen (1999)
 [10] Kropp, private communication, IKV (2001)
 [11] Vieth, Diffusion in and trough polymers, Hanser (1991)
 [12] Scheid, Simulation of polyolefine foam parameters, Blowing agents and foaming processes 2002, Rapra Technology Ltd (2002)

Biographical Notes



extrusion technology since 1990.

Thomas Reiner, born on 10th of May 1954 in Cologne, Germany, studied Mechanical Engineering at the Technical University of Aachen, Germany. After 5 years of research on adhesive bonding at the RWTH Aachen he received his doctorate in 1982. In 1994 he was appointed as Professor of the Engineering Faculty of the RWTH Aachen. Since 1982 he is the president and general manager of SIEBE Engineering. He is involved in the research on foam



Germany. Since 1995, his activities focus on foam extrusion research at Siebe Engineering, Germany.

Horst Scheid, born on 16th of June 1958 in Steinberg, Germany, studied Solid State Physics at the University of Saarbrücken, Germany. Since 1986, he was working in the research group at Arburg, a company that manufactures injection moulding machinery. Between 1990 and 1994, he worked in a research team at the COSY beam accelerator and received his doctoral degree in Nuclear Physics from the University of Bonn, Germany. Since 1995, his activities focus on foam extrusion research at Siebe Engineering, Germany.

Silane Crosslinked Polyethylene Insulation for Cost Effective Overhead Cables

Roger Carlsson

Borealis AB
SE-444 86 Stenungsund, Sweden
+46 303 86 000
roger.carlsson@borealisgroup.com

Detlef Wald

Borealis Polymers NV
Schaliënhovedreef 20 C, B-2800 Mechelen, Belgium
+32 475 71 11 55
detlef.wald@borealisgroup.com

Dr. Bermt-Åke Sultan

Borealis AB
SE-444 86 Stenungsund, Sweden
+46 303 86 000
bermt-ake.sultan@borealisgroup.com

Ola Fagrell

Borealis AB
SE-444 86 Stenungsund, Sweden
+46 303 86 000
ola.fagrell@borealisgroup.com

The public demand for a safer and reliable electricity supply has increased the demand for Covered Conductors (overhead conductor design including a polymeric layer). These lines are an economical solution, compared to underground cables, to distribute energy in rural and fast growing areas across the world. In these designs conductors are encapsulated with one or more layers of polymer, normally crosslinked polyethylene (XLPE). This paper compares XLPE solutions with the proposed CENELEC specification for covered conductors.

It demonstrates the improved properties that can be achieved with a moisture crosslinkable silane-copolymer (EVS). It presents aspects, in addition to those in the specification, that will further assure or extend the lifetime of Covered Conductors. The importance of mechanical strength (crosslinking degree) in achieving optimal tracking and UV performance is highlighted.

Keywords

Covered Conductors, Moisture crosslinking, Tracking.

1. Introduction

The most common way to distribute electricity is through bare overhead wires. However, in the last decade more and more underground cables have been installed to increase the security of the electricity supply and reduced the environmental impact in highly populated areas, however, in rural areas overhead bare wires are still used. As a result of the public demand of higher levels of safety and reliability, covered conductors (CC) are becoming more common today. The first installations were in the 50's in North America and later in Europe. Today, approximately 15000 km of covered conductors are installed in Europe. In Japan the entire 6.6-kV network has been changed to covered conductors for safety reasons. As a result of these good experiences more countries all over the world are showing interest in this construction. The reasons why covered conductors are being considered as an alternative along with underground cables are:

- Lower costs
- Lower capacitance
- Higher rating
- Reduced need for new wayleaves.

When compared to the traditional bare wire solution the advantages of covered conductors are [1]:

- Large reduction in failure rate, minimising fault maintenance.
- Minimising the planned maintenance.
- Significant safety improvement for service operators and third parties.
- Substantial reduction of duration and frequency of interruptions.
- Reduction of the EMF (electromagnetic field), improving perception of the public.
- Space reduction, with consequently less need for tree trimming and right of way.
- In Australia the concern for bush fires has lead to the implementation of covered conductors.

The space between the conductors can be reduced significantly. The distance needed between conductors is 110 cm at bare wires and for covered conductors it can be reduced to 90 cm. For certain constructions requiring a track resistant compounds the distance can be reduced to 10 cm, Table 1. This significantly reduces the tree trimming required and narrows the right of way, leading to reduced costs.

The significant reduction in failure rate can be seen in Figure 1. This reduction is mainly due to that the covered conductors provide a protection against branches, animals and other objects from causing

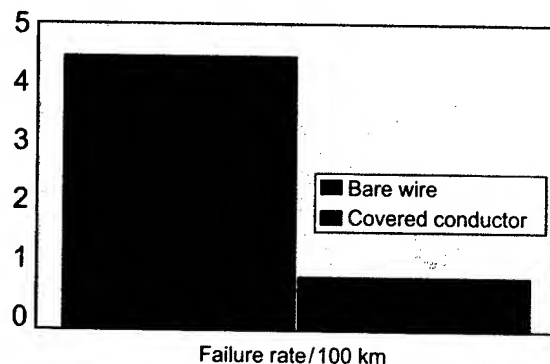


Figure 1. Failure rate per annum/100 km of conductor [2]

The normalised capital cost for a 110 kV distribution line in Poland is presented here as an example [3].

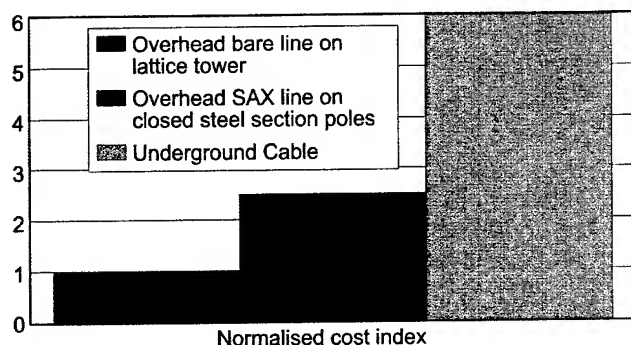


Figure 2. The normalised capital cost of different power supply solutions

In Figure 2 the initial investment costs are compared for the three alternatives, Bare Wires, Covered Conductors and Underground Cable. For a true cost comparison also the other cost elements need to be considered. There has been calculation made and presented comparing the global costs for a specific area and application [1]. This calculation needs however to be done in the specific case to compare the different solutions. The cost calculations should contain cost elements from:

- Initial investment
- Operational costs, including preventive and corrective maintenance
- Social cost, the cost of a power failure.

Their calculations are laborious but will show that in many cases covered conductors are the most cost-effective solution.

This paper presents recent results on cables with XLPE compounds that are compared with requirements of different specifications valid in the world and specifically the latest proposal in the CENELEC specification.

2. Constructions

Several constructions and standards are used around the world. The most commonly installed types in Europe are outlined in Table 1

Table 1. Overview of Constructions

Name	Bare Wires	Tree Wire	Partially Insulated Cable (PIC)	Fully Insulated Overhead Cables	Spacer Cables
N° of polymeric layers	0	1	2	4	3
Phase spacing [cm]	110	50	30	0	15
Areas of use	World	US, Europe	Asia, North Europe, South + Central America	Europe	US, South-East-Asia
Voltage Range		6.6 - 24 kV	10 - 35 kV	10 - 150 kV	10 - 150 kV

2.1 Tree Wire, One Layer Construction

The oldest and simplest construction is a 2.3-mm insulation of a single layer of low-density polyethylene (LDPE) or crosslinked polyethylene (XLPE) on a stranded aluminium conductor. The insulation thickness was determined by the minimum needed to keep the cable working for up to two weeks when trees are hanging against the lines. From an electrical insulation standpoint a thinner thickness would have been sufficient. Here one layer of insulation is giving the mechanical protection against abrasion, the electrical properties against tracking and breakdown and a sufficient adhesion to the conductor to avoid slipping of the conductor inside the cable. The latter is important if the cable is directly clamped with the insulation. Here adhesion forces up to 100 N/mm² are required. In other countries the cable is de-insulated at the clamps. This can create a disturbance of the electrical field. These cables have been in use for several years in the Northern Hemisphere. In Finland these cables are called SAX cables, in Sweden BLX and in the anglophone area they are generally described as Covered Conductors. In these countries the constructions are meant to protect the cables against heavy winds, snowfall and medium weather exposure, like moderate sunshine and lightning.



Figure 3. One layer construction

2.2. Partial Insulated Cables (PIC)

The outages with a one-layer construction are reduced by more than 55 % compared to bare wires and by a further 20% using a two-layer construction, partial insulated cable [2] Figure 4. This type of cable is mainly used in Far East Asia, Sweden, Australia, Japan and South America.

Here an inner semiconductive layer is used additional to the insulation. This improves the adhesion to the conductor and homogenises the electrical field inside the cable. It is utilised in low populated areas where it is possible to put poles and using the three different phases with a distance of approximately 30-cm.

Separate partially insulated cables are fixed with aluminium wire to insulators on brackets. The insulation thickness is depending on the rated voltage varying within 2.8 and 5.4 mm.

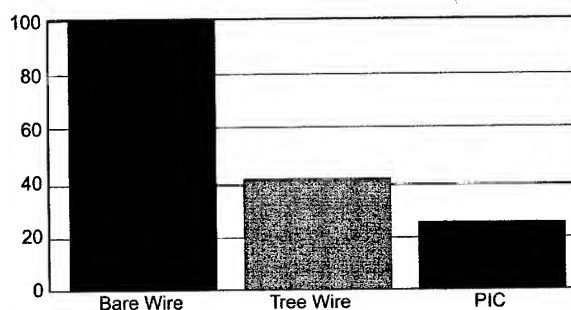


Figure 4. Normalised Failure Rate of different constructions [2]

2.3 Fully Insulated Construction

In the southern part of Europe standard medium voltage cables are used bundled together with or without a supporting wire, Figure 5. This construction is then protected using a high-density polyethylene. Due to the construction the tracking risk is very low, however, it has similar cost in production as a standard underground cable, without the cost of digging.



Figure 5. Fully Insulated Constructions as installed in South and West Europe

3. Requirements Defined by CENELEC

In table 2 different materials are compared with the proposal of the CENELEC.

Table 2. Comparison of different insulator material with the proposed CENELEC specification covering Tree Wire and PIC

Properties/ Test Method	Standard	Typical Values		
Polymer	PrEN50XXX/1 XLPE	Track resistant-XLPE XLPE	XLPE Black Moisture Crosslinkable Copolymer (EVS)	XLPE Black Moisture Crosslinkable MD Copolymer (EVS)
UV stabilisation	>2.0% Carbon Black or UV stabiliser	0.5%	2.5%	0.5% + UV stabiliser
Track Resistance	3.5 kV	3.5 kV	2.8 kV	3.5 kV
Track Resistance	6 h	>300 h	>200 h	>300 h
AC Breakdown Strength	>U	>22 kV/mm	>22 kV/mm	>22 kV/mm
Heat Elongation	<175%	60 - 80%	60%	40%
Tensile Strength	>12.5 MPa	22 MPa	17 MPa	25 MPa
Elongation at Break	>200%	500%	350%	380%
Variation of mechanical properties after 7 days, 135°C	<25%	<25%	<25%	<25%
Variation of mechanical properties after 2000 h UV ageing	<10%	<10%	<10%	<10%

The specification requirements shown in Table 2 detail the foundation for material solutions for Covered Conductors. Experience working in this area shows that additional consideration needs to be given to:

- Abrasion resistance
- Conductor adhesion
- Track resistance after UV exposure
- UV stabilisation

Attention to these areas significantly improves the performance and longevity of Covered Conductors.

3.1 Mechanical Properties

3.1.1. Abrasion Resistance. On the basis of electrical performance the thickness of the insulating layer could be considerably thinner than used in normal practice. The increase is to enable the conductors to operate in emergency situations, laying on the ground or with tree contact. Given the rugged nature of the operation, normal as well as emergency, it is important that the material is immune from abrasion damage. Abrasion could reduce the insulation wall below that required for emergency operation.

Figure 6 shows the abrasion index (Taber mass loss per 1000 cycles) for crosslinked LDPE and crosslinked MDPE. This shows that increasing the density reduces the abrasion. There is a 50% increase in the number of cycles to remove the same amount of the material when moving from LDPE to MDPE.

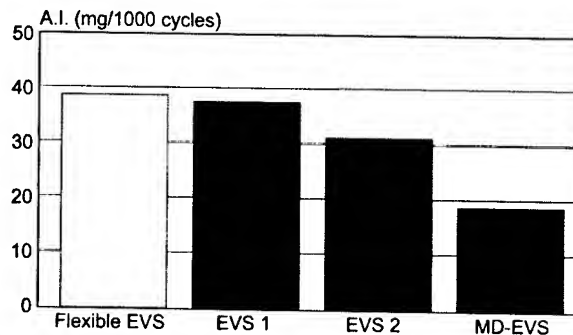


Figure 6. Abrasion Resistance according to Taber

3.1.2. Adhesion to the conductor. Two methods of connecting Covered Conductors to the supports are currently used through out Europe:

- Clamps used around the insulation
- Clamps attached through the insulation and onto the bare wire.

When using the first method it is clear that a very good adhesion is needed between the insulation and the conductor. If the adhesion is too low the insulation might slip creating vibration and other problems. The adhesion issue is further exacerbated by the use of grease to improve the water tightness of the conductor.

The impact of insulation material on the adhesion is shown in Figure 7. The crosslinked MDPE based material exhibits the highest pull out force and gives the best adhesion. Here crosslinked material has one further advantage over thermoplastic material, having better mechanical properties at elevated temperatures.

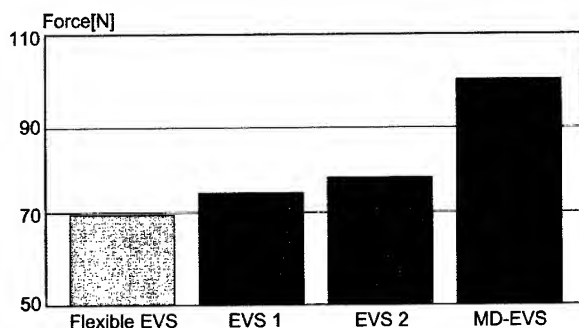


Figure 7. Adhesion to metal according to NFC 33-209

3.2 Electrical Properties

3.2.1. Track Resistance. In the early sixties it was recognised that unshielded power cables, particularly in wet contaminated environments, had surface induced voltages leading to leakage currents. These currents and associated surface discharges are known to combine into a phenomenon generally described as surface tracking. Polyethylene for itself has a very good track resistance, but not a good outdoor performance. The poor outdoor performance comes from degradation under UV exposure. The best protection against UV ageing is the addition of carbon black (CB). It is common practice to add 2.0 % carbon black to give sufficient protection. This is based on the studies done in the Bell laboratories in the 50's. However the original study recommends 1.0 % carbon black as sufficient enough. However 2% of carbon black is already significantly negatively influencing the track resistance of the compound.

Figure 8 shows the effect that the CB added to improve the UV resistance has on the electrical performance, dust and fog test.

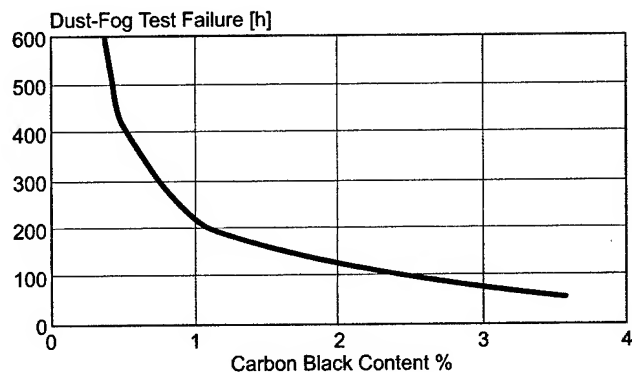


Figure 8. Dependencies of Track Resistance against Carbon Black Content (ASTM D 2132)

To balance the opposing requirements the optimal choice is to have a low amount of CB (0,5% typically) and UV protecting additives make up for the inferior UV absorption at the low CB level. There is also a very strong influence of the carbon black dispersion on cable insulation properties as can be seen in Figure 9. Therefore the adding of the CB via a masterbatch will always be inferior and a more robust grade would have the CB dispersed in the base resin, then one are not dependent of the ability of the cable extruder to disperse the carbon black.

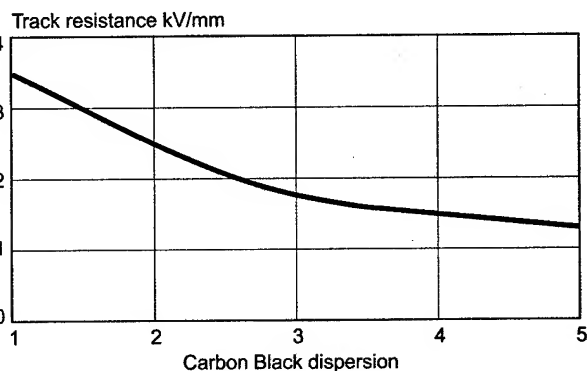


Figure 9. Influence of Carbon Black content and dispersion on Track Resistance (ASTM D 2303)

Carbon Black dispersion index measured in accordance with a slightly modified British Standard 2782 pat 8

The tracking resistance is also depending on the insulation thickness, the dielectric constant and the system voltage. Severe tracking demands are in the proposed European specification. The material should withstand 3.5 kV for 6 hours to pass the test. As outlined in Table 5 there are several materials that are meeting this requirement.

In Figure 10 the EVS and the EVS MD are tested with a carbon black level of 2,5%. The performance would be improved further by the use of the specially developed masterbatch for track resistancy, containing the optimised carbonblack level, however this indicates the robustness of the silane crosslinked compounds in terms of track resistancy.

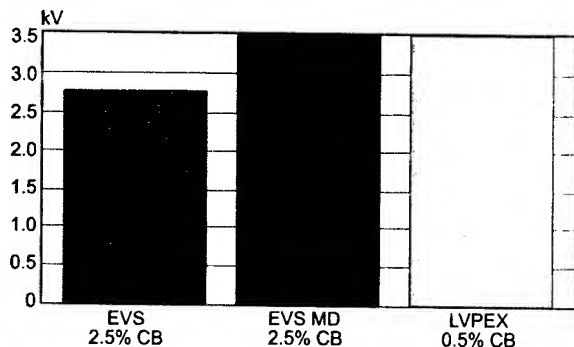


Figure 10. Track Resistance according to ASTM D 2303

3.2.2. Electrical Strength. Covered Conductors are required to operate under AC voltage in emergency conditions when lying on the ground or having tree lie on them. This requires that the Covered Conductor are able to pass an AC voltage test. The CENELEC specification requires that the Covered Conductor are able to withstand rated voltages in water for a minimum of 6 hours. The test does not require that the Covered Conductor maintain this withstand whilst under mechanical load (fallen tree) at operating temperature. However the mechanical strength at high temperature afforded by crosslinking means that XLPE is able to fulfil these requirements. The experience from underground cables has shown that the best way to assure good electrical properties is to use insulation that is essentially free of voids, metal particles and process contaminants, ambers, gels etc.

4. Crosslinking and tracking

It has been shown that a crosslinked polyethylene increases the UV resistance compared to thermoplastic material [4]. In Brazil it was found that materials which passed the laboratory tracking evaluation according to ASTM D-2303 did not provide good service and failed in the field [5]. This indicated that the "real exposure" was more severe. Therefore a more severe tracking test was developed to better imitate the realistic exposure of the cable. In the method, ABRADDEE CODI 3.2.18.23.1/NBR10296, tracking performance are measured both before and after Xenon UV exposure for 2000 hours, the requirements are described in Table 3.

Table 3. Tracking requirements for ABRADDEE CODI 3.2.18.23.1/NBR 10296

ABRADDEE CODI 3.2.18.23.1/NBR10296	Unaged sample	UV exposure 2000 h
Minimum Tracking voltage for passing	2.75 kV	2.5 kV

When applying this test method it was discovered that the thermoplastic materials had an in built deficiency in long term tracking performance in the field, see Figure 11.

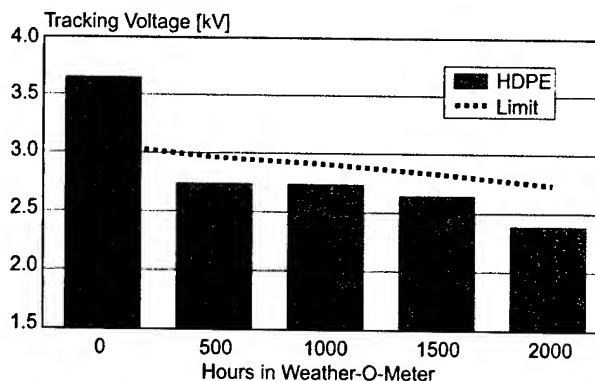


Figure 11 Evolution of tracking performance as a function of UV exposure according to ABRADDEE CODI 3.2.18.23.1/NB10296C [9]

It is seen from this evaluation that even if the HDPE starts at a high level it starts to drop when it is exposed to UV light suggesting a non suitable material for covered conductors when exposed to a high UV radiation. A crosslinked material however shows a much more stable behaviour during UV exposure [5].

This indicates that in order to find an optimal compound for covered conductors one should look for optimisation with in crosslinked polyethylene. Another test that emphasises the advantages of crosslinked PE versus thermoplastic material is the reported in Table 4. Where it is evident that the tracking performance increases significantly when crosslinking take place.

Table 4 Comparison of thermoplastic and crosslinked LDPE

Sample/Dust and Fog (ASTM D 2132)	Cable	Pressed plaques
PEX Non crosslinked	>400 h	250 h
PEX Crosslinked	>600 h	400 h

In the silane crosslinkable compounds it quite common to have a scorch retarder present, this scorch retarder is a low molecular silane compound. The scorch retarder is demoting the wetting of the cable. The hypothesis is that, in case of abrading the surface by e.g. a tree branch, the scorch retarder will migrate to the surface to again prevent good wetting of contaminated water. The wetting is essential

for promoting tracking. This mechanism will distinguish the silane crosslinking material from the peroxide crosslinking and the thermoplastic materials in long term real life track resistance. This advantage will not be detected in the accelerated tracking since the surface are abraded and directly after they are exposed to the tracking method not giving time for the scorch retarder to migrate and demote the wetting. In real life, the abrading is a much slower phenomena and therefore gives time for migration of the scorch retarder.

The European standard proposes a hot set value of 175%. A polyethylene with this value is not sufficient crosslinked to pass any of the requirements and does not give the significant advantage of XLPE. With this high value still a further crosslinking might occur during the operation of the cable, that might result in mechanical damage of the cables. Additionally the tracking resistance is with 175 % far away from being optimal. As seen in Figure 12 the tracking performance is dependent of the crosslinking.

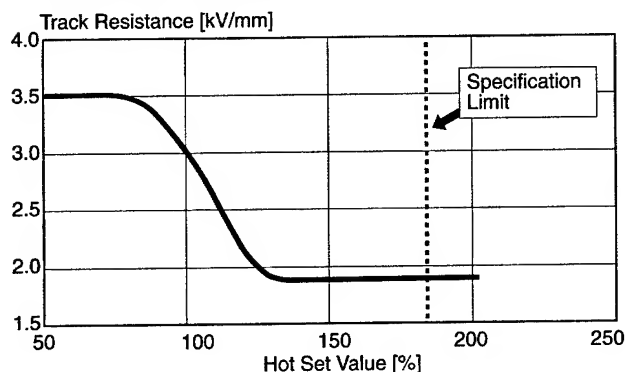


Figure 12. Hot Set Value against Track Resistance (ASTM D 2303)

5. Compounds used for these applications

Low density polyethylene (LDPE) has established itself already in the 1950's as a superior extruded insulation material for power cable insulation this was a result of the selection of its outstanding electrical properties. Today 5% of the polyethylene production are used for Wire & Cable applications. Firstly, used in its thermoplastic form, the need to crosslinked LDPE has quickly evolved (XLPE). This is because XLPE has better properties than polyethylene in terms of:

- ESCR
- Heat deformation
- Mechanical Properties
- Cut Through Resistance
- Impact Strength
- Shear and Compressive Strength
- Creep Strength
- Abrasion Resistance
- Weather Resistance

Other obvious advantages are that a conductor temperature of up to 90°C can be used using XLPE whereas the maximum temperature for LDPE is 70 °C. During a short period of five second it can withstand a temperature of 250°C. For the one- and two-layer construction moisture curing is the preferred solution in Europe. To fully un-

derstand the benefits that are generally achieved with crosslinking and with silane crosslinking specifically, the recent developments in silane crosslinking will be explained, and how it influences the requirements for covered conductors.

5.1 Moisture Curing Process

Sioplas™ was introduced in 1968, in this processes vinyl silane, normally vinyl-trimethoxysile (VTMS), is grafted onto a low-density polyethylene (LDPE) [6]. In all moisture curable processes a crosslinking agent, originally an organo-tin derivative such as di-n-butyltindilaurate (DBTDL), has to be added. In all these processes the crosslinking was originally performed "off line" by introducing the cable core drum into a steam cabinet or water bath heated to 70 °C for several hours. Crosslinkable ethylene-vinyl silane copolymers (EVS), specific for the global wire and cable market were introduced fifteen years ago. The copolymer process solved some of the problems associated with the older silane technologies. As it improved the product consistency resulted in cable manufacturing without any handling of explosive and burnable liquids. Copolymers have superior storage stability and contain no volatiles.

5.2 Optimisation of processing characteristics

Crosslinking reactions occurring during the extrusion process will lead to an increased viscosity and might result in the formation of pre-cured particles (scorch). These particles are un-melttable and can be seen as a contaminant reducing electrical and mechanical properties as well as negatively effecting surface finish and dimension stability. When using reactor copolymers it is possible to produce insulation having superior storage stability and product consistency [7]. Together with a scorch retarder a virtually non scorching material is obtained, Figure 13.

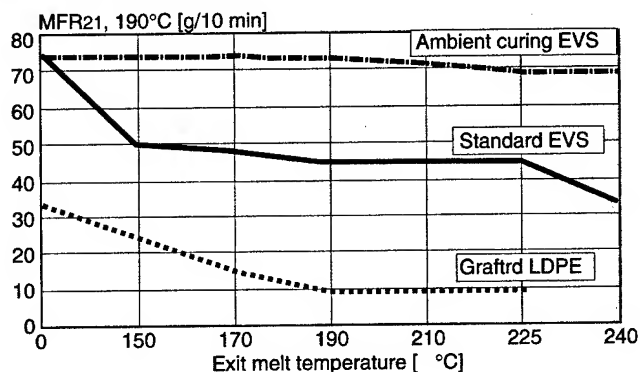


Figure 13. Influence of the scorch retarder additive

In Figure 13 the melt index is shown versus temperature. A drop in MFR indicates that precrosslinking occurs. The processing window of grafted polymers is more narrow than that of standard EVS-polymers or even EVS-polymers for ambient curing. Already at 160°C pre-crosslinking (scorch) can occur, whereas ambient EVS-polymer can be processed up to 210 °C without any problems. Scorch particles can be the origin of surface defects or electrical failures.

5.3. Development of ambient curing

An additive reacting with virtually all the water present during extrusion made it possible to develop compounds with higher crosslinking speed. Organo-tin compounds like DBTL have limita-

tions in crosslinking speed and they are regarded as hazardous substances, as they inhibit the fundamental energy conservation process in mitochondria. Accordingly authorities and cable makers blacklist them. A class of substances is now patented for ambient curing of silane crosslinkable polymers, and provide a less harmful impact on the environment and human exposure [8]. The improved crosslinking can be seen in Figure 14.

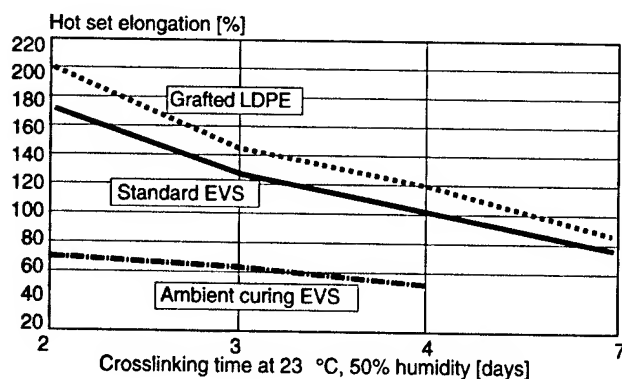


Figure 14. Crosslinking speed

With the new ambient curing EVS-polymers a very low hot-set value can be achieved after three days. As earlier highlighted a very good crosslinking degree is needed to get better outdoor performance of the cable. The crosslinking speed is depending on the cable construction and on the reel size.

6. Practical solutions

As can be seen in Table 5, peroxide crosslinkable LDPE has similar tracking properties, 3.5kV, as the medium density based moisture cured material with standard black catalyst masterbatch. The positive effect of the harder material can be seen as it reaches the same tracking in accordance with ASTM D2303 at a less favourable carbon black content. The results with the optimised CB level in the designed tracking masterbatch needs to be collected but indications from Figure 8 gives that the value will be even higher than for LDPEX. LDPEX performs however better in the dust and fog test, ASTM 2332 compared with the moisture cured low density version, the tracking is increased by 0.7kV to 3.5 kV and the resistance in the dust and fog test is increased from >200 to > 250 hours. However the only combination that meets the Brazilian test is when combining the intrinsic good properties of a medium density silane crosslinkable base resin with the specially designed track resistant catalyst masterbatch.

When weighting all requirements as outlined in Table 5 together with the other important parameters, like abrasion resistance, conductor adhesion, tracking performance after UV exposure and a high crosslinking degree, it is evident that the trackresistant moisture crosslinkable MDPE best balance these different requirements and therefor ought to be the preferred material for Covered Conductors, securing longevity in the field.

Table 5. Comparison of different crosslinkable compounds

Properties/	Covered Conductors, typical requirements	Typical Values			
Polymer	Peroxide crosslinkable PE Moisture Crosslinkable PE Thermoplastic PE	Peroxide Crosslinking LDPE	Moisture Crosslinking LDPE	Moisture Crosslinking MDPE	Track Resistance Moisture crosslinking MDPE
Carbon Black content	>2.0% or lower with combination of a UV protector	0.5%	2.5%	2.5%	0.5%
Track Resistance: ASTM D 2305 ASTM D 2332	>2.0 kV >200 h	3.5 kV >300 h	2.8 kV >200 h	3.5 kV >250 h	3.5kV —
Abradee Code 3.2.18.23.1/ INBR 10296	>2.75 kV >2.5 kV for UV exposed	Fail	Fail	Fail	Pass (3.5 kV)
AC Breakdown	>5 kV/mm	>22 kV/mm	>22 kV/mm	>22 kV/mm	>22 kV/mm
Heat Elongation	<175%	70%	60%	40%	40%
Tensile Strength	>12.5 MP	22 MPa	17 MPa	25 MPa	25 MPa
Elongation at Break	>250%	>500%	>350%	>380%	>380%
Variation of mechanical properties after 7 days at 135°C	<25%	<25%	<25%	<25%	<25%
Variation of mechanical properties after 200 h UV ageing	<10%	<10%	<10%	<10%	<10%
ESCR ASTM D 163	No cracks 1000 h	No cracks >1000 h	No cracks >1000 h	No cracks >1000 h	No cracks >1000 h

7. Conclusions

Covered Conductors have been recognised as an economical and environmentally friendly solution to energy distribute. Today there are compounds on the market that can give a cable manufactures a wide choice of producing cables according to the different demands of the utilities. It is shown that crosslinking in general and silane crosslinking compounds specifically offer unique properties that are of importance for a robust and economical overhead cable construction. The following parameters should be included in an optimal compound:

- Crosslinked, for long term track resistance, UV protection, abrasion resistance.
- 0,5% CB + UV additivition, for tracking resistancy and UV protection.
- Higher density, MDPE, For track resistancy and abrasion resistancy.
- Scorch retarder, for track resistancy, electrical properties and processing.
- Silane crosslinking, for track resistancy and production varsity.
- Fast crosslinking, for track resistancy.

It is recognised that there exists compounds commercially today that fulfils this requirements.

9. Authors

Roger Carlsson received his M.Sc in chemical engineering in 1989 from Chalmers Tekniska Högskola, Gothenburg, Sweden. He joined Borealis Wire & Cable in 1991, where he presently is working in the marketing and development centre as project manager.

Detlef Wald was born 1963 in Gerolstein, Germany. Graduated in 1987 as Diplom Engineer in chemical engineering at the technical university of Aachen, Germany. Joint the Wire & Cable business of at that time BP Chemicals in Geneva, Switzerland 1990 as development chemist. Today responsible for technical service and marketing of Borealis Wire & Cable, based in Mechelen, Belgium.

8. References

- [1] A, M.R. Soares, CEMIG, Brasil, F. Nishimura, ALCOA, Brasil, et al. "Spacer Cable and ABC Distribution Lines a Long-Term Analysis," *IEEE publication* (1996).
- [2] "Reliability of overhead distribution circuits," *Hendrix Publication*
- [3] J.Bucholc et al "A 110 kV SAX line in Poland," *ICCC* (1997).
- [4] Andersson, Hans; Ohrn, Lars. "UV- and acid rain-resistant plastic film or coating for greenhouses or other climate protection.," *PCT Int. Appl., WO 9739058* (1997)
- [5] C. W. Pinheiro et al. "Study of Polymeric Material Characteristics on Covered Conductors Used in Brazil," *IEEE annual report, conference on electrical insulation and dielectric phenomena.* (1996)
- [6] H.G. Scott, Midlands Silciones, Dow Corning "Crosslinking of a polyolfine with a silane," *US patent 3646155*, (1968)
- [7] B-A. Sultan and L-E Ahlstrand, Borealis Holding A/S(Neste Oy), , "Silane Crosslinkable Polymer Composition Containing a Silane Compound as a Precuring Retarder," *European Patent 449939, US Patent 5350812* (1988)
- [8] R. Dammert, B. Gustavsson and B-A. Sultan, Borealis A/S, "Polyethylene Compatible Sulphonic Acids as Crosslinking Catalysts," *European Patent 0736065, WO 95/17463* (1993)

Dr. Bernt-Åke Sultan received his M.Sc in chemical engineering in 1981 from Chalmers Tekniska Högskola, Gothenburg, Sweden, he later obtained a Ph.D. His thesis covered studies of the thermal degradation behaviour of ethylene copolymers. Since 1984 he has been working with product development of Borealis products inteneded for the Wire & Cable application.

Ola Fagrell received his M.Sc in chemical engineering in 1984 from Chalmers Tekniska Högskola, Gothenburg, Sweden. He joined Borealis Wire & Cable in 1989, where he presently is working in the marketing and development centre as project manager.

Antimicrobial Additives for Use in Wire and Cable Applications

Neal J. Earhart
Staff Scientist

Urs Stadler
Senior Staff Scientist

Ciba Specialty Chemicals Corporation
Tarrytown, NY 10591
(914) 785-4518 neal.earhart@cibasc.com

Abstract

During their service life, wires and electrical cables, can be exposed to a variety of detrimental environmental conditions. Beyond the effects of typical light and heat exposure, other environmental conditions can negatively impact the physical properties and performance of a wire or cable during its end-use. Microorganisms can attack polymers that are typically used in wire and cable jacketing formulations and other components of cable construction, such as filling compounds, resulting in a shortening of their service life by causing premature deterioration and discoloration. This paper will review a new range of antimicrobial additives developed, as active ingredients for use in a variety of polymer applications, to meet the fast growing market needs for biocides that can provide antimicrobial surface effects, beyond typical polymer protection.

Introduction

The two major purposes for the use of antimicrobial additives in the polymer industry are as biostabilizers and as antimicrobial active ingredients. Biostabilizers act against microorganisms that can attack the polymeric material resulting in unwanted changes in physical properties or appearance of the material. In addition to this preservative action, active antimicrobial additives provide built-in ability in polymeric products to either maintain surfaces in a sanitary or hygienic state or to provide additional protection such as prevention of odor development and extended product life. As a result, these articles have additional benefits for the user [1].

The three major categories of microorganisms that can grow on polymeric surfaces include bacteria, fungi and algae. Depending on the intended function of antimicrobial additives in polymeric applications, the necessary activity spectrum has to be considered so that a substance with a good efficacy against the targeted microorganism, with no/low toxicity against humans and the environment together with sufficient stability at processing temperatures and end-use conditions is selected. In some cases, a mixture of antimicrobials is recommended in order to protect against a broader spectrum of microorganisms. The active

components of an antimicrobial system can either be organic or inorganic. Organic systems are generally small molecules that are incompatible with the polymer matrix and therefore diffuse to the surface where they interact with microorganisms present. Inorganic systems are based on metal ions, most commonly silver, that are stabilized in a way so that they are unreactive until released in association with another agent, such as moisture. Hence, antimicrobial additives remain stored in the polymer, only being released gradually to the surface, providing continual and long-lasting activity.

In the United States, all antimicrobial additives must be registered with the Environmental Protection Agency (EPA) for intended use in plastic. Under the Federal Insecticide, Fungicide and Rodenticide Act (FIFRA), a company cannot make public health or pesticidal claims for any polymer product distributed or sold unless the product has been approved or licensed by the EPA or covered by an exemption from registration, i.e. treated article exemption [2]. Therefore, the anti-microbial additive supplier should be consulted prior to the use of these products in order to comply with existing regulations.

Experimental

A variety of test methods can determine the susceptibility of a plastic material to microbial degradation and the resistance of a material to microbial settlement. The most commonly used method to assess antimicrobial efficacy is the agar diffusion test. The agar medium is applied uniformly on a petri dish and inoculated with the test microorganisms. The test specimen, 2cm in diameter, is placed on top of the agar medium. The test plate is then incubated for 18-24 hours at 37°C. After incubation, when the microbial growth is visible, the growth of the test organisms is assessed on and around the test specimen. The zone of suppressed microbial growth is measured from the edge of the sample disk to the organism growth front. This is reported as the Zone of Inhibition (ZI). Microbial growth is also assessed on the test specimen surface and is assigned a Vinson rating [3] as illustrated in Figure 1; polymer samples with 0.1% of the antimicrobial additive AM-1 inhibit the growth of gram-negative

and gram-positive bacteria (*Escherichia coli* and *Staphylococcus aureus*, respectively).

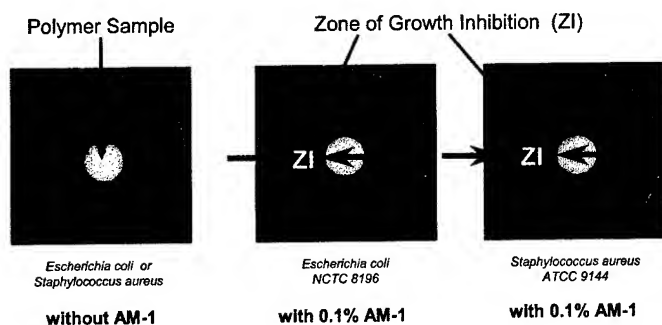


Figure 1: Antimicrobial Activity of Polymer Samples with and without 0.1% AM-1 in Agar Diffusion Tests

Examples of organic antimicrobials (AM-1) in polymers commonly used in wire and cable construction are provided in the following section. Additional evaluations using an inorganic (AM-2) antimicrobial additive, that is known to have a broad activity spectrum against a large number of bacteria and some fungi, a specific anti-algae product (AM-3), and an anti-fungi agent (AM-4) are in progress. More will be reported on the progress of these investigations at a later date.

Discussion

Wire and cables have a myriad of uses; wiring in housing and construction, appliances, electronics, automotive, telecommunications, marine use, and many applications. During their service life, if the environmental conditions are favorable, microorganisms, such as bacteria, algae, and fungi, can colonize and reproduce on the exposed materials. Aggressive microbial growth on the surface of a wire or cable jacketing or in the filling compound, for example, can promote premature deterioration and discoloration, possibly limiting the service life of the product. In applications where a wire or cable has markings for identification, discoloration can cause misinterpretation during servicing or installation. In some applications, the hygienic condition of the wire and cable jacketing may be of concern.

Antimicrobial Additives

In this section of the paper, the performance of a broad-spectrum (organic) antimicrobial, AM-1, will be assessed in molded polypropylene (PP) and high-density polyethylene (HDPE). Each growth inhibition test was performed twice and both results are given in the respective tables. The zone of inhibition (ZI) and Vinson rating are reported.

Tables 1 and 2, present the experimental data for PP and HDPE, respectively. The data show that for the polymer samples that did not contain the AM-1 additive, there was no suppression of either test strain of microorganism growth, ZI=0 and VR=0 in both cases. However, when AM-1 is added at 0.10% in the PP sample, Table 1,

no microorganism growth was detected on the test specimen, VR=4, and a wide zone of suppressed growth was present, ZI = 26mm and 16mm. In the HDPE test specimen, Table 2, two concentrations of AM-1 were evaluated. The results in HDPE are similar to those observed in the PP evaluation; there was complete microorganism growth in the HDPE test specimens that do not contain AM-1. Samples containing the AM-1, there was complete inhibition of growth on the test specimen, VR=4, and an increasing zone of suppression, ZI, with respect to AM-1 concentration.

PP Samples	Staphylococcus Aureus ATCC 9144		Escherichia Coli NCTC 8196	
	ZI (mm)	VR	ZI (mm)	VR
Without AM-1	0 / 0	0 / 0	0 / 0	0 / 0
With 0.10% AM-1	26 / 26	4 / 4	16 / 16	4 / 4

Table 1: Antimicrobial Activity in Molded Polypropylene

ZI = Zone of Inhibition

VR = Vinson rating for growth under the sample disc

4 = No growth (Good Activity)

2 = Weak Growth (Moderate Activity)

0 = Strong Growth (No Activity)

HDPE Samples	Staphylococcus Aureus ATCC 9144		Escherichia Coli NCTC 8196	
	ZI (mm)	VR	ZI (mm)	VR
Without AM-1	0 / 0	0 / 0	0 / 0	0 / 0
With 0.20% AM-1	22 / 22	4 / 4	12 / 12	4 / 4
With 0.50% AM-1	24 / 25	4 / 4	15 / 15	4 / 4

Table 2: Antimicrobial Activity in Molded High-Density Polyethylene

ZI = Zone of Inhibition

VR = Vinson rating for growth under the sample disc

4 = No growth (Good Activity)

2 = Weak Growth (Moderate Activity)

0 = Strong Growth (No Activity)

Conclusions and Summary

The data presented has shown efficacy of the AM-1 antimicrobial additive in polypropylene and high-density polyethylene, two polymers commonly used in wire and cable applications. AM-1 can also be used in a wide range of other polymers, such as PVC, TPE's, polyurethanes, and styrenics. Antimicrobial additives can offer many benefits to both manufactures and consumers. Manufacturers can improve and differentiate themselves from

their competition, by offering products with new ancillary effects and properties that may provide real value in many applications. These products then can offer significant benefits to the consumer by improving longevity with respect to physical properties, appearance, odor, and hygienic conditions.

Acknowledgments

The author wishes to recognize and thank his colleagues for their contribution at the Ciba Specialty Chemicals sites around the world. We would also like to thank our local and global management teams for their continued support and permission to present this work. A special thank you to Melinda Reyes.

References

- [1] D. Ochs , in "Plastics Additives Handbook" ; 5th Edition , Ed.: H. Zweifel , Hanser Publishers , Munich 2001
- [2] 40 CFR 152.25(a) and Pesticide Registration Notice (PRN) 2000-1
- [3] L.J. Vinson, et al., J. Pharm. Sci. 827-830, 1961

Evaluation of ADSS Jacketing Compounds and Environmental Exposure Effects using a New Dry Band Arc Test Methodology

Brian G. Risch, Swati Neogi, George Karady*, Yun Lei*, and Baozhuang Shi***

Alcatel, Fiber Optic Cable R&D, Claremont, NC

*Arizona State University, Department of Electrical Engineering, Tempe, AZ

**To whom correspondence should be addressed.

KEYWORDS: ADSS, electrical testing, dry-band arcing, reliability, high voltage, aerial cables.

pollution levels are proposed to augment older reliability guidelines.

ABSTRACT

All Dielectric Self Supporting (ADSS) cables are seeing increased use as electrical power transmission and distribution rights of way are being used for fiber optic cable deployment. Aerial applications typically offer worst-case scenarios for cable lifetimes due to combined effects of UV radiation, temperature extremes, humidity, salt, and pollution, as well as wind and ice loading. High voltage ADSS installations also have the potential complication of cable damage caused by electrical activity. This paper presents a new methodology to assess electrical reliability of ADSS jacket compounds along with test data on several ADSS jacket materials used in the industry.

Unlike older test methodologies, this new test methodology provides higher resolution of material performance characteristics as well as better performance evaluation data as compared to the pass/fail criteria of older test methodologies. Additionally, up to 5 cable samples can be tested at one time, allowing better statistical analysis of performance data. Versions of this new test methodology have been presented before the Fiber Optic Working Group of the IEEE during the September 2001 and March 2002 meeting, as a replacement for the older salt-fog test methodology that dates back to 1997 and before.

Several commercially available ADSS track resistant and HDPE jacket compounds have been tested according to the new test methodology before and after exposure to UV radiation and results are compared. In this study the various materials are tested at voltages which vary from 4KV up to 25KV and at pollution levels which vary from $10^5 \Omega/\text{M}$ to $10^7 \Omega/\text{M}$. Cable test results on aged and polluted cables obtained using the new test methodology are related to climatological and other environmental factors that were presented by the authors in the 2000 IWCS proceedings.¹ The effect of surface pollution levels is shown to be an extremely important variable, and methodologies for incorporation of the new variables of cable age and

INTRODUCTION

All Dielectric Self-Supporting (ADSS) fiber optic cable offers a rapid and economical solution for utility and telecommunication companies to deploy optical fiber cables along existing electric and telephone utility pole rights of way. ADSS cables offer an alternative solution over other aerial application cables such as lashed or Figure-8 cables. All dielectric solutions are preferred and sometimes mandatory for installation on or near electric power lines on utility structures.

When ADSS optical fiber cables are installed in close proximity to high voltage power lines, two electrical phenomenon known as dry band arching and corona have caused premature failure of cables. Corona is caused by high electric field gradients at the tips of the suspension hardware and has been observed in both field and laboratory environments. While corona can be very damaging to the cable, mitigation devices do exist. When properly installed at each attachment point, these devices dissipate the electrical energy that causes corona discharge and can prevent cables from being damaged.^{2,3}

Dry band arcing is a completely different phenomenon that has proven to be a more elusive problem to solve and is the subject of this paper. While mitigation devices at the attachment points can prevent cable damage due to corona, proper installation guidelines must be followed, and appropriate jacket materials must be selected in order to avoid dry band arcing. Proper installation guidelines must be based on knowledge of the electrical fields surrounding the cable as well as other environmental conditions including climate and pollution.

Events leading to dry-band arching can be described as follows: When first installed, the outer jacket of an ADSS cable is hydrophobic and non-conductive. As a result, cable resistance is very high even when wet, and no appreciable current flows on the surface of the cable. Over time, however, the jacket becomes hydrophilic and in some environments,

significant contamination may accumulate due to pollution in the surrounding air. During wet conditions the contamination layer can become conductive causing capacitively coupled currents from adjacent energized conductor's to flow within this layer. As the contamination layer on the cable surface dries, narrow bands form. These dry bands can have high voltages across them, sufficient to cause arcing. If the current available to the arcs is high enough (i.e. the resistance of the contamination is small enough to allow pre dry-band currents in the milliamperage range) arc heating can degrade the ADSS jacket and cause cable failure.

Measurements of cable resistance in the field⁴ have shown that newly installed ADSS cables have a resistance in excess of $10^9 \Omega/\text{m}$. In areas of relatively low pollution, measurements on cables with varying age showed a reduction in resistance to about $10^{7.7} \Omega/\text{m}$ to $10^{8.2} \Omega/\text{m}$ after several years of service.⁵ With quantified levels of cable resistance (pollution) and space potentials known in these failure free installations combined with available laboratory test results, safe cable installation guidelines can be established. It should be noted that, to date, actual measurements of cable resistance are very limited in number, and restricted to a geographical region that has a very low level of industrial pollutants and less harsh environmental conditions relative to other regions in the world.

Selection of a suitable cable jacket material is very important to guarantee the long-term reliability of the cable. This selection depends upon the phase to phase voltage of the power utility system, the environment, and the position of the ADSS cable within the electrical field. In low space potential environments, a typical high-density polyethylene (HDPE) material may be used. However, in higher space potentials track resistant jacket materials are required to prevent damage due to dry band arcing caused by proximity to high voltage lines. Cross-linked or filled thermoplastic materials have shown the best resistance to electrical activity. Previous research has shown that filled thermoplastic jacket materials containing approximately 2.5% carbon black provide a superior combination of electrical and mechanical properties for protection of the cables.⁶

A thermoplastic track resistant jacket with acceptable carbon black content provides a three pronged solution to dry band arcing. First, the addition of carbon black ensures the ADSS will be resistant to UV aging, thus reducing collection of salt/pollution on the cable jacket, which can lower cable resistance. Second, properly selected filled thermoplastic jacket materials minimize carbon surface tracking better than cross-linked materials. This assures a high electrical stability of the cable jacket. Finally, the filled thermoplastic track resistant jacket is resistant to heat

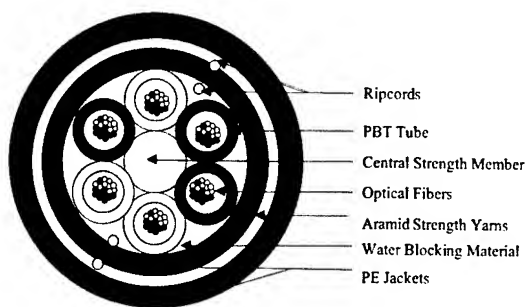
damage by ablation (vaporization of material resulting in pitting), should arcing occur^{7,8}.

Although mid-span space potentials of up to 12-25 kV are recommended by some manufacturers as suitable for ADSS cable installation with special jacket materials^{9,10}, previous studies and installations have shown that without further protection, cable jackets can prematurely fail below these threshold voltages.^{6,11} One major limitation of earlier studies is that they were based on test methodologies that did not cycle between wet and dry conditions, and therefore did not truly duplicate the mechanism behind dry-band arcing. Additionally, these earlier studies did not properly address the high degree of variability possible in cable pollution levels. The current test method has been designed to most accurately duplicate actual dry-band arcing conditions and to be a predictive tool for assessment of risk for ADSS installations in various environments of voltage and pollution. The results presented will illustrate why some cables can be installed in space potentials of 25 KV and higher with no apparent problems, while others can fail in short order in the same, or even lower, space potential.

EXPERIMENTAL

The cables tested were of a similar construction with Polybutylene Terephthalate (PBT) tubes containing optical fibers stranded around a central strength member. Superabsorbent waterblocking materials were used to make the interstices between the tubes watertight.¹² The cable had a Medium Density Polyethylene (MDPE) inner jacket. Aramid strength yarns were applied between the inner jacket and outer jackets. The material of the outer jacket was varied in order to examine the effects of environmental exposure and electrical testing. Various outer jacket materials were investigated in this study as well as earlier studies^{1,6,7,8,11,12} to get a complete representation of all common, commercially available jacket materials. A diagram of the cable construction is shown in Figure 1. Details in the composition of outer jacket materials are outlined in Table 1.

Figure 1. Schematic Representation of the Cross Section of Typical ADSS Cable.



Various track-resistant materials were in this study as well as HDPE. The performance of such compounds relative to crosslinked polyethylene PE has been compared in an earlier studies^{6,7,8,11}.

Table 1: Composition of Cable Jacket Materials.

Sample	Material Composition	Density
Cable A	Filled Thermoplastic/ High Filler; Vendor A	1.17
Cable B	Filled Thermoplastic/ Low Filler; Vendor B	1.10
Cable C	Filled Thermoplastic/ Low Filler; Vendor C	1.10
Cable D	Filled Thermoplastic/ Low Filler; Vendor B; Improved Formulation	1.10
Cable E	HDPE; Vendor C	0.944* 0.956
Cable F	Crosslinked Polyethylene	0.935* 0.947

*Base material density. Other values are with 2.6% carbon black.

Aging of Cable Jacket Materials

UV exposure testing was conducted according to ASTM G-26/G-155 with an irradiance of $0.38\text{W/m}^2/\text{nm}$ at 340nm and approximately 20W/m^2 in the 300-400nm (Total UV) region. Total exposure was 6895KJ/m^2 at 340nm and 363MJ/m^2 in the 300-400nm range. This is equivalent to a little over 1 year of UV exposure in southern Arizona, 1.5 years of UV exposure in southern Florida, or about 3 years of UV exposure in northern or central Europe¹³. With the combined UV and heat of the test, an expected aging acceleration factor would be approximately equivalent to 4-6 years of outdoor exposure in central Europe.¹⁴

Effect of Dry Band Arcing

Effects of dry band arcing on the performance of ADSS cable jackets were studied by subjecting the cables to electrical space potentials before and after aging. Two test methods were compared in order to give correlation between different test methodologies. An older salt-fog test methodology as well as a new electrical test methodology that is under investigation as a new industry standard¹⁵ were compared. The new test method was performed on all materials with some reference data also available from earlier studies with the salt-fog method on selected materials. The design of electrical experiments and details of the test methods are described below.

-Salt-Fog Test

Salt Fog testing was performed on unaged and aged cables according to the earlier IEEE P1222 Draft March 1997 - Annex A. Each cable sample was sealed at both ends and attached to a high voltage brass ferrule

on one end and a grounded cable dead end on the other. The samples were then placed under tension and put into the salt fog chamber. A 1% NaCl (salt) solution was dispensed at a constant rate of 0.4 liters per cubic meter per hour. After the system was energized at 30 kV, the cables were inspected at 50 hours, 100 hours and then every 100 hours thereafter. Values of the parameters used in salt fog test are listed below:

Duration of the test:	1000 hours (42 days)
Test Voltage:	30 kV
Temperature:	15-25°C
Flow rate:	0.4 liters/hr/m ³
NaCl content:	10 kg/m ³
Particle size:	5-20 micron

It is important to note that the Salt Fog test is a constant flow test that simulates conditions that are not likely to occur continuously in nature. This test method has been under review by the IEEE Fiber Optics Standards Committee and a newer method that is the subject of this investigation is being evaluated as a replacement.

-New Accelerated Electrical Test

To simulate environmental conditions more like actual preconditions for dry-band arcing on high voltage networks, an experimental setup subjected the cables to a series of wet and dry cycles. An experimental set-up was built indoors in Arizona State University's High Voltage Laboratory. This test setup is based on the theory of capacitive coupling and uses a Thevenin Equivalent circuit to model the electrical behavior of an ADSS cable installed near phase conductors.¹⁶ Figure 2 shows a schematic diagram of the experimental set-up. Similar to the Salt Fog test which was, at one time, included as part of the draft IEEE 1222 Draft 1997 Annex A standard for ADSS cables, the water reservoir contains water and NaCl (salt) to simulate the effects of precipitation and pollution. Equivalent cable resistance for pollution levels is defined below. Three levels of cable resistance representing a corresponding pollution level have been suggested in previous research on the dry band arcing phenomenon:^{17,18}

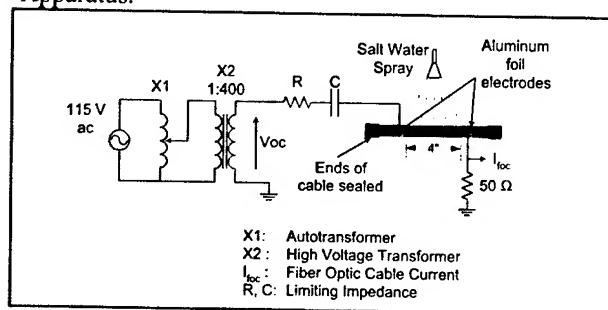
Pollution Level	Equivalent Resistance
1. Light:	$10^7\ \Omega/\text{m}$
2. Medium:	$10^6\ \Omega/\text{m}$
3. Heavy:	$10^5\ \Omega/\text{m}$

Higher pollution results in lower cable resistance and therefore higher current levels during dry-band arcing.

-High Voltage Electrical Setup

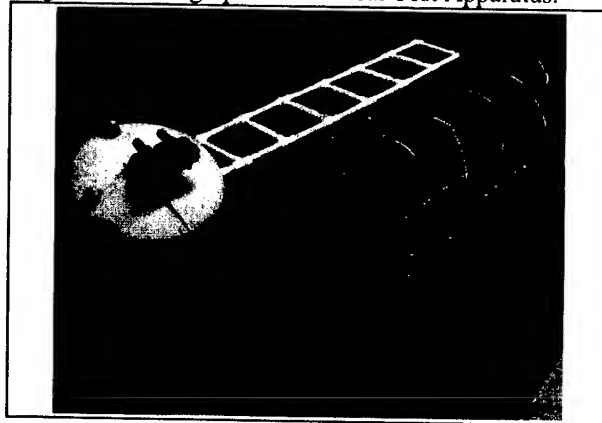
The circuit diagram of the test setup is shown in Figure 2. A small piece of the cable to be tested is prepared by sealing its ends and fixing electrodes on the cable jacket. Each cable is energized through a RC limiting impedance that is built on a PCB. Non-inductive resistors with proper wattage and voltage ratings have to be used to prevent damage due to high frequency components of the arcing current. High-voltage ceramic-disc capacitors are used for the capacitance. The limiting impedance represents the resistance of the pollution layer on the cable and the capacitive coupling of the fiber-optic cable with high voltage and ground. The values of the resistance and capacitance depend on the pollution level. Shunt ($50\ \Omega$) resistances with parallel voltage suppression devices are used to measure the current. High voltage (40 kV) wires are used to connect the RC impedances to the insulators.

Figure 2: Circuit Diagram of Electrical Test Apparatus.



The cable is sprayed with salt water in the region between the electrodes. The salt water forms a conducting layer on the cable surface where current can flow. Since the resistance of the saturated cable is small compared to the limiting impedance, the current through the saturated layer is very close to the short-circuit current. When the spray is turned off, the jacket surface dries forming a dry-band. High voltage appears across the band resulting in arcing. Once the cable dries sufficiently, arcing stops. This on/off spray cycle is repeated until the cable fails or until a fixed number of cycles is exceeded indicating a passing result. Failure is defined as a puncture of the jacket. Figure 3 shows a picture of the electrical test apparatus.

Figure 3: Photograph of Electrical Test Apparatus.



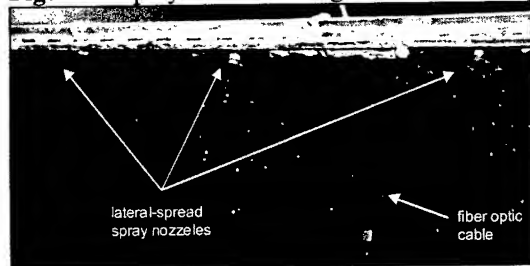
-Housing Tank and Spray System

A stainless steel tank (40" x 30" x 16") was built to provide mechanical support for the cables and other test equipment. A 0.5 hp, self-priming, utility pump is used to circulate the water through the system. A commercial, nylon in-line water filter with a 40 mesh, 420 micron, stainless steel screen is attached at the input of the pump. A mechanical timer is used to control the pump. A typical test cycle time is 15 minutes during which the cable is wetted for 2 minutes and allowed to dry for 13 minutes. A flow meter with a valve is used to measure and control the water flow. The flow rate and water salinity are kept constant during the tests. A salinity of 1 % and a flow rate of 0.5 – 0.8 gpm per nozzle are maintained. Tests have shown that water salinity above 0.75 % does not affect the test results.

There are two drain holes on the sides of the tank about 1" from the base. Hence, the tank will have about 1" of water during normal operation. This water will extinguish any fire, if a burning cable falls into the water. Excess water is returned to the tank.

To generate dry-band arcing, the spray system generates a wet, conductive layer on the cable jacket between the electrodes. In order to achieve some uniformity between spray cycles, the water spray has to saturate the cable surface. Sprinkler nozzles have been used to spray salt water on the cable sample. These nozzles are commercially available gardening watering nozzles, made by Ewing Co.. The opening diameter of the nozzles is 0.012 mm. An example of a spray pattern on a single cable test is shown in Figure 4.

Figure 4: Spray Pattern During Electrical Testing.



-Cable Samples

Aluminum foil electrodes are wrapped around each cable. To ensure that arcing does not occur between the two electrodes, the electrodes should be adequately spaced to prevent electrode to electrode arcing at the maximum test voltage level. Experiments have determined that a 4" (10.16cm) gap is sufficient for a system voltage of 40 kV or lower. Figure 5 shows cable samples with electrodes ready for testing.

Figure 5: Cable Samples Mounted in Test Apparatus.



Aging and Environmental Effects

Performance of cables in electrical fields is highly dependent on the aging of the cable. On a newly installed dry cable, the surface sheath resistance is quite high ($>10^9$ Ohm/m) so the induced currents are insignificant. Additionally, the cable surface is highly hydrophobic so moisture and contaminants are not prone to build up and thereby reduce surface resistance. However, as a cable ages from thermal oxidation and exposure to ultraviolet rays from the sun, contaminants such as salt, pollutants, and moisture adsorb on the cable sheath. The surface impurities can significantly reduce the electrical resistance to current flow on the surface of the cable.

The earlier portion of this study has shown that electrical activity and accumulation of pollutants during electrical testing can influence the surface properties as substantially as several years worth of UV exposure.¹ Additionally, this earlier research indicated that once a certain level of cable pollution is present, pollutant type and concentration rather than jacket material dominate the surface electrical properties of the cable. Therefore, it is expected that if electrical tests have a long enough duration, effects of prior UV exposure should be minimal, as long as a suitably UV stabilized jacket material is used. However, as test duration becomes

shorter and test conditions more severe, the effect of previous sample weathering exposure becomes more significant. The final state of the cable in any test should be the high surface energy state of an aged cable, since this aged state will be the most prone to electrical activity. It is therefore advisable that requirements for passing electrical tests be set such that surface properties of the materials have gone through any transient stages. In our case a cycle limit of 400 cycles was selected. This test-cycle duration also keeps the test duration to within one workweek.

Due to the inherent hydrophobic nature of polyethylene, the newly extruded ADSS jacket is not prone to collection of moisture on its surface. As the cable surface begins to degrade due to heat, UV-radiation, or exposure to ozone the cable sheath material may be wetted by rainfall. Additionally resistance may be lowered from salt or pollution. With a wetted and/or polluted cable surface, dry bands of high resistance surrounded by wetted sections of much lower resistance may develop. As these bands develop the possibility for arcing across the dry band exists, which can damage an unprotected sheath by heat and ablation (vaporizing of jacket material causing pitting).

The rate of aging and the subsequent changes of surface properties of the cable are highly dependent on the region in which the cable is installed. In regions where UV exposure is low and climates are moderate such as northern Europe, aging effects will be minimal. However, in regions such as southern China where average temperature, UV-exposure, and pollution levels are high the risk of dry-band arcing will be greater.

Similarly, other factors such as pollution, ozone, dust, or aerosols can influence the surface properties of cables and/or accelerate material degradation. Pollution levels can vary greatly from nation-to-nation and from locality to locality. Seasonal variation in winds and other factors such as wildfires can also have effects on overall atmospheric particulate matter, and cables installed in coastal regions can experience the added risk of salt-spray. In areas with known high-risk levels of surface contamination, guidelines should be conservative to account for the effects of surface pollution on the electrical properties of the outer jacket.

RESULTS AND DISCUSSION

Table 2 summarizes the results of the salt fog testing carried out in accordance with IEEE P1222 Draft 1997 Annex A. This is a pass/fail test method where very few conclusions can be drawn from the results, other than the fact that Cable E, with a standard HDPE outer jacket, fails in short order under the harsh conditions and 30 kV. No differentiation is noted

between cables A&B and actual service guidelines cannot be deduced from the 30kV test voltage. One thing that can be noted is that aging did not compromise the ability of the materials to pass the test.

Table 2: IEEE P1222 Draft 1997 Annex A Salt Fog Test Results.

	Cable E	Cable A	Cable B
Virgin		Pass	Pass
Heat Aging	N/A	Pass	Pass

Table 3: Average Electrical Test results on Unaged Cables.

n	Isc (mA)	Voc (kV)	A	B	C	D	E	F
5	2.2	14.66						
5	1.6	11.00	Pass (400+)			Pass (400+)		
5	1	7.33	Pass (400+)	Pass (400+)	Pass (400+)	Pass (400+)	Pass (400+)	
5	0.5	3.67	Pass (400+)	Pass (400+)	Pass (400+)	Pass (400+)	Pass (400+)	
6	1	19.40	Pass (400+)	Pass (400+)	Pass (400+)	Pass (400+)	Pass (400+)	
6	0.8	15.52	Pass (400+)	Pass (400+)	Pass (400+)	Pass (400+)	Pass (400+)	
6	0.5	9.70	Pass (400+)	Pass (400+)	Pass (400+)	Pass (400+)	Pass (400+)	
7	0.4	25	Pass (400+)	Pass (400+)	Pass (400+)	Pass (400+)	Pass (400+)	
7	0.35	19.04	Pass (400+)	Pass (400+)	Pass (400+)	Pass (400+)	Pass (400+)	
7	0.25	13.60	Pass (400+)	Pass (400+)	Pass (400+)	Pass (400+)	Pass (400+)	

Resistance = $(10^n \Omega/m)$

n≤5 : High Pollution

n=6 : Intermediate Pollution

n≥7 : Low Pollution

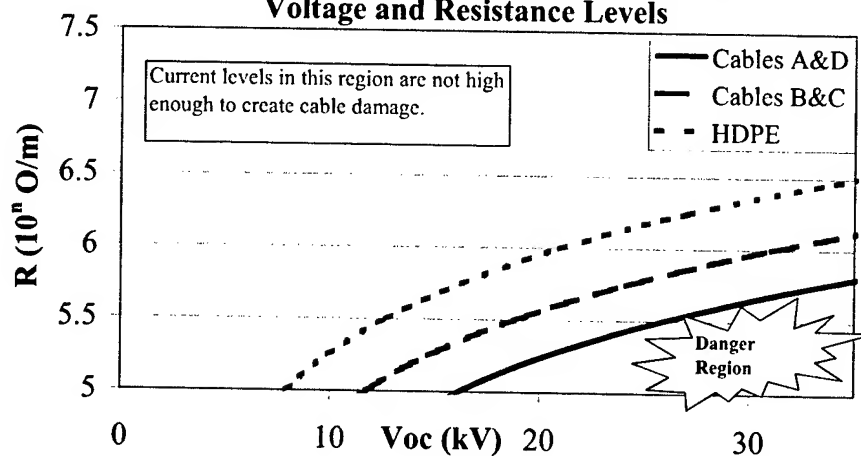
Table 3 summarizes the average cycles to failure for the various unaged cable samples under varying test conditions with the new test method. In each case multiple samples were tested in order to gain information on sample-to-sample reproducibility. In some cases multiple tests were also run in order to obtain data on test-to-test reproducibility.

Figure 6 is a graphical representation of the failure regions represented in Tables 3&4. This figure illustrates the better differentiation between materials and the more substantial relationship to in-service guidelines for materials possible through the new testing methodology. The materials tested fell into three basic performance categories. HDPE was able to withstand the least current during electrical testing, and when current levels exceeded about 1.1mA, HDPE would fail in short order.

Table 4: Average Electrical Test Results on Aged Cables.

n	Isc	Voc	A	B	C	E
5	2.2	14.66	Pass (400+)	Pass (400+)	Pass (400+)	
5	1.6	11.00	Pass (400+)	Pass (400+)	Pass (400+)	Pass (400+)
5	1	7.33	Pass (400+)	Pass (400+)	Pass (400+)	Pass (400+)
7	0.4	25	Pass (400+)	Pass (400+)	Pass (400+)	Pass (400+)

Figure 6: Cable Electrical Failure Limits as A Function of Voltage and Resistance Levels



The filled and crosslinked materials had a greater capacity to absorb electrical energy and resist damage, but the performance characteristics between different materials were clearly evident from the test results. Two track resistant compounds tested (A&D) withstood the full 400 cycle test duration with currents of 1.6mA and were able to withstand many cycles at up to 2.2mA. Track resistant compounds B&C were not able to withstand the full 400 cycles at currents of 1.6mA and above.

The relationship of electrical test results and the corresponding service limitations of materials to induced current rather than voltage is very important, since pollution level has a very substantial effect on the induced current that is obtained at any given space potential. None of the materials, not even HDPE, failed electrical tests corresponding to low pollution environments at voltages up to 25KV. In fact, test results lead to a predicted safe voltage exceeding 30KV for all materials tested as long as cable resistance exceeds $10^7 \Omega/m$. However, HDPE could only withstand 7kV for the full test duration under heavy pollution conditions ($R \leq 10^5 \Omega/m$).

Cables jacketed with compounds A, B, C, as well as HDPE were tested after being subjected to UV exposure. UV exposure did not substantially reduce the time to failure in any of the cable materials tested. The materials studied were all stabilized with 2.6% carbon black; thus, the results indicate that these materials are adequately UV stabilized with this level of carbon black.

Table 5A: Electrical Test Data Set #1; 14.7KV Test, Heavy Pollution, and Material A.(8/1/01)

Sample #	Cycles Survived	Test Result
1	35	Failure
2	15	Failure
3	89	Failure
4	147	Failure
5	252	Failure
Average	108	Failure

Table 5B: Electrical Test Data Set #2; 14.7KV Test, Heavy Pollution, and Material A.(11/6/01)

Sample#	Cycles Survived	Test Result
1	48	Failure
2	20	Failure
3	23	Failure
4	24	Failure
5	133	Failure
Average	50	Failure

Duplicate tests were performed on compounds A, B, and C to verify repeatability and reproducibility of

electrical test results. Data from electrical test results from material A are summarized in Table 5 and data from electrical tests conducted on material B are summarized in Table 6. The overall test results were averaged between multiple tests in order to rank materials.

Table 6A: Electrical Test Data Set #1; 11KV Test , Heavy Pollution, and Material B. (10/31/01)

Sample#	Cycles Survived	Test Result
1	39	Failure
2	73	Failure
3	325	Pass*
4	233	Failure
5	143	Failure
Average	163	Failure

*Test Stopped.

Table 6B: Electrical Test Data Set #2; 11KV Test , Heavy Pollution, and Material B.(11/17/01)

Sample #	Cycles Survived	Test Result
1	280	Failure
2	250	Failure
3	340	Pass*
4	290	Failure
5	300	Failure
Average	336	Failure

*Test Stopped.

Figure 7: Electrical Testing at 14.7KV, Round 1.

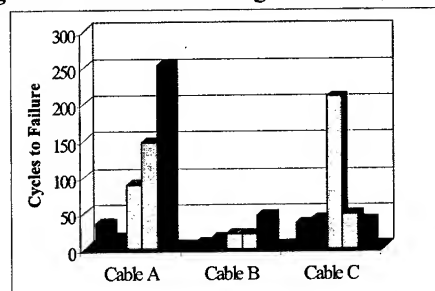
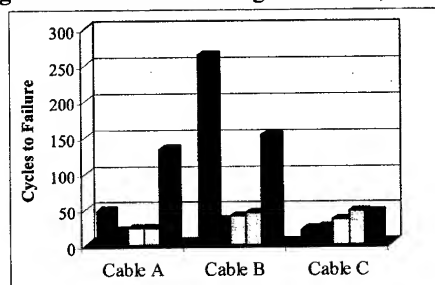


Figure 8: Electrical Testing at 14.7KV, Round 2.



Due to the large number of tests that were conducted, the best overview of the data is presented in Tables 3&4. Electrical tests that produced passing results produced

400 cycles without a jacket puncture in each channel, making the additional detailed charts unnecessary. No dry band arcing activity was observed in tests where surface current did not exceed 1mA. The more detailed data in tables 5&6 reveals that there may be substantial sample to sample variability in electrical test results, necessitating multiple samples in testing for reliable results. The fact that up to 5 samples can be tested at one time is a big advantage for the new test methodology. Figures 7, 8, and 9 illustrate how the statistical data from individual samples is converted to an overall average for cable samples A, B, & C.

Figure 9: Average Electrical Test Results per Channel at 14.7 KV.

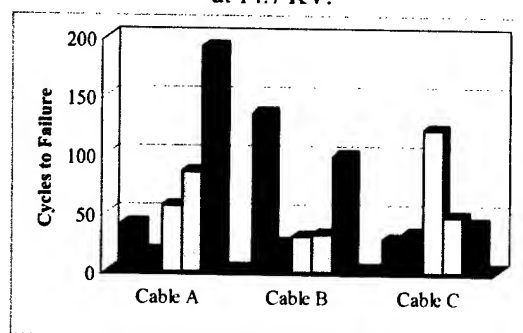
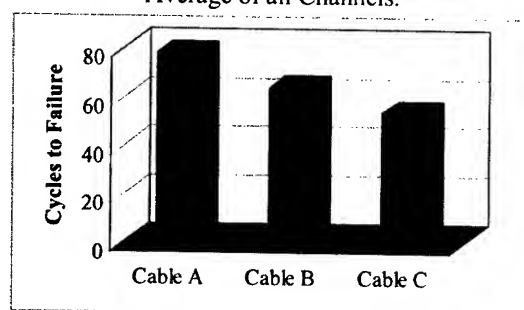


Figure 10: Average Cycles to Failure at 14.7KV: Average of all Channels.



The substantial improvement in resolution of electrical test performance, combined with a reduced test time and the ability to test multiple samples, gives this new test methodology several advantages over the older method. The improved resolution of service parameters gives jacketing compound formulators better feedback on how formulation changes alter electrical performance of the material. The test data also allows resolution into both voltage (space potential) and resistance (pollution) levels, thereby giving cable manufacturers and installers better installation guidelines that can take local environmental effects into account.

One notable result of this study was the fact that the ability to resist electrical damage was correlated, in-part, to the level of filler contained in the material. This result was predicted in earlier work,^{1,7,& 8} but until

now, it had not been experimentally verified in cable electrical tests. Another notable result was that a lower filler material was developed during the course of this study that showed nearly identical performance to a material with a higher level of filler. This improved low filler level material showed electrical performance nearly identical to the high filler level material A.

Another substantial result that was predicted in earlier publications^{1,4,16,17,&18} and experimentally verified in this study was the substantial effect of pollution on the dry-band arcing phenomenon. This laboratory testing has verified the validity of earlier models of dry-band arcing phenomenon. Additionally, these results show that variability in cable pollution levels is the most probable reason why some cable installations have withstood years of service in relatively high space potentials, while other cables have failed rather quickly in similar or lower space potentials.

CONCLUSIONS

Earlier research by the authors confirmed that aging and pollution significantly alter surface properties of ADSS cable jacket materials and thereby contribute to variation in electrical test results. This study clearly shows that cable pollution level can be as important as mid-span potential in determining the long-term electrical reliability of ADSS cables. Cable pollution levels can vary by orders of magnitude as a function of cable installation environment and age. The current findings are significant since pollution levels on cables are largely uncontrollable, and the results clearly illustrate that development of universal and safe ADSS cable installation guidelines must account for both midspan space potential as well as cable pollution levels. Some cable installers have already started to quantify cable pollution levels through direct measurement. Direct measurement required for reliable cable installations in high space potentials. Data on actual cable installations, however, is very limited and currently only available from relatively benign pollution environments.

Damaging electrical activity can start on an ADSS cable surface with a surface current as low as 1mA for standard HDPE jackets and between 1.5mA and 2.2mA for track resistant jackets. To ensure that dry-band arcing does not cause cable damage, the combination of cable surface resistance (pollution level) and mid-span potential must not produce a surface current above the threshold for the jacket material of the cable. If no information is known about pollution levels, a conservative assumption should be made about pollution level in order to avoid cable failure.

A conservative assumption would be to assume high cable pollution ($R=10^5 \Omega/m$) which would result in maximum mid-span potentials of about 12KV for a good

track resistant jacket material and about 7KV for HDPE. Data on actual surface pollution has just recently started to become available, but is very limited. In areas with relatively benign environments with respect to precipitation, UV exposure, and pollution cable surface resistance has remained above $10^7 \Omega/\text{m}$ even after several years of service, making installations in space potentials of 25KV and higher well within the expected safe level for induced surface currents. Many regions, however, have much harsher environments for ADSS installations which can result in surface resistance of $10^5 \Omega/\text{m}$ or below. In these harsh environments, 25KV installations would be catastrophic. Any installations in space potentials above 12KV for track resistant jackets and above 7KV for HDPE jackets should have some quantification of surface resistance so that safe surface current levels will not be exceeded and a long trouble-free cable lifetime will result.

ACKNOWLEDGEMENTS

We would like to thank Alstom UK Ltd. For their contribution on the salt-fog testing. We would also like to thank Monty Tuominen and Ken Edwards for providing technical contributions and background information.

REFERENCES

- 1 William DeWitt, Swati Neogi, Dr. Brian G. Risch, Dr. George Karady, and Johnny Madrid "High Voltage ADSS Reliability Modeling: Environmental and Climatological Effects on Advanced Jacket Material Selection", *Proceedings of the 49th International Wire and Cable Symposium*, November 2000, p.337-346.
- 2 Besztercey, G., Karady, G., and Tuominen, M. W. "Corona Caused Deterioration of ADSS Fiber-optic Cables on High Voltage Lines." *IEEE Transactions on Power Delivery*, 14, No. 4 October 1999, 1438-47.
- 3 Karady, G., et. al. "A Mitigation Method for Dry-band Arcing Caused Deterioration of ADSS Fiber-optic Cables", *Proceedings of The IEEE Power Engineering Society Winter Meeting*, 4, 2000, 2391-6.
- 4 K.S. Edwards, P.D. Pedrow, and R.G. Olsen, "Portable ADSS Surface Contamination Meter Calibrated in High Voltage Environment" *IEEE proceedings*, in press.
- 5 Tuominen, M.W., Bonneville Power Administration, private communications
- 6 Keller, D.A, D.J. Benzel, J.P. Bonicel, C. Bastide, F. Davidson, "Continued Investigation of ADSS Designs and Reliability Considerations with respect to Space Potential Tracking and Cable Installation Practices", *Proceedings of the 46th International Wire and Cable Symposium*, November 1997.
- 7 Vaughan, A.S., S.G. Swingler, M. Lanfear, H. Weingandt, and H. White, "Laser Ablation and Thermal Decomposition Studies of Fiber Optic Cable Sheathing Materials", *IEEE proceedings*, October 1992, 501-510.
- 8 Vaughn A.S., Robbie D A., Hosier I.L., Sutton S.J., "Simulations of Surface Discharge Damage on Self Supporting Fiber Optic Cables", *Plastics in Telecomm Proceedings*, 6E, September 1998, 87-96.
- 9 Carter, C., et al., "Mathematical Model of Dry Band Arcing on Self Supporting All Dielectric Optical Cables on Overhead Power lines", *IEE Proceedings-C*, 139, No 3, May 1992, 185-96.
- 10 Rowland S., et al. "Electrical Aging and Testing of Dielectric Self Supporting Cables for Overhead Power lines", *IEE Proceedings-A*, 140, No 5, September 1993, 351-56.
- 11 Keller, D.A, O. Tatat, R. Girbig, M.Adams, R. Bohme, and C. Larsson, "Design and Reliability Considerations for Long Span High Voltage ADSS Cables", *Proceedings of the 46th International Wire and Cable Symposium*, November 1997. and references contained therein.
- 12 Neogi, S, Risch, B.G., and Soltis, M., "Materials Reliability of Flooded and Dry-Core ADSS Cable", *Proceedings of the 48th International Wire and Cable Symposium*, November 1999, 795-806.
- 13 De Jong, B., *Net Radiation Received by a Horizontal Surface at the Earth*, Delft University Press, 1973.
- 14 Wypych, George, ed., *Weathering of Plastics: Testing to Mirror Real life Performance*, Plastics Design Library, Norwich, NY, 1999.
- 15 IEEE 1222 Draft March 2002 version; Annex A.
- 16 R.G. Olsen, "An Improved Model for the Electromagnetic Compatibility of All-Dielectric Self-Supporting Fiber Optic Cable and High Voltage Power Lines," *IEEE Transactions on Electromagnetic Compatibility*, 41, No 3, August 1999.
- 17 G.G. Karady, S. Devarajan, M. Tuominen, "Novel Technique to Predict Dry Band Arcing Failure of Fiber Optic Cables Installed on High Voltage Lines," *IEEE Power Tech '99 Conference*, Aug-Sept 1999, Paper PBT99-160-30, Budapest, Hungary.
- 18 M.W. Touminen and R.G. Olsen, "Electrical Design of All-Dielectric Self-Supporting Optical Fiber Cable," *IEEE Transactions on Power Delivery*, Vol. PWRD-15, No. 3, July 2000, 940-947.



Brian G. RISCH

*Alcatel
Fiber Optic Cable R&D
2512 Penny Rd.
P.O. Box 39
Claremont, NC 28610*

Brian G. Risch is the Cable Materials Manager at Alcatel. He holds a B.A. degree in physics from Carleton College and a Ph.D. in Materials Science and Engineering from Virginia Polytechnic Institute and State University. His Ph.D. research was in the area of polymer crystallization and structure-property relationships in polymers. Since 1996 Brian has worked for Alcatel's Optical Fiber Cable R&D center specializing in cable materials and fundamental material reliability studies.

Non-contact Measurement of Copper Diameter and Drawdown Through the Insulation

Christine C. Matthias

Zumbach Electronics Corporation

Mount Kisco, New York

+1-914-241-7080 · cmatthias@zumbach.com

Abstract

As manufacturers of copper data communication cable advance to the production of Category 6 products and beyond, the requirement for quantifying every possible variable in the manufacturing process becomes more critical. During the insulating process, it is common for the copper wire to experience a drawdown effect, changing its dimensions and resistivity in the process. By measuring the copper diameter before and after the insulation it is possible to determine drawdown and adjust line tensions to minimize the dimensional differences between start and finish. And, by measuring the electrical properties of the wire, it is possible to pinpoint assignable causes before they reach threshold levels. Further, by utilizing Fast Fourier Transform to analyze these characteristics, the predictability of Structural Return Loss is further enhanced. The end result is a decrease in cross talk and an increase in electrical bandwidth capabilities.

It has been possible for many years to measure the diameter of the copper prior to the insulation step during the production of primary data wires. However, recent refinements in inductive sensor technology and signal evaluation have permitted the measurement of the copper diameter through the insulation in a non-destructive fashion.

Keywords

Drawdown; Fast Fourier Transform; Eddy Current; Structural Return Loss; Resistivity; Capacitance; ID; Cross Talk.

1. Introduction

A cost-critical element in any manufacturing process is the detection and removal of the causes of defects. Locating these assignable causes as quickly as possible will result in materials savings from the reduction of scrap as well as overall process improvement. In the manufacture of copper data communication cable, the more advanced the product, the less room in the process for assignable causes. For example, process variations that were acceptable for Category 3 products are deemed unacceptable for Category 5, 6, 6e, and beyond. Usually these periodic defects manifest themselves as Structural Return Loss at higher frequencies.

For many years, suppliers of measurement instrumentation to wire and cable manufacturers have provided the industry with

the means to measure the diameter of the copper prior to the insulation step during the production of primary data wires for communication cables. However, in the past, the inability to once again measure the copper diameter through the insulation has been a source of some difficulty in the removal of manufacturing causes of Structural Return Loss, Cross Talk, and failure to meet resistivity specifications.

2. Why measure the copper conductor through the insulation?

2.1 Detection of Defects

Current gauging methods have enabled the manufacturer to detect various assignable causes, especially in conjunction with a good Structural Return Loss prediction software package, utilizing Fast Fourier Transform. However, due to the fact that the last location the copper conductor is measured is usually directly before the first extruder, some subsequent problems that affect conductor OD or resistivity and capacitance can either go undetected or become very difficult to remedy.

2.2 The Importance of Controlling Drawdown

During the insulating process, drawdown can occur, which changes the dimensional properties of the copper conductor. Subsequently, an alteration in the dimensional properties equals a change in the resistivity of the copper conductor.

However, in order to be efficient from a manufacturing standpoint, one would want to run the production line at the maximum speed possible before drawdown commences. By utilizing the means to measure the conductor through the insulation material and subsequently calculate the elongation of the conductor, one can ascertain precisely at what speed the drawdown effect is commencing to occur.

Measurement of Drawdown Effect

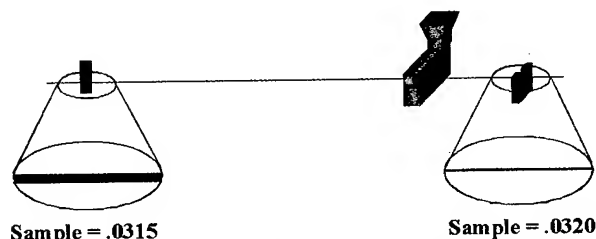


Figure 1. Drawdown of the Conductor

2.3 Ensuring Performance Criteria is Met

There are three common performance criteria for category cables as well as telephone wires. A pair capacitance performance criterion is based on the coaxial capacitance of the individual wires of the pair. A pair resistance criterion is mainly based on the resistance of the individual copper wires making up the pair. And, the unbalance to ground criteria is mainly based on the diameter and coaxial capacitance of the individual wires making up the pair and, to a lesser degree, the pairing and cabling of the wires.

3. A New Method for Non-Contact Measurement of Copper Diameter Through the Insulation

3.1 The Methodology of this Measurement System

Recently, new technology has enabled the development of a gauge that makes measurement of the copper diameter through the insulating material possible. Eddy current technology is utilized, which is a method involving electromagnetic induction that allows for non-destructive testing. This unit then measures a vector (involving current and voltage) from which the mass or diameter can be calculated, which affect capacitance. This vector measurement also allows for the calculation of wire.

3.2 Utilization of Resistivity Measurement

However, it is important to note that this resistivity measurement is highly temperature sensitive and should not be misconstrued as the specific resistance for that material due to the fact that the specific resistance can only be calculated when the copper temperature is known. Specific resistance measurement is usually based on finished product that has cooled to room temperature. However, this relative resistivity measurement is still vital. Resistivity increases in a near-linear fashion in proportion to temperature. By watching the trending of said measurement, one can analyze and prevent changes in the cooling process. If the cooling process is not stable, it is very likely that the cold product will not be within specification. Since category product is wound hot on the take-up reel, issues with the cooling process can become critical. The copper temperature affects capacitance and diameter, since they are related to the thermal expansion of copper and insulation. Also, the dielectric constant will fluctuate with temperature.

Fluctuations in resistivity can also be traced to issues with the annealing process. A properly annealed wire has a certain level of hardness and a certain resistance. If there is a problem with the annealing, a change in resistivity will be observed.

Also, tolerances could be added in order to observe the in process resistivity of the copper conductor.

3.3 ID Variation Equals Capacitance Variation

Even minor fluctuations in inner diameter affect capacitance measurements. Figures 2 and 3 illustrate this point using category 6 product as an example. Even a slight fluctuation in ID

or OD can cause the product to no longer be within specification for capacitance.

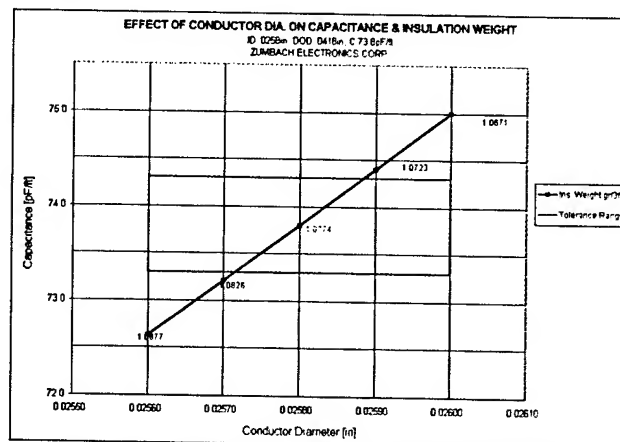


Figure 2. Effect of DOD on Capacitance and Insulation Weight for CAT-6

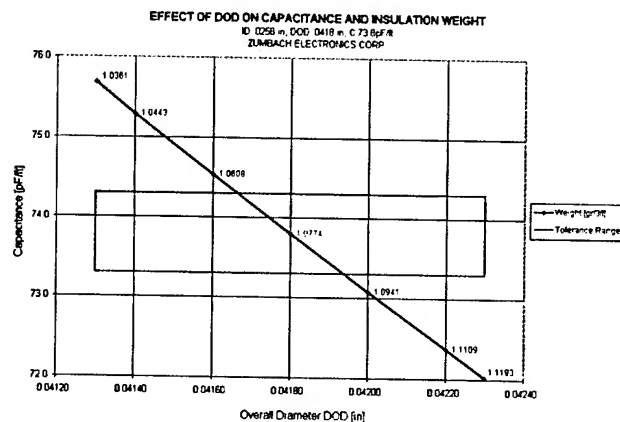


Figure 3. Effect of Conductor Diameter on Capacitance and Insulation Weight for CAT-6

3.4 Features of this Measurement System

An instrument utilizing the above mentioned technology would offer precise measurement of conductor diameter and resistivity. It also would be connectable to a processor unit enabling overall process control in conjunction with other on-line gauging equipment. It is also important to note that, unlike other diameter measurement devices, any type of liquid film on the conductor surface would not affect measurements. At present, this unit is available for diameter ranges from .016 in. to .035 in. (0.4 mm to 0.9 mm) copper OD. Line speed is also not a factor for instrumentation operation. The conductor temperature range should be between 32°F and 203°F (0°C and 95°C for optimum operation). And, by utilizing inductive principles, the accuracy of the copper diameter measurement varies less than plus or minus 0.2 percent while resistance measurement repeatability is plus or minus 0.9% or less than the effect of a 1°F change of temperature.

4. Benefits that Can Be Derived from Measurement of the Conductor through the Insulation

4.1 Successful operation at high line speeds

It is important to be able to successfully monitor the copper diameter at the end of the line and observe indicators of excessive drawdown. By conducting such observations, one can make corrections before scrap cable is produced, thus resulting in significant materials cost savings while producing a highly uniform product.

Another advantage is that, through observation and experimentation, one will be able to operate at the highest possible line speed without affecting the quality of the product. Production efficiency will be increased drastically. This instrument is a process tool that will allow the user to find the optimum line speed for each product. It can also be utilized as a means to locate speed-limiting components of the line.

4.2 Consistent Wire Parameters

Being able to monitor the conductor throughout the process results in more consistent wire parameters. Better transmission

characteristics are the result of a constant category production process. It is important to monitor the conductor during manufacture so that the acquired information can be correlated to capacitance and diameter data also acquired on line. Thus the need for off-line bench measurements of diameter and capacitance is substantially minimized.

5. Conclusion

By being able to measure before and after the insulation process, drawdown can be determined and subsequently, tension and/or line speed can be adjusted to control this effect. This tool can also be used to help locate causes of Structural Return Loss in conjunction with the aforementioned Fast Fourier Transform / Structural Return Loss prediction package. By utilizing this instrument, cross talk problems can be reduced and electrical bandwidth increased.

The correction of all the aforementioned issues result in cost savings and scrap elimination. Also, as tolerances become more and more critical for Category cable manufacturers, the need to have optimal control of the process is paramount.

Composite Cable for Shared Powering System

Sungyul Park, Min Son, Sangki Hong, Youngtark Lee, Joungyuong Ha

¹O643 Optical Cable Technology Team, LG Cable, Kumi, Korea

+82-54-941-7005 · sypark@cable.lg.co.kr

²Optical Access Network Engineering Division., Korea Telecom, Daejeon, Korea

+82-42-870-8694 · freebyrd@kt.co.kr

Abstract

In order to implement FTTC for residential area, there are many issues to be considered such as ONU installation site, ONU coverage, powering options for ONU, environmental controlled outdoor cabinet technologies and so on. This paper presents powering solution for broadband passive optical network (B-PON) with small capacity ONUs that will be installed in residential area and composite fiber/copper cable. The composite cable having optical fiber and copper conductor in one cable enables reduced installation cost and improved service operations and maintenances in shared feeding system. In accordance to the shared feeding system configuration, three types of composite fiber/copper cable have been herein designed. The copper conductor with its' outside diameter of 0.65mm providing the output power feed of up to 400 meters has been selected and general single mode fiber corresponding to KT standard has been applied for the design. Loose tube type structure having advantages for relatively high fiber count and easy midspan access has been adopted, and the 32-fiber cable was designed to have three layers of stranded core. The composite fiber/copper cable containing 32 optical fibers and 18 copper pairs to enable power supply and optical transmission for 32 ONUs with one pair of cable. Also the buffer tubes are placed on outer end layer to facilitate its' access to the fiber in midspan access. The composite cable was confirmed that the cable is in compliance with KT standard for its' mechanical and environmental characteristics.

Keywords

FTTC; composite cable; fiber/copper cable; shared powering; ONU

1. Introduction

Optical access networks have been evolved in response to meet the customers' emerging demands for broadband services. There was a rapid growth in Korean broadband market. According to Korea Network Information Center or KRNIC, the number of broadband service subscribers is about 9.2 million, by June 2002 and it will exceed 10 million, about 70% of total 14.5 million households, by October 2002 [1].

FTTB for business building had been mature and FTTC for densely populated apartment complex (FTTC-A) has been widely deployed since last year. For residential users, however, broadband services were delivered only by existing copper subscriber lines from central office. Now it's time to deploy FTTC for residential area or FTTC-R to improve quality of broadband service.

2. Shared Powering System

2.1 Implementation Strategies for FTTC-R

As the result of surveying existing copper distribution network, we define the concept of ODP (Optical Distribution Point) in order to deploy FTTC-R as shown in figure 1. According to its subscriber capacity, each ODP can be implemented by among these outdoor cabinets as follows; BB(Shelter)-Shelter, BB-Cabinet and BB-Box whose maximum capacities are 2400, 900 and 30 lines, respectively. These ODPs will be implemented in consideration of installation environment and features of copper access network. Each ODP comprises ONU (Optical Network Unit), powering equipments, copper cross-connection modules, fiber box and so on.

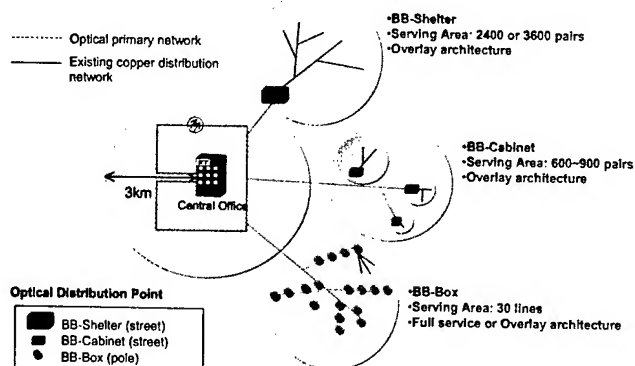


Figure 1. Deployment strategy for FTTC-R

Characteristics of residential area in Korea

In order to deploy FTTC for residential areas, fiber distribution networks such as broadband passive optical network or B-PON that is considered as the most effective broadband access platform have to be additionally installed. The concentration ratio, defined as the number of subscribers per 100m² area, in residential area is about 100 to 150. It is very high and similar to that of MDU(multi dwelling unit) such as apartment complex. This densely populated residential area makes it feasible to implement a 1:32 B-PON comprises an ODP and 32 ONU30s accommodating 1000 customers within 250m² area. When we consider existing copper infrastructure and subscriber distribution, above serving area can be varied.

The ODP where optical splitter, power supply system and back-up batteries are located feeds power and transmits optical signal to each ONU.

2.2 Designing Sheared Powering System

The shared powering system the ONU is one of the most issues in deploying FTTC[2]. In case of BB-Shelter and BB-Cabinet, each ODPs are powered by individual local power source. For BB-Box, however, we concluded that shared powering method, each power node remotely feeds several ONUs, is the appropriate power feeding architecture. Figure 2 shows configuration of SHARP-system (shared powering system). SHARP-cabinet is outdoor cabinet where SHARP-power supply, backup batteries and PON splitter are located in. SHARP-power supply rectifies commercial power and provides power to maximum 32 BB-Boxes. At the final stage of the system, DC/DC converter in ONU feeds powers to each system shelf. Backup batteries are only located in the SHARP-cabinet for easy maintenance and savings in installation space and cost. SHARP-cable is composite cable that composed of power feeding copper pairs and single mode fibers. The management system, called SHARP-DM², which stands for design, management and monitoring manages conditions of power and environment and optical fiber information.

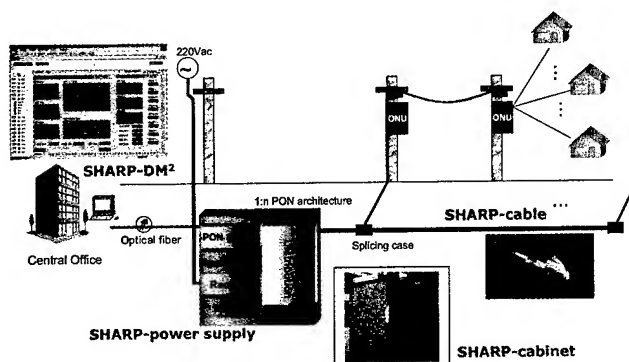


Figure 2. Configuration of SHARP-system

Design criteria-Shared powering system

In order to deploy appropriate powering architecture for FTTC-R, there are many factors to be considered as follows;

- PON splitting ratio, i.e. number of ONU that be fed by each power node
- ONU serving capacity
- ONU power consumption
- Maximum power feeding distance
- Backup capacity
- Voltage drop at power feeding copper pair
- Number of required core for each ONU
- Diameter of power feeding copper pairs

SHARP-power supply

From the consideration ONU power consumption, feeding distance and power feeding cable, we developed power supply system comprises four 2.5kW-rectifying modules. Power supply system has the following specifications:

- Rated input voltage: 220Vac, single phase

- Maximum output current: 50A (10kW@200Vdc)
- Rated output voltage: 200Vdc, CVF type
- Protections: Over-voltage, over-current, over-temperature and battery over-charging
- n+1 parallel operation for redundant powering
- Back-up: 3 hours supplied by fifteen 50AH sealed lead acid batteries
- Temperature compensating battery charging

The SHARP-power supply rectifies commercial power and provides power up to 32 ONUs by constant voltage feeding (CVF). At the final stage of the system, DC/DC converter in ONU feeds powers to each shelf. Back-up batteries are only located in the ODP for easy maintenance and savings in installation space and cost.

3. Fiber/Copper Composite Cable

A Composite cable with optical fibers for broadband signal and copper conductors for electrical power enable cost down of installation and integrated system operation and management[3].

Those factors as follows should be taken into consideration for design the composite cable. For the optical cable, composite cable can contain sufficient count of optical fibers and copper pairs in appropriate outer diameter in order to supply power and optical signals to 32 ONUs. From the viewpoint of frequent midspan access of the shared power feeding system, composite cable should have structures supporting easy fiber access. There should be no optical characteristic decrease that may be caused by the stress from stranded copper and the structure should have the equal optical characteristics as that of conventional optical cables.

For the copper cable, the power of 200Vdc can be supplied up to 400 meters and other components of cable should not be damaged from the heat generated on copper as the power feeds. Also the power of copper cable should be taken into consideration to avoid leakage to communication system.

3.1 Design of Composite Fiber/Copper Cable

3.1.1 Fibers and Conductors Count

The composite fiber/copper cable has been developed as an application for PON network. Accordingly subscriber structure considerably effects to the count of fiber of conductors in the cable, and it can vary at the requirement of transmitting system. Hence the study assumed, when the structure of subscriber network is as shown in Figure 3, that the cable is applied all the way to ONU from the optical dividing point where optical splitter meets optical cable that was withdrawn from optical trunk line.

As indicated on the Figure 3 one pair of cables supports 32 ONU's in common and, when one ONU is considered having two optical fibers and one pair of coppers are provided, main distributing cable comprises 32 optical fibers and 18 pairs of coppers including 2 pairs of spare copper conductors. The cable that is finally led into ONU located in residential area becomes the system composed of two optical fibers and 3 pairs of coppers including spare one pair of

coppers and one pair of ONU monitoring coppers. In the same way, auxiliary distribution cables with 16 optical fibers and 10 pairs of copper can be designed.

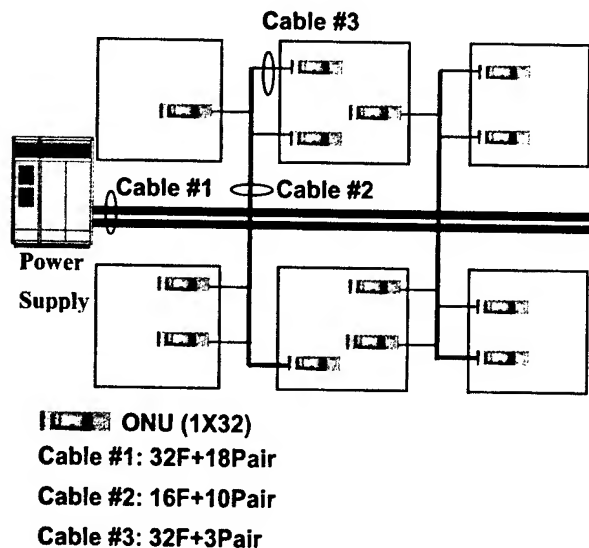


Figure 3. Distribution Structure of subscriber network

3.1.2 Cable Core Structure

The study applied a structure that composite fiber/copper cable has the loose tubes including optical fibers and coppers being stranded around dielectric central strength member in multi-layer. It is advantageous when gathered part and reverse part of optical fiber tubes and coppers are displaced alternatively in order to enable easy midspan access. Central tube type composite cable had to remove the copper layer gathered outside to access necessary optical fiber for midspan access. This newer composite cable improves working efficiency due to enabling the access to the necessary optical fiber without any removal for copper layer by disclosing optical fiber tubes on the outer most layer of core, and it also reduces stresses to optical fiber tube from stranded coppers.

3.1.3 Buffer Tubes and Copper Conductors

The diameter of copper conductors was set to 22AWG(0.65mm outer diameter) in consideration of power transmission length of 200Vdc to the up to 400 meters and proper stiffness to handle the cable. Resistance requirement for copper was set less than 56.5Ω/km in accordance with KT standard. The copper was coated with polyethylene with the thickness of 0.8mm in accordance with the standard for polyethylene insulation, KSC3330. The optical fiber tube was made of PBT materials with outer diameter of 2.25mm that is the same as sheathed copper. In order to prevent deformations of tube that may be caused from outside forces, increased tube thickness is integral, or on the contrary, in order to improve tensile window that resists thermal variation and tensile force applied from installation, it's necessary to reduce tube thickness and increase its' inner diameter. The study has decided 1.4mm for inner diameter of

the tube with considering both above explained characteristics together.

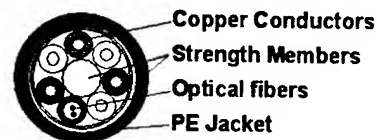
3.2 Manufacturing Composite Fiber/copper Cable

The composite cable has been made under same conditions as conventional loose tube type optical cable. Optical tube units were stranded around the central strength member. Outer dielectric strength member and polyethylene jacket were applied around the core. Figure 4 shows construction of the manufactured composite cables. And Table 1 shows

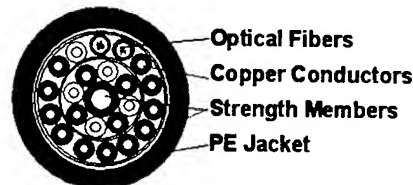
Table 1. Construction of the Composite Cable

Item	# 1	#2	#3
Fiber Count	2	16	32
Copper Conductors	22AWG 3 Pair	22AWG 10 Pair	22AWG 18 Pair
Outer Diameter	12.7 mm	18.5 mm	23.7 mm
Cable Weight	140 kg/km	310 kg/km	510 kg/km

2 Fibers & 3 Copper Pairs



16 Fibers & 10 Copper Pairs



32 Fibers & 18 Copper Pairs

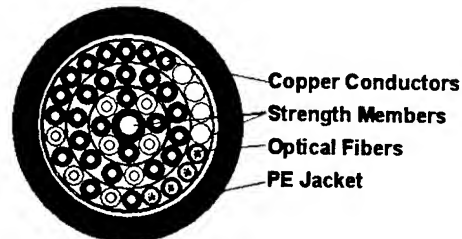


Figure 4. Cross-sectional View of the Composite cables

3.3 performance of the Composite Cable

The previously manufactured composite cable showed favorable characteristics in aspect of optical loss with below 0.35 dB/km at 1310nm wave and below 0.21 dB/km at the wave of 1550nm. Conductor resistance of the copper was below 52.3 Ω /km in average and maximum 52.8 Ω /km, and its' insulation resistance was measured as above 240,000 M Ω .km. The characteristics of dielectric strength showed stable result in DC 2200V/1min. test.

The mechanical and environmental characteristics was tested in accordance with KT Standard and GR-20-CORE and the result showed, as indicated in Table 2, same properties of conventional loose tube cable.

Table 2. Characteristic of the Composite Cable

Parameter	Test condition	Results
Tensile Strength	#1: 270 kg #2: 310 kg #3: 510 kg	Pass
Impact Resistance	#1: 2 kg #2: 3 kg #3: 5 kg	Pass
Compression Strength	220 N/cm	Pass
Cable Twisting	10cycles \pm 360°C	Pass
Repeated Bending	20x Diameter	Pass
Temperature Cycling	30°C~70°C	Pass
Water penetration	1m static head, 1m length	Pass

4. Deploying Shared Powering System

SHARP-cabinet

SHARP-cabinet contains backup batteries, management agent, PON splitter, fiber/copper distribution compartment, and large capacity rectifier, namely SHARP-power supply. It also contains ONU whose height is up to 8U, if necessary.

SHARP DM²-Design, Management & Monitoring

Since each SHARP-system comprise up to 32 ONUs, the maximum subscribers covered by each SHARP-system are 960.

Consequently, we needed to develop an extra management system for power and environment in addition to the EMS(element management system) of the ONU in order to provide reliable services. The developed prototype management system also has the two other functions including design and management for SHARP-system. Its key features and benefits are as follows, which is shown in Figure 5;

- Monitoring the electrical and environmental conditions for SHARP-power supply and SHARP-cabinet, respectively
- Automated network planning and calculation of deployment cost

- Management of fiber core information, splice information, outside plant facilities such as hand-hole, manhole, pole and so on.

SHARP-DM², provides above functions via web-based remote access.

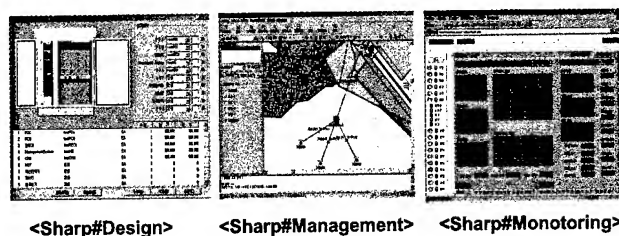


Figure 5. Management and Monitoring System of Shared Powering System

5. Conclusions

There are many factors to be considered such as system types, system capacity, installation site, ONU powering issue and so on when implementing optical access networks. Among other things, powering the small capacity ONU that will covers less than 30 lines is one of important issues in deploying FTTC. After investigating the network characteristics of residential area, we concluded that shared powering method, each remote power node feeds several ONUs, is the appropriate power feeding architecture for B-PON deployment in residential area. We developed power supply system, composite cables, street cabinet and management system for shared powering architecture and they showed reliable test results. The fiber/copper composite cable with maximum 32 optical fibers and 18 pairs of copper could effectively support the shared feeding system providing power from one power supply to 32 ONUs in the scope of 400 meters. Also, since the Composite Cable has advantageous structure to access optical fibers, it is expectable that the consuming time for midspan access can be saved.

6. References

- [1] Korea Network Information Center (KRNIC), www.nic.or.kr
- [2] D. Sorenson, T. H. Sloane, "Powering Fiber in the Local Loop: FTTC and FITL Power Architectures", *National Fiber Optic Engineers Conference*, p.343-354 (1998)
- [3] John Heery, Mike Gimblet, James Register, "Development and Application of a Composite Fiber/copper Cable with Remote Powering Capabilities", *International Wire & Cable Symposium*, 48th, p. 755-763 (1999)

Authors



Sungyul Park received B.E. degree in Electronics Engineering from Kyungbuk University in 1996. He joined LG Cable Ltd. in 1996 as a design engineer in the optical fiber cable part. He is responsible for developing optical fiber cable.



Min Son received B.E. degrees in Electronics Engineering from Kyungbuk University in 1988. He joined LG Cable Ltd. in 1988 and has been engaged in design and development of optical fiber cable. He is now in charge of optical cable technology team in Indong Plant.



Sangki Hong received M.S. degree in Electrical Engineering from Yon-sei University in 2000 and joined Korea Telecom. He is engaged in the engineering of optical access network.



Youngtark Lee received M.S. and Ph.D. degrees in Electronic Engineering from the Sungkyunkwan University in Korea in 1988 and 1999, respectively. Since 1989, he has been with the R&D group at Korea Telecom, where he is currently a director of Optical Access Network Engineering Division. His research includes optical access network engineering, specialty optical fibers and optical fiber Bragg grating applications.



Joungyoung Ha received M.S. degree in Electronics from Kyungbuk National University in 1989 and joined Korea Telecom. He is engaged in the engineering of optical access network.

Development of Flame-Retardant Optical Fiber Cord

Tetsuo Hayano, Osamu Kato, Tsuyoshi Shimomichi, Keiji Oohashi

Research and Development Dept. Telecommunication Cable Division Fujikura Ltd.

1440, Mutsuzaki, Sakura-shi, Chiba, 285-8550, Japan

Phone: +81-43-484-3946 Fax +81-43-484-3997 E-mail: hayano@s.fujikura.co.jp

Abstract

We have developed a non-halogen highly flame-retardant optical cord for use in intra- and inter-apparatus cabling. The jacketing material of this cord is a halogen-free flame-retardant (HFFR) polymer. The cord has an outer diameter of 2-mm and complies with UL VW-1 standards. Performance of the developed cord is comparable to that of the conventional PVC-jacketed optical cord.

Keywords

Halogen Free; Flame Retardant; Optical Fiber Cord

1. Introduction

With the increased use of optical fibers in subscriber communications systems, the demand for optical fiber cords for intra- and inter-apparatus cabling is expected to grow in coming years. Currently, PVC (Polyvinyl Chloride, a polymeric material) is typically employed in the manufacture of the jacketing material. In terms of environmental conservation, the jacketing material of optical cords are expected to be highly flame-retardant, to offer reduced emissions of toxic gases when incinerated, and to minimize the contamination of water and soil with hazardous elements when disposed of as waste. In response to these requirements, we have developed a technique to replace conventional jacketing material with a HFFR-polymer. The main component of the flame retardant adopted in the HFFR-polymer is a hydrate of light metals that is harmless to plants and animals. This material is ecologically safe and does not emit toxic gases when incinerated; nor does it contaminate water and soil with hazardous elements when disposed of in landfills.

2. Structure of Prototype Cord

Figure 1 illustrates the structure of the $\phi 2$ -mm optical fiber-cord we constructed. Aramid yarn serving as a strength member is applied longitudinally to the $\phi 0.9$ -mm single-mode buffered fiber, and the jacketing material is coated on the external surface, resulting in an optical cord with an outer diameter of 2-mm. The jacketing material is composed of a HFFR polymer containing a flame retardant whose main component consists of an inorganic metal hydrate.

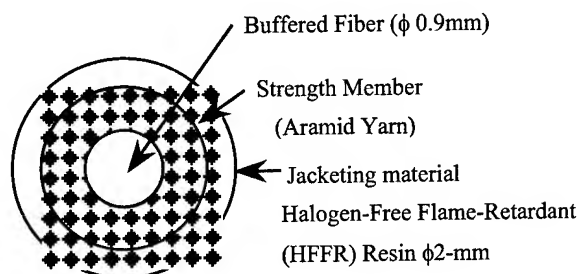


Figure 1. Cross-Sectional Structure of Prototype Cord

3. Flammability of cord components

We tested the flammability of the conventional PVC cord in order to acquire the basic data for the construction of a halogen-free cord. The flammability of each of the three components—jacketing material, strength-member, and buffered fiber—was determined using a cone calorimeter. Cone calorimeter is used to measure the rate of heat generation and the amount of heat generated when a specimen is burned in a cone-shaped heater (shown in Figure 2). This is a highly useful measure of the combustion properties of a specimen. The quantities of component materials for this measurement were equivalent to those in a cord one-meter long. Figure 3 shows the flammability of each component (for comparison, the flammability of the cord itself is shown in this Figure). The following results were obtained.

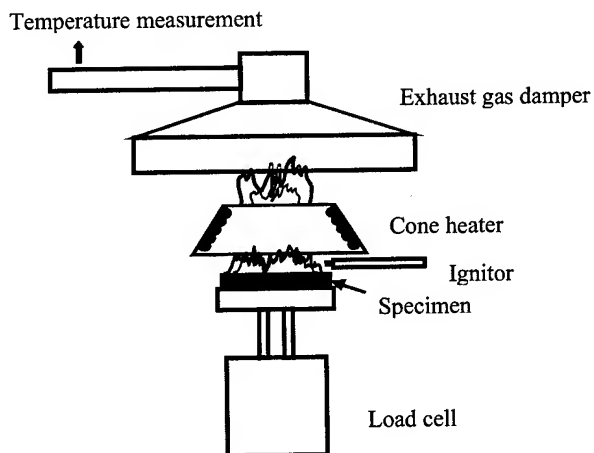


Figure 2. Schematic Structure of the Cone Calorimeter

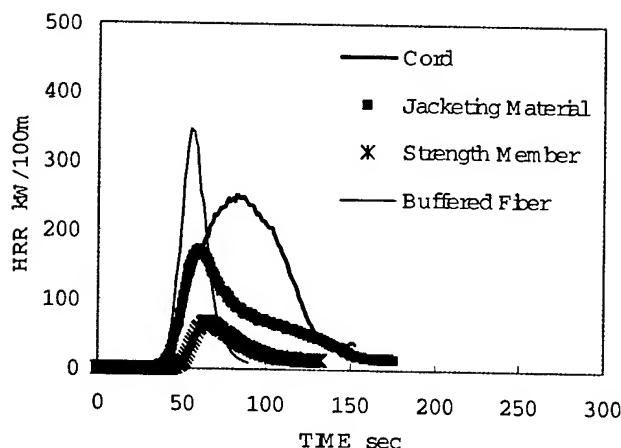


Figure 3. Heat Generation Speed of each Component of the Cord

The Peak top value of generated heat of the jacketing material was approximately half as high as that of the buffered fiber.

We noted the above point during development of the halogen-free cord. Following are descriptions of the selection of the jacketing material and of the process of improving the flame resistance of the buffered fiber.

4. Improvement of the Flame Resistance of each Component

4.1 Selection of the Jacketing Material

The properties of three non-halogen polyolefin resins of different flame-resistance levels were investigated for comparison. Table 1 lists the typical properties of the jacketing material, while Figure 4 shows the heat generation speed of each component, which had been formed into sheets, by a cone calorimeter. (For comparison, the flammability of PVC is shown in this Figure) Then we selected material C, which featured a high OI value and a low heating rate, expecting that this material would show the highest flame resistance. [*1]

Table 1. Typical Properties of the Jacketing Material

Item	A	B	C
O.I.(Oxygen Index/ASTM D 2863)	39	44	53
Peak top value of generated heat(kW/m ²)	234	175	161
Breaking Strength(MPa)	13.2	11.5	9.3
Breaking Elongation(%)	630	130	200
Breaking Strength Retention rate (%)			
After 90°C 48hr	93	102	103
Breaking Elongation Retention rate (%)			
After 90°C 48hr	102	104	125

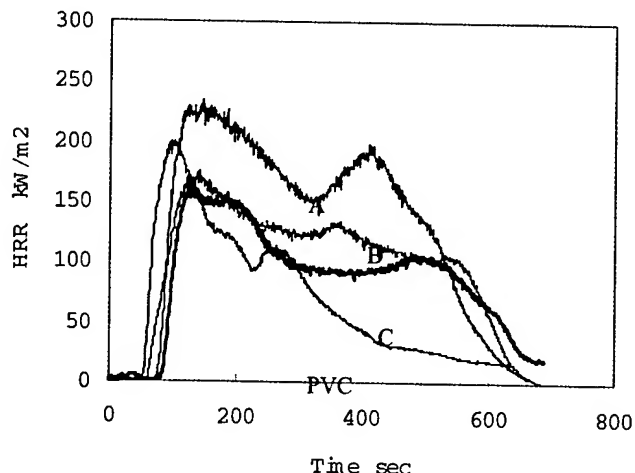


Figure 4. Heat Generation Speed of each Materials

4.2 Improvement of the Flame Resistance of the Buffered Fiber

Polyester-elastomer was employed as the base material because it had an appropriate flexural modulus and featured high reliability in transmission. Two types of inorganic non-halogen flame retardants (I and II) were employed in this experiment. The three test buffered fibers (a, b, and c) included I alone, II alone, and both I and II, respectively. Table 2 shows the combustion test results for the buffered fibers. The combustion test conformed to UL VW-1 Vertical Combustion Test Standards. All the buffered fibers failed the test. Although c did not pass the test, we selected c because it showed higher flame resistance (due to the synergistic effect of flame retardants I and II). For comparison, the test results of core d (featuring a halogen-type flame retardant) are also shown.

Table 2. Combustion Test Results of the Buffered Fibers

Type	Flame Retarder	Combustion of Indicator-Flag	Cotton
a	I	no fired	fired
b	II	fired	no fired
c	I + II	no fired	2/10 fired
d	Halogen	no fired	no fired

5. Combustion Test for the First Prototype Cord

We conducted a VW-1 combustion test on a cord using jacketing material C and buffered fiber c selected as discussed in Section 4. In order to clarify the differences in the flammability of the buffered fiber, we conducted the same combustion test on the cords using a flammable buffered fiber and using a halogen-type VW-1 buffered fiber. As shown in Table 3, all the cords failed the test. And as shown in Figure 5, the Peak top value of generated heat of the PVC-jacketing material cord was smaller than that of the HFFR-jacketing material cords. It thus proved difficult to manufacture a flame-retardant cord by merely improving the flame resistance of the jacketing material and buffered fiber. Thus we focused on the remaining aramid yarn as a strength member.

**Table 3. Combustion Test Results
for the First Prototype Cords**

Jacketing Material	Type			Combustion of	
	Buffered Fiber	Indicator-Flag	Cotton		
C	c	fired	no fired		
C	flammable	fired	no fired		
C	d (halogen)	fired	no fired		

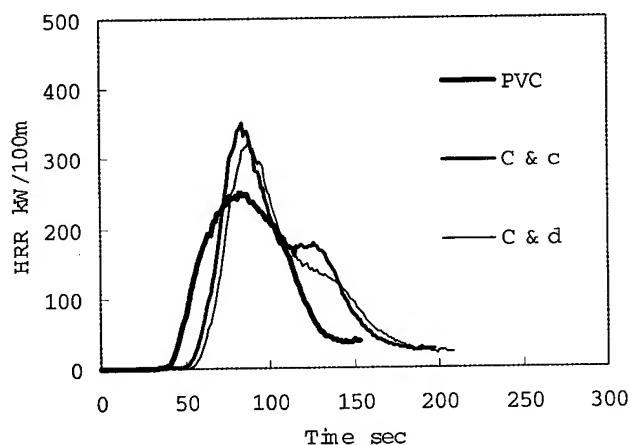


Figure 5. Heat Generation Speed of Various Cords

6. Improvement of the Flame Resistance of the Aramid Yarn

We tried to improve the flame resistance of the aramid yarn coated with a flame retarder. Figure 6 shows the flammability of this coated yarn. The difference attributable to the presence or absence of the coating is also shown for comparison. As shown by the heating value, heating rate, and heating peak height, the flame-retardant coating on the strength member yarn significantly improved flame resistance.

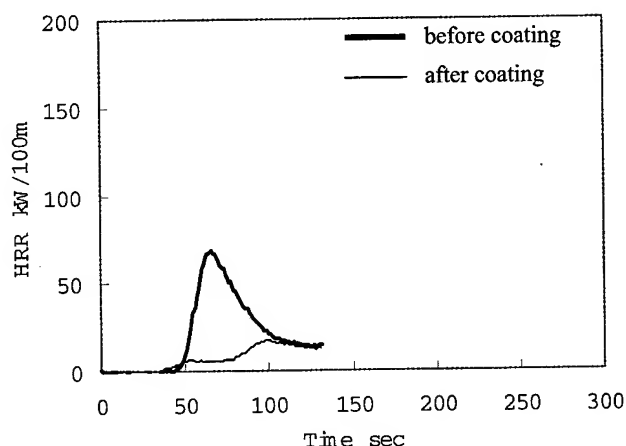


Figure 6. Heat Generation Speed of the Aramid Yarn

7. Combustion Test for the Second Prototype cord

We fabricated prototype cords using the aramid yarn coated with a flame retarder. Table 4 shows the results of the VW-1 combustion test for the fabricated cords. Regardless of whether the buffered fiber was flame retardant or not, the cords passed the test. Figure 7 shows the heat generation speed of the cords. Thus, the aramid yarn coated with a flame-retardant played a role as a heat insulation-layer. It would be surmised that the strength member coated with a flame retarder decreased the heat generation speed of the buffered fiber. Then we determined the various properties of the stable cord whose buffered fiber is flammable.

**Table 4. Combustion Test Results
for the Second Prototype Cords**

Buffered Fiber Type				
		c	flammable	
Combustion-Time	sec	35.6	39.4	at first ignition
Combustion-Length	mm	133	140	at first ignition
Indicator-Flag		no fired	no fired	
Cotton-Flame		no fired	no fired	

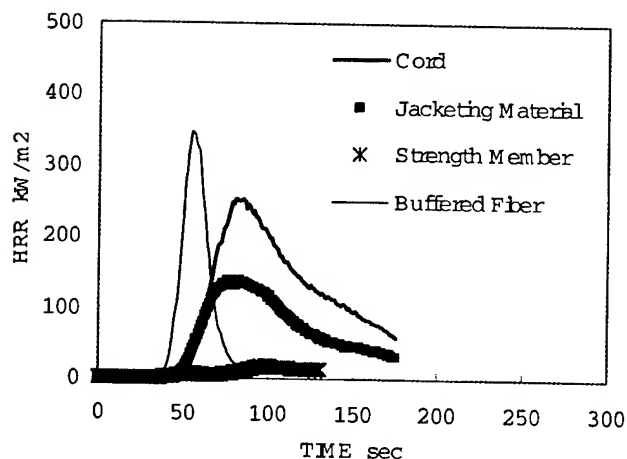


Figure 7. Heat Generation Speed of the Second Prototype Cord with Flammable Buffered Fiber

8. Evaluation of the Final Prototype Cord

We have fabricated the final prototype cord, shown in figure 8, and evaluated its initial properties and long-term reliability. Changes in transmission loss during fabrication, temperature cycling test, lateral-pressure test, and bending test were examined to evaluate the initial properties of the cord. The cord showed excellent results in all performance tests, suggesting no potential problems in practical use. To evaluate long term-reliability of transmission loss, we conducted high temperature-test (85°C×2000hr), wet heat test (60°C×95%RH×2000hr), and low temperature-test (-40°C×2000hr) on the cord. The level of transmission loss in the selected cord proved to be stable over a long period of time. Table 5 summarizes the test results. As an example, Figure 9 shows a wet heat characteristic graph of the cord.

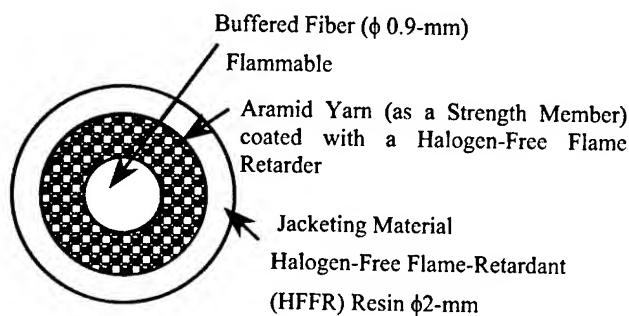


Figure 8. Cross-Sectional Structure of Final Prototype Cord

Table 5. Table of Evaluation Results

Test Item	Method and Condition	Results
Combustion	UL1581 VW-1	Passed
Temperature Cycling I	-20°C to +60°C × 3cyc.	<0.1 dB/km
Temperature Cycling II	-40°C to +85°C × 3cyc.	<0.1 dB/km
Bending	R20mm × 6 turn	<0.01 dB
Lateral Pressure	19.6 N/mm	<0.01 dB
High Temperature	+60°C × 2000hr	<0.1 dB/km
Low Temperature	-20°C × 2000hr	<0.1 dB/km
Wet Heat	+60°C×95%RH× 2000hr	<0.1 dB/km

Measurement Wavelength: 1.55μm

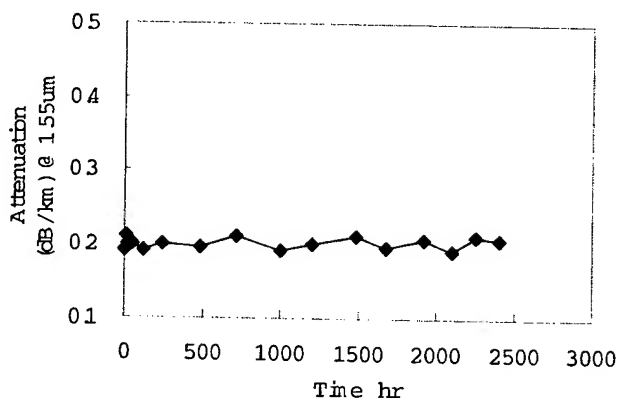


Figure 9. Wet Heat Performance of φ2-mm Cord

9. Conclusions

We have developed a φ2-mm optical cord using a non-halogen flame-retardant material. This cord meets UL VW-1 Test standards. The prototype cord features excellent characteristics with no problems in practical use. The flame resistance of the cord can be considerably improved by coating the aramid yarn with the flame retarder. The flame resistance of the buffered fiber has little impact on the flame resistance of the cord itself.

10. References

- [1] O. Kato, "Development of Optical Fiber Cable with Halogen Free Flame Retardant Jacket" 49th IWCS, p182 (Nov, 2000).

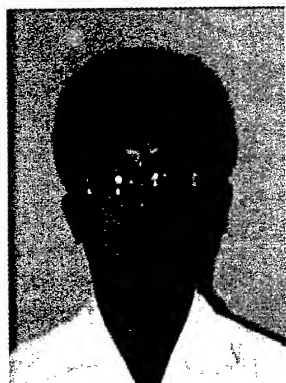


Tetsuo Hayano

R&D Dept. Telecommunication Cable Division Fujikura LTD.

1440 Mutsuzaki, Sakura, Chiba, 285-8550, JAPAN

He was born in 1963. He received the B.E. degree in electronic engineering in 1987 from Kyushu University. He joined Fujikura Ltd. after his graduation and has been engaged in research and development of optical fiber, thin cords and cables. He is now a manager of the Research and Development Department Telecommunication Cable Division and a member of the IEICE of Japan.



Osamu Kato

R&D Dept. Telecommunication Cable Division Fujikura LTD.

1440 Mutsuzaki, Sakura, Chiba, 285-8550, JAPAN

Osamu Kato graduated from Nagoya Institute of Technology with a B.C. degree in 1990. After six years of work as an engineer for material analysis, he has been engaged in research and development of optical fibers. He is now an engineer in the Telecommunication Cable Material Section and a member of the IEICE of Japan.

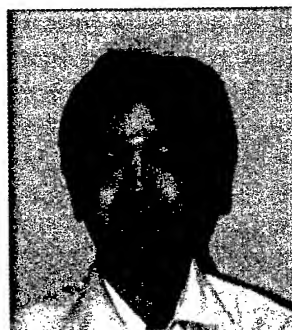


Tsuyoshi Shimomichi

R&D Dept. Telecommunication Cable Division Fujikura LTD.

1440 Mutsuzaki, Sakura, Chiba, 285-8550, JAPAN

He was born in 1960. He joined Fujikura Ltd. after his graduation from Nagasaki University in 1986 with an M.C. degree and has been engaged in research and development of optical fibers and optical fiber coatings. He is now a manager of the Research and Development Department Telecommunication Cable Division and a member of the IEICE of Japan.



Keiji Oohashi

R&D Dept. Telecommunication Cable Division Fujikura LTD.

1440 Mutsuzaki, Sakura, Chiba, 285-8550, JAPAN

He was born in 1956. He graduated from the Tokyo Institute of Technology in 1980 with a B.C. degree in chemistry. After eight years of work as an engineer in the field of materials for motor vehicles, he joined Fujikura LTD. in 1988. He has been engaged in research and development for optical fibers and optical fiber coatings. He is now a general manager of the Research and Development Department Telecommunication Cable Division and a member of the IEICE of Japan.

Development of flame-retardant halogen-free fiber optic cords with shrink-free jacket

Takeshi Honjyo, Masahiro Kusakari, Kazunaga Kobayashi, Keiji Oohashi

Research and development, Telecommunication cable division, Fujikura Ltd.

1440 Mutsuzaki, Sakura-shi, Chiba-ken, 285-8550 Japan

+81-43-484-3945 · thonjyo@s.fujikura.co.jp

Abstract

We have developed flame-retardant halogen-free fiber optic cords with a shrink-free jacket, using simplex($\phi 2.8\text{mm}$)cords. We have devised a new method to ensure that the jacket is shrink-free. The new method of cord manufacture has been optimized so as to minimize residual stress produced by extrusion. Subsequent shrinkage of the jacket may be nearly eliminated by this method. As a result, post-annealing becomes unnecessary when assembling connectors with the cord. Thanks to this shrink-free jacket, optical attenuation increase of the Simplex cord at low temperatures has been significantly reduced. We have also made sure that the Simplex cord displays excellent mechanical and flame-retardant properties.

Keywords

shrink-free; halogen-free; flame-retardant; jacket

1. Introduction

Conventionally, the primary jacket material for flame-retardant optical cords has been PVC. Recently, the development of a halogen-free jacket of the cord required from the viewpoint of environmental conservation. However, significant stress remains in the common flame-retardant halogen-free jacket after it has experienced the usual extrusion. Such a jacket is likely to shrink after extrusion. A number of techniques have been proposed to prevent such post-shrinkage. For example, polycarbonate has been embedded in the cord by co-extrusion, functioning as a melt filament reinforcement (MFR)[1]. Nevertheless, none of the proposed post-shrinkage solutions has proven effective to result in convenient connector coupling at low cost.

When the cord is assembled with connectors, the fiber may bend due to post shrinkage, often resulting in increased attenuation. Occasionally, the cord must be post-annealed at an appropriate temperature to complete jacket shrinkage before assembling with connectors. This post-annealing requires a significant amount of time and labor. For these reasons, there have been great hopes for an optical cord jacket free of post-shrinkage.

2. Design of the cord

2.1 Cord structure

The cord we studied has the structure shown in Fig.1 where a $\phi 0.9\text{mm}$ buffered fiber supported by aramid yarn in the longitudinal direction is coated with a flame-retardant halogen free resin. The outer diameter of the cord is 2.8mm.

We applied a new method to optimize the conditions of cord extrusion in order to avoid post-shrinkage. To compare this new method and the conventional method, we measured properties such as jacket shrinkage, temperature characteristic, mechanical properties, and flame-retardant property in cords fabricated using these different methods.

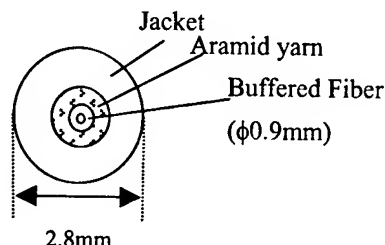


Figure 1. Cord structure

2.2 Selection of jacket materials

We examined several halogen-free resins to determine which was best suited for use in optical cords. The important element of a jacket material is the shrinkage stress at low temperatures. When a halogen-free resin is used in the cord jacket, the attenuation of the cord often increases at low temperatures. Thus the resin used in cord jackets should feature minimal shrinkage stress at low temperatures.

We examined three types of halogen-free flame-retardant resins by thermo-mechanical analysis. For comparison, PVC resin was also used in the test. The resins were cooled from 20°C at a cooling rate of 0.5°C / min. to measure shrinkage stress. Figure 2 shows that the performance of resin A is equal to that of PVC and that resin B shows lower shrinkage stress than PVC. Because the shrinkage stress of resin C was larger than that of PVC at low temperatures, we determined that resin C was not suitable for use in optical cords. Thus we did not use resin C in the performance test described below.

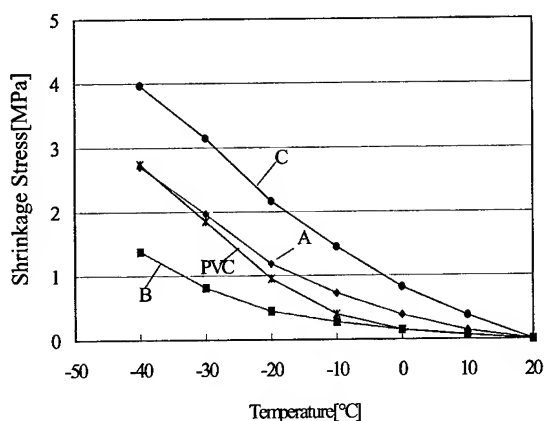
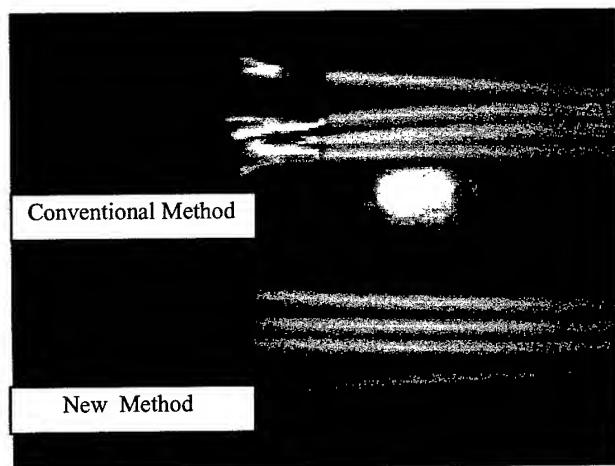


Figure 2. Comparison of shrinkage stress of halogen-free jackets at low temperatures

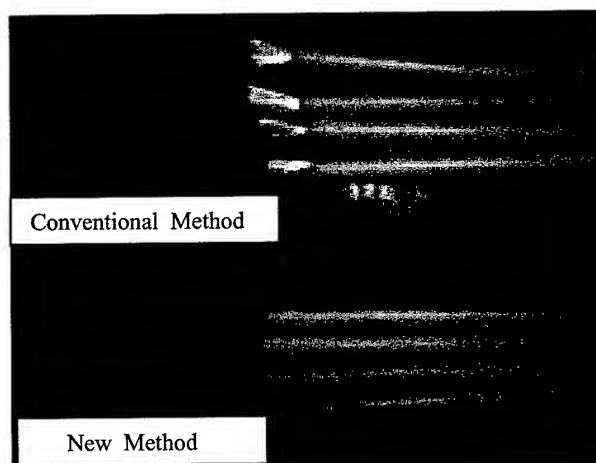
3. Evaluation of the jacket

3.1 Cord heating test

We heated at 85°C a 0.5-m-long cord not assembled with any connectors for 24 hours and measured the length of buffered fiber protrusion from the jacket edge; the more the jacket shrinks through heating, the longer buffered fiber protrudes from the jacket end in this test. We made the cords by using two methods. The conventional method is a usual extrusion. The new method is an extrusion method of minimizing the residual stress of the jacket. In cords fabricated using the conventional method, the average protrusion length after heating (the sum of the protrusion lengths on both ends of the jacket) was 12.5 mm in the resin A jacket and 5.5 mm in the resin B jacket. In contrast, no fiber protrusion was observed at the ends of the jackets made of either resin with cords fabricated using the newly developed method. When connectors are assembled with the ends of a cord fabricated using the conventional method, the fiber will bend near the ends as the jacket shrinks. As a result, attenuation increase may grow or the fiber may be broken. The technique we developed can effectively prevent such problems.



a)



b)

Figure 3. The protrusion of the buffered fiber

after heating; 85°C, 24hours

(Protrusions of both jacket ends were gathered into one side)

a) Resin A b) Resin B

Table 1. The average protrusion length

	The average protrusion length[mm] (The sum of the protrusion lengths on both ends of the jacket)	
	Conventional	New
Resin A	12.5	0
Resin B	5.5	0

3.2 Jacket shrinkage test

We conducted the jacket shrinkage test on the Telcordia GR-409 CORE to determine whether the developed technique would meet the required specifications (acceptable shrinkage from the original length is 5% or less when the jacket alone is heated). The jacket was heated at 110°C for two hours.

In the heating test, the cord jacket fabricated using the new method showed less shrinkage than the jacket fabricated using the conventional method (Fig. 4). Shrinkage of the resin A cord jacket fabricated using the conventional method was approximately 9%, and did not meet the required specifications for the Telcordia GR-409. On the other hand, shrinkage of the resin A cord jacket fabricated using the new method was 5% or less, thus meeting the predetermined specifications. Further, the resin B cord jacket fabricated using the new method showed almost no shrinkage at all in the course of the jacket-shrinkage test.

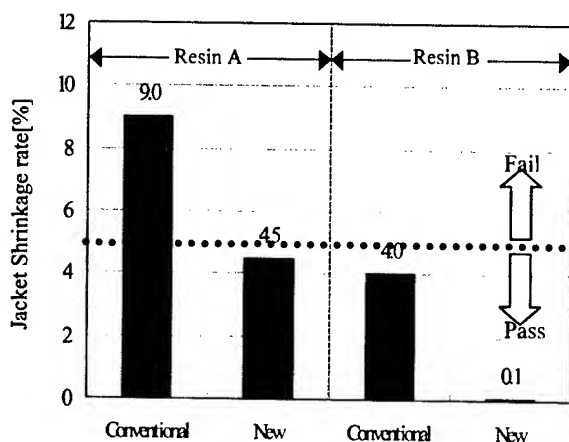


Figure 4. Results of jacket shrinkage tests

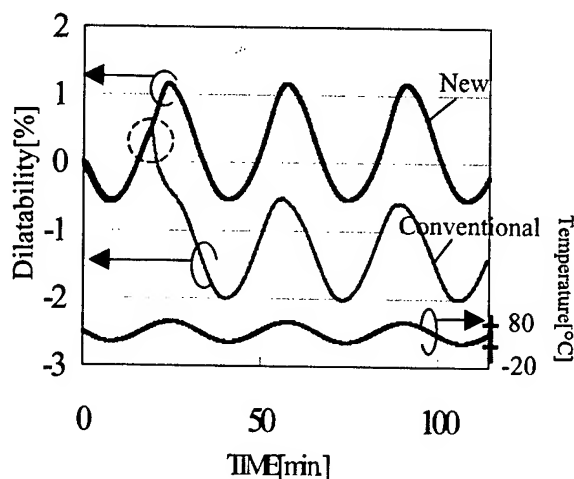


Figure 5. Temperature cycle test of the jacket

3.3 Temperature cycle test of the jacket

We investigated then the relationship between temperature and jacket shrinkage using a thermo-dilatometer. We measured the shrinkage of each jacket at three and half temperature cycles between -20 and 80°C.

As shown in Fig.5, the jacket fabricated using the conventional method began to shrink halfway through the first heating cycle (as indicated in the dotted-line circle). The jacket fabricated using the new method corresponded to the temperature curve. Two dilatibility curves do not look like.

The characteristic of jackets fabricated using the conventional method can be attributed to residual stress produced during extrusion. When the resin of jacket material is elongated in the longitudinal direction under the extrusion process with heat, the strain stress is produced in the resin. Subsequently the resin cools and solidifies with strain stress held. If such a cord is then heated, the residual stress is released and the jacket shrinks in the longitudinal direction. The new method of cord manufacture has been optimized so as to minimize such residual stress produced by extrusion. Thus, as demonstrated in the jacket shrinkage test, jacket shrinkage is extremely low in the cord fabricated using the new method, relative to cords manufactured using the conventional method.

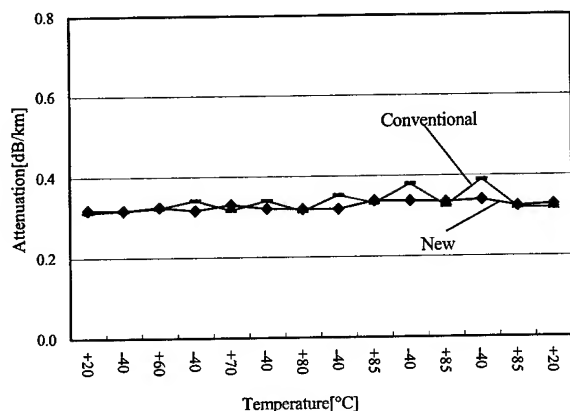
4. Temperature cycle test of the cord

We carried out a temperature cycle test (between -40 and 85°C; the low-temperature side was kept at -40°C and the high-temperature side was heated in steps at each cycle) on resin B cords fabricated using the new and conventional methods and measured the attenuation of those cords by OTDR. The length of the cords were 500-m. The cords used in the measurement had a single mode fiber. As shown in Fig. 6, the attenuation increased at low temperatures for all of the wavelengths—1.31, 1.55, and 1.625 μm —in the cord fabricated using the conventional method in the early stages

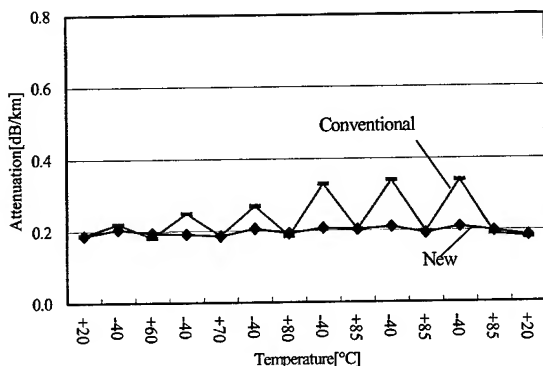
of the temperature cycles. In contrast, there was no attenuation increase in the cord fabricated using the new method.

As indicated in the temperature cycle test of the jacket, the jacket fabricated using the conventional method showed significant shrinkage after subjection to the high-temperature cycles. When cooled to lower temperatures, the jacket shrank further, resulting in bends in the fiber and an eventual increase in attenuation.

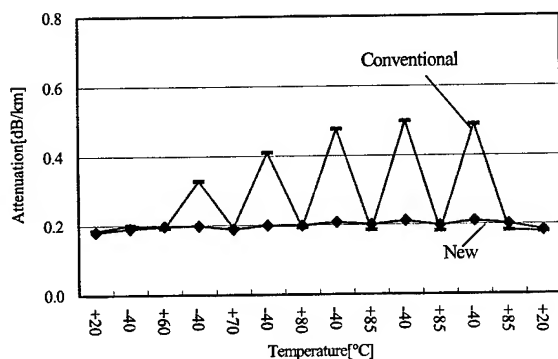
The test results indicated that the jacket fabricated using the conventional method shrank at high temperatures as the stress produced by extrusion was released and that this shrinkage resulted in significant attenuation increase in the cord. The new method, however, can effectively prevent the attenuation increase due to jacket shrinkage. Similar results were obtained in a simplex GI-fiber cord.



a)



b)



c)

Figure 6. Temperature cycle test of the cord
Measurement Wavelength a) 1.31 μ m b) 1.55 μ m
c) 1. 625 μ m

5. Mechanical properties

We conducted mechanical-properties tests on a resin B cord fabricated using the new method with reference to the standards for the Telcordia GR-409 CORE. The test results are shown in Table 3. The cord met the standards for Telcordia GR-409 CORE with excellent test results.

Table 3. Mechanical Properties

ITEM	UNIT	RESULT
Impact resistance	dB	<0.05
Compressive strength	dB	<0.05
Tensile strength of cable	dB	<0.05
Cable twist	dB	<0.05
Cable cyclic flexing	dB	<0.05

6. Flame-retardant property

We conducted a flame-retardant test conforming to IEC60332-3 Cat. C [3] on the resin B cord fabricated using the new method. The cord passed the test with a sufficient margin, as demonstrated in Fig. 7.

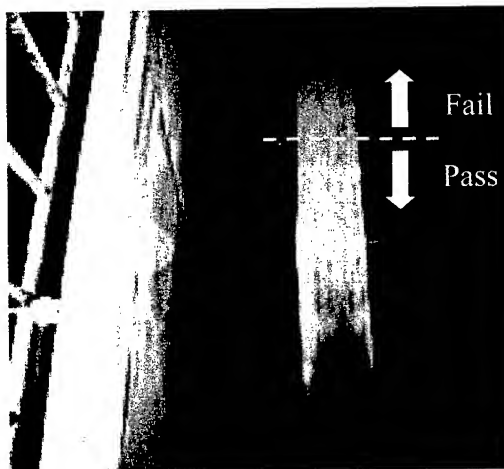


Figure 7. The picture of a flame retardant test

7. Conclusions

Using a halogen-free flame-retardant material, we fabricated a simplex ($\phi 2.8$ mm) cord using an optimized method capable of minimizing residual stress produced by extrusion remaining in the jacket. In the jacket-shrinkage test of the Telcordia GR-409 CORE, we succeeded in reducing jacket shrinkage nearly to zero through the use of the newly developed method. Attenuation increase was not observed at low temperatures due to the minimal post-shrinkage of the cord jacket. In addition, the cord showed excellent mechanical properties and flame-retardant property.

We now intend to apply the newly developed method to the minimization of post-shrinkage in the jackets of multi-core tape-cords and cables.

8. References

- [1] R.Schneider et al. , "Melt Filament Reinforcement" MFR" for Shrink Free Fiber Optic Cable "Proc. 49th International Wire and Cable Symposium, 2000, P287-292
- [2] Telcordia GR-409 -CORE ,Generic Requirements for Premises Fiber Optic Cable (1994)
- [3] IEC60332-3, Tests on Electric Cable under Fire Conditions Part 3-24: Test for vertical flame spread of vertically- mounted bunched wires or cables Category C (2000)

Authors



Takeshi Honjyo

Research and development
department

Telecommunication cable
division

Fujikura Ltd.

1440 Mutsuzaki, Sakura-shi,
Chiba-ken, 285-8550 Japan

Takeshi Honjyo was born in 1969. He graduated Shizuoka University with a M.E. degree in 1997. After four years of work as an engineer in the field of deodorization apparatuses, he joined Fujikura LTD. in 2001. He has been engaged in research and development of optical fiber cables. He is now an engineer in the Telecommunication cable Department and member of the IEICE of Japan.



Kazunaga Kobayashi

Research and development
department

Telecommunication cable
division

Fujikura Ltd.

1440 Mutsuzaki, Sakura-shi,
Chiba-ken, 285-8550 Japan

Kazunaga Kobayashi was born in 1961. He joined Fujikura Ltd. after his graduation from Gunma University with a M.E. degree in 1985 and has been engaged in research and development of optical fiber cables. He is now an engineer in the Telecommunication cable Department and member of the IEICE of Japan.



Mashahiro Kusakari

Research and development
department

Telecommunication cable
division

Fujikura Ltd.

1440 Mutsuzaki, Sakura-shi,
Chiba-ken, 285-8550 Japan

Masahiro Kusakari was born in 1965. He joined Fujikura Ltd. after his graduation from Nagasaki University with a B.E. degree in 1990 and has been engaged in research and development of optical fiber cables. He is now an engineer in the Telecommunication cable Department and member of the IEICE of Japan.



Keiji Oohashi

Research and development
department

Telecommunication cable
division

Fujikura Ltd.

1440 Mutsuzaki, Sakura-shi,
Chiba-ken, 285-8550 Japan

Keiji Oohashi was born in 1956. He graduated from the Tokyo Institute of Technology in 1980 with a B.C. degree in chemistry. After eight years of work as an engineer in the field of materials for motor vehicles, he joined Fujikura LTD. in 1988. He has been engaged in research and development for optical fibers and optical fiber coatings. He is now a general manager of the Research and Development Department Telecommunication Cable Division and a member of the IEICE of Japan.

The prediction of flame retardancy of LSZH optical cable using a small-scale flame test by Cone-calorimeter.

Ho-soon Lee*, Eun-song Um

Samsung Electronics Co., Ltd.

Kumi-City, Republic of Korea.

82-54-479-7164 · hosoon.lee@samsung.com

eunsong.um@samsung.com

Jung-ho Kong

Hanwha Chemical R&D center.

Daejeon-City, Republic of Korea.

82-42-865-6507 · jhkong@hanwha.co.kr

Abstract

As modern industry are requiring and now deploying more environment-friendly and safer optical fiber cable (hereafter OFC) to indoor/outdoor optical transmission system, lots of cable designs have been presented in the market already and they are developing another models with more improved properties. Those, until now, introduced products are focused on improving flame retardancy and suppression of smoke generation and most of them fully meet international standards. Even though those products meet international standards, more and more new products are under development and are introduced.

The main goal of this paper is based on predicting flame retardancy of OFC by knowing the function of char that was formed over Low Smoke Zero Halogen (hereafter LSZH) OFC's outer sheath to flame retardancy of OFC[1][2][3]. So, the function of char over LSZH sheath was deeply studied to determine the degree of flame retardancy of OFC. And small-scale flame testing was also studied to make prediction of flame retardancy of OFC design possible before manufacturing

Keywords

LSZH compound, small scale flame testing, Cone Calorimeter, Smoke generation.

1. Introduction

Determination of OFC construction is focused on satisfying OFC's characteristics to customers' requirements and international standards. Those requirements and standards are simply classified to three parts ; mechanical, environmental and flame properties. Among those requirements and standards, OFC's flame characteristics are heavily dependent on raw materials. In this paper, our study is focused on prediction of flame retardancy of LSZH optical cable using a small-scale flame test by cone-calorimeter

To determine the construction of OFC prior to OFC prototype manufacturing, analysis of LSZH compounds for outer sheath was examined at first using cone calorimeter (FTT Co., hereafter cone test) test (ASTM E-1354 [4][5]) to observe the flame blocking

function and char formation characteristics of them. The basic concept of observing char formation of LSZH compound is that char can suppress flame propagation by blocking evaporation of combustion gas from inner components. From several material tests, only two high effective LSZH compounds were chosen for small-scale flame testing which can present more detail ideas about OFC construction. Small-scale tests were performed according to cone test using OFC-construction-like-sample and main focus of test results is HRR(Heat Release Rate). After small scale testing, real OFCs were manufactured and tested according to IEEE383[6], IEC60332-1[7] and IEC61034-2[8].

2. Experiments

2.1 Test samples

Test samples are prepared for cone test. Figure 1 shows test apparatus and cross-section of test sample.

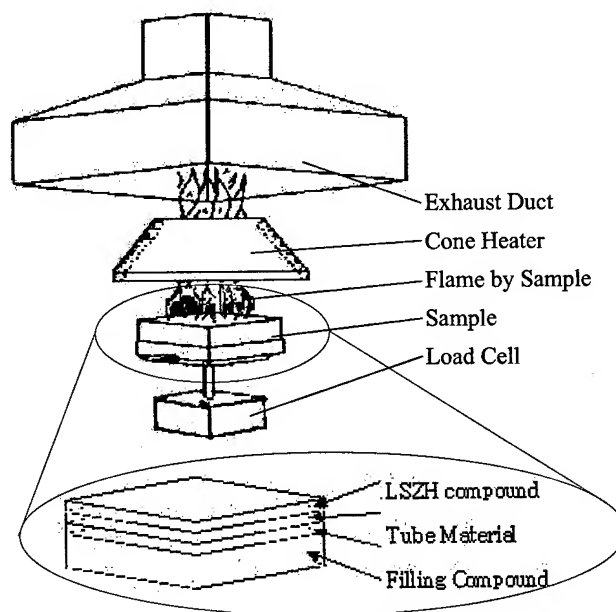


Fig 1. Test apparatus ; Cone Calorimeter

Figure 1 illustrates our test plan of small-scale test. Test Samples are simulation model of OFC to compare test results of samples with those of real OFC's. Prior to small-scale testing, setting of sample construction and material selection was based on OFC construction. Table 1 shows importance index of each components. Components over index 4 were discarded as non-effective to flame retardancy of OFC. We assumed that sample in Figure 1 represents OFC except some unnecessary components. In addition, we postulated that components arrays are same as real OFC construction. After tests, OFC construction for flame testing was determined, and actual OFC was manufactured and tested to verify the results of small-scale testing.

Table 1. Importance index of OFC components

Component	Index	Remarks	Remarks
CSM	4	N.A.	1:Very Effective 2:Effective 3:Moderate 4:less Effective 5:Not Effective
Tube	2	2 models	
Filling Compound	2	2 models	
Binding Tape	5	N.A.	
Yarn Member	3	N.A.	
LSZH Sheath	1	2 models	

2.1.1 LSZH Compound. To select LSZH sheath samples for small scale testing, EVA (Ethylene-Vinyl Acetate) copolymer used with ATH (Aluminum trihydrate, $Al(OH)_3$) and MDH (Magnesium hydroxide, $Mg(OH)_2$) additives ; 3 samples with EVA+ATH, 3 samples with EVA+MDH. During flame testing by cone calorimeter, they showed 2 types of char formation. One has relatively strong char shape (they remain their shape during and after cone test) and the other has weak shape (they were collapsed during cone test). Figure 2 and Figure 3 shows HRR and SEA (Specific Extinction Area) of all the tested samples respectively. HRR value from Figure 2 and time to ignition from Table 2 of LSZH compound sample 'A (EVA+ATH)' and 'F (EVA + MDH)' showed relatively the highest and the lowest value. On the contrary, it was very difficult to observe difference for the SEA value from Figure 3. So, we are mainly focused on HRR value from cone calorimeter and material composition (additives) to select samples for OFC construction. Detail values are listed in Table 2.

Table 2. HRR of LSZH compound

Sample	A	B	C	D	E	F
HRR[KW/m ²], peak	133.9	246	169	217	162.8	292.6
HRR[KW/m ²], 3min	120.7	195	133	140	129.9	206.1
HRR[KW/m ²], avg	112.4	161	119	133	119.4	187.8
SEA[m ² /kg], peak	549.2	435	522	623	826.4	558.3
SEA[m ² /kg], avg	217.1	324	218	307	189.9	262
Time to ignition[sec]	57	35	48	58	56	43
Material Composition	EVA + ATH	EVA + ATH	EVA + ATH	EVA + MDH	EVA + MDH	EVA + MDH

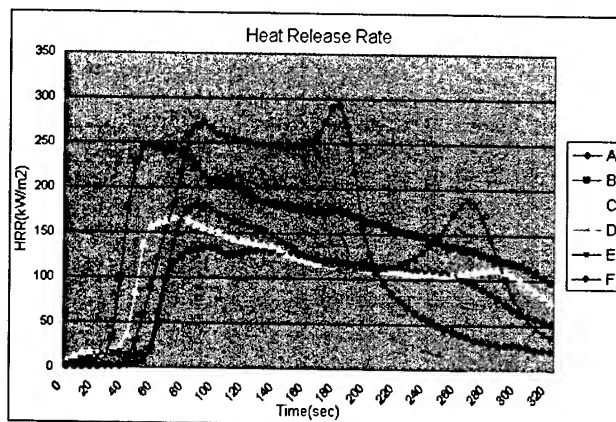


Fig 2. HRR of LSZH compound

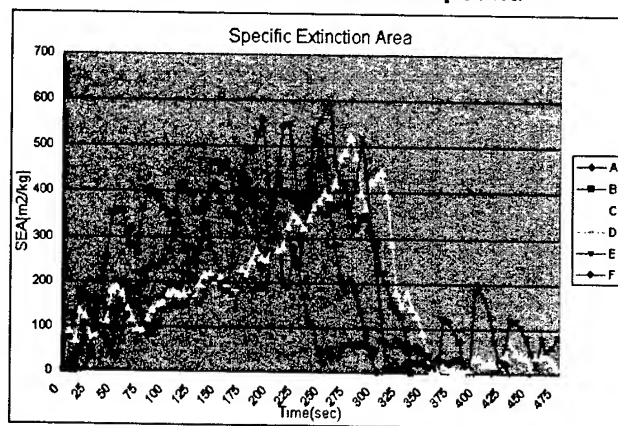


Fig 3. SEA of LSZH compound

2.1.2 Filling Compound and Tube. Materials for tube and filling compound in Table 3 are based on flame retardant properties.

Table 3. Filling compound and Tube material

Items	A	B
Filling Compound	Less flammable	Highly flammable
Tube Material	UL 94 HB	UL 94 V-0

2.2 Small-scale test sample

Table 4 shows samples for small-scale test according to material types. As showed in Table 4, sample #3 shows highly flame retardant characteristics from their material combination – less flammable filling compound + UL 94 V-0 tube material + LSZH compound type 'A' -. On the contrary, sample #6 shows poor flame retardant characteristics when compared with sample #3. Their flammability indexes are sorted according to their material combination. We thought that the function of filling compound is more weighted than tube material. From Table 1, the most important component is LSZH sheath. All the samples were tested by cone calorimeter.

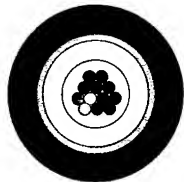
Table 4. Test Samples construction

Sample	Filling Compound	Tube	LSZH Sheath	Flame Retardancy
#1	A	A	A	Good
#2	A	A	F	Normal
#3	A	B	A	Excellent

#4	A	B	F	Normal
#5	B	A	A	Normal
#6	B	A	F	Poor
#7	B	B	A	Good
#8	B	B	F	Normal

2.3 OFC Design

After small-scale testing, OFCs were manufactured and tested by IEEE383, IEC60332-1 and IEC61034-2. Figure 4 shows OFC design and Table 5 describes cable construction.



LSZH Central L/T Cable

- Fiber Count : 12 fibers
- Cable Outer Diameter : 7.0mm
- Cable Weight : 65kg/km

Fig 4. OFC Construction

Table 5. Test Samples construction

Sample No.	#1	#2	#3	#4	#5	#6	#7	#8
Filling Compound	A	A	A	A	B	B	B	B
Loose Tube	A	A	B	B	A	A	B	B
Outer sheath	A	F	A	F	A	F	A	F

3. Test Results

3.1 Small-scale test

3.1.1 Cone test results

LSZH compound in Table 6 and Figure 5~7 shows test results of small-scale flame testing. Based on HRR value, THR (total heat release) in Table 6, Figure 5 and Figure 6, the best material combination to flame retardancy is sample #3 and #7. Sample #3 and #7 showed lower peaks, average HRR values, compared with other samples. Besides, HRR value, time to ignition value also shows similar results as like HRR value. Ignition time was checked without igniter because of sample height and test conditions. As like an HRR value, sample #3 and #7 have longer ignition times that indicates that they can suppress flame propagation. Even though they did not show big difference by SEA value, TSR (total smoke release) value shows that sample #1 and #5 shows the best characteristics to smoke generation. To match small-scale test result to OFC, their effects and interactions were analyzed by Minitab™ in Figure 8.

Table 6. Test Samples construction

Product	#1	#2	#3	#4	#5	#6	#7	#8
HRR, peak [KW/m²]	273	364	188	415	283	507	238	524
HRR, 3min [KW/m²]	201	271	168	285	180	315	187	337
HRR, avg. [KW/m²]	153	210	117	182	151	246	152	275
SEA, peak [m²/kg]	521	675	628	768	622	721	522	652
SEA, avg. [m²/kg]	269	393	382	376	277	407	283	364
Time to ignition[sec]	56	82	98	72	83	71	136	71

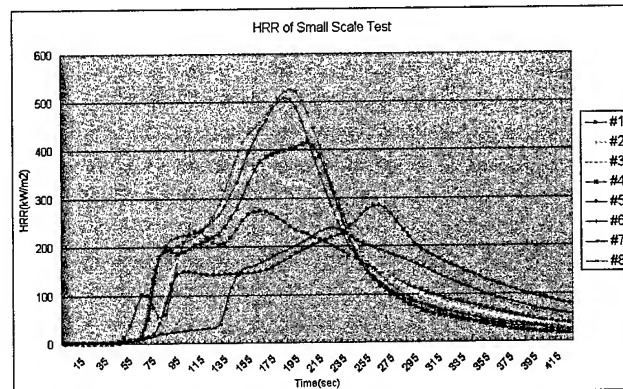


Fig 5. HHR of small-scale test

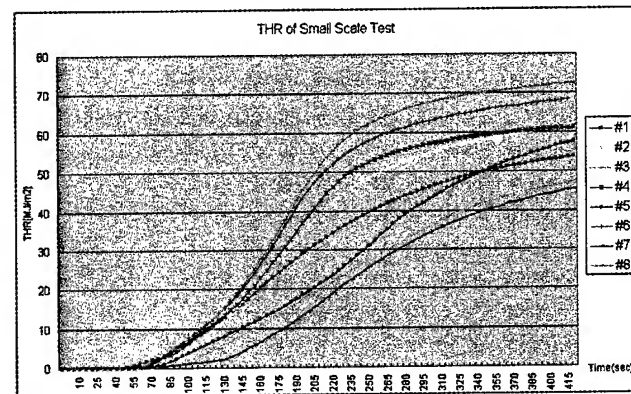


Fig. 6. THR of small-scale tests

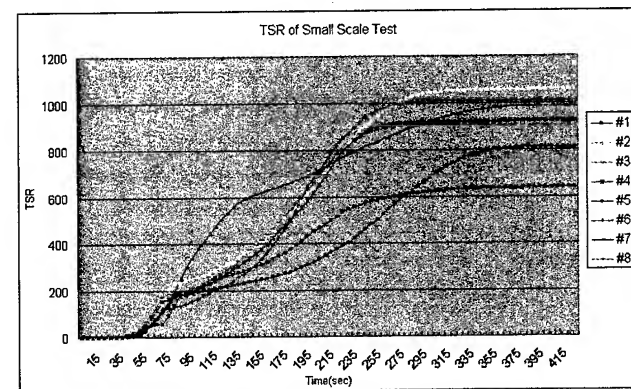


Fig. 7. TSR of small scale test

3.1.2 Char formation characteristics

They showed two trends

- Maintaining char during and after cone test
- Collapse of char during test.

Figure 9 shows two types of char shapes after small-scale test. Sample #3 has good char shape and has strong formation compared with sample #4. Their HHR values also indicate that char formation and keeping characteristics play of LSZH compound plays an important role during fire conditions. They block flame propagation to another parts of OFC and reduces additional effects.

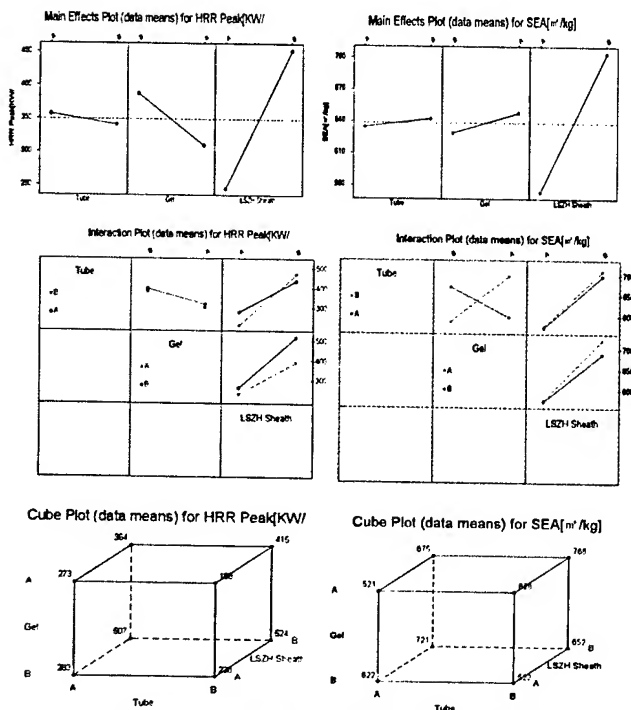


Fig 8. Minitab™ plots of small-scale flame testing (Main-effects, Interaction, Cube Plot)



Fig 9. Char shapes of sample #3 and #4.

3.2 OFC flame testing.

After small-scale flame testing, OFC flame testing was conducted. Their constructions are according to Figure 4 and Table 5 and test results are listed at Table 7.

Table 7. Flame testing results of OFC

OFC type	#1	#2	#3	#4	#5	#6	#7	#8
Char Height accord. to IEEE 383 [Unit:mm]	350	770	300	750	430	890	450	860
Char Length accord. to IEC332-1 [Unit:mm]	110	200	95	200	130	260	150	190
Smoke Density accord. to IEC6034-2 [Unit:%]	88	79	89	84	87	84	88	83

- IEEE 383 vertical tray test ;
- maximum char height is 890mm of sample #6, but that fully

complies requirements.

- sample #3 showed the best result : 300mm char height.
- shows similar results with small-scale test

- IEC 60332-1 single wire, vertical flame test ;
-the maximum height of char is 260mm and that fully complies requirements.
- sample #3 showed the best result.
- shows similar results with small-scale test
- IEC 61034-2 Smoke density test (3 meter cube test)
- minimum smoke density is 79% which complies requirements.
- all the eight samples showed only a little difference between them.
- cannot find difference between tested samples.

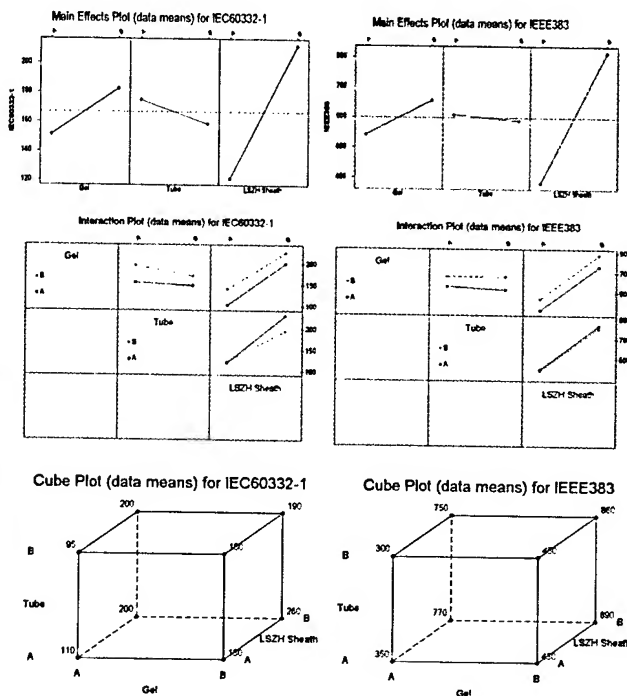


Fig 10. Minitab™ plots of OFC flame testing (Main Effects, Interactions, Cube Plot)

3.3 OFC mechanical test

Tests were conducted according to Telcordia GR-20-CORE, GR-409-CORE and IEC 811. They fully complies requirements.

4. On going research

From the test results described in above work, exact prediction of flame retardancy of OFC by small-scale testing is difficult, because OFC test was conducted to limited cable sample. That means that the amount of sample is too small to analyze quantitatively. To make prediction more precise and quantitatively effective, sample amounts and the number of test should be large enough to analyze. We are now getting more test results to make small-scale testing precise.

5. Discussion

Analyzing Minitab™ graphs of small-scale tests (Figure 8) and OFC flame tests (Figure 10) shows the relationships between them. When comparing plots of Minitab™ - main effect plots, interactions plots and cube plots -, those plot showed similar shapes. It proposed that they have similar functions and characteristics. This proves that simulation test using OFC construction like samples have similar flame retardant behaviors and can make prediction possible. Among three factors, function of LSZH compound is larger than other factors such as tube material and filling compound. Therefore, a proper selection of LSZH compound type decides the most portions of flame retardant properties. Even though small-scale test shows similar characteristics of OFC, it is very difficult to predict complex OFC construction. But, small-scale test can provide more useful information about flame retardant characteristics of OFC before manufacturing OFC.

Regarding smoke generation characteristics of OFC, it is very hard to say that small-scale test represents OFC. But from figure 11, there are some similarities between them although they did not match exactly. We assumed that test result of TSR and smoke density is not accurate because they were not analyzed quantitatively. So exact assumption of smoke characteristics of OFC is very difficult to deduce but lots of test can make smoke density prediction possible even though there are interactions between materials. So, smoke generation characteristics shall be studied continuously and different way of test shall be developed.

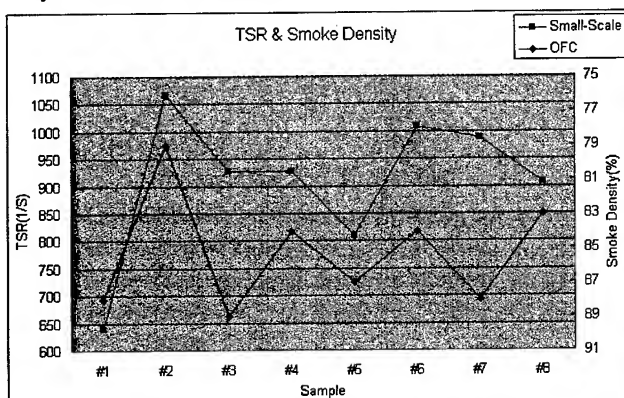


Figure 10. TSR and Smoke Density Comparison

6. Conclusions

Small-scale flame test of OFC-simulated sample can predict the behavior of flame properties of OFC. OFC construction applying small-scale test results showed good flame retardant characteristics and other mechanical/environmental requirements. Eventually small-scale test can make OFC design process simple and cost-effective. Even though small-scale test can give some information about flame retardant characteristics of OFC, more detail study to OFC construction and material selection are required.

7. References

- [1] Dohyun Park, Myeongjin Ahn, Sangcheol Kim, Gunjoo Lee, The synergistic effect of MDH and ATH on flame retardation

and smoke density suppression, *International Wire and Cable Symposium*, 409-414 (2001).

- [2] S.J Grayson, S G Upton. Fire Testing Technology, Predicting the fire performance of products from bench scale fire tests, *Flame retardants*, 15-26, 2000.
- [3] Lai Pinkg Artingstall, Joe Preston, Peter Salthouse, Dudley Sawyer, An innovative breakthrough in the fire retardancy of halogen free cable sheathing materials, *International Wire and Cable symposium*, 433-438(2000).
- [4] ASTM E-1354, Standard test method for heat and visible smoke release rates for materials and products using an oxygen consumption calorimeter, ED 2, 2002, *American Society for Testing and Materials*.
- [5] V.Babrauskas, and S.J.Grayson, Heat release in fires, Elsevier Science Publishers, New York, 1992.
- [6] IEEE 383, IEEE Standard for type test of class IE electric cables, field splices, and connections for nuclear power generating stations. 1992, *Institute of Electrical and Electronics Engineers*.
- [7] IEC 60332-1, Tests on electric cables under fire conditions - part 1. Test on single vertical insulated wire or cable, 1993. *International Electrotechnical Commission*.
- [8] IEC 61034-2, Measurement of smoke density of cables burning under defined conditions - Part 2. Test procedure and requirements. 1997. *International Electrotechnical Commission*.

8. Authors



Hosoon Lee
SAMSUNG Electronics Co., Ltd.
#94-1, Imsoo-Dong Gumi-City, Kyug-Buk, Korea.
Hosoon.lee@samsung.com



Eunsong Um
SAMSUNG Electronics Co., Ltd.
#94-1, Imsoo-Dong Gumi-City, Kyug-Buk, Korea.
Eunsong.um@samsung.com



Jungho Kong
Hanwha Chemical R&D Center
#6, Shinsung-Dong, Yusung0-Gu, Daejeon-City, Korea.
Jhkong@hanwha.co.kr

Nanocomposites as a New Class of Flame Retardants

Dr. Günter Beyer

Kabelwerk Eupen AG

B-4700 Eupen, Belgium

+32 87 59 70 00 · guenter_beyer@eupen.com

Abstract

Flame retardant nanocomposites are synthesized by melt-blending ethylene-vinyl acetate copolymers with modified layered silicates as nanofillers. Thermogravimetric analysis performed under air demonstrates a clear increase in the thermal stability of the layered silicate-based nanocomposites. A cone calorimeter was used to investigate fire hazards. The nanocomposites cause a large decrease in heat release. The char formation is the main important factor for the improvement and its function is outlined. Further improvements of the flame retardancy by combinations of nanofillers and traditional FR-additives on basis metal hydroxides are also studied. The nanocomposites based on nanofillers and ATH can be used as very efficient systems for flame retardant cables. The corresponding results are outlined for a coaxial cable fulfilling the UL 1666 riser test.

Keywords

Cables; wires; nanocomposites; flame retardancy; cone calorimeter; heat release; thermogravimetric analysis; char formation; layered silicates; UL 1666 riser test; aluminium trihydrate; coaxial cable; fire hazards

1. Introduction

Fire hazards are mainly the result of the combination of different factors including

- ◆ ignitability
- ◆ ease of extinction
- ◆ flammability of the generated volatiles
- ◆ amount of the heat released on burning
- ◆ rate of heat release
- ◆ flame spread, smoke obscuration and
- ◆ smoke toxicity.

The most important fire hazards are [1]:

- ◆ heat
- ◆ smoke and
- ◆ toxic gases

A high rate of heat release causes a fast ignition and flame spread. It controls also the fire intensity and is therefore much more important than ignitability, smoke toxicity or flame spread. The time to escape available for fire victims is also controlled by the heat release rate. The smoke production is a further important fire hazard. People get disoriented in the dark smoke and therefore they cannot exit unless they see. On the other side the fire fighters have severe problems to rescue people in dark surroundings.

The acute toxicity of fire gases is mainly controlled by the carbon monoxide content. CO is responsible for over 90 % of people killed by fires [2].

Each year about 5000 people are killed by fire in Europe and more than 4000 people in the USA. The direct property losses are roughly 0,2 % of the gross domestic product and the total costs of fires are around 1 % of the gross domestic product [3].

Therefore it is important to develop well designed flame retardant materials to decrease the fire hazards indicated.

Polymers are used in more and more fields of applications and specific mechanical, thermal and electrical properties are required. One further important property is the flame retardant behaviour of the polymers, which can be fulfilled traditionally by the following routes:

- Use of intrinsically flame retardant polymers like PVC or fluoropolymers.
- Use of flame retardants like aluminium trihydrate, magnesium hydroxide, organic brominated compounds or intumescent systems to prevent the burning of polymers like PE, PP, PA or other polymers.

These flame retardant systems show in some cases considerable disadvantages:

- The applications of aluminium trihydrate (ATH) and also magnesium hydroxide require a very high portion of the filler within the polymer matrix; filling levels of more than 60 weight-% are necessary to achieve a suitable flame retardancy e.g. for cables & wires. Clear disadvantages of these filling levels are the high density and the lack of flexibility of the end products, the low mechanical properties and the problematic compounding and extrusion steps.
- In Europe there are at least reservations about a general use of brominated compounds as flame retardants.
- Intumescent systems are expensive and the electrical requirements can restrict the use of these products.

A new class of materials, called nanocomposites, avoids the outlined disadvantages of the traditional flame retardant systems. Generally the term "nanocomposite" describes a two-phase material with a suitable nanofiller (usually a modified layered silicate) dispersed in the polymer matrix at a nanometer (10^{-9} m) scale.

2. Nanocomposites properties

Compared with virgin polymers the corresponding nanocomposites show tremendous improvements; the content of the modified layered silicates is often ranged between just 2 weight-% and 10 weight-%.

The following list indicates some of the most important improved properties:

- Improvements of mechanical properties like tension, compression, bending and fracture
- Improvements of barrier properties like permeability and solvent resistance
- Improvements of optical properties
- Improvements of ionic conductivity

A review discusses these improvements [4].

Other highly interesting properties of polymer-layered silicate nanocomposites concern their increased thermal stability and ability to promote flame retardancy at very low filling levels. The formation of a thermal insulating and also low permeable char to volatile combustion products caused by a fire is responsible for these improved properties [5-8]. The low filler contents in nanocomposites for the drastic improvement in thermal stability is highly attractive for the industry because the end-products can be made cheaper and easier to process.

3. Experimental

3.1 Materials

A commercial available layered silicate based on montmorillonite modified by dimethyl-distearylammonium cations from Süd-Chemie/Germany was used as nanofiller.

Ethylene-vinyl acetate (EVA) copolymers (Exxon's Escorene types) with different weight-% vinyl acetate were used in this study. Such types of copolymers have demonstrated their ability to promote nanocomposite formation by melt blending with nanofillers [9-11].

Aluminium trihydrate ATH (Martinal OL 104 LE) from Martinswerke GmbH/Germany was used.

3.2 Properties of EVA nanocomposites

Depending on the nature of the filler distribution within the matrix, the morphology of the nanocomposites can evolve from the so-called intercalated structure with a regular alternation of the layered silicates and polymer monolayers to the exfoliated (delaminated) structure with the layered silicates randomly and homogeneously distributed within the polymer matrix. The easiest and technically most attractive way to produce these types of materials is kneading the polymer in the molten state with a modified layered silicate such as montmorillonite. The native Na^+ interlayer cation within the silicate has been exchanged by a quaternary alkylammonium cation. The modified filler is called a nanofiller and is much more compatible with the polymer matrix.

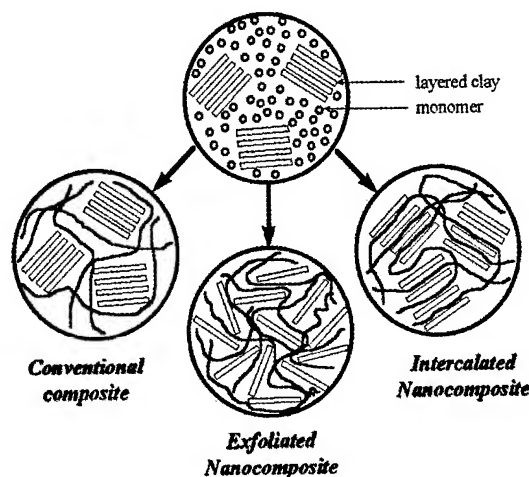
Mixing was done on several compounding machines. Rolling mill and internal mixer as discontinuous compounding machines were used; a BUSS ko-kneader (with a rotating and simultaneously oscillating screw, 11 L/D, 46 mm screw diameter) was used as a continuous compounding machine. Processing temperature of 160°C was used for all the different compounding machines.

Informations on the nanocomposite morphology [figure 1] have been obtained by transmission electron microscopy (TEM) and X-ray diffraction (XRD) observation. Exfoliated silicate sheets are observed together with small stacks of intercalated montmorillonite. This structure may be described as a semi-intercalated semi-

exfoliated structure that does not change principally with the vinyl acetate content of the EVA matrix, even a larger amount of stacks are observed for EVA with lower vinyl acetate contents [10]. There are also no great differences within the morphology of the nanocomposites related to the different compounding routes.

Figure 1

Microcomposites & intercalated and exfoliated morphologies of nanocomposites



4. Results

4.1 Thermal stability

Thermogravimetric analysis (TGA) is widely used to characterize the thermal stability of a polymer. The mass loss of the polymer due to volatilization of products generated by the thermal decomposition is monitored as function of a temperature ramp. Non-oxidative decomposition occurs when the heating of the material is done under an inert gas flow like helium or nitrogen while the use of air or oxygen allows to follow the oxidative decomposition reactions.

The experimental conditions of the degradation highly influences the reaction mechanism of the degradation. The thermal stability of EVA based nanocomposites was investigated [10] as partially intercalated and partially exfoliated structures independent of the EVAs used. TGA under helium (non-oxidative decomposition) and under air (oxidative decomposition) were investigated. EVA is known to decompose in two consecutive steps. The first one is identical to both oxidative and non-oxidative conditions. It occurs between 350 °C and 400 °C and is linked to the loss of acetic acid. The second step involves the thermal decomposition of the obtained unsaturated backbone either by further radical scissions (non-oxidative decomposition) or by thermal combustion (oxidative decomposition). In helium the EVA-nanocomposite has a negligible reduction in the thermal stability compared to the virgin EVA or the EVA filled with Na-montmorillonite (microcomposite). In contrast, when decomposed in air, the same nanocomposite exhibits a rather large increase in the thermal stability because the maximum of the second degradation peak is shifted 40 °C to higher temperatures while the maximum of the first decomposition peak remains unchanged [Table 1]. In this case the explanation for the improved thermal stability is the char formation occurring under oxidative conditions. The char acts as a physical barrier between the

polymer and the superficial zone where the combustion of the polymer is occurring. The results in Table 1 on the maximal temperatures at the main degradation peak for EVA nanocomposites demonstrate that obviously the optimum for the thermal stabilization is already obtained at a layered silicate level of 2,5 - 5,0 weight-%.

Table 1

Maximal temperature of the main degradation peak (DTG) in air, 20°C/min, for EVA and EVA-nanocomposites;

EVA: Escorene UL 00328 with 28 weight % VA

Nanofiller content (weight %)	Maximal temperature peak at the main degradation peak (°C)
0	452.0
1	453.4
2.5	489.2
5	493.4
10	472.0
15	454.0

4.2 Flammability properties

From an engineering point of view, it is important to know what hazards within a fire must be prevented and only then strategies for measurements and improvements can be developed. Extensive research at NIST (National Institute for Standards and Technology, USA) led to the important conclusion which allows significant simplification of the problem for hazards in fires: The heat release rate, in particular the peak heat release rate, is the single most important parameter in a fire and can be viewed as the "driving force" of the fire [12]. Therefore, today the universal choice of an engineering test for flame retardant polymers is the cone calorimeter. The measuring principle is the oxygen depletion with a relationship between the mass of oxygen consumed from the air and the amount of heat released.

The cone calorimeter is standardized as ASTM E 1354 and ISO 5660. In a typical cone calorimeter experiment the polymer sample (as a plate of 100 x 100 x 5 mm) in aluminium dishes is exposed to a defined heat flux (mostly 35 kW/m² or 50 kW/m²).

Simultaneously the properties "heat release rate", "peak of heat release", "time to ignition", "total heat released", "mass loss rate", "mean CO yield", "mean specific extinction area" etc. can be measured.

The flame retardant properties of the EVA nanocomposites have been determined using cone calorimetry under a heat flux of 35 kW/m² (Fig 2). Under such conditions, simulating a small fire scenario, the effect of the nanofiller is already observed for 3 weight-%. A decrease by 47 % of the peak of heat release as well as a shift towards longer times are detected for a nanocomposite containing 5 weight-% of the nanofiller when compared to the virgin matrix EVA. Increasing the filler content to 10 weight-% does not improve any more the reduction of the peak of heat release. As a decrease in the peak of heat release indicates a reduction of the burnable volatiles generated by the degradation of the polymer matrix, such drop clearly indicates the flame retardant effect due to the presence of the nanofiller and its "molecular" distribution

throughout the matrix. The flame retardant properties are further improved by the fact that the peak of heat release is spread over a much longer period of time. The flame retardant properties are due to the formation of a char layer during the nanocomposite combustion. This char acts as an insulating and non-burning material that reduces the emission of volatile products (fuel) into the flame area. The silicate layers of the nanofiller play an active role in the formation of this char but also strengthen it and make it more resistant to ablation.

Cone calorimeter experiments with a heat flux of 35 kW/m² also show that virgin EVA is completely burned without any residue. In contrast to the previous result an early strong char formation is found for the EVA nanocomposite within an analogous cone calorimeter experiment; but now this char is stable and does not disappear by combustion.

Finally, compared to the virgin EVA matrix, the nanocomposite burns without producing burning droplets (UL 94 vertical procedure) [14], a characteristic feature that furthermore limits the propagation of a fire. This is an important characteristic for products to be classified within the new Euroclasses regulating the flame retardancy classes in Europe.

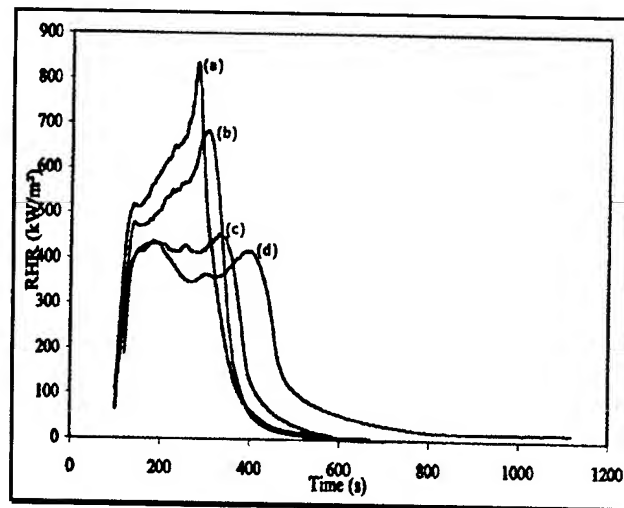


Figure 2

Rate of heat release vs. time measured with a cone calorimeter (heat flux: 35 kW/m²) for various EVA (Escorene UL 00328 with 28 weight-% vinyl acetate content) based materials :

- a) Virgin EVA and EVA with 5 weight-% of Nanomontmorillonite (microcomposite)
- b) EVA + 3 weight-% nanofiller
- c) EVA + 5 weight-% nanofiller
- d) EVA + 10 weight-% nanofiller

4.3 NMR-investigation and FR-mechanism

The degradation of EVA and EVA nanocomposites was investigated by solid phase CP - MAS - ¹³C - NMR spectroscopy. The principles and the measurement method are described in detail by Le Bras et al [16]. EVA (Escorene UL 00112 with 12 weight-% vinyl acetate content) and also a nanocomposite based on EVA (Escorene UL 00112 with 12 weight-% vinyl acetate content) with 5 weight-% of the nanofiller were irradiated within a cone calorimeter by a heat flux of 50 kW/m². Samples were taken out from heat flux

after 50, 100, 150, 200 and 300 s and the presence of EVA and the char formation was measured.

The following results are obtained [17]:

Before irradiation of EVA and EVA nanocomposite:

- ♦ 33 ppm => -CH₂ - by polymer backbone
- ♦ 75 ppm => -CH₃ by acetate group
- ♦ 172 ppm => -C=O by acetate group (small signal)

After irradiation of EVA:

- ♦ 50 seconds: New signals at 130 ppm (char: aromatics & polyaromatics) and 180 ppm (-C=O with beginning of oxidation), EVA signals present
- ♦ 150 seconds: no signals => no organic material present

After irradiation of EVA nanocomposite:

- ♦ 50 seconds: New signals at 130 ppm (char: aromatics and polyaromatics) and 180 ppm (-C=O with beginning of oxidation), EVA signals present
- ♦ 100 seconds: char-formation & EVA signals present
- ♦ 200 seconds: char-formation & EVA signals present
- ♦ > 300 seconds: no signals => no organic material present

Obviously the formation of nanocomposites clearly promotes char formation and delays the degradation of EVA.

4.4 Intercalation versus exfoliation

Often it is reported within the literature that exfoliation is the most effective structure for maximal enhancements of properties improved by nanocomposites. Therefore it was of interest to shift the ratio of mixed intercalated / exfoliated structure that is observed within EVA-nanocomposites [10] to the exfoliated structure. This was done by melt-compounding EVA (Escorene UL 00328) with 5 phr of the nanofiller on a twin-screw extruder. Two screw designs were used: one screw for maximal mixing using mixing elements and the second screw for maximal dispersion using kneading blocs. The screws were used from 300 to 1200 rpm. TEM and XRD demonstrate that for the highest shear rate (1200 rpm) and highest friction (second screw) the mixed structures are shifted to the exfoliated one. Cone calorimeter datas however show that there are no changes on the peak heat release rates for all the melt-compounded nanocomposites. Obviously the mixed intercalated / exfoliated structures within the EVA nanocomposites have already the maximal reduction in peak heat release rates.

5. Combination of the traditional filler

ATH with a nanofiller

To achieve typical flame retardancy for cables required by the most important international cable fire test (IEC 60332-3-24) [15] a ratio of 65 weight-% of ATH and 35 weight-% of a suitable polymer matrix like EVA must often be used for cable outer-sheaths [13]. Therefore the performances of two compounds were compared. Both compounds were prepared on a BUSS ko-kneader (46 mm screw diameter, 11 L/D). One compound was made by 65 weight-% ATH and 35 weight-% EVA Escorene UL 00328 and a second compound was made by 60 weight-% ATH, 5 weight-% of the nanofiller and 35 weight-% EVA Escorene UL 00328. Both

compounds were investigated by TGA in air and by cone calorimeter at 50 kW/m². TGA in air clearly shows the delay in the degradation by the small amount of nanofiller.

The char of the EVA / ATH / nanofiller compound created by the cone calorimeter is very rigid with only very few small cracks; but the char of the EVA / ATH compound is much less rigid (less mechanical strength) and with many big great cracks. This is also the explanation why the peak heat release rate in the case of the nanocomposite is reduced to 100 kW/m² compared to 200 kW/m² for the EVA / ATH compound. To obtain the same decrease for the peak heat release rate by the flame retardant filler ATH only, the content of ATH must to be increased to 78 weight-% within the EVA / ATH compound. The great improvements in flame retardancy by the nanofiller also opens the possibility to decrease the level of ATH within the EVA polymer matrix. To maintain 200 kW/m² as a sufficient peak heat release level, the content of ATH can be decreased from 65 weight-% to 45 weight-% by the presence of only 5 weight-% nanofiller within the EVA polymer matrix. The reduction in the total amount of these fillers results also in improved mechanical and rheological properties of typical EVA-based cable compounds.

6. Coaxial cable passing UL 1666 with a nanocomposite based outer sheath

There are many applications for indoor cables passing the riser test defined by UL 1666 with a 145 kW burner in a two story facility. This very severe fire test defines the following most important points of measurements:

- 12 feet maximum temperature of 850°F
- 12 feet maximum height for flames

For passing this fire test halogen cable compounds are often used. But more and more flame retardant non-halogen (FRNH) cables are requested by the market passing the riser test. Cables based on nanocomposites compounds demonstrate their promising performances for this fire test.

An example for FRNH cables passing UL 1999 is shown in figure 3. The outer sheath is based on a FRNH nanocomposite outer sheath with an EVA / ATH / nanofiller composition. The analogous FRNH coaxial cable is also tested with an outer sheath based on EVA / ATH. In both compounds the relation of polymer / filler was the same and table 2 indicates the results.

The improved flame retardant properties are due to the formation of a char layer during the nanocomposite combustion. This insulating and non-burning char reduces the emission of volatile products from the polymer degradation into the flame area and thus reducing the maximal temperature and height of the flames.

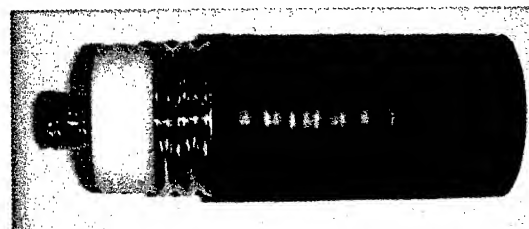


Figure 3

Coaxial cable (1/2") with an FRNH-nanocomposite based outer sheath

Table 2

**Fire performances of FRNH coaxial cables with
EVA / ATH and EVA / ATH / nanofiller outer sheaths**

UL 1666 requirements	EVA / ATH compound	EVA / ATH / nanofiller compound
maximal temperature at 12 feet: < 850°F	1930°F	620°F
maximal flame height: < 12 feet	> 12 feet	6 feet

7. Conclusion

The thermal properties of EVA are improved by very low loadings levels of a suitable nanofiller within the polymer matrix. For these EVA nanocomposites TGA in air shows a delay of the degradation; the peak of heat release measured by a cone calorimeter is dramatically reduced. Char formation in the cases of the nanocomposites is improved and responsible for the better flame retardancy. The results are also valid for EVA nanocomposites in combinations with metal hydroxides like aluminium trihydrate and opens the possibility for new flame retardant compounds for cables with reduced total filler contents.

A coaxial cable with an outer sheath based on flame retardant non halogen nanocomposites passes the UL 1666 riser test.

8. References

- [1] M. Hirschler, *Polymeric Materials: Science and Engineering*, Vol. 83, ACS Meeting August 2000, Washington, DC
- [2] V. Brabrauskas, *Fire and Materials*, 19, 1995, 205
- [3] G.C. Stevens, Conference "Flame Retardants 2000", London, Elsevier Applied Science
- [4] M. Alexandre, Ph. Dubois, *Materials Science and Engineering*, 28, 2000, 1
- [5] G. Beyer, *Polymer News*, November 2001
- [6] M. Le Bras, G. Camino, S. Bourbigot, R. Delobel (editors), *Fire Retardancy of Polymers: The use of Intumescence*, Royal Society of Chemistry, Cambridge, 1998, page 196 ff
- [7] J.W. Gilman, T. Kashiwagi, E.P. Giannelis, J.D. Lichtenhan, *SAMPE J.*, 1997, 4
- [8] J. Lee, T. Takekoshi, E.P. Giannelis, *Mater. Res. Soc. Symp.*, 457, 1997, 513
- [9] G. Beyer, M. Alexandre, C. Henrist, R. Cloots, A. Rulmont, R. Jérôme, Ph. Dubois, World Polymer Congress, IUPAC Macro 2000, 38th Macromolecular IUPAC Symposium, Warsaw, 2000

- [10] G. Beyer, M. Alexandre, C. Henrist, R. Cloots, A. Rulmont, R. Jérôme, Ph. Dubois, *Macromol. Rapid Commun.*, 22, 2001, 643
- [11] M. Zanetti, G. Camino, R. Thomann, R. Mülhaupt, *Polymer*, 42, 2001, 4501
- [12] V. Babrauskas, R.D. Peacock, *Fire Safety J.*, 18, 1992, 255
- [13] M.J. Herbert, S.C. Brown, Conference "Flame Retardants 1992", London, Elsevier Applied Science
- [14] UL 94, Test for flammability of plastic materials for parts in devices and appliances, 1966-10-00, Underwriters Laboratories Inc.
- [15] IEC 60332-3-24, Tests on electrical cables under fire conditions - Part 3-24: Test for vertical flame spread of vertically-mounted bunched wires or cables; Category C, 2000-10-00, International Electrotechnical Commission
- [16] Le Bras et al, *Polymer Degrad. & Stab.*, 64, 1999, 425
- [17] G. Beyer, 12th BCC conference "Flame retardancy of polymeric materials", 2001, Stamford, CT, USA



Dr. Günter Beyer
Kabelwerk EUPEN AG
B - 4700 Eupen

Günter Beyer joined Kabelwerk Eupen AG in 1984 and is responsible for the fire testing stations, material developments and qualification of new materials. He gained his PhD at the university RWTH Aachen / Germany in 1984 and has published more than 60 scientific papers mainly in the field of material science and flame retardancy of polymers. He has been invited for plenary presentations and as chairman on many international conferences. His main research interest for the moment is related to nano-structured flame retardant compounds.

The Characteristics of a Non-Halogen Flame Retardant Compound Using Advanced Thermoplastic Plastomer

Tong Chen*, Allen Hendrix

J. M. Huber Corporation, 251 Gordon Street, Fairmount, GA 30137

Todd Glogovski(1), Robert Butala(2)

Basell USA Inc.

(1) 2727 Alliance Drive, Lansing, MI 48910

(2) 800 Greenbank Road, Wilmington, DE 19808

*Contact for Correspondence

tel: 706-337-3243; fax: 706-337-3384; email: tchen@huber.com

Abstract

This paper investigates performance characteristics of a non-halogen, low-smoke flame retardant thermoplastic compound derived from soft polypropylene-based plastomers and magnesium hydroxide. Performance characteristics of this FR compound are examined from aspects of physical/mechanical properties, fire/flame characteristics, and processing characteristics. The ability to readily and uniformly incorporate Zerogen™ magnesium hydroxide into soft Catalloy Plastomers to achieve excellent FR performance, while maintaining viable material processing behavior is studied. The soft nature characteristic of Catalloy Plastomers and its thermoplastic rigidity impart controlled balance among toughness, low-temperature flexibility and achievable service temperature. The lower density of thermoplastic Catalloy Plastomers relative to other polyolefins also allows for reduced finished wire or cable weight. Results from this study show that soft Catalloy Plastomers along with Zerogen™ offers high performance compounds to the specialty wire and cable applications, such as automotive wires and communications cables where excellent flame retardancy/smoke characteristics and physical/electrical performance are critical to meeting application requirements.

Introduction

Wire and cable producers and end users are continuing to demand superior compound materials that are not only cost/performance effective but meet increasingly stringent industrial and regulatory standards or initiatives. Low-smoke, zero-halogen polyolefin compounds have received broad attention as one of the advanced technology materials that can provide the desired application performance including material handling while being health and environmentally sound. Enhanced wire and cable flame retardancy and flexibility are of keen interest to the end users. This is particularly true for the automotive wire and cable insulation and jacketing applications where plasticized PVC and polyethylene/EVA are among the main polymers currently used. PVC, while inherently a better fire retardant polymer than polyolefins, is always a source of health and environmental concerns due to potentials for release of chlorine-containing chemicals and plasticizer bleed-out. Polyethylene and/or EVA, on the other hand, has certain limitations in incorporating high levels of metal hydrate flame retardants to achieve necessary fire performance while still retaining adequate mechanical properties. In

comparison, polypropylene has an apparent performance advantage over polyethylene/EVA for PP's inherently higher material strength and lower density, which enable PP compounds to maintain desired physical properties even with high flame retardant loadings.

Significant technical effort has been directed to the advancement of reactor based soft plastomers in recent years. This push has been driven by market needs to produce lower cost, higher performance olefin based plastomers. The automotive market is leading this advancement, by such applications as automotive wires where a switch from traditional PVC compounds to polyolefins based products is ongoing.

Advancement in catalysts and reactor technologies in the polyolefins family of resins has resulted in the development of numerous new polyolefins plastomers. This paper provides insights into unique wire and cable performance features for the compounds based on a new propylene-ethylene plastomers, utilizing new catalyst developments by Basell, in combination with a surface-coated and fine particle sized magnesium hydroxide by J. M. Huber. The polyolefins plastomers are ethylene-propylene plastomers contained in a hard PP based network. The combination of a relatively high melting polypropylene resin and a low crystalline plastomer provides a unique combination allowing flexibility in compounding high metal hydrate levels to meet mechanical, fire and electrical requirements for automotive wire applications. Use of surface-coated Zerogen™ magnesium hydroxide provides the wire and cable products with low smoke, excellent FR, good balance of mechanical and thermal/dimensional properties, and good electricals. It is important to note that the low-smoke, zero-halogen soft polypropylene compounds discussed in this paper can have broad applications beyond automotive wire and cable.

Materials

Zerogen™ 50SP, made by J. M. Huber Corporation, is a magnesium hydroxide treated with coupling silane and has average particle size of 0.7 microns and BET surface area of 6.5 m²/g.

Soft thermoplastic polyolefins plastomers (such as Hifax Q100F and Hifax 7334) are made by Basell's Catalloy process. The glass transition temperature of the Catalloy process resins can be varied from -26 C to -47 C by controlling the type and ratio of comonomer used to produce the soft phase of the resin. An intrinsic

property comparison of soft plastomers against PVC is provided in Table 1

Table 1. Comparison of Catalloy Hifax Grade Ethylene-Propylene Plastomers vs. Plasticized PVC

	Hifax Q100F	Hifax 7334	Plasticized PVC
Density, (g/cc)	0.88	0.87	1.20
Hardness, Shore A	85	75	75
1% Secant Modulus, (Mpa)	80	20	14
Tensile Strength, (Mpa)	20	11	11
Strain to Break, %	750	750	400
Heat of Fusion J/g	46	16	-

Results and Discussion

1. Catalloy soft thermoplastic plastomers

Hifax 7334 is a soft plastomer containing a polypropylene hard matrix and an EP soft matrix. Its high molecular weight and low crystallinity facilitate the incorporation of oil, and additions of up to 20% oil can be achieved without modifications to the polymer or compound. This will provide softness down to a Shore A hardness of 55 and tensile modulus down to ~9 MPa for improved material flexibility. Table 2 provides a summary of soft polymer based on Hifax 7334. It is interesting to note that a 10% addition of oil reduced Shore A hardness of Hifax 7334 by 10 units with a corresponding reduction in tensile strength and stiffness.

Table 2. Intrinsic properties of oil-modified Hifax 7334

Sample ID	Hifax 7334	31-3	31-4	47-2	47-3
Oil %	0	10	20	30	40
Hardness Shore A	75	65	55	45	40
Tensile Modulus Mpa	19	14	9.0	3.7	2.8
Tensile Strength Mpa	20	12	9	13	10
Strain @ Break %	750	850	800	1000	900

Figure 1 shows SEM graphs of two Catalloy soft plastomers. Dark and gray areas indicate amorphous EP phases, light areas indicate crystalline PP phase. 7334 shows more of a co-continuous morphology compared to Q100F. The PP-based plastomer polymers have uniform-sized soft domains dispersed in high modulus PP continuous phase, providing higher melting point with good material flexibility relative to PE, as shown by Figure 2 that compares Catalloy PP vs. PE on modulus measured on film samples.

Figure 3 shows the relative performance of XLPE, PVC and PP Plastomer with respect to thermal cut resistance as a function of temperature. The PP-based compound performs similarly to XLPE

and is better than that of PVC. As temperatures approach the melting point of PP (162 C), the XLPE provides better thermal cut resistance. Compared to PVC and XL-PE or PVC, PP has more desirable thermal indentation characteristics in the temperature range of -40 to 145 C. This should make a properly designed PP a better material for wire and cable applications where service temperature is always a performance consideration.



Figure 1. SEM of Catalloy soft plastomers

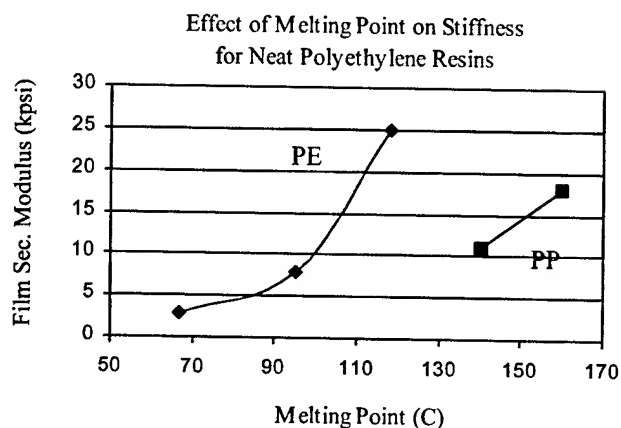


Figure 2. Melting-modulus characteristics of Catalloy soft plastomer vs. PE

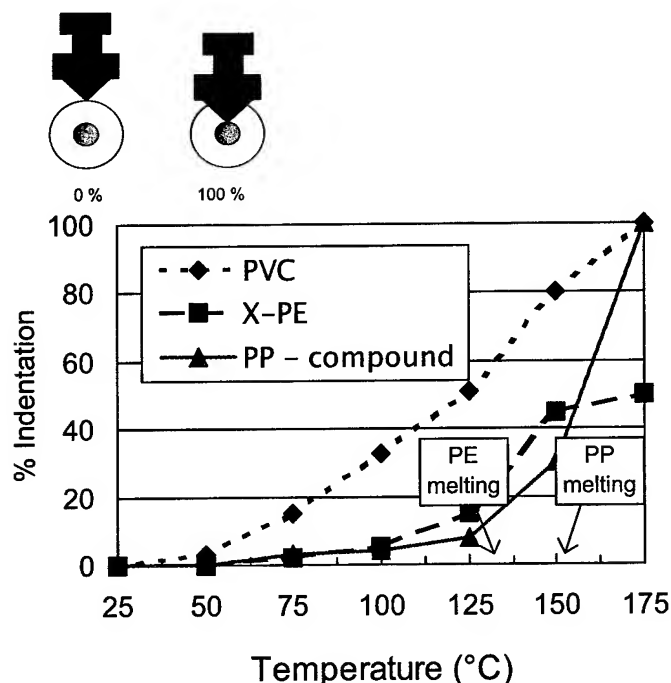


Figure 3. Indentation of PP vs. XL-PE and PVC

2. Flame retardant soft thermoplastic compositions containing magnesium hydroxide

The inherent flame retardant quality and flexibility of PVC make it a natural fit for flame retardant wire and cable applications. However a trend to eliminate halogens or chlorine in specific wire and cable markets has resulted in the development of more advanced halogen-free polyolefins. The main halogen free technology utilized in North America for low voltage, thin wall, automotive wire and cable is crosslinked polyethylene (XLPE) utilizing a peroxide curative. In order to achieve necessary flame retardancy this resin is filled with a non-halogen flame retardant, typically ATH or aluminum trihydrate at levels between 100 and 150 phr. The wire manufacturer will extrude the flame retardant insulation onto the conductor below the activation temperature of the peroxide and then post cure or crosslink the wire. A common method to cure XLPE is by exposing the insulated or jacketed wire or cable to a continuous vulcanizer involving high-pressure steam (250 psi) yielding a temperature of 200 C. Crosslinking of the polyethylene is necessary to achieve the elevated heat performance and toughness required for low voltage automotive wire. In Europe, radiation (e-beam) or silane curative technology is utilized offering its own set of features. The specification followed for automotive wire in North America is SAE J1678. The specification provides requirements for abrasion, flammability, hot knife penetration, heat aging, -40 C winding, dynamic bending, and salt water immersion at elevated temperature.

Polypropylene-based TPO resins offer an alternative to XLPE for low voltage automotive wire. Polypropylene-based TPO Resins provide a higher melting point, eliminating the need for a complex and expensive crosslinking step. Due to higher melting characteristics of PP based plastomers, magnesium hydroxide ($Mg(OH)_2$) is utilized instead of ATH to impart flame retardancy. The higher decomposition temperature of $Mg(OH)_2$ is necessary for production and fabrication of polypropylene-based resins. As with XLPE, high loading of flame-retardant is required to achieve

flammability targets. At those high $Mg(OH)_2$ loadings, proper surface treatment of FR is always vital to assuring good dispersion of hydrates in polymer. Surface treating $Mg(OH)_2$ also enhances greatly the compound performance such as compounding operation and physical properties. These performance features can benefit compound manufacturers and wire and cable producers as well as application end users.

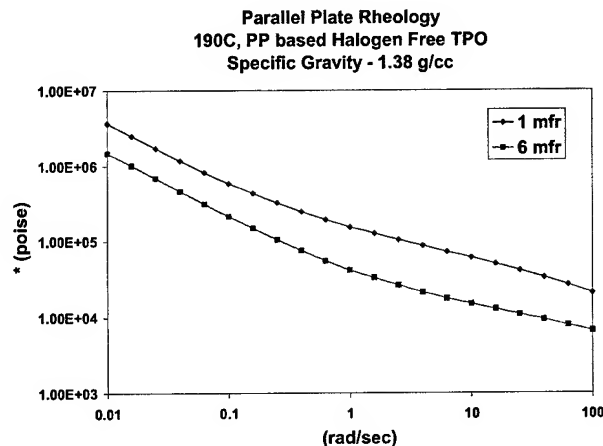


Figure 4a. Low shear rheology

In order to incorporate high levels of flame retardant (100 – 150 phr), high levels of plastomer or low crystallinity are required for the base resin. *Hifax Q100F* is a low crystalline, highly amorphous PP-based plastomer. Using *Hifax Q100F* as the base resin, 60% by weight of silane-treated ($Mg(OH)_2$) was compounded into EXP731 and EXP732. EXP731 has a 1.0 melt flow rate and EXP732 has a 6 melt flow rate.

Figure 4 shows low-shear rheological measurements of EXP731 and EXP732 compounds containing ~60% of treated $Mg(OH)_2$. It is interesting to note that $\tan \delta$ or the ratio of elastic modulus to loss modulus for the two filled compounds behaves quite differently. Increasing MFR delays peak $\tan \delta$ while increasing the maximum $\tan \delta$. By selecting right polymers with appropriate MFR or molecular weight, one can control the modulus response, therefore the compound performance.

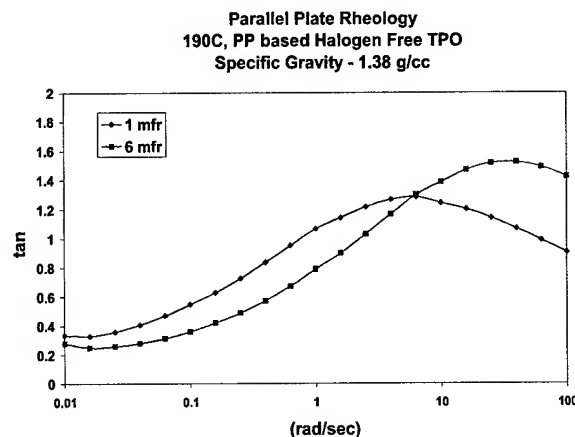


Figure 4b. Low shear rheology

In order for a semi-crystalline polyolefin based resin to impart similar thermoforming characteristics as PVC, some level of melt elasticity is required. Without modifications to the polyolefin plastomer, an abrupt change in rheological behavior would occur at the crystalline melting point or transition temperature of the polymer. This would result in an extreme reduction in stiffness or plastic deformation. Melt elasticity is provided by increasing the network structure of the polymer through use of higher molecular weight, branched, or more entangled polymers.

Improved melt elasticity can be achieved with *Hifax* Q100F through small additions of acrylate coagents cured with peroxide. Coagents provide the saturated EP plastomer in *Hifax* Q100F the ability to crosslink. The coagents utilized affect only the state of cure and, depending on the polymer, they form a crosslinked structure based on ionic and/or covalent bonds. Ionic bonding will provide low tan delta and good fatigue resistance. Small additions of coagents to *Hifax* Q100F will reduce the tan delta at 0.01 radians/second at 180 C from approximately 3.0 to 0.6. This behavior is reflective of a dramatic increase in melt elasticity,

3. Flame and smoke properties

Flame retardant performance is generally increased with increasing $Mg(OH)_2$. Figure 5 indicates such relationship as measured by Limiting Oxygen Index. The increased $Mg(OH)_2$ loading is shown by increased compound density. Our test results also show that soft thermoplastic plastomers containing 60% by weight of $Mg(OH)_2$ can achieve the UL 94 V0 rating at 1/16" thickness.

Compared to XL-PE/EVA, the soft PP has slightly better smoke characteristics as shown by Figure 6, both non-flaming and flaming mode. This difference is probably related to the more reactive chemical nature of EVA polymer chains vs. EP-PP plastomers.

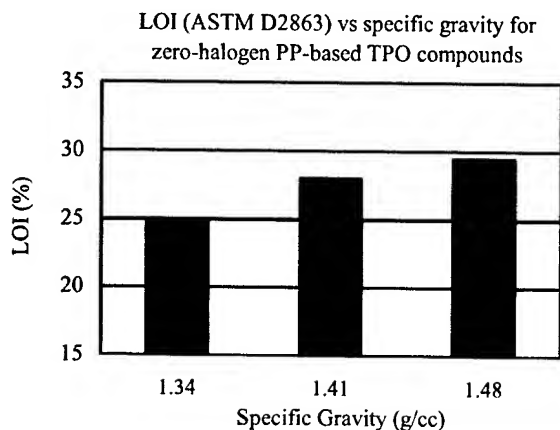


Figure 5. Limiting Oxygen Index vs. compound

4. Mechanical and thermal properties

One of the main concerns with using non-halogen flame retardants is the high loading needed to meet FR performance requirements. As a result, there is reduction of physical properties such as tensile elongation. Figure 7 displays such effect of reduced tensile elongation with increasing $Mg(OH)_2$ use, reported in a form of compound density. However, use of surface-coated $Mg(OH)_2$ can minimize the physical property loss. In addition, choosing specific surface treatment for a given polymer system and application is always critical to achieving desired wire and cable performance.

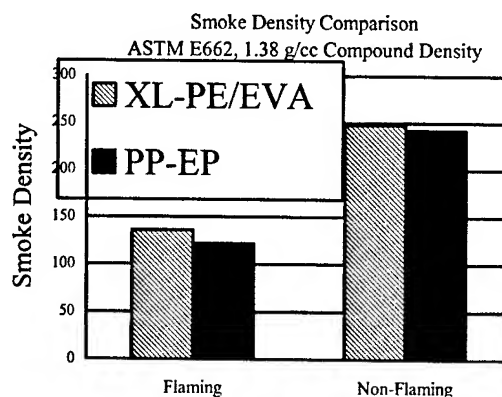


Figure 6. Smoke density comparison of soft PP vs. XLPE/EVA

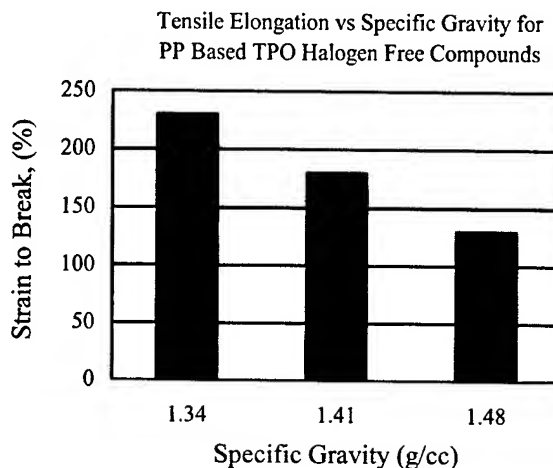


Figure 7. Elongation at break vs. soft PP compound density

Table 3 lists some of key mechanical property measurements comparing two FR compounds using a same amount of $Mg(OH)_2$, one is EVA and another soft thermoplastic plastomer. The soft PP is

Table 3. Mechanical property comparison of $Mg(OH)_2$ -filled Catalloy PP vs. EVA

Property	Unit	EVA compound	Catalloy PP compound
MFR	g/10 min	0.52	0.55
Density	g/cm ³	1.4	1.4
Tensile strength	MPa	13	13.4
Elongation at break	%	20	120
Tensile modulus	MPa	402	430
Taber abrasion	% wt loss	1.05	1.26
Izod impact	kg/m ²	18	20
Brittleness temp	C	11	-24
Vicat	C	68	112

shown to have improved mechanical properties over EVA, particularly tensile elongation at break and low temperature brittleness, both having important value to wire and cable performance. The improved ductility and toughness demonstrated by Catalloy PP is attributed to its unique morphological characteristics where soft EP particles dispersed in the hard matrix act as energy dampers as well as providing good flexibility/stiffness balance.

The $\text{Mg}(\text{OH})_2$ -filled soft PP compound also shows a significantly higher Vicat softening point than does its EVA compound counterpart, 112 C vs. 68 C as shown by Table 3. This will allow for enhanced thermal stability of wire and cable products including dimensional stability, without losing the desirable balance of flexibility vs. stiffness. Figure 8 shows both Vicat softening temperature and brittleness temperature as a function of soft PP compound density. It is clear that increased mineral FR level, as reflected by increased density, tends to reduce the low-temperature performance and at the same time, to improve the Vicat. Therefore, in addition to using its fire performance attribute, $\text{Mg}(\text{OH})_2$ can also be used to control certain thermal properties of wire and cable.

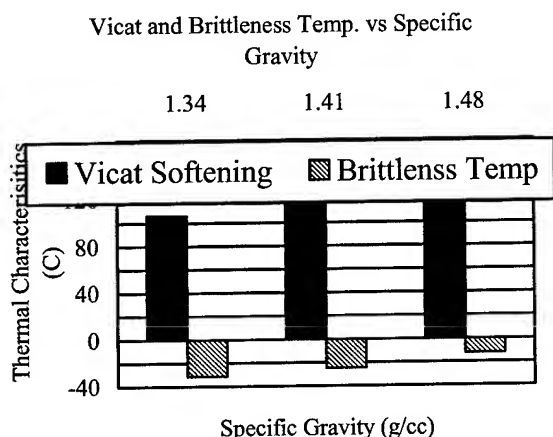


Figure 8. Thermal property of $\text{Mg}(\text{OH})_2$ filled soft PP

5. Electrical properties

Like other polyolefins, PP has excellent electrical properties compared to many other polymers such as PVC. The Catalloy process, using advanced catalyst systems, also provides polymers with very low catalyst residues, thus better electrical properties compared to other polyolefins that contain relatively high impurities from the catalyst. Compared to EVA, PP is also a relatively better material for its chemical nature, i.e., lack of more polar groups present in EVA. Table 4 summarizes several electrical properties comparing 60% of $\text{Mg}(\text{OH})_2$ -filled soft PP and EVA.

Table 4. Electrical property comparison of soft PP and EVA compound

Property	EVA compound	Catalloy PP compound
Dielectric constant	3.93	3.30
Dissipation factor	3.66	3.18
Volume resistivity, ohms-cm	2.9E+15	4.0E+15

Conclusions

Polypropylene-based plastomers provide good elevated temperature performance with a low crystallinity facilitating modification with secondary fillers or additives. The PP-based polymers do not require same crosslinking as used in PE/EVA to achieve elevated temperature performance and toughness when filled with mineral based non-halogen flame retardant.

Soft thermoplastic plastomers made from Catalloy process polypropylene are shown to be an excellent materials for use as a base polymer for wire and cable applications. When combined with fine particle sized, surface-coated magnesium hydroxide, such as Zerogen™ 50SP, these soft plastomers can provide excellent compound properties of value to wire and cable applications such as automotive wires.

Compared to XLPE/EVA, the soft thermoplastic plastomers when combined with properly engineered $\text{Mg}(\text{OH})_2$ offer enhanced thermal and mechanical properties. Flame retardancy and smoke performance of Zerogen™ 50SP-filled soft PP compounds are expected to meet critical requirements in automotive wire and cable applications. The zero-halogen, low-smoke polyolefin compound are considered as better performing alternate to PVC and XLPE counterparts.

Acknowledgement

Authors wish to thank J. M. Huber Corporation and Basell USA, Inc. for permissions to publish this work.

Tong Chen is Technology Manager for Thermoplastics, Wire and Cable Group at J. M. Huber Corporation. Prior to joining Huber in 2001, he was with Union Carbide's Specialty Polyolefins Wire and Cable Business then Dow Chemical. He has worked in areas of polymer research and development since 1991. He received his Doctor of Science degree in chemical engineering/polymer materials science from MIT, and MS in applied chemistry, BS in chemical engineering, both from Tianjin University, China.

Allen Hendrix joined Huber Engineered Materials in 1992 and has worked on development of non-halogen fire retardant and smoke suppression systems for polymer applications. Since 2000, he has served as a technical service and new product specialist supporting the development and commercialization of Huber Engineered Materials products in thermoplastic and wire and cable applications.

Todd Glogovsky is the manager for the Industrial Applications and Product Development Group for Basell Polyolefins. He has worked in the thermoplastics industry since 1985. He has an MS in Polymer Engineering from the University of Akron.

Robert Butala graduated from the University of Minnesota with a bachelor of chemical engineering degree. He began working for Himont USA (now Basell Polyolefins) as an applications development engineer in 1990 following involvement with several manufacturing and engineering assignments in the plastics processing industry.

Overview of Recent Advances in Flame Retardant Compositions UV Stable Flame Retardant Systems; Fully Formulated Antimony Free Flame Retardant Products for Polyolefins

Nikolas Kaprinidis, Neal Earhart and Juerg Zingg*

Ciba Specialty Chemicals Corporation, Plastic Additives
Tarrytown, NY

* Basel, Switzerland

1-800-431-1874 ext 2739, nikolas.kaprinidis@CIBASC.com

Abstract

Over the last several years we have clearly established the utility of novel NOR type hindered amines, such as NOR 1, either as a flame retardant, or flame retardant synergist in polypropylene fibers and thin films. Herein, we will provide an update on the recent advances in flame retardant compositions for polypropylene injection molding substrates including both flame retardant efficacy and UV stability. Overall, we have found that these novel NOR type hindered amines allow for i) substantial reduction in the concentration of the halogenated flame retardants and mineral fillers and ii) the elimination of antimony trioxide. In this report fully formulated antimony free products and UV stable flame retardant systems comprised upon a conventional flame retardant and a light stabilizer for both homopolymer and copolymer injection molding grade polypropylene will be presented.

1. Introduction

The performance and environmental requirements for flame retardants used in the wire and cable industry are continuously evolving. Presently, polyolefins which are used in the wire and cable construction contain flame retardants based on either bromine and phosphorous in combination with fillers and antimony trioxide or magnesium hydroxide. Although these particular systems are very effective in providing flame retardant efficacy at relatively low cost, they raise practical and environmental concerns. For example, there are processing problems such as odor, toxicity, and significant negative impact on the mechanical properties of the polymers associated with the high levels of the flame retardant additives and antimony trioxide.^{1,2} In addition, brominated aromatic flame retardants e.g. Decabromodiphenyl Oxide, detrimentally affect the polymer light stability. Furthermore, in some European countries several proposals have been initiated to ban the use of certain brominated flame retardants and antimony trioxide.^{3,4} Accordingly, an opportunity to replace these conventional systems containing halogenated flame retardants and antimony trioxide has developed.

2. Results and Discussion

2.1 Flame Retardant Efficacy

N-alkoxy hindered amines were first introduced as non-interacting light stabilizers for automotive coatings, flame retarded fiber and agricultural film applications.⁵ Papers have been already presented demonstrating the efficacy of N-alkoxy hindered amines with brominated flame retardants and UV stabilizers.⁶ These papers however, only describe the light stabilization performance and do not show any flame retardant efficacy data. It was believed at that time that the non-interactive nature of NOR HALS with the halogen in the brominated flame retardant positively influenced the performance. Subsequently, when NORs were tested for flame retardancy without the presence of brominated flame retardants, it was observed that they provide flame retardant efficacy to

polypropylene fibers. The efficacy of NOR 1 as a flame retardant in passing flame retardant industry standard tests such as NFPA 701 at surprisingly low concentrations was discussed in a previous paper.⁷ The present report discusses the flame retardant efficacy of fully formulated products containing NOR 1.

Based on the initial range finding work we have carried out in our labs, we were unable to achieve a UL rating with NOR 1 alone in polypropylene molded plaques. Following up the promising results in polypropylene fiber, experimental blends of halogenated and non halogenated flame retardants with NOR 1 were evaluated in polypropylene. The results obtained from products A, B, and C are summarized in Table 1. The concentration (weight percent) of the products in the flame retardant homopolymer grade polypropylene is referring to the total composition (see Table 1).

**Table 1. UL-94 Vertical Burn Test Results in
Polypropylene Plaques (1.6mm)**

Product	Concentration (%) for V-O	Concentration (%) for V-2
A	16	3.5
B	N/A	5.5
C	N/A	17.0

The results suggest that NOR 1 could effectively replace antimony trioxide and achieve the same degree of flame retardant efficacy that traditional halogenated/antimony trioxide systems have provided. The flame retardant efficacy was evaluated according to the UL 94 protocol for injection molded items (please see the experimental section for details). Most notably, a V-0 rating is achieved by the antimony free product A. The flame retardant polymer show less than one second after flame time (self extinguished) and although it is dripping upon application of the flame, the drops do not ignite the cotton underneath the plaque.

Antimony free V-2 ratings are also achieved with remarkably low concentrations of products A and B. The loading (weight percent) for each product is referring to the total composition of the flame retarded polypropylene. The flame retardant polymer in both cases, show less than one second after flame time (self extinguished). However, the dripping in this case ignites the cotton underneath the plaques.

There are numerous advantages to benefit from the new, antimony free, products. It is observed that antimony trioxide free flame retardant products result in substantially decreased smoke density and improved physical and mechanical properties such as density, tensile and impact strength. In addition, the substantially lower effective concentrations of the flame retardant results in polymers with better melt processability, lower density and better physical and mechanical properties.

The non-halogenated, antimony free product C which results in a V-2 performance rating in flame retardant polypropylene molding, is

also very exciting. Again, the product is based on NOR 1 and the concentration (weight percent) is referring to the total composition of the homopolymer polypropylene.

2.2 UV Light Stability

The UV light stability of molded polypropylene items and other polymers containing aromatic brominated flame retardants is an ongoing challenge in many outdoor applications. Aromatic flame retardants are strongly UV absorbing. Exposure to UV radiation will cause the flame retardant to undergo photolytic cleavage, releasing halogen radicals. The halogen radicals abstract hydrogens from the polymer. The reaction inevitably results in chain scission or cross-linking with the consequent rapid loss of polymer physical properties. UV absorbers can be employed to somewhat slow the rate of halogen evolution. However, performance enhancements are often marginal. Light stabilization studies which were conducted with brominated flame retardants and conventional hindered amines (HALS), and NOR HALS confirmed that NORs perform significantly better than conventional light stabilizers in the presence of brominated flame retardants.

The N-alkoxy hindered amines (NOR HALS) are by far less basic than N-H hindered amines (HALS). With their pKa's in the range of 4.2 - 4.7, they experience significantly lower levels of acid/base type interactions compared to traditional HALS. In flame retardant compositions, NORs are not prone to the acid/base reactions and are free to act as UV stabilizers. In non flame retardant formulations they provide a level of performance consistent with traditional HALS.

Weathering of unstable polymer compositions, containing flame retardants and light stabilizer (LS) will lead to premature discoloration and surface cracking. Therefore, the selection of the best combination of flame retardant and light stabilizer becomes critical. The ideal UV stable system is defined by the following criteria:

- To be effective at low concentrations (no effect on mechanical properties)

- To be thermally stable (not decomposed during compounding/molding)

- To be compatible with the polymer matrix (easy to disperse)

- To be UV stable and not pro-degradative to the polymer when exposed to light

- The flame retardant has minimal interaction with light stabilizer,

- the light stabilizer must be highly effective in the chosen matrix

Traditional aliphatic and aromatic flame retardants combined with traditional HALS are not capable of maintaining surface gloss for significant periods of time. System D is comprised upon a halogenated flame retardant and a light stabilizer targeted at achieving a V-2 level of flame retardant efficacy and a high level of UV stability. Gloss retention reaches to several thousand hours, which allows for extended periods of outdoor use for these polymers. Figure 1 shows the change in gloss as a function of accelerated weathering (WOM, wet) of a copolymer grade of polypropylene. A complete loss of gloss will lead to a polymer surface that is chalked or cracked and significantly degraded in appearance.

The resin used in this particular experiment is blown molding grade polypropylene with MFI 0.3 and containing 0.2% Cromophthal Blue 4GNP. The same light stabilizer (LS) was used in all formulations (at 0.5% loading). The flame retardant was used in a concentration to achieve a V-2 UL rating. Flame retardant 1 is aromatic while flame retardant 2 is aliphatic. Figure 2 shows the actual

photographs taken from these polymer formulations after several weathering intervals.

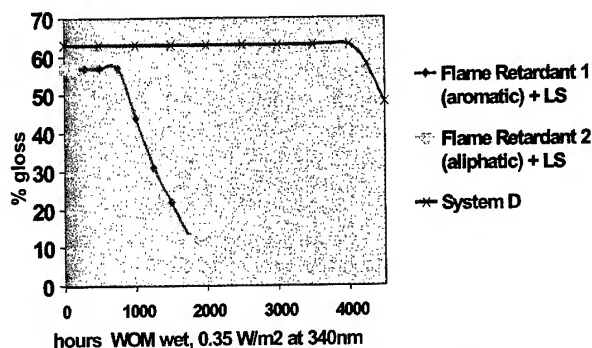


Figure 1: Change of Gloss as a Function of Accelerated Weathering (WOM)

Artificial Weathering: WOM Ci 65, 0.35W/m² 340nm, wet condition

	1000 h	2000 h	3000 h	4000 h
Flame Retardant 1 (aromatic) + LS				
Flame Retardant 2 (aliphatic) + LS				
System D				

Figure 2: Influence of the Flame Retardant on the UV Stability of the Polymer

Figure 3 demonstrates that some non-halogen flame retardants can also have deleterious effects on UV stability. In this example the light stabilizer is the same in all formulations. It is important to recognize that the flame retardant has the most significant impact on the level of UV stability.

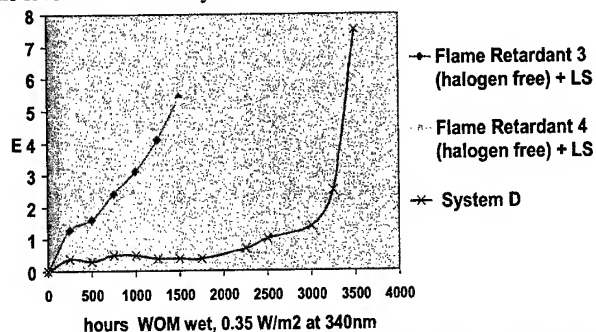
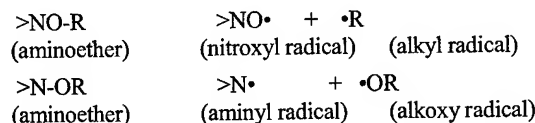


Figure 3: Color Change as a Function of Weathering

2.3 Mechanistic Considerations

It is known from earlier research work that thermolysis of NOR hindered amines may follow two seemingly similar, but distinctly different reaction pathways. The two cleavage processes are as follows:



It can be seen that the thermally induced breakdown of NOR hindered amines may lead to the formation of either alkyl and nitroxyl radicals, or alkoxy and aminyl radicals. The relative extent of these two reactions depends on the chemical structure of the starting NOR aminoether. Aminyl and alkoxy radicals are very reactive and may be involved in the free radical chemical reactions during the combustion process. The effect of aminyl radicals on polyolefins at higher temperatures are under investigation. On the other hand, effect of alkoxy radicals on polyolefins has been widely studied. Alkoxy radicals may promote chain scission or crosslinking reactions in polyolefins depending on the polymer molecular architecture. Alkoxy radicals promote chain scission of polypropylene, while in most cases promote crosslinking or chain enlargement of polyethylene.

Ignition of a polymer results in the formation of volatile combustion products. When these combustion products burn, they release heat. This heat energy from the flame is then fed back to the polymer to sustain the burning process. It is believed that the thermolysis of NOR hindered amines and the consequent generation of the radical species from the NOR significantly reduces the amount of thermal feedback from the flame thereby providing flame retardant efficacy.

Extensive research has been done in the area of using various radical generators as flame retardants and flame retardant synergists.⁸ A possible explanation for the flame retardant performance obtained by using products containing NOR 1 and halogenated flame retardants is the following: generation of aminyl, alkoxy and nitroxyl radicals from the NOR compound can interact with the halogenated compounds and facilitate the release of halogen, thereby improving the flame retardant performance. Also, radical reactions between the NOR, halogenated flame retardant and the polymer may lead to more efficient condensed phase reactions, resulting in improved flame retardant efficacy.

2.4 Experimental Details

Each of the formulations were melt compounded with a twin screw extruder and then injection molded into plaques. The plaques (1.6 mm thickness) were injection molded using a laboratory Boy Injection Molder. The detailed conditions for compounding and injection molding of the plaques are summarized in Appendix 2. The UL-94 testing was performed according to the UL protocol.⁹ The plaques were conditioned prior testing (48 h, room temperature at 50% humidity). Please note, various factors such as homogeneous dispersion of the flame retardant in the polymer, presence of pigments and other additives, material construction, and other sources of variability in the samples may play a role on the measured flame retardant efficacy.¹⁰

The artificial weathering (WOM, wet) was conducted at 0.35 W/m² at 340 nm.

3. Conclusions

The conclusions derived from this investigation can be summarized as follows:

Improved flame retardant efficacy and UV stability can be achieved in polypropylene molded plaques through our light stable flame retardant systems.

In products A, B and C NOR 1 clearly enhances the performance attributes with both halogenated and non halogenated flame retardants in molded items to achieve V-O and V-2 UL ratings. Using this technology, it is possible to design flame retardant polypropylene compositions with lower levels of halogenated or non halogenated flame retardants. It is also possible to eliminate the presence of antimony trioxide.

The lower levels of products A, B and C and the absence of antimony trioxide, provide better processability, lower density,

lower smoke density, improved physical and mechanical properties. In addition, they are in compliance with both existing and anticipated environmental regulations and also provide safer use and recycling.

4. Acknowledgments

The development of new stabilization chemistries and commercial products is the result of hard work by many people. The authors wish to thank their colleagues for their direct and indirect contributions, from the Ciba Specialty Chemical sites around the world. The authors would also like to thank worldwide management for their continued support and commitment as well as permission to publish this paper.

5. References

- [1] Cullis C. F. and Hirschler M. M., "The Combustion of Organic Polymers," Calendron Press, Oxford (1981)
- [2] Marchall A., Delobel R., Le Bras M., Leroy J. and Price D., Polymer Degradation and Stability, **44** (1994) 263-272
- [3] Hardy M. L., Conf. Proceed., Fire Retardant Chemicals Association, (1994) 123-128
- [4] Van Riel, Conf. Proceed., Fire Retardant Chemicals Association, (1994) 167-174
- [5] Guo M., Horsey D., Lelli N. and Bonora M., Conference Proceedings, Polyolefins X, Society of Plastics Engineers (1997) 439
- [6] Davis L., "Recent Developments in UV Stabilization of Polypropylene Fiber Containing Melt Processing Halogenated Flame Retardants" Additives (1996)
- [7] Srinivasan R., Gupta A. and Horsey D., Conference Proceedings, Additives XI, Society of Plastics Engineers (1998)
- [8] Eichom J., Journal of Applied Polymer Science, **8**, (1964) 2497
- [9] Tests for Flammability of Plastic Materials, Underwriters Laboratories Standard (1996)
- [10] Green J., Flame Retardant Polymeric Materials, **3** (1982)

Appendix 1. Description of Stabilization Chemistries

Code Class Trade Name	Stabilizer Function
NOR 1 HALS NOR Flamestab NOR 116	UV Stability; Long Term Thermal Stability Flame Retardant

Appendix 2. Experimental Design

Polymer ID#:	Profax 6501
Compounding:	Dry mixing of all components for 30 min; Leistritz 27mm Twin Screw Extruder; Extruded under nitrogen; 200 °C; 300 RPM
Injection Molding:	400 ° F at Nozzle; 375 ° F at Zone 1,2 and 3; 75 ° C Molding Temperature; 60 Screw Speed
UL-94 Burn Test:	Plaques were prepared, conditioned and tested according to the UL-94 protocol
Weathering:	Xenon Weatherometer WOM Ci 65; Continuous Light; Spray 18 minutes/120; 0.35 W/m ² ; at 340 nm.

Development of a Tough and Flexible Halogen Free Dual Layer Wire Insulation System for Electronics Applications

Akshay H. Trivedi and Anthony Listro

Judd Wire, Inc.

Turners Falls, MA

+1-413-863-4357 · ATrivedi@Juddwire.com

Abstract

Due to strict environmental regulations, insulating materials for electrical wires are required to be not only flame retardant but also generate very low smoke upon flaming. Insulation systems containing halogens evolve harmful hydrogen halide gases upon burning. These gases are acidic and toxic in nature. Due to this reason, there have been increased requirements to use insulation systems that contain halogen free flame retardants. However, in order to impart a similar level of flame retardency as halogen containing compounds, these materials must have a very high level of fillers such as metal hydroxides and other inorganic materials. Unfortunately, such high loadings of halogen free, flame-retarding agents adversely impact the physical and mechanical properties (e.g., toughness, flexibility) and processability of the resulting insulating material.

The present paper describes the development of a low-smoke, halogen free flexible dual layer insulation system (**Flexrad™ HF Dual Wall**), which demonstrates excellent mechanical, thermal and flame characteristics. A key characteristic of this dual wall system is the ratio of the inner to the outer layer thickness. The results of an experiment to determine an optimum ratio of the inside XLPO layer to the outside jacket layer are discussed. We conclude that the thickness of the jacket layer relative to the thickness of the inside insulating layer will influence the ability of the wire to meet the stringent requirements of the UL VW-1 Vertical Flame Test. Further, this thickness ratio influences the ability of the wire to demonstrate very high cut-through resistance.

Keywords

Dual Layer; Halogen-free; Cut through Resistance; VW-1 Flame; IEEE-383; Flexrad™ HF Dual wall.

1. Introduction

Insulation systems used in electronics and telecommunications equipments have in the past relied on halogenated materials. These materials provide the required flame resistance to the overall insulation. They also have good combination of physical and mechanical properties. One of the key requirements for use of wires and cables employing these insulation systems is their flexibility and resistance to physical abuse. A typical application of these wires is in power switching equipment inside buildings. In this application the wire and/or cable is routed through several installations and in doing so comes in contact with sharp metal edges. As a result it is subjected to severe physical abuse.

Consequently the wire or cable is expected to be very flexible and tough. Also since cables are installed inside the building, they are required to have a flame rating of at least VW-1 if rated UL or preferably IEEE-383 vertical tray flame rating.

Over the years, either single or dual wall insulated XLPVC and XLPE wires containing halogenated flame retardants have been used for such applications. But in recent times due to strict environmental regulations regarding recyclability and potentially harmful nature of these materials, they have come under increased scrutiny. The alternative materials, which are being increasingly used, are halogen free polymers. Halogen free polyolefins are excellent candidates since most are readily crosslinked using irradiation crosslinking technology. Irradiation crosslinking significantly increases the heat resistance, chemical resistance and mechanical strength of the insulation. However, in the case of the halogen free polyolefins, the base resin must have excellent filler acceptance. Materials such as ethylene copolymers are typically used since, although these materials tend to be relatively soft in nature, they tend to accept high loadings of halogen free flame retardants. Since the flame retardency of the compound is dependent upon the loading of the halogen free flame retardant in the compound, relatively high loadings of fillers are required to achieve VW-1 flame retardency required for wire used in electronics and telecommunications equipment.

The present paper discusses dual layer insulation systems where the inside layer (first insulating layer) consists of a crosslinked, highly flame retardant, and halogen free polyolefin material (XLPO). A comparison of various jacket layers is made. The first insulating layer provides the overall flame retardency and flexibility to the dual wall insulation system whereas the jacketing materials provide toughness while maintaining flexibility. Flame retardency is usually measured by the Limited Oxygen Index (LOI). The LOI of any material is the percent of oxygen needed in the atmosphere to sustain its combustion. In other words, higher the LOI, the more flame retardant is the material. The LOI of the first insulating material in our study is 48. In order to obtain such high level of flame retardency, high level of filler loading is required which tends to lower the physical and mechanical properties of the first insulating layer. The purpose of this investigation was to enhance the mechanical properties of the wire through the addition of the outer jacket layer. The balance of flame retardency, flexibility and mechanical properties was investigated by adjusting the ratio of the first to the second insulating layer. The goal was to develop a

flexible insulation system that will be easily routed in very tight places. The effect of the thickness of the jacket layer relative to the thickness of the inside insulating layer was investigated to determine its influence on the ability of the wire to meet the stringent requirements of the UL VW-1 Vertical Flame Test. Further, the effect of this thickness ratio on the ability of the wire to demonstrate satisfactory cut through resistance was explored.

2. Experimental

For the purpose of this study, wire samples were extruded on 10 AWG 105 strands tinned copper conductor. The thickness of the first insulating layer, namely halogen free flame retarded polyolefin was kept constant at 0.685 mm. The wire samples were extruded with the said first layer thickness and then crosslinked via electron beam. The jacket layer was then extruded over the crosslinked first layer to make the dual wall insulated wire product. The jacket layer or the second insulating layer thickness was varied from 0.10 mm to 0.25 mm to make different ratios of first to the second layer. For the purpose of this study, several types of jacket layer materials were evaluated to find the best combination which would give a balance of flame and mechanical properties without sacrificing the overall flexibility. In addition to polyamides, HDPE, Thermoplastic Alloy (TPA) and Thermoplastic Elastomer (TPE) were used as jacket materials in various thickness. The two key properties which were measured on the dual layer insulated wire products were (1) VW-1 flame property and (2) Room and high temperature cut through resistance.

2.1 VW-1 Flame Resistance

The insulated wire samples were tested for flame resistance in accordance with the test method set forth in the UL VW-1 Flame Test described in UL 1581 test standard. In this test, insulated wire samples, each measuring approximately 450mm in length, were supported vertically in a rectangular test apparatus housed within a draft-free chamber. The draft-free chamber has greater than or equal to 4m³ of interior volume. The lower end of each wire sample was exposed by a laboratory burner (as described in ANSI/ASTM D 5025-94) positioned at a 20° angle from the vertical plane of the longitudinal axis of the wire, to five-15 second exposures of flame. The period between exposures was: 15 seconds, if flaming ceased in less than or equal to 15 seconds; or, the duration of flaming, if flaming persisted for greater than 15 seconds. A flat, 6mm thick layer of dry, surgical cotton was positioned on a bottom tray of the test apparatus. The bottom tray measured 300mm in width and 355mm in depth, and was positioned 230 to 240mm from the lower end of each wire sample. A kraft paper flag, measuring 10mm in width and 0.5mm in thickness, was placed 250mm above the lower end of each wire sample, where the flame was to touch the sample. The test was deemed passed if: (1) the fire from the flaming wire sample extinguished within 60 seconds for each of the five exposures; and (2) the absorbent cotton and the kraft paper flag did not catch fire.

2.2 Cut through Resistance

The cut-through test measures the resistance of any wire insulation to the penetration of a cutting surface and simulates the type of damage that can occur when a wire is forced by mechanical loading against a sharp edge. The test was performed at room temperature (23°C), at 60°C, and at 90°C, to evaluate the effect of the elevated temperature on the dual layer insulation performance. The standard cutting edge used was stainless steel and had a radius of 0.406 mm. For each test, the wire from an insulated wire sample measuring 75mm in length, was removed and replaced with a steel mandrel having the same outside diameter as the wire. The sample was then clamped in place between a blade and a flat plate within an Instron universal mechanical tester, and the ends of the steel mandrel connected to an 18V DC electrical circuit. The cutting edge of the blade was oriented perpendicularly to the axis of the sample. The cutting edge was then forced through the insulation at a constant rate of 1.27 mm per minute until contact with the steel mandrel occurred. A detection circuit sensed contact of the cutting edge with the steel mandrel and recorded the maximum force encountered during the test. The test was then repeated three times rotating the sample at approximately 90° between tests to offset the effect of eccentric insulation. The reported cut-through resistance was the arithmetic mean of four tests performed on each sample.

3. Results and Discussion

3.1 VW-1 Flame

Table 1 contains all the key data namely VW-1 flame results and the cut through resistance (kgf.) of various dual layer wire samples having different outer layer jackets. As described earlier, for the purpose of this study, the first insulating layer thickness was kept constant at 0.685 mm. This halogen free flame retarded material (XLPO) is UL rated material (AWM Style 3385, 3386) with a VW-1 rating by itself. In other words, it meets this flame requirement in all the conductor sizes and insulation thicknesses. On the other hand, inherent flame retardency of various jacket layer materials evaluated was lower than the inside layer material. As a result the overall flame resistance of the dual layer wire products was compromised by adding the jacket layer. Also this flame resistance decreases as the jacket layer thickness increases. This is evident from the data shown in Table 1. As we can see, except for PA4 and TPE jacket layer, all the samples with jacket thickness more than 0.10 mm failed the VW-1 flame test. The wire samples with PA4 as jacket layer material met this requirement for all thickness evaluated. This is because PA4 selected was a flame retarded polyamide with V-0 rating. This material was a halogen free flame retarded polyamide with LOI of more than 28. The TPE jacket evaluated was inherently flame retardant material and hence met VW-1 with 0.15mm thickness. Besides these two jacket materials, the remaining materials evaluated did not have sufficient flame retardency to extinguish flame within 60 s when subjected to the flame test on wire sample.

3.2 Cut Through Resistance

The other key property measured on the dual layer insulated products was cut through resistance as described earlier in the experimental section. This property strongly depends on the overall toughness of the product. The inside XLPO layer is very flexible and has satisfactory physical properties ($E_b > 150\%$, $T_b > 10.5$ MPa) but is relatively soft in nature. As a result it is not a suitable material to use in applications where wire may be under severe mechanical abuse. On the other hand, all the jacket materials evaluated have

much higher tensile modulus than the first insulating layer. As a result the dual wall products provided toughness to the overall insulation. These materials have varying amount of flexibility and depending on their individual flexural modulus, make the overall dual layer wire product more or less flexible than the single layer insulated wire. As seen in Table 1, the room temperature as well as elevated temperature cut through resistance in general increases with an increase in jacket layer thickness.

Table 1. Flame and Cut through Properties of Various Dual Layer Insulated Wires

	Thickness (mm)	Layer Thickness Ratio	VW-1 Flame (P,F)	Cut Through Resistance (Kg.)		
				at 25°C	at 60°C	at 90°C
First Insulating Layer (XLPO)	0.685					
Second Insulating Layer (Jacket)						
PA1	0.10	1: 0.25	PASS	22.8	12.7	5.5
	0.15	1: 0.22	FAIL	24.7	8.0	7.9
	0.20	1: 0.29	FAIL	23.3	13.0	6.0
	0.25	1: 0.36	FAIL	19.6	8.9	5.8
PA2	0.10	1: 0.25	PASS	23.5	9.5	7.2
	0.15	1: 0.22	FAIL	---	---	---
	0.20	1: 0.29	FAIL	---	---	---
	0.25	1: 0.36	FAIL	---	---	---
PA3	0.10	1: 0.25	PASS	34.1	21.2	17.9
	0.15	1: 0.22	FAIL	---	---	---
	0.20	1: 0.29	FAIL	---	---	---
	0.25	1: 0.36	FAIL	---	---	---
PA4	0.10	1: 0.25	PASS	22.9	10.8	8.9
	0.15	1: 0.22	PASS	23.9	12.6	8.4
	0.20	1: 0.29	PASS	26.8	17.3	9.2
	0.25	1: 0.36	PASS	34.2	21.5	13.0
TPA	0.10	1: 0.25	PASS	25.3	9.9	9.2
	0.15	1: 0.22	FAIL	---	---	---
	0.20	1: 0.29	FAIL	---	---	---
	0.25	1: 0.36	FAIL	---	---	---
TPE	0.10	1: 0.25	PASS	18.3	5.8	3.8
	0.15	1: 0.22	PASS	21.9	8.2	4.5
	0.20	1: 0.29	FAIL	25.4	8.5	6.1
	0.25	1: 0.36	FAIL	27.2	10.5	6.5
HDPE	0.10	1: 0.25	PASS	14.7	7.2	4.8
	0.15	1: 0.22	FAIL	18.2	8.0	4.3
	0.20	1: 0.29	FAIL	24.8	6.6	5.6
	0.25	1: 0.36	FAIL	22.2	9.3	6.4
Control (XLPO)	0.102	N/A	PASS	16.8	4.2	1.3

The elevated temperature cut through value depends on the thermal behavior of the outside jacket layer material. All the jacket materials evaluated were partly crystalline in nature with melting points higher than 100°C. PA1, PA4, TPE and HDPE materials were tested for cut through resistance for all the three temperatures and jacket layer thickness of up to 0.25 mm. Of all the materials evaluated, PA3 had the highest room temperature cut through resistance while PA1 had the highest flexibility amongst all the materials evaluated. Figure 1 shows the bar graph of cut through resistance values at three selected temperatures of all the materials including the control. Figure 1 data shows dual layer samples with jacket layer thickness of 0.10 mm. The control sample is an equivalent thickness wire sample made only with the XLPO material. As seen in Figure 1, the cut through resistance of the inside XLPO layer is inferior to the dual layer systems, especially at elevated temperatures. This is because the nature of this material is such that even though it is crosslinked, it has a tendency to become soft at high temperatures. As a result, its cut through resistance becomes smaller as the temperature increases. The jacket layers have much higher heat resistance and protect the inside layer when subjected to physical and mechanical abuse. Of all the jacket layers evaluated, PA3 was found to have highest elevated cut through resistance but was not tested for higher jacket layer thickness. The reason was because at higher jacket thickness, in addition to not meeting the flame requirement, it was also the most stiff material.

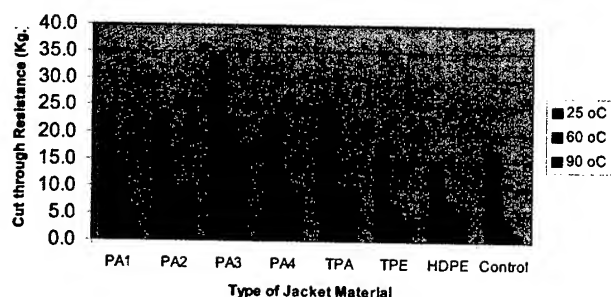


Figure 1. Cut through Resistance of Various Jacketed Materials at different temperatures.

Similarly, PA4 jacketed wire samples met flame requirements in all the thickness evaluated and they also had high cut through resistance. But it was also found to be a stiff product. As it was explained earlier, the most suitable product was to have the highest flame and cut through resistance without sacrificing the overall flexibility of the insulated wire. The flexibility of the wires is an equally important requirement in these applications.

From overall performance of flame, cut through resistance, flexibility and other physical properties, PA1 jacket material was found to have the optimum properties and was chosen for this application. This material has a flexural modulus of less than 10,000 Kg/cm². The insulated wire product made with PA1 as the jacket

material was then later qualified under UL appliance wire (AWM style 3660) and is being currently used in commercial applications. This dual wall product in all conductor sizes also meet or exceed the requirements of IEEE-383 vertical tray flame test as well as smoke density test described in IEC 61034-2 as well as UL 1685 (Limited Smoke). All these properties make this product suitable for use in various electronic appliance wire as well as fireproof electrical cabinets.

4. Conclusions

This paper describes the development of a unique, halogen free flexible dual layer insulation system with superior mechanical and flame characteristics. A key characteristic of this dual wall system is the ratio of the inner XLPO to the outer jacket layer thickness. The balance of flame retardency, flexibility and mechanical properties was achieved by adjusting this ratio. The two key properties measured on various insulation systems were VW-1 flame and cut through resistance. From the data discussed in the paper, we conclude that the thickness of the jacket layer relative to the thickness of the inside insulating layer will influence the ability of the wire to meet the stringent requirements of the UL VW-1 Vertical Flame Test. Further, this thickness ratio influences the ability of the wire to demonstrate excellent cut through resistance. The flexible design of the insulation system makes it suitable to be easily routed in very tight places. The resultant wire product is suitable for internal applications where improved mechanical properties like abrasion, cut through resistance, low deformation as well as flexibility are desired. The product is rated at 105 °C and is recognized by UL under AWM style 3660 and also by CSA under AWM I A/B. It meets flame rating of VW-1 described in UL 94 and vertical tray flame rating of IEEE 383 as well as UL 1685 for low smoke emission.

5. Acknowledgments

The authors would like to thank Mike Bompastore for his invaluable help in preparing and testing wire samples.

6. Authors

Akshay H. Trivedi, Ph.D.
Sr. R&D Engineer
Judd Wire, Inc.
124 Turnpike Road
Turners Falls, MA 01376



Akshay Trivedi earned his B.S. degree in Chemical Engineering from University of Bombay (U.D.C.T). He later had his M.S. degree in Chemical Engineering from Texas A&M, Kingsville University and Ph.D. in Chemical Engineering from University of Akron, Ohio in 1997. Since then, he has been working for Judd Wire, Inc. in R&D department.

Anthony E. Listro

Director of Engineering
Judd Wire Inc.
124 Turnpike Road
Turners Falls, MA 01376



Tony Listro earned his BS and MS degrees in Plastics Engineering from the University of Lowell, Lowell, MA and his MBA from the the University of Massachusetts, Amherst, MA. He has worked as a Research Engineer for Quantum Chemicals from 1989 to 1993. Since 1993 he has worked in various levels of responsibility in Judd Wire's Engineering Department.

Determining Cable Shield Behaviour

Alyse R. Coates

**Alexandros
Gavrilakis**

Alistair P. Duffy

**Kenneth G
Hodge**

Arthur J Willis

De Montfort University, Leicester, UK

alyse@dmu.ac.uk

alex@dmu.ac.uk

apd@dmu.ac.uk

Brand-Rex Ltd, Glenrothes, Scotland

khodge@brand-

rex.com

awillis@brand-

rex.com

Abstract

As technology advances, the role of electromagnetic compatibility becomes more dominant in the design of distributed electronic systems. In high performance applications the leakage of energy into and out of cables is an important source of interference. It is widely acknowledged that cables are often the 'weakest link' of any large electronic system.

This paper examines theoretically the surface transfer impedance of braid-shielded cables and compares these results with those obtained practically. Expressions for the transfer impedance are presented as improved tools for the analysis of tape-shielded cables. The paper then goes on to investigate the shielding effectiveness of a cable with a braided shield using a mode stirred reverberation chamber, then, by using a transfer function, converts the surface transfer impedance results into shielding effectiveness and compares these results with those obtained previously. Whilst this is applicable to other types of cable, this paper concentrates on coaxial systems.

Keywords

transfer impedance, theory, modeling, practical, reverberation chamber.

1. Introduction

Electromagnetic compatibility (EMC) is concerned with designing and operating equipment in such a way that it is immune to electromagnetic interference (EMI) from external sources and does not cause interference in other equipment in close proximity to it. Such susceptibility to interference increases with the complexity of electronic equipment. Recognising this, much effort is put into improving the shielding of this equipment. However such effort is wasted if the equipment is connected with poorly shielded cables that dominate the overall performance of the entire system either by being sources of, or susceptible to interference. Therefore the performance for the cable shield must be predicted at the design stage of development and optimised against several required criteria, such as balancing the braid and hole inductances. Commonly, such optimisation is undertaken with significant empirical input. Then the shield performance must be measured to ensure that it is consistent with the design criteria and sufficiently immune to electromagnetic interference from the lowest frequency (~1MHz) to the highest frequency (~20GHz) of operation.

The cable shielding performance is generally quantified in one of two ways. By calculating the proportion of an electromagnetic field incident on the shield that is transmitted through it (the 'shielding effectiveness' or 'SE'). Or by calculating the ratio of the interfering field, in the form of the current measured on the cable braid, to the voltage it produces between the braid and the

inner conductor (the 'Surface Transfer Impedance', ' Z_T ' or 'STI').

2. Surface Transfer Impedance

The surface transfer impedance of a length (L) of coaxial cable is illustrated in Figure 1. In the figure, the interfering field induces a current (I) on the braid, which causes a potential difference (V) between the inner and outer conductors. The surface transfer impedance is expressed as a per unit length parameter of the cable, and is defined in Equation 1.

$$Z_T = \frac{V}{I \cdot L} \quad (\Omega m^{-1}) \quad (1)$$

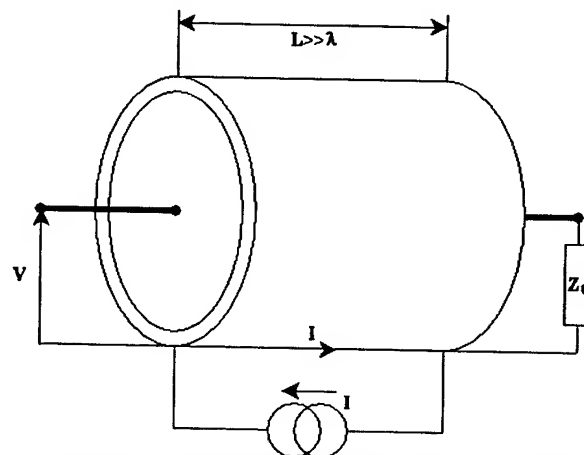


Figure 1. Illustration of the surface transfer impedance.

The surface transfer impedance is independent of both the conditions under which it is measured and the cable length, though the latter defines the upper frequency limit to which it can be measured. Because of this, the surface transfer impedance is a popular method for demonstrating the shielding performance of cables at low frequencies.

2.1 Theoretical Methods for Determining the Surface Transfer Impedance of Braided Cables

The first kind of cable shield to be examined here is one made from braid, as its use has been extensive in the cable industry. The surface transfer impedance is initially theoretically calculated using a model proposed by Katakis [1]. Katakis, after performing a number of measurements, suggested that the radial spindle separation should be taken into account when calculating the mean braid diameter by Tyni's model [2].

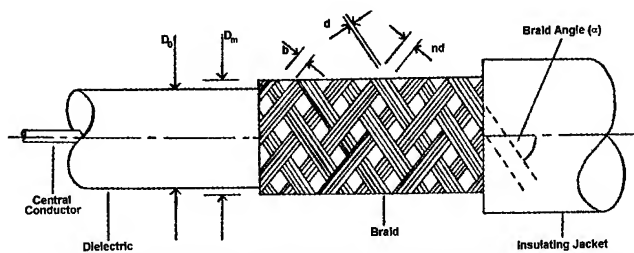


Figure 2. Diagram showing the braid parameters.

There are two types of inductance present on a cable shield; firstly the braid inductance L_b (defined in Equation 2) which arises from the woven nature of the braid.

$$L_b = \frac{-\mu_o h}{4\pi D_m} (1 - \tan^2 \alpha) \quad (2)$$

The second type of inductance is the leakage inductance (L_a), which can be calculated (see Equation 3) from the braid angle (α), the total number of belts or spindles (N) each containing 'n' wires of diameter 'd', the hole width (b), the radial spindle separation (h) and the mean braid diameter (D_m). The mean braid diameter can, in turn be calculated from the external diameter of the dielectric (D_o) as shown in Equation 4.

$$L_a = \frac{\mu_o 2N}{\pi \cos \alpha} \left(\frac{b}{\pi \cdot D_m} \right)^2 \cdot e^{\left(\frac{-\pi \cdot d}{b} - 2 \right)} \quad (3)$$

$$D_m = D_o + 2d + h \quad (4)$$

The surface transfer impedance is then calculated using Equations 2 and 3 to give the approximation:

$$Z_T \approx j\omega(L_b - L_a) \quad (5)$$

Another method by which the theoretical values for the surface transfer impedance can be obtained is to simulate the braid. The simulation tool used in the modelling of the surface transfer impedance in this paper is the Transmission Line Matrix (TLM) method which has been thoroughly analysed in a previous paper by these authors [3].

The advance in this paper is that a more accurate model of Katakis' equations is used. Again, to account for resonances, the length of the cable is split into a number of nodes, whose length is much less than one tenth of the minimum wavelength of the cable examined. Also, the model allows for the different termination conditions required by different measurement techniques or to investigate operational behaviour.

Using the Thevenin circuits for the lumped equivalents of the shield and the inner conductor, the voltages and currents at any point on the surfaces of the inner conductor and the shield can be calculated. The surface transfer impedance is then calculated, by the ratio of the voltage between the inner conductor and the shield (kVT_n) to the current flowing on the shield (kIs_n) at node n, for k iterations, using in Equation 6.

$$Z_T = \frac{kVT_n}{kIs_n} \quad (6)$$

2.2 Practical Methods for Determining the Surface Transfer Impedance

There are a multitude of methods which can be used to find the surface transfer impedance of cables (e.g. [4]), however a majority of these require complicated and time consuming test arrangements. Two much simpler methods have been used in this paper; the 'Current Probe' [5,6] and 'Martin and Mendenhall' [7] methods.

In the current probe method the cable under test is connected between two support brackets using standard coaxial connectors (see Figure 3). These support brackets are in turn bolted onto a metallic ground plate which acts as the current return path. A current probe is then connected around each end of the test cable and a load, matched to the characteristic impedance of the cable, is attached via a connector at one end. The probe at the load end is then connected to the output of a network analyser and becomes the source of the interfering field. Two sets of measurements are then taken, firstly the current on the braid caused by the 'interfering field' is measured by way of the 'monitor probe' (V_M see Figure 4) then, with the input of the network analyser connected to the open end of the cable, the voltage generated by the interfering current is measured (V_C see Figure 5). The interfering current is then calculated from the monitor probe voltage using the probe transfer impedance (Z_{TT}). Then, assuming that the internal impedance of the network analyser is identical to the characteristic impedance of the cable and load, the surface transfer impedance of the cable can be calculated using Equation 7.

$$Z_T = \frac{V_C \cdot Z_{TT}}{L \cdot V_M} \quad (\Omega m^{-1}) \quad (7)$$

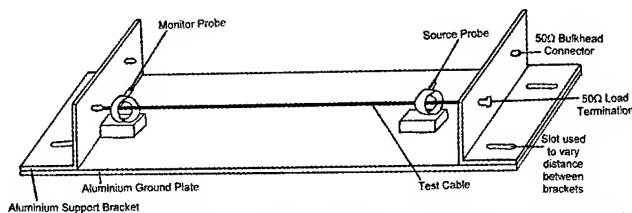


Figure 3. Showing the test arrangement required to perform the current probe method.

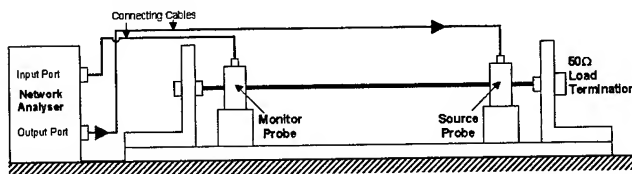


Figure 4. Schematic of the circuit used to measure the monitor probe voltage (V_M).

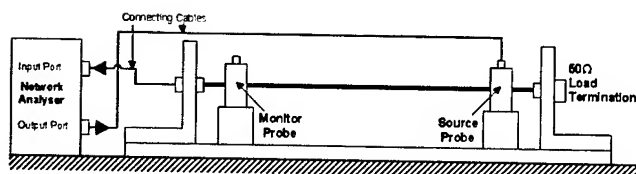


Figure 5. Schematic of the circuit used to measure the cable voltage (V_c).

In the Martin and Mendenhall test method a sample of intact coaxial cable has a length of braid taken from a similar cable 'milked on' over its outer sheath. At one end the milked on braid becomes the outer braid in the end connector whilst the shield under test is connected to the central conductor of the cable. At the other end the milked on braid is connected to the shield under test and both are put into the end connector. The triaxial test cable is then connected to the network analyser and the ratio of the power received at the input port (P_{REC}) to the power transmitted via the output port (P_{TRANS}) is measured for each frequency. A schematic of this circuit is shown in Figure 6. Assuming a 50Ω cable and network analyser and a test cable of length 'L' the surface transfer impedance can be calculated using Equation 8.

$$Z_T = \frac{25}{L} \sqrt{\frac{P_{REC}}{P_{TRANS}}} \quad (\Omega m^{-1}) \quad (8)$$

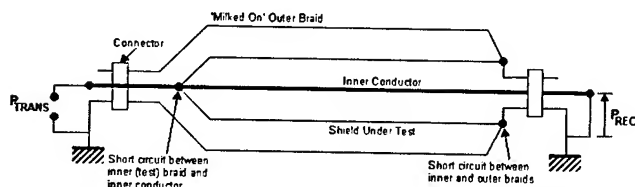


Figure 6. Schematic of Martin and Mendenhall triaxial test cable method.

As previously mentioned, the disadvantage of this test technique, as with all methods for measuring surface transfer impedance, is that it has an absolute upper frequency limit (f_{Max}), which is dependent on the length (L) of the test cable as defined in Equation 9.

$$f_{Max} = \frac{40}{L} \quad (MHz) \quad (9)$$

Therefore, in order to provide accurate measurements up to a frequency of 200MHz, a 0.2 metre cable was used for the measurements.

2.3 Comparison of the Surface Transfer Impedance Results

In order to determine whether the experimental results produced using the above methods were acceptable they were compared with those predicted for an identical cable using a simulation technique [3] and the Katakis theoretical equations [1] as detailed in Section 2.1, see Figure 7.

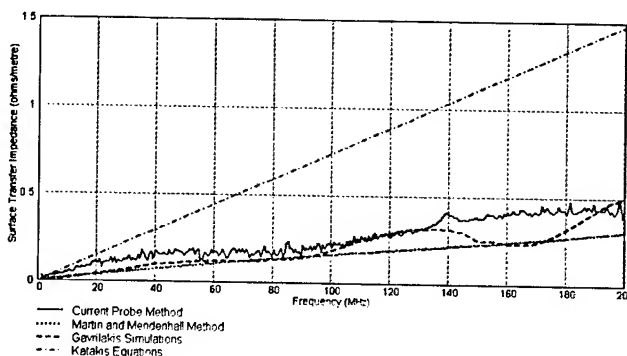


Figure 7. Showing a comparison of the surface transfer impedance results.

The strong correlation between the results from Current Probe and Martin and Mendenhall methods (as seen in Figure 7) suggest that the responses are accurate. The slight differences between them are due to the different losses, etc in the otherwise comparable test methods.

The theoretical surface transfer impedance results produced using the Katakis equations provided a 'worst case' response based entirely on the physical characteristics of the cable braid. Hence, the response obtained by the use of the Katakis equations is somewhat dissimilar to the others. However, the numerical modelling proposed in this paper produced results that predicted the experimental responses extremely well, thus confirming the accuracy of this approach.

3. Theoretical Methods for Determining the Surface Transfer Impedance of Tape Shielded Cables

Recently, cable designers have started to prefer tape shielding to braid shielding; hence this paper also introduces a model for the behaviour of helically wound tape shields. Figure 8 presents the geometry of the helically wound tape shield.

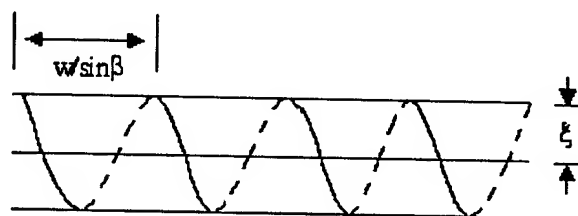


Figure 8. Configuration of a tape wound shield.

Using, Figure 8 the spiral angle (β) is related to width of the tape (w), the width of the overlap between the turns of tape (w_o) and the shield radius (ξ) by Equation 10 [8].

$$\cos \beta = \frac{w - w_o}{2\pi\xi} \quad (10)$$

These parameters also define the number of turns of the tape (N) by Equation 11.

$$N = \frac{\sin \beta}{w - w_0} \quad (11)$$

3.1 Primary Parameters of a Shield

The primary parameters that need to be determined are the shield resistance, the shield inductance and any capacitance present.

To obtain an expression for the resistance (R_s) the equations developed for the transfer impedance by Kaden [9] are used.

$$\begin{aligned} \frac{Z_t}{R_o} &= \frac{(1+j)T/\delta}{\sinh(1+j)T/\delta} \\ &+ \left(\left((1+j)T/\delta \right) \coth(1+j)T/\delta \right. \\ &\left. + j(T/\delta)^{\frac{\xi}{T}} \right) \tan^2 \beta \end{aligned} \quad (12)$$

And:

$$\delta = \frac{1}{\sqrt{\pi f \mu \sigma}} \quad (13)$$

Where, ' R_o ' is the surface resistivity, at the shield radius and ' δ ' the skin depth.

Then, using the fact that the resistance (R_s) represents the real part of the transfer impedance in Equation 12, its value is given as:

$$\begin{aligned} R_s &= \frac{1}{2\pi \xi \sigma T} \left(\left(\frac{T}{\delta} \right) \right) \left(\frac{T}{\sinh \left(\frac{T}{\delta} \right)} \right) \quad (\Omega/m) \quad (14) \\ &+ \frac{\tan^2 \beta}{2\pi \xi \sigma T} \left(\left(\frac{T}{\delta} \right) \coth \left(\frac{T}{\delta} \right) \right) \end{aligned}$$

Where ' T ' is the thickness of the shield tape, ' δ ' is the skin depth and ' σ ' the conductivity of the shield material.

In the case of inductance, the fact that the shield behaves as a solenoid gives:

$$L_s = \frac{\mu_o}{4\pi} \tan^2 \beta \quad (H/m) \quad (15)$$

Where ' μ_o ' is the magnetic permeability of free space.

There are two different capacitances present on the shield: the capacitance between the turns of the overlapped tape and capacitance of the shield to ground.

In the case of the capacitance between the turns, the theory of tubular capacitors [10] is applied. Taking into account that usually the distance between the turns is very small in relation to the overall radius of the cable, the capacitance can be simply calculated by determining the mean length of the tape (l_x) and

treating the overlapping tapes as plates of a parallel plates capacitor:

$$C = \frac{\epsilon \cdot l_x}{d} \quad (16)$$

Where:

$$\epsilon = \epsilon_o \cdot \epsilon_r \quad (17)$$

' ϵ_o ' is the permittivity of free space (8.85×10^{-12} F/m), ' ϵ_r ' is the dielectric constant of the dielectric used and ' d ' is the dielectric thickness between the plates. In cylindrical coordinates, for a spiral forming a tubular capacitor [5].

$$\frac{r}{r_o} = 1 + \left(\frac{t+d}{r_o} \right) \left(\frac{n}{2} + \frac{\phi}{2\pi} \right) \quad (18)$$

' r ' is the radius of the rod at angle ' ϕ ' and ' r_o ' is the radius of the rod in which the spiral has begun.

The thickness of a tape shield is given as:

$$t = (u \cdot T + v)q \quad (19)$$

Where $u=1$ corresponds to a tape metalised on one side $u=2$ for a double sided one, ' v ' is the thickness of the dielectric between tape sides and ' q ' the number of layers being wound.

To find the mean length of the tape, the integral of Equation 18 is required:

$$l_n = \int_0^\phi \frac{r}{r_o} d\phi \quad (20)$$

Where:

$$0 \leq \phi \leq 2q\pi \quad (21)$$

Leading to:

$$l_x = \left(1 + \left(\frac{t}{r_o} \right) \cdot \left(\frac{n}{2} + \frac{\phi}{4\pi} \right) \right) \phi \quad (22)$$

For multi-layered shields, the total capacitance is given as the sum of each individual capacitance between the turns. Hence, the fact that the capacitance between the overlapped turns corresponds only to the overlapped region (w_0/w) then its value can be approximated as:

$$C_s = \left(\frac{\epsilon \cdot r_o \cdot w_0}{d \cdot w} \right) \sum_{x=1}^q \left(\frac{l_x}{r_o} \right) \quad (F/m) \quad (23)$$

Where ' ϵ ' is the dielectric permittivity, ' n ' is a constant depending

on how tight the wrappings are and 'd' is the dielectric thickness. Finally, the capacitance of the shield to ground depends on the distance of the cable from the ground and on the testing facilities of the measurements. It is usually small and the best practice is to determine it experimentally for each set of measurements.

3.2 The Surface Transfer Impedance of a Tape Shield

From the structure of Figure 8, it can be seen that the tape shield can be self-resonant so the frequency spectrum has to be divided into two main areas with the cut off frequency to be determined approximately by the point at which the inductive part (X_L) becomes equal to the capacitive part (X_C).

The transfer impedance at any frequency is generally given by:

$$Z_T \approx R_s \pm jX_y \quad (24)$$

The condition for self-resonance gives:

$$\omega_x = \frac{1}{\sqrt{L_s C_s}} \quad (25)$$

Where ' ω ' is the angular frequency, ' L_s ' is the shield inductance and ' C_s ' the capacitance between turns.

Hence, ignoring any parasitic capacitances, the frequency (f_x) at which the shield becomes self-resonant (f_x) is given by Equation 26.

$$f_x = \frac{1}{2\pi\sqrt{L_s C_s}} \quad (26)$$

When the frequency is less than the resonant frequency the behaviour of the taped shield is inductive and the imaginary part of Equation 24 is:

$$X_y = \omega L_s \quad (27)$$

Similarly, when the frequency exceeds the resonant frequency then the shield is mainly capacitive and the imaginary part of Equation 24 is:

$$X_y = \frac{1}{\omega C_s} \quad (28)$$

3.3 Implementation

There are many trade-offs that must be made during the design stage in the development of a cable shield. For example a good braid shield can have better (i.e. lower) transfer impedance performance than a tape shield however a tape shield is more easily manufactured.

To compare the two types of shield, a 1m RG58 braided cable was examined and was found to give a mutual inductance of about 1.2nH and a transfer impedance of 73mΩ/m at 10MHz. However,

a 1cm wide non-overlapped tape with similar geometrical characteristics as the above RG58 braid (radius of cable 0.25cm and shield diameter 3mm) will give a mutual inductance of 146nH and a transfer impedance of 9.17Ω/m at 10MHz (125 times greater!).

Also the tape shield has a frequency dependent cut-off point usually in the region of few MHz due to the parasitic capacitance between the tape turns which, in some cases, could have a considerable effect on the operation of the shield. A wide gap between the turns would mean a higher cut-off point, something undesirable as the main object of a shield designer is to keep the transfer impedance low at the widest frequency range possible, so less coupling between the shield and the inner conductors is present. This cut-off point can be seen in measurements by Hoeft [11] (see Figure 9) and is predicted in some degree by the theory developed in this section as in Table 1.

For the metalised aluminium tape shield described in Hoeft's paper (Figure 2 of [12]) the prediction accuracy is moderate. The reason for this is that the theory has not included any parasitic components introduced by the measurement procedure, which can affect the resonant frequency point. A prime example of this interference is the drain wire that is used for mechanical support but acts as an inductor and a resistor in series.

Table 1. Prediction of the cut-off point for surface transfer impedance of tale shield.

	This paper	Measurements [12]
Cut-off frequency (MHz)	1	Region between 1 and 11 (Figure 2 in [12])

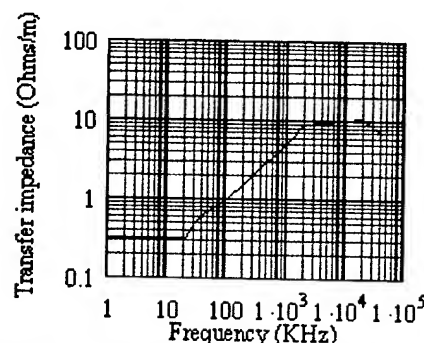


Figure 9. Measured transfer impedance for aluminium tape [11].

4. Shielding Effectiveness

Another parameter for defining the shielding performance is the shielding effectiveness. The shielding effectiveness of a shield is a ratio (in decibels) of the proportion of an electromagnetic field incident on the shield (E_i) to that which is transmitted through it (E_t) as shown in Equation 29 and Figure 10.

$$SE = -20 \cdot \log_{10} \left(\frac{E_t}{E_i} \right) \quad (\text{dB}) \quad (29)$$

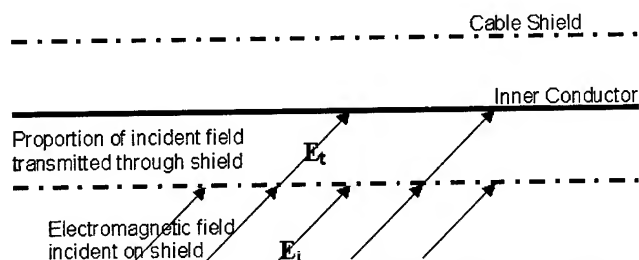


Figure 10. Definition of shielding effectiveness.

The shielding effectiveness is generally used at higher frequencies than the surface transfer impedance and, depending on precisely how it is measured, is dependant on the cable length [12,13]. Shielding effectiveness is used to measure the efficiency of a large variety of shields (not just on cables) therefore the performance of the cables can be compared with other devices in a system.

4.1 Practical Methods for Measuring Shielding Effectiveness

There are many methods for measuring the shielding effectiveness of various forms of shield, which have been redeveloped to measure the shielding effectiveness of cables as the effect of cabling on the overall system electromagnetic compatibility has become more significant. Most of these methods require that the test cable be placed within a metal walled chamber in order to prevent the arbitrarily fluctuating ambient electromagnetic fields outside the chamber from affecting the fields of interest inside the chamber.

Such tests are carried out by injecting an electromagnetic field into the chamber using an antenna then having the cable under test attached to a detector. However such a chamber contains standing waves that add together to form maxima (modes) and minima (nulls) in the electromagnetic field at certain, fixed positions within the chamber hence the amount of power leaking through the shield is dependant on the orientation and location of the device within the chamber, to eliminate this dependency the cable must be tested in a variety of positions. To eliminate the necessity for repeatedly moving and re-testing the cable the positions of the modes and nulls can be altered instead. This can be achieved by installing a rotating reflective surface (or 'stirrer') within the chamber which alters the 'boundary conditions' and causes very large changes in the standing wave patterns and hence the position and magnitude of the modes and nulls. As the stirrer rotates and the modes and nulls move around within the chamber a field within a certain volume (the 'Working Volume', a sub-volume of the 'Uncluttered Volume' shown in Figure 11) is produced that, when averaged over one stirrer revolution, is statistically uniform and hence uniformly illuminates the device under test, which must remain within this volume throughout.

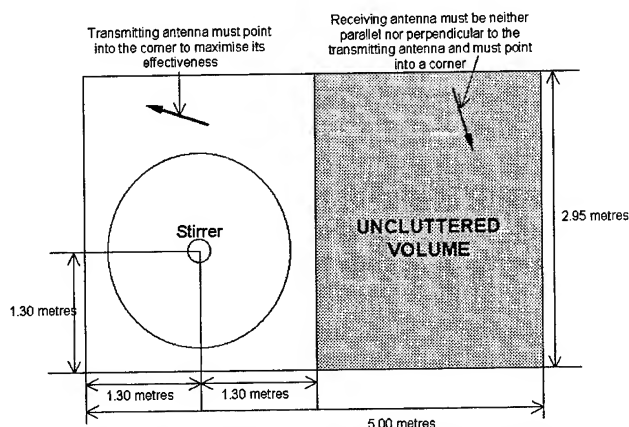


Figure 11. Showing the chamber layout.

The ability of the stirrer to produce this statistically uniform field is dependant on the number of modes within the unperturbed chamber; this in turn is dependant on the frequency and dimensions of the chamber. General rules of thumb suggest that this 'lowest operating frequency' is that which supports 60 modes [14], when this, and the dimensions of the De Montfort University chamber (5.00 metres (a) by 2.95 metres (b) by 2.36 metres (d)), are substituted into Equation 30 [15] they produce a minimum test frequency of 182.5MHz, slightly below the maximum test frequency for the surface transfer impedance methods used previously in this paper. The maximum frequency for which the chamber can be used is defined entirely by the operating frequencies of the equipment used, this gives a maximum frequency of 2GHz. This means that the mode stirred chamber technique is ideal for quickly and easily measuring the shielding effectiveness over a wide frequency range.

$$Ns_f = \frac{8 \cdot \pi}{3} \cdot a \cdot b \cdot d \cdot \left(\frac{f}{c}\right)^3 - (a + b + d) \cdot \left(\frac{f}{c}\right) + \frac{1}{2} \quad (30)$$

There are two methods of operating a mode stirred chamber to obtain shielding effectiveness results. In the 'Mode Stirred Method' 200 sets of measurements are taken whilst the stirrer rotates continuously through 360°. However, because the stirrer is constantly moving no correction or averaging is possible. This contrasts with the 'Mode Tuned Method' where the stirrer is stepped at selected, uniform increments (again 200 per rotation), with the stirrer remaining stationary whilst the measurements are taken and averaged. Due to this averaging the Mode Tuned Method is theoretically more consistent, however it also takes significantly longer to complete each test run.

In order for the mode stirred reverberation chamber to be used to measure the shielding effectiveness of a test cable both the field strength incident on the shield and passing through it must be measured. The field is set up using a transmitting antenna and the power passing through the shield of the standard 1m cable (P_{CAB}) is measured over one stirrer revolution using the arrangement in Figure 12.

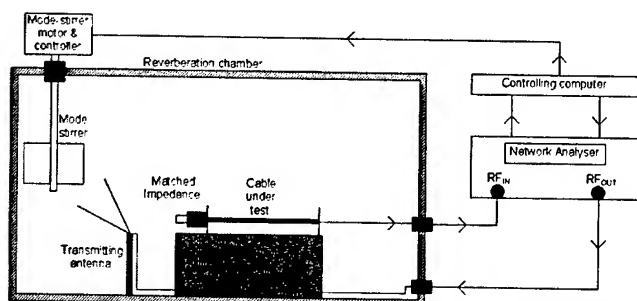


Figure 12. Block diagram of the proposed test set up from [13].

The cable under test in Figure 12 was then replaced with a receiving antenna, which measured the power of the field to which the shield was subjected (P_{REF}) whilst the stirrer was again rotated. Then the maximum power received at each frequency over one rotation of the stirrer was found and used in Equation 31 to calculate the cable shield effectiveness.

$$SE = -10 \cdot \log_{10} \left(\frac{\text{Max}(P_{CAB})}{\text{Max}(P_{REF})} \right) \text{ (dB)} \quad (31)$$

As can be seen from Figure 13 the two mode stirred reverberation chamber methods (mode stirred and mode tuned) produce extremely similar shielding effectiveness responses.

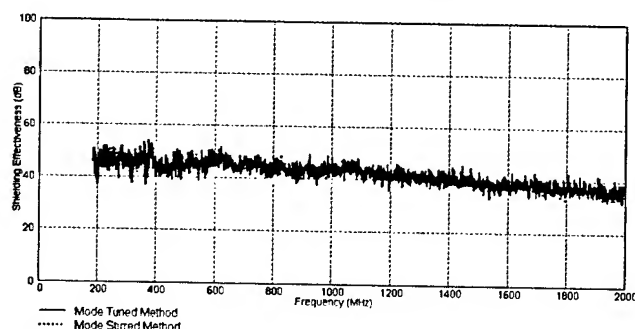


Figure 13. Comparing the results produced using the mode tuned and mode stirred methods.

5. Converting Surface Transfer Impedance into Shielding Effectiveness

Due to the repeatability of the measurements, the short length of time required to perform the tests and the fact that the mode stirred chamber can be used to measure the shielding effectiveness of any device that can fit into the working volume, the mode stirred reverberation chamber method is becoming an increasingly popular test method. However, as has been stated the major problem with this method is that it cannot be used to measure the shielding effectiveness below the minimum operating frequency threshold. As many shielding effectiveness test methods have a similar minimum frequency threshold a simple method for determining the entire shielding effectiveness frequency response of a test cable is essential. As the surface transfer impedance of a cable is usually measured in the frequency range for which the mode stirred chamber does not produce a shielding effectiveness

response, one possibility is to measure the surface transfer impedance in the lower frequency range and the shielding effectiveness in the upper frequency range.

Since the surface transfer impedance and the shielding effectiveness are both measures of how much electromagnetic energy penetrates a shield, it is logical that there should be a relationship between them, by which the responses can be compared. The best proof of this relationship comes from Tsaliovich's cable shielding book [16], however this method is rather too complicated to enact practically. Many other methods have also been formulated which relate the shielding effectiveness and surface transfer impedance [17,17,18], these however are also rather complicated. A much simpler method of converting the surface transfer impedance into shielding effectiveness was proposed by Martin [13] and is shown in Equation 32.

$$SE(f) = 36 - 20 \cdot \log_{10}(L) - 20 \cdot \log_{10}(Z_T(f)) \text{ (dB)} \quad (32)$$

The surface transfer impedance responses produced in Section 2.2 using the two experimental methods and the modelling technique proposed in Section 2.1 of this paper were converted into shielding effectiveness responses using Equation 32 so the results could be compared with those obtained using the mode stirred chamber (see Figure 14). As the cable length differed between the surface transfer impedance (which is a 'per unit length' parameter) and the shielding effectiveness results (which are length dependant) a constant value of 1m was used in Equation 32 to compensate for the variations this would otherwise have caused.

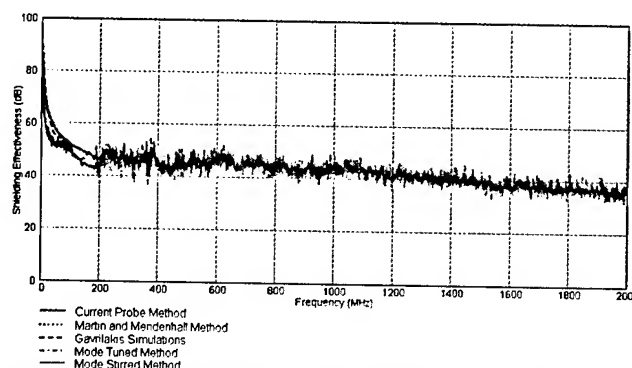


Figure 14. Comparing the shielding effectiveness results.

As can be seen in Figure 14 the transformed surface transfer impedance responses are consistent with the shielding effectiveness responses produced using the mode stirred chamber. Thus a complete shielding effectiveness frequency response is provided. Also the transformed response obtained using the TLM simulations appear to predict the lower frequency shielding effectiveness response, which could be used as a theoretical prediction of the shielding effectiveness response of a cable shield.

6. Conclusions

As can be seen from the practical results produced in this paper, the actual values of the surface transfer impedance for a length of cable, correlate well with those produced using the developed

simulation technique [3]. This provides results that are by far more accurate than those produced using the Katakis equations [1] as it takes into account the resonance phenomenon, unlike the purely theoretical equations. When these surface transfer impedance results were transformed into shielding effectiveness results, there was an extremely high level of agreement between the transformed results and those produced practically in the mode stirred chamber. This is a promising method for theoretically determining the accuracy of shielding effectiveness results. This theoretical support for the shielding effectiveness results is extremely useful, especially as the mode stirred chamber method could be used to test not just coaxial cables (as in this paper) but any type of cable, connector, cable assembly, harness, etc with little or no alteration required between tests.

Also in this paper, theoretical formulae have been presented to predict the surface transfer impedance performance of braid and tape shielded cables. The comparison between the two types of cable shields showed that, although the overlapped tape had mechanical advantages, it also had a high transfer impedance. Also the phenomenon of the cut-off point for tape shielded cables has been explained by the parasitic capacitance between the overlapped turns, and validated with measurements by Hoeft [11]. In future work the developed simulation technique for the braid presented in this paper will be used for the prediction of resonant behavior of tape shields.

7. REFERENCES

- [1] Katakis, J. N., Leakage Through and Optimisation of Braids for Coaxial Cables 1981. Department of Electronic and Electrical Engineering, University of Sheffield.
- [2] Tyni, M., "The Transfer Impedance Of Coaxial Cables With Braided Outer Conductor," *EMC Symposium*, Wroclaw, Poland, Sep 1976, pp. 410-418.
- [3] Coates, A. R., Gavrilakis, A., Al-Asadi, M. M., Duffy, A. P., Hodge, K. G., and Willis, A. J., "EMC Behaviour of Cable Screens," *50th International Wire & Cable Symposium*, Disney's Coronado Springs Resort, Lake Buena Vista, Florida, USA, Nov 2001, pp. 554-563.
- [4] International Standard IEC 61196-1. *Radio frequency cables - Generic specification - General, definitions, requirements and test methods*, 237 pages, International Electrotechnical Commission, 1999.
- [5] Coates, A. R., The Development of a Simple Method For The Evaluation Of The Surface Transfer Impedance Of Coaxial Cables (MEng Thesis) 1997. Department of Electrical and Electronic Engineering, University of Nottingham.
- [6] Atkinson, D. M., A Current Transformer Method For The Surface Transfer Impedance Measurement of Braided Coaxial Cables 1984. Department of Electronic and Electrical Engineering, University of Sheffield.
- [7] Martin, A. R. and Mendenhall, M., A Fast, Accurate and Sensitive Method For Measuring Surface Transfer Impedance *IEEE Transactions On Electromagnetic Compatibility*, vol. EMC-26, pp. 66-70, May, 1984.
- [8] Vance, E. F. *Coupling to Shielded Cables*, New York: Wiley, 1978.
- [9] Kaden, H. *Wirbelstrom und Schirmung in der Nachrichtentechnik*, Berlin: Springer-Verlag, 1959.
- [10] Murphy, A. T. and Young, F. J., High Frequency Design and Performance Tubular Capacitors *IEEE Transactions on Components, Hybrids, and Manufacturing Technology*, vol. 16, pp. 228-237, 1993.
- [11] Hoeft, L. and Hofstra, J. S., "Measured transfer impedance of metallised plastic tape and knitted wire mesh cable shields," *IEEE Symposium on Electromagnetics Compatibility*, 1983, pp. 296-300.
- [12] Dole, C. W. and Kincaid, J. W., "Screening Attenuation of Long Cables," *Proceedings of the Forty-Ninth International Wire and Cable Symposium*, New Jersey, Nov 2000, pp. 135-140.
- [13] Martin, A. R., An Introduction to Surface Transfer Impedance *EMC Technology*, vol. 1, pp. 44-52, Jul, 1982.
- [14] Draft 61000-4-21. *Electromagnetic Compatibility (EMC) - Part4: Testing and measurement techniques - Section 21: Reverberation Chamber Test Methods*, 89 pages, International Electrotechnical Commission, 2000.
- [15] Liu, B.-H., Chang, D. C., and Ma, M. T. *Technical Note 1066: Eigenmodes and the Composite Quality Factor of a Reverberating Chamber*, United States: National Bureau of Standards, 1983.
- [16] Tsaliovich, A. B. *Cable Shielding For Electromagnetic Compatibility*, 468 pages, Van Nostrand Reinhold, 1995.
- [17] Peel, R. J., "Simple Relations Between Shielding Effectiveness and Transfer Impedance/Admittance for Cables," *1988 IEEE International Symposium on Electromagnetic Compatibility*, Seattle, WA, USA, Aug 1988, pp. 134-139.
- [18] Peel, R. J., Finney, R., and Lassise, R. M., "Relationship of Shielding Effectiveness to Transfer Impedance/Admittance for Cable Emission and Susceptibility," *1984 IEEE National Symposium on Electromagnetic Compatibility*, San Antonio, TX, USA, Apr 1984, pp. 55-62.

Author Biographies



Alyse Coates (alyse@dmu.ac.uk) studied for a Master of Engineering with Honours Degree in Electrical and Electronic Engineering at Nottingham University, England graduating in July 1997. She joined the Applied Electromagnetics Research Group at De Montfort University, Leicester, in September 1999. She is currently involved in developing methods for measuring the Electromagnetic Susceptibility of communications cables.



Alexandros Gavrilakis (alex@dmu.ac.uk) holds a BEng (Hons) degree from Staffordshire University, UK and an MSc from the University of Bradford, UK. He joined the Applied Electromagnetics Research Group at De Montfort University, UK in 2000. His research includes developing mathematical and computer modelling methods to calculate the shielding parameters of communications cables.

The biographies for Alistair P. Duffy, Kenneth G Hodge and Arthur J Willis can be found in the paper "Technology Forecasting Techniques in Communications".

Coaxial Drop Cable Shielding Fatigue Analysis

Allen Miller, Ken Dunn

Corning Cable Systems

Hickory, NC

+1-828-901-6042 · allen.miller@corning.com, +1-828-901-6936 · ken.dunn@corning.com

Abstract

Product reliability is always a factor influencing which products cable TV companies utilize in their networks. The reliability of coaxial drop cable has been, historically, problematic. Multiple System Operators (MSOs) typically consume sufficient coaxial drop cable, beyond new build requirements, to replace all of their drop cables every 3 to 5 years.

In developing unique coaxial drop cables, Corning Cable Systems (CCS) designed for a significantly improved service life. As part of that effort, sophisticated analytical techniques were employed to predict eventual failure. Among these were finite element and fatigue analyses, techniques commonly used in industries such as aerospace, automotive and nuclear to prove the reliability of new products. This paper presents fatigue analyses of coaxial cable shielding utilizing finite element and classical analytical methods to determine alternating shielding strains.

Keywords

Finite element; shielding fatigue; coaxial cable; aluminum.

1. Introduction

Life prediction using fatigue analyses required complete characterization of the alternating load history and the resulting strain in the structure for loads including manufacturing, installation and service loads. Strains resulting from these loads along with the corresponding number of cycles and the associated fatigue curve were then used to determine the fatigue usage associated with each type of loading. Utilizing Miner's rule [1], the sum of the individual fatigue usage values must be less than the theoretical fatigue limit of 1.

Loads considered in evaluation of these coaxial drop cables include manufacturing bends, installation bends, aeolian vibration, galloping vibration and temperature cycling. Manufacturing and installation load cycles were experienced independent of the duration of life while the aeolian vibration, galloping vibration and thermal cycling were assumed to occur uniformly distributed over time.

Loads evaluated and the associated number of cycles are shown in Table 1.

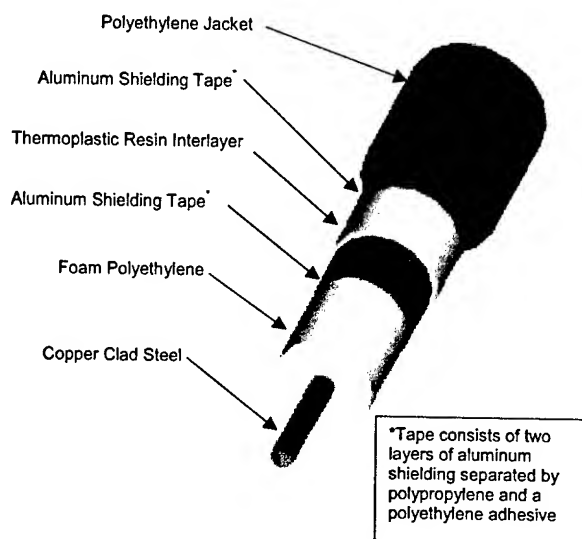


Figure 1 Pentabond™ Cable Geometry

Table 1 Loading

Load	Load Description	Cycles
1	Aeolian Vibration	1e8/20 years ¹
2	Galloping Vibration	1e5/20 years ¹
3	470 mm Diameter Bend	34
4	102 mm Diameter Bend	1
5	356 mm Diameter Bend	1
6	127 mm Diameter Bend	1
7	305 mm Diameter Bend	6
8	76 mm Diameter Bend	1
9	44 °C Thermal	1/day
10	78 °C Thermal	1/year

¹ Assumed 20 year minimum design life for fiber optic cables [2].

2. Cable Geometry and Materials

The coaxial cable construction consisted of a copper-clad steel central member surrounded by a foam polyethylene dielectric. The dielectric had aluminum tape, comprised of two layers of aluminum foil separated by polypropylene, bonded to it. An interlayer of thermoplastic resin was bonded to the inner layer of tape with another layer of aluminum tape bonded to the outside of the interlayer. A polyethylene jacket covered the cable assembly as shown in Figure 1. Table 2 shows the geometry and materials for size 6 and 11 coaxial cables evaluated in this paper.

Material properties used in the analyses are shown in Table 3.

Table 2 Cable Geometry and Materials

Outside Diameter, mm		Description
Size 6	Size 11	
1.02	1.63	Copper Clad Steel Center
4.57	7.11	Dielectric, Foam Polyethylene
4.59	7.13	Tape 1, 1100-O Aluminum
4.64	7.18	Tape 1, Polypropylene
4.65	7.19	Tape 1, 1100-O Aluminum
4.71	7.25	Tape 1, Polyethylene Adhesive
5.39	7.92	Interlayer, Thermoplastic Resin
5.40	7.94	Tape 2, 1100-O Aluminum
5.45	7.99	Tape 2, Polypropylene
5.47	8.01	Tape 2, 1100-O Aluminum
5.48	8.01	Tape 2, Polyethylene Adhesive
7.11	10.06	Jacket, Polyethylene

Table 3 Material Properties

Description	Young's Modulus, MPa	Poisson's Ratio	Coefficient of Thermal Expansion, m/(m-°C)
Copper Clad Steel	1.9e5	0.3	1.3e-5
Foam Polyethylene	1.9e2	0.4	1.4e-4
Aluminum 1100-O	7.0e4	0.33	2.3e-5
Polypropylene	3.8e2	0.4	1.1e-4
Polyethylene	1.9e2	0.4	1.3e-4
Thermoplastic Resin	3.0e1	0.4	1.3e-4

3. Fatigue Curve

Strain based fatigue methods were used to determine the fatigue life of the 1100 aluminum cable shielding. The fatigue data in Figure 2 was obtained from SAE [4] and corrected for a mean strain of yield, surface finish, and reliability based on Equation (1) [1] and [3]

$$S_a' = S_a K_a K_c \left[\frac{S_u}{S_a} \frac{S_b}{S_a} \right] \quad (1)$$

Where:

K_a = surface finish factor based on a cold drawn surface, 0.84.

K_c = reliability factor based on 0.9999 reliability, 0.702.

S_a = completely reversed (zero mean strain) strain amplitude that produces failure in N cycles.

S_a' = the strain amplitude that combined with the maximum possible mean strain produces failure in the same number of cycles as a completely reversed strain amplitude S_a .

S_b = cyclical yield strain of the material, 0.002.

S_u = ultimate strain of the material.

$$\left[\frac{S_u}{S_a} \frac{S_b}{S_a} \right] = \begin{cases} \left[\frac{S_u}{S_a} \frac{S_b}{S_a} \right] & \text{when } S_a \leq S_b \\ 1 & \text{when } S_a > S_b \end{cases}$$

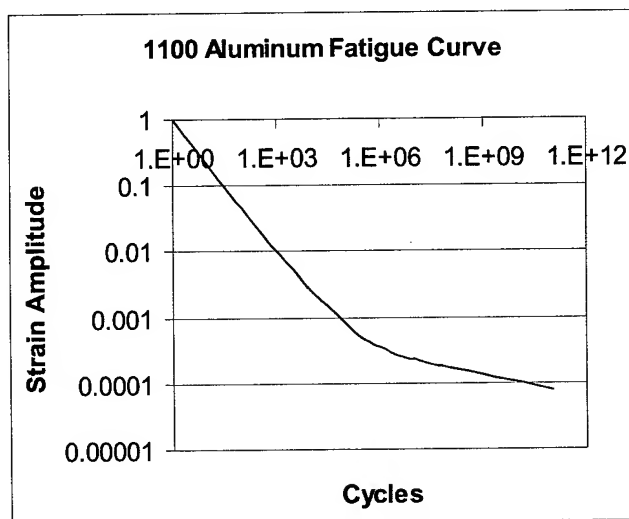


Figure 2 1100-O Aluminum Strain Based Fatigue

4. Analysis

The fatigue analysis was performed by first calculating the strain ranges for each type of loading listed in Table 1. The fatigue usage was then calculated for the fixed cycle load cases and the time dependent load cases as a function of time. Finally, the fatigue life was determined using Miner's rule [1] and setting the sum of the fatigue usage for all the load cases equal to the fatigue limit of 1 and solving for time (fatigue life).

The longitudinal strain calculation for the bends were performed using Equation (2) assuming the neutral axis was at the geometric center of the cable and no slippage occurred at the various material layers in the cable. Hoop strains were calculated by multiplying the longitudinal strains by 0.4, Poisson's ratio for the polymers.

$$\frac{L}{L} \frac{\left(r \frac{d}{2}\right)}{r} \frac{r}{2r} \quad (2)$$

Where: ϵ = longitudinal strain
 L = length, Figure 3
 r = radius of curvature
 d = diameter of shielding
 θ = included angle

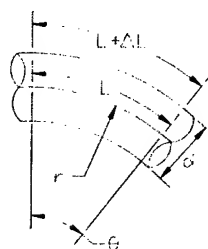


Figure 3 Cable Strain from Bending

Aeolian and galloping vibration loads evaluated were based on those specified in [2] for an assumed 20 year minimum life of self supporting fiber optic cables, refer to Table 4.

For aeolian vibration and galloping vibration, the shape of the cable was assumed to be that of a sine wave during vibration. Assuming an initially straight cable in the unloaded condition, the cable was strained axially to lengthen it into the sinusoidal shape and was also strained in bending by the curvature. Superposition was used to determine the combined effect of these two load conditions.

Equation (3) was used to determine the axial strain in the cable when it was displaced into the sinusoidal shape.

Equation (4) was used to determine the minimum radius of curvature of the cable that was used in Equation (2) to calculate the bending strain from vibration.

Table 4 Vibration Loads

Vibration Type	Cable Size	Span Length, m	Amplitude, mm	Cycles
Aeolian	6	3.33 ¹	1.78 ³	1e8
Aeolian	11	3.33 ¹	2.51 ³	1e8
Galloping	6 & 11	20 ²	399 ⁴	1e5

¹ six loops in 20 meters

² one loop in 20 meters

³ one half of the cable diameter, peak to peak

⁴ span length/25, peak to peak

$$\frac{L}{L_0} \frac{L_0}{L_0} \int_0^{L_0} \sqrt{1 + [f'(x)]^2} dx \quad (3)$$

$$\int_0^{L_0} \sqrt{1 + \left[A \left(\frac{x}{L_0} \right) \cos \left(\frac{x}{L_0} \right) \right]^2} dx \quad L_0$$

Where: A = amplitude (1/2 peak to peak), Figure 4

ϵ = longitudinal strain

L = arc length of sine curve from $x=0$ to $x=L_0$

L_0 = length of the span (half of wave length)

x = location along the span

$$f(x) = A \sin \left(\frac{x}{L_0} \right)$$

$$f'(x) = A \left(\frac{x}{L_0} \right) \cos \left(\frac{x}{L_0} \right)$$

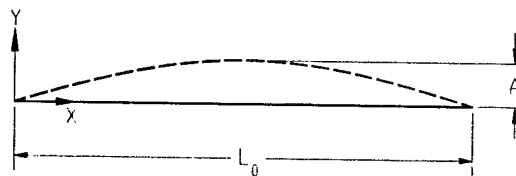


Figure 4 Sinusoidal Vibration of Cable

$$r = \frac{1}{f''(x)} \left(\frac{f'(x)}{2} \right)^2 \quad (4)$$

Where: A , $f'(x)$, L_0 and x were defined in Equation (3)
 r = radius of curvature

$$f''(x) = A \left(\frac{x}{L_0} \right)^2 \sin \left(\frac{x}{L_0} \right)$$

The radius of curvature was a minimum (maximum strain) at $x = L_0/2$, substituting $L_0/2$ in Equation (4) yields:

$$r = \frac{\left(1 - \left(A \left(\frac{L_0}{2} \right) \cos \left(\frac{1}{2} \right) \right)^2 \right)^{\frac{3}{2}}}{\left(A \left(\frac{L_0}{2} \right) \sin \left(\frac{1}{2} \right) \right)^2} = \frac{1}{A \left(\frac{L_0}{2} \right)^2}$$

5. Finite Element Model

Strains in the shielding due to thermal expansion were determined using ANSYS finite element software. Axisymmetric models of transverse slices of the cables were used to determine the thermal strains since the geometry and the loading were axisymmetric, Figure 5. Symmetry boundary conditions were applied to one end of the model ($y = 0$) while the nodes at the other end of the model were coupled in the Y direction to represent a long cable by restricting the motion to planar. The 44 °C temperature change was imposed on the finite element models, FEMs, and the solutions performed to determine the thermal strains. Thermal strains for the 78 °C load case were calculated by multiplying the 44 °C strains by the ratio of the temperature changes (78/44).

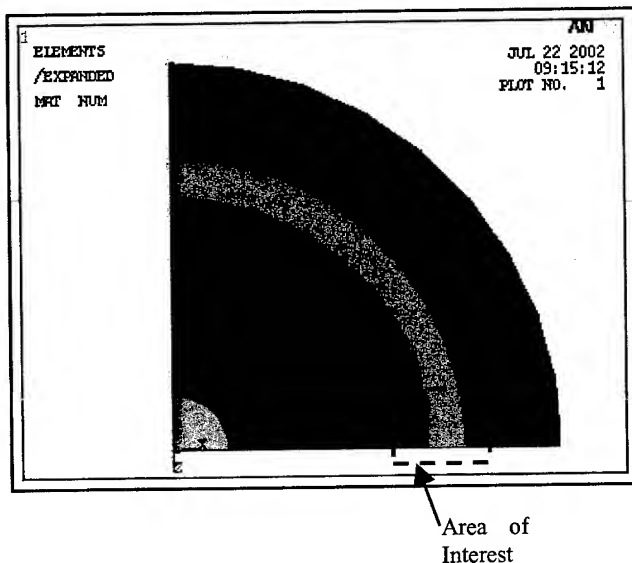


Figure 5 Expanded Axisymmetric Finite Element Model

6. Results

The strain results from the finite element analyses are shown in Figures 6 through 8. From the results, the thermal strains were shown to be most significant in the hoop (circumferential) direction on the inner layer of tape (tape 1 in Table 2) due to the large radial thermal expansion of the relatively stiff foam polyethylene in the cable. The longitudinal growth; however, was limited by the steel central member so the longitudinal strains were not critical for fatigue.

The bending strains due to aeolian and galloping vibrations were calculated using Equation (4) to determine the radius of curvature and Equation (2) to determine the bending strain. Axial strains due to the increased length of the sinusoidal displacements were calculated using Equation (3) and combined with the bending strains using superposition. Bending strains due to manufacturing and installing the cables were determined using Equation 2 and are summarized in Tables 5 and 6 along with the previously discussed strains.

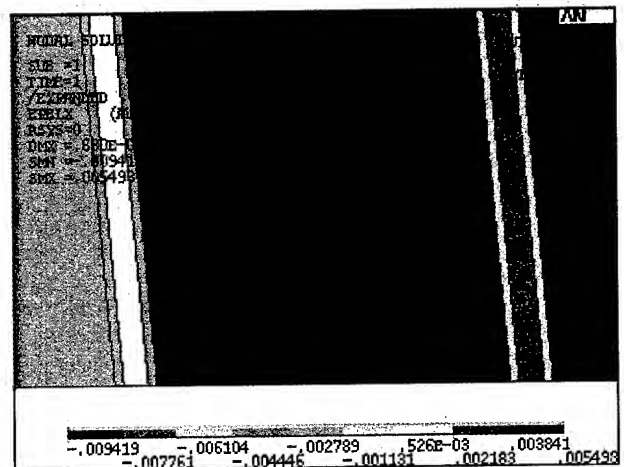


Figure 6 Radial Strain

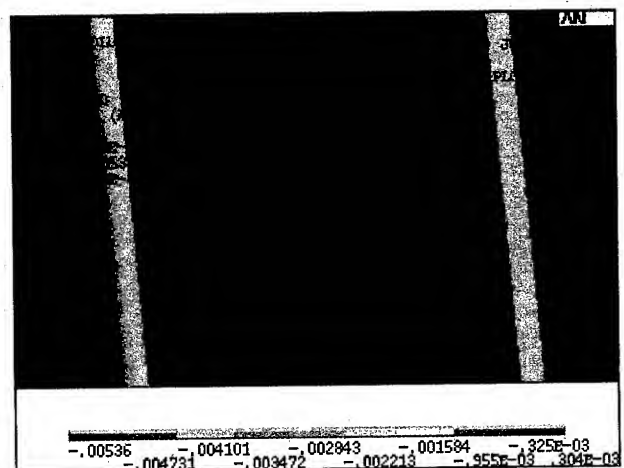


Figure 7 Longitudinal Strain

Table 5 Size 6 Results

Load ¹	Cycles	Alternating Strain Intensity		Fatigue Usage	
		Long - Radial	Hoop - Radial	Long - Radial	Hoop - Radial
1	1.66E+08	3.84E-06	1.54E-06	0.17%	0.17%
2	1.66E+05	1.47E-04	5.87E-05	0.05%	0.00%
3	3.40E+01	5.05E-03	2.02E-03	1.06%	0.21%
4	1.00E+00	2.34E-02	9.35E-03	0.36%	0.09%
5	1.00E+00	6.68E-03	2.67E-03	0.05%	0.01%
6	1.00E+00	1.87E-02	7.48E-03	0.26%	0.06%
7	6.00E+00	7.79E-03	3.12E-03	0.38%	0.08%
8	1.00E+00	3.12E-02	1.25E-02	0.56%	0.14%
9	1.21E+04	6.98E-04	2.36E-03	9.23%	98.56%
10	3.40E+01	1.22E-03	4.13E-03	0.07%	0.76%

¹Refer to Table 1 for load descriptions

Table 6 Size 11 Results

Load ¹	Cycles	Alternating Strain Intensity		Fatigue Usage	
		Long - Radial	Hoop - Radial	Long - Radial	Hoop - Radial
1	1.20E+08	8.32E-06	3.33E-06	0.12%	0.12%
2	1.20E+05	1.59E-04	6.37E-05	0.08%	0.00%
3	3.40E+01	7.76E-03	3.10E-03	2.16%	0.46%
4	1.00E+00	3.59E-02	1.44E-02	0.70%	0.17%
5	1.00E+00	1.03E-02	4.10E-03	0.10%	0.02%
6	1.00E+00	2.87E-02	1.15E-02	0.50%	0.12%
7	6.00E+00	1.20E-02	4.78E-03	0.76%	0.17%
8	1.00E+00	4.78E-02	1.91E-02	1.08%	0.26%
9	8.76E+03	8.06E-04	2.80E-03	8.98%	98.09%
10	2.40E+01	1.41E-03	4.90E-03	0.07%	0.71%

¹Refer to Table 1 for load descriptions

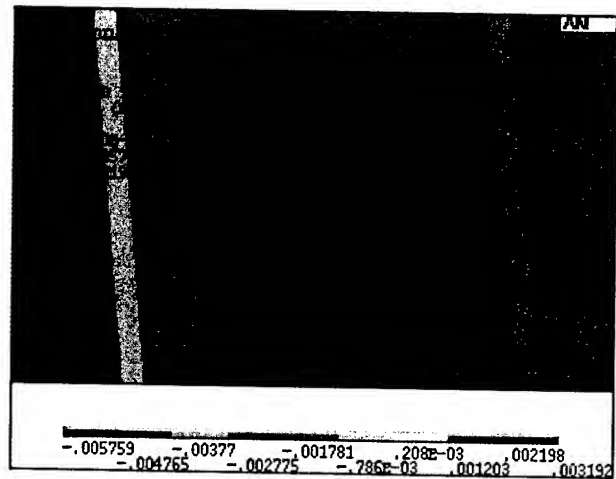


Figure 8 Hoop Strain

7. Conclusions

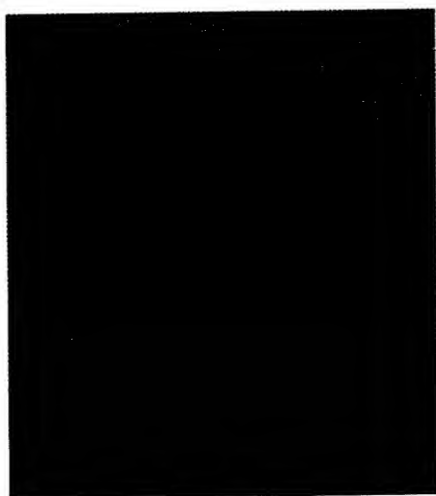
The most significant load contributing to fatigue of the shielding was the daily 44 °C temperature change, which utilized at least 98% of the fatigue life. Radial thermal expansion of the polymers was the most significant loading because it loaded the shielding with significant hoop strain. The longitudinal thermal expansion; however, was limited by the copper-clad steel center conductor.

The theoretical fatigue life of the aluminum shielding was determined to be 34 years and 24 years for the size 6 and size 11 coaxial cables, respectively.

8. References

- [1] Shigley, J. E. and Mitchell, L. D.: "Mechanical Engineering Design," 4th ed., McGraw Hill, 1983.
- [2] Fiber Optics Standards Working Group, "IEEE Standard for All Dielectric Self-supporting Fiber Optic Cable (ADSS) for Use on Overhead Utility Lines," IEEE P1222, Draft, 9/95.
- [3] O'Donnell, W. J. and Langer, B. F.: "Fatigue Design Basis for Zircaloy Components," Nuclear Science and Engineering, 20, 1-12, (1964).
- [4] Chu, C. C., Chairperson, (313) 390-3052, "Fatigue Design & Evaluation Committee of the SAE," <http://fde.uwaterloo.ca/Fde/Materials/dindex.html>, Wrought Aluminum link.

Authors



Allen Miller, P.E., Analytical Engineer, Corning Cable Systems
800 17th Street NW, Hickory, NC 28601

Allen Miller, P.E. joined Corning Cable Systems in 1999, where he performs FE simulations in research and development. Prior to Corning, he worked in defense, nuclear and telecommunication industries as an analyst doing FEA. He received a B.S. in Mechanical Engineering in 1985 from North Dakota State University and a M.E. in Mechanical and Aerospace Engineering in 1997 from the University of Virginia. Allen is an active member of the National Society of Professional Engineers and Professional Engineers of North Carolina.



Ken Dunn, P.E., Product Specialist, Corning Cable Systems
800 17th Street NW, Hickory, NC 28601

Ken Dunn, P.E. joined Corning Cable Systems in 1992, where he works in cable product management and sales development. Prior to this assignment, he worked in process engineering and production. He received a B.S. in Electrical Engineering in 1987 from the U.S. Naval Academy and earned a Professional Engineer license in 1997. Ken is an active member of the Institute of Electrical and Electronics Engineers, National Society of Professional Engineers, and Professional Engineers of North Carolina.

Impedance Calculation of High Frequency Shielded Cables with the Aid of Conformal Mappings

**Alexandros*
Gavrillakis**

**Muhammed
Al-Asadi**

Alistair P. Duffy

**Kenneth G.
Hodge**

Arthur J. Willis

School of Engineering and Technology
De Montfort University
The Gateway, Leicester, UK.
+44 116 257 7056 * alex@dmu.ac.uk

Brand-Rex Ltd.
Viewfield Industrial Estate
Glenrothes, Fife, Scotland

Abstract

This paper presents a new method for the calculation of the impedance of high frequency channels and in particular that of shielded twisted pair cables. Its main advantage is that it uses a more realistic shield geometry instead of the ideal cylindrical case, which most of the related literature is based on. It uses conformal mapping for the conductor-to-conductor capacitance and effective permittivity calculations for extra accuracy. Lastly, characteristic impedance equations are derived. Comparison with measurements is made to show the improvement; practical considerations of the new method are also addressed.

Keywords

Shielded cables, conformal mappings, impedance

1. Introduction

This paper is concerned with high frequency shielded channels. In this configuration two copper conductors, each enclosed in its own insulation are twisted together and are surrounded by a shield. The purpose of the shield is to add extra protection to the pair from electromagnetic interference initiated by external sources. Up to date, the highest frequency is achieved with Category 7 cables that can work up to frequencies of 600 MHz [1]. Significant work has been done to improve the accuracy of Unshielded Twisted Pair (UTP) Cable formulae [2]. However, in the case of Shielded Twisted Pair (STP) cables the literature relating to the formulation of primary parameters as capacitance and inductance of STP cables is more complex and a deeper understanding is required.

In the shielded case the complexity of the configuration increases dramatically, as the number of conducting surfaces from just two in the UTP case (two parallel conductors increases to three (two parallel conductors and the shield) in the STP case. Based on the fact that the structure is usually symmetrical with respect to the centre of the shield, it means that only two capacitance values are required to describe the system. One is the mutual capacitance between the parallel conductors, the other is the capacitance between each individual conductor and the shield. The structure of the paper is as follows. Initially, the relations relating the electrical parameters of the conductors and the shield (charge, potential) are presented and are applicable to any given geometry subject to the determination of a number of constants. The major step then is to obtain these constants by analysing the geometrical structure of the system. Then, conformal transformations are used for the calculation of the mutual capacitance. Furthermore a method to calculate the effective permittivity is introduced.

Finally, expressions for the characteristic impedance are developed and compared with measurements.

2. Capacitance calculation

2.1 Coefficients of potential

In a system consisting of two parallel conductors, surrounded by a grounded shield, as in Figure 1 the potential on the surface of each one,

$$\Phi_1 = r_{11} \cdot q_1 + r_{12} \cdot q_2 \quad (1)$$

$$\Phi_2 = r_{21} \cdot q_1 + r_{22} \cdot q_2$$

(2)

where the r constants depend solely on the geometry of the system

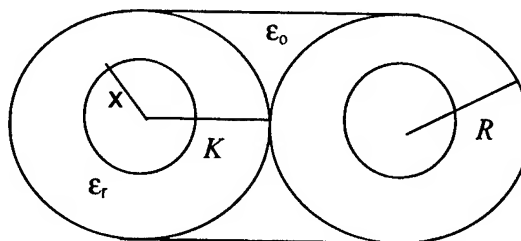


Figure 1: Practical cross-section shape of twisted-pair cable

In order to calculate the potentials Φ_1 and Φ_2 the determination of the r constants is required. First constant to be determined is r_{11} , which relates each conductor with the shield.

The first important point to observe is that the surfaces of the inner conductors, when they are not directly facing each other, they correspond to that ones of a coaxial case. This gives a potential of

$$\Phi_y = \frac{q_y \cdot \ln\left(\frac{R}{x}\right)}{\pi \cdot \epsilon_r} \quad (3)$$

where R is the radius of the dielectric, x the radius of the inner conductor, ϵ_r the dielectric permittivity and $y=1$ or 2 (for each inner conductor).

For a coaxial system

$$C = \frac{q_y}{\Phi_y - \Phi_o} \quad (4a)$$

and $\Phi_o = 0$ (grounded shield), then

$$C_A = \frac{\pi \epsilon_r}{\ln\left(\frac{R}{x}\right)} \quad (4b)$$

The next point to calculate is the conductor to shield capacitance when the shield is not any more cylindrical, but can be represented satisfactory by a straight line.

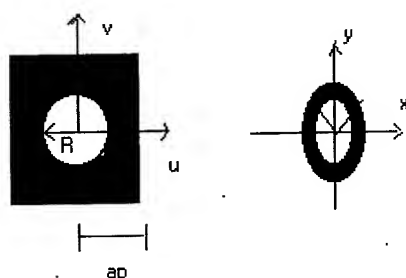


Fig. 2 Approximate conformal mapping of doubly connected region

The following conformal transformation [3], mapping polygons and circles in the w plane into approximate circles in the z plane, as in Figure 2, has been used to account, in part, for the shape of the shield.

$$w = \alpha_p A_p \sum_{j=0}^{\infty} \alpha_j \cdot z^{jp+1} \quad (5)$$

$$\alpha_j = \left(\left(-\frac{2}{p} \right) \right)_j \cdot \frac{1}{jp+1} (-1)^j \quad (6)$$

Where a_p is the apothem of the polygon, p is the number of axes of symmetry and A_p is a constant relating to p . In this method the values of p and A_p is 4 and 1.078 respectively [3].

$$w = \alpha_p (1.078z - 0.108z^5 + 0.045z^9 - 0.026z^{13} + \dots) \quad (7)$$

Having converted this part of the shield into two eccentric circles, then the more simplified coaxial theory can be used. If the dielectric was homogeneous the capacitance C would be

$$C = \frac{\pi \cdot \epsilon_r}{2 \cdot \ln\left(\frac{1.078 \cdot R}{x}\right)} \quad (8)$$

However because in a cable there is an air filling in the area where the dielectric is not present, then,

$$C_B = \frac{\frac{\pi \cdot \epsilon_r}{2 \cdot \ln\left(\frac{R}{x}\right)} \cdot \frac{\pi \cdot \epsilon_o}{2 \cdot \ln(1.078)}}{\frac{\pi \cdot \epsilon_r}{2 \cdot \ln\left(\frac{R}{x}\right)} + \frac{\pi \cdot \epsilon_o}{2 \cdot \ln(1.078)}} \quad (9)$$

As the mapped area represents a coaxial line the capacitances C_A and C_B are in parallel so they add arithmetically and from equation 4 b and 9,

$$C = \frac{\pi \epsilon_r}{\ln\left(\frac{R}{x}\right)} + \frac{\frac{\pi \cdot \epsilon_r}{2 \cdot \ln\left(\frac{R}{x}\right)} \cdot \frac{\pi \cdot \epsilon_o}{2 \cdot \ln(1.078)}}{\frac{\pi \cdot \epsilon_r}{2 \cdot \ln\left(\frac{R}{x}\right)} + \frac{\pi \cdot \epsilon_o}{2 \cdot \ln(1.078)}} \quad (10)$$

and because each conductor has been mapped into a coaxial system, then from equations 1 and 4a and disregarding at this stage the effect of the second conductor the self-potential constant r_{11} is given as,

$$r_{11} = \frac{1}{\frac{\pi \cdot \epsilon_r}{2 \cdot \ln\left(\frac{R}{x}\right)} \cdot \frac{\pi \cdot \epsilon_o}{2 \cdot \ln(1.078)} + \frac{\pi \cdot \epsilon_r}{\ln\left(\frac{R}{x}\right)} + \frac{\pi \cdot \epsilon_r}{2 \cdot \ln\left(\frac{R}{x}\right)} + \frac{\pi \cdot \epsilon_o}{2 \cdot \ln(1.078)}} \quad (11)$$

The rest of the field, is confined mainly between the interaction of the two parallel conductors so it will be used solely for the determination of constant r_{12} .

In order to find the effect of the second conductor into the first one, the method of images is implemented on the path between the two conductors.

Initially, the potential on a arbitrary point Z , due to a charge and its image, is given by

$$\Phi = \Phi_+ + \Phi_- = -\frac{(+q)\ln\left(\frac{p_+}{p_{o+}}\right)}{2\pi\epsilon_{eff}} - \frac{(-q)\ln\left(\frac{p_-}{p_{o+}}\right)}{2\pi\epsilon_{eff}} \quad (12a)$$

where q is the charge on conductor

$-q$ is the charge of the image

p_+ is the distance of the conductor to an arbitrary point Z

p_- is the distance of the image conductor to arbitrary point Z

p_{o+} is the distance of the conductor to the zero potential point

p_{o-} is the distance of the image conductor to the zero potential point

ϵ_{eff} is the effective permittivity of the system which can be calculated using the conformal mappings technique of section 3 of this paper.

The shield will simplify the calculations using the fact that is grounded and the point in question could be assumed to be on the surface of circle with radius $2R$. Furthermore, it is assumed that the charge on the surface of the inner conductors is uniform.

Applying the superposition theorem on the surface of the shield, on the path between the two conductors and the shield regarding initially the *conductors as point charges*, [4], (for simplicity of calculation the outer conductor will initially considered as spherical, as the geometry examined on this paper is mapped similarly in a conductor case)

$$\Phi = \frac{1}{4\pi\epsilon_{eff}} \left[\frac{q_o}{p_{o-}} + \frac{q}{p_{o+}} \right] = 0 \quad (12b)$$

The charge of the image conductor has been assigned for clarity as q_o in this case.

Applying equation 12b to the examined system of Figure 1 gives,

$$\Phi = \frac{1}{4\pi\epsilon_{eff}} \left[\frac{q_o}{|R' - b_i|} + \frac{q}{|R' - K|} \right] = 0 \quad (13)$$

where b_i is the distance from the centre of the shield to the image of the second conductor and R' the maximum distance from center of shield to its surface.

By solving equation 13 and then dividing by R' the first part of the equation and by K the second one,

$$\frac{\frac{q_o}{R'}}{\left| \hat{r} - \frac{b_i}{R'} \hat{z} \right|} = \frac{-\frac{q}{K}}{\left| \hat{r} \frac{R'}{K} - \hat{z} \right|} \quad (14)$$

where, \hat{r} is a unit vector and refers to radius R of the shield and \hat{z} is a unit vector and refers to the distances of the conductors and their images to the center of the shield

Next step is to equate the numerators and the denominators of equation 14.

One of the solutions of equation 14 (equating the numerators) gives

$$\frac{q_o}{R'} = -\frac{q}{K} \Leftrightarrow q_o = -q \frac{R'}{K} \quad (15)$$

From equation 12b,

$$q_o = -q \frac{p_{o-}}{p_{o+}} \quad (16)$$

Then, combining the results in equations 12a, 15 and 16, the potential of a conductor (surrounded by a cylindrical shield) and its image in an *arbitrary point Z* is given in equation 17.

$$\Phi = \frac{q \cdot \ln\left(\frac{p_-}{p_+}\right) \left(\frac{K}{R'}\right)}{2\pi\epsilon_{eff}} \quad (17)$$

where p_- is the distance of the image to the arbitrary point Z

p_+ is the distance of the conductor to the arbitrary point Z

q is the charge of the conductor

If the denominator equality of equation 14 is considered then,

$$\hat{r} - \frac{b_i}{R'} \hat{z} = \frac{R'}{K} \hat{r} - \hat{z} \quad (18)$$

Squaring equation 18 gives,

$$1 - 2\frac{b_i}{R'}(\hat{r} \cdot \hat{z}) + \left(\frac{b_i}{R'}\right)^2 = 1 - 2\frac{R'}{K}(\hat{r} \cdot \hat{z}) + \left(\frac{R'}{K}\right)^2 \quad (19)$$

By equating factors of the left hand and right hand sides of equation 19,

$$b_i = \frac{R'^2}{K} \quad (20)$$

So equation 17 gives,

$$\Phi_1 = \frac{q_2 \cdot \ln\left(\frac{\overline{A_1 B_2} \frac{K}{R'}}{A_1 A_2}\right)}{2\pi\epsilon_{eff}} \quad (21)$$

where $\overline{A_1 B_2}$ is the distance from the first conductor to the image of the second, $\overline{A_1 A_2}$ is the distance between the two conductors.
Using 20 into 21 and substituting the geometrical value of R ,

$$\Phi_1 = \frac{q_2 \cdot \ln \left(\frac{b_i + K}{2 \cdot K} \frac{K}{2 \cdot R} \right)}{2\pi\epsilon_{eff}} \quad (22)$$

and from equation 1,

$$r_{12} = \frac{\Phi_1}{q_2} = \frac{\ln \left(\frac{\left(\left(\frac{2R}{K} \right)^2 + 1 \right) \cdot K}{4R} \right)}{2\pi\epsilon_{eff}} \quad (23a)$$

Because of the symmetry of the structure and the reciprocity being present

$$r_{11} = r_{22}, \quad r_{12} = r_{21} \quad (23b)$$

so there is no need for extra calculations for r_{22} and r_{21} .

2.2 Conductor to shield capacitance

However the system of Figure 1 cannot be treated solely with coaxial theory, so the following procedure is required. In order to calculate the capacitance the potential on each conductor have to be related to both individual charges. By inverting equations 1 and 2,

$$q_1 = \beta_{11} \cdot \Phi_1 + \beta_{12} \cdot \Phi_2 \quad (24)$$

and

$$q_2 = \beta_{21} \cdot \Phi_1 + \beta_{22} \cdot \Phi_2 \quad (25)$$

where,

$$\beta_{11} = \frac{r_{22}}{\Delta} \quad \beta_{12} = -\frac{r_{12}}{\Delta} \quad (26a)$$

$$\beta_{21} = -\frac{r_{21}}{\Delta} \quad \beta_{22} = \frac{r_{11}}{\Delta} \quad (26b)$$

and

$$\Delta = r_{11}r_{22} - r_{12}r_{21} \quad (27)$$

But,

$$\Phi_2 = -(\Phi_1 - \Phi_2) + \Phi_1 = -V_{12} + V_{10} \quad (28)$$

Combining equations 24 and 28,

$$q_1 = (\beta_{11} + \beta_{12}) \cdot V_{10} - \beta_{12} \cdot V_{12} \quad (29)$$

But from electrostatic theory [5], for the geometry considered,

$$q_1 = C_{11} \cdot V_{10} + C_{12} \cdot V_{12} \quad (30)$$

Hence,

$$C_{11} = \beta_{11} + \beta_{12} \quad (31)$$

So by solving equation 31 the conductor to shield capacitance can be calculated.

2.3 Mutual capacitance

The next step is to calculate the mutual capacitance between the parallel conductors. In this case conformal mappings will be used as they can map satisfactory any inhomogeneities between the parallel conductors. The conformal mappings used in [6] for the determination of the capacitance of unshielded cables was used.

w to z plane transformation

$$w = x \cdot \sinh x_1 \coth \frac{z}{2} \quad (32)$$

z to w plane transformation

$$z = \ln \frac{w + R \sinh x_1}{w - R \sinh x_1} \quad (33)$$

$$x_1 = \cosh^{-1} \left(\frac{K}{x} \right) \quad (34)$$

The characteristic of this transformation is that the boundaries of the metal conductors in the w plane are transformed in parallel lines in the z plane and the dielectric boundaries into curved contours respectively. The shield is mapped in the area between the parallel lines as in Figure 3b. Conformal mapping on the boundaries is valid because it retains the angle of refraction of

lines of force on the boundary [6]. The mutual capacitance is calculated by considering the parallel lines as plates of capacitors and obtaining the capacitance in the area where the shield is not present.

Figures 3a and 3b shows an example of a cable with insulation to inner conductor radius ratio equal to 3. Figure 3a shows a replica of Figure 1 represented on the w-plane for the above ratio. Figure 3b shows the corresponding mapping on the z-plane when equations 33 and 34 are used. As it can be seen the parallel straight lines are mapped at $x = \pm 1.76$, as expected from equation 34.

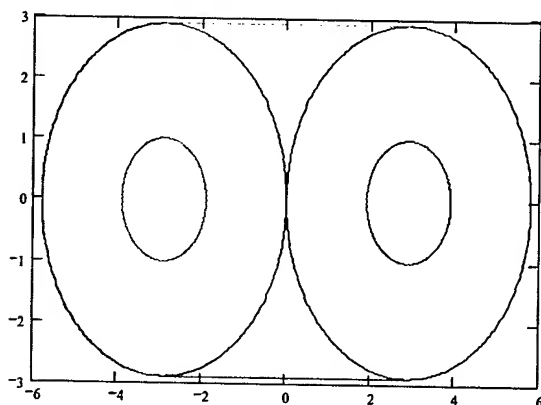


Figure 3a: Cotangent hyperbolic transformation (w-plane)

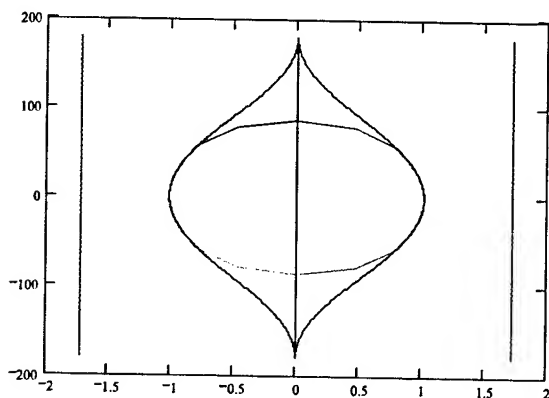


Figure 3b: Cotangent hyperbolic transformation (z-plane)

3. Effective permittivity

This requires calculation of the capacitance (using conformal mappings as in section 2) with and without the dielectric present and then using the ratio of these capacitances to find the effective permittivity. The capacitance required in this step, is calculated by adding arithmetically the conductor to shield and conductor-to-conductor capacitances.

$$\epsilon_{eff} = \frac{C_{11} + C_{12}}{C_{01} + C_{02}} \quad (35)$$

where C_{12} is the mutual capacitance calculated in section 2.3, C_{01} is the conductor to shield capacitance for air medium between them, and C_{02} the mutual capacitance between the inner conductors separated by air medium as well.

4. Impedance calculation

Usually the cable manufacturers specify several nominal parameters for the cable. Two of them are the characteristic impedance and the velocity of propagation. Furthermore the dielectric constant of the medium (insulation) ϵ_r is related to the velocity of propagation, v , by [7],

$$v = \frac{v_o}{\sqrt{\epsilon_r}} \quad (36)$$

where v_o is the velocity of light. So when the velocity of propagation is known the value of the medium permittivity can be calculated.

By calculating the effective permittivity in the previous section, then the line can be treated as homogeneous with the permittivity value the effective one.

Then, for a TEM mode of propagation and a homogeneous medium, the following equation states,

$$LC = \mu\epsilon_{eff} \quad (37)$$

where L is inductance, C is the capacitance and μ the permeability of free space.

Also,

$$Z = \sqrt{\frac{L}{C}} \quad (38)$$

Then, the impedance can be given as function of the capacitance C by

$$Z = \frac{\sqrt{\epsilon_{eff}}}{C \cdot v_o} \quad (39)$$

The final step is to take into account the effect of the twist on the actual length of the cable and consequently on the capacitance per unit length (which in this case will be 1 meter).

Considering that the voltage and the current propagate along the wires of length L , Pythagoras' theorem gives, the propagation constant β in the x-axis is given by

$$\beta' = \frac{\beta}{\sin \alpha} = \beta \frac{\sqrt{P^2 + (\pi D)^2}}{P} \quad (40)$$

Where P is the Lay length

D is the diameter of the pair

So by assigning a constant AD as a correction factor ,

$$AD = \frac{\sqrt{P^2 + (\pi D)^2}}{P} \quad (41)$$

Then the total length of the cable $L\alpha$, will be given by

$$La = Lt \cdot AD \quad (42)$$

5. Results

A PimF cable has been examined in this paper with the following geometrical characteristics.

Conductor diameter: 0.574mm

Insulation diameter: 1.52mm

Dielectric constant of insulation (foam) = 1.93

The twist lay length for the above calculation was assumed to be 20mm which is a characteristic value for this kind of cables.

Table 1: Comparison between theory and measurements

	theory	Measurements
Capacitance to shield (pF/m)	67	69
Mutual capacitance (pF/m)	45	43
Characteristic Impedance (Ω/m)	102	~100

6. Conclusions

A new method of the calculation of the impedance for cables with non-ideal shields has been developed. The advantage of this method is that it can calculate the capacitance for any shields without employing complex modeling techniques such as the Method of Moments (MOM), Finite Element Analysis Method (FEA) etc. Also the use of conformal mappings involves simple calculations (it maps a complex structure to a much simpler one) and have been integrated in the equations given for the conductor to shield and mutual capacitances. The results presented demonstrate the accuracy of the technique.

7. Acknowledgments

The authors would like to thank D. Jackson of Brand-Rex Ltd., for providing the measurements used.

8. References

- [1] ISO/IEC 11801 standard, edition 1.2, January 2000.
- [2] M. M. Al-Asadi, A. P. Duffy, K. Hodge, A. J. Willis "Analysis and modelling of Structured Wiring Communication Channels", IEE Proc.-Sci. Meas. and Techn., 148(3), pp 129-136(May 2001)
- [3] P.A.Laura, L.E.Luisoni, "Approximate Determination of the Characteristic Impedance of the Coaxial Line System Consisting of a Regular Polygon Concentric with a Circle", IEEE Trans. on MTT, 160-162.(Fe. 1977)
- [4] M.H.Nayfeh, M.K.Brussel, "Electricity and Magnetism", John Wiley and Sons, New York, (1985).
- [5] S.Zhang "Calculation of the partial Capacitance in an system of conductors within the Calculable Resistor" IEEE Trans. on Instrum. and Meas., 43,(6), 929-932.(Dec 1994)
- [6] B.N Das, S.B Chakrabarty, and S.R.Rao, "Capacitance of Transmission Line of Parallel Cylinders in the Presence of Dielectric Coating", IEEE Trans. on EMC, 37, (1), 94-96 (Feb1995).
- [7] C.R.Paul, "Introduction to Electromagnetic Compatibility", J.Wiley and Sons, New York, (1992).

Author biographies

Alexandros Gavrilakis can be found in "Determining Cable Shield Behaviour" in these proceedings.

Muhammed Al-Asadi can be found in "Input Impedance of irregular cascaded systems" in these proceedings

Alistair P Duffy, Kenneth G. Hodge and Arthur J. Willis can be found in "Technology Forecasting Techniques in Communications" in these Proceedings

Impact of Environmental Effects upon Transmission Performance Data Grade Cables

J.- H. Walling

Consultant, Beaconsfield, Quebec, Canada
1-(514)-695-8220 ; E-mail: jo.walling@sympatico.ca

Abstract

The performance change of data grade cables is investigated as a function of an environmental treatment. It is shown, that

- the temperature coefficient of attenuation increase, using commercially available jacket materials may be substantially higher than indicated in the standards.

- the sensitivity to humidity of data grade cables is due to the moisture pick-up of the surrounding jacketing material. This effect is reversible at room temperature and to a large extent also at elevated temperature.

- the aging of the jacket material and a migration of the plasticizer into the insulating materials may substantially increase the attenuation. It is shown, that primarily polyolefin insulations are susceptible to plasticizer ingress from the surrounding jacketing material, though at low frequencies, up to approximately 5 MHz, also fluorinated ethylene-propylene insulations are affected as well by aging of the cable. The mechanism leading to this effect could not yet be assessed.

The paper focuses on development of test methods to determine the environmental impacts. It is mandatory to specify such test methods, in order to obtain comparable data.

Some recommendations are given as to the selection of proper cable designs to minimize the environmental impacts.

Keywords

Aging of jacketing materials, temperature coefficient of attenuation increase, plasticizer migration, moisture adsorption, test methods

1. Background

There are basically three common environmental effects which have a direct influence on the transmission performance of cables, i.e. Temperature, Humidity, and Long-term Exposure to Elevated Temperatures.

To take the impact of temperature of data grade cables into account, a so called temperature coefficient of attenuation increase has been standardized. This coefficient has been originally based upon the copper losses alone [1]. Later on the coefficient has been increased to nearly twice this amount [2] for high performance data grade cables. In these cases a flat frequency response has been assumed for the increase of attenuation as a function of temperature. There is no test method indicated so far yet for the determination of the temperature coefficient of attenuation increase.

However such a test procedure is being currently submitted to ASTM for incorporation into the ASTM D 4566.

On the impact of humidity on the transmission performance of data grade cables numerous contributions have been made in the past. However, the relevant standards do not yet reflect this property. The first reporting on this subject was a contribution by the Belden Electronics Division at a TIA/ICEA meeting in Ottawa in 1995. At this time the following phenomena has been reported on patch cables: the attenuation had been measured 24 hours after manufacturing and passed the requirements. Leaving the cable on a shelf for an extended period of time yielded a substantially higher attenuation. It has been inferred at that time, that this effect concerns only stranded patch cords, and it has been conjectured that this might be due to a moisture accumulation in between the strands of the conductor. The effect observed is shown in Fig.1.

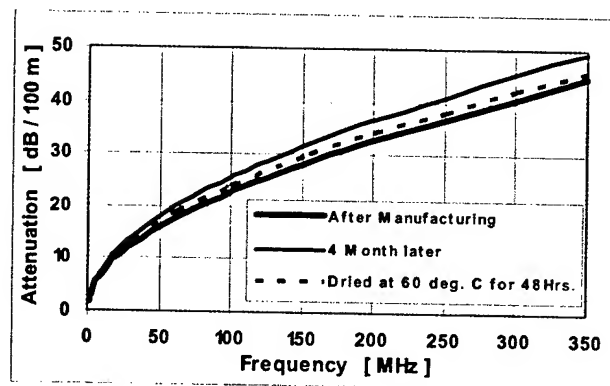


Fig.1: Attenuation of patch cable after manufacturing, 4 month later and after a drying at 60 °C for 48 hours.

It will be shown in this paper that this effect is exclusively due to the impact of humidity on the jacketing compounds. In fact, this effect is due to the water adsorption of the fillers/flame retardants in the jacketing compounds.

The long-term exposure to elevated temperatures is generally simulated by a short-exposure to high temperatures (aging) [3][4]. Thus the aging of cables is a very well established procedure to test their mechanical performance, and the procedures and aging regimes towards this purpose are well reflected in the relevant standards. They take care as well of the different continuous operating temperatures.

These methods have been used to predict life time of cables [5].

Some articles concerned the longevity of coaxial cables, under inclusion of the transmission performance considerations. [6][7]. However the aging and its impact upon the electrical performance of data grade cables in balanced mode transmission has not yet been considered or standardized.

Thus there is no method available yet of how to assess these effects experimentally.

2. Introduction

There are several objectives pursued in this paper. Thus the following subjects are elucidated with the aim:

- to indicate clearly defined and reproducible test methods for assessing the main environmental effects upon the transmission performance of data grade cables we are concerned with here, i.e. Temperature, Humidity, and Long-term Exposure to Elevated Temperatures. In this case the emphasis is placed upon the utilization of relatively small air circulating ovens and climate chambers.
- to demonstrate that the behavior of the temperature coefficient of attenuation increase is more complex, than so far reflected in the standards, and that this fact will have to be reflected mainly, if the performance levels are further increased. Such an increase in performance may be required in the cabling systems for the industrial environment. It should be mentioned, that this may have also an impact upon the "echo forward" performance, hence upon the noise generated in a cabling system, if the heating of the cable is longitudinally inhomogeneous, i.e. alternating over length
- to show that CM or CMR rated cables are generally more susceptible to plasticizer migration than plenum rated cables.
- to highlight the impact of the migration of the commonly used plasticizers into polyolefin insulations.
- to show that mixed insulation types in plenum cables may result in a similar degradation of transmission performance as in the CM or CMR rated cables, as far as it concerns the polyolefin insulated pair(s).
- to show that the majority of commercial jacketing compounds for plenum cables yields a very substantial dependency of the transmission performance to moisture pick-up during long term exposures to higher levels of relative humidity.
- to show the small impact of the plasticizer exuding from the compound at higher temperatures in FEP insulated cables.

To support the findings on the transmission performance of data grade cables, measurements on slabs of different jacketing materials have been made, before and after exposing them to the same environmental treatment as the cables.

3. Methodology

Here the main focus is given to the attenuation performance of the data grade cables, though the propagation speed and the return loss are impacted upon as well.

3.1 The measurement of attenuation

As the cables will have to be measured prior and after exposure to the environmental regime, importance has to be attached to the measurement of the attenuation under the geometrical constraints. Thus the cables need to be coiled due to the dimensional constraints of the air circulating ovens and the climate chambers. However, coiling of UTP cables generally results in "inter winding cross talk", which in turn affects directly the measurement. A typical "attenuation" measurement is shown in Fig. 2. The result is a relatively rough attenuation curve.

This roughness is not to be confounded with the one encountered due to impedance variations along the transmission line (ILD). However, it would result also in an echo forward noise, affecting transmission performance. Therefore it is mandatory to avoid coiled UTP cables in a transmission channel.

As a result it is required to curve fit the attenuation curves, measured before and after exposure to the environmental regime. This is the more important, as the coiled cables, whose ends are fed out of the air circulating oven or climate chamber no more than approx. 12 inches, may shift during the environmental regime due to the thermal expansion and due to vibration and air movement inside the air circulating oven or climate chamber. Such a small shifts will in turn shift also the measurements with respect to the occurrence of the extremes over frequency.

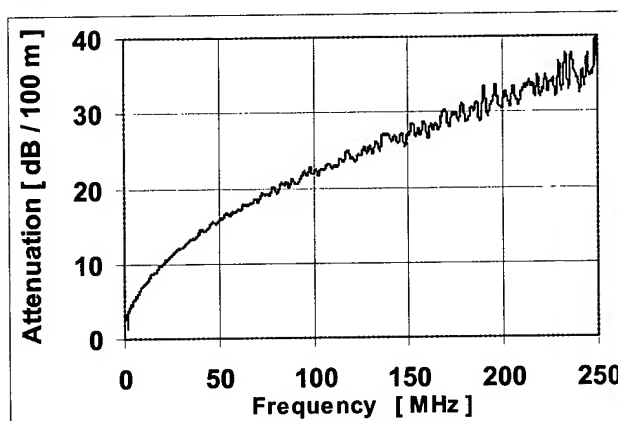


Fig. 2: Typical roughness of the attenuation if the cable is measured in coil form. The roughness is due to inter winding cross talk coupling.

Hence, in order to be able to compare the values at different exposure points during the environmental treatment, a curve fit of the obtained measurement points is mandatory. Since the determination of the temperature coefficient of attenuation increase depends also upon the DC resistance, a four term curve fitting function, suitable for UTP cables has been used:

$$\alpha = a + b \cdot \sqrt{f} + c \cdot f + \frac{d}{\sqrt{f}} \quad (1)$$

where:

- f - is the frequency, and
- a, b, c, d - are the constants of the curve fit.

Thus we obtain for instance for the measurements of Fig. 2 the curve fit depicted in Fig. 3.

The curve fit functions are well suited to compare the measurement data after the different exposures in the environmental regime. In fact, these functions may be used directly to calculate the required values.

3.2 The temperature coefficient of attenuation increase

The temperature coefficient of attenuation increase is defined as:

$$\kappa = \frac{\alpha_T - \alpha_{T_{ref}}}{(T - T_{ref}) \cdot \alpha_{T_{ref}}} \times 100 \text{ [% / } ^\circ\text{C]} \quad (2)$$

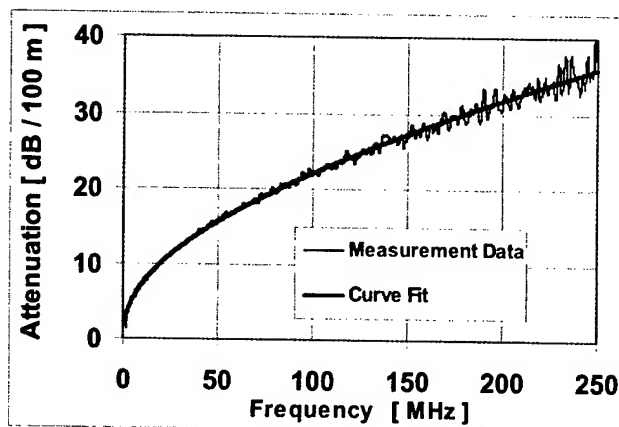


Fig. 3: Curve fit of the measurement data represented in Fig. 2.

where:

- T_{ref} - is the starting reference temperature
- T - is the temperature for which the measurement is to be taken
- α - Is the attenuation measured at the temperature T or the reference temperature

The reference test temperature for these tests has been set to 20 °C, whereas the temperature to determine the temperature coefficient of attenuation increase has been set to 60 °C. It should be mentioned however, that the temperature coefficient of attenuation increase, as far as it concerns that portion exceeding the copper loss, is primarily due to the dielectric losses of the jacketing material. These losses are not necessarily linear with temperature. Thus the temperature coefficient of attenuation increase, measured over lets say half the temperature span than indicated above, may not yield the same result!

3.3 The humidity exposure regime

The attenuation increase λ defined as:

$$\lambda = \frac{\alpha_{T_{Hum}} - \alpha_{T_{ref}}}{\alpha_{T_{ref}}} \times 100 \text{ [%]} \quad (3)$$

where:

- T_{ref} - is the starting temperature at the reference humidity level (20 % RH)
- T_{Hum} - is the temperature of the humidity exposure regime, here for instance 60 °C at 90 % RH
- α - Is the attenuation measured at the temperature T_{Hum} or the reference temperature T_{ref} .

The cables were placed in coil form into a climate chamber with the ends of the cable extending 12 inches out of the chamber. They were then conditioned for 24 hrs at 20 % RH, after which time a base line

measurement of the attenuation has been made. This base line measurement is referred to as 20 °C / 20 % RH, or simply 20 / 20. The temperature was then raised to 60 °C while maintaining the same relative humidity level for 24 hrs. After this time period, a measurement has been taken, to determine the temperature coefficient of attenuation increase, after curve fitting the measurement data 20 / 20 and 60 / 20.

Then the humidity level has been raised to 90 % RH, while maintaining the temperature at 60 °C. The cables are then exposed for 120 hrs to these conditions. A level of 60 °C / 90 % RH for 120 hrs has been selected to accelerate the moisture adsorption of the flame retardant package, based upon the diffusion equation for the moisture adsorption and simulating a long term exposure. After this time the attenuation has been measured as well, to eventually determine the temperature increase of attenuation under simultaneous exposure to humidity.

Then the temperature was lowered again to 20 °C, while maintaining the relative humidity at a level of 90 %. The cables are conditioned under these conditions for another 24 hrs, after which time another measurement of the attenuation has been made. These measurements are referred to also as 20 / 90.

3.4 The aging and the aging regime

As far as the aging concerns, it is logical to use the same aging regime, as used for the mechanical properties. The aging regimes interesting here have been developed for different operating temperatures, and refer to PVC type jackets. Here the aging mechanism is mainly influenced by plasticizer loss. Now it is obvious, that the plasticizer migrating out of the jacket material goes both ways, into the surroundings of the cable as well as to the inside, i.e. towards the insulated wires. The kinetics of the plasticizer migration into polyolefin insulations depends upon the type of plasticizer used. Some plasticizers migrate into the polyolefin in amounts affecting already the attenuation at an amazingly fast rate, which exceeds even the migration rate out of the PVC jacket. Thus it is fully justified, to use the same aging regime as for the mechanical properties also for the electrical transmission performance.

For data grade cable the normally used aging regime is a short term exposure for 168 hours at 100 °C, to simulate a long term operating temperature of 60 °C.

The attenuation increase due to aging η is defined as:

$$\eta = \frac{\alpha_T - \alpha_{T_{ref}}}{\alpha_{T_{ref}}} \times 100 \text{ [%]} \quad (4)$$

where:

- T_{ref} - is the starting reference temperature
- T - is the temperature of the aging regime, here 100 °C
- α - Is the attenuation measured at the temperature T or the reference temperature

It could be conjectured that the increase of attenuation due to temperature may become negative, i.e. it might be an "attenuation decrease" especially for FEP insulations at higher frequencies. This could happen due to an improvement of the cable jacket due

to plasticizer loss and due to the fact that FEP does normally not absorb plasticizers, i.e. it represents normally a very effective barrier against plasticizer migration.

3.5 The types of cables investigated

The following types of cables have been investigated:

1. CM and CMR rated cables
2. CMP rated cables
3. LSOH type cables.

On the LSOH cables results will not be reported, but there will be given some general statements.

Emphasis has been placed to also include cables with mixed insulation material. Such cable designs may be interesting from a cost point of view. Their inclusion in this study seems interesting to assess their viability and potential regarding the environmental impacts.

Therefore, within the second group additionally cables with mixed types of insulation have been used, i.e. cables with 3 pairs which are FEP insulated while one pair which is polyolefin insulated. These types of cables are normally referred to as 3/1 type cables as compared to 4/0 type cables, having four FEP insulated pairs.

3.6 Dielectric performance of commercial jacketing compounds

Several of the tested cables were produced with different commercially available jacketing compounds.

In order to obtain a base line behavior of these jacketing compounds as well, their dielectric behavior has been assessed before and after environmental exposure.

Obviously the jacket materials containing a large flame retardant package are very susceptible to water adsorption to these particulate filling materials, if their surface is not treated to become fully hydrophobic. Therefore one may expect a strong degradation of the dielectric loss of these compounds. This concerns especially those compounds which are used for plenum type cables, as they contain a relatively high amount of flame retardants.

In order to measure the dielectric properties of the jacketing compounds, slabs of suitable thickness have been produced, and these slabs have then been measured at room temperature after conditioning them at 20 % RH for 24 hours. Then these slabs were exposed to the same humidity levels, i.e. 90 % RH for 120 hours, as the cables to measure the impact of humidity on attenuation.

To measure the complex dielectric constant a HP 4291A - RF Impedance / Material Analyzer with HP 16453A Dielectric Material Test Fixture has been used.

As already mentioned, one may expect the dielectric properties of PVC compounds after exposure to an aging regime to improve, as the large part of the dielectric loss of PVC compounds can be attributed to the plasticizer, which migrates out of the jacketing compound upon aging. To measure the dielectric properties before and after aging, similar slabs have been used as above. These slabs were aged for 168 hrs at 100 °C in an circulating air oven conforming to ASTM D 5423, Type II [8].

4. Results

4.1 Temperature coefficient of attenuation increase

The temperature coefficient of attenuation increase is calculated either based on the measured data or the curve fitted data. Both values are shown here sometimes, in order to demonstrate the rather strange behavior up to approximately 5 MHz.

A short look at the data indicates, that mainly CMP type cables meet the specified value of the temperature coefficient of attenuation increase of 0.4 % / °C, where as the CMR or CM type cable exceed this value substantially. This can be attributed to the different types of insulation in conjunction the jacketing materials having very different loss characteristics.

The same is true also for patch cables which show values of up to 0.9 % / °C. For patch cable this does not seem to be important, as the patch cords are hardly seeing temperatures in excess of approximately 35 °C.

However for all types of cables the standards reflect so far only values of 0.4 % / °C, and this flat over the entire frequency range. It should be noted that these values will have to be reevaluated to reflect practical realities, if the cables are to be used at elevated temperatures.

Noteworthy also is the fact that cables with mixed insulation types have a slightly different behavior of the temperature coefficient of attenuation increase for those pairs which have an FEP insulation and those insulated with polyolefin.

In fact the temperature coefficient for polyolefin insulated pairs is markedly higher than the one for pairs insulated with FEP.

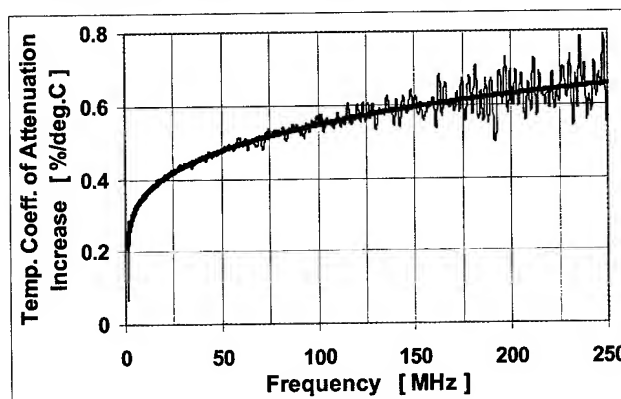


Fig. 4: Temperature coefficient of attenuation increase of a CMR type cable, calculated from measured data and curve fitted data.

4.2 Attenuation increase due to humidity exposure

The Fig. 10 shows the attenuation of a polyolefin insulated pair exposed to 20 % RH at 20 and 60 °C respectively. This pair has been prepared with openings in the insulation every 4 inches over the entire length of 100 m. The holes were approximately 0.25 inch long. The holes in the insulation alternated between the conductors. Thus the stranded conductors were directly exposed to the humidity.

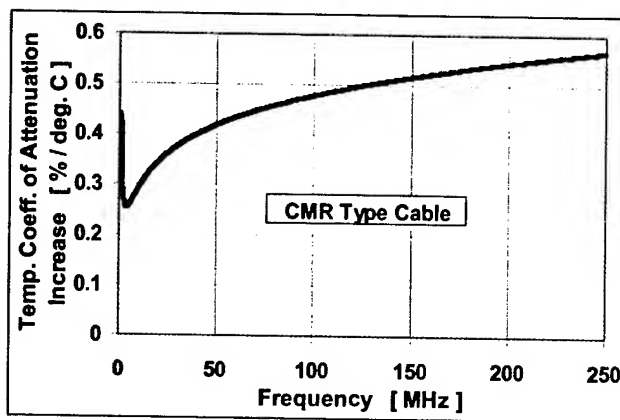


Fig. 5: Typical curve for the temperature coefficient of attenuation increase for a CMR type cable.

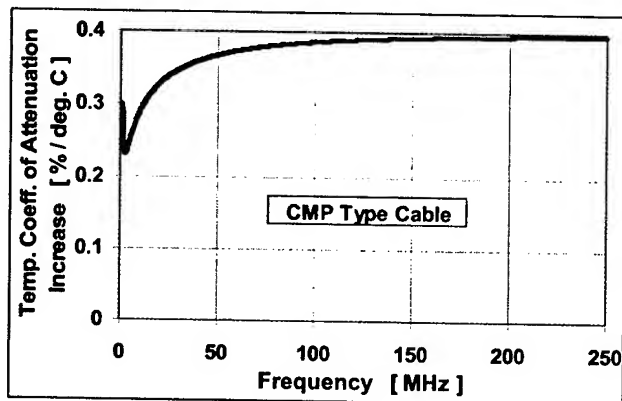


Fig. 6: Typical curve for the temperature coefficient of attenuation increase for a CMP type cable.

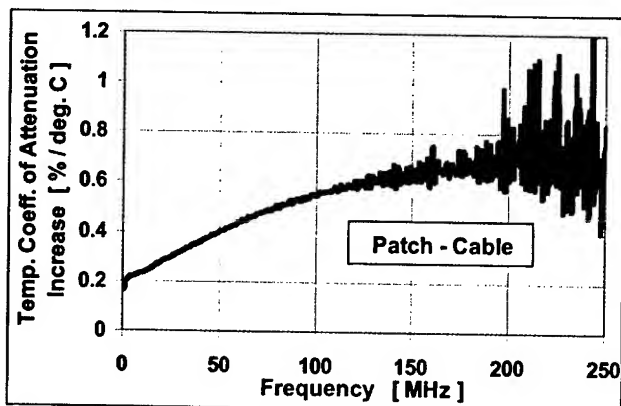


Fig. 7: Temperature coefficient of attenuation increase for a patch cable, based upon measured data.

The Fig. 11 shows the behavior of a typical CMR type cable, exposed to the humidity exposure regime whereas the Fig. 12 shows the same for a typical CMP type cable.

The Fig. 13 and Fig. 14 indicate very clearly the importance of treating the flame retardant package to render it hydrophobic.

Thus the Fig. 14 shows the attenuation difference at 60 °C between the conditions at 20 % RH and 90% RH. It shows clearly the very small difference of attenuation due to moisture

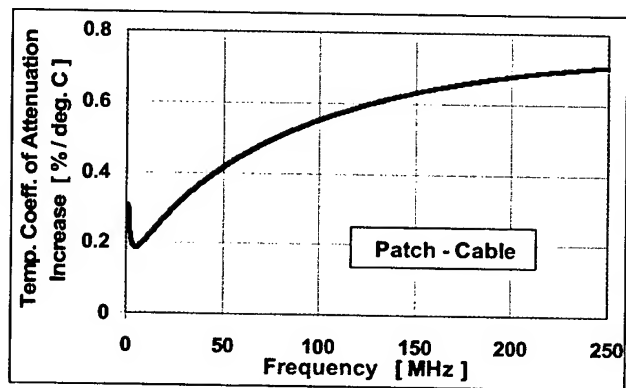


Fig. 8: Temperature coefficient of attenuation increase for the patch cable in Fig. 7, based upon curve fitted data.

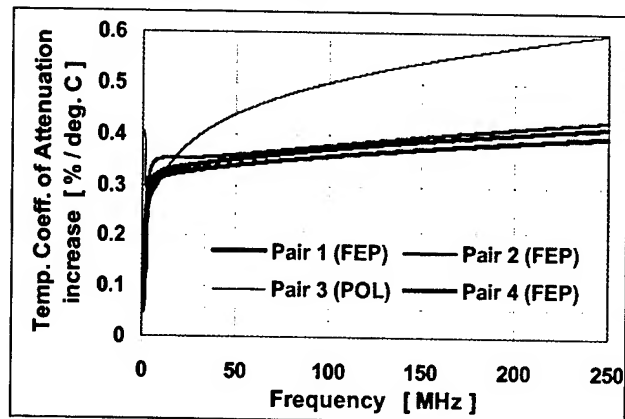


Fig. 9: Temperature coefficient of attenuation increase for a CMP type cable with 3 / 1 FEP / Polyolefin (POL) pairs

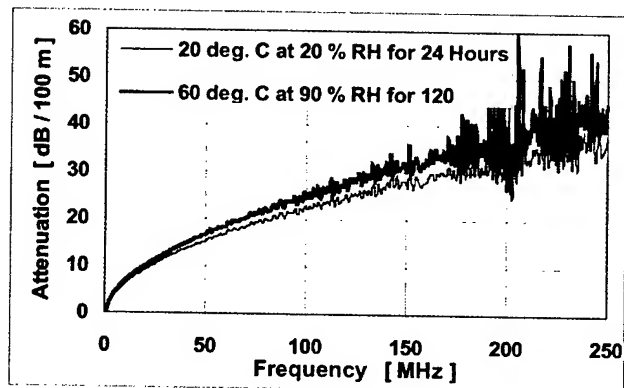


Fig. 10: Attenuation of a patch cable pair without jacket. The insulation has been perforated every 4 inches for approximately for ¼ of an inch, alternating on the conductors. The cable has been measured dry and after exposure for 120 hours to 60 °C and 90 % RH.

pick-up typical for compounds with hydrophobic treated flame retardant packages.

It should be clearly noted that the attenuation increase for the ordinary CMP cables is substantially higher, simply due to the fact, that the majority of the commercially available compounds do not use hydrophobic treated flame retardants.

It is obvious, that this effect can be substantially reduced, by

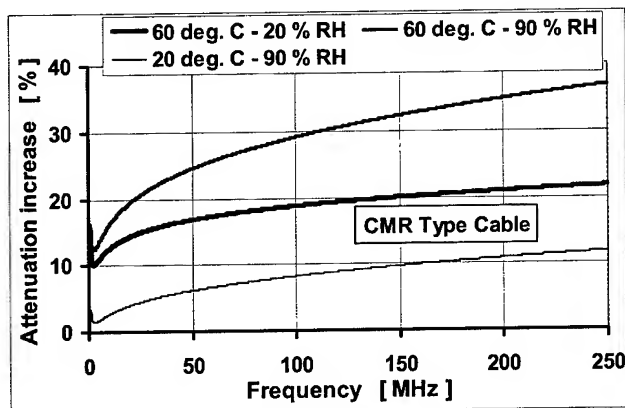


Fig. 11: Attenuation increase for a CMR type cable before, during and after exposure to humidity regime.

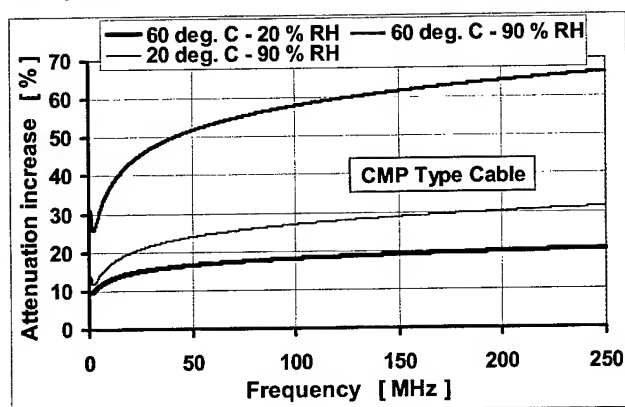


Fig. 12: Attenuation increase for a CMP type cable before, during and after exposure to humidity regime.

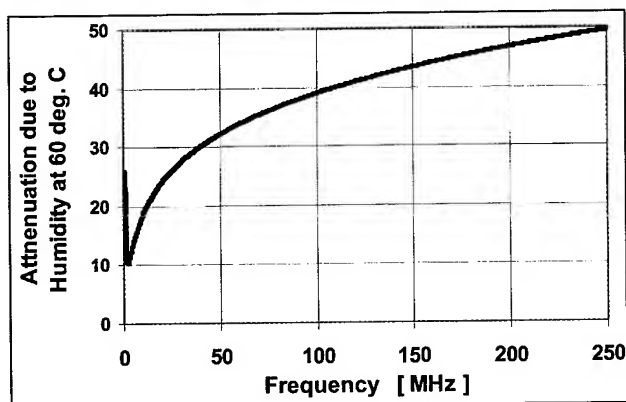


Fig. 13: Attenuation difference at 60 °C between the condition at 20 % RH and 90% RH. It shows clearly the large increase of attenuation due to moisture pick-up typical for compounds with untreated flame retardants.

using hydrophobic treated flame retardant packages. This is shown very clearly in the Fig. 14, where a compound with such treated flame retardants has been used.

4.3 Attenuation increase due to aging

Fig. 15 and Fig. 16 show the results obtained on the same CMR type cable. The attenuation increase is calculated in the first case

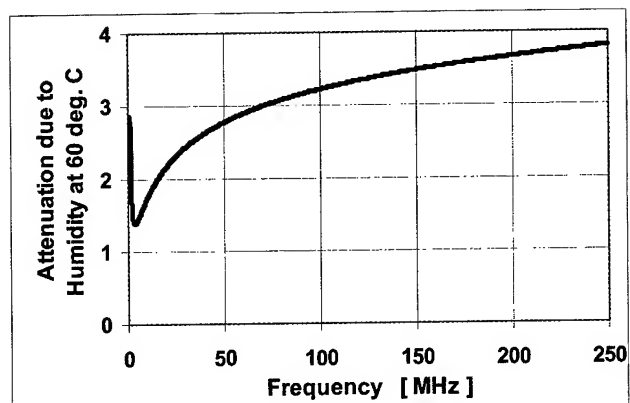


Fig. 14: Attenuation difference at 60 °C between the condition at 20 % and 90 % RH. It shows the small difference of attenuation due to moisture pick-up typical in compounds with hydrophobic treated flame retardants.

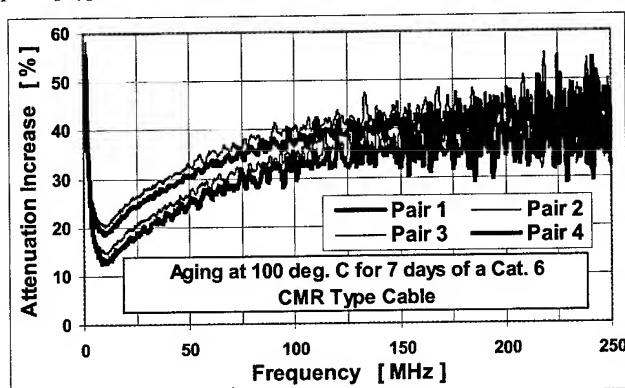


Fig. 15: Attenuation increase for a CMR type cable due to aging after 168 hour aging at 100 °C. Calculation based upon measured values.

based upon the real measurements, whereas in the second case the data are curve fitted. It seems to be important to show these values in both representations, to demonstrate the validity of the curve fitting for the proposed test methods.

The Fig. 17 and Fig. 18 show similar results, but for a CMP type cable. The Fig. 19 and Fig. 20 show the difference of results obtained using the same jacketing compound on pairs insulated with FEP and polyolefin, respectively (CMP and CMR cables).

Fig. 21 and Fig. 22 show the behavior of a CMP type cable with mixed insulations. Noteworthy here is the similarity between the results obtained with the same jacket material on the different insulation types.

The Fig. 23 and Fig. 24 indicate the results obtained when aged cables are additionally subjected to a humidity exposure regime. The CMP type cables showed the normal behavior which is to be expected, falling back to a relatively low value after cooling to 20 °C at 90 % RH. However, the moisture retention of some of the CMP type cables is noteworthy. Thus the value after 24 hours at 20 °C and 90 % RH just falls below the value obtained at 60 °C and 90 % RH. It takes a substantial amount of time to get back close to the original attenuation by drying the cable at 20 °C and 20 % RH.

4.4 Dielectric performance of commercial jacketing compounds

The reporting on the complex dielectric constant is limited to two typical compounds one for each type of cables, i.e. CMR or CMP.

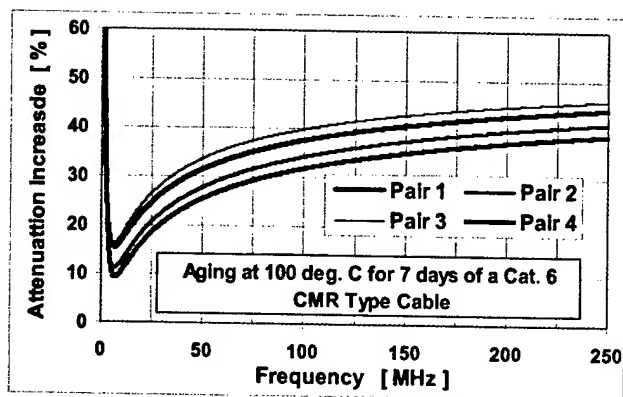


Fig. 16: Attenuation increase for a CMR type cable due to aging after 168 hour aging at 100 °C. Calculation based on curve fitted data of Fig. 15.

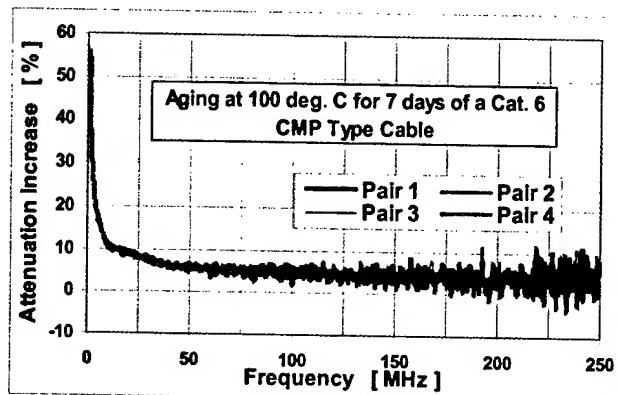


Fig. 17: Attenuation increase for a CMP type cable due to aging after 168 hour aging at 100 °C. Calculation based upon measured values.

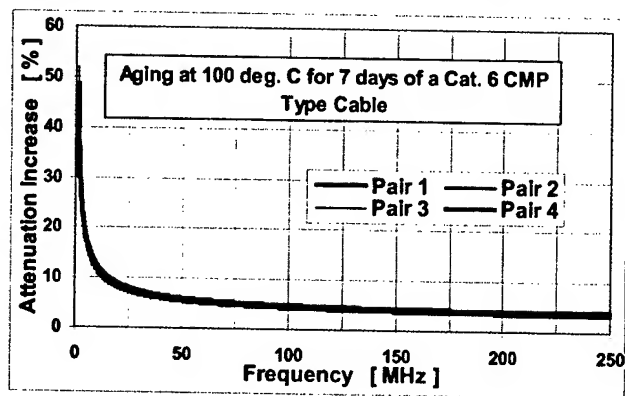


Fig. 18: Attenuation increase for a CMP type cable due to aging after 168 hour aging at 100 °C. Calculation based on curve fitted data of Fig. 17.

The reporting will be limited to the complex dielectric constant, and will not elaborate upon the loss tangent. Hence we have for the dielectric constant:

$$\epsilon = \epsilon' + j \cdot \epsilon'' \quad (5)$$

Though LSOH compound have been measured as well, their results are not reported here.

It should be mentioned that major differences may be found in commercial LSOH compounds. For EVA based compounds little impact

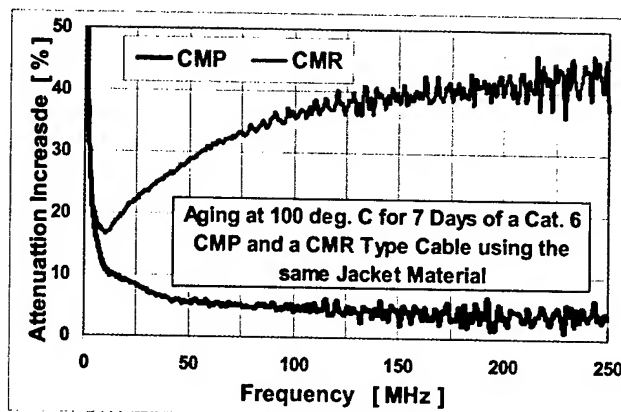


Fig. 19: Attenuation increase for a CMP and CMR type cables due to aging after 168 hour aging at 100 °C. Calculation based upon measured values.

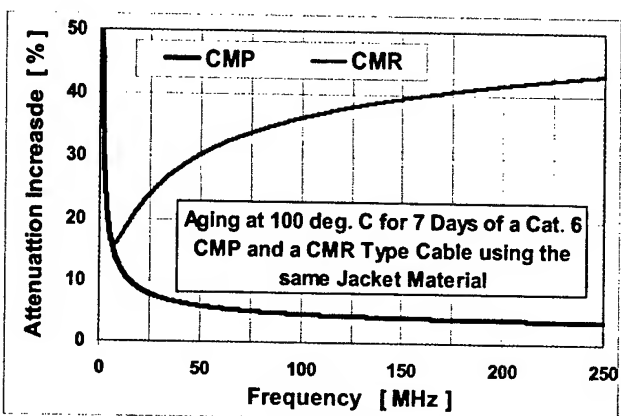


Fig. 20: Attenuation increase for a CMP and CMR type cables due to aging after 168 hour aging at 100 °C. Calculation based on curve fitted data of Fig. 19.

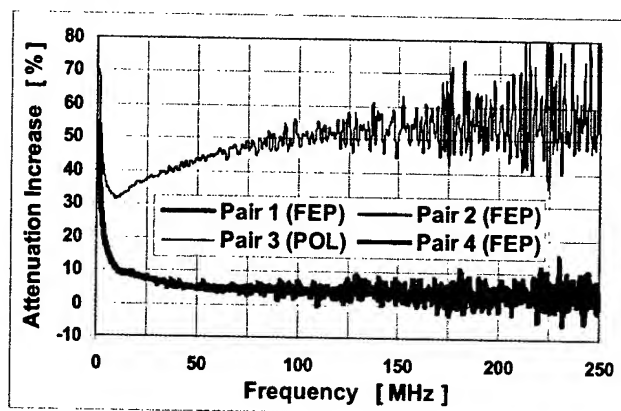


Fig. 21: Attenuation increase for a CMP type cable in a 3/1 FEP/Polyolefin (POL) pair design due to aging after 168 hours aging at 100 °C. Calculation based upon measured values.

from aging or humidity should be expected. This is often not the case.

As far as it concerns the CMR jacketing compounds, they show a relatively limited sensitivity to the humidity. This is obvious, as they contain also relatively small amounts of fillers and/or flame retardants as compared to the CMP jacketing materials.

Therefore they show also much less water adsorption to the particulate matter in the compound. Fig. 25 indicates practically no increase of the real part of the dielectric constant, while Fig. 26 indicates a slight increase of the imaginary part of the complex dielectric constant, responsible for increased losses. Also the aging affects only to a very minor extent the imaginary part of the complex dielectric constant of CMR type compounds, while the real part is not affected at all. See Fig. 27 and Fig. 28.

Fig. 29 and Fig. 30 indicate the complex dielectric constant for a typical plenum rated compound. The real part shows a marked increase which is relatively very high towards the lower frequency end. The imaginary part shows an extreme increase also with a substantial sloping up towards lower frequencies.

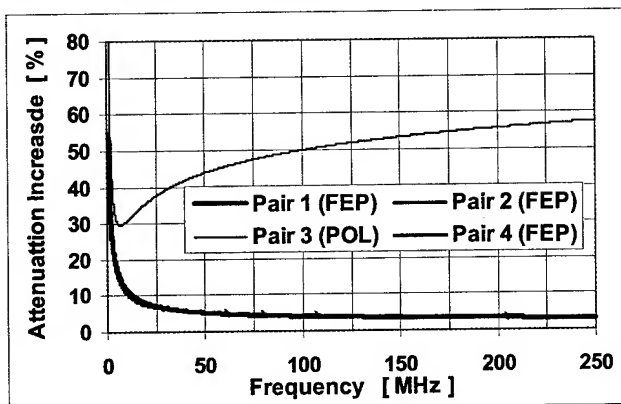


Fig. 22: Attenuation increase for a CMP type cable in 3 / 1 FEP / Polyolefin (POL) pair design due to aging after 168 hours aging at 100 °C. Calculation based on curve fitted data of Fig. 21.

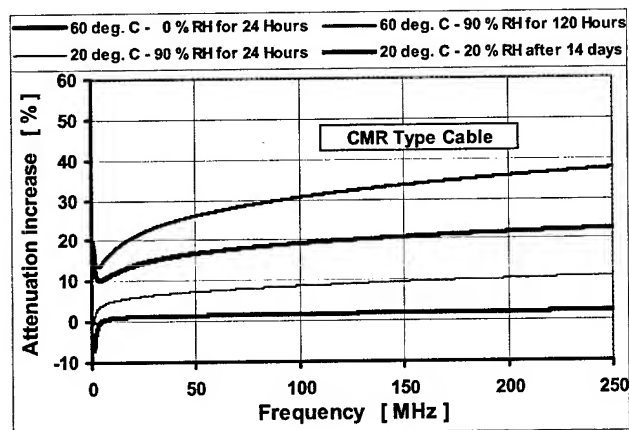


Fig. 23: Attenuation increase for a CMR type cable exposed to the humidity regime after aging. The values are indicated before, during and after exposure to humidity, and after conditioning for 14 days at 29 % RH and 20 °C for drying.

The aging alone of the compounds has practically no impact on the dielectric properties, as is shown in Fig. 31 and Fig. 32. This is also normal. There is no interaction with any insulating material, be it FEP or polyolefin. The aging of the jacketing compounds alone is of little importance, as only the interaction with the insulating material yields the impact on the attenuation and results in an increase.

Work in this direction is under way.

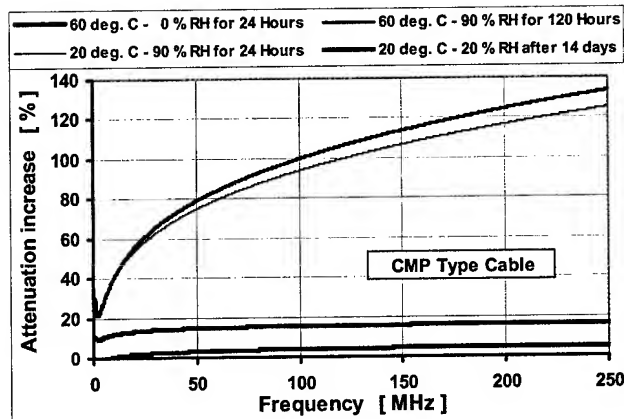


Fig. 24: Attenuation increase for a CMP type cable exposed to the humidity regime after aging. The values are indicated before, during and after exposure to humidity, and after conditioning for 14 days at 29 % RH and 20 °C for drying

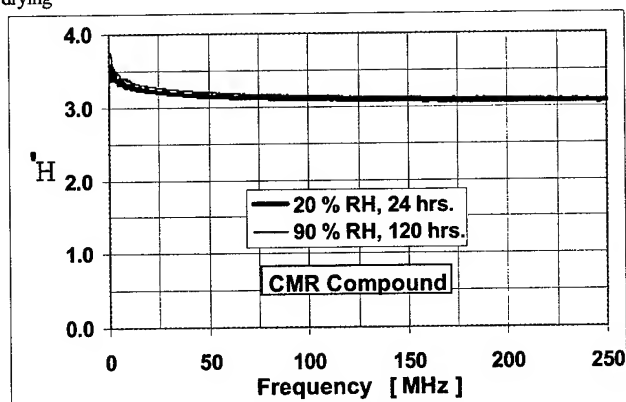


Fig. 25: Real part of the dielectric constant before and after exposure to a humidity regime for a typical CMR compound.

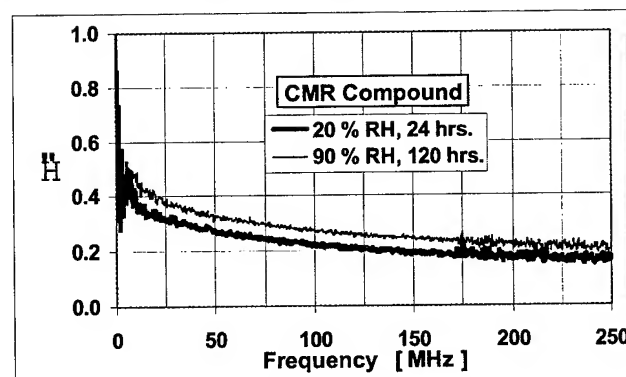


Fig. 26: Real part of the dielectric constant before and after exposure to a humidity regime for a typical CMR compound.

5. Discussion of Results

The results presented indicate very well that the impact of the roughness created by the coiling of the UTP cables can be eliminated by curve fitting. The presented equation (1) to do this is very well suited towards this purpose.

The measurements of the temperature coefficient of attenuation increase indicate furthermore very clearly, that this coefficient

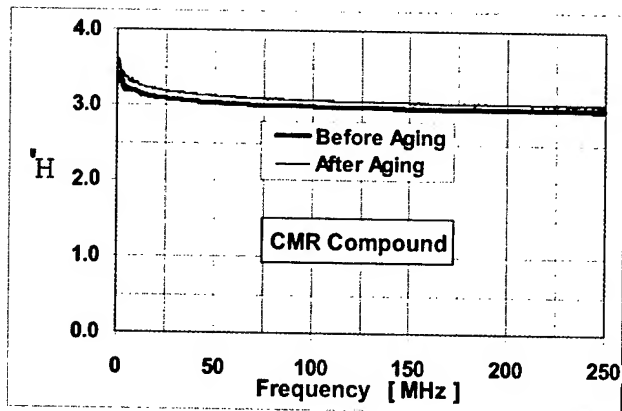


Fig. 27: Real part of the dielectric constant before and after exposure to an aging regime for a typical CMR compound.

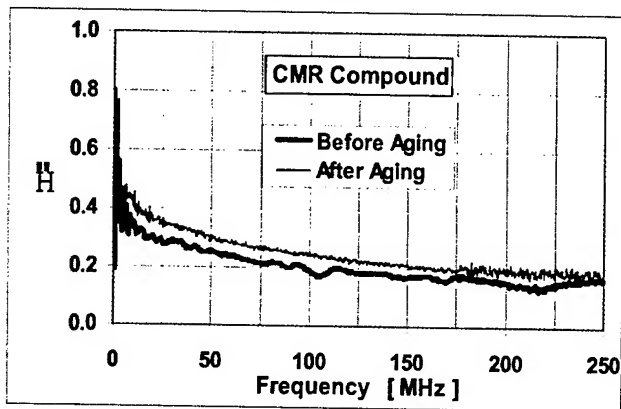


Fig. 28: Imaginary part of the dielectric constant before and after exposure to an aging regime for a typical CMR compound.

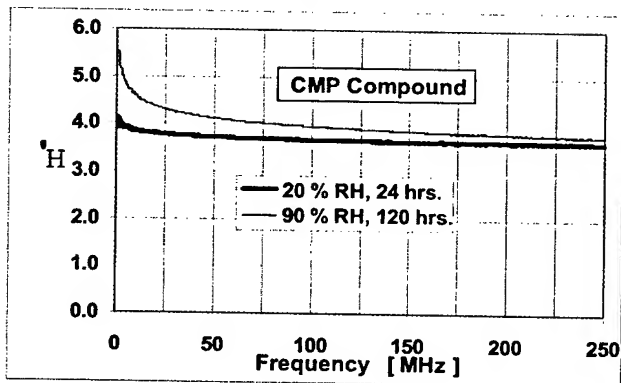


Fig. 29: Real part of the dielectric constant before and after exposure to a humidity regime for a typical CMP compound.

goes up from a value approaching the value of the copper losses at low frequencies to relatively high values at higher frequencies.

It is indicated furthermore, that the value of $0.4 \% / ^\circ\text{C}$ flat over the entire frequency range is for CMP cables sufficient, see Fig. 6. However for CMR and CM type of cables this coefficient has to be raised to approximately $0.6 \% / ^\circ\text{C}$ if only one value over the entire frequency range is intended to be specified, see Fig. 5.

Alternately the temperature coefficient of attenuation increase may be specified as a function of frequency. Also for patch

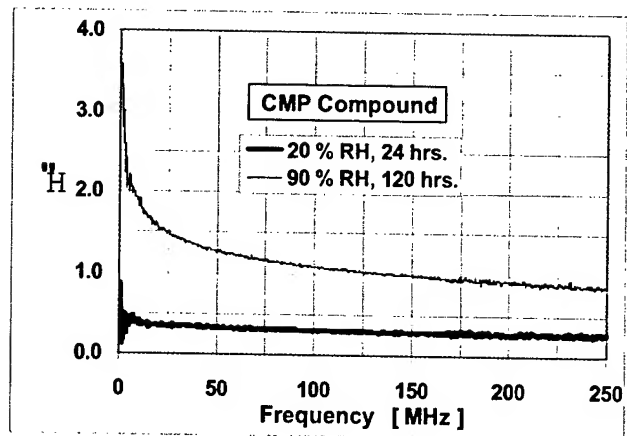


Fig. 30: Imaginary part of the dielectric constant before and after exposure to a humidity regime for a typical CMP compound.

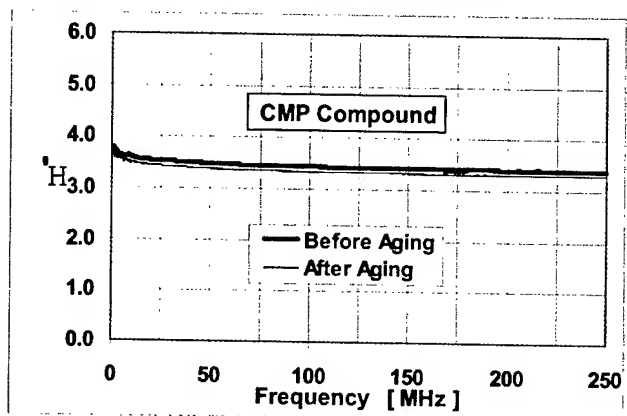


Fig. 31: Real part of the dielectric constant before and after exposure to an aging regime for a typical CMP compound.

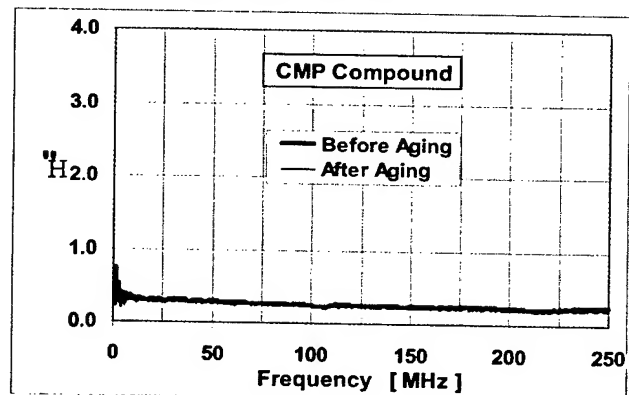


Fig. 32: Imaginary part of the dielectric constant before and after exposure to an aging regime for a typical CMP compound.

cables the coefficient has to be raised to approximately 0.75 or $0.8 \% / ^\circ\text{C}$ if specified flat over the entire frequency range, see Fig. 8.

A problem of course may occur with mixed types of insulations, where the coefficient for plenum rated cables will have to be raised to $0.6 \% / ^\circ\text{C}$.

The moisture pickup of the jacketing materials, especially of the plenum rated commercial compounds, subjected to higher

humidity levels over an extended period of time or in an accelerated test at higher temperature could not be detected gravimetrically. However, it could be easily detected by measuring the complex dielectric constant. The resultant increase of the imaginary part of the dielectric constant is substantially higher at lower frequencies. Together with a slight increase of the real part of the dielectric loss constant, this yields a substantial increase of attenuation in the higher frequencies. This increase of attenuation may be kept very limited, if compounds are used which have inherently hydrophobic flame retardant packages.

The accelerated aging of the cables yields different effects, depending upon the type of plasticizers. The effect of accelerated aging is more pronounced on CM and CMR rated cables, see also Fig. 16. It has been verified with IR-spectrometry that this effect is due to plasticizer migration primarily into polyolefin type insulations. Of course this depends upon the type of plasticizer used in the compound. The increase of attenuation is at low frequencies relatively high, drops off to a minimum at about 5 MHz and increases from there on steadily over frequency, as may be seen in Fig. 16.

On the other hand FEP insulations are affected only in the lower frequency range up to approximately 5 MHz, while the attenuation increase drops asymptotically to zero over increasing frequency, as may be seen very clearly in Fig. 18. The same jacketing compound on the two types of insulation yields nearly an identical attenuation increase at low frequencies below 5 MHz, as can be seen in the Fig. 20. This may suggest a similar mechanism leading to this attenuation increase in both cases. However, a verification using IR-spectrometry yielded on FEP no result. There may be a deposit of plasticizer on the wires or on the inside of the jackets. However this could not yet be confirmed. Therefore the mechanism on FEP insulations yielding the increase at low frequencies remains unanswered.

Interesting in this context is the behavior of mixed insulation materials, i.e. cables with a 3/1 design. Here the attenuation increase of the FEP pairs drops off also asymptotically over frequency to zero, while the polyolefin insulated pairs are affected by plasticizer migration, and increase in their attenuation over frequency after going through a minimum at about 5 MHz. In these cases extreme care has to be taken for the selection of such wires with respect to their jacketing compounds in environments where the cables are extendedly exposed to higher temperatures.

Major problems may be encountered with some compounds, when the cables are run under elevated continuous duty temperatures and at higher humidity levels. In fact, under these conditions the attenuation increase may attain such high levels that channel failures are unavoidable. This is shown very clearly in the fig. 23 and Fig. 24. Mainly in the latter case, i.e. for plenum rated cables there may be a serious problem, depending upon the type of compound used.

The measurements on the slabs of the jacketing material are interesting only if they are submitted to an humidity exposure regime. Then the plenum rated jacketing compounds show a very marked increase of the imaginary part of the dielectric constant, see Fig. 30. In fact this part goes up substantially towards lower frequencies. But also the real part of the dielectric constant goes up in a similar fashion, however proportionally to a much lesser extent, see Fig. 29. The compounds using hydrophobic treated flame retardants show only a very minor variation.

6. Conclusion

Based upon the results obtained the following conclusions can be drawn:

- The relevant standards should be updated with respect to the incorporation of suitable test methods to determine the addressed parameters.
- The values so far specified for the temperature coefficient of attenuation increase will have to be revised at least as far as they concern CM and CMR type cables as well as patch cables.
- A permissible level of attenuation increase due to long term exposure to elevated relative humidity levels should be specified. Suggested is the use of an accelerated test regime for 120 hours at 60 °C and 90 % relative humidity.
- Hydrophobic treated fillers and flame retardants should be used for compounding purposes, especially for CMP rated jacketing compounds
- A permissible value of attenuation increase due to aging has to be specified. The aging regime is already prescribed to test the mechanical properties of cables, which are to be used at a continuous duty temperature of 60 °C. This level has to be specified as a function of frequency.
- The mechanism of attenuation increase at low frequencies due to aging, primarily with respect to FEP insulations will have to be investigated in more detail. Also the mechanism on polyolefin insulations leading to an attenuation increase at lower frequencies will have to be investigated. Suggested is the use of modeling techniques under consideration of the effects of the dielectric behavior of the jackets and their impact on the attenuation of the pairs.
- Cables with mixed insulation types should be avoided for operations under higher environmental demands if they are made with the usual commercial jacketing compounds.
- The interaction of plasticizer of the jacket material with the polyolefin of the insulation will have to be investigated in more detail. A laboratory test towards this purpose will have to be developed.
- Low migrating plasticizers should be used in plenum rated jacketing compounds.

7. References

- [1] ASTM D 4566-98
- [2] TIA/EIA - 568 - B.1
- [3] ASTM D 4565-99
- [4] UL / CSA Bi-National Standard UL 444 / CSA 22.2 No. 214
- [5] Grune, G.I. and T.I. Talarico: An initial investigation on the accelerated aging and lifetime predictions of wire and cable insulations used for local network installations.
IWCS 34 (1985) p. 187-212

- [6] D'Amico, J. N., T. N. Bowmer, O. G. Chavez and L.M. Hore: The deterioration of transmission characteristics and coaxial cable longevity.
IWCS 44 (1995) p. 720-727
- [7] Hore, L. M., V. J. Ferraro, O. G. Chavez and J. N. D'Amico: Thermal aging effects on coaxial cable's transmission and its life expectancy.
IWCS 45 (1996) p. 946-954
- [8] ASTM D 5423

8. Author

Jörg-Hein (Jo) Walling received his diploma in Mechanical Engineering in 1966 at the Technical University of Berlin. In 1974 he obtained a Doctor's degree (Dr.-Ing.) at the same University. In 1974 he joined Northern Electric (later on Northern Telecom and Nortel) in the Research and Development department.

Since 1976 he has been senior engineer at the Lachine Cable Plant. He continued to work at the Nordx/CDT facilities, responsible for the design of Outside Plant and Data Grade Wires and Cables. Since 1999 he is an independent consultant for cables, standards and machinery.



Jo is Canadian head of delegation to ISO/IEC JTC1 25C and IEC 46C, and participates actively as an expert in the development of standards in the working groups ISO/IEC JTC1 25C WG3 and IEC 46C WG7. He was also actively involved in the standards writing activities of ICEA and served as a 1st VP of the communications cable section. He is chairman of the UL-CSA Harmonization Committee, the CSA Subcommittee C22.2 No. 214 (Communication Cables).

Jo is curious and always interested in new challenges.

Temperature and Flexing Effects on Coaxial Cable Insertion Phase, Insertion Loss, and VSWR

Carl W. Dole

Belden Electronics Division
Richmond, Indiana
765-983-5200 · carl.dole@Belden.com

Abstract

This paper will present test methodology, empirical results, and evaluation methods from temperature and flexure testing of flexible coaxial cable testing in accordance with the IEC 60966-1 standard [1]. Measurements of insertion phase and loss, as well as VSWR, were performed to 6 GHz with multiple samples that were simultaneously subjected to temperature increments from -40°C to 85°C. Methods for analyzing and presenting the data, which are not discussed in the IEC standard, are included. These include relating the phase change to temperature, frequency, and sample length in a manner that is easily usable from a system design standpoint. Insertion phase behavior under changing temperature and the time required to stabilize will also be addressed. Flexure involved multiple samples with initial and subsequent insertion phase characterization after multiple flexure cycles, also up to 6 GHz, will be discussed. Statistical analysis establishes mean, maximum, and minimum values for the measurement results.

Keywords

Phase; loss; VSWR; attenuation; coaxial; cable; IEC; 60966-1; temperature; flex.

1. Introduction

Flexible coaxial cable is often used in applications subject to temperature variations and mechanical flexing. These cables may transport signals that require predictable insertion phase and insertion loss characteristics for the system to function properly. For example, an antenna array where the driven elements are interconnected with flexible coaxial cables will be subject to the temperature extremes of an outdoor environment. These variations in temperature will change the insertion phase and loss of the coaxial cables, which could significantly change the antenna radiation pattern due to the altered phasing and amplitude of the signals applied to the antenna elements.

Equipment that involves flexure of coaxial cables may be adversely affected by insertion phase changes in the cable. For example, portable equipment systems with units interconnected with coaxial cable or moveable antenna arrays would have flexure as a concern.

These concerns about temperature and flexure effects led to development of standardized testing methodologies in accordance with IEC 60966-1. Data evaluation methods, which are not addressed in the IEC standard, were also developed. These methods, empirical data, and statistical analysis will be presented.

2. IEC 60966-1 Standard

IEC 60966-1 provides an international standard to use in evaluating phase variation. For temperature (8.8 Phase variation with temperature) the standard specifies a minimum loop diameter of at least ten times the minimum static bend radius, six temperature cycles, and a network analyzer to perform the measurements. The only mention of how to present the data is a suggestion of °el/°C (i.e. degrees of electrical length change per degree Celsius of temperature change) with no explanation. Also, the sample length is not specified.

For flexure (8.6 Stability of electrical length) the standard provides figures of the test sample positions using a mandrel to control the bending and twisting. The dynamic bending radius of the cable is suggested as the mandrel radius. A network analyzer is used for the measurements. Again, the sample length is not specified.

Cable assemblies (i.e. cables with connectors installed) are specified for both temperature and flexure testing. This implies the use of permanently installed connectors. Also, the standard implies the entire cable assembly should be placed in the temperature chamber. The objective of this paper is to evaluate bulk cable rather than assemblies. Therefore, quick-connect, reusable test laboratory type connectors were used. Equal portions of the sample ends remained outside of the temperature chamber with the data analysis taking this into account.

3. Phase, Loss, & VSWR vs. Temperature

3.1 Sample Preparation and Configuration

Ten samples were taken from one bulk reel with each sample carefully cut to 15.24 meters (50 ft.) length (Table 1). Each end was marked 1.52 meters (5 ft.) from each end to standardize the portion that would extend out of the temperature chamber and not be subjected to the temperature variations. All samples were coiled to a diameter of 61 cm (24 in.) in observance of the 10 times minimum static bend radius specified in the IEC standard and placed in the environmental chamber at 20°C. The marked portion of each cable extended out of the chamber to the test equipment. Consequently, all samples would then be simultaneously subjected to the same environmental conditions to reduce this area of variation to the minimum possible.

Table 1. Cable Description

	Diameter (mm)	Description
Conductor	1.47	
Dielectric	3.81	Foamed polyethylene
Shielding tape (inner)		0.09 mm overall thickness Al/Polyester/Al
Braid (outer)	4.55 0.13 (strand)	96.4% coverage
Jacket	6.1	
Impedance		50 ohms
Velocity		86 %

3.2 Equipment Setup and Calibration

The network analyzer was set for a linear frequency sweep of 5 MHz to 6 GHz with 1601 data points per sweep. The network analyzer's internal response calibration was performed for S_{21} measurements of insertion phase and insertion loss. One-port calibration for S_{11} was performed for the VSWR measurements.

The network analyzer is limited to a 360-degree phase range (± 180 degrees). Ambiguity in phase data can result if the phase difference between adjacent data points in the frequency sweep is greater than 180 degrees. To avoid this ambiguity, the first sample was connected to the analyzer and the analyzer's electrical delay setting was adjusted to give a nearly flat phase trace across the entire frequency range. This change of displayed phase is not an issue since only changes in phase are of concern. The electrical delay setting was recorded and remained unchanged throughout all phase versus temperature measurements. The total insertion phase can be calculated from the frequency and electrical delay setting.

3.3 Testing and Data Acquisition

All samples were preconditioned at 20°C for a minimum of two hours prior to the first measurement. Each sample was then characterized for insertion phase (S_{21} phase in degrees), insertion loss (S_{21} log magnitude in dB), and VSWR (S_{11}) while remaining in the temperature chamber.

From this baseline at 20°C, the temperature was changed incrementally in the range of -40°C to 85°C for a total of six cycles (Table 2). Cycles one and six consisted of multiple steps in this temperature range. Cycles two through five included only the temperature extremes, without the intermediate steps, and 20°C. Full sets of insertion phase, insertion loss, and VSWR were obtained for all samples at each temperature.

Table 2. Temperature Sequences

Temperature Cycles	Temperature Sequence (°C)
1 & 6	20, 40, 60, 85, 20, 0, -20, -40, 20
2-5	85, 20, -40, 20

Two hours minimum dwell was allowed at each temperature prior to data acquisition. Figures 1 and 2 show examples of the preliminary phase and temperature versus time testing that was performed to determine this. It is interesting to note in figure 1 that the phase during the temperature transition makes a significant excursion before stabilizing at a lesser phase change. Figure 2 shows a lesser but similar excursion.

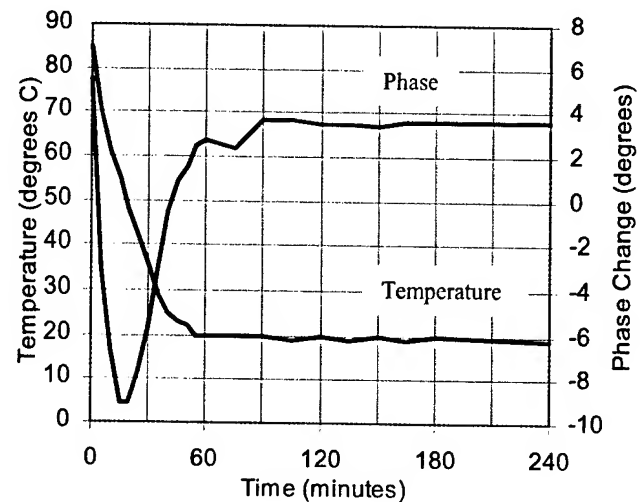


Figure 1. Phase vs. Time (85°C to 20°C)

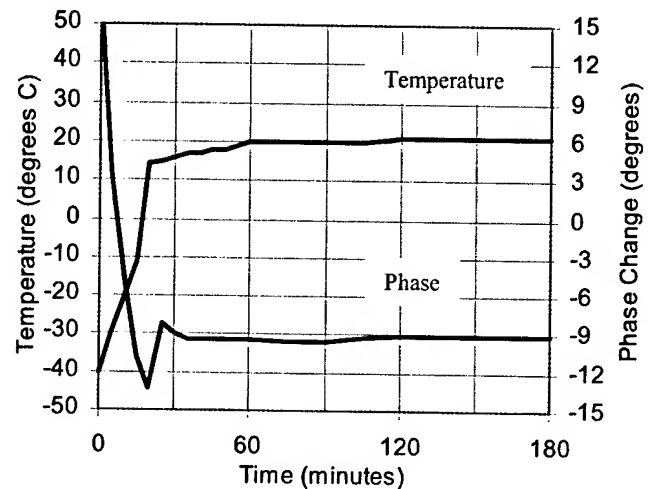


Figure 2. Phase vs. Time (-40°C to 20°C)

3.4 Data Analysis Methods

3.4.1 Phase The network analyzer only has a 360-degree range (± 180 degrees) of phase. When the insertion phase exceeds this range the display makes an abrupt 360-degree transition, resulting in a sawtooth pattern with many transitions possible (Figure 3) [2].

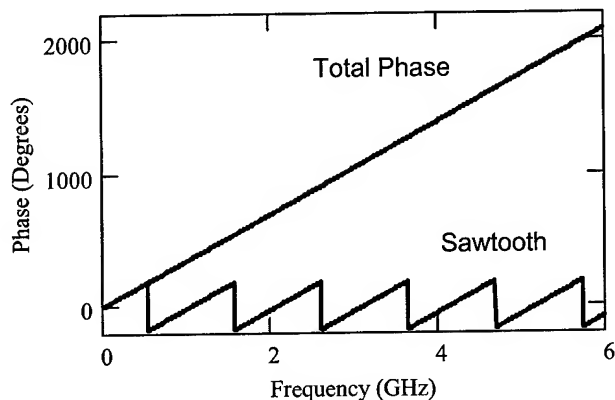


Figure 3. Sawtooth and Total Phase

The initial setting of the network analyzer electrical delay removed most of these transitions, but phase changes due to the temperature changes and small variations between samples resulted in some transitions. Removal of these transitions is necessary to obtain the total phase of the cable for proper data analysis. The transitions were automatically removed by writing equation 1 into a program routine in a math software package [3].

$$\text{total} = \text{na} + k * 360 \quad (1)$$

Where: total = Total phase (degrees)
 na = Phase from network analyzer (degrees)
 k = Integer number of 360 degree phase transitions (e.g. 0, 1, 2, etc.)

The sample length and frequency indicated initializing k to zero at the lowest frequency (5 MHz). The k value was then incremented or decremented by one at each transition. It was incremented if the slope prior to the transition was positive or decremented for a negative slope. This was done automatically in the program routine. The resulting total phase is shown with the sawtooth waveform in figure 3.

The initial total insertion phase at 20°C was used as a baseline phase reference for each sample. It was subtracted from each of the subsequent measurements for that sample to obtain the phase change at each frequency of the sweep (Equation 2).

$$\Delta = \text{total} - \text{ref} \quad (2)$$

Where: Δ = Phase change from reference (degrees)
 total = Total phase from equation 1 (degrees)
 ref = Phase at initial 20°C (degrees)

Analysis was applied to the phase change data to obtain mean, minimum, and maximum values across the frequency sweep at each temperature.

The phase change versus frequency has a nearly constant slope, which allows for a simplified expression of the phase change by relating it to frequency and length (Equation 3). This calculation has a nearly constant value across the frequency span (Figure 7). It is similar to group delay which is the derivative of phase with respect to frequency. The advantage of using the elect deg/GHz/m value is that the phase change can be calculated for any frequency and length.

$$\text{elect deg/GHz/m} = \frac{\Delta}{\text{Freq} * \text{Leng}} \quad (3)$$

Where: elect deg/GHz/m = electrical degrees/GHz/meter
 Δ = Phase change from reference (degrees)
 Freq = Frequency (GHz)
 Leng = Length of sample (meters)

Parts per million (ppm) is another way to express the phase change (Equation 4). This calculation results in a nearly constant value across a frequency span.

$$\text{ppm} = \frac{\Delta * 10^6}{\text{AbsRef}} \quad (4)$$

Where: ppm = Parts per million phase change (degrees)
 Δ = Phase change from reference (degrees)
 AbsRef = Absolute total reference phase (degrees)

It should be noted that AbsRef is the absolute total phase of the cable without the effect of the network analyzer electrical delay setting. This offset can be removed by equation 5.

$$\text{AbsRef} = \text{total} - 360 * \text{Freq} * \text{Delay}_{\text{na}} \quad (5)$$

Where: AbsRef = Absolute total reference phase (degrees)
 total = Total phase (degrees)
 Delay_{na} = Delay setting of network analyzer (sec.)
 Freq = Frequency (Hz)

3.4.2 Loss The insertion loss data was analyzed in a similar manner as the insertion phase data. The initial measurement of each sample at 20°C was used as the baseline for that sample. The change in insertion loss was calculated for each sample across the entire frequency sweep (Equation 6). All insertion loss data from the network analyzer was converted to positive values so that positive ΔIL represents an increased loss and negative ΔIL represents decreased loss. Analysis was applied to obtain mean values (Figure 5).

$$\Delta \text{IL} = \text{IL}_{\text{meas}} - \text{IL}_{\text{ref}} \quad (6)$$

Where: ΔIL = Insertion loss change (dB)
 IL_{meas} = Insertion loss measured (dB)
 IL_{ref} = Insertion loss reference at 20°C (dB)

3.4.3 VSWR The VSWR data was subdivided into frequency bands and the highest VSWR value was extracted from each band (Figure 4). This seemed an appropriate manner to evaluate VSWR change since specifications for VSWR are typically a single value across a frequency range(s).

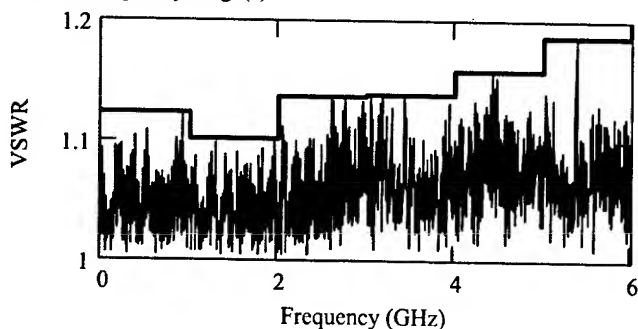


Figure 4. Extracting VSWR Maximum

The 20°C VSWR measurements served as the benchmark to calculate the change in each band (Equation 7). Mean, maximum, and minimum calculations were applied to the Δ VSWR values.

$$\frac{\text{VSWR} - \text{VSWR}_{\text{temp}}}{\text{VSWR}_{\text{ref}}} \quad (7)$$

Where: Δ VSWR = VSWR change
 $\text{VSWR}_{\text{temp}}$ = VSWR at new temperature
 VSWR_{ref} = VSWR reference at initial 20°C

3.5 Results

3.5.1 Phase The mean phase change for the first half of temperature cycle one is shown (Figure 5). Several things should be noted. The phase did not return to its original value when the temperature returned to 20°C after being at 85°C. Also, this 20°C phase change is greater than at 40°C and 60°C.

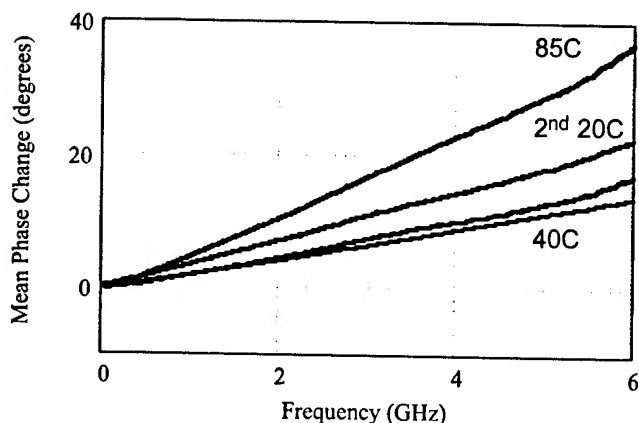


Figure 5. Mean Phase Change (40°C to 85°C, Cycle 1)

The phase change for the other half of temperature cycle one is shown (Figure 6). Again, the phase at 20°C did not return to its original value. The phase changes at 0°C, -20°C, and -40°C were nearly the same, but the greatest change did not occur with the greatest temperature change of -40°C.

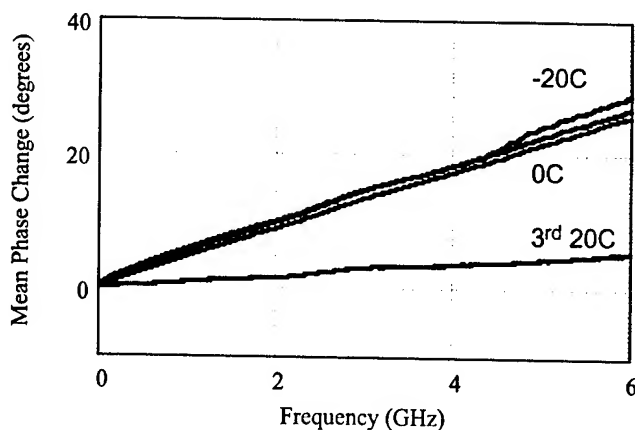


Figure 6. Mean Phase Change (0°C to -40°C, Cycle 1)

All phase changes were positive with the greatest change at the highest frequency. The nearly constant phase slope produces a nearly constant elect deg/GHz/m (Figure 7). The data was started at 200 MHz because of the sensitivity of the calculation to small phase changes at low frequencies, which produced abnormally large excursions. The extremes of phase change did not necessarily occur at the temperature extremes as was anticipated.

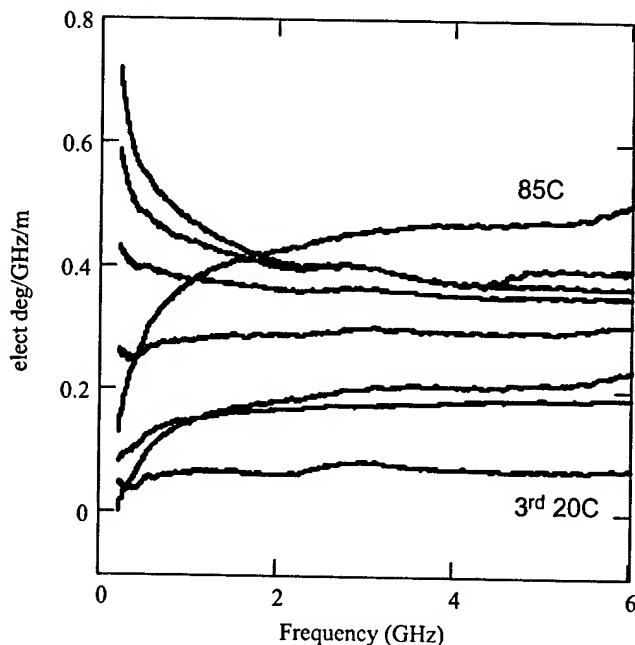


Figure 7. Mean Elect Deg/GHz/m (Cycle 1)

The phase changes for the sixth and final temperature cycle are shown (Figure 8). Again, the extremes of change did not occur at the temperature extremes. Interestingly, the most negative phase excursion occurred with the final 20°C measurement.

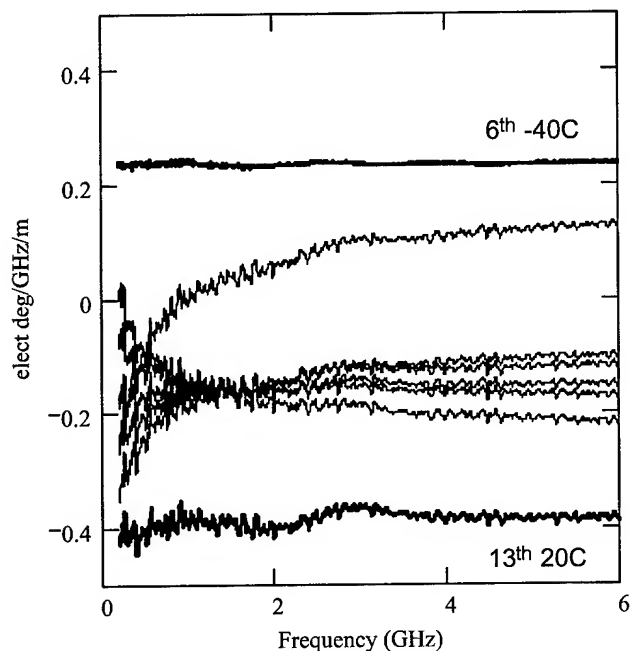


Figure 8. Mean Elect Deg/GHz/m (Cycle 6)

The extremes of phase change for all measurements of temperature cycles one through six were captured (Figure 9 & Table 3). The greatest positive phase changes did not all occur at the same temperature for all frequencies (Table 4). The extremes of elect deg/GHz/m across the six cycles were calculated from the phase extremes (Figure 10 & Tables 5).

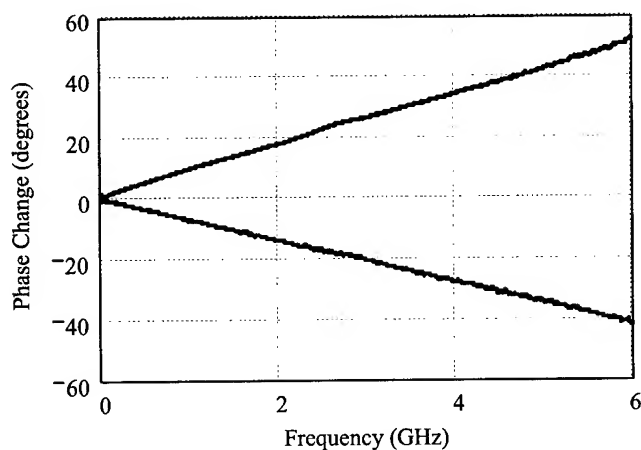


Figure 9. Phase Change Extremes (Cycles 1-6)

Table 3. Extremes of Phase Change (degrees)
Cycles 1-6

Frequency (GHz)	Maximum Positive	Maximum Negative	Mean Total (Initial 20°C)
1	9.7	-7.3	16988
2	17.7	-13.9	33879
3	26.6	-20.5	50832
4	34.4	-27.7	67784
5	42.5	-34.7	84734
6	52.7	-41.8	101685

Table 4. Occurrence of Phase Extremes

Frequency (GHz)	Maximum Positive Change	Maximum Negative Change
1	-40°C, Cycle 1	11 th 20°C, Cycle 5
2	-40°C, Cycle 1	11 th 20°C, Cycle 5
3	-40°C, Cycle 1	11 th 20°C, Cycle 5
4	-40°C, Cycle 1	11 th 20°C, Cycle 5
5	85°C, Cycle 2	11 th 20°C, Cycle 5
6	85°C, Cycle 1	11 th 20°C, Cycle 5

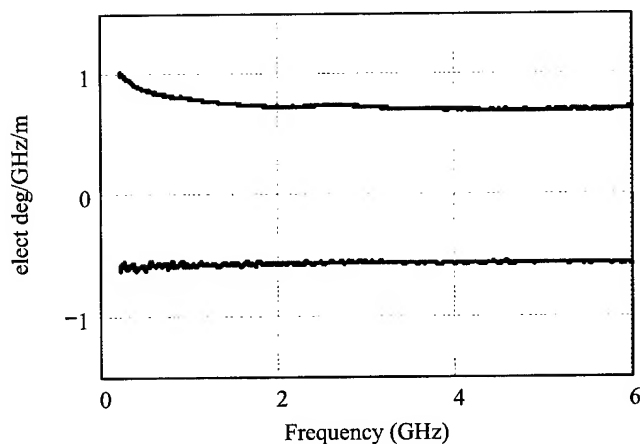


Figure 10. Elect Deg/GHz/m Extremes (Cycles 1-6)

Table 5. Elect Deg/GHz/m (Cycles 1-6)

Frequency (GHz)	Maximum Positive	Maximum Negative
0.2	1.0	-0.62
1	0.80	-0.60
2	0.73	-0.57
3	0.73	-0.56
4	0.70	-0.57
5	0.70	-0.57
6	0.72	-0.57
0.2-6	1.0	-0.63

The phase changes for the sixth and final temperature cycle are shown (Figure 8). Again, the extremes of change did not occur at the temperature extremes. Interestingly, the most negative phase excursion occurred with the final 20°C measurement.

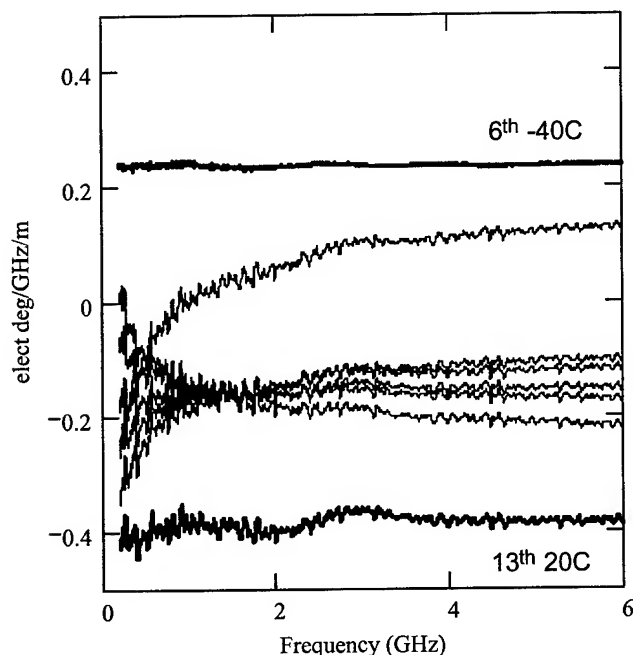


Figure 8. Mean Elect Deg/GHz/m (Cycle 6)

The extremes of phase change for all measurements of temperature cycles one through six were captured (Figure 9 & Table 3). The greatest positive phase changes did not all occur at the same temperature for all frequencies (Table 4). The extremes of elect deg/GHz/m across the six cycles were calculated from the phase extremes (Figure 10 & Tables 5).

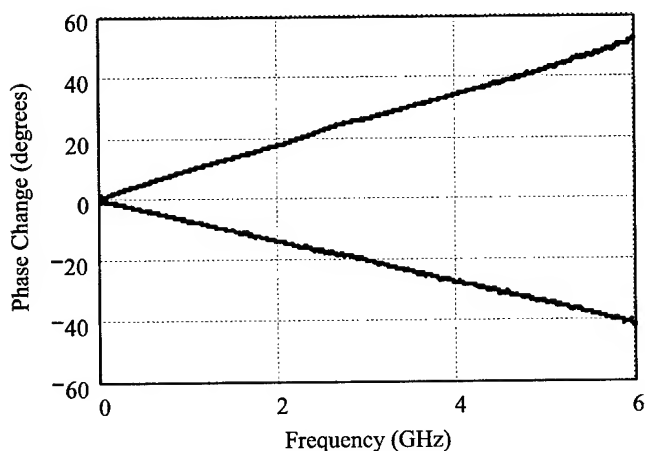


Figure 9. Phase Change Extremes (Cycles 1-6)

**Table 3. Extremes of Phase Change (degrees)
Cycles 1-6**

Frequency (GHz)	Maximum Positive	Maximum Negative	Mean Total (Initial 20°C)
1	9.7	-7.3	16988
2	17.7	-13.9	33879
3	26.6	-20.5	50832
4	34.4	-27.7	67784
5	42.5	-34.7	84734
6	52.7	-41.8	101685

Table 4. Occurrence of Phase Extremes

Frequency (GHz)	Maximum Positive Change	Maximum Negative Change
1	-40°C, Cycle 1	11 th 20°C, Cycle 5
2	-40°C, Cycle 1	11 th 20°C, Cycle 5
3	-40°C, Cycle 1	11 th 20°C, Cycle 5
4	-40°C, Cycle 1	11 th 20°C, Cycle 5
5	85°C, Cycle 2	11 th 20°C, Cycle 5
6	85°C, Cycle 1	11 th 20°C, Cycle 5

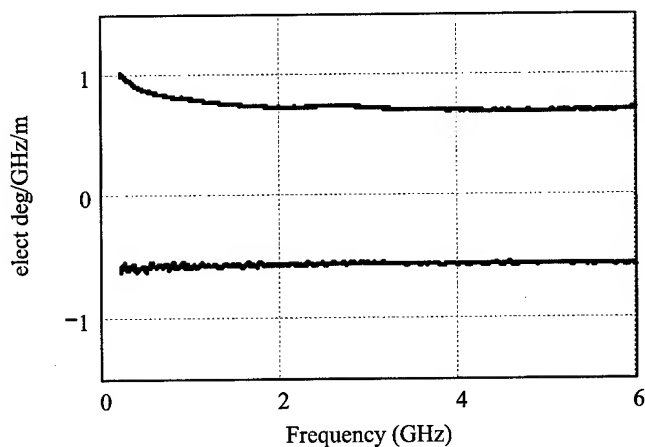


Figure 10. Elect Deg/GHz/m Extremes (Cycles 1-6)

Table 5. Elect Deg/GHz/m (Cycles 1-6)

Frequency (GHz)	Maximum Positive	Maximum Negative
0.2	1.0	-0.62
1	0.80	-0.60
2	0.73	-0.57
3	0.73	-0.56
4	0.70	-0.57
5	0.70	-0.57
6	0.72	-0.57
0.2-6	1.0	-0.63

The insertion phase exhibited a hysteresis, where by the phase did not return to its original value at a given temperature (Figure 11). All samples were tested 13 times at 20°C and this figure shows the mean phase change from the initial measurement at 1 GHz increments. The greatest phase change occurred at 6 GHz and the hysteresis effect occurred at all frequencies. Note how the change was positive for the beginning cycles and changed to negative for the later ones.

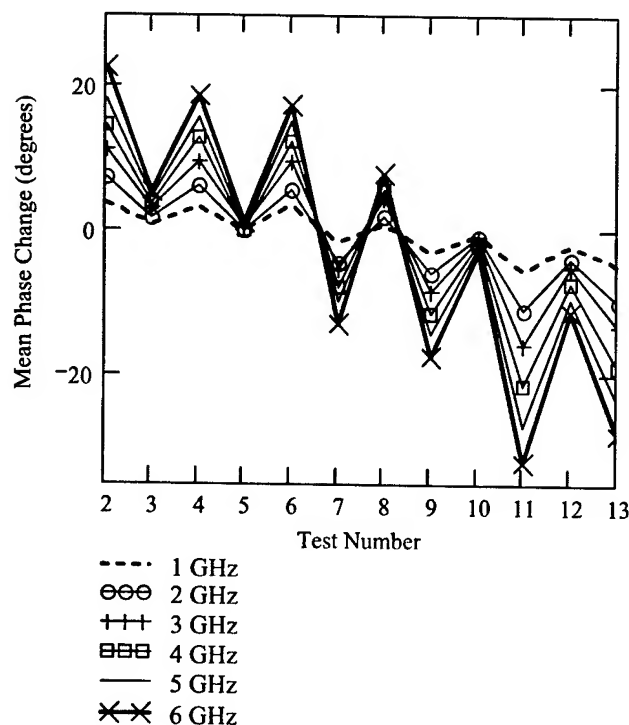


Figure 11. Mean Phase Change at 20°C (6 cycles)

3.5.2 Loss Insertion loss exhibited a positive temperature coefficient throughout the range -40°C to 85°C (Figures 12 & 13). The greatest decreases in insertion loss were in the 3.5 - 4 GHz range rather than at 6 GHz, as was the case with insertion loss increases. The maximum changes for all samples and all temperatures for the six cycles are tabulated at 1 GHz increments (Table 6)

Table 6. Insertion Loss (dB/100m), Cycles 1-6

Frequency (GHz)	Maximum Increase	Maximum Decrease	Mean Total (Initial 20°C)
1	3.7	-3.3	24.5
2	5.6	-4.4	35.2
3	6.7	-5.5	44.3
4	10.4	-5.7	51.2
5	13.2	-4.6	56.9
6	19.2	-0.8	59.9

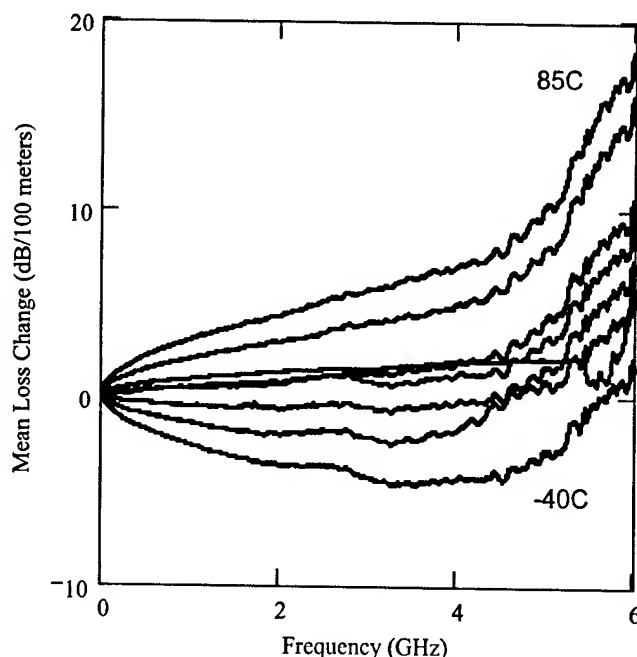


Figure 12. Mean Insertion Loss Change (Cycle 1)

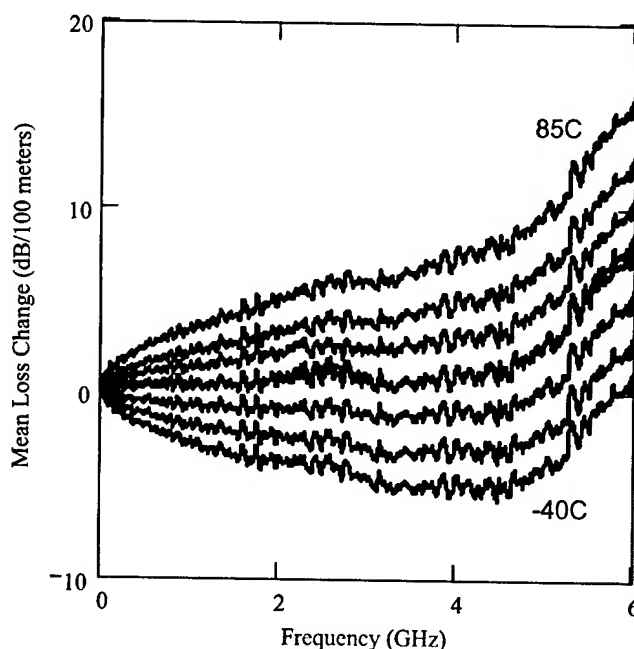


Figure 13. Mean Insertion Loss Change (Cycle 6)

3.5.3 VSWR The VSWR exhibited essentially no change due to temperature variations (Figure 14, Table 7). The mean change was nearly zero, which suggests that what little change was observed was due to measurement error. A measurement system evaluation would confirm this suspicion.

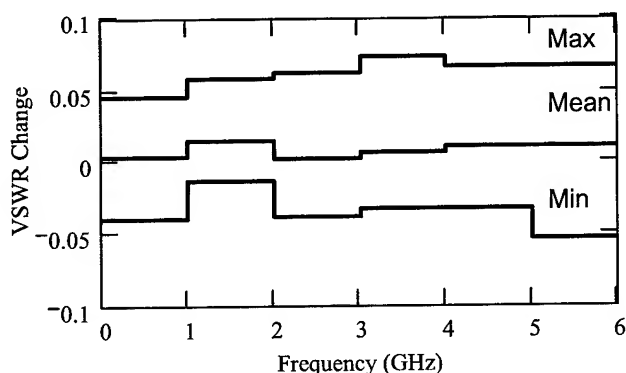


Figure 14. VSWR Max, Mean, and Min (Cycles 1-6)

Table 7. VSWR Change (Cycles 1-6)

	Frequency (GHz)					
	.005-1	1-2	2-3	3-4	4-5	5-6
Maximum	.044	.058	.062	.073	.066	.066
Mean	.004	.015	.002	.006	.01	.01
Minimum	-.039	-.014	-.038	-.033	-.032	-.053

4. Phase vs. Flexure

4.1 Sample Preparation and Configuration

Ten samples of 2 meters (6.56 ft.) each were prepared.

4.2 Equipment Setup and Calibration

The network analyzer was set up the same as for the phase versus temperature measurements. A through normalization was performed for S_{21} . The analyzer electrical delay setting was adjusted for a nearly flat trace and remained at this setting for all phase versus flexure measurements.

4.3 Testing and Data Acquisition

Each sample was connected to the network analyzer once to avoid additional movement that might introduce additional phase variation. Initial characterization for insertion phase (S_{21} degrees) in the position 1 (Table 8) served as the baseline for each sample. Positions 1-8 comprised one cycle of flexing. Insertion loss and VSWR data were not gathered because of the difficulty in measuring these accurately on such a short sample.

Table 8. Bending and Twisting Positions

Position	Description	IEC 60966-1 Figure
1	Bending start position	1a
2	First bend	1b
3	Second bend	1c
4	Bending start position	1a
5	Twisting start position	3a
6	First twist	3b
7	Second twist	3c
8	Twisting start position	3a

The samples were individually subjected to 25 cycles of bending and twisting while connected to the network analyzer. A mandrel diameter of 127 mm was used. Insertion phase data was gathered only in the eight positions of cycles 1 and 25.

4.4 Data Analysis

Analysis followed a similar methodology as phase versus temperature. The baseline for each sample was the phase at position 1 of cycle 1. Equations 1 and 2 were applied to each sample measurement to obtain the total phase and phase change. Maximum and minimum phase change across the frequency span was extracted from all phase change calculations (i.e. all samples, all positions) and converted to elect deg/GHz/m (Equation 3).

4.5 Results

The summary of all flex testing is shown (Figure 15, Table 8). This covers all samples, all positions, and all cycles.

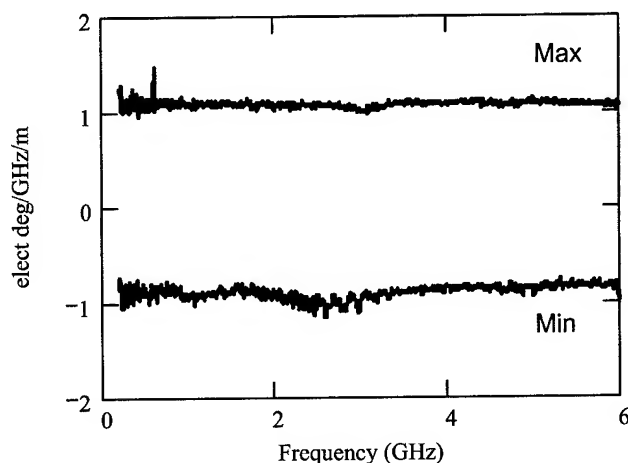


Figure 15. Elect Deg/GHz/m (Flex Cycles 1 & 25)

Table 8. Elect Deg/GHz/m (Flex Cycles 1 & 25)

Frequency (GHz)	Maximum Positive	Maximum Negative
0.2	1.2	-0.87
1	1.1	-0.94
2	1.0	-0.95
3	1.0	-0.96
4	1.1	-0.85
5	1.1	-0.93
6	1.1	-0.89
0.2-6	1.5	-1.2

5. Areas for Further Investigation

The number of temperature cycles could be extended to see long-term effects and determine if sample conditioning occurs. The flexing cycles could be extended to see long-term flexing effects prior to conductor and/or shield breakage. Phase and loss at low

frequencies (e.g. down to 5 MHz) could be determined more accurately by using longer samples. Insertion loss and VSWR versus flexing could be investigated. This might also require longer samples with only a portion of cable subjected to flexing.

Additional samples of the type used for this paper could be tested to obtain a more accurate statistical analysis. Different types and sizes of flexible coaxial cable could be tested. A measurement system evaluation (MSE) could be performed on each of the tests.

6. Conclusions

A consistent relationship was not observed between the coaxial cable insertion phase change and the temperature. The maximum insertion phase change from the reference phase at 20°C did not necessarily occur at the maximum temperature excursions. Insertion phase did not return to its original value after temperature cycling. The largest changes were +1.0 and -0.63 elect deg/GHz/m for 200 MHz to 6 GHz.

Insertion loss has a positive coefficient versus temperature. It behaves in a more predictable manner than insertion phase. Increased temperature consistently increases the loss and vice versa. The largest changes were +19.2 and -5.7 dB per 100 meters.

The VSWR is essentially unaffected by temperature changes. The largest changes were +0.073 and -0.053. The largest mean change was 0.015. What little change was observed could easily fall within the realm of measurement error.

Insertion phase change with cable flexure has a similar magnitude to the change versus temperature. The largest changes were +1.5 and -1.2 elect deg/GHz/m for 200 MHz to 6 GHz.

7. Acknowledgments

Thanks to the Belden Engineering Center laboratory staff for performing the testing that produced the data for this paper. Special thanks go to Ben Willett for his many hours spent on testing.

8. References

- [1] International Electrotechnical Commission, Standard 60966-1
- [2] Mathsoft Engineering & Education, *Mathcad 2001i User's Guide with Reference Manual*.
- [3] American Society for Testing and Materials, D-4566.



Carl W. Dole

Carl is a Product Engineer and has been with the Belden Engineering Center of Belden Electronics Division for nearly thirteen years. He currently holds one U.S. patent. His academic achievements include a B.S. degree in Electrical Engineering Technology ("With Highest Distinction") from Purdue University. Prior to joining Belden, Carl worked 10 years in television broadcast engineering, is a Certified Senior Broadcast Engineer, and has a lifetime FCC General Class Radiotelephone License. His areas of responsibility include developing improved electrical test methodologies, writing technical papers, and working on new product development teams. He is a member of SMPTE, IEEE, and SBE.

Low Cost Assessment Of Connector Performance

**Alyse R.
Coates**

**Alexandros
Gavrilakis**
De Montfort University, Leicester, UK

**Muhammed
Al-Asadi**

**Alistair P.
Duffy**

**Kenneth G
Hodge**

**Arthur J
Willis**

Brand-Rex Ltd, Glenrothes,
Scotland

alyse@dmu.ac.uk alex@dmu.ac.uk

apd@dmu.ac.uk khodge@brand- awillis@brand-
rex.com rex.com

Abstract

From an electromagnetic interference perspective, it is widely acknowledged that connectors are the most sensitive components in cascaded copper systems. Twisted pair connectors are inherently poorly suited to radiation rejection through their design. It is useful, therefore, to be able to quantify the radiation performance for connectors to enable quantitative assessments of interference rejection or to provide input to numerical models used to predict interference performance of cascaded systems. This latter point is particularly important, as direct incorporation of connectors into numerical models using a reasonable computational resource in a reasonable time is generally extremely difficult due to the complexity of the connectors. In this paper the electromagnetic emissions from a plug-in-socket combination and from a cable with no connector are measured using a 'Stripline Cell' and the dipole moments for each device and each twisted pair are presented.

Keywords

Radiation, dipole moment, theory, measurement, emissions.

1. Introduction

In order to create a better connector, many different designs could be produced, prototyped and tested, however this is expensive, time consuming and unpredictable. Another technique is to simulate the different designs, but this requires a lot of processing power and modelling the fine details can make the simulations overly complicated. These approaches are particularly inefficient if the performance of an installed system is required, taking into account the general EMC performance of local structures. It is perhaps sensible therefore to use a combination of testing and modelling to simplify the modelling by eliminating the need for simulating some of the fine detail. For example, if the emissions from a standard plug and connector combination are known in terms of E_x , E_y , E_z , H_x , H_y and H_z then it can simply be inserted into the simulation as a 'black box' that reacts to certain stimuli in a predefined manner. Simplifying the modelling in this manner should provide the ability to simulate scenarios more rapidly and hence lead to faster prototyping.

In such measurement techniques as the mode stirred chamber method (see 'Determining Cable Shield Behaviour') only the total power emitted from the device under test can be measured. However, this is not sufficient, when the electromagnetic emissions from the device need to be broken down into the three orthogonal directions. The most convenient method of doing this is to calculate the 'dipole moments' of the device. The dipole moments can best be viewed as a method of decomposing the emissions from a device into six radiating components, three orthogonal electric field radiators (E_x , E_y , E_z) and three orthogonal

magnetic field radiators (H_x , H_y , H_z). All of these are functions of frequency and can be determined by taking measurements of the radiating device in a manner that allows both the directivity and magnitude of the fields to be taken into account.

2. Obtaining the Dipole Measurements for the Device Under Test

Measurements for the dipole moments were taken using a parallel plate 'Stripline Cell' (which is shown diagrammatically in Figure 1). The stripline is a lower cost alternative to the TEM (or Crawford) Cell, which uses three parallel plates and has enclosed sides to improve the accuracy of the field definition within the measurement environment. The stripline cell consists of two metallic plates, which are parallel in the middle section, which forms a cube of 0.8m, but taper together at their ends, forming two output ports. The tapers are designed to maintain constant impedance along the length of the cell. This apparatus is placed above a ground plane at a distance equal to its height. The device under test is then placed in the centre of the cell and connected to the output port of a network analyser. To ensure adequate field uniformity, the test object was limited to a cube of no more than 200mm on each side. The output ports of the cell are then connected via a junction to the input port of the network analyser. The open sides of the stripline are not a significant issue, providing the cell is sufficiently distant from other structures to avoid interference with the fringing fields. The parallel plates permit transverse electromagnetic (TEM) propagation with a reasonably well-defined and well-conditioned electric field. Hence, for a device under test, the radiated power (in the direction between the plates) can be measured at the tapered ends of the stripline using a combiner (or splitter) and a network analyser.

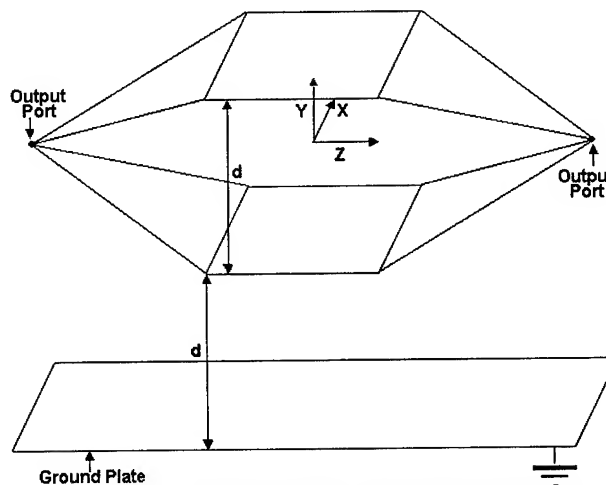


Figure 1. A schematic of the stripline cell.

When an arbitrary current source (the device under test) is introduced inside the waveguide it will generate electric and magnetic fields in both the forward direction (E^+ , H^+) and the backward direction (E^- , H^-). The simplest way to calculate these fields [1] is when both the current source and the power at each output port are known. The total field is the sum of an expansion coefficient a_n or b_n (which are functions of the current source value) and the field at each transverse electromagnetic mode (n).

$$\overline{E}^{(+)} = \sum a_n \overline{E}_n^{(+)} \quad (1)$$

$$\overline{E}^{(-)} = \sum b_n \overline{E}_n^{(-)} \quad (2)$$

$$\overline{H}^{(+)} = \sum a_n \overline{H}_n^{(+)} \quad (3)$$

$$\overline{H}^{(-)} = \sum b_n \overline{H}_n^{(-)} \quad (4)$$

If a parallel plate waveguide is used, where the guide has no sides and the source is placed at the centre of the cell only the dominant TEM mode ($n=0$) is present therefore only the a_0 and b_0 coefficients need to be determined for Equations 1-4.

However, in virtually all circumstances the detail of the current source is unknown so the concept of dipole moments has to be introduced into the determination of the values of the a_0 and b_0 coefficients. The coefficients a_0 and b_0 are related to the electric (m_e) and magnetic (m_m) dipole moments using Equation 5 and 6.

$$a_0 = -\frac{1}{2} (\overline{m}_e + jk \overline{M}) \cdot \overline{e}_0 \quad (5)$$

$$b_0 = -\frac{1}{2} (\overline{m}_e - jk \overline{M}) \cdot \overline{e}_0 \quad (6)$$

Where \overline{e}_0 , q and \overline{M} are defined in Equations 7, 8 and 9 respectively.

$$\overline{e}_0 = q \overline{y} \quad (7)$$

$$q = \frac{\sqrt{Z_0 \cdot P}}{b} \quad (8)$$

$$\overline{M} = \overline{m}_m \times \overline{z} \quad (9)$$

Where \overline{z} is the unit vector along the longitudinal axis of the cell, \overline{e}_0 is the normalized transverse vector electric field inside the cell, \overline{y} is the unit vector perpendicular to the parallel plates, Z_0 is the impedance of the cell (150Ω), P is the power supplied to the cell, b is the separation distance between plates in metres (0.8m) and k is the free space wave number as defined in Equation 10.

$$k = \frac{2 \cdot \pi \cdot f}{c} \quad (10)$$

Where f is the frequency and c is the speed of electromagnetic propagation in free space (2.99792×10^8 m/s).

Hence the dipole moments (m_e and m_m) can be used to quantify precisely the emissions from a dipole. But if it is assumed that any device can be represented by three orthogonally directed dipoles, then the emissions can be broken down into their constituent parts (E_x , E_y , E_z , H_x , H_y and H_z) using the dipole moments and reconstructed from the magnitudes (m) and phases (ψ) using Equations 11 to 16.

$$E_x = m_{ex} \angle \Psi_{ex} \quad (11)$$

$$E_y = m_{ey} \angle \Psi_{ey} \quad (12)$$

$$E_z = m_{ez} \angle \Psi_{ez} \quad (13)$$

$$H_x = m_{mx} \angle \Psi_{mx} \quad (14)$$

$$H_y = m_{my} \angle \Psi_{my} \quad (15)$$

$$H_z = m_{mz} \angle \Psi_{mz} \quad (16)$$

The ubiquitous nature of four pair UTP cable is the reason that this was used throughout this paper, the method works equally well with other connector systems or small devices. The main limitation on the method is that the device under test should not be more than $\frac{1}{3}$ of the height of the cell.

The devices under test in this paper were firstly a length of UTP cable with a plug and socket as the device under test. Then, for comparison purposes, just a length of UTP cable was tested. For each 'device' one end was connected to the output of the network analyser via a balun whilst the other end was connected to a matching load via a second balun. Each coloured pair of twisted wires (see Figure 2) was measured separately so the overall contribution to the emissions from each pair could be determined.

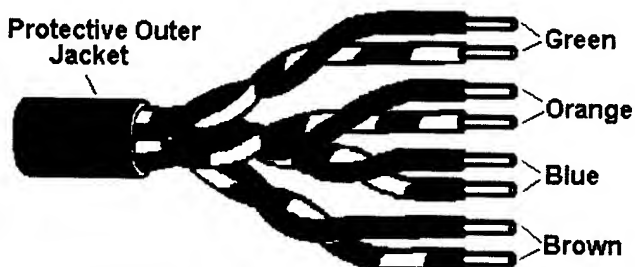


Figure 2. Diagram of twisted pair cable.

In order to measure the dipole moments, the devices under test had to be positioned in six different orientations as specified in Figure 3. Both the axes of the cell (X , Y and Z) and of the device under test (x , y and z) remain constant relative to what they describe (cell or device under test) throughout, though they are rotated relative to each other. The devices under test were placed between the parallel plates using a low dielectric constant mount.

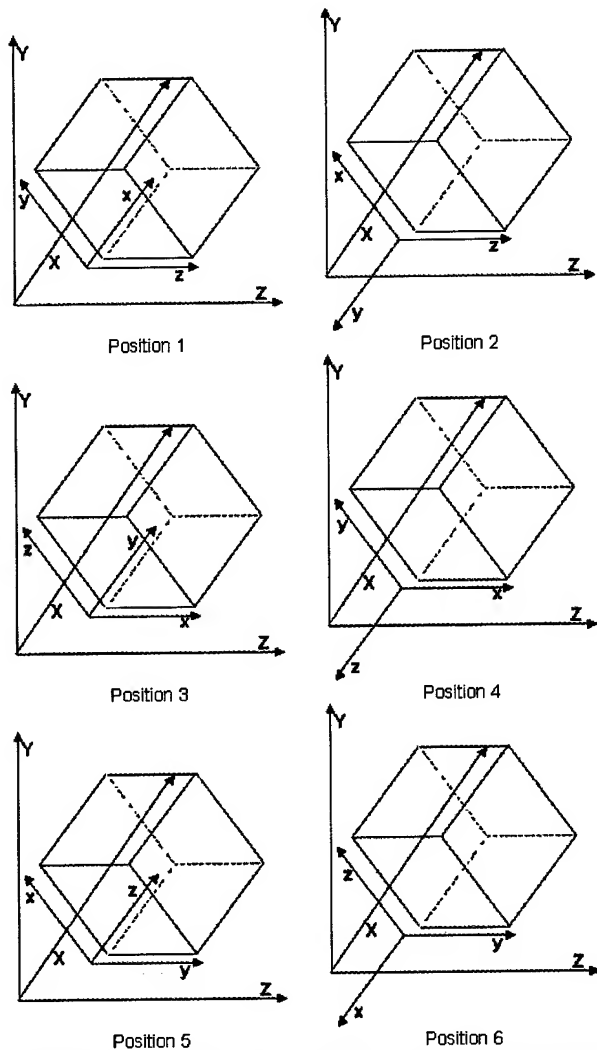


Figure 3. Showing the positioning of the device under test in the cell.

In order to separate the contributions of the electric and magnetic dipole moments simple addition (electric dipole moments) and subtraction (magnetic dipole moments) of the coefficients a_0 and b_0 is required. This addition and subtraction is carried out whilst the measurements are being taken by inserting either a 0° hybrid junction (see Figure 4) or a 180° hybrid junction (see Figure 5) in between the outputs of the cell and the input of the network analyser.

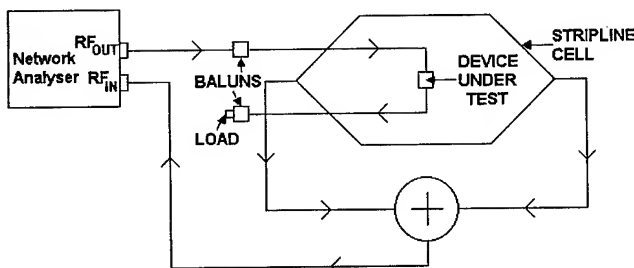


Figure 4. Schematic of the circuit to measure the sum of the outputs (P_s).

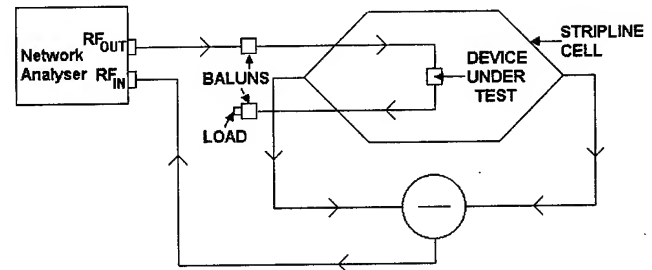


Figure 5. Schematic of the circuit to measure the difference of the outputs (P_d).

The powers detected at the output of the junction which relate to the sum of coefficients (P_{si}) and their difference (P_{di}) are given by Equations 17 and 18, where the 'i' stands for the power at the i^{th} device under test orientation (1 to 6, see Figure 3).

$$P_{si} = |a_0 + b_0|^2 = |\overline{m_e} \cdot \overline{e_0}|^2 \quad (17)$$

$$P_{di} = |a_0 - b_0|^2 = k^2 |\overline{M} \cdot \overline{e_0}|^2 \quad (18)$$

In order to obtain the electric and magnetic dipole moment amplitudes (m_e and m_m) from the power responses at the 6 different orientations Equations 19 to 24 are used. The relative phases between the moments can also be found [1], however these are not used herein.

$$m_{ex}^2 = \frac{(P_{S1} + P_{S2} - P_{S3} - P_{S4} + P_{S5} + P_{S6})}{2 \cdot q^2} \quad (19)$$

$$m_{ey}^2 = \frac{(P_{S1} + P_{S2} + P_{S3} + P_{S4} - P_{S5} - P_{S6})}{2 \cdot q^2} \quad (20)$$

$$m_{ez}^2 = \frac{(-P_{S1} - P_{S2} + P_{S3} + P_{S4} + P_{S5} + P_{S6})}{2 \cdot q^2} \quad (21)$$

$$m_{mx}^2 = \frac{(P_{d1} + P_{d2} - P_{d3} - P_{d4} + P_{d5} + P_{d6})}{2 \cdot k^2 \cdot q^2} \quad (22)$$

$$m_{my}^2 = \frac{(P_{d1} + P_{d2} + P_{d3} + P_{d4} - P_{d5} - P_{d6})}{2 \cdot k^2 \cdot q^2} \quad (23)$$

$$m_{mz}^2 = \frac{(-P_{d1} - P_{d2} + P_{d3} + P_{d4} + P_{d5} + P_{d6})}{2 \cdot k^2 \cdot q^2} \quad (24)$$

Finally the amplitude of the total power emitted by the devices (P_t) can then be obtained from the moment amplitude results using Equation 25.

$$P_t = \frac{40 \cdot \pi^2}{\lambda^2} \left[m_{ex}^2 + m_{ey}^2 + m_{ez}^2 + k^2 (m_{mx}^2 + m_{my}^2 + m_{mz}^2) \right] \quad (25)$$

3. Results

Each of the devices under test (the cable and the connector) were tested using the method described in this paper. For each device, each pair of twisted wires were connected up and measured separately, so any differences between the responses could be examined. Also the contribution of each pair to the total emitted power could be observed.

Figures 6 and 7 show the differences and similarities between the sums of the emitted powers received at the outputs of the stripline cell (P_s), for firstly the cable and then the connector when the device under test is placed in the six positions indicated in Figure 3. It can be clearly seen that the emissions from a specified pair (in this case the brown pair) have many similar features in all six positions. It can also be seen that the emissions from the connector are greater than those from just the cable.

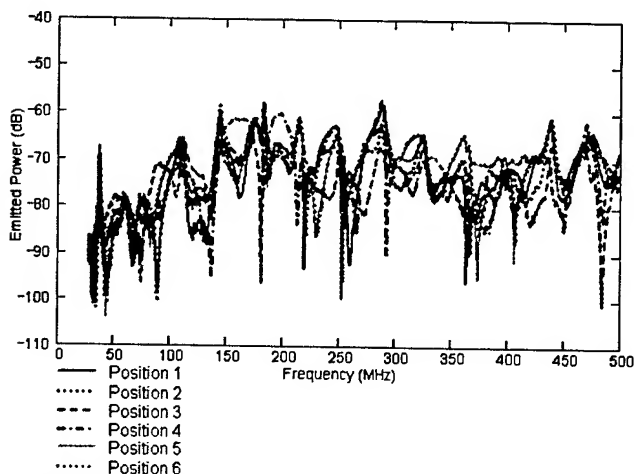


Figure 6. The emissions from the brown pair in the cable measured using the addition junction.

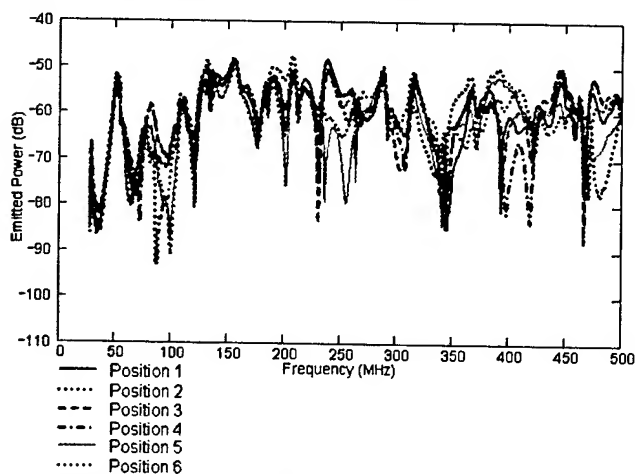


Figure 7. The emissions from the brown pair in the connector measured using the addition junction.

In Figures 8 and 9 the difference of the emitted powers (P_d) measured at the outputs of the stripline cell are shown for all the twisted pairs whilst the devices under test remain stationary in position 5. It can be seen that whilst each of the responses have similar sharp features to those observed in Figures 6 and 7, the responses for the different wire pairs vary greatly from each other.

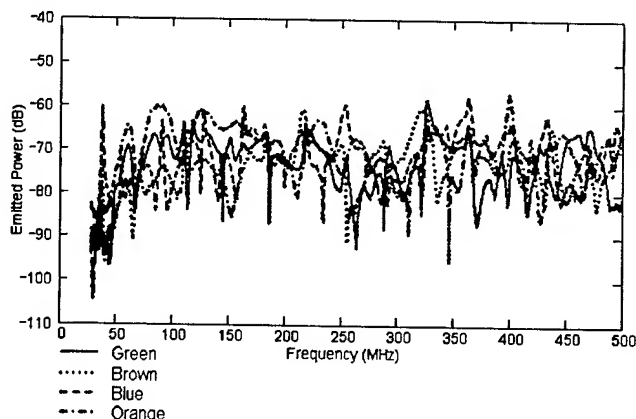


Figure 8. The emissions measured in position 5 for the cable, using the subtraction junction.

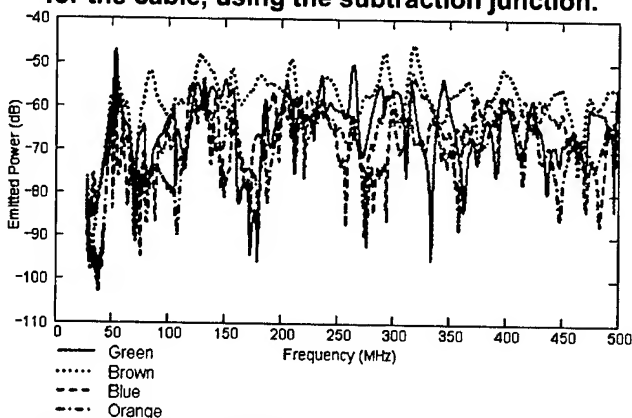


Figure 9. The emissions measured in position 5 for the connector, using the subtraction junction.

It can be seen from Figures 6 to 9 that all of the emission responses contain strong features (sudden peaks or troughs) and the amplitude of the responses vary greatly with frequency. It can also be seen that whilst the emission responses remain reasonably consistent for a specific pair whilst the device position is altered, the responses for the different twisted pairs vary widely from each other. It has also been noted that the responses obtained for the two devices under test are very different from each other in terms of both amplitude and the positioning of the features, in order to closer examine these differences the emissions from the same pair of wires in the same position for each device were compared.

When the emissions from an identical pair of wires passing through the connector and through just the cable are compared it is immediately evident that the emissions from the connector exceed those from just the cable on its own, as would be expected. However, the magnitude of the difference can clearly be seen in Figures 10 to 13.

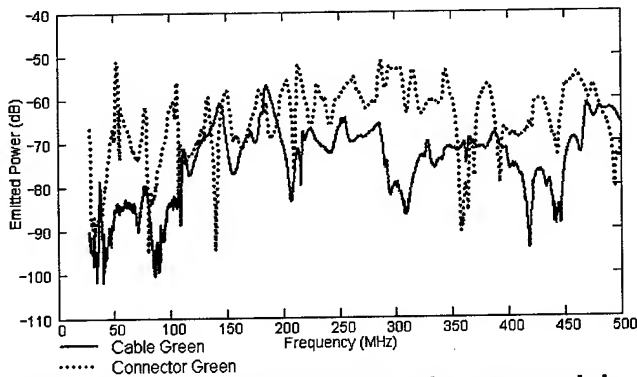


Figure 10. The emissions from the green pair in position 3 measured using the addition junction.

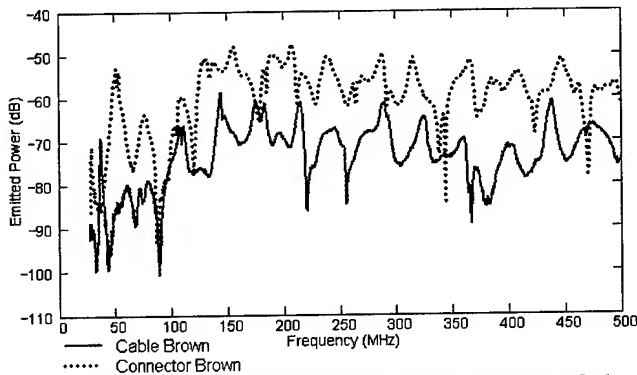


Figure 11. The emissions from the brown pair in position 3 measured using the addition junction.

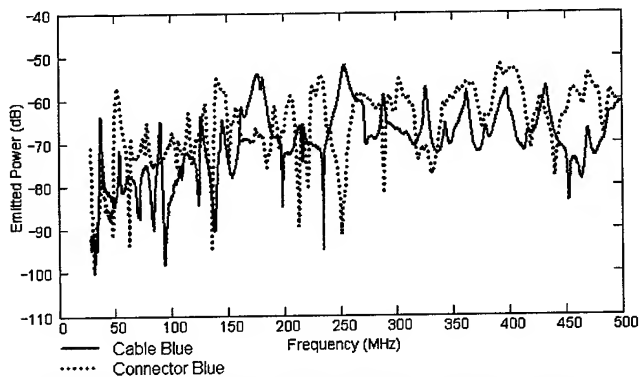


Figure 12. The emissions from the blue pair in position 4 measured using the subtraction junction.

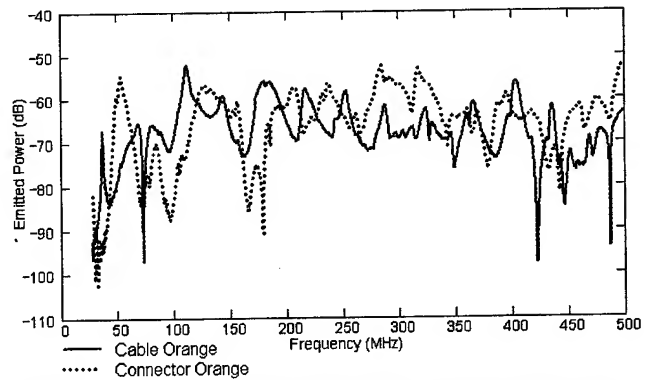


Figure 13. The emissions from the orange pair in position 4 measured using the subtraction junction.

When the electric dipole moments were calculated from the emissions responses using Equations 19 to 21, the differences between the cable and connector results were immediately evident (see Figures 14 to 17).

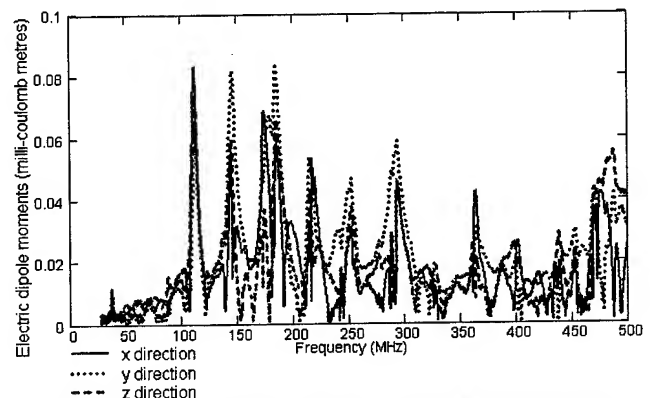


Figure 14. Electric dipole moments from the green pair in the cable.

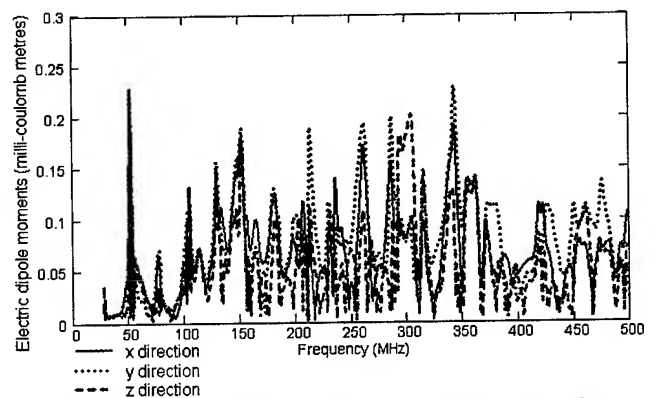


Figure 15. Electric dipole moments from the green pair in the connector.

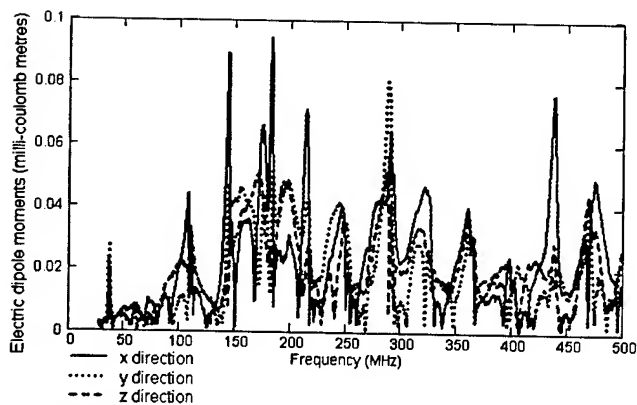


Figure 16. Electric dipole moments from the brown pair in the cable.

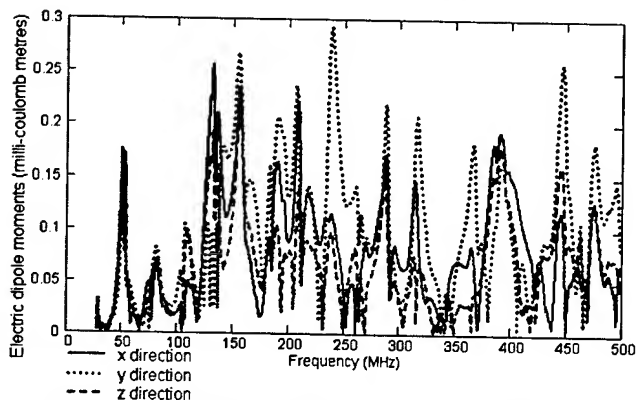


Figure 17. Electric dipole moments from the brown pair in the connector.

The magnetic dipole moment amplitudes were obtained from the emissions responses using Equations 22 to 24, as can be seen in Figures 18 to 21. As with the electric dipole moments, the amplitude of the responses varied greatly between the two devices.

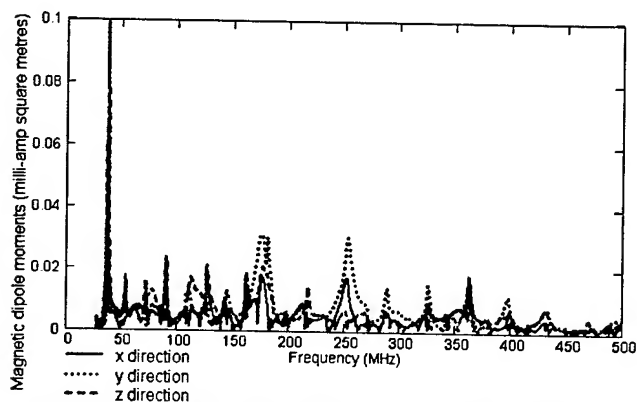


Figure 18. Magnetic dipole moments from the blue pair in the cable.

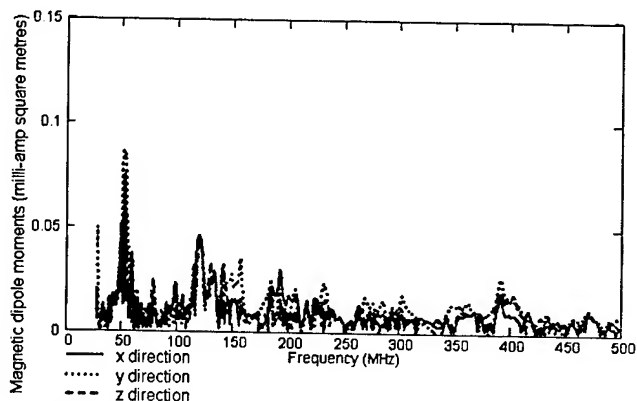


Figure 19. Magnetic dipole moments from the blue pair in the connector.

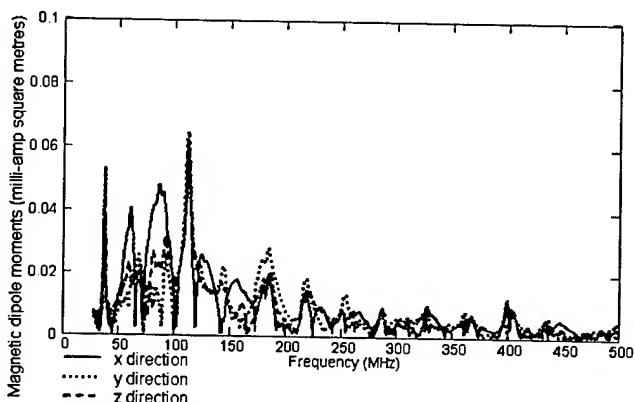


Figure 20. Magnetic dipole moments from the orange pair in the cable.

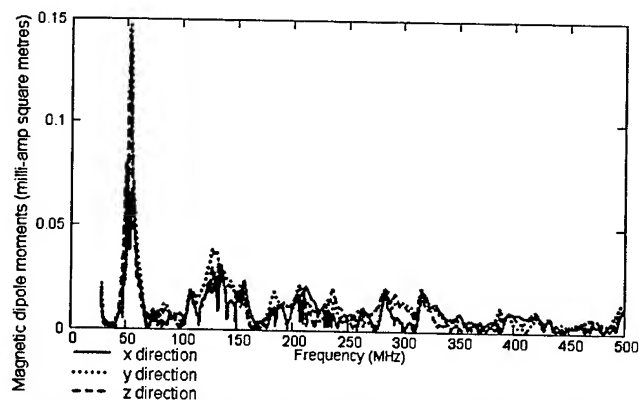


Figure 21. Magnetic dipole moments from the orange pair in the connector.

Both sets of dipole moment responses show strong features that are consistent between the three orthogonal dipoles that represent a specific device and twisted pair. However, the dipole moment responses vary greatly between the different pairs, suggesting that the total emitted power contributed by each pair is also different. This hypothesis was tested by using the dipole moment responses to calculate the total power emitted by each pair in each device using Equation 25.

It can be seen from Figure 22 that the total power emitted by each pair in the cable is rather similar, though the emitted power does vary with both pairs and frequency. However, the total power emitted by the connector is strongly dependant on the twisted pair being tested, see Figure 23. It can be seen by comparing Figures 22 and 23 that more power is emitted from the connector than from just the cable, to quantify this difference the total power emitted by each pair in each device was averaged over the entire frequency range, these results are shown in Table 1.

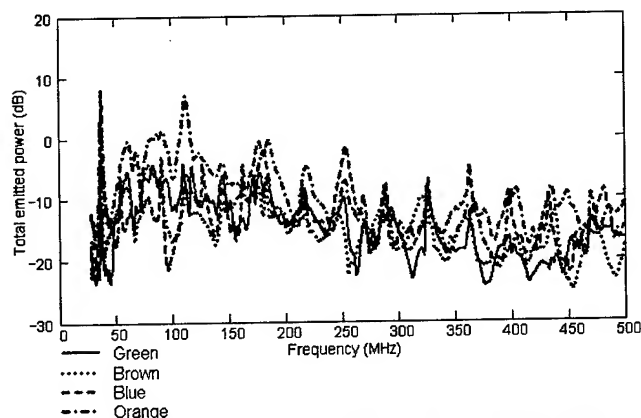


Figure 22. Total power emitted from the cable.

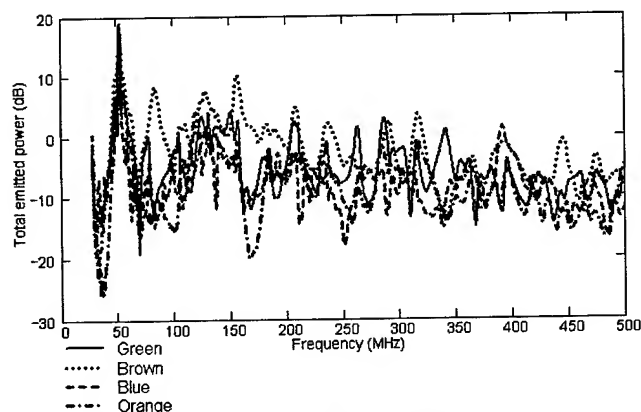


Figure 23. Total power emitted from the connector.

It can be seen from Table 1 that the average power emitted by a pair in the connector is up to 13dB greater than that which is emitted by the same pair in just the cable on its own. It can also be seen that the amount of power emitted by each cable pair is different, probably due to the positioning of the pair within the cable.

Table 1. Showing the average 'total emitted power' (in decibels) for each device and pair.

	Green	Brown	Blue	Orange
Cable	-14.8	-15.1	-12.8	-10.4
Connector	-5.6	-2.8	-7.9	-9.0

4. Conclusion

The method described in this paper can be used to obtain the dipole moments of any device (provided certain criteria, such as device size, are met), quickly, easily and relatively inexpensively. These dipole moments can, in turn, be used to predict the total emitted power and (if phase is taken into consideration) the radiation patterns from the device.

The dipole moments obtained for both a cable and a connector were used in this manner to obtain the total emitted power as a function of frequency. These results show how much extra power is radiated from a connector relative to a cable and hence demonstrate the need to fully characterise and examine these emissions.

In this paper a method has been demonstrated by which a complex electromagnetic device can be broken down into six dipoles that can be used to represent its behaviour. These representative dipoles can then be used in, for example, numerical modelling to predict the emissions from systems of which this device is only a part.

5. References

- [1] Koepke, G. H., Ma, M. T., and Bensema, W. D. *NIST Technical Note 1326: Theory and Measurements of Radiated Emissions Using a TEM Cell*, United States: National Institute of Standards and Technology, 1989.

Author Biographies

Biographies for Alyse R. Coates and Alexandros Gavrilakis can be found in the paper "Determining Cable Shield Behaviour" in Session 16.

The biography for Muhammed Al-Asadi can be found in the paper "Input Impedance of Irregular Cascaded Systems" in Session 11.

The biographies for Alistair P. Duffy, Kenneth G Hodge and Arthur J Willis can be found in the paper "Technology Forecasting Techniques in Communications" in Management Session 1.

PMD Improving by Fiber Profile Design

Tiejun Wang, Yuqing Cao, Jie Luo

Yangtze Optical Fiber and Cable Co. Ltd. Wuhan, CHINA 430073

+8627-87802541-3115 · wangtiejun@yofc.com

Abstract

PMD is the limiting factor in long haul and high bit rate transmission. In this paper, fiber refractive index (RI) profile and dopant are investigated to reduce PMD. The higher relative refractive index between core and adjacent cladding is a critical factor leading to worse PMD. Gradient profile is introduced in profile designing to reach the same optical characters but with lower PMD. The stress distribution in radius which can contribute to the PMD is also analyzed by experiment. A series of tests are implemented to analyze the impact of profile distribution on PMD. Results show that core circularity can be improved by 20%, and PMD can be reduced by 27% for DCF.

Keywords

Refractive index profile; dopant; inner stress; PMD

1. Introduction

It is well known that PMD is the limiting factor in long haul and high bit rate transmission. Fiber and cable manufactures are working hard to improve PMD. PMD compensator is also under studied and commercial product is available now, but with very high cost. Although PMD is very complex and is a random parameter during fiber is working, one is still hoping that PMD is small and stable in fiber. In this paper, fiber refractive index (RI) profile and dopant are investigated to reduce PMD.

For any kinds of transmission fiber: G652, G653, G655, or even DCF (dispersion compensation fiber), multi-cladding are used to present a required optical character and transmission performance. Normally, a sharp core is in the center of the profile. The higher relative refractive index between core and adjacent cladding is a critical factor leading to worse PMD. This is performed in two aspects: one is the suddenly dopant changing from core to cladding makes the core circularity worse; another is that inner stress between core and cladding is not homogeneous because of the large difference of material expanding coefficient between core and cladding. All these impacts will contribute to a higher PMD.

In this paper, the contribution on PMD of RI profile and dopant in core and cladding are analyzed. Gradient profile is introduced in profile designing to reach the same optical characters but with lower PMD. The plasma chemical vapor deposition (PCVD) process is used in our experiments. The thickness of every deposition layer in preform is less than 1micron in PCVD process. With PCVD process, we can produce fiber with smooth and triangle shape profile. The small lean in the core can give both a better core circularity and a more homogenous inner stress.

The stress distribution is a big issue and has been analyzed in many papers. But those papers focus on the stress effect on fiber strength, crack formation and aging performance. This paper will focus on the stress distribution in radius which can contribute to the PMD.

A series of tests are implemented to analyze the impact of profile distribution on PMD. Results show that core circularity can be improved by 5%, and PMD can be reduced by 3% For G.655. The detail situation on inner stress is under testing.

2. Analyzing on PMD and profile doping

2.1 Preform prepared by PCVD process

Plasma-active Chemical Vapor Deposition (PCVD) is known as its high deposition efficiency of doped silica together with the precise control of the refractive index profile in preform making. During PCVD process, the desired gas mixtures, a combination of SiCl_4 , GeCl_4 , C_2F_6 and O_2 are fed into the substrate tubes at a low pressure. C_2F_6 is only used in PCVD process in standard fiber manufacturing. Thus, material characters are different from other preform making process. A moving non-isothermal plasma area is generated inside the tube by a microwave (2.45GHz). Reactions are stimulated and deposition of the desired glass components on the inner wall of the substrate tubes occurs in this plasma area. During deposition the substrate temperature is kept constant at a temperature at about 1200°C by a stationary furnace over the whole unit. In the PCVD process, the microwave energy required to maintain the plasma and to stimulate the reactions is coupled directly into the gasphase without influenced by heat transfer problem. So the transverse speed of the resonator can be high, and the deposition layer is very thin (micron thickness), which makes the profile accurate and precise. It is also a positive factor to control the profile shape in the view of PMD reduction.

2.2 PMD reduction during manufacture

From the cause of PMD, the most directly way to reduce PMD is to manufacture fiber with its core as circular as possible and stress in both radial and axial directions as homogeneous as possible. Both geometrical circularity and optical circularity of core are mostly determined by the even deposition. During deposition, gas pressure inside deposition tube is kept low to guarantee the uniform distribution of gas mixture concentration. The gasflow is carefully controlled by MFC to keep the residence time of the reactive gas in the plasma zone, constant to get the same deposition yield of SiO_2 and GeO_2 . Different MFC are also used to maintain the same materials structure in the reactive zone. The applied plasma power is kept stable and proportional to the deposition rate, no any power varying available. The deposition is also strongly related to the inner wall temperature of the substrate tube, so beside the plasma power, the stationary furnace temperature should also be kept constant. The even deposition is also guaranteed by the resonator transverse speed. We maintain it to make it stable and proportional to the deposition rate.

The second reason causing PMD is inner stress. It is well known that preparation of preform is always associated with the generation of stress because that different doped regions forming the core and the cladding usually have different thermal expansion coefficients. Especially for non-zero dispersion shift fiber or dispersion compensation fiber which have quite different dopant in core and cladding. To reduce the stress to a low level can benefit PMD at the following process steps. Refractive index profile is specially designed and doped at the interface of core and cladding is controlled by more accurate deposition to make the profile smoother, therefore, inner stress is decreased. At the collapse step, the pressure inside and outside the deposited tube are adjusted in order to prevent tube deforming to get a balanced state. If there is tube deformed at previous process, flame is used to reshape that deformed part and inner stress is also released at the same time.

2.3 Theoretical background of stress

Stress generated due to difference of thermal expansion coefficients in a preform, axial stress σ_z can be expressed by^[3]:

$$\sigma_z = \int_{T_{room}}^{T^*} \frac{E(T)}{1-\nu(T)} [\alpha(r,T) - c(T)] dT \quad (1)$$

By integration, the radial stress can be obtained:

$$\sigma_r = \frac{1}{r^2} \int_0^r \sigma_z(r') r' dr' \quad (2)$$

Where

$$c(T) = \int_0^R \alpha(r,T) r dr \quad (3)$$

T^* is a virtual temperature above room temperature where stress starts to develop during cooling. $\alpha(r,T)$ is the thermal expansion coefficient at the radial position r and the temperature T , $E(r,T)$ and $\nu(r,T)$ are the elastic modulus and Poisson's ratio respectively, R is the preform diameter.

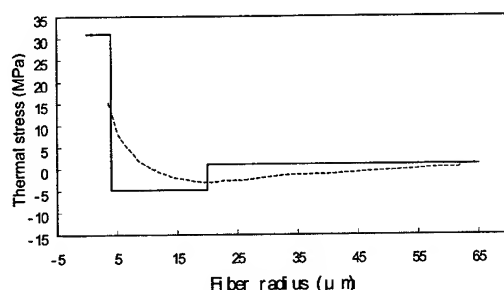


Figure 1 Thermal stress profile of Fluorine doping fiber

In a preform with F-doped in cladding, the radial stress can be calculated basing on above equations and is shown in fig.1. In fig. 1, solid line is refractive index profile and dashed line is radial

stress profile. It can be seen that the maximum is at the interface of core and cladding where the dopant is different.

2.4 Stress characters of doping material

The PCVD materials, the fluorine doped materials in special, have new properties. The density of the material decreases with about 0.5% per weight % of fluorine concentration^[4] (see fig. 2). This character can be used to balance the density in core and cladding.

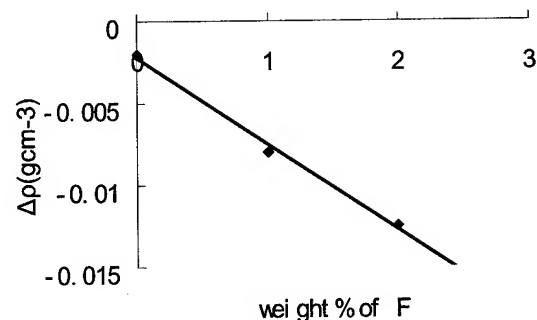


Figure 2 Density decrease of F-doped PCVD quartz

The major concerning of materials characters is the thermal expansivity of materials which contributes the PMD of fiber. Generally speaking, Germanium doped material have a thermal expansion coefficient that increases proportional to the germanium concentration. Fluorine doped materials seems to have smaller expansion coefficient than pure quartz. The deposition is basing on pure quartz. The stresses that arise between quartz as substrate and deposition materials are shown in fig. 3. It can be seen that germanium doped quartz exerts positive stresses and fluorine doped materials generate negative stresses up to concentrations which yield 1% refractive index difference. Because the stresses are determined by the dopant concentrations^[6], it is possible to design the RI profile and doping in core and cladding to keep the PMD less influenced by inhomogeneous stresses.

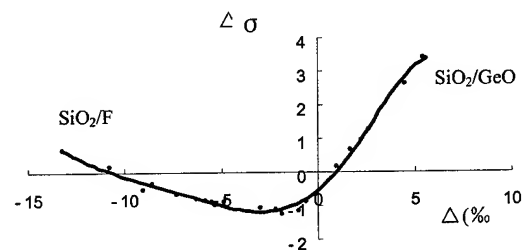


Figure 3 Mechanical stress in doped PCVD material vs refractive index

In the F doping material, the variation of the thermal stress with the relative refractive index difference is completely different from the germanium doping material. For most kinds of fiber, the relative refractive index in F doping cladding is: $0 > \Delta > -1.0\%$ where the relative stress values are negative with respect to the

substrate tube materials. In some cases of dispersion compensation fiber, the relative refractive index of depressed cladding can be less than -1.0% and in this case, the relative stress change its sign and continues to increase for more negative Δ values. See fig. 3.

The stress behavior induced during drawing process has been discussed in many papers^{[1][2]}. The inhomogeneous stress in radius induced by drawing process is a big issue for PMD reduction and the drawing condition and hot zone should be carefully designed. It is not analyzed in this article.

3. Experiment and results

From the theory analyzed above, it is known that PMD is proportion to birefringence rate. There two reasons causing birefringence: the geometrical and stresses birefringence. They cannot be eliminated completely. What we can do is to decrease their effect on PMD as low as possible through fiber profile designing, including the wave-guide structure and the doping concept.

Experiments have been done about the relationship between PMD and fiber profile design. The experiment conditions are:

- All of the substrate tubes and the jacket tubes are Heraus' F-300 glass tubes.
- All of the substrate tubes have the same size and the similar geometrical specification, and also jacket tubes.
- With the same PCVD process and the same collapsing process.
- The core non-circularity in perform is measured by PK2600.
- With the same drawing conditions (tower, drawing tension and drawing speed).
- PMD is measured by PMD400.

For each profile concept, at least 800km fiber were drawn and used for PMD analyzing.

3.1 The relationship between RI profile shape and PMD

In order to guarantee the required wave-guide characteristics, high refractive index in core and thin core diameter are necessary. For example: from G.652 to G.655 and DCF fiber, the refractive index in core is higher and higher, while the core diameter gets thinner and thinner. Those varying will make PMD worse. Higher RI in core is to makes the stress inhomogeneous. A relative thinner fiber core diameter can contribute to a bad geometrical core circularity, and that's the reason of geometrical birefringence. Therefore, the PMD of DCF is higher than that of G.655 and G.652 fiber. The refractive index profiles of G.652 fiber, G.655 fiber and DCF are shown in figure 4. As a typical fiber, G.655 fiber is tested with two profile shapes: step core and gradient core. Both profile concepts have the same transmission characters.

The data of different RI profile and PMD are compared in table 1. During testing, all the fiber manufacturing conditions are kept same to find the effect of profile and material doping.

Table 1. The PMD value of G.652, G.655 and DCF fiber.

	G.652	G.655-gradient	G.655-step	DCF
core data(%)	0.35	0.66	0.64	1.7
core dia.(μm)	4.64	3.66	3	1.82
PMD avg.(ps/km ^{1/2})	0.03	0.033	0.038	0.08

From the comparing, core should be a gradient shape instead of step one when refractive index of core is relative high. For the concerning of fiber PMD and manufacturing, the profile concept of decreasing the RI in core and enlarging the core diameter as possible are recommended in fiber profile design.

3.2 The smoother the RI profile between different layers, the lower the PMD

In order to match the requirement of the long haul and high bit rate optical transmission system, multi-cladding fiber profile design is necessary. As an example G.655 fiber has a sharp core in the center of the profile and 2 or 3 claddings. The higher relative refractive index between core and adjacent cladding is a critical factor leading to worse PMD. This is performed in two aspects: one is the suddenly dopant changing from core to cladding makes the core circularity worse; another is that inner stress between core and cladding is not homogeneous because of the large difference of material expanding coefficient between core and cladding. All these impacts will contribute to a higher PMD.

Three samples of G.655 fiber with different profile slope are tested. The profiles of testing samples are shown in fig.5. Fiber profile of sample 2 is shown in fig. 6. The PMD values are in table 2. From the experiment results we can find that gradient RI profile design in fiber core can reduce the sudden varying of the thermal expansion coefficient between different material in core and cladding.

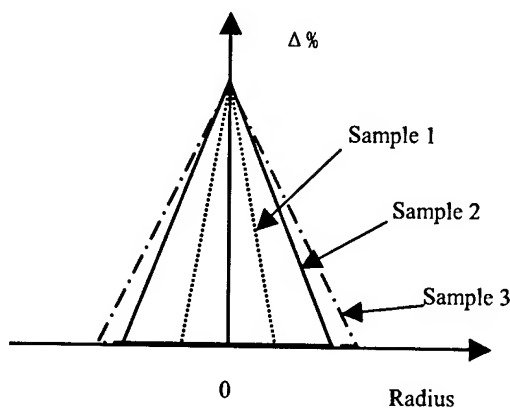


Figure 5. Profiles of G655 fiber with different slopes

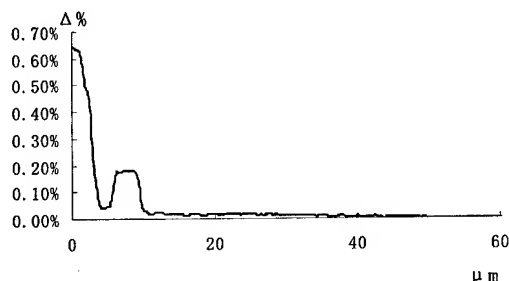


Figure 6. fiber profile of sample 2

With PCVD process, it is relative easy to deposit gradient profile shape and keep the gradient profile smooth with thin deposited layers.

Table 2 Fiber results of different profiles

	core non-cir.(%) avg.in preform	PMD avg.(ps/km ^{1/2})	fiber loss avg. at 1550nm(dB/km)
Sample 1.	1.2%	0.15	0.51
Sample 2.	1.0%	0.10	0.53
Sample 3.	0.6%	0.06	0.56

3.3 Experiment on doping with different concentration in deposition

The doping material in SiO₂ can help us get the expected RI profile, and at the same time, the glass transition temperature T_g can also be changed. Whatever Freon dopant or Germanium

dopant in SiO₂, both of them can decrease T_g. Lower T_g make it easier to collapse a deposited tube into a perform. We can keep a better core circularity level in perform under a relative lower T_g. On the other hand, a relative lower T_g means a relative small drawing tension when using the same drawing temperature and drawing speed. The small drawing tension can depress the non-isotropy of stress in fiber and decrease the fiber PMD.

Too much doping can also increase the fiber nature attenuation finally. So doping in core and cladding is specially designed to reach a balance between decreasing fiber PMD and controlling fiber attenuation.

In this experiment, DCF profile designing is tested in different doping to investigate the doping effect on PMD. The RI profile is kept the same, and mol. concentration of dopant is varied. Therefore, the glass transition temperature will be changed in addition. Th experiment results are shown in Table 3. The RI profile of DCF has been shown in Figure 4.

From table 3, we can see that the relative lower glass transition temperature T_g design can be helpful for keeping good circularity of perform and decreasing drawing tension, and the PMD can be controlled within a low level easily. Core circularity of example 2 is improved 20% comparing with that of example 1, and PMD of example 2 is decreased 27%.

4. Conclusion

In this paper, we analyze the contribution on PMD of RI profile and dopant in core and cladding. Different slope of gradient profile is tested to investigate the impact of profile shape on PMD. The tested preforms are prepared by PCVD process which is easy to control the RI profile shape. The small lean in the core can give both a better core circularity and a more homogenous inner stress. The stress distribution is also discussed in the view of PMD improving.

Table 3. The different doping mol. Concentration of Fluorine and Germanium in DCF

	doping mol.concentration(%)		core non-cir.(%) in preform avg.	PMD avg.(ps/km ^{1/2})	fiber loss at 1550nm(dB/km) avg.
	Ge in core	Fr in core			
example 1.	55.3%	0.0%	1.5%	0.11	0.53
example 2.	63.0%	0.3%	1.2%	0.08	0.58
example 3.	70.7%	0.6%	0.9%	0.06	0.67

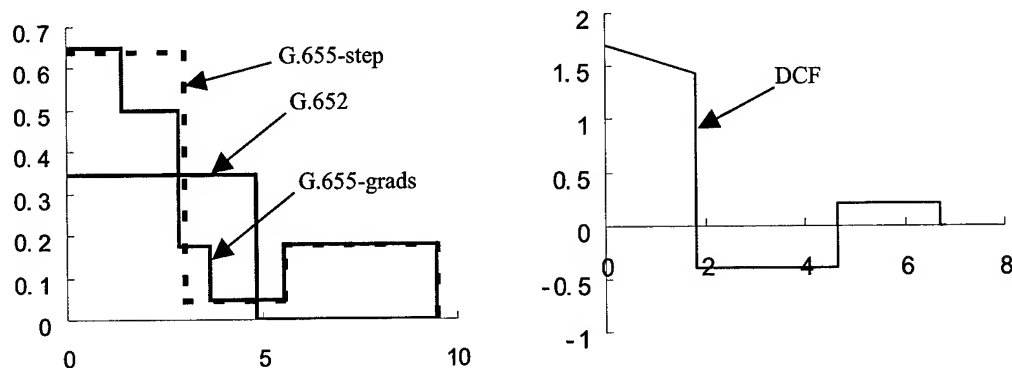


Figure 4. The RI profile of G.652, G.655 and DCF

A series of tests are implemented to analyze the impact of profile distribution on PMD. Results show that core circularity can be improved by 20%, and PMD can be reduced by 27%.

5. References

- [1]. P. Ledoux, J. Auge, etc., "Stress Measurements on fibers and preforms" Journal of Lightwave Technology. Vol.7, No.8, August, 1989
- [2]. Y. Park, K. Oh, etc., "Residual stresses in a doubly clad fiber with depressed inner cladding (DIC)" Journal of Lightwave Technology. Vol.17, No.10, October, 1999
- [3]. P.K. Bachmann, W. Hermann, etc., "Stress in optical waveguide" Applied Optics, Vol.25, No.7, April, 1986
- [4]. H. Wehr, D. Wiechert, Mat. Res. Bull., 21(1986)
- [5]. P. L. Chu, T. Whitbread, "Measurement of stress in optical fiber and preform." Appl. Opt., Vol.21, No.23, P.4241-4245, Dec.1,1982.
- [6]. P. L. Chu, T. W. Whitbread, "Stress modification in optical fiber." Electron. Lett., Vol.20, No.11, P449-450, May, 1984.

SPEAKER BIOGRAPHY



Tiejun Wang
Yangtze optical fiber & Cable
co.Ltd.(YOFC)
Wuhan, 430073 P.R. CHINA
Wangtiejun@yofc.com

Tiejun Wang was born in 1969. He received his B.S. degree in optical engineering from Huazhong university of science and technology(HUST) in 1992 and M.S. degree in optoelectronics in 1998 from HUST. Since 1998, he works in YOFC as a chief engineer in R&D Dept. His responsibilities focus on new fiber product, specialty fiber, and process optimizing.

Application of Statistical Models to Estimate PMD Coefficient in Telecommunications Optical Links

Carlos E. P. Blume¹, Alexandre A. P. Pohl¹, Januncio A. de Medeiros Neto²,

Jeancarlo Dotto³, Lucio F.G. Marques³, Renato F. Cruz³

CEFET-PR-Departamento de Eletronica¹ – Curitiba-PR-Brazil

CITS-Centro Internacional de Tecnologia de Software² Curitiba-PR-Brazil

Furukawa Industrial S.A. Produtos Elétricos³ Curitiba-PR-Brazil

phone 55-41-341-3510 email: januncio@furukawa.com.br

Abstract

This paper presents a characterization of Polarized Mode Dispersion (PMD) by using different statistical models describes on the bulletin TIA/EIA TSB107. The numerical simulations were based on experimental data obtained from different loose tube optical cables with standard single-mode fibers. The results showed that from a certain number of cable section ($N > 20$) the maximum admissible PMD coefficient in the optical link converges to a fixed value, and do not depend on the statistical model employed. The results obtained for $N < 10$ showed a reasonable variation in the estimated values.

Keywords

Fiber; Optical Cable; Optical Link; PMD coefficient

1. Introduction

Low PMD value is a fundamental requirement for current optical transmission rates at 10 Gbit/s and beyond. For example, high PMD is a serious issue for WDM network, particularly when the bit rate increases up to more than 40 Gb/s. Actually, high PMD values emerges as severe constraints on long-haul multi-channel high data-rate systems^[1]. The PMD effect arises in single mode fiber when circular symmetry is broken by the presence of an elliptical core or by non-circularly symmetric stresses, which are induced during manufacture process. In perfect single mode (SM) fibers having perfect cylindrical geometry, there are two degenerate modes polarized in two orthogonal directions. The deviation from the geometrical symmetry breaks the mode degeneracy and causes a birefringence resulting in the polarization modes propagating with different group velocities along two orthogonal axes. The temporal delay between the two polarization modes at a given wavelength is known as the differential group delay (DGD). The average of DGD values across wavelengths yields the PMD Value. The birefringence in optical fiber is also perturbed by microbends, twists, temperature change, etc., which are randomly distributed along the fiber. These mechanisms induce an power exchange between the fast and the slow mode, resulting in a random variation of DGD. In this case, theoretically, polarization mode dispersion must be treated statistically. The DGD is an intrinsic function of the wavelength and of the environmental conditions, to which the fibers are submitted. For optical cable, the variation in DGD value in time and wavelength follows a Maxwell distribution^[2].

Differential group delay (DGD) is usually measured in a pico-second scale and it represents a singular result of a statistical process. In the other hand, PMD value represents the expected value (mean) of that same process. In a practical way, a parameter denominated PMD coefficient is defined as the value of PMD divided by the square root of the length (ps / $\sqrt{\text{km}}$) of a cable section or link. This definition is consistent with results observed experimentally, where PMD value assumes, for long fiber lengths, a dependence with the square root of the distance^[3].

There are several studies on the PMD phenomenon, but only recently works regarding PMD phenomena in installed optical cable fibers have been published^[4,5,6]. The few works found in literature are associated with the difficult of measuring PMD in a real link, since beside mechanical effects, PMD can be strongly influenced by physical surrounding in which cables are installed^[7]. The difficulty in measuring PMD coefficient on installed links has raised the attention on statistical methods to estimate such parameter in long-distance links. These methods use the approach of concatenated cables sections to estimate an allowed PMD coefficient of the link (PMD_q), in a probability basis. The Bulletin TIA/EIA TSB107 describes different methods to estimate allowed PMD coefficient, but is not so clearly presented^[8]. Our objective in this work is to describe, implement, and apply such models using loose-tube optical cable configurations.

2. Statistical Characterization of PMD

The PMD phenomena is a stochastic attribute on a fundamental level: it varies in magnitude randomly over time and wavelength. It is well known that the PMD of a long and ultra-long optical link at a given wavelength change in response to its environment. This means that this parameter can not be expressed by an individual number, but by means of a probability distribution function^[7]. However, cabled fiber PMD shall be characterized on a statistical basis not on an individual fiber basis. One approach is to consider the statistical properties of the PMD distribution generated from the cabling process. Two method can be used to specify the characteristics of the PMD distribution: The first one is related to PMD coefficient variation of concatenated links and the other one is related to the variation of DGD value in concatenated links. This work applies the first mentioned method, which uses the approach of concatenation by quadrature average. In this case, the PMD coefficient of a link is defined as the square root of the sum of squares of PMD values of the cable sections that are used to form the link

$$X_N = \sqrt{\frac{\sum_{i=1}^N x_i^2}{N}} \quad (1)$$

Where:

N Number of equal length cable sections comprising the link

x_i The PMD coefficient of fiber in an individual cable(ps/sqrt(km))

X_N The PMD coefficient of a concatenated link of N cables(ps/sqrt(km))

The Probability distribution of link PMD coefficients depends on the distribution of the individual cable PMD values and the number of cable sections in the link, N. In a statistical distribution, the value assumed by a random variable can be calculated through the probability of occurrence of that value. Therefore, to each value of the PMD coefficient of a given distribution in a link comprised by M cable sections, is associated an occurrence probability. The maximum link PMD coefficient X_Q , is defined in terms of a small value of probability Q, such that, the probability that a link PMD coefficient X_N is greater than X_Q , is smaller than the probability Q:

$$\Pr(X_N > X_Q) < Q$$

Q should necessarily assume a low value. In this work, Q was considered equal to 10^{-4} . The probability density functions and the respective maximum link coefficient for a given distribution (X_Q) is obtained by using different mathematical methods, such as Monte Carlo, Gamma Model, and Generalized Central Limit Theorem. These methods are defined in terms of a small probability level, Q, which is the probability that a link PMD coefficient exceeds the maximum PMD coefficient X_Q .

2.1 Monte Carlo Technique

In order to build the probability distribution using Monte Carlo method, the PMD coefficient for each cable section, x_i , is chosen randomly from individual PMD values of cabled fibers obtained from the manufacture process. The values are added in quadrature, according to equation (1), in order to calculate the link PMD coefficient, X_N , comprised by N cable sections. The process is repeated K times, where $K \geq 10/Q$. For $Q = 10^{-4}$, there are 100.000 possible link values. The maximum PMD coefficient is determined from the accumulated probability density function given by

$$c_m = \sum_{k=1}^m p_k \quad (2)$$

where p_k represents the normalized relative frequency in which the values of the link PMD coefficient appear in the distribution. The maximum PMD coefficient of the link, X_Q , is the first value of X_N that satisfy the condition $c_m \geq 1 - Q$.

2.2 Gamma Model Technique

The Gamma function^[9,10,11] is a model widely used to represent many natural physical phenomena. The gamma family distribution derived from gamma model can be used to represent both individual PMD value and link coefficient distributions. The model is based on the assumption that the square of the PMD coefficient of individual cables sections follow a distribution in agreement with a random variable of the Gamma type. The same way, the distribution of PMD coefficients of a link with many cable sections connected, may be also represented by the same variable and can be used to estimate the parameters that define the distribution of probabilities for the link. The probability distribution function Gamma is expressed by:

$$f(X, \alpha, \beta, N) = 2 \frac{(N\beta)^{M\alpha}}{\Gamma(\alpha)} X^{2M\alpha-1} \exp[-N\beta X^2] \quad (3)$$

Where X are the PMD coefficient values for the link, α and β are parameters that define, respectively, the shape and scale parameter of the distribution and M is the number of cables sections that are connected to form the link. The characterization of the Gamma distribution is made by determining the values of α and β respectively. These parameters can be calculated using the Moments Method^[8] or the Maximum likelihood Method^[12,13], as described below.

2.2.1 Method of moments

This is an iterative method based on the assumption that $N\alpha \geq 5$, because the parameter values are estimated before the verification of this inequality. In order to implement this estimative, the Monte Carlo method is required again with the objective to ensure the assumption of the inequality. Theoretically, the expected value or the mean of the Gamma distribution (1st order moment related to the origin of the distribution) is presented by α/β ^[14]. The Monte Carlo technique permits to generate a distribution of PMD coefficients, calculate the mean of the squares of these values and compare it with the mean of the Gamma function, as described by equation 4:

$$\frac{\alpha}{\beta} = v^2 = \frac{1}{k} \sum_{i=1}^k X_i^2 \quad (4)$$

where k is the number of Monte Carlo iterations (>100,000)

The variance of the Gamma function can be approximated by the variance related to squares mean (2nd order moment, related to the mean of the distribution) as:

$$\frac{1}{4N\beta} \cong \text{Average of } [(X - v)^2] \quad (5)$$

$$\frac{1}{4N\beta} = \frac{1}{k} \sum_{i=1}^k [X_i - v]^2 \quad (6)$$

By using equations (4) and (6), the α and β parameters can be estimated and the probability distribution function Gamma given by equation 3 is obtained.

2.2.2 Maximum Likelihood Method

This method starts directly from measurements of PMD coefficients on individual cable sections. A log-likelihood function [16] is defined by:

$$G(\alpha, \beta, x_i) = \sum_{i=1}^n \ln\left(\frac{2}{x_i}\right) - n \ln(\Gamma(\alpha)) + \alpha \sum_{i=1}^n \ln(\beta x_i^2) - \beta \sum_{i=1}^n x_i^2 \quad (7)$$

where n represents the number of measurements on individual cable sections (100 measures in the case of this work) and x_i is the PMD coefficient value of an individual cable section.

The shape and scale parameter, α and β , respectively, are values that maximize the G function. These values are calculated by taking the second derivate of $G(\alpha, \beta, x_i)$ with respect to α and β , and applying the following condition:

$$\ln(\alpha) - \psi(Sn) + 2gn = 0 \quad (8)$$

$$\beta = \alpha / Sn \quad (9)$$

where,

$$Sn = \frac{1}{n} \sum_{i=1}^n x_i^2, \quad gn = \frac{1}{n} \sum_{i=1}^n \ln(x_i)$$

$\psi(\alpha)$ is the Digamma function^[15,16].

Equation (8) is resolved by calculating the nulls of the function α . With the computed values of α and β , the PMD coefficients distribution can be constructed using equation (3). The maximum link PMD coefficient is estimated applying the following condition: for a given value of Q , the probability of finding a value of PMD coefficient higher than P_Q is given by

$$\int_0^{P_Q} \frac{y^{a-1}}{\Gamma(a)} \exp(-y) dy = 1 - Q \quad (10)$$

where, $a \equiv N\alpha$ and $y \equiv N\beta(X_N)^2$. N represents the number of cable sections and X_N is the PMD coefficient of the link. Therefore, to obtain the solution of this integral, it is necessary to find a value for p_Q in order to satisfy the condition $1-Q$. The Maximum PMD coefficient of the link is given by

$$X_Q = \left(\frac{P_Q}{N\beta} \right)^{1/2} \quad (11)$$

2.3 Generalized Central Limit Theorem

In this method, the individual PMD coefficients of individual cable sections are used to calculate the following moments

$$\mu_1 = \frac{1}{n} \sum_{i=1}^n x_i^2 \quad (12)$$

$$\mu_2 = \frac{1}{n-1} \sum_{i=1}^n (x_i^2 - \mu_1)^2 \quad (13)$$

$$\mu_3 = \frac{1}{n-1} \sum_{i=1}^n (x_i^2 - \mu_1)^3 \quad (14)$$

where,

x_i - PMD coefficient measured in a cable section (ps/√km);

n - number of measurements

The maximum PMD coefficient of the link obtained from the accumulated probability density function^[17] is given by

$$X_Q \approx \left[\mu_1 + z_Q \left(\frac{\mu_2}{N} \right)^{1/2} + \frac{\mu_3}{6\mu_2 N} (z_Q^2 - 1) \right]^{1/2} \quad (15)$$

where z_Q is a variable that depends on the value attributed to Q [6] e N indicates the number of cable sections in the link.

3. Experimental

In order to realize the numerical simulation, we choose from manufacture production four loose tube optical cables with 24, 72, 96, and 144 standard single-mode fibers, respectively. The length of each configuration was 5 km. For each cable configuration 100 PMD values were measured taking cabled fibers chosen randomly from manufacture production, and using the interferometer technique with a 1.55 μm light source^[18]. The

PMD of all cabled fibers were measured in a room where temperature was kept constant at 21 °C. The statistical results of individual PMD coefficients are summarized in table 1. Fig. 1 shows the PMD distribution obtained for the configuration of 24 fiber. It is noticed that the distribution fits very well the theoretically predicted Maxwellian distribution ^[19,20].

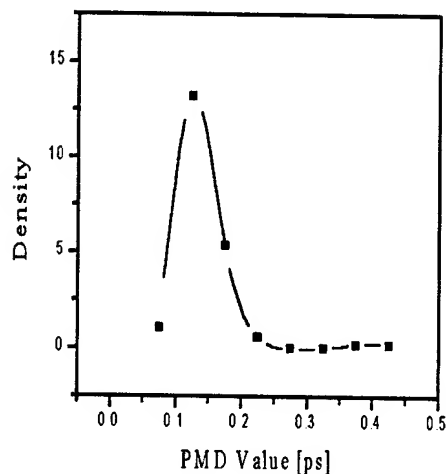


Fig.1 – PMD distribution obtained from a loose tube optical cable – 24 fibers

Table 1 . Experimental values of the PMD coefficient (ps/√km)

	24 fibers	72 fibers	96 fibers	144 fibers
Average	0,065	0,04974	0,06356	0,06321
Máximum	0,196	0,102	0,126	0,101
Minimum	0,037	0,022	0,049	0,045

4. Result and Discussion

Figures 2 and 3 shows the probability density function obtained by Monte Carlo's method for two links comprised of 10 and 200 cable sections, respectively. The simulation results were obtained using the experimental PMD parameters for optical cables with 24, 72, 96 and 144 fibers. These figures show the influence of the number of sections on the density function. It is clearly observed that the increase of the link length results on the reduction of the dispersion of all PMD coefficient distribution curves. From theory, the maximum PMD coefficient of the link, X_Q , is defined as the first value of X_N that satisfies the condition $c_m \geq 1 - Q$. This means that if the curves became narrower with the increase of the cable sections, the result for the maximum PMD coefficient parameter on the link may be strongly influenced by the number of cable section considered on the numerical simulation. From a practical point of view, the fact of having long-distance fiber link implies, statistically, that the maximum PMD coefficient estimated will be smaller than the short-distance fiber link one. For example, the PMD coefficient distribution curve for a hypothetical cable links comprised of 10 (corresponding to 50 km) and 200 cable (1000 km) sections using 72 fibers, gives values for maximum PMD coefficient of 0.077 and 0.058 ps/√km, respectively.

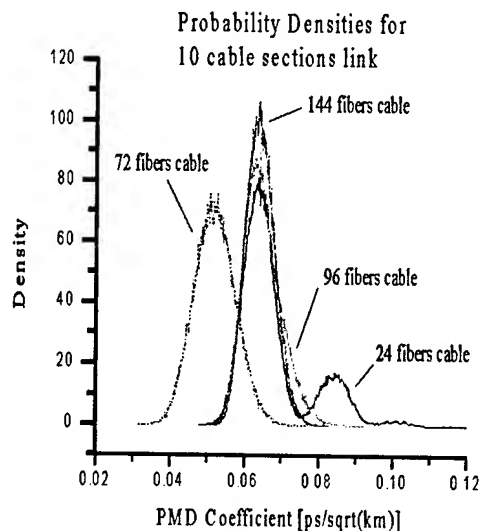


Fig. 02 –PMD coefficients distribution calculated by Monte Carlo method for a concatenated link comprised of 10 cable sections (50 km).

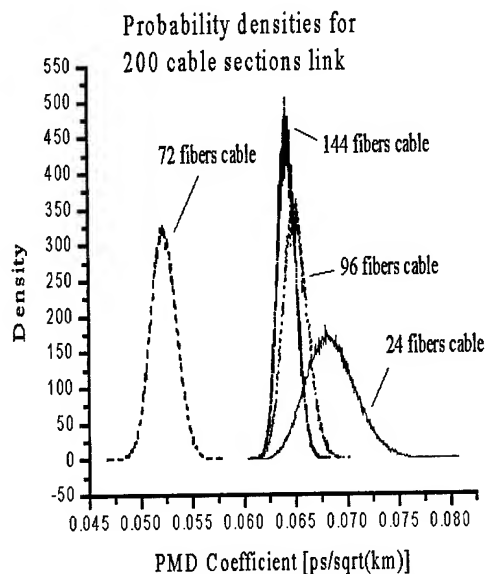


Fig. 03 – PMD coefficients distribution calculated by Monte Carlo method for a concatenated link comprised of 200 cable sections (1000 km).

Figure 4 shows the distribution curves using Monte Carlo and Gamma Model for a link comprised by 10 cable sections. The result of the numerical simulation shows a significant discrepancy between the methods, especially for the maximum likelihood method. If the number of cable section are added to the total link, it is observed again a reduction of the dispersion between the distribution curves. For a link comprised of 50 cable sections, the mean values for all curves starts to converge to the same value as shown in fig. 5.

Increasing the number of cable sections to 200, the results obtained by Monte Carlo and moment technique have almost identical distribution curves, as shown in figure 6. This result evidences a fundamental result of statistics, expressed by the Central Limit Theorem. This theorem affirms that different distributions tend to a normal distribution (gaussian) when the number of points tends to infinite^[14]. The numerical simulation shows also that for the maximum likelihood method, the convergence to normal distribution is not so fast than the others two methods. The most important is that the maximum value of the PMD coefficient is very close to the estimated by the other two methods.

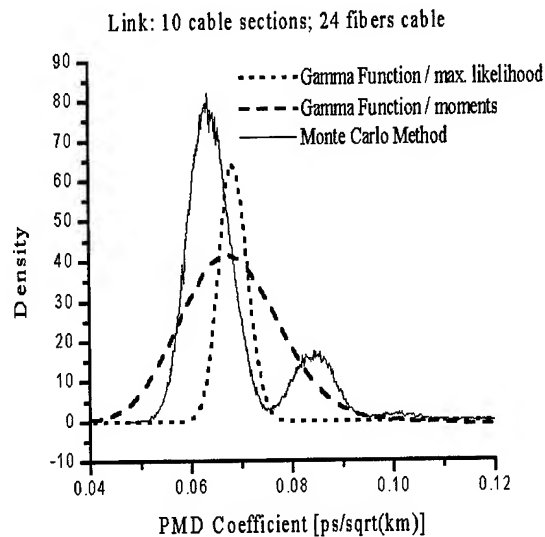


Fig. 04 - PMD distribution coefficients using Monte Carlo and Gamma Function methods, for a concatenated link of 50 sections (250km) using a loose tube optical cable – 24 fibers

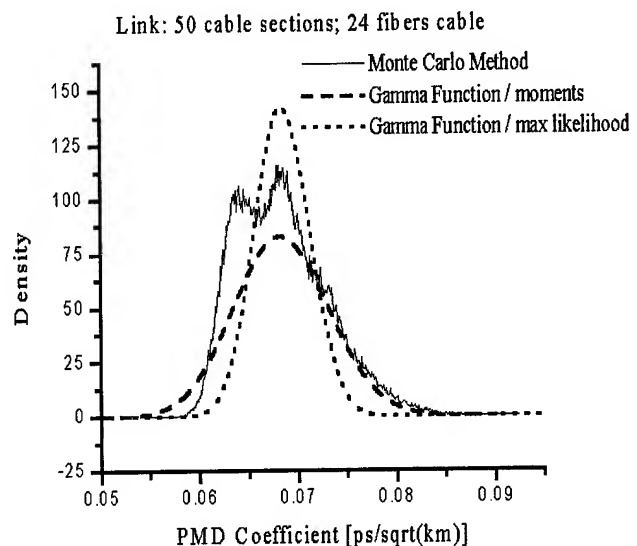


Fig. 05 - PMD distribution coefficients using Monte Carlo and Gamma Function methods, for a concatenated link of 50 sections (250km) using a loose tube optical cable – 24 fibers

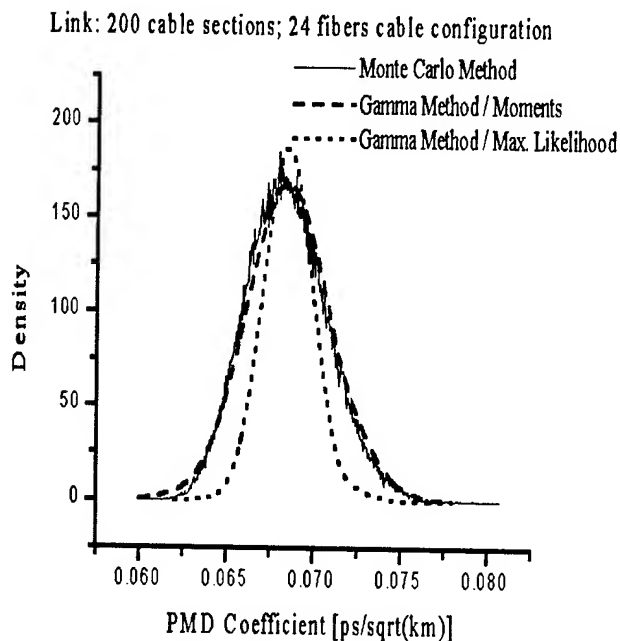


Fig. 06 - PMD distribution coefficients using Monte Carlo and Gamma Function methods, for a concatenated link of 200 sections (1000km) using a loose tube optical cable – 24 fibers

For the 72 fibers cable configuration, the PMD coefficient distribution curves obtained were almost identical, even considering a concatenated link comprised by a small number of cable sections. This is an indication that the final PMD coefficient distribution function has a strong dependence on the individuals PMD coefficients used on the simulation. The results are shown in Fig. 7.

Figure 08 shows the distribution of PMD coefficients for a link comprised of 200 cable sections. It is observed again that the dispersion of the distribution decreases with the increase of the number of cable sections. This result can be associated with a higher frequency of optical power coupling among the propagation modes along the space, inducing an equalization of the observed delays between the polarization modes.

Fig. 09 shows the behavior of maximum admissible PMD coefficient X_Q , calculated as a function of the number of cable sections N . The calculus was made considering a value of Q equal to 10^{-4} . The results showed clearly the dependence of the methods with the number of the cable section considered in the numerical simulation. For a link with length below 100 Km, the maximum admissible PMD coefficient value differs reasonably from method to method. For example, the maximum PMD obtained by using central limit technique is approximately 40 % higher than the value obtained by using the maximum likelihood method. For $N > 20$ it is observed a fast convergence for a low value with the Monte Carlo, Maximum likelihood and Moment method. For the Generalized Central limit method, this convergence is smoother. Finally, if N tends to infinite, the maximum PMD converges to the same value, no matter which method has been applied. Table

2 summarizes the values of X_Q , calculated considering a link with $N = 20$ and with probability of 10^{-4} to exceed this limit.

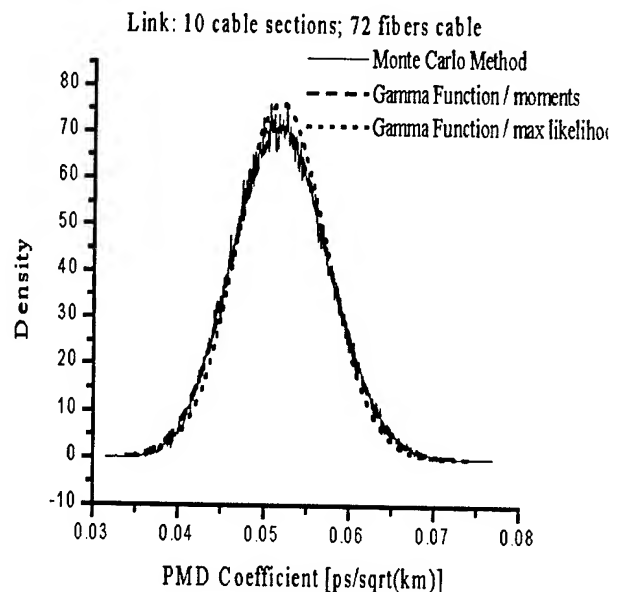


Fig. 07 - PMD distribution coefficients using Monte Carlo and Gamma Function methods, for a concatenated link of 10 sections (50km) using a loose tube optical cable – 72 fibers

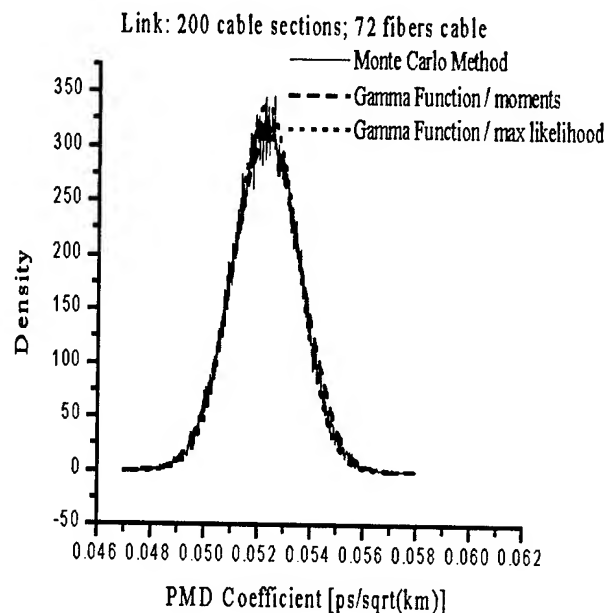


Fig. 08 - PMD distribution coefficients using Monte Carlo and Gamma Function methods, for a concatenated link of 200 sections (1000km) using a loose tube optical cable – 72 fibers

Tab 2. Values of X_Q for a link comprised of 20 cable sections

Method	Maximum admissible PMD Coefficient X_Q $Q = 10^{-4}$
Monte Carlo	0,105294
Gama Function	0,106144
CentralLimit Theorem	0, 106415

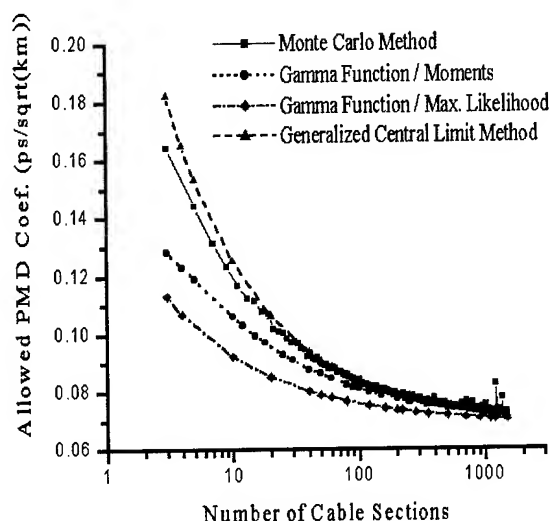


Fig. 09 – Maximum admissible PMD coefficient as function of the number of cable sections calculated by using different models.

In order to access the impact of the maximum PMD coefficient in the performance of an optical communication system, it is necessary to associate this parameter with the maximum link length and bit rate. This can be done by defining a small value of probability, from which the enlargement of the pulse inside of the bit slot, provoked by the polarization mode dispersion (maximum admissible PMD coefficient), would not degrade the performance of the system. This probability is expressed as ^[12]

$$P[X > \frac{fa \cdot 1000}{B \cdot \sqrt{L_{\max}}}] \approx 10^{-4} \quad (16)$$

$$L_{\max} = (\frac{1000 \cdot fa}{B \cdot X_{\max}})^2 \quad (17)$$

and f_a represents the tolerance for temporal enlarging of the pulse, inside the bit slot.

Figure 10 shows the behavior of the maximum link length, as function of X_Q , without taking into account the effect of chromatic dispersion of the fiber (that is, the chromatic dispersion have to be null or previously compensated). The simulation was realized with rates of 10 and 40 Gb/s, considering a tolerance, f_a , between 10 and 15% of the temporal enlarging of the pulse inside the bit slot. The results show, as expected, a strong dependence of the PMD with bit rate and the maximum transmission distance. For 40 Gbit/sec optical system, we have a dramatic reduction of link length, even using newer low-PMD fibers.

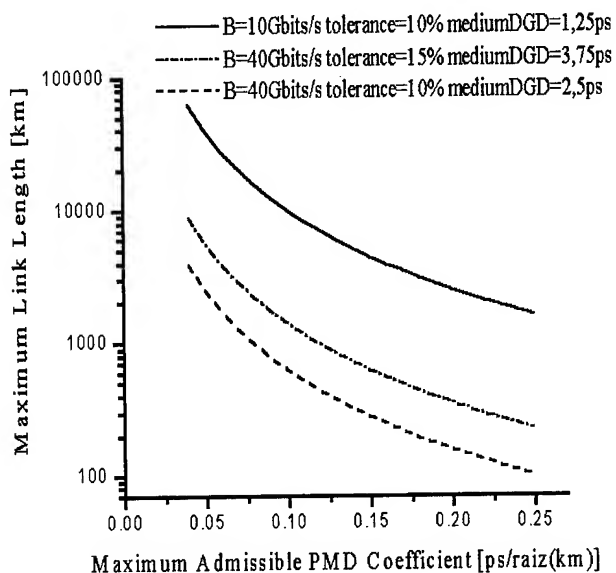


Fig. 10 – Maximum length of a link, in function of bit rates

5.0 Conclusion

Through the use of different statistical models, it was possible to build distribution functions for the PMD coefficient of links, starting from data obtained experimentally in cables with length of 5 km in the tube loose configuration. The results showed that from a certain number of sections ($N > 20$) the maximum admissible PMD coefficient converges to a fixed value, and do not depend on the statistical model employed. However, results obtained for $N < 10$ showed a reasonable variation in the estimated values. It was observed a heavy dependence of the PMD coefficient on the bit rate. The increase of the transmission rate (> 40 Gb/s) implied a significant reduction of the link length, when the system is not compensated. This reduction shows the need for compensation of the PMD phenomenon, operating at high bit rates.

6. Acknowledgments

The authors wish to acknowledge the support of many people in our organization that working with us in the laboratory measurements. Special thanks to Marcos Boulos for his assistance in the computer analysis.

7. References

- [1] P.A.Andrekson , OFC 2000, paper TuP2
- [2] F. Curti, B. Daino, G. DeMaris and F. Matera, "Statistical Treatment of the Evolution of the Principal States of Polarization in Single-Mode Fibers", J. Lightwave Technol., vol. 8, pp. 1162-1166, Agosto 1990.
- [3] N. Gisin, J.-P. Van der Weid and J.-P. Pellaux, "J. Lightwave Technol., vol. 9, no. 7, pp. 821-827, 1991.
- [4] H. Sunnerud, B.-E. Olsson, M. Karlsson, P.A. Andrekson e J. Brentel,"Polarization-Mode Dispersion Measurements Along Installed Optical Fibers Using Gated Backscattered Light and a Polarimeter", J. Lightwave Technol., vol. 18, pp. 897-904, Julho 2000
- [5] M. Karlsson, J. Brentel e P.A. Andrekson, "Long-Term Measurement of PMD and Polarization Drift in Installed Fibers", J. Lightwave Technol., vol. 18, pp. 941-951, Julho 2000.
- [6] A. Galtarossa, L. Palmieri, A. Pizzinat, M. Schiano e T. Tambosso, "Measurement of Local Beat Length and Differential Group Delay in Installed Single-Mode Fibers", J. Lightwave Technol., vol. 18, pp. 1389-1394, Outubro 2000.
- [7] H. Sunnerud, B.-E. Olsson, M. Karlsson, P.A. Andrekson e J. Brentel,"Polarization-Mode Dispersion Measurements Along Installed Optical Fibers Using Gated Backscattered Light and a Polarimeter", J. Lightwave Technol., vol. 18, pp. 897-904, Julho 2000.
- [8] TIA/EIA TSB107 "Guidelines for the Statistical Specification of Polarization Mode Dispersion on Optical Fiber Cables" – November 1999
- [9] P. L. Meyer, "Probabilidade: aplicações à estatística", Livros Técnicos e Científicos Editora, Rio de Janeiro, 1981.
- [10] Abramowitz, M., e Stegun, I.: 'Handbook of Mathematical Functions', Dover Publications, New York, 1970.
- [11] Press, W., Teukolsky, S., Vetterling, W., e Flanner Y, B.: 'Numerical Recipes in Fortran', Cambridge University Press, 1992.
- [12] S.A. Jacobs, J.J. Refi e R.E. Fangmann, "Statistical Estimation of PMD Coefficients for System Design", Electron. Lett., vol. 33, pp. 619-621, Março 1997.
- [13] Breimann, L.: 'Statistics: with a view toward applications' Houghton Mifflin Company, Boston, 1973.
- [14] P. L. Meyer, "Probabilidade: aplicações à estatística", Livros Técnicos e Científicos Editora, Rio de Janeiro, 1981.
- [15] Abramowitz, M., e Stegun, I.: 'Handbook of Mathematical Functions', Dover Publications, New York, 1970.
- [16] Press, W., Teukolsky, S., Vetterling, W., e Flanner Y, B.: 'Numerical Recipes in Fortran', Cambridge University Press, 1992.
- [17] J. Patel e C. Read, "Handbook of the Normal Distribution", Marcel Dekker Inc., New York, 1982.
- [18] R. Cross, "PMD Measurements Methods", Fiberoptic Product News, pp.27-29, Junho 1995.
- [19] B. W. Hakki, "Polarization Mode Dispersion in a Single Mode Fiber", J. Lightwave Technol., vol. 14, no. 10, pp. 2202-2208, 1996.
- [20] N. Gisin, R. Passy, J. C. Bishoff and B. Perny, "Experimental Investigations of the Statistical Properties Polarization Mode Dispersion in Single Mode Fibers", IEEE Photonics Techn. Lett., vol. 5, no. 7, pp 819-821, 1993.
- [21] L.F. Marques, A. M. Simião, R. F. Cruz, J.A. Medeiros e M.R. Boulos,"Statistical Analyses of PMD Using Monte Carlo Method for Different Configuration of Loose Tube Optical Cable", in Proceedings of OFC'2001, 2001, paper WDD12

8.0 Authors



Jeancarlo Dotto received his B.S. degree as an Electrical Engineer from Federal Center of Technological Education (CEFET-PR) in 2000. In the same year his joined Furukawa Industrial S/A and since than his is evolved with optical fiber and cables evaluation for Quality Department



Januncio A. Medeiros Neto² received his B. S. degree from Federal University of Rio Grande do Norte (UFRN) and M. S. and PhD in Physics from University of Campinas (UNICAMP) in 1991. After post doctoral appointment at ORC-University of Southampton – England, he joined UNICAMP as research associated. In 1998, he joined Furukawa Industrial S/A. as consultant. Since April, 2002 he is technical supervisor at the Centro Internacional de Tecnologia de Software (CITS).



Renato Flávio Cruz³ received his Chemical Engineer degree from Universidade Federal do Paraná (UFPR) in 1988. He joined Furukawa Industrial S/A. in February 1989 and since then he has been involved in research and development of products for telecommunication cables. He is now Manager of cable Development Engineering.



Lúcio F. G. Marques³ received his B.S. degree as an Electrical Engineer from Federal University of Paraná (UFPR) in 1995. He joined Furukawa Industrial S/A. in 1997. He is currently Product Engineering



Alexandre A. P. Pohl¹ received the B.S. and M. Sc. degree in Physics from the Universidade Estadual de Campinas (Unicamp), Brazil. From 1990 to 1994 he worked as a visiting researcher at the Institut für Hochfrequenz Technik of the Technische Universität Braunschweig, Germany, where he obtained the Dr.-Ing in Electrical Engineering. In 1995 he joined the telecommunications systems division of Furukawa Industrial S.A. Since 2001 he has been with the Centro Federal de Educação Tecnológica do Paraná (CEFET-PR).



C. E. P. Blume¹ has a technical degree in Mechanics from the Centro Federal de Educação Tecnológica do Paraná (CEFET-PR). Since 1999 he has been working toward the B.S degree in mechanical engineering at the CEFET-PR. As a research student he worked on mechanical and optical properties of optical fibers in the group led by Mr. Januncio A. Medeiros Neto.

PMD Evaluation in Backbones – A Comparison Between the PMD Value Expected by Calculus and the Field Measurements

J. A. Brito Jr, A. Cieslak

Intelig Telecomunicações Ltda/ Network Implementation Dept.
Av. Praia de Botafogo, 370 Zip Code 22250-909 Rio de Janeiro, RJ, Brazil
55-21-2323-6616 · joao.brito@intelig.net.br/agnaldo.cieslak@intelig.net.br

Abstract

The articles, up to now, mention that the PMD value quantification due to concatenation of some spliced fibers into laboratory is slightly higher than the measured value of this supposed link. Another point discussed in these articles is the link PMD characterization where the maximum limit is obtained by statistical analysis considering PMD as stochastic attribute [1]. In this paper we present the analysis determining the real differences between these mentioned methods, taking into consideration a great data base based on measured values of two backbones, under securely known conditions.

Keywords

Optical Fiber; Polarization Mode Dispersion Coefficient; Concatenation by Quadrature Average; Monte Carlo Technique; Measurements, As-Built.

1. Introduction

Intelig is a new carrier company in Brazil, set up after privatization of Telecommunication market. Since 1999 more than 15.000 km of optical fiber cables were deployed in backbones and metropolitan networks located in the ten most important cities. During the implementation of these backbones from 1999 to 2001, the evaluation of the links characteristics as attenuation, chromatic dispersion and PMD was done intensively in order to guarantee the backbones performance for higher hierarchies and accumulating information for further implementations.

This paper is centered on the PMD evaluation due to the absence of a PMD compensation method, differently from chromatic dispersion that can be corrected by adding dispersion-compensator modules as Bragg grating, DCF fiber etc.

This concern regards to the fact that at 10 Gbit/sec, PMD is a problem only for long-haul systems, while at 40 Gbit/sec, PMD can become a significant issue for metro/regional systems as well [2].

There is a leak of historical information from the PMD characteristics of backbones that had been deployed previously and either we can't find studies comparing PMD values obtained by calculus with field measurements. Intelig was the first telecom company that evaluated PMD characteristics of its backbones with real data, requiring the PMD measurements from its suppliers.

It is known that the averaging process arising from concatenation of cables leads to a link PMD coefficient value lower than the

individual cable PMD coefficient value [5]. The question is: What is the real difference between the backbones links PMD values and the fiber PMD values after cabling?

In this paper we will show the results obtained evaluating two different backbones: 565 Km and 1650 Km long.

2. Deployment Conditions

2.1 Infrastructure Specifications

The bulk of backbones were deployed along the railroads, including the two mentioned above. The infrastructure specification as trench depth and wide, type of ducts (inner and outer diameter), splice box, manholes, etc. was exactly the same for all backbones.

2.2 Optical Fiber and Cable Specification

In the same way the optical fiber and cable specification were the same for all backbones. The optical cable used was Single Jacket Loose tube for duct application [3] with 72 and 48 single mode fibers [4].

3. Calculus Methodology

The PMD value specified for each link was 0,2 ps/Km^{1/2}.

There are two methods for statically quantifying a PMD link according to the EIA/TIA [5]. Method 1 defines the statistical PMD performance of a distribution of fibers in a link providing a statistical upper bound (PMD link value). This upper bound provides a more realistic indication of maximum PMD likely to be encountered in a concatenated link. The second method is expressed in terms of a maximum DGD value, and the probability that a DGD on a given link and wavelength exceeds this maximum.

We used Method 1 for this study because it is recommended for the fiber and cable manufactures, systems sellers and end users.

Additionally to method 1, the data were analysed by the concatenation by quadrature average, taking into account the As-Built information of cables deployment along the routes.

3.1 Concatenation by Quadrature Average

According to the TIA/EIA-TSB107, the PMD value of a link is given by the square root of the sum of squares of the PMD values of the cable sections that are used to make the link. This leads to a similar relationship between the link PMD coefficient and the cable section PMD coefficients.

The quadrature total yielding d_{link} is:

$$d_{link} = \left(\sum_{i=1}^N d_i^2 \right)^{1/2} \quad (1)$$

The relationship of link PMD coefficient, d_{c-link} , to cable section PMD coefficients, d_{c-i} , is then:

$$d_{c-link} \cdot L_{link}^{1/2} = \left(\sum_{i=1}^N d_{c-i}^2 \cdot L_i \right)^{1/2} \quad (2)$$

If one assumes that all cable section lengths are less than some common value, L_{cab} and, simultaneously reducing the number of assumed cable sections to $M=L_{link}/L_{cab}$ then:

$$d_{c-link} \leq \left(L_{cab} / L_{link} \cdot \sum_{i=1}^M d_{c-i}^2 \right)^{1/2} = \left(1 / M \cdot \sum_{i=1}^M d_{c-i}^2 \right)^{1/2} \quad (3)$$

Where: d_{link} = PMD of the link

d_i = PMD value of N cable sections

d_{c-link} = PMD coefficient of the link

L_{link} = Link length

d_{c-i} = Cable section PMD coefficient

L_i = Cable section length

M = Number of equal length cable sections comprising the link

The concatenation by quadrature average (equation 3) of the backbones was performed by taking the As-Built information into account and each cable section used in each of the links of these two backbones.

The cable manufactures measured the fiber PMD coefficient after cabling according to a sample criteria, adopted in order to permit the evaluation by concatenation by quadrature and after the cables deployment permits the comparison with the field measurements.

3.2 Monte Carlo Technique according to Method 1 by TIA/EIA – TSB107

According to this method, we used the PMD coefficients of the fibers measured by the manufactures after cabling to calculate the PMD coefficient for a single fiber path in a concatenated link.

The PMD link coefficient was calculated by a routine selecting randomly M values from the measured individual fiber PMD coefficients, and performs the quadrature average according to equation 3 to create one random link. The calculating process of link PMD coefficient was repeated $K=100,000$ times to create K random link coefficient values. The values were placed in a high resolution histogram. The minimum values of K is given in terms of Q:

$$K \geq 10/Q \quad (4)$$

Number of interactions: 100.000

Q=small probability value, were for $Q=100\text{ppm}$, PMD_Q is the 99,99% of the link PMD coefficients.

The cumulative probability function was computed as:

$$C_m = \sum_{K=1}^m p_k \quad (5)$$

The value of PMD_Q is the first value, d_{c-m} , at which $C_m \geq 1-Q$.

The typical link created for backbone A was $L=110\text{ Km}$, Cable section lengths = 5,5 Km.

The typical link created for backbone B was $L=120\text{ Km}$, cable section lengths = 8 Km.

4. Field Measurements

The links of each backbone were measured in order to compare the theoretical values obtained by two evaluations mentioned previously in item 3 with the field measurements.

The equipment used was based on the interferometer methodology [6].

The fibers path was measured according to the same sample criteria adopted to permit the evaluation by concatenation by quadrature average.

The values obtained of each fiber path are an average of three measurements that were done consecutively.

In order to check the repetitiveness of results, some of the fibers were measured some time later and the results were confirmed.

5. Data Evaluation - Graphics

5.1 Backbone A Evaluation

This Backbone is composed by 6 links. The optical cables drums came from the same manufacturer that used its own optical fiber. Taking aleatory values of the fiber PMD coefficients measured after cabling (Figure 1) and using a routine to calculate the link PMD coefficient (PMD_Q) by Monte Carlo technique, it was found out 0,076 $\text{ps/km}^{1/2}$ as result. All the fiber paths of these 6 links might have 99,99% probability of being below this value.

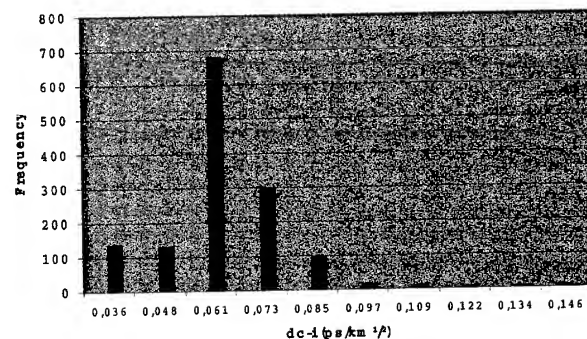
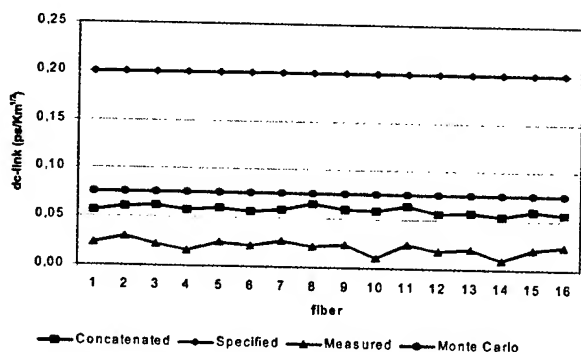


Figure 1. Distribution of d_{c-i} from Manufacturer A

The concatenated value is valid for each individual fiber path unlikely the PMD_Q value that is valid for all fiber paths of all links.

Figure 2 shows Link 1 graphic, which is representative of all links of this backbone because all links presented the same behaviour.

We can observe that the value obtained from the concatenation (d_{c-link}) was about 150% superior to the measured value of each fiber



path. The PMDQ result by Monte Carlo presented a value about 200% higher than the measured value.

We can conclude that the average difference between the PMD_Q value and the concatenated value (d_{c-link}) is around 50% for all links.

Figure 2. Link 1 (74,56 km) from Backbone A

The PMD coefficient measured in the fiber paths in this link is around $0,02 \text{ ps/km}^{1/2}$. In all the other links this result was the same.

Considering the maximum allowed PMD value as one-tenth of the bit period for non-impairments system performance [7, 8, 9] and taking the results exposed above we could guarantee that this 585 Km backbone could support 40Gbps bit rate.

5.2 Backbone B Evaluation

This Backbone is composed by 16 links and 2 regenerations. The optical cables drums came from two different manufacturers, B and C that used their own optical fiber. The procedures to calculate the PMD coefficients by Monte Carlo and by Concatenation of this backbone were the same adopted in backbone A.

We chose random values of the fiber PMD coefficients measured after cabling from the two manufactures B and C¹ (figure 3 and 4 respectively) and using a routine to calculate the link PMD coefficient (PMD_Q). It was found out $0,119 \text{ ps/km}^{1/2}$ as a result. All the fiber paths of these 16 links would have 99,99% probability of being bellow this value.

The concatenated value is valid for each individual fiber path unlikely the PMD_Q value that is valid for all fiber paths of all links.

¹ The manufacturer C performed larger sampling than the officially one requested by Intelig.

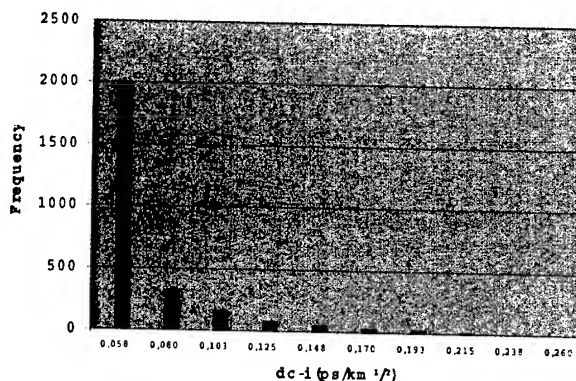


Figure 3. Distribution of d_{c-i} from Manufacturer B

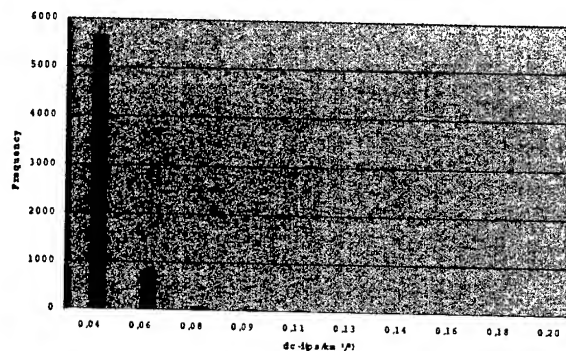


Figure 4. Distribution of d_{c-i} from Manufacturer C

This backbone evaluation can be classified in two different reference patterns accordingly to the PMD link coefficient behaviour (see figures 5 and 6). These patterns are related to the differences between the concatenated and measured values compared with the value obtained by the Monte Carlo technique.

In case of first pattern link (figure 5), the fibers used are from manufacturer B. This manufacturer has presented non-uniformity in the concatenated values but the average value is similar to link 1 backbone A.

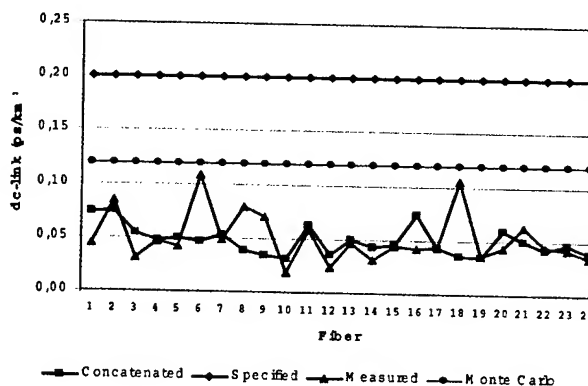


Figure 5. Link 2 (108 km) from Backbone B

Beyond the non-uniformity of individual PMD values reflected in the measured link PMD, probably there was a residual stress after installation. This residual stress kept and, in some cases, amplified this result probably due to the association of cable design, process control and optical fiber used.

In case of second pattern link (figure 6), it was used fibers from manufacturer C. This pattern presented the same behaviour as link 1 (backbone A) in terms of measured and concatenated results.

We can observe that the value obtained through concatenation (d_{c-link}) fixed around 80% superior than the measured value of each fiber path. This difference shows that probably this manufacturer presented low stress in the fibers just after cabling.

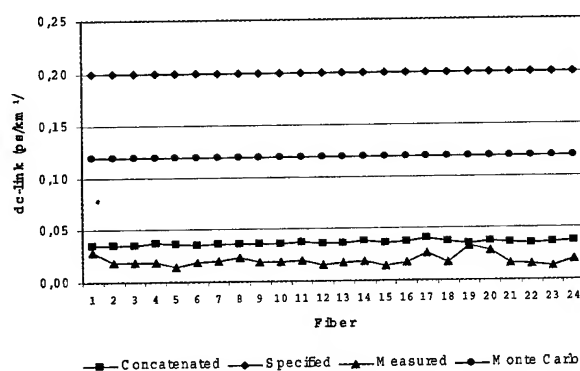


Figure 6. Link 3 (120 km) from Backbone B

About Monte Carlo result certain analysis about difference between concatenation and measured values can be plotted. Monte Carlo value was obtained taking values from those two manufacturers B and C, but the second pattern behaviour is related to manufacturer C where d_{c-i} presented lower steps than manufacturer B. So Monte Carlo value was over-estimated for links that follow this pattern.

An analysis that should be considered for all links is about lower measured PMD in comparison with concatenation and Monte Carlo results. Beyond the concatenation, in fact the measurement of PMD after cabling is done while optical cable was wounded in the bobbin. This leads to an extra stress point. After cable deployment the stress points relaxed reducing the optical fiber PMD.

Another explanation relates to a certain DGD values measured by manufacturer were out of dynamic range of the used equipment. When the equipment software calculates the PMD, some penalty was imputed and the values were fixed in the lower possible value of equipment.

Finally the higher variations between calculated and measured values occurred, mainly in the fiber paths with lower measured values, reinforcing that previous explanation.

6. Conclusions

For first time all three values were compared: the PMD fiber measured value vs. the concatenated by quadrature average value vs. the obtained value through Monte Carlo technique.

It was possible to quantify the differences between real values, field measurements, with theoretical values.

It was proved that the Monte Carlo technique used to determine the PMD coefficient is around 2,5 times higher, in the majority, if compared with measured values.

Due to the fibers state of art and the optical cables project control a 40 Gbps per channel is possible.

7. Acknowledgments

The authors are grateful to the contributions of several individuals specially including Jean Pierre Von der Weid, José Roberto F. Rocha and Marcos Barreto.

8. References

- [1] N. Gisin, B. Gisin, J. P. Von der Weid, R. Passy, "How accurately can one measure a statistical quantity like polarization-mode dispersion?," IEEE Photonics Technology Letters, Vol. 8, N° 12, pp 1671-1673 (December, 1996).
- [2] S. A. Jacobs, J. J. Refi and R. E. Fangmann, "Statistical estimation of PMD coefficients for system design", Electronic letter, Vol. 33, No 7 (1997).
- [3] CTO-NT-TE-0108 - CFOA-SM-DDP-G-XX- Intelig Telecomunicações Standard (August, 2001)
- [4] ITU-T G.652 "Characteristics of a single-mode optical fibre cable" (November, 2000).
- [5] TIA/EIA TSB107 "Guideline for the Statistical Specification of Polarization Mode Dispersion on Optical Fiber Cables," (November, 1999).
- [6] ITU-T G.650 Definition and test methods for the relevant parameters of single-mode fibers," (November, 1999).
- [7] ITU-T G.691 "Optical interfaces for single channel STM-64, STM-256 systems and other SDH systems with optical amplifiers," (November, 2000).
- [8] S. A. Jacobs, J. J. Refi and R. E. Fangmann, "Statistical estimation of PMD coefficients for system design", Electronic letter, Vol 33, No 7 (1997).
- [9] H. Bulow, "System Outage Probability Due to First and Second Order PMD," IEEE Photonics Technology Letters, Vol.10, N° 5, (May, 1998).
- [10] F. Kapron, A. Dori, J. Peters, H. Knehr, "Polarization-Mode Dispersion: Should you be concerned?," NFOEC'96, pp. 757-768 (September, 1996).

9. Authors



João Arlindo Brito Junior – Intelig Telecomunicações Ltda.
370, Praia de Botafogo Ave, Zip Code: 22250-909
Rio de Janeiro – RJ – Brazil. Joao.brito@intelig.net.br

João A. Brito Jr. received B. S. degree as an Electrical Engineer from Federal University of Paraná (UFPR) and P. G. degrees in Telecommunications Administration from FESP and Administration from FGV. Going on M. S. in Optical Communications at Pontifícia Universidade Católica do Rio de Janeiro (PUC-RJ). He is a Contract Manager for the implementation of transmission and data equipment.



Agnaldo Cieslak – Intelig Telecomunicações Ltda.
370, Praia de Botafogo Ave, Zip Code: 22250-909
Rio de Janeiro–RJ–Brazil. agnaldo.cieslak@intelig.net.br

Agnaldo Cieslak received his B. S. degree as an Electrical Engineer from Federal Center of Technological Education of Paraná (CEFET-PR) and P. G. degree in Telecommunications Administration from FESP. Going on M. S. in Optical Communications at Pontífica Universidade Católica do Rio de Janeiro (PUC-RJ). He is a Contract Manager for the implementation of transmission and data equipment.

The Behavior of PMD Parameter in an Optical Cable Link due to Temperature Cycling

Marcelo M. Simião¹, Jeancarlo Dotto¹, Lucio F.G. Marques¹, Renato F. Cruz¹,
Januncio A. de Medeiros Neto²

Furukawa Industrial S.A. Produtos Elétricos¹, Curitiba - PR - Brazil
CITS-Centro Internacional de Tecnologia de Software², Curitiba-PR-Brazil
Phone 55-41-341-4060, email: msimiao@furukawa.com.br

Abstract

This paper presents a characterization of PMD parameter in optical cable links under thermal cycle using conventional Single-Mode Fiber (SMF-G.652) and Non-Zero Dispersion Shifted Fiber (NZDF-G.655). The expected PMD value for the link comprised NZDF-G.655 exhibits a much larger variation than the results obtained with the link SMF-G.652. Measurement of the cable links after the end of the thermal cycle shows that the expected PMD value remains almost the same to the value measured at the beginning of the experiment, especially for the link comprised of SMF-G.652 fibers. From the practical point of view this results are very important, since than as the thermal cycle represent conditions that affect the optical cable during its lifetime, this means that the system designer may consider the initial expected PMD values without significant modification of the PMD distribution during cable's lifetime.

Keywords

PMD Coefficient; Optical Link; Optical Fiber; Temperature Cycle

1. Introduction

Polarization-Mode Dispersion (PMD) is considered to be the limiting mechanism in high-capacity single-mode fiber-optic transmission systems when chromatic and waveguide dispersion effects are compensated for^[1]. In an ideal single-mode fiber the fundamental mode is indeed split into two polarization modes that propagate with the same group velocity along perpendicular axes. The dispersion of the polarization modes arises when circular symmetry is broken by the presence of an elliptical core or by non-circular symmetric stresses, which are induced during the fiber drawing and packaging process. Therefore, from the practical point of view, it is imperative that optical cable manufacturers be able to guarantee a low PMD in their products. As the PMD value of a single piece of cable provides only a limited insight into the phenomenon, one should take into consideration the variation of the PMD in an optical cable link as a whole. This approach allows manufacturers, in a feedback process, to optimize all parameters and improve design and

fabrication conditions. It has been demonstrated that a variation in the temperature leads to a fluctuation in PMD and that the rate of fluctuation follows the rate of temperature change^[2].

In this paper we present results concerning the behavior of PMD coefficient associated with a thermal cycle using two types of optical fiber. The idea is to simulate strong temperature changes that may occur during the optical cable lifetime. In order to simulate as near as possible a fiber-optic transmission system, we built two optical links comprised of Standard Single-Mode Fiber (SMF-G.652) and Non-Zero Dispersion Shifted Fiber (NZDF-G.655) for thermal analysis. The experimental links data were also compared with the statistical analysis based on PMD distribution generated from the individual PMD coefficients cabled fibers.

2. Cable Design

In order to experimentally simulate the dependence of PMD in function of the temperature changes in a link comprised of N cable sections, we use an underground in duct loose tube cable with SMF-G.652 and NZDF-G.655 optical fiber. Table 1 summarized the principal parameters of the cable used in this study. The use of different types of fibers in the same cable structure allowed us to induce the same mechanical stress along the entire fiber length. With this experimental procedure, we expected that the PMD variation associated with mechanical effects are equivalent for both types of fibers inside the cable, since it is well known that the variation on the birefringence in cabled fibers is strongly dependent on the cable design^[3].

Table 1. Cable Parameters

Design	Loose Tube Optical Cable	
	SMF-G.652	NZDF-G.655
Outer diameter	11.2 mm	
Number of tube	2	2
Fiber per tube	6	6
Lay Length	80 mm	
Cable Length	4.5 km	

3. Theory - Statistical analysis

The PMD effect arises in optical fiber when circular symmetry is broken by the presence of an elliptical core or by non-circularly symmetric stresses induced during cabling process. The loss of circular symmetry removes the degeneracy and causes an intrinsic birefringence resulting in the two polarization modes propagating with different group velocities. Besides, fibers are submitted to tension, bend, and compression during the cabling process and field installation. All these mechanisms induce a complex and random variation of the birefringence. Consequently, the PMD should be treated statistically^[4].

The temporal delay between the two polarization modes at a given wavelength is defined as the Differential Group Delay (DGD). This parameter is usually measured in a picoseconds scale and it represents a singular result of a statistical process. On the other hand, PMD value represents the expected values (mean) of that same process. From the practical point of view, the parameter denominated PMD coefficient is defined as the PMD value of a cable section or link divided by the square root of its length (ps/√ km). This definition is consistent with results observed experimentally^[5]. As PMD of a long and ultra-long optical link at a given wavelength change in response to its environment, this requires that it be expressed not as a single number, but by means of a probability distribution function^[6]. Two methods can be used to specify the characteristics of the PMD distribution^[7]. This work applies the method which uses the approach of the concatenation by quadrature average, which is defined as the square root of the sum of squares of PMD values of the cable sections used to form the optical link:

$$X_n = \sqrt{\frac{\sum_{i=1}^n x_i^2}{N}} \quad (1)$$

Where:

N - number of equal length cable comprising the link

x_i -The PMD coefficient of fiber in an individual cable (ps/√km)

X_n - The PMD coefficient of a concatenated link of N cables (ps/√kmrequest)

4. Experiments

The probability distribution of link PMD coefficients depends on the distribution of the individual cable PMD values and the number of cable sections that comprise the link. Different methods can be applied to obtain the PMD coefficients distribution. In this paper we use the Monte Carlo method.

In order to realize the numerical simulation, PMD values for both types of fibers were measured on cabled fibers chosen randomly from manufacture production cables with the same design. The numerical simulations were made using 100 individual PMD coefficient values for the SMF-G.652 fiber and 80 for the NZDF-G.655 fiber. The individual PMD measurements were made under stable ambient temperature conditions, using an AGG

PMD4000 equipment with a 1.55 μm light source. The statistical results of the individual PMD coefficients are summarized in table 2. Fig. 1 and 2 shows the measured PMD coefficients distribution for the SMF-G.652 and NZDF-G.655 fibers respectively.

Table 2. PMD coefficient of cabled fibers (ps/√km)

	SMF-G.652	NZDF- G655
Average	0.0399	0.0467
Stdev	0.0139	0.0198
Maximum	0.1100	0.1260
Minimum	0.0300	0.0310

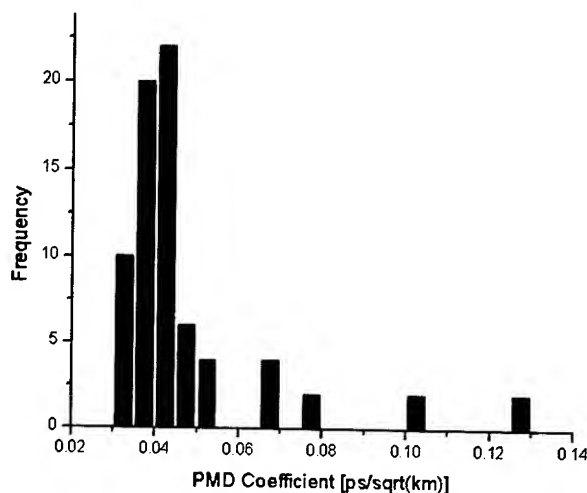


Fig.2 – PMD coefficient distribution for NZDF-G.655- cabled fibers

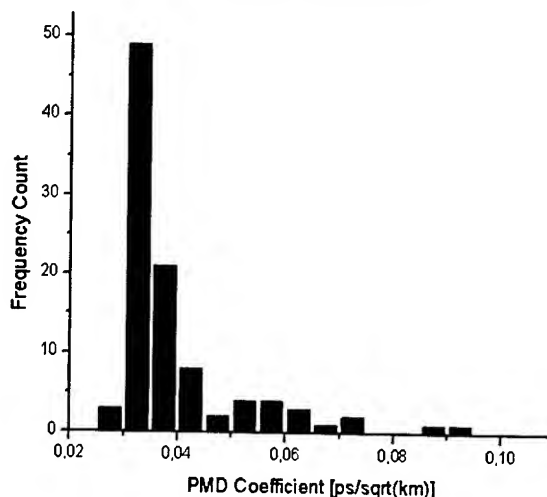


Fig.3 – PMD coefficient distribution for SMF-G.652 cabled fibers

Fig.3 shows the probability density function, obtained by Monte Carlo's method for the two links comprised each of 20 cable sections. The simulation was made using the experimental PMD parameters described in the fig.1 and fig.2. The difference between the two curves is associated with the experimental PMD coefficients used on the simulation. As the SMF-G.652 fiber presents a more narrow curve distribution compared with NZDF-G.655, the numerical results for the maximum PMD coefficient in the link (probability of 10^{-4} to exceed this value) comprised of this type of fiber will give PMD values smaller than for the link comprised of NZDF-G.655 fiber. The table 3 summarizes the results of the numerical simulation.

Fig.3 – PMD coefficient distribution for a link comprised of SMF-G.652 and NZDF-G.655 optical fiber

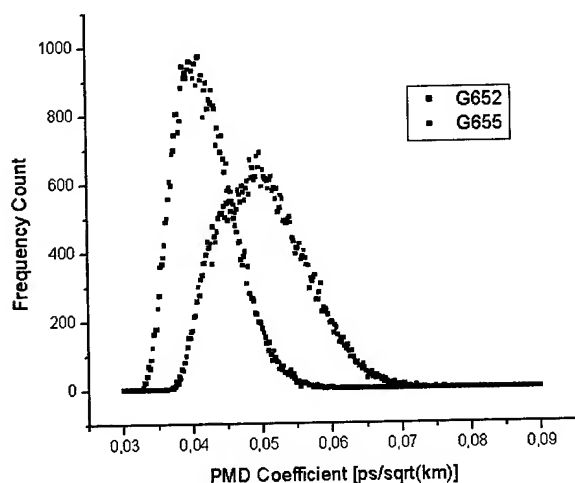


Table 4. Summary of the statistics analysis of the PMD parameter obtained by using Monte Carlo Method

	SMF-G.652	NZDF-G.655
Average	0.04203	0.05033
stdev	0.00423	0.00617
Minimum	0.03190	0.03520
Maximum	0.06320	0.08235

Two links were constructed for temperature tests. Table 4 summarized the optical link parameters

Table 4. Optical Link parameters

Link	A	B
Type of Fiber	SMF-G.652	NZDF-G.655
Number Cable section – N	11	
Total Length (km)	54	
Total Optical Loss (dB)	10,5	10,9

The links were placed in a controlled-temperature chamber, which were then connected externally to an AGG PMD4000 equipment operating at 1.55 μm . Prior to beginning the thermal cycle, the PMD coefficient of the links were measured at ambient temperature in order to characterize the initial conditions.

The temperature cycling applied for both links consisted of the alternated steps of low-high temperatures. Low temperature was set at -40°C and high temperature at $+85^\circ\text{C}$. After the end of each step, the temperature was ramped linearly at 44°C per hours in order to reach the new temperature level. The total time spent for a complete temperature cycle was of the 360 hours. The PMD measurements for each cycle were made following the sequence: reference at 25°C , two step of -40°C to 70°C , one aging cycle at 85°C during 120 hs, two cycle of -40°C to 70°C and other reference at 25°C . Between the first and second cycle was made an interval of one week. The PMD data were collected only in the last two hours of each temperature step, allowing this way the stabilization of the fibers inside the cable and the minimization of the mechanical stress associated with cable design. Hundreds of data were taken in each step and the PMD coefficient ($\text{ps}/\sqrt{\text{km}}$) were calculated automatically by the equipment. After the end of the PMD measurements in each temperature step were made also measurements of the optical loss in order to verify if dimensional changes in the cable were stable enough to guarantee optical stability. After the end of the each temperature cycling, the PMD coefficient of the link was measured again at ambient temperature in order to correlate measured values before and after the experiment

5.0 Result and Discussion

Figs. 4.a and 4.b shows the typical dispersion of measured points related to each step of the temperature cycling. As discussed before, the measurements were made only after the ensemble reached the isothermal conditions. The 660 data points plotted in each figure represent testing performed over a period of 720 hours. The experimental results for both links shows clearly the stochastic nature of the PMD phenomenon. Fig.5.a, fig.5.b, fig.6.a and fig.6.b show the boxplot distribution for PMD coefficient obtained using the experimental data described in fig. 4.a and 4.b respectively.

The evolution of the PMD coefficients in the first thermal cycle for the links comprised of the two types of fiber shows different trends. The expected value of the PMD coefficient obtained at ambient temperature before the beginning the thermal cycle for the SMF-G.652 fiber was approximately 0.0156 ps / $\sqrt{\text{km}}$ and the value upon its completion was 0.0186 ps / $\sqrt{\text{km}}$, which means an increase of about 19% between the values before and after the thermal cycle. For the link comprised of NZDF-G.655 fibers, the initial value of the PMD coefficient was approximately 0.0260 ps / $\sqrt{\text{km}}$, and after the end of the thermal cycle was observed one reduction of 30 %. In this case, the link showed a behavior diametrically opposite to the one obtained using SMF-G.652 fibers. Regarding the expected values during the alternated steps of low-high temperature, the boxplot distribution described in the fig.5.a and fig 5.b for the first cycle indicates a rather broad distribution for the link comprised of NZDF-G.655 and a narrow distribution of PMD for the link comprised of SMF-G.652 fibers respectively. Another feature is that the mean PMD for the link NZDF-G.655 exhibits a much larger variation than the results obtained with the link SMF-G.652. The well-behaved characteristic of the link comprised of SMF-G.652 fibers, may suggest that the fiber stress conditions inside the cable have been stabilized and that the smaller observed PMD fluctuation compared with the link NZDF-G.655 can be associated with the small sensibility of the SMF-G.652 fiber to temperature. As a check, measurements made at ambient temperature one week after the completion of the first thermal cycle showed that the PMD coefficient for the link SMF-G.652 is almost identical to value measured at the beginning of the experiment. Regarding the second cycle, the expected PMD values for both links present a behavior very similar to the first cycle.

When compared with the Monte-Carlo simulation, was observed that the most of the expected experimental PMD values obtained during the thermal cycle were below of the minimum value obtained in the numerical simulation. The discrepancies observed between theoretical e experimental results is associated to the fact that the numerical algorithm used in the Monte-Carlo simulation does not taking into account the components between the fiber that present polarization dependence loss^[7]. On the other hand, the small values obtained experimentally for both links are associated to the high mode coupling present for both types of fibers, which equalizes the propagation times of the two polarization mode, reducing PMD value in the optical link^[8]. Regarding optical stability, the experimental results obtained by monitoring the optical loss during the full thermal cycle showed a cable design with a very stable dimensional changes. The optical loss variation was less than 0.01 dB/km.

6. Conclusion

A thermal cycle consisting of low-high temperature steps was applied in two different optical links. The expected value of the PMD coefficient in each step was calculated and compared to corresponding values measured prior to and after the cycle. The expected PMD value for the link comprised NZDF-G.655 exhibits a much larger variation than the results obtained with the link SMF-G.652. Measurement of the cable links a week after the end of the first cycle shows that the expected PMD value remains almost the same to the value measured at the beginning of the

experiment, especially for the link comprised of SMF-G.652 fibers.

As the thermal effects represent conditions that affect the optical cable during its lifetime, the experimental results obtained showing insignificant PMD fluctuation due to temperature changes may have important implications from the practical point of view. For example, the system designer may consider the initial expected PMD values without significant modification of the PMD distribution during cable's lifetime. Therefore, a link can be designed to accommodate this estimated values obtained from cable suppliers and ensure that the network outages will be less than a few minutes per year.

7. Acknowledgments

The authors wish to acknowledge the support of many people in our organization that working with us in the laboratory measurements. Special thanks to Marcos Boulos for his assistance in the computer analysis.

8. References

- [1] P.A.Andreckson , OFC 2000, paper TuP2
- [2] J. Cameron, L. Chen, X. Bao and J. Stears, "Time Evolution of Polarization Mode Dispersion in Optical Fibers", IEEE Photon. Technol. Lett, 10, 1265-1267 (1998).
- [3] Jeancarlo Dotto, Januncio A.M.Neto, L.F. Marques and Rentato . F. Cruz, "The influence of mechanical and environmental effects on PMD coefficient in loose tube optical cable design" 50th IWC, pp 493-497 (2001),
- [4] G.J. Foschini and C.D. Poole, "Statistical Theory of Polarization Mode Dispersion in Single Mode Fibers", J. Lightwave Technol., 9, 1439-1456 (1991).
- [5] N. Gisin, J.-P. Van der Weid and J.-P. Pellaux, "J. Lightwave Technol., vol. 9, no. 7, pp. 821-827, 1991.
- [6] F. Curti, B. Daino, G. DeMaris and F. Matera, "Statistical Treatment of the Evolution of the Principal States of Polarization, J.Lightwave Technol.. vol.8, pp. 1162-1166, 1990.
- [7]A.J.Barlow. D.N.Payne, M.R.Hadley and R.J.Mansfield, Electronics Letters, Vol.17, October 1981, pp 725-726
- [8] B.huttner and N.Gisin, Optics Letters, Vol.22 April 1997, pp. 504-506

9. Authors



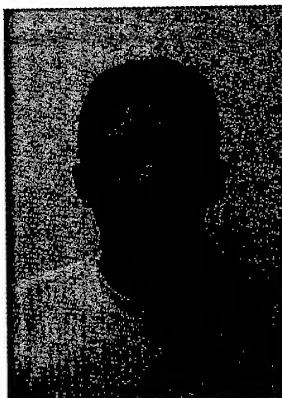
Marcelo Machado Simião received his B.S. degree as an Electrical Engineer from Federal Center of Technological Education (CEFET-PR) in 1997. He joined Furukawa Industrial S/A in the same year. He is involved in the optical fiber and cables evaluation for Engineering Process Department



Jeancarlo Dotto received his B.S. degree as an Electrical Engineer from Federal Center of Technological Education (CEFET-PR) in 2000. He joined Furukawa Industrial S/A in the same year. He is involved in the optical fiber and cables evaluation for Quality Department



Lúcio F. G. Marques received his B.S. degree as an Electrical Engineer from Federal University of Paraná (UFPr) in 1995. He joined Furukawa Industrial S/A. in 1997. He is currently Product Engineering



Januncio A. Medeiros Neto received his B. S. degree from Federal University of Rio Grande do Norte (UFRN) and M. S. and PhD in Physics from University of Campinas (UNICAMP) in 1991. After post doctoral appointment at ORC-University of Southampton – England, he joined UNICAMP as research associated. In 1998, he joined Furukawa Industrial S/A. as consultant and CEFET-PR as research fellow. Since April, 2002 he is technical supervisor at the Centro Internacional de Tecnologia de Software (CITS).



Renato Flávio Cruz received his Chemical Engineer degree from Universidade Federal do Paraná (UFPr) in 1988. He joined Furukawa Industrial S/A. in February 1989 and since then he has been involved in research and development of telecommunication cables. He is now Manager for development cable engineering Department.

Fig. 4.a – Thermal cycle diagram for a link comprised of the NZDF-G.655 optical fiber. Dot line represents PMD coefficient and full line shows temperature

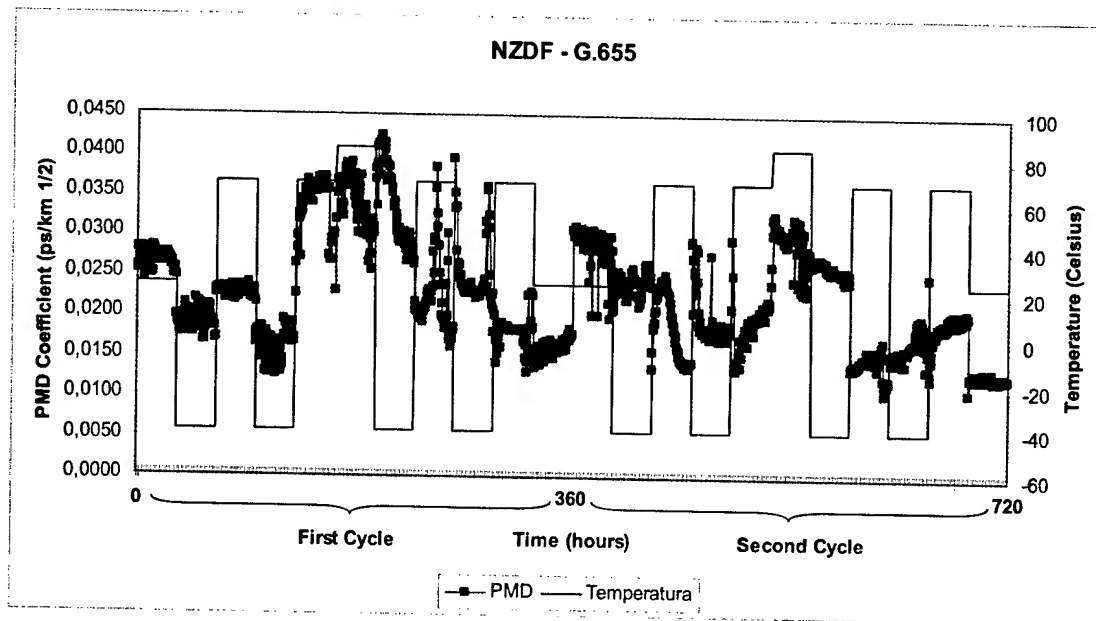
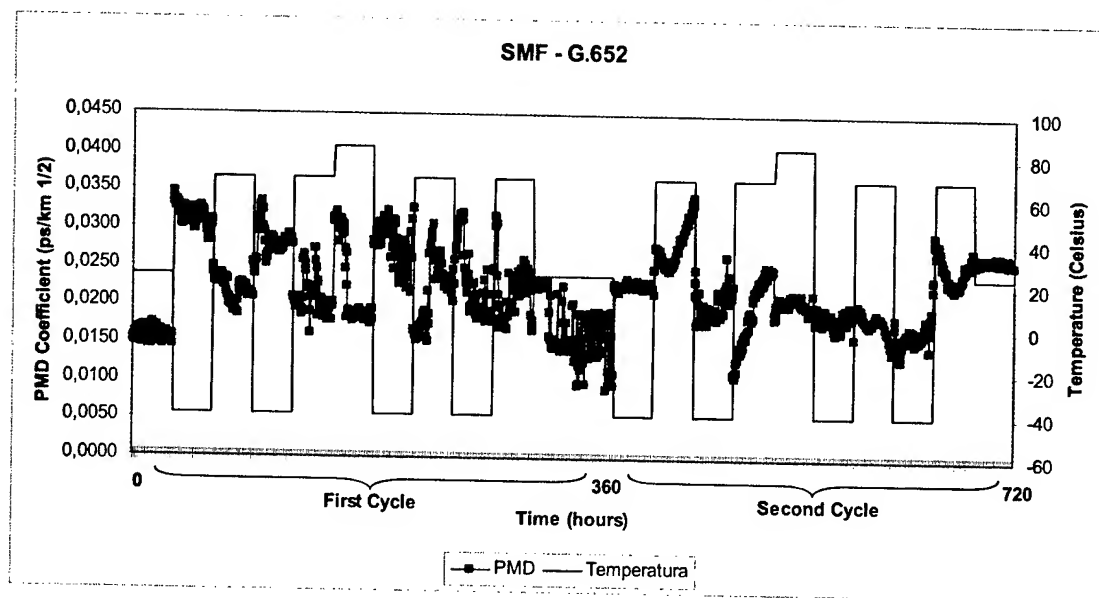
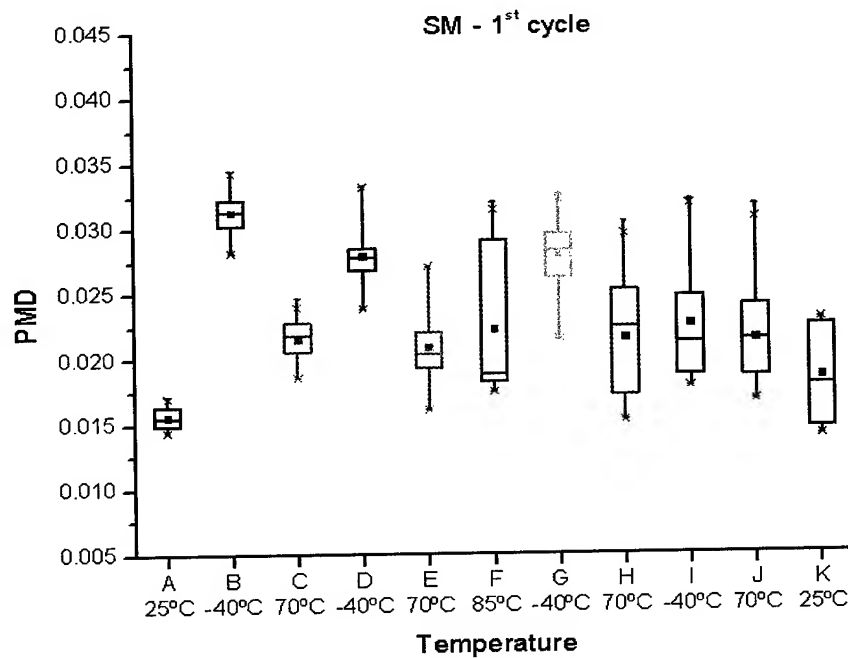
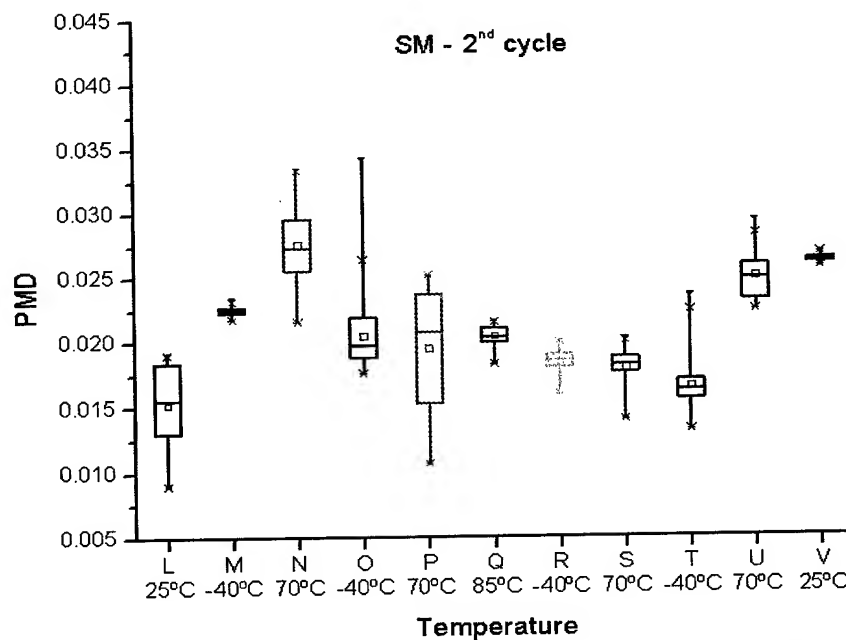


Fig. 4.b – Thermal cycle diagram for a link comprised of the SMF-G.652 optical fiber. Dot line represents PMD coefficient and full line shows temperature

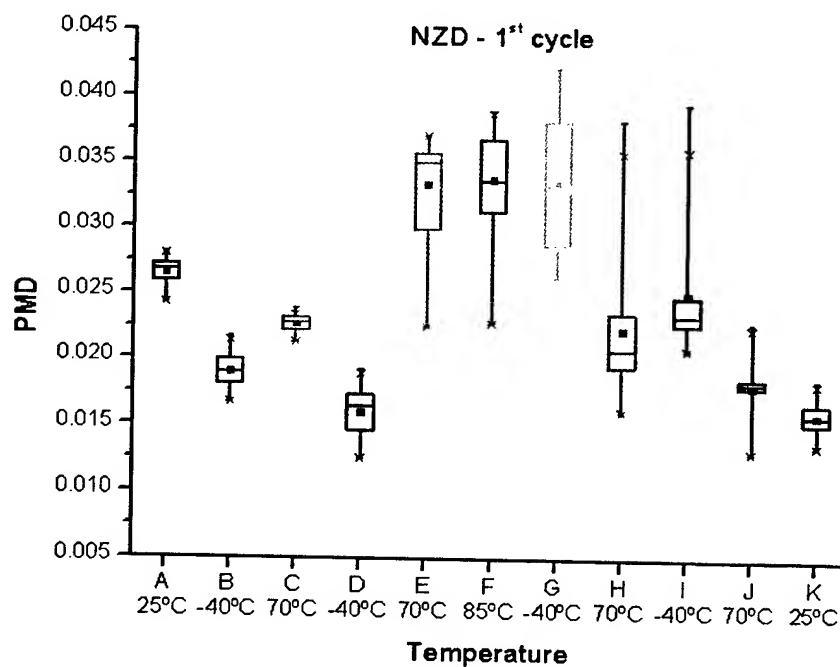




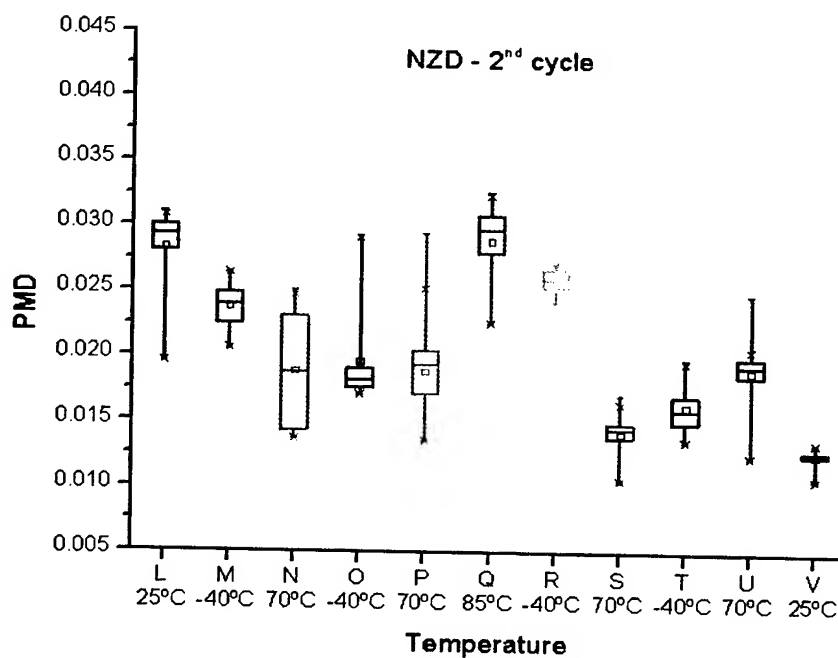
5.a PMD statistics for a link comprised of the SMF-G.652 fiber obtained during the first temperature cycle



5.b PMD statistics for a link comprised of the SMF-G.652 fiber obtained during the second temperature cycle



6.a. PMD statistics for a link comprised of NZDF- G655 fiber obtained during the first temperature cycle



6.b. PMD statistics for a link comprised of NZDF- G655 fiber obtained during the second temperature cycle

Temperature and Humidity Dependence of PMD in Dispersion Compensating Fiber

Jian ZHOU, Kazuhide NAKAJIMA

NTT Access Network Service Systems Laboratories,
NTT Corporation
1-7-1, Hanabatake, Tsukuba, Ibaraki, 305-0805 JAPAN
+81-298-68-6430 · zhou@ansl.ntt.co.jp
nakaji@ansl.ntt.co.jp

Masaharu OHASHI

Osaka Prefecture University
1-1, Gakuen-cho, Sakai, Osaka, 599-8531 JAPAN
+81-72-254-9255 · ohashi@uopmu.ees.osakafu-u.ac.jp

Abstract

In this paper, we describe the temperature and humidity characteristics of polarization mode dispersion (PMD) in dispersion compensating fiber (DCF) both experimentally and numerically.

Our experimental results show that the PMD of a test DCF tends to increase with a decrease in ambient temperature or humidity. We also study the wavelength dependence of the differential group delay (DGD) with respect to temperature and humidity. Moreover, we show that the temperature and humidity characteristics of the PMD in DCF are strongly related to strain variation between the fiber coating and fiber glass by comparison with numerical calculation results.

Keywords

Polarization mode dispersion; dispersion compensating fiber; temperature dependence; humidity dependence; strain

1. Introduction

In recent years, transmission capacity has increased rapidly due to the introduction of various kinds of Internet service, and various kinds of transmission system have been proposed with the aim of realizing even larger capacity. Of these proposed systems, the interest in hybrid transmission line has been growing recently with a view to building a high performance system for long-span high-bit-rate transmission.^[1] DCF with a large negative dispersion is commonly used in hybrid transmission line to optimize the chromatic dispersion and dispersion slope.

In long haul or high-bit-rate transmission systems, PMD limits the transmission capacity, and so has been receiving increasing attention.^[2] Due to small fiber core anisotropies and residual strains in single-mode fibers, lights in orthogonal polarization states appear significantly with different group delays associated with local fiber birefringence. However, the PMD characteristics in existing transmission systems have not been evaluated sufficiently because PMD experiences the combined influence of a variety of environmental factors.

The effects of temperature on various transmission characteristics have been widely investigated.^{[3]-[6]} However, the temperature /

humidity dependence of PMD in an optical fiber has not been clarified enough.^{[5] [6]} In this paper, we report the temperature and humidity dependence of PMD in a DCF both experimentally and numerically.

2. Temperature and Humidity Dependence

2.1 Fiber sample and experimental condition

The fiber sample we used was 4 km long and its parameters are given in Table 1.

Table 1. Characteristics of the test fiber

Attenuation (dB/km)	Dispersion (ps/nm/km)	Dispersion Slope (ps/nm ² /km)
0.681	-110.91	-0.31

$\lambda=1550\text{nm}$

The fiber sample was placed in a thermostatic chamber. We removed the fiber from the bobbin in order to avoid the influence of external strain induced by the deformation of bobbin with changes in ambient temperature and humidity.

We used the Johns Matrix Eigen (JME) analysis method to measure the DGD in the 1480 to 1570 nm wavelength range. And the measurement step was set at 1 nm. This was to ensure that, from one test wavelength to the next, the polarization output state rotated less than 180 degrees about the principal states axis of the Poincaré sphere. The DGD was measured every 30 minutes as a function of wavelength and time.

2.2 Variation in PMD

Figure 1 shows the measured variations in the PMD coefficient (ps/rkm), which corresponds to the average DGD for the whole measurement wavelength region, against ambient temperature with a constant humidity of 50% and against humidity with a constant temperature of 20°C. The solid line shows the temperature or humidity change in the thermostatic chamber and the open circles show the measured PMD coefficient.

From Fig. 1, it is found that the PMD coefficient tends to decrease with increases in temperature and relative humidity. The change is approximately 0.1 ps/rkm for a 100°C temperature variation and 0.03 ps/rkm for an 80% humidity variation. Moreover, we showed that the value of the PMD coefficient becomes stable over time after a change in the ambient conditions, which indicates that PMD is sensitive to temperature and humidity.

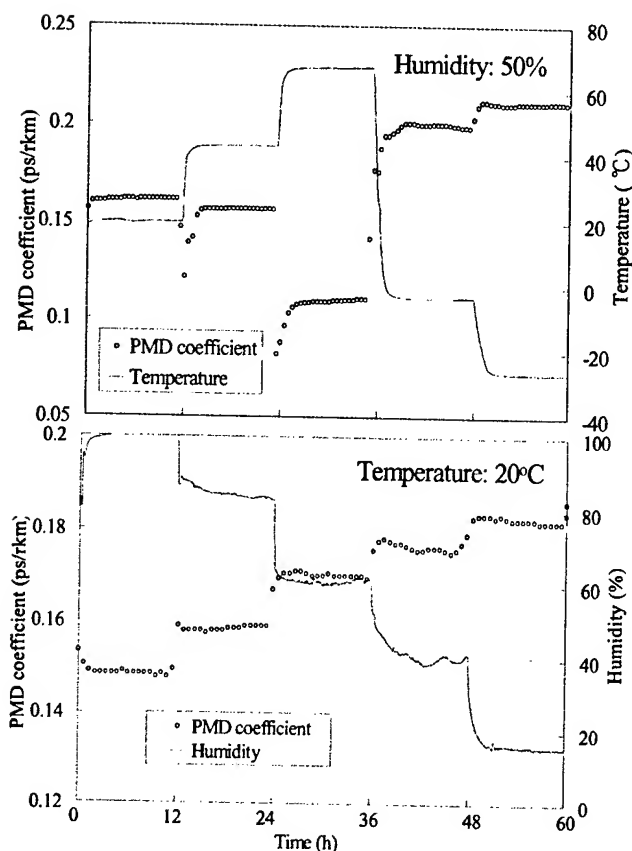


Figure 1. PMD versus time

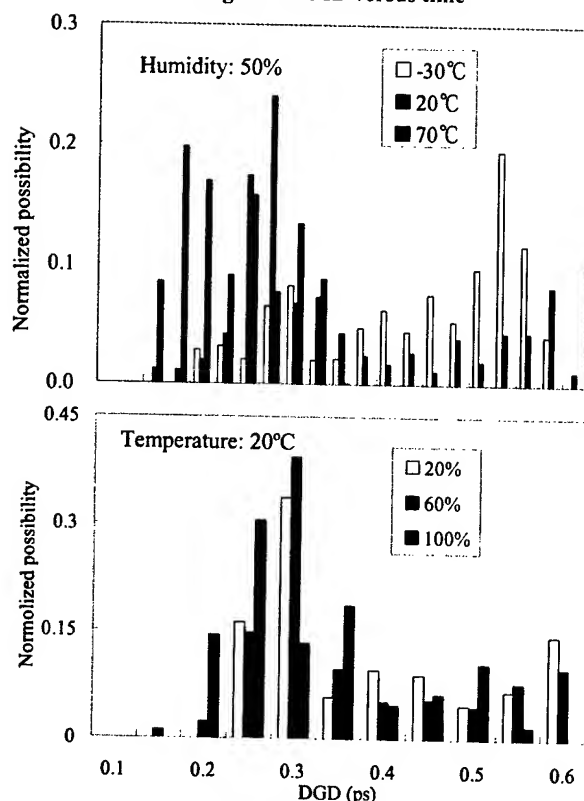


Figure 2. Histogram of DGD levels

2.3 Statistical characteristics of DGD

It is well known that PMD has a stochastic attribute in that it varies randomly with time, wavelength, etc.^[7] In this work, we investigated the statistical characteristics of DGD by using data obtained in both temperature and humidity experiments.

Figures 2 shows histograms of the DGD in relation to temperature and humidity, respectively. The white, gray and black columns show the measurement results at specified temperatures (-30°C, 20°C and 70°C), and humidity levels (20%, 60% and 100%), respectively.

We found that the peaks and distributions of the histograms moved to the low DGD side with increases in temperature or humidity. In both cases, we superimposed the Maxwellian curve on the histogram and calculated the cross-correlation coefficient between the Maxwellian curve and the histogram for each condition. The cross-correlation coefficients were no more than 0.8. Therefore, the DGD distribution plots under isothermal conditions obtained as a function of time do not follow a Maxwellian function, which has also been indicated by Hakki.^[6]

2.4 Wavelength dependence of DGD

Figure 3 shows samples of spectra measured for different temperatures and humidity conditions. From Fig. 3, it is clear that when the ambient temperature or humidity changes, there is a change not only in the average DGD value over the whole wavelength range but also in the spectral characteristics. This implies that the wavelength dependence of DGD is also sensitive to temperature and humidity.

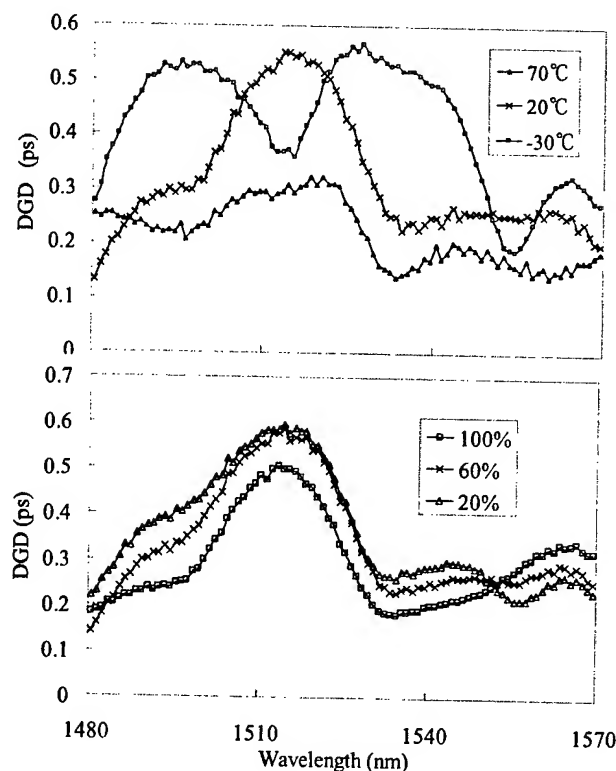


Figure 3. DGD wavelength spectrum

We then investigated the correlation coefficient of the DGD wavelength spectrum against time. To do that, we assumed that the DGD data six hours after starting the measurement had become stable and treated it as a reference. We calculated its correlation coefficient with all previous and succeeding DGD wavelength spectra. The correlation coefficient C_c was calculated using the formula (1):

$$C_c = \frac{\frac{1}{N} \sum_{i=1}^N (\tau_{xi} - \langle \tau_x \rangle)(\tau_{yi} - \langle \tau_y \rangle)}{\sigma_x \sigma_y} \quad (1)$$

where τ_x and τ_y are the two DGD wavelength spectra, $\langle \tau_x \rangle$, $\langle \tau_y \rangle$ and σ_x , σ_y are their averages and standard deviations, respectively.

Figure 4 shows the result of the correlativity calculation. It is found that the correlation coefficient is high when there are no change in the ambient temperature or humidity and it decreases when the temperature or humidity changes.

Based on the result in section 2.2, which showed that the PMD can remain stable when the ambient temperature and humidity remain unchanged, we can draw the conclusion that the DGD at a specified wavelength would be constant if the ambient condition remains stable.

It is important to have a clear grasp of DGD's wavelength dependence when one wants to apply system operating at different wavelength such as wavelength division multiplexing (WDM) system. We then investigated the variation range of the DGD coefficient at each wavelength.

Figure 5 shows the maximum and minimum value of DGD at each wavelength within the experimental ambient temperature and humidity range. From Fig. 5, it is found that the maximum of DGD coefficient variations range at specified wavelengths is 0.24ps/rkm with respect to a 100°C temperature change and 0.09ps/rkm with respect to an 80% change in relative humidity. Our result shows that the DGD at a specified wavelength varies when the ambient temperature and humidity are changed.

Here, we assumed a 320km long transmission line with the longitudinally uniform DGD coefficient of 0.17ps/rkm at the operating wavelength. If the transmission system applies non-return to zero (NRZ) format at a bit rate of 40Gbps, the variations of DGD coefficient according to Fig. 5 correspond to the system penalty variation of 0.5 dB with respect to a 100°C temperature change and 0.2 dB with respect to an 80% change in relative humidity.^[8] This shows that the system performance strongly depends on the ambient temperature or humidity variation. Therefore, it is necessary to know the characteristics of the DGD due to ambient temperature or humidity condition at each operating wavelength for designing future high-bit-rate WDM transmission system.

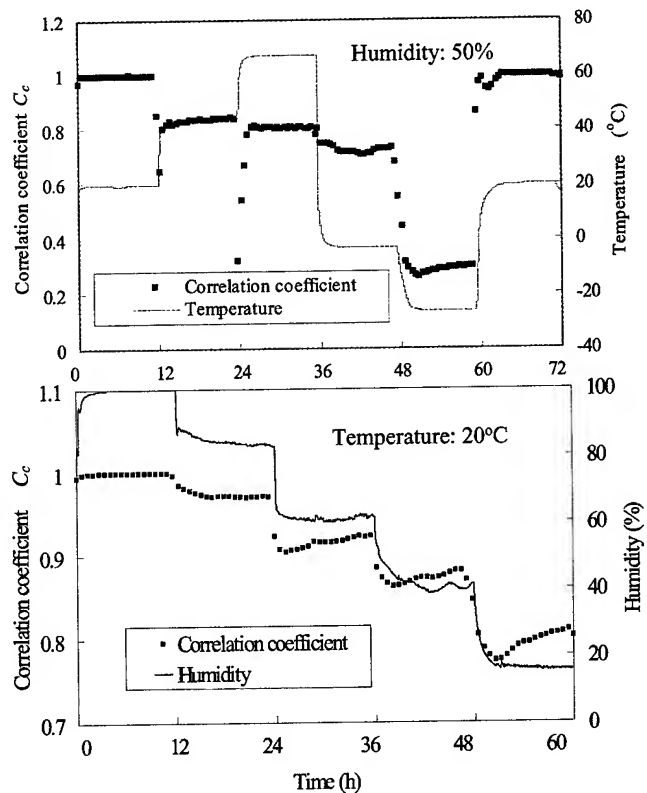


Figure 4. Correlativity versus time

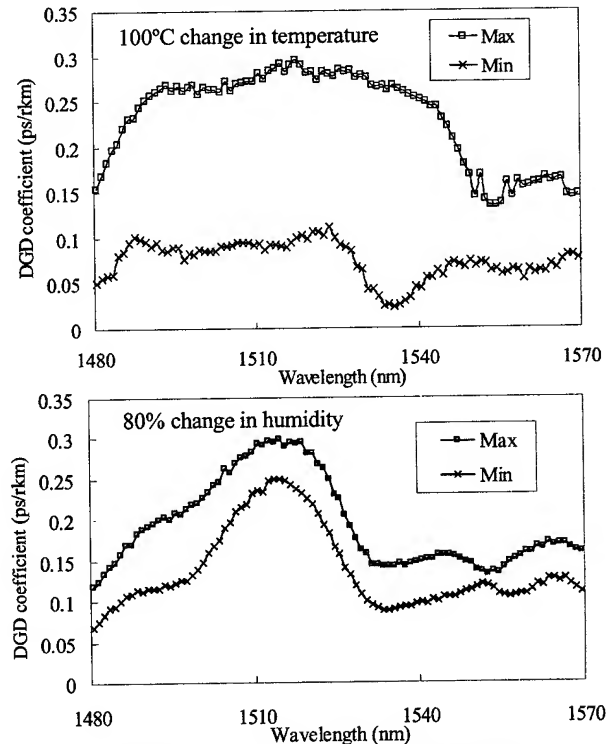


Figure 5. DGD variation range for change in ambient condition

3. An examination of the mechanism

3.1 Calculation Model

Strain anisotropy in a fiber generally results when noncircular regions of the fiber's cross-section have different thermal-expansion coefficients. We assumed that the fiber has an elliptical cladding structure and the mismatch between the thermal expansion of the cladding and the UV coating yields the strain distribution.

We assumed a fiber with an elliptical structure in which the mismatch is given by the product of the difference between the thermal-expansion coefficients ($\alpha_c - \alpha_g$) of the coating material (α_c) and the fiber glass (α_g) and the temperature difference ($T_h - T$) between the UV curing temperature T_h and room temperature T . We found that the DGD ($\Delta\tau$) of the fiber can be calculated by the following formula [9]

$$\Delta\tau = \frac{L}{2c} (p_{11} - p_{12}) \frac{a-b}{a+b} \frac{E_c}{E_g} \frac{[\eta + (\alpha_c - \alpha_g)(T_h - T)]}{1 - \nu^2} \cdot n^3 \quad (2)$$

Here, L is the length of the birefringent fiber, n is the mean refractive index. p_{11} and p_{12} are the components of the photoelastic tensor, and E_c , E_g are the Young's moduli of the UV coating and the glass. ν is Poisson's ratio of the fiber material. Assumed to be elastically homogeneous throughout the fiber, a and b are the semi-axes of the ellipse along the long and short coordinate directions, respectively. And η represents the curing shrinkage of the UV coating material.

In this work, we assume that the fibers, which have random mode coupling characteristics, can be divided into N segments as shown in Fig. 6. The fiber is assumed to be jointed with many birefringent fibers with their birefringent axes at all possible angles and the model without mode coupling between polarization modes. [10]

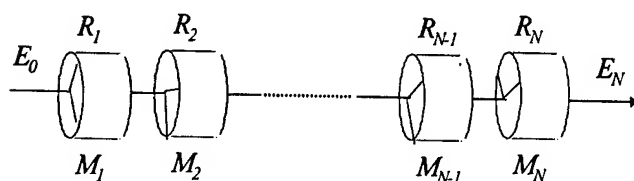


Figure 6. Calculation model

Each of the birefringent fibers is characterized by a local DGD calculated by Eq. 2 in consideration of the material parameter characteristics in relation to the ambient temperature and humidity. Adjacent fibers are connected with axes of a given orientation α_i , which is assumed to be wavelength independent. Random coupling of polarization modes along the fiber is then simulated by randomizing the elemental delays and rotations. The Jones matrix M_i and the rotation matrix R_i at the angular frequency ω corresponding to the i th ($i=1,2,\dots,N$) element are given respectively by

$$M_i = \begin{bmatrix} \exp(j\omega\Delta\tau/2) & 0 \\ 0 & \exp(-j\omega\Delta\tau/2) \end{bmatrix}$$

$$R_i = \begin{bmatrix} \cos\alpha_i & \sin\alpha_i \\ -\sin\alpha_i & \cos\alpha_i \end{bmatrix} \quad (3)$$

The fiber transfer matrix is then given by

$$E_N = M_N R_N \cdots M_2 R_2 M_1 R_1 E_0 \quad (4)$$

where E_0 and E_N are the input and output Jones vector respectively.

We calculated the intensity distribution of the output light where the interference method is simulated. The optical source is assumed to have a range of 200 nm and a Gaussian distribution is assumed for the interference fringe to allow us to calculate the PMD of the whole fiber.

3.2 Calculation result

A typical daily temperature variation was simulated here. The simulation was performed with the method described above using a 100 element model. Figure 7 shows the experimental and numerical calculation results of the PMD relative variation as well as the temperature and humidity variation. The filled triangles indicate the experimental result and the solid line shows the numerical calculation result.

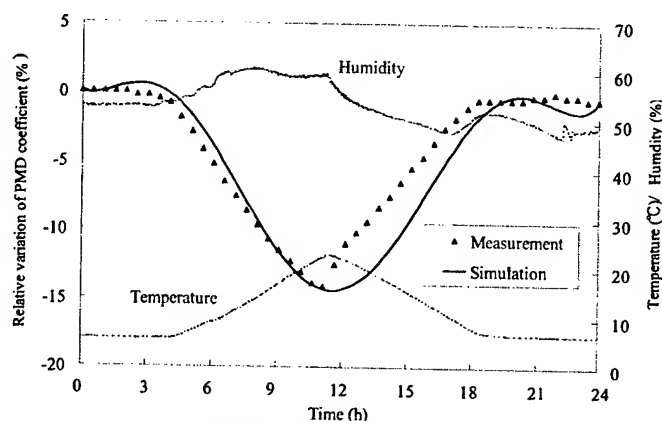


Figure 7. Simulation result

From Fig. 7, it is obvious that the calculation result agrees very well with the experimental result, which suggests that the calculation model proposed here is feasible. We found that the variation in the strain between the coating and the fiber is one of the important factors which influence the PMD/DGD dependence on temperature and humidity. In order to limit the PMD/DGD variation when the ambient conditions change, we would choose proper fiber material as well as realize a perfectly circular fiber cross-section.

4. Conclusions

We investigated the relationship between PMD variation and ambient temperature / humidity. Our results show that the PMD coefficient tends to decrease with increases in temperature and relative humidity. We also showed that, when the ambient temperature or humidity changes, there is a change not only in the PMD but also in the characteristics of the DGD spectrum as the function of wavelength, which implies that the DGD at a specified wavelength is sensitive to the ambient temperature and humidity.

Moreover we proposed a numerical calculation model to explain the PMD dependence on temperature and humidity. The simulation results showed that the strain between the coating and the fiber is one of the probable causes.

5. Acknowledgments

We offer special thanks to K. Tajima, K. Sato and N. Sato for beneficial discussions and encouragement.

6. References

- [1] E. Sasaoka et al., APCC/OECC'99, p. 378, 1999.
- [2] R. Morgan et al., Electron. Lett., **26**, p. 937, 1990.
- [3] P. R. Morkel et al., Electron. Lett., **30**, p. 806, 1994.
- [4] G. Ghosh, J. Lightwave Technol., **12**, p. 1338, 1994.
- [5] M. Nakano et al., IWCS2001, p. 499, 2001.
- [6] B. W. Hakki, J. Lightwave Technol., **14**, p. 2202, 1996.
- [7] G. J. Foschini et al., J. Lightwave Technol., **9**, p. 1439, 1991.
- [8] P. J. Winzer et al., OFC'02, Tu11, 2002.
- [9] Eric Udd, "Fiber Optic Smart Structures", John Wiley & Sons Inc, 1995.
- [10] K. Mochizuki, Appl. Opt., **23**, p. 3284, 1984.

Authors

Jian Zhou received B.E. degree in instrument engineering from the



Shanghai Jiaotong University and M.E. degree in mechanical engineering from the Tokyo institute of technology in 1995 and 2000, respectively. In 2000 he joined the NTT Access Network Service Systems Laboratories, where he has been engaged in the research on optical fiber and cable. Mr. ZHOU is a member of the IEICE of Japan.

Kazuhide Nakajima received the B.S. and M.S. degree in



electrical engineering from Nihon University, Chiba, Japan, in 1992 and 1994, respectively. In 1994, he joined NTT Access Network Systems laboratories, Ibaraki, Japan, where he has been engaged in research on optical fiber design for suppressing optical nonlinearities and related measurement techniques. Mr. Nakajima is a member of the IEICE of Japan. He received a

Best Paper Award of the first OECC in 1996.

Masaharu Ohashi received B.E. degree in electrical engineering



from Nagoya Institute of Technology in 1977, and M.E. and Ph.D. degrees in electrical communication engineering from Tohoku University in 1979 and 1987, respectively. In 1979, he joined the NTT Ibaraki Electrical Communication Laboratory. Since 2002, he has been with Osaka Prefecture University, Osaka, Japan. He has engaged in research on

transmission characteristics in relation to optical fiber designs, new fiber materials for low-loss fiber, fiber design for suppressing optical nonlinear effects and related measurement techniques. Dr. Ohashi is a senior member of the IEEE and Rapporteur in SG15 of ITU-T.

Downsized and Enhanced Optical Fiber Cable Transfer Splicing System

Kuniaki Tanaka, Masahiro Zaima, Masao Tachikra, Minoru Nakamura

NTT Access Network Service Systems Laboratories, Nippon Telegraph and Telephone Corporation

1-7-1, Hanabatake, Tsukuba-city, Ibaraki, 305-0805 Japan

+81-298-52-4834 tanaka@ansl.ntt.co.jp

Abstract

We have downsized and enhanced our original optical fiber transfer splicing system so that it can be applied to all regions in optical access networks. This paper describes methods for applying this system to aerial optical fiber cables, where it is already used, to optical fiber cables, which are composed of ribbons with different numbers of fibers, and to optical fiber cables without optical fibers for synchronous control. The equipment was miniaturized to enable aerial cable work to be undertaken more easily. We then added a function that allows us to control the optical fiber CATS system synchronously at three work sites, and to synchronize this system by using a cellular phone. We succeeded in reducing the size to about half that of a conventional device by changing the switch movement from the vertical to the horizontal direction. In addition we developed an algorithm so that an optical fiber CATS system could be controlled synchronously at three different locations. Moreover, the synchronous switch enabled by the cellular phone provided the same accuracy as a synchronous control that uses optical fiber by changing from the currently used subordination synchronization to independent synchronization. Then, we evaluated the performance of a prototype system, and used it in a cable removal simulation. As a result, we confirmed the suitability of this system for practical use.

Keywords

Optical fiber CATS system; MT-connector; Switching device; Synchronous control; Aerial optical cable

1. Introduction

NTT is constructing optical fiber networks that extend from trunk systems to subscriber systems, and today's "information society" is supported by these networks, which are capable of transmitting vast amounts of data. When an active route has to be changed to another route in the optical fiber network because of, for example, road construction, the influence on the service provided to users is difficult to estimate. The optical fiber cable transfer splicing system (optical fiber CATS system) [1][2] has been introduced in these expanding optical fiber networks to minimize circuit-releasing time and to prevent any reduction in the service provided to the user.

Figure 1 is a diagram showing optical cable removal using the optical fiber CATS system. This system is chiefly composed of a switching device and a controller. These two components are set up in mechanically transferable connectors (MT connectors) [3] in the active cable, and user side and telephone office side connectors (hereafter referred to as transfer ferrules,) are moved to the connector of the new cable (route) in synchronization with this system. The transfer time is several tens of milliseconds. Initially, we only had to assume that this system would be used underground since this is where most optical fiber cable is

installed. However, the following three demands have been newly imposed on optical fiber CATS systems because the use of aerial optical fiber cable has increased in optical access networks. (1) Optical fiber CATS systems can be employed with aerial optical fiber cable. (2) Optical fiber CATS systems can be synchronously controlled at three different work sites. We require synchronous transfer technology for three locations because underground and aerial optical fiber cables are composed of ribbons with different numbers of fibers. Namely, when an aerial cable with a 4-fiber ribbon structure is connected to an underground cable with an 8-fiber ribbon structure, the 8-fiber ribbon is divided into two and connected to two 4-fiber ribbons. Synchronous transfer technology for a total of three work sites is needed where the optical fiber cable facilities consist of one work site on the 8-fiber ribbon side and two work sites on the 4-fiber ribbon side (hereafter referred to as the distribution line). (3) Optical fiber CATS systems can be synchronously controlled with a cellular phone. Because the fiber use rate of aerial optical fiber cable is increasing, it is not easy to use unemployed fiber in the aerial cable as the synchronous control line.

We have therefore developed devices for this system based on the two design concepts outlined below in order to satisfy the requirements derived from (1) to (3).

(i) The development of safe equipment that does not require special skill to operate. (This concept corresponds to (1). We describe this in section 2.1).

(ii) The development of equipment that is compatible with the current optical access networks mentioned above. (This concept corresponds to points (1) to (3). We describe this in section 2.2).

We then evaluated the performance of a prototype system, and used it in a cable removal simulation.

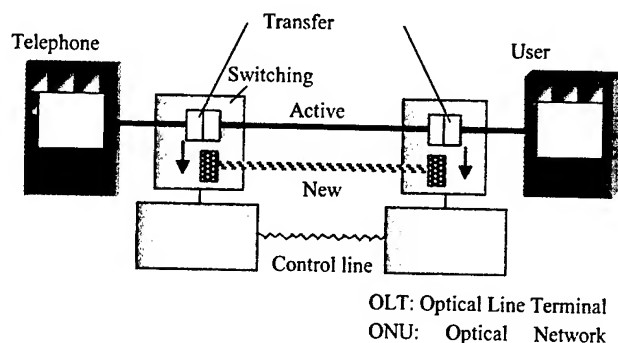


Figure 1. Cable removal using optical fiber CATS system

2. Optical fiber CATS system based on design concept

2.1 Safe and simple aerial work

In terms of aerial work, aerial equipment should be easy to use and smaller than equipment designed for ground use from the viewpoint of safety. In this work, we succeeded in miniaturizing the switch device by making the switch mechanism horizontal rather than vertical (the conventional direction), and this led to an improvement in connector handling. Moreover, the size and shape of the synchronous controller were examined taking into consideration the narrow workspace afforded by a bucket truck. Figure 2 shows the conventional transfer splicing mechanism. The conventional device shortens the stroke of the transferable ferrule (It is called "Ferrule before being fixed" in this figure.) by in that the replacement ferrule is positioned to the right of and below the ferrule to be replaced, which is an active ferrule for the purpose of shortening the transfer time. As a result, a high-speed transfer is achieved by moving the ferrule holder vertically. However, the scale of the device becomes large because of the need to house the upper replaced ferrule holder. Even worse, the work becomes inefficient because the upper replaced holder covers the lower ferrule.

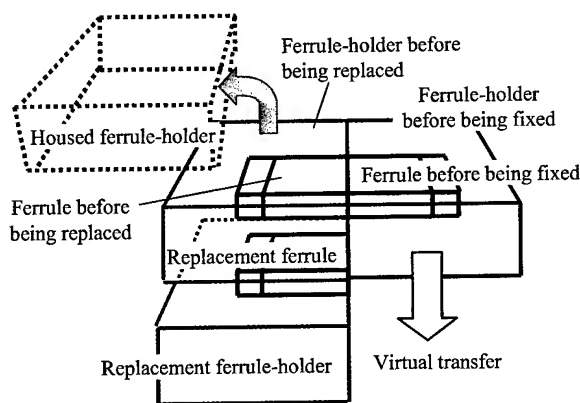


Figure 2. Conventional transfer splicing mechanism

Figure 3 shows our proposed transfer splicing mechanism. We miniaturized the switching device and simplified the connector handling by changing the ferrule movement from the vertical to the horizontal direction. Because the simplification results from the fact that the upper ferrule holder need not be housed.

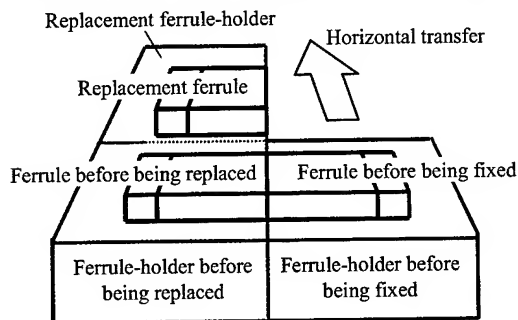


Figure 3. Proposed transfer splicing mechanism

Figure 4 shows the transfer splicing procedure with the MT connector in the horizontal direction that is the subject of this study (1) Pressure is applied to four points on the active connector to keep the connection intact. (2) The clamp spring, which maintains the connection between the ferrules, is removed. (3) The guide pins are pushed from the ferrule being replaced into the ferrule before transfer. (4) The unfixed ferrule (It is called "Ferrule before being fixed" in this figure.) is moved so that it butts with the replacement ferrule at high speed as the ferrule before being replaced is separated from the unfixed ferrule. (5) At this time, pressure is applied, fixing the previously unfixed ferrule in position, so that both the now fixed ferrule and the replacement ferrule keep the connection intact. The guide pins on the fixed ferrule side are inserted into the replacement ferrule simultaneously. (6) The clamp spring is attached to the replacement ferrule and the fixed ferrule newly connected. (7) The pressure applied to the four corners of the connector is released. Steps (4) and (5) in this process are executed at a speed of tens of milliseconds.

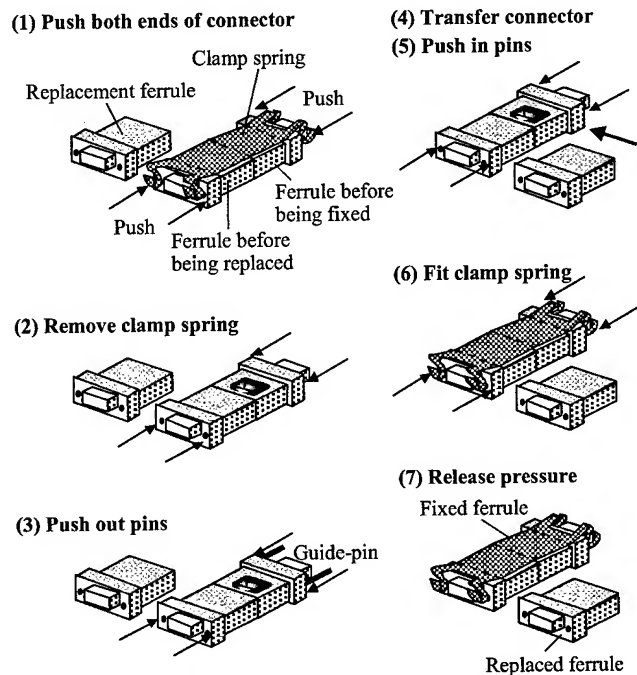


Figure 4. Transfer splicing procedure of MT connector

Then, we designed a synchronous controller that could be hung on the sidewall of the bucket because of the confined workspace afforded by the bucket truck. The battery is built into this synchronous controller.

2.2 Suitability for current optical access network facilities

Optical cable with a 4-fiber ribbon structure and optical cable with an 8-fiber ribbon structure can be found together in optical access networks, and they are connected by distribution lines. For

instance, it is used to connect underground cable with aerial cable. In this case, since the 8-fiber ribbon is divided into two and connected with two 4-fiber ribbons, one switching device (henceforth called the master) is necessary in 8-fiber ribbon, and two switching devices (hereafter referred to as slaves) are necessary in 4-fiber ribbons. Moreover, it is assumed to be impossible to secure a fiber for synchronous control since there are fewer fibers in aerial optical fiber cables than in underground optical fiber cables and optical service demand is increasing. Therefore, we need a synchronous control method to replace that using optical fiber.

In order to solve the above-mentioned problem, we added a function to control the optical fiber CATS system synchronously at three work sites, and examined a method for synchronizing this system by using a cellular phone. The gap in the transfer timing caused by the distance between the work sites is adjusted on the master device side using optical fiber-based synchronous control. Firstly, the first transfer signal is transmitted from the master device to a slave device. Next, the slave device transmits the received signal to the master device side immediately upon receipt of the signal. The switch has yet to be operated. The master device calculates the difference in the transfer timing by using the first transfer signal and the received signal. Finally, a second transfer signal transmitted from the master device to the slave, and the slave device, which receives this signal, executes the switch immediately. At this time, the master device retards only the difference in the calculated switch timing, and executes the transfer. Here, we calculate the switch timing in the access network system. The distance between work sites is about 5 km at most in the access network system. The timing difference is about 0.03 ms, considering the speed of light in the optical fiber. Since this is only about 0.1% of the transfer time (about 25 ms), this timing difference does not greatly influence the transfer time. This process is important when the optical fiber CATS system is applied to a trunk system operating over a long distance and with a large transmission capacity because the lack of information caused by this slight transfer timing difference cannot be disregarded.

In contrast, synchronous control realized by using a cellular phone is different from that using optical fiber since the control signal is transmitted and received via public networks. The difference in the transfer timing is 200 ms or more on average. Moreover, the dispersion is also large. Therefore, the method for correcting the synchronous control by using an optical fiber

cannot be incorporated in the cellular phone method. To overcome this problem, we changed from the currently used subordination synchronization to independent synchronization. That is, although the transfer timing of the master device has thus far been matched to that of the slave device, we changed the way of adjusting the transfer timing difference with the master device to a method involving the independent transfer of both devices in absolute time. In fact, the number is counted independently by using an efficient quartz oscillator installed in both synchronous controllers at different work sites. The switch signal is transmitted from the master device to the slave device and the transfer is executed. As a result, the transfer timing does not increase greatly although the problem of the synchronous error margin-accuracy of the quartz oscillator remains. In our study, we used a quartz oscillator, which resulted in an error margin of about 0.01 ms in a maximum of one hour. Here, the synchronous error margin reached a maximum value of about 0.06 ms when assuming that the optical fiber CATS system was used for 6 hours a day. Since this is only about 0.2% of the transfer time (about 25 ms), the optical fiber CATS system provides a similar transfer performance to synchronous control using optical fiber.

3. Prototypes

3.1 Functions and features

Figure 5 shows our developed optical CATS system. This system consists mainly of three components, that is, an MT connector switching device, a synchronous controller and a control panel. Table 1 compares the main functions and features of the developed device with those of the conventional device. These components are about 1/4 the size of the conventional components and their total weight is about 12 kg. This system has a function for synchronously transfer splicing from existing to newly installed cables at three different work sites. Furthermore, we can control the system by using a cellular phone when it is impossible to employ a fiber for synchronous control during the cable transfer splicing work. This system is easily capable of undertaking transfer splicing work at aerial sites, and can also be applied to distribution lines where two aerial cables are connected with 4-fiber ribbon joints and an underground cable with an 8-fiber ribbon joint. With this proposed system, cable can be transferred faultlessly with only a slight interruption to working transmission systems, and circuit quality degradation is suppressed.

Table 1. Main functions and features of the developed optical fiber CATS system

Item	Developed optical fiber CATS system	Conventional optical fiber CATS system
Application region	Telephone office, Underground, Aerial	Telephone office, Underground
Application case	Synchronous transfer at two locations, Synchronous transfer at three locations	Synchronous transfer at two locations
Transfer time	About 24 ms	About 22 ms
Size(Relative comparison)	About 1/4	1
Weight	About 12 kg / set	About 28 kg / set
Synchronous method	Synchronous control with optical fiber, Synchronous control by cellular phone	Synchronous control with optical fiber
Transfer mechanism	Horizontal movement	Vertical movement

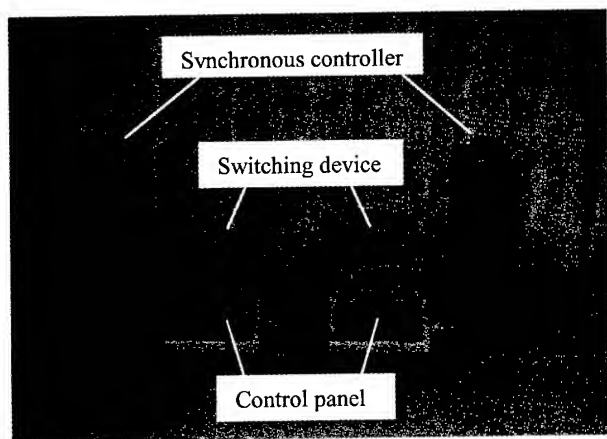


Figure 5. Developed optical fiber CATS system

3.2 Performance evaluations

Figure 6 shows the transfer waveform of our optical fiber CATS system. This figure shows that it takes about 25 ms to connect the unfixed ferrule to the replacement ferrule.

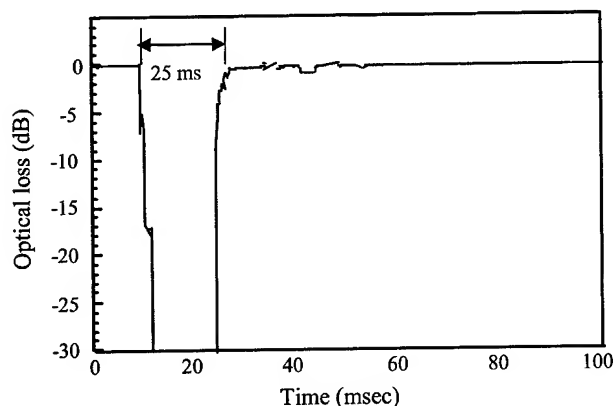


Figure 6. Transfer waveform

A histogram of the measured transfer time is shown in Fig. 7. The transfer splicing was executed 292 times for 30 samples. The average transfer time was 24.2 ms, and the standard deviation was about 2.4 ms. Moreover, even the longest transfer time was only 32.2 ms. The characteristics at this transfer time are not very different from those of a conventional optical fiber CATS system [1]. Figure 8 shows the change in the transfer time with transfer splicing frequency. Transfer splicing was executed 700 times, and

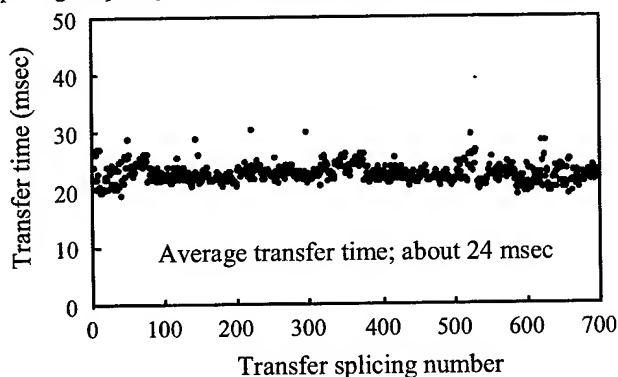


Figure 8. Change in transfer time with transfer splicing frequency

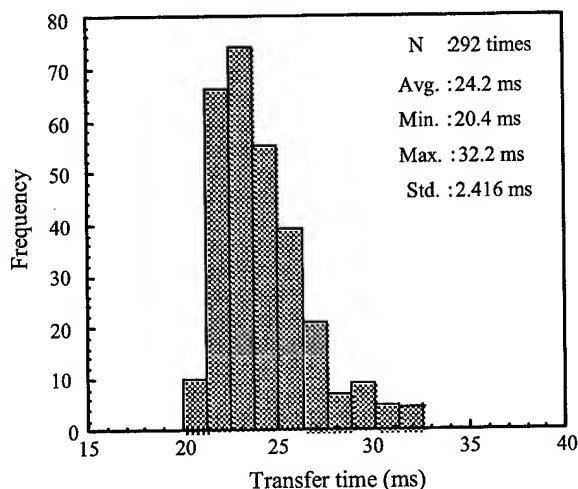
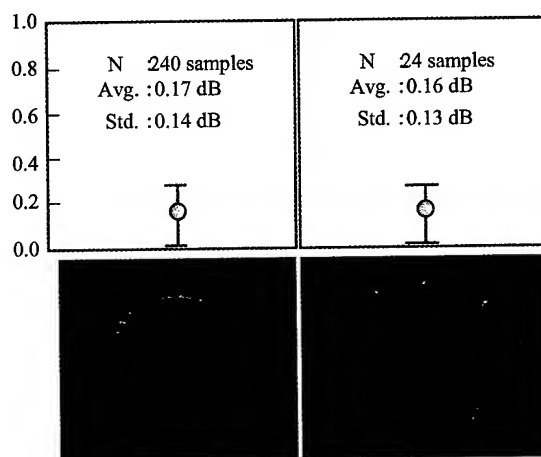


Figure 7. Histogram of measured transfer time

the degradation in the performance of the switching device with increases in transfer frequency was evaluated. This figure shows that there was no large change in the transfer time through 700 transfer splicing operations, and it confirms that the switching device provided mechanically steady operation. The average transfer time was about 24 ms. We then investigated the influence of the switching device on the MT connector. Figure 9 shows the MT connector before and after the transfer splicing. Figure 9(a) is a photograph of the pinhole of the MT connector obtained with an optical microscope prior to the transfer splicing, and the connection loss. We measured 240 samples, and the average value and standard deviation of the connection loss were 0.17 and 0.14 dB respectively. Figure 9(b) is a photograph of the pinhole of the MT connector after 60 transfer splicing operations, and the connection loss. Although we observed that the edge of the pinhole was worn out, the connection loss was no problem as there was little damage caused by pinhole scuffing. As evidence of this, there were no great differences in the average connection loss or the standard deviation before and after the transfer splicing.



(a) Before transfer splicing (b) After transfer splicing

Figure 9. Comparison of MT connectors pinholes before and after transfer splicing

4. Field trial using this prototype

Figure 10 shows the set up for an aerial cable removal experiment using a cellular phone. We used this practical example because the construction of communication facilities in Japan involves the widespread use of aerial optical cable. The optical fiber CATS system was installed in aerial closures, and we switched from an active route to another route using a cellular phone to synchronize the changeover. The distance between the two work sites was about 200 m. During cable removal, we monitored the installed optical fiber with an optical time domain reflectometer (OTDR) from the telephone office. This is because it is necessary to monitor the optical loss change caused by transfer splicing work, and the change in connection loss before and after transfer splicing.

The main working time related to the cable transfer is as follows. The time needed to install the synchronous controller in the bucket and the switching device on the aerial worktable is about 15 minutes. About 20 minutes is needed to prepare the telephone call line and the synchronous control line. It took about 10 minutes per fiber ribbon from fiber identification to cable transfer splicing. And, about 5 minutes were spent on the OTDR

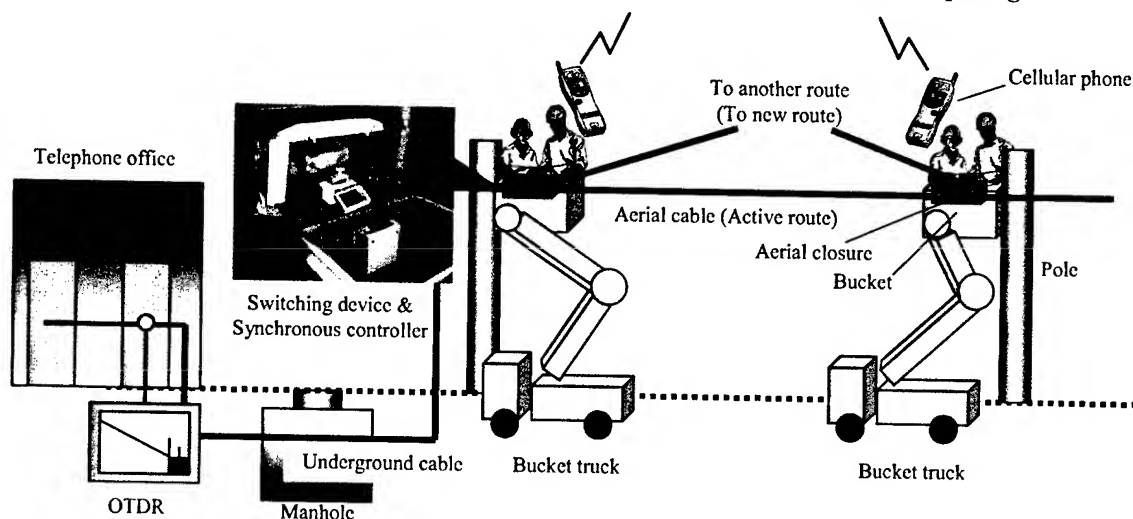


Figure 10. Aerial cable removal experiment using cellular phone

examination performed after the transfer splicing. We were able to shorten the time of the process from fiber identification to cable transfer splicing by about 20 minutes compared with that needed for a conventional device. This is because our approach makes it possible for the first time to work simultaneously at two work sites. This is because no optical loss fluctuation was generated when the connector was handled [4].

The workspace for aerial optical cable is shown in the photograph in Fig. 10. The worker can work freely in the bucket because the switching device, which is a component of the optical fiber CATS system, was downsized to the same size as a fusion splice device for aerial optical cable [5]. There is sufficient space for two workers to work in the bucket.

OTDR waveforms before and after the transfer splicing in the cable removal work are shown in Fig. 11. From this figure, the connection loss and the connector reflection remained unchanged

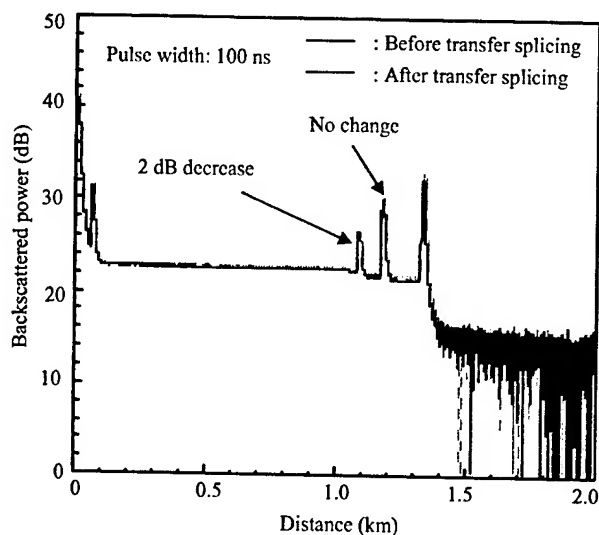


Figure 11. OTDR waveforms before and after transfer splicing

at both work sites. Moreover, there was no optical loss change at either work site during the transfer splicing work.

5. Conclusions

We have developed a miniaturized switching device whose use does not require special skill, so that we may expand the application region of the optical fiber CATS system to aerial cable facilities. Moreover, we added a function that allows us to control the optical fiber CATS system synchronously at three work sites, and to synchronize this system by using a cellular phone. We then constructed a prototype optical fiber CATS system for aerial cable, and evaluated its performance. Furthermore, we applied this prototype to aerial optical cable outdoors and confirmed its efficacy in aerial transfer splicing work. These experimental results confirmed that our optical fiber CATS system, which we developed for aerial optical cable, is practically viable. As a result,

since the application region of the optical fiber CATS system can be extended from underground to aerial cable facilities, the use of this system during cable re-routing or replacement will reduce circuit-releasing time and improve customer service.

6. Acknowledgments

The authors thank Takaaki Aihara, Hiromichi Isogai, Toshinobu Izumi, Akihiko Harada, and for valuable discussions and assistance. We also thank Kiminori Sato, and Nobuo Tomita for their helpful advice and encouragement.

7. References

- [1] I. Watanabe, H. Saito, H. Kobayashi, and S. Takashima, "Subscriber optical fiber cable transfer splicing using mechanically transferable connectors", *IEEE J. Lightwave Technol.*, 10(6), pp. 720-727 (June, 1992).
- [2] H. Kobayashi, M. Shimizu, I. Watanabe, and Y. Chijiwa, "Development of optical fiber transfer splicing system", *Nat. Conv. Rec. IEICE Japan* (March, 1990).
- [3] S. Nagasawa, H. Furukawa, M. Makita, and H. Murata, "Mechanically transferable single-mode multifiber connectors", (*IOOC'89*), paper 21C21, (1989).
- [4] K. Tanaka, M. Tachikura, and M. Nakamura, "Reduction of loss fluctuation in optical fiber cable transfer splicing technique using mechanically transferable connectors", *TECHNICAL REPORT OF IEICE, OFT2000-92(2001-3)*, pp. 31-35, Japan (March 2001).
- [5] H. Taya, S. Yaguchi, T. Sato, and M. Yoshinuma, "Fusion splicing technique for aerial optical cables in access networks", *IEICE, Trans. Electron., Vol. E80-C, No.1 Japan* (January, 1997).

Authors



Kuniaki TANAKA

NTT Access Network Service Systems Laboratories, Nippon Telegraph and Telephone Corporation, 1-7-1 Hanabatake, Tsukubacity, Ibaraki-ken, 305-0805 Japan

Kuniaki Tanaka is a research engineer at NTT Access Network Service Systems Laboratories. Since he joined NTT Network systems development center in 1990, he has been engaged in research & development of optical fiber testing system for subscriber and trunk line, testing device for optical distribution networks. More recently he has been engaged in the development of optical fiber identifier and optical fiber cable transfer splicing system. He is a member of IEICE.



Masahiro ZAIMA

NTT Access Network Service Systems Laboratories, Nippon Telegraph and Telephone Corporation, 1-7-1 Hanabatake, Tsukubacity, Ibaraki-ken, 305-0805 Japan

Masahiro Zaima is a research engineer at NTT Access Network Service Systems Laboratories. He joined NTT Access Network Service Systems Laboratories in 2000. He then engaged in research on optical fiber connection techniques and optical fiber cable transfer splicing system. More recently he has been engaged in the development of optical fiber identifier.



Masao TACHIKURA

NTT Access Network Service Systems Laboratories, Nippon Telegraph and Telephone Corporation, 1-7-1 Hanabatake, Tsukubacity, Ibaraki-ken, 305-0805 Japan

Masao Tachikura is a Senior Research Engineer at NTT Access Network Service Systems Laboratories. He joined NTT Electrical Communication Laboratories in 1976. He has been engaged in research on fiber splicing and connection techniques, the mechanical reliability of optical fibers, and fiber switching techniques. He is currently engaged in the research and development of optical cords and a management system for a central office fiber distribution system. He is a member of OSA, IEICE, JSME (The Japan Society of Mechanical Engineers), and JSAP (The Japan Society of Applied Physics).



Minoru NAKAMURA

NTT Access Network Service Systems Laboratories, Nippon Telegraph and Telephone Corporation, 1-7-1 Hanabatake, Tsukubacity, Ibaraki-ken, 305-0805 Japan

Minoru Nakamura is an executive research engineer at NTT Access Network Service Systems Laboratories. He joined Nippon Telegraph and Telephone Corporation in 1980. Recently, he has been engaged in the development of an optical access network system.

Improvements in Splicing Dissimilar Fibers for Dispersion-Managed Ultra Long Haul Network

Masakazu Nakano*, Harish C. Chandan, Jian Luo, Louis R. Pritchett, Tarek Ellithi,

Torben Veng, Andrew D. Yablon, and John F. Ryan

OFS, 2000 N.E. Expressway, Norcross, GA 30071 U.S.A.

Abstract

Dispersion-managed ultra long haul (ULH) submarine and terrestrial networks typically require transmission fiber spans, which consist of two fibers – one with a positive dispersion and the other with a negative dispersion. Generally, the mode field diameter (MFD) of these fibers is very different. Due to large mismatches in mode field diameters, typical splice loss of these fiber combinations is ~ 1.0 dB at 1550 nm. Not only is the splice loss large, it also has wavelength dependence across the C-Band (1530 to 1565 nm) and the L-Band (1565 to 1625 nm) transmission windows, the wavelength range for the Dense Wavelength Division Multiplexing (DWDM). Four solutions were evaluated for reducing the splice loss of these dissimilar fiber combinations, thermally expanded core (TEC) technique including Pretreatment, Post treatment, Arc scanning and bridge fiber splicing with optimized program. On average, the 1550 nm was less than 0.2 dB with low wavelength dependence in the 1530-1625 nm range.

Keywords

Dissimilar fiber splice; Dispersion management network; High strength splice; TEC; Bridge fiber splice

1. Introduction

Future ULH, 40 Gb/s and 80 Gb/s transmission network will require dispersion balanced spans that have low attenuation and polarization mode distortion. These kind of networks are classified under two major management design mappings: (1) positive-dispersion fiber followed by inverse-dispersion fiber per one network span (A+B management)[1][2][3][4][5], (2) inverse-dispersion fiber section is sandwiched between two positive-dispersion fiber sections (A+B+A management)[4][5][6]. Both of these dispersion-managed spans require splicing dissimilar fibers. Mode field size and shape play a significant role in determining the splice loss between these fibers. These fibers typically have a factor of two difference in mode field diameter. Furthermore, the mode field shape, which is related to the chromatic dispersion characteristics, is very different for these two fibers. The splice loss between such dissimilar fibers can approach 1.0 dB at 1550 nm as compared to the typical 0.1 dB splice loss between more conventional single-mode ITU-T G.652 fibers and Non-Zero Dispersion Shifted Fibers (NZDSF) ITU-T G.655 for terrestrial use, both use positive dispersion fibers profiles.

Copyright © 2002
Fitel USA Corp, All rights reserved

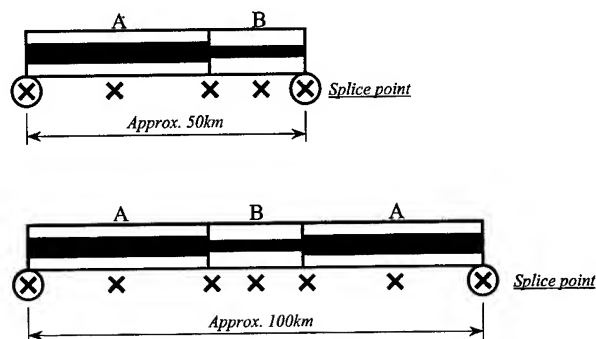


Figure 1. Dispersion managed network

Figure 1 illustrates the splice requirements for A+B and A+B+A type spans. To reduce the splice loss, in principle, one has to create a gradual transition of mode field diameter between the two fibers. We have investigated two major techniques – the bridge fiber technique and the thermally expanded core (TEC) techniques. Careful consideration was given to the splicing technology requirements. Splices deployed in submarine networks (factory splice) need both high strength and low splice losses where terrestrial networks (field splice) must support heat shrinkable splint protection.

2. Fiber characteristics

Table 1 shows typical splice loss results and basic fiber characteristics of the fibers used in our study. In this paper, we described SLA (Super Large effective Area) fiber as positive dispersion fiber and IDF (Inverse Dispersion Fiber) as negative dispersion fiber.

Table 1. Basic fiber characteristics for dispersion-managed network (@1550nm)

Fiber type		A fiber	B fiber
		SLA	IDF
Attenuation	(dB/km)	<0.19	<0.25
MFD	(μm)	11.9	6.2
Aeff	(μm^2)	106	30
Dispersion	(ps/nm/km)	+20	-40
Splice loss (dB)	Same fiber	0.04	0.15
	Dissimilar	>1.0	

3. Splice loss improvements

Dispersion-managed networks typically have three different splice conditions in one network span. It includes two major splice scenarios, which are 1) same fiber type splice such as SLA-SLA and IDF-IDF and 2) dissimilar fiber splice such as SLA-IDF. The fusion-splice difficulty has a strong relation to MFD mismatch between spliced fibers. It is very difficult to get low splice loss with the SLA-IDF fiber splice because the MFD mismatch is approximately $5.7 \mu\text{m}$ at 1550 nm . That kind of dissimilar fiber splice loss performance has been reported in several previous papers [7][8][9]. Reported results show that it was approximately 0.5 dB (Aeff difference was approximately $70 \mu\text{m}^2$) on direct splice [7], 0.28 dB at 1550 nm average (MFD mismatch was approximately $8.9 \mu\text{m}$) with bridge fiber technique [8] and 0.122 dB average (MFD mismatch was approximately $3 \mu\text{m}$) with the arc sweep technique [9]. In this section, we focus on splice loss improvement of the SLA-IDF fiber combination.

3.1 Bridge fiber technique

The bridge fiber method involves making two splices (see Figure 2), which are some distance apart. This length of bridge fiber is necessary to control the effect of modal noise on optical transmission. SLA is first spliced to a short length of a fiber that has an intermediate mode field diameter (bridge fiber). Splice loss is minimized by an appropriate choice of bridge fiber. In our study, we chose a $9.5 \mu\text{m}$ MFD negative dispersion fiber on the basis of matching the mode field shapes. The other end of the bridge fiber is then spliced to IDF. Total splice loss is the combined splice loss of SLA - bridge fiber and bridge fiber - IDF. Table 2 lists the splice losses obtained using the bridge fiber technique. Note that this splice loss depends upon a good match between the bridge fiber and SLA and IDF fibers and the fiber design for large mode field and small mode field diameter fibers. In the factory, one can recoat these two splices but in the field this configuration requires two heat shrinkable protection splints for the splices. A typical two-splint storage scheme is illustrated in Figure 3.

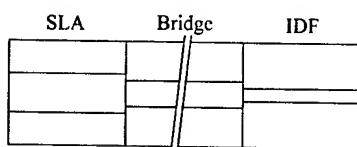


Figure 2. Bridge fiber splice

Table 2. Bridge fiber results for various splicing devices (dB)

Splicer	A	B	C	D	E
Splicer for	Field	Field	Field / Factory	Factory	Factory
SLA - Bridge	0.186 [0.038]	0.166	0.228 [0.015]	0.127 [0.030]	0.113
Bridge - IDF	0.250 [0.019]	0.290	0.257 [0.016]	0.240 [0.021]	0.400
SLA - IDF	0.436	0.456	0.485	0.367	0.513

Mean / [Standard deviation]

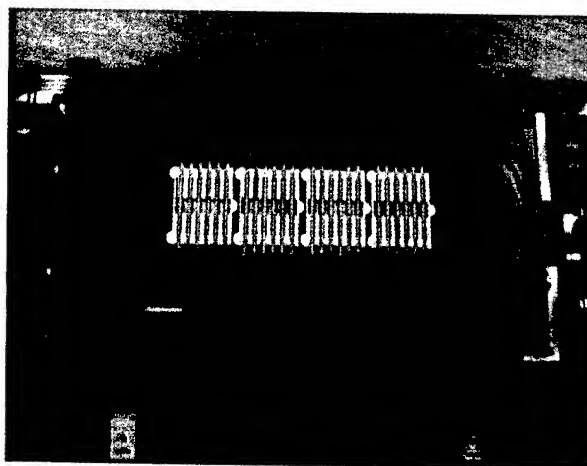


Figure 3. Double splint splices arranged in a splice enclosure

Using a Monte Carlo Simulation, Table 3 shows the estimated splice loss populations based on our measurement result at several wavelengths. These were calculated on the best combination on both for the field splice and factory splice. In the factory splice, the optimized splice program balanced reasonable strength performance with low splice loss and low wavelength dependence splice loss.

Table 3a. Wavelength dependence splice loss using field splicer (dB)

Combination	SLA - Bridge				Bridge - IDF			
	Field splicer A				Field / Factory splicer C			
Wave-length	1530 nm	1550 nm	1565 nm	1625 nm	1530 nm	1550 nm	1565 nm	1625 nm
Ave.	0.190	0.187	0.184	0.175	0.252	0.256	0.261	0.300
M.D.	0.184	0.183	0.181	0.172	0.252	0.256	0.261	0.299
S.D.	0.049	0.040	0.033	0.032	0.019	0.016	0.014	0.026
Max.	0.45	0.41	0.35	0.34	0.38	0.36	0.32	0.41
Min.	0.07	0.08	0.09	0.09	0.19	0.20	0.21	0.22

Count	10,000	10,000	10,000	10,000	10,000	10,000	10,000	10,000
-------	--------	--------	--------	--------	--------	--------	--------	--------

Table 3b. Wavelength dependence splice loss using factory splicer (dB)

Combination	SLA - Bridge				Bridge - IDF			
Splicer	Factory splicer D				Factory splicer D			
Wave-length	1530 nm	1550 nm	1565 nm	1625 nm	1530 nm	1550 nm	1565 nm	1625 nm
Ave.	0.125	0.127	0.128	0.130	0.229	0.240	0.250	0.325
M.D.	0.122	0.124	0.124	0.127	0.228	0.239	0.249	0.321
S.D.	0.029	0.030	0.030	0.030	0.024	0.021	0.021	0.053
Max.	0.27	0.30	0.29	0.30	0.34	0.32	0.34	0.60
Min.	0.05	0.05	0.05	0.06	0.16	0.17	0.18	0.17
Count	10,000	10,000	10,000	10,000	10,000	10,000	10,000	10,000

The differences between the splicing process for field and factory splicing are as follows.

- 1) Stripping method of coating material (tools [scissor type vs. hot stripper], and length [long vs. short])
- 2) Cleaning method during fiber end face preparation process [hand wiping vs. ultrasonic cleaner]
- 3) Fiber clamping method [bare fiber clamp vs. coating clamp]

For field splicing, the splicing time per splice is more important than strength performance. However, in the factory splice, the splice points are typically in the cable. Consequently, the splice points need to satisfy the fiber proof test level. To meet these two objectives the optimized program consists of different settings for each of the parameters.

The splice loss results from the applied optimized program show that the wavelength dependence splice loss was extremely low in C-Band and it will be acceptable in L-Band on both field splice and factory splice.

3.2 TEC techniques

The second technique involves expanding the mode field using heat treatment. This technique requires only one direct splice between SLA and IDF and technique has two advantages. It avoids the possibility of mode -mixing due to the bridge fiber and needs only one protection splint which makes the splice storage in the field easier. There are two variations of this technique - pre-splice treatment [10] and post-splice treatment, with 2 different post-treatment approaches. The first post treatment method involves applying a flame following the direct splice by commercial splicer. The other method uses an arc scanning technique following the commercial splicer [9]. All of TEC techniques make a gradual change in mode field shape near the splice point. The key technology will be the length of the MFD change around the fiber contact point.

3.2.1 Pretreatment

This technique has strong possibility to reduce the splice loss because of its advantage of matching the MFD of small MFD fiber side to large MFD fiber before making the initial splice. The disadvantage is that it is difficult to monitor the splice loss change during the treatment process, because this technique is only applied on the small MFD fiber (IDF) before the fusion splice.

Table 4 shows the experiment results of this technique applied to the SLA-IDF splice. The results indicate extremely low splice loss at the reference wavelength (1550 nm), low wavelength dependence splice loss in C-Band and acceptable wavelength dependence splice loss in L-Band.

Table 4. Splice loss result of SLA-IDF using pretreatment technique (dB)

Items	1530nm	1550nm	1565nm	1625nm
Average	0.122	0.132	0.142	0.222
Median	0.118	0.129	0.140	0.212
Std dev	0.046	0.044	0.042	0.061
Maximum	0.24	0.24	0.24	0.36
Minimum	0.06	0.08	0.09	0.11
Count	34	34	34	34

Splice loss reduction can be accredited to a fiber's Reflective Index Profile (RIP) changes over the splice point. Gradually increasing the smaller core fiber's MFD allows for a uniform transfer of optical light between the fibers to occur. Thus taper allows more uniform optical light transfer between the spliced fibers. Figure 4 graphs the SLA-IDF splice loss verse MFD gap relationship for pretreated IDF to SLA fusions.

These results show that the lowest splice loss point corresponds to a gap of approximate +1.0 μm . The reason for this is that we used variable aperture far field technique to measure the MFD on treated IDF fibers. This means that the fiber has a gradual RIP change related treatment time. Therefore the measurement of the MFD will have an offset to the large side. Consequently, the gap between treated IDF and untreated SLA has some measurement error related to the MFD taper. Using the lowest splice loss treatment condition, which can be achieved when the gap between the treated IDF and SLA is +1.0 μm , produces the minimum splice loss at 1550 nm. Measured results of 0.075dB with virtually no wavelength dependency loss verify this conclusion.

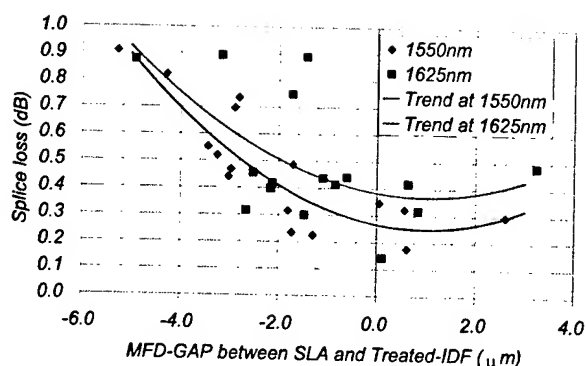


Figure 4. The relationship between MFD gap and splice loss

3.2.2 Post treatment

Some of the advantages of flame post treatment is the ability to monitor the splice loss change during the treatment process, easy to control the treatment time to achieve the lowest loss and the process is very production friendly. However, the flame treatment requires precise positioning of the splice point in the flame.

Table 5 shows the splice loss results of this technique on the SLA-IDF splice. As the result shows it also achieved low splice loss and low wavelength dependence splice on this fiber combination.

Table 5. Splice loss result of SLA-IDF using flame post treatment technique (dB)

Items	1530nm	1550nm	1565nm	1625nm
Average	0.160	0.192	0.223	0.419
Median	0.152	0.184	0.210	0.440
Std dev	0.049	0.047	0.053	0.120
Maximum	0.29	0.29	0.34	0.61
Minimum	0.11	0.14	0.15	0.17
Count	13	13	13	13

Based on RIP measurement result over the splice point, the MFD over all length change at the contact point was slightly shorter than that of pretreatment technique. This seems to be the primary reason for the difference in average splice loss and wavelength dependence splice loss between the two methods.

3.2.3 Arc scanning

This technique has an advantage in the area of fiber handling, including 1) preparation process (stripping, cleaning and cleaving), 2) extremely short splice time and, 3) single station processing (no need to relocate the fiber ends for additional treatment). The splice process is the same as standard fiber splicing, except for the splice program. Therefore it is easy to transfer the splice process to the operator of both the field and factory. Unfortunately, the splice loss result with a pre-optimized program was higher than the above TEC techniques (Table 6).

However, the advantages of this technique may outweigh the higher splice loss in certain cases (such as field splicing).

Table 6. Splice loss result of SLA-IDF using arc scanning technique (dB)

Items	1530nm	1550nm	1565nm	1625nm
Average	0.510	0.529	0.549	0.689
Median	0.519	0.538	0.559	0.684
Std dev	0.057	0.058	0.059	0.088
Maximum	0.61	0.61	0.63	0.83
Minimum	0.41	0.43	0.44	0.55
Count	18	18	18	18

3.3 Summary of SLA-IDF splice improvement

Table 7 shows our study results of the existing techniques for reducing the splicing loss of dissimilar fibers.

As shown, TEC techniques have an advantage in both the field splice and factory splice. The pretreatment and post treatment techniques are better choices for the factory splice. For the field splice, the pretreatment and arc scanning technique are better than other techniques. A disadvantage of the flame TEC technique is that open flames may pose a safety hazard in the field and in the factory. Also, the open flame is sensitive to environmental conditions, including temperature, humidity and altitude. The arc scanning technique will also be affected by environmental conditions; however the impact will be lower than for a flame. Table 8 shows the splice loss results of same fiber splice (SLA-SLA and IDF-IDF) using optimized program and basic result of SLA-IDF direct splice.

Table 7. Comparison of each splicing techniques on SLA-IDF splice

Splice method		Splice loss	Wavelength dependence	Handling	
				Factory	Field
Direct Splice		High	Acceptable	Good	Good
Bridge fiber splice		Acceptable	Acceptable	Acceptable	Acceptable
TEC technique	Pre treatment	Low	Low	Acceptable	Possible
	Post treatment by flame	Low	Low	Acceptable	Difficult
	Arc scanning technique	Acceptable	Acceptable	Good	Good

Table 8. Splice loss characteristics of same fiber type splicing and SLA-IDF direct splice loss without TEC or bridge splice technique (dB)

Splice type	Wavelength	1530nm	1550nm	1565nm	1625nm
Field splicer C	SLA-SLA	0.011 [0.005]	0.011 [0.004]	0.010 [0.005]	0.010 [0.005]
	IDF-IDF	0.047 [0.020]	0.054 [0.020]	0.062 [0.021]	0.112 [0.018]
Factory splicer D	SLA-SLA	0.030 [0.020]	0.032 [0.017]	0.035 [0.018]	0.035 [0.018]
	IDF-IDF	0.100 [0.045]	0.113 [0.047]	0.127 [0.049]	0.240 [0.072]
	SLA-IDF	0.980 [0.105]	0.965 [0.091]	0.953 [0.079]	0.948 [0.098]

4. Investigation of span loss of dispersion managed network

In this section, we estimated the network splice loss distributions, based our study results, using the Monte Carlo Simulation method.

4.1 Submarine dispersion-managed network

Table 9 and Figure 5 show the estimation results of span splice loss distribution related on A+B and A+B+A dispersion-managed network, calculated for several wavelengths. The basic network was presented on Figure 1. The typical cable segment of this network is approximately 14 km and one span length is 50 km and 100 km, respectively.

Table 9a. The result of span splice loss estimation for A+B management (Submarine) (dB)

Wavelength	1530nm	1550nm	1565nm
Average	0.245	0.264	0.293
Median	0.234	0.255	0.286
Std Dev	0.082	0.072	0.075
Maximum	0.78	0.74	0.77
Minimum	0.06	0.08	0.10
Count	10,000	10,000	10,000

Table 9b. The result of span splice loss estimation for A+B+A management (Submarine) (dB)

Wavelength	1530nm	1550nm	1565nm
Average	0.490	0.527	0.586
Median	0.480	0.521	0.580
Std Dev	0.104	0.094	0.097
Maximum	1.14	1.07	1.12
Minimum	0.21	0.26	0.32
Count	10,000	10,000	10,000

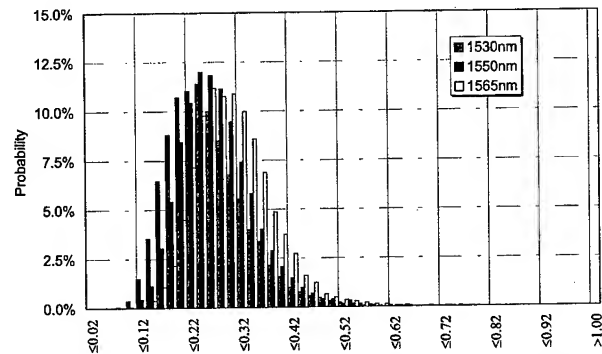


Figure 5a. The result of span splice loss estimation for A+B management (Submarine)

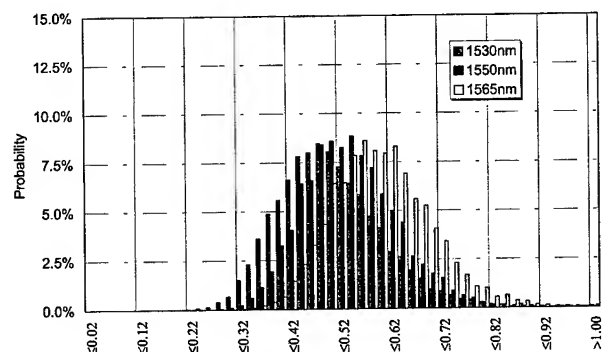


Figure 5b. The result of span splice loss estimation for A+B+A management (Submarine)

4.2 Terrestrial dispersion-managed network

In this section we estimated the terrestrial span splice loss distribution on both dispersion management designs (see Table 10 and Figure 6). The difference from submarine network was the length of the average cable segment. A terrestrial network typically consists of an average cable length of 4 km. This layout requires many splice points in one span.

Table 10a. The result of span splice loss estimation for A+B management (dB)

Wavelength	1530nm	1550nm	1565nm
Average	0.716	0.748	0.782
Median	0.711	0.743	0.780
Std Dev	0.069	0.063	0.058
Maximum	1.04	1.15	1.03
Minimum	0.51	0.56	0.61
Count	10,000	10,000	10,000

Table 10b. The result of span splice loss estimation for A+B+A management (dB)

Wavelength	1530nm	1550nm	1565nm
Average	1.433	1.496	1.565
Median	1.428	1.492	1.563
Std Dev	0.097	0.089	0.082
Maximum	1.89	1.95	1.90
Minimum	1.14	1.20	1.25
Count	10,000	10,000	10,000

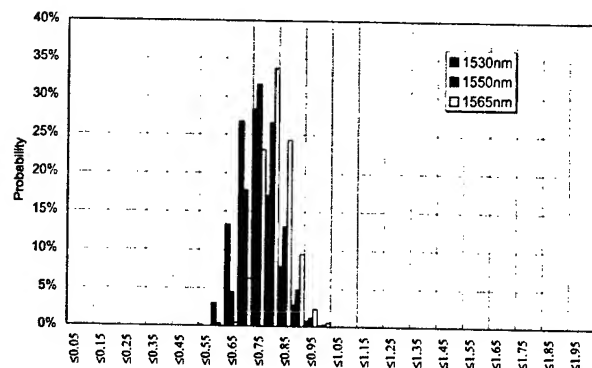


Figure 6a. The result of span splice loss estimation for A+B management (Terrestrial)

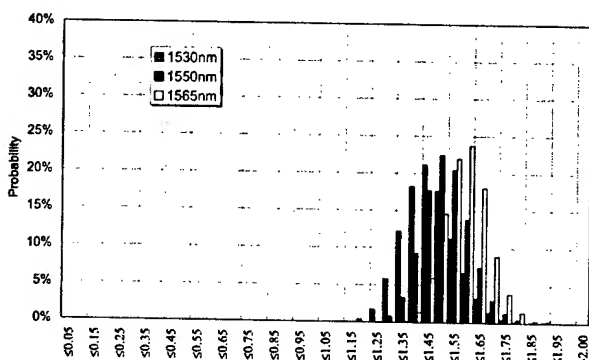


Figure 6b. The result of span splice loss estimation for A+B+A management (Terrestrial)

When using dispersion-managed solutions in the terrestrial applications it is necessary to consider the methodologies for network restoration and network rerouting of installed cables. These considerations will affect the choice of SLA-IDF splice method deployed in the field and how network cable management will be done in the future. Either of these conditions lends support to making a SLA-IDF splice with high strength in the factory. Then install this splice point in the cable of initial construction. This method has three advantages; 1) it can reduce the SLA-IDF splice loss, 2) in the field condition it will be splicing same fiber type (SLA-SLA and IDF-IDF), 3) it has no concern to make a double

splint splice. However it would be more difficult to manage the installed network.

Instead of the Monte Carlo technique, a first order estimate of network splice loss can also be made via a direct analytical combination of the constituent splice loss distributions. If the individual splice loss distributions are approximated by normal distributions, each characterized by a mean and standard deviation, predicting the network splice loss is particularly simple. The expected average span splice loss is simply given by the sum of the means for the constituent splice losses while the standard deviation of the splice loss is given by the square root of the sum of the squares of the standard deviations of the constituent splice losses. As we would expect, the average span splice loss and standard deviation of the span splice loss predicted by this simple technique agrees with the Monte Carlo results presented in Tables 9 and 10 to within 15% or better. This simple first order estimate is expected to be particularly accurate when the standard deviations of the constituent splice losses are small compared to their mean values. The limitation of this simple analytical technique is that a normal splice loss distribution approximation can lead to negative splice loss values.

4.3 Summary of network loss estimation

Analyzing the estimation results of splice loss distribution on one network span and the average splice losses at several key wavelengths appears to have no significant differences between A+B and A+B+A dispersion management design (Based on the splice loss ratio related to span length). However, in the actual network, both span end fibers of the A+B+A designed span will be of the SLA type (large MFD fiber). Because it is easy to splice SLA to repeater cover fibers, which usually have large MFD, this could be an advantage in the field.

Table 11. Example of network loss estimation at 1550nm

Network Design	Splice technique	Total loss (dB)	Fiber loss (dB)		Splice loss (dB)		
		Splice loss ratio (%)	SLA	IDF	SLA-SLA	IDF-IDF	SLA-IDF
A-B	Previous	11.39	6.27	4.25	0.04	0.15	0.69
		7.66%	10.52		0.87		
	Bridge w/ optimized	11.04	6.27	4.25	0.03	0.12	0.37
		4.70%	10.52		0.52		
	Pretreat w/ optimized	10.80	6.27	4.25	0.03	0.12	0.13
		2.58%	10.52		0.28		
A-B-A	Previous	22.74	13.49	7.5	0.07	0.31	1.37
		7.68%	20.99		1.75		
	Bridge w/ optimized	22.03	13.49	7.5	0.06	0.23	0.74
		4.71%	20.99		1.04		
	Pretreat w/ optimized	21.55	13.49	7.5	0.06	0.23	0.26
		2.59%	20.99		0.56		

Table 11 results indicate that applying the Bridge fiber technique with optimized splice programs on dissimilar fiber and same fiber type splices, the splice loss ratio on one network span could be less than 5 %. Applying the pretreatment technique on dissimilar fiber splice could further reduce it to 2.5 %.

5. Conclusions

We have shown splice loss improvement on dissimilar fiber fusion splice of 0.13 dB average splice loss at 1550 nm with extremely low wavelength dependence splice loss, on fibers with a MFD difference of 5.7 μm , using a pretreatment technique. Also our experiment results indicate that other splicing techniques could be useful to achieve the reasonable splicing performance, when considering handling and splice process time in addition to splice loss.

Based on splice loss, the pretreatment technique is the best method to obtain the low splice loss. However we would recommend taking into consideration the environmental conditions when choosing a technique for reducing the dissimilar fiber splice loss. Any technique involving a flame will be very sensitive to environmental conditions. To apply this technique to the field splice, which includes onboard ship splices and terrestrial field splices, additional work to improve the stability of these techniques is required.

For all fusion splices, it is difficult to guarantee the field condition. However, the methods shown here will provide lower splice loss and allow for easier splicing to obtain the optimum network loss.

6. Acknowledgments

We would like to acknowledge Anthony Parker and Rodney Casteel of OFS for double splint bridge splice arrangement in a splice enclosure; Latha Venkatraman and Eric Mies of Vytran for the thermal diffuser prototype unit, Tom Liang of Fitel Interconnectivity Corp. for a field splicer and Doug Duke of Alcoa-Fujikura for a field splicer.

7. References

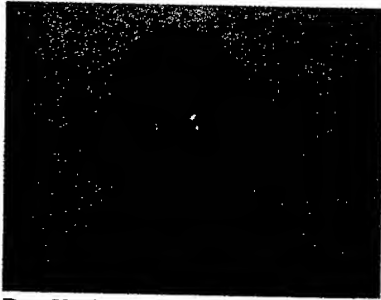
- [1] D. G. Foursa et. al., "2.56Tb/s (256x10 Gb/s) transmission over 11,000km using hybrid Raman/EDFAs with 80nm of continuous bandwidth", OFC March, FC3-1 (2002)
- [2] J. -X. Cai et. al., "Transmission of Thirty-Eight 40 Gb/s Channels (>1.5 Tb/s) Over Transoceanic Distance", OFC March, FC4-1 (2002)
- [3] H. Sugahara et. al., "6,050km transmission of 32x42.7 Gb/s DWDM signals using Raman-amplified quadruple-hybrid span configuration", OFC March, FC6-1 (2002)
- [4] M. Vasilyev et. al., "Raman noise-figure improvement and multipath interference mitigation in effective-area-optimized dispersion-managed cable", OFC March, ThQ4 (2002)

- [5] I. Tomkos, et. al., "80x10.7 Gb/s Ultra-Long-Haul (+4200km) DWDM network with reconfigurable "Broadcast & Select" OADMs", OFC March, FC1-1 (2002)
- [6] F. Liu et. al., "1.6 Tbit/s (40x42.7 Gbit/s) transmission over 3600km UltraWaveTM fiber with all-Raman amplified 100km terrestrial spans using ETDM transmitter and receiver", OFC March, FC7-1 (2002)
- [7] K. Mukasa et. al., "New type of dispersion management transmission line with MDFSD for long-haul 40 Gb/s transmission", OFC March, ThGG2 (2002)
- [8] K. Ohsono et. al., "The Study of Ultra Large Effective Area Fiber & Mating Dispersion Slope Compensating Fiber for Dispersion Flattened Hybrid Optical Fiber DWDM Link", 50th IWCS, 483-487 (2001)
- [9] K. Takahashi et. al., "Development of a New Factory Fusion Splicer", 50th IWCS, 68-76 (2001)
- [10] Thermal Diffuser Station, Patent pending, Vytran Corporation, 1400 Campus Drive West, Morganville, N.J. 07751, U.S.A.

8. Authors



M. Nakano was a Member of Technical Staff at OFS in Norcross, Georgia. He has been engaging in Bell laboratory of Lucent Technologies in 2001. His main work was development of splicing technologies on submarine fibers in Post draw R&D.



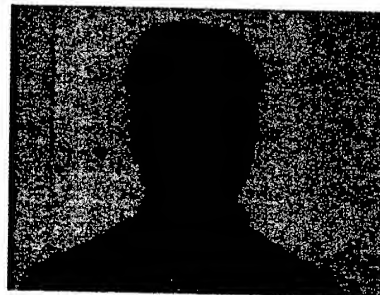
Dr. Harish C. Chandan is a Distinguished Member of Technical Staff at OFS in Norcross, Georgia. At OFS, he is responsible for fiber reliability, fiber failure analysis, fiber qualification, microbending and splicing. He is Chairman of the Fiber Reliability and Coatings Working Group in the Telecommunications Industry Association. Harish has taught a short course on fiber reliability at IWCS in 2000 and 2001, and plans to teach it in 2002. Harish is the author of 33 technical papers and 2 patents.



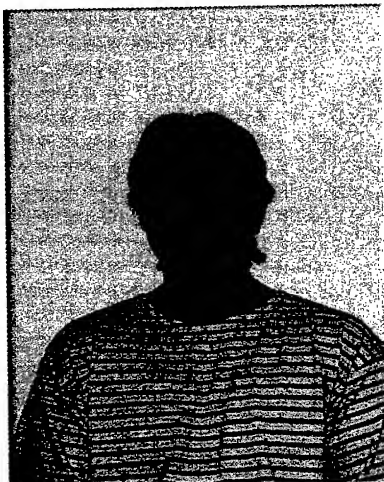
L. Pritchett was a Member of Technology Staff at OFS in Norcross, Georgia. At OFS his main responsibility was splicing process development and experimentation.



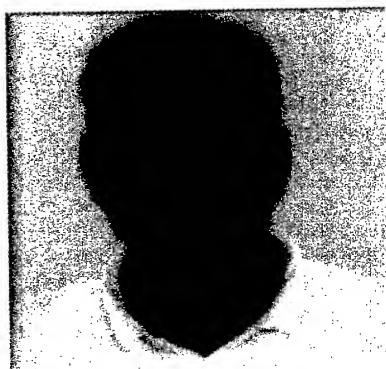
Jian Luo graduated from Tsinghua University (Beijing, China) in 1994 with dual B.E. degrees in Materials S&E, and Electronics and Computer Technology. He received his M.S. (Materials S&E, 1999) and Ph.D. (Ceramics, 2001) degrees from MIT. In June 2001 he joined the optical fiber division of Lucent Technologies Inc. Bell Laboratories in Norcross, Georgia. He is currently conducting optical fiber R&D at OFS. He has authored and co-authored 19 publications in the fields of materials characterization, materials process, oxide surface, nanostructure, and fiber optics.



Tarek Ellithi received his B.S. in ChE degree from Northeastern University (Boston, Mass.) in 1995. He has been with OFS (formerly part of Lucent Technologies Bell Labs) as a Member of Technical Staff-1 since June 2000. He is currently conducting process development and experimentation in splicing technologies on submarine fibers in Post draw R&D.



T. Veng received the Ph.D. degree in Technical Physics from Technical University of Denmark in 1997. Same year he joined Lucent Technologies Denmark I/S, now OFS Fitel Denmark I/S, where he has been working mainly with Dispersion Shifted Fibers and techniques for fusion splicing of Dispersion Compensating Fibers.



Andrew D. Yablon is a Member of Technical Staff at OFS Laboratories, formally Bell Laboratories Optical Fiber Research, in Murray Hill, New Jersey. His main research interests include optical fiber measurements, splicing, and connectorization. Prior to joining Bell Laboratories, Andrew was a Senior Research Scientist at Vytran Corporation in Morganville, New Jersey. He holds the Ph.D. degree from MIT.



J.F. Ryan received his MS in ME from Georgia Institute of Technology in 1996. He has been with OFS (formerly part of Lucent Technologies Bell Labs) since 1996. He is currently the Technical Manager responsible for the research and development of splicing technologies on submarine fibers and systems.

Development of Buffer Tube Storage Solution for 1728 Fibers

By Parke K. Strong and Jason C. Lail

Corning Cable Systems
Hickory, NC
parke.strong@corning.com

Abstract

Higher fiber count cable development continues to be driven by bandwidth demand in the metropolitan network. Service providers wish to maximize the capacity of their networks and minimize the installation cost per fiber meter. These requirements drive the development of even higher fiber count optical cables and closures. As fiber count increases, fiber optic cables and closures are becoming larger and more difficult to handle in the field. During the recent development of a 1728-fiber loose tube ribbon cable and the corresponding 1728-fiber closure, a critical customer requirement was addressed in order to provide a robust solution. The requirement was the customer's desire to store buffer tubes containing ribbons inside the closure.

Section 1.0 provides an introduction to the customer requirement followed by Section 2.0 which discusses the technical issues concerning the customer's desire to store buffer tubes inside the closure instead of ribbons. Section 3.0 presents methods and results for evaluating the kink resistance of buffer tubes in order to successfully store buffer tubes inside closures. Section 4.0 discusses field testing methods and results for various buffer tubes and closure prototypes. Section 5.0 discusses attenuation testing performed to simulate field performance. Finally, Section 6.0 summarizes the conclusions of the study.

Keywords

Closure; Ribbon; Cable; Tube; Coil

1.0 Introduction

During the development of the 1728-fiber cable and closure solution it was critical to meet industry requirements for both the cable and the closure. While meeting industry requirements is an important common ground for the supplier and the customer, a complete understanding of additional technical issues is essential for providing a robust solution for the customer. In the case of the 1728-fiber solution one of the key customer requirements focused on the cable and closure interface.

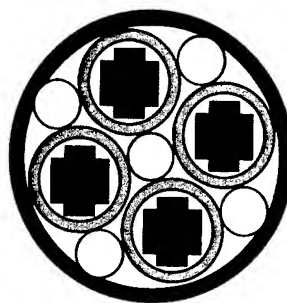
The requirement was the customer's desire to store buffer tubes containing ribbons inside the closure. Storing buffer tubes in the closure allows the installer to avoid the time-consuming task of exposing, cleaning, and storing unspliced ribbons inside the closure. Customer's also prefer to store buffer tubes to better protect unspliced fibers and for easier fiber identification and organization. Excess lengths of buffer tube and/or ribbon are typically stored in case any issues arise with the cable, closure, or fiber splices. Excess length allows the customer to re-enter the closure and troubleshoot potential fiber breaks or rework fiber splices.

This paper focuses on the technical concerns of storing buffer tubes inside closures and identifies the methods and results used

to develop the optimum 1728-fiber loose tube ribbon cable and corresponding 1728-fiber closure design.

Figure 1 shows a cross-section of the cable design utilized in the evaluation. Each buffer tube contains eight 12-fiber ribbons and fourteen 24-fiber ribbons in a combination ribbon stack design.

Figure 1. 1728-fiber Cable Cross-section

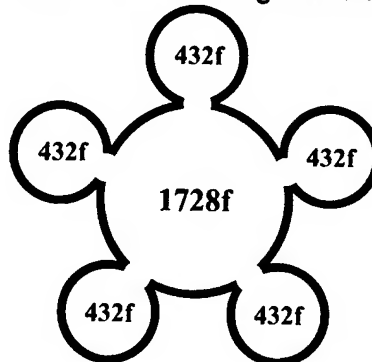


2.0 Buffer Tube Storage

In addition to meeting industry requirements for both the cable and closure design, the most critical requirement was the customer's desire to store buffer tubes containing ribbons inside the closure. Storing ribbons inside of the buffer tubes saves cleaning time when only accessing a portion of the fibers in the cable, provides better protection for the remainder of the unutilized fibers, and helps with fiber identification and organization.

To illustrate the importance of storing buffer tubes, consider a metro-ring around a large city containing a 1728-fiber loose tube ribbon cable and five 432-fiber feeder cables. See Figure 2. At each 432-fiber feeder ring, the 1728-fiber cable is mid-span accessed and 432 fibers are spliced to the feeder cable. There are a total of ten splice points, two at each 432-fiber feeder ring.

Figure 2. Metro Ring Scenario



In the previous scenario, consider two closure storage options: ribbon and tube. If the buffer tubes are not stored in the closure, then all four tubes in the 1728-fiber cable must be opened so that the ribbons can be routed in the closure. If the tubes are stored, only one tube in the 1728-fiber cable must be opened. Table 1 summarizes the quantity of 12-fiber ribbons that must be exposed, cleaned, and stored using the ribbon storage and the tube storage options.

Table 1. Storage Options Inside Closure

Storage Option	Exposed, Cleaned and Stored		
	Spliced 12FRs	Unspliced 12FRs	Total 12FRs
Ribbon	360	1080	1440
Tube	360	0	360

Notice that with tube storage the quantity of 12-fiber ribbons that must be exposed, cleaned, and stored is reduced from 1440 to only 360. This reduction in the number of ribbons that must be exposed, cleaned, and stored saves many hours for the installer. The storage of buffer tubes also improves organization, identification and protection of ribbons inside the closure.

In order to store buffer tubes inside closures it is important to understand the procedure for buffer tube storage. During buffer tube storage, 10-20 feet of each buffer tube is typically formed into small-diameter coils. This amount of tube is needed to ensure that enough ribbon slack will be available for future splicing needs. For the 4-tube 1728-fiber design, this results in a maximum length of 80 feet of buffer tube for storage inside the closure. After the buffer tubes are coiled they are then placed or pushed into the closure. In order to perform this procedure successfully, the buffer tube must not kink during coiling or during placement inside the closure. A kink resistant buffer tube is essential for performing the procedure successfully. If the buffer tube kinks during coiling or placement, fibers may experience increased attenuation or in extreme cases may even break.

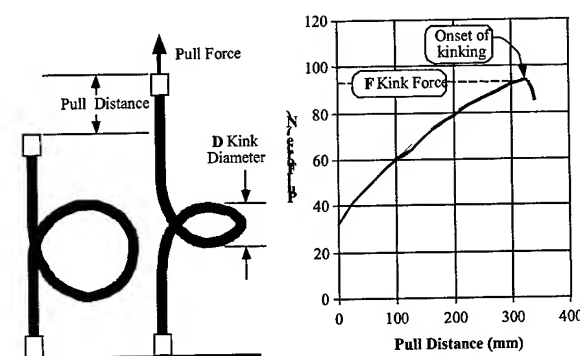
In addition to having a kink resistant buffer tube, it is critical to ensure that there is minimal attenuation change once the buffer tubes are placed in the closure. It is also important to ensure minimal attenuation increase across the entire operating temperature range.

3.0 Kink Resistance

3.1 Published Kink Resistance Methods

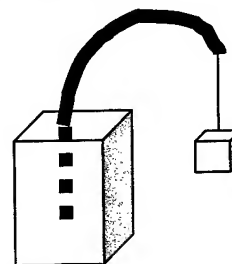
In order to place buffer tubes inside closures, the tubes are formed into slack coils. During coiling and placement in the closure, buffer tubes are susceptible to kinking. There are many methods used to evaluate the kink resistance of buffer tubes and cables. One method used by Logan, "forms a cable into a loop on a tensile tester. The cable loop is pulled while monitoring the pull force and pull distance. The onset of cable kinking is noted by a sudden drop in the pull force" [1]. Figure 3 is an excerpt from Logan's paper and shows the test configuration along with the resulting graph of pull force versus pull distance. In Logan's paper, the kink force and kink diameter were utilized to compare various cable designs and for correlation of the laboratory test to actual field performance at room temperature.

Figure 3. Kink Test Configuration & Graph



Another method for evaluating kink resistance was published by Okuno. Okuno states, "One end of a sample cord is inserted into a hole on a sample holding implement, and a weight is attached and hung from the other end of the cord. The weight weighs 5 grams to simulate an actual connector. The distance from the top surface of the sample holding implement to the highest point of the bent sample cord is measured and used as the kink-resistance index" [2]. Figure 4 shows the test configuration utilized by Okuno. In the test configuration the tube is placed in a rectangular mount and a 5 gram weight is suspended from the end of the tube. The resulting deformation of the tube is then utilized to determine the kink-resistance index. Similar to Logan, Okuno presented a method for comparing different cable and buffer tube prototypes and also assumptions for correlating the laboratory testing to actual field-testing.

Figure 4. Okuno Kink Resistance Method



The method utilized by Logan was ideal for buffer tubes or cables that required kink forces of 50-100 N. Okuno's method was ideal for buffer tubes or cables that required smaller kinking forces. While both methods addressed the primary issues of kink resistance and field performance, the development team for the 1728-fiber solution had several additional concerns.

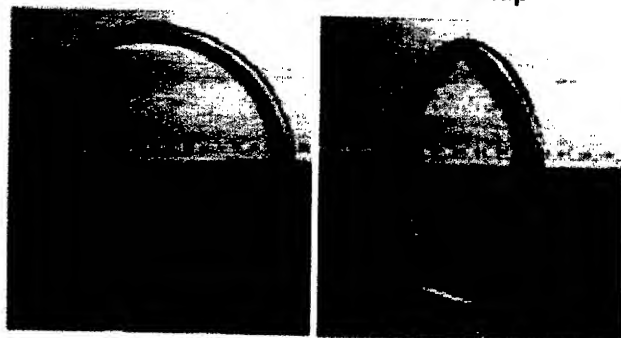
3.2 New Kink Resistance Procedure

In addition to measuring kink resistance and correlation to field performance, there were several additional requirements for the new procedure.

1. Minimal time to setup and perform.
2. Ability to perform test from -40°C to $+70^{\circ}\text{C}$.
3. Ability to always test buffer tube to kink failure.

In order to address the additional concerns of the development team. A manual kink resistance procedure was created and used to evaluate the kink resistance of each tube sample. Figure 5 shows the setup of the manual kink test and the resulting kink failure.

Figure 5. Manual Kink Test Setup



To perform the manual procedure, the buffer tube sample was placed at a coil diameter of approximately 200-mm. Gripping the ends of the buffer tube sample, the tester slowly increased the distance between their hands at a constant rate, approximately 150 mm/min. This movement decreased the initial 200-mm coil diameter. As the coil diameter was decreased, the buffer tube eventually kinked as shown in Figure 5.

At the point of failure, the kink diameter was measured and utilized for comparisons of different buffer tube samples. Because the test procedure did not require any electronic equipment, the procedure could be easily utilized across the entire cable operating temperature range from -40°C to $+70^{\circ}\text{C}$. Additionally, because the test was quick and simple results could be gathered rather easily.

In order to confirm that the manual kink resistance procedure was repeatable and reliable, it was compared to similar laboratory methods. Buffer tubes were evaluated utilizing the manual kink resistance procedure and a laboratory procedure similar to Logan's. Kink diameters were determined with both procedures. Table 2 shows the correlation between the two methods. While, the kink diameters were not equal using each method, the correlation between the two methods was very consistent. As a result, the manual kink resistance procedure was selected for evaluating buffer tubes for the 1728-fiber solution.

Table 2. Comparison of Kink Procedures

Sample #	Manual Kink Diameter (mm)	Laboratory Kink Diameter (mm)	% Differ
1	100	125	11.1
2	117	145	10.7
3	132	163	10.5
4	145	177	9.9
5	163	198	9.7

3.3 Kink Resistance Results

While kink resistance is essential for storing buffer tubes inside closures, it is also important to consider the compression

resistance of the buffer tubes as well. Adequate compression resistance is essential for meeting the customer's cable compression requirements. For this evaluation, buffer tubes of different materials and dimensions were evaluated to optimize compression and kink resistance. The materials chosen for the evaluation were medium density polyethylene (MDPE), high density polyethylene (HDPE) and polypropylene (PP). Buffer tubes of various dimensions and materials were manufactured and tested. Table 3 shows the materials and dimensions of the buffer tubes.

Table 3. Buffer Tube Dimensions and Materials

Inner Diameter (mm)	Tube Material	Wall Thickness (mm)	Compression Resistance
Small	MDPE	0.9 - 3.0	0.35 - 6.80
	HDPE	0.5 - 2.2	0.16 - 5.70
	PP	0.5 - 2.0	0.14 - 5.35
Large	MDPE	0.7 - 2.6	0.13 - 3.75
	HDPE	0.4 - 1.8	0.04 - 2.75
	PP	0.3 - 1.7	0.04 - 2.65

The buffer tube wall thickness was varied with each material type to create three levels of compression resistance. The compression resistance is a function of the inside diameter and wall thickness. The minimum compression resistance needed to meet the customer's requirements is 1.0. The technical challenge is to balance the compression resistance to meet the customer's requirements and the kink resistance to allow the customer to adequately store 80 feet of buffer tube inside the closure.

Figure 6 shows the results of the evaluation of the small tubes utilizing the manual kink resistance procedure. The results show that buffer tubes with higher compression resistance generally had smaller kink diameters (or higher kink resistance). The results also showed that MDPE buffer tubes had the smallest kink diameters and PP buffer tubes had the largest kink diameters.

Figure 6. Summary of Small Buffer Tubes

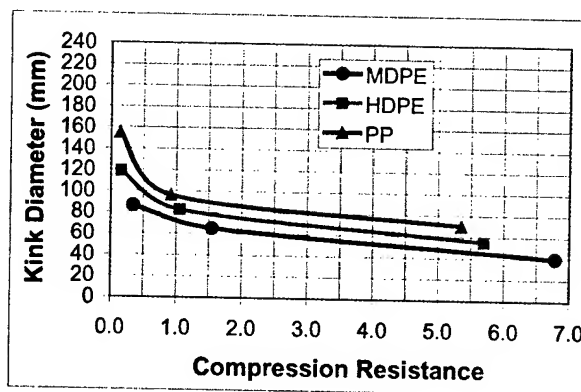


Figure 7 shows the results of the evaluation of the large buffer tubes using the manual kink procedure. The results again show buffer tubes with higher compression resistance also had smaller kink diameters. It is also apparent that buffer tubes with larger inside diameters exhibited larger kink diameters. The small tubes had kink diameters from 40-160 mm, while the large tubes exhibited larger kink diameters from 60-240 mm.

Figure 7. Summary of Large Buffer Tubes

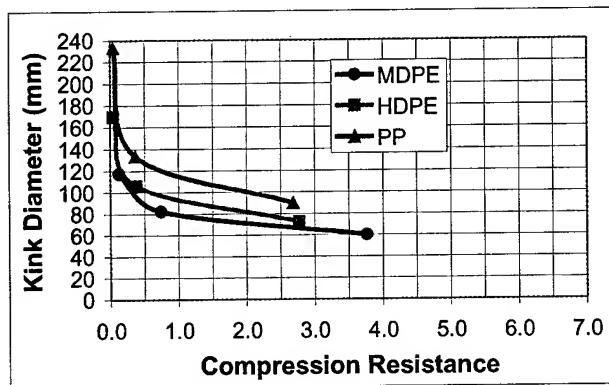
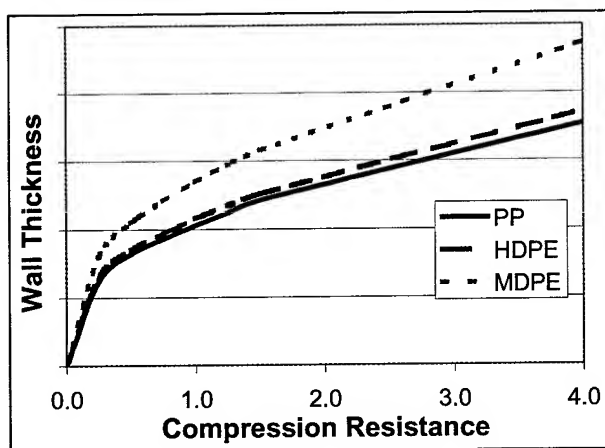


Figure 8 shows the wall thickness needed for different materials at various levels of compression resistance. Tubes manufactured with MDPE will require thicker walls to maintain the minimum compression resistance of 1.0.

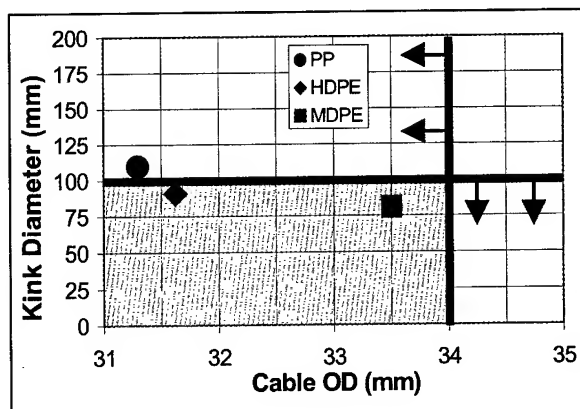
Figure 8. Wall Thickness Comparison



Based on the manual kink testing results, MDPE provided the highest kink resistance but required a larger wall thickness to achieve the minimum compression resistance. The PP tubes required a thinner wall thickness to meet the minimum compression resistance, but had the least kink resistance, exhibiting the largest kink diameters. Figure 9 shows a summary of the kink resistance evaluation, comparing kink diameter and cable diameter. A kink diameter of less than 100 mm and a cable outside diameter (OD) of less than 34 mm were requirements established by the project team. PP required the smallest cable OD, but had the least kink resistant tubes. Tubes made of MDPE had the best kink resistance but produced large cable diameters. The material that provided the optimum combination of

compression resistance, kink resistance and cable diameter was HDPE and it was selected for additional field test evaluations.

Figure 9. Cable OD vs. Kink Diameter



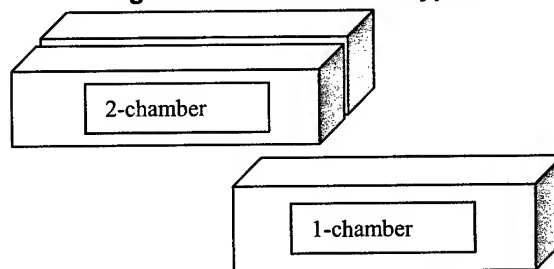
4.0 Field Testing in Closure Prototypes

After the kink testing results were complete, additional HDPE buffer tubes were manufactured and evaluated in two closure prototypes. The objective of the evaluation was to confirm that the selected buffer tube could be adequately coiled and placed inside the closure prototypes as performed in an actual field test. The initial target was the successful storage of four 20-foot buffer tube coils or 80 total feet of buffer tube inside the closure without any evidence of buffer tube kinking.

4.1 Field Test Procedure

Two closure prototypes were used in this evaluation. The 2-chamber closure contained two chambers as shown in Figure 10. Each chamber was 28.0" long, 2.4" wide, and 7.1" tall. The 2-chamber closure contained a total volume of 954 cubic inches. The 1-chamber closure contained a single chamber located in the middle of the closure also shown in Figure 10. The single chamber was 25.5" long, 3.5" wide, and 9.3" tall for a total volume of 830 cubic inches.

Figure 10. Closure Prototypes



The procedure for the field test consisted of coiling buffer tubes into various coils and then placing the coils into the closure prototypes. The coils had to fit completely into the closure and the buffer tube was then removed and inspected for any evidence of kinking. Table 4 summarizes the procedures that were utilized.

Table 4. Summary of Field Test Procedures

Closure Prototype	Buffer Tube Coil Geometry
1-chamber	Oval
1-chamber	Round
2-chamber	Oval
2-chamber	Round

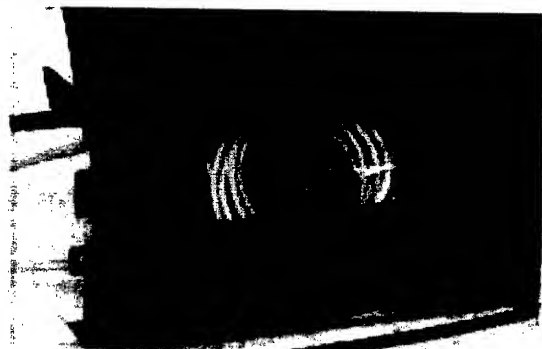
Figure 11 shows pictures of the oval buffer tube coils and the round buffer tube coils. The oval coil was approximately 9 x 25 inches, while the round coil was approximately 9 inches in diameter.

Figure 11. Oval and Round Coil Geometry



Figure 12 shows a round coil placed in the 2-chamber closure prototype. All other samples were inserted into the closure prototypes in a similar fashion.

Figure 12. Round Coil in 2-chamber Closure



4.2 Field Test Results

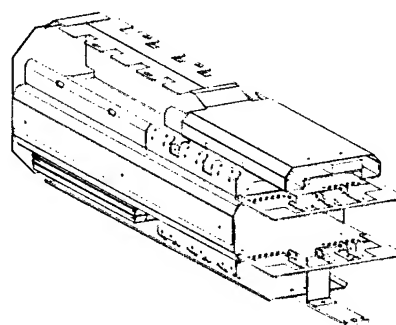
The results of field testing in the two closure prototypes were very conclusive. Table 5 shows a summary of the testing. For each test three trials were performed and inspected for evidence of kinking. Based on the results round coils performed better than oval coils and the 1-chamber closure performed better than the 2-chamber closure. However, round coils were very difficult and time consuming to prepare. Therefore, the chosen field test procedure was to utilize oval coils in the 1-chamber closure design.

Table 5. Summary of Field Testing

Closure Prototype	Buffer Tube Coil Geometry	Evidence of Kinking
1-chamber	Oval	No
1-chamber	Round	No
2-chamber	Oval	Yes
2-chamber	Round	No

The final closure prototype design is shown in Figure 13.

Figure 13. Final 1-chamber Closure Design



5.0 Attenuation Performance

After the HDPE buffer tube material was selected based on the kink resistance study and the 1-chamber closure design was selected based on the field testing results, the final step in the evaluation was to determine the potential for attenuation increases in small-diameter coils.

5.1 Published Attenuation Standards

There are several industry standards that address attenuation performance. A typical requirement is a change of less than 0.15 dB/km in standard cable mechanical testing and in any testing requiring temperature cycling. Other standards include some guidance on cable termination in closures and some closure specific attenuation requirements. However, no standard specifically addresses attenuation increases associated with buffer tube storage inside closures. Additionally, because the length of buffer tube is only 20 feet for each tube, characterization of attenuation performance is difficult.

5.2 Attenuation Performance Procedure

To evaluate attenuation performance a procedure was developed specifically for storing buffer tubes inside closures. To conduct the test, buffer tubes were placed in large-diameter coils and initial attenuation measurements were taken. These values were utilized to simulate the attenuation performance of an installed cable resting in a duct or coiled in a manhole. The buffer tubes were then formed into small-diameter coils, and placed into the closures similar to the field testing procedure discussed in Section

4.0. The attenuation was measured again and the attenuation change was determined.

5.3 Attenuation Performance Results

The results from the evaluation were very clear. Table 6 summarizes the results utilizing oval and round coils with coil lengths of 20 feet.

Table 6. Summary of Attenuation Results

Coil Geometry	Coil Length (ft)	Temperature (°C)	Attenuation Change (dB)
Oval	20	23	0.04
Oval	20	-30	0.11
Oval	20	-40	0.40
Round	20	23	0.01
Round	20	-30	0.04
Round	20	-40	0.10

Both the oval and round coils showed minimal attenuation change at room temperature, 23 °C. In the oval coil, the maximum -30°C attenuation change was 0.11 dB and up to 0.40 dB at -40°C. While the increases are significant and measurable, the level of increase is similar to a splice loss and should be included in splice loss calculations when designing the network. All attenuation returned to the initial measurements after the temperature cycling was completed.

6.0 Conclusions

The development of a buffer tube storage solution for a 1728-fiber loose tube ribbon cable and the corresponding 1728-fiber closure was successful. Kink resistance studies for various buffer tube materials and dimensions were conducted to select the optimum buffer tube for the 1728-fiber cable design. Field testing in closure prototypes was also conducted to select the most robust closure design with respect to buffer tube storage. Finally, attenuation testing was conducted to ensure minimal attenuation changes with buffer tube coils stored inside the final closure prototype. The result of the development work is a 1728-fiber loose tube ribbon cable. The cable contains four HDPE buffer tubes with 432 fibers per tube. Additionally, the final closure design can contain 144 12-fiber ribbon splices and 288 additional single fiber splices with adequate space for storing up to 80 feet of buffer tube.

7.0 References

- [1] Logan, "Evaluating High Fiber Count Cable Designs for Field Performance," 1998 NFOEC Proceedings, Volume 1, pp. 385-395.
- [2] Okuno, et al. "Development of Kink-Resistant Non-Halogen Flame-Retardant Optical Fiber Cord," 2000 IWCS Proceedings, pp. 187-191.



Parke K. Strong is a Product Development Engineer in the Ultra-High Fiber Count Ribbon Cable Development group at the Corning Cable Systems R,D&E facility in Hickory, NC. Parke received his Bachelor of Science degree in Mechanical Engineering from North Carolina State University. He has been employed with Corning Cable Systems for seven years.



Jason C. Lail is the supervisor of Ultra-High Fiber Count Ribbon Cable Development at Corning Cable Systems R,D&E facility in Hickory, NC. Jason has a B.S. degree in Mechanical Engineering and a B.A. degree in Business Communication from North Carolina State University. Jason has four previous publications, over 40 internal technical reports, over 40 records of invention, and holds four patents. Jason's focus is on evolutionary high fiber count ribbon cable designs and revolutionary designs to create increased value for the customer.

Mid-span Access Tool Designs and Their Impact on Fiber Reliability

Geoff Witt, Brian Risch, Bill Chapman, Pierre Coat, Ray Lovie, and Bob Overton

Alcatel Fiber Optic Technology
Claremont, NC 28610

Abstract

Mid-span accessing of buffer tubes is frequently done to extract a subset of the fibers inside. The buffer tube access tools used for mid-span access have three requirements: 1) they must open the buffer tube to allow access to the optical fibers inside, 2) they must not interrupt traffic on active fibers, and 3) they must not damage the optical fibers. However, many mid-span access tools cannot meet all three of these requirements. This paper presents a detailed study of the potential for fiber damage resulting from the use of various mid-span access tools currently used in the field.

Keywords

Mid-span access tool, branch, blades, fiber damage, reliability, drop, buffer tube.

1. Introduction

This study of fiber damage resulting from the use of mid-span access tools was undertaken in response to two developments in the communications industry. The first development is the fact that mid-span access is becoming increasingly more common as networks spread closer to the end user. As this happens, small numbers of fibers (6, 4, or even 1) are dropped off of feeder lines. Since buffer tubes typically contain 12 fibers, the tube must be opened in mid-span to allow the desired fibers to be cut and spliced to a drop cable.

The second development is the emergence of unique cables especially designed to carry a large number of fibers in a small cross-section. These "high fiber density" cables are miniaturized to take advantage of unusual right-of-ways and innovative installation techniques that reduce the cost of deployment.^{1,2,3,4 and 5} For example, special cables have been installed in sewers, water lines, gas lines, tiny trenches in roadways, and in miniaturized ducts^{6,7}. Instead of carrying 12 fibers in a 3mm buffer tube, some of these cables carry 24 fibers in a 2.4mm buffer tube, or 12 fibers in a 1.5mm buffer tube.

These two developments create an urgent need for a reliable and effective mid-span access tool that can address buffer tubes with higher packing density. In order to develop a reliable tool for mid-span access, several different tools, which are now commonly used in the field, were tested with the buffer tubes they were

designed to open. The purpose of this study was to benchmark the effectiveness of current tools.

2. Variables

Samples of loose tube optical fiber cable, and the corresponding recommended access tools, were procured from three major cable manufacturers. The buffer tubes were removed from the cable structure using conventional techniques, and each manufacturer's tool was used to access the buffer tubes for which it was designed. A fourth mid-span access tool, expressly designed for mid-span access of "high fiber density" buffer tubes, designated as "tool A2", was also tested with buffer tubes made by each of the three cable manufacturers. Three duplicate tools of each type were paired with three different buffer tubes, e.g. blue, orange, green, to achieve the variation in tools and buffer tubes that might occur in the field.

Standard buffer tubes from each manufacturer were used. Two of the cable designs used a 3mm tube containing 12 fibers, and one design used a 2.8mm tube containing 12 fibers.

Buffer Tube	Tool #1	Tool #2
Vendor A 3mm/12 fiber	Tool A1	Tool A2
Vendor B 2.8mm/12 fiber	Tool B	Tool A2
Vendor C 3mm/12 fiber	Tool C	Tool A2

Photographs of the various access tools and respective cutting channels are shown in Figures 1A-C. Tools A1 and A2 both have a blade that shaves off part of the tube with minimal intrusion into the tube interior. Tools B and C have blades that cut through the tube and penetrate substantially into the tube interior.

Tool A2 incorporates design features that makes it especially suited for mid-span access of "high fiber density" buffer tubes. Specifically, the blade is designed so that the bottom of the blade can safely contact optical fibers during access without causing

coating damage. This is achieved by positioning the cutting edge of the blade some distance above the bottom of the blade. This distance is the "blade edge height" and is illustrated in Figure 2A. Additionally, the channel of Tool A2 is integral to replaceable inserts that are precision machined. In this way, the depth of cut is carefully controlled by the "step height" illustrated in Figure 2B. These inserts are made for a specific buffer tube geometry and can be easily replaced in the tool depending on the tube that is to be accessed. Figure 3 illustrates the wide range of tube geometries that can be accessed with tool A2 and a series of inserts.

Figure 1A: Access Tools A1, B, and C.

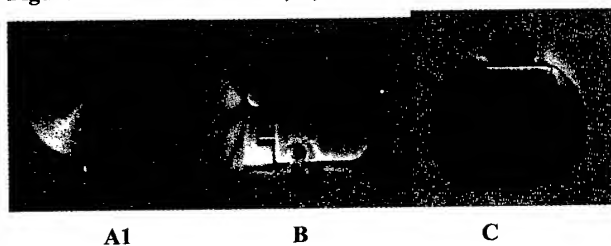


Figure 1B: Access Tool A2 in Cae with 2.5mm, 2.8mm, and 3.0mm Inserts.

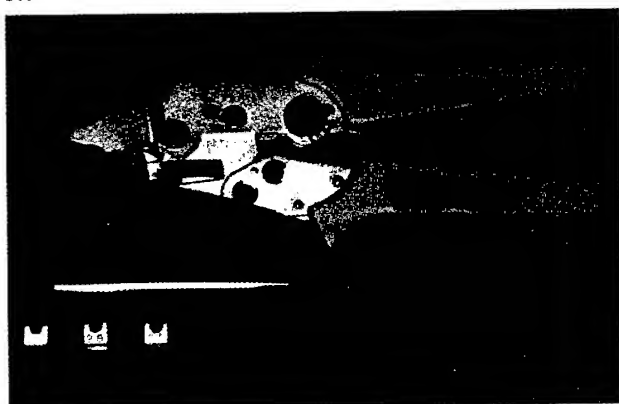


Figure 1C: View Through the Access Channels of the Tools.

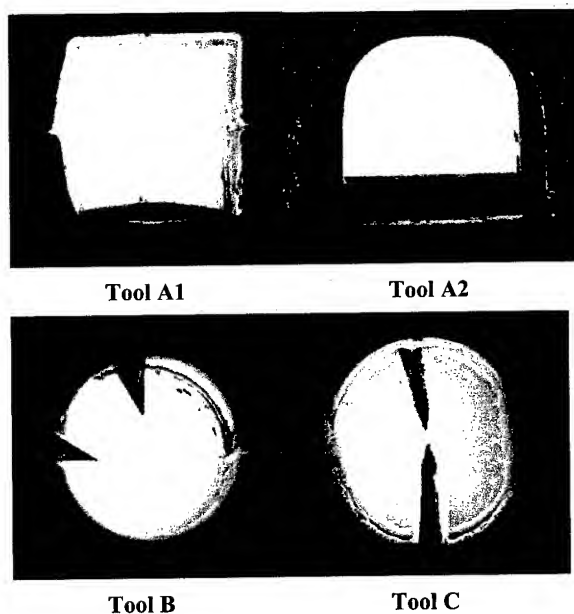


Figure 2A: Drawing of the Cutting Blade Profile of the High Fiber Density Access Tool A2.

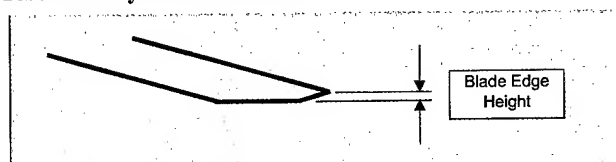


Figure 2B: Illustration of the Insert Used in the High Fiber Density Access Tool A2.

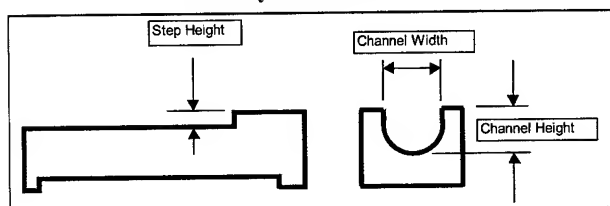
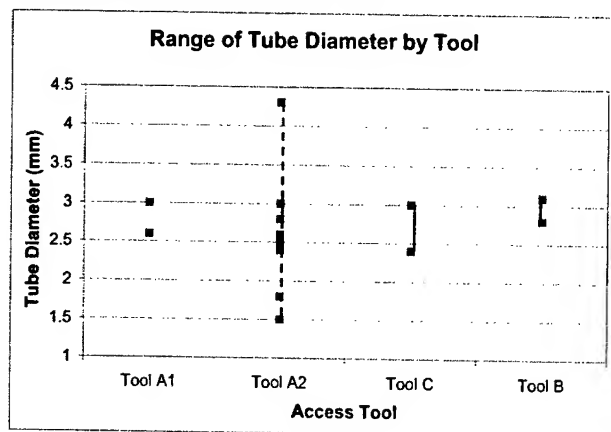


Figure 3: An Illustration of the Range of Buffer Tube Sizes that Can be Accessed with Each Tool.



3. Procedure

First, three access tools of each type were paired with three buffer tubes from the same cable. Each tool was then used to open a 2m length of buffer tube in accordance with the tool manufacturer's instructions. The fibers were carefully removed and hung vertically to prevent contact with damaging surfaces. Thirty-six accessed fibers were obtained for each toolmaker / buffer tube maker combination. After the fibers were extracted from the opened buffer tube, they were cleaned with gel solvent and alcohol. Then, the entire length of each fiber was inspected under a microscope at 100x magnification, to look for signs of coating damage resulting from fiber contact with cutting tool blades.

The level of damage was noted for each fiber. Damage was categorized into three levels: no damage, damage to the secondary coating only, and damage to both secondary and primary coating. Note that glass damage could not be quantified with this inspection method, so some damage recorded as primary coating damage may actually have included glass damage as well.

4. Results

A summary of the damage rates observed on fibers from the various tube access trials is shown in Figure 4. The aforementioned tool for "high fiber density" buffer tubes, tool A2, was tested on all tube types with zero fiber damage being evident. In contrast, other tools produced damage rates as high as 97%. Examples of coating damage observed through optical microscopy are shown in Figures 5 and 6.

Tools A1 and A2 did not produce observable coating damage in the tube sizes used in this study. The reduction in fiber damage rates with tools A1 and A2 is explained by the greatly reduced penetration of the cutting blade into the interior of the tube as well as by the design features described previously. An important distinction between Tool A1 and Tool A2 is that Tool

A2 is designed for use with buffer tubes having fiber densities greater than those in this study but Tool A1 is not.

With the level of coating damage observed in many of the fibers that were damaged by access tools, there is a significant reduction in the protection afforded to the glass. Since fibers within splice enclosures typically see the increased stresses due to lower bending radii and increased handling, coating damage should be avoided especially in fibers that do not have the additional protection of the cable and buffer tube.

Figure 4: Fiber Damage Observed with Various Access Tools and Buffer Tubes

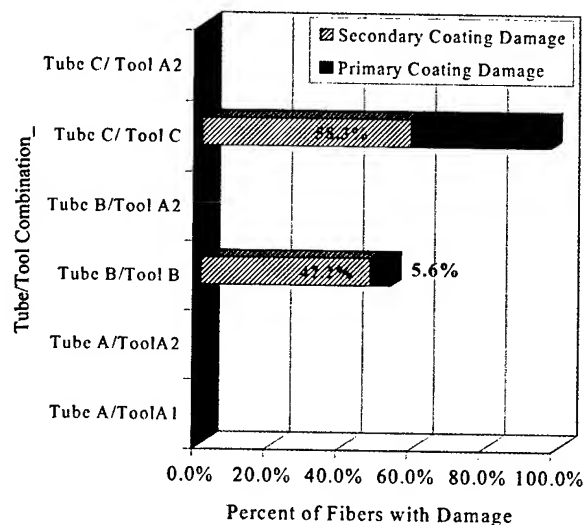


Figure 5A: Fiber Damage on a Red Fiber from Tube B Accessed with Tool B.



Figure 5B: Fiber Damage on a Blue Fiber from Tube B Accessed with Tool B.

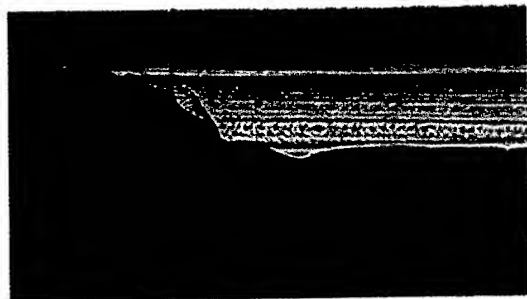


Figure 6A: Fiber Damage on an Orange Fiber from Tube C Accessed with Tool C.

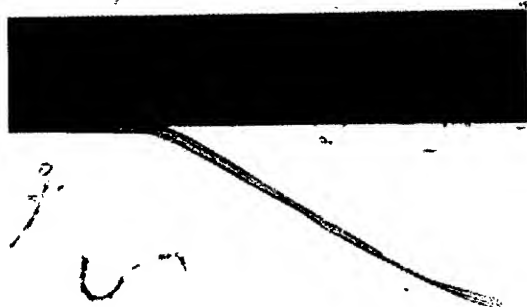


Figure 6B: Fiber Damage on a Green Fiber from Tube C Accessed with Tool C.



Figure 6C: Fiber Damage along a Substantial Length of an Orange Fiber from Tube C Accessed with Tool C.



Figure 6D: A Section of Fiber with Secondary Coating Almost Entirely Removed by Tool C.



The fibers accessed with the different tools were aged for 50 days in an environmental chamber controlled at 85°C and 85% relative humidity in order to assess the effects of the coating damage on the long-term fiber reliability and strength. After aging the fibers were placed in the chamber in a stress-free state for the duration of the aging period. Following the accelerated aging, the tensile strength of the fibers was measured per the procedure of FOTP-28C for half meter tensile testing. The results are shown in Figures 7A – 7C. Note that flaws outside of the half meter gauge length would not affect strength measurements.

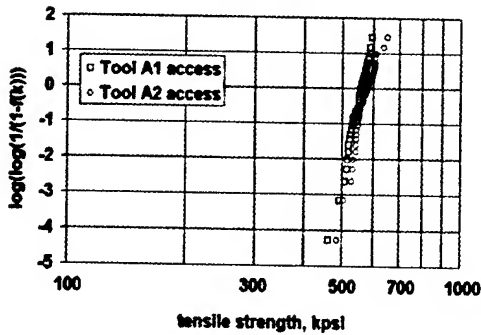
Tube A fibers show little difference in the strength distribution whether accessed with Tool A1 or Tool A2. The median strength of the fibers accessed with Tool A1 is somewhat lower, but there is an absence of low stress breaks that might have been a result of damage from either tool.

Tube B fibers also do not show substantial variation in median strength when accessed with either Tool A2 or Tool B. However, several large flaws in fibers accessed with Tool B were indicated by the low stress breaks in the tensile distribution as shown in Figure 7B.

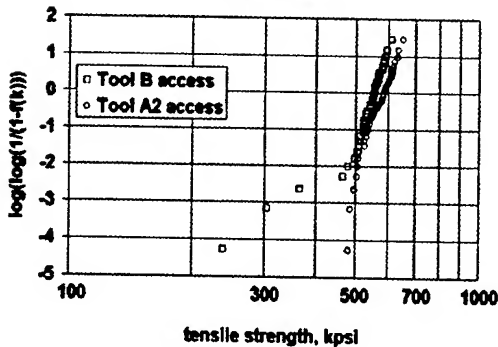
Tube C fibers showed the most substantial variation in median strength as a function of access tool. Tool C resulted in the most severe effects on fiber strength, where several flaws of a strength less than 200 kpsi are seen in this 36 fiber data set, Figure 7C. Flaws this weak can lead to fiber breaks during subsequent handling of the fibers. Again, Tool A2 did not cause coating or glass damage that affected the tensile strength of the fibers from tube C even after aging.

Figures 7A-C. Tensile Strength After 50 Days Aging
85°C/85% RH.

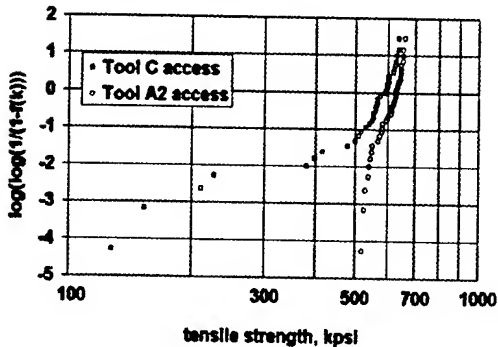
7A. DYNAMIC TENSILE STRENGTH, TUBE A FIBERS
FOTP-28C



7B. DYNAMIC TENSILE STRENGTH, TUBE B FIBERS
FOTP-28C



7C. DYNAMIC TENSILE STRENGTH, TUBE C FIBERS
FOTP-28C



5. Conclusions

The primary conclusions of this study are:

1. Some commonly used mid-span access tools have the potential to cause severe coating damage.
2. Substantial coating damage may go unnoticed during normal fiber access since careful inspection, sometimes requiring microscopy, is needed for detection.
3. Coating damage caused by access tools may increase the risk of fiber breaks due to static fatigue, handling, or other mechanical forces in splice closures.
4. A survey of various tool technologies available to the industry and a concurrent tool development effort has produced a buffer tube access tool that virtually eliminates the risk of coating damage. This tool is compatible with a variety of buffer tube materials and geometries.

The need for reliable mid-span access tools will grow more acute as fiber densities in buffer tubes increase. As fiber densities increase, the tolerance inside a tube for an invasive cutting tool decreases, thereby increasing the risk of coating damage. A flexible, reliable, access tool is needed to ensure that as fiber density increases, risk of fiber damage does not. This research has produced a tool that has successfully produced reliable and repeatable tube access without fiber damage with tubes of varying geometry and from various manufacturers.

6. Acknowledgments

Thanks to Kelly Felmet for inspecting the fibers, and thanks to Pierre Coat for capturing the images of fiber damage.

7. References

- ¹ M. Garcia, *et. al.*, "Very High Transmission Density Cables Including Multicore Fibers", *Proceedings of the 47th International Wire and Cable Symposium*, November 1998, p.57-65.
- ² E. R. Logan, H.M. Nassar, and R.S. Wagman, "The Status and Future of High Fiber Count Cable Designs", *Proceedings of the 48th International Wire and Cable Symposium*, November 1999, p.12-19.
- ³ E. Park, *et. al.*, "Semi-Tight Bound Type Fiber Optic Cable", *Proceedings of the 48th International Wire and Cable Symposium*, November 1999, p.141-146.
- ⁴ P. Gaillard, *et. al.*, "Optimization of Loose Tube Cable Designs: The Next Step", *Proceedings of the 47th International Wire and Cable Symposium*, November 1998, p.913-920.
- ⁵ M.G. Soltis, R. Lovie, and G. Witt, and C. Hutton, "Next Generation Loose-Tube Cables: reduce the Size, Not the Performance", *Proceedings of the 49th International Wire and Cable Symposium*, November 2000, p.155-163.
- ⁶ H.G. Haag, *et. al.*, "Experiences from Construction and Operation of Fiber Optic Cable Plants in Sewer Systems", *Proceedings of the 48th International Wire and Cable Symposium*, November 1999, p.176-183.
- ⁷ P.E. Gregor, L. Kuhn, and A. Weiss, "Optical Fiber Cable Links within Gas Pipelines as an Alternative Telecommunications Route Technology", *Proceedings of the 48th International Wire and Cable Symposium*, November 1999, p.176-183.

Development of a Mass Fusion Splicing System for up to 24-Fiber Ribbon

Toshiro Mizushima, Sachie Morita, Hiroshi Sugawara,

Takeshi Sato, Shonosuke Yaguchi

Precision Instruments Research & Development Dept., Fujikura Ltd.

1440 Mutsuzaki, Sakura, Chiba, 285-8550, JAPAN

+81 43 484 3962 mizushima@opt.fujikura.co.jp

Abstract

A mass fusion splicer has been developed for splicing all fiber counts up to 24-fiber ribbon and including single fibers. Accessories, including a cleaver, hot jacket stripper, and fiber protection sleeve, have also been developed for splicing and protecting 24-fiber ribbons. The splicer is designed to be small and light weight, and is capable of repeatable and reliable performance in harsh field conditions, including aerial or underground environments.

1. Introduction

Until recently, the demand for high fiber-count ribbon cables constantly increased. To meet this need, cables using 24-fiber ribbon have become increasingly common. [1] Initially, these cables contained up to 432 fibers, but recently, 864 fiber-count cables have been deployed. [2] In the past year, cables with up to 1,728 fibers have been demonstrated utilizing 24-fiber ribbon. [3] However, up to now, no splicer has been capable of splicing 24-fiber ribbon. Furthermore, while development of 24-fiber mass fusion splicing capability was previously reported, [4] it has previously been impossible to achieve low loss splicing of all counts of fiber (from single fibers up to 24-fiber ribbons) with conventional arc fusion techniques. This paper provides details concerning final development of a new mechanism known as EDS (Electrode Driving System) that has been developed in order to achieve acceptable low loss splicing for all fiber counts up to 24-fiber ribbon.

Another difficulty concerning 24-fiber mass fusion splicing operations is that hot jacket stripping of 24-fiber ribbon requires double the stripping pulling force as compared with stripping 12-fiber ribbon. Furthermore, the clamping pressure must also be significantly higher in order to prevent slipping during the stripping operation. A new mechanism developed to address these issues is also introduced in this paper.

2. EDS - Electrode Driving System

2.1 Relation between Actual Loss and the Fusion Arc Heating Profile

In order to achieve low loss splice results when splicing multiple fibers simultaneously, there are several important parameters. Examples are: the pre-splice fiber offset, cleave angles, arc time, arc power, fiber stuff distance, etc. However, the most important consideration for successful ribbon splicing is to distribute adequate and uniform heat across the entire ribbon fiber array. If this is not achieved, it is difficult to obtain consistent low splice

loss even if all of the other important parameters are changed and optimized. Therefore, in order to splice 24-fiber ribbons with low loss, it is necessary to design a system that provides adequate and uniform heat across the entire 24-fiber ribbon array. Figure 1 shows the relation between actual loss and the arc fusion arc heating profile.

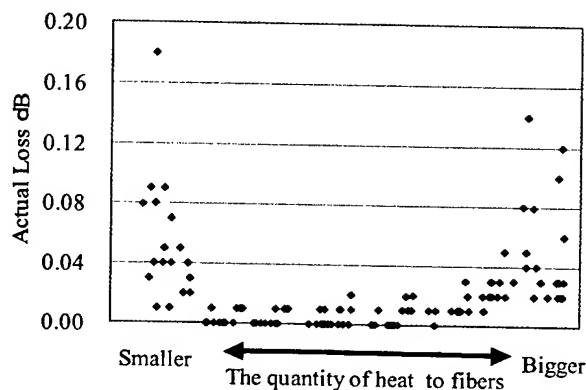


Figure 1. Relation between actual loss and the fusion arc heating

2.2 Relation between Electrode position and the Arc Heating Profile

The most important parameter to apply heat equally across all the fibers in a ribbon is the electrode position relative to the fibers.

When splicing 24-fiber ribbons, it is necessary to set the gap between the electrodes as well as the offset of the electrode axis (relative to the plane of the fibers) to positions suitable for 24-fiber ribbon.

Figure 2 illustrates the various temperature regions produced across the electrode gap. The lower part of Figure 2 illustrates the important considerations of the electrode position relative to the ribbon fiber array (i.e., electrode gap, and the electrode axis offset relative to the plane of the fibers). The fusion arc temperature profile has a typical characteristic such that in the regions close to the tips of the two electrodes, the arc plasma field has the highest temperature. Therefore, when splicing with the plane of the fibers aligned with the axis of the electrodes (Electrode Offset = 0), it is impossible to heat all fibers equally. The fibers on each end of the ribbon array (which are close to electrodes) are exposed to very high heat, and consequently they melt too much. Fibers in the center of the ribbon array receive either adequate heat, or too little heat. It is therefore important that the electrode gap and electrode offset are set at suitable positions to heat all of the fibers within the 24-fiber ribbon equally.

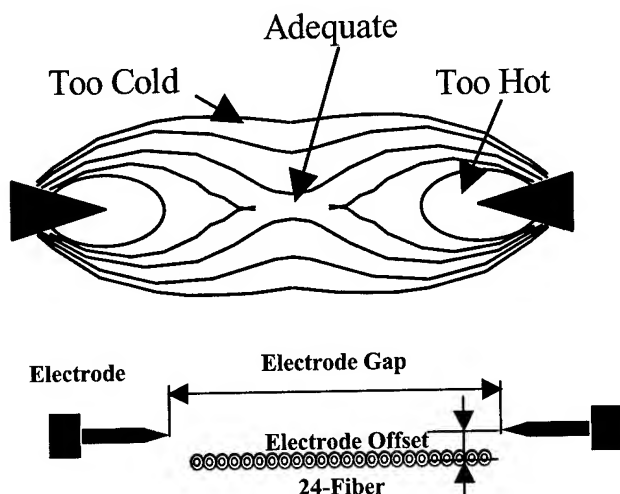
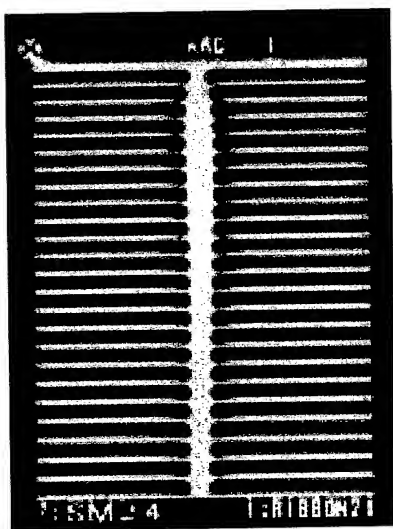


Figure 2. Straight Arc Discharge with Wide Gap

The temperature distribution across the ribbon fiber array can be analyzed by measuring the melt back amount of the fibers by use of an arc test. Figure 3 shows the 24-fiber ribbon image that is produced after a melt back test is performed when the electrode positions is suitable for 24-fiber ribbon. In this case, the electrode gap is wider than the width of 24-fiber ribbon, the electrode offset is set at an acceptable position, and other techniques are used to stabilize and control the arc shape. As shown, the test results with the 24-fiber ribbon are within a uniform and acceptable melt back range. Unfortunately, not all fiber counts from single fiber splicing through every ribbon size all the way up to 24-fiber ribbon can be spliced with this electrode position



**Figure 3. Melt Back Results, 24-Fiber Ribbon
(Electrode Position Optimized for 24-Fibers)**

Figure 4 shows the fiber melt back image for 16-fiber ribbon that results from an arc test when the electrode position is set to the position established as suitable for 24-fiber ribbon. As this test result demonstrates, the electrode position optimized for 24-fiber ribbon is not suitable for 16-fiber ribbon. Therefore, fibers at both ends of the 16-fiber array are melting too much. With this condition, it is impossible to achieve low loss splicing of 16-fiber ribbon. In order to solve this problem, either the electrode gap or the electrode offset needs to be changed to a position optimized for 16-fiber splicing.

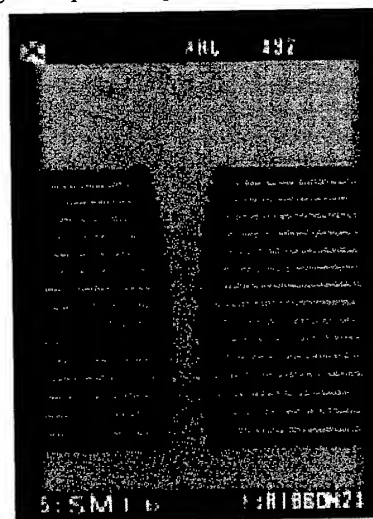


**Figure 4. Melt Back Results, 16-Fiber Ribbon
(Electrodes Set at 24-Fibers Position)**

If the electrode offset relative to the plane of the ribbon fibers is varied, the temperature variation is sudden. Therefore, adjusting the electrode offset to a suitable position is extremely difficult and may not produce results that are repeatable and stable. Hence, if the electrode offset is changed in order to heat the fibers in a 16-fiber ribbon equally, it is necessary to adjust the electrode offset with extremely high precision. Therefore, it has been determined that it is better to set the electrode offset position relative to any size ribbon to a fixed value that is suitable for 24-fiber ribbon, and to adjust only the electrode gap for splicing numbers of fibers less than 24.

Figure 5 shows the arc test result for 16-fiber ribbon with adjustment of the electrode gap to an adequate position. Clearly, by changing only the electrode gap position, adequate heat can be distributed to the entire 16-fiber ribbon array.

Similar issues can be observed if the electrode position for 24-fiber ribbon is used in a melt back test for 12-fiber ribbon. Adequate and uniform heat cannot be distributed across the entire 12-fiber ribbon with the 24-fiber electrode position. Therefore, it is necessary to adjust the electrodes to an adequate position for 12-fiber ribbon. It has been determined that adjusting only the electrode gap (while leaving the electrode offset position at the offset value previously established for 24-fiber splicing) is sufficient to achieve adequate and uniform heat across the entire 12-fiber ribbon. Figure 6 illustrates the result. Moreover, it has been confirmed that the 12-fiber electrode gap position produces an adequate and balanced heat distribution for splicing all numbers of fibers less than and up to 12-fiber ribbon, including single fiber splicing. This indicates

that the new splicer has a single balanced and adequate electrode position for splicing 1-12 fibers just like the conventional 12-fiber splicer. [5]

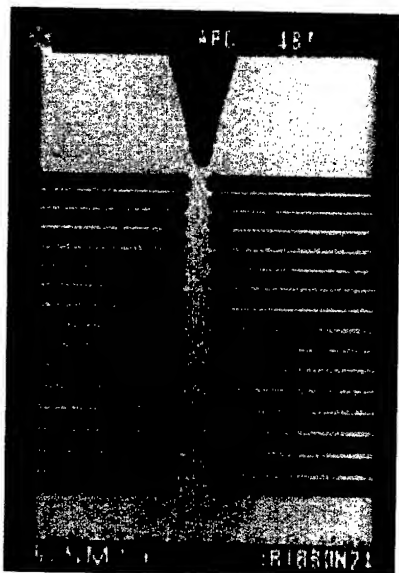


Figure 5. Arc Test with 16 Fiber Ribbon

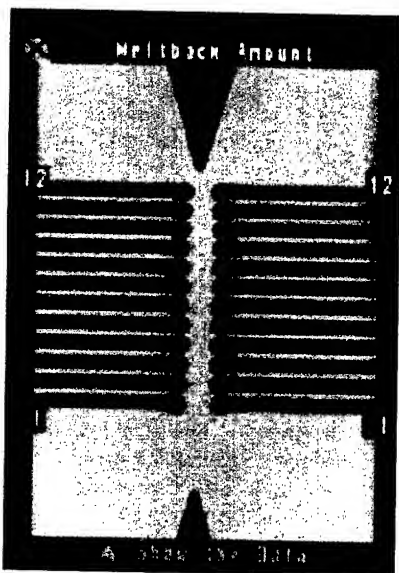


Figure 6. Melt Back Results, 12-Fiber Ribbon
(Electrode Gap Optimized for 12-Fibers)

Table 1. The Relation Between Electrode Gap and Splice Loss

Fiber Number	Distance of Electrode		
	1-12mode	16mode	24mode
1	OK	NG	NG
2	OK	NG	NG
4	OK	NG	NG
8	OK	NG	NG
12	OK	NG	NG
16		OK	NG
24			OK

Note: The crosshatched areas in the Table 1 correspond to conditions in which the width of the ribbon fiber array is larger than the electrode gap. Hence, in such a condition it is impossible to splice, and this condition is not applicable.

We confirmed from the developments and experiments detailed above that all ribbon fiber counts as well as single fiber splicing can be performed with three electrode gap positions: (1) One electrode position is suitable for splicing 1-12 fibers, (2) Another electrode gap position is optimized for 16-fiber ribbon, (3) A third electrode gap position is utilized for 24-fiber ribbon splicing. Therefore, the electrode gap must be moved to the suitable position relative to the number of fibers to be spliced. Hence, the Mass Fusion Splicing System features the new automated EDS (Electrode Driving System) mechanism.

2.3 Performance of 1-24 Fiber Ribbon Splice

Based upon the experimental results, a splicer has been developed that utilizes EDS in order to automatically set the electrode gap to the appropriate one of three optimum positions (depending upon the number of fibers to be spliced). Single mode fiber splice loss results for this splicer are shown in Figure 7, Figure 8, and Figure 9 for 24-fiber ribbon, 16-fiber ribbon, and single fiber splicing respectively. In each case, the average splice loss is less than 0.02dB, clearly indicating that the electrode condition is suitable for each fiber count.

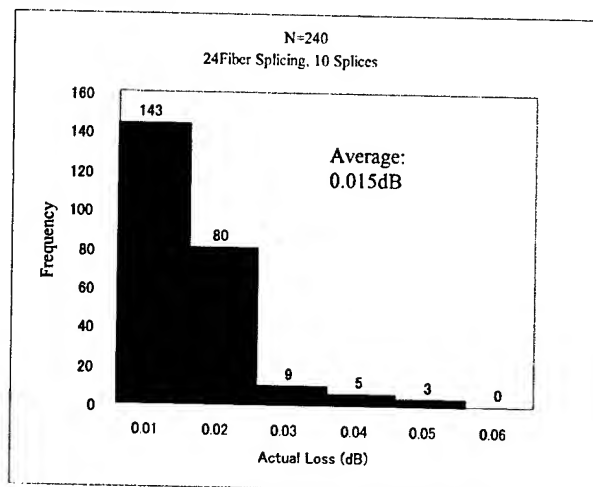
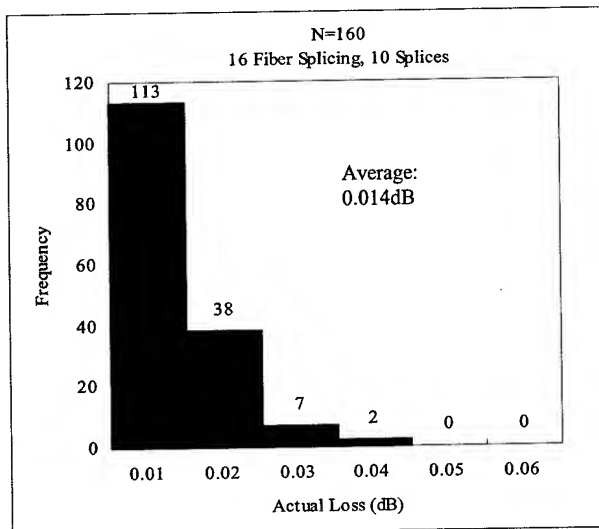
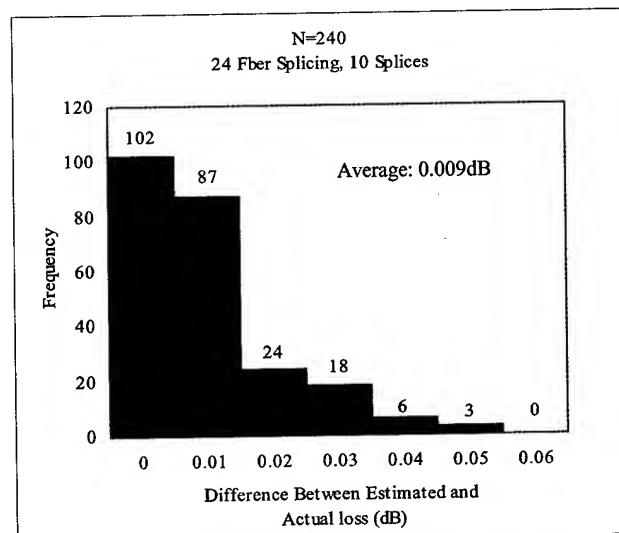


Figure 7. Splice Loss Results
(24-Fiber SMF spliced to 24-Fiber SMF)



**Figure 8. Splice Loss Results
(16-Fiber SMF Spliced to 16-Fiber SMF)**



**Figure 10. Estimated vs. Actual Loss
(24-Fiber SMF Spliced to 24-Fiber SMF)**

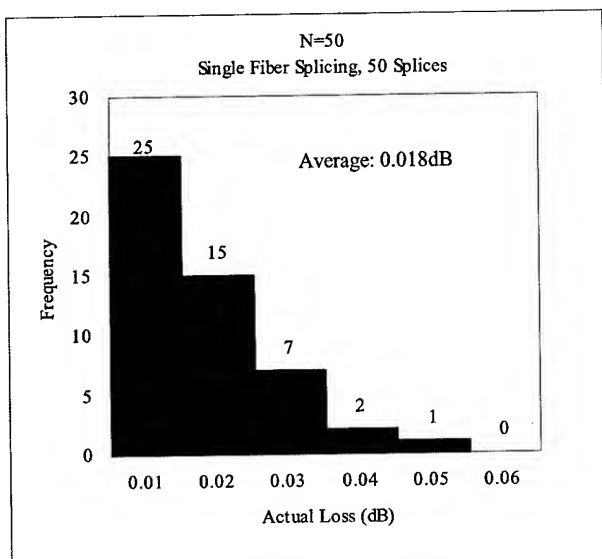


**Figure 9. Splice Loss Results
(Single SMF Spliced to Single SMF)**

The correlation between estimated and actual splice losses can be seen in Figure 10 (in this case, the estimated versus actual splice loss data is for the 24-fiber SM ribbon splicing). As this figure shows, the mean difference between estimated and measured splice loss is 0.009dB.

Splicing tests have also been performed with 12 and 24-fiber ribbons containing TrueWave RS fiber, as well as 24-fiber ribbons containing LEAF fiber. This test data is shown in Figures 11-13. In every case, the average splice loss is less than 0.05dB. Hence, we have confirmed that use of the Electrode Driving System (EDS) allows the new mass fusion splicer to achieve performance results when splicing 1-24 fibers ribbon that are equivalent to conventional 12-fiber mass fusion results, even in the case of the more difficult to splice Non-Zero Dispersion fibers such as TrueWave and LEAF.

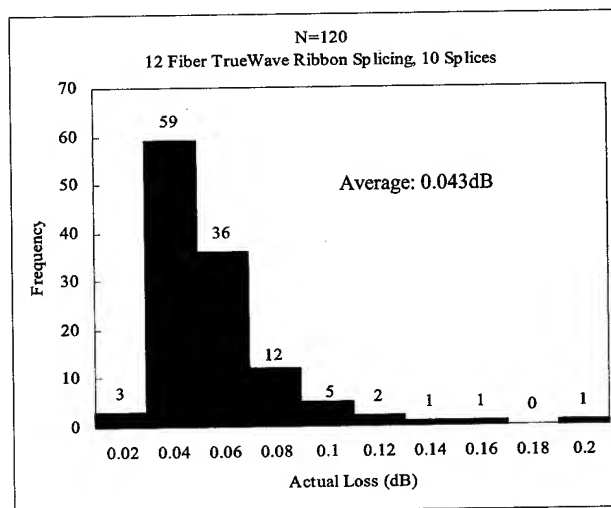


**Figure 11. Splice Loss Results for TrueWave RS
(12-Fiber Ribbon Splicing)**

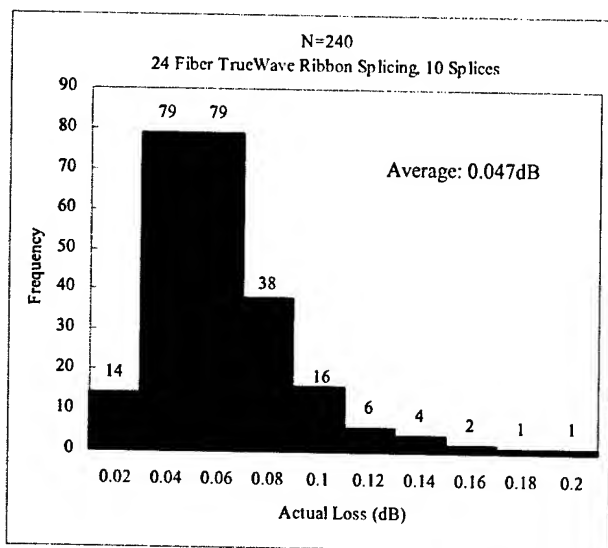


Figure 12. Splice Loss Results for TrueWave RS (24-Fiber Ribbon Splicing)

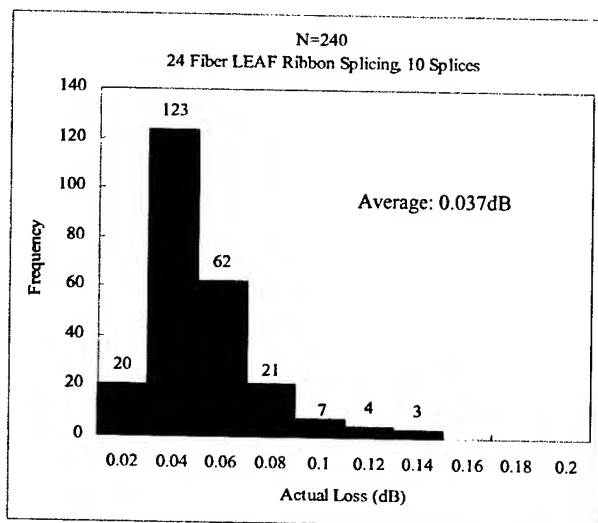


Figure 13. Splice Loss Results for LEAF (24-Fiber Ribbon Splicing)

3. Complete Splicing System

The splicing process for 24-fiber ribbons can be divided into 4 stages: (1) Strip the fiber, (2) Cleave the fiber, (3) Splice the fiber, and (4) Protect the fiber. The proper tools are necessary at each stage in order to complete each part of the 24-fiber ribbon splicing process.

3.1 Stripping the Fiber

In order to splice up to 24-fiber ribbons, a stripping tool is required that is capable of performing the stripping task. Unfortunately, the stripping force required to strip a 24-fiber ribbons is significantly greater than that required to strip a 12-fiber ribbon. Therefore, a stripping tool has been developed with a power assist system, which makes it easy to strip 24-fiber ribbon.

3.1.1 Clamping Force

When stripping a traditional 12-fiber ribbon, an operator is required to clamp the fiber in a fiber holder with enough force such that the fiber does not slip through the fiber holder or that the blades do not slip during the stripping process. Therefore the operator must clamp two lids simultaneously and continuously.

Figure 14 shows about the relation between clamping force required to strip the ribbon and ribbon fiber count. An operator can easily strip the fiber easily for 12-fiber ribbon and lower fiber counts. However, it is difficult to strip 24-fiber ribbon as the clamping force for 24-fiber ribbon is much larger than other ribbon fiber counts. To solve this problem, a latch was added to both lids. Once enough clamping force is added to close the lids, the operator is not required to continuously provide a clamping force to the lids, and ensures proper clamping force regardless of the operator's skill level.

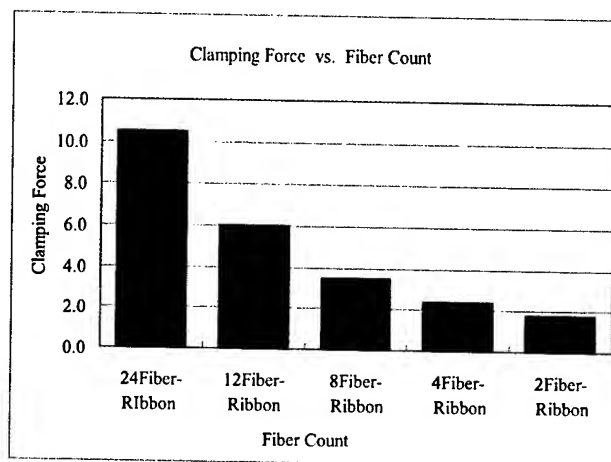


Figure 14. Relation between clamping force and fiber counts.

3.1.2 Pulling Force

The other force required to strip the 24-fiber ribbon is pulling force. As expected, the higher the fiber count of the ribbon, the more pulling force is required. This pulling force is the largest when the stripping process is started. Figure 15 shows about relation between pulling force and ribbon fiber counts. Since requiring an operator to consistently apply this amount of force to strip a fiber, an alternative method was needed. An assist mechanism was attached to the stripper base to solve this problem and significantly reduce the strip force required from the operator. Figure 16 illustrates the power assist on the ribbon stripping tool.

By pulling the assist mechanism lever, it is possible to strip the fiber coating easily. The pulling force required to strip a length of ribbon is inversely affected by the length of ribbon to strip. Figure 17 illustrates the relationship between strip length and pulling force. The shorter the length to strip, the higher the pulling force required. The assist mechanism is designed such that a limited amount of upward pull force on the assist lever is needed to strip a very short length of ribbon.

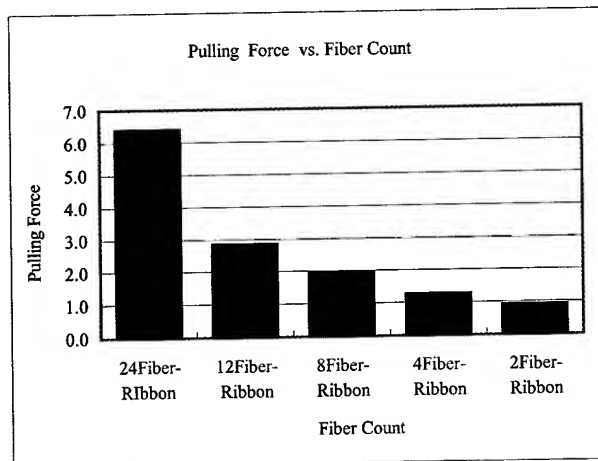


Figure15. Relation between pulling force and ribbon fiber count.

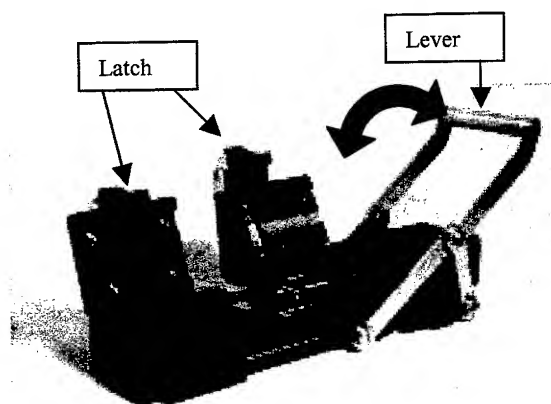


Figure16. Fiber Stripper with locking latches and assist lever

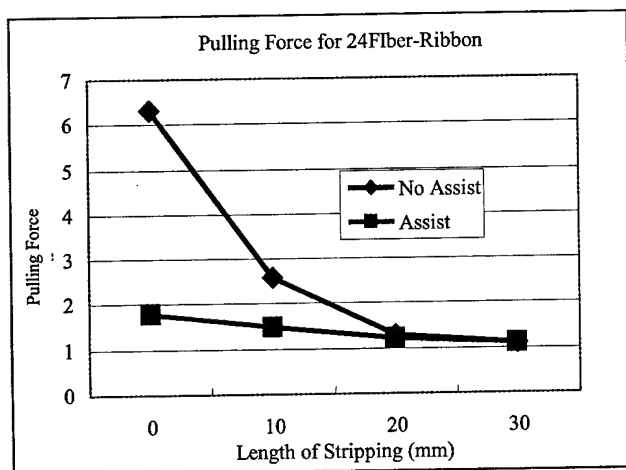


Figure 17. Relation between length strip length and pulling force

3.2 Cleaving the Fiber

Figure 18 shows a new and advanced fiber cleaver. This cleaver has expanded capability in order to cleave up to 24-fiber ribbons. In addition, it has other new and helpful features. For example, the new cleaver performs precision cleaving with just a simple one-step operation. The only action required by the operator is to push downward on the top of the cleaver. Cleaving performance is the same as the previous high precision cleaver, despite the greatly simplified operation. In addition, an optional cleaved-fiber scrap recovery attachment is available. This device easily recovers each cleaved fiber scrap. This is a significant benefit for ribbon splicing in which case each cleaving operation results in multiple cleaved fiber scraps that must otherwise be removed manually by the operator. This feature is of even greater benefit when cleaving 24-fiber ribbons. In addition, cleaver blade life is much longer than previous one.

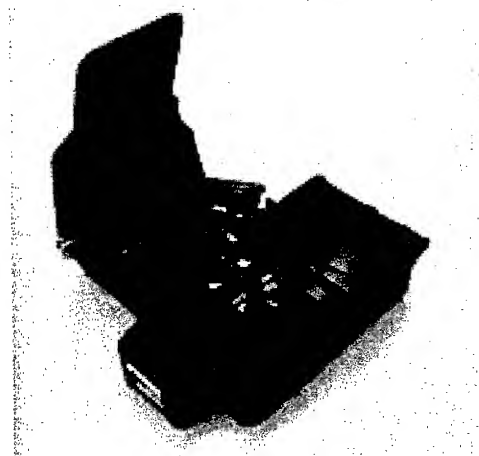


Figure 18. Fiber Cleaver

3.3 Protecting the Fiber

After splicing the 24-fiber ribbon, the spliced region is protected with an exclusive new splice protection sleeve. The splice protection sleeve for 24-fiber ribbon is larger in width than former ribbon splice sleeves, but is similar in thickness to the splice protection sleeve for 12-fiber ribbon. Therefore it fits into many existing splice organizers and splice storage trays. However, due to its greater size and thermal mass, the new sleeve requires more heat for the shrinking process. A completed and heat-shrunk 24-fiber splice sleeve is shown in Figure 19.

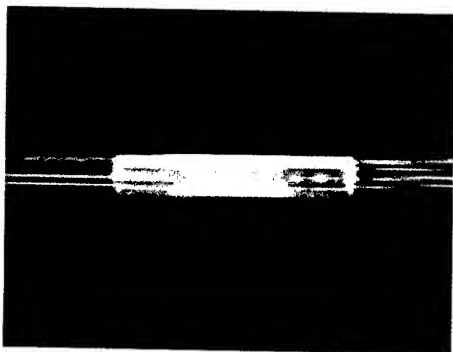


Figure19. Fiber Protection Sleeve

4. Conclusions

A new 24-fiber ribbon splicer has been developed, capable of splicing from 1 to 24 fibers.

- 1) Stable splicing performance with low loss has been realized, even with Non-Zero Dispersion fibers. This performance is achieved by use of the Electrode Driving System that ensures a suitable electrode position and condition relative to the number of fibers to be spliced.
- 2) The splicer is small, lightweight, and suitable for use in harsh outdoor field conditions, including high wind environments.
- 3) The new stripping tool incorporates a power assist system, which makes it possible to strip 24-fiber ribbon with ease.

- 4) The new cleaver provides high-precision cleaving performance with up to 24-fiber ribbons, greater ease of use than the previous model, a scrap disposal system that provides great convenience for ribbon splicing, and improved maintenance features.
- 5) The new tube heater system and 24-fiber splice protection sleeve provide the same heat shrink time as with previous ribbon splice sleeves, therefore doubling productivity of the heat shrink process relative to 12-fiber splicing.

5. References

- [1] David Gibson, Howard Kemp, Kris Kathiresan, Ruben Travieso, Greg Karl, George Mackie, "Field Deployment and Test Results for High Fiber Count Cables", Proc. of NFOEC '97, Volume 1, pp. 333-341.
- [2] K.W. Jackson, N.E. Hardwick, M.D. Kinard, M.R. Santana, R. Travieso, "Optimal Design Strategies for Central Tube Ribbon Cables Comprising 864 Fibers and Beyond", Proc. of IWCS 1999, pp. 118-126
- [3] P. Strong and D.S. Hedrick, "OSP Loose Tube Ribbon Cable - Approaching 2000 Fibers -"Proc. of IWCS 2001 pp.643-649
- [4] H. Sugawara, et al, "Development of 24-Fiber Mass Fusion Splicer", Proc. of IWCS 2000, pp. 203-206
- [5] T. Kusayanagi, et al, "New Mass Fiber Fusion Splicer FSM-30R", Fujikura Technical Review, No.27, pp. 13-16.

Authors



Toshiro Mizushima
Precision Instruments
R&D Dept.
Fujikura Ltd.
1440, Mutsuzaki, Sakura,
Chiba, 285-8550, JAPAN
mizushima@opt.fujikura.co.jp

Toshiro Mizushima received his M.M. degree in Mechanical Engineering from Shinshu University in 1998. He joined Fujikura Ltd. in 1998 and has been engaged in the research and development of optical fiber fusion splicers.



Takeshi Sato
Precision Instruments
R&D Dept.
Fujikura Ltd.
1440 Mutsuzaki, Sakura,
Chiba, 285-8550, JAPAN
tsatoh@opt.fujikura.co.jp

Takeshi Sato graduated in mechanical engineering from Chiba University in 1984. He joined Fujikura Ltd. in 1984 and currently is an assistant manager of the Precision Instruments R&D department.



Sachie Morita
Precision Instruments R&D
Dept.
Fujikura Ltd.
1440, Mutsuzaki, Sakura,
Chiba, 285-8550, JAPAN
sashie@opt.fujikura.co.jp

Sachie Morita graduated in a Electrical Engineering from Chiba University in 1999. She joined Fujikura Ltd. in 1999 and has been engaged in the research and development of optical fiber fusion splicers.



Shonosuke Yaguchi
Precision Instruments
R&D Dept.
Fujikura Ltd.
1440, Mutsuzaki, Sakura,
Chiba, 285-8550, JAPAN
syaguchi@opt.fujikura.co.jp

Shonosuke Yaguchi graduated in mechanical engineering from Keio University in 1979. He joined Fujikura Ltd. in 1979 and has been engaged in the Plant Engineering Section for 12 years and currently is a general manager of the Precision Instruments R&D department.



Hiroshi Sugawara
Precision Instruments
R&D Dept.
Fujikura Ltd.
1440 Mutsuzaki, Sakura,
Chiba, 285-8550, JAPAN
hsugawar@opt.fujikura.co.jp

Hiroshi Sugawara received his M.E. degree in Electrical Engineering from Chiba University in 1995. He joined Fujikura Ltd. in 1995 and has been engaged in the research and development of optical fiber fusion splicers.

A New Cost-Effective Approach to Coastal Underwater Cable Installation

Svend Hopland

Telenor Networks, Infrastructure Division
Oslo, NORWAY

+47 977 00805 · svend.hopland@telenor.com

Abstract

In this paper, we investigate and evaluate two alternative depth data sources for the use in terrain modelling to be used for advanced fiberoptic underwater cable installation along the Norwegian coast. We have shown that a new method using depth data available from the Norwegian Hydrographic Service in so-called fair sheets combined with limited on-site corrective depth measurements with the cable ship's single beam echosounder equipment, is suitable for this purpose. As a consequence, the multibeam echo sounder survey is avoided, thereby reducing the costs significantly. We also describe methods for remote assistance during laying which may contribute to the reduction of costs.

Keywords

Underwater; installation; cost-effective.

1. Introduction

Telenor Network has through the last 10-12 years used an advanced concept for fibreoptic underwater cable installation in our rugged coastal underwater terrain. The details of the concept have been presented several times at IWCS [1], [2], [3]. In the later years we have investigated the possibility of simplifying parts of the installation process in order to achieve lower cost and at the same time maintain the high quality of the installation.

A major and important task is to provide an adequate description of the rugged sea bottom terrain along the cable routes. Earlier a survey ship used to perform a multibeam echo sounder survey of the seabed from which detailed route maps were calculated by advanced data processing. Evidently this is costly, time consuming and possibly in many cases an "overkill" with respect to the amount of depth data actually needed.

In this paper we present and describe a new and more simple method of calculating the route maps and the detailed bottom profiles along which the cables are laid.

2. Depth data sources

If a survey ship performs multibeam echo sounder (MBE) scans of the sea bottom along the cable route, large amounts of data are generated. Subsequent data processing results in a detailed topographical map of the sea bottom, from which the accurate bottom profile along the selected cable route may be calculated. All depth data are given in the World Geodetic System (WGS-84), the official worldwide international horizontal datum at sea.

This method for data gathering results in accurate information, but is costly, and requires a long planning time.

Another possibility is to use depth data available from the Norwegian Hydrographic Service (NHS), contained in so-called hydrographical fair sheets. The fair sheets include considerable amounts of bathymetric data collected during the surveying operations performed by NHS. Coastlines are also included as well as other useful sailing information.

The graticule of the fair sheets has been drawn in different horizontal datums. Up to 1957, Norwegian Datum was used, whereas newer charts have been drawn in European Datum, ED-50. In later years, the graticule is drawn in WGS-84. As a result of improved surveying methods, the amount of data in the fair sheets as well as the accuracy of the data, has increased during the years.

Copies of hydrographic fair sheets may be obtained upon application to NHS which will be forwarded to naval authorities for approval.

This alternative method for data gathering is far less costly, and provided that the accuracy is satisfactory, it stands out as preferable.

3. Comparison of data

3.1 Purpose of bathymetric data

The purpose of the bathymetric data base is diverse. It should provide an adequate description of the sea bottom terrain in order to be able to select an optimal cable route. Also, it should provide a good prediction of the cable length necessary for the installation.

The most important quality, however, is the ability to provide the accurate bottom profile along the full length of the chosen cable route, since this profile is used for calculating the cable pay out during laying. It is recognized that the quality of the installation depends to a great extent on the accuracy of this parameter.

The total amount of depth data constitutes a terrain model which is used to generate a three-dimensional surface grid. This grid is accordingly used for calculating the sea bottom topography and other terrain features such as cable route depth profile and total cable length.

In order to be able to handle the data electronically, the individual depths are characterized with its position; that being northing and easting coordinate values, and its depth value. All data points should be given in the horizontal datum used by the cable ship, which we have chosen to be WGS-84.

3.2 Number of data points

3.2.1 Fair sheets. In Figure 1 is shown the layout of the fair sheet covering the area near one of the landing points for a cable route on the west coast of Norway. The total number of depth data

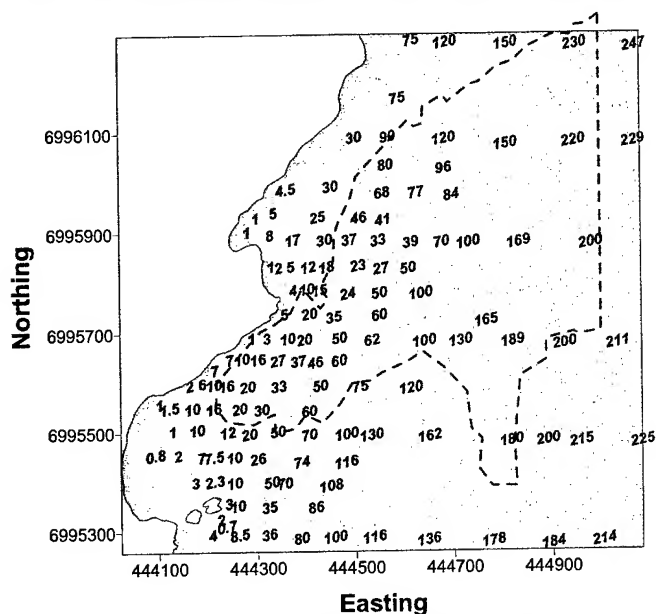


Figure 1. Fair sheet with depth data.

points is 132, which constitutes the terrain model in this case. A MSE survey was performed on a selected part of this area.

3.2.2 MSE-survey.

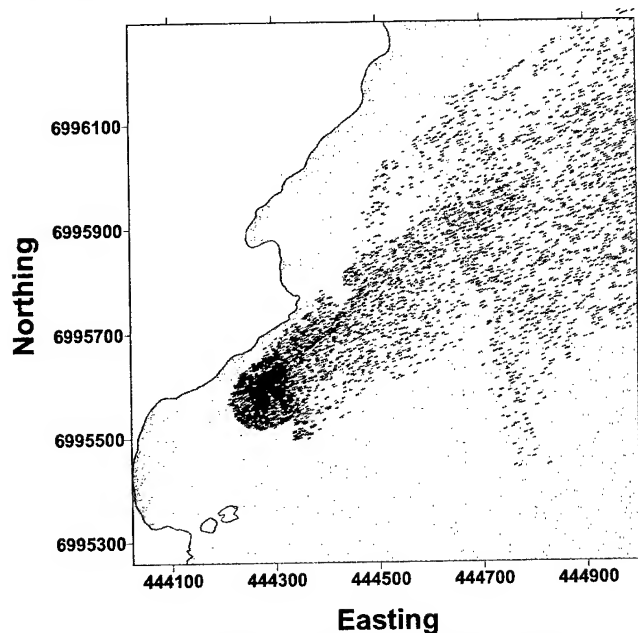
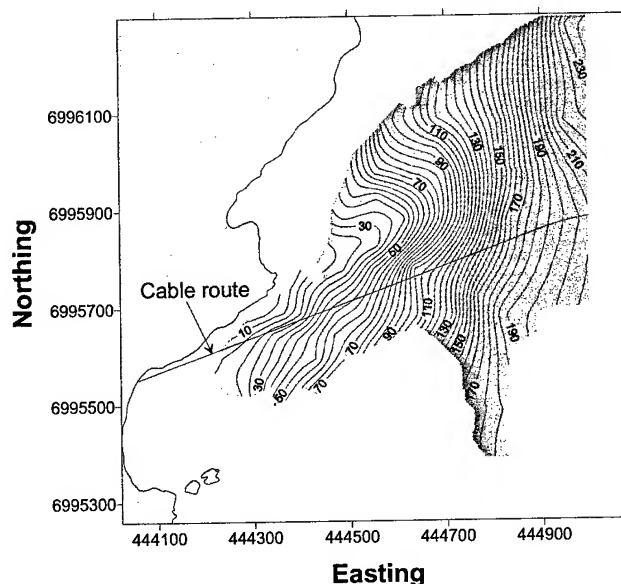


Figure 2. MSE-survey with depth data.

In Figure 2 are shown 5 % of the data points from the MSE survey in the same area. The total number of data points in this case is 119500, which constitutes the terrain model in this case. We note that there are approximately 3 orders of magnitude more data points in the MSE model compared with the FS model.

3.3 Contour maps

3.3.1 Fair sheets. We have used standard scientific contouring PC-software to create a 3D surface grid from the FS terrain model, and a contour map of the FS area has been constructed. In Figure 3 is shown the contour map drawn inside the selected area. The contour interval is 5 m.



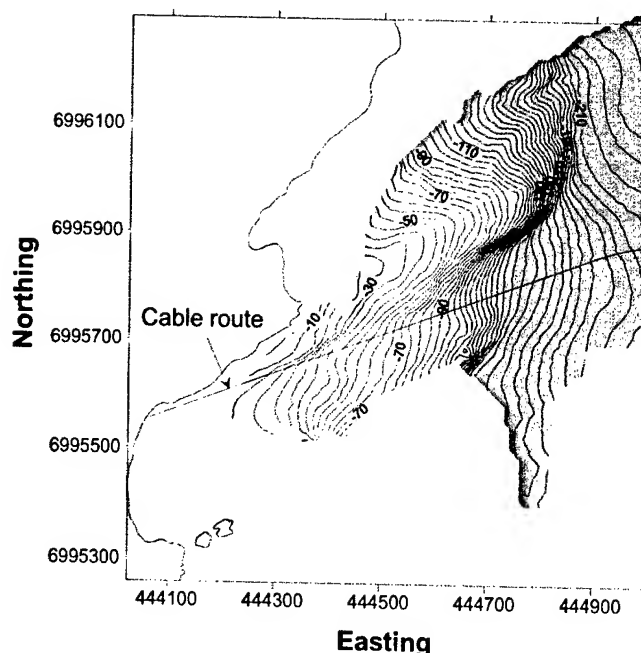


Figure 4. Contour map from MSE-survey.

3.4 Depth profile along cable route

When the cable route is selected, the cable route depth profiles can be calculated using the surface grids. We have calculated the FS depth profile on basis of the FS-grid, and the MBE depth profile on basis of the MBE-grid through the full length of the cable route. In Figure 5 are shown the two profiles near both landing points.

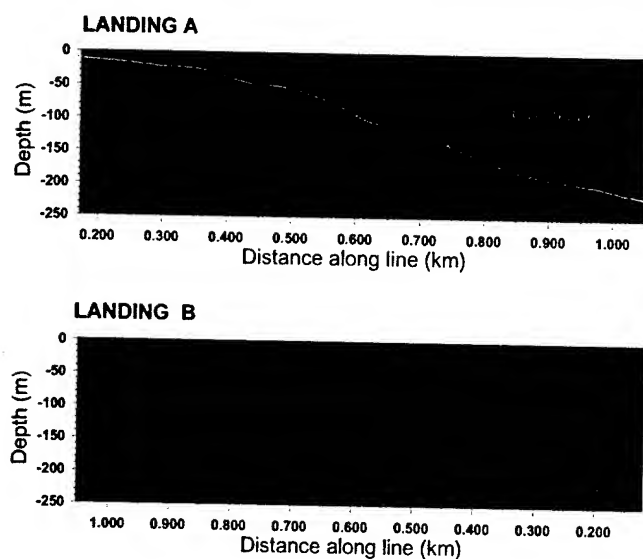


Figure 5. Calculated bottom profiles near landing points.

We observe that the FS-profile closely follows the MSE-profile, except from smaller areas along the slopes. However, even here the discrepancies are rather small.

In the middle part of the cable routes, in areas where the variations in the depth profile are less pronounced, we have found as a general rule that the FS-profile is very close to the MSE-profile.

It is thus possible to use the as-calculated FS-profile for the cable laying through a major part of the cable route. However, during cable laying we depend on high accuracy in all parts of the of the depth profile, and therefore a correction of the profile should be made in areas where the slopes of the depth profile are pronounced.

Clearly, it is possible to use the uncorrected FS-profile for the precalculation of total cable length.

3.5 Method for correcting FS-profile

It is widely recognized that the depth profile along one specific line can be accurately measured with a narrow single beam echo sounder (SBE). It is possible with SBE equipment to obtain depth values with accuracy equivalent to, or better, than the accuracy in a MSE-survey.

The cable ship is equipped with SBE which we use for correcting depth measurements near the landing points and, if necessary, elsewhere along the cable route.

By studying the fair sheets data and the thereof calculated contour maps and depth profiles, we decide which part(s) of the route should be pointed out for corrective measurements.

These measurements are performed at the time when the cable ship is on site for the actual cable laying. The normal pre-laying procedure for the cable ship is to check the navigational sailing and landfall conditions. Adding to these routines, the corrective depth measurements impose little extra time consumption.

The measurement data are transferred to a remote assistant by means of high speed data transmission in Telenor's cellular phone network. Corrective depth data are inserted into the FS-profile and a new and more accurate depth profile is constructed and returned to the cable ship. This takes only a minimum of time, thereby allowing the cable ship to continue its preparation for cable laying without delay.

4. Remote assistance

We are exploring the possibilities of using remote assistance of expert knowledge in order to reduce personnel on board and travel costs.

As pointed out, we now use routinely Telenor's cellular phone high speed data link system to exchange data in connection with the on-site FS depth profile correction.

We also routinely use online laying support via cellular phone. In order to facilitate the on-line laying support, we have developed a lap-top based combined 3D/2D view of the laying process.

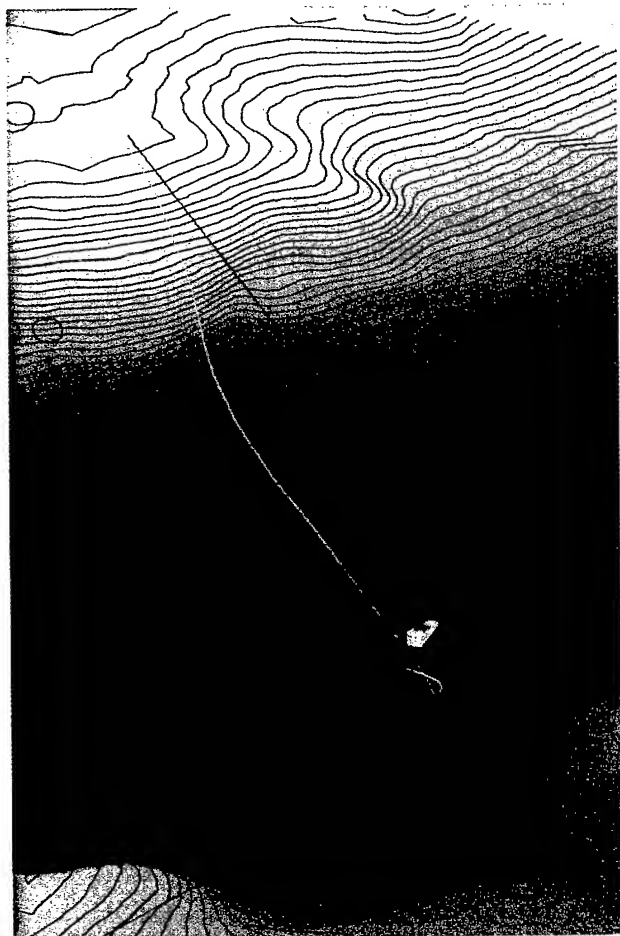
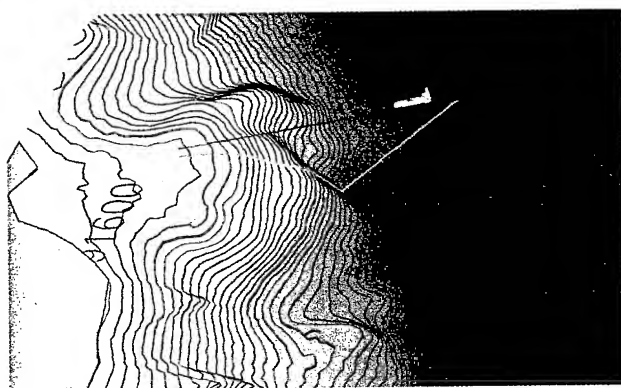


Figure 6: 3D views of cable laying



Using the 3D module, we are able to monitor the cable laying from any wanted angle of view, which give an excellent overview of the current laying situation. This point is illustrated in Figure 6, showing the cable ship from two different view angles.

Simultaneously, we are able to watch a synchronous 2D view of the laying as shown in Figure 7. In the 2D view, the cable catenary and the bottom slopes stand out clearly thus adding a valuable supplement to the 3D view.

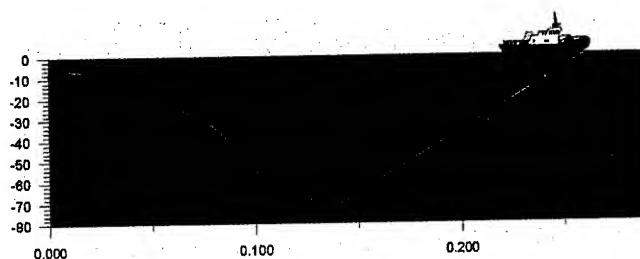


Figure 7: 2D view of cable laying.

5. Conclusions

We have investigated and compared bathymetric data available from the Norwegian Hydrographic Service in so-called fair sheets (FS) with data from a full multibeam echo sounder survey (MSE). The data point density were typically 3 orders of magnitude higher for the MSE data set compared with the FS data set. We utilised standard scientific terrain modelling PC-software for calculating cable route maps and bottom profiles using the vastly different data point densities.

The results have shown that the FS data point density is sufficient to give a adequate description of the terrain which allows for a optimal cable route selection and an accurate total cable length pre-calculation. Even the calculated FS bottom profile follows closely the MSE bottom profile for most parts of the cable routes.

However, in order to determine the bottom profile with high accuracy in all areas, corrections have been made on the pre-calculated FS-profile. By studying the fair sheets and the thereof calculated maps, we locate part(s) of the depth profile, commonly near the landing points where the slopes are steep, where better accuracy is required. In these areas, the profile is measured on site by the cable ship's single beam echo sounder just prior to cable laying.

Corrective depth data are transferred to a remote assistant via Telenor's cellular phone high speed data link system, and a new and accurate profile is constructed and returned to the cable ship within few minutes.

We have explored the feasibility of remote assistance of expert knowledge during cable laying. We now use routinely the Norwegian cellular phone high-speed data link system for exchange of data in connection with on-site profile building as well as online support during laying. We have in addition developed a combined 3D/2D-view of the cable laying process in order to facilitate remote assistance.

6. Acknowledgments

Special thanks to Magnar Greve, Telenor, who is responsible for the operation of Telenor's cable laying system on board the cable ship.

7. References

- [1] Svend Hopland and Albert Klykken: "Installation of submarine fiberoptic cables in rugged coastal terrain". Proceedings IWCS 1992, Reno Nevada, pp. 492-496.
- [2] Svend Hopland: "Investigation of cable behaviour in water during laying of fiberoptic submarine cables". Proceedings IWCS 1993, St. Lois Missouri, pp.734-739.
- [3] S. Hopland: "Alter course cable behaviour in water during laying of fiberoptic submarine cables." Proceedings IWCS 1995, Philadelphia, Pennsylvania, pp.592-598.

High-Voltage Performance and Reliability of Insulated Products in Undersea Cable Systems

Steven Bernstein, Mitchell L. Jackson, Maurice E. Kordahi, Chung-Shin Ma, Seymour Shapiro, Qian Zhong

Tyco Telecommunications (US), Inc.
Eatontown, New Jersey

Abstract

Undersea cable systems are constructed with a series of cable, optical amplifiers, and joints. These systems are typically operated with considerably high DC voltages since optical amplifiers, essential to the transmission of the communication signal and located at periodic intervals within the system, are powered from shore stations. High-voltage breakdown of the power path is catastrophic and generally renders the system inoperable. The long design service life and extremely low repair allowance place a very stringent requirement on the performance and reliability of insulated components, such as cable and joints, in these systems. In this work, we report our recent study on critical factors influencing the high-voltage breakdown of these insulated components as well as those impacting the prediction of service lifetime.

The initial phase of the program emphasized the development of a reproducible and reliable test protocol. Using the established methodology, we then examined the insulated components under accelerated test conditions. The high-voltage performance was evaluated, and potential failure mechanisms were further studied, both analytically through material characterizations and statistically by correlating them to the breakdown data. These findings are significant in the accomplishment of our robust design of products, as well as contribute to the fundamental understanding of high-voltage DC insulation breakdown phenomena.

Keywords

Undersea cable systems; high-voltage performance and reliability; insulation materials; polyethylene; DC electrical breakdown; cable and joints

1. Introduction

The use of optical amplifiers in undersea telecommunication systems requires that they be powered by high DC voltage, which must be insulated from the sea ground. A number of insulated components are used in a typical undersea system. For example, polyethylene jacketed cable is connected with polyethylene overmolded joints to ensure optical, electrical, and mechanical continuity. Each component has a unique geometry, and therefore a different electrical field stress, when the system voltage is applied. Furthermore, the selection of materials and processing

conditions can vary, making it challenging to characterize the high-voltage performance of the overall system [1].

To further complicate testing, DC high-voltage test methodology for undersea system components is specific to each component, as they have their unique material, manufacturing, and electrical characteristics. Much ambiguity is further introduced when various test setups are considered [2].

In this paper, we report our continuing effort with a systematic approach to address the robustness of insulated components used in undersea cable systems. By standardizing the test protocols used, we will demonstrate that our preliminary results provide a more reliable benchmark for the high-voltage performance of various insulated components used in our system. We will also report our initial results attempting to delineate the effects of materials and processing conditions on the electrical properties of the insulation. Lastly, our data of various insulated components illustrate that the overall undersea cable system has a significant design margin in its high-voltage performance.

2. Test Protocol

2.1 Test Methods

Two test regimes were used: DC ramp-to-failure (RTF) test and DC lifetime (LT) test. In both cases, samples of insulated components were submerged in artificial ocean solution whose salinity and conductivity are typical of ocean environments. High voltage, typically negative in polarity, was applied to the conductor. In RTF tests, voltage was ramped at a constant rate, typically 60 kV/min until the breakdown occurred. In LT tests, constant voltage was applied to the samples, and time to breakdown was monitored.

2.2 Sampling Statistics

Weibull statistics were used to model the breakdown data. Undoubtedly, more data points would provide more accurate representation of the "true" probability distribution and most likely increased confidence levels. Nevertheless, constraints such as resource availability, cost, sample quantity available for testing, and time etc., preclude us from arbitrarily increasing the sample size. With an assumption that test accuracy is high and variability is small and thus negligible, we used a Monte Carlo method to determine the bounds on the slope (β) and characteristic breakdown voltage (η) of the Weibull distribution by varying the

number of samples. Our analysis indicated that a sample size of 10 provides a good compromise between an accurate representation of probability distributions and the diminishing return at a considerably increased price of a relatively small accuracy and confidence enhancement.

2.3 Termination Preparation

When high voltage is applied to test samples, particularly in the case of RTF test of insulated components with significantly high breakdown voltage (e.g., >200 kV), proper termination preparation is critical in ensuring the minimization of voltage "flashover" and "triple-point" breakdown (a triple point is defined as insulation, air, and water interface), commonly known artifacts of the test.

Several strategies were employed to eliminate flashover and triple-point failures in long-term tests, and to raise the threshold voltage of these termination failures during RTF tests to allow failure of the insulated product. Among the techniques investigated were:

1) Greater termination length, measured from the water surface to the electrode, resulted in higher RTF voltage. Increased termination length tends to raise the threshold voltage of direct water-to-electrode flashover (independent of the cable), and provides a longer path for resistive grading of surface charge.

2) The use of a field (or stress) control tube (SCT) that is applied coaxially over the cable termination. When electrically connected to the electrode and water, the SCT can provide resistive grading to prevent charge accumulation that could lead to overstress or corona discharge. The use of various SCT configurations, however, did not show significant improvement in flashover suppression.

3) Initially a U-shaped sample configuration, with terminals widely separated, was employed for RTF tests; this configuration exhibited no shielding effect at all. Configuring two or more cable terminations (at isotopotential) in parallel (Figure 1), in close proximity, demonstrates a significant shielding effect. As a result, the threshold voltage for flashover was observed to increase. Triple-point breakdown voltage was also much increased in the parallel termination configuration.

4) Application of an oil layer above the water surface gave mixed results. Oil-water interface failure usually occurred with flashover; this is believed to be related to leakage current at the dissimilar liquid interface.

3. Test Results

3.1 Electrical Field Stress of Samples

The samples used for the study are the representative insulated components in undersea cable systems. They are designated as Insulated Components A through D, as they differ in geometry, material, and processing conditions. The electrical field stresses

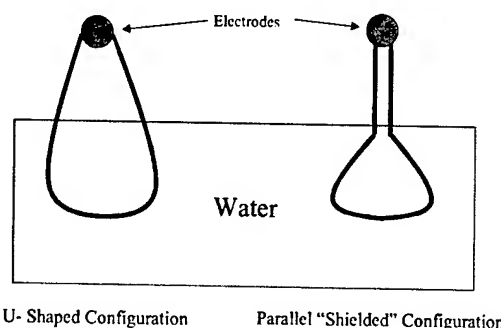


Figure 1: Schematic of test sample configuration

generated in these samples at the test voltages are summarized in Tables 1 and 2 below:

Table 1. Electrical Field Stress of RTF Test

Sample	Testing Voltage (kV)	Field Stress (kV/mm)
Insulated Component A	<800	280
Insulated Component B	<500	325
Insulated Component C	<300	180
Insulated Component D	<400	265

Table 2. Electrical Stress of LT Test

Sample	Testing Voltage (kV)	Field Stress (kV/mm)
Insulated Component A	500, 200, 150, 120, 100	176, 70, 53, 42, 35
Insulated Component B	100	65
Insulated Component C	100	85
Insulated Component D	100	65

3.2 Test Conditions

In RTF tests, samples were usually controlled in a water bath at room temperature. To evaluate material capability, RTF tests at different temperatures were also performed. For the LT test, temperature control is critical. Without temperature control, the breakdown life (time to failure) may have a 10 to 15% error. To minimize this, ideally, a cooling/heating system is needed to control the temperature of the water tank. A more cost effective approach is to set the water temperature at different levels above room temperature in the test, and to use steam to control the tank temperature in a narrow range. Two to three temperature levels were planned for each of the voltage level of the LT test.

For RTF test, the rate of the voltage ramp was about 60 kV/min. Flashover was monitored carefully during each RTF test.

3.3 Test Data

3.3.1 Component benchmarking. Table 3 summarizes characteristic RTF breakdown voltage for the components tested at room temperature.

Table 3 Summary of RTF Breakdown Voltages

Sample	Low Breakdown Voltage (kV)	High Breakdown Voltage (kV)
Insulated Component A	-	>500
Insulated Component B	245	500
Insulated Component C	185	260
Insulated Component D	350	360

3.3.2 Effect of temperature. The sea bottom temperature is fairly uniform at about 4 C except near the shores and volcanic hot spots. The insulated product is sometimes exposed to 20 C near the shore. This is also where the voltages are typically the highest. Therefore ambient temperature testing is appropriate, and modestly conservative. The literature shows that insulation properties increase exponentially with temperature decrease between 40 and 4 C. However, most of the data was taken with AC voltage loads.

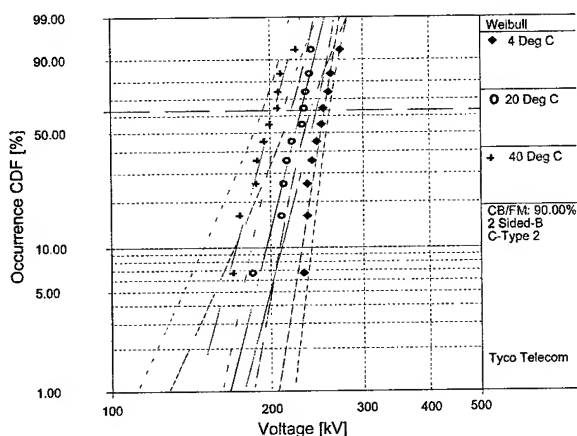


Figure 2: RTF data of Insulated Component C at various temperatures.

To better understand the design margins under DC load at various temperatures, RTF and LT tests were performed at multiple

temperatures. Results are reported herein for Insulated Component C, which contains multiple interfaces. Figure 2 shows that the characteristic RTF breakdown voltage [the characteristic breakdown voltage is defined as the voltage at which the cumulative probability of failure is equal to $1-(1/e)$, or 0.632] of about 253 kV at 4 C vs. 229 kV at 20 C vs. 204 kV at 40 C.

The Insulated Component C samples were also tested at 100 kV at 18 and 4 C. The characteristic time to failure was about 4 hr. at 18 C compared to about 29 hr. at 4 C, as shown in Figure 3.

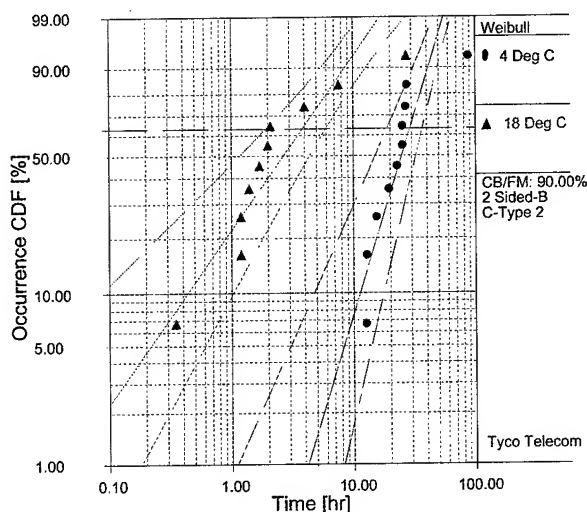


Figure 3: Breakdown data of Insulated Component C tested at 100 kV, at various temperatures.

3.3.3 Effect of interfaces. The effect of interfaces and aging on high-voltage breakdown performance was evaluated. The results from samples of Insulated Component B are shown in this report. Insulation repairs are occasionally done on cable jackets to restore insulation continuity for the components. This provides a meaningful sample since the repair introduces two amalgamated interfaces and maintains its cylindrical geometry. Figure 4 shows schematically the configuration of the sample. Two sample conditions were evaluated: one was electrically aged for 1000 hr. at 100 kVDC, and the other was pristine without any aging. Both samples were then subjected to RTF test. Figure 5 shows the breakdown voltage for both aged vs. pristine Insulated Component B samples with interfaces.

3.3.4 Effect of dielectric discontinuity. One example of dielectric discontinuities is an air gap between an insulator and a

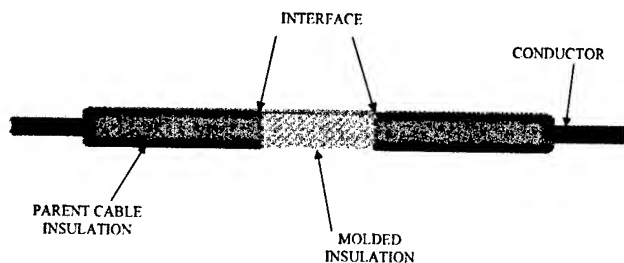


Figure 4: Schematic of Insulated Product B

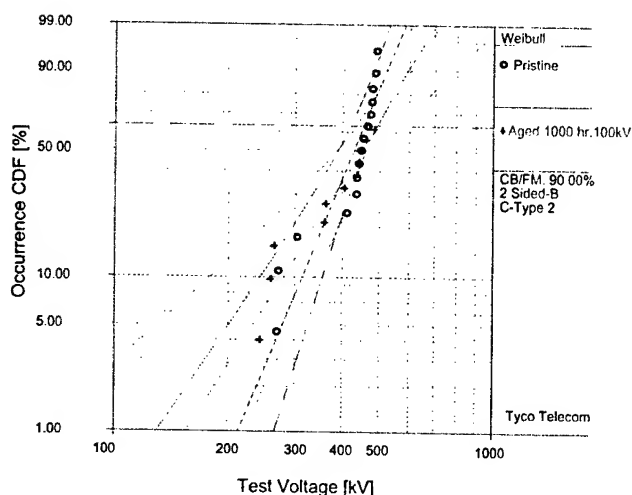


Figure 5: Breakdown data for aged vs. pristine samples

conductor. A dielectric discontinuity occurs due to the difference in dielectric constants in the adjacent media. Figure 6 (dielectric discontinuity size vs. life at 100 kV) shows the general relationship between the life and normalized dimension of the discontinuity for long-term high voltage testing.

4. Analysis and Discussions

The ability to follow a repeatable and methodical testing protocol allows us to benchmark high-voltage performance for various insulated components that constitute the undersea cable system.

Our results revealed the importance of an appropriate setup for the test. One key issue is the ambiguity created by the termination, in particular, when the insulated components were tested at high voltage (e.g., > 200 kV). Although the leakage current and the triple point pose a significant experimental challenge, we have demonstrated repeatability of test data through minimization of leakage currents by using multiple parallel samples, installing a large field suppression toroid on the terminal electrode, and

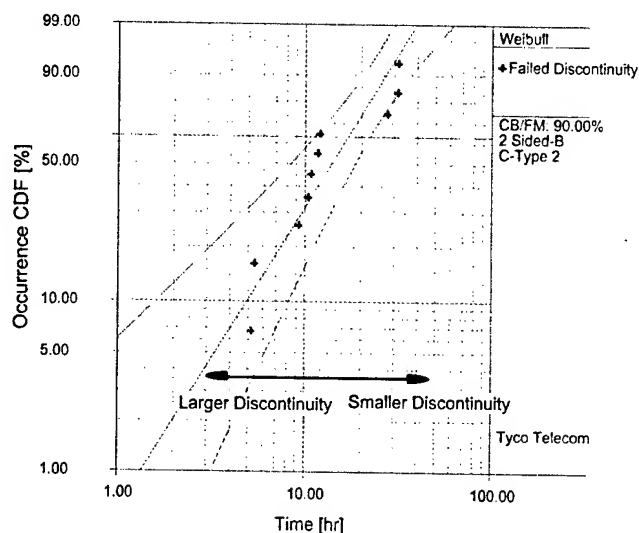


Figure 6: Insulation lifetime at 100 kV as a function of discontinuity size

employing longer sample terminal lengths, all of which significantly mitigated the problems associated with the triple-point failure as well as flashover.

The dependence of breakdown voltage (or time) on the temperature is encouraging as it confirms the conservative margin in our routine tests that are typically conducted at ambient temperatures. Further work is needed to quantify the temperature dependence of the breakdown voltage for various components, although it is likely that a thermally activated process is responsible for the temperature dependence.

The data from Insulated Component B samples illustrate the reduction of characteristic breakdown voltage for those containing an interface, although the difference is small due to the use of ultra-clean materials and stringent processing conditions. One of the important findings in this work is to demonstrate the value of material selection. A number of critical parameters are engineered into the selection of the polyethylene insulation compound. For example, a high degree of cleanliness minimizes local electrical field enhancement due to contaminants. Minute metallic particulates are particularly harmful at the amalgamation zone.

Another interesting result is manifested in the aging data. One commonly attributed reason for electrical degradation at the interface is the lack of amalgamation due to thermal degradation of polymeric materials during processing. In this case, the by-product of oxidized polyethylene can pose a serious threat for the molded interface. By using an optimized stabilizer package, one can achieve a robust interface that is essentially of the same quality as the parent material. Our data suggest that aged samples were no less robust than unaged samples under identical test conditions (Figure 6). One also should pay particular attention to the thermal history of a

given resin, in that ample qualification activities should be carried out to minimize the thermal-mechanical stress and chemical degradation that are typically seen in the molded zones.

The presence of hydrostatic pressure in the ocean bottom environment in most cases serves to "close up" defects such as air gaps. Therefore, our current testing scheme of ambient pressure, in fact, provides additional design margin for insulation robustness. While the high-voltage testing data from our insulated components are consistent with the expected compromise of the breakdown voltage for components with increased field stress due to geometry, multiple interfaces or complicated thermal history, all the components tested demonstrated a significant safety margin for the longevity of service life for an undersea system. Additional life tests are currently in progress in an attempt to continue to refine the lifetime model and provide more reliable prediction of system life.

5. Conclusions

Our continuing efforts in the high-voltage program demonstrated that a repeatable test protocol allowed us to benchmark insulated components in our undersea cable system containing complex geometry, material and processing differences. Our data show significant design margin based upon the temperature dependence of the breakdown performance. In addition, with optimized selection of materials and processing conditions, we are able to minimize the detrimental effect due to amalgamation interfaces.

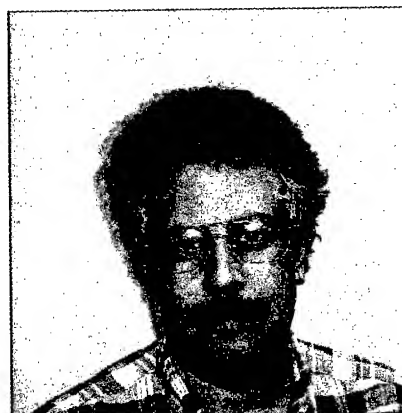
6. Acknowledgments

The authors wish to acknowledge Lorence Augh, Marios Avgousti, Ray Tuminaro, and Li-Ming Zhou for their significant contributions to this program, and Gary Gullo and George Bruno for their support in the sample preparation.

7. References

- [1] L.A. Dissado, I. Doble, S. V. Wolfe, P. A. Norman, A.E. Davies, G. Chen, Q. Zhong, W. B. Wargotz, M. M. Sanders, "Electrical Reliability of dc-operated Submarine Telecommunications Cables," *IEEE Trans. Dielectrics and Elec. Insulation*, 4(1), 1-9 (February 1997).
- [2] L.A. Dissado and J.C. Fothergill, *Electrical Degradation and Breakdown in Polymers*, Peter Peregrinus, U.K., (1992).

8. Authors



Steven Bernstein

Tyco Telecommunications (US), Inc., Eatontown, NJ 07724

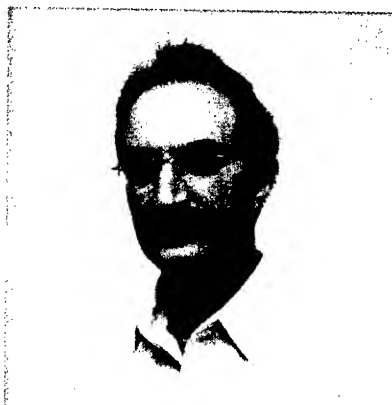
Steven Bernstein is a Distinguished Member of Technical Staff at Tyco Telecommunications Laboratories. He has been employed by AT&T Undersea Systems and then Tyco since 1982. He has worked on joint and coupling, insulation process development and high-voltage testing. Steve has a BSME from Fairleigh Dickinson University and an MSE-ME from the University of Michigan.



Mitchell L. Jackson

Tyco Telecommunications (US), Inc., Eatontown, NJ 07724

Mitch Jackson received a B.S. in Engineering Science and Mechanics (1989) and an M.S. in Engineering Mechanics (1993) from Virginia Polytechnic Institute (VPI). After a fellowship at the Oak Ridge National Laboratory he returned to VPI to complete his Ph.D. in Materials Engineering Science in 1999. He then joined Tyco Telecommunications as a member of the System Reliability group working on materials issues related to electronic and optical components, and undersea repeaters. He is currently a Sr. Member of Technical Staff working with the Cable Development group of Tyco Telecommunications.



Maurice E. Kordahi
Tyco Telecommunications (US), Inc., Eatontown, NJ 07724

Maurice Kordahi is Director of the Wet Plant Mechanical Development group and has been in the undersea cable business with Tyco Telecommunications Laboratories (formerly part of AT&T Bell Laboratories) since 1984. He is currently responsible for cable jointing, and repeater mechanical design. He has been instrumental in the design and development of methods, procedures, and equipment for installation and maintenance of submarine cable systems. Dr. Kordahi received his B.S. degree from the University of Dayton in Ohio, and both an M.S. and Ph.D. degrees from the University of Kansas in Lawrence, all in mechanical engineering.



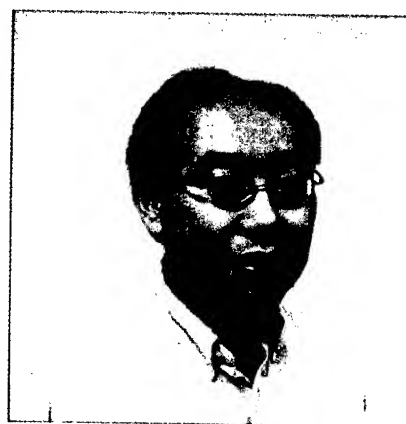
Seymour Shapiro
Tyco Telecommunications (US), Inc., Eatontown, NJ 07724

Seymour Shapiro is Managing Director of Undersea Cable and Mechanical Development at Tyco Telecommunications Laboratories and has been in the undersea cable business for over two decades. He joined AT&T Bell Laboratories in 1969 after he obtained his undergraduate degree from the City College of New York. His graduate degrees are from Columbia University; all in mechanical engineering. He is currently responsible for providing leadership in all aspects of mechanical design and development in undersea cable systems.



Chung-Shin Ma
Tyco Telecommunications (US), Inc., Eatontown, NJ 07724

Chung-Shin Ma is a Technology Director in the R&D of Tyco Telecommunications. He has been working in the undersea cable business since middle of 80's and joined Tyco Telecommunications in 1997. His interest is in the cable developing and related areas such as: cable design, manufacture, and fiber/cable characterization.



Qian Zhong
Tyco Telecommunications (US), Inc., Eatontown, NJ 07724

Qian Zhong is Director of Cable Development at Tyco Telecommunications Laboratories (formerly part of AT&T Bell Laboratories). He joined AT&T Bell Laboratories in 1992 after receiving his Ph.D. in Materials Science and Engineering from the University of Pennsylvania. He is currently responsible for the design, development, and implementation of cable, fiber, and materials in undersea telecommunications systems.

Nonferrous Armor Cable Termination: Ironing Out the Details

David A. Giordano, Maurice E. Kordahi, Ralph J. Rue, Robert K. Stix

Tyco Telecommunications Laboratories
Eatontown, NJ

Abstract

A new undersea cable termination has been developed and qualified to couple armor strength members of nonferrous undersea fiber-optic cable in couplings and joints.¹ Its use covers repeater couplings, double-armored cable joints, and single-armored cable joints. The termination holds nonferrous armor strength members (rods) without slippage and without reducing their tensile strength. This is accomplished using a novel way of fastening the rods in an underlying matrix.

This method of terminating nonferrous (Aramid) rods is unique since it does not use standard termination methods. It reduces the overall length of the termination while making it stronger. A standard Aramid rod termination would be considerably longer. Another essential feature in this termination design is the even load sharing amongst all of the Aramid rods. The connecting matrix is essential for this and transfers the tensile load from the rods to the load-bearing housing.

This paper presents the mechanics of the termination along with results from experimental testing. In addition, the pertinent termination parameters are discussed.

Keywords

Cable; Termination; Coupling; Joint; Undersea; Optical Fiber; Aramid; Nonferrous; Submarine

1. Introduction

A Branching Unit (BU) is a special underwater housing that has a single cable on one side (Trunk Cable) and two branch cables on the other side (Leg Cables) as shown in Figure 1.

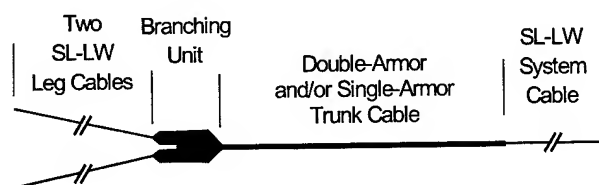


Figure 1. Example Branching Unit Configuration

The first application was targeted at BUs. Early fiber-optic submarine systems deployed BUs at water depth less than 2000 meters where conventional deep-water cable has sufficient strength to serve as a trunk cable.

Recently, submarine cable systems have required BUs to be deployed to greater depths. A new trunk cable with higher

tensile strength-to-weight ratio was developed to allow the BUs to be deployed and recovered from such depths. The selected cable uses Aramid rods² added externally to the polyethylene-insulated core³ cable. These rods have an excellent strength-to-weight ratio that provides the required tensile strength with minimum additional cable weight. Therefore, a method of terminating the Aramid strength members was needed.

Although this undersea cable termination was initially developed for use in BU couplings and associated joints, it can also be used in both nonferrous and ferrous applications not associated with BUs.

2. Applications

2.1 Cable Types

There are two typical varieties of nonferrous Aramid armor cables. One is a double-armored (DA) design and the other is a single-armored (SA) design. The cross sections of the two armored cables are shown in Figure 2.

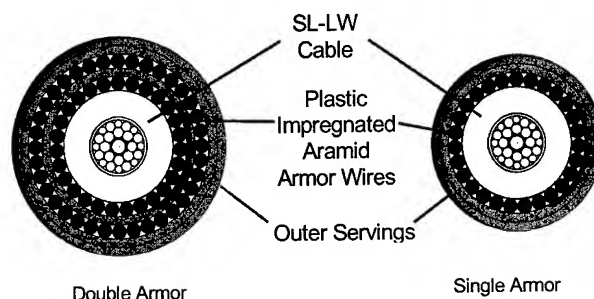


Figure 2. Cable Structure

2.2 Application Environment

Undersea cable terminations are assembled in both factory and field environments. The majority is constructed in a factory environment.

Terminations are assembled during the following three phases of a system's life: (1) system assembly (usually in a factory), (2) system installation (including shipping), and (3) system maintenance (usually in the field after installation). For some installations, terminations are applied after the cable has been shipped from the factory but before it has been deployed. In these cases, the work is done on a ship or barge—either dockside or at-sea.

¹ This termination design approach is also suitable for steel-armored cable types.

² These are used in place of traditional zinc-coated steel wires.

³ The core cable and its termination are not discussed in this paper.

Termination designers are keenly aware of the variety of conditions that must be considered in selecting and perfecting a termination method. Salt air, open decks, lighting, vibration, and temperature variations are among the factors addressed. In addition, the tools, materials, handling, logistics, and regulations for each assembly area must be accounted for. For example, the equipment and materials must be portable, shippable, and storable in factories, depots, and on ships, as needed.

3. Functional Requirements

The following are typical requirements for terminations:

- The termination itself shall be recoverable by the conventional deep water system cable in foul weather conditions.
- The termination shall meet typical factory and shipboard handling requirements for undersea fiber-optic joints.
- The termination shall have sufficient strength to recover repeaters and branching repeaters at water depths up to 6000 meters. This shall include tension, torque, and bending stresses.
- The terminations shall withstand the hydrostatic pressure associated with a depth of 6000 meters.
- The termination shall have a typical undersea design life.

During development and qualification, a variety of aggressive tests are performed to validate that terminations are capable of meeting these requirements.

4. Termination Description

4.1 Repeater Coupling

A *cable-to-repeater* coupling terminates double-armor or single-armor cables to either a repeater or BU. In addition, it transfers torque to the repeater and restricts bending of the cable. Figure 3 shows a sketch of a typical repeater coupling. The mechanism for transferring the cable load is shown in Figure 4.

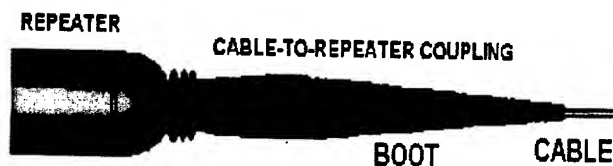


Figure 3. Repeater Coupling

4.2 Cable Joints

A *cable-to-cable* joint transmits tension and torque from one cable to another. In addition, it restricts the bending of the cable at the entry points. Cable-to-cable joints can be used to connect the following combinations of cables:

- DA to DA
- DA to SA
- SA to SA

All of these joint assemblies use identical components as shown in Figure 5.

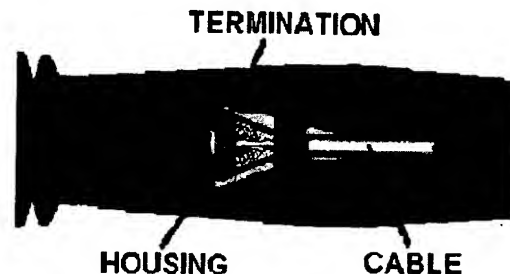


Figure 4. Coupling Cross Section



Figure 5. Cable Joint Arrangement

Joints are symmetrical about the center of the housing. The loading of the cable is transmitted to the termination then to the housing as depicted in Figure 6.

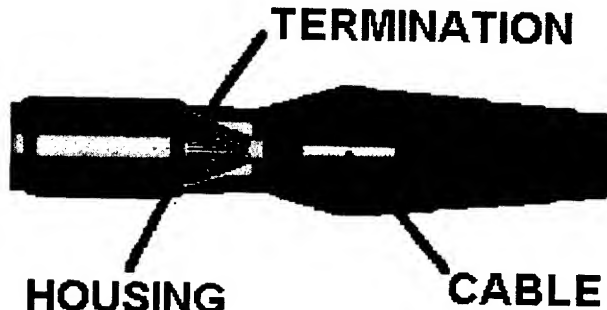


Figure 6. Joint Cross Section

5. Termination Design

5.1 Termination Features

This novel termination combines swaged ferrules, Spelter-type socketing,⁴ and adhesive potting—all in one compact assembly. The Aramid rods are individually crimped and equally spaced to allow uniform distribution of the potting matrix. This

⁴ Spelter-type sockets originally were constructed with molten zinc cast into cone-shaped baskets around broomed-out wires of the cable or rope that they are fastened to. Newer socketing methods replace zinc with epoxy or similar material.

combination of features reduces the overall length of the termination and provides a stronger termination.

The connecting matrix provides a load-bearing surface for the ferrules and is essential for maintaining an even load amongst the Aramid rods. In addition, it eliminates the need for complex and costly shimming arrangements that are typically used to even out the loading among strength members.

By using an adhesive potting material, the termination is suitable for environments that are ordinarily more corrosive for ferrous-based materials typically used in armored cable terminations. The epoxy blocks seawater entry and associated corrosion and, at the same time, isolates the strength members from the external hardware. In this application, the cable strength members can be either ferrous or nonferrous since there is no Galvanic corrosion, limited oxygen access, and protection from seawater.

Matrix or potting material selection is based on compressive strength, cure time, shrinkage, cure temperature, viscosity, shelf life, and seawater resistance.

5.2 Ferrule Strength

Ferrule (i.e. Aramid rod termination) strength is related to the properties of the radial crimp and the strength member (rod). The governing equation for the termination strength, F_R , is given in Equation 1.

$$F_R = \int_0^{L_c} \mu P(2\pi R) \cdot \delta L \quad (1)$$

where μ is the coefficient of friction, P is the radial pressure induced, R is the Aramid rod diameter, L is the ferrule length and L_c is critical ferrule length.

6. Test Results

6.1 Termination & Ferrule

The first phase of the testing involved determining the relationship between ferrule strength and crimping length. During ferrule development, crimp pressure, material, diameter, and length were all evaluated and selected to provide sufficient design margin to account for process variations. Using experimental results in conjunction with Equation 1, the ferrule parameters were finalized.

Figure 7 provides a comparison of the new termination method and the standard termination method. It shows that the new termination method significantly reduces the critical termination length. Standard termination methods, which have a considerably lower coefficient of friction, can result in slippage between the Aramid Rod and adhesive.

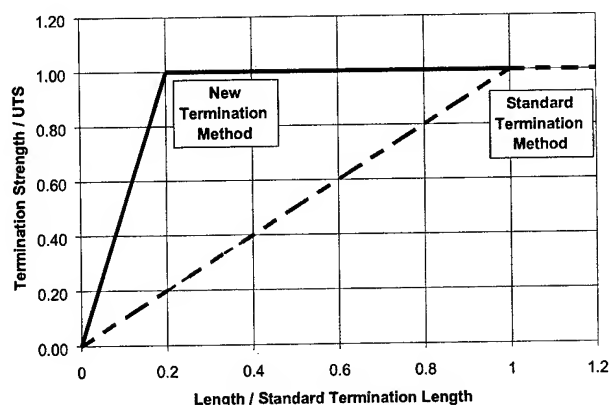


Figure 7. Termination Strength and Critical Length

Without the ferrules, the termination would be considerably longer. This shortening is made possible because the force developed between the Aramid Rods and radial crimp is much greater than the adhesion between the Aramid Rods and epoxy. Typical epoxy-only terminations are weaker due to the relatively low adhesion which results in slippage between the Aramid Rods and epoxy.

6.2 Coupling and Joint

Coupling, joints, and cables were subjected to a series of standard undersea qualification tests to simulate the most severe in-service environmental conditions expected in the field. These included tension, bending, temperature, and pressure testing.

Results of the double-armored termination ultimate tensile strength are indicated in Figure 8. This figure indicates that the strength of the double armor termination exceeds the rated cable UTS.

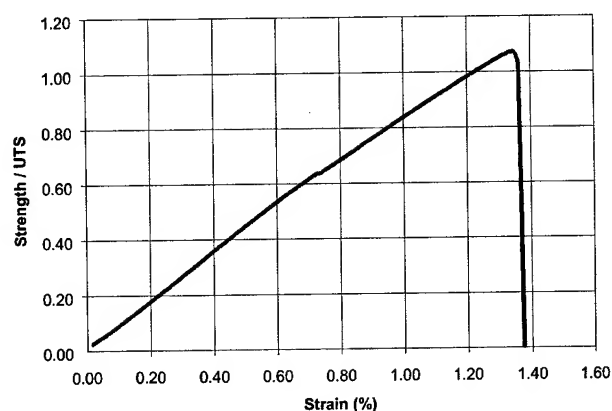


Figure 8. Double Armored Joint / Coupling Ultimate Tensile Strength Test Results

Upon test completion the joints and couplings were meticulously dissected and inspected. Dissection revealed no damage to any components. The design met all of the imposed mechanical, electrical, and optical requirements and demonstrated that the performance of the new termination design is robust.

7. Conclusions

A new undersea cable termination has been developed and qualified to couple armor strength members of nonferrous (and ferrous) undersea fiber-optic cables in couplings and joints. Thorough testing has proven this termination design to be both robust and fully capable for use and deployment in undersea systems.

This approach achieves numerous advantages through savings in cost, reduced assembly times, improved performance, and wider versatility. It is suitable for a variety of applications including BU couplings, repeater couplings, double-armored cable joints, and single-armored cable joints. In addition to holding armor strength members without slippage, this compact termination method reduces the overall length of the termination without sacrificing performance.

We anticipate that as short-cycle development needs arise to create and deploy armor terminations for new applications this versatile design will be cost-effectively applied.

8. Acknowledgments

We are grateful for the diligent support and guidance we received from numerous people including: Dr. R. F. Gleason, S. Shapiro, J. Mendez, G. Gullo, P. Durant, T. S. Fong, R. Stathum, and T. C. Lee. All of whom are either current or former Tyco Telecommunications colleagues.

9. References

- [1] T. C. Chu, D. A. Giordano, T. V. Kutt, R. J. Rue, "Special Trunk Cable for Deploying Branching Repeaters in Deep Ocean" in: *The Proceedings from the 50th International Wire and Cable Symposium*, November 2001.

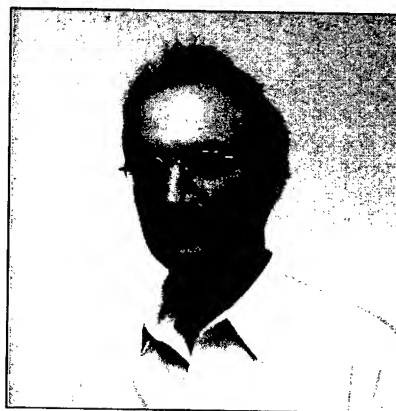
10. Authors



David A. Giordano

Tyco Telecommunications (US) Inc., Eatontown, NJ 07724

Mr. Giordano, Member of Technical Staff, has been in the undersea cable business with Tyco Telecommunications Laboratories (formerly part of AT&T Bell Laboratories) since 1997. He received his B.S.M.E. in 1996 and M.S.M.E. in 2002, both from Stevens Institute of Technology. Mr. Giordano has been developing undersea cable joints and couplings for both factory and field applications. Currently, he is responsible for developing new cable jointing techniques in the Undersea Cable & Development Department.



Maurice E. Kordahi

Tyco Telecommunications (US) Inc., Eatontown, NJ 07724

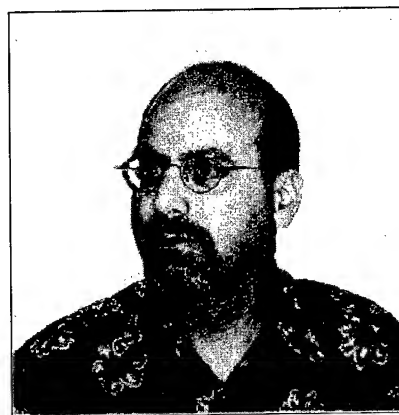
Dr. Kordahi is Director of the Wet Plant Mechanical development group and has been in the undersea cable business with Tyco Telecommunications Laboratories (formerly part of AT&T Bell Laboratories) since 1984. He is currently responsible for cable jointing, and repeater mechanical design. He has been instrumental in the design and development of methods, procedures, and equipment for installation and maintenance of submarine cable systems. Dr. Kordahi received his B.S. degree from the University of Dayton in Ohio, and both an M.S. and Ph.D. degrees from the University of Kansas in Lawrence, all in mechanical engineering.



Ralph J. Rue

Tyco Telecommunications (US) Inc., Eatontown, NJ 07724

Mr. Rue, Senior Member of Technical Staff, has been in the undersea cable business with Tyco Telecommunications Laboratories (formerly part of AT&T Bell Laboratories) since 1984. He received his AAE-MET degree from Vermont Technical College and his BS-MET degree from Trenton State College. His work has been focused on development and qualification testing and analysis of fiber optic undersea cable designs and related hardware. His responsibilities span across cable, joint, and coupling design development and include sea trial qualifications and shipboard handling guidelines.



Robert K. Stix

Tyco Telecommunications (US) Inc., Eatontown, NJ 07724

Mr. Stix, Distinguished Member of Technical Staff, has been in the undersea cable business with Tyco Telecommunications Laboratories (formerly part of AT&T Bell Laboratories) since 1980. He received his B.S.M.E. from Purdue University 1979 and M.S.M.E from Stanford University in 1981. His experience is highly diverse and includes cabling, cable jointing, installation, and maintenance. In addition, he has contributed to undersea cable technology in the areas of Passive Optical Components, Project Management, and Shipboard Equipment.

Design of an Efficient Cooling Tube for Optical Fiber Manufacturing at High Draw Speeds

Denis Tschümperlé, Aurélien Léon

Alcatel, Optical Fiber Division

Conflans, France

+ 33 1 39 19 12 00 · denis.tschumperle@alcatel.fr

Abstract

During the draw phase in optical fiber manufacturing, the fiber temperature needs to be lowered quickly after it exits the furnace in order to allow coating by polymer materials. With increasing draw speeds, the need arises for more efficient designs of cooling tubes.

This paper will outline the steps that led to the design and realization of a new cooling device named Heole (High Efficiency coOLing tube). A numerical modeling tool using the CFD software Fluent has been created to simulate fiber cooling for various tube configurations. It computes the fluid flow in the tube, the mixing of different gas species and the heat transfer. The computed fiber temperature is compared to measurements which were made with an infrared camera on an operating draw tower.

The calculations aided in the design and manufacturing of an improved prototype which will be tested and compared to the earlier prototypes as well as other cooling tubes.

Keywords

Optical fiber, draw, cooling device, CFD, gas flow, heat transfer.

1. Introduction

With increasing draw speeds, the need arises of more efficient cooling tubes. In the existing cooling tubes, the efficiency of the cooling is directly related to the amount of cooling gas inside the tube [2]. Higher cooling gas flow rates are thus needed to ensure that no external air is allowed inside the tube. For the existing tubes, the cooling efficiency quickly reaches a plateau value and subsequent increases in the gas flowrate does not further enhance the cooling of the fiber.

The goal of this work is to develop a cooling device of higher efficiency at lower gas flows. The Heole tube principle is to periodically strip off the thermal boundary layer that travels with the fiber by impinging successive cooling jets closely along the fiber surface as it passes in the tube. This method is discussed and described in an earlier patent [3]. We will use numerical modeling to study how the multiple jets can increase the heat transfer coefficient, h , between the fiber and the surrounding gas.

With some simplifications (see [1]), the normalized temperature θ of the fiber can be written as a function of axial coordinate x :

$$\theta = \frac{T - T_x}{T_0 - T_x} = \exp\left(-\frac{2h}{\rho_S C_S U_0 r_0} x\right)$$

where ρ_S , C_S , U_0 and r_0 are fixed properties of the fiber. Hence it can be seen that in order to decrease the fiber temperature, the heat exchange coefficient h must be increased.

The first cooling device prototype, following with a description of the numerical model will be described firstly. The second part outlines the validation of the modeling tool by comparison with experiment. Finally, the use of the numerical model to enhance the cooling device's design will be discussed.

2. Presentation of the cooling device and numerical study

2.1 Presentation of Heole

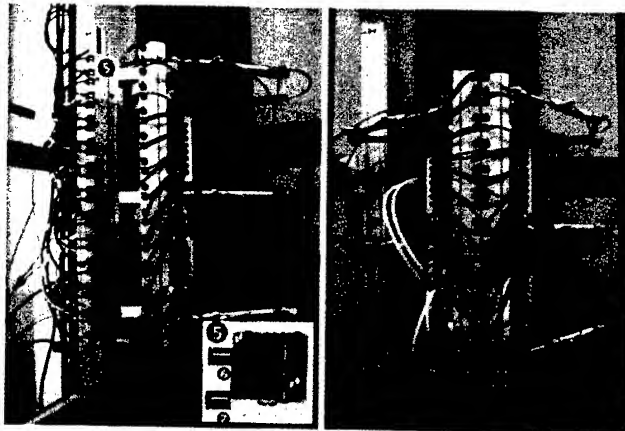


Figure 1: views of Heole prototype: open (left) and closed (right). Insert shows one module's half

Figure 1 shows views of the Heole cooling tube prototype. The tube is open on left image (with one chamber detailed on insert) and closed on right image. Cooling water ❶ is circulated around the chambers to maintain a set temperature. Pure Helium is injected using a distribution device which divides the incoming gas flux ❷. The insert shows a half chamber with its tube plug for injecting ❸ and pumping ❹. The modules are mounted on a clamshell closing type device. Each of the 24 pumping holes ❺ is closed by caps, but each can be connected to a gas recycling device.

The system is highly modular with each chamber having a low cost and it can be modified to ensure optimal design for individual draw tower configuration and speed.

2.2 Numerical study

A study of the cooling device was made using Computational Fluid Dynamics (CFD) tools. The CFD software Fluent v5.6 was used to compute the gas flow and heat transfer inside the cooling tube. The parameters used in previous studies of fiber cooling in air [1] and in other cooling tubes [2] using the Fluent software were applied in this study. Gas and silica properties, such as thermal conductivity and specific heat, are temperature dependent. Due to moderate overall temperatures (600°C max.), no radiation model was used. Due to small tube diameters, Reynolds numbers are low, thus it is assumed that no significant turbulence effects will need to be computed.

The studied tube is comprised of 12 identical modules as shown in Figure 2. The software computes the mixing of the air that enters the tube along the fiber with the injected helium. Heat transfer occurs between the hot fiber, the gases, and the external water cooled wall (at 16°C in the reference case). Note that all the fiber velocities, U , are normalized to a reference velocity U_0 .

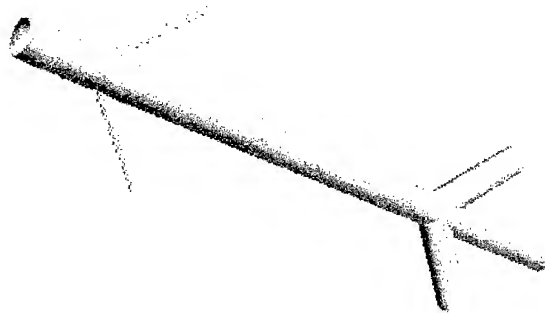


Figure 2: 3D view of one modeled module

A 2D axisymmetric model of the entire tube was used to obtain the pressure in each section. This model provided an estimate of the final temperature and of the gas distribution. To have a better understanding of the heat transfer phenomena for each injection approaching the fiber, a 3D model was also developed. It was used to optimize the design by increasing the cooling efficiency of the Heole tube as compared to the existing design.

3. Model validation

3.1 Pressure distribution

Due to the important effect of the pressure in the tube on the gas distribution, a model of the entire tube of twelve modules was needed to obtain the pressure distribution. Modeling the entire tube in 3D is not possible given the geometric aspect ratio, hence a 2D axisymmetric model was used for this work.

The mesh is comprised of triangular cells, with a boundary layer of quadrangular cells near the fiber surface and in the injectors. The typical number of cells is approximately 20,000. Each injection/aspiration inlet is represented as an annular slit having a surface area identical to the actual inlet.

For the calculations, the injected helium is supposed to be divided equally into each injection. This is not possible in the actual tube given the actual pressure differences that lead to different amounts of gas flowrates at each injector. Thus a redesign of the gas injecting path may be needed. This is one source of discrepancy between the calculation and experiment.

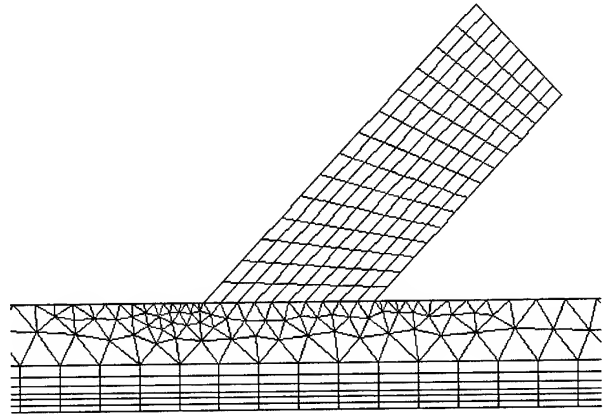


Figure 3: grid view near an aspiration for 2D model

The aspiration outlets were all sealed except for one which was used for pressure measurements using a PPC500 device. A total flowrate of 5 l/min of helium was injected. The measured pressures were normalized to the peak value.

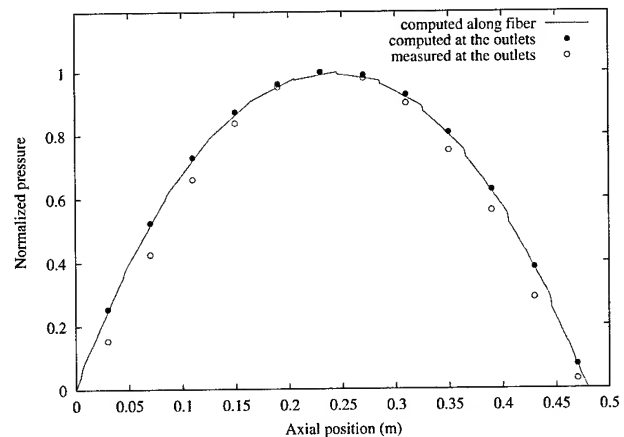


Figure 4: Measured and calculated pressure in the tube

Figure 4 shows the measured and computed pressure curves normalized by their maximum pressure value. The agreement is good between the computed and measured values. Absolute pressure values are lower for the measurements (168 Pa peak value) than for calculation (630 Pa peak value). The calculation does not take into account two effects: the pressure drop due to the flexible tube length between the cooling tube and the PPC500 device, as well as the pressure drop that can occur at each module's end due to a deficient air sealing between each chamber.

With a given temperature of the fiber at the top of the domain, the calculation computes the temperature at the exit. Here it is

preferred to use the values given by the more accurate 3D model to compare with the experiments. The important data given by the 2D model are the pressure values at the beginning and the end of each module, which will be used for the 3D calculation.

3.2 3D Model

A 3D calculation was executed for each individual module. Although it is necessary to have the correct impact of the effects of the jets on the fiber, these calculations are time consuming. Therefore, only the first 5 modules were studied. The temperature values of the fiber were then extrapolated with an exponential curve to give the temperature at the tube exit. As in the 2D case, the mesh is comprised of tetrahedral elements except near the fiber and in the injections/aspirations with a typical grid size of 250,000 cells.

Figure 2 shows the model geometry of one module containing only the fluid zone. Helium is introduced by the two upper injectors and can be pumped out by the two lower aspirations. The fiber runs through the tube center.

The gas inlets are treated as velocity inlets in the model and the aspirations can be taken into account by assuming a negative value for those inlet velocities. The upper and lower bounds of the domain are pressure outlets where the pressure is given by the 2D calculation results. The model was planned to be able to predict the effect of non-symmetric injections and aspirations, so a whole module, instead of only one half, was modeled. After the first module simulation, the temperature of both the fiber and the gas as well as the mass fraction of air at the exit of one module are known. These values are then re-injected into the next module's calculation. This process is then repeated for four successive modules. The final temperature is then extrapolated with an exponential curve to obtain the fiber temperature at the tube's exit.

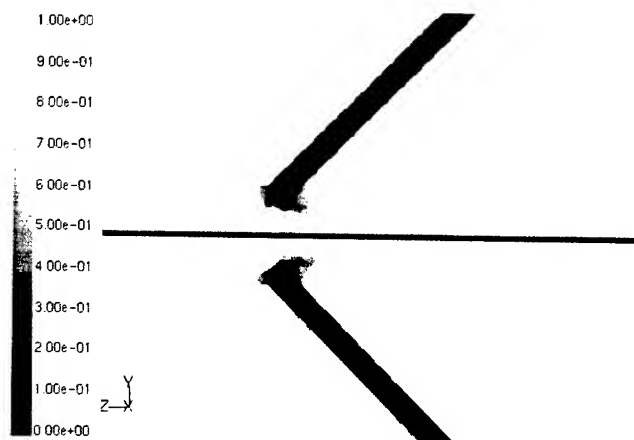


Figure 5: Mass fraction of air near first injector; U=1, 1 l/min of Helium

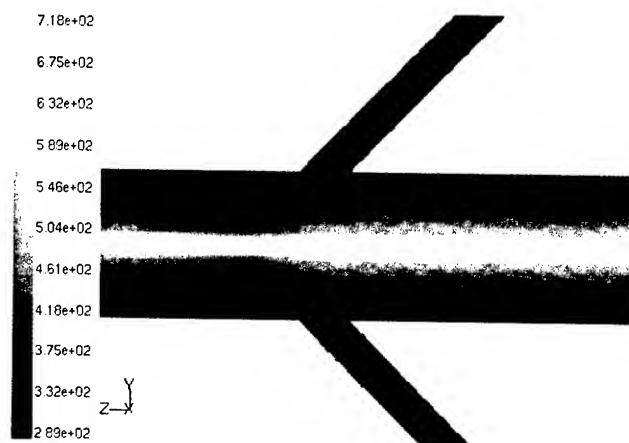


Figure 6: Temperature profile in K near first injector; U=1, 5 l/min of Helium

Figure 5 shows air entering the first module and then mixing with the injected helium at a low flowrate. The gas in the module is mainly composed of air in this case. In Figure 6 one can see the thermal boundary layer being stripped away due to the two gas jet impacts. These two figures illustrate two different cooling mechanisms. The less air present in the tube, the more efficient the cooling will be due to helium having a higher heat exchange coefficient than air. It is then necessary to minimize the quantity of air inside the tube. There is a second effect due to the impact of helium jets directly onto the fiber which is due to the high gradients in the heat transfer coefficient between the fiber and the gas that are apparent in the region near the inlet locations (see Figure 8 and 9).

3.3 Validation: comparison with experimental results

Calculated values were compared with temperature measurements made at normalized draw speeds of U equal to 1 and 1.36 with helium injected at various flowrates. Gas is pumped only into the fifth module at 1 l/min where the oxygen fraction of the gas mixture is then measured. All other aspirations are sealed.

Table 1. Exit fiber temperature and O₂ volume fraction for experiments and model

U	He (l/min)	Temp. exper. (°C)	Temp. model. (°C)	O ₂ exp. (%)	O ₂ model. (%)
1	1	372	344	13.8	6.47
	3	317	334	4.8	4.06
	5	300	282	0.91	0
	10	282	268	0.02	0
1.36	1	484	509	15.2	9.5
	3	433	445	5.8	0
	5	398	430	0.02	0

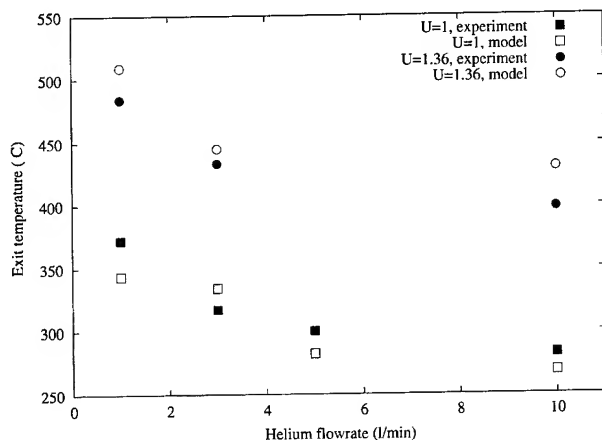


Figure 7: Exit fiber temperature in °C as a function of helium flowrate

The agreement between measurement and calculation is fairly good, bearing in mind the differences between the simulation details and actual system used in the measurements. For example, during the experiments, the actual draw speed U can fluctuate while it is maintained at a constant value in the calculations. Secondly, the 'airtight-ness' of the device as a whole is not perfect which can generate slight pressure drops and allow more air to penetrate. This likely explains the higher oxygen quantities observed in the measurements. Another effect approximated in the model is the cooling due to the water-jacket surrounding the tube. Because no solid zone is modeled in our case, it is assumed that the external wall temperature is at the water temperature (16°C) which is of course, not strictly the case in actuality.

4. Optimizing fiber cooling

As discussed earlier, the cooling efficiency of the tube is directly linked to the value of the heat transfer coefficient h ($\text{W/m}^2\text{-K}$) between the fiber and the surrounding gas. This value is related to the thickness of the thermal boundary layer around the fiber. The curves of h were thus studied. The coefficient typically consists of a mean value with perturbations due to the gas injections and aspirations. The modeling effort's approach was to globally increase this heat transfer coefficient value in order to lower the fiber temperature. The methods used will be discussed next.

4.1 Air sealing

It is important to ensure that the minimum amount of air is allowed to penetrate the tube. To achieve this, flowrate of helium as well as pressure inside the tube must be maintained high. Pressure in the first modules rises naturally into the tube when no helium is pumped (cf. Figure 4) which prevents the air from entering.

The heat transfer coefficient h is plotted for various helium flowrates for both the 2D and 3D calculations at draw speed $U=1$ in the figures below. The coefficient h derived from the 3D simulations is plotted on a line on the fiber surface directly in

front of the inlets. Thus the values are necessarily higher than for the 2D case where the value of h is an average over the entire fiber surface. For a low helium flowrate (Figure 8), much air enters the tube, and thus the value of h starts low and increases which each successive injection of cooling gas. For higher flowrates, helium completely surrounds the fiber and the value of h reaches a plateau. After which, the only way to increase h is from the effect of the jet which locally induces a peak of h as can be seen in Figure 9. A higher flowrate increases the gas velocity impinging the fiber which results in a higher h peak value.

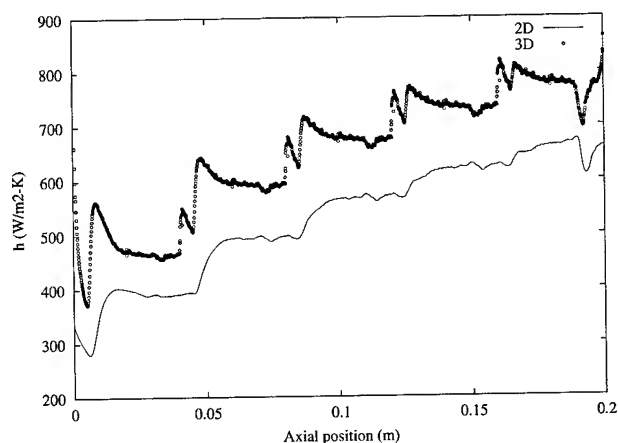


Figure 8: heat transfer coefficient h in $\text{W/m}^2\text{-K}$ along the fiber; $U=1$, 1 l/min of He

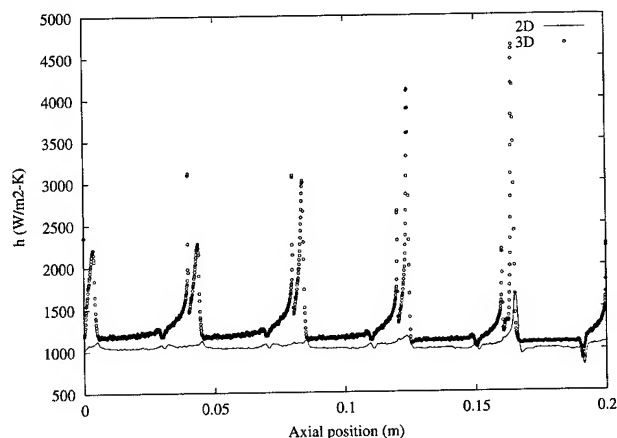


Figure 9: heat transfer coefficient h in $\text{W/m}^2\text{-K}$ along the fiber; $U=1$, 5 l/min of He

The 3D model gives a more precise description of the variation of h , thus it was used in the following parametric studies.

4.2 External cooling

In order to decrease the fiber temperature, ways of increasing the mean value of the heat transfer coefficient h along the fiber were studied. Because this value is linked to the thickness of the thermal boundary layer, the simplest method to increase it was to reduce the tube diameter. However, due to the fiber vibrations and the risk of fiber breaks, it cannot be decreased under a few mm.

The remaining solution then becomes to lower the wall temperature.

For example, if we consider cooling with liquid nitrogen, the external wall temperature could be well below the temperature obtained by water cooling. For a wall temperature of 77 K (-196°C), we can compare the results with the standard case of a 289 K (16°C) water cooled wall. For the following cases, no gas is pumped in the tube and the aspiration outlets are sealed.

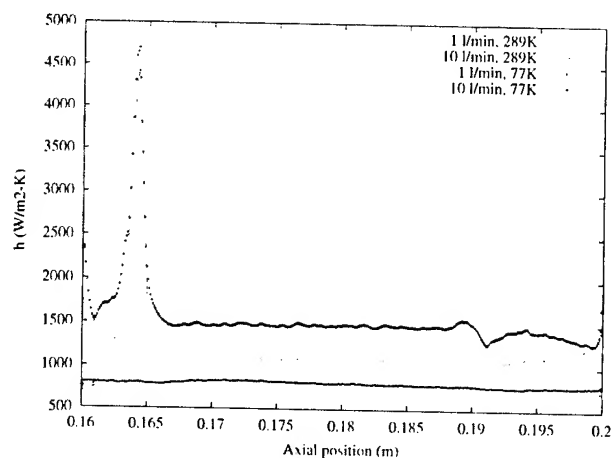


Figure 10: heat transfer coefficient h in W/m^2-K in fifth module for various wall temperatures and helium flowrates; $U=1.36$

The gain in the coefficient h is more pronounced for cases of high helium flowrates, when no air is present along the fiber. The gain in the mean value of h is then an increase of 37%. The decrease in exit fiber temperature is 8°C for 1 l/min of helium and 33°C for 10 l/min.

4.3 Changing the injector shape

Another method to increase the overall value of h is to increase the thickness of the peak zone near the gas inlets. For this, the influence of enlarged gas injectors with a shape to be hereafter referred to as a 'pencil' injector (see Figure 11) was tested.

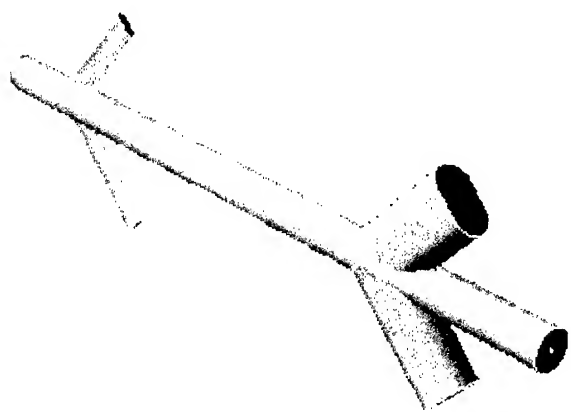


Figure 11: module with enlarged pencil-type injector and aspiration

To ensure that no air is allowed to enter the tube, no gas was pumped in the first 3 modules, thus allowing the pressure to rise at the tube's top end. Then 0.5 l/min was then pumped in the remaining modules for a total of 4.5 l/min of helium. For the standard case, 6 l/min (0.5 l/min per module) was injected at a draw speed of $U=1$. Since the surface area of the pencil injector is larger than the round injector, the gas velocity for a given flowrate was lower. Therefore, 20.9 l/min of helium was injected to result in a velocity equivalent to that of the standard injector.

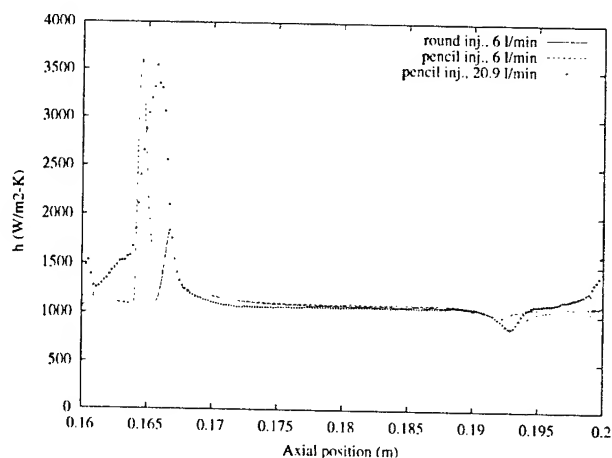


Figure 12: heat transfer coefficient h in W/m^2-K in fifth module for round and pencil injector; $U=1$

Figure 12 shows the h curves corresponding to those cases. For the pencil injector at 6 l/min, the maximum value of h is significantly lower due to the lower velocities. For equivalent gas velocities, the maximum peak values are the same, but the peak thickness is larger for the pencil injector. The temperature decrease in the entire tube for the cases of round injector at 6 l/min, pencil injector at 6 l/min and 20.9 l/min is respectively $\Delta T=159, 162$ and $177^\circ C$. For 20.9 l/min, the overall pressure in the tube is higher, thus less air can enter in the tube which affects the output temperature as well as enlarging the peak of h .

5. Conclusions

A computer model to simulate the cooling behavior of an optical fiber during draw passing through a new concept of cooling tube has been validated by comparing the results obtained both experimentally and by calculation. Periodical air stripping effect due to the helium jets has been studied. A numerical study to improve the efficiency of this new cooling tube was made and various parameters were shown to have an impact on the fiber cooling.

The heat transfer coefficient curves have shown that the value of h is directly related to the quantity of air inside the tube which reaches a constant value when no air is left. The coefficient value can be increased by lowering the temperature of the external wall cooling. The remaining method of increasing h is then to periodically direct cooling gas jets on the fiber in order to locally induce a peak of the heat transfer coefficient.

6. Acknowledgments

The authors would like to thank Olivier Schuepbach, for designing the first Heole prototype. All people involved in this project shall be warmly thanked for their kind help.

7. References

- [1] D. Tschümperlé, M. Nicolardot, "Fiber Cooling Modelisation During Draw Using CFD", *ASME PVP- Vol. 424-1*, 211-217 (2001).

- [2] D. Tschümperlé, J.-F. Bourhis, S. Dubois, A. Léon, "Study of Cooling Tubes for Fiber Draw using CFD", *Proc. Of 50th IWCS, Lake Buena Vista, FL*, 28-33 (2001).
- [3] A. Léon, D. Tschumperlé, O. Schuepbach, J.-F. Bourhis, French Patent 0204344 deposited at INPI 08/04/2002 and Letters Patent for the USA 104345/RV/OOFD.



Denis Tschümperlé is a R&D Modeling Engineer within the Alcatel Optical Fiber Division. He graduated from Ecole Centrale de Nantes in 1995. He obtained his Ph.D. in Fluid Dynamics working with the French Army (DCN) in 2000. He joined Alcatel in Conflans in 2000.



Aurélien Léon is a R&D Engineer responsible of the cooling technology for Fiber Draw within the AOFD. He obtained his Ph.D. in Physics from University Paris VI (France) working with Laboratoire de Physique Statistique de l'Ecole Normale Supérieure in 2001. He joined Alcatel in 2001.

Optical Fiber Coating Delamination Using Model Coating Materials

Charles Aloisio, Arturo Hale, Kariofilis Konstadinidis, Rob Moore, Mahmood Tabaddor, John Turnipseed

OFS

2000 Northeast Expressway, Norcross, GA 30071

+1-770-798-2824 · cjalosio@ofsoptics.com

Copyright © 2002

Fitel USA Corp.

All rights reserved

Abstract

The design of coatings for optical fibers often necessitates establishing a critical balance between competing performance demands. The bond at the primary-glass interface requires particular attention because the coating must remain reliably attached until it is removed, and then it must be easily separated from the glass without substantial residues. In this paper, we present results from a designed evaluation of four factors affecting the adhesion of the primary coating to the glass and its resistance against delamination. The factors are the adhesion promoter concentration, the primary polarity, the glass transition temperature of the secondary coating, and the primary modulus. We develop model optical fiber coatings to meet the parameters of the experiment. As responses, we measure the pull out force, the primary modulus measured in situ, and the force required to achieve a 50% probability of delaminating the primary coating.

Keywords

Optical fiber; coating; non-uniform adhesion; delamination; design of experiment; coating formulation; coating chemistry; finite element analysis.

1. Introduction

The delamination resistance is an important performance property consideration in the design of coatings systems. It must be high enough to prevent damage to the primary-glass interface during routine handling, as when the fiber is drawn, rewound, colored, or cabled. It must also be low enough to permit stripping the coating from ribboned fiber without leaving substantial residue.

It is well known that delamination resistance is affected by the coating formulation and chemical composition [1], but these effects have not been quantified. To better understand this dependence and establish guidelines for the design of future coating systems, we designed an experiment to study the effects of four fundamental coating properties on the delamination resistance. The factors were the primary coating polarity, the secondary coating glass transition temperature (T_g), the concentration of the adhesion promoter, and the primary coating

modulus. These are the four material properties we believed to have the greatest influence on delamination resistance. Other properties, such as primary tear strength, we deemed to have less of an effect and were left out to minimize the number of experiments required to determine the strengths of the principal factors. To vary these factors, we developed a series of primary and secondary coatings using only commercially available coating components. We measured the secondary T_g with differential scanning calorimetry (DSC) and the primary moduli of cured sheets using oscillatory mechanical tests (dynamic mechanical analysis, or DMA). Then, after drawing optical fiber with the coatings, we measured the pull out force, the in situ modulus, and the force required to achieve a 50% probability of delaminating the primary coating. We used a twenty-trial designed experiment to make the greatest use of the data.

2. Experimental Design

2.1 Factors

Table 1 shows the ranges we chose for the four experimental factors. They are representative of coating formulations available commercially. The formulation strategy used to achieve these ranges is described in the next section.

Table 1. Factors of the experimental design

Factor	L	M	H
Primary coating modulus (PRIMOD) at 23°C, psi	160	225	290
Primary coating polarity (POLAR), arbitrary units	-1	-	1
Primary coating adhesion promoter (ADHPROM), wt. %	0	1	2
Secondary Coating T_g (SECTG), °C	82	-	128

The origins of the primary coating polarity in Table 1 are in the chemical functionalities of the polymer chains, whose effects we

could only estimate. We assigned a relative polarity based on the contact angle of a water droplet on the cured coatings films, and on the films' water absorption. (These methods are described in section 3.) In Table 1, high polarity coatings (+1) have higher water absorption and lower contact angle. The secondary T_g s in Table 1 are DSC results, as noted in the introduction, but we also measured T_g with DMA, and those numbers were close to the DSC values (88°C and 136°C).

The primary moduli reported in Table 1 are those of the low-polarity coating. The high-polarity coating moduli were comparable, although the modulus of the high-modulus formulation was somewhat higher (340 psi). The midpoint modulus, 225 psi, was interpolated with a least-squares fit from the results of a designed experiment in which the adhesion promoter was varied in the high and low-modulus, low-polarity formulations. The error from this extrapolation, as measured by the residuals, was comparable to the experimental error in the measurement.

2.2 Responses

In addition to the delamination resistance, we included two other fiber-coating properties as responses, the primary coating "in situ" modulus, or the modulus on the fiber, and the fiber pull out force. The in situ modulus differs in general from the sheet modulus, as the fiber temperature during cure and film thickness can have a substantial impact. The pull out force is the force required to pull a 1 cm section of glass out of the coating and is a measure of the adhesion of the primary coating to the glass. These methods are described in the next section.

A full design with 4 factors, 2 of which have 3 levels, would require at least 36 trials ($3 \times 3 \times 2 \times 2$). To reduce this number, we used the full factorial design for 4 factors with 2 levels each (16 trials) and ran four more trials with the primary coating modulus and adhesion promoter at their mid-point values and the other two parameters at their low and high values. The resulting design is shown in Table 2.

We analyzed the results of the experiment using a commercial software package, STRATEGY (Process Builder, Bremerton, WA). The package computes the least-squares fits to the four factors plus interactions and displays the responses in three-dimensional charts. Examples of these charts are included in the results section of the paper. The four trials at the midpoints of the modulus and adhesion promoter were withheld from the calculation and were used to check the predictions of the linear model.

Having only two levels of the secondary coating T_g is not a significant assumption in determining its effect on delamination resistance. The adhesion at the primary-glass interface, and by extension the delamination resistance, is expected to decrease linearly as T_g increases [2]. The effect of the polarity of the coating, the other two-level factor, may not be linear but should be monotonic. The adequacy of the linear fit to the 3-level

factors, the modulus and the adhesion promoter, is discussed in section 7.

Table 2. Experimental design.

Run order	POLAR	PRIMOD	ADHPROM	SECTG
1	-1	160	0	82
2	1	290	0	82
3	-1	160	2	82
4	-1	290	2	82
5	1	160	2	82
6	1	290	2	82
7	-1	160	0	128
8	-1	290	0	128
9	1	160	0	128
10	1	290	0	128
11	-1	290	2	128
12	1	160	2	128
13*	-1	225	1	128
14*	1	225	1	82
15	1	160	0	82
16	-1	160	2	128
17*	-1	225	1	82
18	-1	290	0	82
19	1	290	2	128
20*	1	225	1	128

* Withheld points used to test the model predictions

3. Characterization Techniques

3.1 Sheet Tests

3.1.1 Dynamic Mechanical Analysis (DMA) The dynamic moduli for the coatings were measured with a Rheometrics Scientific RSA-II at a frequency of 1 rad/sec in tensile mode. The storage modulus (E'), the loss modulus (E'') and $\tan \delta$ curves were measured at temperatures ranging from -150°C to 200°C for secondary coatings and -150°C to 100°C for primary coatings at intervals of 2°C. The sample was held for 10 seconds at each temperature before measurement. The sample sheets were all cured at 0.7 J/cm² in a nitrogen environment. The DMA samples cut from the sheets were 9.4 mm X 4 mm X 120 μ m thick.

The DMA data show the high and low glass transition temperature of the secondary coatings (Figure 1.). The peak in the value of $\tan \delta$ agreed in general with the midpoint of the glass transition determined by DSC, which was our expectation [3].

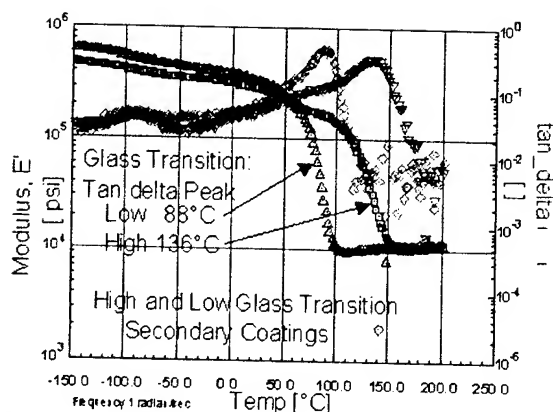


Figure 1. DMA curves of the high and low T_g secondary coatings.

3.1.2 Polarity Measurements. We used water absorption and water contact angle measurements to rank the primary coatings with regard to polarity. Films of the coatings were prepared by spin coating on polypropylene sheets and curing at 100 mJ/cm^2 . The film thickness was approximately 100 microns. Water content of the films at $25^\circ\text{C}/50\% \text{ RH}$ was measured using Karl Fischer's reagent. The water contact angle was measured using deionized water.

3.1.3 Equilibrium Tensile Modulus The equilibrium tensile modulus of the primary coating control formulations was measured using a Rheovibron DDV-II-c manufactured by Toyo-Baldwin. Measurements were performed at room temperature in the manual mode. Rectangular strips ($25\text{mm} \times 5\text{mm} \times 0.28\text{mm}$) were stretched in strain increments of 0.2 mm (about 0.8%) and the equilibrium force was measured at each point. The modulus was calculated as the slope of a stress versus strain line obtained from a linear regression of eight experimental points. Correlation coefficients were always 0.99 or better.

3.2 In situ Tests

Twenty trial fibers were manufactured from the model fiber coating systems utilizing standard production towers under commercial operational conditions. The in situ modulus and pull out force were measured immediately thereafter.

3.2.1 In situ modulus. We determined the in situ modulus (ISM) by gluing a 1 cm section of one end of the fiber onto an immobile substrate, attaching a weight on the free end, and measuring the fiber displacements [1, 2]. We made five measurements with weights ranging from 10 to 70 grams. The shear modulus is given by $G = [a^2/2p]EA \ln(R_2/R_1)$ [4], where E is the glass modulus, A is the area of the fiber, R_2 and R_1 are the outside and inside radii of the primary, and a is defined by $Fl/(dEA) = (a) \tanh(a)$. (This expression includes a correction for glass stretch.) Here, d is the displacement, l is the gauge length, and F is the force on the fiber. We assumed a rubbery Poisson's ratio of $1/2$ and reported 3 times G as a tensile modulus. The

repeatability of the test is about 5 psi, and the variation between samples drawn on different days is about 10 psi. The visual examination required by the specimen preparation for the ISM testing also revealed the immediate delamination of the primary coating from the glass substrate for several of the developmental coating systems.

3.2.2 Fiber pull out force. The fiber pull out force is a measure of the tensile shear resistance of the primary coating at the glass substrate surface. It correlates well with the in situ modulus in general, although not always, making it another helpful indication of process-related coating characteristics such as cure dependence on the UV dose. We used the OFS-standard method to measure the pull out force [1.5]. We attached the ends of the fiber samples onto paper tabs with an acrylate glue and made an incision in the coating 1 cm from one end of the fiber. We then recorded the maximum force measured by an Instron test machine to pull the fiber out of the coating at a cross-head speed of 0.2 in/min (0.085 mm/s). The pull out force was the maximum averaged over seven samples. The standard deviation was typically 0.1 lb/cm; if it was larger than 0.2 lb/cm, the test was repeated using seven new samples.

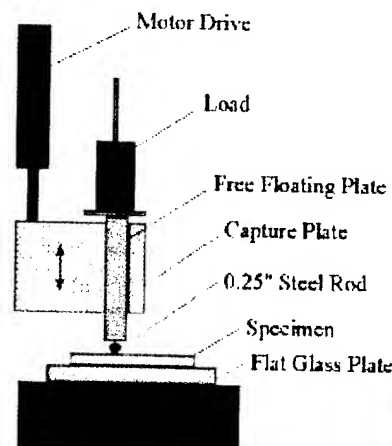


Figure 2. Delamination test set-up.

3.2.3 Delamination testing. Figure 2 illustrates the test setup we used to measure delamination resistance. An optical fiber was placed on a glass slide fixed to an aluminum block on the delaminator so that the fiber is aligned with the center. A free-floating plate connected to a $1/4$ " diameter rod was loaded with a desired test weight and lowered at a speed of 1.7 mm/sec onto the fiber. The loaded rod was allowed to rest on the fiber for 5 seconds and then raised off the sample. The block was moved $1/4$ " to expose a new test region, and the test was repeated. After 30 sites were impacted, the slide was removed from the delaminator, and a liquid matching the coating's index of refraction was applied to the fiber. The impacted areas were then examined with an optical microscope at 400X magnification. The probabilities of

delamination, the ratios of the number of damaged sites to the total sites (i.e. 30), were plotted versus load in grams. These data were fit by linear regression and the load for 50% delamination (called D50 in this paper) was determined. A typical delamination generated is shown in Figure 3.

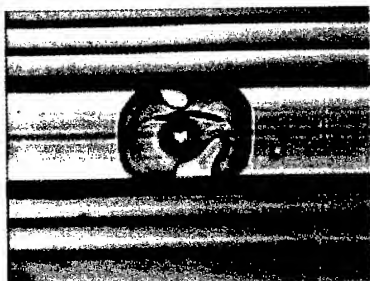


Figure 3. Typical delamination observed during testing

4. Model Coating Formulation

4.1 Primary Coatings

As discussed previously, the primary coating properties studied in this work are polarity, elastic modulus, and adhesion to glass. Our strategy was to formulate two families of coatings, each based on a different oligomer, a "high polarity" and a "low polarity" oligomer. Within each family, we changed the modulus by varying small amounts of monomers, and the adhesion to glass was modified by the use of silane coupling agents (adhesion promoters). We designed all of the formulations to have a viscosity of approximately 6,500 cps at 23°C to ensure consistent fiber coating application.

The oligomers chosen were off-the-shelf commercially available urethane-acrylate oligomers marketed for flexible, low Tg coatings. These oligomers consist of a polymer backbone with a molecular weight on the order of a few thousand, end-capped with acrylate groups through urethane linkages. The original intention was to employ a polyester backbone as the "high polarity" oligomer and a polyether backbone as the "low polarity" oligomer. Infrared analysis, however, showed that the polyether-based oligomer contained a much larger concentration of urethane groups than the polyester-based oligomer (presumably indicating that the polyether backbone is shorter than the polyester backbone). This higher urethane concentration provides the polyether-based oligomer with a higher polarity. Water absorption and contact angle measurements on cured coatings indeed confirmed that the high-urethane polyether oligomer is more polar than the low-urethane polyester oligomer. The results are shown in Table 3.

Table 3. Water absorption and contact angle results

Coating	%Water absorption	Contact angle, deg
Polyether-based coatings	0.98±0.08	75±3
Polyester-based coating	0.6±0.00	80±5

4.1.1 High polarity formulations. As a starting point, a control coating formulation was designed to have a viscosity of 6,500 cP and an elastic modulus of 1.1 MPa, with no silane coupling agent. The commercial polyether oligomer employed is provided neat, without a diluent, and has a very high viscosity. To decrease both the viscosity and the cross-link density to achieve the desired values, we added monomeric ethoxylated nonyl phenyl acrylate (ENPA) and lauryl acrylate (LA). The use of ENPA was dictated by two important features: a) the aromatic moiety in this monomer raises the refractive index of the liquid formulation to values consistent with the requirements of the fiber drawing operation, and b) its relatively high viscosity as compared to other monomers permits the use of a relatively large amount of this monomer to lower the cross-link density without lowering the viscosity to unacceptable levels. We used lauryl acrylate to fine-tune the crosslink density. In addition, since the cross-link density needed to be lower than that achievable with the aforementioned components (while keeping the right viscosity), we added a chain-transfer agent, iso-octyl mercaptopropionate (IOMP). IOMP also acts as a control for the silane coupling agent, as explained below. The composition of the high polarity, low modulus, no adhesion promoter primary coating formulation (control) is:

Polyether urethane acrylate oligomer	68 parts (wt)
Ethoxylated nonyl phenyl acrylate (ENPA)	21 parts
Lauryl acrylate (LA)	5 parts
Iso-octyl mercaptopropionate(IOMP)	4 parts
Photoinitiator (Ciba Irgacure 1700)	2 parts

Within this high polarity family, we modified the modulus by replacing the lauryl acrylate with 1,6-hexanediol diacrylate (HDDA). The use of a diacrylate instead of a mono-acrylate increases the cross-link density. Thus, the "high modulus" "polar" coatings have 5 parts HDDA instead of LA. We prepared the "high adhesion" coatings by substituting 2 parts of IOMP with 2 parts of -mercaptopropyl trimethoxysilane (MPTMS). MPTMS, a commonly-used adhesion promoter, improves adhesion by reacting covalently with both the polymer network (through the mercaptan functionality) and the glass substrate (through the alkoxysilane functionality). By using IOMP as the control for MPTMS, no change in crosslink density is caused by substituting one for the other, since both have the mercaptan functionality to react with the polymer network. Some formulations have a "medium" modulus. These coatings contain 2.5 parts LA and 2.5 parts HDDA. Likewise, the "medium" adhesion promoter formulations have only 1 part MPTMS.

4.1.2 Low polarity formulations. We designed a control formulation based on the low-urethane polyester oligomer to have a viscosity of about 6,500 cP and a modulus of 1.1 MPa. The oligomer we used comes with ENPA as diluent. In this case, because of the higher molecular weight of the oligomer backbone, it was necessary to add multifunctional monomers to the control formulation to increase the cross-link density and achieve the

desired modulus. In particular, a high viscosity monomer was needed to avoid dropping the viscosity of the formulation to undesirable values. We used pentaerythritol triacrylate for this purpose. Even though this introduces a hydroxyl functionality to the low polarity formulations, it should be kept in mind that the high urethane concentration in the high polarity formulations still dominates, as demonstrated by water absorption and contact angle measurements. The monofunctional acrylate used in this formulation was ethoxyethoxyethyl acrylate. A small amount of tetraethyleneglycol diacrylate was also employed to fine-tune the modulus. Since there was no need to use a chain transfer agent to lower the cross-link density, the amount of IOMP used was only as much as needed as a control for the adhesion promoter MPTMS. The composition of the low polarity, low modulus, no adhesion promoter formulation is:

Polyester urethane acrylate oligomer	79.3 parts
Pentaerythritol triacrylate (PETA)	7 parts
Ethoxyethoxyethyl acrylate (EEEE)	6.8 parts
Tetraethyleneglycol diacrylate (TEGA)	2.9 parts
Iso-octyl mercaptopropionate (IOMP)	2 parts
Photoinitiator (Ciba Irgacure 1700)	2 parts

Within this low polarity family, the high modulus formulations were generated by substituting 5 parts of EEEA with 5 parts of diethyleneglycol diacrylate (DEGDA), and the high adhesion formulations were obtained by replacing the IOMP with MPTMS. As before, the "medium modulus" formulations were obtained by replacing 2.5 parts of EEEA with 2.5 parts of DEGDA, and the "medium adhesion" samples were formulated by replacing 1 part of IOMP with one part MPTMS.

4.2 Secondary Coatings

Only one variable was manipulated in the secondary coatings: the glass transition temperature (T_g). The "low T_g " coating was formulated using a commercially available aromatic polyether urethane acrylate oligomer diluted with tripropyleneglycol diacrylate to obtain the right viscosity. The glass transition of the cured coating (as measured by differential scanning calorimetry) was 82°C.

We formulated the "high T_g " coating from a low molecular weight polyester urethane acrylate oligomer diluted with 1,6-hexanediol diacrylate. The glass transition of the fully cured coating was measured to be 128°C.

5. Designed Experiment Output

5.1 Coated fiber characterization

The primary coating in situ moduli and fiber pull out forces, measured as described in sections 3.2.1-2, are shown in Table 4. The standard deviation for the in situ modulus is 10 psi and for the fiber pull out force 0.1-0.2 lb/cm.

5.2 Delamination testing

The delamination results are presented in Table 4 as the force required to achieve a 50% probability of delaminating the primary coating (see section 3.2.3). A value of zero indicates spontaneous delamination during draw or handling.

Table 4. In situ modulus, fiber pull out force, and delamination results.

Run order	POLAR	PRIMOD	ADHPROM	SECTG	ISM	PO	D50
1	-1	160	0	82	132	1.41	203
2	1	290	0	82	182	2.37	433
3	-1	160	2	82	229	1.52	189
4	-1	290	2	82	306	1.99	172
5	1	160	2	82	166	2.21	428
6	1	290	2	82	232	2.64	470
7	-1	160	0	128	114	0.66	0
8	-1	290	0	128	173	1.52	196
9	1	160	0	128	69	1.17	0
10	1	290	0	128	177	2.20	0
11	-1	290	2	128	173	1.52	207
12	1	160	2	128	158	2.17	0
13*	-1	225	1	128	150	2.27	495
14*	1	225	1	82	205	1.71	0
15	1	160	0	82	84	1.78	122
16	-1	160	2	128	219	0.82	0
17*	-1	225	1	82	197	1.788	216
18	-1	290	0	82	202	1.70	203
19	1	290	2	128	217	2.30	656
20*	1	225	1	128	126	1.93	0

* Withheld points used to test the model predictions

6. Finite Element Analysis

In this section, we describe a finite element calculation we used to predict the mechanics of delamination. The model of the fiber on a pin is shown in Figure 4. The fiber end furthest from the pin is fixed and placed under tension. The revealed section for the pin and the fiber end sitting on the pin are symmetry conditions where the pin is pushed up against the fiber. Using the Ansys 5.5 commercial finite-element program, we are able to track the stresses that develop in this composite structure. Specifically, for delamination, tensile radial stresses at the glass-primary coating interface are a necessary precursor. The model uses 3-D brick elements for the coatings, fiber and pin. The principal mechanism for generating stresses is the contact between the coated fiber and the pin, which requires contact elements.

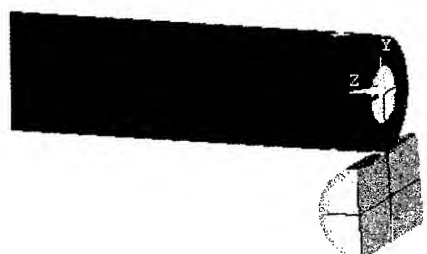


Figure 4. Symmetric finite element model for the fiber on a pin

Figure 5 shows the radial stress contours on the surface of the optical fiber for one set of material and geometric properties. The shaded regions on the lower section of the fiber indicate the shape and magnitude of these tensile radial stresses. This section of the fiber is directly above the pin. The calculated tensile radial stress distribution agreed well with photographs of delaminations (not shown here).

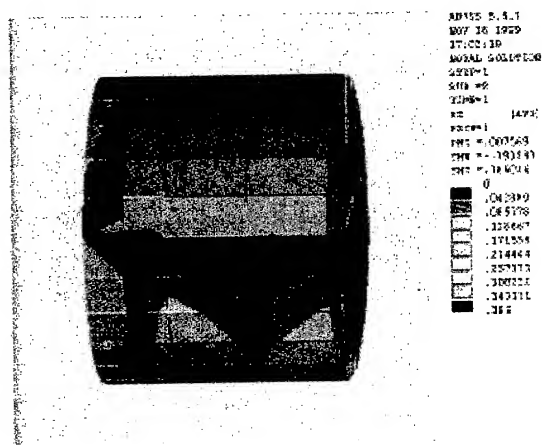


Figure 5. Radial Tensile Stresses at the surface of the fiber above the pin.

7. Results and Conclusions

Table 5 shows the least-square coefficients of the main effects and interactions for normalized factors, i.e., -1 to +1 variation. B_0 is the intercept of the least-squares line, and the other numbers are the slopes associated with each main effect (factor) or interaction. A positive slope indicates positive correlation, so that, for example, increasing the primary modulus from 160 to 280 psi (-1 to +1) increases the in situ modulus by about 61 psi (2×30.6) when the interactions are zero (all other factors at midpoints). Negative correlations show the reverse behavior, so e.g. increasing the secondary T_g from 80°C to 130°C decreases the delamination force required to achieve a 50% probability of delamination (D50) by about 145 grams, again in the absence of interactions.

Table 5. Least square coefficients

	Main effects and interactions	IM, psi	PO, lb/cm	D50, g
B0	Intercept	177.1	1.75	204.9
x1	POLAR	-16.3	0.35	58.7
x2	PRIMOD	30.6	0.28	87.2
x3	ADHPROM	35.6	0.15	60.3
x4	SECTG	-14.6	-0.20	-72.6
	x1x2	10.9	-0.01	38.9
	x1x3	-2.8	0.08	64.6
	x1x4	9.3	0.06	-27.1
	x2x3	-11.2	-0.06	23.8
	x2x4	-8.2	0.06	45.2
	x3x4	-6.3	0.01	23.1

7.1 Main effects

The largest main effects on the in situ modulus are the adhesion promoter concentration and the primary modulus of the sheets, the magnitudes of which are the same within the experimental error. Polarity may have a greater influence on the pull out force than the adhesion promoter concentration; the dependence of the resistance on the modulus is the subject of a recent patent [6]. The delamination resistance depends about equally on all four factors.

Note that all three responses correlate negatively with the secondary T_g . The effects on pull out force and delamination resistance we believe are owing to thermal expansion differences between the primary and secondary coatings. The secondary contracts rapidly as the fiber cools down after exiting the ultraviolet curing lamps until it reaches its T_g , where the rate of contraction slows considerably. The primary coating continues to contract at the same rate, however, as it is still well above its T_g . As the primary is adhered to the secondary coating, its continuing shrinkage leads to increased tension at the primary-glass interface, which reduces the adhesive forces. (Reference 2 contains a detailed analytical calculation of these effects.) The resulting effect on the delamination force was graphically demonstrated in this evaluation: Many of the high glass transition secondary fibers could not be tested. The primary-glass interface either failed upon take-up on the draw spool or during handling prior to delamination testing.

The negative effect of the secondary T_g on the in situ modulus may be also the result of the increased tension, perhaps because the higher T_g secondary had more reactive functional groups, which would raise the enthalpy of reaction and the fiber temperature, which would reduce the primary modulus.

The delamination resistance increase observed with an increasing primary modulus is owing to a reduction of the stress

delivered to the primary-glass interface when the fiber is mechanically perturbed. In other words, a higher-modulus primary absorbs more of the stress from deformation than a lower-modulus material. The stress redistribution is confirmed by the finite element analysis discussed in Section 6.

7.2 Interactions

Interactions between the main effects are most significant for the delamination resistance response. The largest of these is the positive interaction between the polarity and the adhesion promoter (x_1x_3 in Table 5), which means that higher polarity increases the effect of the adhesion promoter on D50 and higher adhesion promoter increases the effect of polarity. In fact, looking at Figure 6, there is no effect of the adhesion promoter at low polarity and no effect of polarity with zero adhesion promoter. (The surfaces in these 3-D figures represent the linear least-squares fit to the data. The curvature of the surfaces is larger when the interactions between factors are greater.) This reflects greater uncertainty in the measurement at very low adhesion. The samples with higher secondary T_g were especially likely to delaminate spontaneously. Figure 6 represents estimates taken at the T_g midpoint, which is the reason D50 is not zero at the vertices, and is the likely cause of the lack of dependence in Figure 6 at the extremes of low polarity and zero adhesion promoter.

The second largest interaction is x_2x_4 , or primary modulus and secondary T_g , which is again positive. Figure 6 shows that a combination of a low-modulus primary and high T_g secondary results in spontaneous delamination. Higher-modulus primaries ameliorate the reduction in tension caused by the thermal shrinkage through the stress-reduction mechanism discussed above.

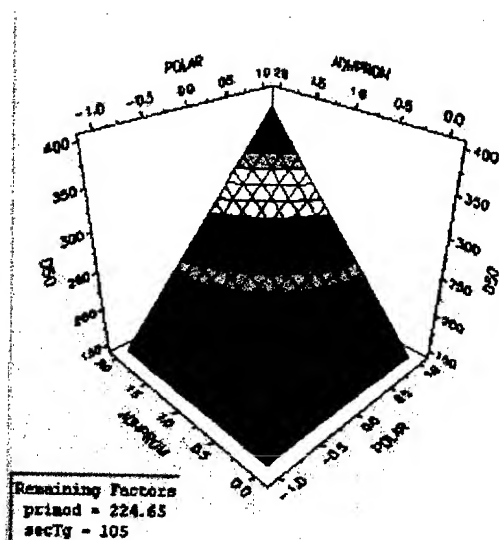


Figure 6. Effect of adhesion promoter and primary coating polarity on delamination resistance.

Decreasing primary polarity reduces the effect the primary modulus has in increasing delamination resistance, as shown in Figure 8, and this is the third-largest interaction (x_1x_2 ; considering the error of the measurement, the magnitude is comparable to x_2x_4).

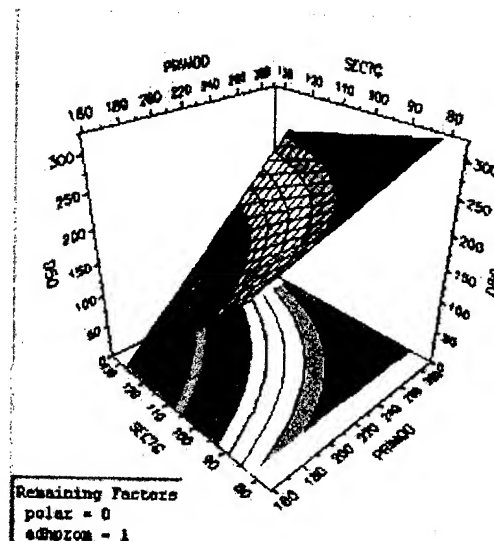


Figure 7. Effect of secondary coating T_g and primary coating modulus on delamination resistance.

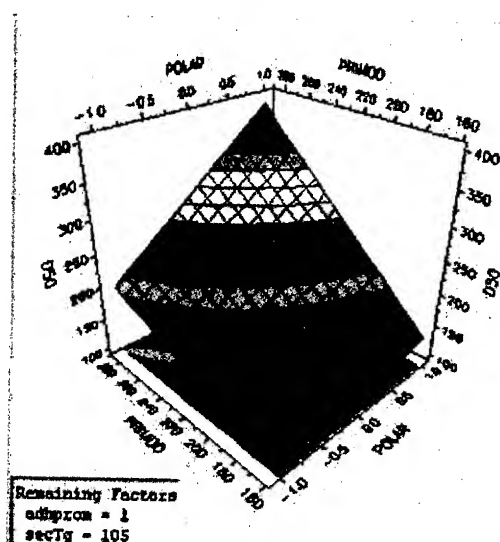


Figure 8. Effect of primary coating polarity and primary coating modulus on delamination resistance.

Table 6 indicates that the high-polarity primary coatings have lower in situ moduli than the corresponding low-polarity coatings. This behavior is presumably owing to a different reaction pathway at the high temperatures experienced in the fiber draw tower. The high-polarity formulations employ a larger concentration of mercaptan chain transfer agent in order to adjust the room-temperature modulus. In addition, they are

based on a polyether backbone, which is prone to chain transfer reactions because it can undergo hydrogen abstraction by free radicals [7], thus affecting the way in which the material crosslinks during cure. It has been proposed that the temperature sensitivity of chain transfer reactions may be responsible for the lower moduli of UV-cured acrylates reacted at high temperatures [8]. Note in Figure 9 that the equilibrium modulus of the high-modulus variant of the low-polarity coating is about the same as that of the low-modulus coating, as the modulus decreases substantially as the temperature increases. In contrast, as shown in Figure 10, the modulus of the high-modulus, higher-polarity coating increases slightly with temperature, which is the expected behavior for rubbers. A closer look at Figure 9 reveals a shoulder to the right of the tan delta peak of the "high modulus" coating, indicating perhaps the existence of a two-phase system. The coatings of Figure 9 consist of a polyester backbone and several monomers, including a diacrylate and a triacrylate. The high-modulus version has an additional diacrylate. The apparent two-phase behavior of this coating, together with its unexpectedly low equilibrium rubbery modulus, may be explained by hypothesizing that the additional diacrylate utilized to increase the modulus contributed to the development of a heterogeneous crosslinked structure consisting of two domains: a relatively lightly crosslinked domain where the crosslink density is determined by the oligomer molecular weight, and a small second phase of rigid nodules formed by the diacrylate and triacrylate monomers. On the other hand, the polyether-based coatings of Figure 10, which have a shorter oligomer backbone and fewer crosslinking monomers, proved to be more homogeneous.

The reduced cross-linkage may also account for the reduction in the delamination resistance at lower polarity. Per the above discussion, this would reduce the capability of the primary coating to absorb the stress of an imposed deformation.

Table 6. Effect of primary polarity on in situ modulus.

Secondary T_g	In situ Modulus in psi			
	Low polarity		High polarity	
	High modulus	Low modulus	High modulus	Low modulus
low	161	112	147	75
high	137	99	141	64

The effect of adhesion promoter and primary modulus on the in situ modulus is shown in Fig. 11. This is the x_2x_3 interaction, which is negative according to Table 5. This means that increasing adhesion promoter decreases the dependence of the in situ modulus on the primary modulus. On the other hand, the in situ modulus is uniformly higher at higher promoter concentrations. The adhesion promoter increases the cross-link density, and it interacts strongly with the cross-linking agent.

The least-squares expression for the modulus of sheets of the low-polarity primaries was $(M_A) = 1.0*(M_0) + 325*(A) + 0.54*(M_0)*(A) + 9.35$, where M_0 is the modulus (psi) without adhesion promoter (AP), M_A is the modulus with AP, and A is the concentration of AP. The large interaction coefficient shows that cross-linking agent added to increase the modulus boosted the modulus by more than expected when an adhesion promoter was present. The least-squares expression for the ISM from Table 5 is $M(30.6+10.9P-11.2A-8.2T) - P(16.3+2.8A-9.3T) + A(35.6-6.3T) - 14.6T + 177.1$, where P is the polarity, M the sheet modulus, T the secondary T_g , and A the adhesion promoter concentration. Analogous to the behavior on sheets, ISM increases as A increases (the negative $A-M$ interaction is more than offset by the positive sign and magnitude of the A coefficient.)

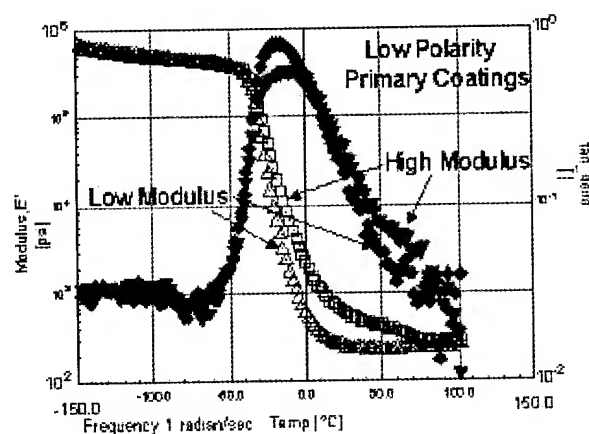


Figure 9. DMA curves of low and high modulus, low polarity primary coatings.

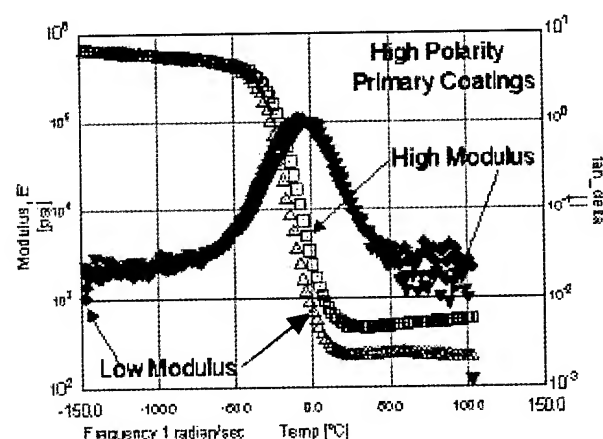


Figure 10. DMA curves of low and high modulus, high polarity primary coatings.

7.3 Linearity assumption

Table 7 shows the residuals of the four trials that were added to the factorial design at the midpoints of the modulus and the adhesion promoter and not included in the analysis.

Table 7. Residuals = Estimates-Measurements

Trial	13	14	17	20
In situ modulus	19.6	-38.5	20.3	29.4
pull out force	-1.13	0.53	-0.12	0.03
D50	-395	363	-24	164

The linearity assumption is worst for trials 13 and 14 for all three responses but particularly for the pull out force and the delamination resistance. Accurate prediction of these responses over the full range might require additional trials between the vertices of the design.

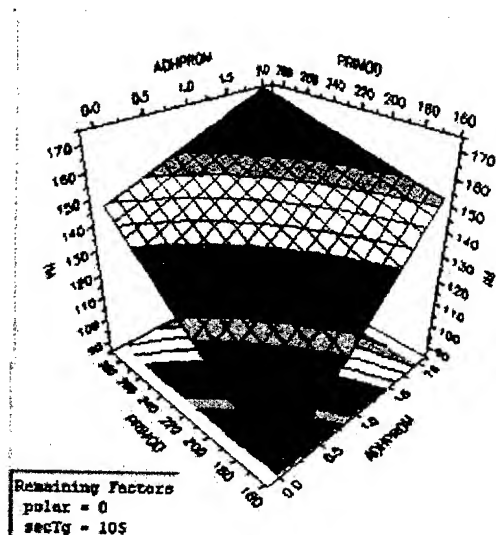


Figure 11. Effect of adhesion promoter and primary modulus on in situ modulus.

8. Summary

Because most commercial fiber coating formulations are proprietary to the suppliers, measuring the critical properties of optical fiber coating systems in which details of the chemistry are known represents an unusual opportunity for a fiber manufacturer. With these systems, we have been able to establish a quantitative relationship between a coating system's molecular structure and its mechanical and adhesive properties on glass. Our designed experiment has enabled us to extract the maximum amount of information from the responses, which will be helpful to our suppliers and us in formulating next-generation coatings.

9. Acknowledgments

Special thanks go to Claire Plagianis for the generation of the DMA results and Danny Harper for drawing the fiber. Valerie Kuck is acknowledged for the valuable delamination resistance data. The water absorption and contact angle data were provided by SEI laboratories. Thanks to Yasuo Matsuda and Tomoyuki Hattori of SEI for these data and many helpful discussions. Lee Blyler and Fred Wight are also acknowledged for their many contributions to this project.

10. References

- [1] P. L. Tabaddor, C. J. Aloisio, C.H. Plagianis, C. R. Taylor, V. Kuck and P. G. Simpkins, "Mechanics of Delamination Resistance Testing," Proceedings 47th International Wire and Cable Symposium, 725-731 (1998).
- [2] C. J. Aloisio, W. W. King and R. C. Moore, "A Viscoelastic Analysis of Thermally Induced Residual Stresses in Dual Coated Optical Fibers," Proceedings 44th International Wire and Cable Symposium, 139-145 (1995).
- [3] Achorn, P.J., and Ferrillo, R.G., "Comparison of Thermal Techniques for Glass Transition Measurements of Polystyrene and Cross-linked Acrylic Polyurethane films," *J. Appl. Polym. Sci.*, 54(13), 2033, (1994).
- [4] Suhir, E, "Analytical modeling of the interface shearing stress in dual-coated optical fiber specimens subjected to tension," *Applied Optics*, 32(16), 3024 (1993).
- [5] B. J. Overton and C. R. Taylor, *Proc. of SPE ANTEC*, p392, April 18-21, 1988.
- [6] C.J. Aloisio, A. Hale, V.J. Kuck, J.F. Malluck, P.G. Simpkins, and H. Tornqvist, "Coated optical fiber with increased modulus and thermally enhanced strippability", US Patent # 6,243,523, June 5, 2001.
- [7] N. S. Allen, P. J. Robinson, and N. J. White, "Photo-oxidative stability of electron-beam and UV cured triacrylate resin films: influence of the structure of the multifunctional monomer", *Polymer Degradation and Stability*, 23, 245 (1989).
- [8] R. Levin, A. Hale, A. L. Harris, N. J. Levinos, and F. C. Schilling, "The effect of cure temperature on the reaction kinetics and elastic modulus of a UV-cured acrylate system," *Polym. Mat. Sci. Eng.*, 72, 524 (1995).

Biographies



Charles J. Aloisio

2000 NE Expressway, Norcross, GA 30071

Charles Aloisio began his career with AT&T Bell Laboratories in 1952. He worked in the Materials Group with Bell Labs in Indianapolis from 1967 to 1972, while obtaining his MS and Ph.D. from Purdue University. He is currently a Distinguished Member of the Technical Staff in the OFS Material Technology Group and has worked on applying rheology and viscoelasticity to a variety of materials such as polypropylene and polyethylene for cable sheathing and DEPIC insulation, copper and optical fiber coatings.



Arturo Hale

700 Mountain Avenue, Murray Hill, NJ 07974

Arturo Hale is a Member of Technical Staff in the Optical Fiber Research Department at OFS Laboratories in Murray Hill, New Jersey. He received his B.S. in chemical engineering from the Universidad Autónoma Metropolitana in Mexico City in 1982 and his Ph.D. in chemical engineering from the University of Minnesota in 1988. He works on research and development of new polymeric materials for optical fibers and specialty photonic devices.



Kariofilis Konstadinidis

2000 NE Expressway, Norcross, GA 30071

Kariofilis Konstadinidis is a Member of Technical Staff in the Materials Technology group at OFS, Norcross, GA. He is involved in the development, qualification, and implementation of UV curable materials for optical fiber applications. He received his Ph.D. in Chemical Engineering from the University of Minnesota in 1992. He did his post-doctoral work at AT&T Bell Laboratories in Murray Hill, NJ prior to transferring to Norcross in 1995.



Robert C. Moore

2000 NE Expressway, Norcross, GA 30071

Rob Moore is a Consulting Member of Technical Staff for OFS in Norcross, Georgia, where he works on glass and optical fiber manufacture and fiber coating design and application. He earned an A.B. in Physical Sciences from the University of California,

Berkeley, an M.S. in Chemical Engineering from the University of Washington in Seattle, and a Ph.D. in Chemical Engineering from the University of California, Berkeley. He joined AT&T's Engineering Research Center in New Jersey in 1986 and transferred to Norcross in 1990.



Mahmood Tabaddor

2000 NE Expressway, Norcross, GA 30071

Mahmood Tabaddor is a Member of Technical Staff with the Optical Fiber Division of OFS. Mahmood has his MS and PhD degrees from University of Michigan and Virginia Tech, respectively, in the field of mechanical engineering. Mahmood has worked on the numerical modeling of products, processes and tests related to optical fibers and ribbons.



John M. Turnipseed

2000 NE Expressway, Norcross, GA 30071

John Turnipseed is a Distinguished Member of Technical Staff in the Materials Technology group at OFS, where he is engaged in the development and implementation of radiation curable materials intended for use in telecommunications products. He received B.S. and M.S. degrees in Analytical Chemistry from the University of Virginia prior to joining the Western Electric Company in 1972.

Micro-mechanical On-fiber Analysis of the Interface Between Outer Primary and UV-cured Ink

Kathleen Hoekstra

DSM Desotech

Elgin, IL

847-214-3844 · kathleen.hoekstra@dsm.com

Abstract

One important performance parameter for UV curable fiber optic inks is adhesion between the color-coding ink layer and underlying outer primary coating. The adhesion performance is difficult to quantify, especially on the fiber itself. Flat film sandwiches of ink and outer primary do not represent the actual geometry, dimensions, and cure conditions of the coatings on fiber. A current industry practice to quantify adhesion on fiber is to perform a solvent-rub test until ink delaminates. However, solvent and mechanical contributions cannot be separated and solvent diffusion plays a significant role in the interfacial failure during the rub test. Micro-mechanical properties of film interfaces can be characterized with scratch instrumentation. This paper describes scratch investigations of ink and coating layers on optical fibers. The utility of micro-scratch and nano-scratch techniques, and of blade versus traditional tip shapes, for characterizing coatings on optical fiber, is explored. The nature and threshold for ink delamination are compared for inks differing in mechanical properties and rub test performance.

Keywords

Optical fibers; coatings; micro-mechanical; adhesion; UV-curable; on-fiber analysis; micro-scratch.

1. Introduction

Optical fibers are typically colored with UV-curable inks for visual identification of individual fibers assembled into ribbons or loose tubes. A polymeric ink layer (3-6 μm) colors each fiber (125 μm diameter) that has been coated with inner and outer primary coatings (40 to 60 μm each). Adhesion between the ink and outer primary is important for the fiber to retain its color under handling and aging stresses.

Methods to quantify adhesion of optical fiber inks are not straightforward. The cure conditions and dimensions of thin films on cylindrical fibers cannot accurately be reproduced with flat film sandwiches. On fiber coatings will be subjected to different geometrical stresses, line speeds, lamp distances, exposure times, temperatures, and oxygen permeation depths than flat films. Many adhesion methods are designed for macroscopic flat film measurements and are not suitable to measure coatings on fiber. Tensile tests to measure coating adhesion on fiber^{1,2} can be

complicated by shearing of low modulus coatings in a multiple coating system of this nature.

Industry has adopted a solvent rub method to qualify adhesion of inks on optical fibers. Inked fiber held between solvent-saturated Kimwipes® is rubbed back and forth with a set force across a fixed distance. Ink passes the adhesion test when it remains intact beyond 200 double rubs. Experiments performed in our labs have indicated that solvent diffusion is a primary contributor to ink failure in the rub test. Variations in ink thickness significantly affect the number of rubs to ink failure. Design of coatings with specific adhesion behavior will require quantification of relative adhesion values for coatings on fiber independent of solvent impact on coating integrity.

Sampling and test procedures that minimize alteration of the sample itself would be valuable to clarify the interfacial behavior of the coatings. Surfaces can be studied by force microscopy with or without the sample being exposed to solvent. Samples are most often flat substrates coated with a single film; optical fiber coatings are more difficult to analyze because of the geometry and scale of the films and fiber, and very little analysis has been reported for optical fiber coating interfaces. Özgür, Gebizliouglu, and Kurkjian³ used an atomic force microscope (AFM) with a nanoindentation / nanoscratch tip to look at surface cleanliness of optical fiber after stripping, but were measuring residual roughness on the order of nanometers, and did not measure adhesion. For our system, sampling the interface between intact micron-scale fiber coatings would require a larger probe that can penetrate through the upper layer, or a means to access the interface end-on. We have observed that fiber coatings are easily damaged when embedded and microtomed to create end-on samples. Another way to examine the coating interface is by indentation and scratch techniques that can penetrate the upper film. Scratch and indentation techniques have been used to measure coating durability, wherein load to film failure is taken as an indicator of adhesion.⁴ Microscratch with a diamond blade was used to examine fracture of 200 nm metallic coatings on optical fiber, but has not been reported for polymer films on optical fiber or for multi-coat films on fiber.⁵ We set out to investigate the utility of the scratch technique for characterizing the ink-secondary coating interface on fiber.

2. Experimental

Optical fiber samples were characterized with a nanoscratch tester (NST) and with a microscratch tester (MST) from CSEM at Micro Photonics (Irvine, CA). Fibers were glued flat onto microscope slides that were mounted onto the sample stage. The scratch experiment involved drawing a small stylus along the longitudinal axis of the coated fiber, while a progressive normal load was applied to the stylus at a fixed rate. The depth of the stylus was profiled and critical loads (L_c) for failure were identified as the scratch was optically monitored (50x-1000x) to observe fracture events. The NST with a medium load cell had a force range of 10 μ N to 100 mN, and the range of the MST was 5 mN to 30 N. A tungsten carbide (WC) Rockwell conical indenter with 10 μ m radius and a 75° diamond blade were used with the MST, and a 2 μ m WC Rockwell conical indenter with the NST. Example instrument operating parameters we used are shown in Table 1.

Table 1. Typical operating parameters used.

Parameter	MST, 75° blade	NST, 2 μ m tip
Prescan load, mN	---, 5	---
Initial load, mN	5	0.1
Final load, mN	700	130
Loading rate, mN/min	700	130
Speed, mm/min	2	1.4
Scratch length, mm	2	1.4

Fibers (125 μ m) were coated with different types of ink (3-6 μ m) over UV-cured outer and inner primary layers (40-60 μ m each) that were identical for every sample. Inks were also characterized for tensile, elongation and modulus (Instron tensile testing of 3 mil flat films), and for resistance to MEK solvent rubs (on fiber). Here we compare inks with good solvent-rub performance to an ink with poor performance. These properties are shown in Table 2.

Table 2. Physical characterization of samples.

Ink type	MEK* rubs	TEM* (MPa / % / MPa)
A	>200	25 / 15 / 600
B	>200	25-30 / 2-4 / 1450-1650
C	20-30	26 / 16 / 724

*MEK(methylethylketone), T(tensile), E(elongation), M(modulus)

The outer primary coating has TEM properties similar to that of the inks, while the inner primary coating is a much lower modulus, more flexible coating.

3. Results and Discussion

3.1 Ink B

Ink B was characterized by both nanoscratch and microscratch methods. The NST equipped with the 2 μ m tip and medium load cell was not sufficient to characterize more than the outer ink layer itself. The experiment produced a surface scratch that exhibited a brittle fracture pattern consistent with the low flexibility of the ink, as shown in Figure 1.

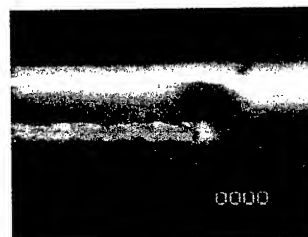


Figure 1. Optical image of scratch of on-fiber Ink B, with 2 μ m tip by NST.

The profile of the scratch showed that the tip moved steadily into the sample without sudden changes in probe depth. The higher load range available with the MST gave us the opportunity to scratch the sample to a greater depth. The ink was tested on the MST with both the conical 10 μ m tip and the 75° blade. Alignment of the blade along the axis of the fiber was much easier than the 10 μ m round tip, because the tip had a tendency to slide off of the side of the fiber due to its curved shape. These experiments yielded the same type and sequence of coating failure events. This sequence of failure events and the associated loads were consistent from run to run. Critical load (L_c) values averaged over three runs (Table 3) verify the reproducibility of the test.

Table 3. Reproducibility of Fracture Events for Ink B with 75° Blade on MST.

Ink B, Fracture Event	L_c , mN	Standard deviation
compression	370	7
initial fracture	406	11
coating removal	514	8

The scratch profile is shown in Figure 2 and optical images of fracture events are shown in Figure 3. The first noticeable change in the sample appeared to be an internal compression of inner coatings that occurred without any fracture of the ink surface itself. The tip or blade exerted enough pressure to cause the compression at this load level, but not enough to break through the hard outer shell of the high modulus ink. Compression was followed by brittle fracture of the outer ink surface; the image shows the cuts produced by the knife as it chatters along the ink. This phase is accompanied by a small depth change consistent with the thickness of the ink. The knife finally breaks through the ink, delaminating one or more of the coatings beneath. This event

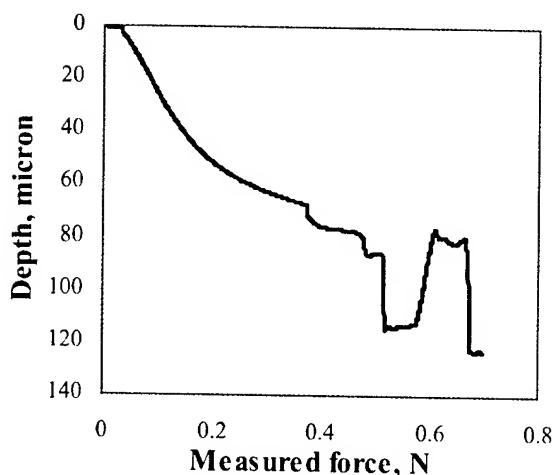


Figure 2. Scratch profile of Ink B on Fiber using 75° blade on MST.

is accompanied by a final sharp depth change, and the fiber core soon breaks if the test is continued beyond this point. More than one coating may delaminate at once, because the load is high enough to cut into any of the coatings at this point; ink would not separate from the secondary if sufficient adhesion exists between them.



Figure 3. Optical images of fracture events during scratch testing of Ink B with 75° blade on MST. Upper: initial compression. Center: initial fracture of outer ink surface. Lower: coating delamination. 200x

3.2 Inks A & C

Inks A and C have similar physical properties with the distinction that one performed well in the solvent-rub test while the other did not. Both inks are more flexible and lower in modulus than ink B, and this is apparent in the images of fracture shown by way of example in Figure 4 for ink C. These two inks exhibited nearly the same scratch response, with the distinction that the ink with poor solvent-rub performance completely delaminated at lower critical load (Table 4). Even though the outer surface of inks A and C fractured under similar loads, as high a load was required to break through the lower interface of ink A as with ink B. This suggests that inks with better solvent-rub performance hold up better to delamination under scratch. Fracture of the outer surface of the ink should relate more to TEM properties than to interfacial adhesion.



Figure 4. Optical image of fracture of Ink C with 75° blade on the MST. Upper: compression of the coatings. Center: ink fracture. Lower: silica core. 200x

Table 4. Comparison of critical loads for ink fracture and delamination.

Ink	Lc, mN ink fracture	Lc, mN ink delamination
A	121	543
B	406	514
C	140	316

4. Conclusion

The drive for higher performance optical fiber coatings will place an increasing reliance on characterization methods that accurately portray coating performance on fiber. We have reported, to our knowledge, the first implementation of scratch methods to characterize UV cured inks directly on coated optical fibers. Nanoscratch and microscratch measurements offer the opportunity to analyze micromechanical properties of coatings "as-are" – minimizing the need for complex preparation schemes that might alter properties, and eliminating sampling configurations and test conditions that don't accurately represent the state of the coating. A blade-shaped probe worked very well with the cylindrical fiber geometry. Our study, which differentiated inks varying in mechanical behavior and solvent resistance, shows scratch measurement to be a promising technique for characterizing performance of coatings on fiber.

5. Continuing Research

Continuing research avenues include to:

- Analyze a number of inks by microscratch. Gain a better understanding of how physical properties affect coating behavior in scratch tests.
- Further establish the scratch behavior of inks that perform well or poorly in solvent-resistance tests.
- Distinguish solvent versus adhesion contributions by correlating ink failure to extent of solvent exposure.

6. Acknowledgements

The author would like to thank Pierre Leroux and Ethel Poiré of Micro Photonics for their assistance and valuable input. Ed Murphy of DSM Desotech is recognized for enthusiastically supporting this project.

7. References

- [1] J. Rayss, W. M. Podkoscielny, J. Widomski, A. Gorgol, "Determinatin of Adhesion of UV-Curable Protective Coatings of Optical Fibers," *J. Appl. Poly. Sci.*, 53, 1833-1834 (1994).
- [2] A. Apicella, L. Nicolais, D. Ciuomo, I. Ferri, "Adhesion of Coatings on Glass : A New Measurement Method," *EFOC/LAN 91, Ninth Annual European Fibre Optic Communications aned Local Area Network Conference*, 100-104 (June 19-21).
- [3] M.R. Özgür, O.S. Gebizlioglu, C.R. Kurkjian, "Evaluation of Fiber Coating Stripping Methods by Atomic Force Microscopy of Fiber Surfaces," *Proceedings of the 50th IWCS*, 257-266 (2001).
- [4] K.L. Mittal, ed., *Adhesion Measurement of Films and Coatings*, VSP, Netherlands, 95-102, 161-174, 175-188, 189-215 (1995).
- [5] Micro Photonics website, www.microphotonics.com

Prediction of Ribbon Friction by Matrix Resin Upjacketing of Single Fibers

Edwin Currie*, Keqi Gan, Kelly A. Hawkinson, Brett A. Register, Edward P. Zahora

DSM Desotech, Inc
Elgin, Illinois
+1-847-697-0400

*DSM Research
Geleen, The Netherlands
+31-46-476-0160

Abstract

As the trend of fiber to the home (FTTH) persists, it is beneficial for ribbon matrix and buffer coatings to possess an intrinsic low coefficient of friction without the lubricating action of external greases. In order to test the friction properties of new matrix or buffer coatings without the time and materials necessary to produce a high fiber count ribbon, a test has been devised in which a single fiber is upjacketed with the candidate resin. The single buffered fiber is pulled along a control ribbon without any lubricating additives. This test method is based on published methodology that is used in the industry to generate CoF data for ribbon to ribbon contact. Since the single buffered fiber has been coated on typical fiber optic coloring and ribboning equipment with the proper thickness of the resin, the authors observed good rank order correlation between the measured sliding friction of the single fiber and a typical twelve-fiber ribbon of standard configuration. This method has proved a significant advantage in saving time and materials, and provides a much better coefficient of friction performance prediction than flat film analyses. Examples are presented in this paper that demonstrate this correlation between buffered single fiber to ribbon and ribbon to ribbon coefficient of friction results.

Keywords

buffered fiber; CoF; ribbon matrix; sliding friction; upjacketed fiber

1. Introduction

Cable manufacturers require the sliding friction of a matrix material to be low in order to isolate the fibers from microbending forces and allow easy slippage between adjacent ribbons, thereby minimizing fiber strain^[1]. Microbending occurs when large lateral forces are acting between fibers and this increases attenuation resulting in signal loss. Therefore, it is important that a ribbon sliding test accurately predicts the CoF of a matrix material, which determines how a fiber ribbon interacts with adjacent ribbons in multiple cable designs.

In the past, flat film testing was utilized to obtain slip data on matrix materials. This test involved dragging a weighted sled with an attached film of the material over a flat film of the same material^[2]. This test was unable to accurately predict either a trend or an absolute value that correlated to what was observed by customers producing ribbons with the same matrix material. Analysis reveals that the mechanics of the mandrel test differ strongly from those of a flat film test as will be described in the Section 2 (Frictional Properties). The amount of weight necessary to attain similar

stresses in the flat film testing are unrealistic, and would cause the sled to plow through the sample causing deformation to the surface.

A difference also exists in the final surface of a flat film and ribbon due to the different methods of curing the samples. When a material is cured as at flat film it is exposed to UV light via a Fusion unit at a speed of approximately 10 to 20 m/min. In contrast, a ribbon sample made on a Nextrom ribboning machine is exposed to UV light at 400 m/min, and the time between the creation of the film and the curing of the surface is approximately 1 ms. This difference in time prior to cure has a large impact on the diffusion of surface active additives, i.e. lubricants, and thus the slip properties.

Therefore, a ribbon to ribbon test was employed utilizing previously published methodology^[3,4,5]. We were able to predict what the customer observed on ribbon, since the analyzed samples were of similar geometry. However, ribbon to ribbon testing can be expensive and is dependent on processing conditions. Ribbons need a high degree of planarity to ensure that only the slip properties of the material are being measured. Surface roughness of the ribbon is one of the parameters that determine the sliding friction of a material. If the fibers are not properly aligned, the surface becomes irregular. Also in order to process a ribbon, multiple fibers have to be coated and a matrix resin is deposited over these fibers. This can become expensive when materials are in the developmental stage. As a result, a single buffered fiber to ribbon CoF test was developed. The test is based on the same principle as the ribbon to ribbon test, with a few modifications. Also the application and cure conditions of the upjacketed fiber are similar to that of a ribbon, in comparison to the large differences that exist between those of a flat film and a ribbon. Studies to date indicate the results are comparable and that the same frictional properties are being measured.

2. Frictional Properties

When discussing the friction of polymeric surfaces, the coefficient of friction is sometimes represented as a material parameter only. The CoF is a complex function of surface topology, processing conditions, and testing conditions and this is especially important in the case of UV-curable resins with lubricating additives. In order to interpret the results of the sliding friction of ribbons correctly, one must understand and control the conditions of curing, processing, and testing.

The lateral sliding friction of polymeric surfaces is generally analyzed utilizing a polymer adhered to a steel sled and pulling it over a surface of the same material at a controlled rate^[2]. The sliding speeds generally range from 1 to 10 mm/s and the normal contact pressure is in the range of 0.02 to 0.2 MPa, assuming full contact

between the film and the sled. In contrast, the mandrel set-up devised by Keesec, et al.^[3] for measuring the sliding friction of ribbons, has an estimated contact pressure of 1 to 20 MPa as illustrated in Figure 1. This high value of the normal pressure is due to two factors. First, the circular geometry induces an exponential increase of the overall tensile force as a function of the arc angle (φ) and the CoF (μ) as shown in the following relationship^[6] where mg is the initial force:

$$F_{ten}(\varphi) = mg e^{\mu\varphi} \quad (1)$$

Secondly, the uneven surface of a ribbon results in low contact areas when pressed against each other. The effective contact area is a function of the local curvature and the modulus of the matrix^[7]. The increase in overall normal load and small contact areas combined results in significantly higher normal pressures than those attained in flat film testing. Using Hertzian mechanics this local normal pressure was estimated to be^[7]:

$$p_0(\varphi) = \left(\frac{mgE}{\pi n R_{man} R} \right)^{1/2} \left(\sin \varphi + \frac{e^{\mu\varphi} - 1}{\mu} \right)^{1/2} \quad (2)$$

In the above equation E is the modulus of the matrix, R_{man} is the radius of the mandrel (10 cm), R is the radius of the optical fibers in the ribbon (~150 μ m), and n is the number of fibers in contact with each other (estimated to be 12 for simplicity). In Figure 1 the estimated normal pressure is plotted as a function of the arc φ for values of μ ranging from 0 to 1. It is clear that the local contact pressure may become rather high, and considerably above that attained in flat film tests.

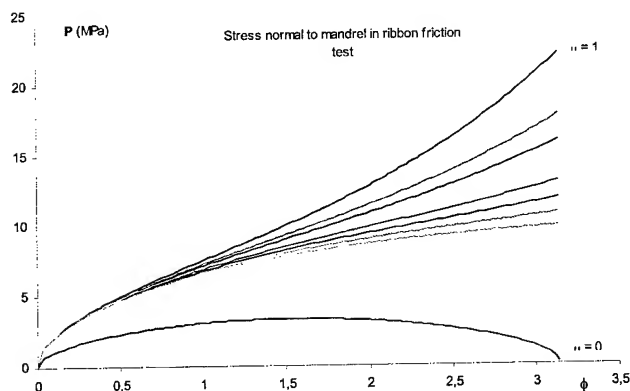


Figure 1. Normal Pressure for μ varying from 0, 0.1, ..., 1 as a function of the arc angle

Due to this large difference in contact pressure the mandrel CoF test may differentiate formulations that have an equal performance in a flat film test. The reason for this is as follows: At high normal pressures mobile lubricants can be squeezed from the contact area, resulting in dry polymeric contact areas^[8,9]. The pressure at which the lubricant film breaks is determined by the affinity of the lubricant for the polymeric surface. Estimation of such critical

pressures showed these to be in the same regime as the normal pressure in the mandrel CoF test. This is shown in Figure 2, together with the estimated radius of such holes in the lubricant layer. The details of this analysis can be found in references 8 and 9. Thus, in our opinion the mandrel ribbon CoF test is a more critical test for the performance of lubricating additives than film tests.

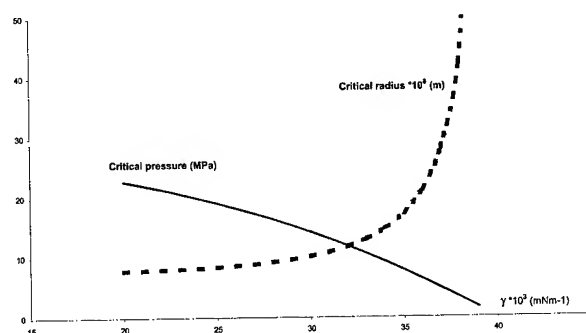


Figure 2. Critical Pressure and Critical Lubricant Hole Size as a Function of the Lubricant Surface Tension

The fabrication of ribbons is time consuming; therefore it was our goal to develop an alternative CoF test, which predicts the rank order of new matrix candidates in studies, which often involve a large number of formulations. In order to achieve the normal pressures observed in ribbon to ribbon analysis, a similar circular geometry and low contact areas are necessary. To accomplish this we developed the buffered single-fiber test, in which a single fiber with an outer layer of matrix material is pulled across a twelve-fiber ribbon whose matrix is without any lubricating additives. The buffered single fiber has a diameter similar to that of the twelve-fiber ribbon with similar contact area and since the matrix of the underlying ribbon does not contain lubricating additives, all lubricating action can be attributed to the formulation on the single fiber.

3. Experimental Design

3.1 Processing Conditions For Ribbon and Single Buffered Fiber

The twelve-fiber ribbon samples were processed on a Nextrom OFC-21 ribbon machine with 254 μ m colored single fibers. A slight in-house modification was made with the machine allowing the oxygen concentration in the nitrogen purge gas to consistently be below 100 ppm when measuring with a calibrated oxygen analyzer (Thermox CG-1000 manufactured by AMETEK).

The OFC-21 ribbon machine is equipped with two UV lamps. The first in line lamp is an 11 mm, 6-inch D bulb with 500 W/in functioning at 100% of power. The second lamp is mounted opposite of the first and is a 13 mm, 10-inch H bulb with 600 W/in functioning at 60%. The nitrogen flow rate for both lamps is 40 L/min. The purity of the nitrogen purge gas is greater than 99.9%. The tested ribbon samples were processed at 400 m/min. The entry die size is 3188 x 271 μ m, while the exit die size is 3219 x 350 μ m.

Final ribbon thickness is about 300 μm , resulting in an average matrix thickness of 23 μm .

We attempted to match the processing conditions of the single upjacketed fiber samples as close as possible to the twelve-fiber ribbon samples. The fiber was upjacketed with the Nextrom OFC-52 color machine. The first in line lamp is an 11 mm, 10-inch D bulb with 600 W/in functioning at 67% power, followed by a 13 mm, 10-inch H bulb with 600 W/in also functioning at 67% power. The nitrogen and the flow rate parameters were the same as the ribbon machine. All of the testing samples were processed at 400 m/min. The measured oxygen content in the processing environment was consistently less than 100 ppm. The entry and exit dies are both 275 μm . Smaller diameter (235 μm) uncolored fibers were chosen for the analyses to achieve the final unjacketed fiber diameter of 265 μm , resulting in an average matrix thickness of 15 μm .

3.2 Test Method

The single buffered fiber to ribbon test is based on the ribbon to ribbon CoF test^[3,4,5] that is currently used in the field and at our facility to obtain CoF values for different matrix materials. A ribbon containing multiple fibers is fastened around a steel mandrel with a diameter of 20 cm and a groove width for a twelve-fiber ribbon of 3.2 mm. The mandrel is attached to the crosshead of an Instron. The ribbon does not contain any lubricating additives that are added to the matrix composition in order to decrease the friction of the material. The single buffered fiber is attached to a clamp at the base of the Instron and then draped over the mandrel containing the ribbon. A 200 g weight is attached to the end of the single buffered fiber. Care must be taken to ensure that the single buffered fiber is properly aligned along the ribbon and is not allowed to touch either side of the mandrel. The single buffered fiber is pulled across the ribbon at 25 mm/min. The main differences that exist between the two tests are: the ribbon to ribbon test utilizes a higher weight of 1600g attached to the top ribbon sample, and the ribbon that is pulled along the fixed ribbon in the mandrel are both coated with the same matrix material. The instrument configuration can be found in Figure 3. The maximum load is reported and allows the coefficient of friction to be calculated. The following equation is used to determine the coefficient of friction:

$$\mu = 1/\pi \ln[F_{\text{tot}}/(M \times g) - 1] \quad (3)$$

The coefficient of friction is represented by μ , F represents the maximum peak force, M represents the weight attached to the single buffered fiber, and the acceleration due to gravity is represented by g. Each matrix material is analyzed at least three times in order to ensure that the value is accurate and to provide an estimate of test variance. Each time a material is evaluated a new single buffered fiber is wrapped over a new ribbon on the mandrel.

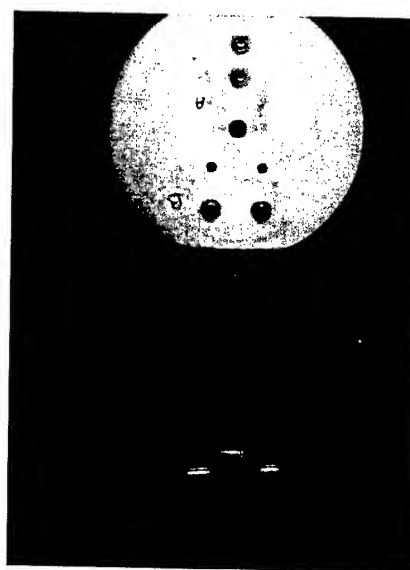


Figure 3. COF Mandrel Configuration

3.3 Materials

Typical acrylate-based matrix materials were prepared for this study as illustrated in U.S. patents 6,052,503 and 6,319,549^[10,11].

3.4 Results

The experiment was set up in three different phases. In the first phase the CoF data obtained from ribbon to ribbon and the single buffered fiber to ribbon analyses were directly compared. This experiment included a ladder study of lubricating additives used in the same base matrix formulation. The numerical data can be found in Table 1. The results of the study and the repeatability of the data can be found in Figure 4.

Table 1. Comparison of Ribbon-to-Ribbon and Single Buffered Fiber Analysis for Lubricating Additives Ladder study

Lubricating Additives (%)	Ribbon to Ribbon CoF	Single Buffered Fiber to Ribbon CoF
2	0.71 (0.06)	0.73 (0.03)
3	0.64 (0.04)	0.80 (0.03)
4	0.49 (0.10)	0.63 (0.03)
5	0.48 (0.10)	0.63 (0.03)
6	0.47 (0.01)	0.62 (0.04)

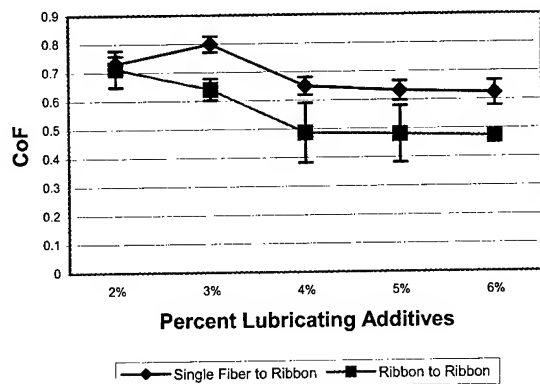


Figure 4. CoF Comparison of Single Fiber to Ribbon Versus Ribbon to Ribbon Analysis

The results indicate that differences in the CoF of a material can be determined from both the ribbon to ribbon and the single fiber to ribbon analysis. The numerical values differ slightly between the two analyses, but the same trend and rank order are observed. A trend in the CoF of a material is noted between two and six percent addition of lubricating additives. The CoF decreases from two to four percent and then levels off between four and six percent.

In the second phase of the study, we wanted to evaluate the relationship between formulation composition and the effective slip properties. The formulation was altered, but the tensile properties were kept constant. A similar ladder study with lubricating additives was performed on these coatings. The results of the study and the repeatability of the data can be found in Figure 5. The numerical data can be found in Table 2.

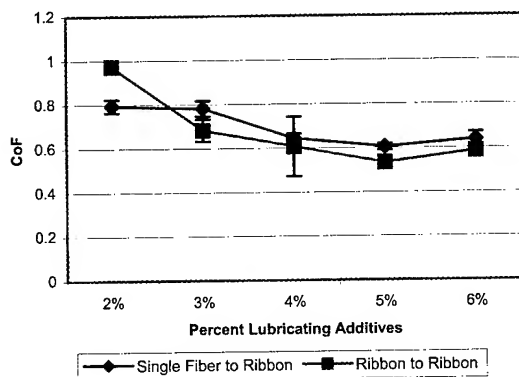


Figure 5. CoF Comparison of Single Fiber to Ribbon Versus Ribbon to Ribbon Analysis for alternant Formulations

The results demonstrate in the case of both formulations the same trend is observed with the single fiber and the ribbon to ribbon test, regardless of the specific chemical composition of the formulation.

The third phase of the study evaluated matrix materials of low, medium, and high CoF values; and measured the CoF values via the

ribbon to ribbon and single buffered fiber to ribbon methods. The data can be found in Table 3.

Table 2. Comparison of Ribbon-to-Ribbon and Single Buffered Fiber Analysis for Lubricating Additives Ladder study Alternant Formulations

Lubricating Additives (%)	Ribbon to Ribbon CoF	Single Buffered Fiber to Ribbon CoF
2	0.97 (0.01)	0.79 (0.03)
3	0.68 (0.05)	0.78 (0.04)
4	0.61 (0.14)	0.65 (0.02)
5	0.53 (0.02)	0.61 (0.01)
6	0.59 (0.01)	0.64 (0.03)

Table 3. Comparison of Ribbon to Ribbon and Single Buffered Fiber to Ribbon Analysis for Multiple Matrix Materials

Material	Ribbon to Ribbon CoF	Single Buffered Fiber to Ribbon CoF
Formulation A	0.61 (0.07)	0.66 (0.01)
Formulation B	0.74 (0.04)	0.78 (0.06)
Formulation C	0.82 (0.14)	0.76 (0.02)
Formulation D	0.97 (0.02)	0.78 (0.04)
Formulation E	1.06 (0.001)	0.95 (0.02)

The results demonstrate that the single buffered fiber to ribbon analysis can be utilized to obtain reliable rank order CoF data for matrix materials. The values are similar to that obtained from ribbon to ribbon analysis. Both methods can be used to differentiate the slip properties of different matrix formulations. Also the single buffered fiber to ribbon data always has a repeatable low standard deviation. The ribbon to ribbon analysis standard deviation varies from sample to sample.

4. Conclusions

The single buffered fiber to ribbon CoF test is a useful research and development tool in predicting the slip properties and rank order of matrix materials. Also the single buffered fiber to ribbon analysis is more economical in comparison to the ribbon to ribbon analysis. The results that are obtained from this analysis are repeatable and similar to those obtained from ribbon to ribbon CoF analysis. The test adequately predicts the sliding characteristics of multiple ribbons when they are placed into a cable design.

5. Acknowledgments

The authors would like to acknowledge the contributions of Todd Anderson and Loretta Bradley whose work allowed us to generate the results of this study. Ed Murphy and David Szum are also recognized for enthusiastically supporting this project.

6. References

- [1] Wagman, R.S., et al. "Design Concepts for a 4000-Fiber Cable with Thinly Coated Fiber." *International Wire and Cable Symposium Proceedings*, 12-21 (1994).
- [2] "Static and Kinetic Coefficients of Friction of Plastic Film and Sheeting." *ASTM D-1894*.
- [3] J.R. Keesee, et al. "A Comprehensive Approach To Ribbon Design With A Focus On Materials." *International Wire and Cable Symposium Proceedings*, 430-438 (1994).
- [4] G.A. Lochkovic, et al. "Cable Containing Fiber Ribbons With Optimized Frictional Properties." *US Patent 5,561,730* (1996).
- [5] T. Hattori, et al. "Coated Tape Form Optical Fiber Wire." *US Patent 5,524,164* (1996).
- [6] J.A. Eytelwein. *Handbuch der Mechanik fester Korper und der Hydraulik*. Berlin. F.T. Lagarde (1801).
- [7] K.L. Johnson. *Contact Mechanics*, Cambridge University Press, Cambridge (1985)
- [8] B.N.J Persson. *Sliding Friction*, Springer, Berlin (2000)
- [9] B.N.J. Persson and E. Tosatti. *Phys. Rev. B*, 50, 5590 (1994)
- [10] J.J. Schouten, et al. "Optical Glass Fiber Ribbon Assembly and Radiation Curable Matrix Forming Composition," *US Patent 6,052,503*
- [11] D.M. Szum and A. Abel "Ribbon Unit. A Method of Making the Ribbon Unit. And A Method of Providing Mid-Span Access," *US Patent 6,054,217* (2000)



Kelly Hawkinson is a chemist on a Fiber Optics Materials technical team with the responsibility for the development of matrix resins. She holds a B.S. degree in biology from the University of St. Francis and a B.S. degree in chemistry from North Central College.
(kelly.hawkinson@dsm.com)



Brett Register is a laboratory specialist on the Applied Research team, with responsibilities in physical testing, microscopy, and thermal analysis. He holds a B.S. degree in microbiology from the University of Wisconsin at La Crosse.
(brett.register@dsm.com)

7. Biography



Edwin Currie studied physical chemistry at the University of Leiden, The Netherlands. He received his PhD cum laude at the University of Wageningen in the field of polymer physics. Since January 2000 he is employed by DSM Research in Geleen, the Netherlands.
(edwin.currie@dsm.com)



Edward Zahora is a senior research chemist on a Fiber Optics Materials technical team with responsibility for development of UV cure inks and matrix resins. He holds a B.S. degree in chemistry from Westmont College, and has pursued graduated studies at Illinois State University.
(ed.zahora@dsm.com)



Keqi Gan is an application engineer on Fiber Optics Materials with responsibility for the coating process. He holds a Ph.D. degree in polymer science from Lehigh University and M.S. and B.S. degrees in physical chemistry and radiochemistry from Peking University.
(keqi.gan@dsm.com)

Fiber Optic Coating System Effect Upon Fiber Performance

Gregory L Workman II

Borden Chemical, Inc.
Cincinnati, OH 45215 USA
1.513.782.6200 · workmangl@bordenchem.com

Abstract

UV Curable Fiber Optic coating systems from the three largest suppliers were analyzed by an independent industry authority. The purpose of the study was to determine and provide objective evidence of commercial coating systems relative strengths and weaknesses. Commercial fibers were purchased on the open market and submitted to Telcordia (Bellcore) for testing per the basic GR-20 [2] standard test schedule. The results of those tests show that there are some differential benefits provided by different coating systems. All of the coating system choices passed the GR-20 requirements. However, within those allowable results, the coating system choice can affect where within the specification the results lie.

Keywords

Optical Fiber; Outside Plant Performance; UV Curable Coatings; GR-20 CORE; Attenuation; Strip Force; Dynamic Tensile Strength; Environmental Exposure Resistance.

1. Introduction

Fiber Optic coating systems from the three largest suppliers of UV Curable fiber optic coatings (Borden Chemical, Desotech/DSM, and JSR) were analyzed by an independent industry authority. The purpose of the study was to determine and provide objective evidence of commercial coating systems relative strengths and weaknesses. Commercial fibers were purchased on the open market and submitted to Telcordia (Bellcore) for testing. The results of those tests show that there are some differential benefits provided by different coating systems. The testing also shows that there can also be differentiating effects based upon process conditions. This is demonstrated in that the same coating system used by two different manufactures shows some subtle differentiating results.

The basic GR-20 standard test schedule for tests that can be affected by coating system was commissioned. The following GR-20 tests were performed: Fiber Macro-bending, Fiber attenuation coefficient at 1310 and 1550nm, Geometrical Requirements, Coating Strip Force, Dynamic Tensile Strength, Stress Corrosion Parameter, and Wasp Spray Exposure. In addition to that standard test scheme, DMTA was performed on the fibers to help explain some of the observed phenomena and Borden analyzed the aged fibers via video microscopy to determine the effects.

All of the coating system choices passed the GR-20 Standards. Within those allowable results however, the coating system choice can affect where within the specification the results lie. For example: the micro-bending attenuation, upon temperature cycling and environmental exposure, resistance are affected by the choice of coating systems. Tensile strength varied among those tested and the DMTA analysis explained why some coatings have greater low temperature micro-bending attenuation losses. Conversely, none of the systems showed any significant degradation upon wasp spray exposure and all showed a reduction of stress corrosion factor.

2. Coating System Analysis

Eight Optical Fiber Spools were purchased on the open market from some of the World's best fiber manufacturers. These fibers were then submitted to Telcordia Technologies, (formerly Bellcore) for an independent analysis of the Outside Plant Performance characteristics of those fibers with respect to the GR-20 CORE [2] requirements that could be affected by selection of UV Curable Coating Systems. As a control, two of the fibers (numbers four and five) were from the same manufacturer purportedly using the same coating system. As a further study, the same coating system utilized by two different manufactures half a world apart were also chosen to detail the effect that processing might have upon the overall performance of these coating systems. Fiber number 2 has the Borden Advanced Coating materials and is our control sample. It is believed that the coatings for fibers 1, 4, & 5 are from the same supplier, fiber coatings on 3, 6, & 7 are believed to be from another supplier, and fiber 8 is the 2nd manufacturer using the same coatings as in Borden control fiber number 2.

Telcordia was contacted and after a discussion regarding appropriate testing, the following test program was agreed upon:

Table 2-1: Summary of Borden Chemical Fiber/Coating Test Plan [1]

GR-20-CORE, Reference Section	Test Description	Specific Test Information
4	GR-20 Sect #GR-20-CORE, Issue 2	
4.2	Optical Requirements	Test at 23 C
4.2.6	Fiber Macro Bend	Test at 23 C
4.2.1	Attenuation Coefficient Test	Test at -40 C, 23 C and 70 C (see 6.6.3)
4.3	Geometrical Requirements	Test at 23 C
4.4	Mechanical Requirements	
4.4.2	Coating Strip Force	Test at 23 C unaged, temperature and humidity aged, water soak
4.4.3	Dynamic Tensile Strength	Test at 23 C unaged, temperature and humidity aged
4.4.4	Stress Corrosion Parameter	Test at 23 C unaged, temperature and humidity aged
6	Requirements and Test Procedures for Optical Cables (Applicable Sections Only)	
6.6.8	Wasp Spray Exposure	Test at 23 C strip force, dynamic tensile strength

Fiber samples were submitted to Telcordia with the manufacturer's identities withheld. Each fiber was supplied on a single 25 Km shipping spool and numbered one through eight. Telcordia proceeded to excise the required amount of fiber from each spool. They choose an amount of approximately 1.5 Km of each to utilize for testing.

Each fiber was fully tested according to the above protocol. Each fiber passed the requirements as set forth in the GR-20 CORE. However some general trends could be observed within the data sets. All of the data in this report is from the independent test facility [1] except for the microscopic photography that was done internally at Borden. Some general comments proffered by Telcordia for the fibers are bulleted below [1]:

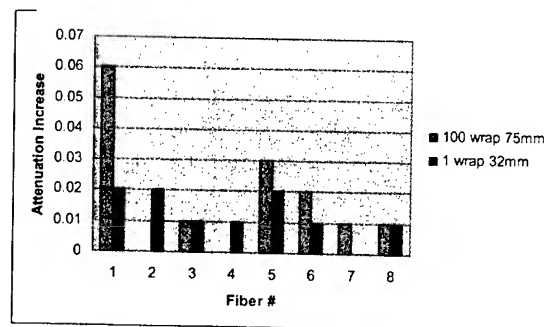
- None of the fibers appeared to be susceptible to the effects of microbending.
- Fiber 1 experienced the greatest effect from the microbending exposure, a 0.06 dB increase in attenuation, followed by Fiber 5 with a 0.03 dB attenuation.
- At 1310 nm Fiber 4 consistently showed the lowest attenuation in temperature cycling from -40°C to 70°C, followed closely by Fiber 2. Fiber 5 consistently showed the greatest attenuation at 1310 nm throughout the temperature cycling.
- At 1550 nm Fibers 2 and 8 consistently showed the lowest attenuation in temperature cycling from -40°C to 70°C. Fiber 4 consistently showed the greatest attenuation at 1550 nm throughout the temperature cycling.
- The geometrical measurements showed Fiber 4 to have the thinnest primary coating (182.8-mm diameter). Fiber 3 was measured with the thickest primary coating (194.6-mm diameter).
- Fibers 4 and 5 consistently were measured with the greatest mean strip force for the unaged and aged (temperature/humidity and water soak).

- Fibers 4 and 5 were measured with the greatest tensile strength for unaged fiber. Fiber 7 was found to have the lowest tensile strength.
- Fiber 5 was measured with the greatest tensile strength for aged fiber. Fiber 7 was found to have the lowest tensile strength. Aged fiber experience a greater spread in tensile strength for the population of test samples than the same number of test samples of unaged fiber.
- The stress corrosion factor for each of the fibers tested was significantly reduced between the results of the unaged and aged samples for each fiber.
- None of the fibers (strip force or tensile strength) were significantly affected by the exposure to wasp spray.

2.1 Data and Borden Interpretation:

The first set of testing was for macrobending resistance. Fiber one was the most sensitive to an increase in attenuation due to macrobending. The others were all similar in increase.

Figure 2-1 Macrobending Attenuation



Another test performed was temperature cycling attenuation. The following charts depict the change in attenuation at 1310 and 1550 with exposure to temperature. This is one test that shows the effect of processing, in that fibers number two and number eight were processed by different manufacturers using the same coatings. One can see that number eight has an increase in attenuation at -40 C whereas fiber 2 has a slight decrease at 1550nm. All of the fibers were slightly sensitive to an increase in temperature at both 1310 and 1550nm. Fibers 6,7, & 8 were sensitive to decreased temperatures at 1550nm only.

Figure 2-2 Temperature/ Attenuation Change (1310)

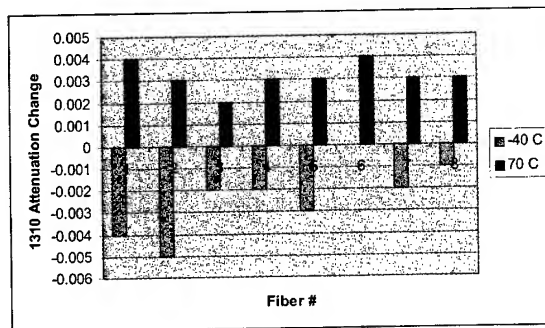
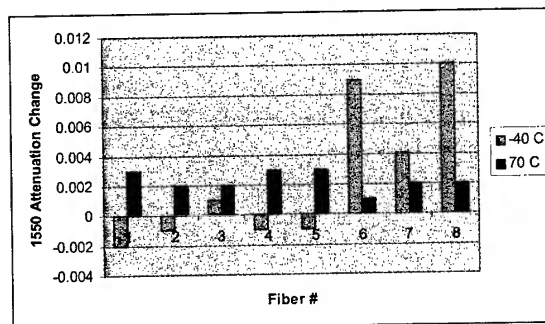


Figure 2-3 Temperature/ Attenuation Change (1550)



The next criteria observed were that of the physical geometry of the fibers. The table below depicts the coating geometry as applied to the glass fibers. Fiber three had the smallest Secondary diameter, wherein fiber five had the largest Secondary diameter. Fiber four had a smaller Primary diameter versus fiber five with the largest Primary diameter. Fibers four and six had poor concentricity, whereas fiber eight had exceptionally good concentricity as compared to the other fibers.

Table 2-2 Geometric Measurements of Fiber Coatings (μm) [1]

	Secondary Coating Diameter	Primary Coating Diameter	Secondary Concentricity	Primary Concentricity
Fiber 1	241.92	184.06	5.03	1.41
Fiber 2	241.89	184.67	4.57	1.84
Fiber 3	239.97	194.58	1.52	1.29
Fiber 4	243.45	182.82	8.46	4.79
Fiber 5	250.24	197.38	2.36	1.83
Fiber 6	244.94	192.48	4.77	3.66
Fiber 7	244.78	192.12	1.22	0.43
Fiber 8	245.13	192.70	0.72	0.34

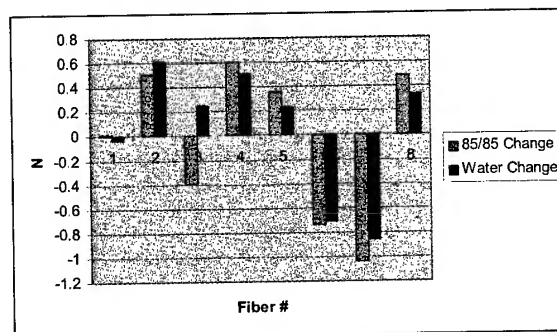
The next table represents the glass geometry of the fibers. Although glass geometry is not coating related it is included for completeness. There were no significant differences, one to another, in the glass geometry.

Table 2-3 Geometrical Measurements of Fiber Glass (μm) [1]

	Cladding Diameter	Cladding Non-circularity	Core Diameter	Core Non-circularity	Concentricity
Fiber 1	124.86	0.294	10.06	2.035	0.122
Fiber 2	125.09	0.193	10.14	3.228	0.093
Fiber 3	125.01	0.144	10.36	3.220	0.125
Fiber 4	124.83	0.150	10.08	2.908	0.570
Fiber 5	125.29	0.146	10.53	2.465	0.318
Fiber 6	125.17	0.129	10.64	3.099	0.132
Fiber 7	125.02	0.1917	9.99	4.712	0.200
Fiber 8	124.94	0.1638	9.71	3.092	0.168

Strip force measurements were taken on the fiber. The fibers were then exposed to environmental aging. (85C/ 85%RH and also Water soak). Some of the fibers stayed the same or actually increased adhesion to the glass upon aging. Others were significantly reduced by as much as 30%. This points to the lack of environmental exposure resistance by some of the coatings, especially numbers six and seven.

Figure 2-4 Aged Fiber Max Strip Force Change



Dynamic Tensile Strength was performed for each fiber. In comparison to each other, fibers 3,6 & 7 were shown to be weaker than fibers 2,4 & 5. Whereas fibers 1 and 8 were similarly average.

Figure 2-5 Dynamic Tensile Strength Weibull Probability Unaged Fibers [1]

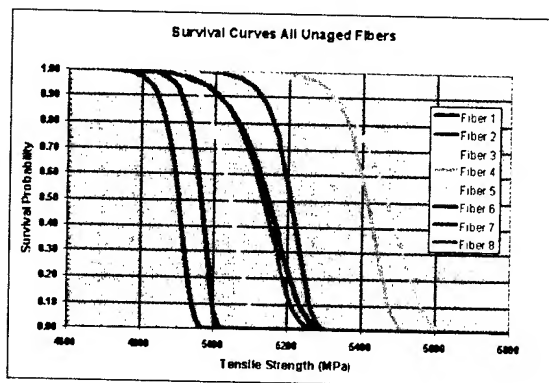
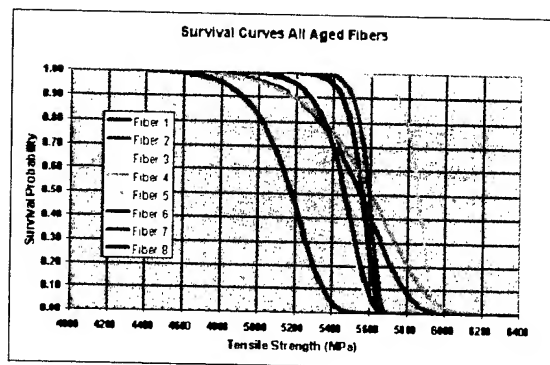
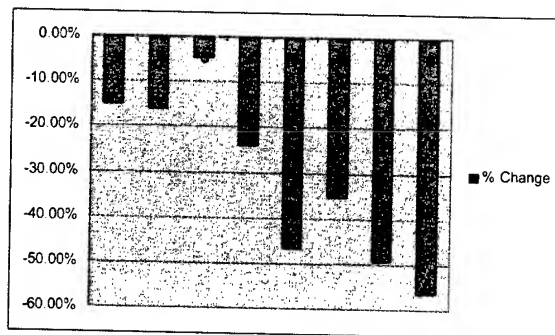


Figure 2-6 Dynamic Tensile Strength, Weibull Probability Aged Fibers [1]



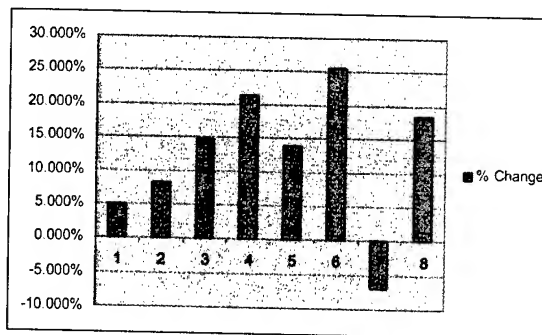
The stress corrosion factor was analyzed and each fiber had a reduction in value upon aging. Fibers one through four were below average in loss. While fibers five through eight had more than average losses.

Figure 2-7 Stress Corrosion Change Upon Aging



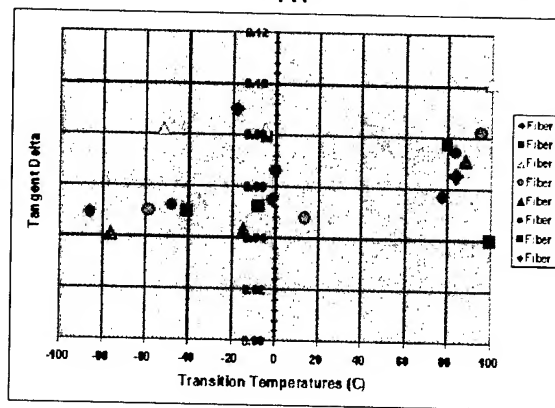
Fibers were also tested for Wasp Spray resistance. Only fiber seven was found to have a loss of adhesion upon exposure to commercial grade insecticide. All others had similar or increased strip force.

Figure 2-8 Wasp Spray Exposure Change in Max Strip Force (N)



The final analysis by Telcordia was that of DMTA on the fibers. Each was analyzed for Tg. At least one lower and only one upper Tg were identified for each set of coatings. The following figure summarizes the findings.

Figure 2-9 DMTA Transition Temperatures [1]



The concluding analysis performed on each fiber was that of video microscopy. Telcordia aged fibers were returned to Borden for a microscopic analysis. This proved to be quite interesting. Some of the fibers showed significant changes to the primary coating upon standard 85C/85RH (30 day) and Water (25C-14day) aging. For several of these fibers the aging effects upon the primary coating was one of crystalline development. In the primary coating small crystal "spots" developed with exposure to the above environmental conditions. In some cases the coatings developed bubbles and ultimately large crystal growth. Fibers 1 and 7 had spot growth. Fiber 6 had spots and bubbles. Fiber 3 had significant crystalline growth. Those fibers that exhibited this phenomenon also were the

same fibers that had a loss of adhesion to glass (lower strip force) upon being aged. Of anecdotal interest is that those fibers with the lowest Dynamic Tensile Strength were also those with this developing crystal incident. The Borden control as well as fibers 4, 5 and 8 did not exhibit any visual changes upon aging.

Figure 2-10 Fiber #7 After Aging

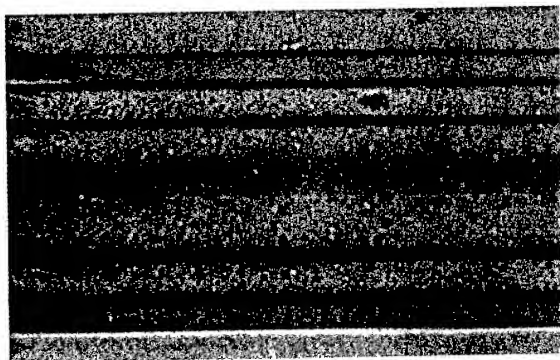


Figure 2-11 Fiber #6 After Aging

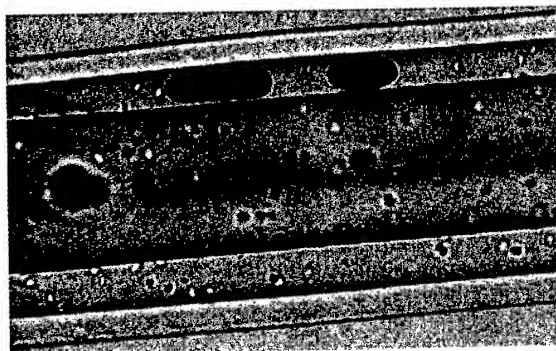


Figure 2-12 Fiber #3 After Aging

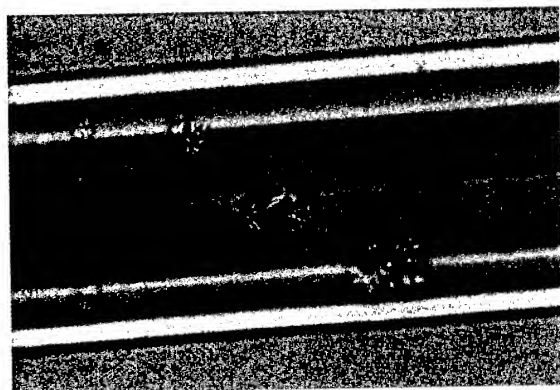
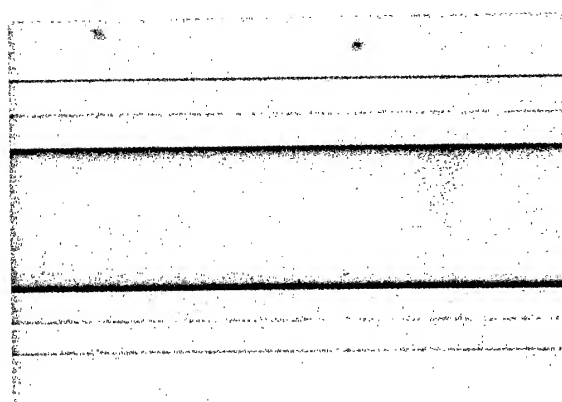


Figure 2-13 Fiber #2 After Aging



3. Conclusions

Although all modern commercial coating formulations available in the marketplace passed the GR-20 CORE requirements, some differentiation and added value can be gleaned from selection within this field. Coating chemistry as well as processing parameters can improve the fiber's resistance to temperature-induced attenuation. Process condition optimization seems the remedy for fiber geometry improvements as opposed to coating choice. The DMTA of the fibers help to clarify the relationship of test results. Most coatings are adequate at insecticide resistance. Of particular note is that some formulations are much better at environmental resistance than others. This is proven out in the aged strip force analysis as well as the visual changes developed by some of the less resistant coating chemistries.

4. Acknowledgments

Special thanks to the staff of Telcordia for the independent professional analysis of our submitted fiber samples. [1]

5. References

- [1] Telcordia Technologies; Telcordia Distributable Technical Analysis Report: DA-1353, Volume 1, Issue 1, June 2002. "Optical Fiber/ Coating Study: Borden Chemical, Inc"
- (Copies available in .pdf format upon email request to the author)
- [2] GR-20-CORE, Generic Requirements for Optical Fiber and Optical Fiber Cable, Issue 2, July, 1998 (GR-20). Telcordia Technologies

6. Author Biography



Gregory L Workman II

630 Glendale- Milford Road
Cincinnati, OH 45215

Gregory L Workman II is the ISO-Quality Manager for Borden Chemical Inc. Specialty Coatings Division located in Cincinnati, OH. This division designs and manufactures UV curable coatings for the Telecommunication, Data Storage, Automotive, and Military markets. He joined the Borden team in 1997. He holds an A.S. from Ohio University, a B.S. Chemistry Degree (ACS) from Otterbein College and is a Certified Quality Manager (ASQ). He is a member of the American Chemical Society, the American Society for Quality, and is an affiliate of IUPAC. He has filed for one process related patent.

Author Index

Author	Page Number	Author	Page Number
A			
Aderogba, S.	26, 37, 288	Cottino, E.	84
Agresta, J.	330	Cressan, E.	176
Ahn, M. J.	391	Cruz, R. F.	165, 653, 667
Aihara, T.	72	Cui, H. L.	448
Akasaka, N.	56	Currie, E.	752
Al-Asadi, M.	423, 616, 641	D	
Aloisio, C.	738	Dammert, R. C.	348
Andrade, M. A.	382	Davis, C. S.	251
Artiglia, M.	471	de Medeiros Neto, J. A.	653, 667
Arvidsson, B.	260	Debban Jr., H. P.	251
B		DiMarcello, F.	339
Barnes, J. P.	14	Do, M. H.	44, 281, 362, 482, 516
Beckett, J.	186	Dole, C. W.	633
Beetz, C.	330	Dotto, J.	653, 667
Bernstein, S.	721	Duffy, A. P.	1, 423, 602, 616, 641
Beyer, G.	584	Dunn, K.	610
Bing, Y.	475	E	
Bise, R. T.	339	Earhart, N.	594, 548
Björk, A.	221	Ellithi, T.	687
Blume, C. E. P.	653	Engel, R.	519
Boerstler, R.	330	Enomoto, Y.	72
Bonvin, P.-Y.	103	F	
Boukalov, A.	143	Fagrell, O.	540
Bow, K. E.	239	Fang-rong, H.	17
Brito Jr., J. A.	662	Fauchoux, F.	158, 176
Brown, G. D.	129	Fay, P. J.	13
Bulsari, A.	267	Federighi, R. C.	382
Busch, R.	294	Fitz, J. G.	488
Butala, R.	589	G	
C		Gafney, H. D.	68
Cao, Y.	648	Gan, K.	752
Carlsson, R.	540	Garms, M. A.	382
Carnahan, D. L.	321, 443	Gavrilakis, A.	602, 616, 641
Casals, L.-R. S.	494	Gibson, A.	117
Chakrabarty, K.	26, 288	Giersig, M.	321
Chandan, H. C.	687	Ginocchio, A.	494
Chang, S.	98	Giordano, D. A.	727
Chapman, B.	702	Glogovski, T.	589
Chen, H.	288	Goodson III, T.	318
Chen, T.	589	Gravely, R. G.	227
Cheng, X.	365	Gregor, P. E.	150
Chiasson, D. W.	371	Greven, W.	244
Cho, H.	281	Griffioen, W.	244
Choi, I. S.	78	Guan, Y.	387
Choi, J.-S.	281	Guida, T. J.	9
Chou, S.-H.	397	Gunther, M. F.	443
Cieslak, A.	662		
Coat, P.	702		
Coates, A. R.	602, 641		

Author Index

Author	Page Number	Author	Page Number
Ren, Z. F.	321	Sunil, D.	68
Ren-jie, T.	17	Suwarow, B.	117
Reorda, P. S.	150		
Risch, B.	551, 702	T	
Rossi, M. S.	251	Tabaddor, M.	738
Rue, R. J.	727	Tachikra, M.	680
Rush, G.	275	Tajima, H.	403
Ryan, J. F.	687	Tamekuni, Y.	56
Rybczynski, J.	321	Tanaka, H.	507
		Tanaka, K.	680
S		Tanaka, R. T.	165
Sakurai, W.	48	Tanaka, S.	500
Salo, P.	260	Tanana, M.	466
Sang, A. K.	443	Tang, R.-j.	17
Sato, K.	72	Tashiro, T.	72
Sato, T.	708	Thio, T.	344
Scheid, H.	531	Thomas, A. C. R.	176
Schloemer, T. S.	124	Tiesmäki, J.-P.	260
Schnee, P.	150	Törnqvist, E.	143
Schottke, L.	294	Tozze, O.	382
Sennett, M.	321	Trevor, D. J.	339
Shapiro, S.	721	Trivedi, A. H.	597
Shi, B.	551	Tschümperlé, D.	732
Shi, H.	31	Tu, Y.	321
Shigemoto, T.	93	Turnipseed, J.	738
Shih, H. C.	418	Turunen, H.	357
Shimizu, F.	171		
Shimomichi, T.	569	U	
Shimoshio, Y.	524	Ueda, T.	48
Shinoda, M.	437	Ueda, T.	56
Shirley, A.	275	Um, E.-s.	579
Shirosawa, T.	475		
Shmukler, M.	26	V	
Shukushima, S.	108	Vaughn, R.	22
Silva, A. C.	165	Veng, T.	687
Simião, M. M.	667	Virolainen, E. P.	211
Skutnik, B.	68		
Sneck, S.	267	W	
Solanki, R.	326	Wakiyasu, H.	461
Son, M.	564	Wald, D.	540
Stadler, U.	548	Walling, J.-H.	622
Steeves, D.	321	Wan, W. Z.	108
Stevenson, P.	443	Wang, D. Z.	321
Stewart, W. M.	136	Wang, J. H.	418
Stix, R. K.	727	Wang, S.	31
Strong, P. K.	696	Wang, T.	648
Stucky, G. D.	311	Wang, Y.	31
Suda, Y.	403	Wartschinski, D.	519
Suematsu, K.	437	Wasserman, S. H.	129
Sugawara, H.	708	Wei, Z.-c.	17
Sukegawa, T.	475	Weimann, P. A.	192, 202, 251
Sultan, B.-A.	540	Wen, J. G.	321

Author Index

Author	Page Number	Author	Page Number
Wetherell, A. D.....	9	Yasutomi, T.....	432
Will, S.....	519	Yoon, S. m.	78
Willis, A. J.	1, 423, 602, 616, 641	Yu, C.	31
Winn, D.	330		
Witt, G.	702	Z	
Workman II, G. L.....	757	Zahora, E. P.....	752
Wright, R.	330	Zaima, M.	680
		Zamzow, P. E.....	150
Y		Zhang, Y.	448
Yablon, A. D.....	687	Zhong, Q.	721
Yaguchi, S.....	708	Zhong-cheng, W.....	17
Yamamoto, N.	524	Zhou, J.	675
Yang, J. S.	482	Zingg, J.	59
Yang, Y. G.	78		